Bridge Engineering Handbook
SECOND EDITION

SEISMIC DESIGN

EDITED BY

Wai-Fah Chen and Lian Duan

CRC Press
Taylor & Francis Group

Bridge Engineering Handbook

SECOND EDITION

SEISMIC DESIGN

Bridge Engineering Handbook, Second Edition

Bridge Engineering Handbook, Second Edition: Fundamentals

Bridge Engineering Handbook, Second Edition: Superstructure Design

Bridge Engineering Handbook, Second Edition: Substructure Design

Bridge Engineering Handbook, Second Edition: Seismic Design

Bridge Engineering Handbook, Second Edition: Construction and Maintenance

Bridge Engineering Handbook

SECOND EDITION

SEISMIC DESIGN

EDITED BY

Wai-Fah Chen and Lian Duan

CRC Press
Taylor & Francis Group
Boca Raton London New York

CRC Press is an imprint of the
Taylor & Francis Group, an **informa** business

CRC Press
Taylor & Francis Group
6000 Broken Sound Parkway NW, Suite 300
Boca Raton, FL 33487-2742

Version Date: 20130923

International Standard Book Number-13: 978-1-4398-5232-3 (eBook - PDF)

Contents

Foreword

Throughout the history of civilization bridges have been the icons of cities, regions, and countries. All bridges are useful for transportation, commerce, and war. Bridges are necessary for civilization to exist, and many bridges are beautiful. A few have become the symbols of the best, noblest, and most beautiful that mankind has achieved. The secrets of the design and construction of the ancient bridges have been lost, but how could one not marvel at the magnificence, for example, of the Roman viaducts?

The second edition of the *Bridge Engineering Handbook* expands and updates the previous edition by including the new developments of the first decade of the twenty-first century. Modern bridge engineering has its roots in the nineteenth century, when wrought iron, steel, and reinforced concrete began to compete with timber, stone, and brick bridges. By the beginning of World War II, the transportation infrastructure of Europe and North America was essentially complete, and it served to sustain civilization as we know it. The iconic bridge symbols of modern cities were in place: Golden Gate Bridge of San Francisco, Brooklyn Bridge, London Bridge, Eads Bridge of St. Louis, and the bridges of Paris, Lisbon, and the bridges on the Rhine and the Danube. Budapest, my birthplace, had seven beautiful bridges across the Danube. Bridge engineering had reached its golden age, and what more and better could be attained than that which was already achieved?

Then came World War II, and most bridges on the European continent were destroyed. All seven bridges of Budapest were blown apart by January 1945. Bridge engineers after the war were suddenly forced to start to rebuild with scant resources and with open minds. A renaissance of bridge engineering started in Europe, then spreading to America, Japan, China, and advancing to who knows where in the world, maybe Siberia, Africa? It just keeps going! The past 60 years of bridge engineering have brought us many new forms of bridge architecture (plate girder bridges, cable stayed bridges, segmental prestressed concrete bridges, composite bridges), and longer spans. Meanwhile enormous knowledge and experience have been amassed by the profession, and progress has benefitted greatly by the availability of the digital computer. The purpose of the *Bridge Engineering Handbook* is to bring much of this knowledge and experience to the bridge engineering community of the world. The contents encompass the whole spectrum of the life cycle of the bridge, from conception to demolition.

The editors have convinced 146 experts from many parts of the world to contribute their knowledge and to share the secrets of their successful and unsuccessful experiences. Despite all that is known, there are still failures: engineers are human, they make errors; nature is capricious, it brings unexpected surprises! But bridge engineers learn from failures, and even errors help to foster progress.

The *Bridge Engineering Handbook*, second edition consists of five books:

Fundamentals
Superstructure Design
Substructure Design
Seismic Design
Construction and Maintenance

Fundamentals, Superstructure Design, and *Substructure Design* present the many topics necessary for planning and designing modern bridges of all types, made of many kinds of materials and systems, and subject to the typical loads and environmental effects. *Seismic Design* and *Construction and Maintenance* recognize the importance that bridges in parts of the world where there is a chance of earthquake occurrences must survive such an event, and that they need inspection, maintenance, and possible repair throughout their intended life span. Seismic events require that a bridge sustain repeated dynamic load cycles without functional failure because it must be part of the postearthquake lifeline for the affected area. *Construction and Maintenance* touches on the many very important aspects of bridge management that become more and more important as the world's bridge inventory ages.

The editors of the *Bridge Engineering Handbook*, Second Edition are to be highly commended for undertaking this effort for the benefit of the world's bridge engineers. The enduring result will be a safer and more cost effective family of bridges and bridge systems. I thank them for their effort, and I also thank the 146 contributors.

Theodore V. Galambos, PE
Emeritus professor of structural engineering
University of Minnesota

Preface to the Second Edition

In the approximately 13 years since the original edition of the *Bridge Engineering Handbook* was published in 2000, we have received numerous letters, e-mails, and reviews from readers including educators and practitioners commenting on the handbook and suggesting how it could be improved. We have also built up a large file of ideas based on our own experiences. With the aid of all this information, we have completely revised and updated the handbook. In writing this Preface to the Second Edition, we assume readers have read the original Preface. Following its tradition, the second edition handbook stresses professional applications and practical solutions; describes the basic concepts and assumptions omitting the derivations of formulas and theories; emphasizes seismic design, rehabilitation, retrofit and maintenance; covers traditional and new, innovative practices; provides over 2500 tables, charts, and illustrations in ready-to-use format and an abundance of worked-out examples giving readers step-by-step design procedures. The most significant changes in this second edition are as follows:

- The handbook of 89 chapters is published in five books: *Fundamentals, Superstructure Design, Substructure Design, Seismic Design,* and *Construction and Maintenance*.
- *Fundamentals,* with 22 chapters, combines Section I, Fundamentals, and Section VI, Special Topics, of the original edition and covers the basic concepts, theory and special topics of bridge engineering. Seven new chapters are Finite Element Method, High-Speed Railway Bridges, Structural Performance Indicators for Bridges, Concrete Design, Steel Design, High Performance Steel, and Design and Damage Evaluation Methods for Reinforced Concrete Beams under Impact Loading. Three chapters including Conceptual Design, Bridge Aesthetics: Achieving Structural Art in Bridge Design, and Application of Fiber Reinforced Polymers in Bridges, are completely rewritten. Three special topic chapters, Weigh-In-Motion Measurement of Trucks on Bridges, Impact Effect of Moving Vehicles, and Active Control on Bridge Engineering, were deleted.
- *Superstructure Design,* with 19 chapters, provides information on how to design all types of bridges. Two new chapters are Extradosed Bridges and Stress Ribbon Pedestrian Bridges. The Prestressed Concrete Girder Bridges chapter is completely rewritten into two chapters: Precast–Pretensioned Concrete Girder Bridges and Cast-In-Place Posttensioned Prestressed Concrete Girder Bridges. The Bridge Decks and Approach Slabs chapter is completely rewritten into two chapters: Concrete Decks and Approach Slabs. Seven chapters, including Segmental Concrete Bridges, Composite Steel I-Girder Bridges, Composite Steel Box Girder Bridges, Arch Bridges, Cable-Stayed Bridges, Orthotropic Steel Decks, and Railings, are completely rewritten. The chapter Reinforced Concrete Girder Bridges was deleted because it is rarely used in modern time.
- *Substructure Design* has 11 chapters and addresses the various substructure components. A new chapter, Landslide Risk Assessment and Mitigation, is added. The Geotechnical Consideration chapter is completely rewritten and retitled as Ground Investigation. The Abutments and

Retaining Structures chapter is divided in two and updated as two chapters: Abutments and Earth Retaining Structures.

- *Seismic Design,* with 18 chapters, presents the latest in seismic bridge analysis and design. New chapters include Seismic Random Response Analysis, Displacement-Based Seismic Design of Bridges, Seismic Design of Thin-Walled Steel and CFT Piers, Seismic Design of Cable-Supported Bridges, and three chapters covering Seismic Design Practice in California, China, and Italy. Two chapters of Earthquake Damage to Bridges and Seismic Design of Concrete Bridges have been rewritten. Two chapters of Seismic Design Philosophies and Performance-Based Design Criteria, and Seismic Isolation and Supplemental Energy Dissipation, have also been completely rewritten and retitled as Seismic Bridge Design Specifications for the United States, and Seismic Isolation Design for Bridges, respectively. Two chapters covering Seismic Retrofit Practice and Seismic Retrofit Technology are combined into one chapter called Seismic Retrofit Technology.
- *Construction and Maintenance* has 19 chapters and focuses on the practical issues of bridge structures. Nine new chapters are Steel Bridge Fabrication, Cable-Supported Bridge Construction, Accelerated Bridge Construction, Bridge Management Using Pontis and Improved Concepts, Bridge Maintenance, Bridge Health Monitoring, Nondestructive Evaluation Methods for Bridge Elements, Life-Cycle Performance Analysis and Optimization, and Bridge Construction Methods. The Strengthening and Rehabilitation chapter is completely rewritten as two chapters: Rehabilitation and Strengthening of Highway Bridge Superstructures, and Rehabilitation and Strengthening of Orthotropic Steel Bridge Decks. The Maintenance Inspection and Rating chapter is completely rewritten as three chapters: Bridge Inspection, Steel Bridge Evaluation and Rating, and Concrete Bridge Evaluation and Rating.
- The section on Worldwide Practice in the original edition has been deleted, including the chapters on Design Practice in China, Europe, Japan, Russia, and the United States. An international team of bridge experts from 26 countries and areas in Africa, Asia, Europe, North America, and South America, has joined forces to produce the *Handbook of International Bridge Engineering, Second Edition*, the first comprehensive, and up-to-date resource book covering the state-of-the-practice in bridge engineering around the world. Each of the 26 country chapters presents that country's historical sketch; design specifications; and various types of bridges including girder, truss, arch, cable-stayed, suspension, and so on, in various types of materials—stone, timber, concrete, steel, advanced composite, and of varying purposes—highway, railway, and pedestrian. Ten benchmark highway composite girder designs, the highest bridges, the top 100 longest bridges, and the top 20 longest bridge spans for various bridge types are presented. More than 1650 beautiful bridge photos are provided to illustrate great achievements of engineering professions.

The 146 bridge experts contributing to these books have written chapters to cover the latest bridge engineering practices, as well as research and development from North America, Europe, and Pacific Rim countries. More than 80% of the contributors are practicing bridge engineers. In general, the handbook is aimed toward the needs of practicing engineers, but materials may be re-organized to accommodate several bridge courses at the undergraduate and graduate levels.

The authors acknowledge with thanks the comments, suggestions, and recommendations made during the development of the second edition of the handbook by Dr. Erik Yding Andersen, COWI A/S, Denmark; Michael J. Abrahams, Parsons Brinckerhoff, Inc.; Dr. Xiaohua Cheng, New Jersey Department of Transportation; Joyce E. Copelan, California Department of Transportation; Prof. Dan M. Frangopol, Lehigh University; Dr. John M. Kulicki, Modjeski and Masters; Dr. Amir M. Malek, California Department of Transportation; Teddy S. Theryo, Parsons Brinckerhoff, Inc.; Prof. Shouji Toma, Horrai-Gakuen University, Japan; Dr. Larry Wu, California Department of Transportation; Prof. Eiki Yamaguchi, Kyushu Institute of Technology, Japan; and Dr. Yi Edward Zhou, URS Corp.

We thank all the contributors for their contributions and also acknowledge Joseph Clements, acquiring editor; Jennifer Ahringer, project coordinator; and Joette Lynch, project editor, at Taylor & Francis/CRC Press.

Preface to the First Edition

The *Bridge Engineering Handbook* is a unique, comprehensive, and state-of-the-art reference work and resource book covering the major areas of bridge engineering with the theme "bridge to the twenty-first century." It has been written with practicing bridge and structural engineers in mind. The ideal readers will be MS-level structural and bridge engineers with a need for a single reference source to keep abreast of new developments and the state-of-the-practice, as well as to review standard practices.

The areas of bridge engineering include planning, analysis and design, construction, maintenance, and rehabilitation. To provide engineers a well-organized, user-friendly, and easy-to-follow resource, the handbook is divided into seven sections. Section I, Fundamentals, presents conceptual design, aesthetics, planning, design philosophies, bridge loads, structural analysis, and modeling. Section II, Superstructure Design, reviews how to design various bridges made of concrete, steel, steel-concrete composites, and timbers; horizontally curved, truss, arch, cable-stayed, suspension, floating, movable, and railroad bridges; and expansion joints, deck systems, and approach slabs. Section III, Substructure Design, addresses the various substructure components: bearings, piers and columns, towers, abutments and retaining structures, geotechnical considerations, footings, and foundations. Section IV, Seismic Design, provides earthquake geotechnical and damage considerations, seismic analysis and design, seismic isolation and energy dissipation, soil–structure–foundation interactions, and seismic retrofit technology and practice. Section V, Construction and Maintenance, includes construction of steel and concrete bridges, substructures of major overwater bridges, construction inspections, maintenance inspection and rating, strengthening, and rehabilitation. Section VI, Special Topics, addresses in-depth treatments of some important topics and their recent developments in bridge engineering. Section VII, Worldwide Practice, provides the global picture of bridge engineering history and practice from China, Europe, Japan, and Russia to the U.S.

The handbook stresses professional applications and practical solutions. Emphasis has been placed on ready-to-use materials, and special attention is given to rehabilitation, retrofit, and maintenance. The handbook contains many formulas and tables that give immediate answers to questions arising from practical works. It describes the basic concepts and assumptions, omitting the derivations of formulas and theories, and covers both traditional and new, innovative practices. An overview of the structure, organization, and contents of the book can be seen by examining the table of contents presented at the beginning, while the individual table of contents preceding each chapter provides an in-depth view of a particular subject. References at the end of each chapter can be consulted for more detailed studies.

Many internationally known authors have written the chapters from different countries covering bridge engineering practices, research, and development in North America, Europe, and the Pacific Rim. This handbook may provide a glimpse of a rapidly growing trend in global economy in recent years toward international outsourcing of practice and competition in all dimensions of engineering.

In general, the handbook is aimed toward the needs of practicing engineers, but materials may be reorganized to accommodate undergraduate and graduate level bridge courses. The book may also be used as a survey of the practice of bridge engineering around the world.

The authors acknowledge with thanks the comments, suggestions, and recommendations during the development of the handbook by Fritz Leonhardt, Professor Emeritus, Stuttgart University, Germany; Shouji Toma, Professor, Horrai-Gakuen University, Japan; Gerard F. Fox, Consulting Engineer; Jackson L. Durkee, Consulting Engineer; Michael J. Abrahams, Senior Vice President, Parsons, Brinckerhoff, Quade & Douglas, Inc.; Ben C. Gerwick, Jr., Professor Emeritus, University of California at Berkeley; Gregory F. Fenves, Professor, University of California at Berkeley; John M. Kulicki, President and Chief Engineer, Modjeski and Masters; James Chai, Senior Materials and Research Engineer, California Department of Transportation; Jinrong Wang, Senior Bridge Engineer, URS Greiner; and David W. Liu, Principal, Imbsen & Associates, Inc.

We thank all the authors for their contributions and also acknowledge at CRC Press Nora Konopka, acquiring editor, and Carol Whitehead and Sylvia Wood, project editors.

Editors

Dr. Wai-Fah Chen is a research professor of civil engineering at the University of Hawaii. He was dean of the College of Engineering at the University of Hawaii from 1999 to 2007, and a George E. Goodwin Distinguished Professor of Civil Engineering and head of the Department of Structural Engineering at Purdue University from 1976 to 1999.

He earned his BS in civil engineering from the National Cheng-Kung University, Taiwan, in 1959, MS in structural engineering from Lehigh University in 1963, and PhD in solid mechanics from Brown University in 1966. He received the Distinguished Alumnus Award from the National Cheng-Kung University in 1988 and the Distinguished Engineering Alumnus Medal from Brown University in 1999.

Dr. Chen's research interests cover several areas, including constitutive modeling of engineering materials, soil and concrete plasticity, structural connections, and structural stability. He is the recipient of several national engineering awards, including the Raymond Reese Research Prize and the Shortridge Hardesty Award, both from the American Society of Civil Engineers, and the T. R. Higgins Lectureship Award in 1985 and the Lifetime Achievement Award, both from the American Institute of Steel Construction. In 1995, he was elected to the U.S. National Academy of Engineering. In 1997, he was awarded Honorary Membership by the American Society of Civil Engineers, and in 1998, he was elected to the Academia Sinica (National Academy of Science) in Taiwan.

A widely respected author, Dr. Chen has authored and coauthored more than 20 engineering books and 500 technical papers. His books include several classical works such as *Limit Analysis and Soil Plasticity* (Elsevier, 1975), the two-volume *Theory of Beam-Columns* (McGraw-Hill, 1976 and 1977), *Plasticity in Reinforced Concrete* (McGraw-Hill, 1982), and the two-volume *Constitutive Equations for Engineering Materials* (Elsevier, 1994). He currently serves on the editorial boards of more than 15 technical journals.

Dr. Chen is the editor-in-chief for the popular *Civil Engineering Handbook* (CRC Press, 1995 and 2003), the *Handbook of Structural Engineering* (CRC Press, 1997 and 2005), the *Earthquake Engineering Handbook* (CRC Press, 2003), the *Semi-Rigid Connections Handbook* (J. Ross Publishing, 2011), and the *Handbook of International Bridge Engineering* (CRC Press, 2014). He currently serves as the consulting editor for the *McGraw-Hill Yearbook of Science & Technology* for the field of civil and architectural engineering.

He was a longtime member of the executive committee of the Structural Stability Research Council and the specification committee of the American Institute of Steel Construction. He was a consultant for Exxon Production Research on offshore structures, for Skidmore, Owings, and Merrill in Chicago on tall steel buildings, and for the World Bank on the Chinese University Development Projects, among many others. Dr. Chen has taught at Lehigh University, Purdue University, and the University of Hawaii.

Dr. Lian Duan is a senior bridge engineer and structural steel committee chair with the California Department of Transportation (Caltrans). He worked at the North China Power Design Institute from 1975 to 1978 and taught at Taiyuan University of Technology, China, from 1981 to 1985.

He earned his diploma in civil engineering in 1975, MS in structural engineering in 1981 from Taiyuan University of Technology, China, and PhD in structural engineering from Purdue University in 1990.

Dr. Duan's research interests cover areas including inelastic behavior of reinforced concrete and steel structures, structural stability, seismic bridge analysis, and design. With more than 70 authored and coauthored papers, chapters, and reports, his research focuses on the development of unified interaction equations for steel beam-columns, flexural stiffness of reinforced concrete members, effective length factors of compression members, and design of bridge structures.

Dr. Duan has over 35 years experience in structural and bridge engineering. He was lead engineer for the development of Caltrans *Guide Specifications for Seismic Design of Steel Bridges*. He is a registered professional engineer in California. He served as a member for several National Highway Cooperative Research Program panels and was a Transportation Research Board Steel Committee member from 2000 to 2006.

He is the coeditor of the *Handbook of International Bridge Engineering,* (CRC Press, 2014). He received the prestigious 2001 Arthur M. Wellington Prize from the American Society of Civil Engineers for the paper, "Section Properties for Latticed Members of San Francisco-Oakland Bay Bridge," in the *Journal of Bridge Engineering,* May 2000. He received the Professional Achievement Award from Professional Engineers in California Government in 2007 and the Distinguished Engineering Achievement Award from the Engineers' Council in 2010.

Contributors

Mahamad Akkari
California Department of Transportation
Sacramento, California

Fadel Alameddine
California Department of Transportation
Sacramento, California

Michel Bruneau
University at Buffalo
Buffalo, New York

Gian Michele Calvi
IUSS Pavia and Eucentre Foundation
Pavia, Italy

Lian Duan
California Department of Transportation
Sacramento, California

Marc Eberhard
University of Washington
Seattle, Washington

Paolo Franchin
Sapienza University of Rome
Rome, Italy

Yoshiaki Goto
Nagoya Institute of Technology
Nagoya, Japan

Roy A. Imbsen
Imbsen Consulting
Fair Oaks, California

Kevin I. Keady
California Department of Transportation
Sacramento, California

Mervyn J. Kowalsky
North Carolina State University
Raleigh, North Carolina

Steven L. Kramer
University of Washington
Seattle, Washington

Qian Li
Research Institute of Highway
The Ministry of Transport
Beijing, China

Yue Li
Research Institute of Highway
The Ministry of Transport
Beijing, China

Jiahao Lin
Dalian University of Technology
Dalian, China

Jack Moehle
University of California
Berkeley, California

Joseph Penzien
International Civil Engineering Consultants, Inc.
Berkeley, California

Paolo Emilio Pinto
Sapienza University of Rome
Rome, Italy

M. J. Nigel Priestley
IUSS Pavia and Eucentre Foundation
Pavia, Italy

Thomas E. Sardo
Parsons Group
Irvine, California

Charles Scawthorn
University of California
Berkeley, California

and

SPA Risk
San Francisco, California

Jian Ren Tao
HNTB Corporation
San Jose, California

Semyon Treyger
HNTB Corporation
Bellevue, Washington

Keh-Chyuan Tsai
National Taiwan University
Taipei, Republic of China

Wen-Shou Tseng
Paul C. Rizzo Associates, Inc.
Oakland, California

Chia-Ming Uang
University of California
San Diego, California

Shigeki Unjoh
Public Works Research Institute
Ibaraki, Japan

Murugesu Vinayagamoorth
California Department of Transportation
Sacramento, California

Kehai Wang
Research Institute of Highway
The Ministry of Transport
Beijing, China

Han Wei
Research Institute of Highway
The Ministry of Transport
Beijing, China

Larry Wu
California Department of Transportation
Sacramento, California

Mark Yashinsky
California Department of Transportation
Sacramento, California

Wei Zhang
Taiyuan University of Technology
Taiyuan, China

Yahui Zhang
Dalian University of Technology
Dalian, China

Yan Zhao
Dalian University of Technology
Dalian, ChinaContents

1

Geotechnical Earthquake Considerations

Charles Scawthorn
University of California

Steven L. Kramer
University of Washington

1.1 Introduction

Earthquakes are naturally occurring broad-banded vibratory ground motions, due to a number of causes, including tectonic ground motions, volcanism, landslides, rockbursts, and man-made explosions, the most important of which are caused by the fracture and sliding of rock along tectonic faults within the earth's crust. For most earthquakes, shaking and/or ground failure are the dominant and most widespread agents of damage. Shaking near the actual earthquake rupture lasts only during the time when the fault ruptures, a process that takes seconds or at most a few minutes. The seismic waves generated by the rupture propagate long after the movement on the fault has stopped; however, spanning the globe in about 20 minutes. Typically earthquake ground motions are powerful enough to cause damage only in the near field (i.e., within a few tens of kilometers from the causative fault)—in a few instances, long-period motions have caused significant damage at great distances, to selected lightly damped structures, such as in the 1985 Mexico City earthquake, where numerous collapses of mid- and high-rise buildings were due to a Magnitude 8.1 earthquake occurring at a distance of approximately 400 kilometers from Mexico City.

1.2 Seismology

Plate Tectonics: In a global sense, tectonic earthquakes result from motion between a number of large plates comprising the earth′s crust or lithosphere (approximately 15 large plates in total, with many smaller "platelets"). These plates are driven by the convective motion of the material in the earth′s mantle, which in turn is driven by heat generated at the earth′s core. Relative plate motion at the fault interface is constrained by friction and/or asperities (areas of interlocking due to protrusions in the fault surfaces). However, strain energy accumulates in the plates, eventually overcomes any resistance, and causes slip between the two sides of the fault. This sudden slip, termed *elastic rebound* by Reid (1910) based on his studies of regional deformation following the 1906 San Francisco earthquake, releases large amounts of energy, which constitute the earthquake. The location of initial radiation of seismic waves (i.e., the first location of dynamic rupture) is termed the *hypocenter*, whereas the projection on the surface of the earth directly above the hypocenter is termed the *epicenter*. Other terminology includes *near-field* (within one source dimension of the epicenter, where source dimension refers to the length of faulting), *far-field* (beyond near-field) and *meizoseismal* (the area of strong shaking and damage). Energy is radiated over a broad spectrum of frequencies through the earth, in body waves and surface waves (Bolt, 1993). Body waves are of two types: P waves (transmitting energy via push–pull motion), and slower S waves (transmitting energy via shear action at right angles to the direction of motion). Surface waves are also of two types: horizontally oscillating Love waves (analogous to S body waves) and horizontally and vertically oscillating Rayleigh waves.

Faults are typically classified according to their sense of motion (Figure 1.1). Basic terms include *transform* or *strike slip* (relative fault motion occurs in the horizontal plane, parallel to the strike of the fault), and *dip-slip* (motion at right angles to the strike, up- or down-slip), which includes normal (dip-slip motion, two sides in tension, move away from each other), reverse (dip-slip, two sides in compression, move toward each other) and thrust (low-angle reverse) faulting.

Generally, earthquakes will be concentrated in the vicinity of faults, faults that are moving more rapidly than others will tend to have higher rates of seismicity, and larger faults are more likely than others to produce a large event. Many faults are identified on regional geological maps, and useful information on fault location and displacement history is available from local and national geological surveys in areas of high seismicity. An important development has been the growing recognition of blind thrust faults, which emerged as a result of the several earthquakes in the 1980s, none of which were accompanied by surface faulting (Stein and Yeats, 1989).

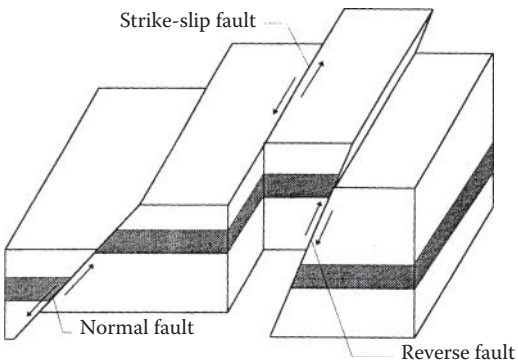

FIGURE 1.1 Fault types.

1.3 Measurement of Earthquakes

Magnitude: An individual earthquake is a unique release of strain energy—quantification of this energy has formed the basis for measuring the earthquake event. C.F. Richter (1935) was the first to define earthquake magnitude, as

$$M_L = \text{Log}\, A - \text{Log}\, A_o \tag{1.1}$$

where M_L is local magnitude (which Richter only defined for Southern California), A is the maximum trace amplitude in microns recorded on a standard Wood–Anderson short-period torsion seismometer, at a site 100 km from the epicenter, Log A_o is a standard value as a function of distance for instruments located at distances other than 100 km and < 600 km. A number of other magnitudes have since been defined, the most important of which are surface wave magnitude M_S, body wave magnitude m_b and moment magnitude M_W. Magnitude can be related to the total energy in the expanding wave front generated by an earthquake, and thus to the total energy release—an empirical relation by Richter is

$$\log_{10} E_s = 11.8 + 1.5M \tag{1.2}$$

where E_S is the total energy in ergs. Owing to the observation that deep-focus earthquakes commonly do not register measurable surface waves with periods near 20 seconds, a body wave magnitude m_b was defined (Gutenberg and Richter, 1956), which can be related to M_S (Darragh et al., 1994):

$$m_b = 2.5 + 0.63\, M_S \tag{1.3}$$

Body wave magnitudes are more commonly used in stable continental regions, because of the deeper earthquakes. Seismic moment has been employed to define moment magnitude M_W (Hanks and Kanamori, 1979; also denoted as bold face $\boldsymbol{M}$), which is now the most widely used measure of earthquake magnitude:

$$\text{Log}\, \boldsymbol{M_o} = 1.5\, \boldsymbol{M_W} + 16.0 \tag{1.4}$$

where seismic moment M_o (dyne-cm) is defined as (Lomnitz, 1974)

$$M_o = \mu\, A\, \overline{u} \tag{1.5}$$

where μ is the material shear modulus, A the area of fault plane rupture, and $\overline{u}$ the mean relative displacement between the two sides of the fault (the averaged fault slip). Comparatively, M_W and M_S are numerically almost identical up to magnitude 7.5. Figure 1.2 indicates the relationship between moment magnitude and various magnitude scales.

From the foregoing discussion, it can be seen that magnitude and energy are related to fault rupture length and slip. Slemmons (1977), Bonilla et al (1984) and (Wells and Coppersmith, 1994) have determined statistical relations between these parameters, for worldwide and regional data sets, aggregated and segregated by type of faulting (normal, reverse, strike-slip). (Wells and Coppersmith, 1994) provide regressions for rupture area, length, width, displacement, and surface rupture length and displacement as a function of faulting type, the latter of which are given in Table 1.1, which indicates, for example, that for $M_w = 7$, the average fault rupture length (fault type undifferentiated) is approximately 41 km. (and the average displacement is approximately 1m).

Intensity: In general, seismic intensity is a metric of the effect, or the strength, of an earthquake hazard at a specific location. Although the term can be generically applied to engineering measures such as peak ground acceleration (PGA), it is often employed for qualitative measures of location-specific earthquake effects, based on observed human behavior and structural damage. Numerous intensity scales developed in preinstrumental times—the most common in use today are the Modified Mercalli

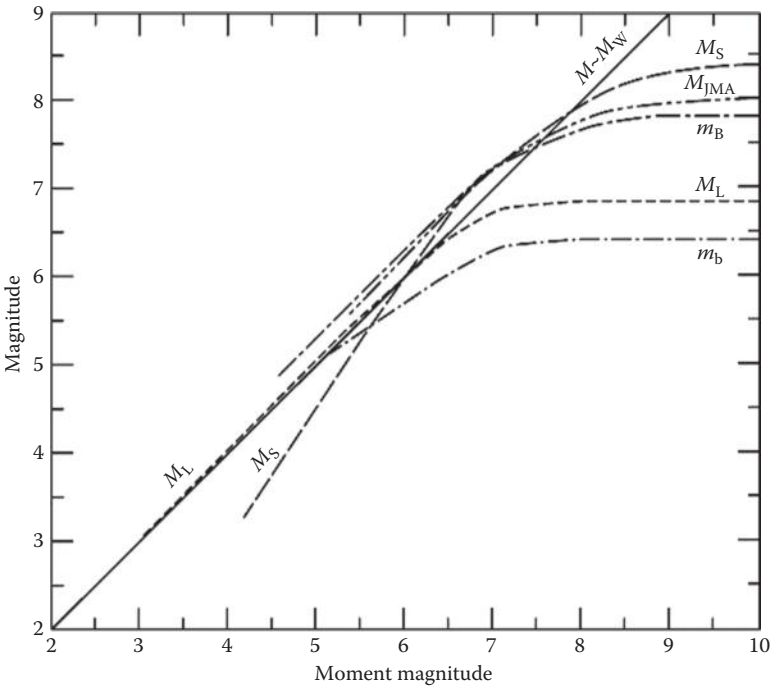

FIGURE 1.2 Relationship between moment magnitude and various magnitude scales. (From Campbell, K. W., *Earthquake Spectra*, 1(4), 759–804, 1985. With permission; after Heaton, T.H., Tajima. F., and Mori, A.W., *Surveys in Geophysics*, 8(1), 25–83, 1986.)

(MMI) (Wood and Neumann, 1931), Table 1.2, Rossi-Forel (R-F), Medvedev–Sponheur–Karnik (MSK-64, 1981), and Japan Meteorological Agency (JMA) scales.

Time History: Strong motion seismometers have been available since the 1930s, and record actual ground motions specific to their location (Figure 1.3). Typically, the ground motion records, termed "seismograms" or "time histories," have recorded acceleration (these records are termed "accelerograms"), for many years in analog form on photographic film and, recently, digitally.

Time histories theoretically contain complete information about the motion at the instrumental location, recording three *traces* or orthogonal records (two horizontal and one vertical). Time histories (i.e., the earthquake motion at the site) can differ dramatically in duration, frequency content, and amplitude. The maximum amplitude of recorded acceleration is termed PGA (also termed the zero period acceleration [ZPA])—peak ground velocity (PGV) and peak ground displacement (PGD) are the maximum respective amplitudes of velocity and displacement. Acceleration is normally recorded, with velocity and displacement being determined by integration; however, velocity and displacement meters are deployed to a lesser extent. Acceleration can be expressed in units of cm/sec^2 (termed *gals*), but is often also expressed in terms of the fraction or percent of the acceleration of gravity (980.66 gals, termed 1 g). Velocity is expressed in cm/sec (termed *kine*). Recent earthquakes (1994 Northridge, M_W 6.7 and 1995 Hanshin (Kobe) M_W 6.9) have recorded PGA's of approximately 0.8 g and PGV's of approximately 100 kine, whereas almost 2 g was recorded in the 1992 Cape Mendocino earthquake.

Elastic Response Spectra: If a single degree of freedom mass is subjected to a time history of ground (i.e., base) motion similar to that shown in Figure 1.3, the mass or elastic structural response can be readily calculated as a function of time, generating a structural response time history, as shown in Figure 1.4 for several oscillators with differing natural periods. The response time history can be calculated direct integration in the time domain, or by solution of the Duhamel integral. However,

TABLE 1.1 Regressions of Surface Rupture Length and Displacement

Equation[a]	Slip Type[b]	Number of Events	Coefficients and Standard Errors		Standard Deviation (s)	Correlation Coefficient (r)	Displacement Range (m)	Rupture Length Range (km)
			a(sa)	b(sb)				
log (MD) = a + b log (SRL)	SS	55	–1.69(0.16)	1.16(0.09)	0.36	0.86	0.01–14.6	1.3–432
	{R[c]	21	–0.44(0.34)	0.42(0.23)	0.43	0.38	0.11–6.5	4–148
	N	19	–1.98(0.50)	1.51(0.35)	0.41	0.73	0.06–6.4	3.8–75
	All	95	–1.38(0.15)	1.02(0.09)	0.41	0.75	0.01–14.6	1.3–432
log (SRL) = a + b log (MD)	SS	55	1.49(0.04)	0.64(0.05)	0.27	0.86	0.01–14.6	1.3–432
	{R	21	1.36(0.09)	0.35(0.19)	0.39	0.38	0.11–6.5	4–148}
	N	19	1.36(0.05)	0.35(0.08)	0.20	0.73	0.06–6.4	3.8–75
	All	95	1.43(0.03)	0.56(0.05)	0.31	0.75	0.01–14.6	1.3–432
log (AD) : = a + b log (SRL)	SS	35	–1.70(0.23)	1.04(0.13)	0.32	0.82	0.10–8.0	3.8–432
	{R	17	–0.60(0.39)	0.31(0.27)	0.40	0.28	0.06–2.6	6.7–148}
	N	14	–1.99(0.72)	1.24(0,49)	0.37	0.59	0.08–2.1	15–75
	All	66	–1.43(0.18)	0.88(0.11)	0.36	0.71	0.06–8.0	3.8–432
log (SRL) = a + b log (AD)	SS	35	1.68(0.04)	0.65(0.08)	0.26	0.82	0.10–8.0	3.8–432
	{R	17	1.45(0.10)	0.26(0.23)	0.36	0.28	0.06–2.6	6.7–148}
	N	14	1.52(0.05)	0.28(0.11)	0.17	0.59	0.08–2.1	15–75
	All	66	1.61(0.04)	0.57(0.07)	0.29	0.71	0.06–8.0	3.8–432

[a] SRL is surface rupture length (km); MD maximum displacement (m); AD average displacement (m).
[b] SS is strike slip; R reverse; N normal.
[c] Regressions for reverse-slip relationships shown in italics and brackets are not significant at a 95% probability level.
Source: Data from Wells, D. L., and Coppersmith, K. J., *Bull. Seismol. Soc. Am.*, 84, 974–1002, 1994.

TABLE 1.2 Modified Mercalli Intensity Scale of 1931

I	Not felt except by a very few under especially favorable circumstances.
II	Felt only by a few persons at rest, especially on upper floors of buildings. Delicately suspended objects may swing.
III	Felt quite noticeably indoors, especially on upper floors of buildings, but many people do not recognize it as an earthquake. Standing motor cars may rock slightly. Vibration like passing truck. Duration estimated.
IV	During the day felt indoors by many, outdoors by few. At night some awakened. Dishes, windows, and doors disturbed; walls make creaking sound. Sensation like heavy truck striking building. Standing motorcars rock noticeably.
V	Felt by nearly everyone; many awakened. Some dishes, windows, etc., broken; a few instances of cracked plaster; unstable objects overturned. Disturbance of trees, poles, and other tall objects sometimes noticed. Pendulum clocks may stop.
VI	Felt by all; many frightened and run outdoors. Some heavy furniture moved; a few instances of fallen plaster or damaged chimneys. Damage slight.
VII	Everybody runs outdoors. Damage negligible in buildings of good design and construction slight to moderate in well-built ordinary structures; considerable in poorly built or badly designed structures. Some chimneys broken. Noticed by persons driving motor cars.
VIII	Damage slight in specially designed structures; considerable in ordinary substantial buildings, with partial collapse; great in poorly built structures. Panel walls thrown out of frame structures. Fall of chimneys, factory stacks, columns, monuments, and walls. Heavy furniture overturned. Sand and mud ejected in small amounts. Changes in well water. Persons driving motor cars disturbed.
IX	Damage considerable in specially designed structures; well-designed frame structures thrown out of plumb; great in substantial buildings, with partial collapse. Buildings shifted off foundations. Ground cracked conspicuously. Underground pipes broken.
X	Some well-built wooden structures destroyed; most masonry and frame structures destroyed with foundations; ground badly cracked. Rails bent. Landslides considerable from river banks and steep slopes. Shifted sand and mud. Water splashed over banks.
XI	Few, if any (masonry), structures remain standing. Bridges destroyed. Broad fissures in ground. Underground pipelines completely out of service. Earth slumps and land slips in soft ground. Rails bent greatly.
XII	Damage total. Waves seen on ground surfaces. Lines of sight and level distorted. Objects thrown upward into the air.

Source: Adapted from Wood, H. O., and Neumann, F., *Bull. Seis. Soc. Am.*, 21, 277–283, 1931.

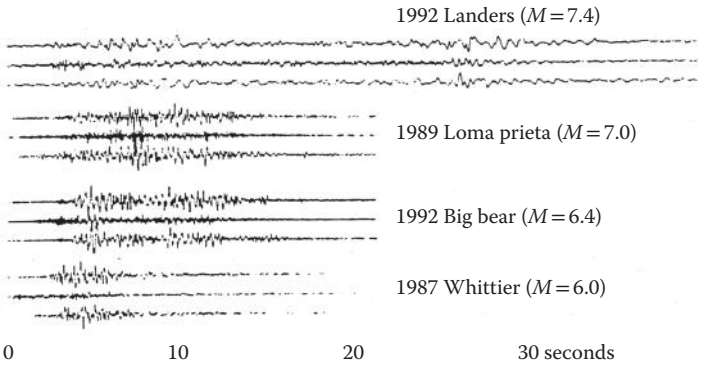

FIGURE 1.3 Typical earthquake accelerograms. (From Darragh et al. *Proceedings of Fifth U.S. National Conference Earthquake Engineering*, vol. III, 99–108, Earthquake Engineering Research Institute, Oakland CA, 1994. With permission.)

this is time-consuming, and the elastic response is more typically calculated in the frequency domain (Clough and Penzien, 1975).

For design purposes, it is often sufficient to know only the maximum amplitude of the response time history. If the natural period of the single degree of freedom oscillator (SDOF) is varied across a spectrum of engineering interest (typically, for natural periods from 0.03 to 3 or more sec., or frequencies

of 0.3 to 30 + Hz), then the plot of these maximum amplitudes is termed a *response spectrum*. Figure 1.4 illustrates this process, resulting in S_d, the *displacement response spectrum*, whereas Figure 1.5 shows (1) the S_d, displacement response spectrum, (2) S_v, the *velocity response spectrum* (also denoted PSV, the pseudo-spectral velocity, pseudo to emphasize that this spectrum is not exactly the same as the relative velocity response spectrum [Hudson, 1979]), and (3) S_a, the acceleration *response spectrum*. Note that

$$S_v = \frac{2\pi}{T} S_d = \varpi S_d \tag{1.6}$$

and

$$S_a = \frac{2\pi}{T} S_v = \varpi S_v = \left(\frac{2\pi}{T}\right)^2 S_d = \varpi^2 S_d \tag{1.7}$$

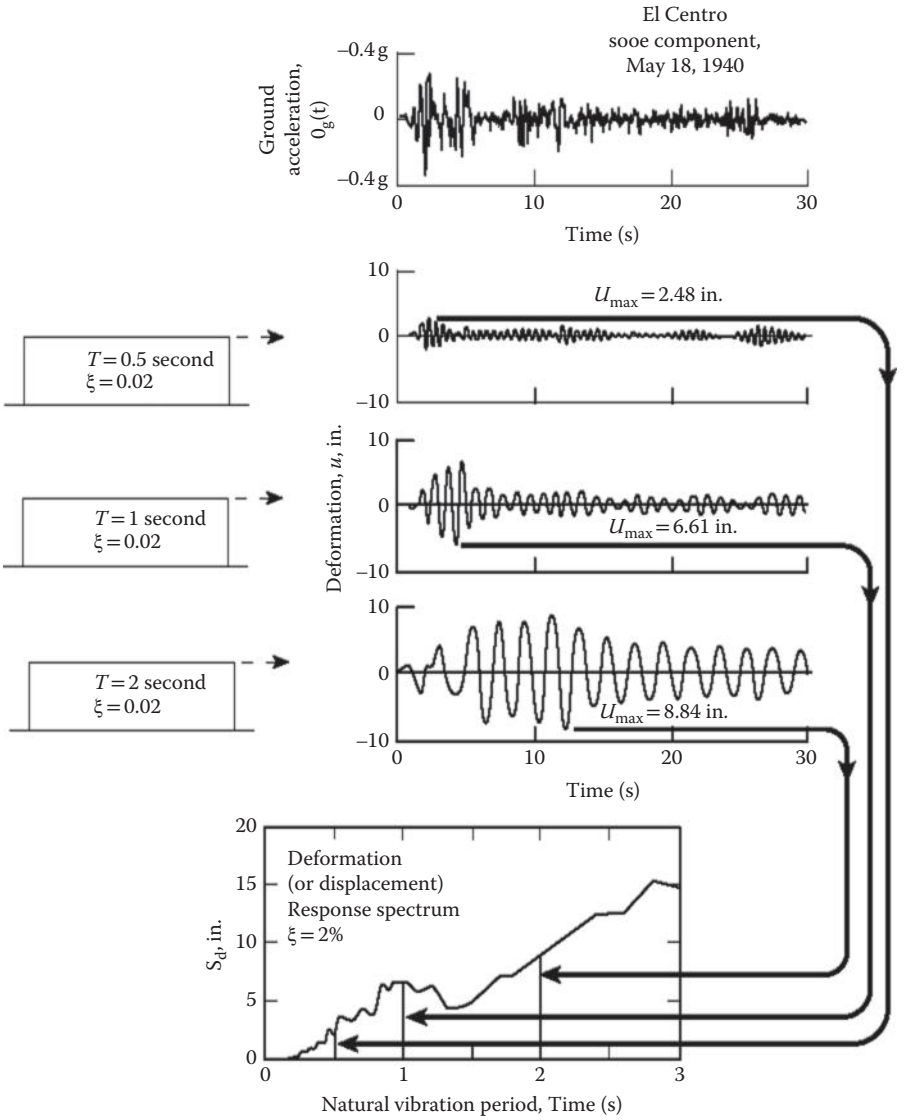

FIGURE 1.4 Computation of deformation (or displacement) response spectrum. (From Chopra, A.K., *Dynamics of Structures: A Primer*. Earthquake Engineering Research Institute, Oakland, CA, 1981.)

Response spectra form the basis for much modern earthquake engineering structural analysis and design. They are readily calculated if the ground motion is known. For design purposes however, response spectra must be estimated, either by methods of probabilistic seismic hazard analysis using period-specific attenuation relations, by adjusting an idealized response spectral shape such as shown in Figure 1.7 combined with estimates of peak ground acceleration and peak ground velocity, or by following code procedures as shown in Figure 1.8. Response spectra may be plotted in any of several ways, as shown in Figure 1.5 with arithmetic axes, and in Figure 1.6, where the velocity response spectrum is plotted on tripartite logarithmic axes, which equally enables reading of displacement and acceleration response. Response spectra are most normally presented for 5% of critical damping.

Inelastic Response Spectra: Although the foregoing discussion has been for elastic response spectra, most structures are not expected, or even designed, to remain elastic under strong ground motions. Rather, structures are expected to enter the *inelastic* region—the extent to which they behave inelastically can be defined by the ductility factor, μ:

$$\mu = \frac{u_m}{u_y} \tag{1.8}$$

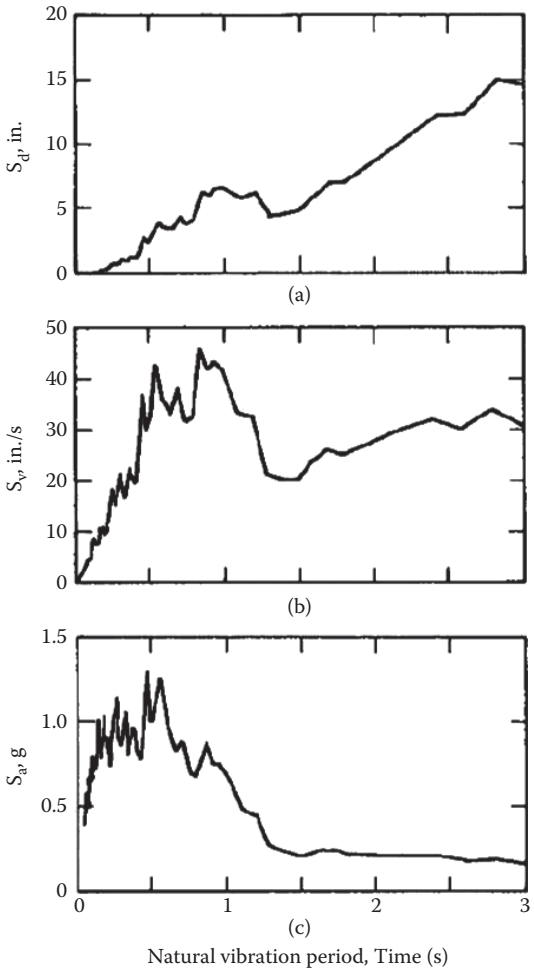

FIGURE 1.5 Response spectra spectrum. (From Chopra, A.K., *Dynamics of Structures: A Primer*. Earthquake Engineering Research Institute, Oakland, CA, 1981.)

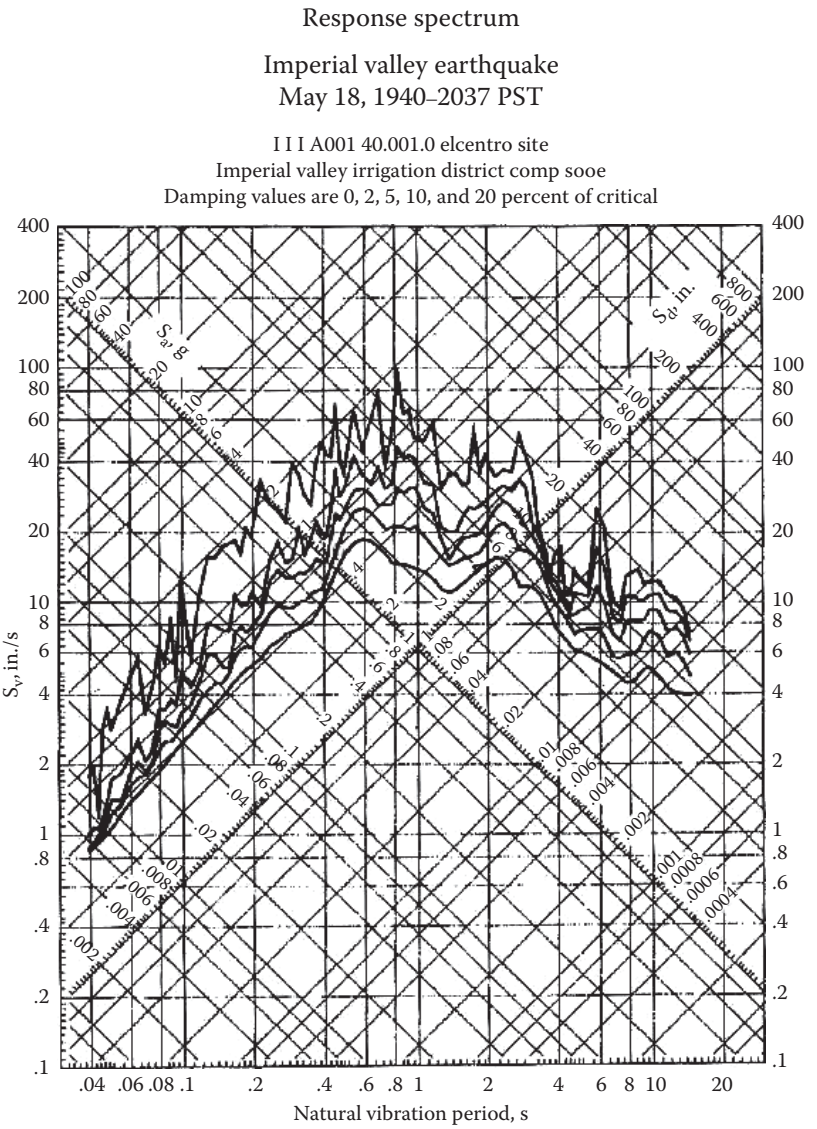

FIGURE 1.6 Response spectra, tri-partite plot (El Centro S 0° E component). (From Chopra, A.K., *Dynamics of Structures: A Primer*. Earthquake Engineering Research Institute, Oakland, CA, 1981.)

where u_m is the actual displacement of the mass under actual ground motions, and u_y is the displacement at yield (i.e., that displacement that defines the extreme of elastic behavior). Inelastic response spectra can be calculated in the time domain by direct integration, analogous to elastic response spectra but with the structural stiffness as a nonlinear function of displacement, $k = k(u)$. If elastoplastic behavior is assumed, then elastic response spectra can be readily modified to reflect inelastic behavior (Newmark and Hall, 1982), on the basis that (1) at low frequencies (0.3 Hz<) displacements are the same, (2) at high frequencies (>33 Hz), accelerations are equal, and (3) at intermediate frequencies, the absorbed energy is preserved. Actual construction of inelastic response spectra on this basis is shown in Figure 1.9, where $DVAA_o$ is the elastic spectrum, which is reduced to D′ and V′ by the ratio of $1/\mu$ for frequencies <2Hz, and by the ratio of $1/(2\mu-1)^{1/2}$ between 2 and 8 Hz. Above 33 Hz there is no reduction. The result is the inelastic acceleration spectrum ($D'V'A'A_o$), whereas $A''A_o'$ is the inelastic displacement spectrum. A specific example, for ZPA = 0.16 g, damping = 5% of critical and $\mu = 3$ is shown in Figure 1.10.

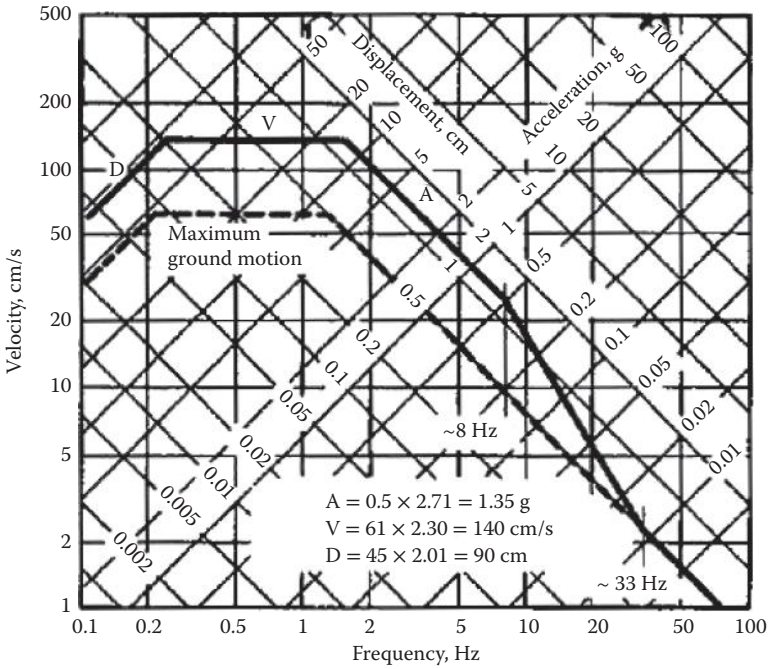

FIGURE 1.7 Idealized elastic design spectrum, horizontal motion (ZPA = 0.5 g, 5% damping, one sigma cumulative probability. (From Newmark, N. M. and Hall, W. J., *Earthquake Spectra and Design*. Earthquake Engineering Research Institute, Oakland, CA, 1982.)

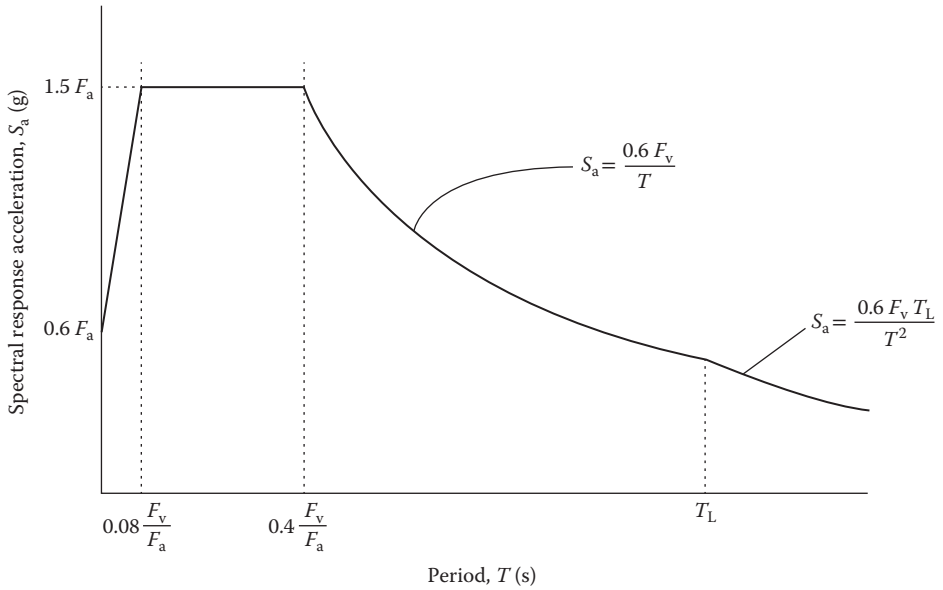

FIGURE 1.8 Deterministic lower limit on MCER response spectrum. (From ASCE 7-10, *Minimum Design Loads for Buildings and Other Structures, Sei/Asce 7-10.* American Society of Civil Engineers, Reston, VA, 2010.)

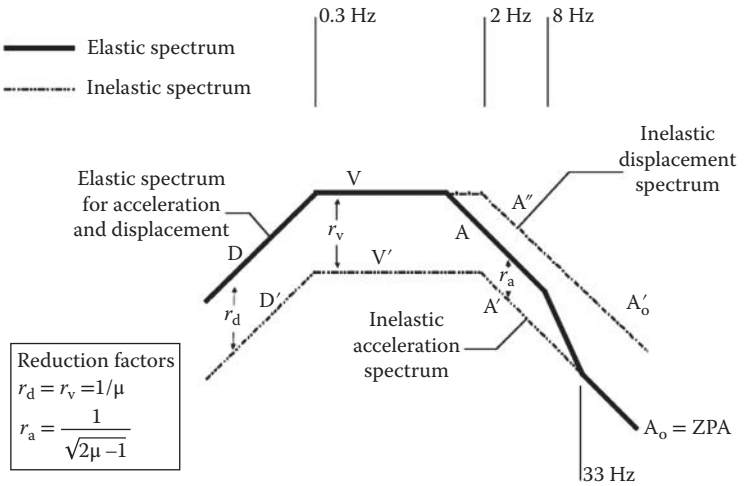

FIGURE 1.9 Inelastic response spectra for earthquakes. (After Newmark, N. M. and Hall, W. J., *Earthquake Spectra and Design*. Earthquake Engineering Research Institute, Oakland, CA, 1982.)

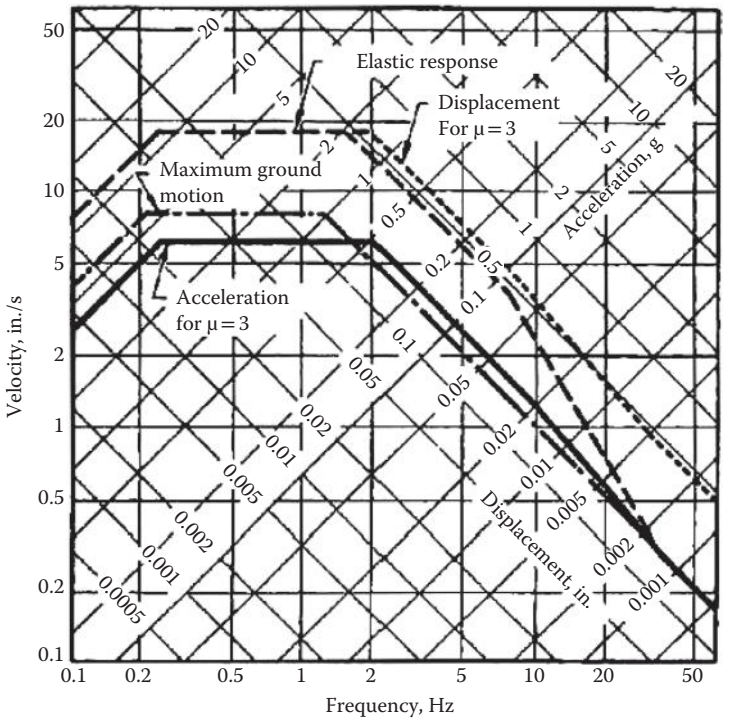

FIGURE 1.10 Example inelastic response spectra. (From Newmark, N. M. and Hall, W. J., *Earthquake Spectra and Design*. Earthquake Engineering Research Institute, Oakland, CA, 1982.).

1.4 Strong Motion Attenuation and Duration

The rate at which earthquake ground motion decreases with distance, termed *attenuation*, is a function of the regional geology and inherent characteristics of the earthquake and its source. Equations for estimation of attenuation are termed *ground-motion prediction equations* (GMPEs), and until a decade or two ago were thought to vary significantly among many different regions. Douglas (2011) offers an

excellent review of more than 450 such relations developed during the period 1964–2010, many of which are now mainly of historical or only local interest. With the availability of more data, the consensus is emerging (see for example Stafford et al. [2008]) that attenuation may be relatively similar within a broader classification of regions, three of which are currently favored: (1) active tectonic regions, (2) stable continental regions, and (3) subduction zones.

Starting about 2005, a series of projects has developed a strong ground motion database (http://peer .berkeley.edu/products/strong_ground_motion_db.html) that has formed the basis for development of empirical GMPEs for active tectonic regions. Five GMPEs for active tectonic regions, termed the Next Generation Attenuation (NGA) equations for PGA, PGV and response spectral ordinates, have been developed and are presented in the February 2008 Special Issue of *Earthquake Spectra* (Stewart et al., 2008). Comparable NGA relations for stable continental regions and subduction zones are currently under development. The NGA models mark a significant advancement in the state-of-the-art in empirical ground-motion modeling and include many effects not generally previously accounted for. The remainder of this section discusses the five NGA equations in general, and presents selected details for one of the NGA equations—the reader is referred to the Special Issue for details.

The five NGA models are (Abrahamson and Silva, 2008; Boore and Atkinson, 2008; Campbell and Bozorgnia, 2008; Chiou and Youngs, 2008; Idriss, 2008) referred to as AS08, BA08, CB08, CY08 and I08, respectively. As noted above, they are meant for estimation of strong ground motion because of shallow crustal earthquake in active tectonic regions. The approach for all five relations, while informed by theoretical considerations, was largely empirical and consisted of regressing data from (depending on the equation) 942 to 2754 recordings from 58 to 135 different earthquakes. Function forms of the NGA models are indicated in Table 1.3, where it can be seen that style-of-faulting, depth of rupture, nonlinear site amplification and hanging wall (HW) effects are considered by all or most of the models. All models use moment magnitude as the earthquake size metric and V_{s30} (shear wave velocity for top 30 meters of the soil column) as the soil column stiffness metric, but vary as to the way in which the primary distance measure is calculated, with BA08 using the "Joyner–Boore distance" (R_{jb}, the closest horizontal distance to the surface projection of the rupture plane), whereas the others employ R_{rup}, the closest distance to the rupture plane, Figure 1.11. (Abrahamson et al., 2008) present further details on comparisons of the five models.

TABLE 1.3 Functional Forms of NGA Models

	AS08	BA08	CB08	CY08	I08
Saturation at short distances	X	X	X	X	X
Style-of-faulting factor	X	X	X	X	X
Rupture depth factor	X	Implicit through R_{JB}	X (RV only)	X	
HW factor	X	Implicit through R_{JB}	X	X	
Nonlinear site amplification	Constrained (Walling et al., 2008)	Constrained (Stewart, 2005)	Constrained (Walling et al., 2008)	X	N/A
Soil/sediment depth factor	Constrained (Shallow: Silva, 2005; deep: Day et al., 2005)		Constrained deep: Day et al. (2005)	X	N/A
Magnitude dependent σ	X			X	X
Nonlinear effects on σ	Intra-event and intra-event terms		Intra-event term only	Intra-event and intra-event terms	

Source: Data from Abrahamson, N. et al., *Earthquake Spectra*, 24, 45–66, 2008.

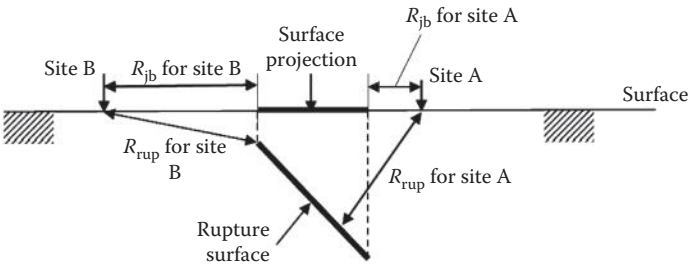

FIGURE 1.11 Common GMPE distance measures.

CB08 is typical of the five models and the following discussion excerpted from Campbell and Bozorgnia (2008). CB08′s basic equation is

$$\ln Y = f_{mag} + f_{dis} + f_{flt} + f_{hng} + f_{site} + f_{sed} \tag{1.9}$$

where Y is the ground motion parameter of interest (e.g., PGA, PGV, spectral acceleration), and f_{mag} is the magnitude parameter:

$$f_{mag} = \begin{cases} c_0 + c_1 \boldsymbol{M}; & \boldsymbol{M} \le 5.5 \\ c_0 + c_1 \boldsymbol{M} + c_2(\boldsymbol{M} - 5.5); & 5.5 < \boldsymbol{M} \le 6.5 \\ c_0 + c_1 \boldsymbol{M} + c_2(\boldsymbol{M} - 5.5) + c_3(\boldsymbol{M} - 6.5); & \boldsymbol{M} > 6.5 \end{cases} \tag{1.10}$$

the distance parameter is

$$f_{dis} = (c_4 + c_5 \boldsymbol{M}) \ln\left(\sqrt{R_{RUP}^2 + c_6^2}\right) \tag{1.11}$$

the style-of-faulting (fault mechanism) term is given by the expressions

$$f_{flt} = c_7 F_{RV} f_{flt,Z} + c_8 F_{NM} \tag{1.12}$$

$$f_{flt,Z} = \begin{cases} Z_{TOR}; & Z_{TOR} < 1 \\ 1; & Z_{TOR} \ge 1 \end{cases} \tag{1.13}$$

the HW term is given by the expressions

$$\begin{aligned} f_{hng} &= c_9 f_{hng,R} f_{hng,M}, f_{hng,Z}, f_{hng,\delta} \\ f_{hng,R} &= \begin{cases} 1; & R_{JB} = 0 \\ \left[\max\left(R_{RUP}, \sqrt{R_{JB}^2 + 1}\right) - R_{JB}\right] / \max\left(R_{RUP}, \sqrt{R_{JB}^2 + 1}\right); & R_{JB} > 0, Z_{TOR} < 1 \\ \left(R_{RUP} - R_{JB}\right) / R_{RUP}; & R_{JB} > 0, Z_{TOR} \ge 1 \end{cases} \\ f_{hng,M} &= \begin{cases} 0; & \boldsymbol{M} \le 6.0 \\ 2(\boldsymbol{M} - 6.0); & 6.0 < \boldsymbol{M} < 6.5 \\ 1; & \boldsymbol{M} \ge 6.5 \end{cases} \\ f_{hng,Z} &= \begin{cases} 0; & Z_{TOR} \ge 20 \\ (20 - Z_{TOR}) / 20; & 0 \le Z_{TOR} < 20 \end{cases} \\ f_{hng,\phi} &= \begin{cases} 1; & \delta \le 1 \\ (90 - \delta) / 20; & \delta > 70 \end{cases} \end{aligned} \tag{1.14}$$

the shallow site response term is given by the expression

$$f_{\text{site}} = \begin{cases} c_{10}\ln\left(\frac{V_{S30}}{k_1}\right) + k_2\left\{\ln\left[A_{1100} + c\left(\frac{V_{S30}}{k_1}\right)^n\right] - \ln\left[A_{1100} + c\right]\right\}; & V_{S30} < k_1 \\ (c_{10} + k_2 n)\ln\left(\frac{V_{S30}}{k_1}\right); & k_1 \le V_{S30} < 1100 \\ (c_{10} + k_2 n)\ln\left(\frac{1100}{k_1}\right); & V_{S30} \ge 1100 \end{cases} \tag{1.15}$$

the basin response term is given by the expression

$$f_{\text{sed}} = \begin{cases} c_{11}\left(Z_{2.5} - 1\right); & Z_{2.5} < 1 \\ 0; & 1 \le Z_{2.5} \le 3 \\ c_{12}k_3 e^{-0.75}\left[1 - e^{-0.25\left(Z_{2.5}-3\right)}\right]; & Z_{2.5} > 3 \end{cases} \tag{1.16}$$

and Y is the median estimate of the geometric mean horizontal component (referred to as GMRotI50) (Boore et al., 2006) of PGA (g), PGV (cm/s), PGD (cm) or PSA (g); **M** is moment magnitude; R_{RUP} is the closest distance to the coseismic rupture plane (km); R_{JB} is the closest distance to the surface projection of the coseismic rupture plane (km); F_{RV} is an indicator variable representing reverse and reverse-oblique faulting, where $F_{\text{RV}} = 1$ for $30° < \lambda < 150°$, $F_{\text{RV}} = 0$ otherwise, and λ is rake defined as the average angle of slip measured in the plane of rupture between the strike direction and the slip vector; F_{NM} is an indicator variable representing λ for normal and normal-oblique faulting, where $F_{\text{NM}} = 1$ for $-150° < \lambda < -30°$ and $F_{\text{NM}} = 0$ otherwise; Z_{TOR} is the depth to the top of the coseismic rupture plane (km); δ is the dip of the rupture plane (°); V_{S30} is the time-averaged shear-wave velocity in the top 30 m of the site profile (m/s); A_{1100} is the median estimate of PGA on a reference rock outcrop (V_{S30} = 1,100 m/s) from Equation 1.15 (g); and $Z_{2.5}$ is the depth to the 2.5 km/s shear-wave velocity horizon, typically referred to as basin or sediment depth (km). The empirical coefficients *ci* and the theoretical coefficients *c, n* and *ki* are listed in Table 1.4. When PSA < PGA and $T \le 0.25$ s, PSA should be set equal to PGA to be consistent with the definition of pseudo-absolute acceleration. This condition occurs only at large distances and small magnitudes.

1.4.1 OpenSHA Attenuation Calculator

OpenSHA (discussed further in Section 1.5) has implemented an open-source Java applet termed the "Attenuation Calculator," available at http://www.opensha.org/glossary-attenuationRelation-USGS_COMBO_2004. The calculator implements the NGA and a number of other GMPEs and permits calculation or comparison of various GMPEs, for specified values. Figure 1.12 shows the calculator plotting CB08 for moment magnitude 5.5 and 7.5 events, as a function of distance, with other parameters fixed as indicated. The calculator is easy to use, and also provides the data in tabular form.

TABLE 1.4 Coefficients for the Geometric Mean and Arbitrary Horizontal Components of the Median Ground Motion Model

T (s)	c_0	c_1	c_2	c_3	c_4	c_5	c_6	c_7	c_8	c_9	c_{10}	c_{11}	c_{12}	k_1	k_2	k_3
0.010	–1.715	0.500	0.530	–0.262	–2.118	0.170	5.60	0.280	–0.120	0.490	1.058	0.040	0.610	865	–1.186	1.839
0.020	–1.680	0.500	0.530	–0.262	–2.123	0.170	5.60	0.280	–0.120	0.490	1.102	0.040	0.610	865	–1.219	1.840
0.030	–1.552	0.500	–0.530	–0.262	–2.145	0.170	5.60	0.280	–0.120	0.490	1.174	0.040	0.610	908	–1.273	1.841
0.050	–1.209	0.500	–0.530	–0.267	–2.199	0.170	5.74	0.280	–0.120	0.490	1.272	0.040	0.610	1,054	–1.346	1.843
0.075	–0.657	0.500	–0.530	–0.302	–2.277	0.170	7.09	0.280	–0.120	0.490	1.438	0.040	0.610	1,086	–1.471	1.845
0.10	–0.314	0.500	–0.530	–0.324	–2.318	0.170	8.05	0.280	–0.099	0.490	1.604	0.040	0.610	1,032	–1.624	1.847
0.15	–0.133	0.500	–0.530	–0.339	–2.309	0.170	8.79	0.280	–0.048	0.490	1.928	0.040	0.610	878	–1.931	1.852
0.20	–0.486	0.500	–0.446	–0.398	–2.220	0.170	7.60	0.280	–0.012	0.490	2.194	0.040	0.610	748	–2.188	1.856
0.25	–0.890	0.500	–0.362	–0.458	–2.146	0.170	6.58	0.280	0.000	0.490	2.351	0.040	0.700	654	–2.381	1.861
0.30	1.171	0.500	–0.294	–0.511	–2.095	0.170	6.04	0.280	0.000	0.490	2.460	0.040	0.750	587	–2.518	1.865
0.40	–1.466	0.500	–0.186	–0.592	–2.066	0.170	5.30	0.280	0.000	0.490	2.587	0.040	0.850	503	–2.657	1.874
0.50	–2.569	0.656	–0.304	–0.536	–2.041	0.170	4.73	0.280	0.000	0.490	2.544	0.040	0.883	457	–2.669	1.883
0.75	–4.844	0.972	–0.578	–0.406	–2.000	0.170	4.00	0.280	0.000	0.490	2.133	0.077	1.000	410	–2.401	1.906
1.0	–6.406	1.196	–0.772	–0.314	–2.000	0.170	4.00	0.255	0.000	0.490	1.571	0.150	1.000	400	–1.955	1.929
1.5	–8.692	1.513	–1.046	–0.185	–2.000	0.170	4.00	0.161	0.000	0.490	0.406	0.253	1.000	400	–1.025	1.974
2.0	–9.701	1.600	–0.978	–0.236	–2.000	0.170	4.00	0.094	0.000	0.371	–0.456	0.300	1.000	400	–0.299	2.019
3.0	–10.556	1.600	–0.638	–0.491	–2.000	0.170	4.00	0.000	0.000	0.154	–0.820	0.300	1.000	400	0.000	2.110
4.0	–11.212	1.600	–0.316	–0.770	–2.000	0.170	4.00	0.000	0.000	0.000	–0.820	0.300	1.000	400	0.000	2.200
5.0	–11.684	1.600	–0.070	–0.986	–2.000	0.170	4.00	0.000	0.000	0.000	–0.820	0.300	1.000	400	0.000	2.291
7.5	–12.505	1.600	–0.070	–0.656	–2.000	0.170	4.00	0.000	0.000	0.000	–0.820	0.300	1.000	400	0.000	2.517
10.0	–13.087	1.600	–0.070	–0.422	–2.000	0.170	4.00	0.000	0.000	0.000	–0.820	0.300	1.000	400	0.000	2.744
PGA	–1.715	0.500	–0.530	–0.262	–2.118	0.170	5.60	0.280	–0.120	0.490	1.058	0.040	0.610	865	–1.186	1.839
PGV	0.954	0.696	–0.309	–0.019	–2.016	0.170	4.00	0.245	0.000	0.358	1.694	0.092	1.000	400	–1.955	1.929
PGD	–5.270	1.600	–0.070	0.000	–2.000	0.170	4.00	0.000	0.000	0.000	–0.820	0.300	1.000	400	0.000	2.744

Note: $c = 1.88$ and $n = 1.18$ for all periods (T); PGA and PSA have units of g; PGV and PGD have units of cm/s and cm, respectively.
Source: Data from Campbell, K., and Bozorgnia, Y., *Earthquake Spectra*, 24, 139–171, 2008.

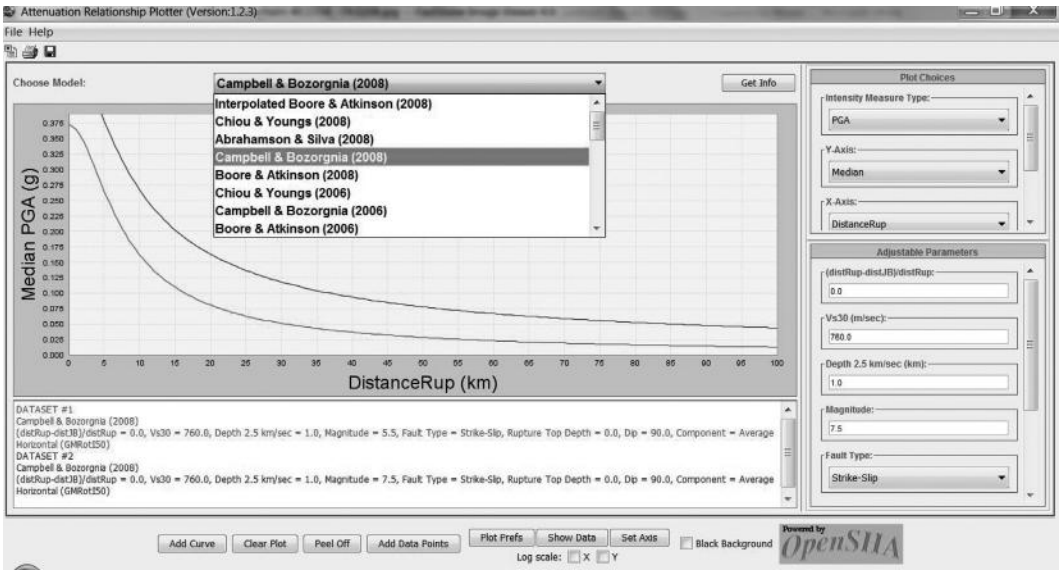

FIGURE 1.12 OpenSHA Attenuation Calculator showing example plot of PGA versus distance for M_w 5.5 (lower curve) and M_w 7.5 (upper curve), other variables fixed as shown.

1.5 Probabilistic Seismic Hazard Analysis

The Probabilistic Seismic Hazard Analysis (PSHA) approach entered general practice with Cornell's (1968) seminal paper, and basically employs the theorem of total probability to formulate

$$P(Y) = \sum_F \sum_M \sum_R p(Y|M,R)p(M)p(R) \tag{1.17}$$

where

Y is a measure of intensity, such as PGA, response spectral parameters PSV, and so on
p(Y|M,R) is the probability of *Y* given earthquake magnitude *M* and distance *R* (i.e., attenuation)
p(M) is the probability of a given earthquake magnitude *M*,
P(R) is the probability of a given distance, *R*, and
F indicates seismic sources, whether discrete such as faults, or distributed

This process is illustrated in Figure 1.13, where various seismic sources (faults modeled as line sources and dipping planes, and various distributed or area sources, including a background source to account for miscellaneous seismicity) are identified, and their seismicity characterized on the basis of historic seismicity and/or geologic data. The effects at a specific site are quantified on the basis of strong ground motion modeling, also termed "attenuation." These elements collectively are the seismotectonic model—their integration results in the seismic hazard.

There is an extensive literature on this subject (National Academy, 1988; Reiter, 1990) so that only key points will be discussed here. Summation is indicated, as integration requires closed form solutions, which are usually precluded by the empirical form of the attenuation relations. The *p(Y|M,R)* term represents the full probabilistic distribution of the attenuation relation—summation must occur over the full distribution, because of the significant uncertainty in attenuation. The *p(M)* term is referred to as the magnitude-frequency relation, which was first characterized by Gutenberg and Richter (1954) as

$$\log N(m) = a_N - b_N m \tag{1.18}$$

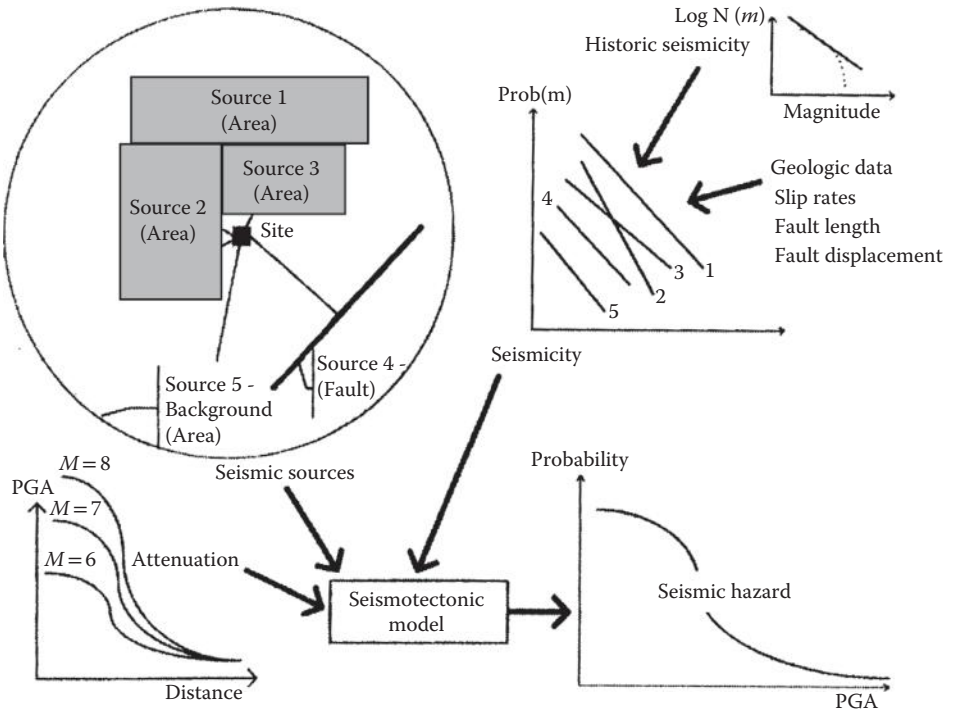

FIGURE 1.13 Elements of seismic hazard analysis—seismotectonic model is composed of seismic sources, whose seismicity is characterized on the basis of historic seismicity and geologic data, and whose effects are quantified at the site via strong motion attenuation models.

where N(m) = the number of earthquake events equal to or greater than magnitude m occurring on a seismic source per unit time, and a_N and b_N are regional constants (10^{a_N} = the total number of earthquakes with magnitude >0, and b_N is the rate of seismicity; b_N is typically 1 ± 0.3). The Gutenberg–Richter relation can be normalized to

$$F(m) = 1 - \exp\left[-B_M(m - M_o)\right] \tag{1.19}$$

where F(m) is the cumulative distribution function (CDF) of magnitude, B_M is a regional constant and M_o is a small enough magnitude such that lesser events can be ignored. Combining this with a Poisson distribution to model large earthquake occurrence (Esteva, 1976) leads to the CDF of earthquake magnitude per unit time:

$$F(m) = \exp\left[-\exp\{-a_M(m - \mu_M)\}\right] \tag{1.20}$$

which has the form of a Gumbel (1958) extreme value type I (largest values) distribution (denoted $EX_{I,L}$), which is an unbounded distribution (i.e., the variate can assume any value). The parameters a_M and μ_M can be evaluated by a least squares regression on historical seismicity data, although the probability of very large earthquakes tends to be overestimated. Several attempts have been made to account for this (e.g., Cornell and Merz, 1973). Yegulalp and Kuo (1974) have used Gumbel's Type III (largest value, denoted $EX_{III,L}$) to successfully account for this deficiency. This distribution

$$F(m) = \exp\left[-\left(\frac{w - m}{w - u}\right)^k\right] \tag{1.21}$$

has the advantage that w is the largest possible value of the variate (i.e., earthquake magnitude), thus permitting (when w, u, and k are estimated by regression on historical data) an estimate of the source's largest possible magnitude. It can be shown (Yegulalp and Kuo, 1974) that estimators of w, u, and k can be obtained by satisfying Kuhn–Tucker conditions although, if the data is too incomplete, the $EX_{III,L}$ parameters approach those of the $EX_{I,L}$. Determination of these parameters requires careful analysis of historical seismicity data, which is highly complex and something of an art (Donovan and Bornstein, 1978), and the merging of the resulting statistics with estimates of maximum magnitude and seismicity made on the basis of geological evidence (i.e., as discussed in Section 1.3, maximum magnitude can be estimated from fault length, fault displacement data, time since last event, and other evidence, and seismicity can be estimated from fault slippage rates combined with time since last event; see Schwartz [1988] for an excellent discussion of these aspects). In a full PSHA, many of these aspects are treated fully or partially probabilistically, including the attenuation, magnitude–frequency relation, upper and lower bound magnitudes for each source zone, geographical bounds of source zones, fault rupture length, and many other aspects. The full treatment requires complex specialized computer codes, which incorporate uncertainty via use of multiple alternative source zonations, attenuation relations, and other parameters (Electric Power Research Institute [EPRI], 1986; Bernreuter et al., 1989) often using a logic tree format. A number of codes have been developed using the public domain FRISK (Fault Risk) code first developed by McGuire (1978).

1.5.1 Open Source PSHA Tools

There are a number of open source PSHA tools now available on the web—two of these stand out and are worthy of mention (Figures 1.14 and 1.15):

OpenSHA is a suite of open source software developed by the U.S. Geological Survey, available at http://www.opensha.org/. "As an object-oriented framework, OpenSHA can accommodate arbitrarily complex (e.g., physics based) earthquake rupture forecasts (ERFs), ground-motion models, and engineering-response models, which narrows the gap between cutting-edge geophysics and state-of-the-art hazard and risk evaluations." OpenSHA is now used to develop the U.S. National Seismic Hazard Maps, and significantly lowers the barriers to entry for performing PSHA. The site not only offers calculational tools, but also tutorials and in-depth reference materials.

OpenQuake is the open source implementation of a calculational engine developed by the Global Earthquake Model (www.globalquakemodel.org) and is available at http://beta.globalquakemodel.org/openquake/about/. "OpenQuake refers to all tools, apps and IT-infrastructure being developed to support stakeholders in assessing risk. The core of OpenQuake is the web-based risk assessment platform, which will offer an integrated environment for modeling, viewing, exploring, and managing earthquake risk. But there is more: a variety of tools and even databases can be used independently, so users can use GEM's resources and tools in a flexible way, adjusted to their needs." The goal of OpenQuake, which incorporates significant elements from OpenSHA, is to go beyond PSHA to PSRA—Probabilistic Seismic Risk Analysis—that is, the probabilistic estimation of earthquake damage and loss.

1.6 Site Response

When seismic waves reach a site, the ground motions they produce are affected by the geometry and properties of the geologic materials at that site. At most bridge sites, rock will be covered by some thickness of soil that can markedly influence the nature of the motions transmitted to the bridge structure as well as the loading on the bridge foundation. The influence of local site conditions on ground response has been observed in many past earthquakes, but specific provisions for site effects were not incorporated in codes until 1976.

The manner in which a site responds during an earthquake depends on the near-surface stiffness gradient and on how the incoming waves are reflected and refracted by surface topography, near-surface material boundaries, and deeper basin geometries. The interaction between seismic waves and

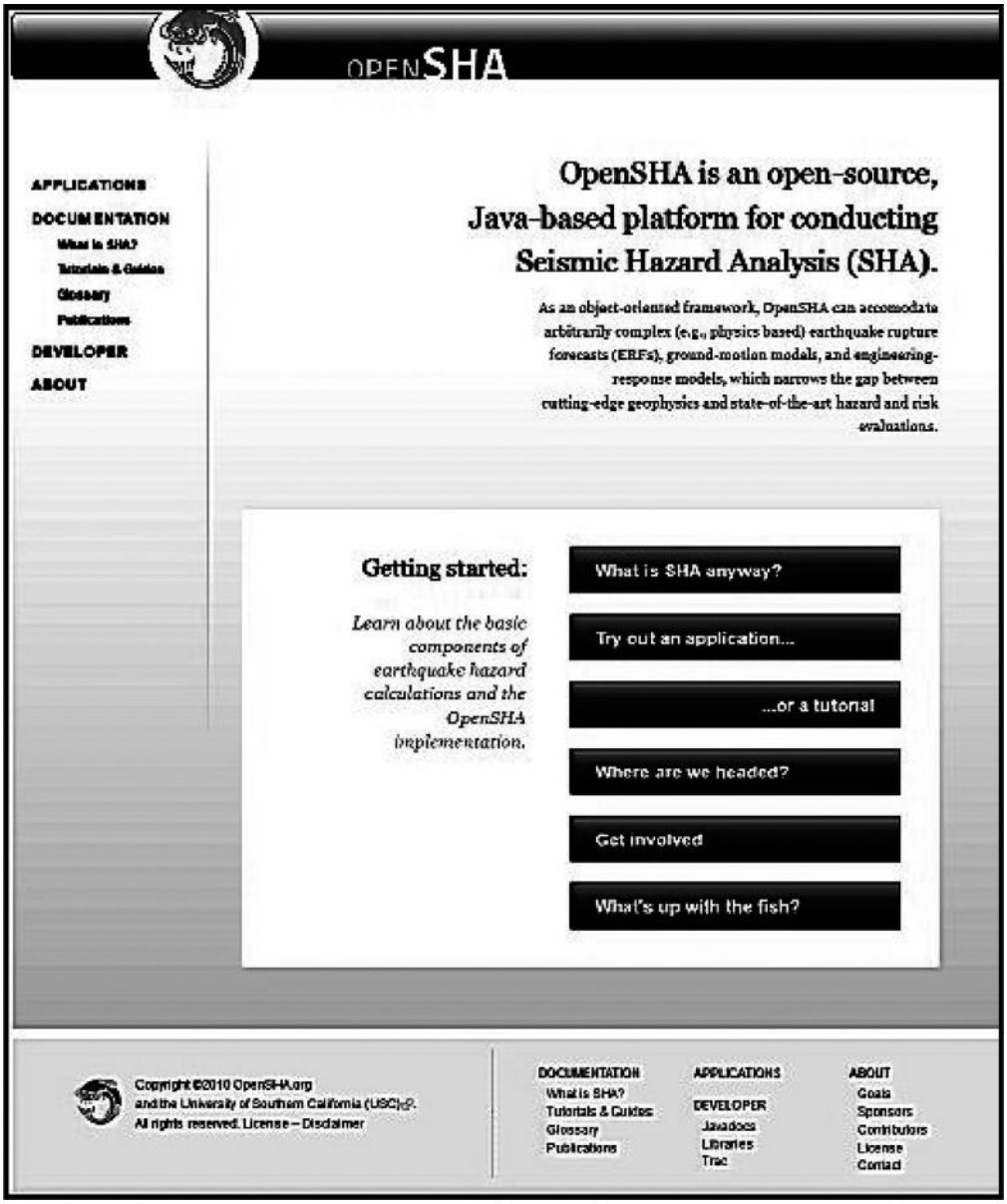

FIGURE 1.14 OpenSHA home page (http://www.opensha.org/).

near-surface materials can be complex, particularly when surface topography and/or subsurface stratigraphy are complex. Quantification of site response has generally been accomplished by empirical or analytical methods.

1.6.1 Evidence for Local Site Effects

Theoretical evidence for the existence of local site effects has been supplemented by instrumental and observational evidence in numerous earthquakes. Nearly 200 years ago (MacMurdo, 1824), variations in damage patterns were correlated to variations in subsurface conditions; such observations have been repeated on a regular basis since that time. With the advent of modern seismographs and strong motion

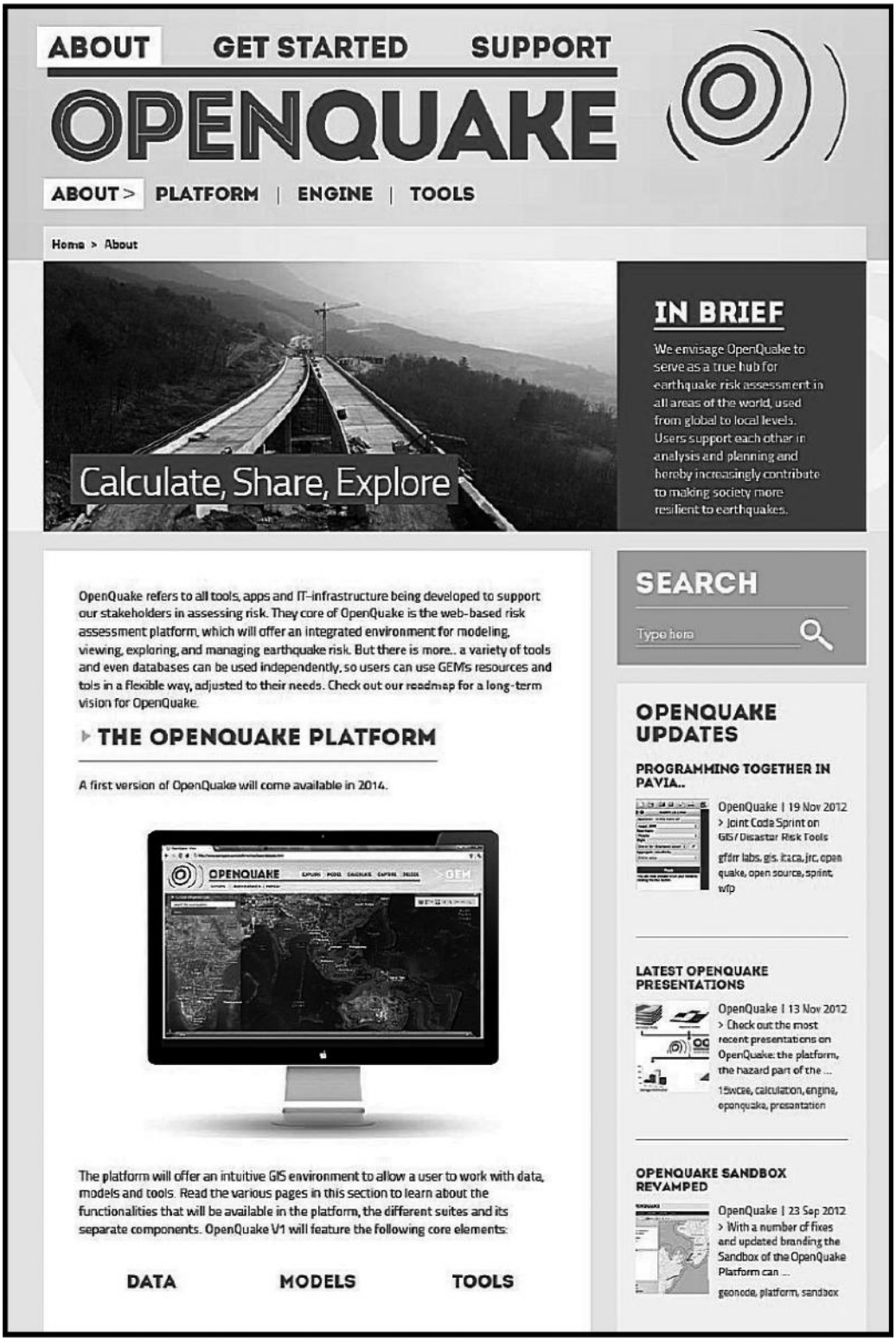

FIGURE 1.15 OpenQuake home page (http://beta.globalquakemodel.org/openquake/about/).

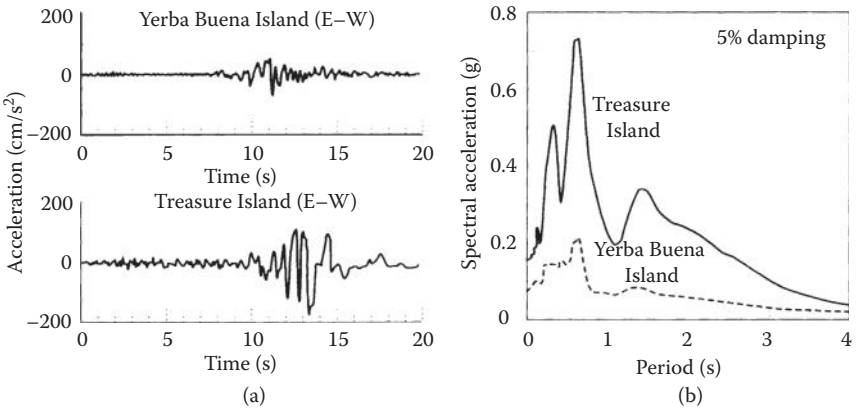

FIGURE 1.16 Ground surface motions at Yerba Buena Island and Treasure Island in the Loma Prieta earthquake (From Kramer, S. L. 1996. *Geotechnical Earthquake Engineering*, Prentice-Hall, Upper Saddle River, NJ, Figure 8.9, 1996. With permission.)

instruments, quantitative evidence for local site effects is now available. In the Loma Prieta earthquake, for example, strong motion instruments at Yerba Buena Island and Treasure Island were at virtually identical distances and azimuths from the hypocenter. However, the Yerba Buena Island instrument was located on a rock outcrop and the Treasure Island instrument on approximately 14 m of loose hydraulically placed sandy fill underlain by nearly 17 m of soft San Francisco Bay Mud. The measured motions, which differed significantly (Figure 1.16), illustrate the effects of local site effects.

Site effects are taken here to include local ground response, topographic effects, and basin effects. Local ground response refers to the amplification or de-amplification of ground motions associated with (nearly) vertically propagating body waves by near-surface geologic materials. Topographic effects are those associated with amplification or de-amplification by two- and three-dimensional topographic irregularities (i.e., features that deviate from level-ground-surface conditions). Basin effects are associated with reflection and refraction of waves at inclined subsurface boundaries and the generation of surface waves near basin edges.

1.6.2 Methods of Evaluation

Development of suitable design ground motions, and estimation of appropriate foundations loading, generally requires evaluation of anticipated site response. This is usually accomplished using empirical or analytical methods. For small bridges, or for projects in which detailed subsurface information is not available, the empirical approach is more common. For larger and more important structures, a subsurface exploration program is generally undertaken to determine whether site effects can be evaluated empirically, or if site-specific analytical evaluation of site response is required.

1.6.2.1 Empirical Methods

In the absence of site-specific information, local site effects can be estimated on the basis of empirical correlation to measured site response from past earthquakes. The database of strong ground motion records has increased tremendously over the past 30 years. Division of the records within this database according to general site conditions has allowed the development of empirical correlations for different site conditions.

Since that time, a number of approaches have been taken to the empirical estimation of site effects. Most express site effects in terms of period-dependent amplification factors defined as the ratio of ground surface response spectral acceleration (usually 5% damping) to reference motion spectral acceleration for a given site condition. The available methods use different characteristics to describe site conditions, and some use different definitions of reference motions.

Reference motions are generally taken as recorded rock motions (Boatwright et al., 1991), most commonly "soft rock" such as that commonly associated with the western United States, having a typical shear wave velocity of 760 m/sec. In other cases (e.g., Field and Jacob, 1995; Sokolov, 1997), median rock spectra from GMPEs are used for the reference motion values. Site conditions have been characterized in terms of surficial geology, geotechnical classification (Seed and Idriss, 1982; Dickenson, 1994; Rodriguez-Marek et al., 2001), and near-surface shear wave velocity (Borcherdt, 1994; Choi and Stewart, 2005; BSSC, 2009). The latter approach, in which site conditions are characterized by the average shear wave velocity of the upper 30 m of a profile, that is,

$$V_{s30} = \frac{30m}{t_t} = \frac{30m}{\sum_{i=1}^{n} h_i / V_{s,i}} \tag{1.22}$$

where t_t = travel time for shear wave in upper 30 m of profile, h_i = thickness of i^{th} sublayer in upper 30 m, and n = number of sublayers comprising upper 30 m of profile, has become common. Choi and Stewart (2005) proposed that a median amplification factor could be estimated as

$$AF = \exp\left[c \ln\left(\frac{V_{s30}}{V_{ref}} \right) + b \ln\left(\frac{PHA_{rock}}{0.1} \right) \right] \tag{1.23}$$

where V_{ref} = reference site velocity, PHA_{rock} is the reference site peak acceleration (in g), and b and c are factors obtained by regression. The second term in the brackets in Equation 1.23 accounts for nonlinear response, in which the degree of amplification depends on the amplitude of the input motion. The value of b, therefore, is negative with an effect that increases with decreasing V_{s30}. Values of the amplification factor for periods between 0.3 and 1.0 seconds are shown in Figure 1.17 amplification at 1.0 seconds is

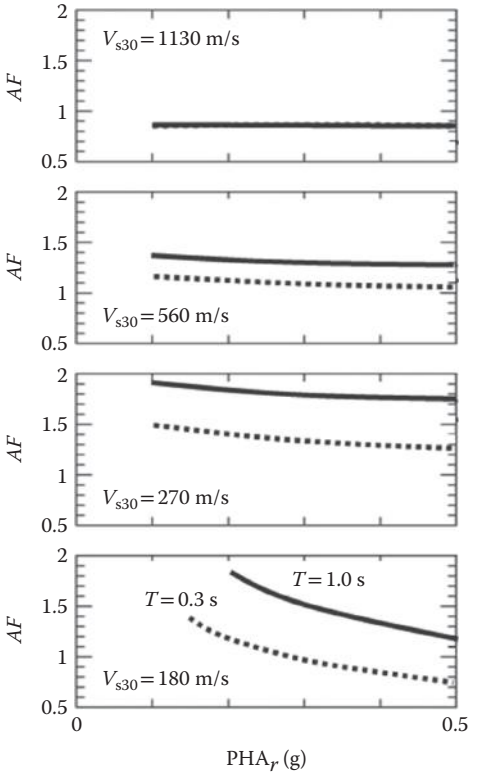

FIGURE 1.17 Variation of amplification factors for $S_a(0.3)$ and $S_a(1.0)$ as function of peak rock acceleration for different V_{s30} values.

TABLE 1.5 Estimation of Site Class

Site Class	Soil Profile Name	Soil Shear Wave Velocity, $\overline{v}_s$, (ft./s)	Standard Penetration Resistance, $\overline{N}$	Soil Undrained Shear Strength, $\overline{s}_u$ (psf)
A	Hard rock	$\overline{v}_s > 5000$	N/A	N/A
B	Rock	$2500 < \overline{v}_s \leq 5000$	N/A	N/A
C	Very dense soil and soft nock	$1200 < \overline{v}_s \leq 2500$	$\overline{N} > 50$	>2000 psf
D	Stiff soil profile	$600 \leq \overline{v}_s < 1200$	$15 \leq \overline{N} \leq 50$	1000 to 2000 psf
E	Stiff soil profile	$\overline{v}_s < 600$	$\overline{N} < 15$	<1000 psf
E	—	Any profile with more than 10 ft. of soil having the characteristics 1. Plasticity index $PI > 20$ 2. Moisture content $w \geq 40\%$ 3. Undrained shear strength $\overline{s}_u < 500$ psf		
F	—	Any profile containing soils having one or more of the following characteristics 1. Soils vulnerable to potential failure or collapse under seismic loading such as liquefiable soils, quick and highly sensitive days, collapsible weakly cemented soils 2. Peats and/or highly organic clays ($H > 10$ ft. of peat and/or highly organic clay where H = thickness of soil) 3. Very high plasticity clays ($H > 25$ ft. with plasticity index $PI > 75$) 4. Very thick soft/medium stiff clays ($H > 120$ ft.)		

Source: AASHTO. *Guide Specifications for LRFD Seismic Bridge Design*, 1st Edition. American Association of State Highway and Transportation Officials, Washington, DC, 2011.

generally greater than at 0.3 seconds by an amount that increases with decreasing V_{s30}. The effects of nonlinearity, reflected in the slopes of the amplification factor curves, also increase with decreasing V_{s30} and decreasing structural period.

Recent GMPEs have included site terms with function forms similar to those of recent amplification functions. The manner in which the site term coefficients are determined vary from one GMPE to another, but the basic trends of amplification factor with V_{s30} and input motion amplitude are similar.

Bridge codes have historically used relatively simple site classification schemes. The AASHTO code (AASHTO, 2011) determines site class based on V_{s30} but also allows average standard penetration test (SPT) resistances or average undrained strengths to be used when shear wave velocity data is not available. The average SPT resistances and undrained strengths are computed as

$$\overline{N} = \frac{30m}{\sum_{i=1}^{n} h_i / N_i} \quad \overline{s}_u = \frac{30m}{\sum_{i=1}^{n} h_i / s_{u,i}} \tag{1.24}$$

and the criteria indicated in Table 1.5 used to classify the soil profile into one of the six types.

The reasonableness of empirically based methods for estimation of site response effects depends on the extent to which site conditions match the site conditions in the databases from which the empirical relationships were derived. Whether in the form of amplification factors or GMPEs, empirical expressions of site effects are based on regression analyses, and therefore correspond best to sites with characteristics, such as shear wave velocity profiles, that are similar to the average characteristics of the profiles in the databases upon which the expressions are based. It is important to recognize the empirical nature of such methods and the significant uncertainty inherent in the results they produce.

1.6.2.2 Analytical Methods

When sufficient information to characterize the geometry and dynamic properties of subsurface soil layers is available, local site effects may be computed by site-specific ground response analyses. Site-specific analyses are most useful for sites whose characteristics are significantly different than those

of "average" sites with the same value of V_{s30}—sites with highly variable V_s profiles, sites with strong impedance contrasts (i.e., abrupt changes in stiffness), or other unusual characteristics. Site response analyses are also useful for prediction of stresses and deformations below the ground surface, which can be important for a number of applications but are not provided by amplification factors or GMPEs. Ground response analyses may be conducted in one, two, or three dimensions; one-dimensional analyses are most common, but the topography of many bridge sites may require two-dimensional analyses.

1.6.2.3 Basic Concepts

The simplest possible case of site response would consist of a uniform layer of visco-elastic soil of density, ρ, shear modulus, G, viscosity, η, and thickness, H, resting on rigid bedrock and subjected to vertically propagating shear waves (Figure 1.18). The response of the layer would be governed by the wave equation,

$$\rho\frac{\partial^2 u}{\partial t^2} = G\frac{\partial^2 u}{\partial z^2} + \eta\frac{\partial^3 u}{\partial z^2 \partial t} \tag{1.25}$$

which has a solution that can be expressed in the form of upward and downward traveling waves. At certain frequencies, these waves interfere constructively to produce increased amplitudes; at other frequencies, the upward and downward traveling waves tend to cancel each other and produce lower amplitudes. Such a system can easily be shown to have an infinite number of natural frequencies and mode shapes (Figure 1.18) given by

$$\omega_n = \frac{v_s}{H}\left(\frac{\pi}{2} + n\pi\right) \quad \text{and} \quad \phi_n = \cos\left[\frac{z}{H}\left(\frac{\pi}{2} + n\pi\right)\right] \tag{1.26}$$

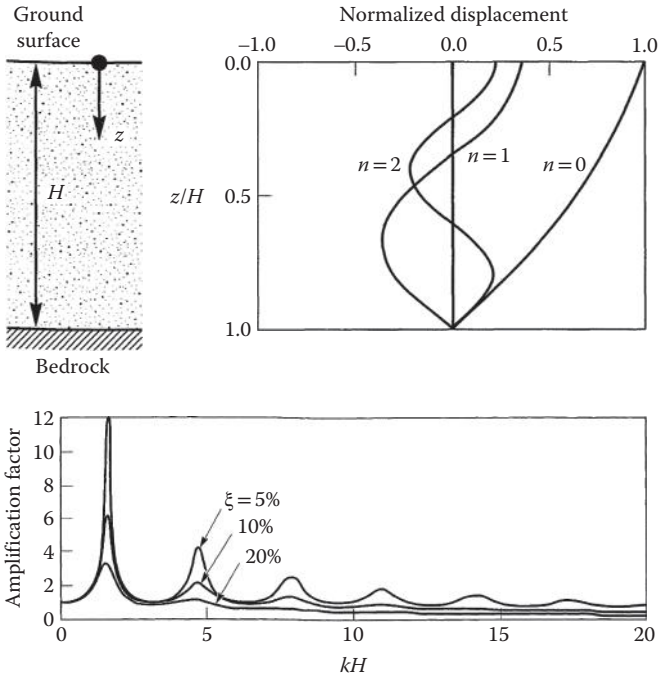

FIGURE 1.18 Illustration of (top) mode shapes and (bottom) amplification function for uniform elastic layer underlain by rigid boundary. (From Kramer, S. L., *Geotechnical Earthquake Engineering*, Prentice-Hall, Upper Saddle River, NJ, 1996. With permission.)

Note that the fundamental, or characteristic site period, is given by $T_s = 2\pi/\omega_o = 4H/v_s$. The ratio of ground surface to bedrock amplitude can be expressed in the form of an "amplification function" as

$$A(\omega) = \frac{1}{\sqrt{\cos^2\left(\omega H/v_s\right) + \left[\xi\left(\omega H/v_s\right)^2\right]}} \tag{1.27}$$

Figure 1.18 shows the amplification function that illustrates the frequency-dependent nature of site amplification. The amplification factor reaches its highest value when the period of the input motion is equal to the characteristic site period. More realistic site conditions produce more complicated amplification functions, but all amplification functions are frequency-dependent. In a sense, the surficial soil layers act as a filter that amplifies certain frequencies and de-amplifies others. The overall effect on site response depends on how these frequencies match up with the dominant frequencies in the input motion.

The example illustrated above is mathematically convenient, but unrealistically simple for application to actual sites. First, the assumption of rigid bedrock implies that all downward-traveling waves are perfectly reflected back up into the overlying layer. Although generally quite stiff, bedrock is not perfectly rigid and therefore a portion of the energy in a downward-traveling wave is transmitted into the bedrock to continue traveling downward—as a result, the energy carried by the reflected wave that travels back up is diminished. The relative proportions of the transmitted and reflected waves depend on the ratio of the specific impedance of the two materials on either side of the boundary. At any rate, the amount of wave energy that remains within the surficial layer is decreased by waves radiating into the underlying rock. The resulting reduction in wave amplitudes is often referred to as "radiation damping." Second, subsurface stratigraphy is generally more complicated than that assumed in the example. Most sites have multiple layers of different materials with different specific impedances. The boundaries between the layers may be horizontal or may be inclined, but all will reflect and refract seismic waves to produce wavefields that are much more complicated than described here. This is often particularly true in the vicinity of bridges located in fluvial geologic environments where soil stratigraphy may be the result of an episodic series of erosional and depositional events. Third, site topography is generally not flat, particularly in the vicinity of bridges, which may be supported in sloping natural or man-made materials, or on man-made embankments. Topographic conditions can strongly influence the amplitude and frequency content of ground motions. Finally, subsurface conditions can be highly variable, particularly in the geologic environments in which many bridges are constructed. Conditions may be different at each end of a bridge and even at the locations of intermediate supports—this effect is particularly true for long bridges. These factors, combined with the fact that seismic waves may reach one end of the bridge before the other, can reduce the coherence of ground motions. Different motions transmitted to a bridge at different support points can produce loads and displacements that would not occur in the case of perfectly coherent motions.

Unlike most structural materials, soils are highly nonlinear, even at very low strain levels. This nonlinearity causes soil stiffness to decrease and material damping to increase with increasing strain amplitude. The variation of stiffness with strain can be represented in two ways—by nonlinear backbone (stress–strain) curves or by modulus reduction curves, both of which are related as illustrated in Figure 1.19. The modulus reduction curve shows how the secant shear modulus of the soil decreases with increasing strain amplitude. To account for the effects of nonlinear soil behavior, ground response analyses are generally performed using one of two basic approaches: the equivalent linear approach or the nonlinear approach.

In the equivalent linear approach, a linear analysis is performed using shear moduli and damping ratios that are based on an initial estimate of strain amplitude. The strain level computed using these properties is then compared with the estimated strain amplitude and the properties adjusted until the computed strain levels are very close to those corresponding to the soil properties. Using this iterative approach, the effects of nonlinearity are approximated in a linear analysis by the use of strain-compatible soil properties. Modulus reduction and damping behavior has been shown to be influenced by soil plasticity, with highly plastic soils

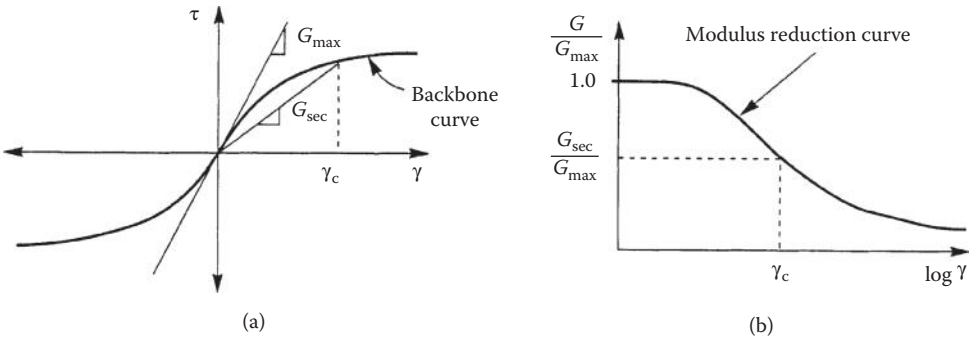

FIGURE 1.19 Relationship between (a) backbone curve and (b) modulus reduction curve.

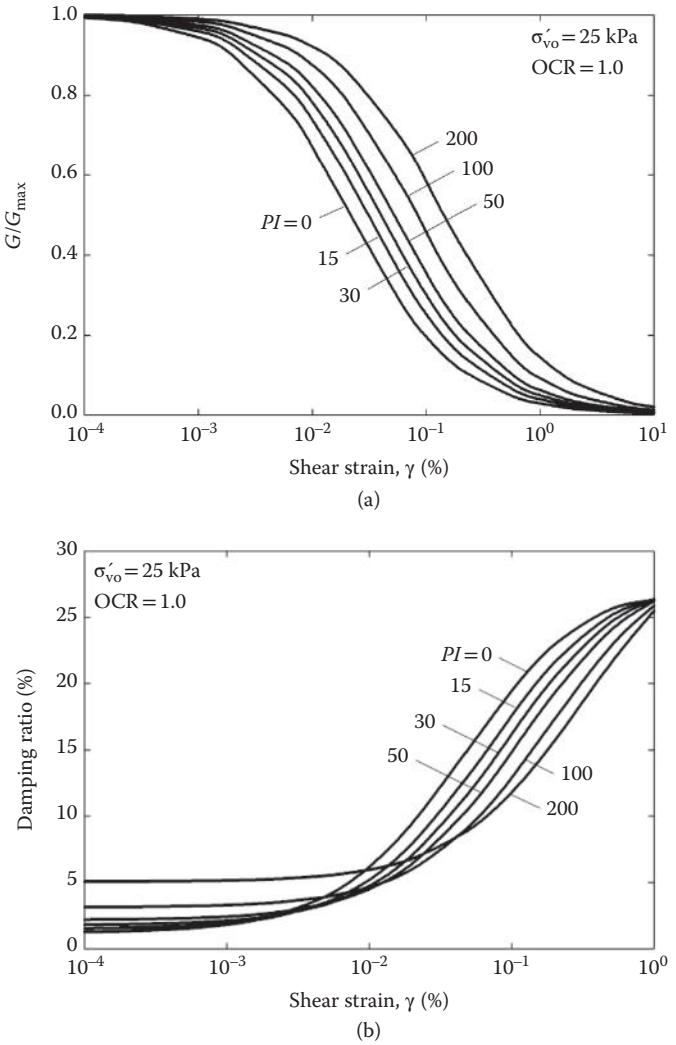

FIGURE 1.20 Equivalent linear soil behavior: (a) modulus reduction curves and (b) damping curves from relationships of Darendeli (2001) (From Darendeli, M. B., *Ph. D. Dissertation*, University of Texas at Austin, Austin, TX, 2001.)

exhibiting higher linearity and lower damping than low plasticity soils (Figure 1.20). The equivalent linear approach has been incorporated into such computer programs as SHAKE (Schnabel et al., 1972), ProShake (EduPro Civil Systems, Inc., 1998), Shake2000 (Ordonez, 2011), and DeepSoil (Hashash and Park, 2001) for one-dimensional analyses, Quad4M (Hudson et al., 1994), Quake/W (GeoSlope, 2012), and FLUSH (Lysmer et al., 1975) for two-dimensional analyses, and TLUSH (Kagawa et al., 1981) for three-dimensional analyses.

In the nonlinear approach, the equations of motion are assumed to be linear over each of a series of small time increments. This allows the response at the end of a time increment to be computed from the conditions at the beginning of the time increment and the loading applied during the time increment. At the end of the time increment, the properties are updated for the next time increment. In this way, the stiffness of each element of soil can be changed depending on the current and past stress conditions and hysteretic damping can be modeled directly. For seismic analysis, the nonlinear approach requires a constitutive (stress–strain) model that is capable of representing soil behavior under dynamic loading conditions. Such models can be complicated, and can require calibration of a large number of soil parameters by extensive laboratory testing. With a properly calibrated constitutive model, however, nonlinear analyses can provide reasonable predictions of site response and have two significant advantages over equivalent linear analyses. First, nonlinear analyses are able to predict permanent deformations such as those associated with ground failure (Section 1.8). Second, nonlinear analyses are able to account for the generation, redistribution, and eventual dissipation of porewater pressures, which makes them particularly useful for sites that may be subject to liquefaction and/or lateral spreading. The nonlinear approach has been incorporated into such computer programs as DeepSoil (Hashash and Park, 2001), DMOD2000 (Matasovic and Ordonez, 2011), TESS (Pyke, 2000), and SUMDES (Li et al., 1992) for one-dimensional analysis, and TARA (Finn et al., 1986) for two-dimensional analyses. General purpose programs such as FLAC (Itasca Consulting Group, 1995) and Plaxis (2012) can also be used for nonlinear two-dimensional analyses. In practice, however, the use of nonlinear analyses has lagged behind the use of equivalent linear analyses, principally because of the difficulty in characterizing nonlinear constitutive model parameters.

1.6.3 Site Effects for Different Soil Conditions

As indicated previously, soil deposits act as filters—amplifying response at some frequencies and de-amplifying it at others. The greatest degree of amplification occurs at frequencies corresponding to the characteristic site period, $T_s = 4H/v_s$. Because the characteristic site period is proportional to shear wave velocity and inversely proportional to thickness, it is clear that the response of a given soil deposit will be influenced by the stiffness and thickness of the deposit. Thin and/or stiff soil deposits will amplify the short-period (high frequency) components and thick and/or soft soil deposits will amplify the long-period (low frequency) components of an input motion. As a result, generalizations about site effects for different soil conditions are generally based on the average stiffness and thickness of the soil profile.

These observations of site response are reflected in bridge design codes. For example, the 2009 Standard Specifications for Highway Bridges (AASHTO, 2011) require the use of design spectrum based on ground motions with a 975-yr return period. The AASHTO design spectrum is based on three mapped spectral acceleration values—zero-period spectral acceleration (or PGA), a short-period spectral acceleration, S_s, and a longer-period (1.0 second) spectral acceleration, S_1. These values are modified by factors (F_{PGA}, F_a, and F_v—see Tables 1.6 through 1.8) intended to account for local site effects to obtain the design values

$$\begin{aligned} A_s &= F_{PGA}\text{PGA} \\ S_{DS} &= F_a S_s \\ S_{D1} &= F_v S_1 \end{aligned} \tag{1.28}$$

TABLE 1.6 Values of F_{PGA}

	Mapped Peak Ground Acceleration, PGA				
Site Class	≤0.1	0.2	0.3	0.4	≥0.5
A	0.8	0.8	0.8	0.8	0.8
B	1.0	1.0	1.0	1.0	1.0
C	1.2	1.2	1.1	1.0	1.0
D	1.6	1.4	1.2	1.1	1.0
E	2.5	1.7	1.2	0.9	0.9

TABLE 1.7 Values of F_a

	Short-Period Acceleration Parameter, S_s				
Site Class	≤0.25	0.5	0.75	1.0	≥1.25
A	0.8	0.8	0.8	0.8	0.8
B	1.0	1.0	1.0	1.0	1.0
C	1.2	1.2	1.1	1.0	1.0
D	1.6	1.4	1.2	1.1	1.0
E	2.5	1.7	1.2	0.9	0.9

TABLE 1.8 Values of F_v

	1 Second Acceleration Coefficient, S_1				
Site Class	≤01	0.2	0.3	0.4	≥0.5
A	0.8	0.8	0.8	0.8	0.8
B	1.0	1.0	1.0	1.0	1.0
C	1.7	1.6	1.5	1.4	1.3
D	2.4	2.0	1.8	1.6	1.5
E	3.5	3.2	2.8	2.4	2.4

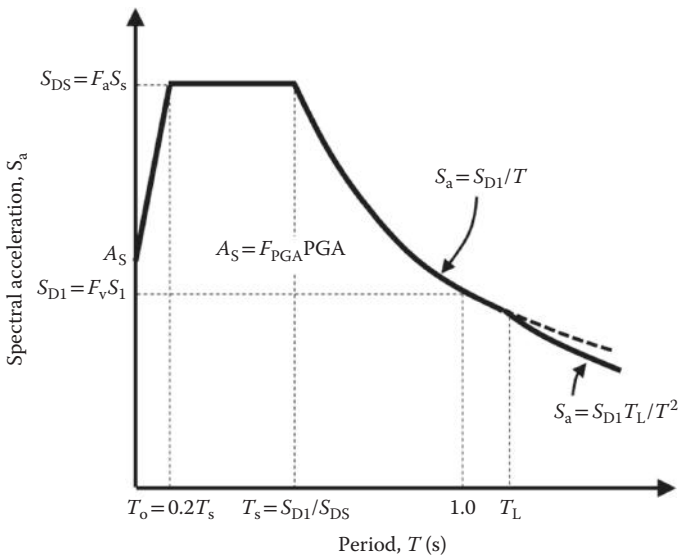

FIGURE 1.21 Construction of AASHTO design spectrum. (After AASHTO. *Guide Specifications for LRFD Seismic Bridge Design*, 2nd Edition. American Association of State Highway and Transportation Officials, Washington, DC, 2011.)

These values are then used, along with a mapped long-period value, T_L, to define the design spectrum as indicated in Figure 1.21.

1.7 Earthquake-Induced Settlement

Settlement is an important consideration in the design of bridge foundations. In most cases, settlement results from *consolidation*, a process that takes place relatively slowly as porewater is squeezed from the soil as it seeks equilibrium under a new set of stresses. Consolidation settlements are most significant in fine-grained soils such as silts and clays. However, the tendency of coarse-grained soils (sands and gravels) to densify because of vibration is well known, in fact, it is frequently relied upon for efficient compaction of sandy soils. Densification because of the cyclic stresses imposed by earthquake shaking can produce significant settlements during earthquakes. Although caused by consolidation or earthquakes, bridge designers are concerned with total settlement and, because settlements rarely occur uniformly, also with differential settlement. Differential settlement can induce very large loads in bridge structures.

Although bridge foundations may settle due to shearing failure in the vicinity of abutments (Chapter 6 of *Bridge Engineering Handbook, Second Edition: Substructure Design*), shallow foundations (Chapter 8, of *Bridge Engineering Handbook, Second Edition: Substructure Design*), and deep foundations (Chapter 9 of *Bridge Engineering Handbook, Second Edition: Substructure Design*), this section deals with settlement due to earthquake-induced soil densification. Densification of soils beneath shallow bridge foundations can cause settlement of the foundation. Densification of soils adjacent to deep foundations can cause downdrag loading on the foundations (and bending loading if the foundations are battered). Densification of soils beneath approach fills can lead to differential settlements at the ends of the bridge that can be so abrupt as to render the bridge useless.

Accurate prediction of earthquake-induced settlements is difficult. Errors of 25%–50% are common in estimates of consolidation settlement, so even less accuracy should be expected in the more complicated case of earthquake-induced settlement. Nevertheless, procedures have been developed that account for the major factors known to influence earthquake-induced settlement and that have been shown to produce reasonable agreement with many cases of observed field performance. Such procedures are generally divided into cases of dry sands and saturated sands.

1.7.1 Settlement of Dry Sands

Dry sandy soils are often found above the water table in the vicinity of bridges. The amount of densification experienced by dry sands depends on the density of the sand, the amplitude of cyclic shear strain induced in the sand, and on the number of cycles of shear strain applied during the earthquake.

Laboratory studies (Seed and Silver, 1972; Youd, 1972; Tokimatsu and Seed, 1987; Duku et al., 2008) have determined the primary factors that control the volumetric strain induced in dry sand specimens subjected to cyclic testing- soil density, amplitude and duration of shaking, and cyclic shear strain amplitude. Tokimatsu and Seed (1987) developed a procedure for estimation of volumetric strain, ε_v, due to seismic shaking, and proposed that settlements for one-dimensional compression (i.e., for level-ground sites) could be estimated by integrating volumetric strain over the thickness of the sand layer, that is,

$$\Delta H = \int \varepsilon_v \, dz \approx \sum_{i=1}^{n} \varepsilon_{v,i} \Delta z_i \tag{1.29}$$

where n is the number of sand sublayers and ε_v was determined as a function of relative density or SPT resistance and cyclic shear strain amplitude. Following the results of Pyke et al. (1975), the volumetric strain was recommended to be doubled to account for the effects of multi-directional shaking. The Tokimatsu and Seed (1987) procedure required a somewhat cumbersome iterative procedure for

estimation of shear strain amplitude; Pradel (1998) developed an approximation that eliminated the need for iteration while producing results that were consistent with those of Tokimatsu and Seed (1987).

Recently, Duku et al. (2008) used cyclic simple shear test data from a variety of sands and found that the volumetric strain after N cycles of shear strain of amplitude, γ_c, could be estimated as

$$\varepsilon_{v,N} = 5.38\left(0.29\ln(N)+0.215\right)\left(\frac{\sigma'_{vo}}{p_a}\right)^{-0.29}\exp\left(-0.023D_r\right)\left(\gamma_c-\gamma_{tv}\right)^{1.2} \tag{1.30}$$

where σ'_{vo} = initial vertical effective stress, p_a = atmospheric pressure, D_r = relative density, and γ_{tv} = volumetric threshold shear strain (typically 0.01%–0.03%). The influence of such factors as degree of saturation (from 0%–90%), frequency, soil fabric, composition, and particle angularity were all found to be small. Little case history data for dry sand settlement is available to date, so volumetric strains must be based on laboratory test results. Because of the high air permeability of sands, settlement of dry sands occurs almost instantaneously.

1.7.2 Settlement of Saturated Sands

The dissipation of excess porewater pressures generated in saturated sands (reconsolidation) can lead to settlement following earthquakes. Settlements of 50–100 cm were observed on Port Island and Rokko Island in Kobe, Japan following the 1995 Hyogo-ken Nambu earthquake. Large and widespread settlements were observed across the area surrounding Christchurch, New Zealand following the M_w 6.2 Christchurch earthquake of February, 2012; damaging settlements of up to 1 m were observed in residential areas east of downtown Christchurch. Because water flows much more slowly through soil than air, settlements of saturated sands occur much more slowly than earthquake-induced settlements of dry sands. Nevertheless, the main factors that influence the magnitude of saturated soil settlements are basically the same as those that influence the dry sands.

Several investigators (Tokimatsu and Seed, 1984; Ishihara and Yoshimine, 1992; Shamoto et al., 1998; Ohsaki, 1970) have proposed procedures for estimating postearthquake settlement of saturated sands. The procedures generally involve prediction of volumetric strain as a function of some measure of soil density (most commonly SPT or CPT resistance) and level of ground shaking (e.g., CSR or FS_L), followed by integration of volumetric strain over depth as in Equation 1.31 (dry sand section). For some models, a weighting, or correction, factor is included in the integration to better match case history data. Cetin et al. (2009) proposed that the median settlement, s, of a profile containing saturated sand could be estimated from

$$s = 1.15\frac{\sum_{i=1}^{n} t_i\left(1-d_i/18\right)\varepsilon_{v,i}}{\sum_{i=1}^{n} t_i\left(1-d_i/18\right)}\sum_{i=1}^{n} t_i \tag{1.31}$$

where t_i = thickness of ith layer, d_i = depth to center of ith layer in meters, and

$$\varepsilon_{v,i} = 1.879\ln\left[\frac{780.416\ln CSR_{SS,20,1D,1atm}-(N_1)_{60,cs}+2442.465}{636.613(N_1)_{60,cs}+306.732}\right]+5.583 \tag{1.32}$$

The cyclic stress ratio (CSR) used in this expression corresponds to 20 cycles of uniform, unidirectional, cyclic simple shear loading at an initial vertical effective stress of 100 kPa, and is computed as

$$CSR_{SS,20,1D,1atm} = \frac{CSR_{field}}{K_{md}K_{M_w}K_\sigma} \tag{1.33}$$

where K_{md}, K_{Mw}, and K_σ are correction factors for multi-directional shaking, ground motion duration, and initial effective stress, respectively. The correction factors are computed as

$$K_{md} = 0.361 \ln D_r - 0.579$$
$$K_{M_w} = 87.1 / M_w^{2.217} \tag{1.34}$$
$$K_\sigma = \left(\sigma'_{vo}/p_a\right)^{-0.005 D_r}$$

1.8 Ground Failure

Strong earthquake shaking can produce dynamic response of soils that is so energetic that the stress waves exceed the strength of the soil. In such cases, ground failure characterized by permanent soil deformations may occur. Ground failure may be caused by weakening of the soil or by temporary exceedance of the strength of the soil by transient inertial stresses. The former case results in phenomena such as liquefaction and lateral spreading and the latter in inertial failures of slopes and retaining wall backfills.

1.8.1 Liquefaction

The term "liquefaction" has been widely used to describe a range of phenomena in which the strength and stiffness of a soil deposit is reduced because of the generation of porewater pressure. It occurs most commonly in loose, saturated sands, although it has also been observed in gravels and nonplastic silts. The effects of liquefaction can range from massive landslides with displacements measured in tens of meters to relatively small slumps or spreads with small displacements. Many bridges, particularly those that cross bodies of water, are located in areas with geologic and hydrologic conditions that tend to produce liquefaction.

The mechanisms that produce liquefaction-related phenomena can be divided into two categories. The first, flow liquefaction, can occur when the shear stresses required for static equilibrium of a soil mass are greater than the shear strength of the soil in its liquefied state. Although not common, flow liquefaction can produce tremendous instabilities known as flow slide failures. In such cases, the earthquake serves to trigger liquefaction, but the large deformations that result are actually driven by the preexisting static stresses. The second phenomenon, cyclic mobility, occurs when the initial static stresses are less than the strength of the liquefied soil. The effects of cyclic mobility lead to deformations of sloping ground that develop incrementally during the period of earthquake shaking, and are commonly referred to as "lateral spreading." Lateral spreading can occur on very gentle slopes, in the vicinity of free surfaces such as river banks, and beneath and adjacent to embankments. Lateral spreading occurs much more frequently than flow failure, and can cause significant distress to bridges and their foundations.

1.8.2 Liquefaction Susceptibility

The first step in an evaluation of liquefaction hazards is the determination of whether the soil is susceptible to liquefaction. If the soils at a particular site are not susceptible to liquefaction, liquefaction hazards do not exist and the liquefaction hazard evaluation can be terminated. If the soil is susceptible, however, the issues of initiation and effects of liquefaction must be considered.

Liquefaction occurs most readily in loose, clean, uniformly graded, and saturated soils. Therefore, geologic processes that sort soils into uniform grain size distributions and deposit them in loose states produce soil deposits with high liquefaction susceptibility. As a result, fluvial deposits, and colluvial and aeolian deposits when saturated, are likely to be susceptible to liquefaction. Liquefaction also occurs in alluvial, beach, and estuarine deposits, but not as frequently as in those previously listed. Because bridges are commonly constructed in such geologic environments, liquefaction is a frequent and important consideration in their design.

The composition of a soil will also influence its susceptibility to liquefaction. Clean sands are highly susceptible to liquefaction, and extensive liquefaction has also been observed in coarse, nonplastic silts

and silty sands. The susceptibility of soils of low plasticity is a subject of ongoing research. Idriss and Boulanger (2004) considered soils with plasticity index, $PI < 3$ to be "sand-like" and therefore susceptible to liquefaction, soils with $PI > 8$ to be "clay-like" and thus not susceptible to liquefaction (although still potentially susceptible to softening/weakening through mechanisms other than liquefaction), and soils of intermediate PI to be in a transitional zone best addressed by laboratory testing. Idriss and Boulanger (2006) suggested that $PI = 7$ represented a conservative upper limit for soils exhibiting sand-like behavior. Bray and Sancio (2006) considered soils with $PI < 12$ and $w_c/LL > 0.85$ to be susceptible to liquefaction, soils with $PI > 18$ or $w_c/LL < 0.80$ to be nonsusceptible, and other soils to be potentially susceptible and best characterized by laboratory testing.

1.8.3 Initiation of Liquefaction

The fact that a soil deposit is susceptible to liquefaction does not mean that liquefaction will occur in a given earthquake. Liquefaction must be triggered by some disturbance, such as earthquake shaking, with sufficient strength to exceed the liquefaction resistance of the soil. Even a liquefaction-susceptible soil will have some liquefaction resistance. Evaluating the potential for the occurrence of liquefaction (liquefaction potential) involves comparison of the loading imposed by the anticipated ground motion with the liquefaction resistance of the soil. Liquefaction potential is most commonly evaluated using the cyclic stress approach in which both earthquake loading and liquefaction resistance are expressed in terms of cyclic stresses, thereby allowing direct and consistent comparison.

A number of procedures for evaluation of liquefaction potential have been developed. Youd et al. (2002) developed a procedure based on the consensus views of leading researchers and practitioners in the mid-1990s. Idriss and Boulanger (2004) used new data and a critical state-influenced framework to develop updated procedures that produced results generally consistent with those of Youd et al. (2002); the following illustration of liquefaction potential evaluation is based on the procedure of Idriss and Boulanger (2004).

1.8.3.1 Characterization of Earthquake Loading

The level of porewater pressure generated by an earthquake is related to the amplitude and duration of earthquake-induced shear stresses. Such shear stresses can be predicted in a site-response analysis using either the equivalent linear method or nonlinear methods. Alternatively, they can be estimated using a simplified approach that does not require site response analyses.

Early methods of liquefaction evaluation were based on the results of cyclic triaxial tests performed with harmonic (constant amplitude) loading, and it remains customary to characterize loading in terms of equivalent shear stress amplitude:

$$\tau_{cyc} = 0.65\,\tau_{max} \tag{1.35}$$

When sufficient information is available to perform site response analyses, it is advisable to compute τ_{max} in a site response analysis and use Equation 1.35 to compute τ_{cyc}. When such information is not available, τ_{cyc} at a particular depth can be estimated (Seed and Idriss, 1971) as

$$\tau_{cyc} = 0.65\frac{a_{max}}{g}\sigma_v r_d \tag{1.36}$$

where a_{max} is the peak ground surface acceleration, g is the acceleration of gravity, σ_v is the total vertical stress at the depth of interest, and r_d is the value of a site response reduction factor that can be estimated from

$$r_d = \exp\left[\alpha(z) + \beta(z)M_w\right] \tag{1.37}$$

where z is the depth of interest in meters and

$$\alpha(z) = -1.012 - 1.126 \sin\left(\frac{z}{11.73} + 5.133\right) \tag{1.38}$$

$$\beta(z) = 0.106 + 0.118 \sin\left(\frac{z}{11.28} + 5.142\right) \tag{1.39}$$

For evaluation of liquefaction potential, it is common to normalize τ_{cyc} by the initial (pre-earthquake) vertical effective stress, thereby producing the CSR

$$\mathrm{CSR}_{M_w=7.5} = \frac{\tau_{cyc}}{\sigma'_{vo}} \cdot \frac{1}{\mathrm{MSF}} \tag{1.40}$$

where MSF is a magnitude scaling factor that accounts for the increasing number of loading cycles that occur in the longer duration motions produced by larger magnitude earthquake, computed as

$$\mathrm{MSF} = \min\left\{\begin{array}{c} 6.9 \exp[-M_w/4] - 0.058 \\ 1.8 \end{array}\right\} \tag{1.41}$$

1.8.3.2 Characterization of Liquefaction Resistance

Although early liquefaction potential evaluations relied on laboratory tests to measure liquefaction resistance, increasing recognition of the deleterious effects of sampling disturbance on laboratory test results has led to the use of field tests for measurement of liquefaction resistance. Although the use of soil freezing and sampling techniques provide the potential for acquisition of undisturbed samples, liquefaction resistance is currently evaluated using in situ tests such as the SPT and the cone penetration test (CPT) and observations of liquefaction behavior in past earthquakes.

In this approach, liquefaction resistance is expressed as the lowest CSR for which liquefaction has been observed in the field case histories, and an in situ test measurement is generally used as a proxy for density. Two in situ tests are commonly used—the SPT that produces the resistance parameter, $(N_1)_{60}$, and the CPT that produces the resistance parameter, q_{c1N}. These parameters are computed from measured values, N_m and q_{cm}, respectively as

$$(N_1)_{60} = C_N \frac{ER}{60} N_m \tag{1.42}$$

and

$$q_{c1N} = C_N \frac{q_{cm}}{p_a} \tag{1.43}$$

where

$$C_N = \min\left\{\begin{array}{c} \left(p_a/\sigma'_{vo}\right)^n \\ 1.7 \end{array}\right\} \tag{1.44}$$

and $n = 0.784 - 0.0768\sqrt{(N_1)_{60}}$ or $n = 1.338 - 0.249 q_{c1N}^{0.264}$. An iterative procedure is required to determine C_N because it is a function of the same parameter ($(N_1)_{60}$ or q_{c1N}) it is used to compute.

Recent review of SPT- and CPT-based procedures for characterization of cyclic resistance ratio (CRR) (Idriss and Boulanger, 2004) resulted in recommendation of the curves shown in Figures 1.22 and 1.23. Because the value of the CSR given by the curve represents the minimum CSR required to produce liquefaction, it is commonly referred to as the "cyclic resistance ratio," (CRR). The SPT curve is for a

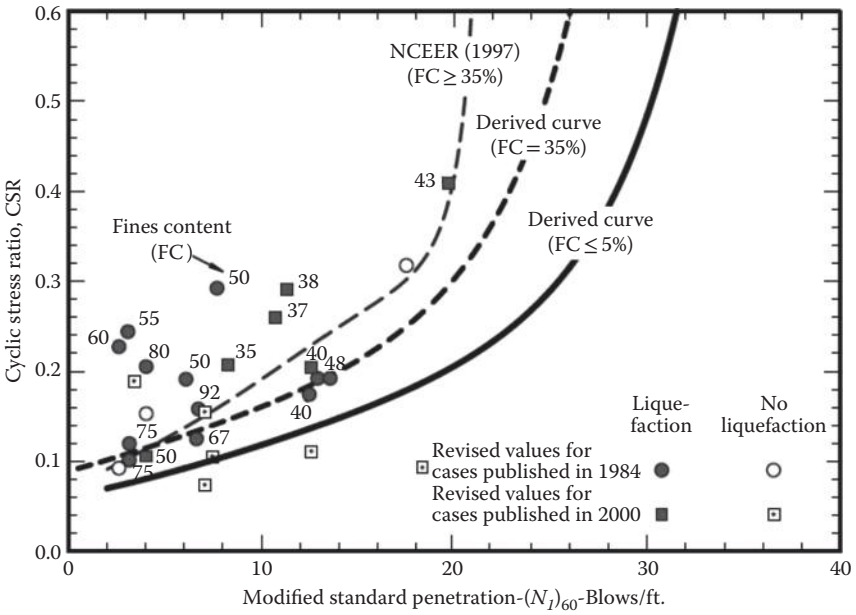

FIGURE 1.22 Relationship between cyclic resistance ratio and SPT resistance. (After Boulanger, R. W. and Idriss, I. M., *Report No. UCD/CGM- 04/01*. Center for Geotechnical Modeling, Dept. of Civil and Environmental Engineering, University of California, Davis, CA, 2004.)

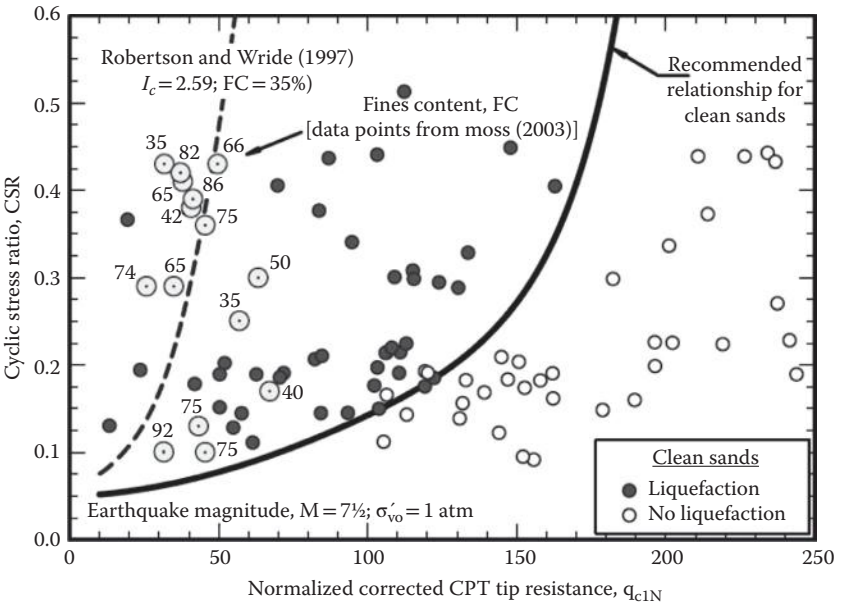

FIGURE 1.23 Relationship between cyclic resistance ratio and CPT resistance. (After Boulanger, R. W. and Idriss, I. M., *Report No. UCD/CGM- 04/01*. Center for Geotechnical Modeling, Dept. of Civil and Environmental Engineering, University of California, Davis, CA, 2004.)

clean sand and describes the liquefaction resistance of an element of soil at an initial vertical effective stress of 1 atm under level ground (zero initial shear stress) conditions subjected to ground motion from a magnitude 7.5 earthquake.

For silty sand with fines content, FC, an equivalent clean sand SPT resistance can be computed from

$$(N_1)_{60,cs} = (N_1)_{60} + \Delta(N_1)_{60} \tag{1.45}$$

where

$$\Delta(N_1)_{60} = \exp\left[1.63 + \frac{9.7}{FC} - \left(\frac{15.7}{FC}\right)^2\right] \tag{1.46}$$

and FC is in percent. For an arbitrary initial vertical effective stress, σ'_{vo}, the CSR can be computed as

$$CRR_{M=7.5,\sigma'_{vo}} = K_\sigma \cdot CRR_{M=7.5,\sigma'_{vo}=1atm} \tag{1.47}$$

where

$$K_\sigma = 1 - C_\sigma \ln\left(\frac{\sigma'_{vo}}{p_a}\right) \tag{1.48}$$

with

$$C_\sigma = \frac{1}{19.9 - 2.55\sqrt{(N_1)_{60}}} \text{ or } C_\sigma = \frac{1}{37.3 - 8.27\left(q_{c1N}\right)^{0.264}} \tag{1.49}$$

The CPT offers two distinct advantages over the SPT for evaluation of liquefaction resistance. First, the CPT provides a nearly continuous profile of penetration resistance, a characteristic that allows it to identify thin layers that can easily be missed in an SPT-based investigation. Second, the CPT shows greater consistency and repeatability than the SPT. However, the CPT has a shorter history of use, particularly in the United States, there is less case history data available for it than for the SPT, and it provides no sample for examination or index testing. Other procedures for CPT-based evaluation of liquefaction potential include those of Seed and De Alba (1986), Mitchell and Tseng (1990), Robertson and Wride (1977), and Olson (1997).

Liquefaction resistance has also been correlated to other in situ test measurements such as shear wave velocity (Stokoe et al., 1988; Tokimatsu et al., 1991; Andrus et al., 2004), and dilatometer index (Reyna and Chameau, 1991). In addition, probabilistic approaches that yield a probability of liquefaction have also been developed (Liao et al., 1988; Youd and Noble, 1997).

1.8.3.3 Characterization of Liquefaction Potential

After loading and resistance have both been characterized, the potential for initiation of liquefaction is commonly expressed in terms of a factor of safety against liquefaction, which is defined as

$$FS_L = CRR/CSR$$

A factor of safety less than 1.0 indicates that liquefaction is expected to occur. Liquefaction potential can also be characterized probabilistically as

$$P_L = P[FS_L, 1.0] = P[CRR < CSR]$$

1.8.4 Lateral Spreading

Lateral spreading has often caused damage to bridges and bridge foundations in earthquakes. Lateral spreading generally involves the lateral movement of soil at and below the ground surface, often in the form of relatively intact surficial blocks riding on a mass of softened and weakened soil. The lateral soil

movement can impose large lateral loads on abutments and wing walls, and can induce large bending moments in pile foundations. The damage produced by lateral spreading is closely related to the magnitude of the lateral soil displacements.

Because cyclic mobility, the fundamental phenomenon that produces lateral spreading, is so complex, analytical procedures for prediction of lateral spreading displacements have not yet reached the point at which they can be used for design. As a result, currently accepted procedures for prediction of lateral spreading displacements are empirically based.

Bartlett and Youd (1992) used multiple regression on a large database of lateral spreading case histories to develop empirical expressions for lateral spreading ground surface displacements. Youd et al. (2002) used an expanded and corrected version of the 1992 database to develop the predictive relationship

$$\log D_H = b_0 + b_1 M_w + b_2 \log R^* + b_3 R + b_4 \log W + b_5 \log S + b_6 \log T_{15} + b_7 \log(100 - F_{15}) + b_8 \log(D50_{15} + 0.1\,\text{mm}) \tag{1.50}$$

where D_H = horizontal displacement in meters, M_w = moment magnitude, W and S are as defined in Figure 1.24, T_{15} = cumulative thickness of saturated layers with $(N_1)_{60} < 15$, F_{15} = average fines content of soils comprising T_{15}, $D50_{15}$ = average mean grain size of soils comprising T_{15}, and $R^* = R + 10^{-0.89 M_w - 5.64}$. The values of the coefficients are presented in Table 1.9. The ranges of the variables used in the Youd et al. (2002) relationship are indicated in Figure 1.25 (note the region of verification as indicated in the figure within the table).

Zhang et al. (2004) made use of a laboratory test-based relationship between "maximum cyclic shear strain," relative density, and factor of safety against liquefaction (Ishihara and Yoshimine, 1992) to develop a cumulative shear strain model for prediction of lateral spreading displacement. Maximum cyclic shear strains were defined by Ishihara and Yoshimine (1992) as the maximum shear strain (in any direction) under transient loading conditions. Zhang et al. (2004) capped the maximum cyclic shear strains by the limiting shear strains proposed by Seed (1979) and used empirical relationships between relative density and penetration resistance (SPT or CPT) to allow lateral spreading displacement to be predicted in the following series of steps:

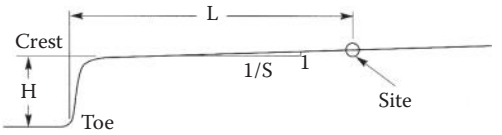

L = Distance from toe of free face to site
H = Height of free face (crest elev.–toe elev.)
W = Free-face ratio = (H/L) (100), in percent
S = Slope of natural ground toward channel in percent

FIGURE 1.24 Slope geometry notation for Youd et al. (2002) model. (After Youd, T. L., Hansen, C. M. and Bartlett, S. F. (2002). *J. Geotech. Geoenviron. Eng.*, 128(12), 1007–1017, 2002.)

TABLE 1.9 Coefficients for Youd et al. (2002) Model

Model	b_0	b_1	b_2	b_3	b_4	b_5	b_6	b_7	b_8
Ground slope	–16.213	1.532	–1.406	–0.012	0	0.338	0.540	3.413	–0.795
Free face	–16.713	1.532	–1.406	–0.012	0.592	0	0.540	3.413	–0.795

Variable	Description	Range
T_{15}	Equivalent thickness of saturated cohesionless soils (clay content ≤ 15%) in meters	1–15 m
M	Moment magnitude of the earthquake	6.0–8.0
Z_T	Depth to top of shallowest layer contributing to T_{15}	1–15 m
W	Free face ratio	1%–20%
S	Ground slope	0.1%–6%

F_{15}, $D50_{15}$

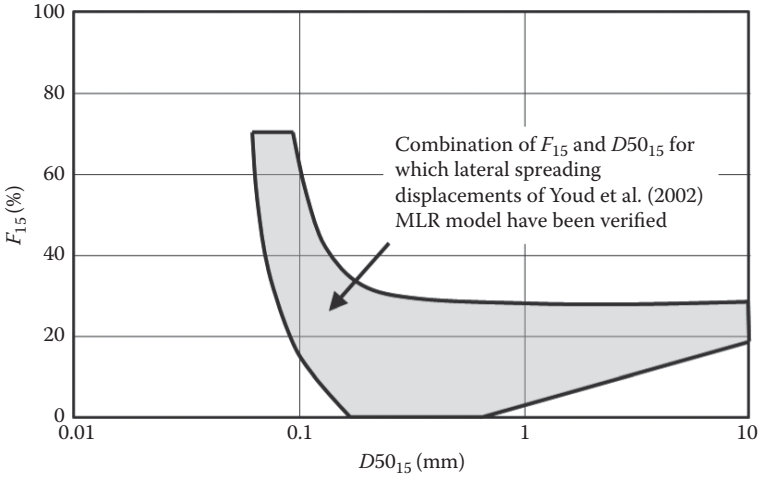

FIGURE 1.25 Recommended range of variable values for the Youd et al. (2002) predictive equation.

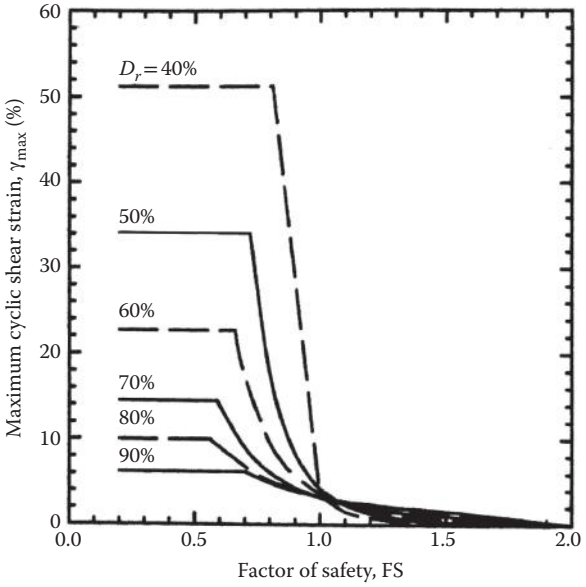

FIGURE 1.26 Variation of maximum cyclic shear strain with factor of safety and relative density. (After Zhang, G., Robertson, P. K., and Brachman, R. W. I., *J. Geotech. Geoenviron. Eng.*, 130(8), 861–871, 2004.)

1. Characterize the slope of interest as a ground slope case or a free-face case
2. Using Figure 1.24, compute the ground slope inclination, *S*, for ground slope cases, or the free-face ratio, *W*, for free-face cases
3. Divide the soil profile into a series of sublayers and determine the average SPT or CPT resistance for each sublayer
4. Compute the factor of safety against liquefaction for each sublayer
5. Using the penetration resistance and factor of safety against liquefaction, use Figure 1.26 to determine the maximum shear strain, τ_{max}
6. Compute the lateral displacement index, LDI by integrating maximum shear strains with depth over all potentially liquefiable layers, that is

$$\text{LDI} = \int_0^{z_{max}} \gamma_{max} dz \tag{1.51}$$

7. Compute the expected lateral spreading displacement as

$$D_H = \begin{cases} (S + 0.2) \cdot \text{LDI} & \text{ground slope case} \\ 6W^{-0.8} \cdot \text{LDI} & \text{free-face case} \end{cases} \tag{1.52}$$

1.8.5 Global Instability

Ground failure may also occur because of the temporary exceedance of the shear strength of the soil by earthquake-induced shear stresses. These failures may take the form of large, deep-seated soil failures that can encompass an entire bridge abutment or foundation. The potential for such failures, often referred to as global instabilities, must be evaluated during design.

Historically, inertial failures were evaluated using pseudo-static methods in which the transient, dynamic effects of earthquake shaking were represented by constant, pseudo-static accelerations. The resulting destabilizing pseudo-static forces were included in a limit equilibrium analysis to compute a pseudo-static factor of safety. A pseudo-static factor of safety greater than one was considered indicative of stability. However, difficulty in selection of the pseudo-static acceleration, interpretation of the significance of computed factors of safety <1.0, and increasing recognition that serviceability is closely related to permanent deformations led to the development of alternative approaches.

The most common current procedure uses pseudo-static principles to establish the point at which permanent displacements would begin, but then uses a simple slope analogy to estimate the magnitude of the resulting permanent displacements. This procedure is commonly known as the sliding block procedure (Newmark, 1965). Using the common assumptions of rigid, perfectly plastic behavior embedded in limit equilibrium analyses, a potentially unstable slope is considered to be analogous to a block resting on an inclined plane (Figure 1.27) in the sliding block procedure. In both cases, base accelerations above a certain level will result in permanent relative displacements of the potentially unstable mass.

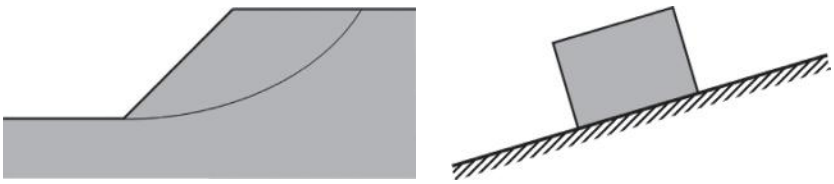

FIGURE 1.27 Illustration of analogy between (a) potentially unstable zone of soil and (b) sliding block for evaluation of permanent slope.

In the sliding block procedure, a pseudo-static analysis is performed to determine the horizontal pseudo-static acceleration that produces a factor of safety of 1.0. This pseudo-static acceleration, referred to as the yield acceleration, represents the level of acceleration above which permanent slope displacements are expected to occur. When the input acceleration exceeds the yield acceleration, the shear stress between the sliding block and the plane exceeds the available shear resistance and the block is unable to accelerate as quickly as the underlying plane. As a result, there is a relative acceleration between the block and the plane that lasts until the shear stress drops below the strength long enough to decelerate the block to zero relative acceleration. Integration of the relative acceleration over time yields a relative velocity, and integration of the relative velocity produces the relative displacement between the block and the plane. By this process, illustrated in Figure 1.28, the sliding block procedure allows estimation of the permanent displacement of a slope.

Saygili and Rathje (2008) performed sliding block analyses on a number of slopes with different yield accelerations using numerous ground motions, and evaluated the accuracy with which different ground motion intensity measures (and combinations of intensity measures) could predict computed displacements. For slopes with relatively shallow failure surfaces, the single (scalar) intensity measure that predicted permanent displacements with the lowest variability was peak acceleration; the predicted displacements were found to be log normally distributed with a median

$$D = \exp\left[5.52 - 4.43\left(\frac{k_y}{\text{PGA}}\right) - 20.39\left(\frac{k_y}{\text{PGA}}\right)^2 + 42.61\left(\frac{k_y}{\text{PGA}}\right)^3 - 28.74\left(\frac{k_y}{\text{PGA}}\right)^4 + 0.72\ln(\text{PGA})\right] \quad (1.53)$$

and standard deviation $\sigma_{\ln D} = 1.113$. Saygili and Rathje (2008) found that the variability in the predicted displacement could be substantially reduced with the addition of more ground motion information, and that by using two intensity measures, PGA and PGV, the median displacement could be expressed as

$$D = \exp\left[-1.56 - 4.58\left(\frac{k_y}{\text{PGA}}\right) - 20.84\left(\frac{k_y}{\text{PGA}}\right)^2 + 44.75\left(\frac{k_y}{\text{PGA}}\right)^3 - 30.50\left(\frac{k_y}{\text{PGA}}\right)^4 - 0.64\ln(\text{PGA}) + 1.55\ln\text{PGV}\right] \quad (1.54)$$

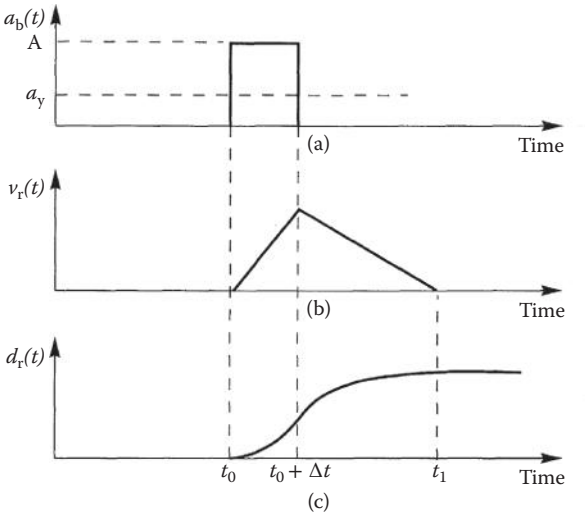

FIGURE 1.28 Illustration of computation of permanent slope displacements using sliding block method.

and the standard deviation would be reduced to $\sigma_{\ln D} = 0.41 + 0.52(k_y/\text{PGA})$.

For deeper failure mechanisms, Bray and Travasarou found that using spectral acceleration at a lengthened period (50% higher than the fundamental period) was better able to predict permanent slope displacements, and proposed that median displacements could be estimated as

$$D = \exp\left[-1.10 - 2.83\ln k_y - 0.333\left(\ln k_y\right)^2 + 0.566\ln k_y \ln S_a(1.5T_s) + 3.04\ln S_a(1.5T_s) - 0.244\left(\ln S_a(1.5T_s)\right)2 + 1.5T_s + 0.278(M-7)\right] \tag{1.55}$$

with a standard deviation $\sigma_{\ln D} = 0.66$.

1.8.6 Retaining Structures

Earth retaining structures are commonly constructed as parts of bridge construction projects and, in the form of abutment walls and wing walls, as parts of bridge structures themselves. However, there are many different types of retaining structures, several of which have developed in recent years. Historically, rigid retaining structures have been most commonly used; their static design is based on classical earth pressure theories. However, newer types of retaining structures, such as flexible anchored walls, soil nailed walls, and reinforced walls, have required the development of new approaches, even for static conditions. Under seismic conditions, classical earth pressure theories can be extended in a logical way to account for the effects of earthquake shaking, but seismic design procedures for the newer types of retaining structures remain under development.

Free-standing rigid retaining structures typically maintain equilibrium through the development of active and passive earth pressures that develop as the wall translates and rotates under the action of the imposed stresses. By assuming that static stresses develop through mobilization of the shear strength of the backfill soil on a planar potential failure surface, Coulomb earth pressure theory predicts a static active thrust of

$$P_A = \frac{1}{2}K_A\gamma H^2 \tag{1.56}$$

where

TABLE 1.10 Typical Interface Friction Angles

	Interface Materials	Interface Friction Angle δ
Mass concrete against:	Clean sound rock	35
	Clean gravel, gravel-sand mixtures, coarse sand	29–31
	Clean fine to medium sand, silty medium to coarse sand, silty or clayey gravel	24–29
	Clean fine sand, silty or clayey fine to medium sand	19–24
	Fine sandy silt, nonplastic silt	17–19
	Medium-stiff and stiff clay and silty clay	17–19
Formed concrete against:	Clean gravel, gravel-sand mixture, well-graded rock fill with spalls	22–26
	Clean sand, silty sand-gravel mixture, single-size hard rock fill	17–22
Steel sheet piles against:	Silty sand, gravel, or sand mixed with silt or clay	14
	Fine sandy silt, nonplastic silt	11
	Clean gravel, gravel-sand mixture, well-graded rock fill with spalls	22
	Clean sand, silty sand-gravel mixture, single-size hard rock fill	17

Source: After NAVFAC, *Foundations and Earth Structures, Design Manual 7.02*. Naval Facilities Engineering Command, Alexandria, VA, 1982.

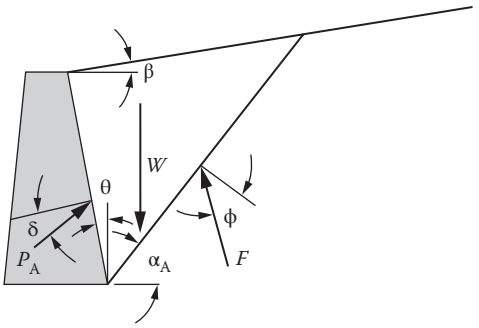

FIGURE 1.29 Illustration of variables for computation of active earth thrust.

$$K_A = \frac{\cos^2(\phi - \theta)}{\cos^2\theta\cos(\delta + \theta)\left[1 + \sqrt{\dfrac{\sin(\delta + \phi)\sin(\phi - \beta)}{\cos(\delta + \phi)\cos(\beta - \theta)}}\right]^2} \tag{1.57}$$

δ is the angle of interface friction between the wall and the soil, (Table 1.10), and β and θ are as shown in Figure 1.29.

Under earthquake shaking, active earth pressures tend to increase above static levels. In one of the first geotechnical earthquake engineering analyses, Okabe (1926) and Mononobe and Matsuo (1929) developed a pseudo-static extension of Coulomb theory to predict the active earth thrust under seismic conditions. Assuming pseudo-static accelerations of $a_h = k_h g$ and $a_v = k_v g$ in the horizontal and vertical directions, respectively, the Mononobe–Okabe total thrust is given by

$$P_{AE} = \frac{1}{2} K_{AE} \gamma H^2 (1 - k_v) \tag{1.58}$$

where $\phi - \beta \geq \psi$ and $\psi = \tan^{-1}\left[k_h / 1 - k_v\right]$. Although the assumptions used in the Mononobe–Okabe analysis imply that the total active thrust should act at a height of $H/3$ above the base of the wall, experimental results indicates that it acts at a higher point. The total active thrust of Equation 1.58 can be divided into a static component, P_A (given by Equation 1.56), and a dynamic component

$$\Delta P_{AE} = P_{AE} - P_A \tag{1.59}$$

which acts at a height of approximately $0.6H$ above the base of the wall. On this basis, the total active thrust can be taken to act at a height

$$h = \frac{P_A \, H/3 + \Delta P_{AE}(0.6H)}{P_{AE}} \tag{1.60}$$

above the base of the wall. Some recent experimental studies (e.g., Al-Atik and Sitar, 2010; Lew et al., 2010) have suggested that the Mononobe–Okabe method may over predict the dynamic active pressures acting on full-scale retaining structures; additional research on this topic is continuing.

When retaining walls are braced against lateral movement at top and bottom, as can occur with abutment and basement walls, the shear strength of the soil will not be fully mobilized under static or seismic conditions. As a result, the limiting conditions of minimum active or maximum passive conditions cannot be developed. In such cases, it is common to estimate lateral earth pressures using the elastic solution of

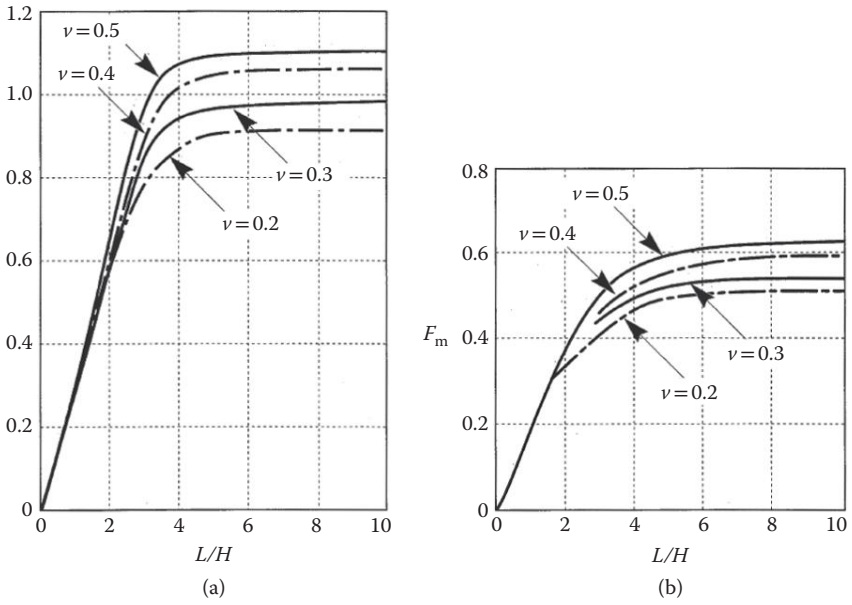

FIGURE 1.30 Charts for determination of (a) dimensionless thrust factor and (b) dimensionless moment factor for various geometries and Poisson's ratios.

Wood (1973) for a linear elastic material of height, H, trapped between rigid walls separated by a horizontal distance, L. For motions at less than half the fundamental frequency of the unrestrained backfill ($f_o = v_s/4H$), the dynamic thrust and dynamic overturning moment (about the base of the wall), can be expressed as

$$\Delta P_{eq} = \gamma H^2 \frac{a_h}{g} F_p \tag{1.61}$$

$$\Delta M_{eq} = \gamma H^3 \frac{a_h}{g} F_m \tag{1.62}$$

where a_h is the amplitude of the harmonic base acceleration and F_p and F_m are dimensionless factors that can be obtained from Figure 1.30. It should be noted that Equations 1.62 and 1.63 refer to dynamic thrusts and moments; static thrusts and moments must be added to obtain total thrusts and moments.

1.9 Soil Improvement

When existing subsurface conditions introduce significant seismic hazards that adversely affect safety or impact construction costs, improved performance may be achieved through a program of soil improvement. A variety of techniques are available for soil improvement and may be divided into four main categories: densification, drainage, reinforcement, and grouting/mixing. Each soil improvement technique has advantages and disadvantages that influence their cost and effectiveness under different circumstances. Soil improvement techniques for both seismic and nonseismic areas are described in detail in such references as Welsh (1987), Van Impe (1989), Hausmann (1990), Broms (1991), Bell (1993), and Mosely (1993).

1.9.1 Densification Techniques

Virtually all mechanical properties of soil (e.g., strength, stiffness, etc.) improve with increasing soil density. This is particularly true when earthquake problems are considered—the tendency of loose soils to densify under dynamic loading is responsible for such hazards as liquefaction, lateral spreading, and earthquake-induced settlement. This tendency can be used to advantage, however, as most densification techniques rely on vibrations to efficiently densify granular soil. Because fines inhibit densification for much the same reason as they inhibit liquefaction, densification techniques are most efficient in clean sands and gravels.

Vibratory densification of large volumes of soil can be accomplished most economically by dynamic compaction. In this procedure, a site is densified by repeatedly lifting and dropping a heavy weight in a grid pattern across the surface of the site. Using weights that can range from 53 to 267 kN and drop heights of 10 to 30 m, densification can be achieved to depths of up to 12 m. The process is rather intrusive in terms of ground surface disturbance, noise, dust, and vibration of surrounding areas, so it is used primarily in undeveloped areas. Vibrations from probes that penetrate below the ground surface have also proved to be effective for densification. Vibroflotation, for example, is accomplished by lowering a vibrating probe into the ground (with the aid of water jets, in some cases). By vibrating the probe as it is pulled back toward the surface, a column of densified soil surrounding the vibroflot is produced. Gravel or crushed stone may be introduced into the soil at the surface or, using a bottom feed vibroflot, at the tip of the probe to form stone columns. Blasting can also be used to densify cohesionless soils. Blast densification is usually accomplished by detonating multiple explosive charges spaced vertically at distances of 3–6 m in borings spaced horizontally at distances of 5–15 m. The charges at different elevations are often detonated at small time delays to enhance the amplitude, and therefore the densification capacity, of the blast waves. Two or three rounds of blasting, with later rounds detonated at locations between those of the earlier rounds, are often used to achieve the desired degree of densification. Finally, densification may be achieved using static means using compaction grouting. Compaction grouting involved the injection of very low slump (usually < 25 mm) cementitious grout into the soil under high pressure. The grout forms an intact bulb or column that densifies the surrounding soil by displacement. Compaction grouting may be performed at a series of points in a grid or along a line. Grout points are typically spaced at distances of approximately 1–4 m, and have extended to depths of 30 m.

1.9.2 Drainage Techniques

Excessive soil and foundation movements can often be eliminated by lowering the groundwater table, and construction techniques for dewatering are well developed. The buildup of high porewater pressures in liquefiable soils can also be suppressed using drainage techniques, though drainage alone is rarely relied upon for mitigation of liquefaction hazards. Stone columns provide means for rapid drainage by horizontal flow, but also improve the soil by densification (during installation) and reinforcement.

1.9.3 Reinforcement Techniques

The strength and stiffness of some soil deposits can be improved by installing discrete inclusions that reinforce the soil. Stone columns are columns of dense angular gravel or crushed stone (stone columns) that reinforce the soil in which they are installed. Stone columns also improve the soil because of their drainage capabilities and the densification and lateral stress increase that generally occurs during their installation. Granular soils can also be improved by the installation of compaction piles, usually prestressed concrete or timber, driven in a grid pattern and left in place. Compaction piles can often increase relative densities to 75%–80% within a distance of 7–12 pile diameters. Drilled inclusions such as drilled shafts or drilled piers have been used to stabilize many slopes, though the difficulty in drilling

through loose granular soils limits their usefulness for slopes with liquefiable soils. Soil nails, tiebacks, micropiles, and root piles have also been used.

1.9.4 Grouting/Mixing Techniques

The characteristics of many soils can be improved by the addition of cementitious materials. Introduced by injection or mixing, these materials both strengthen the contacts between soil grains and fill the space between the grains. Grouting involves injection of cementitious materials into the voids of the soil or into fractures in the soil; in both cases, the particle structure of the majority of the soil remains intact. In mixing, the cementitious materials are mechanically or hydraulically mixed into the soil, completely destroying the initial particle structure.

Permeation grouting involves the injection of low-viscosity grouts into the voids of the soil without disturbing the particle structure. Both particulate grouts (aqueous suspensions of cement, fly ash, bentonite, microfine cement, etc.) and chemical grouts (silica and lignin gels, or phenolic and acrylic resins) may be used. The more viscous particulate grouts are generally used in coarser-grained soils with large voids such as gravels and coarse sands; chemical grouts can be used in fine sands. The presence of fine can significantly reduce the effectiveness of permeation grouting. Grout pipes are usually arranged in a grid pattern at spacings of 1.2–2.4 m and can produce grouted soil strengths of 350–2100 kPa. Intrusion grouting involves the injection of more viscous (and hence stronger) cementitious grouts under pressure to cause controlled fracturing of the ground. The first fractures generally follow weak bedding planes or minor principal stress planes; after allowing the initially placed grout to cure, repeated grouting fractures the soil along additional planes, eventually producing a three-dimensional network of intersecting grout lenses.

Using a mechanical system consisting of hollow stem augers and rotating paddles, soil mixing produces an amorphous mixture of soil and cementitious material. The soil mixing process produces columns of soil–cement that can be arranged in a grid pattern or in a linear series of overlapping columns to produce subsurface walls and/or cellular structures. Soil mixing, which can be used in virtually all inorganic soils, has produced strengths of 1400 kPa and improvement to depths of 60 m. In jet grouting, cement grout is injected horizontally under high pressure through ports in the sides of a hollow rod lowered into a previously drilled borehole. Jet grouting begins at the bottom of the borehole and proceeds to the top. Rotation of the injection nozzle as the process occurs allows the jet to cut through and hydraulically mix columns of soil up to 2.4 m in diameter. Air or air and water may also be injected to aid in the mixing process. Jet grouting can be performed in any type of inorganic soil to depths limited only by the range of the drilling equipment.

Defining Terms

Selected terms used in this section are compiled here.

Amplification function: A function that describes the ratio of ground surface motion to a reference (usually bedrock) motion as a function of frequency.

Attenuation: The rate at which earthquake ground motion decreases with distance.

Backbone curve: The nonlinear stress–strain curve of a monotonically loaded soil.

Blind thrust faults: Faults at depth occurring under anticlinal folds—since they have only subtle surface expression, their seismogenic potential can only be evaluated by indirect means (Greenwood, 1995). Blind thrust faults are particularly worrisome because they are hidden, are associated with folded topography in general, including areas of lower and infrequent seismicity, and therefore result in a situation where the potential for an earthquake exists in any area of anticlinal geology, even if there are few or no earthquakes in the historic record. Recent

major earthquakes of this type have included the 1980 M_w 7.3 El Asnam (Algeria), 1988 M_w 6.8 Spitak (Armenia) and 1994 M_w 6.7 Northridge (California) events.

Body waves: Vibrational waves transmitted through the body of the earth, and are of two types: P waves (transmitting energy via dilatational or push-pull motion), and slower S waves (transmitting energy via shear action at right angles to the direction of motion).

Coherence: The similarity of ground motion at different locations. The coherence of ground motions at closely spaced locations is higher than at greater spacings. At a given spacing, the coherence of low-frequency (long wavelength) components is greater than that of high-frequency (short wavelength) components.

Cyclic mobility: A phenomenon involving accumulation of porewater pressure during cyclic loading in soils for which the residual shear strength is greater than the shear stress required to maintain static equilibrium.

Cyclic resistance ratio (CRR): The ratio of equivalent shear stress amplitude required to trigger liquefaction to the initial vertical effective stress acting on the soil.

Cyclic stress ratio (CSR): The ratio of equivalent shear stress amplitude induced by an earthquake ground motion to the initial vertical effective stress acting on the soil.

Damping curve: A plot of equivalent viscous damping ratio as a function of shear strain amplitude.

Damping: Represents the force or energy lost in the process of material deformation (damping coefficient c = force per velocity).

Differential settlement: The relative amplitudes of settlement at different locations. Differential settlement may be particularly damaging to bridges and other structures.

Dip: The angle between a plane, such as a fault, and the earth's surface.

Dip-slip: Motion at right angles to the strike, up- or down-slip.

Ductility factor: The ratio of the total displacement (elastic plus inelastic) to the elastic (i.e., yield) displacement.

Epicenter: The projection on the surface of the earth directly above the hypocenter.

Equivalent linear analysis: An analysis in which the nonlinear stress–strain behavior of the soil is approximated by a secant shear modulus and damping ratio that, through a process of iteration, are compatible with the level of shear strain induced in the soil.

Far-field: (Beyond near-field), also termed teleseismic.

Fault: A zone of the earth's crust within which the two sides have moved—faults may be hundreds of miles long, from one to over one hundred miles deep, and not readily apparent on the ground surface.

Flow failure: A soil failure resulting from flow liquefaction. Flow failures can involve very large deformations.

Flow liquefaction: A phenomenon that can occur when liquefaction is triggered in a soil with a residual shear strength lower than the shear stress required to maintain static equilibrium.

GMPE: Ground motion prediction equation, used to estimate strong ground motion. Formerly referred to as attenuation relationship.

Hypocenter: The location of initial radiation of seismic waves (i.e., the first location of dynamic rupture).

Intensity: A metric of the effect, or the strength, of an earthquake hazard at a specific location, commonly measured on qualitative scales such as MMI, MSK, and JMA.

Lateral spreading: A phenomenon resulting from cyclic mobility in soils with some nonzero initial shear stress. Lateral spreading is characterized by the incremental development of permanent lateral soil deformations.

Magnitude: A unique measure of an individual earthquake's release of strain energy, measured on a variety of scales, of which the moment magnitude M_w (derived from seismic moment) is preferred.

Magnitude-frequency relation: The probability of occurrence of a selected magnitude—the most common is $\log_{10} n(m) = a - bm$ (Gutenberg and Richter, 1954).

Meizoseismal: The area of strong shaking and damage.

Modulus reduction curve: The ratio of secant shear modulus at a particular shear strain to maximum shear modulus (corresponding to very low strains) plotted as a function of shear strain amplitude.

Near-field: Within one source dimension of the epicenter, where source dimension refers to the length or width of faulting, whichever is less.

Nonlinear approach: An analysis in which the nonlinear, inelastic stress–strain behavior of the soil is explicitly modeled.

Normal fault: A fault that exhibits dip-slip motion, where the two sides are in tension and move away from each other.

Peak ground acceleration (pga): The maximum amplitude of recorded acceleration (also termed the ZPA, or zero period acceleration).

Pseudo-static approach: A method of analysis in which the complex, transient effects of earthquake shaking are represented by constant accelerations. The inertial forces produced by these accelerations are considered, along with the static forces, in limit equilibrium stability analyses.

Radiation damping: A reduction in wave amplitude because of geometric spreading of travelling waves, or radiation into adjacent or underlying materials.

Response spectrum: A plot of maximum amplitudes (acceleration, velocity, or displacement) of a single degree of freedom oscillator (SDOF), as the natural period of the SDOF is varied across a spectrum of engineering interest (typically, for natural periods from 0.03 to 3 or more seconds. Or frequencies of 0.3 to 30 + hz).

Reverse fault: A fault that exhibits dip-slip motion, where the two sides are in compression and move away toward each other.

Seismic hazards: The phenomena and/or expectation of an earthquake-related agent of damage, such as fault rupture, vibratory ground motion (i.e., shaking), inundation (e.g., tsunami, seiche, dam failure), various kinds of permanent ground failure (e.g., liquefaction), fire, or hazardous materials release.

Seismic moment: The moment generated by the forces generated on an earthquake fault during slip.

Seismotectonic model: A mathematical model representing the seismicity, attenuation, and related environment.

Specific impedance: Product of density and wave propagation velocity.

Spectrum amplification factor: The ratio of a response spectral parameter to a corresponding reference ground motion parameter (where parameter indicates acceleration, velocity, or displacement).

Strike: The intersection of a fault and the surface of the earth, usually measured from north (e.g., the fault strike is N 60° W).

Subduction: Refers to the plunging of a tectonic plate (e.g., the Pacific) beneath another (e.g., the North American) down into the mantle, because of convergent motion.

Surface waves: Vibrational waves transmitted within the surficial layer of the earth, and are of two types: horizontally oscillating LOVE waves (analogous to s body waves) and vertically and horizontally oscillating Rayleigh waves.

Thrust fault: Low-angle reverse faulting (blind thrust faults are faults at depth occurring under anticlinal folds—they have only subtle surface expression).

Total settlement: The total amplitude of settlement at a particular location.

Transform or strike slip fault: A fault where relative fault motion occurs in the horizontal plane, parallel to the strike of the fault.

Uniform hazard spectra: Response spectra with the attribute that the probability of exceedance is independent of frequency.

Yield acceleration: The horizontal acceleration that produces a pseudo-static factor of safety of 1.0. Accelerations greater than the yield acceleration are expected to produce permanent deformations.

References

AASHTO. 2011. *Guide Specifications for LRFD Seismic Bridge Design*, (2nd edition). American Association of State Highway and Transportation Officials, Washington, DC.

Abrahamson, N., Atkinson, G., Boore, D., Bozorgnia, Y., Campbell, K., Chiou, B., Idriss, I. M., Silva, W. and Youngs, R. 2008. Comparisons of the Nga ground-motion relations. *Earthquake Spectra*, 24(1), 45–66.

Abrahamson, N., and Silva, W. 2008. Summary of the Abrahamson & Silva Nga ground-motion relations. *Earthquake Spectra*, 24(1), 67–97.

Al Atik, L., and Sitar, N. 2010. Seismic earth pressures on cantilever retaining structures. *J. Geotech. Geoenviron. Eng.*, 136(10), 1324–1333.

Andrus, R. D., Stokoe, K. H., II, and Juang, C. H. 2004, Guide for shear wave-based liquefaction potential evaluation, *Earthquake Spectra*, 20(2), 285–308.

Anil K., and Chopra, A. K. 1981. *Dynamics of Structures: A Primer*, Earthquake Engineering Research Institute, Oakland, CA.

ASCE 7-10 2010. *Minimum Design Loads for Buildings and Other Structures, Sei/Asce 7-10*. American Society of Civil Engineers, Reston, VA.

Bartlett, S. F., and Youd, T. L. 1992. Empirical analysis of horizontal ground displacement generated by liquefaction-induced lateral spread. *Technical Report NCEER-92-0021*. National Center for Earthquake Engineering Research, Buffalo, NY.

Bell, F. G. (1993). *Engineering Treatment of Soils*. E & FN Spon, London, p. 302.

Bernreuter, D. L., Savy, J. B., Mensing, R. W., and Chen, J. C. 1989. *Seismic Hazard Characterization of 69 Nuclear Power Plant Sites East of the Rocky Mountains*. U.S. Nuclear Regulatory Commission, NUREG/CR-5250.

Bolt, B. A. 1993. *Earthquakes*. W.H. Freeman and Co., New York, NY.

Bonilla, M. G., Mark, R. K., and Lienkaemper, J. J. 1984. Statistical relations among earthquake magnitude, surface rupture length, and surface fault displacement. *Bulletin Seis. Soc. Am.*, 74(6), 2379–2411.

Boore, D. M., and Atkinson, G. M. 2008. Ground-motion prediction equations for the average horizontal component of Pga, Pgv, and 5%-damped Psa at spectral periods between 0.01 S and 10.0 S. *Earthquake Spectra*, 24(1), 99–138.

Boore, D. M., Watson-Lamprey, J., and Abrahamson, N. A. 2006. Orientation-independent measures of ground motion. *Bull. Seismological Soc. Am.*, 96, 1502–1511.

Borcherdt, R. D. 1994. Estimates of site-dependent response spectra for design (methodology and justification), *Earthquake Spectra*, 10(4), 617–653.

Boulanger, R. W., and Idriss, I. M. 2004. Evaluating the potential for liquefaction or cyclic failure of silts and clays, *Report No. UCD/CGM- 04/01*, Center for Geotechnical Modeling, Dept. of Civil and Environmental Engineering, Univ. of California, Davis, CA.

Bray, J., and Sancio, R. 2006. Assessment of the liquefaction susceptibility of fine-grained soils, *J. Geotech. Geoenviron. Eng.*, 132(9), 1165–1177.

Broms, B. 1991. Deep compaction of granualr soil. In: H.-Y. Fang (Ed.), *Foundation Engineering Handbook* (2nd edition). Van Nostrand Reinhold, New York, pp. 814–832.

BSSC. 2009. *NEHRP Recommended Seismic Provisions for New Buildings and Other Structures, Part 1: Provisions; Part 2: Commentary*, (FEMA P-750 2009 edition). Building Seismic Safety Council, Washington, DC.

Campbell, K. W. 1985. Strong ground motion attenuation relations: A ten-year perspective. *Earthquake Spectra*, 1(4), 759–804.

Campbell, K., and Bozorgnia, Y. 2008. Nga ground motion model for the geometric mean horizontal component of Pga, Pgv, Pgd and 5% damped linear elastic response spectra for periods ranging from 0.01 to 10 S. *Earthquake Spectra*, 24(1), 139–171.

Cetin, K. O., and Ozan, C. 2009. CPT-based probabilistic soil characterization and classification. *J. Geotech. Geoenvir. Eng.*, 135 (1), 84–107.

Chiou, B. S. J., and Youngs, R. R. 2008. An Nga model for the average horizontal component of peak ground motion and response spectra. *Earthquake Spectra*, 24(1), 173–215.

Choi, Y. and Stewart, J. P. 2005. Nonlinear site amplification as function of 30 m shear wave velocity, *Earthquake Spectra*, 24(1), 1–30.

Clough, R. W., and Penzien, J. 1975. *Dynamics of Structures*. McGraw-Hill, New York, NY.

Cornell, C. A. 1968. Engineering seismic risk analysis. *Bull. Seis. Soc. Am*., 58(5), 1583–1606.

Cornell, C. A., and Merz, H. A. 1973. Seismic risk analysis based on a quadratic magnitude frequency law. *Bull. Seis. Soc. Am*., 63(6), 1992–2006.

Crouse, C. B. 1991. Ground-motion attenuation equations for earthquakes on the Cascadia subduction zone. *Earthquake Spectra*, 7(2), 201–236.

Darendeli, M. B. 2001. Development of a new family of normalized modulus reduction and material damping curves, *Ph. D. Dissertation*, University of Texas at Austin, Austin, TX.

Darragh, R. B., Huang, M. J., and Shakal, A. F. 1994. Earthquake engineering aspects of strong motion data from recent California earthquakes. *Proceedings of Fifth U.S. National Conference Earthquake Engineering*, Earthquake Engineering Research Institute, Oakland CA, Vol. III, 99–108.

Day, S. M., Bielak, J., Dreger, D., Graves, R., Larsen, S., Olsen, K., and Pitarka, A. 2005. 3D ground motion simulations in basins, *Final report for Lifelines Project 1A03*, Pacific Earthquake Engineering Research Center, University of California, Berkeley, CA.

Duku, P. M., Stewart, J. P., Whang, D. H., and Yee, E. 2008. Volumetric strains of clean sands subject to cyclic loads, *J. Geotech. Geoenviron. Eng*., 134 (8), 1073–1085.

Donovan, N. C., and Bornstein, A. E. 1978. Uncertainties in seismic risk procedures. *J. Geotech. Div*., 104(GT7), 869–887. Am. Soc. Civil Engrs., NY.

Douglas, J. 2011. *Ground-Motion Prediction Equations*. Pacific Earthquake Engineering Research Center, University of California, Berkeley, CA, p. 455.

EduPro Civil Systems, Inc. 1998. *ProShake User's Manual*. EduPro Civil Systems, Inc., Redmond, Washington, p. 52.

Electric Power Research Institute. 1986. *Seismic Hazard Methodology for the Central and Eastern United States*, EPRI NP-4726, Menlo Park, CA.

Esteva, L. 1976. Seismicity, chapt. In: C. Lomnitz and E. Rosenblueth (Eds.), *Seismic Risk and Engineering Decisions*. Elsevier, New York, NY.

Field, E. H., and Jacob, K. H. 1995. A comparison and test of various site response estimation techniques including three that are not reference-site dependent, *Bull. Seismol. Soc. Am*., 85, 1127–1143.

Finn, W. D. L., Martin, G. R., and Lee, K. W. 1977. An effective stress model for liquefaction, *J. Geotech. Eng. Div*., 103(6), 517–533.

Finn, W. D. L., Yogendrakumar, M., Yoshida, M., and Yoshida, N. 1986. *TARA-3: A program to compute the response of 2-D embankments and soil-structure interaction systems to seismic loadings*. Department of Civil Engineering, University of Brirish Columbia, Vancouver, Canada.

Geo-Slope International. 2012. *Quake/W*, (http://www.geo-slope.com/products/quakew.aspx).

Greenwood, R. B. 1995. Characterizing blind thrust fault sources—an overview. In: M. C. Woods and W. R. Seiple. (Eds.), *The Northridge California Earthquake of 17 January 1994*. California Department Conservation, Div. Mines and Geology, Special Publ. 116, p. 279–287.

Gumbel, E. J. 1958. *Statistics of Extremes*. Columbia U, Press, New York, NY.

Gutenberg, B., and Richter, C. F. 1954. *Seismicity of the Earth and Associated Phenomena*. Princeton U, Press, Princeton, NJ.

Gutenberg, B., and Richter, C. F. 1956. Magnitude and energy of earthquakes. *Annali de Geofisica*, 9(1), 1–15.

Hanks, T. C., and Kanamori, H. 1979. A moment magnitude scale, *J. Geophys. Res*., 84, 2348–2350.

Hashash, Y.M.A. and Park D. 2001. Non-linear one-dimensional wave propagation in the Mississippi Embayment, *Engineering Geology*, 62 (1–3), 185–206.

Hausmann, M. R. 1990. *Engineering Principles of Ground Modification*. McGraw-Hill Publishing Company, New York, p. 632.

Heaton, T. H., Tajima. F., and Mori, A. W. 1986. Estimating ground motions using recorded accelerograms, *Surveys in Geophysics*, 8(1), 25–83.

Hudson, D. E. 1979. *Reading and Interpreting Strong Motion Accelerograms*, Earthquake Engineering Research Institute, Oakland, CA.

Hudson, M., Idriss, I.M., and Beikae, M. 1994. *QUAD-4M: A Computer Program to Evaluate the Seismic Response of Soil Structures Using Finite Element Procedures and Incorporating a Compliant Base, User's Manual*, Center for Geotechnical Modeling, University of California, Davis, CA. 73 pp.

Idriss, I. M. 2008. An Nga empirical model for estimating the horizontal spectral values generated by shallow crustal earthquakes. *Earthquake Spectra*, 24(1), 217–242.

Ishihara, K., and M. Yoshimine, M. 1992. Evaluation of settlements in sand deposits following liquefaction during earthquakes, *Soils and Foundations*, 32(1), 173–188.

Itasca Consulting Group 1995. FLAC: Fast Lagrangian Analysis of Continua. *User's Manual*, Itasca Consulting Group, Minneapolis, MN.

Kagawa, T., Mejia, L., Seed, H. B., and Lysmer, J. 1981. TLUSH—A computer program for three-dimensional dynamic analysis of earth dams, *Report No. UCB/EERC-81/14*, University of California, Berkeley, CA.

Kramer, S. L. 1996. *Geotechnical Earthquake Engineering*. Prentice-Hall, Upper Saddle River, NJ.

Lawson, A. C., and Reid, H. F. 1908–1910. *The California Earthquake Of April 18, 1906. Report Of The State Earthquake Investigation Commission*. State Earthquake Investigation Commission, Carnegie Institution of Washington, Washington, DC.

Lew, M., Sitar, N., and Al Atik, L. 2010. Seismic earth pressures: Fact or fiction. *Proceedings of the Earth Retention Conference 3*, Geo-Institute of ASCE, Bellevue, WA.

Li, X. S., Wang, Z. L., and Shen, C. K. 1992. SUMDES, a nonlinear procedure for response analysis of horizontally layered sites subjected to multidirectional earthquake loading. *Report*, Department of Civil Engineering, University of California, Davis, CA.

Liao, S. S. C., Veneziano, D., and Whitman, R. V. 1988. Regression models for evaluating liquefaction probability. *J. Geotech. Eng*., ASCE, 114(4), 389–411.

Lomnitz, C. 1974. *Global Tectonics and Earthquake Risk*, Elsevier, New York, NY.

Lysmer, J., Udaka, T., Tsai, C. F., and Seed, H. B. 1975. FLUSH—A computer program for approximate 3-D analysis of soil-structure interaction problems. *Report No. EERC 75-30*, Earthquake Engineering Research Center, University of California, Berkeley, CA, p. 83.

MacMurdo J. 1824. Papers relating to the earthquake which occurred in India in 1819. *Philosophical Magazine*, 63, 105–177.

McGuire, R. K. 1978. FRISK: Computer program for seismic risk analysis using faults as earthquake sources. U.S. Geological Survey, Reports. United States Geological Survey Open file 78-1007, 71 p. 1978.

Meeting on Up-dating of MSK-64 1981. Report on the Ad-hoc panel meeting of experts on up-dating of the MSK-64 seismic intensity scale, Jene, 10-14 March 1980, *Gerlands Beitr. Geophys*., *Leipzeig*, 90(3), 261–268.

Mitchell, J. K., and Tseng, D.-J. 1990. Assessment of liquefaction potential by cone penetration resistance. In: J. M. Duncan (Ed.), *Proceedings*, H. Bolton Seed: Memorial Symposium, Berkeley, CA, Vol. 2, pp. 335–350.

Mononobe, N., and Matsuo, H. 1929. On the determination of earth pressures during earthquakes. *Proceedings*, World Engineering Congress, Tokyo, Vol. 9.

Mosely, M. P. (ed.) 1993. *Ground Improvement*. Blackie Academic & Professional, London, p. 218.

National Academy Press 1988. *Probabilistic Seismic Hazard Analysis*. National Academy of Sciences, Washington, DC.

NAVFAC. 1982. *Foundations and Earth Structures, Design Manual 7.02*. Naval Facilities Engineering Command, Alexandria, VA.

Newmark, N. 1965. Effects of earthquakes on dams and embankments. *Geotechnique*, 15(2), 139–160.

Newmark, N. M., and Hall, W. J. 1982. *Earthquake Spectra and Design*, Earthquake Engineering Research Institute, Oakland, CA.

Ohsaki, Y. 1970. Effects of sand compaction on liquefaction during Tokachioki earthquake. *Soils and Foundations*, 10(2), 112–128.

Okabe, S. 1926. General theory of earth pressures," *J. Japan Soc. Civil Eng*., 12(1).

Olson, R.S. 1997. Cyclic liquefaction based on the cone penetrometer test. In: T. L. Youd and I. M. Idriss (Eds.), *Proceedings of the NCEER Workshop on Evaluation of Liquefaction Resistance of Soils, Technical Report NCEER-97-0022*, National Center for Earthquake Engineering Research, Buffalo, NY, p. 280.

Ordonez, G. 2011. *SHAKE2000: A Computer Program for the 1-D Analysis of Geotechnical Earthquake Engineering Problems, User's Manual*, GeoMotions, LLC, Lacey, WA, 264 pp.

Plaxis. 2012. *PLAXIS 2D: User's Manual*, Plaxis bv, Delft, The Netherlands (http://www.plaxis.nl/files/files/2D2012-2-Reference.pdf), 320 pp.

Pyke, R. M., Seed, H. B., and Chan, C. K. 1975. Settlement of sands under multi-directional loading. *J. Geotech. Eng. Div*., ASCE, 101(GT4), 379–398.

Pyke, R. M. 2000. *TESS: A computer program for nonlinear ground response analyses*. TAGA Engineering Systems & Software, Lafayette, CA.

Reid, H. F. 1910. The mechanics of the earthquake. *The California Earthquake of April 18*, 1906, Report of the State Investigation Committee, vol. 2, Carnegie Institution of Washington, Washington, DC.

Reiter, L. 1990. *Earthquake Hazard Analysis, Issues and Insights*, Columbia U. Press, New York, NY.

Reyna, F., and Chameau, J. L. 1991. Dilatometer based liquefaction potential of sites in the Imperial Valley. *Proceedings, 2nd International Conference on Recent Advances in Geotechnical Earthquake Engineering and Soil Dynamics*, St. Louis, Missouri, Vol. 1, pp. 385–392.

Richter, C. F. 1935. An instrumental earthquake scale. *Bull. Seismological Soc. Am*., 25, 1–32.

Robertson, P. K., and Wride, C. E. 1997. Cyclic liquefaction and its evaluation based on the SPT and CPT. *Proceedings, NCEER Workshop on Evaluation of Liquefaction Resistance*, Technical Report NCEER-97-0022, National Center for Earthquake Engineering Research, Buffalo, NY.

Saygili, G., and Rathje, E. M. 2008. Empirical predictive models for earthquake-induced sliding displacements of slopes," *J. Geotech. Geoenviron. Eng*., 134(6), 790–803.

Schnabel, P. B., Lysmer, J., and Seed, H. B. 1972. SHAKE: A computer program for earthquake response analysis of horizontally layered sites. *Report No. EERC 72-12*, Earthquake Engineering Research Center, University of California, Berkeley, CA.

Schwartz, D. P. 1988. Geologic characterization of seismic sources: Moving into the 1990s. In: J. L. Thun (Ed.), *Earthquake Engineering and Soil Dynamics II—Recent Advances in Ground-Motion Evaluation*. Geotechnical Special Publication No. 20. American Soc. Civil Engrs., New York, NY.

Schwartz, D. P., and Coppersmith, K. J. 1984. Fault behavior and characteristic earthquakes: Examples from the Wasatch and San Andreas Faults. *J. Geophys. Res*., 89, 5681–5698.

Seed, H.B. and Idriss, I.M. 1971. Simplified Procedure for Evaluating Soil Liquefaction Potential, *J. Soil Mech. Foundations Div*., 107(SM9), 1249–1274.

Seed, H. B. 1979. Soil liquefaction and cyclic mobility evaluation for level ground during earthquakes," *J. Geotech. Eng. Div*., 105(2), 201–255.

Seed, H. B., and De Alba, P. 1986. Use of SPT and CPT tests for evaluating the liquefaction resistance of sands. *Specialty Conference on Use of In-Situ Testing in Geotechnical Engineering, INSITU'86, Geotechnical Special Publication No. 6*, American Society of Civil Engineers, New York, NY. 281–302.

Seed, H. B., and Silver, M. L. 1972. Settlement of dry sands during earthquakes. *J. Soil Mech. Foundations Div*., 98(SM4), 381–397.

Shamoto, Y., Zhang, J. M., and Tokimatsu, K. 1998. Methods for evaluating residual post-liquefaction ground settlement and horizontal displacement, *Soils Found*., 2(2), 69–83.

Silva, W. J. 2005. Site response simulations for the NGA project. *Report prepared for the Pacific Earthquake Engineering Research Center*, University of California, Berkeley, CA.

Slemmons, D. B. 1977. State-of-the-art for assessing earthquake hazards in the United States, Report 6: Faults and earthquake magnitude, U.S. Army Corps of Engineers, Waterways Experiment Station, Misc. Paper s-73-1, p. 129.

Sokolov, V. Y. 1997. Empirical models for estimating Fourier-amplitude spectra of ground acceleration in the northern Caucasus (Racha seismogenic zone), *Bull. Seism. Soc. Am*., 87, 1401–1412.

Stafford, P. J., Strasser, F., and Bommer, J. J. 2008. An Evaluation of the applicability of the Nga models to ground-motion prediction in the Euro-Mediterranean region. *Bull Earthquake Eng*., 6, 149–177.

Stein, R. S., and Yeats, R. S. 1989. Hidden Earthquakes, *Sci. Am*., 260, 48–57.

Stewart, J. P., Archuleta, R. J., and Power, M. S. 2008. Preface. *Earthquake Spectra*, 24(1), 1–2.

Stokoe, K. H. II, Roesset, J. M., Bierschwale, J. G., and Aouad, M. 1988. Liquefaction potential of sands from shear wave velocity. *Proceedings, 9th World Conference on Earthquake Engineering*, Tokyo, Japan, Vol. 3, p. 213–218.

Tokimatsu, K., and Seed, H. B. 1984. Simplified procedures for the evaluation of settlements in sands due to earthquake shaking, *Report No. UCB/EERC-84/16*, Earthquake Engineering Research Center, University of California, Berkeley, CA.

Tokimatsu, K., and Seed, H. B. 1987. Evaluation of settlements in sand due to earthquake shaking. *J. Geotech. Eng*., ASCE, 113(8), 861–878.

Tokimatsu, K., Kuwayama, S., and Tamura, S. 1991. Liquefaction potential evaluation based on Rayleigh wave investigation and its comparison with field behavior. *Proceedings, 2nd International Conference on Recent Advances in Geotechnical Earthquake Engineering and Soil Dynamics*, St. Louis, Missouri, Vol. 1, pp. 357–364.

Van Impe, W. F. 1989. *Soil improvement techniques and their evolution*, A.A. Balkema, Rotterdam, the Netherlands, p. 125.

Walling, M., Silva, W., and Abrahamson, N. A. 2008. Nonlinear site amplification factor for constraining the NGA modles, *Earthquake Spectra*, 24(1), 243–255.

Wells, D. L., and Coppersmith, K. J. 1994. New empirical relationships among magnitude, rupture length, rupture width, rupture area, and surface displacement. *Bull. Seismol. Soc. Am*., 84, 974–1002.

Welsh, J. P. 1987. *Soil improvement: A ten year update*. Geotechnical Special Publication No. 12, ASCE, New York, NY, p. 331.

Wood, H. O., and Neumann, Fr. 1931. Modified Mercalli intensity scale of 1931, *Bull. Seis. Soc. Am*., 21, 277–283.

Wood, J. 1973. Earthquake-induced soil pressures on structures. *Report No. EERL 73-05*, California Institute of Technology, Pasadena, CA, p. 311.

Yegulalp, T. M., and Kuo, J. T. 1974. Statistical prediction of the occurrence of maximum magnitude earthquakes. *Bull. Seis. Soc. Am*., 64(2), 393–414.

Youd, T. L. 1972. Compaction of sands by repeated straining, *J. Soil Mech. Found. Div*., 98(SM7), 709–725.

Youd, T. L., Hansen, C.M., and Bartlett, S. F. 2002. Revised Multilinear Regression Equations for Prediction of Lateral Spread Displacement." *J. Geotech. Geoenviron. Eng*., 128(12), 1007–1017.

Youd, T. L., and Noble, S. K. 1997. Liquefaction criteria based on probabilistic analyses. *Proceedings, NCEER Workshop on Evaluation of Liquefaction Resistance*, Technical Report NCEER-97-0022, National Center for Earthquake Engineering Research, Buffalo, NY.

Zhang, G., Robertson, P. K., and Brachman, R. W. I. 2004. Estimating liquefaction-induced lateral displacements using the standard penetration test or cone penetration test, *J. Geotech. Geoenviron. Eng*., 130(8), 861–871.

2

Earthquake Damage to Bridges

Mark Yashinsky
California Department of Transportation

Jack Moehle
University of California

Marc Eberhard
University of Washington

2.1 Introduction

2.1.1 Lessons Learned from Recent Earthquakes

Bridge engineers make changes to seismic design practice (American Association of State Highway and Transportation Officials [AASHTO], 2011; ATC, 1981; ATC, 1996; Caltrans, 1997; 2010a–d, 2011a, 2011b, 2013; China-MOT, 2008; JRA, 2002) based on lessons learned after earthquakes, through tests in laboratories, and from analytical studies. However, it has usually been bridge damage from earthquakes that has been the impetus for changes to seismic practice.

Engineers in California began designing bridges for a lateral force based on the acceleration records from the 1940 El Centro earthquake. However, California did not update its seismic design criteria (SDC) after the 1964 M9.2 Prince William Sound, Alaska Earthquake despite plenty of bridge damage (NAS, 1973). The M7.5 Niigata Japan earthquake occurred the same year and damaged several bridges, but like the Alaska earthquake it was of interest mostly to geotechnical engineers.

A damaging earthquake in California apparently makes a great deal of difference because damage during the 1971 M6.6 San Fernando Earthquake (Jennings, 1971) was the impetus for big changes to earthquake engineering practice in California. Requirements for site specific ground motions, the establishment of a

post-earthquake investigation team (PEQIT), new SDC, the first seismic retrofit program, annual earthquake exercises, and many other changes resulted from the widespread bridge damage in 1971 (EERI, 1995a).

Each subsequent earthquake provided additional lessons (or at least some clues) about bridge seismic behavior. The 1980 M7.2 Trinidad (Eureka) California earthquake caused the collapse of one of the two Field's Landing Bridges. The short hinge seats and room for superstructure movement contributed to the collapse of the southbound bridge. However, why the right bridge remained standing and how the severe skew contributed to the collapse is still an issue of debate.

The 1987 M5.9 Whittier Narrows Earthquake (EERI, 1988) in Los Angeles caused only moderate bridge damage, but diagonal shear cracks on the columns of the Route 605/5 Separation worried the California Department of Transportation (Caltrans) so much that they began a research and screening program for column retrofits. Unfortunately, that program was not fully implemented when the 1989 M6.9 Loma Prieta earthquake caused a great deal of additional bridge damage. However, those bridges that were designed after the 1971 San Fernando earthquake performed well, which was encouraging. The 1989 Loma Prieta earthquake (like the 1964 quakes) could be considered a geotechnical earthquake because almost all the bridge damage occurred on weak soil, often many miles from the fault (Zelinski, 1994).

Although Caltrans was retrofitting its bridges, the 1994 M6.7 Northridge earthquake occurred before the retrofit program could be completed. Again there was not only a great deal of bridge damage, but also many valuable lessons. Of particular interest were the large recorded ground motions at Rinaldi and Pacoima Dam. These recordings provided support for those seismologists who had been warning about near-fault effects. Bridge engineers now had to be concerned with large, long-period velocity pulses for bridges close to the fault (approximately 50% of the bridges in California). Also, retrofitted bridges performed very well during Northridge. Often a retrofit would sit undamaged next to a collapsed bridge. The biggest lesson was the problem of unbalanced bridges. Several bridges with tall bents near the middle of the bridge collapsed because the shorter bents at the ends could not handle the displacement.

The 1995 M6.9 Hyogo-Ken Nanbu (Kobe), Japan earthquake reinforced the problem of near-fault ground motion. Very large ground motion knocked over long sections of the elevated expressway in downtown Kobe (EERI, 1995b; Chung et al., 1996; Kawashima and Unjoh, 1997). For the Japanese, this was particularly startling because they had been only designing for a large offshore earthquake at that time. After the Kobe earthquake, Japanese bridge engineers began designing for two earthquakes, a subduction event similar to the 1923 Great Kanto Earthquake and a large crustal earthquake.

Several large earthquakes in 1999 made surface faulting a bigger concern for bridge engineers. The M7.6 Kocaeli Turkey Earthquake showed what happened to a bridge that crossed a strike-skip fault. Even more disturbing was the M7.6 Chi Chi Taiwan earthquake caused by a thrusting fault. Several bridges collapsed when portions of the bridge were lifted up to 18 ft. in the air. The 2002 M7.9 Denali Alaska earthquake provided encouraging news when the strike-slip fault displaced 13 ft. under the Alyeska Oil Pipeline with only moderate damage.

In 2004, the M9.1 Sumatra–Andaman Island earthquake alerted the world to the dangers of a large tsunami. Besides the tragic loss of life, it alerted engineers to a tsunami's ability to knock over bridges with waves, automobiles, ships, and anything else in its path. Among the many lessons were better notification systems, an evaluation of the tsunami hazard along the United States coastline, an inventory of bridges at risk to tsunami, research on tsunami forces on bridges, and so on.

In 2008, the M7.9 Wenchuan earthquake in Sichuan, China (Lee, 2008) showed how fragile roads and bridges are to strong shaking in a mountain setting. Landslides caused quake lakes that washed away bridges. Bridges on unstable slopes fell apart. Damage to roads and bridges isolated the people in the mountains.

The 2010 M8.8 earthquake in Chile and the 2011 M9.0 earthquake in Tohoku, Japan were important because they provided previously unrecorded ground shaking data for higher magnitude earthquakes and for subducting faults. They also reminded bridge engineers about tsunami hazards (especially the Japan earthquake) and about vulnerable bridge details (especially the Chile earthquake).

2.1.2 Organization of Chapter

The purpose of this chapter is to identify and classify types of damage to bridges that earthquakes commonly induce and, where possible, to identify the causes of the damage. This task is not straightforward. Damage usually results from a complex and interacting set of contributing variables. The details of damage often are obscured by the damage itself, so that some speculation is required in reconstructing the event. In many cases, the cause of damage can be understood only after detailed analysis, and even then, the actual causes and effects may be elusive.

Even when the cause of a particular collapse is well understood, it is difficult to generalize about the causes of bridge damage. In past earthquakes, the nature and extent of damage that each bridge suffered has varied with the characteristics of the ground motion at the particular site and the construction details of the particular bridge. No two earthquakes or bridge sites are identical. Design and construction practices vary extensively throughout the world and even within the United States. These practices have evolved with time, and in particular, seismic design practice improved significantly in the Western United States during the 1970s as a result of experience gained from the 1971 San Fernando earthquake.

Despite these uncertainties and variations, one can learn from past earthquake damage, because many types of damage occur repeatedly. By being aware of typical vulnerabilities that bridges have experienced, it is possible to gain insight into structural behavior and to identify potential weaknesses in existing and new bridges. Historically, observed damage has provided the impetus for many improvements in earthquake engineering codes and practice.

An effort is made to distinguish damage according to two classes, as follows:

1. Primary damage—damage caused by earthquake ground shaking or deformation that was the primary cause of damage to the bridge, and that may have triggered other damage or collapse
2. Secondary damage—damage caused by earthquake ground shaking or deformation that was the result of structural failures elsewhere in the bridge, and was caused by redistribution of internal actions for which the structure was not designed

The emphasis in this chapter is on primary damage. It must be accepted, however, that in many cases the distinction between primary and secondary damage is obscure because the bridge geometry is complex or, in the case of collapse, because it is difficult to reconstruct the failure sequence. In this chapter, the word "damage" and "collapse" are used somewhat interchangeably. For most bridges, earthquake damage that does not include collapse is considered a success. Only recently, bridge engineers have begun designing bridges to stay in service and that is usually for smaller earthquakes.

The following sections are organized according to which element in the overall set of contributing factors appears to be the primary cause of the bridge damage. Section 2.2 addresses general issues and parameters influencing ground shaking damage and how to determine the remaining seismic capacity of bridges. Section 2.3 focuses on the ground shaking damage to Standard Bridges. Section 2.4 describes typical types of ground shaking damage to Nonstandard Bridges including arch, truss, cable-supported, and movable bridges, Section 2.5 describes damage because of other seismic hazards. Section 2.6 provides a summary of lessons learned.

2.2 Parameters That Influence Ground Shaking Damage

2.2.1 Geotechnical Parameters

There are several parameters that affect the intensity of ground shaking and bridge damage. The most obvious one is proximity to the fault. Bridges closer to the fault rupture are subject to higher levels of ground shaking as can be seen by the many attenuation relationships developed from recorded ground motion. However, as we shall see, there are other parameters that can modify or even reverse this trend.

Greater magnitude can increase ground shaking. Bridge maintenance engineers seldom bother to check for bridge damage for earthquakes with magnitudes less than approximately 6.0. Bridges are very

stable structures and it is typical to see buildings lying in ruins beside undamaged bridges at lower magnitudes. However, magnitude is related to fault area and so magnitudes larger than approximately 8.0 just impact larger areas without producing significantly higher levels of ground motion.

A relationship exists between the fault mechanism and the level of ground shaking. Bridges on the hanging wall of faults are designed for higher ground motion. Dipping faults can cause higher ground motion because the fault plane extends under a larger area. The ground motion for subducting faults is smaller than crustal faults based on current records. Perhaps the new data from Chile and Japan will alter the current attenuation relationships for subducting faults. In general, the level of ground shaking is related to the amount of asperities on the fault. Some faults are smooth and produce low levels of shaking, whereas faults with a lot of rough spots cause strong shaking.

Bridges very close (within 15 km or 9.3 miles) of the fault rupture are subject to near-fault effects that can greatly increase ground shaking. The fault rupture produces a forward directivity pulse that enhances ground motion perpendicular to the fault. When this "velocity pulse" has a long period, it causes severe damage as we have seen in Kobe and many other earthquakes (Figure 2.1).

Other near-fault effects include strong vertical accelerations and static deformations, but the velocity pulse provides the biggest problem for bridge engineers. Near-fault effects challenge many of our current practices for analyzing and designing bridges.

The most straightforward relationship is between site conditions and ground shaking. Shear and compression waves travel through rock to the bridge site. The site conditions can amplify the resulting ground motion at periods that can damage bridges. Post-earthquake investigations often find similar structures that are undamaged or have collapsed within a few hundred yards from each other. For instance, during the 1989 M6.9 Loma Prieta earthquake, the portion of the Cypress Viaduct on weak soil (with a low shear wave velocity) collapsed, whereas the portion of the structure on competent soil (a higher shear wave velocity) was undamaged (Figures 2.2 and 2.3).

During the 1989 Loma Prieta earthquake, the Cypress Viaduct was about 60 miles (96 km) from the fault so the ground motion was low. However, the portion of the bridge supported on soft clay collapsed (Housner, 1990).

It is seen from Figure 2.4 that soft soil has a higher acceleration at longer periods close to the fault but it has a much higher acceleration than stiffer soil at all periods far from the fault (Housner, 1990). Therefore, vulnerable bridges can remain at high risk on soft soil far from the fault rupture.

This was certainly the case during the Loma Prieta earthquake where most of the bridge damage was on Bay Mud far to the north of the earthquake epicenter (Figure 2.5). Similar circumstances resulted in damage to tall buildings in Mexico City, which was about 200 miles from the epicenter of the 1985 M8.0 Michoacan, Mexico Earthquake.

FIGURE 2.1 Bridge damage because of near fault velocity pulse during 1995 Kobe earthquake.

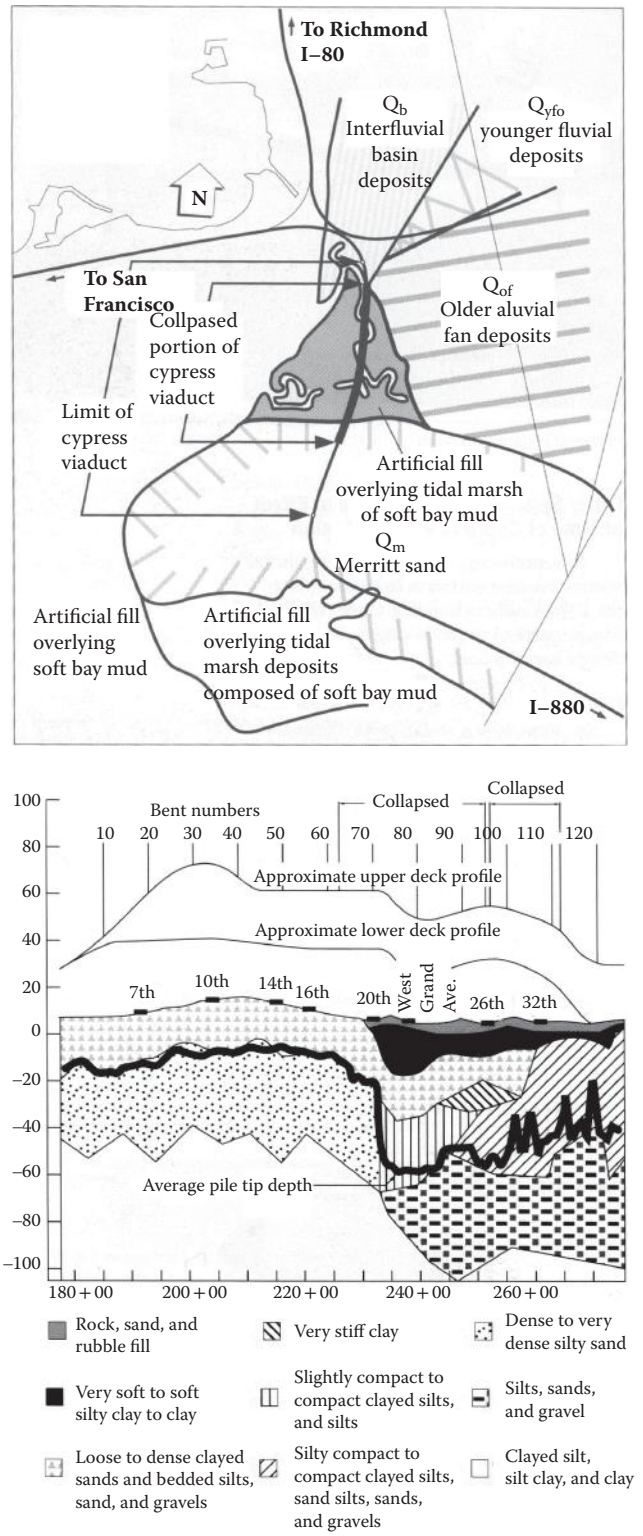

FIGURE 2.2 Site conditions for the Cypress Viaduct (from competing against time).

FIGURE 2.3 Portion of Cypress Viaduct from Bent # 30 (upper right) to Bent #80 (lower left).

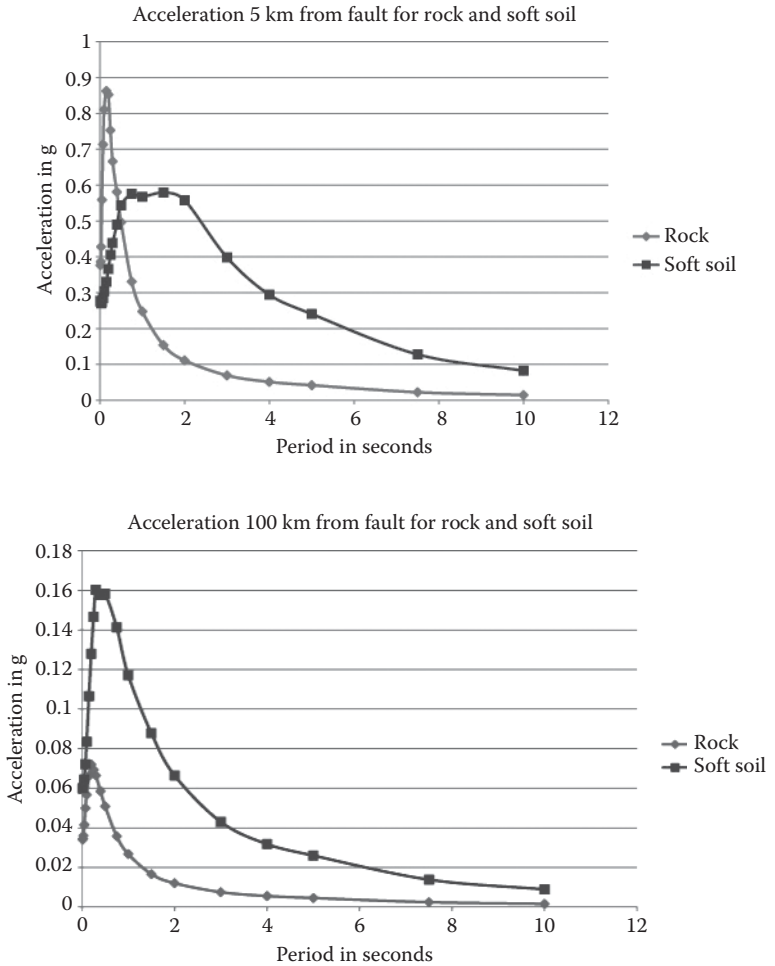

FIGURE 2.4 Ground motion for Campbell–Bozorgnia NGA model.

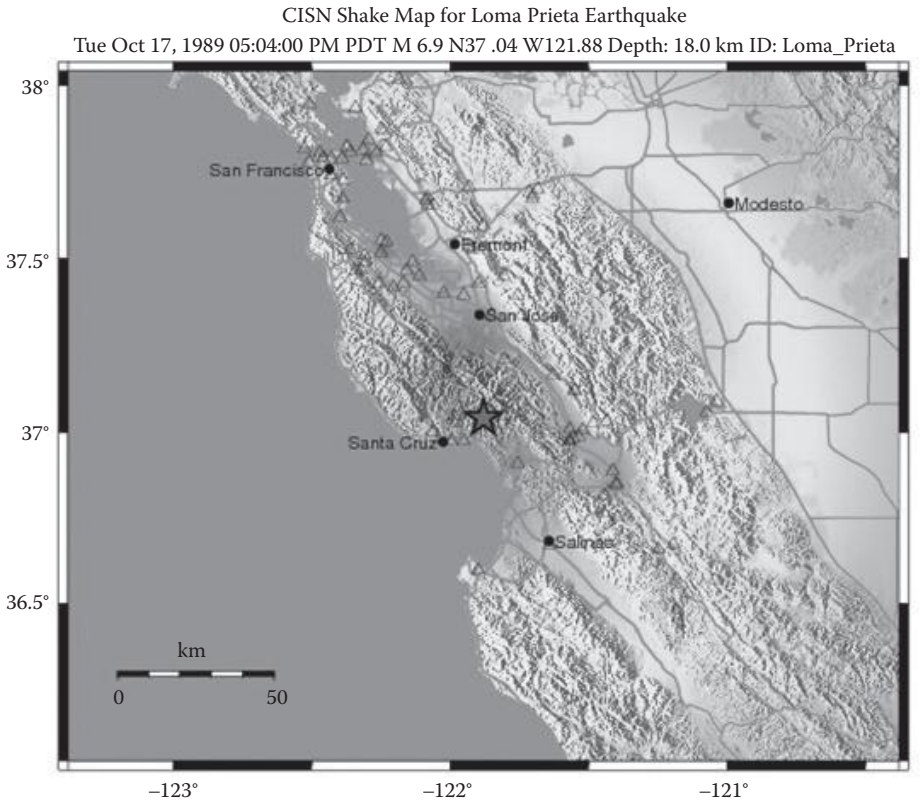

PERCEIVED SHAKING	Not felt	Weak	Light	Moderate	Strong	Very Strong	Severe	Violent	Extreme
POTENTIAL DAMAGE	None	None	None	Very Light	Light	Moderate	Moderate/Heavy	Heavy	Very Heavy
PEAK ACC(%g)	< .17	.17–1.4	1.4–3.9	3.9–9.2	9.2–18	18–34	34–65	65–124	> 124
PEAK VEL(cm/s)	< 0.1	0.1–1.1	1.1–3.4	3.4–8.1	8.1–16	16–31	31–60	60–116	> 116
INSTRUMENTAL INTENSITY	I	II-III	IV	V	VI	VII	VIII	IX	X+

FIGURE 2.5 Shake map for the 1989 M6.9 Loma Prieta, California earthquake.

So, an important site condition for bridge damage is the shear wave velocity of the top 30 m (98 ft.) of the ground (v_{s30}). Far from the fault rupture softer soils are amplified and can damage vulnerable bridges. Longer period structures also see higher accelerations on soft soil. Only very short period structures are negatively impacted on rock.

Other site conditions that affect ground motion include deep (2.5 km) basins filled with alluvium. Shear waves traveling through these basins can be amplified, especially along the edges of the basin. Topographical features also have an effect on ground motion, especially enhancing the amplitude of surface waves.

2.2.2 Structural Parameters

Certain parameters can prevent bridges from collapsing during strong ground shaking. For instance, good development of reinforcement or "continuity" can prevent concrete bridge elements from being pulled apart during earthquakes. During the 1971 San Fernando earthquake, concrete girder bridge columns pulled out of pile caps and pile shafts as the bridge moved back and forth, contributing to their collapse. After the earthquake Caltrans required all column reinforcement on new bridges to be fully developed through the foundation and bent cap. Similarly, during the 1989 Loma Prieta earthquake, poor

development of column reinforcement on the Cypress Viaduct allowed the columns supporting the upper deck to pull out of the connections at the column base and resulted in about a mile (1.67 km) of the upper bridge deck smashing onto the lower deck. Similarly, the longitudinal reinforcement in the pile extensions on Struve Slough Bridge was not adequately developed into the bent cap resulting in the superstructure and the piles pulling apart and collapsing. Inadequate development of reinforcement of the precast girders on the Napa River Bridge pulled out of the diaphragms above the bents and almost collapsed. Providing good development of reinforcement for precast girder bridges continues to be an issue at Caltrans.

The first aspect of continuity is ample seats to support the ends of girders. Caltrans typically designs cast-in-place bridges with fewer girder ends to become unseated. However, during the 1971 San Fernando earthquake, unseating of bridges led to their collapse and resulted in Caltrans requiring new bridges to be designed for a minimum 24 in. (0.6 m) seat and requiring existing bridges to be retrofitted with catchers and restrainers. Today, bridge seats are designed for the combined displacement of the adjacent bridge frames plus additional length for factors such as skew, horizontal curve, and so on.

The second important parameter to prevent collapse is ample "confinement" in concrete columns to allow them to displace without failing in flexure or shear. After the San Fernando earthquake Caltrans required all new bridges to have columns with larger diameter spiral reinforcement at a closer spacing. This increase in transverse reinforcement prevents the longitudinal reinforcement from buckling, increases the stress and strain of concrete and prevents it from escaping the columns, and it prevents shear forces from breaking the columns. Today at Caltrans it is typical to see closely spaced #8 hoops providing confinement for new bridges (Caltrans, 2010c).

The final parameter affecting bridge vulnerability is "regularity." Tall and short columns in the same bent, tall and short bents in a frame, and tall and short frames in a bridge cause the shorter elements to fail since they cannot displace as much as the longer elements (among other problems). Not only is it important for the elements on a bridge to be regular and balanced but parts of bridge elements should also be regular. For instance, nonprismatic elements like flared columns often fail during earthquakes. The strong flare forces plastic hinging into the short column below it. The shorter column gets a bigger shear force ($V_p = M_p/L$), which can fail the column. Bridge elements arranged in parallel need to have about the same stiffness, carry about the same mass, and have about the same period. Bridge elements arranged in series need to have about the same strength and stiffness to prevent the weaker element from failing prematurely.

Experience indicates that a bridge is most likely to be vulnerable if (1) excessive deformation demands occur in a few brittle elements, (2) the structural configuration is complex, or (3) a bridge lacks redundancy. The bridge designer needs to recognize the potential consequences of these irregularities, and design accordingly to either reduce the irregularity or toughen the structure to compensate for it.

There are other parameters that are effective in reducing bridge damage but continuity, confinement, and regularity can eliminate most bridge collapses resulting from strong ground shaking during earthquakes.

2.2.3 Remaining Bridge Capacity

Many concrete bridge columns have been tested during the past 20 years. Researchers have created databases of the resulting column damage for a variety of purposes. One goal is to provide tools to determine the remaining column capacity on a bridge after an earthquake. For instance, five damage states (DS) from hundreds of column tests as shown in Figure 2.6 are identified by Saiidi (2011).

The trick is to identify how ductile or brittle the concrete column is and then study the damage to determine where you are on the curve and how much capacity you have left. For instance, if we were aware that there is not a lot of transverse reinforcement in a column and it is at DS-3, than there is little capacity remaining, and so this column would be shored and replaced. This type of capacity assessment can be done for other vulnerable bridge elements such as girders, girder/column joints, foundations, abutments/shear keys, hinge seats, bearings, and so on.

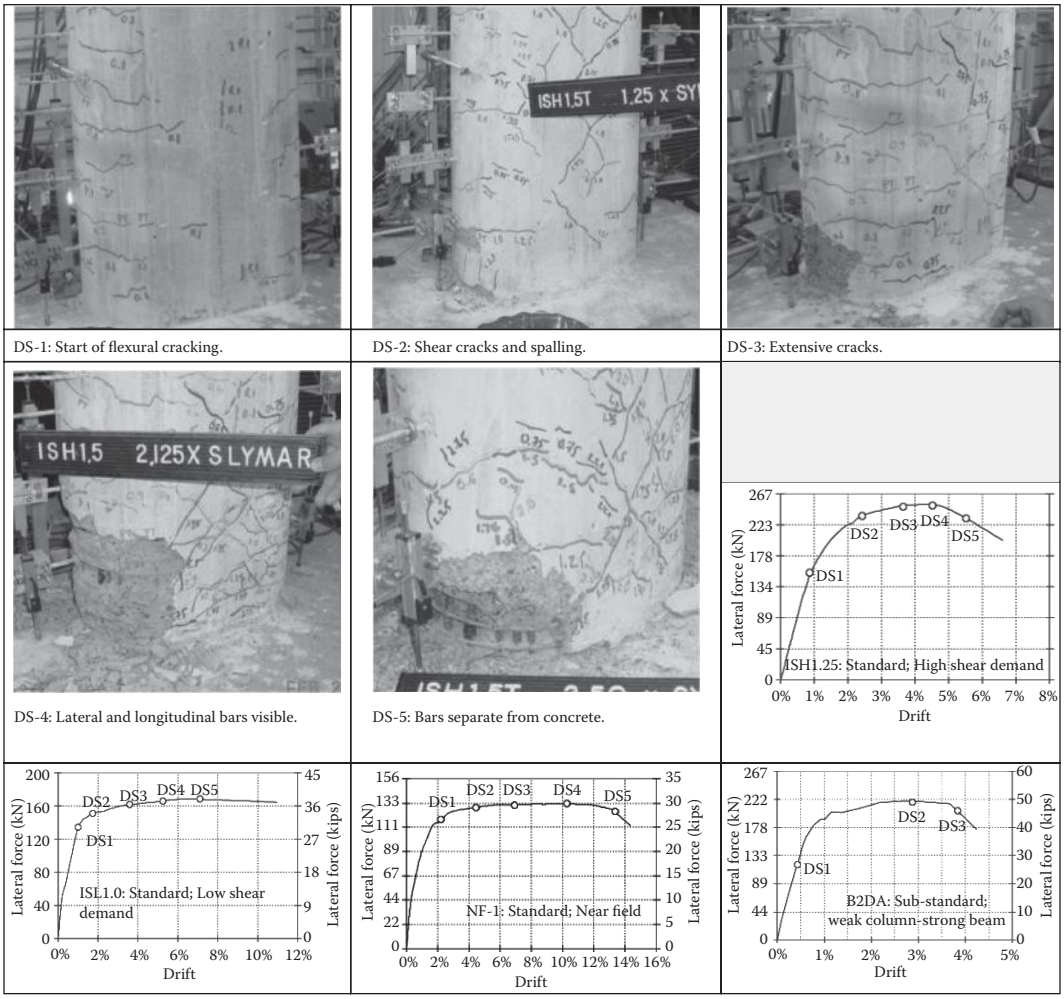

FIGURE 2.6 Using "damage states" to determine remaining bridge capacity.

2.3 Ground Shaking Damage to Standard Girder Bridges

2.3.1 Damage to Superstructures

It is usually at discontinuities in the superstructure where damage occurs. For instance, an expansion joint is often provided in the superstructure to release stresses because of thermal movement of the superstructure, post-tensioned superstructure shortening, creep and shrinkage, and relative settlement of supports. Expansion joints are located over abutment seats, bent caps, and at in-span hinges. When the ends of the girders sit on a narrow seat, the bridge is vulnerable to collapse. After the 1971 San Fernando earthquake, engineers began putting cable restrainers at expansion joints. However, that practice is discouraged today. It is unlikely that enough cables can be provided to prevent unseating or to support the superstructure if it falls. Since unseating is related to column displacement, the seats at expansion joints must be longer than the combined earthquake displacement of adjacent bents and frames.

Sometimes the girders fall off the bearings but not the seat. Although this can be a headache to repair, it is much better than having the girders fall off the seat and dropping the span. Girders falling off bearings can destroy the expansion joint device, which is a danger to inattentive drivers (Figure 2.7a).

(a)

(b)

(c)

FIGURE 2.7 Damage to Superstructure. (a) Girders on the Wangan Expressway came off their bearings during the Kobe earthquake, which posed a hazard to drivers. (b) When the Bolu Viaduct in Turkey became unseated during the 1999 Duzce earthquake. (c) The well-designed deck prevented a collapse.

If the superstructure is continuous, then the superstructure can move off the bearings without much danger of becoming unseated. This is a much better situation since injuries are unlikely to occur. Generally, only the deck is made continuous over simply supported girders. Here the situation is more uncertain. An extremely well-designed deck can sometimes support the girders as they become unseated (Figure 2.7b and c), but the downward force is usually enough to break the deck in two.

In order for a bridge girder to become unseated, the distance between supports must become larger than the length of the girders. Usually the bents move in the same direction during an earthquake. However, if bents or frames have different stiffness or periods, then it is possible for them to move in opposite directions (or some to move farther than others). For instance, the portions of the Kobe Route 3 Expressway in Figure 2.9 show several simple spans with fixed (pinned) and movable (roller) bearings on opposite ends and an expansion joint between them. During the 1995 Kobe earthquake, the spans moved to the west and fell off the bent caps at Pier 40 and Pier 41 but not at Pier 39 (Figure 2.8a and b). Stiff Pier 39 acted like an anchor, whereas Pier 41 and 42 moved in the opposite direction, pulling the spans off Pier 40 and Pier 41 (Figure 2.9a, b, and c).

A similar situation occurred to the Llacolen Bridge over the Bio River in Concepcion, Chile. At the north end of the bridge, several connectors come together on to a long, stiff bent with a short seat. The more flexible connectors moved to the north during the 2010 M8.8 Chile earthquake, pulling their end spans off the stiffer river bridge (Figure 2.10).

Many superstructures fell off their seats during the 2010 Chile earthquake. Newer bridges were built with short seats, weak shear keys, and without end diaphragms between the girders. The Puente Los Echevers on the Vespucio Norte Expressway was parallel to three span precast I girder bridges. During the earthquake, the spans of the newer bridge rotated enough to push over the steel keeper plates and unseat all three spans. Note the parallel bridge (with concrete shear keys and end diaphragms) was undamaged (Figure 2.11a and b).

FIGURE 2.8 Unseating at Piers 41 and 40 and column damage at Pier 39 during the Kobe EQ.

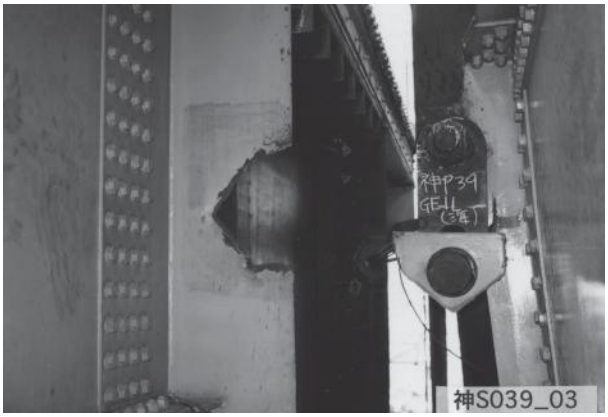

(a)

(b)

(c)

FIGURE 2.9 Route 3 after the Kobe earthquake. (a) Top of Pier 39. (b) Pier 40. (c) Pier 42.

FIGURE 2.10 Collapsed connectors to the Puente Llacolen.

(a)

(b)

FIGURE 2.11 Puente Los Echevers on Vespucio Norte after the 2010 earthquake. (a) Overview. (b) Side view.

Bridges usually do not unseat transversely, but two span overcrossings over Route 5 in Chile had a main mode of vibration that was rotation around the center bent. Because of the lack of an end diaphragm many of the girders were able to fall off their abutments (Figure 2.12a). Many of these bridges had good slope paving that caught the girders (Figure 2.12b), although not all the overcrossings were so lucky. Chile's Ministry of Transportation required all new bridges to have end diaphragms after the earthquake.

Curved and skewed bridges become unseated because transverse movement can become longitudinal movement at the joint and because the center of stiffness and mass are some distance apart (Figure 2.13a, b, and c).

(a)

(b)

FIGURE 2.12 Highway bridge unseated transversely. (a) Bridge over Route 5 in Chile—typical highway overcrossings without a diaphragm to provide continuity at the ends of spans. (b) Bridge unseated.

(a)

(b)

(c)

FIGURE 2.13 Damage to curved and skewed bridges. (a) The Minatagawa Interchange after the Kobe earthquake. (b) Fields Landing OC after the 1980 Trinidad, CA earthquake. (c) Gavin Canyon Undercrossing after Northridge.

2.3.2 Damage to Substructures

The other main cause of bridge collapse is because of poorly designed substructures. If the superstructure is firmly attached to the substructure then the forces must be carried through the substructure as the ground moves back and forth and the superstructure's mass is excited. Substructures are more likely to be damaged when the superstructure is cast monolithically with the substructure. If the superstructure can move on its seat, then the forces to the substructure are reduced. That is why there is less column damage when there is a lot of unseating (like in Chile). Usually you see some unseating and some substructure damage. However, if the substructure has ample confinement and continuity and it is prismatic and regular then it is unlikely to break even though it may sustain considerable damage during an earthquake.

The forces being carried by the substructure are mainly shear (especially for short, stiff substructures) and bending (especially for tall, flexible substructures). There may be some axial forces (especially as multi-column bents move transversely) and there is occasionally torsion (especially when the inertia force is not centered over the columns).

When coming upon a bridge after an earthquake, it is always a good idea to try to draw what the displaced shape of the structure was during ground shaking. Cracks on the substructure can show how the bridge moved. Unfortunately, when a bridge collapses, most of the evidence is destroyed. Figure 2.14 shows a reinforced concrete single-column bent that collapsed because the horizontal shear force exceeded the column's capacity. This section of the Kobe Expressway moved in a longitudinal direction until the column broke and fell into the ground with the span that pushed the column over still laying on top and the span that was pushed out of the way lying beside it on the ground.

More visual information is provided before the pier collapses. Figure 2.15 shows another pier, quite close by, that was supporting two continuous steel box girders. It is seen that the transverse reinforcement has failed and the stiff column has split diagonally into two. This is the worst possible design for a seismic member. It was designed to be extra stiff but it immediately failed in shear. On the positive side, the continuous superstructure was so strong that it easily handled the loss of the support.

The cast-in-place concrete box girder bridge is popular, especially in California. The superstructure, consisting of reinforced concrete box girders with longitudinal steel reinforcement and post-tensioned tendons, is usually rigidly connected to the substructure columns. Expansion and contraction are permitted at in-span transverse joints and/or transverse joints over piers and abutments. Figure 2.16 shows damage to

FIGURE 2.14 Collapsed Pier 167 on Route 3 after the 1995 Kobe earthquake.

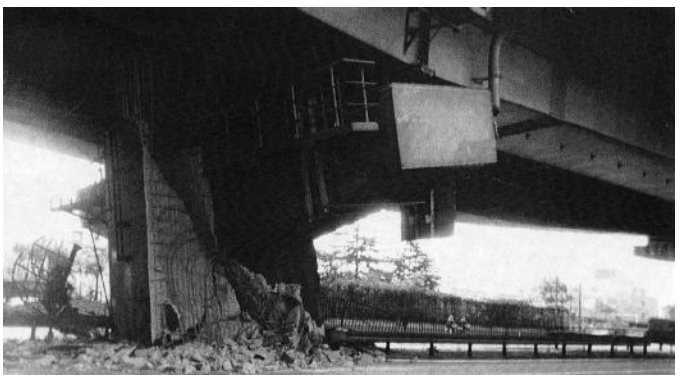

FIGURE 2.15 Pier 150 on Route 3 with shear damage after the 1995 Kobe earthquake.

a cast-in-place box girder bridge from the 1994 Northridge earthquake. As short, stiff Bent 2 collapsed near the abutment, a large positive moment developed in the prestressed superstructure at Bent 3. The prestressing tendons were incapable of handling the excess moment and failed in tension. Once the tendons broke, the spans on both sides of Bent 3 fell into the ground. This is also an example of how difficult it is to see the cause of bridge damage once the superstructure has collapsed on top of the supports.

Although the collapse was because of the failure at Bent 2, concern about the observed performance of this type of superstructure prompted changes in design practice. More longitudinal reinforcing steel is now placed at the top and bottom of girders over the supports and at midspan. Also, the maximum strain for prestressing tendons is limited to 3% where a plastic hinge is expected to develop at the top of the columns.

In most modern seismic criteria, a bridge column is designed to withstand shear forces corresponding to the column's plastic hinge capacity. The maximum induced shear in the column is limited to the plastic hinge moment (or moments) divided by the column length. For this simple strategy to be successfully implemented, the effective column length must be ascertained in the design stage and kept constant

FIGURE 2.16 The southbound separation and overhead after the 1994 Northridge earthquake. (Photo courtesy of Professor Frieder Seible.)

FIGURE 2.17 Multi-column bent damage on the Mission Gothic Undercrossing after the 1994 Northridge earthquake.

during the life of the bridge. Figure 2.17 shows a failed column of the Mission Gothic Undercrossing after the 1994 Northridge earthquake. The column design assumed that a plastic hinge would form at the top of the column. However, the added nonstructural flares reduced the effective length of the column, substantially increasing the induced horizontal shear, exceeding the design capacity, and resulting in failure during the earthquake.

Substructures with inherent ductility have performed well during recent earthquakes, such as the Ruffner Avenue Overcrossing in Northridge. Figure 2.18 shows a 1500 mm diameter hexagonal column section from this overcrossing with #14 (45 mm) longitudinal reinforcement and #5 (16 mm) spiral reinforcement at 90 mm spacing. The column was designed and constructed in the 1970s. During the 1994 Northridge earthquake, the cover concrete spalled off. However, the longitudinal reinforcement was protected from buckling, and the core concrete was prevented from crumbling by the transverse reinforcement. This kind of damage is anticipated and considered acceptable in a strong earthquake. As long as the transverse reinforcement remains intact and the cracked concrete does not spill out, the bridge should continue to support substantial forces until it is repaired or replaced.

Another common bridge substructure element is the reinforced concrete pier wall. This element has usually performed well during earthquakes. The damage shown in Figure 2.19 was caused by vertical reinforcement that went only halfway up the pier wall. As the bridge moved longitudinally, these bars pushed off the cover concrete, weakening the pier wall, which failed in shear. Testing has shown that pier walls, even those with minimal stirrups and ties (but with sufficiently lapped or continuous vertical reinforcement), have a displacement ductility of 2–3 in the longitudinal direction (Haroun, 1993). However, such pier walls are very stiff in the transverse direction and can attract large forces that may cause foundation damage. There is also concern that thin pier walls (<60 cm thick) may become unstable because of the longitudinal displacement that occurs during strong ground motion.

FIGURE 2.18 Damage to a column on the Ruffner Avenue Overcrossing after the 1994 Northridge earthquake.

FIGURE 2.19 Damaged reinforced concrete pier wall at Moribe Viaduct on the Meishin Expressway after the 1995 Kobe earthquake.

FIGURE 2.20 The precast girders on the Napa River Bridge had holes drilled at the ends, #8 rebar inserted into the holes, and diaphragms cast at the ends. However, during the 1989 Loma Prieta earthquake, the girders pulled out of the diaphragms and almost unseated.

2.3.3 Damage to Connections

There are a variety of connections between bridge members. In the longitudinal direction, adjacent spans can be continuous over the support and they can also be free or fixed (for translation and rotation) to the supports. It is easier to provide reliable connections between cast-in-place members. Adjacent precast girder spans are often poorly connected and can pull apart during earthquakes. During the 1989 Loma Prieta earthquake the supposedly continuous precast spans of the Napa River Bridge pulled apart and almost fell off their supports (Figure 2.20).

In the transverse direction the connection between the superstructure and the substructure can be just as diverse. When the girders sit on a drop bent cap, each girder can be supported on a bearing

or the girders can be connected to an end diaphragm with bearings between the end diaphragm and the bent cap. The connection from the bent cap to the columns can be well-behaved 'T' joints that have ample concrete on both sides of the column, but sometimes the exterior columns are placed too close to the end of the cap, creating weak 'knee' joints that are often damaged during earthquakes (Figure 2.21).

For a capacity-protected design to be effective, the connections at the top and bottom of columns must be strong enough to force plastic hinging in the columns. If the connections are poorly designed, the damage will occur in the connection instead, with less reliable results. The most common damage of this type is because of inadequate development of reinforcement through the connection. This can occur between the girders and the columns, which was seen during the 1995 Kobe earthquake (Figure 2.22),

(a)

(b)

FIGURE 2.21 Weak "knee" joints like the connection to this outrigger on the China Basin Viaduct are subject to large opening and closing moments as the bridge moves back and forth.

FIGURE 2.22 The column reinforcement was not sufficiently developed into the knee joints on the Benton Viaduct in Downtown Kobe and the connection fell apart during the 1995 Kobe earthquake.

or between the columns and the foundation, which occurred during the San Fernando earthquake (Figure 2.23), (or even more devastating) between the top and bottom columns of double-deck structures like the Cypress Viaduct (Figure 2.24).

Another type of connection damage that is often observed after earthquakes is because of lack of confinement in the joint region. When the connection is required to transfer bending moments and shear forces between members, then a lot of reinforcement is required to prevent joint shear damage.

2.3.4 Damage to Foundations

A problem with foundation damage is that it occurs underground where it may not be detected (although disturbance of the ground surface is sometimes observed). The lack of visual evidence of foundation damage is such a concern that some bridge owners require plastic hinging above the ground surface where it can be more easily detected. However, the excellent behavior of pile shafts that are allowed to form plastic hinges and the expense of preventing all damage to the foundation has made some foundation damage during large earthquakes inevitable.

There has been little foundation damage observed after earthquakes in competent soil. Most foundation damage occurs in weak or liquefied soil as we shall see in Section 2.5.1. In stiff soil there is little foundation movement and without movement there can be little damage. After the Kobe earthquake, the piles were exposed (or drilled from above and studied with television cameras) but little damage was found (Figure 2.25).

Damage to piles or a pile cap usually does not result in loss of lateral stability for bridges. Areas of concern for foundations in competent soil are loss of bearing capacity because of rocking of the foundation, pile "fence posting" because of inadequate embedment into the ground, and damage to the connections at the top of batter piles.

(a)

(b)

FIGURE 2.23 The column reinforcement was not sufficiently developed into the pile shafts on the Route 210/5 Separation and Overhead, which contributed to bridge toppling over during the 1971 San Fernando earthquake.

FIGURE 2.24 The column reinforcement supporting the top deck of the Cypress Viaduct was not sufficiently developed at the bottom and pulled out during the 1989 Loma Prieta earthquake.

FIGURE 2.25 The pile foundation of severely damaged Pier 126 on the Route 3 Expressway was uncovered after the 1995 Kobe earthquake but only moderate cracking was found at the top of the piles. This was the most severe foundation damage that was found on the expressway.

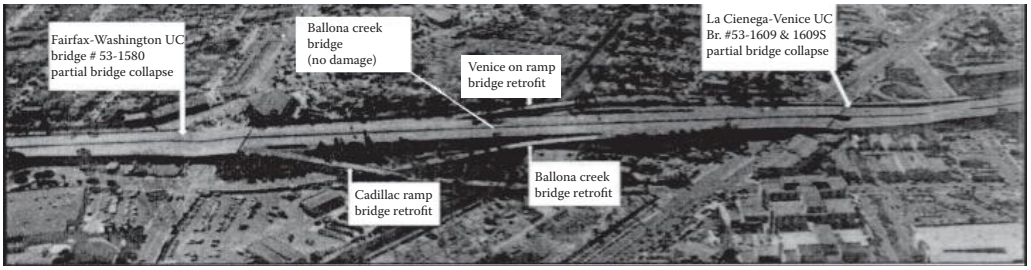

FIGURE 2.26 The collapsed bridges on the Santa Monica (I-10) Expressway sit next to several undamaged retrofits after the 1994 Northridge earthquake.

2.3.5 Damage to Retrofits

After the 1994 Northridge earthquake, a careful survey was made to the many retrofitted bridges in areas where peak ground acceleration (PGA) was >0.2 g. In many cases these bridges were sitting undamaged next to collapsed unretrofitted bridges (Figure 2.26). None of the retrofitted bridges had serious damage and the conclusion (by George Housner of Caltrans Seismic Advisory Board) was that if the retrofit program had been completed, there would have been little bride damage during the Northridge earthquake.

During the 2001 M6.8 Nisqually Earthquake, a major via duct in downtown Seattle with steel jacketed columns had no damage (Figure 2.27). However, ground shaking in the Seattle was low and it will take a much stronger earthquake to test this retrofitted bridge.

After the 2011 Christchurch New Zealand earthquake two bridges that had undergone seismic retrofits as part of the New Zealand Transport Agency (NZTA) seismic retrofit program were studied. The Port Hills Overbridge and the Horotane Overbridge were within 200 m (656 ft.) of each other and both retrofits were designed to link the spans together and to the abutments (Figure 2.28) to make these precast girder bridges behave more like monolithic, cast in place bridges. This type of retrofit appears to have worked well, and although both bridges sustained damage, they were able to go back in service soon after the earthquake. The Port Hills Overbridge suffered some pier damage because of transverse ground shaking and the bolts that tied the spans to the abutments had elongated. The Horotane Overbridge suffered abutment damage and a small slope failure

FIGURE 2.27 Undamaged steel jackets on columns of a major viaduct in Seattle after the 2001 Nisqually earthquake.

FIGURE 2.28 Retrofitted pier cap on Port Hills Overbridge after the 2011 Christchurch, New Zealand earthquake. (Photo courtesy of L. Hogan.)

of the embankments. The ties between spans and at the abutments also elongated and pulled out as they had in the Port Hills Overbridge. Additionally, approximately 60% of the bolts that attached the soffit of the precast concrete beams to the abutment seat extension sheared off (Figure 2.29). Although initially alarming, this failure of the retrofitted bolts highlights the necessity of bridge retrofits. If these spans had not been tied together and the seats not extended it is quite likely the spans would have collapsed.

FIGURE 2.29 Sheared bolt at Horotane Overbridge abutment retrofit after the 2011 Christchurch, New Zealand earthquake. (Photo courtesy of J. Allen.)

2.4 Ground Shaking Damage to Nonstandard Bridges

Bridges with continuous superstructures, balanced, regular elements, and good reinforcing details are straightforward to analyze and design for earthquakes. However, special circumstances require special bridges, which may have more complicated behavior and may be more vulnerable to ground shaking hazards. Caltrans Memos to Designers 20-1 defines Nonstandard Bridges as structures that have features that require a more detailed analysis in order to capture their complex response during earthquakes. The following Nonstandard Bridges have been observed to have characteristic types of ground shaking damage during large earthquakes.

2.4.1 Highway Interchanges

Interchanges usually have several levels of ramps to provide drivers with connections between different routes where two or more highways come together. These connectors may have tall and short bents and are often connected to other bridges with different stiffness and period. Considerable effort has been made recently to develop criteria for "urban interchanges," that provide the same level of convenience but with better seismic performance. However, because the interstate highway system was largely completed many years ago, few new "urban interchanges" have been built. Much of the damage to conventional interchanges has been described in the previous sections. Figure 2.10 shows the problems when several connectors come together onto a short stiff bent. Figure 2.13a shows the problem of short radius connectors moving off their supports. Figure 2.16 illustrates the problem of short and tall bents that allow connectors to climb over and under other connectors on the 14/5 Interchange.

The 14/5 Interchange was being constructed during the 1971 San Fernando earthquake and suffered a great deal of damage. The interchange was rebuilt only to again suffer significant damage during the

FIGURE 2.30 Damage to the 14/5 Interchange during the 1994 Northridge, California earthquake.

1994 Northridge earthquake (Figure 2.30). Unlike a Standard Bridge where a detour can be provided on a nearby surface street, the closure of the 14/5 Interchange required a long detour and a 45-minute delay for commuters trying to get into Los Angeles from the north.

2.4.2 Arch and Truss Bridges

Until recently, engineers would often use arches or trusses for medium-span bridges. Today, they are not designed as often but there are still a lot of these bridges around. There are a great variety to arches and trusses but they all have long spans with large inertia forces during earthquakes.

The San Francisco-Oakland Bay Bridge east span, a through-truss structure, dropped a 15 m long span during the 1989 Loma Prieta earthquake. The easternmost frame, consisting of 14 truss spans 90 m long, was supported laterally by the stiff Pier E9. The frame moved 30.5 cm longitudinally during the earthquake, shearing all the bolts at the truss bearings at Pier E9 and pulling the top and bottom deck spans off their supports.

Truss bridges are held together with hundreds of connections. Unless the connections, usually gusset plates, are carefully designed for longitudinal and transverse earthquake forces, they can be damaged during earthquakes. For instance, in the 2011 Tohoku, Japan earthquake the Arakawa Truss Bridge had dozens of gusset plates that ripped apart by transverse shaking (Figure 2.31) even though it was far from the fault and had a PGA of about 0.2 g.

To prevent collapse, long-span structures such as arch and truss bridges must be carefully designed with ample reserve capacity and ductility for unexpectedly large earthquakes. The Rokko Island Bridge is an arch bridge with a span of 214 m and a height of 36 m. During the 1995 Kobe earthquake, the arch superstructure moved 3 m transversely and would have fallen off its piers if it had not been caught by a jacking platform (Figure 2.32). This movement damaged the arch, requiring that it be removed and replaced by a new superstructure.

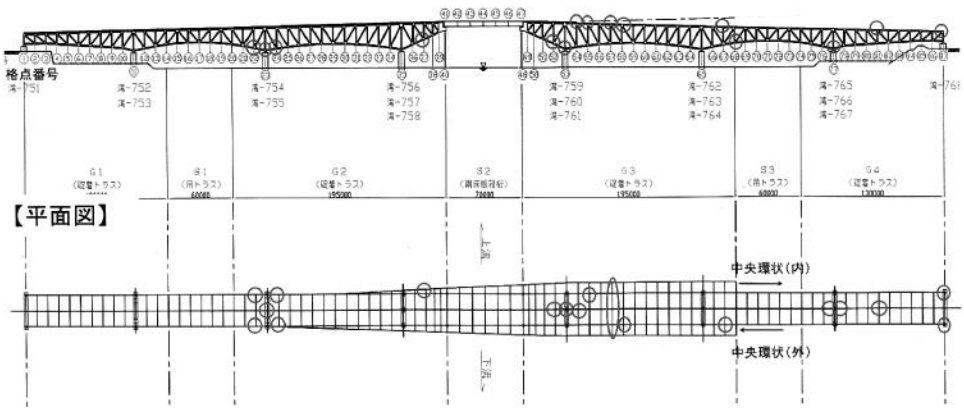

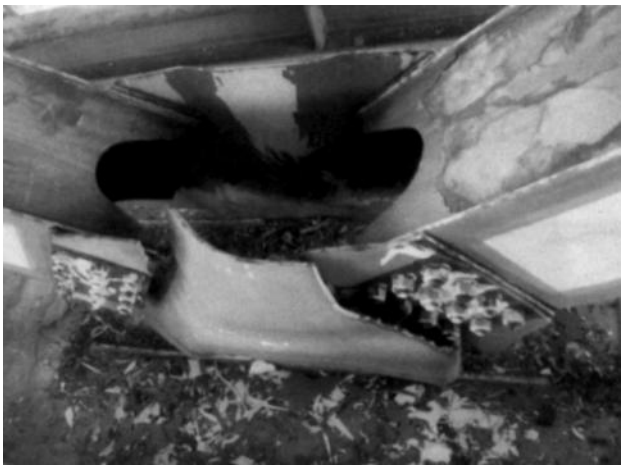

FIGURE 2.31 Damage to the Arakawa (deck truss) Bridge during the 2011 M9.1 Tohoku Japan earthquake.

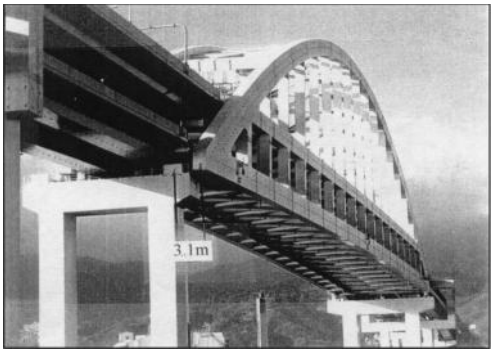

FIGURE 2.32 Damage to the Rokko Island (tied arch) Bridge during the 1995 M6.9 Kobe, Japan earthquake.

FIGURE 2.33 Collapsed Puente Rio Claro (masonry arch) during the 2010 M8.9 Maule, Chile earthquake.

The Rio Clara Bridge was built in 1870 and had survived many large earthquakes. However, strong ground motion can vary. Just because a structure has survived previous earthquake does not guarantee that it is well designed. Many old arch bridges are made of stone masonry that can fall apart because of tension or bending. During the 2010 Maule, Chile earthquake this bridge was finally shaken apart (Figure 2.33).

2.4.3 Cable-Stayed and Suspension Bridges

If the performance of truss and arch bridges with their longer spans has been poor, then the performance of the longer cable-stayed and suspension bridges is even more problematic. Because of the very large inertia forces of long-span bridges, the best way to prevent damage is to isolate the towers from the bridge deck.

Cable-stayed bridges have sustained moderate damage during every earthquake. The Higashi-Kobe Bridge broke a cable during the 1995 Kobe Japan earthquake along with most of the bearings, dampers, and hold-downs connecting the deck to the supports (Figure 2.34). The end spans of the single-tower Chi-Lu Bridge were badly damaged during the 1999 Chi-Chi earthquake along with a broken cable and a lot of spalling (Figure 2.35). A single-tower design may not be a good idea in areas of high

FIGURE 2.34 The Higashi Kobe Cable-Stayed Bridge after the 1995 Kobe, Japan earthquake.

FIGURE 2.35 The Chi-Lu Cable-Stayed Bridge after the 1999 Chi Chi, Taiwan earthquake.

seismicity since the structure has a tendency to rotate about the tower. The tie rods and wind shoes of the Yokohama Bay Bridge were damaged during the 2011 Tohoku Japan earthquake (Figure 2.36) despite being far away from the fault and with a PGA of <0.2 g.

There has not been a great deal of damage to suspension bridges because of ground shaking but they have been sensitive to other seismic hazards. During the 2011 Christchurch, New Zealand earthquake the Mandeville Suspension Bridge had considerable damage because of movement of the cable anchors (Figure 2.37). Also, the Groynes Footbridge, a concrete suspension bridge sustained major damage (Figure 2.38) despite being considerable distance from the fault rupture. Suspension

FIGURE 2.36 The Yokohama Bay Cable-Stayed Bridge after the 2011 Tohoku, Japan earthquake.

FIGURE 2.37 The Mandeville Pedestrian Suspension Bridge after the 2011 Christchurch, New Zealand earthquake.

FIGURE 2.38 The Groynes Pedestrian Suspension Bridge after the 2011 Christchurch, New Zealand earthquake.

FIGURE 2.39 The West Seattle Swing Bridge after the 2001 Nisqually, Washington State earthquake.

bridges are long-period structures that are sensitive to low amplitude, long-period ground motion from distant earthquakes. For instance, the Vincent Thomas Bridge was shaken and sustained minor damage from the Northridge and from other earthquakes that are many miles away.

2.4.4 Movable Bridges

Movable bridges allow ships access through channels and rivers. However, many of these bridges use counterweights that create large eccentric forces that can cause significant damage during earthquakes. Swing bridges are a better alternative, but they have locking devices at the ends of the spans and machinery at the towers that are vulnerable to earthquake motion. The West Seattle Swing Bridge was subjected to a peak ground motion of 0.25 g during the 2001 Nisqually earthquake. This motion broke the shims and locking devices on the bridge (Figure 2.39) and the channel was closed to ship traffic for several weeks after the earthquake.

2.5 Damage Caused by Other Seismic Hazards

Originally, bridge engineers were mostly concerned with preventing ground shaking damage to bridges during earthquakes. This was because most of the damage during earthquakes was caused by ground shaking. However, as bridge engineers began paying more attention to earthquakes around the world, they became aware that other hazards could be equally damaging to bridges. Today, bridges are designed for the design earthquake that includes all seismic hazards that can occur at the bridge site.

2.5.1 Liquefaction and Lateral Spreading

Saturated loose sandy and silty layers of soil can liquefy when shaken by an earthquake. Liquefaction reduces soil stiffness and can cause a loss of bearing capacity at bridge foundations. The increased pore pressure can create lateral forces that push against piles and move bridge piers toward adjacent bodies of water. This was noted by pioneering geotechnical engineers during the 1964 Great Alaska and Niigata, Japan earthquakes. They carefully studied the behavior of liquefied soils and documented the collapse of several bridges, including the newly constructed Showa Bridge across the Shinano River. During the 1964 M7.5 Niigata Japan earthquake, the soil around this 11 span bridge liquefied resulting in the collapse of the two center piers and the loss of six spans (Figure 2.40). Liquefied soil has played a large role in bridge damage during subsequent earthquakes. For instance, very similar damage occurred to the Rokko Bridge in Ibaraki Prefecture during the 2011 Tohoku, Japan earthquake. The soil around the bridge liquefied and the center two piers collapsed resulting in the loss of the center three bridge spans (Figure 2.41).

FIGURE 2.40 The Showa Bridge after the 1964 Niigata, Japan earthquake.

FIGURE 2.41 The Rokko Bridge after the 2011 Tohoku, Japan earthquake.

Lateral spreading has also damaged bridges in recent earthquakes. During the 1995 Kobe earthquake the piers on the Wangan Expressway moved toward the Shukugawa River almost dropping one of the spans (Figure 2.42a). What are bridge owners supposed to do when the bridge piers have moved? In this case, they simply built a corbel on the edge of the bent cap and set the girders on new bearings (Figure 2.42b). After the 2003 Zemourri, Algeria earthquake, lateral spreading around the Isser River Bridge caused similar movement of the piers, which resulted in cutting the girders into manageable segments before moving them back in place (Figure 2.43a and b).

During the 2007 M6.8 Niigata, Japan earthquake, a great deal of lateral spreading occurred at river crossings, but the strong piles continued to support the bridge and prevented severe damage (Figure 2.44). However, during the 2011 Christchurch, New Zealand earthquake, lateral spreading behind the abutments resulted in many broken piles (Figure 2.45) leaving the bridge owner with only two options: replace the piles or replace the bridges.

(a)

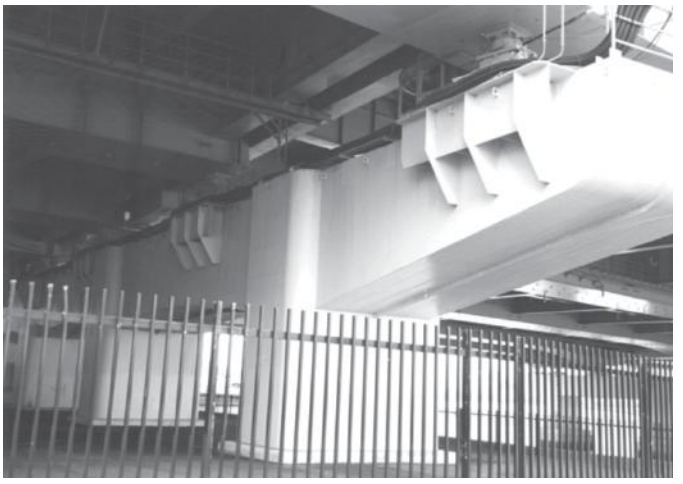

(b)

FIGURE 2.42 (a) The Wangan Expressway over the Shukugawa River after the 1995 Kobe, Japan earthquake. (b) Repair to the Wangan Expressway over the Shukugawa River after the 1995 Kobe, Japan earthquake.

(a)

(b)

FIGURE 2.43 (a) The Isser River Bridge after the 2003 Zemourri, Algeria earthquake. (b) Repair to the Isser River Bridge after the 2003 Zemourri, Algeria earthquake.

FIGURE 2.44 Tremendous lateral spread at the Heisei Hashi over the Sabaishi river with no bridge damage after the 2007 Niigata earthquake.

FIGURE 2.45 Tremendous lateral spread at Fitzgerald Avenue Bridge over the river Avon with broken abutment piles after the 2011 Christchurch, New Zealand earthquake.

2.5.2 Tsunami

Tsunamis are waves generated by undersea earthquakes that displace large volumes of water. In the deep ocean, such waves are almost unnoticeable, but as they approach the shore, they can reach heights of 30 m. Tsunami can originate thousands of kilometers from shore, giving people a chance to evacuate, or they can originate locally, leaving no time for evacuation.

The shape of the continental shelf and/or the shoreline plays a large role in the destructiveness of a tsunami. Long, shallow shelves such as those along the eastern shore of the United States dissipate much of a tsunami's energy before the waves reach land. Short, steep coastlines such as those along Japan and Hawaii receive the brunt of any tsunami formed in the Pacific.

During the 1964 Prince William Sound earthquake, bridges in Alaska—as well as in Washington, Oregon, and California—were damaged. Two very dramatic aspects of this earthquake were the tectonic subsidence and the tsunami, both of which did tremendous damage to Prince William Sound and Kodiak Island. Kodiak Island residents were assessing the relatively light damage from the earthquake when a tsunami struck 38 minutes after the shaking had subsided. The sea slowly rose from 0 to 4 m in about 10 minutes and then slowly subsided to about 3 m below sea level and then swelled again when a train of 9 m waves struck the island. It was reported that the two bridges at Women's Bay were undamaged by the first incoming wave, but they were torn apart by the outgoing and subsequent waves. The bridge shown in Figure 2.46 collapsed because of damage to the piles. The second bridge at Women's Bay was washed away. All the bridges on Kodiak Island's Chiniak Highway were destroyed by the tsunami, except for those that had already been washed away by tectonic subsidence that had lowered them below sea level (NAS, 1973). The tsunami from this earthquake damaged bridges along much the Pacific Coast. A bridge over the Copalis River was damaged several hours later when the tsunami struck the coast along the state of Washington. The bridge was damaged by debris that had been carried downstream by the returning wave (Figure 2.47).

There has been a recent spate of undersea earthquakes accompanied by terribly damaging tsunami. The 2004 Sumatra earthquake and tsunami killed a quarter of a million people and damaged bridges all along the coast of the Indian Ocean (Figure 2.48). The 2010 Maule earthquake and tsunami damaged

FIGURE 2.46 Tsunami damaged Women's Bay Bridge on Kodiak Island's Chiniak Highway after the 1964 Great Alaska earthquake.

FIGURE 2.47 Tsunami damaged Copalis River Bridge in Washington State after the 1964 Great Alaska earthquake.

FIGURE 2.48 Tsunami damaged Pazhayar River Bridge in Kanyakumari District, Tamil Nadu, India after the 2004 Sumatra earthquake.

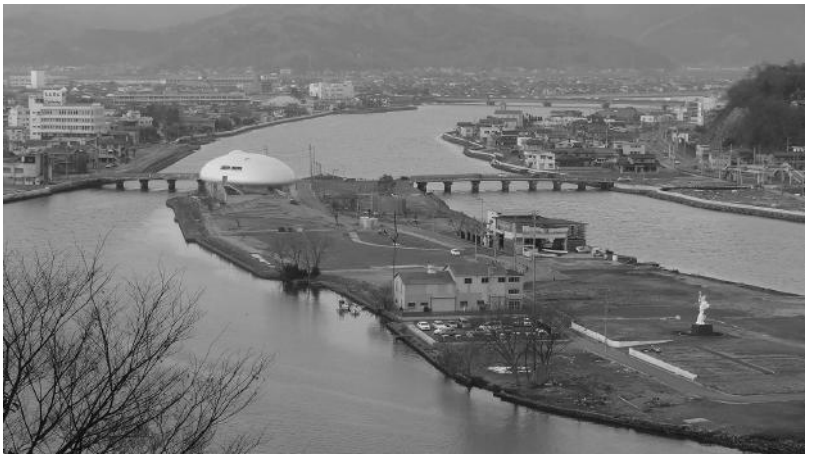

FIGURE 2.49 Comic Book Museum Bridges in Ishinomiya were overtopped by tsunami but relatively undamaged after the 2011 Tohoku, Japan earthquake.

bridges along Chile's coast. The 2011 Tohoku, Japan earthquake and tsunami damaged bridges along 700 km of Japan's Pacific Coast, but even of more interest, did not damage many more bridges that were overtopped by the tsunami waves. We saw during this earthquake that well designed and engineered structures were able to survive the tsunami with little damage (Figure 2.49). Based on current observations, the amplitude of the tsunami hazard appeared to be less important than the bridge details in causing bridge collapse.

2.5.3 Surface Rupture

The 1999 Kocaeli and Chi-Chi earthquakes illustrated how vulnerable bridges were to nearby surface fault ruptures. The Kocaeli earthquake occurred on the North Anatolian Fault Zone (NAFZ), a shallow right-lateral strike-slip fault 1300 km long that has experienced numerous ruptures over the past 100 years. During that earthquake, a surface rupture occurred on 161 km of the NAFZ that is roughly parallel to the Trans-European Motorway (TEM). The TEM is an east–west highway with long viaducts carrying the motorway over rivers and with short overcrossings carrying traffic over the TEM. Figure 2.50 shows the Arifiye Overcrossing after the earthquake. The superstructure consisted of four simple spans attached to a continuous cast-in-place bridge deck and supported on pier walls and seat-type abutments. The bridge crossed over the TEM, two frontage roads, and the fault very close to where the fault crosses the TEM. During the earthquake, the fault pushed the north abutment and pier far enough apart to drop the north span. The other bridge spans also fell, perhaps because the superstructure was pulled to the north before breaking apart.

Even more problematic are bridges that span thrusting faults, such as the Bei-Feng Bridge near Shargang, Taiwan, which spanned the Dajia River, and the Cherlongpu Fault. During the 1999 Chi-Chi earthquake, this fault moved more than 6 m vertically, pushing the south end of the bridge high into the air and causing the three southern spans to drop (Figure 2.51).

2.5.4 Colocation Hazards

A problem that is encountered during almost every earthquake is the failure of nearby buildings, waterlines, and so on that results in damage to bridges that happen to be nearby. The cells of cast-in-place box girders and the space between premanufactured girders are often used to carry gas lines,

(a)

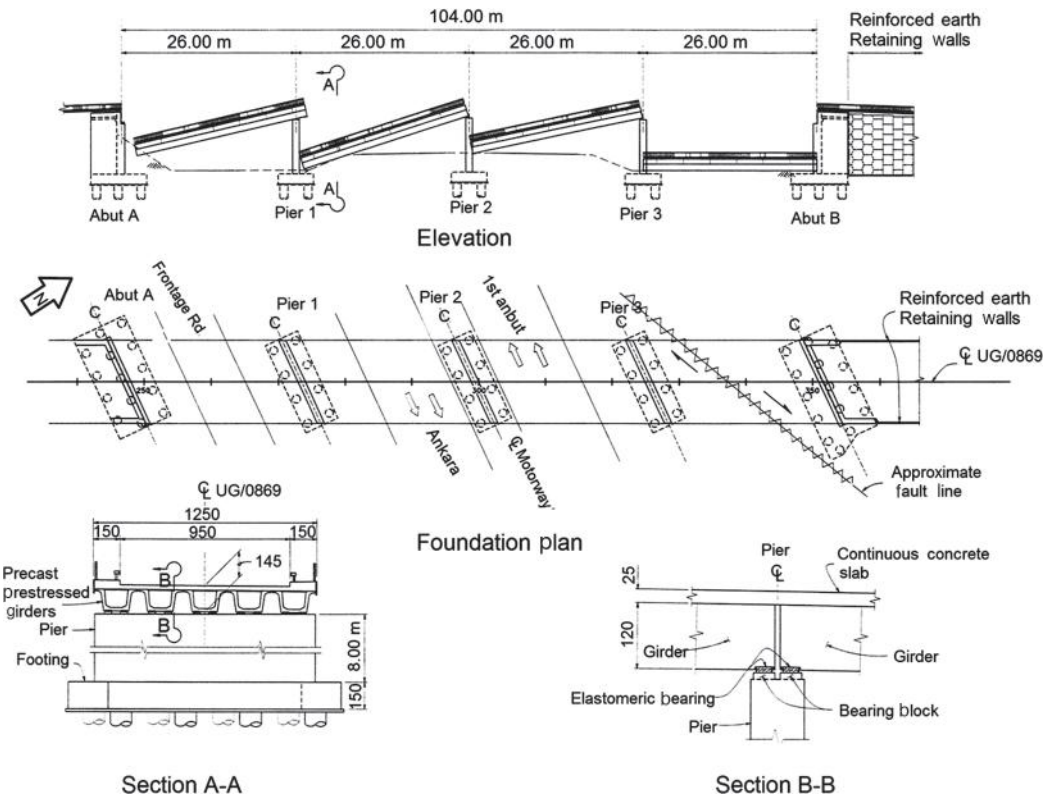

(b)

FIGURE 2.50 Arifiye Overcrossing over the TEM was pulled apart by the strike-slip NAFZ after the 1999 Kocaeli, Turkey earthquake.

(a)

(b)

FIGURE 2.51 Bei-Feng Bridge near Shargang that spanned the Dajia River and the Cherlongpu Thrust Fault had the southern piers lifted 6 m during the 1999 Chi Chi, Taiwan earthquake.

high-pressure water lines, electrical or telephone cables, and other utilities that can be damaged during earthquakes. Such collocation of lifelines and their interaction during earthquakes have become a significant urban planning issue in Wellington, New Zealand (Brunsdon, 2000) and in other seismically active regions. In many cases, utilities carried on a bridge must have flexible joints to accommodate the relative movement between the superstructure and the abutment or embankment. On the Balboa Boulevard Overcrossing during the 1994 Northridge earthquake, the movement between the backfill and the concrete abutment ruptured a high-pressure water line, which washed out the surrounding fill and exposed the abutment pile foundation (Figure 2.52a). The bridge was closed until new backfill could be placed around the abutment. Figure 2.52b shows the utilities carried on this overcrossing.

Adjacent structures often cause bridge damage. A building fell against Pier 352 of Route 3 during the 1995 Kobe earthquake (Figure 2.53a), causing buckling of stiffeners, cross-bracing, and girders (Figure 2.53b), bearing damage, and also some damage to the bottom of Pier 353 (not shown). During the 1971 San Fernando earthquake, the tall Route 210-5 Separation and Overhead collapsed onto the Northwest Connector causing that span also to collapse (Figure 2.54). However, adjacent structures are sometimes helpful during large earthquakes. For instance, storage buildings under

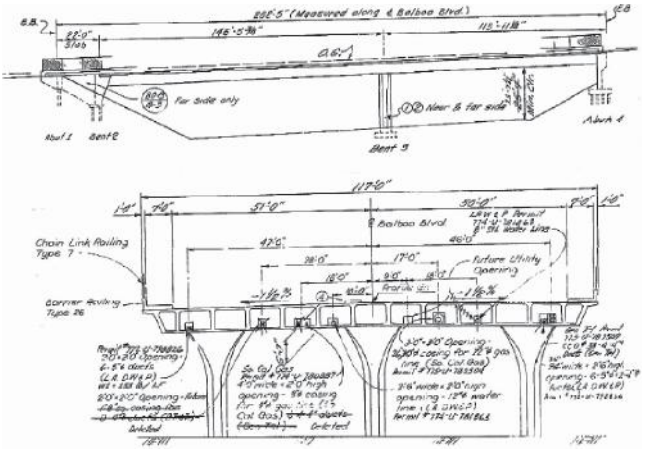

(a)

(b)

FIGURE 2.52 (a) and (b) Balboa Boulevard Overcrossing had the embankment soil around the abutment washed out by a broken waterline after the 1994 Northridge earthquake.

the La Cienega-Venice Undercrossing caught it when its columns failed during the 1994 Northridge earthquake (Figure 2.55).

Addressing colocation hazards is not always easy. Caltrans requires oversized utility openings on its bridges to accommodate the resulting displacement without damage to the pipeline or to the bridge. Utility shut-off valves are required at both ends of the bridge. The utility is required to move onto the median at both ends to facilitate repairs without obstructing the roadway. Box girder bridges carrying waterlines have large weep-holes in the soffit so the bridge does not collapse from the weight of the liquid if the water or sewer lines break and fill the bays.

It would be expensive to require a right-of-way wide enough to prevent the collapse of nearby buildings from impacting bridges. It might be cheaper to help pay the cost of retrofitting seismically vulnerable buildings, railroad bridges, and so on, that are nearby.

The goal is to facilitate colocation planning so that reliable roadways are available to hospitals, to tsunami shelters, and to the military during a disaster and to prevent the compounding of disaster upon disaster that turns a small emergency into a larger one.

(a)

(b)

FIGURE 2.53 (a) and (b) Pier 352 of Route 3 was damaged when a building fell against it after the 1995 Kobe earthquake.

FIGURE 2.54 Tall Route 210-5 Separation and Overhead collapsed onto the Northwest Connector during the 1971 San Fernando earthquake.

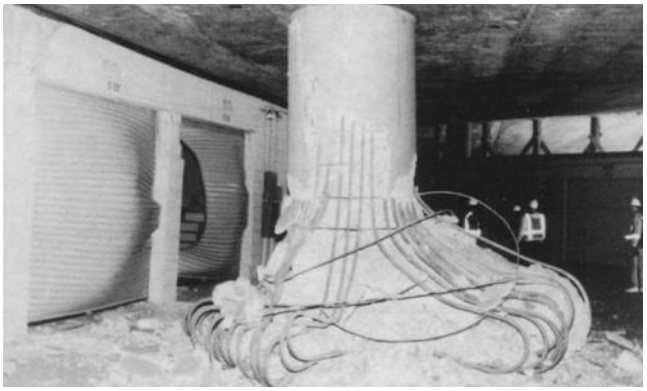

FIGURE 2.55 La Cienega-Venice Undercrossing on the Santa Monica Expressway had column damage but did not collapse because of storage building sitting under the bridge during the 1994 Northridge earthquake.

2.6 Summary

This chapter has reviewed various types of damage that can occur in bridges during earthquakes. Damage to a bridge can have severe consequences for a local economy, because bridges provide vital links in the transportation system of a region. In general, the likelihood of damage increases if the ground motion is particularly intense, the soils are soft, the bridge was constructed before modern codes were implemented, or the bridge configuration is irregular. Even a well-designed bridge can suffer damage if nonstructural modifications and structural deterioration have increased the vulnerability of the bridge.

Depending on the ground-motion, site conditions, overall configuration, and specific details of the bridge, the damage induced in a particular bridge can take many forms. Despite these complexities, the record is clear. Damage within the superstructure is rarely the primary cause of collapse. Although exceptions exist, most of the severe damage to bridges is due to the lack of continuity between bridge elements, the lack of balance between bridge elements, or the lack of transverse reinforcement in substructure elements to prevent shear and flexural damage.

One of objectives of this chapter is to show bridge damage as it relates to current seismic design practice. Damage can have several meanings. DS can be used as indicators of remaining bridge capacity before collapse. It was shown how damage relates to the ability of the bridge to remain in service. However, more research will be needed before there is better certainty on serviceability issues. It is believed that current seismic bridge designs have enough robustness to keep a bridge in service after the design earthquake, but it will probably take several earthquakes to find out for sure. Moreover, the currently available data on the bridge inventory does not include many parameters that can be used as predictors of bridge vulnerability.

Those parts of a bridge whose failure will cause collapse and those parts of a bridge whose failure can cause closure were identified, but those parts of a bridge whose failure does not impact life-safety or serviceability were not discussed. Differences in the behavior of Standard and Nonstandard Bridges were studied. Seismic criteria for more kinds of bridges are going to be developed in the future. Currently there is a big push for accelerated bridge construction and so work is going on to develop seismic criteria for steel and precast bridges that will have the same robustness as cast-in-place box girder bridge design. Bridge performance for the different seismic hazards besides ground shaking was examined. The goal is to give bridge analysts and designers simple rules to design for all the seismic hazards at the bridge site.

Acknowledgments

This work was made possible through the reconnaissance work of many individuals. The writers acknowledge the significant effort and risk made by those experts, as well as the funding agencies, in particular the National Science Foundation, Pacific Earthquake Engineering Research Center, Earthquake Engineering Research Institute, American Society of Civil Engineers Technical Council on Lifeline Earthquake Engineering, Federal Highway Administration, and California Department of Transportation.

Defining Terms

AASHTO American Association of State Highway and Transportation Officials.
Bearing An element used to support bridge girders on bent or abutment seats.
Bent (or pier) An intermediate support under the superstructure.
Box Girder A superstructure composed of two or more girders, top and bottom horizontal diaphragms, and transverse vertical diaphragms.
Cable-Stayed Bridge A bridge having one or more towers strung with taut, diagonal cables supporting the bridge deck. The cables are placed parallel to one another in a harp configuration, or they can radiate outward in a fan configuration.
Cap A horizontal element that joins vertical elements together. A bent cap connects the tops of the columns. A pile cap connects the tops of the piles. A dropped bent cap sits below the girders, whereas an integral bent cap is part of the superstructure.
Capacity The amount of strain, curvature, displacement an element can undergo before it loses its ability to resist a load.
Confinement Transverse reinforcement such as spirals, hoops, stirrups, and so on, that support longitudinal reinforcement and concrete.
Deck The horizontal riding surface on a bridge.
Demand The amount of strain, curvature, displacement an element undergoes because of an earthquake.
Design Earthquake The seismic hazards that a structure is designed to resist.
Ductility The ability of a structural element to deform without breaking.
Embankment Soil on sides of a road or other obstacle to provide a ramp on and off of a bridge.
Expansion Joint A transverse joint that accommodates superstructure expansion and contraction.
Fault Crossing A bridge that is over an earthquake fault.
Faults Boundary between tectonic plates that can slowly slip (causing creep) or suddenly rupture (causing an earthquake).
FHWA Federal Highway Administration.
Interchange Elevated structures at intersection of highways that allow drivers to continue or change direction without stopping.
Isolation Devices with small lateral stiffness used to reduce the inertia force below the device.
Key An element that limits superstructure movement.
Knee Joint The connection to the bent cap for columns that are too close to the end of the bent cap.
Lateral Bracing Transverse elements between girders to prevent out-of-plane displacements caused by wind and seismic loads.
Lateral Spreading Tendency for loose soil to move after it liquefies.
Liquefaction Tendency for the pore pressure in loose soil to increase during earthquakes, resulting in loss of bearing capacity, reduction of soil stiffness, and soil movement.
Magnitude Measurement of the size of earthquakes.
Movable Bridge A water crossing that moves to allow the passage of boats underneath.
Near-Fault Effects Enhancement to ground shaking close to the fault.

Ordinary Bridges Bridges that do not justify the considerable expense to keep them in service following earthquakes.
Outrigger When a support cannot be placed directly under a superstructure because of an obstacle, an outrigger bent is used to straddle the obstacle.
Overcrossing A bridge that carries roads or city streets over a highway.
PGA Peak ground acceleration.
Pier This is the same as a bent, which is defined above.
Pier Wall A solid, reinforced-concrete bent whose height is <2.5 times its width.
Pile Shaft A large-diameter pile that directly supports the bent cap.
Plastic Hinge Location on an element where yielding and deformation can occur.
Restrainer A steel rod, steel cable, rubber-impregnated chain, or similar device that prevents a superstructure from becoming unseated during an earthquake.
SDC Seismic design criteria.
Shear Key A concrete element that resists forces up to a certain point and then fails in shear.
Skew The angle between the centerline of the superstructure and a horizontal line perpendicular to the abutments or bents.
Slab Bridge A solid reinforced-concrete superstructure supported over two or more bents.
Soffit The underside of the superstructure.
Standard Bridges Well-designed box girder bridge with good reinforcement details.
Stiffener A horizontal or vertical plate that is bolted or welded to steel bridge members like girder webs, to prevent buckling.
Substructure Elements such as piers, abutments, and foundations that support the superstructure.
Superstructure The bridge elements supported by the substructure.
Suspension Bridge A bridge constructed by draping a steel cable over two towers.
Truss Bridge Bridge designed with a top chord in compression and a bottom chord in tension.
Undercrossing A bridge carrying a highway over a road or city street.
Underpass A bridge carrying a railroad over a highway, road, or city street.
Viaduct A very long elevated structure that carries vehicles over a series of obstacles.

References

AASHTO. 2011. *Guide Specifications for LRFD Seismic Bridge Design* (2nd Edition). American Association of State Highway and Transportation Officials, Washington, DC.

ATC. 1981. *ATC-6 Seismic Design Guideline for Highway Bridges*. FHWA Contract No. DOT-FH-11-9295. Applied Technology Council, Berkeley, CA.

ATC. 1996. *ATC-32 Improved Seismic Design Criteria for California Bridges: Provisional Recommendations*. Applied Technology Council, Redwood City, CA.

Brunsdon, D. 2000. A decade of lifelines engineering in New Zealand. Paper 2798. *Twelfth World Conference on Earthquake Engineering Proceedings*, New Zealand Society for Earthquake Engineering, Upper Hutt, NZ.

Caltrans. 1997. *San Francisco—Oakland Bay Bridge West Spans Seismic Retrofit Design Criteria*. Duan, L. (Ed.), California Department of Transportation, Sacramento, CA.

Caltrans. 2010a. *Seismic Design Criteria, Version 1.6*. California Department of Transportation, Sacramento, CA.

Caltrans. 2010b. *Bridge Memo to Designers Section 20—Seismic*. California Department of Transportation, Sacramento, CA.

Caltrans. 2010c. *Bridge Memo to Designers (20-1)—Seismic Design Methodology*. California Department of Transportation, Sacramento, CA.

Caltrans. 2010d. *Bridge Memo to Designers (20-4)—Seismic Retrofit Guidelines for Bridges in California*. California Department of Transportation, Sacramento, CA.

Caltrans. 2011a. *Seismic Design Criteria, Version 1.6*. California Department of Transportation, Sacramento, CA.

Caltrans. 2011b. Seismic Retrofit Program. http://www.dot.ca.gov/hq/paffairs/about/retrofit.htm (accessed June 20, 2011).

Caltrans. 2013. *Guide Specifications for Seismic Design of Steel Bridges* (2nd Edition). California Department of Transportation, Sacramento, CA.

China-MOT. 2008. *Guidelines for Seismic Design of Highway Bridges, Recommended Standard of China Ministry of Transport*. JTG/T B02-01-2008, Ministry of Transport, People's Communications Press, Beijing, China. (in Chinese)

Chung, R. 1996. *The January 17, 1995 Hyogoken-Nanbu (Kobe) Earthquake*. NIST Special Publication 901, National Institute of Standards and Technology, Gaithersburg, MD, p. 544.

EERI. 1988. *The Whittier Narrows Earthquake of October 1, 1987*. Earthquake Spectra, Vol. 4. no. 2, Earthquake Engineering Research Institute, Oakland, CA, p. 409.

EERI. 1995a. *Northridge Earthquake Reconnaissance Report*. Earthquake Spectra, Special Supplement to Vol. 11, Earthquake Engineering Research Institute, Oakland, CA, p. 523.

EERI. 1995b. *The Hyogo-Ken Nanbu Earthquake. Preliminary Reconnaissance Report*, Earthquake Engineering Research Institute, Oakland, CA, p. 116.

Haroun, M. A. 1993. *Cyclic Behavior of Bridge Pier Walls for Retrofit*. RTA 59N974, University of California, Irvine, CA.

Housner, G. 1990. Competing Against Time. *Report to Governor George Deukmejian from the Governor's Board of Inquiry on the 1989 Loma Prieta Earthquake*, Office of Planning and Research, State of California, Sacramento, California, p. 264.

Jennings, P. C. (ed.). 1971. *Engineering Features of the San Fernando Earthquake of February 9*. Report ERL 71-02, California Institute of Technology, Pasadena, CA.

JRA. 2002. *Design Specifications of Highway Bridges, Part V: Seismic Design*, Road Association, Tokyo, Japan.

Kawashima, K., and Unjoh, S. 1997. The Damage of Highway Bridges in the 1995 Hyogo-Ken Nanbu Earthquake and its Impact on Japanese Seismic Design. *Journal of Earthquake Engineering*, 1(3), 505–541.

Lee, C. G. 2008. *The 512 Wenchuan Earthquakeof China—A Preliminary Report*. Department of Civil, Structural and Environmental Engineering, MCEER, University at Buffalo, NY.

NAS. 1973. *The Great Alaska Earthquake*. Publication 1603, National Academy of Sciences, Washington, DC.

Saiidi, M. 2011. *Personal Correspondence*. University of Nevada, Reno, NV.

Zelinski, R. 1994. *Post Earthquake Investigation Team Report for the Loma Prieta Earthquake*. California Department of Transportation, Division of Structures, Sacramento, CA.

Further Reading

Priestley, M. N. J., Seible, F., and Calvi, G. M. 1996. *Seismic Design of Bridge Structures*. Wiley, New York.

Relevant Websites

http://www.dot.ca.gov/hq/esc/earthquake_engineering/
http://peer.berkeley.edu/
http://mceer.buffalo.edu/

3

Dynamic Analysis

Wei Zhang
Taiyuan University of Technology

Murugesu Vinayagamoorth
California Department of Transportation

Lian Duan
California Department of Transportation

3.1 Introduction

The primary purpose of this chapter is to present dynamic methods for analyzing bridge structures when subjected to earthquake loads. Basic concepts and assumptions used in typical dynamic analysis are presented first. Various approaches to bridge dynamics are then discussed. Several examples are presented to illustrate their practical applications.

3.1.1 Static versus Dynamic Analysis

The main objectives of a structural analysis are to evaluate structural behavior under various loads and to provide the information necessary for design such as forces, moments, and deformations. Structural analysis can be classified as "static" or "dynamic, whereas statics deals with time-independent loading, dynamics considers any load where the magnitude, direction, and position vary with time. Typical dynamic loads for a bridge structure include vehicular motions and wave actions such as winds, stream flow, and earthquakes.

3.1.2 Characteristics of Earthquake Ground Motions

An earthquake is a natural ground movement caused by various phenomena including global tectonic processes, volcanism, landslides, rock-bursts, and explosions. The global tectonic processes are continually producing mountain ranges and ocean trenches at the earth's surface and causing earthquakes.

This section briefly discusses the earthquake input for seismic bridge analysis. Detailed discussions of ground motions are presented in Chapter 1.

The ground motion is represented by the time history or seismograph in terms of acceleration, velocity, and displacement for a specific location during an earthquake. Time history plots contain complete information about the earthquake motions in the three orthogonal directions (two horizontal and one vertical) at the strong-motion instrument location. Acceleration is usually recorded by strong-motion accelerograph and the velocities and displacements are determined by numerical integration. The accelerations recorded at locations that are approximately same distance away from the epicenter may differ significantly in duration, frequency content, and amplitude because of the different local soil conditions. Figure 3.1 shows several time histories of recent earthquakes.

From a structural engineering view, the most important characteristics of an earthquake are the peak ground acceleration (PGA), duration, and frequency content. The PGA is the maximum acceleration and represents the intensity of a ground motion. Although the ground velocity may be a more significant measure of intensity than the acceleration, it is not often measured directly, but determined using supplementary calculations (Clough and Penzien, 1993). The duration is the length of time between the first and the last peak exceeding a specified strong motion level. The longer the duration of a strong motion, the more energy is imparted to a structure. Because the elastic strain energy absorbed by a structure is very limited, a longer strong earthquake has a greater possibility to enforce a structure into inelastic range. The frequency content can be represented by the number of zero crossings per second in the accelerogram. It is well understood that when the frequency of a regular disturbing force is the same as the natural vibration frequency of a structure (resonance), the oscillation of structure can be greatly magnified and effects of damping become minimal. Although earthquake motions are never as regular as a sinusoidal waveform, there is a usually a period that dominates the response.

Because it is impossible to measure detailed ground motions for all structure sites, the rock motions or ground motions are estimated at a fault and then propagated to the earth surface using a computer

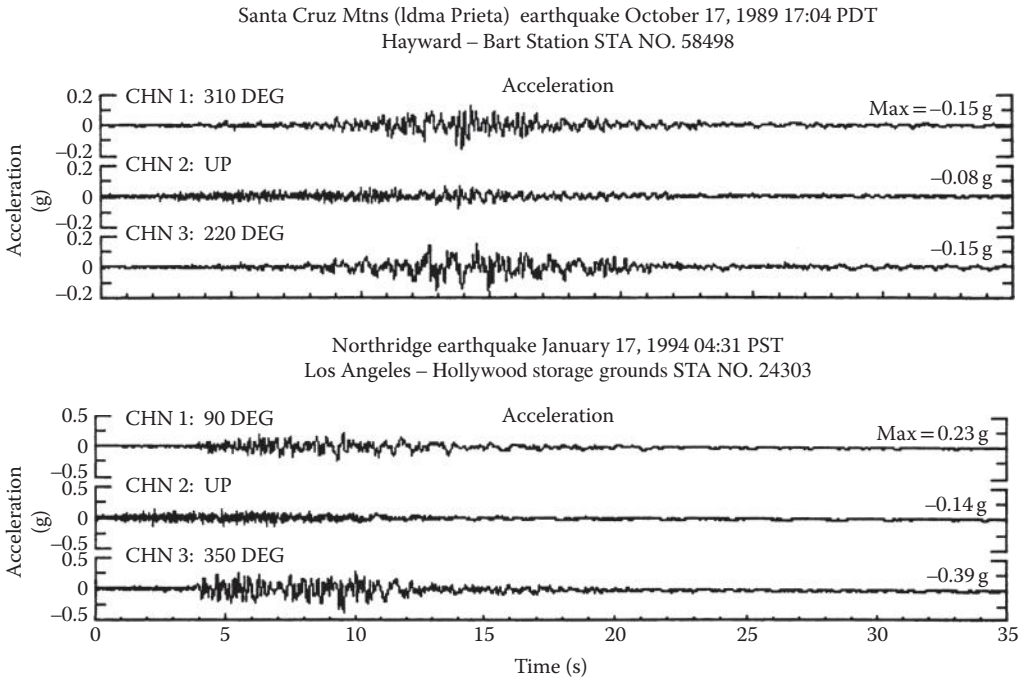

FIGURE 3.1 Ground motions recorded during 1989 Loma Prieta and 1994 Northridge earthquakes.

program considering the local soil conditions. Two guidelines (Caltrans, 1996a and 1996b) developed by the California Department of Transportation provide the methods to develop seismic ground motions for bridges.

3.1.3 Dynamic Analysis Methods for Seismic Bridge Design

Depending on the seismic zone, geometry, and importance of the bridge, the following analysis methods may be used for seismic bridge design:

- The single-mode method (single-mode spectral and uniform load analysis) (AASHTO, 2011) assumes that seismic load can be considered as an equivalent static horizontal force applied to an individual frame in either the longitudinal or transverse direction. The equivalent static force is based on the natural period of a single degree of freedom (SDOF) and code-specified response spectra. Engineers should recognize that the single-mode method (sometimes referred to as equivalent static analysis) is best suited for structures with well-balanced spans with equally distributed stiffness.
- Multi-mode spectral analysis assumes that member forces, moments, and displacements because of seismic load can be estimated by combining the responses of individual modes using the methods such as Complete Quadratic Combination (CQC) method and the Square Root of the Sum of the Squares (SRSS) method. The CQC method is adequate for most bridge systems (Wilson et al., 1981; Wilson, 2009; Menun and Kiureghian, 1998) and the SRSS method is best suited for combining responses of well-separated modes.
- The multiple support response spectrum (MSRS) method provides response spectra and the peak displacements at individual support degrees of freedom (DOF) by accurately accounting for the spatial variability of ground motions including the effects of incoherence, wave passage, and spatially varying site response. This method can be used for multiply supported long structures (Kiureghian et al., 1997).
- Time history method is a numerical step-by-step integration of equation of motions. It is usually required for critical/important or geometrically complex bridges. Inelastic analysis provides a more realistic measure of structural behavior when compared to an elastic analysis.

Selection of the analysis method for a specific bridge structure should not purely be based on performing structural analysis, but be based on the effective design decisions (Powell, 1997). The detailed discussions of above methods are presented in the following sections.

3.2 Single Degree of Freedom System

The familiar spring-mass system represents the simplest dynamic model and is shown in Figure 3.2a. When the idealized, undamped structures are excited by either moving the support or by displacing the mass in one direction, the mass oscillates about the equilibrium state forever without coming to rest. But, real structures do come to rest after a period of time because of a phenomenon called *damping*. To incorporate the effect of the damping, a massless viscous damper is always included in the dynamic model as shown in Figure 3.2b.

In a dynamic analysis, the number of displacements required to define the displaced positions of all the masses relative to their original positions is called the number of DOF. When a structural system can be idealized with a single-mass concentrated at one location and moved only in one direction, this dynamic system is called SDOF system. Some of the structures such as a water tank supported by a single column, one-story frame structure, and two-span bridges supported by a single column could be idealized as SDOF models (Figure 3.3).

In the SDOF system shown in Figure 3.3c, mass of the bridge superstructure is the mass of the dynamic system. The stiffness of the dynamic system is the stiffness of the column against the sidesway and viscous damper of the system is the internal energy absorption of the bridge structure.

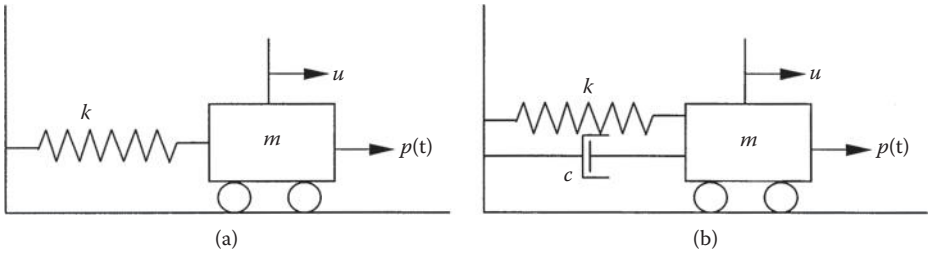

FIGURE 3.2 Idealized dynamic model (a) undamped SDOF system; (b) damped SDOF system.

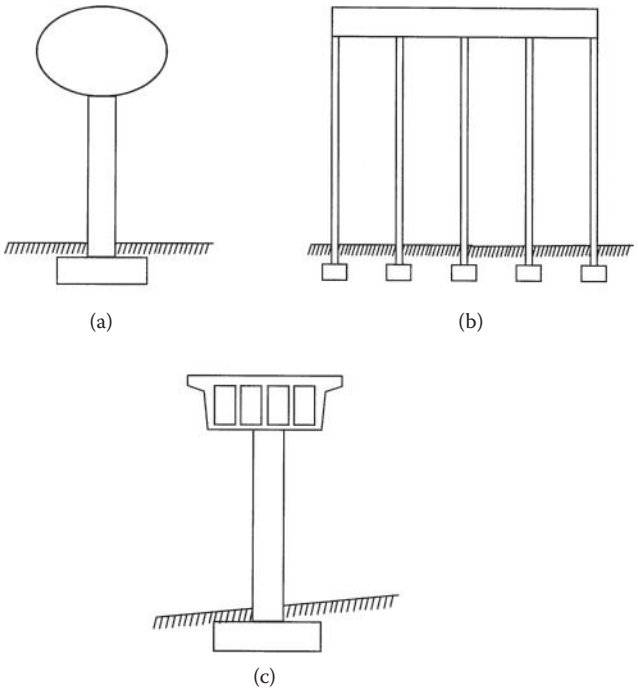

FIGURE 3.3 Examples of SDOF structures (a) water tank supported by single column; (b) one-story frame building; (c) two-span bridge supported by single column.

3.2.1 Equation of Motion

The response of a structure depends on its mass, stiffness, damping, and applied load or displacement. The structure could be excited by applying an external force $p(t)$ on its mass or by a ground motion $u(t)$ at its supports. In this chapter, since the seismic loading is induced by exciting the support, we focus mainly on the equations of motion of a SDOF system subjected to a ground excitation.

The displacement of the ground motion u_g, the total displacement of the single mass u_t, and the relative displacement between the mass and ground u (Figure 3.4) are related by

$$u_t = u + u_g \tag{3.1}$$

By applying the Newton's law and D'Alembert's principle of dynamic equilibrium, it can be shown that

$$f_I + f_D + f_S = 0 \tag{3.2}$$

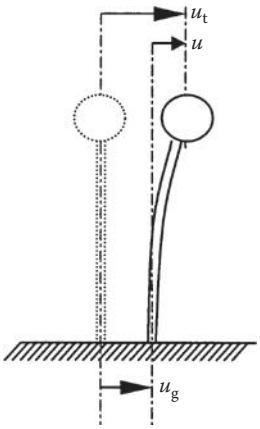

FIGURE 3.4 Earthquake-induced motion of a SDOF system.

where f_I is the inertial force of the single mass and related to the acceleration of the mass by $f_I = m\ddot{u}_t$; f_D is the damping force on the mass and related to the velocity across the viscous damper by $f_D = c\dot{u}$; f_S is the elastic force exerted on the mass and related to the relative displacement between the mass and the ground by $f_S = ku$, where k is the spring constant; c is the damping ratio; and m is the mass of the dynamic system.

Substituting these expressions for f_I, f_D, and f_S into Equation 3.2 gives:

$$m\ddot{u}_t + c\dot{u} + ku = 0 \tag{3.3}$$

The equation of motion for a SDOF system subjected to a ground motion can then be obtained by substituting the Equation 3.1 with Equation 3.3, and is given by

$$m\ddot{u} + c\dot{u} + ku = -m\ddot{u}_g \tag{3.4}$$

3.2.2 Characteristics of Free Vibration

To determine the characteristics of the oscillations such as the time to complete one cycle of oscillation (T_n) and number of oscillation cycles per second (ω_n), we first look at the free vibration of a dynamic system. Free vibration is typically initiated by disturbing the structure from its equilibrium state by an external force or displacement. Once the system is disturbed, the system vibrates without any external input. Thus, the equation of motion for free vibration can be obtained by setting $\ddot{u}_g$ to zero in Equation 3.4 and is given by

$$m\ddot{u} + c\dot{u} + ku = 0 \tag{3.5}$$

Dividing the Equation 3.5 by its mass m will result in

$$\ddot{u} + \left(\frac{c}{m}\right)\dot{u} + \left(\frac{k}{m}\right)u = 0 \tag{3.6}$$

$$\ddot{u} + 2\xi\omega_n + \omega_n^2 u = 0 \tag{3.7}$$

where $\omega_n = \sqrt{k/m}$ the natural circular frequency of vibration or the undamped frequency; $\xi = \dfrac{c}{c_{cr}}$ the damping ratio; $c_{cr} = 2m\omega_n = 2\sqrt{km} = \dfrac{2k}{\omega_n}$ the critical damping coefficient.

Figure 3.5a shows the response of a typical idealized, undamped SDOF system. The time required for the SDOF system to complete one cycle of vibration is called natural period of vibration (T_n) of the system and is given by

$$T_n = \frac{2\pi}{\omega_n} = 2\pi\sqrt{\frac{m}{k}} \tag{3.8}$$

Furthermore, the natural cyclic frequency of vibration f_n is given by

$$f_n = \frac{\omega_n}{2\pi} = 2\pi\sqrt{\frac{k}{m}} \tag{3.9}$$

Figure 3.5b shows the response of a typical damped SDOF structure. The circular frequency of the vibration or damped vibration frequency of the SDOF structure, ω_d, is given by

$$\omega_d = \omega_n\sqrt{1-\xi^2}$$

The damped period of vibration (T_d) of the system is given by

$$T_d = \frac{2\pi}{\omega_d} = \frac{2\pi}{\sqrt{1-\xi^2}}\sqrt{\frac{m}{k}} \tag{3.10}$$

When $\xi = 1$ or $c = c_{cr}$ the structure returns to its equilibrium position without oscillating and is referred to as critically damped structure. When $\xi > 1$ or $c > c_{cr}$, the structure is "overdamped" and comes to rest without oscillating, but at a slower rate. When $\xi < 1$ or $c < c_{cr}$, the structure is "underdamped" and oscillates about its equilibrium state with progressively decreasing amplitude. Figure 3.6 shows the response of SDOF structures with different damping ratios.

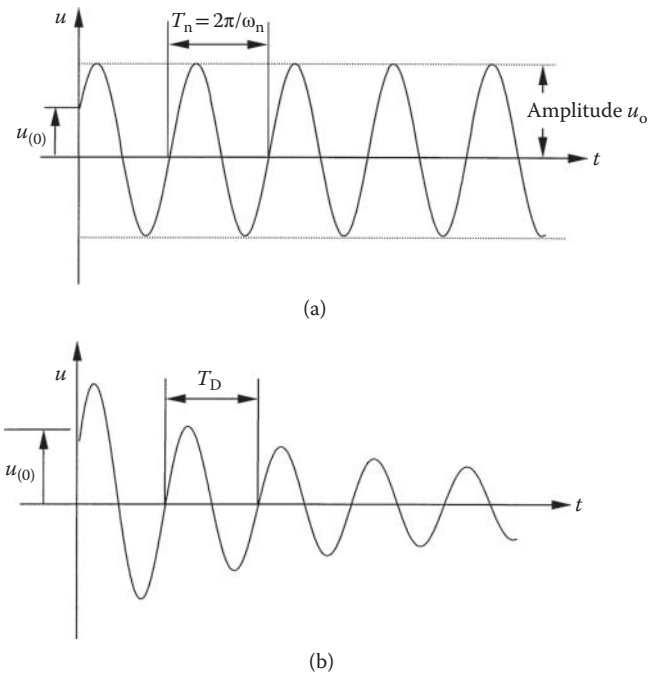

FIGURE 3.5 Typical response of an idealized SDOF system (a) undamped; (b) damped.

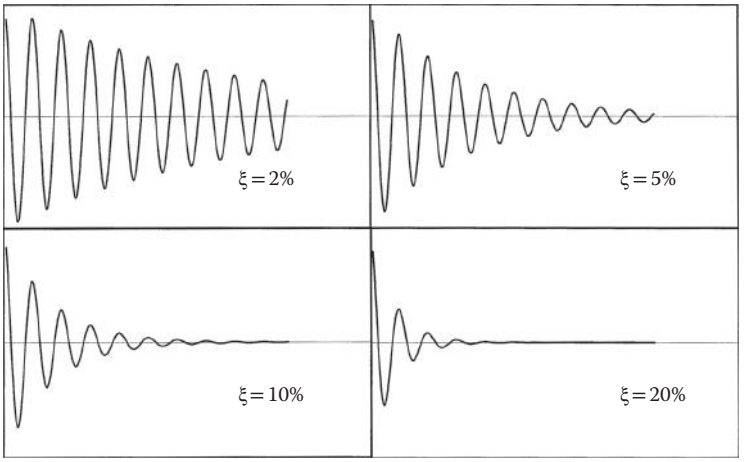

FIGURE 3.6 Response of SDOF system for various damping ratios.

For structures such as buildings, bridges, dams, and offshore structures, the damping ratio is <0.15 and thus can be categorized as underdamped structures. The basic dynamic properties estimated using damped or undamped assumptions are approximately the same. For example, when $\xi = 0.10$, $\omega_d = 0.995\omega_n$ and $T_d = 1.01T_n$.

Damping dissipates the energy out of a structure in opening and closing of micro cracks in concrete, stressing of nonstructural elements, and friction at connection of steel members. Thus, damping coefficient accounts for all energy dissipating mechanisms of the structure and can only be estimated by experimental methods. Two seemingly identical structures may have slightly different material properties and may dissipate energy at different rates. Since damping does not play an important quantitative role except for resonant responses in structural responses, it is common to use an average damping ratios based on types of construction materials. Relative damping ratio for common types of structures such as welded metal of 2%–4%, bolted metal structures of 4%–7%, prestressed concrete structures of 2%–5%, reinforced concrete structures of 4%–7%, and wooden structures of 5%–10% are recommended by Chmielewski et al. (1996).

3.2.3 Response to Earthquake Ground Motion

A typical excitation of an earth movement is shown in Figure 3.7. The basic equation of motion of a SDOF system is expressed in Equation 3.4. Since the excitation force $m\ddot{u}_g$ cannot be described by simple mathematical expression, closed form solutions for Equation 3.4 are not available. Thus, the entire ground excitation needs to be treated as a superposition of short-duration impulses to evaluate the response of the structure to the ground excitation. An impulse is defined as the product of the force times duration. For example, the impulse of the force at time τ during the time interval $d\tau$ equals $-m\ddot{u}_g(\tau)d\tau$ and is represented by the shaded area in Figure 3.7. The total response of the structure for the earthquake motion can then be obtained by integrating all responses of the increment impulses. This approach is sometimes referred to as "Time History Analysis." Various solution techniques are available in technical literature on structural dynamics (Clough and Penzien, 1993; Chopra, 2007).

In seismic structural design, designers are interested in the maximum or extreme values of the response of a structure as discussed in the following sections. Once the dynamic characteristics (T_n and ω_n) of the structure are determined, the maximum displacement, moment, and shear on the SDOF system can easily be estimated using basic principles of mechanics.

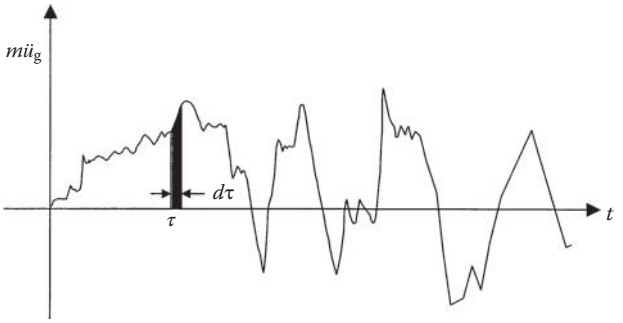

FIGURE 3.7 Induced earthquake force versus time on a SDOF system.

3.2.4 Response Spectra

The response spectrum is defined as a relationship of the peak values of a response quantity (acceleration, velocity, or displacement) with a structural dynamic characteristic (natural period or frequency). The core concept of the response spectrum in earthquake engineering provides a much more convenient and meaningful measure of effects of an earthquake than any other single quantity. It represents the peak response of all possible SDOF systems to a particular ground motion.

3.2.4.1 Elastic Response Spectrum

The elastic response spectrum is the response spectrum of an elastic structural system and can be obtained by the following steps (Chopra, 2007):

1. Define the ground acceleration time history (typically at a 0.02 second interval).
2. Select the natural period T_n and damping ratio ξ of an elastic SDOF system.
3. Compute the deformation response $u(t)$ using any numerical method.
4. Determine u_o, the peak value of $u(t)$.
5. Calculate the spectral ordinates by $D = u_o$, $V = 2\pi D/T_n$ and $A = \left(2\pi/T_n\right)^2 D$.
6. Repeat steps 2 and 5 for a range of T_n and ξ values for all possible cases.
7. Construct results graphically to produce three separate spectra as shown in Figure 3.8 or a combined tripartite plot as shown in Figure 3.9.

It is noted that although three spectra (displacement, velocity, and acceleration) for a specific ground motion contain the same information, each of them provides a physically meaningful quantity. The displacement spectrum presents the peak displacement. The velocity spectrum is related directly to the peak strain energy stored in the system. The acceleration spectrum is related directly to the peak value of the equivalent static force and base shear.

A response spectrum (Figure 3.9) can be divided into three ranges of periods (Chopra, 2007):

- Acceleration-sensitive region (very short-period region): A structure with a very short period is extremely stiff and expected to deform very little. Its mass moves rigidly with the ground and its peak acceleration approximately equals to the ground acceleration.
- Velocity-sensitive region (intermediate period region): A structure with an intermediate period responds greatly to the ground velocity than other ground motion parameters.
- Displacement-sensitive region (very long-period region): A structure with a very long period is extremely flexible and expected to remain stationary while the ground moves. Its peak deformation is closer to the ground displacement. The structural response is most directly related to ground displacement.

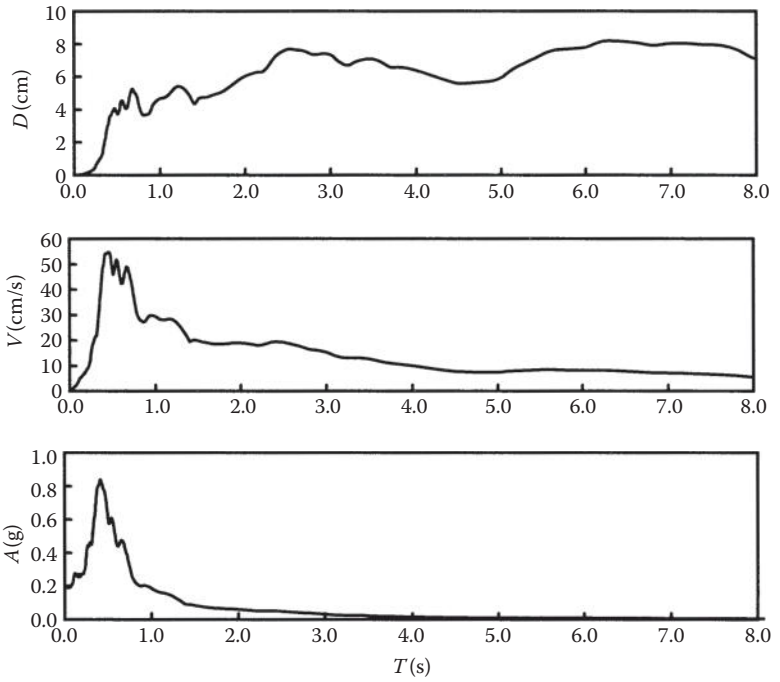

FIGURE 3.8 Example of response spectra (5% critical damping) for 1989 Loma Prieta earthquake.

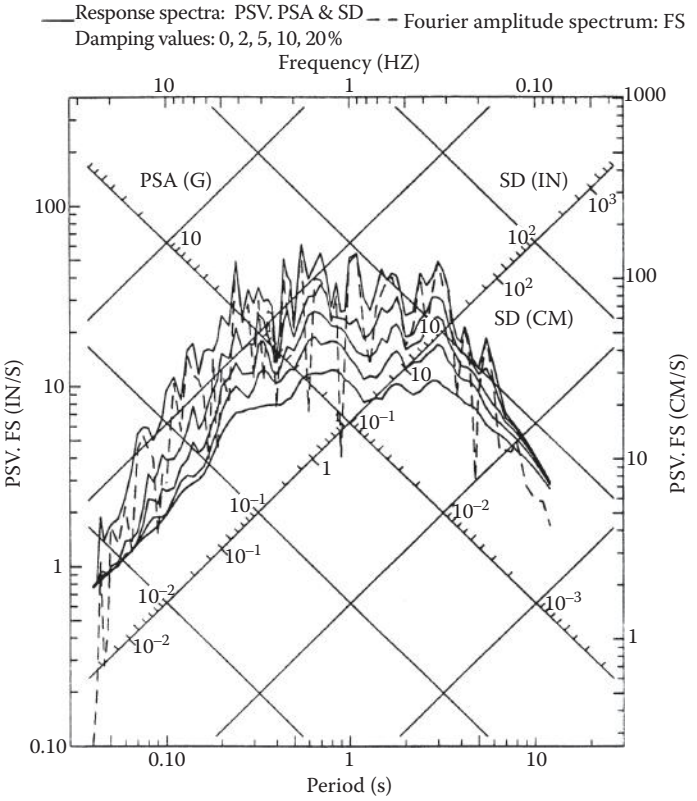

FIGURE 3.9 Tripartite plot—response spectra (Northridge earthquake, Arleta—Rordhoff Ave. Fire Station).

3.2.4.2 Elastic Design Spectrum

Since seismic bridge design is intended to resist future earthquakes, use of a response spectrum obtained from a particular past earthquake motion is inappropriate. In addition, jagged spectrum values over small ranges would require an unreasonable accuracy in the determination of the structure period (Lindeburg, 1998). It is also impossible to predict a jagged response spectrum in all its details for a ground motion that may occur in the future. To overcome these shortcomings, the elastic design spectrum, a smoothened idealized response spectrum is usually developed to represent the envelopes of ground motions recorded at the site during past earthquakes. The development of elastic design spectrum is based on statistical analysis of the response spectra for the ensemble of ground motions. Figure 3.10 shows a set of elastic design spectrum in Caltrans Seismic Design Criteria (SDC) (Caltrans, 2013). Figure 3.11 shows project-specific acceleration response spectra for the California Sonoma Creek Bridge.

Engineers should recognize the conceptual differences between a response spectrum and a design spectrum (Chopra, 2007). A response spectrum is only the peak response of all possible SDOF systems because of a particular ground motion, whereas a design spectrum is a specified level of seismic design forces or deformations and is the envelope of two different elastic design spectra. The elastic design spectrum provides a basis for determining the design force and deformation for elastic SDOF systems.

3.2.4.3 Inelastic Response Spectrum

A bridge structure may experience inelastic behavior during a major earthquake. The typical elastic and elasto-plastic responses of an idealized SDOF to severe earthquake motions are shown in Figure 3.12. The input seismic energy received by a bridge structure is dissipated by both viscous damping and yielding (localized inelastic deformation converting into heat and other irrecoverable forms of energy). Both viscous damping and yielding reduce the response of inelastic structures compared to elastic structures. Viscous damping represents the internal friction loss of a structure when deformed and is approximately a constant because it depends mainly on structural materials. Yielding, however, varies depending on structural materials, structural configurations, and loading patterns and histories. Damping has negligible effects on the response of structures for the long- and short-period systems and is most effective in reducing response of structures for intermediate-period systems.

In seismic bridge design, a main objective is to ensure that a structure is capable of deforming in a ductile manner when subjected to a larger earthquake loading. It is desirable to consider inelastic response of a bridge system to a major earthquake. Although a nonlinear inelastic dynamic analysis is not difficult in concept, it requires careful structural modeling and intensive computing effort (Powell, 1997). To consider inelastic seismic behavior of a structure without performing a true nonlinear inelastic analysis, the ductility-factor method can be used to obtaining the inelastic response spectra from the elastic response spectra. The ductility of a structure is usually referred as the displacement ductility factor μ defined by (Figure 3.13)

$$\mu = \frac{\Delta_u}{\Delta_y} \tag{3.11}$$

where Δ_u is ultimate displacement capacity and Δ_y is yield displacement.

A simplest approach to develop the inelastic design spectrum is scale the elastic design spectrum down by some function of the available ductility of a structural system

$$\mathrm{ARS}_{\mathrm{inelastic}} = \frac{\mathrm{ARS}_{\mathrm{elastic}}}{f(\mu)} \tag{3.12}$$

$$f(\mu) = \begin{cases} 1 & \text{For } T_n \le 0.03 \text{ s} \\ 2\mu - 1 & \text{For } 0.03 \text{ s} < T_n \le 0.5 \text{ s} \\ \mu & \text{For } T_n > 0.5 \text{ s} \end{cases} \tag{3.13}$$

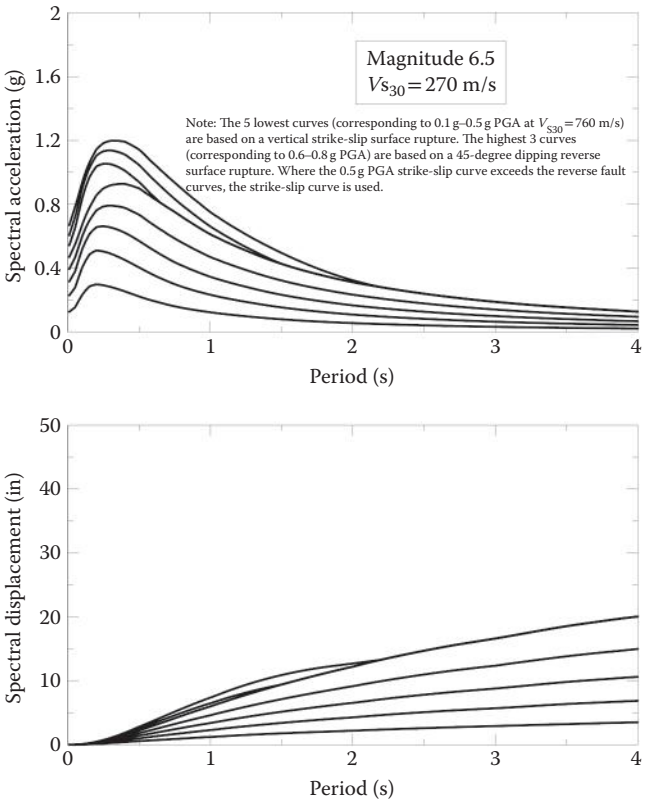

FIGURE 3.10 Typical Caltrans elastic design response spectra.

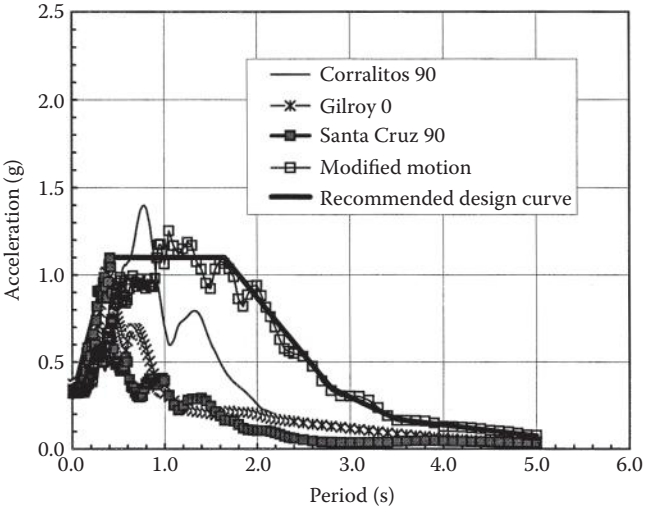

FIGURE 3.11 Acceleration response spectra for Sonoma Creek Bridge.

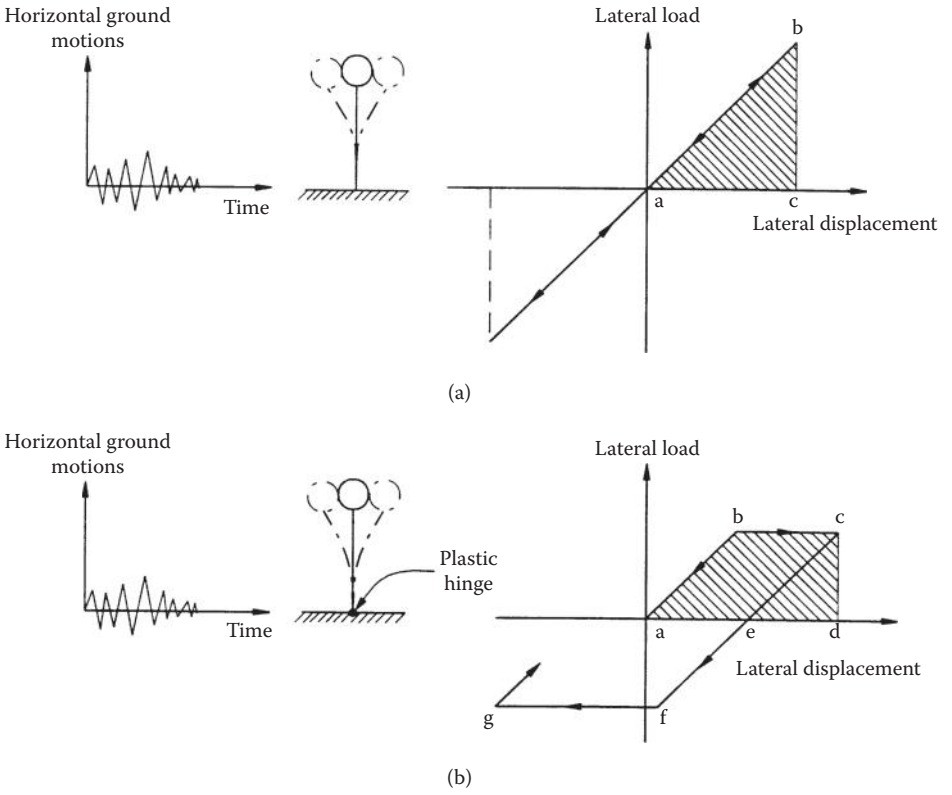

FIGURE 3.12 Response of a SDOF to earthquake ground motion (a) elastic system; (b) inelastic system.

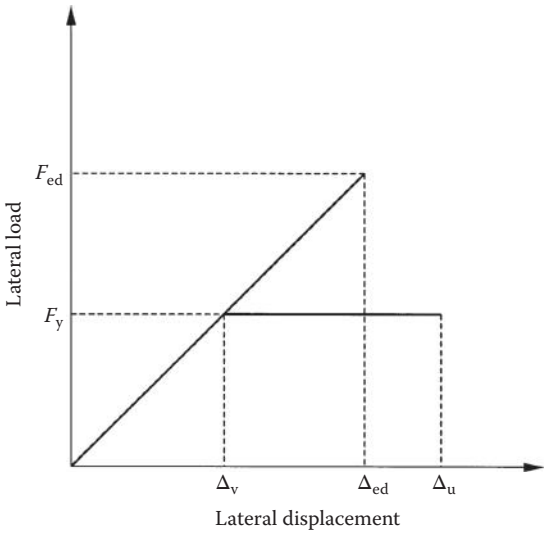

FIGURE 3.13 Lateral load—displacement relations.

For very short period ($T_n \leq 0.03$ s) in the acceleration-sensitive region, the elastic displacement demand Δ_{ed} is less than displacement capacity Δ_u (see Figure 3.13). The reduction factor $f(\mu)=1$ implies that the structure should be designed and remained at elastic to avoid excessive inelastic deformation. For intermediate period ($0.03 \text{ s} < T_n \leq 0.5$ s) in the velocity sensitive region, elastic displacement demand Δ_{ed} may be greater or less than displacement capacity Δ_u and reduction factor is based on the equal energy concept. For the very-long period ($T_n > 0.5$ s) in the displacement-sensitive region, the reduction factor is based on the equal displacement concept.

3.2.5 Example of a Single Degree of Freedom System

Given: A SDOF bridge structure is shown in Figure 3.14. To simplify the problem, the bridge is assumed to move only in longitudinal direction. The total resistance against the longitudinal motion comes in the form of friction at bearings and this could be considered as a damper. Assume the following properties for the structure: damping ratio $\xi = 0.05$; area of superstructure $A = 38.43$ ft^2 (3.57 m^2); moment of column $I_c = 12$ ft^4 (0.1036 m^4); E_c of column = 3,000 ksi (20,700 MPa); material density $\rho = 150$ lb/ft^3 (2,400 kg/m^3); length of column $L_c = 30$ ft (9.14 m); and length of the superstructure $L_s = 120$ ft (36.6 m). The acceleration response curve of the structure is given in the Figure 3.11. Determine (1) natural period of the structure, (2) damped period of the structure, (3) maximum displacement of the superstructure, and (4) maximum moment in the column.

Solution:

$$\text{Stiffness: } k = \frac{12E_cI_c}{L_c^3} = \frac{12(3{,}000)(12)(12^2)}{30^3} = 2{,}304 \text{ kip/ft} \quad (33{,}624{,}346 \text{ N/m})$$

$$\text{Mass: } m = \frac{AL_s\rho}{g} = \frac{(38.43)(120)(0.15)}{32.174} = 20.878 \text{ kip/ft/s}^2 \quad (313{,}768 \text{ kg})$$

$$\text{Natural circular frequency } \omega_n = \sqrt{\frac{k}{m}} = \sqrt{\frac{2{,}304}{20.878}} = 10.35 \text{ rad/s}$$

$$\text{Natural cyclic frequency } f_n = \frac{\omega_n}{2\pi} = \frac{10.35}{2\pi} = 1.65 \text{ cycles/s}$$

$$\text{Natural period of the structure } T_n = \frac{1}{f_n} = \frac{1}{1.65} = 0.606 \text{ s}$$

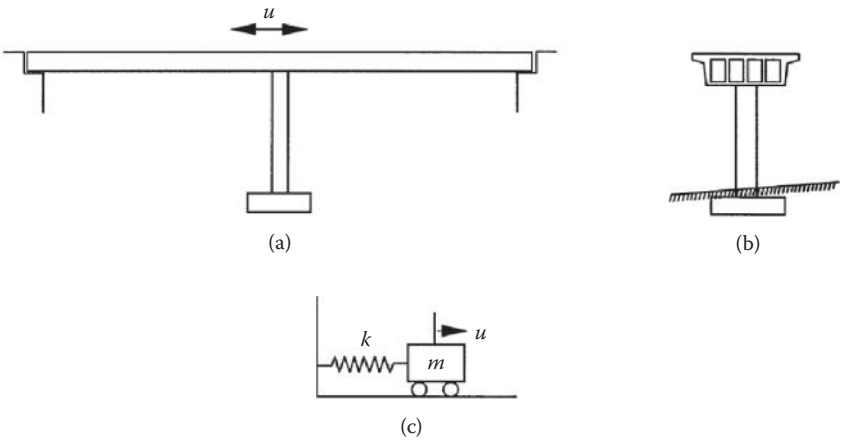

FIGURE 3.14 SDOF bridge example (a) two-span bridge schematic diagram; (b) single-column bent; (c) idealized equivalent model for longitudinal response.

The damped circular frequency is given by,

$$\omega_d = \omega_n\sqrt{1-\xi^2} = 10.36\sqrt{1-0.05^2} = 10.33\,\text{rad/sec}$$

The damped period of the structure is given by

$$T_d = \frac{2\pi}{\omega_d} = \frac{2\pi}{10.33} = 0.608\,\text{sec}$$

From the ARS curve, for a period of 0.606 seconds, the maximum acceleration of the structure will be 0.9 g = 0.9 × 32.174 = 28.96 ft/s² (11.10 m/s²).

Then, the force acting on the mass

$$F = m(28.96) = (20.878)(28.96) = 604.63\text{ kip } (2.69\,\text{MN})$$

The maximum displacement

$$u_{max} = \frac{F}{k} = \frac{604.42}{2{,}304} = 0.262\text{ ft } (0.079\text{ m})$$

The maximum moment in the column

$$M = \frac{FL_c}{2} = \frac{(604.63)(30)}{2} = 9{,}069.45\text{ kip-ft } (12.30\,\text{MN-m})$$

3.3 Multi-Degree of Freedom System

The SDOF approach may not be applicable for complex structures such as multilevel frame structure and bridges with several supports. To predict the response of a complex structure, the structure is discretized with several members of lumped masses. As the number of lumped masses increases, number of displacements required to define the displaced positions of all masses increases. The response of a multi degree of freedom (MDOF) system is discussed in this section.

3.3.1 Equation of Motion

The equation of motion of a MDOF system is similar to the SDOF system, but the stiffness k, mass m, and damping c are matrices. The equation of motion to a MDOF system under ground motion can be written as

$$[M]\{\ddot{u}\} + [C]\{\dot{u}\} + [K]\{u\} = -[M]\{B\}\ddot{u}_g \tag{3.14}$$

The stiffness matrix $[K]$ can be obtained from standard static displacement-based analysis models and may have off-diagonal terms. The mass matrix $[M]$ because of the negligible effect of mass coupling can best be expressed in the form of tributary lumped masses to the corresponding displacement DOFs, resulting in a diagonal or uncoupled mass matrix. The damping matrix $[C]$ accounts for all the energy dissipating mechanisms in the structure and may have off-diagonal terms. The vector $\{B\}$ is a displacement transformation vector that has values 0 and 1 to define DOFs to which the earthquake loads are applied.

3.3.2 Free Vibration and Vibration Modes

To better understand the response of MDOF systems, we look at the undamped, free vibration of N degrees of freedom (N-DOF) system first.

3.3.2.1 Undamped Free Vibration

By setting $[C]$ and $\ddot{u}_g$ to zero in the Equation 3.14, the equation of motion of undamped, free vibration of *N*-DOF system can be shown as

$$[M]\{\ddot{u}\}+[K]\{u\}=0 \tag{3.15}$$

where $[M]$ and $[K]$ are $n \times n$ square matrices.

Equation 3.15 could then be rearranged to

$$\left[[K]-\omega_n^2[M]\right]\{\phi_n\}=0 \tag{3.16}$$

where $\{\phi_n\}$ is the deflected shape matrix. Solution to this equation can be obtained by setting

$$\left|[K]-\omega_n^2[M]\right|=0 \tag{3.17}$$

The roots or eigenvalues of the Equation 3.17 will be the *N* natural frequencies of the dynamic system. Once the natural frequencies (ω_n) are estimated, Equation 3.16 can be solved for the corresponding *N* independent, deflected shape matrices (or eigenvectors), $\{\phi_n\}$. In other words, a vibrating system with *N*-DOFs will have *N* natural frequencies (usually arranged in sequence from smallest to largest), corresponding *N* natural periods T_n, and *N* natural mode shapes $\{\phi_n\}$. These eigenvectors are sometimes referred to as natural modes of vibration or natural mode shapes of vibration. It is important to recognize that the eigenvectors or mode shapes represent only the deflected shape corresponding to the natural frequency, not the actual deflection magnitude.

The *N* eigenvectors can be assembled in a single $n \times n$ square matrix $[\Phi]$, modal matrix, where each column represents the coefficients associated with the natural mode. One of the important aspects of these mode shapes is that they are orthogonal to each other. Stated mathematically

$$\text{If, } \omega_n \neq \omega_r \quad \{\phi_n\}^T[K]\{\phi_r\}=0 \text{ and } \{\phi_n\}^T[M]\{\phi_r\}=0 \tag{3.18}$$

$$[K^*] = [\Phi]^T[K][\Phi] \tag{3.19}$$

$$[M^*] = [\Phi]^T[M][\Phi] \tag{3.20}$$

where $[K]$ and $[M]$ have off diagonal elements, whereas $[K^*]$ and $[M^*]$ are diagonal matrices.

3.3.2.2 Damped-Free Vibration

When damping of the MDOF system is included, the free vibration response of the damped system will be given by

$$[M]\{\ddot{u}\}+[C]\{\dot{u}\}+[K]\{u\}=0 \tag{3.21}$$

The displacements are first expressed in terms of natural mode shapes, and later they are multiplied by the transformed natural mode matrix to obtain the following expression:

$$[M^*]\{\ddot{Y}\}+[C^*]\{\dot{Y}\}+[K^*]\{Y\}=0 \tag{3.22}$$

where, $[M^*]$ and $[K^*]$ are diagonal matrices given by Equations 3.19 and 3.20 and

$$[C^*] = [\Phi]^T[C][\Phi] \tag{3.23}$$

Although $[M^*]$ and $[K^*]$ are diagonal matrices, $[C^*]$ may have off diagonal terms. When $[C^*]$ has off diagonal terms, the damping matrix is referred to as nonclassical or nonproportional damping matrix. When $[C^*]$ is diagonal, it is referred to as classical or proportional damping matrix. Classical damping is an appropriate idealization when similar damping mechanisms are distributed throughout the structure. Nonclassical damping idealization is appropriate for the analysis when the damping mechanisms differ considerably within a structural system.

Since most bridge structures have predominantly one type of construction material, bridge structures could be idealized as classical damping structural system. Thus, the damping matrix of Equation 3.22 will be a diagonal matrix for most bridge structures. And, the equation of *n*th mode shape or generalized *n*th modal equation is given by

$$\ddot{Y}_n + 2\xi_n \omega_n \dot{Y}_n + \omega^2 Y_n = 0 \tag{3.24}$$

Equation 3.24 is similar to the Equation 3.7 of a SDOF system. And, the vibration properties of each mode can be determined by solving the Equation 3.24.

3.3.2.3 Rayleigh Damping

The damping of a structure is related to the amount of energy dissipated during its motion. It could be assumed that a portion of the energy lost because of the deformations and thus damping could be idealized as proportion to the stiffness of the structure. Another mechanism of energy dissipation could be attributed to the mass of the structure and thus damping is idealized as proportion to the mass of the structure. In Rayleigh damping it is assumed that the damping is proportional to the mass and stiffness of the structure.

$$[C] = a_o [M] + a_1 [K] \tag{3.25}$$

The generalized damping of *n*th mode, is then given by

$$C_n = a_o M_n + a_1 K_n \tag{3.26}$$

$$C_n = a_o M_n + a_1 \omega_n^2 M_n \tag{3.27}$$

$$\xi_n = \frac{C_n}{2M_n\omega_n} \tag{3.28}$$

$$\xi_n = \frac{a_o}{2}\frac{1}{\omega_n} + \frac{a_1}{2}\omega_n \tag{3.29}$$

Figure 3.15 shows the Rayleigh damping variation with natural frequency. The coefficients a_o and a_1 can be determined from specified damping ratios at two independent dominant modes (say *i*th and *j*th modes). Expressing Equation 3.29 for these two modes will lead to the following equations:

$$\xi_i = \frac{a_o}{2}\frac{1}{\omega_i} + \frac{a_1}{2}\omega_i \tag{3.30}$$

$$\xi_j = \frac{a_o}{2}\frac{1}{\omega_j} + \frac{a_1}{2}\omega_j \tag{3.31}$$

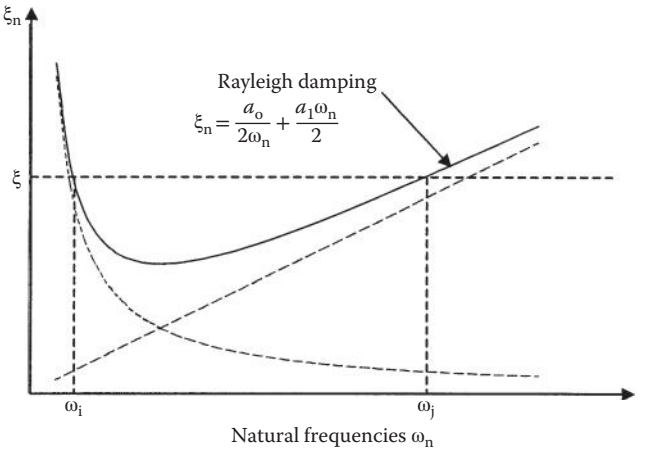

FIGURE 3.15 Rayleigh damping variation with natural frequency.

When the damping ratio at both *i*th and *j*th modes is the same and equals ξ, it can be shown that

$$a_o = \xi \frac{2\omega_i \omega_j}{\omega_i + \omega_j} \quad a_1 = \xi \frac{2}{\omega_i + \omega_j} \tag{3.32}$$

It is important to note that the damping ratio at a mode between the *i*th and *j*th mode is less than ξ. And, in practical problems the specified damping ratios should be chosen to ensure reasonable values in all the mode shapes that lie between the *i*th and *j*th mode shapes.

3.3.3 Modal Analysis and Modal Participation Factor

In previous sections, we have discussed the basic vibration properties of a MDOF system. Now, we will look at the response of a MDOF system to earthquake ground motion. The basic equation of motion of the MDOF for an earthquake ground motion is given by the Equation 3.14, which is repeated here:

$$[M]\{\ddot{u}\} + [C]\{\dot{u}\} + [K]\{u\} = -[M]\{B\}\ddot{u}_g$$

The displacement is first expressed in terms of natural mode shapes, and later it is multiplied by the transformed natural mode matrix to obtain the following expression:

$$[M^*]\{\ddot{Y}\} + [C^*]\{\dot{Y}\} + [K^*]\{Y\} = -[\Phi]^T[M]\{B\}\ddot{u}_g \tag{3.33}$$

And, the equation of *n*th mode shape is given by

$$M_n^* \ddot{Y}_n + 2\xi_n \omega_n M_n^* \dot{Y}_n + \omega^2 M_n^* Y_n = L_n \ddot{u}_g \tag{3.34}$$

where

$$M_n^* = \{\phi_n\}^T [M]\{\phi_n\} \tag{3.35}$$

$$L_n = -\{\phi_n\}^T [M][B] \tag{3.36}$$

The L_n is referred to as the "modal participation factor" of nth mode.

By dividing the Equation 3.34 by M_n^*, the generalized modal equation of nth mode becomes

$$\ddot{Y}_n + 2\xi_n \omega_n \dot{Y}_n + \omega^2 Y_n = \left(\frac{L_n}{M_n^*}\right)\ddot{u}_g \tag{3.37}$$

Equation 3.34 is similar to the equation motion of a SDOF system and thus Y_n can be determined by using similar methods described for SDOF systems. Once Y_n is established, the displacement because of the nth mode will be given by $u_n(t)=\phi_n Y_n(t)$. The total displacement because of combination of all mode shapes can then be determined by summing up all displacements for each mode and is given by

$$u(t)=\sum \varphi_n Y_n(t) \tag{3.38}$$

This approach is sometimes referred to as classical mode superposition method. Similar to the estimation of the total displacement, the element forces can also be estimated by adding the element forces for each mode shapes.

3.3.4 Example of a MDOF System

Given: The bridge shown in Figure 3.16 is a three-span continuous frame structure. Details of the bridge are as follows: Span lengths are 60 ft + 80.4 ft + 60 ft (18.3 m + 24.5 m + 18.3 m); column length is 30.17 ft (9.5 m); area of superstructure is 60.1 ft^2 (5.58 m^2); moment of inertia of superstructure is 9,356 ft^4 (70.77 m^4); moment of inertia of column is (25.25 ft^4) 0.218 m^4; modulus of elasticity of concrete is 3,000 ksi (20,700 MPa). Determine the vibration modes and frequencies of the bridge.

Solution: As shown in Figure 3.16b, c, and d, five DOF are available for this structure. Stiffness and mass matrices are estimated separately and the results are given here.

$$[K]=\begin{bmatrix} 126318588 & 0 & 0 & 0 & 0 \\ 0 & 1975642681 & -1194370500 & -1520122814 & -14643288630 \\ 0 & -1194370500 & 1975642681 & 14643288630 & 1520122814 \\ 0 & -1520122814 & 14643288630 & 479327648712 & 119586857143 \\ 0 & -14643288630 & 1520122814 & 119586857143 & 479327648712 \end{bmatrix}$$

$$[M]=\begin{bmatrix} 81872 & 0 & 0 & 0 & 0 \\ 0 & 286827 & 0 & 0 & 0 \\ 0 & 0 & 286827 & 0 & 0 \\ 0 & 0 & 0 & 0 & 0 \\ 0 & 0 & 0 & 0 & 0 \end{bmatrix} \text{Kg}$$

Condensation procedure will eliminate the rotational DOF and will result in three DOF. (Condensation procedure is done separately and the result is given here.) The equation of motion of free vibration of the structure is

$$[M]\{\ddot{u}\} + [K]\{u\} = \{0\}$$

Substituting condensed stiffness and mass matrices with the above equation gives

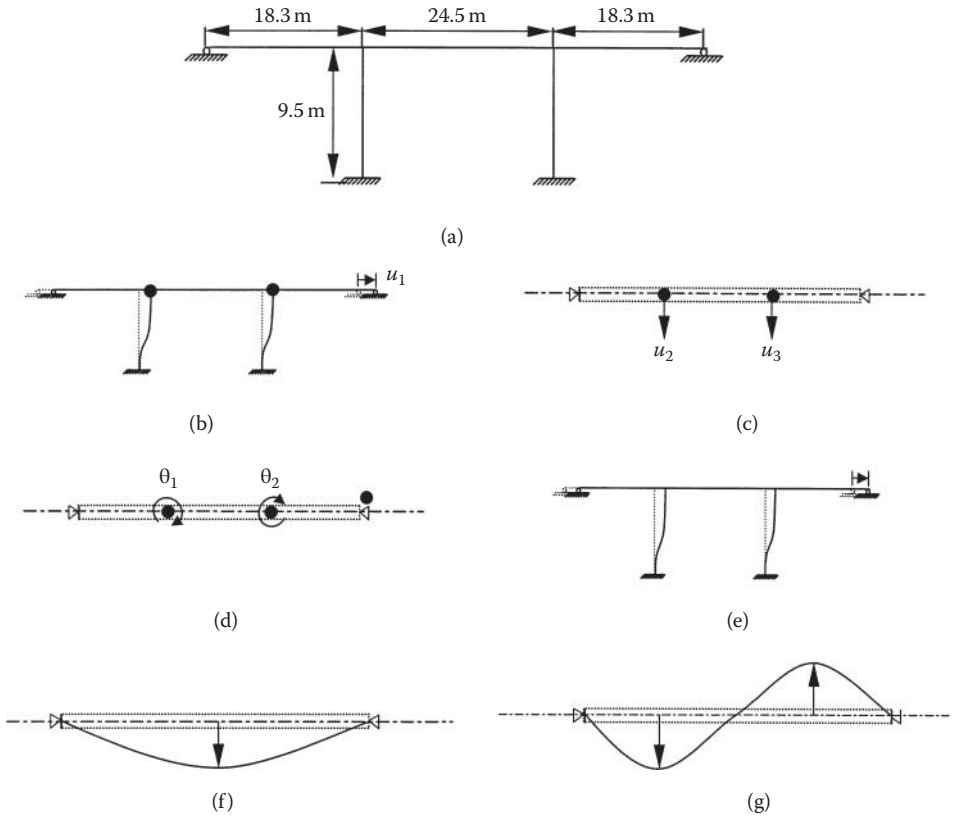

FIGURE 3.16 Three-span continuous framed bridge structure of MDOF example. (a) Schematic diagram; (b) longitudinal degree of freedom; (c) transverse degree of freedom; (d) rotational degree of freedom; (e) mode shape 1; (f) mode shape 2; (g) mode shape 3.

$$\begin{bmatrix} 81872 & 0 & 0 \\ 0 & 286827 & 0 \\ 0 & 0 & 286827 \end{bmatrix} \begin{Bmatrix} \ddot{u}_1 \\ \ddot{u}_2 \\ \ddot{u}_3 \end{Bmatrix} + \begin{bmatrix} 126318588 & 0 & 0 \\ 0 & 1975642681 & -1194370500 \\ 0 & -1194370500 & 1975642681 \end{bmatrix} \begin{Bmatrix} u_1 \\ u_2 \\ u_3 \end{Bmatrix} = \begin{Bmatrix} 0 \\ 0 \\ 0 \end{Bmatrix}$$

Above equation can be rearranged in the following form:

$$\frac{1}{\omega^2}[M]^{-1}[K]\{\phi\} = \{\phi\}$$

Substitution of appropriate values in the above expression gives the following:

$$\frac{1}{\omega_n^2} \begin{bmatrix} \frac{1}{818172} & 0 & 0 \\ 0 & \frac{1}{286827} & 0 \\ 0 & 0 & \frac{1}{286827} \end{bmatrix} \begin{bmatrix} 126318588 & 0 & 0 \\ 0 & 1518171572 & -1215625977 \\ 0 & -1215625977 & 1518171572 \end{bmatrix} \begin{Bmatrix} \phi_{1n} \\ \phi_{2n} \\ \phi_{3n} \end{Bmatrix} = \begin{Bmatrix} \phi_{1n} \\ \phi_{2n} \\ \phi_{3n} \end{Bmatrix}$$

$$\frac{1}{\omega_n^2}\begin{bmatrix} 154.39 & 0 & 0 \\ 0 & 5292.9 & -4238.2 \\ 0 & -4238.2 & 5292.9 \end{bmatrix}\begin{Bmatrix} \phi_{1n} \\ \phi_{2n} \\ \phi_{3n} \end{Bmatrix} = \begin{Bmatrix} \phi_{1n} \\ \phi_{2n} \\ \phi_{3n} \end{Bmatrix}$$

By assuming different vibration modes, natural frequencies of the structure can be estimated. Substitution of vibration mode $\{100\}^T$ will result in the first natural frequency.

$$\frac{1}{\omega_n^2}\begin{bmatrix} 154.39 & 0 & 0 \\ 0 & 5292.9 & -4238.2 \\ 0 & -4238.2 & 5292.9 \end{bmatrix}\begin{Bmatrix} 1 \\ 0 \\ 0 \end{Bmatrix} = \frac{1}{\omega_n^2}\begin{bmatrix} 154.39 \\ 0 \\ 0 \end{bmatrix} = \begin{Bmatrix} 1 \\ 0 \\ 0 \end{Bmatrix}$$

Thus, $\omega_n^2 = 154.39$ and $\omega_n = 12.43$ rad/s

By substituting the vibration modes of $\{0\ 1\ 1\}^T$ and $\{0\ 1\ -1\}^T$ in the above expression, other two natural frequencies are estimated as 32.48 rad/s and 97.63 rad/s.

3.3.5 Multiple-Support Excitation

So far we have assumed that all supports of a structural system undergo the same ground motion. This assumption is valid for structure with foundation supports close to each other. However, for long-span bridge structures, supports may be widely spaced. As described in Section 3.1.2, earth motion at a location depends on localized soil layer and distance from the epicenter. Thus, bridge structures with supports lie far from each other may experience different earth excitation. For example, Figure 3.17 shows the predicted earthquake motions at Pier-W3 and Pier-W6 of the San Francisco Oakland Bay Bridge (SFOBB) of California. The distance between Pier-W3 and Pier-W6 of the SFOBB is approximately 1411 m (Figure 3.17b). These excitations are predicted by the California Department of Transportation by considering the soil and rock properties in the vicinity of SFOBB and expected earth movements at San Andreas Fault and Hayward fault (Caltrans, 1997). Note that the earth motion at Pier-W3 and Pier-W6 are very different. Furthermore, Figures 3.17c, d, and e indicates that the earth motion not only varies with the location, but also varies with direction. Thus, to evaluate the response of long, multiply supported, and complicated bridge structures, use of the actual earthquake excitation at each support is recommended.

The equation of motion of a multi-support excitation would be similar to the Equation 3.14, but the only difference is now that $\{B\}\ddot{u}_g$ is replaced by a displacement array $\{\ddot{u}_g\}$. And, the equation of motion multi-support system becomes

$$[M]\{\ddot{u}\} + [C]\{\dot{u}\} + [K]\{u\} = -[M]\{\ddot{u}_g\} \tag{3.39}$$

where, $\{\ddot{u}_g\}$ has the acceleration at each support locations and has zero value at nonsupport locations. By using uncoupling procedure described in the previous sections, the modal equation of nth mode can be written as

$$\ddot{Y}_n + 2\xi_n \omega_n \dot{Y}_n + \omega^2 Y_n = -\sum_{l=1}^{N_g} \frac{L_n}{M_n^*}\ddot{u}_g \tag{3.40}$$

where N_g is the total number of externally excited supports.

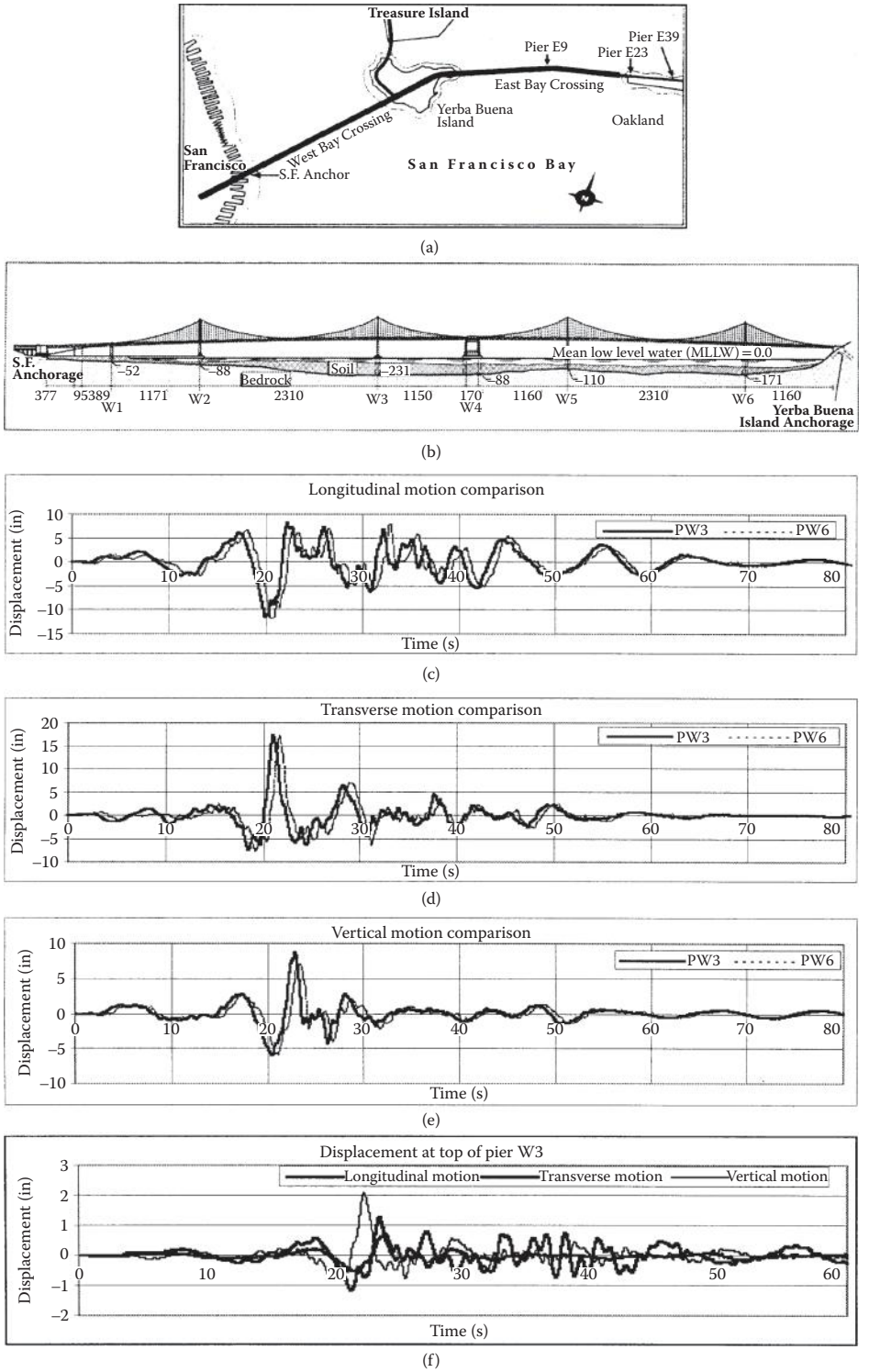

FIGURE 3.17 San Francisco Oakland Bay Bridge (SFOBB) West Spans. (a) Vicinity map; (b) general plan elevation; (c) longitudinal motion at rock level; (d) transverse motion at rock level; (e) vertical motion at rock level; (f) displacement response at top of Pier W3.

The deformation response of the *n*th mode can then be determined as described in Section 3.3.3. Once the displacement response of the structure for all the mode shapes are estimated, the total dynamic response can be obtained by combining the displacements.

3.3.6 Time History Analysis

When the structure enters the nonlinear range, or has nonclassical damping properties, modal analysis cannot be used. A numerical integration method sometimes referred to as time history analysis, is required to get more accurate responses of the structure.

In a time history analysis, the time scale is divided into a series of smaller steps, $d\tau$. Let us say the response at *i*th time interval has already determined and is denoted by $u_i, \dot{u}_i, \ddot{u}_i$. Then, the response of the system at *i*th time interval will satisfy the equation of motion (Equation 3.39).

$$[M]\{\ddot{u}_i\} + [C]\{\dot{u}_i\} + [K]\{u_i\} = -[M]\{\ddot{u}_{gi}\} \tag{3.41}$$

The time stepping method enables us to step ahead and determine the responses $u_{i+1}, \dot{u}_{i+1}, \ddot{u}_{i+1}$ at $i+1$th time interval by satisfying the Equation 3.39. Thus, the equation of motion at $i+1$th time interval will be

$$[M]\{\ddot{u}_{i+1}\} + [C]\{\dot{u}_{i+1}\} + [K]\{u_{i+1}\} = -[M]\{\ddot{u}_{gi+1}\} \tag{3.42}$$

Equation 3.42 needs to be solved before proceeding to the next time step. By stepping through all the time steps, the actual response of the structure can be determined at all time instants.

3.3.6.1 Example on Time History Analysis

The Pier W3 of San Francisco Oakland Bay Bridge West Spans was modeled using ADINA (1995) Program and nonlinear analysis was performed using the displacement time histories. The displacement time histories in three directions are applied at the bottom of the Pier W3 and the response of the Pier W3 was studied to estimate the demand on the Pier W3. One of the results, the displacement response at top of the Pier W3 is shown in Figure 3.17f.

3.4 Response Spectrum Analysis

Response spectrum analysis is an approximate method of dynamic analysis that gives the maximum response (acceleration, velocity, or displacement) of a SDOF system with the same damping ratio, but with different natural frequencies, responding to a specified seismic excitation. Structural models with *n* DOF can be transformed to *n* single-degree systems and response spectra principles can be applied to systems with many DOF. For most ordinary bridges a complete time history is not required. Because the design is generally based on the maximum earthquake response and response spectrum analysis is probably the most common method used in the design offices to determine the maximum structural response because of transient loading. In this section, we will discuss basic procedures of response spectrum analysis for bridge structures.

3.4.1 Single-Mode Spectral Analysis

The single-mode spectral analysis is based on the assumption that earthquake design forces for structures respond predominantly in the first mode of vibration. This method is most suitable to regular linear elastic bridges to compute the forces and deformations, but not applicable for irregular bridges (unbalanced spans, unequal stiffness in the columns, etc.) because higher modes of vibration affects the

distribution of the forces and resulting displacements significantly. This method can be applied to both continuous and noncontinuous bridge superstructures in either the longitudinal or transverse direction. Foundation flexibility at the abutments can be included in the analysis.

The single-mode analysis is based on Rayleigh's energy method—an approximate method, which assumes a vibration shape for a structure. The natural period of the structure is then calculated by equating the maximum potential and kinetic energies associated with the assumed shape. The inertial forces $p_e(x)$ are calculated using the natural period and the design forces and displacements are then computed using static analysis. The detailed procedure can be described in the following steps:

1. Apply uniform loading P_o over the length of the structure and compute the corresponding static displacements $u_s(x)$. The structure deflection under earthquake loading, $u_s(x,t)$ is then approximated by the shape function, $u_s(x)$, multiplied by the generalized amplitude function, $u(t)$, which satisfies the geometric boundary conditions of the structural system. This dynamic deflection is shown as

$$u(x,t) = u_s(x)\ u(t) \tag{3.43}$$

2. Calculate the generalized parameters α, β, and γ using the following equations:

$$\alpha = \int u_s(x)\,dx \tag{3.44}$$

$$\beta = \int w(x)\,u_s(x)\ dx \tag{3.45}$$

$$\gamma = \int w(x)\left[u_s(x)\right]^2 dx \tag{3.46}$$

where $w(x)$ is the weight of the dead load of the bridge superstructure and tributary substructure.

3. Calculate the period T_n

$$T_n = 2\pi\sqrt{\frac{\gamma}{p_o g \alpha}} \tag{3.47}$$

where g is acceleration of gravity (ft/s^2) and p_o a uniform load arbitrarily set equal to 1.0 (kip/ft).

4. Calculate the static loading $p_e(x)$, which approximates the inertial effects associated with the displacement $u_s(x)$ using the ARS curve or following equation (AASHTO, 2011 and 2012):

$$p_e(x) = \frac{\beta\, C_{sm}}{\gamma} w(x)\ u_s(x) \tag{3.48}$$

$$C_{sm} = \frac{1.2AS}{T_m^{2/3}} \tag{3.49}$$

where C_{sm} is the dimensionless elastic seismic response coefficient; A the acceleration coefficient from the acceleration coefficient map; S the dimensionless soil coefficient based on the soil profile type; T_n the period of the structure as determined above; $p_e(x)$ is the intensity of the equivalent static seismic loading applied to represent the primary mode of vibration (kip/ft).

5. Apply the calculated loading $p_e(x)$ to the structure as shown in the Figure 3.18 and compute the structure deflections and member forces.

This method is an iterative procedure, and the previous calculations are used as input parameters for the new iteration leading to a new period and deflected shape. The process is continued until the assumed shape matches the fundamental mode shape.

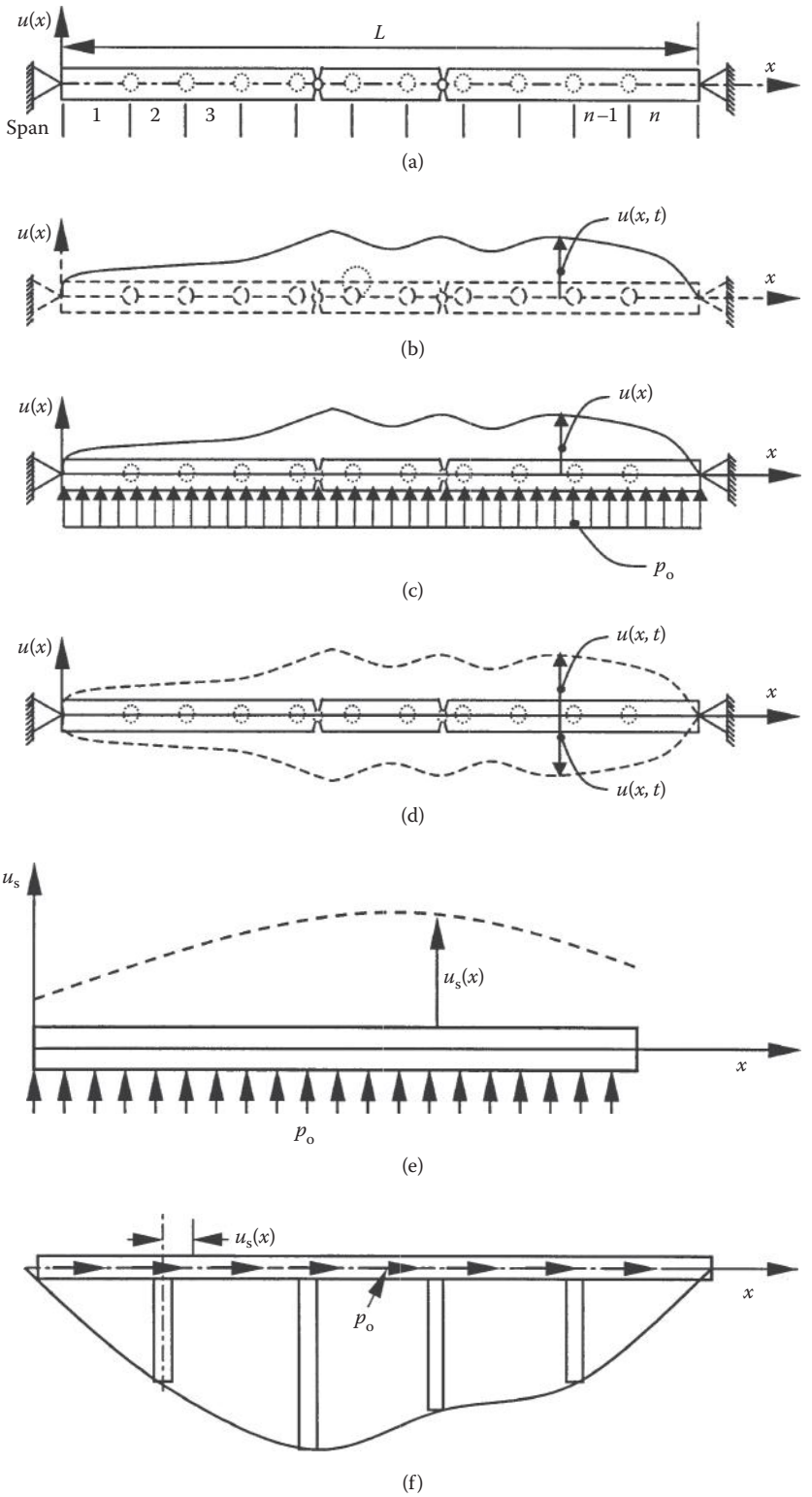

FIGURE 3.18 Single-mode spectral analysis method.

3.4.2 Uniform Load Method

The uniform load method is essentially an equivalent static method that uses the uniform lateral load to compute the effect of seismic loads. For simple bridge structures with relatively straight alignment, small skew, balanced stiffness, relative light substructure, and with no hinges, uniform load method may be applied to analyze the structure for seismic loads. This method is not suitable for bridges with stiff substructures such as pier walls. This method assumes continuity of the structure and distributes earthquake force to all elements of the bridge and is based on the fundamental mode of vibration in either longitudinal or transverse direction (AASHTO, 2011 and 2012). The period of vibration is taken as that of an equivalent single mass-spring oscillator. The maximum displacement that occurs under the arbitrary uniform load is used to calculate the stiffness of the equivalent spring. The seismic elastic response coefficient C_{sm} or the ARS curve is then used to calculate the equivalent uniform seismic load using, which the displacements and forces are calculated. The following steps outline the uniform load method:

1. Idealize the structure into a simplified model and apply a uniform horizontal load (p_o) over the length of the bridge as shown in Figure 3.19. It has units of force/unit length and may be arbitrarily set equal to 1 kip/ft.
2. Calculate the static displacements $u_s(x)$ under the uniform load P_o using static analysis.
3. Calculate the maximum displacement $u_{s,MAX}$ and adjust it to 1 ft adjusting the uniform load P_o.
4. Calculate bridge lateral stiffness K using the following equation:

$$K = \frac{p_o L}{u_{s,MAX}} \tag{3.50}$$

   where L is total length of the bridge (ft); and $v_{s,MAX}$ maximum displacement (ft).
5. Calculate the total weight W of the structure including structural elements and other relevant loads such as pier walls, abutments, columns, and footings by

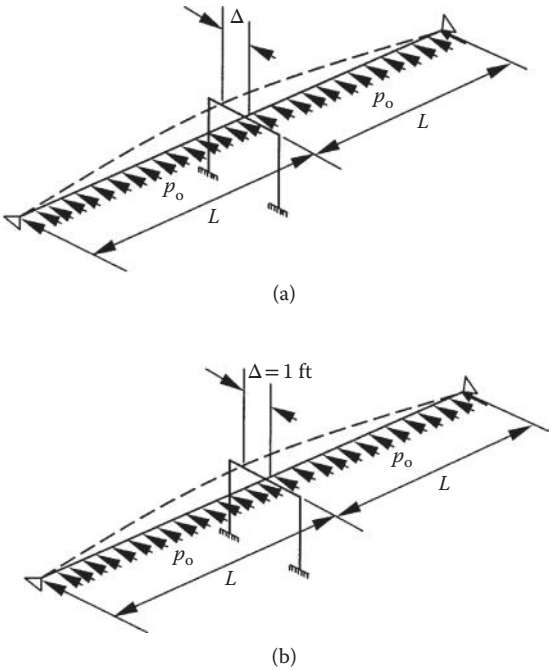

FIGURE 3.19 Structure idealization and deflected shape for uniform load method. (a) Structure idealization; (b) deflected shape with maximum displacement of 1 ft.

$$W = \int w(x)\,\mathrm{d}x \tag{3.51}$$

where $w(x)$ is nominal, unfactored dead load of the bridge superstructure, and tributary substructure.

6. Calculate the period of the structure T_n using the following equation:

$$T_n = 2\pi\sqrt{\frac{W}{gK}} \tag{3.52}$$

where g is acceleration of gravity (ft/s^2).

7. Calculate the equivalent static earthquake force P_e using the ARS curve or using the following equation:

$$p_e = \frac{C_{sm}W}{L} \tag{3.53}$$

8. Calculate the structure deflections and member forces by applying p_e to the structure.

3.4.3 Multi-Mode Spectral Analysis

3.4.3.1 Basic Concept

The multi-mode spectral analysis method is more sophisticated than single-mode spectral analysis and is very effective in analyzing the response of more complex linear elastic structures to an earthquake excitation. This method is appropriate for structures with irregular geometry, mass, or stiffness. These irregularities induce coupling in three orthogonal directions within each mode of vibration. Also, for these bridges, several modes of vibration contribute to the complete response of the structure. A multi-mode spectral analysis is usually done by modeling the bridge structure consisting of three-dimensional frame elements with structural mass lumped at various locations to represent the vibration modes of the components. Usually, five elements per span are sufficient to represent the first three modes of vibration. A general rule of thumb is to capture ith mode of vibration, the span should have at least $(2i–1)$ elements. For long-span structures many more elements should be used to capture all the contributing modes of vibration. To obtain a reasonable response, the number of modes should be equal to at least three times the number of spans. This analysis is usually performed with a dynamic analysis computer programs such as ADINA (2011), SAP2000 (2011), and ANSYS (2010). For bridges with outrigger bents, C-bents, and single-column bents, rotational moment of inertia of the superstructure should be included. Discontinuities at the hinges and abutments should be included in the model. The columns and piers should have intermediate nodes at quarter points in addition to the nodes at the ends of the columns.

3.4.3.2 Analysis Procedure

Using the programs mentioned in Section 3.4.4.1, frequencies, mode shapes, member forces, and joint displacements can be computed. The following steps summarize the equations used in the multi-mode spectral analysis (AASHTO, 2011 and 2012).

1. Calculate the dimensionless mode shapes $\{\phi_i\}$ and corresponding frequencies ω_i by

$$\left[[K] - \omega^2[M]\right]\{u\} = 0 \tag{3.54}$$

where

$$u_i = \sum_{j=1}^{n} \phi_j y_j = \Phi y_i \tag{3.55}$$

y_j = modal amplitude of jth mode; φ_j = shape factor of jth mode; Φ = mode-shape matrix.

The periods for ith mode can then be calculated by

$$T_i = \frac{2\pi}{\omega_i} \quad (i = 1, 2, \ldots\ldots, n) \tag{3.56}$$

2. Determining the maximum absolute mode amplitude for the entire time history is given by

$$Y_i(t)_{\max} = \frac{T_i^2 S_a(\xi_i, T_i)}{4\pi^2} \frac{\{\phi_i\}^T [M]\{B\}\ddot{u}_g}{\{\phi_i\}^T [M]\{\phi_i\}} \tag{3.57}$$

where $S_a(\xi_i, T_i) = gC_{sm}$ is the acceleration response spectral value; C_{sm} is the elastic seismic response coefficient for mode $m = \frac{1.2AS}{T_n^{2/3}}$; A is the acceleration coefficient from the acceleration coefficient map; S the dimensionless soil coefficient based on the soil profile type; T_n the period of the nth mode of vibration.

3. Calculate the value of any response quantity $Z(t)$ (shear, moment, displacement) using the following equation:

$$Z(t) = \sum_{i=1}^{n} A_i Y_i(t) \tag{3.58}$$

where coefficients A_i are functions of mode shape matrix (Φ) and force displacement relationships.

4. Compute the maximum value of $Z(t)$ during an earthquake using the mode combination methods described in Section 3.4.3.3.

3.4.3.3 Modal Combination Rules

Mode combination method is a very useful tool for analyzing bridges with large number of DOF. In a linear structural system maximum response can be estimated by mode combination after calculating natural frequencies and mode shapes of the structure using free vibration analysis. The maximum response cannot be computed by adding the maximum response of each mode because different modes attain their maximum values at different times. The absolute sum (AS) of the individual modal contributions provides an upper bound that is generally very conservative and not recommended for design. The following are several commonly used mode combination methods to compute the maximum total response. The variable Z represents the maximum value of some response quantity (displacement, moment, shear, etc.), Z_i is the peak value of that quantity in the ith mode and N the total number of contributing modes.

1. AS: The AS is sum of the modal contributions

$$Z = \sum_{i=1}^{N} |Z_i| \tag{3.59}$$

2. Square root of sum of squares (SRSS) or root mean square (RMS) method. This method computes the maximum by taking the SRSS of the modal contributions.

$$Z = \left[\sum_{i=1}^{N} Z_i^2 \right]^{1/2} \tag{3.60}$$

3. CQC: Cross correlation between all modes are considered.

$$Z = \left[\sum_{i=1}^{N} \sum_{j=1}^{N} Z_i \rho_{ij} Z_j \right]^{1/2} \tag{3.61}$$

$$\rho_{ij} = \frac{8\sqrt{\xi_i \xi_j}\left(\xi_i + r\xi_j\right) r^{3/2}}{\left(1-r^2\right)^2 + 4\xi_i \xi_j r\left(1+r^2\right) + 4\left(\xi_i^2 + \xi_j^2\right) r^2} \tag{3.62}$$

where

$$r = \frac{\omega_j}{\omega_i} \tag{3.63}$$

4. CQC with three components (CQC3):

$$Z = [Z_0^2 + a^2 Z_{90}^2 - (1-a^2)(Z_0^2 - Z_{90}^2)\sin^2\theta + 2(1-a^2) Z_{0-90}^2 \sin\theta\cos\theta + Z_z^2]^{\frac{1}{2}} \tag{3.64}$$

$$Z_0^2 = \sum_i \sum_j Z_{0i} \rho_{ij} Z_{0j} \tag{3.65}$$

$$Z_{90}^2 = \sum_i \sum_j f_{90i} \rho_{ij} f_{90j} \tag{3.66}$$

$$Z_{0-90}^2 = \sum_i \sum_j f_{0i} \rho_{ij} f_{90j} \tag{3.67}$$

$$Z_Z^2 = \sum_i \sum_j f_{zi} \rho_{ij} f_{zj} \tag{3.68}$$

where Z_{0i} and Z_{90i} are the modal values produced by 100% of the lateral spectrum applied between 0 and 90°, respectively; Z_{zi} the modal response from the vertical spectrum that can be different from the lateral spectrum; θ an arbitrary angle between one computation axis and one of directions of basic horizontal input spectra; and a the ratio (between 0 and 1.0) of two basic horizontal input spectra.

It is important to note that for equal spectra $a = 1.0$, the value F is not a function of θ and the selection of the analysis reference system is arbitrary, that is

$$Z = \sqrt{Z_0^2 + Z_{90}^2 + Z_z^2} \tag{3.69}$$

5. Percentage combination (AASHTO, 2011; Caltrans, 2013).
100% of the prescribed seismic effects in one direction plus 30% or 40% of the prescribed seismic effects applied in the perpendicular direction. For examples, AASHTO Guide Specifications for LRFD Seismic Bridge Design (AASHTO, 2011) and Caltrans SDC (Caltrans, 2013) specify the following load cases:
   a. Seismic load case 1: 100% transverse + 30% longitudinal + 30% vertical
   b. Seismic load case 2: 30% transverse + 100% longitudinal + 30% vertical
   c. Seismic load case 3: 30% transverse + 30% longitudinal + 100% vertical

3.4.3.4 Remarks

- Theoretically all mode shapes must be included to calculate the response but fewer mode shapes can be used when the corresponding mass participation is over 85% of the total structure mass. In general, the factors considered to determine the number of modes required for the mode combination are dependent on structural characteristics of the bridge, spatial distribution, and frequency content of the earthquake loading.
- AS is the most conservative method. It assumes that the maximum modal values for all modes occur at the same time.
- SRSS is a very common approach and is suitable for structures with well-spaced modes. It assumes that all of the maximum modal values are statistically independent. For three-dimensional structures in which a large number of frequencies are almost identical, this assumption is not justified (Wilson, 2009).
- CQC is based on random vibration theories and has been accepted by most experts in earthquake engineering (Wilson et al., 1981). For an undamped structure, the CQC is identical to the SRSS. For structures with closely spaced dominant mode shapes the CQC method is precise, whereas the SRSS estimates inaccurate results. Closely spaced modes are those within 10% of each other in terms of natural frequency.
- CQC3 combines the effects of three orthogonal spectra (Menun and Kiureghian, 1998). For $a = 1$, the CQC3 reduces to the SRSS. For three-dimensional response spectra analyses, the CQC3 method should be used if a value of $a < 1.0$ can be justified. It will produce realistic results that are not a function of the user-selected reference system. At the present time, no specific guidelines have been suggested for the value of a.
- Percentage rule (100/30) is the simplest and recommended by the AASHTO (2011) and Caltrans (2013). However, it is empirical and can underestimate the design forces in certain members and produces a member design that is relatively weak in one direction.

3.4.4 Multiple Support Response Spectrum Method

Records from recent earthquakes indicate that seismic ground motions can significantly vary at different support locations for multiply supported long structures. When different ground motions are applied at various support points of a bridge structure, the total response can be calculated by superposition of response because of independent support input. This analysis involves combination of dynamic response from single input and pseudo-static response resulting from the motion of the supports relative to each other. The combination effects of dynamic and pseudo-static forces because of multiple support excitations on a bridge depend on the structural configuration of the bridge and ground motion characteristics. Kiureghian et al. (1997) presented a comprehensive study on the MSRS method based on fundamental principles of stationary random vibration theory for seismic analysis of multiply supported structures that accounts for the effects of variability between the support motions. Using MSRS combination rule, the response of a linear structural system subjected to multiple support excitations can be computed directly in terms of conventional response spectra at the support DOF and a coherency function describing the spatial variability of the ground motion. This method accounts for the three important effects of ground motion spatial variability, namely, the incoherence, the wave passage, and the site response effect. These three components of ground motion spatial variability can strongly influence the response of multiply supported bridges and may amplify or de-amplify the response by one order of magnitude. Two important limitations of this method are nonlinearities in the bridge structural components and/or connections and the effects of soil structure interaction. This method is an efficient, accurate, and versatile solution and requires less computational time than a true time history analysis. Following are the steps that describe the MSRS analysis procedure.

1. Determine the necessity of variable support motion analysis: Three factors that influence the response of the structure under multiple support excitations are the distance between the supports of the structure, rate of variability of the local soil conditions, and the stiffness of the structure. The first factor, the distance between the supports influences the incoherence and wave passage effects. The second factor, the rate of variability of the local conditions influences the site response. The third factor, the stiffness of the superstructure plays an important role in determining the necessity of variable support motion analysis. Stiff structures such as box girder bridges may generate large internal forces under variable support motion, whereas flexible structures such as suspension bridges easily conform to the variable support motion.
2. Determine the frequency response function for each support location. Programs such as SHAKE (Idriss et al., 1991) can be used to develop these functions using borehole data and time-domain site response analysis. Response spectra plots, peak ground displacements in three orthogonal directions for each support location, and a coherency function for each pair of DOF are required to perform the MSRS analysis. The comprehensive report by Kiureghian et al. (1997) provides all the formulas required to account for the effect of nonlinearity in the soil behavior and the site frequency involving the depth of the bedrock.
3. Calculate the structural properties such as effective modal frequencies, damping ratios, influence coefficients, and effective modal participation factors (ω_i, ξ_i, a_k, and b_{ki}) are to be computed externally and provided as input.
4. Determine the response spectra plots, peak ground displacements in three directions, and a coherency function for each pair of support DOF required to perform MSRS analysis. The three components of coherency function are incoherence, wave passage effect, and site response effect. Analysis by array of recordings is used to determine incoherence component. The models for this empirical method are widely available (Abrahamson et al., 1991). Parameters such as shear wave velocity, the direction of propagation of seismic waves, and the angle of incidence are used to calculate the wave passage effect. Frequency response function determined in the previous steps is used to calculate the site response component.

3.4.5 Remarks

It should be understood clearly that the response spectrum method is an approximate method used to estimate maximum peak values of displacements and forces (Wilson, 2009) and must be used very carefully. It is strictly limited to linear elastic analysis where damping properties can only be estimated with a low degree of confidence. The use of nonlinear spectra has very little theoretical background, and this approach should not be applied in the analysis of complex three-dimensional structures (Wilson, 2009).

3.5 Inelastic Dynamic Analysis

3.5.1 Equations of Motion

Inelastic dynamic analysis is usually performed for the safety evaluation of important bridges to determine the inelastic response of bridges when subjected to design earthquake ground motions. Inelastic dynamic analysis provides a realistic measure of response because the inelastic model accounts for the redistribution of internal actions because of the nonlinear force displacement behavior of the components (I&A, 1992; ATC, 1996; Bathe, 1996; Priestly et al., 1996; Buchholdt, 1997; Paz and Leigh, 2004). Inelastic dynamic analysis considers nonlinear damping, stiffness, load deformation behavior of members including soil, and mass properties. A step-by-step integration procedure is the most powerful method used for nonlinear dynamic analysis. One important assumption of this procedure is that the acceleration varies linearly, whereas the properties of the system such as damping and stiffness remain

constant during the time interval. Using this procedure, a nonlinear system is approximated as series of linear systems and the response is calculated for a series of small equal intervals of time Δt and equilibrium is established at the beginning and end of each interval.

The accuracy of this procedure depends on the length of the time increment Δt. This time increment should be small enough to consider rate of change of loading $p(t)$, nonlinear damping and stiffness properties, and the natural period of the vibration. A SDOF system and its characteristics are shown in Figure 3.20. The characteristics include spring and damping forces, forces acting on mass of the system, and arbitrary applied loading. The force equilibrium can be shown as

$$f_i(t) + f_d(t) + f_s(t) = p(t) \tag{3.70}$$

and the incremental equations of motion for time t can be shown as

$$m\,\Delta\ddot{u}(t) + c(t)\,\Delta\dot{u}(t) + k(t)\,\Delta u(t) = \Delta p(t) \tag{3.71}$$

Current damping $f_d(t)$, elastic forces $f_s(t)$ are then computed using the initial velocity $\dot{u}(t)$, displacement values $u(t)$, nonlinear properties of the system, damping $c(t)$, and stiffness $k(t)$ for that interval.

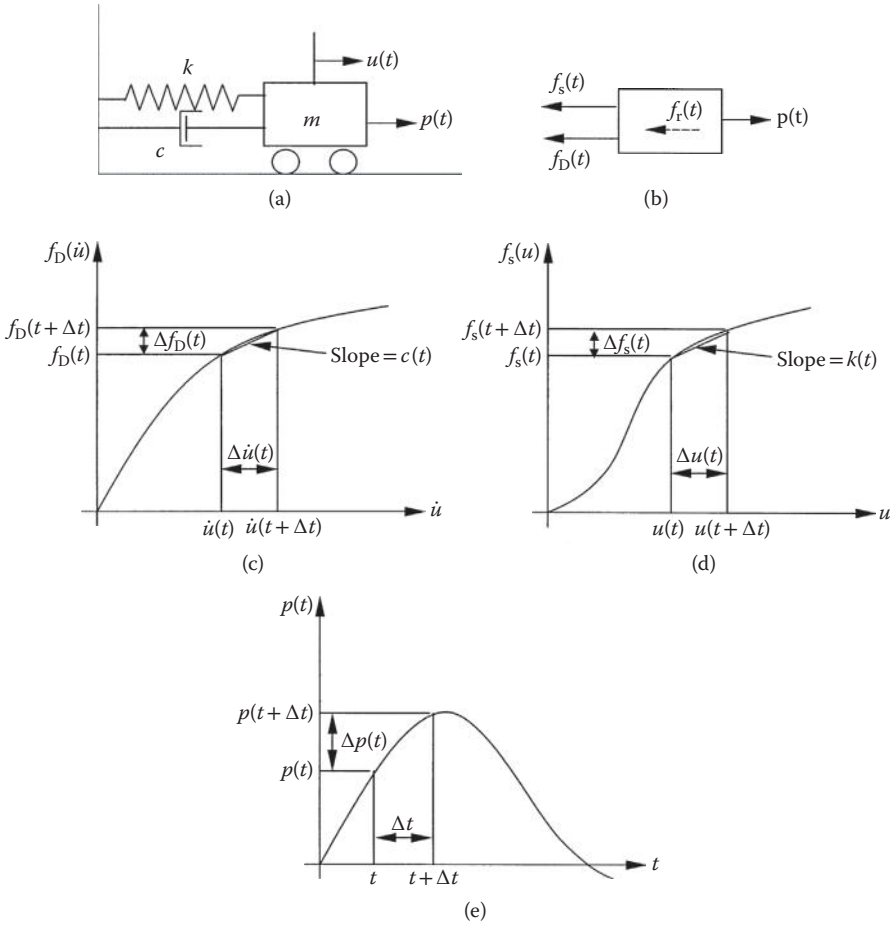

FIGURE 3.20 Definition of nonlinear dynamic system. (a) Basis SDOF structure; (b) force equilibrium; (c) nonlinear damping; (d) nonlinear stiffness; (e) applied load.

New structural properties are calculated at the beginning of the each time increment based on the current deformed state. The complete response is then calculated by using the displacement and velocity values computed at the end of each time step as the initial conditions for the next time interval and repeating until the desired time.

3.5.2 Modeling Considerations

A bridge structural model should have sufficient DOF and proper selection of linear/nonlinear elements such that a realistic response can be obtained. Nonlinear analysis is usually preceded by a linear analysis as a part of a complete analysis procedure to capture the physical and mechanical interactions of seismic input and structure response. Output from the linear response solution is then used to predict which nonlinearities will affect the response significantly and model them appropriately. In other words, engineers can justify the effect of each nonlinear element introduced at the appropriate locations and establish the confidence in the nonlinear analysis. Although discretizing the model, engineers should be aware of the tradeoffs between the accuracy, computational time, and use of the information such as the regions of significant geometric and material nonlinearities. Nonlinear elements should have material behavior to simulate the hysteresis relations under reverse cyclic loading observed in the experiments. A detailed discussion is presented in Chapter 12 of Volume I-Fundamentals.

The general issues in modeling of bridge structures include geometry, stiffness, mass distribution, and boundary conditions. In general, abutments, superstructure, bent caps, columns and pier walls, expansion joints, and foundation springs are the elements included in the structural model. The mass distribution in a structural model depends on the number of elements used to represent the bridge components. The model must be able to simulate the vibration modes of all components contributing to the seismic response of the structure.

Superstructure: Superstructures are usually modeled using linear elastic three-dimensional beam elements. Detailed models may require nonlinear beam elements.

Columns and pier walls: Plastic hinge zones in columns and pier walls are usually modeled using nonlinear beam-column (frame) elements having response properties with a yield surface described by the axial load and biaxial bending. Outside plastic hinge zone are modeled using linear elastic beam-column elements. Some characteristics of the column behavior include, initial stiffness degradation because of concrete cracking, flexural yielding at the fixed end of the column, strain hardening, pinching at the point of load reversal. Shear actions can be modeled using either linear or nonlinear load deformation relationships for columns. For both columns and pier walls, torsion can be modeled with linear elastic properties. For out-of-plane loading, flexural response of a pier wall is similar to that of columns where as for in-plane loading, the nonlinear behavior is usually shear action. Effective cross-section properties including area, moment of inertia, and torsional constant should be used.

Cap Beam: For multi-column bent bridges, the cap beam should be modeled as an elastic beam element. The torsional constant of the cap beam J should be modified by an amplification factor with a minimum value of in order of 100 (Aviram et al., 2008).

Expansion joints: Expansion joints can be modeled using gap elements that simulate the nonlinear behavior of the joint. The variables include initial gap, shear capacity of the joint, and nonlinear load deformation characteristics of the gap.

Abutments: Abutments are modeled using nonlinear spring and gap elements to represent the backfill soil material, abutment back wall, the piles, bearings, and gaps at the seat.

Foundations: Foundations are typically modeled using nonlinear spring elements to represent the translational and rotational stiffness of the foundations to simulate the expected behavior during a design earthquake.

3.6 Summary

This chapter has presented the basic principles and methods of dynamic analysis for seismic design of bridges. Response spectrum analysis—the SDOF or equivalent SDOF-based equivalent static analysis is efficient, convenient, and most frequently used for ordinary bridges with simple configurations. Elastic dynamic analysis is required for bridges with complex configurations. A MSRS analysis developed by Kiureghian et al. (1997) using a lumped-mass beam element mode may be used in lieu of an elastic time-history analysis.

Inelastic response spectrum analysis is a useful concept, but the current approaches apply only to SDOF structures. An actual nonlinear dynamic time-history analysis may be necessary for some important and complex bridges, but linearized dynamic analysis (dynamic secant stiffness analysis), and inelastic static analysis (static push-over analysis) (Chapters 5 and 6) are the best possible alternatives (Powell, 1997) for the most bridges.

References

AASHTO. 2011. *AASHTO Guide Specifications for LRFD Seismic Bridge Design* (2nd Edition). American Association of State Highway and Transportation Officials, Washington, DC.

AASHTO. 2012. *AASHTO LRFD Bridge Specifications*. Customary US Units, American Association of State Highway and Transportation Officials, Washington, DC.

Abrahamson, N. A., Schneider, J. F., and Stepp, J. C. 1991. Empirical Spatial Coherency Functions for Application to Soil-Structure Interaction Analysis, *Earthquake Spectra,* 7, 1–28.

ADINA. 1995. *Users Guide*, Adina R&D, Inc., Watertown, MA.

ADINA. 2011. Version 8.5 *Users Guide*, Adina R&D, Inc., Watertown, MA.

ANSYS. 2010. Release 13.0 *User's Manual*, ANSYS Inc., Canonsburg, PA.

ATC. 1996. *Improved Seismic Design Criteria for California Bridges: Provisional Recommendations,* ATC-32, Applied Technology Council, Redwood City, CA.

Aviram, A., Mackie, K. R., and Stojadinović, B. 2008. *Guidelines for Nonlinear Analysis of Bridge Structures in California*, Report UCB/PEER 2008/03, Pacific Earthquake Engineering Research Center, University of California, Berkeley, CA.

Bathe, K-J. 1996. *Finite Element Procedures*, Prentice-Hall Inc., Englewood Cliffs, NJ.

Buchholdt, H. A. 1997. *Structural Dynamics for Engineers* (1st Edition). Thomas Telford, London, UK.

Caltrans. 1996a. *Guidelines for Generation of Response—Spectrum-Compatible Rock Motion Time History for Application to Caltrans Toll Bridge Seismic Retrofit Projects*. The Caltrans Seismic Advisor Board Ad Hoc Committee on Soil-Foundation-Structure Interaction, California Department of Transportation, Sacramento, CA.

Caltrans. 1996b. *Guidelines for Performing Site Response Analysis to Develop Seismic Ground Motions for Application to Caltrans Toll Bridge Seismic Retrofit Projects*, The Caltrans Seismic Advisor Board Ad Hoc Committee on Soil-Foundation-Structure Interaction, California Department of Transportation, Sacramento, CA.

Caltrans. 1997. *San Francisco–Oakland Bay Bridge West Spans Seismic Retrofit Design Criteria* (prepared by Reno, M., and Duan, L.). Duan, L. (Ed.), California Department of Transportation, Sacramento, CA.

Caltrans. 2013. *Seismic Design Criteria*, Version 1.7, California Department of Transportation, Sacramento, CA.

Chmielewski, T., Kratzig, W. B., Link, M. Meskouris, K., and Wunderlich, W. 1996. Phenomena and Evaluation of Dynamic Structural Responses. In: *Dynamics of Civil Engineering Structures*, Wilfried B. Kratzig, and H.-J. Niemann (eds.), A.A. Balkema Publishers, Leiden, The Netherlands.

Chopra, A. K. 2007. *Dynamics of Structures: Theory and Applications to Earthquake Engineering* (3rd Edition), Prentice Hall Inc., Englewood Cliffs, NJ.

Clough, R. W., and Penzien, J. 1993. *Dynamics of Structures* (2nd edition). McGraw-Hill, New York, NY.

Idriss, I. M., Sun, J. I., and Schnabel, P. B. 1991. *User's manual for SHAKE91: A Computer Program for Conducting Equivalent Linear Seismic Response Analyses of Horizontally Layered Soil Deposits*, Report of Center for Geotechnical Modeling, Department of Civil and Environmental Engineering, University of California at Davis, CA.

I&A. 1992. *Seismic Design of Highway Bridges*. Imbsen & Associates, Sacramento, CA.

Kiureghian, A. E., Keshishian, P., and Hakobian, A. 1997. *Multiple Support Response Spectrum Analysis of Bridges Including the Site-Response Effect and the MSRS Code*, Report No. UCB/EERC-97/02, University of California, Berkeley, CA.

Lindeburg, M. 1998. *Seismic Design of Building Structures: A Professional's Introduction to Earthquake Forces and Design Details*, Professional Publications, Inc., Belmont, CA.

Menun, C., and Kiureghian, A. D. 1998. A Replacement for 30%, 40% and SSRC Rules for Multicomponents Seismic Analysis. *Earthquake Spectra*, 14(1), 153–163.

Paz, M., and Leigh, W. 2004. *Structural Dynamics—Theory and Computation* (5th edition). Kluwer Academic Publishers, Norwell, MA.

Powell, G. H. 1997. *Concepts and Principles for the Application of Nonlinear Structural Analysis in Bridge Design,* Report No.UCB/SEMM-97/08, Department of Civil Engineering, University of California, Berkeley, CA.

Priestly, M. J. N., Seible, F., and Calvi, G. M. 1996. *Seismic Design and Retrofit of Bridges*, John Wiley & Sons, Inc., New York, NY.

SAP2000. 2011. *User's Manual*, Version 14, Computers and Structures Inc., Berkeley, CA.

Wilson, E. L., Der Kiureghian, A., and Bayom, E. P. 1981. A Replacement for SSRS Method in Seismic Analysis, *Earthquake Engineering and Structural Dynamics*, 9, 187–192.

Wilson, E. L. 2009. *Static and Dynamic Analysis of Structures*, Computers and Structures Inc., Berkeley, CA.

4

Seismic Random Response Analysis

Jiahao Lin
Dalian University of Technology

Yahui Zhang
Dalian University of Technology

Yan Zhao
Dalian University of Technology

4.1 Basic Concepts

4.1.1 Random Variables and Random Processes

A random process is a family of n-dependent random variables related to a similar phenomenon that may be functions of one or more independent variables. For a discrete random variable X, let $x_1, x_2,\ldots, x_i$ be the values it can take, then the probability of $X = x_i$ called the probability distribution of X has the following form:

$$p_i(x_i) = P(X = x_i) \quad (i = 1,2,\cdots) \tag{4.1}$$

For a continuous random variable, define the probability density function $p(x)$ as

$$p(x) = \lim_{\Delta x \to 0} \frac{P(x \le X < x + \Delta x)}{\Delta x} \tag{4.2}$$

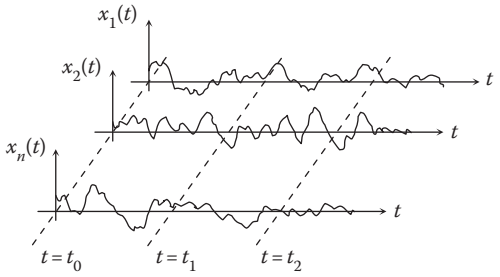

FIGURE 4.1 An ensemble of random time functions.

where $P(x \le X < x + \Delta x)$ is the probability of X lying between x and $x + \Delta x$. Therefore, the probability of X lying between a and b can be written as

$$P(a \le X < b) = \int_a^b p(x)\mathrm{d}x \tag{4.3}$$

For any time $t \in T$ (T is a fixed time domain), if $X(t)$ is a random variable, the ensemble of the random variables $[X(t),\ t \in T]$ can be called a random process. As shown in Figure 4.1, $x_1(t_0), x_2(t_0), \ldots, x_n(t_0)$ are samples of the random variable $X(t_0)$.

A random process is strictly stationary when all the probability distributions associated with it are time invariant. It is weakly stationary if only its first and second moments are time invariant. A random process is said to be ergodic if its statistical properties (such as its mean and variance) can be deduced from a single, sufficiently long sample (realization) of the process. A random process is nonstationary when its probability functions are time-dependent. Most random physical phenomena of interest to engineers can usually be approximated as being stationary.

The expected or mean value of a random process $X(t)$ is given by

$$E[X(t)] = \int_{-\infty}^{+\infty} xp(x)\mathrm{d}x \tag{4.4}$$

where $p(x)$ is the probability density function. It specifies the probability, $p(x)\mathrm{d}x$, that a random variable lies in the range x to $x + \mathrm{d}x$. For a stationary random process, $E[X(t)] = E[X]$. This is because a stationary random process is time invariant. It is sometimes referred to as the first statistical moment. The second statistical moment, or the mean-square value, $E[X^2]$, is the average value of X^2 and is given by

$$E[X^2] = \int_{-\infty}^{+\infty} x^2 p(x)\mathrm{d}x \tag{4.5}$$

If $X(t)$ is ergodic, Equations 4.4 and 4.5 can be written as

$$E[X] = \lim_{T\to\infty} \frac{1}{T}\int_0^T x(t)\mathrm{d}t,\ E[X^2] = \lim_{T\to\infty} \frac{1}{T}\int_0^T x^2\,\mathrm{d}t \tag{4.6}$$

4.1.2 Correlation Functions of Stationary Random Processes

In order to investigate the relation between the values of a stationary random process $X(t)$ at two different times, the auto-correlation function of $X(t)$ is defined as

$$R_{XX}(\tau) = E[X(t)X(t+\tau)] = \int_{-\infty}^{+\infty}\int_{-\infty}^{+\infty} x_1(t)x_2(t+\tau)p(x_1,t;x_2,t+\tau)\mathrm{d}x_1\,\mathrm{d}x_2 \tag{4.7}$$

The cross-correlation function between two different stationary random processes $X(t)$ and $Y(t)$ is

$$R_{XY}(\tau) = E\left[X(t)Y(t+\tau)\right] = \int_{-\infty}^{+\infty}\int_{-\infty}^{+\infty} x(t)y(t+\tau)p(x,t;y,t+\tau)\,\mathrm{d}x\,\mathrm{d}y \tag{4.8}$$

4.1.3 Power Spectral Density Function of Stationary Random Processes

A stationary random process, denoted as $X(t)$, is not absolutely integrable in a region of $t\in(-\infty,\infty)$. Therefore, a subsidiary function $\overline{X}_T(t)$ is defined

$$\overline{X}_T(t) = \begin{cases} X(t) & \text{when} \quad -T/2 \le t \le T/2 \\ 0 & \text{elsewhere} \end{cases} \tag{4.9}$$

Obviously, $\overline{X}_T(t)$ is absolutely integrable within $t\in(-\infty,\infty)$. Therefore, its Fourier's transformation can be executed by

$$X_T(\omega) = \frac{1}{2\pi}\int_{-\infty}^{\infty} \overline{X}_T(t)e^{-i\omega t}\,\mathrm{d}t \tag{4.10}$$

Let

$$S_{XX}(\omega) = \lim_{T\to\infty}\frac{1}{T}\left|X_T(\omega)\right|^2 \tag{4.11}$$

Equation 4.11 is the definition of the auto-power spectral density (PSD) function of $X(t)$.

Note that the repeated subscripts in R_{XX} or S_{XX} can be reduced by one, that is, they can be denoted as R_X or S_X. When $X(t)$ is a zero-mean stationary random process, its variance is

$$\sigma_X^2 = \int_{-\infty}^{\infty} S_{XX}(\omega)\mathrm{d}\omega \tag{4.12}$$

Wiener and Khintchine proved that for an arbitrary stationary random process $X(t)$, its auto-PSD $S_{XX}(\omega)$ and auto-correlation function $R_{XX}(\tau)$ are a Fourier transform pair, that is

$$S_{XX}(\omega) = \frac{1}{2\pi}\int_{-\infty}^{\infty} R_{XX}(\tau)e^{-i\omega\tau}\,\mathrm{d}\tau \tag{4.13}$$

$$R_{XX}(\tau) = \int_{-\infty}^{\infty} S_{XX}(\omega)e^{i\omega\tau}\,\mathrm{d}\omega \tag{4.14}$$

According to this theorem, if either of $S_{XX}(\omega)$ or $R_{XX}(\tau)$ is found, the other can be obtained immediately.

If stationary random processes $X(t)$ and $Y(t)$ are both ergodic, their cross-correlation functions can be computed in terms of their sample functions $X(t)$ and $Y(t)$:

$$R_{XY}(\tau) = \lim_{T\to\infty}\frac{1}{T}\int_{-\frac{T}{2}}^{\frac{T}{2}} x(t)y(t+\tau)\mathrm{d}t \tag{4.15}$$

$$R_{YX}(\tau) = \lim_{T\to\infty}\frac{1}{T}\int_{-\frac{T}{2}}^{\frac{T}{2}} y(t)x(t+\tau)\mathrm{d}t \tag{4.16}$$

and their cross-PSD functions can be defined by means of the Fourier transforms of the corresponding cross-correlation functions

$$S_{XY}(\omega) = \frac{1}{2\pi}\int_{-\infty}^{\infty} R_{XY}(\tau)e^{-i\omega\tau}\,\mathrm{d}\tau \tag{4.17}$$

$$S_{YX}(\omega)=\frac{1}{2\pi}\int_{-\infty}^{\infty}R_{YX}(\tau)e^{-i\omega\tau}\,d\tau \tag{4.18}$$

For more details, see Lin (1967).

4.1.4 Impulse Response Functions and Frequency Response Functions

For a single-degree of freedom (SDOF) system that is initially at rest, the equation of motion under a unit impulse $\delta(t)$ at time $t = 0$ is

$$\begin{cases} m\ddot{x}+c\dot{x}+kx=\delta(t) \\ x(0)=0;\dot{x}(0)=0 \end{cases} \tag{4.19}$$

$\delta(t)$ can be regarded as a constant force $1/\mu$ acting in a very short time interval μ, and it is also regarded as the Dirac delta function.

Using the impulse theorem, it can be shown that $m\Delta v = p\Delta t = \frac{1}{\mu}\mu = 1$. Hence, at time $t = \mu$, the equation of motion of the system is simply ($\mu \to 0$)

$$\begin{cases} m\ddot{x}+c\dot{x}+kx=0 \\ x(0)=0;\dot{x}(0)=1/m \end{cases} \tag{4.20}$$

Its solution, denoting $x(t) = h(t)$, can then be expressed as

$$h(t)=\begin{cases} \dfrac{1}{m\omega_\varepsilon}e^{-\varsigma\omega_0 t}\sin\omega_\varepsilon t & t\geq 0 \\ 0 & t<0 \end{cases} \tag{4.21}$$

where $\omega_0=\sqrt{k/m}$ and $\varsigma=c/(2m\omega_0)$ are the undamped natural frequency and damping factor of the system, respectively, and $\omega_\varepsilon=\omega_0\sqrt{1-\varsigma^2}$ is the damped natural frequency of the system.

The response to unit impulse, $h(t)$, is also called the impulse response function. For an arbitrary load $p(t)$ acting in time interval $[0,t]$, the overall response is

$$x(t)=\int_0^t p(\tau)h(t-\tau)\,d\tau \tag{4.22}$$

It can also be written as

$$x(t)=\int_{-\infty}^{\infty}p(\tau)h(t-\tau)\,d\tau \tag{4.23}$$

By introducing the change of variable $\theta = t-\tau$, an alternative version of the convolution integral is obtained as

$$x(t)=\int_{-\infty}^{\infty}p(t-\theta)h(\theta)\,d\theta \tag{4.24}$$

Equations 4.22 through 4.24 are commonly known as Duhamel's integral, or the convolution integral.

Consider a SDOF system subjected to a harmonic load $e^{i\omega t}$, its equation of motion is

$$m\ddot{x}+c\dot{x}+kx=e^{i\omega t} \tag{4.25}$$

Assume

$$x=H(\omega)e^{i\omega t} \tag{4.26}$$

Substituting Equation 4.26 with 4.25 gives

$$H(\omega)=\frac{1}{k-\omega^2 m+i\omega c} \tag{4.27}$$

$H(\omega)$ is known as the frequency response function. $h(t)$ and $H(\omega)$ are the Fourier transform pairs, that is

$$H(\omega)=\int_{-\infty}^{\infty} h(\theta)e^{-i\omega\theta}\,\mathrm{d}\theta \tag{4.28}$$

$$h(t)=\frac{1}{2\pi}\int_{-\infty}^{\infty} H(\omega)e^{i\omega t}\,\mathrm{d}\omega \tag{4.29}$$

4.1.5 Conventional Algorithm for Structural Stationary Random Responses

For a linear system subjected to a stationary random excitation, some basic formulae of the random response are given below.

Assume the n-dimensional excitation vector is $\mathbf{X}(t)=\{X_1(t),X_2(t),...,X_n(t)\}^T$, and its expected value $\mathbf{m}_X$, auto-correlation function matrix $\mathbf{R}_{XX}(\tau)$, and auto-PSD matrix $\mathbf{S}_{XX}(\omega)$ are known. $\mathbf{H}(\omega)$ and $\mathbf{h}(t)$ are the frequency response function matrix and the impulse response function matrix. Denote $\mathbf{Y}(t)=\{Y_1(t),Y_2(t),...,Y_m(t)\}^T$ as the m-dimensional random response vector.

The expected value vector of the response is given by

$$E[\mathbf{Y}(t)]=E\left[\int_{-\infty}^{\infty}\mathbf{h}(\theta)\boldsymbol{X}(t-\theta)\mathrm{d}\theta\right]=E[\boldsymbol{X}(t)]\int_{-\infty}^{\infty}\mathbf{h}(\theta)\mathrm{d}\theta \tag{4.30}$$

Equation 4.30 can be written as

$$\mathbf{m}_Y=\mathbf{H}(0)\,\mathbf{m}_X \tag{4.31}$$

Equation 4.31 shows that the expected value vector of the responses can be easily obtained from that of the excitations by using the traditional statics method.

The auto-correlation function matrix of the responses is given by

$$\mathbf{R}_{YY}(\tau)=\int_{-\infty}^{\infty}\mathbf{h}(\theta_1)\int_{-\infty}^{\infty}\mathbf{R}_{XX}(\tau+\theta_1-\theta_2)\,\mathbf{h}^T(\theta_2)\,\mathrm{d}\theta_1\mathrm{d}\theta_2 \tag{4.32}$$

The cross-correlation function matrices between the response and the excitation vectors are given by

$$\begin{aligned}\mathbf{R}_{XY}(\tau)&=E[\mathbf{X}(t)\boldsymbol{Y}^T(t+\tau)]=E\left[\mathbf{X}(t)\int_{-\infty}^{\infty}\mathbf{X}^T(t-\theta+\tau)\mathbf{h}^T(\theta)\mathrm{d}\theta\right]\\&=\int_{-\infty}^{\infty}\mathbf{R}_{XX}(\tau-\theta)\mathbf{h}^T(\theta)\mathrm{d}\theta\end{aligned} \tag{4.33}$$

$$\begin{aligned}\mathbf{R}_{YX}(\tau)&=E[\mathbf{Y}(t)\mathbf{X}^T(t+\tau)]=E\left[\int_{-\infty}^{\infty}\mathbf{h}(\theta)\mathbf{X}(t-\theta)\mathbf{X}^T(t+\tau)\mathrm{d}\theta\right]\\&=\int_{-\infty}^{\infty}\mathbf{h}(\theta)\mathbf{R}_{XX}(\tau+\theta)\mathrm{d}\theta\end{aligned} \tag{4.34}$$

The auto-PSD matrix of the response vectors is

$$\mathbf{S}_{YY}(\omega)=\int_{-\infty}^{\infty}\mathbf{R}_{YY}(\tau)e^{-i\omega\tau}\,\mathrm{d}\tau=\mathbf{H}^*\mathbf{S}_{XX}(\omega)\,\mathbf{H}^T \tag{4.35}$$

and the cross-PSD matrices between the input and the response vectors are

$$\mathbf{S}_{XY}(\omega) = \mathbf{S}_{XX}(\omega)\,\mathbf{H}^T \tag{4.36}$$

$$\mathbf{S}_{YX}(\omega) = \mathbf{H}^*\mathbf{S}_{XX}(\omega) \tag{4.37}$$

4.1.6 Basic Concepts of Nonstationary Random Vibration

Nonstationary random processes are generally short in duration. Their basic characteristic is that the statistical properties vary significantly with time. The process of a typical earthquake record is such an example, for which the medium flat segment is often regarded as a stationary random process in order to simplify the structural analysis. However, such simplification sometimes causes significant errors. For instance, some long-span bridges with fundamental periods of approximately 10–20 seconds are very flexible. The period of the strong earthquake portion of a typical earthquake record is only approximately 20–30 seconds. For such flexible long-span bridges, the seismic excitations exhibit evident nonstationary characteristics. In order to avoid computational complexities in the structural analyses, such excitations are usually assumed to be stationary random processes. It is shown in this chapter that the analysis of such nonstationary random responses has been made very simple by using the pseudo-excitation method (PEM).

Nonstationary random processes are not ergodic because their statistical properties vary with time. In earthquake engineering, the evolutionary random process defined by Priestley (1967) has been extensively investigated. It is expressed in terms of the Riemann–Stieltjes integration as follows:

$$F(t) = \int_{-\infty}^{\infty} A(\omega,t)\exp(i\omega t)\,\mathrm{d}\alpha(\omega) \tag{4.38}$$

in which $\alpha(\omega)$ satisfies the following relations

$$X(t) = \int_{-\infty}^{\infty} \exp(i\omega t)\,\mathrm{d}\alpha(\omega) \tag{4.39}$$

$$E\left[\mathrm{d}\alpha^*(\omega_1)\mathrm{d}\alpha(\omega_2)\right] = S_{XX}(\omega_1)\delta(\omega_2-\omega_1)\mathrm{d}\omega_1\mathrm{d}\omega_2 \tag{4.40}$$

Here $X(t)$ is a zero-mean stationary random process, with auto-PSD $S_{XX}(\omega)$; $A(\omega, t)$ a deterministic slowly varying nonuniform modulation function and; δ a Dirac function. The variance of $F(t)$ is

$$\sigma_F^2(t) = \int_{-\infty}^{\infty} S_{FF}(\omega)\,\mathrm{d}\omega = \int_{-\infty}^{\infty} |A(\omega,t)|^2\, S_{XX}(\omega)\,\mathrm{d}\omega \tag{4.41}$$

The PSD of $F(t)$

$$S_{FF}(\omega,t) = |A(\omega,t)|^2\, S_{XX}(\omega) \tag{4.42}$$

is known as an evolutionary power spectrum density function.

Responses of structures subjected to nonstationary random excitations expressed by Equation 4.38 are not easy to compute. Therefore, the nonuniform modulation assumption is often replaced by a uniform modulation assumption, that is the nonuniform modulation function $A(\omega,t)$ is replaced by a uniform modulation function $g(t)$. Thus, Equation 4.38 reduces to

$$F(t) = \int_{-\infty}^{\infty} g(t)\exp(i\omega t)\,\mathrm{d}\alpha(\omega) = g(t)X(t) \tag{4.43}$$

Equations 4.38 and 4.43 are known as the nonuniformly modulated and uniformly modulated evolutionary random processes, respectively.

4.2 Seismic Random Excitations

4.2.1 Spatial Variation of Seismic Ground Motions

The seismic ground motion is assumed to be a normal stationary random process. If a structure has N supports, their ground accelerations $\ddot{u}_i$ $(i=1,2,...,N)$ along the earthquake wave traveling direction can be written as the N dimensional vector

$$\ddot{\mathbf{u}}_b(t)=\left\{\ddot{u}_1(t)\ \ddot{u}_2(t)\cdots\ddot{u}_N(t)\right\}^T \tag{4.44}$$

where superscript T denotes transpose. The spatial variability of the ground motion is characterized by the cross-power spectral density function in the frequency domain. For ground accelerations $\ddot{u}_k(t)$ and $\ddot{u}_l(t)$ at the kth and lth supports this function can be written as

$$S_{kl}(\omega)=\rho_{kl}(\omega)\sqrt{S_{kk}(\omega)S_{ll}(\omega)} \tag{4.45}$$

where ω is the circular frequency; $S_{kk}(\omega)$, $S_{ll}(\omega)$, and $S_{kl}(\omega)$ are the auto-power spectral density functions of the accelerations at the kth and lth supports and their cross-power spectral density function, respectively; and $\rho_{kl}(\omega)$ is the coherency function of the accelerations at the kth and lth supports, which can be expressed as

$$\rho_{kl}(i\omega)=\left|\rho_{kl}(i\omega)\right|\exp\left[i\theta_{kl}(\omega)\right] \tag{4.46}$$

Its norm must satisfy the relation $\left|\rho_{kl}(i\omega)\right|\le 1$. The values of $S_{kk}(\omega)$ and $S_{ll}(\omega)$ in Equation 4.45 can be different because of the local effects. However, earthquake records show that the structural responses because of the difference between $S_{kk}(\omega)$ and $S_{ll}(\omega)$ are in general of relatively low significance. The factor $\exp\left[i\theta_{kl}(\omega)\right]$ expresses the wave passage effect, which can be further expressed as

$$\exp\left[i\theta_{kl}(\omega)\right]=\exp\left[-i\omega d_{kl}^L/v_{\text{app}}\right] \tag{4.47}$$

in which d_{kl}^L is the projection of d_{kl} (the horizontal distance between the two supports) along the propagation direction of the seismic waves and v_{app} is the apparent velocity of seismic waves along the surface. Assume that the time lags between the supports and the origin of the reference coordinate system are $T_1, T_2, \ldots, T_N$, respectively. Without losing generality, let $T_l \ge T_k$ (when $l>k$). Then $d_{kl}^L/v_{app}=T_l-T_k$, and so Equation 4.47 becomes

$$\exp\left[i\theta_{kl}(\omega)\right]=\exp\left[i\omega\left(T_k-T_l\right)\right] \tag{4.48}$$

The factor $\left|\rho_{kl}(i\omega)\right|$ reflects the incoherence effect (Der Kiureghian and Neuenhofer, 1992). A number of coherence models have been established based on practical earthquake records. A few of them are as follows:

1. Harichandran–Vanmarcke model

$$\left|\rho_{kl}\left(\omega,\mathrm{d}_{kl}\right)\right|=A\exp\left[-\frac{2\mathrm{d}}{\alpha\theta(\omega)}(1-A+\alpha A)\right]+(1-A)\exp\left[-\frac{2\mathrm{d}}{\alpha\theta(\omega)}(1-A+\alpha A)\right] \tag{4.49}$$

in which

$$\theta(\omega) = K\left[1 + \left(\omega/\omega_0\right)^b\right]^{-\frac{1}{2}} \tag{4.50}$$

According to the acceleration records of the SMART-1 array (Harichandran and Vanmarcke, 1986), the parameters in Equations 4.49 and 4.50 are: $A = 0.736$, $\alpha = 0.147$, $K = 5210$, $\omega_0 = 6.85$ rad/s, $b = 2.78$.

2. Loh–Yeh model

$$\left|\rho_{kl}(\omega, d_{kl})\right| = \exp\left[-\alpha\frac{\omega d_{kl}}{2\pi v_{\text{app}}}\right] \tag{4.51}$$

in which α is the wave number of the seismic waves. According to 40 selected acceleration records of the SMART-1 array (Loh and Yeh, 1988), $\alpha = 0.125$ is proposed. Parameters v_{app} and d_{kl} have been explained above.

3. Luco–Wong model

$$\left|\rho_{kl}\right| = \exp\left[-\left(\frac{\alpha\omega d_{kl}}{v_s}\right)^2\right] \tag{4.52}$$

in which α is the coherence factor, d d_{kl} the horizontal distance between the kth and lth supports, and v_s the shear wave velocity (Luco and Wong, 1986).

4. QWW model

Qu, Wang and Wang (1996) proposed the following model:

$$\left|\rho_{\text{kl}}\right| = \exp\left[-a(\omega)d_{\text{kl}}^{b(\omega)}\right] \tag{4.53}$$

in which

$$a(\omega) = a_1\omega^2 + a_2,\ b(\omega) = b_1\omega + b_2,\ b(\omega) = b_1\omega + b_2 \tag{4.54}$$

with $a_1 = 0.00001678$, $a_2 = 0.001219$, $b_1 = -0.0055$, and $b_2 = 0.7674$. This model was established based on the statistics of dozens of records from four closely located arrays with SMART-1 as the leading one. This model has given reasonable results in some applications in China.

Therefore, the PSD matrix of the ground acceleration vector $\ddot{\mathbf{u}}_b(t)$ for the N supports has the form

$$\mathbf{S}_{\ddot{u}_b\ddot{u}_b}(\omega) = \begin{bmatrix} |\rho_{11}|S_{11} & |\rho_{12}|e^{i\omega(T_1-T_2)}\sqrt{S_{11}S_{22}} & \cdots & |\rho_{1N}|e^{i\omega(T_1-T_N)}\sqrt{S_{11}S_{NN}} \\ |\rho_{21}|e^{i\omega(T_2-T_1)}\sqrt{S_{22}S_{11}} & |\rho_{22}|S_{22} & \cdots & |\rho_{2N}|e^{i\omega(T_2-T_N)}\sqrt{S_{22}S_{NN}} \\ \vdots & \vdots & \ddots & \vdots \\ |\rho_{N1}|e^{i\omega(T_N-T_1)}\sqrt{S_{NN}S_{11}} & |\rho_{N2}|e^{i\omega(T_N-T_2)}\sqrt{S_{NN}S_{22}} & \cdots & |\rho_{NN}|S_{NN} \end{bmatrix} \tag{4.55}$$

in which $S_{kk}(k = 1,2,\ldots, N)$ stands for $S_{kk}(\omega)$.

Obviously, this can be decomposed as

$$\mathbf{S}_{\ddot{u}_b\ddot{u}_b}(\omega) = \mathrm{B}^*\mathrm{JRJB} \tag{4.56}$$

in which * denotes complex conjugate, and

$$\mathbf{B} = \mathrm{diag}\left[\exp(-i\omega T_1), \exp(-i\omega T_2), \cdots, \exp(-i\omega T_N)\right] \tag{4.57}$$

$$\mathbf{J} = \mathrm{diag}\left[\sqrt{S_{11}}\ \sqrt{S_{22}}\ \cdots\ \sqrt{S_{NN}}\right] \tag{4.58}$$

$$\mathbf{R} = \begin{bmatrix} 1 & |\rho_{12}| & \cdots & |\rho_{1N}| \\ |\rho_{21}| & 1 & \cdots & |\rho_{2N}| \\ \cdots & \cdots & \cdots & \cdots \\ |\rho_{N1}| & |\rho_{N2}| & \cdots & 1 \end{bmatrix} \tag{4.59}$$

4.2.2 Generation of Ground Acceleration PSD Curves from Acceleration Response Spectrum Curves

In order to perform the seismic random vibration analysis for some important long-span bridges, the local seismic motion equivalent PSD (usually the acceleration PSD) must be established by geotechnical engineers. For standard bridges however, such seismic acceleration PSD can be derived from the site-specific acceleration response spectrum (ARS) curves. Two methods to perform the transformation are given in the following sections.

4.2.2.1 Kaul Method

Kaul (1978) proposed an approximate transformation method, which consists of the two equations

$$S(\omega_0) = \frac{4\xi R_a^2(\xi, \omega_0)}{\pi \omega_0 r^2} \tag{4.60}$$

$$r^2 = 2\ln\left[(-\frac{\pi}{\omega_0 T_s}\ln p)^{-1}\right] \tag{4.61}$$

in which $R_a(\xi, \omega_0)$ is the ARS curve of the seismic absolute acceleration when the damping ratio is ξ and the natural angular frequency is ω_0; usually ξ taken as 0.05; $S(\omega_0)$ the equivalent PSD curve corresponding to the given ARS curve; T_s is the seismic duration and; p the probability of the peaks that do not cross with the given positive or negative barriers—usually $p = 0.85$ is assumed. However, investigation has shown that $p = 0.5$ is better in most cases (see Figure 4.2) (Zhang et al., 2007).

4.2.2.2 Iteration Scheme

An iteration-based scheme for the transformation has been proposed (Sun and Jiang, 1990), which produces more accurate equivalent PSD curve than the Kaul method. For a given ARS curve $R_a(\xi, \omega_0)$, in order to transform it into an equivalent PSD curve $S(\omega)$, specify its initial values $S^0(\omega_i) = S_i$, for $i = 1,2,\ldots, N$. Then the standard deviation of the acceleration response for a SDOF system can be computed from

$$\sigma_0(\xi, \omega_0) = \left[\int_0^\infty S(\omega) \frac{1 + 4\xi^2(\omega/\omega_0)^2}{(1-(\omega/\omega_0)^2)^2 + 4\xi^2(\omega/\omega_0)^2} \mathrm{d}\omega\right]^{1/2} \tag{4.62}$$

The peak factor r is

$$r = \sqrt{2\ln(vT_s)} + 0.5772/\sqrt{2\ln(vT_s)} \tag{4.63}$$

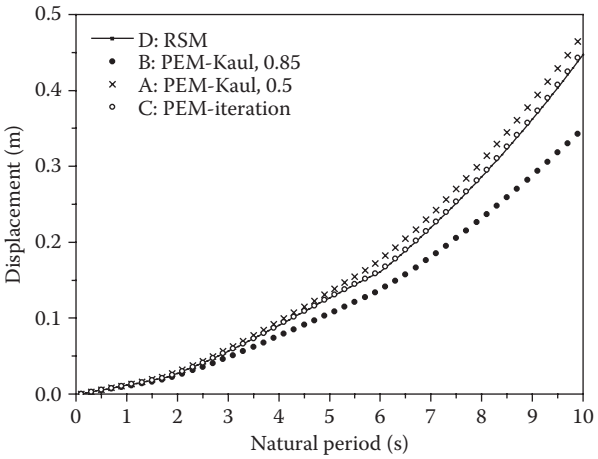

FIGURE 4.2 Displacements of SDOF systems computed by RSM and PEM.

in which T_s is the duration of the strong earthquake portion. The average zero-crossing rate is approximately $\nu = \sqrt{\lambda_2/\lambda_0}/\pi \approx \omega_0/\pi$.

The acceleration responses computed by means of Equations 4.62 and 4.63 are

$$A_m(\xi, \omega_0) = r\sigma_0(\xi, \omega_0) \tag{4.64}$$

The percentage errors between $R_a(\xi, \omega_0)$ and $A_m(\xi, \omega_0)$ can be computed from

$$E(\omega_0) = \frac{\left|R_a(\xi, \omega_0) - A_m(\xi, \omega_0)\right|}{R_a(\xi, \omega_0)} \times 100\% \tag{4.65}$$

Compute $E(\omega_0)$ for each frequency. If $E(\omega_0)$ is found to be greater than the given tolerance ε for at least one frequency, modify all PSD values according to the following equation:

$$S^{k+1}(\omega_i) = S^k(\omega_i) R_a^2(\xi, \omega_i) / A_m^2(\xi, \omega_i), \quad i = 1, 2, \cdots, N \tag{4.66}$$

and then repeat the computations of Equations 4.62 through 4.65. The above process is continued until Equation 4.65 is satisfied at all frequencies.

Figure 4.2 shows the displacement curves computed by the Kaul method (for $p = 0.50$ and 0.85), the iterative method and the standard response spectrum method (RSM) for a number of SDOF systems with their natural periods ranging over (0–10)s. These curves are labeled A, B, C, and D, respectively. Clearly, the curves C and D are extremely close to each other. The errors at all frequencies are <1.2%. Therefore the ground acceleration PSD curve calculated from the corresponding ARS curve based on the iterative method perfectly meets the requirements of the "Guidelines" (CMC, 2008). However the maximum differences of curve A and B from curve D are 10% and 19.1%, respectively. Therefore the Kaul method with $p = 0.5$ produces a better equivalent ground acceleration PSD curve than that with $p = 0.85$, which is already near the margin of the tolerance (20%). For five realistic bridges, four in China and one in the United States, their deck forces were computed based on the Chinese "Guidelines" (CMC, 2008) and the "CALTRANS Seismic Design Criteria"(Caltrans, 2010), respectively. When the equivalent ground acceleration PSD curve was calculated from Kaul ($p = 0.85$), the maximum difference of the beam internal forces based on the PEM and RSM is over 16%, whereas this was reduced to under 7% by

taking $p = 0.5$. This difference was further reduced to 4.5% when the iterative method was used in the determination of the equivalent ground acceleration PSD curve.

4.2.3 Seismic Equations of Motion of Long-Span Structures

For long-span structures subjected to differential ground motion, the equations of motion in the global coordinate system (assumed to be fixed to the center of the earth) can be written in partitioned form as

$$\begin{bmatrix} \mathbf{M}_s & \mathbf{M}_{sb} \\ \mathbf{M}_{sb}^T & \mathbf{M}_b \end{bmatrix} \begin{Bmatrix} \ddot{\mathbf{x}}_s \\ \ddot{\mathbf{x}}_b \end{Bmatrix} + \begin{bmatrix} \mathbf{C}_s & \mathbf{C}_{sb} \\ \mathbf{C}_{sb}^T & \mathbf{C}_b \end{bmatrix} \begin{Bmatrix} \dot{\mathbf{x}}_s \\ \dot{\mathbf{x}}_b \end{Bmatrix} + \begin{bmatrix} \mathbf{K}_s & \mathbf{K}_{sb} \\ \mathbf{K}_{sb}^T & \mathbf{K}_b \end{bmatrix} \begin{Bmatrix} \mathbf{x}_s \\ \mathbf{x}_b \end{Bmatrix} = \begin{Bmatrix} 0 \\ \mathbf{p}_b \end{Bmatrix} \tag{4.67}$$

in which the subscript m represents the master degrees of freedom, that is, the support displacements, whereas the subscript s represents the slave degrees of freedom. The absolute displacement vector $\mathbf{x}_s$ can be decomposed into the two parts

$$\mathbf{x}_s = \mathbf{y}_s + \mathbf{y}_r \tag{4.68}$$

where $\mathbf{y}_s$ is the quasi-static displacement vector (Clough and Penzien, 1993), which satisfies

$$\mathbf{y}_s = -\mathbf{K}_s^{-1}\mathbf{K}_{sb}\mathbf{x}_b \tag{4.69}$$

Substituting Equations 4.68 and 4.69 with 4.67 gives

$$\mathbf{M}_s\ddot{\mathbf{y}}_r + \mathbf{C}_s\dot{\mathbf{y}}_r + \mathbf{K}_s\mathbf{y}_r = \mathbf{M}_s\mathbf{K}_s^{-1}\mathbf{K}_{sb}\ddot{\mathbf{x}}_b + \left(\mathbf{C}_s\mathbf{K}_s^{-1}\mathbf{K}_{sb} - \mathbf{C}_{sb}\right)\dot{\mathbf{x}}_b \tag{4.70}$$

It should be pointed out that Equation 4.70 cannot be reduced to the conventional equation of motion when $\mathbf{x}_m$ represents uniform ground displacements (Clough and Penzien, 1993). This is because Equation 4.67 assumes the damping forces to be proportional to the absolute velocity vector $\left\{\dot{\mathbf{x}}_s^T, \dot{\mathbf{x}}_m^T\right\}^T$. In order to avoid this inconsistency, the damping forces should be assumed to be proportional to the relative velocity vector $\left\{\dot{\mathbf{y}}_r^T, 0\right\}^T$ in Equation 4.67. This leads to the equation

$$\mathbf{M}_s\ddot{\mathbf{y}}_r + \mathbf{C}_s\dot{\mathbf{y}}_r + \mathbf{K}_s\mathbf{y}_r = \mathbf{M}_s\mathbf{K}_s^{-1}\mathbf{K}_{sb}\ddot{\mathbf{x}}_b \tag{4.71}$$

4.2.4 Seismic Waves and Their Geometrical Expressions

Seismic waves or ground motions can be divided into body waves and surface waves. Body waves include the longitudinal waves (or pressure waves, primary waves or *P* waves) and the transverse waves (or shear waves, secondary waves or *S* waves). Surface waves include Rayleigh waves and Love waves. For *P* waves, the soil particles move parallel to the traveling direction of waves; for *S* waves, however, their motions are normal to the wave traveling direction (see Figure 4.3). For horizontal shear waves (SH waves), all particles move horizontally; for vertical shear waves (SV waves), all particles move vertically.

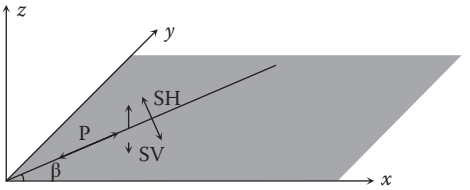

FIGURE 4.3 Particle motion directions for P and S waves.

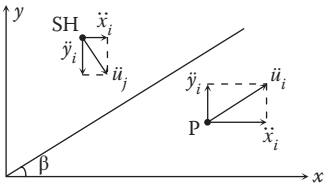

FIGURE 4.4 Transformation of ground acceleration components.

Assume that both the *x* and *y* axes lie in the horizontal plane. The angle between axis *x* and the horizontal traveling direction of these waves is β, as shown in Figures 4.3 and 4.4. Thus, the acceleration components along the coordinate axes can be expressed by the components parallel or normal to the wave traveling direction, that is for *P* waves

$$\ddot{x}_i = \ddot{u}_i \cos\beta, \ddot{y}_i = \ddot{u}_i \sin\beta, \ddot{z}_i = 0 \tag{4.72}$$

for SH waves

$$\ddot{x}_i = -\ddot{u}_j \sin\beta, \ddot{y}_i = \ddot{u}_j \cos\beta, \ddot{z}_i = 0 \tag{4.73}$$

and for SV waves

$$\ddot{x}_i = 0, \ddot{y}_i = 0, \ddot{z}_i = \ddot{u}_k \tag{4.74}$$

For a structure with *N* supports, the *m* dimensional ground acceleration vector in Equation 4.67 is

$$\ddot{\mathbf{x}}_b = \left\{\ddot{x}_1, \ddot{x}_2, \cdots, \ddot{x}_m\right\}^T \tag{4.75}$$

Thus the relation between $\ddot{\mathbf{x}}_b$ and $\ddot{\mathbf{u}}_b$ is

$$\ddot{\mathbf{x}}_b = \mathbf{E}_{mN}\ddot{\mathbf{u}}_b \tag{4.76}$$

in which $\mathbf{E}_{mN}$ is a $m \times N$ block-diagonal matrix

$$\mathbf{E}_{mN} = \text{diag}\left[\mathbf{e}_\beta, \mathbf{e}_\beta, ..., \mathbf{e}_\beta\right]_{m\times N} \tag{4.77}$$

If only three translations are considered for each support, then $m = 3N$ and each submatrix $\mathbf{e}_\beta$ would be $\begin{Bmatrix}\cos\beta\\ \sin\beta\\ 0\end{Bmatrix}$, $\begin{Bmatrix}-\sin\beta\\ \cos\beta\\ 0\end{Bmatrix}$ and $\begin{Bmatrix}0\\ 0\\ 1\end{Bmatrix}$ for the P, SH, and SV waves, respectively.

Using Equations 4.76, 4.69, and 4.71 can be rewritten as

$$\mathbf{y}_s = -\mathbf{K}_s^{-1}\mathbf{K}_{sb}\,\mathbf{E}_{mN}\mathbf{u}_b \tag{4.78}$$

$$\mathbf{M}_s\ddot{\mathbf{y}}_r + \mathbf{C}_s\dot{\mathbf{y}}_r + \mathbf{K}_s\mathbf{y}_r = \mathbf{M}_s\mathbf{K}_s^{-1}\mathbf{K}_{sb}\,\mathbf{E}_{mN}\ddot{\mathbf{u}}_b \tag{4.79}$$

4.2.5 Three Conventional Methods for Structural Seismic Analysis

4.2.5.1 Response Spectrum Method

The equations of motion of a linear multiple degrees of freedom (MDOF) structure subject to a ground acceleration excitation $\ddot{x}_g(t)$ can be written as

$$\mathbf{M}\ddot{\mathbf{y}} + \mathbf{C}\dot{\mathbf{y}} + \mathbf{K}\mathbf{y} = -\mathbf{M}\mathbf{e}\ddot{x}_g(t) \tag{4.80}$$

in which **M**, **C**, and *K* are the $n \times n$ mass, damping and stiffness matrices of the structure and **e** is the index vector of inertia forces. For short-span structures, all supports can be assumed to move uniformly with the same ground acceleration $\ddot{x}_g(t)$. If the structure under consideration has a very large number of degrees of freedom, Equation 4.80 can be solved by using the mode-superposition scheme. First, the lowest q natural angular frequencies ω_j ($j = 1, 2, \ldots, q$, $q<<n$) and the corresponding $n\times q$ mass normalized mode matrix Φ should be extracted. Second $\mathbf{y}(t)$ can be decomposed in terms of these modes

$$\mathbf{y}(t) = \Phi\mathbf{u}(t) = \sum_{j=1}^{q} u_j\varphi_j \tag{4.81}$$

With proportional damping assumed, Equation 4.80 can be decoupled into q SDOF equations

$$\ddot{u}_j + 2\varsigma_j\omega_j\dot{u}_j + \omega_j^2 u_j = -\gamma_j\ddot{x}_g(t) \tag{4.82}$$

in which ς_j is the *j*th damping ratio and γ_j is the *j*th modal participation factor

$$\gamma_j = \varphi_j^T\mathbf{M}\mathbf{e} \tag{4.83}$$

According to the response spectrum theory, the solution of Equation 4.82 is

$$u_j = \gamma_j\alpha_j g/\omega_j^2 \tag{4.84}$$

in which g is the gravity acceleration and α_j is the value of the ground acceleration response spectrum at frequency ω_j. If the kth element of y, denoted as y_k, is required, then the kth elements of all $\mathbf{y}_j$ ($j = 1,2,\ldots,q$) are taken to compose a vector $\mathbf{y}_k$, which is then used in the computation of the response (or demand) y_k

$$y_k = \sqrt{\mathbf{y}_k^T\mathbf{R}_c\,\mathbf{y}_k} \tag{4.85}$$

Here $\mathbf{R}_c$ is the correlation matrix representing the degree of correlation between all participating modes. Based on the white-noise assumption of random vibration theory, Wilson and Der Kiureghian (1981) have derived the expression for its elements as

$$R_{ij} = \frac{8\sqrt{\zeta_i\zeta_j}(\zeta_i + r\zeta_j)r^{3/2}}{(1-r^2)^2 + 4\zeta_i\zeta_j r(1+r^2) + 4(\zeta_i^2+\zeta_j^2)r^2} \tag{4.86}$$

in which $r = \omega_j/\omega_i$. Equation 4.86 is the widely used complete quadratic combination (CQC) algorithm in the RSM. If the correlation coefficients between all modes are neglected, that is if $R_{ij} = \delta_{ij}$ (Dirac function), then $\mathbf{R}_c$ becomes a unit matrix and Equation 4.85 reduces to the square root of the sum of squares (SRSS) algorithm.

The above RSM is very popular in the seismic analysis of short-span structures. Some extensions have been published (Dumanoglu and Severn, 1990; Berrah and Kausel, 1992; Der Kiureghian and Neuenhofer, 1992; Heredia-Zavoni and Vanmarcke, 1994) in order to deal with the seismic analysis of long-span structures. However, the efficiency and accuracy still need further improvement before they can be widely used in practical engineering.

4.2.5.2 Time History Method

It is still assumed that all supports move uniformly with the same acceleration $\ddot{x}_g(t)$, which is now given in a discrete numerical form. The equations of motion (Equation 4.80) can now be solved using the Newmark method or the Wilson-θ method (Bathe and Wilson, 1976). By means of such time history methods, the structural parameters can be modified at any time. Therefore, this method is good for nonlinear problems for which structural parameters may vary with time frequently, for example for seismic elasto-plastic analysis. A major disadvantage of time history methods is that the computational results rely heavily on the selected ground acceleration records. In general, a number of records must be selected for structural analyses, and statistical results are then used in the designs. In order to reduce the computational effort, usually only approximately 3–10 records are used for statistical purposes.

When the wave passage effect needs be taken into account, the same ground acceleration record is applied to different supports with time lags, and this generates $\ddot{\mathbf{x}}_b$ on the right-hand side of Equation 4.71. If the incoherence effect between the supports must also be considered, the process for generating $\ddot{\mathbf{x}}_b$ is rather complicated. In fact, real records like these are difficult to find.

4.2.5.3 Random Vibration Method (Traditional)

Let us begin with Equation 4.80, which also apply to structures subjected to uniform stationary random ground excitations. Now $\ddot{x}_g(t)$ is a zero-mean Gaussian stationary random process with a known auto-PSD $S_a(\omega)$, representing acceleration excitations uniformly applied to all supports of the structure. By means of the mode superposition scheme, that is Equations 4.81 through 4.83, the traditional CQC method can be established (Clough and Penzien, 1993).

$$\mathbf{S}_{yy}(\omega) = \sum_{j=1}^{q}\sum_{k=1}^{q} \gamma_j \gamma_k \varphi_j \varphi_k^T H_j^*(\omega) H_k(\omega) S_a(\omega) \tag{4.87}$$

in which φ_j and γ_j are the jth mode and modal participation factor, and

$$H_j = \left(\omega_j^2 - \omega^2 + 2i\varsigma_j \omega \omega_j\right)^{-1} \tag{4.88}$$

is the jth frequency response function. For a real long-span bridge, the numbers of ω and the degrees of freedom of its finite element model usually range from 10^3 to 10^4, and the number of q typically ranges from 10^2 to 10^3. Equation 4.87 includes all quadratic terms of the participating modes, and it must be repeatedly computed for hundreds or thousands of frequencies. Although it is the simplest form of excitation, the computational effort is still unacceptable. Therefore, in practical engineering, the following SRSS method, obtained by neglecting all $j \neq k$ terms in Equation 4.87, is generally used in place of the above CQC method, that is

$$\mathbf{S}_{yy}(\omega) = \sum_{j=1}^{q} \gamma_j^2 \varphi_j \varphi_j^T \left|H_j(\omega)\right|^2 S_a(\omega) \tag{4.89}$$

This is frequently recommended in academic publications. The SRSS formula is an approximation of Equation 4.87, which neglects the cross-correlation items between participating modes, thereby reducing the computational effort to approximately $1/q$ of that required by Equation 4.87. However, this approximation can be used only for lightly damped structures for which the participating frequencies must be sparsely spaced. For most structures (in particular their 3D structural models), there are always some closely spaced participating frequencies. Hence, the applicability of the SRSS approximation is rather questionable.

The above mentioned random vibration analysis is executed in terms of the power spectrum densities in the frequency domain and therefore it is also referred to as the power spectrum method.

A diagonal element $S_{\xi\xi}$ in the PSD matrix represents the auto-PSD of a random response ξ. Assume that this response is significant only within the frequency domain $\omega \in [\omega_L, \omega_U]$. Thus the ith spectral moment of ξ can be computed by

$$\lambda_i = 2\int_0^{\infty} \omega^i S_{\xi\xi}(\omega)\mathrm{d}\omega \approx 2\int_{\omega_L}^{\omega_U} \omega^i S_{\xi\xi}(\omega)\mathrm{d}\omega \tag{4.90}$$

The above PSD values at negative frequencies do not have intuitive physical significance and so the single-sided PSD $G_{xx}(\omega)$ is defined for application convenience as

$$G_{xx}(\omega) = \begin{cases} 2S_{xx}(\omega) & \omega \geq 0 \\ 0 & \omega < 0 \end{cases} \tag{4.91}$$

Thus Equation 4.90 becomes

$$\lambda_i = \int_0^{\infty} \omega^i G_{\xi\xi}(\omega)\mathrm{d}\omega \approx \int_{\omega_L}^{\omega_U} \omega^i G_{\xi\xi}(\omega)\mathrm{d}\omega \tag{4.92}$$

For general multiple input $\mathbf{x}(t) = \{x_1(t), x_2(t), ..., x_n(t)\}^T$ and multiple output $\mathbf{y}(t) = \{y_1(t), y_2(t), ..., y_m(t)\}^T$ problems, the response (i.e., output) PSD matrix $\mathbf{S}_{yy}(\omega)$ can be computed using the excitation (i.e., input) PSD matrix $\mathbf{S}_{xx}(\omega)$

$$\mathbf{S}_{yy}(\omega) = \mathbf{H}^* \mathbf{S}_{xx}(\omega)\mathbf{H}^T \tag{4.93}$$

in which H is the frequency response function matrix.

It is inconvenient for engineers to take such PSD and their spectral moments for practical designs. However, some approaches have been suggested to estimate structural responses (or demands) in terms of these spectral moments. The popular approach is as follows.

With seismic excitations assumed to be zero-mean stationary Gaussian processes, an arbitrary linear response of the structure subjected to such excitations, denoted $y(t)$, will also possess this probabilistic characteristic. It is also assumed that if a given barrier (threshold) a is sufficiently high, the peaks of $y(t)$ above this barrier will appear independently. Let $N(t)$ be the number of up-crossing a within the time interval $(0, t)$, then $N(t)$ will be a Poisson process with a stationary increment (Davenport, 1961). Denote the extreme value of $y(t)$ (i.e., the maximum value of all peaks by their absolute values) within the earthquake duration $[0, T_s]$ as y_e, and the standard deviation of $y(t)$ as σ_y. Define η as the dimensionless parameter of y_e, and ν as the mean zero-crossing rate, which can be expressed as

$$\eta = y_e/\sigma_y, \nu = \sqrt{\lambda_2/\lambda_0}/\pi \tag{4.94}$$

Based on the above assumptions, the probabilistic distribution of η can be derived as

$$P(\eta) = \exp\left[-\nu T_s \exp\left(-\eta^2/2\right)\right], \quad \eta > 0 \tag{4.95}$$

The expected value of η, known as the peak factor, is approximately

$$E[\eta] \approx (2\ln \nu T_s)^{1/2} + \gamma/(2\ln \nu T_s)^{1/2} \tag{4.96}$$

and its standard deviation is

$$\sigma_\eta \approx \pi/(12\ln \nu T_s)^{1/2} \tag{4.97}$$

in which $\gamma = 0.5772$ is the Euler constant, whereas the expected value of y_e is approximately

$$E[y_e] = E[\eta]\sigma_y \tag{4.98}$$

This quantity is the demand usually required by engineers.

4.2.5.4 Comparisons among the Three Seismic Analysis Methods

The RSM is the most popular method for the seismic analysis of short-span structures. Some extensions have been made to allow this method to be used in the aseismic analysis of long-span structures. However, the accuracy and efficiency still need further improvements for practical applications. The time history method can be used in the seismic analysis of long-span structures without theoretical difficulties. Its major disadvantages are that it requires a reasonable selection of the ground acceleration record samples and its tremendous computational cost. The random vibration method is appealing because of its statistical nature. Previously, the random vibration computation of complex structures was very costly. This issue has received extensive attention in the last two decades. The PEM, as will be described in Section 4.3, has remarkably improved this situation. Now, long-span structures with thousands of degrees of freedom and dozens of supports can be computed very quickly and accurately on personal computers.

4.3 Pseudo Excitation Method for Bridge Random Vibration Analysis

4.3.1 Bridges Subjected to Stationary Random Excitations

4.3.1.1 Single Stationary Random Excitations

The basic principle of PEM for structural stationary random vibration analysis can be explained by means of Figure 4.5.

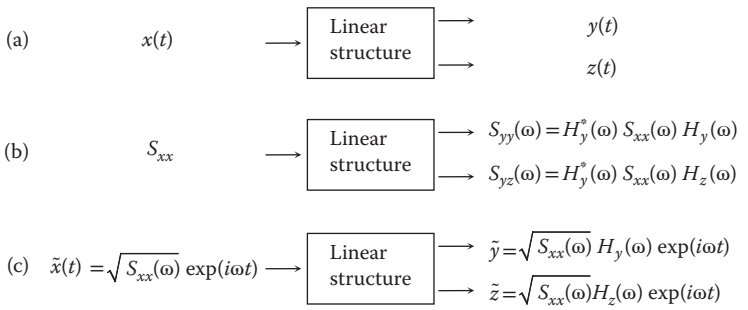

FIGURE 4.5 Basic principle of pseudo excitation method (stationary analysis).

Consider a linear system subjected to a zero-mean stationary random excitation $x(t)$ with a given PSD $S_{xx}(\omega)$ (see Figure 4.5a). Suppose for two arbitrarily selected responses $y(t)$ and $z(t)$, the auto-PSD $S_{yy}(\omega)$ and cross-PSD $S_{yz}(\omega)$ are desired. Figure 4.5b gives the conventional formulas for computing these PSD functions, where $H_y(\omega)$ and $H_z(\omega)$ are the frequency response functions, that is, if $x(t)$ is replaced by a sinusoidal excitation $exp(i\omega t)$, the harmonic responses of $y(t)$ and $z(t)$ will be $H_y(\omega)\exp(i\omega t)$ and $H_z(\omega)\exp(i\omega t)$, respectively. Thus, if $x(t)$ is replaced by a pseudo sinusoidal excitation

$$\tilde{x} = \sqrt{S_{xx}(\omega)}\exp(i\omega t) \tag{4.99}$$

where the symbol "~" represents the deterministic pseudo quantity, the pseudo responses of $y(t)$ and $z(t)$ would be $\tilde{y} = \sqrt{S_{xx}(\omega)}H_y(\omega)\exp(i\omega t)$ and $\tilde{z} = \sqrt{S_{xx}(\omega)}H_z(\omega)\exp(i\omega t)$ (see Figure 4.5c). It can be readily verified that

$$\begin{aligned}\tilde{y}^*\tilde{y} &= \sqrt{S_{xx}(\omega)}H_y^*(\omega)\exp(-i\omega t)\cdot\sqrt{S_{xx}(\omega)}H_y(\omega)\exp(i\omega t)\\ &= \left|H_y(\omega)\right|^2 S_{xx}(\omega) = S_{yy}(\omega)\end{aligned} \tag{4.100}$$

$$\begin{aligned}\tilde{y}^*\tilde{z} &= \sqrt{S_{xx}(\omega)}H_y^*(\omega)\exp(-i\omega t)\cdot\sqrt{S_{xx}(\omega)}H_z(\omega)\exp(i\omega t)\\ &= H_y^*(\omega)S_{xx}(\omega)H_z(\omega) = S_{yz}(\omega)\end{aligned} \tag{4.101}$$

If $\mathbf{y}(t)$ and $\mathbf{z}(t)$ are two arbitrarily selected random response vectors of the structure, and $\tilde{\mathbf{y}} = \mathbf{a}_y\exp(i\omega t)$ and $\tilde{\mathbf{z}} = \mathbf{a}_z\exp(i\omega t)$ are the corresponding harmonic response vectors because of the pseudo excitation (99), it can also be verified that the PSD matrices of $\mathbf{y}(t)$ and $\mathbf{z}(t)$ are

$$\mathbf{S}_{yy}(\omega) = \tilde{\mathbf{y}}^*\tilde{\mathbf{y}}^T = \mathbf{a}_y^*\mathbf{a}_y^T \tag{4.102}$$

$$\mathbf{S}_{yz}(\omega) = \tilde{\mathbf{y}}^*\tilde{\mathbf{z}}^T = \mathbf{a}_y^*\mathbf{a}_z^T \tag{4.103}$$

This means that the auto- and cross-PSD functions of two arbitrarily selected random responses can be computed using the corresponding pseudo harmonic responses.

4.3.1.2 Multiple Stationary Random Excitations

Consider a linear structure subjected to a number of stationary random excitations, which are denoted as an m dimensional stationary random process vector $\mathbf{x}(t)$ with known PSD matrix $\mathbf{S}_{xx}(\omega)$. It is a Hermitian matrix and so it can be decomposed, for example by using its eigenpairs φ_j and d_j ($j = 1, 2, \ldots, r$) into

$$\mathbf{S}_{xx}(\omega) = \sum_{j=1}^{r} d_j\varphi_j^*\varphi_j^T \quad (r \le m) \tag{4.104}$$

in which r is the rank of $\mathbf{S}_{xx}(\omega)$. Next, constitute r pseudo harmonic excitations

$$\tilde{\mathbf{x}}_j(t) = \sqrt{d_j}\varphi_j\exp(i\omega t) \quad (j = 1, 2, \cdots, r) \tag{4.105}$$

By applying each of these pseudo harmonic excitations, two arbitrarily selected response vectors $\mathbf{y}_j(t)$ and $\mathbf{z}_j(t)$ of the structure, which can be displacements, internal forces or other linear responses, may be easily obtained and expressed as

$$\tilde{\mathbf{y}}_j(t) = \mathbf{a}_{yj}(\omega)\exp(i\omega t) \tag{4.106}$$

$$\tilde{\mathbf{z}}_j(t) = \mathbf{a}_{zj}(\omega)\exp(i\omega t) \tag{4.107}$$

The corresponding PSD matrices can be computed by means of the following formulas:

$$\mathbf{S}_{yy}(\omega) = \sum_{j=1}^{r} \tilde{\mathbf{y}}_j^*(t)\tilde{\mathbf{y}}_j^T(t) = \sum_{j=1}^{r} \mathbf{a}_{yj}^*(\omega)\mathbf{a}_{yj}^T(\omega) \tag{4.108}$$

$$\mathbf{S}_{yz}(\omega) = \sum_{j=1}^{r} \tilde{\mathbf{y}}_j^*(t)\tilde{\mathbf{z}}_j^T(t) = \sum_{j=1}^{r} \mathbf{a}_{yj}^*(\omega)\mathbf{a}_{zj}^T(\omega) \tag{4.109}$$

In order to prove Equations 4.108 and 4.109, note that

$$\tilde{\mathbf{y}}_j = \mathbf{H}_y\tilde{\mathbf{x}}_j, \tilde{\mathbf{z}}_j = \mathbf{H}_z\tilde{\mathbf{x}}_j \tag{4.110}$$

Therefore

$$\sum_{j=1}^{r} \tilde{\mathbf{y}}_j^*\tilde{\mathbf{z}}_j^T = \sum_{j=1}^{r} \mathbf{H}_y^*\ \tilde{\mathbf{x}}_j^* \cdot \tilde{\mathbf{x}}_j^T\mathbf{H}_z^T = \mathbf{H}_y^* \sum_{j=1}^{r} \left(\tilde{\mathbf{x}}_j^* \cdot \tilde{\mathbf{x}}_j^T\right)\mathbf{H}_z^T = \mathbf{H}_y^*\mathbf{S}_{xx}(\omega)\mathbf{H}_z^T = S_{yz}(\omega) \tag{4.111}$$

Thus Equation 4.109. Equation 4.108 can be similarly proved.

The way to decompose $\mathbf{S}_{xx}(\omega)$ into the form of Equation 4.104 is not unique. In fact, the complex Cholesky scheme is perhaps the most efficient and convenient way to do it, that is $\mathbf{S}_{xx}(\omega)$ is decomposed into

$$\mathbf{S}_{xx}(\omega) = \mathbf{L}^*\mathbf{D}\mathbf{L}^T = \sum_{j=1}^{r} \mathrm{d}_j\mathbf{l}_j^*\mathbf{l}_j^T \quad (r \le m) \tag{4.112}$$

in which L is a lower triangular matrix with all its diagonal elements equal to unity and $\boldsymbol{D}$ is a real diagonal matrix with r nonzero diagonal elements d_j.

In general $\mathbf{S}_{\ddot{u}_b\ddot{u}_b}(\omega)$ in Equation 4.55 is a nonnegative definite Hermitian matrix, whereas R is a nonnegative definite real symmetric matrix that can be decomposed into the product of a real lower triangle matrix Q and its transposition

$$\mathbf{R} = \mathbf{Q}\mathbf{Q}^T \tag{4.113}$$

Thus Equation 4.55 can be written as

$$\mathbf{S}_{\ddot{u}_b\ddot{u}_b}(\omega) = \mathbf{P}^*\mathbf{P}^T \tag{4.114}$$

in which

$$\mathbf{P} = \mathbf{B}\mathbf{J}\mathbf{Q} \tag{4.115}$$

If all ground joints have equal $S_{kk}(k = 1,2,\ldots, N)$, denoted as S_0, then Equation 4.115 becomes

$$\mathbf{P} = S_0\mathbf{J}\mathbf{Q} \tag{4.116}$$

In order to solve Equation 4.79, the random ground acceleration $\ddot{\mathbf{u}}_b$ on its right hand side should be replaced by the pseudo ground acceleration

$$\ddot{\tilde{\mathbf{U}}} = \mathbf{P}e^{i\omega t} \tag{4.117}$$

Then Equation 4.79 is transformed into a deterministic harmonic equation

$$\mathbf{M}_s\ddot{\tilde{\mathbf{Y}}}_r+\mathbf{C}_s\dot{\tilde{\mathbf{Y}}}_r+\mathbf{K}_s\tilde{\mathbf{Y}}_r=\mathbf{M}_s\mathbf{K}_s^{-1}\mathbf{K}_{sb}\,\mathbf{E}_{mN}\mathbf{P}e^{i\omega t} \tag{4.118}$$

Solving Equation 4.118 gives the pseudo relative dynamic displacement $\tilde{\mathbf{Y}}_r$, whereas the pseudo quasi-static displacement $\tilde{\mathbf{Y}}_s$ can be obtained from Equations 4.78 and 4.117 as

$$\tilde{\mathbf{Y}}_s=-\frac{1}{\omega^2}\mathbf{K}_s^{-1}\mathbf{K}_{sb}\,\mathbf{E}_{mN}\mathbf{P}e^{i\omega t} \tag{4.119}$$

Thus, the pseudo absolute displacement can be obtained from

$$\tilde{\mathbf{X}}_s=\tilde{\mathbf{Y}}_s+\tilde{\mathbf{Y}}_r \tag{4.120}$$

If necessary, an arbitrarily selected pseudo internal force matrix $\tilde{\mathbf{N}}_s$ can be computed from $\tilde{\mathbf{X}}_s$ in terms of the standard FEM, and the corresponding internal force PSD matrix is

$$\mathbf{S}_{N_sN_s}(\omega)=\tilde{\mathbf{N}}_s^*\tilde{\mathbf{N}}_s^T \tag{4.121}$$

Provided only the wave passage effect is under consideration, then all $\left|\rho_{ij}\right|=1$ in Equation 4.55 and $S_{11}=S_{22}=\cdots=S_{NN}$, denoted as S_0. Thus matrix P in Equation 4.115 reduces to a vector

$$\mathbf{P}=\sqrt{S_0}\,\mathbf{e} \tag{4.122}$$

in which e is a complex vector

$$\mathbf{e}=\left\{e^{-i\omega T_1}\quad e^{-i\omega T_2}\quad\cdots\quad e^{-i\omega T_N}\right\}^T \tag{4.123}$$

Therefore, Equation 4.79 reduces to

$$\mathbf{M}_s\ddot{\tilde{\mathbf{Y}}}_r+\mathbf{C}_s\dot{\tilde{\mathbf{Y}}}_r+\mathbf{K}_s\tilde{\mathbf{Y}}_r=\mathbf{M}_s\mathbf{K}_s^{-1}\mathbf{K}_{sb}\,\mathbf{E}_{mN}\mathbf{e}\sqrt{S_0}e^{i\omega t} \tag{4.124}$$

Provided that the structure is subjected to uniform ground excitations, Equation 4.115 can be further reduced to

$$\mathbf{P}=\sqrt{S_0}\,\mathbf{I}_0 \tag{4.125}$$

in which $\mathbf{I}_0$ is a vector with all elements being unity.

4.3.2 Bridges Subjected to Nonstationary Random Excitations

A typical strong motion earthquake record includes three stages. In the first stage, the intensity of the ground motion increases, which mainly reflects the motion of *P* waves. The intensity of the ground motion remains the strongest in the second stage, which mainly reflects the motion of *S* waves. The ground motion will die down in the last stage. Such a complete seismic motion is usually regarded as a nonstationary random process. If the nonstationary property is assumed to takes place only for the intensity of the motion, this random process is regarded as a uniformly modulated evolutionary random process. However, if the shape of the ground motion PSD curve also varies with time, in other words, the intensity and the distribution with frequency of the ground motion energy both depend on time; the ground motion is regarded as a nonuniformly modulated evolutionary random process. It is usually accepted that when the intensity of the seismic motion in the second stage appears quite stationary, and in the meanwhile, the time interval of this stage is much longer (say, three times

or over) than the basic period of the structure under consideration, a simplified, stationary-based random analysis may be acceptable as a replacement of the nonstationary analysis. As a matter of fact, the basic periods of many long-span bridges range from 10 to 20 seconds, and the stationary portion of a typical strong earthquake is usually <1 minute, being only 20–30 seconds in most cases. Therefore, nonstationary analyses are appropriate for such problems. Previously, such nonstationary random analyses have been considered very difficult. However, by using the pseudo excitation method combined with the precise integration method, such analyses have become rather easy.

Some popular uniform modulation functions are listed below:

$$g(t)=\begin{cases} I_0\left(t/t_1\right)^2 & 0\le t\le t_1 \\ I_0 & t_1\le t\le t_2 \\ I_0\exp\left\{c\left(t-t_2\right)\right\} & t\ge t_2 \end{cases} \tag{4.126}$$

$$g(t)=\begin{cases} 1 & t\ge 0 \\ 0 & t<0 \end{cases} \tag{4.127}$$

$$g(t)=a\left[\exp\left(-\alpha_1 t\right)-\exp\left(-\alpha_2 t\right)\right],\ 0\le\alpha_1<\alpha_2 \tag{4.128}$$

$$g(t)=\sin\beta t \tag{4.129}$$

Nonuniform modulation models have rarely been investigated. Lin et al. (1997) suggested a nonuniform modulation model as follows:

$$A(\omega,t)=\beta(\omega,t)g(t)=\exp\left(-\eta_0\frac{\omega t}{\omega_\alpha t_\alpha}\right)g(t) \tag{4.130}$$

in which $g(t)$ is an amplitude modulation function; $\beta(\omega, t)$ a frequency modulation function and; ω_α and t_α are the referential frequency and time that are introduced to transform ω and t into dimensionless parameters. In principle ω_α and t_α can be arbitrarily selected. Once they have been selected, the factor $\eta_0(\eta_0>0)$ can been accordingly adjusted to make the high-frequency components of the nonstationary random process decay more quickly than the low-frequency components, and thus simulate the seismic motion more reasonably. When $\eta_0=0$, that is $\beta(\omega,t)=1$, $A(\omega,t)$ reduces to the uniform modulation function $g(t)$.

For nonuniformly modulated multi-excitation problems, the pseudo excitation for the corresponding stationary problems, that is Equation 4.117, is extended to (Lin and Zhang, 2005)

$$\ddot{\mathbf{U}}(\omega,t)=\mathbf{A}(\omega,t)\mathbf{P}e^{i\omega t} \tag{4.131}$$

in which the kth diagonal element of the $N\times N$ diagonal matrix $\mathbf{A}(\omega,t)$ is the modulation function $A_k(\omega,t)$ of the excitation that is applied to the kth support of the structure. In the case of uniformly modulated excitations, it is only necessary to replace all the nonuniform modulation functions $A_k(\omega,t)$ by the uniform modulation functions $g_k(t)$. Other formulas remain entirely unchanged. The $N\times r$ matrix P can be generated by means of Equations 4.114 and 4.115. Each column of $\ddot{\mathbf{U}}(\omega,t)$ can be regarded as a deterministic acceleration excitation vector. By substituting it into the right-hand side of Equation 4.118 and solving the equations of motion, a column of the matrix $\tilde{\mathbf{Y}}_r(\omega,t)$ can be produced.

Because $A_j(\omega,t)$ is a time-dependant slowly varying function, the pseudo ground displacement matrix can be computed approximately from

$$\tilde{\mathbf{U}}(\omega,t) = -\frac{1}{\omega^2}\ddot{\tilde{\mathbf{U}}}(\omega,t) \tag{4.132}$$

The pseudo quasi-static displacement matrix $\tilde{\mathbf{Y}}_s(\omega,t)$ can then be computed from Equation 4.93. Then the PSD matrix of the absolute displacement vector $\mathbf{X}_s(\omega,t)$ is

$$\mathbf{S}_{X_s X_s}(\omega,t) = \left(\tilde{\mathbf{Y}}_r(\omega,t) + \tilde{\mathbf{Y}}_s(\omega,t)\right)^* \left(\tilde{\mathbf{Y}}_r(\omega,t) + \tilde{\mathbf{Y}}_s(\omega,t)\right)^T \tag{4.133}$$

If a group of pseudo internal forces, denoted as $\mathbf{N}_e$, has been computed, the PSD matrix of the corresponding internal forces $\mathbf{N}_e$ can be computed from

$$\mathbf{S}_{N_e N_e}(\omega,t) = \mathbf{N}_e^* \mathbf{N}_e^T \tag{4.134}$$

When the ground acceleration PSD matrix is known, the corresponding pseudo acceleration vector $\ddot{\tilde{\mathbf{u}}}_b$ is easy to generate according to Equations 4.114 through 4.117. If instead, the ground displacement PSD matrix or velocity PSD matrix is known, then the acceleration PSD matrix can be obtained by multiplying the displacement or velocity PSD matrices by ω^4 or ω^2, respectively.

The evaluation of the peak amplitude responses of structures subjected to nonstationary seismic excitations has also received much attention (Shrikhande and Gupta, 1997; Zhao and Liu, 2001). Previously, only very simple structures could be computed. By using the PEM, complicated structures can be dealt with, as is briefly described at the end of this section.

In order to evaluate the expected extreme value responses of a structure subjected to nonstationary Gaussian excitations, the duration for which the intensity of the excitation peaks exceeds 50% of the maximum peak intensity, denoted by $[t_0, t_0 + \tau]$, is taken as the equivalent stationary duration in order to use Equations 4.94 through 4.98 to evaluate the desired expected extreme values. Provided that the time-dependant PSD of any arbitrary response $y(t)$, that is $S_{yy}(\omega,t)$, has been computed over that equivalent duration using the PEM, then the equivalent stationary PSD over that duration is

$$S'_{yy}(\omega) = \frac{1}{\tau}\int_{t_0}^{t_0+\tau} S_{yy}(\omega,t)\,\mathrm{d}t \tag{4.135}$$

To compute the extreme value responses based on Equation 4.126, the parameters t_0 and τ are

$$t_0 = t_1/\sqrt{2},\ \tau = t_2 + \ln 2/c - t_1/\sqrt{2} \tag{4.136}$$

Thus the equivalent stationary random responses are obtained, and the following processing can still use Equations 4.94 through 4.98.

4.3.3 Precise Integration Method

The precise integration method proposed by (Zhong, 1993) is a highly accurate and efficient direct integration method. So far, it has been extensively developed in many fields because of its powerful functions and superior adoptability. Its use in combination with PEM is very successful, and will be briefly introduced here.

The equation of motion of an n-degree-of-freedom system can be written as

$$\mathbf{M}\ddot{\mathbf{y}} + \mathbf{c}\dot{\mathbf{y}} + \mathbf{K}\mathbf{y} = \mathbf{f}(t) \tag{4.137}$$

in which $\mathbf{f}(t)$ is the given external force vector and M, C, and K are assumed to be time invariant $n \times n$ matrices. The initial displacement y and the initial velocity $\dot{\mathbf{y}}$ of the system are both null. The equation of motion (4.137) combined with the identity $\dot{\mathbf{y}} = \dot{\mathbf{y}}$ leads to the first-order equations of motion in the state space being

$$\dot{\mathbf{v}} = \mathbf{H}\mathbf{v} + \mathbf{r}(t) \tag{4.138}$$

in which

$$\mathbf{H} = \begin{bmatrix} \mathbf{0} & \mathbf{I} \\ \mathbf{B} & \mathbf{D} \end{bmatrix}, \quad \mathbf{v} = \begin{Bmatrix} \mathbf{y} \\ \dot{\mathbf{y}} \end{Bmatrix}, \quad \mathbf{r} = \begin{Bmatrix} \mathbf{0} \\ \mathbf{M}^{-1}\mathbf{f} \end{Bmatrix} \tag{4.139}$$
$$\mathbf{B} = -\mathbf{M}^{-1}\mathbf{K}, \quad \mathbf{D} = -\mathbf{M}^{-1}\mathbf{C}$$

The homogenous solution of Equation 4.138 is

$$\mathbf{v}_h(t) = \mathbf{T}(\tau)\mathbf{c} \tag{4.140}$$

in which

$$\mathbf{T}(\tau) = \exp(\mathbf{H}\tau) \tag{4.141}$$

Consider the current integration interval $t \in [t_k, t_{k+1}]$, $\tau = t - t_k$. When $\tau = 0$ or $t = t_k$, $\mathbf{T}(\tau) = \mathbf{I}$ and therefore c is a constant vector. If the particular solution to Equation 4.138, $\mathbf{v}_p(t)$, is temporarily assumed to have been found, then the general solution of Equation 4.138 is

$$v(t) = \mathbf{T}(\tau)\left(\mathbf{v}(t_k) - \mathbf{v}_p(t_k)\right) + \mathbf{v}_p(t) \tag{4.142}$$

Now, let $\tau = t_{k+1} - t_k$, which represents a full step size. In order to compute $\mathbf{T}(\tau)$ accurately, it is desirable to subdivide the step τ into $m = 2^N$ equal intervals, that is

$$\Delta t = \tau / m = 2^{-N}\tau \tag{4.143}$$

For application purposes, the use of $N = 20$ is sufficient, because it leads to $\Delta t \approx 10^{-6}\tau$. Such a small Δt is in general much less than the highest natural period of any practical discretized system.

Using a Taylor expansion

$$\exp(\mathbf{H} \times \Delta t) \approx \mathbf{I} + \mathbf{T}_{a0} \tag{4.144}$$

in which

$$\mathbf{T}_{a0} = (\mathbf{H} \times \Delta t) + (\mathbf{H} \times \Delta t)^2/2! + (\mathbf{H} \times \Delta t)^3/3! + (\mathbf{H} \times \Delta t)^4/4! \tag{4.145}$$

Substituting Equation 4.144 with Equation 4.141 gives

$$T(\tau) = \left(\exp(\mathbf{H} \times \Delta t)\right)^m = \left(\mathbf{I} + \mathbf{T}_{a0}\right)^m \tag{4.146}$$

Note that

$$\mathbf{I} + \mathbf{T}_{ai} = \left(\mathbf{I} + \mathbf{T}_{a,i-1}\right)^2 = \left(\mathbf{I} + 2 \times \mathbf{T}_{a,i-1} + \mathbf{T}_{a,i-1} \times \mathbf{T}_{a,i-1}\right), \quad (i = 1, 2, \cdots, N) \tag{4.147}$$

so that clearly

$$\mathbf{I} + \mathbf{T}_{aN} = \left(\mathbf{I} + \mathbf{T}_{a,N-1}\right)^2 = \left(\mathbf{I} + \mathbf{T}_{a,N-2}\right)^4 = \cdots = \left(\mathbf{I} + \mathbf{T}_{a0}\right)^m = \mathbf{T}(\tau) \tag{4.148}$$

Equations 4.147 and 4.148 suggest the following computing strategy. In order to avoid the loss of significant digits in the matrix $\mathbf{T}(\tau)$, it is necessary to compute $\mathbf{T}_{a1}$ directly from $\mathbf{T}_{a0}$, $\mathbf{T}_{a2}$ directly from $\mathbf{T}_{a1}$, and so on, by using

$$\mathbf{T}_{ai} = 2\times\mathbf{T}_{a,i-1}+\mathbf{T}_{a,i-1}\times\mathbf{T}_{a,i-1} \qquad (i=1,2,...,N) \tag{4.149}$$

Then $\mathbf{T}(\tau)$ should be computed from

$$\mathbf{T}(\tau) \approx \mathbf{I} + \mathbf{T}_{aN} \tag{4.150}$$

In Equation 4.150, the approximation is caused by the truncation of the Taylor expansion of Equation 4.145. It is generally negligibly small because when $N = 20$, the first term ignored by the truncation is of the order $O(\Delta t^5) = 10^{-30} O(\tau^5)$, which is of the order of the round-off errors of ordinary computers. In Equation 4.142, $\mathbf{v}_p(t)$ can be found analytically for some widely used loading forms, as following (Lin et al., 1995; Zhong and Williams, 1995).

4.3.3.1 Linear Loading (HPD-L Form)

Assume that the loading varies linearly within the time step $[t_k, t_{k+1}]$, that is

$$\mathbf{r} = \mathbf{r}_0 + \mathbf{r}_1 \times (t - t_0) \tag{4.151}$$

in which $\{r_0\}$ and $\{r_1\}$ are time invariant vectors. The particular solution of Equation 4.138 is then

$$\mathbf{v}_p(t) = \left(\mathbf{H}^{-1} + \mathbf{I}t\right)\left(-\mathbf{H}^{-1}\mathbf{r}_1\right) - \mathbf{H}^{-1}\left(\mathbf{r}_0 - \mathbf{r}_1 t_k\right) \tag{4.152}$$

Substituting Equation 4.151 with Equation 4.142 gives the HPD-L (high precision direct integration—linear) formula

$$\mathbf{v}(t_{k+1}) = T(\tau)\left(\mathbf{v}(t_k) + \mathbf{H}^{-1}\left(\mathbf{r}_0 + \mathbf{H}^{-1}\mathbf{r}_1\right)\right) - \mathbf{H}^{-1}(\mathbf{r}_0 + \mathbf{H}^{-1}\mathbf{r}_1 + \mathbf{r}_1\tau) \tag{4.153}$$

The time interval is $\tau = t_{k+1} - t_k$

4.3.3.2 Sinusoidal Loading (HPD-S Form)

If the applied loading is sinusoidal within the time region $t \in [t_k, t_{k+1}]$, then

$$\mathbf{r}(t) = \mathbf{r}_1 \sin\omega t + \mathbf{r}_2 \cos\omega t \tag{4.154}$$

in which $\mathbf{r}_1$ and $\mathbf{r}_2$ are time invariant vectors. Substituting Equation 4.154 with Equation 4.138 enables the particular solution to be obtained as

$$\mathbf{v}_p(t) = \mathbf{v}_1 \sin\omega t + \mathbf{v}_2 \cos\omega t \tag{4.155}$$

in which

$$\begin{aligned} \mathbf{v}_1 &= \left(\omega\mathbf{I} + \mathbf{H}^2/\omega\right)^{-1}\left(\mathbf{r}_2 - \mathbf{H}\mathbf{r}_1/\omega\right) \\ \mathbf{v}_2 &= \left(\omega\mathbf{I} + \mathbf{H}^2/\omega\right)^{-1}\left(-\mathbf{r}_1 - \mathbf{H}\mathbf{r}_2/\omega\right) \end{aligned} \tag{4.156}$$

Substituting Equation 4.155 into Equation 4.142 gives the general solution of Equation 4.138, that is the HPD-S direct integration formula

$$\mathbf{v}_p(t_{k+1}) = \mathbf{T}(\tau)\left(\mathbf{v}(t_k) - \mathbf{v}_1 \sin\omega t_k - \mathbf{v}_2 \cos\omega t_k\right) + \mathbf{v}_1 \sin\omega t_{k+1} + \mathbf{v}_2 \cos\omega t_{k+1} \tag{4.157}$$

The time interval $\tau = t_{k+1} - t_k$ can cover an arbitrary segment, or even many periods, of a sinusoidal wave because, no matter how large the step size may be, exact responses will be obtained provided the matrix $\mathbf{T}(\tau)$ has been generated accurately, without any instability occurring.

4.3.3.3 Polynomial-Modulated Sinusoidal Loading (HPD-P Form)

If the applied loading is polynomial-modulated sinusoidal within the time region $t \in [t_k, t_{k+1}]$

$$\mathbf{r}(t) = \left(\mathbf{r}_0 + \mathbf{r}_1 t + \mathbf{r}_2 t^2\right)\left(\alpha \sin\omega t + \beta \cos\omega t\right) \tag{4.158}$$

in which $\mathbf{r}_0$, $\mathbf{r}_1$, and $\mathbf{r}_2$ are time invariant vectors and α and β are given constants, then the particular solution of Equation 4.138 is

$$\mathbf{v}_p(t) = \left(\mathbf{a}_0 + \mathbf{a}_1 t + \mathbf{a}_2 t^2\right)\sin\omega t + \left(\mathbf{b}_0 + \mathbf{b}_1 t + \mathbf{b}_2 t^2\right)\cos\omega t \tag{4.159}$$

in which

$$\begin{aligned} \mathbf{a}_i &= \left(\mathbf{H}^2 + \omega^2 \mathbf{I}\right)^{-1}\left(-\mathbf{H}\mathbf{P}_{ia} + \omega \mathbf{P}_{ib}\right) \\ \mathbf{b}_i &= \left(\mathbf{H}^2 + \omega^2 \mathbf{I}\right)^{-1}\left(-\mathbf{H}\mathbf{P}_{ib} - \omega \mathbf{P}_{ia}\right) \left(i = 2,1,0\right) \end{aligned} \tag{4.160}$$

and

$$\begin{aligned} \mathbf{P}_{2a} &= \alpha \mathbf{r}_2 & \mathbf{P}_{2b} &= \beta \mathbf{r}_2 \\ \mathbf{P}_{1a} &= \alpha \mathbf{r}_1 - 2\mathbf{a}_2 & \mathbf{P}_{1b} &= \beta \mathbf{r}_1 - 2\mathbf{b}_2 \quad (i = 2,1,0) \\ \mathbf{P}_{0a} &= \alpha \mathbf{r}_0 - \mathbf{a}_1 & \mathbf{P}_{0b} &= \beta \mathbf{r}_0 - \mathbf{b}_1 \end{aligned} \tag{4.161}$$

4.3.3.4 Exponentially Decaying Sinusoidal Loading (HPD-E Form)

Suppose that the applied loading varies according to the following exponentially decaying sinusoidal law within the time region $t \in [t_k, t_{k+1}]$

$$\mathbf{r}(t) = \exp(\alpha t)\left(\mathbf{r}_1 \sin\omega t + \mathbf{r}_2 \cos\omega t\right) \tag{4.162}$$

in which $\mathbf{r}_1$ and $\mathbf{r}_2$ are time invariant vectors. Substituting Equation 4.162 into Equation 4.138 enables the particular solution to be obtained as

$$v_p(t) = \exp(\alpha t)\left(\boldsymbol{\nu}_1 \sin\omega t + \boldsymbol{\nu}_2 \cos\omega t\right) \tag{4.163}$$

in which

$$\begin{aligned} \mathbf{v}_1 &= \left[\left(\alpha \mathbf{I} - \mathbf{H}^2\right) + \omega^2 \mathbf{I}\right]^{-1}\left[\left(\alpha \mathbf{I} - \mathbf{H}\right)\mathbf{r}_1 + \omega \mathbf{r}_2\right] \\ \mathbf{v}_2 &= \left[\left(\alpha \mathbf{I} - \mathbf{H}^2\right) + \omega^2 \mathbf{I}\right]^{-1}\left[\left(\alpha \mathbf{I} - \mathbf{H}\right)\mathbf{r}_2 - \omega \mathbf{r}_1\right] \end{aligned} \tag{4.164}$$

Then substituting Equation 4.164 with Equation 4.142 gives the general solution of Equation 4.138, that is the HPD-E direct integration formula

$$\begin{aligned} \mathbf{v}_p(t_{k+1}) = \mathbf{T}(\tau)\Big(\mathbf{v}(t_k) - \exp(\alpha t_k)\left(\mathbf{v}_1 \sin\omega t_k + \mathbf{v}_2 \cos\omega t_k\right)\Big) \\ + \exp(\alpha t_k)\left(\mathbf{v}_1 \sin\omega t_{k+1} + \mathbf{v}_2 \cos\omega t_{k+1}\right) \end{aligned} \tag{4.165}$$

FIGURE 4.6 Overview of the Liaohe Bridge.

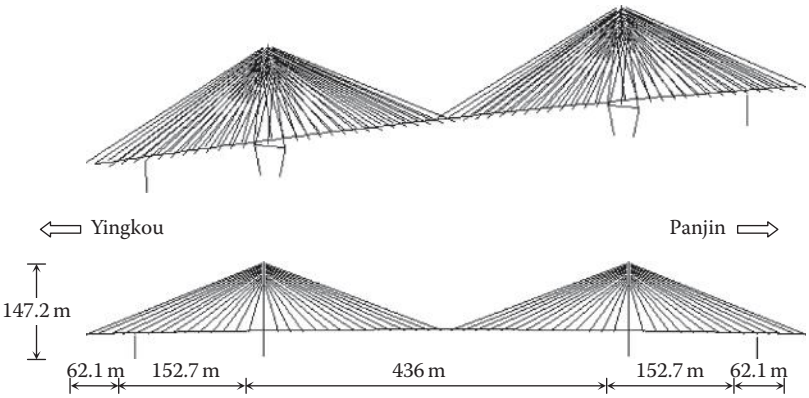

FIGURE 4.7 FE model of the Liaohe Bridge.

4.4 Case Study

The Liaohe Bridge (Figure 4.6) lying between Yingkou and Panjin in Liaoning Province, China is chosen as a numerical example. The main structure spanning the Liao River is a five-span cable-stayed bridge of total length 62.3 + 152.7 + 436+152.7 + 62.3 = 866 m.

The finite element model (Figure 4.7) had 429 nodes (including 6 supports), 310 elements, and 1156 degrees of freedom (DOFs). The deck and towers were modeled by 3D beam elements with stiff arms on both ends and each cable was modeled by a 1-D cable element. The first 200 modes were used in the mode-superposition, with the corresponding natural periods ranging within [0.046, 6.135]s, and a damping ratio of 0.05 was assumed for all participant modes. Under the action of SH and SV waves traveling horizontally along the bridge, the horizontal shear force and vertical shear force distributions along the deck were computed (see Figures 4.8 and 4.9). The effective frequency region was taken as $\omega \in [0.0, 100]$rad/s and the frequency step size was $\Delta\omega = 0.2$ rad/s. The static nonlinearly deformed nodal positions because of the cable internal forces were taken as the equilibrium position for the dynamic analysis.

4.4.1 Stationary Random Responses

The ground acceleration response spectrum used was based on the Chinese code (CMC, 2001) with regional fortification intensity 7, site-type 2, and seismic classification 1. To generate the ground acceleration PSD curves, the Kaul method, that is Equations 4.60 and 4.61, was used with $p = 0.4$. The following analysis models were used for comparison:

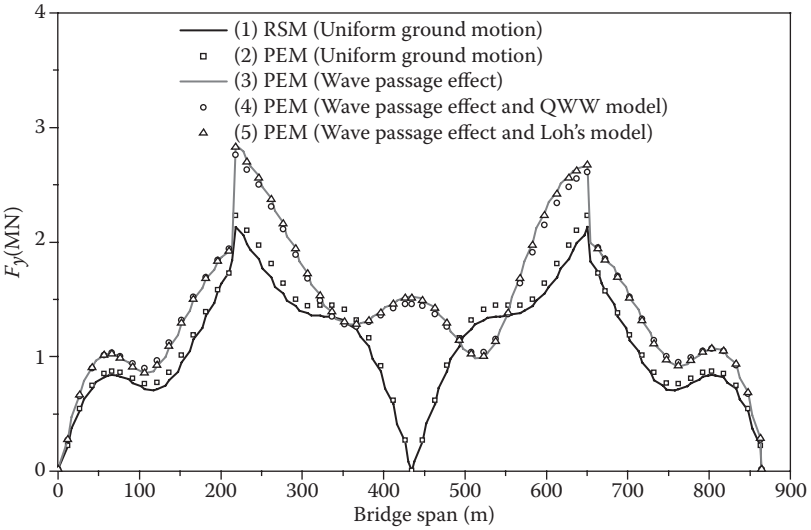

FIGURE 4.8 Transverse shear force distribution along the deck under SH waves.

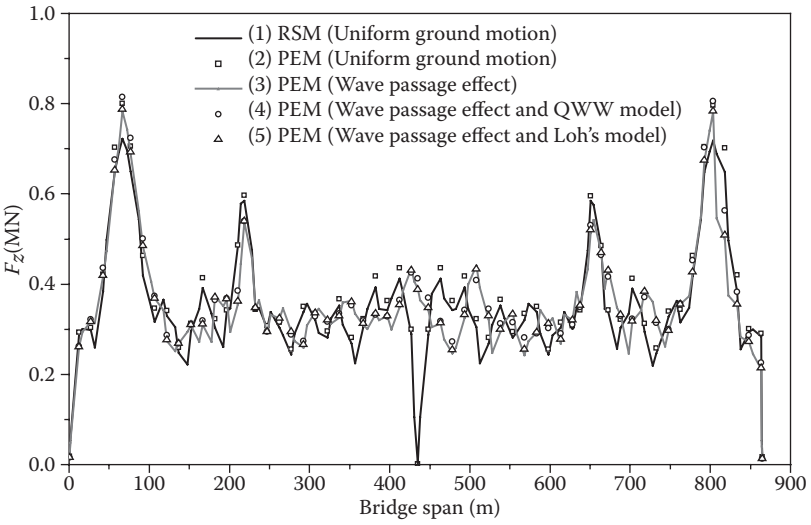

FIGURE 4.9 Vertical shear force distribution along the deck under SV waves.

1. The conventional RSM with uniform ground motion assumed
2. PEM with uniform ground motion assumed
3. PEM with the wave passage effect taken into account, using seismic apparent wave speed $v_{app} = 2000$ m/s both for SH and SV waves
4. PEM with the wave passage effect and QWW coherence model taken into account
5. PEM with the wave passage effect and Loh's coherence model taken into account

In Figures 4.8 and 4.9, curves 1 and 2 show that under uniform ground motion, the responses computed by the random vibration approach (PEM) are very close to those computed by the conventional RSM. The maximum difference between the largest responses in curves 1 and 2 is approximately 5% for Figure 4.8 and 4% for Figure 4.9. However, when $p = 0.85$ was used in Equations 4.60 and 4.61 these two

TABLE 4.1 Computing Time Required by the Five Curves of Figures 4.8 or 4.9

	Curve 1	Curve 2	Curve 3	Curve 4	Curve 5
	RSM	PEM			
Compute 200 Modes	Uniform Ground Motion	Uniform Ground Motion	Wave Passage Effect	QWW Coherence Model	Loh's Coherence Model
38 s	21 s	7 s	8 s	49 s	49 s

errors became 8.7% and 9.2%, respectively. Chen (2005) performed such computations for five bridges and they all led to similar conclusions.

Curves 3 in both figures show that the wave passage effect may lead to considerably different seismic responses. Finally, curves 4 and 5 show that when computing responses incoherence appears to be less important than the wave passage effect.

From the above comparisons the wave passage effect is seen to be of particular importance in the analysis of seismic responses, especially because if it is neglected the computed responses could be bigger, smaller, or almost unchanged, depending upon position along the bridge. It would be very difficult to predict such variation tendencies before performing the numerical computations and therefore such computations are necessary for long-span bridges. Whenever the regional apparent wave speed is not available, the computation should be performed for a few possible speeds with the maximum responses used in the design. The increase of computation time is not a problem because for each additional wave speed, only 8 seconds were required on the computer described as is listed in Table 4.1.

The computing times for the five curves presented above are listed in Table 4.1 when a Pentium-4 personal computer with main frequency 3.0 GHz and 512M memory was used. Clearly, the computational expense required by PEM, that is for curves 2 through 5, is quite acceptable.

4.4.2 Nonstationary Random Responses

The nonstationary random excitation model $z(t) = g(t)x(t)$ was used in which the auto-PSD of $x(t)$ is assumed to be identical to that used for the stationary analyses. The modulation function had the form of Equation 4.126 with $t_1 = 8.0$ s, $t_2 = 20.0$ s, and $c = 0.20$. The duration of the earthquake was $t \in [0, 25]$ s and the time step-size was $\Delta t = 0.5$ s. The precise integration method was used with the HPD-P, HPD-S, and HPD-E forms for the three parts of $g(t)$.

The following analyses were executed with SH or SV waves traveling along the deck, respectively:

1. All supports were subjected to stationary uniform ground acceleration.
2. All supports were subjected to nonstationary uniform ground acceleration.
3. All supports were subjected to stationary ground acceleration with the wave passage effect taken into account.
4. All supports were subjected to nonstationary ground acceleration with the wave passage effect taken into account.
5. All supports were subjected to stationary ground acceleration with the wave passage and incoherent effects both taken into account.
6. All supports were subjected to nonstationary ground acceleration with the wave passage and incoherent effects both taken into account.

PEM was used for all these stationary and nonstationary analyses by means of a program DDJ-B jointly developed by Chongqing Communications Research & Design Institute and Dalian University of Technology. The numerical results are shown in Figures 4.10 and 4.11. Hence comparison of the results for nonstationary random vibration analyses with those because of the corresponding stationary random vibration analyses shows that the wave passage effect is quite important in the seismic analysis of

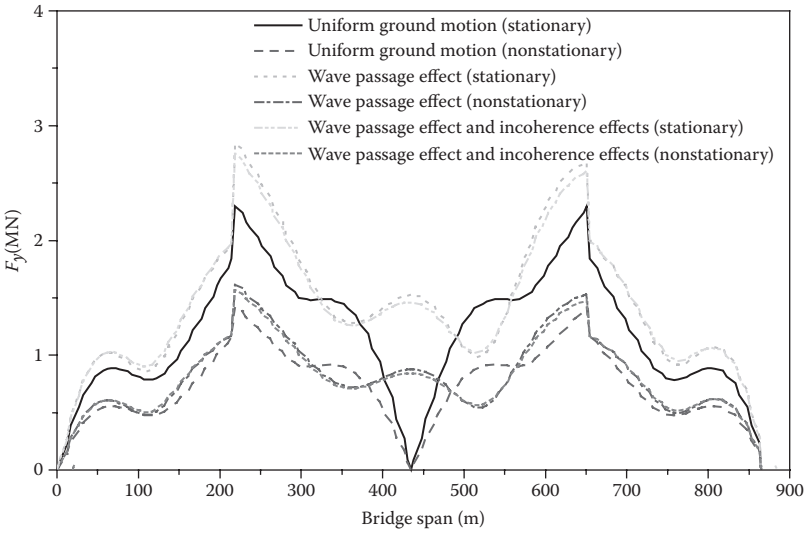

FIGURE 4.10 Transverse shear force distribution along the deck under SH waves.

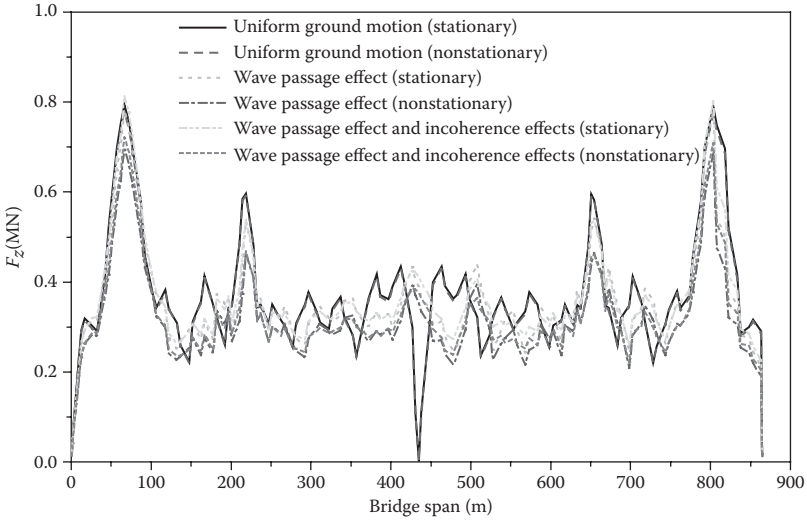

FIGURE 4.11 Vertical shear force distribution along the deck under SV waves.

TABLE 4.2 Computing Time Required by Different Models of Figures 4.10 or 4.11

	Stationary (PEM)			Nonstationary (PEM)		
Computing 200 modes	Uniform ground motion	Wave passage effect	Incoherence effect	Uniform ground motion	Wave passage effect	Incoherence effect
38 s	7 s	8 s	49 s	557 s	652 s	3801 s

long-span bridges; whereas the further inclusion of the incoherence effect is less significant. In addition, whether for uniform ground motion or for differential ground motion, the nonstationary responses are always smaller than the corresponding stationary responses, approximately by 10%–20%. For more flexible bridge structures, such nonstationary effects may become stronger.

The computation times for the six curves in Figures 4.10 or 4.11 are listed in Table 4.2, with a Pentium-4 personal computer with 3.0 GHz main frequency and 512M memory again used. The computational times required by the nonstationary analyses with SH or SV waves are almost equal, being approximately 10 minutes for the case of uniform ground motion and also when the wave passage effect was taken into account, or approximately 60 minutes if the incoherence effect is taken into account. Such high efficiency is quite acceptable for practical engineering designs.

4.4.3 PEM Analysis of Actual Long-Span Bridges

In China, PEM has been used in the seismic analysis of a number of actual long-span cable-stayed bridges, for example the second Nanjing Yangtze River Bridge (main span 628 m), the Chongqing DAFOSI Yangtze River Bridge (main span 846 m); the Sutong Yangtze River bridge (main span 1088m); and some suspension bridges, for example the Guangdong Jin-Ma Bridge (Main span 686 m). The "Guidelines for Seismic Design of Highway Bridges" JTG/T B01-01 were published by the Chinese Ministry of Communications (2008), in which PEM is recommended as a basic tool for seismic analysis of bridges. Therefore these "Guidelines" are applicable to bridges when considering wave passage effects, incoherence effects, and local site effects. A program "LongQiao" based on these "Guidelines" was developed (CCRDI and DUT, 2007) to facilitates the use of the "Guidelines" by engineers.

4.5 Summary

For long-span bridges not only the seismic spatial effects but also the nonstationary effects should be taken into account by designs. Previously, it was very complicated and difficult to execute such analyses. However by using the proposed PEM combined with the precise integration method all computational difficulties have been overcome. These spatial and nonstationary effects can now be computed conveniently, accurately, and very efficiently. For nonstationary excitations, the difficulty is now not the computation of the response PSD but instead is the determination of the ground motion PSD as well as the way to compute the demands.

References

Bathe, K. J. and Wilson, E. L. 1976. *Numerical Methods in Finite Element Analysis*. Prentice-Hall Inc., New Jersey.

Berrah, M. and Kausel, E. 1992. Response spectrum analysis of structures subjected to spatially varying motions. *Earthquake Eng. Struct. Dyn*., 21, 461–470.

Caltrans. 2010. *Seismic Design Criteria, Version 1*.6. California Department of Transportation, Sacramento, CA.

CCRDI and DUT. 2007. *LongQiao User's Guide*. Chongqing Communications Research & Design Institute and Dalian University of Technology, China.

Chen, Y. 2005. *Some Numerical Investigations for the Revision of Earthquake Resistant Specifications for Design of Highway Bridges*. Master thesis, Dalian University of Technology, Dalian, China (In Chinese).

Clough, R. W. and Penzien, J. 1993. *Dynamics of Structures*, McGraw-Hill Inc., New York, NY.

CMC. 2001. *Code for Seismic Design of Buildings GB 50011-2001*. China Ministry of Construction, Chinese Architectural Industry Press, Beijing (in Chinese).

CMCs. 2008. *Guidelines for Seismic Design of Highway Bridges (JTG/T B02-01)*. Chinese Ministry of Communications, China Communications Press, Beijing.

Davenport, A. G. 1961. The application of statistical concepts to the wind loading of structures. *Proc. Inst. Civil Eng*., 19(4), 449–472.

Der Kiureghian, A. and Neuenhofer, A. 1992. Response spectrum method for multisupport seismic excitations. *Earthquake Eng. Struct. Dyn*., 21, 713–740.

Dumanoglu, A. and Severn, R. T. 1990. Stochastic response of suspension bridges to earthquake forces. *Earthquake Eng. Struct. Dyn*., 19, 133–152.

Harichandran, R. S. and Vanmarcke, E. H. 1986. Stochastic variation of earthquake ground motion in space and time. *J. Eng. Mech*., ASCE, 112(2), 154–175.

Heredia-Zavoni, E. and Vanmarcke, E. H. 1994. Seismic random vibration analysis of multi-support structural systems. *J. Eng. Mech*., ASCE, 120(5), 1107–1128.

Kaul, M. K. 1978. Stochastic characterization of earthquake through their response spectrum. *Earthquake Eng. Struct. Dyn*., 6(5), 497–510.

Lin, J. H. and Zhang, Y. H. 2005. Seismic random vibration of long-span structures. In: *Shock and Vibration Handbook*. De Silva, C. W. (ed.), 30, 1–41, Boca Raton, CRC Press.

Lin, J. H., Shen, W. P., and Williams, F. W. 1995. A high precision direct integration scheme for structures subjected to transient dynamic loading. *Comp. Struct*., 56(1), 113–120.

Lin, J. H. Sun, D. K., Sun, Y., and Williams, F. W. 1997. Structural responses to non-uniformly modulated evolutionary random seismic excitations. *Commun. Num. Methods Eng*., 13, 605–616.

Lin, Y. K. 1967. *Probabilistic Theory of Structural Dynamics*, McGraw-Hill, New York, NY.

Loh, C. H. and Yeh, Y. T. 1988. Spatial variation and stochastic modeling of seismic differential ground movement. *Earthquake Eng. Struct. Dyn*., 16(5), 583–596.

Luco, J. E. and Wong, H. L. 1986. Response of a rigid foundation to a spatially random ground motion. *Earthquake Eng. Struct. Dyn*., 14(6), 891–908.

Priestley, M. B. 1967. Power spectral of non-stationary random responses. *J. Sound Vib*., 6, 86–97.

Qu, T. J., Wang, J. J., and Wang, Q. X. 1996. A practical power spectrum model for spatially varying seismic motion. *J. Seismol*., 18(1), 55–62.

Shrikhande, M. and Gupta, V. K. 1997. A generalized approach for the seismic response of structural systems. *Euro. Earthquake Eng*., 11(2), 3–12.

Sun, J. J. and Jiang, J. R. 1990. Parameters of Kanai-Tajimi power spectrum according to the response spectrum of Chinese code. *J. World Earthquake Eng*., 8(1), 42–48 (in Chinese).

Wilson, E. L. and Der Kiureghian, A. 1981. A replacement for the SRSS method in seismic analysis. *Earthquake Eng. Struct. Dyn*., 9, 187–192.

Zhang, Y. H., Chen, Y., Li, L. Y., and Lin, J. H. 2007. Seismic random vibration analysis of bridges and production of input power spectrum. *J. Dalian University of Technol*., 47(6), 786–792 (in Chinese).

Zhao, F. X. and Liu, A. W. 2001. Relationship between power-spectral-density functions and response spectra of earthquake ground motions. *Earthquake Eng. and Eng. Vib*., 21(2), 30–35 (in Chinese).

Zhong, W. X. 1993. *Computational Structural Mechanics and Optimal Control*. Dalian University of Technology Press, Dalian.

Zhong, W. X. and Williams, F. W. 1995. A precise time step integration method. *Proc. Inst. Mech. Engrs*., 208C, 427–430.

5

Nonlinear Analysis

Mahamad Akkari
California Department of Transportation

Lian Duan
California Department of Transportation

5.1 Introduction

In last two decades, nonlinear bridge analysis has gained a greater momentum because of the need to assess inelastic structural behavior under seismic loads. Common seismic design philosophies for ordinary bridges allow some degree of damage without collapse. To control and evaluate damage, a postelastic nonlinear analysis is required. A nonlinear analysis is complex and involves many simplifying assumptions. Engineers must be familiar with those complexities and assumptions to design bridges that are safe and economical.

Many factors contribute to the nonlinear behavior of a bridge. These include factors such as material inelasticity, geometric or second-order effects, nonlinear soil-foundation-structure interaction, gap opening and closing at hinges and abutments locations, time-dependent effects because of concrete creep and shrinkage, and so on. The subject of nonlinear analysis is extremely broad and cannot be covered in detail in this chapter. Only material and geometric nonlinearities as well as some of the basic formulations of nonlinear static analysis with their practical applications to seismic bridge design will be presented here. The reader is referred to the excellent papers, reports, and books (Clough and Penzien, 1993; Fung, 1994; Bathe, 1996; Priestley et al., 1996; Powell, 1997; Arici and Granata, 2005; Chen, 2007; Chen and Han, 2007; Chopra, 2007; Aviram et al., 2008) that cover this type of analysis in more detail.

In this chapter, some general guidelines for nonlinear static analysis are presented. These are followed by discussion of the formulations of geometric and material nonlinearity for section and frame analysis. Two examples are given to illustrate the applications of static nonlinear push-over analysis in bridge seismic design.

5.2 Analysis Classification and General Guidelines

Engineers use structural analysis as a fundamental tool to make design decisions. It is important that engineers have excess to several different analysis tools and understand their development assumptions and limitations. Such an understanding is essential to select the proper analysis tool to achieve design objectives.

Figure 5.1 shows lateral load versus displacement curves of a frame using several structural analysis methods. Table 5.1 summarizes basic assumptions of those methods. It can be seen from Figure 5.1 that the first-order elastic analysis gives a straight line and no failure load. A first-order inelastic analysis predicts the maximum plastic load-carrying capacity on the basis of the undeformed geometry. A second-order elastic analysis follows elastic buckling process. A second-order inelastic analysis traces load-deflection curves more accurately.

5.2.1 Classifications

Structural analysis methods can be classified on the basis of different formulations of equilibrium, the constitutive and compatibility equations as discussed below.

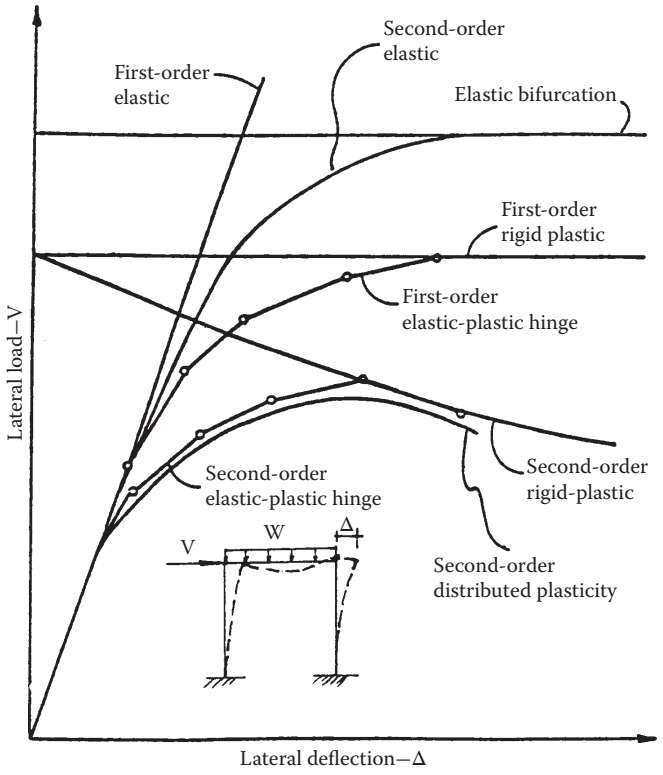

FIGURE 5.1 Lateral load-displacement curves of a frame.

TABLE 5.1 Structural Analysis Methods

		Features		
Methods		Constitutive Relationship	Equilibrium Formulation	Geometric Compatibility
First order	Elastic	Elastic	Original	Small strain and
	Rigid plastic	Rigid plastic	Undeformed	small displacement
	Elastic-plastic hinge	Elastic perfectly plastic	Geometry	
	Distributed plasticity	Inelastic		
Second order	Elastic	Elastic	Deformed	Small strain and
	Rigid plastic	Rigid plastic	Structural	moderate rotation
	Elastic plastic hinge	Elastic perfectly plastic	Geometry (P-Δ and P-δ)	(displacement may be large)
	Distributed plasticity	Inelastic		
True large Displacement	Elastic	Elastic	Deformed	Large strain and
	Inelastic	Inelastic	Structural	large deformation
			Geometry	

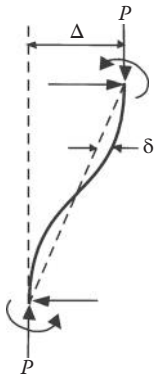

FIGURE 5.2 Second-order effects.

5.2.1.1 Classification Based on Equilibrium and Compatibility Formulations

First-order analysis: An analysis in which equilibrium is formulated with respect to the undeformed (or original) geometry of the structure. It is based on small strain and small displacement theory.

Second-order analysis: An analysis in which equilibrium is formulated with respect to the deformed geometry of the structure. A second-order analysis usually accounts for the *P*-Δ effect (influence of axial force acting through displacement associated with member chord rotation) and the *P*-δ effect (influence of axial force acting through displacement associated with member flexural curvature) (see Figure 5.2). It is based on small strain and small member deformation, but moderate rotations and large displacement theory.

True large deformation analysis: An analysis for which large strain and large deformations are taken into account.

5.2.1.2 Classification Based on Constitutive Formulation

Elastic analysis: An analysis in which elastic constitutive equations are formulated.
Inelastic analysis: An analysis in which inelastic constitutive equations are formulated.
Rigid-plastic analysis: An analysis in which elastic rigid-plastic constitutive equations are formulated.

Elastic-plastic hinge analysis: An analysis in which material inelasticity is taken into account by using concentrated "zero-length" plastic hinges.

Distributed plasticity analysis: An analysis in which the spread of plasticity through the cross sections and along the length of the members are modeled explicitly.

5.2.1.3 Classification Based on Mathematical Formulation

Linear analysis: An analysis in which equilibrium, compatibility, and constitutive equations are linear.

Nonlinear analysis: An analysis in which some or all of the equilibrium, compatibility, and constitutive equations are nonlinear.

5.2.2 General Guidelines

The following guidelines may be useful in the analysis-type selection:

- A first-order analysis may be adequate for short-to-medium span bridges. A second-order analysis should always be encouraged for long-span, tall, and slender bridges. A true large displacement analysis is generally unnecessary for bridge structures.
- An elastic analysis is sufficient for strength-based design. Inelastic analyses are recommended for displacement-based design.
- The bowing effect (effect of flexural bending on member's axial deformation), the Wagner effect (effect of bending moments and axial forces acting through displacements associated with the member twisting), and shear effects on solid-webbed members can be ignored for most of bridge structures.
- Yielding must be taken into account when considering steel nonlinearity. Strain hardening and fracture may be considered. For concrete nonlinearity, a complete strain–stress relationship (in compression up to the ultimate strain) should be used. Concrete tension strength can be neglected.
- Other nonlinearities, such as soil-foundation-structural interaction, seismic response modification devices (dampers and seismic isolations), connection flexibility, gap close and opening, should be carefully considered.

5.3 Geometric Nonlinearity Formulation

Geometric nonlinearities can be considered in the formulation of element stiffness matrixes. The general force–displacement relationship for the prismatic element as shown in Figure 5.3 can be expressed as follows:

$$\{\boldsymbol{F}\} = [\boldsymbol{K}]\{\boldsymbol{D}\} \tag{5.1}$$

where $\{\boldsymbol{F}\}$ and $\{\boldsymbol{D}\}$ are force and displacement vectors and $[\boldsymbol{K}]$ is stiffness matrix.

For a two-dimensional analysis as shown in Figure 5.3a

$$\{\boldsymbol{F}\} = \{P_{1a}, F_{2a}, M_{3a}, P_{1b}, F_{2b}, M_{3b}\}^T \tag{5.2}$$

$$\{\boldsymbol{D}\} = \{u_{1a}, u_{2a}, \theta_{3a}, u_{1b}, u_{2b}, \theta_{3b}\}^T \tag{5.3}$$

For a three-dimensional analysis as shown in Figure. 5.3b

$$\{\boldsymbol{F}\} = \{P_{1a}, F_{2a}, F_{3a}\, M_{1a}, M_{2a}, M_{3a}, P_{1b}, F_{2b}, F_{3b}, M_{1b}, M_{2b}, M_{3b}\}^T \tag{5.4}$$

$$\{\boldsymbol{D}\} = \{u_{1a}, u_{2a}, u_{3a}\, \theta_{1a}, \theta_{2a}, \theta_{3a}, u_{1b}, u_{2b}, u_{3b}, \theta_{1b}, \theta_{2b}, \theta_{3b}\}^T \tag{5.5}$$

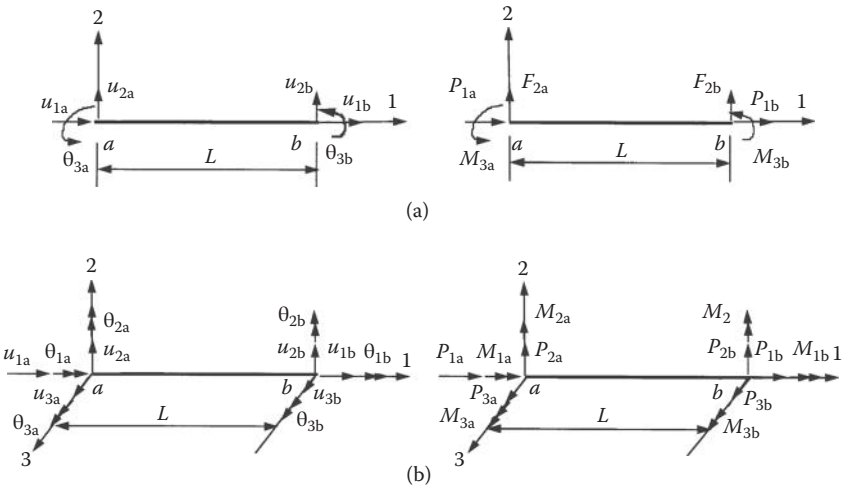

FIGURE 5.3 Degrees of freedom and nodal forces for a framed element.

Two sets of formulations of stability function-based and finite element-based stiffness matrixes are presented in the following section.

5.3.1 Two-Dimensional Analysis

For a two-dimensional analysis of a prismatic element as shown in Figure 5.3a, the stability function-based stiffness matrix (Chen and Lui, 1987) is as follows:

$$[K] = \begin{bmatrix} \frac{AE}{L} & 0 & 0 & -\frac{AE}{L} & 0 & 0 \\ & \frac{12EI}{L^3}\phi_1 & \frac{-6EI}{L^2}\phi_2 & 0 & \frac{-12EI}{L^3}\phi & \frac{-6EI}{L^2}\phi_2 \\ & & 4\phi_3 & 0 & \frac{6EI}{L^2}\phi_2 & 2\phi_4 \\ & & & \frac{AE}{L} & 0 & 0 \\ & & & & \frac{12EI}{L^3}\phi & \frac{6EI}{L^2}\phi_2 \\ & & & & & 4\phi_3 \end{bmatrix} \tag{5.6}$$

where A is cross-section area; E the material modulus of elasticity; L the member length; ϕ_1, ϕ_2, ϕ_3, and ϕ_4 can be expressed by stability equations listed in Table 5.2. Alternatively, ϕ_i functions can also be expressed in the power series derived from the analytical solutions (Goto and Chen, 1987) as listed in Table 5.3.

Assuming polynomial displacement functions, the finite element-based stiffness matrix (Allen and Bulson, 1980; White and McGuire, 1985) has the following form:

$$[K] = [K_e] + [K_g] \tag{5.7}$$

TABLE 5.2 Stability Function-Based φ_i Equations for 2-D Analysis

	Axial Load (P)		
ϕ	Compression	Zero	Tension
ϕ_1	$\dfrac{(kL)^3 \sin kL}{12\phi_c}$	1	$\dfrac{(kL)^3 \sinh kL}{12\phi_t}$
ϕ_2	$\dfrac{(kL)^2(1-\cos kL)}{6\phi_c}$	1	$\dfrac{(kL)^2(\cosh kL-1)}{6\phi_t}$
ϕ_3	$\dfrac{(kL)(\sin kL - kL\cos kL)}{4\phi_c}$	1	$\dfrac{(kL)(kL\cosh kL - \sinh kL)}{4\phi_t}$
ϕ_4	$\dfrac{(kL)(kL-\sin kL)}{2\phi_c}$	1	$\dfrac{(kL)(\sin kL - kL)}{2\phi_t}$

Note: $\phi_c = 2-2\cos kL - kL\sin kL \quad \phi_t = 2-2\cosh kL - kL\sinh kL \quad k=\sqrt{P/EI}$

TABLE 5.3 Power Series Expression of φ_i Equations

ϕ_1	$\dfrac{1+\sum_{n=1}^{\infty}\dfrac{1}{(2n+1)!}\left[\mp(kL)^2\right]^n}{12\phi}$
ϕ_2	$\dfrac{\frac{1}{2}+\sum_{n=1}^{\infty}\dfrac{1}{(2n+2)!}\left[\mp(kL)^2\right]^n}{6\phi}$
ϕ_3	$\dfrac{\frac{1}{3}+\sum_{n=1}^{\infty}\dfrac{2(n+1)}{(2n+3)!}\left[\mp(kL)^2\right]^n}{4\phi}$
ϕ_4	$\dfrac{\frac{1}{6}+\sum_{n=1}^{\infty}\dfrac{1}{(2n+3)!}\left[\mp(kL)^2\right]^n}{2\phi}$
ϕ	$\frac{1}{12}+\sum_{n=1}^{\infty}\dfrac{2(n+1)}{(2n+4)!}\left[\mp(kL)^2\right]^n$

Note: Minus sign—compression Plus sign—tension

where $[\boldsymbol{K}_e]$ is the first order conventional linear elastic stiffness matrix and $[\boldsymbol{K}_g]$ the geometric stiffness matrix that considers the effects of axial load on the bending stiffness of a member.

$$[\boldsymbol{K}_e] = \begin{bmatrix} \frac{AE}{L} & 0 & 0 & -\frac{AE}{L} & 0 & 0 \\ & \frac{12EI}{L^3} & \frac{-6EI}{L^2} & 0 & \frac{-12EI}{L^3} & \frac{-6EI}{L^2} \\ & & 4 & 0 & \frac{6EI}{L^2} & 2 \\ & & & \frac{AE}{L} & 0 & 0 \\ & \text{sym.} & & & \frac{12EI}{L^3} & \frac{6EI}{L^2} \\ & & & & & 4 \end{bmatrix} \tag{5.8}$$

$$\left[\boldsymbol{K}_{\mathrm{g}}\right]=\mp\frac{P}{L}\begin{bmatrix} 0 & 0 & 0 & 0 & 0 & 0 \\ & \frac{6}{5} & \frac{-L}{10} & 0 & \frac{-6}{5} & \frac{-L}{10} \\ & & \frac{2L^2}{15} & 0 & \frac{L}{10} & -\frac{L^2}{30} \\ & & & 0 & 0 & 0 \\ & \text{sym.} & & & \frac{6}{5} & \frac{L}{10} \\ & & & & & \frac{2L^2}{15} \end{bmatrix} \tag{5.9}$$

It is noted (Schilling, 1983) that Equations 5.8 and 5.9 exactly coincide with the stability function-based stiffness matrix when taken only the first two terms of the Taylor series expansion in Equation 5.6.

5.3.2 Three-Dimensional Analysis

For a three-dimensional analysis of a frame element as shown in Figure 5.3b, the stability function-based stiffness matrix has the following form (Ekhande et al., 1989):

$$[\boldsymbol{K}]=\begin{bmatrix} \phi_{s1} & 0 & 0 & 0 & 0 & 0 & -\phi_{s1} & 0 & 0 & 0 & 0 & 0 \\ & \phi_{s7} & 0 & 0 & 0 & \phi_{s6} & 0 & -\phi_{s7} & 0 & 0 & 0 & \phi_{s6} \\ & & \phi_{s9} & 0 & -\phi_{s8} & 0 & 0 & 0 & -\phi_{s9} & 0 & -\phi_{s8} & 0 \\ & & & \frac{GJ}{L} & 0 & 0 & 0 & 0 & 0 & -\frac{GJ}{L} & 0 & 0 \\ & & & & \phi_{s4} & 0 & 0 & 0 & \phi_{s8} & 0 & \phi_{s5} & 0 \\ & & & & & \phi_{s2} & 0 & -\phi_{s6} & 0 & 0 & 0 & \phi_{s3} \\ & & & & & & \phi_{s1} & 0 & 0 & 0 & 0 & 0 \\ & & & & & & & \phi_{s7} & 0 & 0 & 0 & -\phi_{s6} \\ & & \text{Sym.} & & & & & & \phi_{s9} & 0 & \phi_{s8} & 0 \\ & & & & & & & & & \frac{GJ}{L} & 0 & 0 \\ & & & & & & & & & & \phi_{s4} & 0 \\ & & & & & & & & & & & \phi_{s2} \end{bmatrix} \tag{5.10}$$

where G is shear modulus of elasticity; J the torsional constant; φ_{s1} to φ_{s9} are expressed by stability equations listed in Table 5.4.

Finite element-based stiffness matrix has the form (Orbison, 1982):

$$[K_e] = \begin{bmatrix} \phi_{e1} & 0 & 0 & 0 & 0 & 0 & -\phi_{e1} & 0 & 0 & 0 & 0 & 0 \\ & \phi_{e7} & 0 & 0 & 0 & \phi_{e6} & 0 & -\phi_{e7} & 0 & 0 & 0 & \phi_{e6} \\ & & \phi_{e9} & 0 & -\phi_{e8} & 0 & 0 & 0 & -\phi_{e9} & 0 & -\phi_{e8} & 0 \\ & & & \frac{GJ}{L} & 0 & 0 & 0 & 0 & 0 & -\frac{GJ}{L} & 0 & 0 \\ & & & & \phi_{e4} & 0 & 0 & 0 & -\phi_{e8} & 0 & \phi_{e5} & 0 \\ & & & & & \phi_{e2} & 0 & -\phi_{e6} & 0 & 0 & 0 & \phi_{e3} \\ & & & & & & \phi_{e1} & 0 & 0 & 0 & 0 & 0 \\ & & & & & & & \phi_{e7} & 0 & 0 & 0 & -\phi_{e6} \\ & & \text{Sym.} & & & & & & \phi_{e9} & 0 & \phi_{e8} & 0 \\ & & & & & & & & & \frac{GJ}{L} & 0 & 0 \\ & & & & & & & & & & \phi_{e4} & 0 \\ & & & & & & & & & & & \phi_{e2} \end{bmatrix} \tag{5.11}$$

TABLE 5.4 Stability Function-Based φ_{si} for 3-D Analysis

		Stability Functions (S_i)	
ϕ_{si}		Compression	Tension
$\phi_{s1} = S_1 \frac{EA}{L}$	S_1	$\frac{1}{1-\frac{EA}{4P^3L^2}\left[H_y + H_z\right]}$	$\frac{1}{1-\frac{EA}{4P^3L^2}\left[H'_y + H'_z\right]}$
$\phi_{s2} = S_2 \frac{(4+\phi_y)EI_Z}{(1+\phi_y)L}$	S_2	$\frac{(\alpha L)(\sin\alpha L - \alpha L\cos\alpha L)}{4\phi_\alpha}$	$\frac{(\alpha L)(\alpha L\cosh\alpha L - \sinh\alpha L)}{4\phi_\alpha}$
$\phi_{s3} = S_2 \frac{(2-\phi_y)EI_Z}{(1+\phi_y)L}$	S_3	$\frac{(\alpha L)(\alpha L - \sin\alpha L)}{2\phi_\alpha}$	$\frac{(\alpha L)(\sinh\alpha L - \alpha L)}{2\phi_\alpha}$
$\phi_{s4} = S_4 \frac{(4+\phi_z)EI_y}{(1+\phi_z)L}$	S_4	$\frac{(\beta L)(\sin\beta L - \beta L\cos\beta L)}{4\phi_\beta}$	$\frac{(\beta L)(\beta L\cosh\beta L - \sinh\beta L)}{4\phi_\beta}$
$\phi_{s5} = S_2 \frac{(2-\phi_z)EI_y}{(1+\phi_z)L}$	S_5	$\frac{(\beta L)(\beta L - \sin\beta L)}{2\phi_\beta}$	$\frac{(\beta L)(\sinh\beta L - \beta L)}{2\phi_\beta}$
$\phi_{s6} = S_6 \frac{6EI_Z}{(1+\phi_y)L^2}$	S_6	$\frac{(\alpha L)^2(1-\cos\alpha L)}{6\phi_\alpha}$	$\frac{(\alpha L)^2(\cosh\alpha L - 1)}{6\phi_\alpha}$
$\phi_{s7} = S_7 \frac{12EI_Z}{(1+\phi_y)L^3}$	S_7	$\frac{(\alpha L)^3\sin\alpha L}{12\phi_\alpha}$	$\frac{(\alpha L)^3\sinh\alpha L}{12\phi_\alpha}$
$\phi_{s8} = S_8 \frac{6EI_y}{(1+\phi_z)L^2}$	S_8	$\frac{(\beta L)^2(1-\cos\beta L)}{6\phi_\beta}$	$\frac{(\beta L)^2(\cosh\beta L - 1)}{6\phi_\beta}$
$\phi_{s9} = S_9 \frac{12EI_y}{(1+\phi_z)L^3}$	S_9	$\frac{(\beta L)^3\sin\beta L}{12\phi_\beta}$	$\frac{(\beta L)^3\sinh\beta L}{12\phi_\beta}$
$\alpha = \sqrt{P/EI_Z}$	ϕ_α	2−2 cosαL−αLsinαL	2−2 coshαL+αLsinhαL
$\beta = \sqrt{P/EI_y}$	ϕ_β	2−2 cosβL−βLsinβL	2−2 coshβL+βLsinhβL

TABLE 5.4 (*Continued*) Stability Function-Based φ_{si} for 3-D Analysis

$$H_y = \beta L(M_{ya}^2 + M_{yb}^2)(\cot\beta L + \beta L\cos ec^2\beta L) - 2(M_{ya} + M_{yb})^2 + 2\beta L M_{ya}M_{yb}(\cos ec\beta L)(1+\beta L\cot\beta L)$$

$$H_z = \alpha L(M_{za}^2 + M_{zb}^2)(\cot\alpha L + \alpha L\cos ec^2\alpha L) - 2(M_{za} + M_{zb})^2 + 2\alpha L M_{za}M_{zb}(\cos ec\alpha L)(1+\alpha L\cot\alpha L)$$

$$H'_y = \beta L(M_{ya}^2 + M_{yb}^2)(\coth\beta L + \beta L\cos ech^2\beta L) - 2(M_{ya} + M_{yb})^2 + 2\beta L M_{ya}M_{yb}(\cos ech\beta L)(1+\beta L\coth\beta L)$$

$$H'_z = \alpha L(M_{za}^2 + M_{zb}^2)(\coth\alpha L + \alpha L\cos ech^2\alpha L) - 2(M_{za} + M_{zb})^2 + 2\alpha L M_{za}M_{zbb}(\cos ech\alpha L)(1+\alpha L\coth\alpha L)$$

TABLE 5.5 Elements of Finite Element-Based Stiffness Matrix

Linear Elastic Matrix	Geometric Nonlinear Matrix
$\phi_{e1} = \dfrac{AE}{L}$; $\phi_{e2} = \dfrac{4EI_Z}{L}$	$\phi_{g1} = 0$; $\phi_{g2} = \phi_{g4} = \dfrac{2F_{xb}L}{15}$; $\phi_{g3} = \phi_{g5} = \dfrac{F_{xb}L}{30}$
$\phi_{e3} = \dfrac{2EI_z}{L}$ $\phi_{e4} = \dfrac{4EI_y}{L}$	$\phi_{g7} = \phi_{g9} = \dfrac{6F_{xb}}{5L}$; $\phi_{g6} = \phi_{g8} = \dfrac{F_{xb}}{10}$; $\phi_{g10} = \dfrac{M_{za} + M_{zb}}{L^2}$
$\phi_{e5} = \dfrac{2EI_y}{L}$; $\phi_{e6} = \dfrac{6EI_Z}{L^2}$	$\phi_{g11} = \dfrac{M_{ya} + M_{yb}}{L^2}$; $\phi_{g12} = \dfrac{M_{ya}}{L}$;
	$\phi_{g13} = \dfrac{M_{xb}}{L}$ $\phi_{g14} = \dfrac{M_{yb}}{L}$; $\phi_{g15} = \dfrac{M_{za}}{L}$; $\phi_{g16} = \dfrac{M_{zb}}{L}$
$\phi_{e7} = \dfrac{12EI_Z}{L^3}$; $\phi_{e8} = \dfrac{6EI_y}{L^2}$	$\phi_{g17} = \dfrac{F_{xb}I_p}{AL}$; $\phi_{g18} = \dfrac{M_{zb}}{6} - \dfrac{M_{za}}{3}$; $\phi_{g19} = \dfrac{M_{ya}}{3} - \dfrac{M_{yb}}{6}$
$\phi_{e9} = \dfrac{12EI_y}{L^3}$	$\phi_{g20} = \dfrac{M_{za} + M_{zyb}}{6}$; $\phi_{g21} = \dfrac{M_{ya} + M_{yb}}{6}$

I_z and I_y are moments of inertia about z–z and y–y axis, respectively.
I_p is the polar moment of inertia

$$[\boldsymbol{K}_g] = \begin{bmatrix} \phi_{g1} & \phi_{g10} & -\phi_{g11} & 0 & 0 & 0 & 0 & -\phi_{g10} & \phi_{g11} & 0 & 0 & 0 \\ & \phi_{g7} & 0 & \phi_{g12} & \phi_{g13} & \phi_{g6} & -\phi_{g10} & -\phi_{g7} & 0 & \phi_{g14} & -\phi_{g13} & \phi_{g6} \\ & & \phi_{g9} & \phi_{g15} & -\phi_{g6} & \phi_{g13} & \phi_{g11} & 0 & -\phi_{g9} & \phi_{g16} & -\phi_{g6} & -\phi_{g13} \\ & & & \phi_{g17} & \phi_{g18} & \phi_{g19} & & -\phi_{g12} & -\phi_{g15} & -\phi_{g17} & -\phi_{g20} & \phi_{g21} \\ & & & & \phi_{g4} & 0 & 0 & -\phi_{g13} & \phi_{g6} & -\phi_{g20} & -\phi_{g5} & \phi_{g13} \\ & & & & & \phi_{g2} & 0 & -\phi_{g6} & -\phi_{g13} & \phi_{g21} & -\phi_{g13} & -\phi_{g3} \\ & & & & & & \phi_{g1} & \phi_{g10} & -\phi_{g11} & 0 & 0 & 0 \\ & & & & & & & \phi_{g7} & 0 & -\phi_{g14} & \phi_{g13} & -\phi_{g6} \\ & & \text{Sym.} & & & & & & \phi_{g9} & -\phi_{g16} & \phi_{g6} & \phi_{g13} \\ & & & & & & & & & \phi_{g17} & \phi_{g18} & \phi_{g19} \\ & & & & & & & & & & \phi_{g4} & 0 \\ & & & & & & & & & & & \phi_{g2} \end{bmatrix} \tag{5.12}$$

where φ_{ei} and φ_{gi} are given in Table 5.5.

Stiffness matrixes considering warping degree of freedom and finite rotations for a thin-walled member were derived by Yang and McGuire (1986a and 1986b).

In conclusion, both sets of the stiffness matrixes have been used successfully when considering geometrical nonlinearities (P-Δ and P-δ effects). The stability function-based formulation gives an accurate

solution using fewer degrees of freedom when compared to the finite element method. Its power series expansion (Tables 5.3) can be implemented easily without truncation to avoid numerical difficulty.

The finite element-based formulation produces an approximate solution. It has a simpler form and may require dividing the member into a large number of elements in order to keep (*P/L*) term a small quantity to obtain accurate results.

5.4 Material Nonlinearity Formulations

5.4.1 Structural Concrete

Concrete material nonlinearity is incorporated into analysis using a nonlinear stress–strain relationship. Figure 5.4 shows idealized stress–strain curves for unconfined and confined concrete in uniaxial compression. Tests have shown that the confinement provided by closely spaced transverse reinforcement can substantially increase the ultimate concrete compressive stress and strain. The confining steel prevents premature buckling of the longitudinal compression reinforcement and increases the concrete ductility. Extensive research has been made to develop concrete stress–strain relationships (Hognestad, 1951; Popovics, 1970; Kent and Park, 1971; Park and Paulay, 1975; Wang and Duan, 1981; Mander et al., 1988a and 1988b; Hoshikuma et al., 1997).

5.4.1.1 Compression Stress–Strain Relationship

5.4.1.1.1 Unconfined Concrete

A general stress–strain relationship proposed by Hognestad (1951) is widely used for plain concrete or reinforced concrete with a small amount of transverse reinforcement. The relation has the following simple form:

$$f_c = \begin{cases} f'_{co}\left[\dfrac{2\varepsilon_c}{\varepsilon_{co}} - \left(\dfrac{\varepsilon_c}{\varepsilon_{co}}\right)^2\right] & \varepsilon_c \le \varepsilon_{co} \\ f'_{co}\left[1 - \beta\left(\dfrac{\varepsilon_c - \varepsilon_o}{\varepsilon_u - \varepsilon_{co}}\right)\right] & \varepsilon_{co} < \varepsilon_c \le \varepsilon_u \end{cases} \tag{5.13}$$

$$\varepsilon_{co} = \frac{2f'_{co}}{E_c} \tag{5.14}$$

where f_c and ε_c are the concrete stress and strain; f'_{co} the peak stress for unconfined concrete usually taken as the cylindrical compression strength f'_c; ε_{co} strain at peak stress for unconfined concrete usually taken as 0.002; ε_u is the ultimate compression strain for unconfined concrete taken as 0.003; E_c

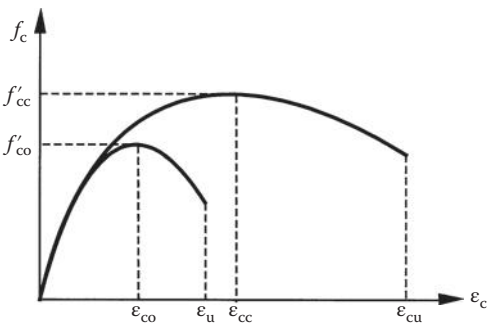

FIGURE 5.4 Idealized stress–strain curves of concrete in uniaxial compression.

the modulus of elasticity of concrete; and β a reduction factor for the descending branch usually taken as 0.15. Note that the format of Equation 5.13 can be also used for confined concrete if the concrete confined peak stress and strain are known or assumed and substituted for f'_{co} and ε_{cu}, respectively.

5.4.1.1.2 Confined Concrete—Mander's Model

Analytical models describing the stress–strain relationship for confined concrete depend on the confining transverse reinforcement type (such as hoops, spiral, or ties) and shape (such as circular, square, or rectangular). Some of those analytical models are more general than others in their applicability to various confinement types and shapes. A general stress–strain model (Figure 5.5) for confined concrete applicable (in theory) to a wide range of cross sections and confinements was proposed by Mander et al. (1988a and 1988b) and has the following form:

$$f_c = \frac{f'_{cc}\left(\varepsilon_c/\varepsilon_{cc}\right)r}{r-1+\left(\varepsilon_c/\varepsilon_{cc}\right)^r} \tag{5.15}$$

$$\varepsilon_{cc} = \varepsilon_{co}\left[1+5\left(\frac{f'_{cc}}{f'_{co}}-1\right)\right] \tag{5.16}$$

$$r = \frac{E_c}{E_c - E_{sec}} \tag{5.17}$$

$$E_{sec} = \frac{f'_{cc}}{\varepsilon_{cc}} \tag{5.18}$$

where f'_{cc} and ε_{cc} are peak compressive stress and corresponding strain for confined concrete. f'_{cc} and ε_{cu}, which depend on the confinement type and shape, are calculated as follows:

Confined Peak Stress

1. For concrete circular section confined by circular hoops or spiral (Figure 5.6a)

$$f'_{cc} = f'_{co}\left(2.254\sqrt{1+\frac{7.94f'_l}{f'_{co}}}-\frac{2f'_l}{f'_{co}}-1.254\right) \tag{5.19}$$

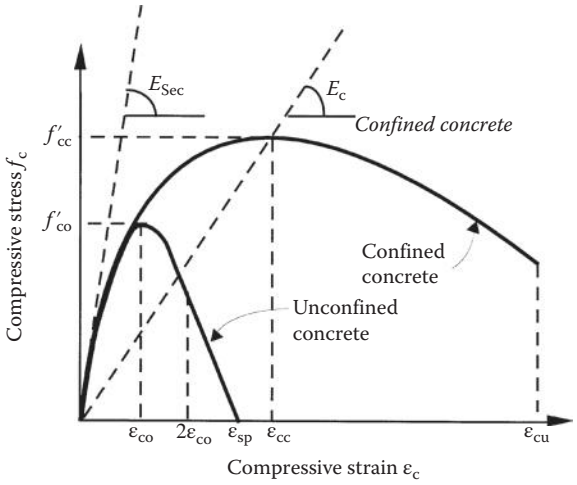

FIGURE 5.5 Stress–strain curves of concrete—Mander model.

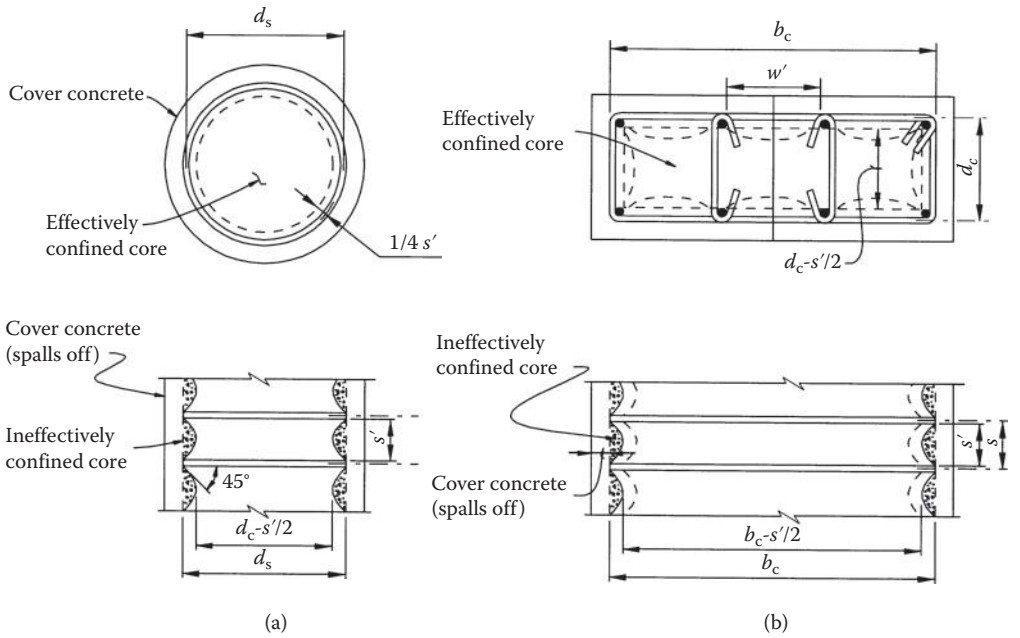

FIGURE 5.6 Confined core for hoop reinforcement.

$$f_l' = \frac{1}{2} K_e \rho_s f_{yh} \tag{5.20}$$

$$K_e = \begin{cases} \left(1 - s'/2d_s\right)^2 / \left(1 - \rho_{cc}\right) & \text{for circular hoops} \\ \left(1 - s'/2d_s\right) / \left(1 - \rho_{cc}\right) & \text{for circular spirals} \end{cases} \tag{5.21}$$

$$\rho_s = \frac{4A_{sp}}{d_s s} \tag{5.22}$$

where f_l' is the effective lateral confining pressure, K_e confinement effectiveness coefficient, f_{yh} the yield stress of the transverse reinforcement, s' the clear vertical spacing between hoops or spiral; s the center to center spacing of the spiral or circular hoops, d_s centerline diameter of spiral or hoops circle, ρ_{cc} the ratio of the longitudinal reinforcement area to the cross-section core area, ρ_s is the ratio of the transverse confining steel volume to the confined concrete core volume, and A_{sp} the bar area of transverse reinforcement.

2. For rectangular concrete section confined by rectangular hoops (Figure 5.6b)

The rectangular hoops may produce two unequal effective confining pressures f_{lx}' and f_{ly}' in the principal x- and y-direction defined as follows:

$$f_{lx}' = K_e \rho_x f_{yh} \tag{5.23}$$

$$f_{ly}' = K_e \rho_y f_{yh} \tag{5.24}$$

$$K_e = \frac{\left[1 - \sum_{i=1}^{n} \frac{(w_i')^2}{6b_c d_c}\right]\left(1 - \frac{s'}{2b_c}\right)\left(1 - \frac{s'}{2d_c}\right)}{\left(1 - \rho_{cc}\right)} \tag{5.25}$$

$$\rho_x = \frac{A_{sx}}{s\,d_c} \tag{5.26}$$

$$\rho_y = \frac{A_{sy}}{s\,b_c} \tag{5.27}$$

where f_{yh} is yield strength of transverse reinforcement; w_i' the ith clear distance between adjacent longitudinal bars; b_c and d_c core dimensions to centerlines of hoop in x and y direction (where $b \geq d$), respectively; A_{sx} and A_{sy} are the total area of transverse bars in x and y direction, respectively.

Once f_{1x}' and f_{1y}' are determined, the confined concrete strength f_{cc}' can be found using the chart shown in Figure 5.7 with f_{1x}' being greater or equal to f_{1y}'. The chart depicts the general solution of the "five-parameter" multi-axial failure surface described by William and Warnke (1975).

As an alternative to the chart, the authors derived the following equations for estimating f_{cc}':

$$f_{cc} = \begin{cases} Af_{lx}^2 + Bf_{lx} + C & f_{ly} < f_{lx} \text{ and } f_{ly} \leq 0.15 \\ \dfrac{f_{lx} - f_{ly}}{0.3 - f_{ly}} D + C & f_{ly} < f_{lx} \text{ and } f_{ly} > 0.15 \\ C & f_{ly} = f_{lx} \end{cases} \tag{5.28}$$

$$A = 196.5 f_{ly}^2 + 29.1 f_{ly} - 4 \tag{5.29}$$

$$B = -69.5 f_{ly}^2 - 8.9 f_{ly} + 2.2 \tag{5.30}$$

$$C = -6.83 f_{ly}^2 + 6.38 f_{ly} + 1 \tag{5.31}$$

$$D = -1.5 f_{ly}^2 - 0.55 f_{ly} + 0.3 \tag{5.32}$$

where $f_{cc} = \dfrac{f_{cc}'}{f_{co}'};\ f_{ly} = \dfrac{f_{ly}'}{f_{co}'};\ f_{lx} = \dfrac{f_{lx}'}{f_{co}'}$.

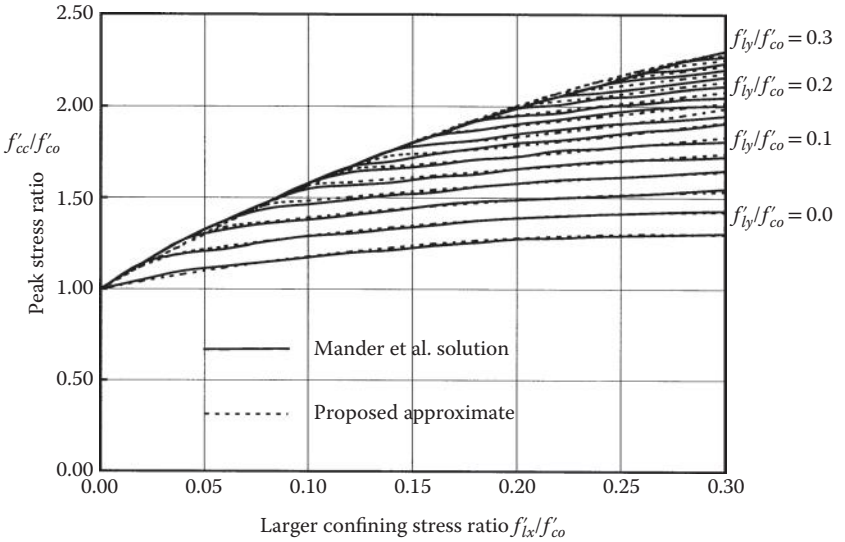

FIGURE 5.7 Peak stress of confined concrete.

Note that setting $f_1' = 0.0$ in Equations 5.19, 5.16, and 5.15 will produce Mander's expression for unconfined concrete. In this case and for concrete strain $\varepsilon_c > 2\,\varepsilon_{co}$, a straight line that reaches zero stress at the spalling strain ε_{sp} is assumed.

Confined Concrete Ultimate Compressive Strain Experiments have shown that a sudden drop in the confined concrete stress–strain curve takes place when the confining transverse steel first fractures. Defining the ultimate compressive strain as the longitudinal strain at which the first confining hoop fracture occurs, and using the energy balance approach, Mander et al. (1984) produced an expression for predicting the ultimate compressive strain that can be solved numerically.

A conservative and simple equation for estimating the confined concrete ultimate strain is given by Priestley et al. (1996).

$$\varepsilon_{cu} = 0.004 + \frac{1.4\rho_s f_{yh}\varepsilon_{su}}{f'_{cc}} \tag{5.33}$$

where ε_{su} is the steel strain at maximum tensile stress for rectangular section $\rho_s = \rho_x + \rho_y$ as defined previously. Typical values for ε_{cu} range from 0.012 to 0.05.

Equation 5.33 is formulated for confined sections subjected to axial compression. It is noted that when Equation 5.33 is used for section in bending or combined bending and axial then it tends to be conservative by at least 50%.

Chai et al. (1990) used an energy balance approach to derive the following expression for calculating the concrete ultimate confined strain as

$$\varepsilon_{cu} = \varepsilon_{sp} + \begin{cases} \rho_s\varepsilon_{su}\dfrac{\gamma_2 f_{yh}}{\gamma_1 f'_{cc}} & \text{confined by reinconcement} \\ \rho_{sj}\varepsilon_{suj}\dfrac{\gamma_2 f_{yi}}{\gamma_1 f'_{cc}} & \text{confined by steel jackets} \end{cases} \tag{5.34}$$

where ε_{sp} is the spalling strain of the unconfined concrete (usually = 0.003–0.005), γ_1 an integration coefficient of the area between the confined and unconfined stress–strain curves and γ_2 an integration coefficient of the area under the transverse steel stress–strain curve. The confining ratio for steel jackets $\rho_{sj} = 4t_j/(D_j - 2t_j)$; D_i and t_j are outside diameter and thickness of the jacket, respectively; f_{yj} yield stress of the steel jacket. For high- and mild-strength steels and concrete compressive strengths of 4–6 ksi (27.58–41.37 MPa), Chai et al. (1990) proposed the following expressions:

$$\frac{\gamma_2}{\gamma_1} = \begin{cases} \dfrac{2000\rho_s}{\left(1+(1428\rho_s)^4\right)^{0.25}} & \text{for Grade 40 Steel} \\ \dfrac{2000\rho_s}{\left(1+(1480\rho_s)^{0.25}\right)^{0.4}} & \text{for Grade 60 Steel} \end{cases} \tag{5.35}$$

5.4.1.1.3 Confined Concrete—Honshihuma's Model

In additional to Mander's model, Table 5.6 lists a stress–strain relationship for confined concrete proposed by Hoshikuma et al. (1997). The Hoshikuma model was based on the results of a series experimental tests covering circular, square, and wall-type cross sections with various transverse reinforcement arrangement in bridge piers design practice in Japan.

5.4.1.2 Tension Stress–Strain Relationship

Two idealized stress–strain curves for concrete in tension are shown in Figure 5.8. For plain concrete, the curve is linear up to cracking stress f_r. For reinforced concrete, there is a descending branch because

TABLE 5.6 Hoshikuma's Stress–Strain Relationship of Confined Concrete

$$f_c = \begin{cases} E_c\varepsilon_c\left[1-\frac{1}{n}\left(\frac{\varepsilon_c}{\varepsilon_{cc}}\right)^{n-1}\right] & \varepsilon_c \le \varepsilon_{cc} \\ f'_{cc} - E_{des}\left(\varepsilon_c - \varepsilon_{cc}\right) & \varepsilon_{cc} < \varepsilon_c \le \varepsilon_{cu} \end{cases}$$

$$n = \frac{E_c\varepsilon_{cc}}{E_c\varepsilon_{cc} - f'_{cc}};\ \varepsilon_{cu} = \varepsilon_{cc} + \frac{f'_{cc}}{2E_{des}};\ E_{des} = 11.2\frac{f'^2_{cc}}{\rho_s f_{yh}}$$

$$\frac{f'_{cc}}{f'_{co}} = \begin{cases} 1.0 + 3.8\frac{\rho_s f_{yh}}{f'_{co}} & \text{for circular section} \\ 1.0 + 0.76\frac{\rho_s f_{yh}}{f'_{co}} & \text{for square section} \end{cases}$$

$$\varepsilon_{cc} = \begin{cases} 0.002 + 0.033\frac{\rho_s f_{sh}}{f'_{co}} & \text{for circular section} \\ 0.002 + 0.013\frac{\rho_s f_{sh}}{f'_{co}} & \text{for square section} \end{cases}$$

Source: Hoshikuma, J. et al., *J. Struct. Eng.* ASCE, 123(5), 624–633, 1997.

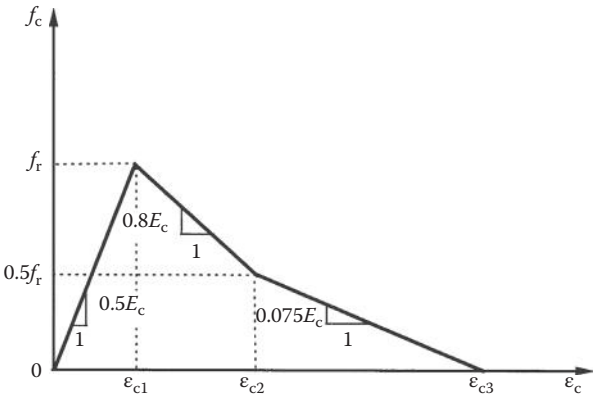

FIGURE 5.8 Idealized stress–strain curve of concrete in uniaxial tension.

of bond characteristics of reinforcement. A tri-linear expression proposed by Vebo and Ghali (1977) is as follows:

$$f_c = \begin{cases} 05E_c\varepsilon_c & \varepsilon_c \le \varepsilon_{c1} = 2f_r / E_c \\ f_r\left[1-0.8E_c\left(\varepsilon_c - 2f_r / E_c\right)\right] & \varepsilon_{c1} < \varepsilon_c \le \varepsilon_{c2} = 2.625 f_r / E_c \\ f_r\left[0.5-0.075E_c\left(\varepsilon_c - 2.625 f_r / 4E_c\right)\right] & \varepsilon_{c2} < \varepsilon_{c3} = 9.292 f_r / E_c \end{cases} \quad (5.36)$$

where f_r is modulus of rupture of concrete.

5.4.2 Structural Steel and Reinforcement

For structural steel and nonprestressed steel reinforcement, its stress–strain relationship can be idealized as four parts: elastic, plastic, strain hardening, and softening as shown in Figure 5.9. The simplest multilinear expression is

$$f_s = \begin{cases} E_s\varepsilon_s & 0 \le \varepsilon_s \le \varepsilon_y \\ f_y & \varepsilon_{sy} < \varepsilon_s \le \varepsilon_{sh} \\ f_y + \dfrac{\varepsilon_s - \varepsilon_{sh}}{\varepsilon_{su} - \varepsilon_{sh}}\left(f_u - f_y\right) & \varepsilon_{sh} < \varepsilon_s \le \varepsilon_{su} \\ f_u\left[1 - \dfrac{\varepsilon_s - \varepsilon_{su}}{\varepsilon_{sb} - \varepsilon_{su}}\left(f_{su} - f_{sb}\right)\right] & \varepsilon_{su} < \varepsilon_s \le \varepsilon_{sb} \end{cases} \tag{5.37}$$

where f_s and ε_s is stress of strain in steel; E_s the modulus of elasticity of steel = 29,000 ksi (200, 000 MPa); f_y and ε_y yield stress and strain; ε_{sh} hardening strain; f_{su} and ε_{su} maximum stress and corresponding strain; and f_{sb} and ε_{sb} rupture stress and corresponding strain.

For the reinforcing steel, the following nonlinear form can also be used for the strain-hardening portion (Chai et al., 1990):

$$f_s = f_y\left[\frac{m(\varepsilon_s - \varepsilon_{sh}) + 2}{60(\varepsilon_s - \varepsilon_{sh}) + 2} + \frac{(\varepsilon_s - \varepsilon_{sh})(60 - m)}{2(30r + 1)^2}\right] \quad \text{for } \varepsilon_{sh} < \varepsilon_s \le \varepsilon_{su} \tag{5.38}$$

$$m = \frac{(f_{su}/f_y)(30r + 1)^2 - 60r - 1}{15r^2} \tag{5.39}$$

$$r = \varepsilon_{su} - \varepsilon_{sh} \tag{5.40}$$

$$f_{su} = 1.5 f_y \tag{5.41}$$

$$\varepsilon_{sh} = \begin{cases} 14\varepsilon_y & \text{for Grade 40} \\ 5\varepsilon_y & \text{for Grade 60} \end{cases} \tag{5.42}$$

$$\varepsilon_{su} = \begin{cases} 0.14 + \varepsilon_{sh} & \text{for Grade 40} \\ 0.12 & \text{for Grade 60} \end{cases} \tag{5.43}$$

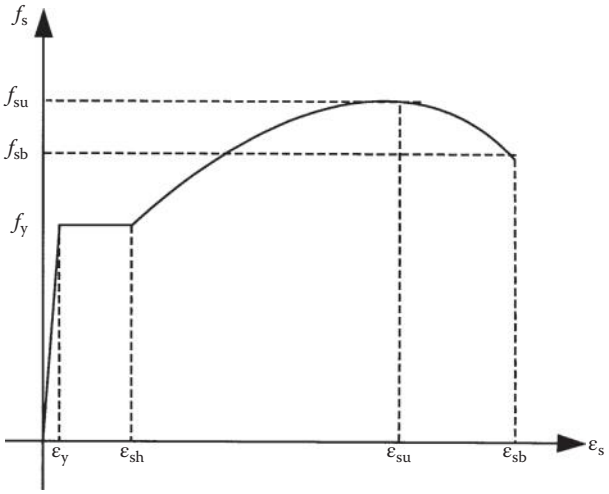

FIGURE 5.9 Idealized stress–strain curve of structural steel and reinforcement.

TABLE 5.7 Nominal Limiting Values for Structural Steel Stress–Strain Curves

f_y ksi (MPa)	f_u ksi (MPa)	ε_y	ε_{sh}	ε_{su}	ε_{sb}
40 (280)	80 (550)	0.00138	0.0230	0.140	0.200
60 (420)	106 (730)	0.00207	0.0060	0.087	0.136
75 (520)	130 (900)	0.00259	0.0027	0.073	0.115

For both strain-hardening and softening portions, Holzer et al. (1975) proposed the following expression:

$$f_s = f_y\left[1+\frac{\varepsilon_s-\varepsilon_{sh}}{\varepsilon_{su}-\varepsilon_{sh}}\left(\frac{f_u}{f_y}-1\right)\exp\left(1-\frac{\varepsilon_s-\varepsilon_{sh}}{\varepsilon_{su}-\varepsilon_{sh}}\right)\right] \quad \text{for } \varepsilon_{sh} < \varepsilon_s \le \varepsilon_{sb} \tag{5.44}$$

The nominal limiting values for stress and strain proposed by Holzer et al. (1975) are shown in Table 5.7.

For prestressing steel, the stress–strain behavior is different from the nonprestressed steel. There is no obvious yield flow plateau in its response. Typical stress–strain curves for prestressing steel can be approximated by the following equations:

For Grade 250 (PCI, 2011)

$$f_s = \begin{cases} 28{,}500\varepsilon_s \ \text{(ksi)} & \text{for } \varepsilon_s \le 0.0076 \\ 250 - \dfrac{0.04}{\varepsilon_s - 0.0064} \ \text{(ksi)} & \text{for } \varepsilon_s > 0.0076 \end{cases} \tag{5.45}$$

For Grade 270 (PCI, 2011)

$$f_s = \begin{cases} 28{,}500\ \varepsilon_s \text{(ksi)} & \text{for } \varepsilon_s \le 0.0086 \\ 270 - \dfrac{0.04}{\varepsilon_s - 0.007} \ \text{(ksi)} & \text{for } \varepsilon_s > 0.0086 \end{cases} \tag{5.46}$$

For Bars Grade 150

$$f_s = \begin{cases} 30{,}000\ \varepsilon_s \ \text{(ksi)} & \text{for } \varepsilon_s \le 0.004 \\ 150 - \dfrac{0.028}{\varepsilon_s - 0.003} & \text{for } \varepsilon_s > 0.004 \end{cases} \tag{5.47}$$

5.5 Nonlinear Section Analysis

5.5.1 Basic Assumptions and Formulations

The main purpose of section analysis is to study the moment-thrust-curvature behavior. In a nonlinear section analysis the following assumptions are usually made:

- Plane section before bending remains plane after bending.
- Shear and torsional deformation is negligible.
- Stress–strain relationships for concrete and steel are given.
- For reinforced concrete, a prefect bond between concrete and steel rebar is assumed.

The mathematical formulas used in the section analysis are (Figure 5.10)

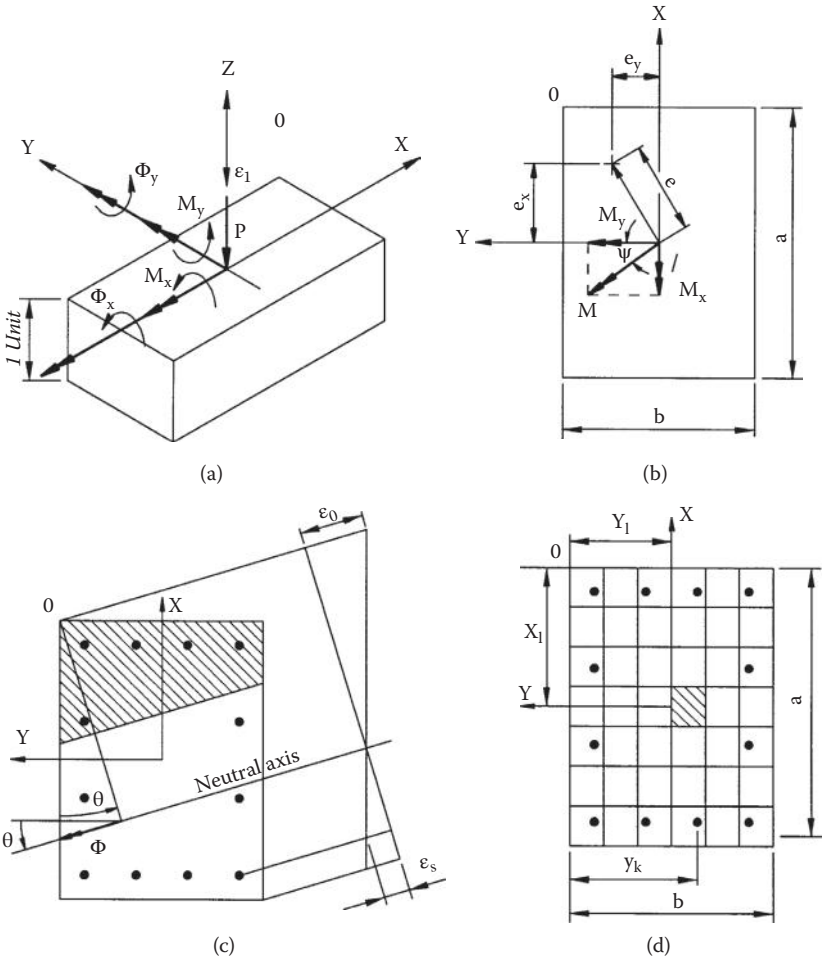

FIGURE 5.10 Moment-curvature-strain of cross-section.

Compatibility equations

$$\varphi_x = \varepsilon / y \tag{5.48}$$

$$\varphi_y = \varepsilon / x \tag{5.49}$$

Equilibrium equations

$$P = \int_A \sigma \, dA = \sum_{i=1}^{n} \sigma_i A_i \tag{5.50}$$

$$M_x = \int_A \sigma y \, dA = \sum_{i=1}^{n} \sigma_i y_i A_i \tag{5.51}$$

$$M_y = \int_A \sigma x \, dA = \sum_{i=1}^{n} \sigma_i x_i A_i \tag{5.52}$$

5.5.2 Modeling and Solution Procedures

For a reinforced concrete member, the cross section is divided into a proper number of concrete and steel layers or filaments representing the concrete and reinforcing steel as shown in Figure 5.10. Each concrete and steel layer or filament is assigned its corresponding stress–strain relationships. Confined and unconfined stress–strain relationships are used for the core concrete and for the cover concrete, respectively.

For a structural steel member, the section is divided into steel layers or filaments and a typical steel stress–strain relationship is used for tension and compact compression elements, and an equivalent stress–strain relationship with reduced yield stress and strain can be used for a noncompact compression element.

The analysis process starts by selecting a strain for the extreme concrete (or steel) fiber. Using this selected strain and assuming a section neutral axis (N.A) location, a linear strain profile is constructed and the corresponding section stresses and forces are computed. Section force equilibrium is then checked for the given axial load. By changing the location of the N.A, the process is repeated until equilibrium is satisfied. Once the equilibrium is satisfied for the assumed strain and the given axial load, the corresponding section moment and curvature are computed by Equations 5.48–5.52.

Moment-curvature (M–Φ) diagram for a given axial load is constructed by incrementing the extreme fiber strain and finding the corresponding moment and the associated curvature. An interaction diagram (M–P) relating axial load and the ultimate moment is constructed by incrementing the axial load and finding the corresponding ultimate moment using the above procedure.

For a reinforced concrete section, the yield moment is usually defined as the section moment at onset of yielding of the tension reinforcing steel. The ultimate moment is defined as the moment at peak moment capacity. The ultimate curvature is usually defined as the curvature when the extreme concrete fiber strain reaches ultimate strain or when the reinforcing rebar reaches its ultimate (rupture) strain (whichever take place first). Figure 5.11a shows typical M–P–Φ curves for a reinforced concrete section.

For a simple steel section, such as rectangular, circular-solid and thin-walled circular section, a closed-form of M–P–Φ can be obtained using the elastic perfectly plastic stress–strain relations (Chen and Han, 2007; Chen and Atsuta, 2008). For all other commonly used steel section, numerical iteration techniques are used to obtain M–P–Φ curves. Figure 5.11b shows typical M–P–Φ curves for a wide-flange section.

5.5.3 Yield Surface Equations

The yield or failure surface concept has been conveniently used in inelastic analysis to describe the full plastification of steel and concrete sections under action of axial force combined with biaxial bending. This section will present several yield surface expressions for steel and concrete sections suitable for use in a nonlinear analysis.

5.5.3.1 Yield Surface Equations for Concrete Sections

The general interaction failure surface for a reinforced concrete section with biaxial bending, as shown in Figure 5.12a, can be approximated by a nondimensional interaction equation (Bresler, 1960):

$$\left(\frac{M_x}{M_{xo}}\right)^m + \left(\frac{M_y}{M_{yo}}\right)^n = 1.0 \tag{5.53}$$

where M_x and M_y are bending moments about x–x and y–y principal axes, respectively; M_{xo} and M_{yo} the uniaxial bending capacity about the x–x and y–y axes under axial load P. The exponents m and n depend on the reinforced concrete section properties and axial force. They can be determined by a numerical analysis or experiments. In general, the values of m and n usually range from 1.1 to 1.4 for low and moderate axial compression.

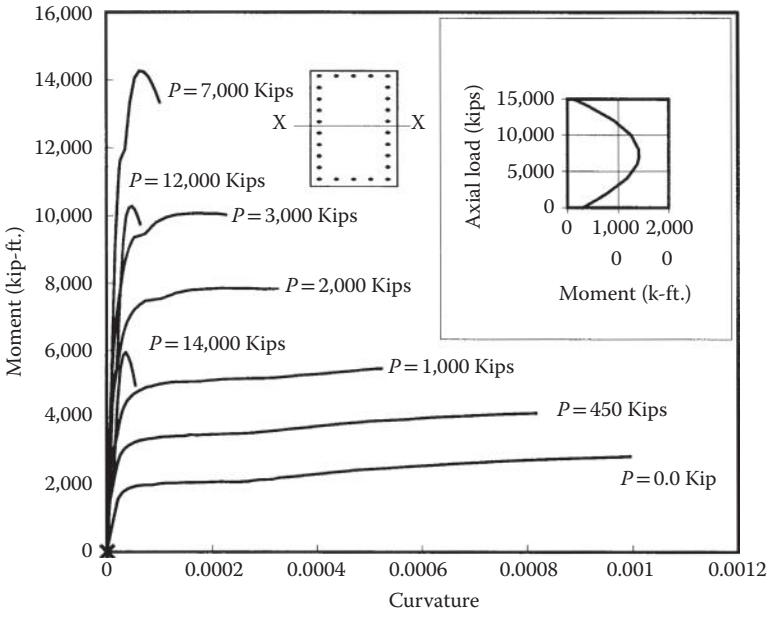

(a)

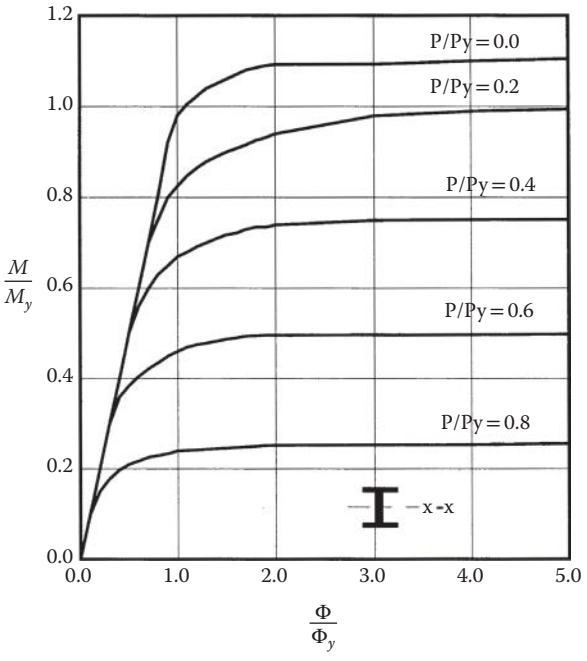

(b)

FIGURE 5.11 Moment-thrust-curvature curves.

5.5.3.2 Yield Surface Equation for Doubly Symmetrical Steel Sections

The general shape of yield surface for a doubly symmetrical steel section as shown in Figure 5.12b can be described approximately by the following general equation (Duan and Chen, 1990):

$$\left(\frac{M_x}{M_{pcx}}\right)^{\alpha_x} + \left(\frac{M_y}{M_{pcy}}\right)^{\alpha_y} = 1.0 \tag{5.54}$$

where M_{pcx} and M_{pcy} are the moment capacities about respective axes, reduced for the presence of axial load; they can be obtained by the following formulas:

$$M_{pcx} = M_{px}\left[1 - \left(\frac{P}{P_y}\right)^{\beta_x}\right] \tag{5.55}$$

$$M_{pcy} = M_{py}\left[1 - \left(\frac{P}{P_y}\right)^{\beta_y}\right] \tag{5.56}$$

where P is axial load; M_{px} and M_{py} the plastic moments about x–x and y–y principal axes, respectively; α_x, α_y, β_x, and β_y the parameters that depend on cross-sectional shapes and area distribution listed in Table 5.8.

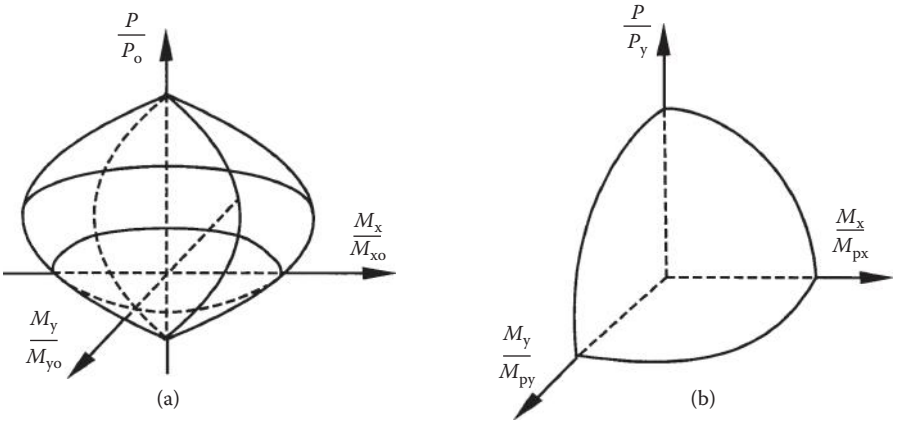

FIGURE 5.12 General yield surfaces.

TABLE 5.8 Parameters for Doubly Symmetrical Steel Sections

Section Types	α_x	α_y	β_x	β_y
Solid rectangular	$1.7 + 1.3\,(P/P_y)$	$1.7 + 1.3\,(P/P_y)$	2.0	2.0
Solid circular	2.0	2.0	2.1	2.1
I-shape	2.0	$1.2 + 2\,(P/P_y)$	1.3	$2 + 1.2\,(A_w/A_f)$
Thin-walled box	$1.7 + 1.5\,(P/P_y)$	$1.7 + 1.5\,(P/P_y)$	$2 - 0.5\,\bar{B} \geq 1.3$	$2 - 0.5\,\bar{B} \geq 1.3$
Thin-walled circular	2.0	2.0	1.75	1.75

where $\bar{B}$ is ratio of width to depth of box section with respect to bending axis

Equation 5.54 represents a smooth and convex surface in the three-dimensional stress–resultant space. It meets all special conditions and is easy to implement in a computer-based structural analysis.

Orbison (1982) developed the following equation for a wide-flange section by trial and error and curve fitting:

$$1.15\left(\frac{P}{P_y}\right)^2+\left(\frac{M_x}{M_{\text{px}}}\right)^2+\left(\frac{M_y}{M_{\text{py}}}\right)^4+3.67\left(\frac{P}{P_y}\right)\left(\frac{M_x}{M_{\text{px}}}\right)^2$$
$$+3.0\left(\frac{P}{P_y}\right)^2\left(\frac{M_y}{M_{\text{py}}}\right)^2+4.65\left(\frac{M_x}{M_{\text{px}}}\right)^4\left(\frac{M_y}{M_{\text{py}}}\right)^2=1.0 \tag{5.57}$$

5.6 Nonlinear Frame Analysis

Both the first- and second-order inelastic frame analyses may be categorized into three types of analysis: (1) elastic-plastic hinge, (2) refined plastic hinge, and (3) distributed plasticity. This section will discuss the basic assumptions and applications of those analyses.

5.6.1 Elastic-Plastic Hinge Analysis

In an elastic-plastic hinge (lumped plasticity) analysis, material inelasticity is taken into account using concentrated "zero-length" plastic hinges. The traditional plastic hinge region is defined as a "zero-length" region (or a point) along the structure member that can rotate freely but maintain plastic moment capacity. When the section reaches its plastic capacity (e.g., the yield surface as shown in Figures 5.12 or 5.13), a plastic hinge is formed and element stiffness is adjusted (Levy et, al., 1997; King, et al., 1992). For regions in a framed member outside of the plastic hinge region, elastic behavior is assumed.

For a framed member subjected to end forces only, the elastic-plastic hinge method usually requires only one element per member making the method computationally efficient. It does not, however, accurately represent the distributed plasticity and associated *P*-δ effects. This analysis predicts an upper bound solution (see Figure 5.1).

5.6.2 Refined Plastic Hinge Analysis

In the refined plastic hinge analysis (Chen and Toma, 1994), a two-surface yield model considers the reduction of plastic moment capacity at the plastic hinge region because of the presence of axial force, and an effective tangent modulus accounts for the stiffness degradation because of distributed plasticity along a frame member. This analysis is similar to the elastic-plastic hinge analysis in efficiency and simplicity and also accounts for distributed plasticity. The approach has been developed for advanced design of steel frames, but detailed considerations for concrete structures still need to be developed.

5.6.3 Distributed Plasticity Analysis

Distributed plasticity analysis models the spread of inelasticity through the cross sections and along the length of the members. This is also referred to as plastic zone analysis, spread-of-plasticity analysis, and elasto-plastic analysis by various researchers. In this analysis, a member needs to be subdivided into several elements along its length to model the inelastic behavior more accurately. There are two main approaches that have been successfully used to model plastification of members in a second-order distributed plasticity analysis:

1. Cross sectional behavior is described as an input for the analysis by means of moment-thrust-curvature (*M*–*P*–Φ) and moment-trust-axial strain (*M*–*P*–ε) relations that may be obtained separately from

section analysis as discussed in Section 5.5 or approximated by close-form expressions (Chen and Atsuta, 2008).
2. Cross sections are subdivided into elemental areas and the state of stresses and strains are traced explicitly using the proper stress–strain relations for all elements during the analysis.

In summary, the elastic-plastic hinge analysis is the simplest one but provides an upper bound solution. Distributed plasticity analysis is considered the most accurate and is generally computationally intensive for larger and complex structures. Refined plastic hinge analysis seems to be an alternative that can reasonably achieve both computational efficiency and accuracy.

5.6.4 Modeling of Standard Ordinary Bridges

The *Guidelines for Nonlinear Analysis for Bridge Structures in California* (Aviram et al., 2008) presents a collection of general recommendations for the modeling and analysis of highway bridges and overpasses subjected to earthquake ground motions, required for the design or evaluation of the capacity and ductility of critical bridge components and systems. Figure 5.13 summarizes the primary modeling aspects of the major components of a Standard Ordinary Bridge in California (Aviram et al., 2008). Definition of Standard Ordinary Bridge in California is discussed in Chapter 15.

5.7 Nonlinear Analysis of Ordinary Bridges Crossing Fault-Rupture Zones

Recently, Goel and Chopra (2008, 2009a and 2009b) studied analysis of ordinary bridges crossing fault-rupture zones. The seismic demands for ordinary bridges crossing fault-rupture zones can be estimated by superposition of the peak values of the quasi-static and dynamic parts of the response as shown in the following equation:

$$r^{t} = r^{t}_{o+g} + r_{o} \tag{5.58}$$

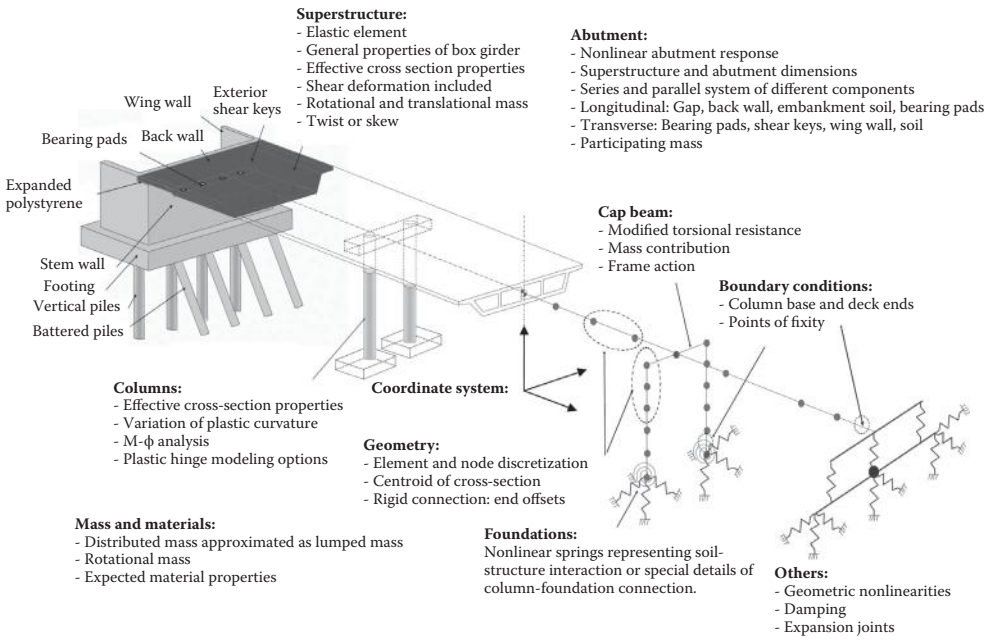

FIGURE 5.13 Primary modeling aspects of a standard ordinary bridge.

where r_{o+g} is peak value of the quasi-static part of the response including the effects of gravity loads, and r_o is peak value of the dynamic part of the response.

The peak value of the quasi-static part of the response, including the effects of gravity loads, is computed by nonlinear static analysis of the bridge because of peak ground displacements applied simultaneously at all supports. The peak value of the dynamic part of the response can be estimated by modal pushover analysis, linear dynamic analysis, and linear static analysis. The linear static analysis procedure, which is much simpler than the other two approximate procedures, is recommended for practical analysis of "ordinary" bridges because it eliminates the need for mode shapes and vibration periods of the bridge.

5.8 Practical Applications

In this section, the concept and procedures of displacement-based design and the bases of the static push-over analysis are discussed briefly. Two real bridges are analyzed as examples to illustrate practical application of the nonlinear static push-over analysis approach for bridge seismic design. Additional examples and detailed discussions of nonlinear bridge analysis can be found in the established literature (Priestley et al., 1996; Aschheim et al., 1997) and Chapter 6.

5.8.1 Displacement-Based Seismic Design

5.8.1.1 Basic Concept

In recent years, displacement-based design has been used in the bridge seismic design practice as a viable alternative approach to strength-based design. Using displacements rather than forces as a measurement of earthquake damage allows a structure to fulfill the required function (damage-control limit state) under specified earthquake loads.

In a common design procedure, one starts by proportioning the structure for strength and stiffness, performs the appropriate analysis and then checks the displacement ductility demand against available capacity. This procedure has been widely used in bridge seismic design in California since 1994. Alternatively, one could start with the selection of a target displacement, perform the analysis and then determine strength and stiffness to achieve the design level displacement. Strength and Stiffness do not enter this process as variables; they are the end results (Priestley, 1993; Kowalsky et al., 1994). Chapter 6 presents a detailed discussion about direct displacement-based seismic design.

In displacement-based design, the designer needs to clearly define a criterion for acceptable structural deformation (damage) based on postearthquake performance requirements and the available deformation capacity. Such criteria are based on many factors including structural type and importance.

5.8.1.2 Available Ultimate Deformation Capacity

Because structural survival without collapse is commonly adopted as a seismic design criterion for ordinary bridges, inelastic structural response, and some degradation in strength can be expected under seismic loads. Figure 5.14 shows a typical load-deformation curve. A gradual degrading response as shown in Figure 5.14 can be because of factors such as P-Δ effects and/or plastic hinge formulation. The available ultimate deformation capacity should be based on how great a reduction (degradation) in structure load-carrying capacity response can be tolerated (Park and Paulay, 1975).

In general, the available ultimate deformation capacity can be referred to as the deformation that a structure can undergo without losing significant load-carrying capacity (Duan and Cooper, 1995). It is, therefore, reasonable to define available ultimate deformation as that deformation when the load-carrying capacity has been reduced by an acceptable amount after the peak load, say 20% as shown in Figure 5.14. This acceptable reduction amount may vary depending on required performance criteria of the particular case.

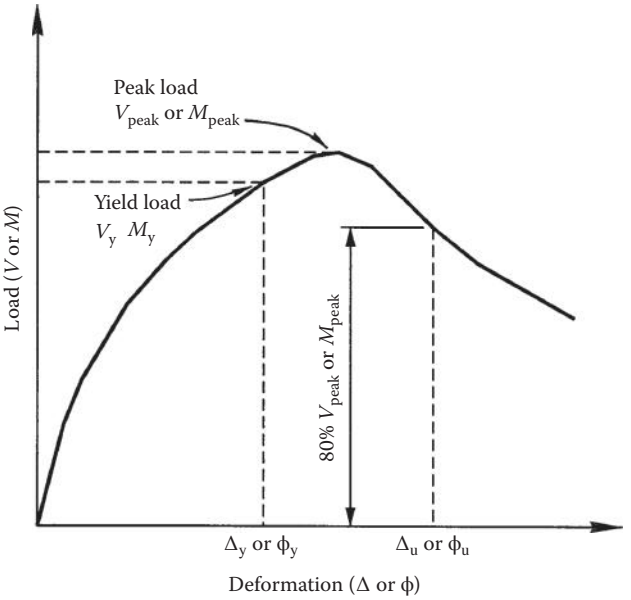

FIGURE 5.14 Load-deformation curves.

The available deformation capacity based on the design criteria requirements needs not correspond to the ultimate member or system deformation capacity. For a particular member cross section, the ultimate deformation in terms of the curvature depends on the section's shape, material properties and loading conditions (i.e., axial load, biaxial bending) and corresponds to the condition when the section extreme fiber reaches its ultimate strain (ε_{cu} for concrete and ε_{sp} for steel). The available ultimate curvature capacity φ_u can be chosen as the curvature that corresponds to the condition when section moment capacity response reduces by say 20% from the peak moment.

For a framed structure system, the ultimate deformation in terms of the lateral displacement depends on both structural configurations, section behavior and loading conditions, and corresponds to a failure state of the frame system when a collapse mechanism forms. The available lateral displacement capacity Δ_u can be chosen as the displacement that corresponds to condition when lateral load carrying capacity reduces by some amount, say 20% from its peak load. In current seismic design practice in California, the available frame lateral displacement capacity corresponds to the first plastic hinge reaching its ultimate rotational capacity.

5.8.1.3 Analysis Procedures

Seismic analysis procedures used in displacement-based design can be divided into three groups:

1. Group I: Seismic displacement and force demands are estimated from an elastic dynamic time history or a response spectrum analysis with effective section properties. For concrete structures, cracked section properties are usually used to determine displacement demands and gross section properties are used to determine force demands. Strength capacity is evaluated from nonlinear section analysis or other code specified methods and displacement capacity is obtained from a static or cyclic nonlinear push-over analysis.
2. Group II: Seismic displacement demand is obtained from specified response spectrum and initial effective stiffness or a substitute structural model (Priestley, 1993) considering both the effective stiffness and the effective damping. Effective stiffness and displacement capacity are estimated from a nonlinear static or cyclic push-over analysis.

3. Group III: A nonlinear inelastic dynamic time history analysis is performed. Bridge assessment is based on displacement (damage) comparisons between analysis results and the given acceptance criteria. This group of analyses is complex and time consuming and used only for important structures.

5.8.2 Static Push-Over Analysis

In lieu of a nonlinear time history dynamic analysis, bridge engineers in recent years have used static push-over analyses as an effective and simple alternative when assessing the performance of existing or new bridge structures under seismic loads. Given the proper conditions, this approximate alternative can be as reliable as the more accurate and complex ones. The primary goal of such analysis is to determine the displacement or ductility capacity, which is then compared with displacement or ductility demand obtained for most cases from linear dynamic analysis with effective section properties. However, under certain conditions, this push-over analysis can also be used in the assessment of the displacement demand as will be illustrated in the examples to follow.

In this analysis, a stand-alone portion from a bridge structure (such as bent-frame with single or multi-columns) is isolated and statically analyzed taking into account whatever nonlinear behavior deemed necessarily (most importantly and commonly, material and geometric nonlinear behavior). The analysis can utilize any of the modeling methods discussed in Section 5.6 but plastic hinge or distributed plasticity model are commonly used. The analytical frame model is first subjected to the applied tributary gravity load and then is pushed laterally in several load (or displacement) increments until a collapse mechanism or a given failure criterion is reached. Figure 5.15 shows a flow chart outlining a procedure using static push-over analysis in seismic design and retrofit evaluation.

When applying static push-over analysis in seismic design, it is assumed that such analysis can predicts with reasonable accuracy the dynamic lateral load-displacement behavior envelope, and that an elastic acceleration response spectrum (ARS) can provide the best means for establishing required structural performance.

5.8.3 Example 1—Reinforced Concrete Multicolumn Bent Frame with *P*-Δ Effects

5.8.3.1 Problem Statement

The as-built details of a reinforced concrete bridge bent frame consisting of a bent cap beam and two circular columns supported on pile foundations are shown in Figure 5.16. An as-built unconfined concrete strength of 5 ksi (34.5 MPa) and steel strength of 40 ksi (275.8 MPa) are assumed. Owing to lack of adequate column transverse reinforcement, the columns are retrofitted with 0.5 in. (12.7 mm) thick steel jacket. The bottom of the column is assumed to be fixed, however, since the footing lacks top mat and shear reinforcement, a column bottom with a pinned connection is also to be considered. The frame is supported on a stiff pile-foundation and the soil-foundation-structure interaction is to be ignored.

Use static nonlinear push-over analysis to study the extent of *P*-Δ effect on the lateral response of the bent frame when the columns are assumed to be fixed at the base in one case and pinned in another case. Assume the columns are retrofitted with steel jacket in both cases and determine if the footing retrofit is also required. Use 0.7 g ground acceleration and the ARS spectrum with 5% damping as shown in Figure 5.17.

5.8.3.2 Analysis Procedure

The idealized bent frame consisting of the cap beam and the two retrofitted column members is discretized into a finite number of beam elements connected at joints as shown in Figure 5.18. The idealized column and cap beam cross sections are divided into several concrete layers and reinforcing steel layers as shown. Two different concrete material properties are used for the column and cap beam

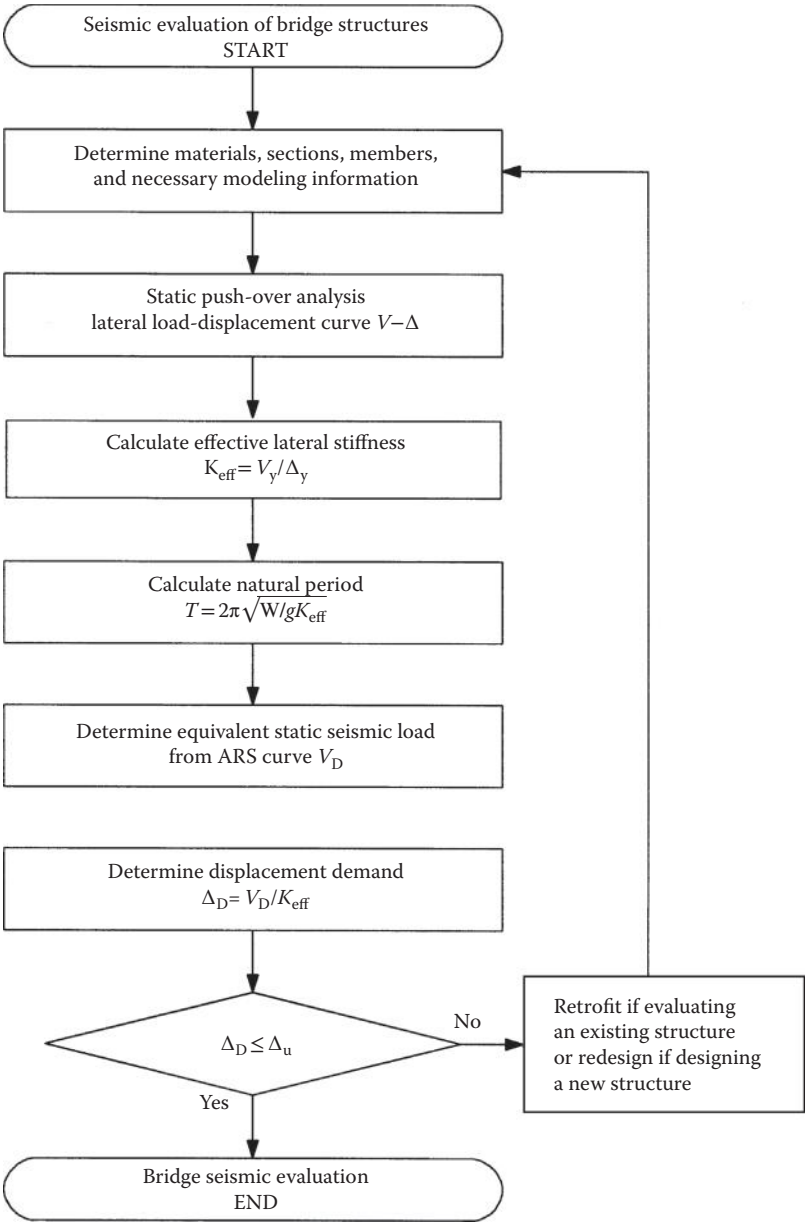

FIGURE 5.15 An alternative procedure for bridge seismic evaluation.

cross sections. The column concrete properties incorporated the increase in concrete ultimate stress and strain because of the confinement provided by the steel jacket. In this study the column confined ultimate concrete compressive stress and strain of 7.5 ksi (51.7 MPa) and 0.085 are used, respectively. The total tributary superstructure dead load of 1160 kips (5160 kN) is applied uniformly along the length of the cap beam. The frame is pushed laterally in several load increments until failure is reached.

For this study, failure is defined as the limit state when one of the following conditions first takes place:

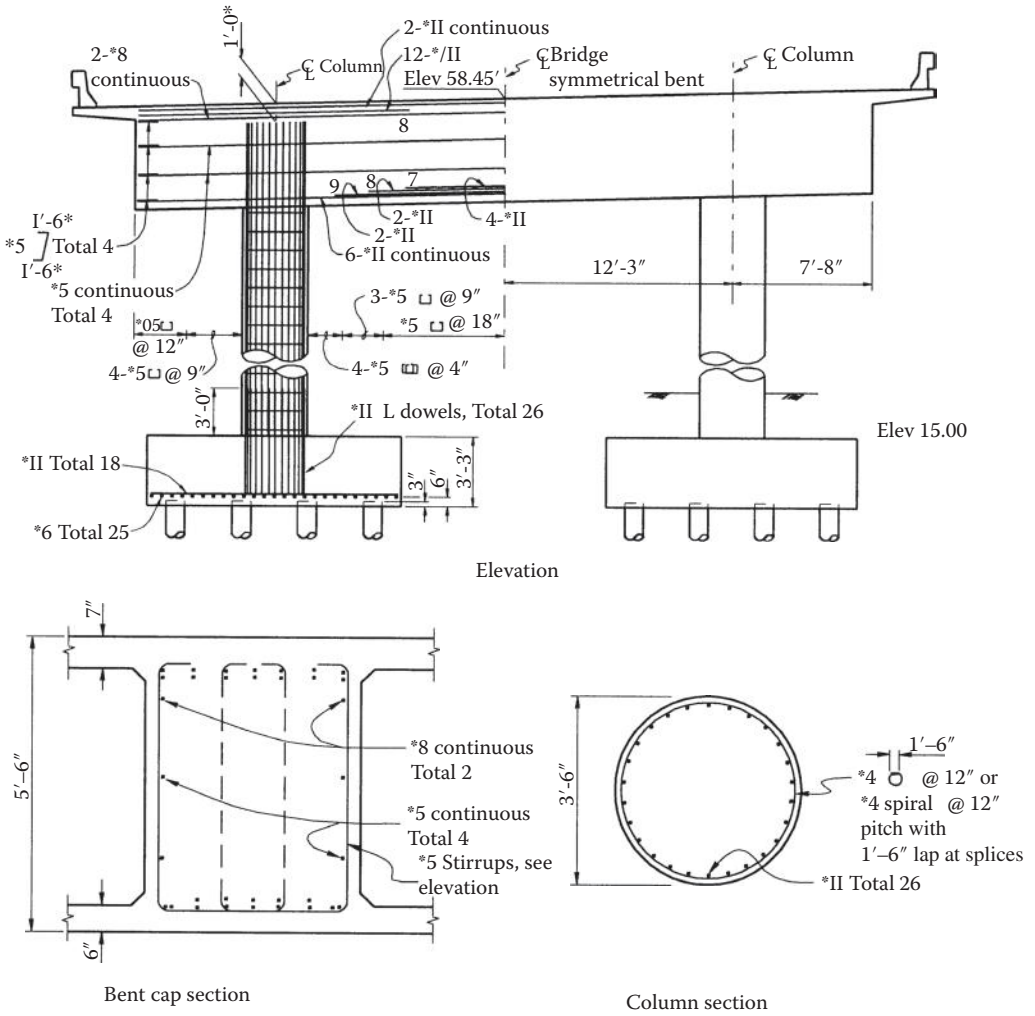

FIGURE 5.16 As-built plan—example 5.1.

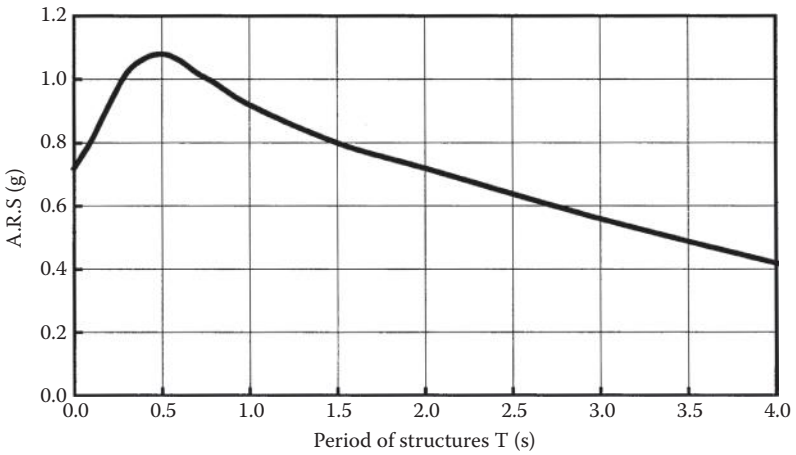

FIGURE 5.17 Specific ARS curve—example 5.1.

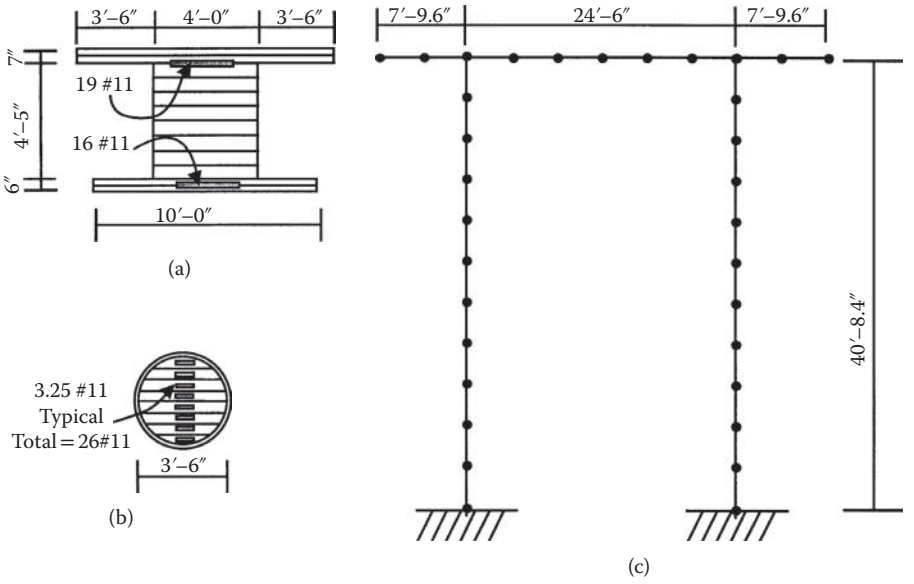

FIGURE 5.18 Analytical model—example 5.1.

1. A concrete layer strain reaches the ultimate compressive strain at any element section.
2. A steel layer strain reaches the rupture strain at any element section.
3. A 20% reduction from peak lateral load of the lateral load response curve (this condition is particularly useful when considering *P*-Δ).

The lateral displacement corresponding to this limit state at the top of the column defines the frame failure (available) displacement capacity.

A nonlinear analysis computer program NTFrame (Akkari, 1993a and 1993b) is used for the push-over analysis. The program is based on distributed plasticity model and the *P*-Δ effect is incorporated in the model second-order member stiffness formulation.

5.8.3.3 Discussion of the Results

The resulting frame lateral load versus displacement responses are shown in Figure 5.19 for the cases when the bottom of column is fixed and pinned. Both cases will be discussed next followed by concluding remarks.

Column fixed at bottom case: In this case the column base is modeled with a fixed connection. The lateral response with and without the *P*-Δ effect is shown in Figure 5.19a. The sharp drop in the response curve is because of several extreme concrete layers reaching their ultimate compressive strain at the top of the column. The effect of *P*-Δ at failure can be seen to be considerable but not as severe as shown in Figure 5.19b with the pinned connection. Comparing Figures 5.19a and b, one can observe that fixing the bottom of the column resulted in stiffer structural response.

Using the curve shown in Figure 5.19a, the displacement demand for the fixed column case with *P*-Δ effect is calculated as follows:

Step 1: Calculate the initial effective stiffness K_{eff}

The computer results showed that the first column extreme longitudinal rebar reached yield at lateral force of 928 kips(4128 kN) at a corresponding lateral yield displacement of 17 in. (431.8 mm), therefore

$K_{eff} = 928/17 = 55$ k/in. (9.63 kN/mm).

Step 2: Calculate an approximate fundamental period T_f

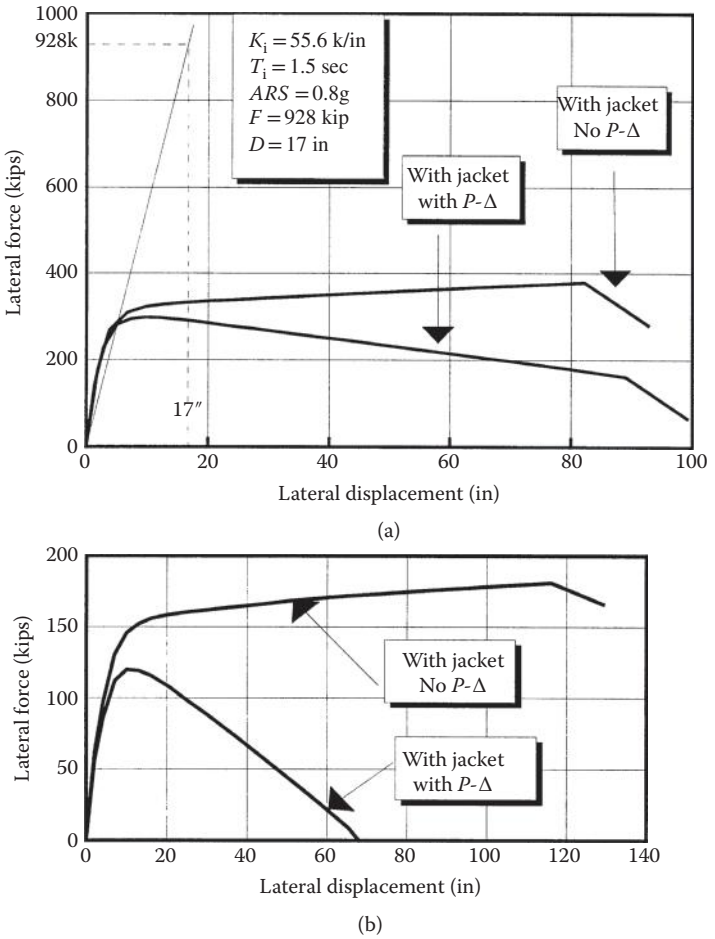

FIGURE 5.19 Lateral load versus displacement responses—example 5.1.

$$T_f = 0.32\sqrt{\frac{W}{K_{eff}}} = 0.32\sqrt{\frac{1160}{55}} = 1.5 \text{ s}$$

Step 3: Determine the damped elastic ARS at the site in g's.
Using the given site spectrum shown in Figure 5.17 and the above calculated period, the corresponding ARS for 5% damping is 0.8.

Step 4: Calculate the displacement demand D_d

$$D_d = \frac{\text{ARS}(W)}{K_{ef}} = \frac{0.8(1160)}{55} = 16.9 \text{ in.} \quad (429.3 \text{ mm})$$

(in this case the yield and demand displacements found to be practically equal).

In many of seismic design practice in California, the effect of P-Δ is usually ignored if the P-Δ moment is <20% of the design maximum moment capacity. Adopting this practice and assuming the reduction

in the moment is directly proportional to the reduction in the lateral force, one may conclude that at displacement demand of 16.9 in. (429.3 mm), the reduction in strength (lateral force) is <20% and as a result the effects of *P*-Δ is negligible.

The displacement demand of 16.9 in. (429.3 mm) is less than the failure state displacement capacity of approximately 40 in. (1016 mm) (based on a 20% lateral load reduction from the peak). Note that for the fixed bottom case with *P*-Δ, the displacement when the extreme concrete layer at the top of the column reached its ultimate compressive strain, is approximately 90 in. (2286 mm).

Column pinned at bottom case: In this case the column bottom is modeled with a pinned connection. Note that the pinned condition assumption is based on the belief that in the event of a maximum credible earthquake the column/footing connection would quickly degenerate (degrade) and behave like a pinned connection. The resulting lateral responses with and without the *P*-Δ effect are shown in Figure 5.19b. In this case the effects of *P*-Δ are shown to be quite substantial.

When considering the response without the *P*-Δ one obtains a displacement demand of 38 in. (965.2 mm) (based on a calculated initial stiffness of 18.5 k/in. (3.24 kN/mm) and a corresponding structure period of 2.5 seconds). This displacement demand is well below the ultimate (at failure) displacement capacity of approximately 115 in. (2921 mm). As a result one would conclude that the retrofit measure of placing a steel jacket around the column with no footing retrofit is adequate.

The actual response, however, is the one that includes the *P*-Δ effect. In this case the effect of *P*-Δ resulted in a slight change in initial stiffness and frame period (15.8 k/in. (2.77 kN/mm) and 2.7 seconds, respectively). However beyond the initial stages, the effects are quite severe on the load displacement response. The failure mode in this case will most likely be controlled by dynamic instability of the frame. MacRae et al. (1993) performed analytical studies of the effect of *P*-Δ on single degree of freedom bilinear oscillators (i.e., single-column frame) and proposed some procedures on how to obtain a limiting value at which the structure becomes dynamically unstable. The process requires the generation of the proper hysteresis loops and the determination of what is termed "the effective bilinear stiffness factor." Setting aside the frame dynamic instability issue, the calculated initial stiffness displacement demand is approximately 38 in. (965.2 mm) and the displacement capacity at 20% reduction from peak load is 24 in. (609.6 mm).

Referring to the curves with *P*-Δ in Figure 5.19, it is of interest to mention, and as pointed out by Mahin and Boroschek (1991), that continued pushing of the frame will eventually lead to a stage when the frame structure becomes statically unstable. At that stage the forces induced by the *P*-Δ effect overcome the mechanical resistance of the structure. Note that the point when the curve with *P*-Δ effect intersects the displacement axis in (as shown Figure 5.19b) will determine the lateral displacement at which the structure becomes statically unstable. Dynamic instability limits can be 20%–70% less than the static instability depending on the ground motion and structural characteristic (Mahin and Boroschek, 1991). Note that dynamic instability is assumed not to be a controlling factor in the previous case with fixed column.

In conclusion, if the as-built column-footing connection can support the expected column moment obtained from the fixed condition case, (which is unlikely) then retrofitting the column with steel jacket without footing retrofit is adequate. Otherwise, the footing should also be retrofitted to reduce (limit) the effect of *P*-Δ.

It should be pointed out that in this example the analysis is terminated at the completion of the first plastic hinge, (conservative) whereas in other types of push-over analysis such as event-to-event analysis, the engineer may choose to further push the frame till it forms a collapse mechanism. Also, unlike the substitute structure procedure described by Priestly at al. (1996) in which both the effective system stiffness and damping ratio are adjusted (iterated) several times before final displacement demand is calculated, here only the initial effective stiffness and a constant specified structure damping are used.

As a final remark, the *P*-Δ effect in bridge analysis is normally assumed small and is usually ignored. This assumption is justified in most cases under normal loading conditions. However,

as this example is illustrated, under seismic loading, the *P*-Δ effect should be incorporated in the analysis, when large lateral displacements are expected before the structure reaches its assumed failure state. In the design of a new bridge the lateral displacement and the effect of *P*-Δ can be controlled. When assessing an existing bridge for possible seismic retrofit, accurate prediction of the lateral displacement with *P*-Δ effects can be an essential factor in determining the retrofit measures required.

5.8.4 Example 2—Steel Multicolumn Bent Frame Seismic Evaluation

5.8.4.1 Problem Statement

The as-built details of a steel bridge bent frame consisting of a bent cap plate girder and two built-up columns supported on a stiff pile-foundations as shown in Figure 5.20. Steel is Grade A36. Site specific displacement response spectra are given in Figure 5.21. For simplicity and illustration purposes, fixed bases of columns are assumed and the soil-foundation-structure interaction is ignored.

Evaluate lateral displacement capacity by using static nonlinear push-over analysis. Estimate seismic lateral displacement demands by using the substitute structure approach considering both the effective stiffness and the effective damping. The effective damping ξ can be calculated by Takeda's (1970) formula:

$$\xi = 0.05 + \frac{\left(1 - \frac{0.95}{\sqrt{\mu_{\Delta d}}} - 0.05\sqrt{\mu_{\Delta d}}\right)}{\pi} \tag{5.59}$$

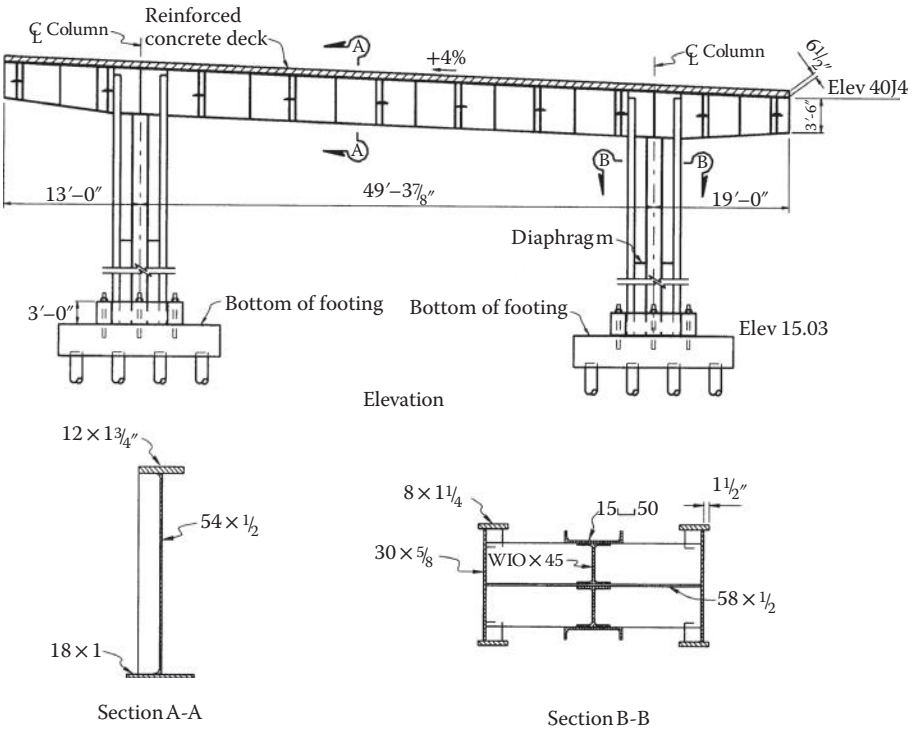

FIGURE 5.20 As-built plane—example 5.2.

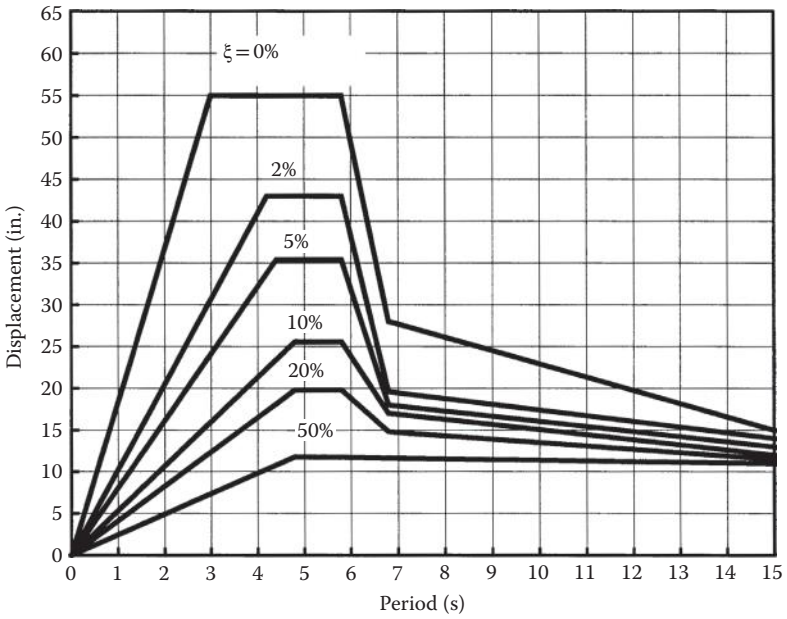

FIGURE 5.21 Specific ARS curves—example 5.2.

$$\mu_{\Delta d} = \frac{\Delta_{ud}}{\Delta_y} \tag{5.60}$$

where $\mu\Delta_d$ is displacement ductility demand; Δ_{ud} and Δ_y the displacement demand and yield displacement, respectively.

5.8.4.2 Analysis Modeling

The bent frame members are divided into several beam elements as shown in Figure 5.22. The properties of beam elements are defined by two sets of relationships for moment-curvature, axial force-strain, and torsion-twist for the cap beam and columns, respectively. The available ultimate curvature is assumed 20 times of yield curvature. The total tributary superstructure dead load of 880 kips (3914 kN) is applied at longitudinal girder locations. A lateral displacement is applied incrementally at the top of the bent column until a collapse mechanism of the bent frame is formed.

5.8.4.3 Displacement Capacity Evaluation

The displacement capacity evaluation is performed by push-over analysis using the ADINA (1994) analysis program. Large displacements are considered in the analysis. The resulting lateral load versus displacement response at the top of columns is shown in Figure 5.23. The sudden drops in the response curve are because of the several beam elements reaching their available ultimate curvatures. The yield displacement $\Delta_y = 1.25$ in. (31.8 mm) and the available ultimate displacement capacity (corresponding to 20% reduction from the peak lateral load) $\Delta_u = 4.8$ in. (121.9 mm) are obtained.

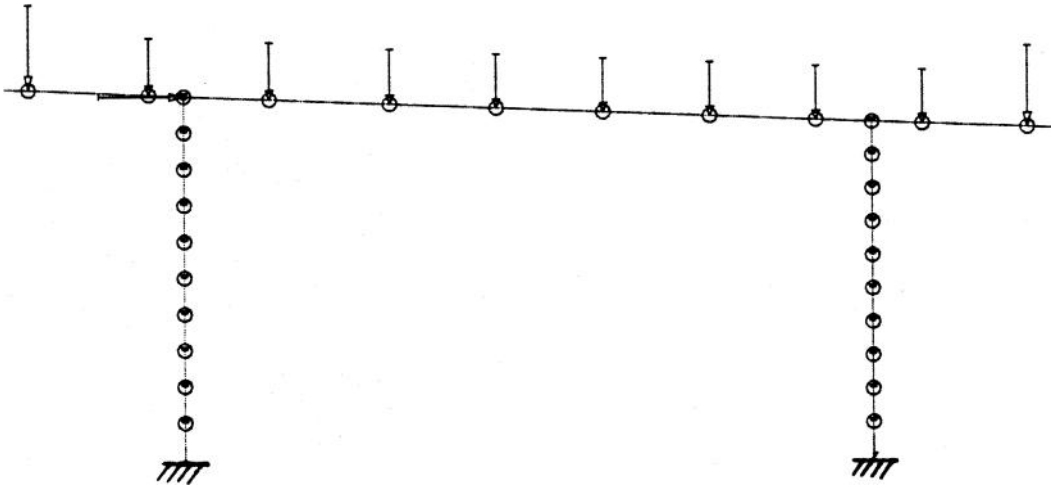

FIGURE 5.22 Analytical model—example 5.2.

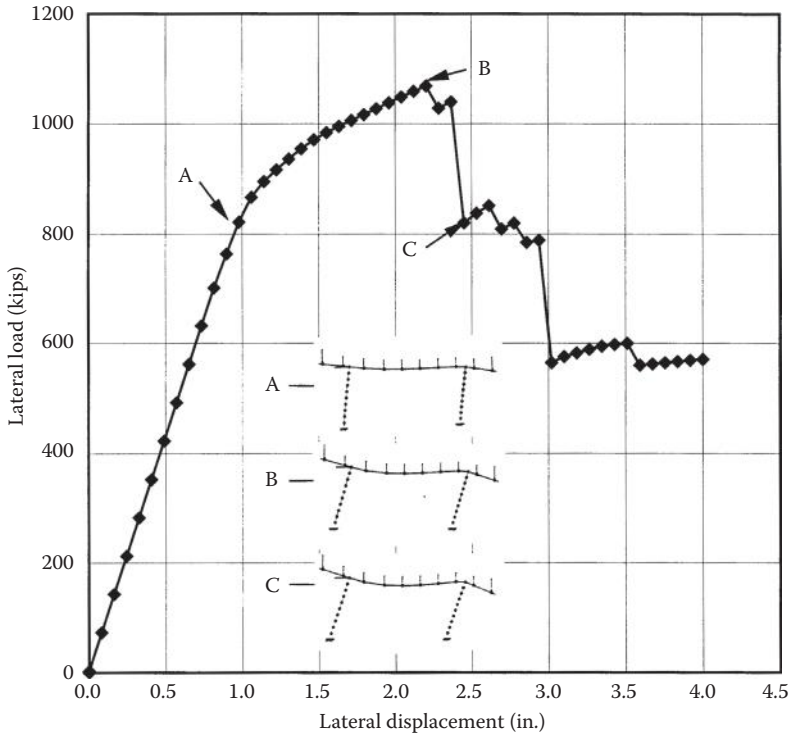

FIGURE 5.23 Lateral load versus displacement—example 5.2.

5.8.4.4 Displacement Demand Estimation

A substitute structure approach with the effective stiffness and effective damping will be used to evaluate displacement demand.

1. Assume $\Delta_{ud} = 4.8$ in. (121.9 mm), from Equations 5.58, 5.59, and Figure 5.21, we obtain

$$K_{eff} = \frac{\text{Lateral Load}}{\text{Displacement}} = \frac{740}{4.8} = 154.17 \text{ kips/in. } (27.0 \text{ kN/mm})$$

$$T_{ef} = \frac{1}{\pi}\sqrt{\frac{M}{gK_{eff}}} = 0.32\sqrt{\frac{W(\text{kips})}{K_{eff}(\text{kips/in.})}} = 0.32\sqrt{\frac{850}{154.17}} = 0.751 \text{ s}$$

$$\mu_{\Delta d} = \frac{\Delta_{ud}}{\Delta_y} = \frac{4.8}{1.25} = 3.84$$

$$\xi = 0.05 + \frac{\left(1 - \frac{0.95}{\sqrt{3.84}} - 0.05\sqrt{3.84}\right)}{\pi} = 0.183$$

From Figure 5.21, find $\Delta_d = 3$ in. $< \Delta_{ud} = 4.8$ in. (121.9 mm)

2. Try $\Delta_{ud} = 3$ in. (76.2 mm), from Figure 5.21, Equations 5.59 and 5.60, we obtain

$$K_{eff} = \frac{850}{3} = 283.3 \text{ kips/in. } (49.61 \text{ kN/mm})$$

$$T_{eff} = 0.32\sqrt{\frac{W(\text{kips})}{K_{eff}(\text{kips/in.})}} = 0.32\sqrt{\frac{850}{283.3}} = 0.554 \text{ s}$$

$$\mu_{\Delta d} = \frac{\Delta_{ud}}{\Delta_y} = \frac{3}{1.25} = 2.4$$

$$\xi = 0.05 + \frac{\left(1 - \frac{0.95}{\sqrt{2.4}} - 0.05\sqrt{2.4}\right)}{\pi} = 0.15$$

From Figure 5.21, find $\Delta_d = 2.5$ in. $< \Delta_{ud} = 3$ in. (76.2 mm)

3. Try $\Delta_{ud} = 2.5$ in. (63.5 mm), from Figure 5.21, Equations 5.58 and 5.59, we obtain

$$K_{eff} = \frac{800}{2.5} = 320 \text{ kips/in. } (56.04 \text{ kN/mm})$$

$$T_{eff} = 0.32\sqrt{\frac{W(\text{kips})}{K_{eff}(\text{kips/in.})}} = 0.32\sqrt{\frac{800}{320}} = 0.51 \text{ s}$$

$$\mu_{\Delta d} = \frac{\Delta_{ud}}{\Delta_y} = \frac{2.5}{1.25} = 2$$

$$\xi = 0.05 + \frac{\left(1 - \frac{0.95}{\sqrt{2}} - 0.05\sqrt{2}\right)}{\pi} = 0.13$$

From Figure 5.21, find $\Delta_d = 2.45$ in. (62.2 mm) close to $\Delta_{ud} = 2.5$ in. (63.5 mm) O.K.
Displacement demand $\Delta_d = 2.45$ in. (62.2 mm).

5.8.4.5 Discussion

It can be seen that the displacement demand Δ_d of 2.45 in. (62.2 mm) is less than the available ultimate displacement capacity of $\Delta_u = 4.8$ in. (121.9 mm). It should be pointed out that in the actual seismic evaluation of this frame, the flexibility of the steel column to the footing bolted connection should be considered.

5.9 Summary

General guidelines for nonlinear static analysis for bridge structures are presented. Basic formulations of geometric and material nonlinearity for section and frame analysis are summarized. Practical applications are illustrated by two examples of static nonlinear push-over analysis in bridge seismic design. For nonstandard and important bridges, engineers are encouraged to pay special attentions on bridge structures with greater geometric irregularities or high degree of nonlinear actions such as: modeling of backbone curves for the longitudinal, transverse, and vertical response of the abutments, participating mass of the adjacent soil, and associated damping properties of the system, soil-structure interaction effects for the abutments and column foundations, as well as the effect of nonlinear foundation springs and degree of semi-rigidity of column bases on the overall seismic demand and structural response of the bridge.

References

ADINA. 1994. *ADINA-IN for ADINA Users Manual*. ADINA R & D, Inc., Watertown, MA.

Akkari, M. M. 1993a. Nonlinear Push-over Analysis of Reinforced and Prestressed Concrete Frames. *Structure Notes*, State of California, Department of Transportation, Sacramento, CA.

Akkari, M. M. 1993b. Nonlinear Push-over Analysis With P-Delta Effects. *Structure Notes*, State of California, Department of Transportation, Sacramento, CA.

Allen, H. G. and Bulson, P. S. 1980. *Background of Buckling*, McGraw-Hill, UK.

Arici, M. and Granata, M. F. 2005. A General Method for Nonlinear Analysis of Bridge Structures. *Bridge Struct.*, 1(3), 223–244.

Aschheim, M., Moehle, J. P., and Mahin S. A. 1997. *Design and Evaluation of Reinforced Concrete Bridges for Seismic Resistance*, Report, UCB/EERC-97/04, University of California, Berkeley, CA.

Aviram, A., Mackie, K. R., and Stojadinović, B. 2008. Guidelines for Nonlinear Analysis of Bridge Structures in California. *Report UCB/PEER 2008/03*, Pacific Earthquake Engineering Research Center, University of California, Berkeley, CA.

Bathe, K. J. 1996. *Finite Element Procedures*, Prentice Hall Engineering, Science & Math, Englewood Cliffs, NJ.

Bresler, B. 1960. Design Criteria for Reinforced Concrete Columns under Axial Load and Biaxial Bending. *Journal ACI*, 57(6), 481–490.

Chai, Y. H., Priestely, M. J. N., and Seible, F. 1990. Flexural Retrofit of Circular Reinforced Bridge Columns by Steel Jacketing, *Report No. SSRP-91/05*, University of California, San Diego, CA.

Chen, W. F. 2007. *Plasticity in Reinforced Concrete*, J. Ross Publishing, Inc., Fort Lauderdale, FL.

Chen, W. F. and Atsuta, T. 2008. *Theory of Beam-Columns* (Vol. 1 and 2). J. Ross Publishing, Inc., Fort Lauderdale, FL.

Chen, W. F. and Han, D. J. 2007. *Plasticity for Structural Engineers*. J. Ross Publishing, Inc., Fort Lauderdale, FL.

Chen, W.F. and Lui, E. M. 1987. *Structural Stability: Theory and Implementation*. Elsevier, New York, NY.

Chen, W. F. and Toma, S. 1994. *Advanced Analysis of Steel Frames*, CRC Press, Boca Raton, FL, 1994.

Chopra, A. K. 2007. *Dynamics of Structures: Theory and Applications to Earthquake Engineering* (3rd Edition). Prentice-Hall Inc., Englewood Cliffs, NJ.

Clough, R. W. and Penzien, J. 1993. *Dynamics of Structures* (2nd Edition). McGraw-Hill Book Company, New York, NY.

Duan, L. and Chen, W. F. 1990. A Yield Surface Equation for Doubly Symmetrical Section. *Eng. Struct*. 12(2), 114–119.

Duan, L. and Cooper, T. R. 1995. Displacement Ductility Capacity of Reinforced Concrete Columns. *ACI Concrete Int*. 17(11), 61–65.

Ekhande, S. G., Selvappalam, M., and Madugula, M. K. S. 1989. Stability Functions for Three-Dimensional Beam-Column. *J. Struct. Eng*. ASCE, 115(2), 467–479.

Fung, Y. C., 1994. *First Course in Continuum Mechanics* (3rd Edition), Prentice-Hall Engineering, Science & Math, Englewood Cliffs, NJ.

Goel, R. K. and Chopra, A. K. 2008. Analysis of Ordinary Bridges Crossing Fault-Rupture Zones. *Report. No. UCB/EERC-2008/01*, Earthquake Engineering Research Center, University of California, Berkeley, CA.

Goel, R. K. and Chopra, A. K. 2009a. Linear Analysis of Ordinary Bridges Crossing Fault-Rupture Zones. *J. Bridge Eng*. 14(3), 203–215.

Goel, R. K. and Chopra, A. K. 2009b. Nonlinear Analysis of Ordinary Bridges Crossing Fault Rupture Zones. *J. Bridge Eng*. 14(3), 216–244.

Goto, Y. and Chen, W. F. 1987. Second-Order Elastic Analysis for Frame Design. *J. Struct. Eng*., ASCE, 113(7), 1501–1519.

Hognestad, E. 1951. *A Study of Combined Bending and Axial Load in Reinforced Concrete Members*. University of Illinois Engineering Experimental Station, Bulletin Series No. 399, Urbana, IL.

Holzer, S. M., Baker, R. M., and Somers, A. E. 1975. *SINDER: A Computer Code for General Analysis of Two-Dimensional Reinforced Concrete Structures*. AFWL-TR-74-228, Vol.1, Air Force Weapons Laboratory, New Mexico.

Hoshikuma, J., Kawashima, K., Nagaya, K., and Taylor, A. W. 1997. Stress-Strain Model for Confined Reinforced Concrete in Bridge Piers. *J. Struct. Eng*. ASCE, 123(5), 624–633.

Kent, D.C. and Park, R. 1971. Flexural Members with Confined Concrete. *J. Struct. Div*. ASCE, 97(ST7), 1969–1990.

King, W. S., White, D. W., and Chen, W. F. 1992. Second-Order Inelastic Analysis Methods for Steel-Frame Design. *J. Struct. Eng*. ASCE, 118(2), 408–428.

Kowalsky, M. J., Priestley, M. J. N., and MacRae G. A. 1994. Displacement-Based Design. *Report No. SSRP-94/16*, University of California, San Diego, CA.

Levy, R., Joseph, F., and Spillers, W. R. 1997. Member Stiffness with Offset Hinges. *J. Struct. Eng*. ASCE, 123(4), 527–529.

MacRae, G. A., Priestly, M. J. N., and Tao, J. 1993. P-Delta Design in Seismic Regions. *Report No. SSRP-93/05*, University of California, San Diego, CA.

Mahin, S. and Boroschek, R. 1991. *Influence of Geometric Nonlinearities on the seismic Response and Design of Bridge Structures*. Background Report to California Department of Transportation, Division of Structures, Sacramento, CA.

Mander, J. B., Priestley, M. J. N., and Park, R. 1988a. Theoretical Stress-Strain Model for Confined Concrete. *J. Struct. Eng*. ASCE, 114(8), 1804–1826.

Mander, J. B., Priestley, M.J.N., and Park, R. 1988b. Observed Stress-Strain Behavior of Confined Concrete. *J. Struct. Eng*. ASCE, 114(8), 1827–1849.

Mander, J. B., Priestley, M.J.N., and Park, R. 1984. Seismic Design of Bridge Piers. *Research Report No. 84-2*, University of Canterbury, New Zealand.

Orbison, J. G. 1982. *Nonlinear Static Analysis of Three-dimensional Steel Frames*, Department of Structural Engineering, Cornell University, NY.

Park, R. and Paulay, T. 1975. *Reinforced Concrete Structures*, John Wiley & Sons, New York, NY.

PCI. 2011. *PCI Bridge Design Manual* (3rd Edition), Prestressed Concrete Institute, Chicago, IL.

Popovics, S. 1970. A Review of Stress-Strain Relationships for Concrete. *J. ACI*, 67(3), 243–248.

Powell, G.H. 1997. Concepts and Principles for the Applications of Nonlinear Structural Analysis in Bridge Design. *Report No. UCB/SEMM-97/08*, Department of Civil Engineering, University of California, Berkeley, CA.

Priestley, M. J. N. 1993. Myths and Fallacies in Earthquake Engineering - Conflicts Between Design and Reality. In *Proceedings of Tom Paulay Symposium—Recent Development in Lateral Force Transfer in Buildings*, University of California, San Diego, CA.

Priestley, M. J. N., Seible, F., and Calvi, G. M. 1996. *Seismic Design and Retrofit of Bridges*, John Wiley & Sons, Inc., New York, NY.

Schilling, C. G. 1983. Buckling of One Story Frames. *AISC Engrg. J*. 2, 49–57.

Takeda, T., Sozen, M. A., and Nielsen, N. N. 1970. Reinforced Concrete Response to Simulated Earthquakes. *J. Struct. Div*. ASCE, 96(ST12), 2557–2573.

Vebo, A. and Ghali, A. 1977. Moment-Curvature Relations of Reinforced Concrete Slab. *J. Struct. Div*., ASCE, 103(ST3), 515–531.

Wang, W. C. and Duan, L. 1981. The Stress-Strain Relationship for Concrete. *J. Taiyuan Inst. Technol*., 1, 125–138.

White, D.W. and McGuire, W. 1985. Method of Analysis in LRFD. *Reprints of ASCE Structure Engineering Congress '85*, Chicago, IL.

William, K.J. and Warnke, E. P. 1975. Constitutive Model for Triaxial Behavior of Concrete. *Proc*., IABSE, 19, 1–30.

Yang, Y. B. and McGuire, W. 1986a. Stiffness Matrix for Geometric Nonlinear Analysis. *J. Struct. Eng*. ASCE, 112(4), 853–877.

Yang, Y. B. and McGuire, W. 1986b. Joint Rotation and Geometric Nonlinear Analysis. *J. Struct. Eng*. ASCE, 112(4), 879–905.

6

Displacement-Based Seismic Design of Bridges

M. J. Nigel Priestley
IUSS Pavia and EUCENTRE Foundation

Mervyn J. Kowalsky
North Carolina State University

Gian Michele Calvi
IUSS Pavia and EUCENTRE Foundation

6.1 Introduction—Problems with Force-Based Design

6.1.1 Overview

This chapter provides a summary of the displacement-based seismic design method as applied to bridge structures. The first section describes the shortcomings of traditional force-based design methods and is followed by a discussion of the seismic input for displacement-based design in the second section and the fundamentals of the method in the third section. The chapter concludes with three design examples illustrating the application of the method to bridge structures.

Given the interest in performance-based earthquake engineering (PBEE) it is essential to have a design methodology that engineers can employ to accomplish the goals of PBEE. As noted by the Structural Engineers Association of California (SEAOC, 1999), the primary objective of PBEE is to design a structure to achieve predictable levels of performance under defined levels of seismic input, within definable levels of reliability. In order to accomplish these goals, it is essential that the design procedures used are capable of controlling structural performance. Such a requirement is the primary limitation of traditional force-based methods. Structural performance can be characterized by various parameters such as strains, curvature, rotations, displacement, drift, or ductility, which are of course all deformation

quantities. This is of obvious importance since structures are designed to respond inelastically under even moderate earthquakes. Forces, however, are poor indicators of damage potential and any attempt to control inelastic structural behavior by controlling forces is likely to fail. The sections that follow will discuss this issue in more detail.

6.1.2 Stiffness Estimation

Force-based design methods invariably start with estimation of structural stiffness (utilized for calculation of structural period and distribution of forces between members later), which is based upon initial geometric properties of the structural members. In many cases, allowances for cracking in the case of reinforced concrete are employed by reducing the gross-section stiffness by a prescribed amount. Alternatively, estimation of stiffness is bypassed and approximate code-based period equations are employed that are based on rough geometric parameters. In either case, the assumption is that the stiffness of the structural elements can be obtained without reference to the strength of element.

Consider the moment curvature response of a cross section. The cracked section stiffness can be readily calculated by Equation 6.1 where M_N is the nominal moment capacity and ϕ_y is the section yield curvature. For sections with different moment capacities, keeping other variables such as geometry constant, force-based design assumes that the response would be as shown in Figure 6.1a. However, actual response is more appropriately characterized by the behavior shown in Figure 6.1b where it is the section yield curvature that remains constant with changing strength, not the stiffness. As a consequence, it is not possible to perform an accurate analysis of either the elastic structural periods, nor of the elastic distribution of required strength throughout the structure, until the member strengths have been determined. Because the required member strengths are the end product of force-based design, the implication is that successive iteration must be carried out before an adequate elastic characterization of the structure is obtained. Although this iteration is simple, it is rarely performed by designers, and does not solve additional problems associated with initial stiffness representation (Priestley et al., 2007).

$$EI = \frac{M_N}{\phi_y} \tag{6.1}$$

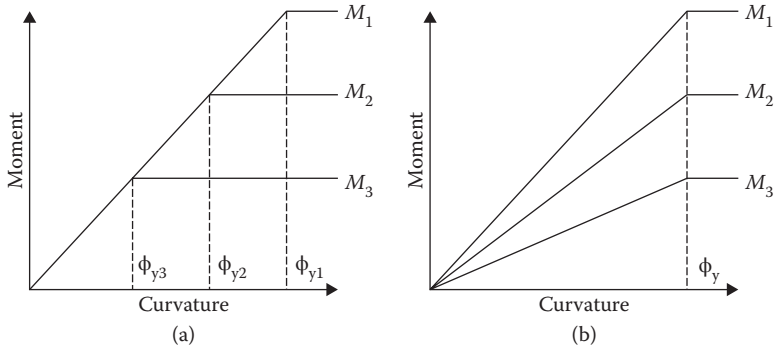

FIGURE 6.1 Influence of strength on moment–curvature relationship. (a) Design assumption (constant stiffness). (b) Realistic conditions (constant yield curvature). (From Priestley, M. J. N. et al., *Direct Displacement-Based Seismic Design of Structures*, IUSS Press, Pavia Italy, 2007. With permission.)

6.1.3 Force-Reduction Factors

The primary purpose of force-reduction factors in force-based design methods is to reduce the elastic response force by a level that is consistent with the implied ductility capacity of the structure under consideration. The shortfall in strength is compensated by inelastic deformation capacity (i.e., ductility). The level of required ductility is obtained by relationships between force reduction factor, R, displacement ductility, μ, and period, T. Such relationships are termed R-μ-T relationships, the most common of which is the "equal displacement approximation" where $R = \mu$.

Although not directly identified in many modern codes, the force-based design practice is based largely on variations of the equal displacement approximation where it is assumed that the inelastic response of a system under the influence of reduced seismic forces is equal to elastic response of the same system under the influence of the unreduced seismic forces. This is manifested in some design codes in the form of "displacement amplification factors" where the elastic response of a structure under the influence of reduced seismic forces is multiplied by a factor that provides an estimate of the nonlinear response displacement. In some cases, the displacement amplification factor, which is often defined as Cd, is equal to the force reduction factor, R, which by definition implies the equal displacement approximation. In other cases, it is similar to R, implying subtle variations from the equal displacement approximation. In either case, it is well established that the equal displacement approximation is inappropriate for very short or very long-period structures and is also of doubtful validity for medium-period structures when the hysteretic characteristic of the inelastic system deviates significantly from elasto-plastic. With regard to bridge practice in the United States, the 2011 AASHTO Guide Specifications for LRFD Seismic Bridge Design (AASHTO, 2011) calculates displacement demand using an R-μ-T relationship that considers short- and long-period modifications.

Further, there has been difficulty in reaching consensus within the research community as to the appropriate definition of yield and ultimate displacements. With reference to Figure 6.2b, the yield displacement has variously been defined as the intersection of the line through the origin with initial stiffness, and the nominal strength (point 1), the displacement at first yield (point 2), and the intersection of the line through the origin with secant stiffness through first yield, and the nominal strength (point 3), among other possibilities. Typically, displacements at point 3 will be 1.8–4 times the displacements at point 1. Displacement capacity, or ultimate displacement, also has had a number of definitions, including displacement at peak strength (point 4), displacement corresponding to 20% or 50% (or some other percentage) degradation from peak (or nominal) strength, (point 5) and displacement at initial fracture of transverse reinforcement (point 6), implying imminent failure.

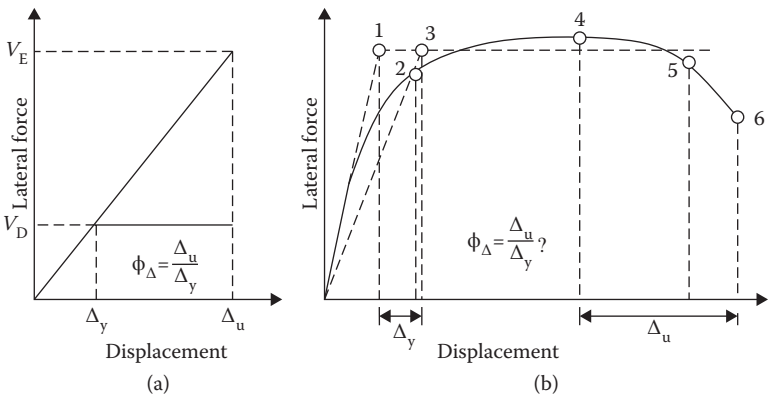

FIGURE 6.2 Ductility capacity and the equal displacement approximation. (a) Equal displacement approximation. (b) Definition of yield and ultimate displacement. (From Priestley, M. J. N. et al., *Direct Displacement-Based Seismic Design of Structures*, IUSS Press, Pavia Italy, 2007. With permission.)

Clearly, with such a wide choice of limit displacements, there has been considerable variation in the assessed experimental displacement ductility capacity of structures. This variation in assessed ductility capacity has, not surprisingly, been expressed in the codified force-reduction factors of different countries. In the United States of America, force-reduction factors as high as 8.0 are permitted for reinforced concrete frames (ICC, 2006). In other countries, notably Japan and Central America, maximum force-reduction factors of approximately 3.0 apply for frames. With such a wide diversity of opinions as to the appropriate level of force-reduction factor, the conclusion is inescapable that the absolute value of the strength is of relatively minor importance (Priestley et al., 2007).

6.1.4 Distribution of Base Shear

After the design base shear force is obtained by dividing the elastic base shear by the force-reduction factor, it is then applied to each degree of freedom in the structure in accordance with the assumed modal response, which is usually the first mode. Structural analysis then follows where base shear is distributed between structural members in proportion to the elastic stiffness of each member.

To further examine the implications of the distribution of force with regard to elastic stiffness, consider Figure 6.3, which represents a bridge crossing a valley, and hence having piers of different heights. Under longitudinal seismic response, the lateral deflections at the top of the piers will be equal. Assuming a pinned connection between the pier tops and the superstructure (or alternatively, fixed connections, and a rigid superstructure), force-based design will allocate the seismic design force between the columns in proportion to their elastic stiffnesses. If the columns have the same cross-section dimensions, as is likely to be the case for architectural reasons, the design shear forces in the columns, V_A, V_B, and V_C, will be in inverse proportion to H_A^3, H_B^3, and H_C^3, respectively, since the stiffness of column i is given by Equation 6.2.

$$K_i = \frac{C_1 E I_{i.e}}{H_i^3} \tag{6.2}$$

In Equation 6.2, $I_{i.e}$ is the effective cracked-section stiffness of column i, typically taken as $0.5I_{gross}$, for all columns. The consequence of this design approach is that the design moment at the bases of the piers will be given by Equation 6.3, which is in inverse proportion to the square of the column heights (Note that C_1 and C_2 are constants dependent on the degree of fixity at the pier top). Consequently the shortest piers will be allocated much higher flexural reinforcement contents than the longer piers.

This has three undesirable effects. First, allocating more flexural strength to the short piers will increase their elastic flexural stiffness, $EI_{i.e}$, even further, with respect to the more lightly reinforced longer piers, as has been discussed in relation to Figure 6.1. A redesign should strictly be carried out with revised pier stiffnesses, which in accordance with Equation 6.2 would result in still higher shear and moment demands on the shorter piers. Second, allocating a large proportion of the total seismic design force to the short piers increases their vulnerability to shear failure. Third,

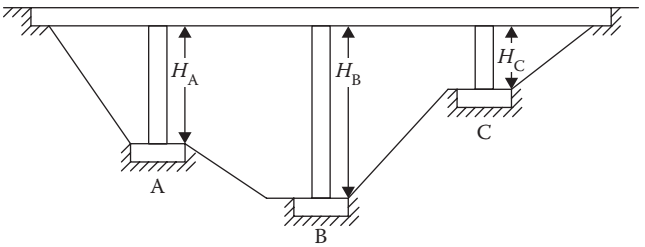

FIGURE 6.3 Bridge with unequal column heights. (From Priestley, M. J. N. et al., *Direct Displacement-Based Seismic Design of Structures*, IUSS Press, Pavia Italy, 2007. With permission.)

the displacement capacity of the short piers will clearly be less than that of the longer piers. The displacement capacity of heavily reinforced columns is reduced as the longitudinal reinforcement ratio increases, and hence the force-based design approach will tend to reduce the displacement capacity (Priestley et al., 2007).

$$M_{Bi} = C_2 V_i H_i = \frac{C_1 C_2 E I_{i,e}}{H_i^2} \tag{6.3}$$

6.1.5 Bridges with Multiple Load Paths

Another serious deficiency of force-based design is apparent in structures that possess more than one seismic load path, one of which remains elastic, whereas the others respond inelastically at the design earthquake level. A common example is the bridge of Figure 6.4a, when subjected to transverse seismic excitation, as suggested by the double-headed arrows. Primary seismic resistance is provided by bending of the piers, which are designed for inelastic response. However, if the abutments are restrained from lateral displacement transversely, superstructure bending also develops. Current seismic design philosophy requires the superstructure to respond elastically. The consequence is that a portion of the seismic inertia forces developed in the deck is transmitted to the pier footings by column bending (path 1 in Figure 6.4b), and the remainder is transmitted as abutment reactions by superstructure bending (path 2). Based on an elastic analysis the relative elastic stiffnesses of the two load paths are indicated by the two broken lines in Figure 6.4b, implying that column flexure (path 1) carries most of the seismic force. A force-reduction factor is then applied, and design forces determined.

The inelastic response of the combined resistance of the columns is now shown by the solid line (path 3, in Figure 6.4b), and on the basis of the equal displacement approximation it is imagined that the maximum displacement is Δ_{max}, the value predicted by the elastic analysis. If the superstructure is designed for the force developed in path 2 at the column yield displacement, it will be seriously underdesigned, since the forces in this path, which are required to be within the elastic range, continue to rise with increasing displacement. Thus the bending moment in the superstructure, and the abutment reactions at A and E are not reduced by column hinging, and a force-reduction factor should not be used in their design.

It is also probable that the maximum response displacement will differ significantly from the initial elastic estimate, since at maximum displacement, the effective damping of the system will be less than expected, as hysteretic damping is only associated with load path 3, which carries <50% of the seismic force at peak displacement response in this example. This may cause an increase in displacements.

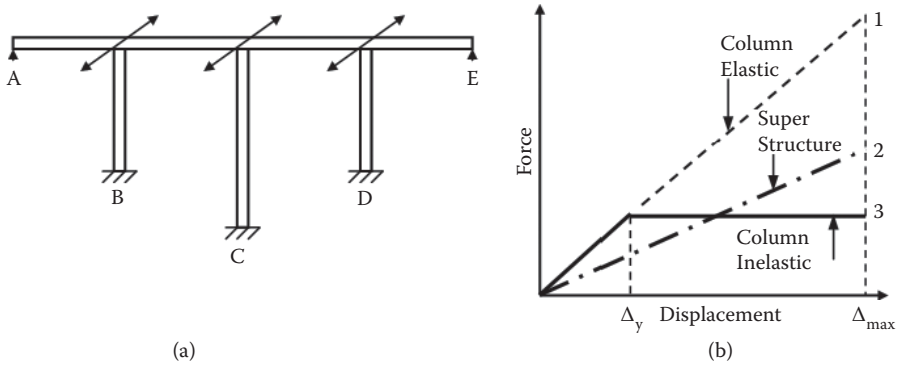

FIGURE 6.4 Bridge with dual seismic load paths under transverse response. (a) Structure. (b) Load path characteristics. (From Priestley, M. J. N. et al., *Direct Displacement-Based Seismic Design of Structures*, IUSS Press, Pavia Italy, 2007. With permission.)

However, the higher strength associated with the increased postyield stiffness of load path 2 may result in reduced displacement demand. Elastic analysis and the force-reduction factor approach give no guidance to these considerations (Priestley et al., 2007).

6.1.6 Bridges with Superstructure Isolation

For bridges with superstructure isolation, the pier responds essentially elastic, whereas inelastic deformation is concentrated in the isolation system. In the case of bridges with unequal column heights, the isolation system can regularize the response, thus minimizing the effects of reduced stiffness of shorter column in force distribution. This of course requires a higher degree of inelastic deformation for the isolator in a shorter pier than a longer pier, and as a consequence, different levels of isolator force-deformation response and ductility. Consideration of these issues in the context of force-based design is not possible when using a single force reduction factor for the bridge. Such systems are, however, well suited to a displacement-based approach.

6.2 Seismicity Representation for Displacement-Based Design

6.2.1 Displacement Spectra

Although force-based design methods utilize acceleration response spectra (ARS) for design, displacement-based design utilizes displacement response spectra (DRS). Before discussion of how DRS are obtained, it is worth to discuss their characteristics. Consider Figure 6.5, which represents the acceleration and DRS from three historical earthquakes—Whittier (15 km distance), Northridge (6 km distance), and Kobe (1 km distance). Some interesting conclusions can be drawn from examination of these figures. The Whittier accelerogram has a peak ground acceleration (PGA) of approximately 0.4 g (see Figure 6.5a), and a peak response acceleration of more than 0.8 g at a period of approximately 0.25 seconds. This might be considered to represent reasonably strong ground motion, since design PGA's and peak response accelerations for high-seismicity regions are often in the range 0.4–1.0 g, respectively. However, when we examine the displacement spectra from the same accelerogram, we find that the peak response displacement is <20 mm (0.79 in.), for a damping level of 5% of critical damping. Thus, if a given structure is capable of sustaining this very minor peak response displacement within the elastic range of response, no damage would be expected, despite the high peak response acceleration.

Another point of interest is apparent from Figure 6.5a. Information from the ARS cannot be extracted for periods of $T > 1.5$ sec since the response accelerations are so low. The displacement spectra provide much more readily accessible information for the medium to long period range, but indicate surprisingly regular displacements at periods greater than approximately 2 seconds. In fact this is false data, since the accelerogram was recorded by an analogue, rather than digital accelerograph, and a filter at 3 seconds was used to determine the displacement response. Akkar and Bommer (2007) have shown that the roll-off associated with filtering makes the response spectra unreliable for periods greater than approximately 2/3 of the filter period. Thus the data in the displacement spectra of Figure 6.5a are meaningless for periods greater than approximately 2 seconds.

The Northridge Sylmar acceleration spectra of Figure 6.5b show peak acceleration response for 5% damping of approximately 2.7 g—about three times the response for the Whittier earthquake. The displacement spectra, which result from a digital accelerograph, and are reliable up to significantly longer periods, indicate peak displacement response of approximately 800 mm (31.5 in.)—more than 40 times that of the Whittier record. Clearly this record would be expected to have much greater potential for damage than the Whittier record. Note that after reaching a peak response at approximately 3 seconds, displacement response decreases at higher periods. The Kobe record of Figure 6.5c also has high peak displacement response, and somewhat similar characteristics to the Sylmar record, though the peak displacement response appears to occur at a reduced period (Priestley et al., 2007).

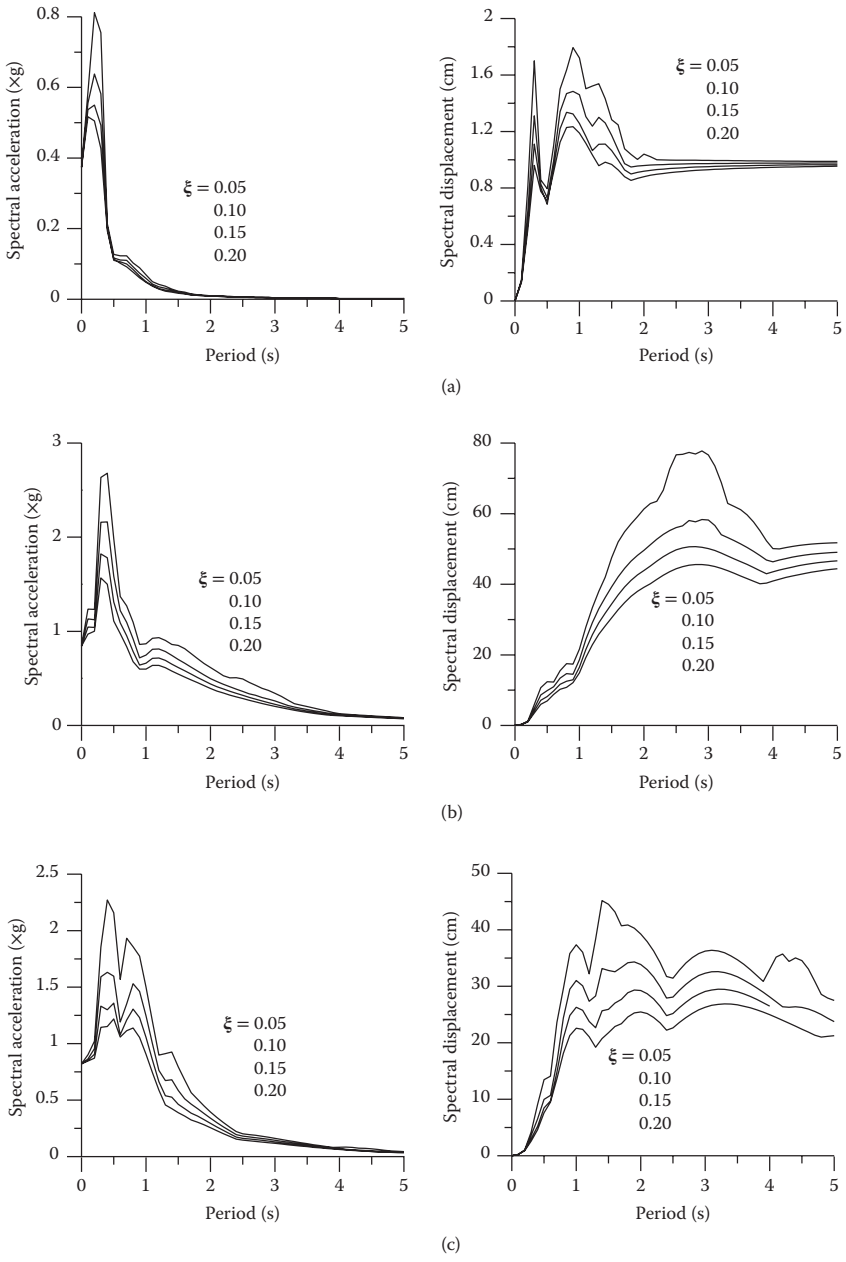

FIGURE 6.5 Acceleration and displacement response spectra. (a) Whittier ($M_w = 6.0$). (b) Sylmar (Northridge, 1994 $M_w = 6.7$). (c) Kobe ($M_w = 6.9$). (From Priestley, M. J. N. et al., *Direct Displacement-Based Seismic Design of Structures*, IUSS Press, Pavia Italy, 2007. With permission.)

6.2.2 Obtaining Design Displacement Response Spectra from Design Acceleration Response Spectra

Currently, seismic hazards around the world are generally characterized on the basis of ARS, with the exception of the EuroCode 8 (CEN 2005), which does offer the possibility of direct calculation of DRS. As a consequence, in order to apply displacement-based design the engineer must develop DRS. Fortunately, this is readily obtainable from ARS. In the United States, ARS are defined using USGS data,

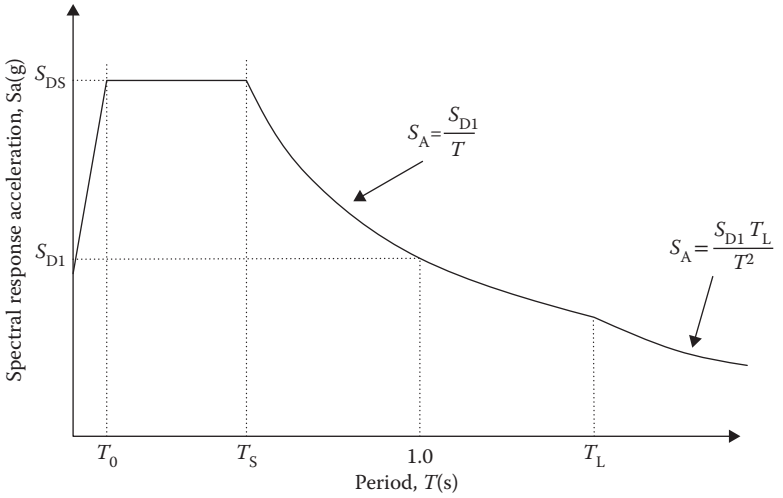

FIGURE 6.6 ASCE 7-10 (ASCE, 2010) design ARS.

which has been distilled into maps for both short (Ss) and 1 (S1) second response acceleration, which are then adjusted for soil type. The basic shape of the ARS as defined in ASCE 7-10 (ASCE, 2010) is shown in Figure 6.6. Details of the generation of design ARS are available in ASCE 7-10 and are not repeated here, however, the long-period transition variable, T_L, (commonly referred to as the "corner period" when discussing DRS) is worth noting. Before the 2002 edition of ASCE 7, design ARS did not contain the long-period transition variable. A consequence of this is that DRS obtained from the ARS linearly increased without a plateau, which is of course not consistent with reality. In the case of force-based design methods, this is inconsequential, however, for displacement-based design, the long-period transition variable is important as it identifies the "corner period" of the displacement spectra that places an upper bound on response displacement. Since the 2002 edition of ASCE 7, long-period transition maps have been developed to address this concern. It is important to note that the design ARS in the 2011 AASHTO Guide Specifications for LRFD Seismic Bridge Design (AASHTO, 2011) does not contain the long-period transition variable. It is the opinion of the authors that until better data is available, the T_L maps provided in ASCE 7-10 should be used in conjunction with the 2011 AASHTO design ARS when developing DRS for bridge design.

Obtaining design DRS from the design ARS in Figure 6.6 is a straightforward operation that involves division of the ARS ordinates by the square of the circular frequency. This relationship is expressed as Equation 6.4 where S_a is in units of 'g'. Application of Equation 6.4 to the spectral shape of Figure 6.6 yields a DRS such as shown in Figure 6.7d.

$$\Delta_{(T)} = \frac{T^2}{4\pi^2} S_{A(T)} g \tag{6.4}$$

6.2.3 Obtaining Design DRS from Magnitude/Distance Relationships

Recent work by Faccioli et al. (2004) and Faccioli and Villani (2009) who analyzed a large number of high-quality digital records has provided new information on the factors influencing the shape of displacement spectra. The records investigated included the very large data set from the large 1999 Chi-chi (Taiwan) earthquake, (magnitude $M_w = 7.6$), and a number of moderate European and Japanese earthquakes in the magnitude range $5.4 < M_w < 6.9$.

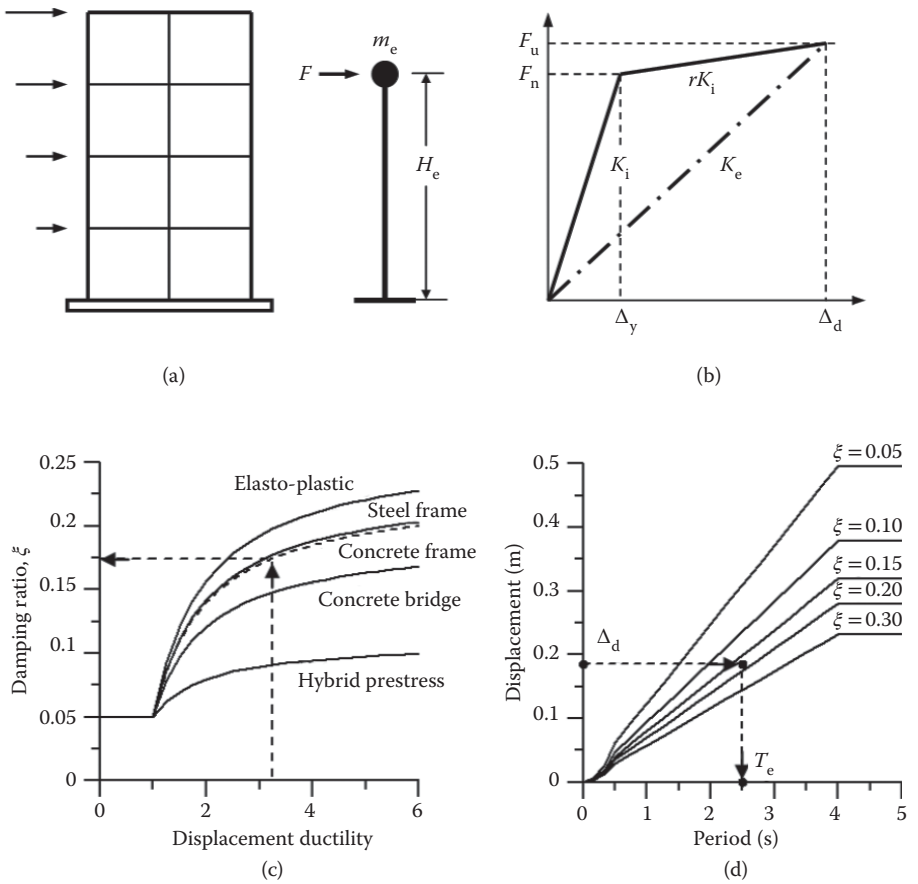

FIGURE 6.7 Fundamentals of direct displacement-based design. (a) SDOF simulation. (b) Effectiveness K_e. (c) Equivalent damping versus ductility. (d) Design displacement spectra. (From Priestley, M. J. N. et al., *Direct Displacement-Based Seismic Design of Structures,* IUSS Press, Pavia Italy, 2007. With permission.)

Their findings include the following points:

- The 5% damped displacement spectra tend to increase essentially linearly with period up to a "corner period." Beyond this, the response displacement either stays essentially constant (for large earthquakes), or tends to decrease (for moderate earthquakes). It is thus conservative to assume a constant spectral displacement for periods higher than the corner period.
- The 10 second spectral displacement for 5% damping can be considered to be a measure of the peak ground displacement.
- Soil amplification of displacement occurs throughout the period range, up to 10 seconds. There is a slight tendency for the corner period to increase for soft soils with large earthquakes, but this is less obvious for moderate earthquakes.
- Soft soil amplification is more pronounced at longer distances (30–50 km) for both moderate and large earthquakes.
- The corner period appears to increase almost linearly with magnitude. For earthquakes with moment magnitude greater than $M_w = 5.7$, the following relationship seems conservative:

$$T_c = 1.0 + 2.5(M_w - 5.7)\text{seconds} \tag{6.5}$$

- Peak response displacement, δ_{max}, depends on the magnitude, the epicentral distance r km (or nearest distance to the fault plane for a large earthquake), and the stress drop during rupture (generally in the range 1–10 MPa). Based on analytical considerations, Faccioli et al. (2004) derive the following relationship for peak response displacement, δ_{max}, in cm, for firm ground conditions

$$\log_{10}\delta_{max} = -4.46 + 0.33\log_{10}\Delta\sigma + M_w - \log_{10} r \text{ (cm)} \tag{6.6}$$

where $\Delta\sigma$ is the stress drop, in MPa, M_w the moment magnitude, and r the epicentral (or fault plane) distance in km. Substituting an average value of $\Delta\sigma = 6$ MPa, and reformatting as a power expression, with δ_{max} in mm

$$\delta_{max} = C_S \cdot \frac{10^{(M_w - 3.2)}}{r} \text{ (mm)} \tag{6.7}$$

where $C_S = 1.0$ for firm ground. The response displacements resulting from Equation 6.7 should be modified for other than firm ground. Tentative suggestions are as follows:

Rock: $C_S = 0.7$
Firm ground: $C_S = 1.0$
Intermediate soil: $C_S = 1.4$
Very soft soil: $C_S = 1.8$

These tentative coefficients for C_S have been interpreted from typical acceleration modifiers for PGA and period T_S (see Figure 6.6). More refined estimates can be expected as further analyses of digital records become available (Priestley et al., 2007).

6.2.4 Modification of Displacement Spectra for Damping

For direct displacement-based design (DDBD), response spectra for damping other than 5% will be needed. Numerous relationships have been proposed in the literature, which relate the response spectrum at damping higher than 5% to the spectrum at 5%. Review of these relationships has indicated the expression presented in the 1998 EuroCode (see Equation 6.8) is most appropriate. In the case of forward directivity velocity pulse cases, it has been suggested (Priestley, 2003) that Equation 6.9 be utilized. In either case, to obtain the response spectra at a damping of ξ, the 5% damped spectra is multiplied by R_ξ.

$$R_\xi = \left(\frac{0.07}{0.02 + \xi}\right)^{0.5} \tag{6.8}$$

$$R_\xi = \left(\frac{0.07}{0.02 + \xi}\right)^{0.25} \tag{6.9}$$

6.3 Fundamentals of Direct Displacement-Based Design for Bridges

6.3.1 Basic Formulation of the Method

The design procedure known as DDBD has been developed over the past 10 years (Priestley, 1993, 1997, and 2000; Priestley and Kowalsky, 2000) with the aim of mitigating the deficiencies in force-based design as previously noted. The fundamental difference from force-based design is that DDBD characterizes the structure to be designed by a single-degree-of-freedom (SDOF) representation of performance at peak

displacement response, rather than by its initial elastic characteristics. This is based on the substitute structure approach pioneered by Gulkan and Sozen (1974) and Shibata and Sozen (1976).

The fundamental philosophy behind the design approach is to design a structure that would achieve, rather than be bounded by, a given performance limit state under a given seismic intensity. This would result in essentially uniform-risk structures, which is philosophically compatible with the uniform-risk seismic spectra incorporated in design codes. The design procedure determines the strength required at designated plastic hinge locations to achieve the design aims in terms of defined displacement objectives. It must then be combined with capacity design procedures to ensure that plastic hinges occur only where intended, and that nonductile modes of inelastic deformation do not develop (Paulay and Priestley, 1992). Capacity design requirements are generally less onerous than those for force-based designs, resulting in more economical structures.

The design method is illustrated with reference to Figure 6.7, which considers a SDOF representation of a frame building (Figure 6.7a), though the basic fundamentals apply to all structural types. The bi-linear envelope of the lateral force-displacement response of the SDOF representation is shown in Figure 6.7b. An initial elastic stiffness K_i is followed by a post yield stiffness of rK_i.

Although force-based seismic design characterizes a structure in terms of elastic, preyield, properties (initial stiffness K_i, elastic damping), DDBD characterizes the structure by secant stiffness K_e at maximum displacement Δ_d (Figure 6.7b), and a level of equivalent viscous damping ξ, representative of the combined elastic damping and the hysteretic energy absorbed during inelastic response. Thus, as shown in Figure 6.7c, for a given level of ductility demand, a structural steel frame building with compact members will be assigned a higher level of equivalent viscous damping than a reinforced concrete bridge designed for the same level of ductility demand, as a consequence of "fatter" hysteresis loops.

With the design displacement at maximum response determined, and the corresponding damping estimated from the expected ductility demand, the effective period T_e at maximum displacement response, measured at the effective height H_e (Figure 6.7a) can be read from a set of displacement spectra for different levels of damping, as shown in the example of Figure 6.7d. The effective stiffness K_e of the equivalent SDOF system at maximum displacement can be found by inverting the normal equation for the period of a SDOF oscillator to provide

$$K_e = \frac{4\pi^2 m_e}{T_e^2} \tag{6.10}$$

where m_e is the effective mass of the structure participating in the fundamental mode of vibration. From Figure 6.7b, the design lateral force, which is also the design base shear force is thus

$$F = V_{Base} = K_e \Delta_d \tag{6.11}$$

The design concept is thus very simple, with much of the effort related to determination of the "substitute structure" characteristics, the determination of the design displacement, and development of design displacement spectra. Careful consideration is however also necessary for the distribution of the design base shear force V_{Base} to the different discretized mass locations, and for the analysis of the structure under the distributed seismic force. These will be discussed later.

The formulation of DDBD described above with reference to Figure 6.7c and d has the merit of characterizing the effects of ductility on seismic demand in a way that is independent of the hysteretic characteristics, because the damping/ductility relationships are separately generated for different hysteretic rules. It is comparatively straightforward to generate the influence of different levels of damping on the DRS (see Section 6.2.2.3), and hence figures similar to Figure 6.7d can be generated for new seismic intensities, or new site-specific seismicity using standard techniques (Gasparini and Vanmarcke, 1976).

6.3.2 Single-Degree-of-Freedom Bridges

6.3.2.1 Yield Displacement

As shown in Figure 6.1, the yield curvature is a fundamental property of a cross section and is only a function of section yield strain and depth. Equations 6.12a through 6.12e represent values for yield curvature based on section analysis (Priestley et al., 2007). It is worth noting that these equations represent the equivalent yield curvature that is defined as the first yield curvature extrapolated to the nominal moment capacity.

$$\text{Circular concrete column: } \phi_y = \frac{2.25\varepsilon_y}{D} \tag{6.12a}$$

$$\text{Rectangular concrete column: } \phi_y = \frac{2.10\varepsilon_y}{h_c} \tag{6.12b}$$

$$\text{Rectangular concrete wall: } \phi_y = \frac{2.00\varepsilon_y}{l_w} \tag{6.12c}$$

$$\text{Symmetrical steel section: } \phi_y = \frac{2.10\varepsilon_y}{h_s} \tag{6.12d}$$

$$\text{Flanged concrete beam: } \phi_y = \frac{1.70\varepsilon_y}{h_b} \tag{6.12e}$$

Once the yield curvature is established, calculation of yield displacement follows by direct application of the moment area method for deflections. When including the component of strain penetration into a footing and/or cap beam, the expression for the yield displacement of a column in single bending is given by Equation 6.13a, and for double bending in Equation 6.13b. Further modifications are possible for columns that are somewhere in between single and double bending, or for pile-columns that develop plastic hinges below ground level as noted in Priestley et al. (2007). In Equation 6.13, L_{SP} is the strain penetration length given by Equation 6.14 and H is the clear column height.

$$\Delta_y = \frac{\phi_y (H + L_{SP})^2}{3} \tag{6.13a}$$

$$\Delta_y = \frac{\phi_y (H + 2L_{SP})^2}{6} \tag{6.13b}$$

$$L_{SP} = 0.022 f_{ye} d_{bl} \quad (f_{ye} \text{in MPa}) \tag{6.14}$$

6.3.2.2 Design Displacement

The design displacement for a bridge column is a function of the performance limit state under consideration, as well as how that limit state is defined, which may be on the basis of material strains, drift, or ductility. In the case of material strains, limit state curvatures are defined on the basis of Equation 6.15 where the variable c defines the neutral axis depth at the design limit state. The more critical of Equation 6.15 are then utilized to obtain the limit state plastic displacement with Equation 6.16. This is then combined with the appropriate yield displacement as obtained from Equation 6.13 to obtain the design displacement as shown in Equation 6.17. In Equation 6.16, L_P represents the column plastic hinge length that is given by Equation 6.18 (Priestley et al., 2007) where L_C is the length from the point of maximum moment to the point of contraflexure. The variable k is given in Equation 6.19.

$$\phi_{ls,c} = \frac{\varepsilon_{c,ls}}{c} \left(\text{concrete compression}\right) \tag{6.15a}$$

$$\phi_{ls,s} = \frac{\varepsilon_{s,ls}}{(d-c)} \left(\text{reinforcement tension}\right) \tag{6.15b}$$

$$\Delta_{d,ls} = (\phi_{ls} - \phi_y) L_p H \tag{6.16}$$

$$\Delta_{d,ls} = \Delta_y + \Delta_p \tag{6.17}$$

$$L_p = kL_C + L_{SP} \geq 2L_{SP} \tag{6.18}$$

$$k = 0.2\left(\frac{f_u}{f_y} - 1\right) \leq 0.08 \tag{6.19}$$

For limit states defined on the basis of drift, the limit state displacement is given by Equation 6.20, whereas for limit states defined on the basis of displacement ductility, the limit state displacement is defined by Equation 6.21.

$$\Delta_{d,ls} = \theta_{ls} H \tag{6.20}$$

$$\Delta_{d,ls} = \mu_{ls} \Delta_y \tag{6.21}$$

In all cases, selection of limit state strains, drifts, or ductility are at the discretion of the engineer for the limit state under consideration. With regard to strain limits, at the serviceability limit state, a concrete compression strain limits of 0.004 (onset of crushing) and tensile steel strain limit of 0.015 (residual crack widths requiring repair) have been proposed (Priestley et al., 2007). In the case of a damage control limit state, a concrete compression strain limit consistent with crushing of confined core concrete is appropriate as is a tensile steel strain limit that characterizes the onset of reinforcement bar buckling.

6.3.2.3 Equivalent Viscous Damping

As noted in Section 6.3.1, the DDBD method utilizes the concept of equivalent linearization to characterize the nonlinear response of a structure with properties of equivalent stiffness and damping. The equivalent stiffness has been previously defined as the secant stiffness to the design limit state under consideration. Similarly, the equivalent damping represents the combined viscous and hysteretic damping at the design limit state.

The concept of hysteretic damping can be traced back to the work of Lydik Jacobsen (1930, 1960). Application of Jacobsen's approach is straightforward as it relies solely upon the area of a hysteretic response, thus making it possible to derive relationships for hysteretic damping based on either experimental data or assumed hysteretic loop shapes. However, because of various assumptions made in Jacobsen's approach, agreement with nonlinear time history analysis is variable. As a result, studies were undertaken in an effort to calibrate Jacobsen's approach for various hysteretic responses (Dwairi et al., 2007; Grant et al., 2005).

In addition to hysteretic damping, it is important to also consider the role of elastic viscous damping. Elastic damping is used in inelastic time-history analysis to represent damping not captured by the hysteretic model adopted for the analysis. This may be from the combination of a number of factors, of which the most important is the typical simplifying assumption in the hysteretic model of perfectly linear

response in the elastic range (which therefore does not model damping associated with the actual elastic nonlinearity and hysteresis). Additional damping also results from foundation compliance, foundation nonlinearity and radiation damping, and additional damping from interaction between structural and nonstructural elements. The damping coefficient, and hence the damping force depends on what value of stiffness is adopted. In most inelastic analyses, this has been taken as the initial stiffness. This, however, results in large and spurious damping forces when the response is inelastic, which is inappropriate, and that tangent stiffness should be used as the basis for elastic damping calculations. With tangent stiffness, the damping coefficient is proportionately changed every time the stiffness changes (Petrini et al., 2008).

However, in DDBD, the initial elastic damping adopted is related to the secant stiffness to the design limit state, whereas it is normal in inelastic time-history analysis to relate the elastic damping to the initial (elastic) stiffness, or more correctly, as noted above, to a stiffness that varies as the structural stiffness degrades with inelastic action (tangent stiffness). Since the response velocities of the "real" and "substitute" structures are expected to be similar under seismic response, the damping forces of the "real" and "substitute" structures, which are proportional to the product of the stiffness and the velocity, will differ significantly. Grant et al. (2005) has determined the adjustment that would be needed to the value of the elastic damping assumed in DDBD (based on either initial-stiffness or tangent-stiffness proportional damping) to ensure compatibility between the "real" and "substitute" structures. Without such an adjustment, the verification of DDBD by inelastic time-history analysis would be based on incompatible assumptions of elastic damping.

The adjustments depend on whether initial-stiffness damping (conventional practice), or tangent-stiffness damping (correct procedure) is adopted for time-history analysis. If initial-stiffness damping is chosen, the elastic damping coefficient used in DDBD must be larger than the specified initial-stiffness damping coefficient; if tangent-stiffness is chosen, it must be less than the specified tangent-stiffness coefficient.

The two components of damping have been combined based on these studies and equations developed (see Equation 6.22) that characterize the equivalent viscous damping as a function of displacement ductility. In general, for bridge design, Equation 6.22a, c, e, and f are applicable. It is important to note that Equation 6.22 assume 5% tangent stiffness proportional damping in conjunction with the hysteretic damping component. In the event that hysteretic characteristics other than those used to derive the expressions below are desired, the reader is referred to Priestley et al. (2007) for instructions on how they may be developed. Also, recent work by Pennucci et al. (2011) proposes a method to combine equivalent viscous damping and damping reduction factors (see Section 6.2.4) into one expression that is a function of ductility.

$$\text{Concrete Bridge Columns and Walls: } \xi_{eq} = 0.05 + 0.444\left(\frac{\mu - 1}{\mu\pi}\right) \tag{6.22a}$$

$$\text{Concrete Frame Building: } \xi_{eq} = 0.05 + 0.565\left(\frac{\mu - 1}{\mu\pi}\right) \tag{6.22b}$$

$$\text{Steel frame building: } \xi_{eq} = 0.05 + 0.577\left(\frac{\mu - 1}{\mu\pi}\right) \tag{6.22c}$$

$$\text{Hybrid prestressed frame: } \xi_{eq} = 0.05 + 0.186\left(\frac{\mu - 1}{\mu\pi}\right) \tag{6.22d}$$

$$\text{Friction slider: } \xi_{eq} = 0.05 + 0.670\left(\frac{\mu - 1}{\mu\pi}\right) \tag{6.22e}$$

$$\text{Bilinear isolation system } (r = 0.2): \xi_{eq} = 0.05 + 0.519\left(\frac{\mu - 1}{\mu\pi}\right) \tag{6.22f}$$

6.3.2.4 Design Base Shear Equation

The DDBD approach, which consist of a series of discrete steps as noted in Section 6.3.1, can be collected into one base shear equation if it is assume that the DRS is linear to the corner period. The resulting equation is shown in Equation 6.23 where $\Delta_{c,5}$ and T_c define the corner displacement (at 5% damping) and corner period from the design response spectrum; m_e the effective mass, ξ the equivalent viscous damping from the appropriate of Equation 6.22, and Δ_d the design target displacement from Section 6.3.2.2, and $\alpha = 0.5$ and 0.25 for normal and velocity pulse conditions, respectively.

$$V_{Base} = K_e\Delta_d = \frac{4\pi^2 m_e}{T_c^2}\cdot\frac{\Delta_{c,5}^2}{\Delta_d}\cdot\left(\frac{0.07}{0.02+\xi}\right)^{2\alpha} \tag{6.23}$$

6.3.2.5 Design When Displacement Capacity Exceeds Spectral Demand

There will be occasions, with very tall or flexible structures, when the design displacement capacity exceeds the maximum possible spectral displacement demand for the damping level. For example, with reference to the response spectra set of Figure 6.7d, it will be seen that if the design displacement Δ_d is calculated to be 0.35 m, and the corresponding damping is 20%, there is no possible intersection between the design displacement and the 20% damping curve. At the corner period of 4 seconds the peak displacement in Figure 6.7d for 20% damping is 0.282 m. In such cases there are two possible conditions to be considered:

(a) Yield displacement exceeds 5% damping value at the corner period: With extremely flexible structures, or when the design seismic intensity is low, it is possible that the yield displacement exceeds the 5% damping elastic response displacement ($\Delta_{c,5}$) at the corner period T_c (in Figure 6.7d this is $\Delta_{c,5} = 0.5$ m). In this case the calculated elastic response period will be larger than T_c, the response displacement will be equal to $\Delta_{c,5}$, and the design base shear force is given by

$$V_{Base} = K_{el}\Delta_{c,5} \tag{6.24}$$

where K_{el} is the elastic stiffness. Note, however, that a unique design solution cannot be found because the stiffness, K_{el}, depends on the elastic period, which depends, in turn, on the strength.

(b) Yield displacement is <5% damping value at the corner period: This case will be more common. Inelastic response will occur, but not at the level of ductility corresponding to the displacement or drift capacity of the structure. Note that if the yield displacement is $<\Delta_{c,5}$, this means that the elastic period is $<T_c$. As the structure softens, a final effective period of $T \geq T_c$ will be achieved, with a displacement response level that is compatible with the damping implied by that displacement. The following trial and error solution method is recommended:

1. Calculate the displacement capacity Δ_{dc}, and the corresponding damping, ξ_c. Confirm that the two are incompatible with the displacement spectra set, as above.
2. Estimate the final displacement response Δ_{df}. This will be somewhere between $\Delta_{c,\xi c}$ and Δ_{dc}.
3. Calculate the displacement ductility demand corresponding to Δ_{df}: ($\mu = \Delta_{df}/\Delta_y$).
4. Calculate the damping ξ corresponding to the ductility demand μ.
5. Calculate the displacement response Δ at T_c corresponding to ξ.
6. Use this value Δ as the new estimate for the final displacement Δ_{df}.
7. Repeat steps 3 to 6 until a stable solution is found. Typically this requires only one or two iterations.

Again there is no unique solution, as the effective stiffness could correspond to any period $T \geq T_c$. Any value of design base shear $<V_{Base} = 4\pi^2 m_e\Delta_{df}/T_c^2$ will satisfy the design assumptions. A higher value will imply a response at an effective period $<T_c$, and hence the response displacement will be incompatible with the effective damping. In both cases discussed above the provided strength will not affect the

displacement response. Minimum strength requirements for *P*-Δ effects or gravity loads will govern the required strength (Priestley et al., 2007).

6.3.2.6 P-Δ Design

As a structure displaces laterally, the presence of axial load induces additional bending moment that are a function of the axial load and displacement. The net effect is to reduce the second slop stiffness of the force deformation response. The significance of *P*-Δ effects is recognized in most seismic design codes, and is typically quantified by some form of "stability index", θ_Δ, which compares the magnitude of the *P*-Δ effect at either nominal yield, or at expected maximum displacement, to the design base moment capacity of the structure. The stability index is often of the form shown in Equation 6.25 (Priestley et al., 2007).

$$\theta_\Delta = \frac{P\Delta_{\max}}{M_D} \tag{6.25}$$

Inelastic time history analysis indicates that the extent of the *P*-Δ effect is a function of the force-displacement hysteretic response. For example, in the case of an elastic-plastic response, instability will eventually occur if the earthquake time history is long enough because of the ratchetting effect of increased deformations in one direction of loading because of unequal strengths in each direction (Priestley et al., 2007). For hysteretic systems that have an unloading stiffness that is softer than the reloading stiffness, or for self-correcting system such as unbonded posttensioned construction, instability requires a higher level of *P*-Δ moment.

For displacement-based design, consideration of the *P*-Δ effect is straightforward since the design displacement is established at the start of the design process. The basic concept is to increase the design lateral force in proportion to the *P*-Δ moment as shown in Equation 6.26, where V_{Base} is from Equation 6.23. For steel structures, application of Equation 6.26 is triggered when the stability index defined in Equation 6.25 exceeds 0.05, whereas for concrete structures the trigger is a value of 0.10. In Equation 6.25, the moment M_D is equal to $V_{\text{base}}H$. Furthermore, for steel structures *C* is 1 and for concrete it is suggested to be 0.5. These differences between steel and concrete are a function of the force-displacement responses of the respective materials. Steel structures follow a response where the unloading stiffness is nearly equal to the initial stiffness, which results in an increase in the ratchetting effect previously discussed. Concrete structures tend to have a reloading stiffness that points more toward origin, thus mitigating, to a certain extent, the *P*-Δ effect. It is suggested that in all cases, the stability index should be <0.33 (Priestley et al., 2007):

$$F = V_{\text{Base}} + C \cdot \frac{P\Delta_d}{H} \tag{6.26}$$

6.3.3 Simulation of Multi-Degree-of-Freedom Bridges

6.3.3.1 Displacement Shapes

The previous section discussed the formulation of the DDBD method and its application to SDOF structures such as single-column bridges. For multi-degree-of-freedom (MDOF) systems such as multi-span bridges in the transverse direction of response, several adjustments are required, the first of which is selection of the target displaced shape.

With bridges it is less easy to initially determine a design displacement profile, particularly for transverse seismic response. Figure 6.8 illustrates two possible bridge configurations out of a limitless potential range. The example of Figure 6.8a has piers of uniform height, whereas those in Figure 6.8b vary in height. The transverse displacement profiles will depend strongly on the relative column stiffnesses, and more significantly, on the degree of lateral displacement restraint provided at the abutment, and the superstructure lateral stiffness. For each bridge type, three possible transverse displacement profiles are shown,

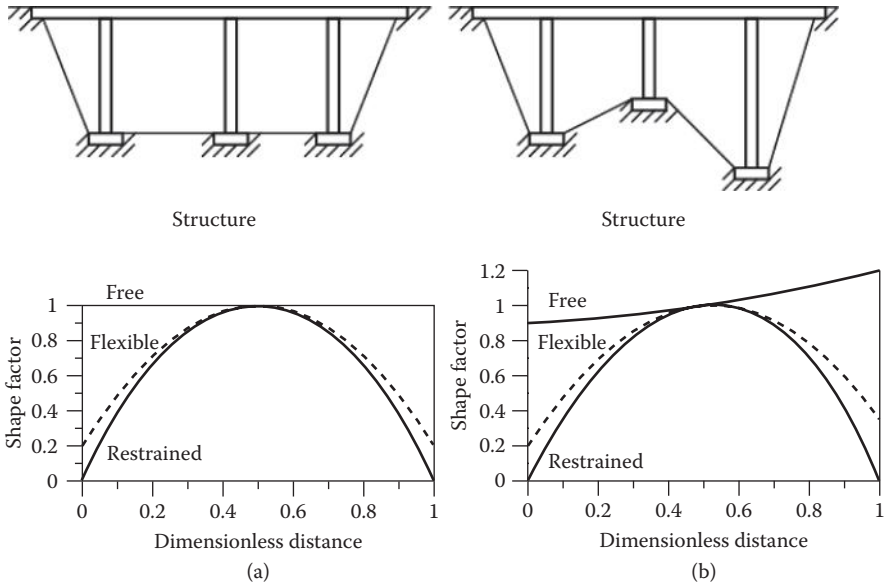

FIGURE 6.8 Transverse displacement shapes for bridges. (a) Uniform height piers. (b) Irregular height piers.

corresponding to an abutment fully restrained against transverse displacement, a completely unrestrained abutment, and one where the abutment is restrained, but has significant transverse flexibility.

For Figure 6.8a, the critical pier will be the central one, whereas for the irregular bridge of Figure 6.8b the critical pier may not be immediately apparent, and some iteration may be required. Iteration may also be required for the case of finite translational flexibility of the abutments for both the regular and irregular bridges to determine the relative displacements of abutment and the critical pier. Generally a parabolic displacement shape between abutments and piers can be assumed for initial design. Details of the calculation of the target displacement shape will be discussed in Section 6.3.3.5.

6.3.3.2 Effective Displacement

The characteristic design displacement of the substitute structure depends on the limit state displacement or drift of the most critical member of the real structure, and an assumed displacement shape for the structure. This displacement shape is that which corresponds to the inelastic first mode at the design level of seismic excitation. Thus, the changes to the elastic first-mode shape resulting from local changes to member stiffness caused by inelastic action in plastic hinges are taken into account at the beginning of the design. Representing the displacement by the inelastic rather than the elastic first-mode shape is consistent with characterizing the structure by its secant stiffness to maximum response. In fact, the inelastic and elastic first-mode shapes are often very similar. The design displacement (generalized displacement coordinate) is thus given by Equation 6.27 where m_i and Δ_i are the masses and displacements of the n significant mass locations, respectively.

$$\Delta_d = \frac{\sum_{i=1}^{n}(m_i\Delta_i^2)}{\sum_{i=1}^{n}(m_i\Delta_i)} \tag{6.27}$$

For bridges, the mass locations will normally be at the center of the mass of the superstructure above each column, but the superstructure mass may be discretized to more than one mass per span to improve validity of simulation. With tall columns, such as may occur in deep valley crossings, the column may also be discretized into multiple elements and masses.

6.3.3.3 Effective Mass

By applying force equilibrium between the MDOF system and the equivalent SDOF system, the effective mass is obtained as Equation 6.28. The effective mass represents the mass that participates in the assumed modal response of the structure. In the case of a simple regular bridge structure with abutments free to translate, the effective mass is nearly equal to the sum of the masses at each degree of freedom. For bridges with more parabolic or irregular displaced shapes, the effective mass would reduce.

$$m_e = \frac{\sum_{i=1}^{n}(m_i \Delta_i)}{\Delta_d} \tag{6.28}$$

6.3.3.4 Effective Damping

For SDOF systems, the equivalent viscous damping was a function of displacement ductility and hysteretic loop shape as shown in Section 6.3.2.3. For MDOF systems such as multispan bridges, there are numerous components that contribute to the effective damping of the entire system. These include the columns, superstructure, and abutments, as well as any isolation bearing or supplemental energy dissipation devices. As a consequence, the individual contributions to effective damping for each of these elements must be combined to obtain the effective damping for the system.

Among the possibilities for obtaining a system effective damping is a straight average. Although such an approach is suitable for a frame building where individual member damping values do not vary greatly and where there are numerous plastic hinges, in a bridge structure, there are fewer members contributing to damping, and it is possible that each of the members will exhibit very different levels of damping. For example, a bridge with unequal column heights may have some columns behaving elastically (5% damping), whereas an adjacent column performing inelastically with correspondingly high damping. Coupled with the superstructure, which responds elastically, and isolation bearing that could be at very high level of damping and the situation becomes more complex.

As a consequence, it is suggested that the effective damping for an MDOF bridge be obtained using a weighted average, where the weighting factor is the work done by the element under consideration. Such an approach is similar to the approach suggested by Shibata and Sozen (1976) where they weighted member damping values in a multistorey building according to the strain energy of each plastic hinge in the building. The general form of the equation for the effective damping of a bridge in the transverse direction is shown as Equation 6.29.

$$\xi_e = \frac{x(\Delta_d - \Delta_a)\xi_{SS} + x\Delta_a\xi_a + (1-x)\dfrac{\left(\sum_{i=2}^{4}\dfrac{1}{H_i}\cdot\Delta_i\xi_i\right)}{\sum_{i=2}^{4}\dfrac{1}{H_i}}}{x(\Delta_d - \Delta_a) + x\Delta_a + (1-x)\dfrac{\left(\sum_{i=2}^{4}\dfrac{1}{H_i}\cdot\Delta_i\right)}{\sum_{i=2}^{4}\dfrac{1}{H_i}}} \tag{6.29}$$

In Equation 6.29, ξ_i is the equivalent viscous damping for each column in accordance with Equation 6.22, H_i the column height, and Δ_i the column displacement in accordance with the assumed displaced shape. ξ_a and Δ_a represent the abutment damping and displacement, whereas ξ_{SS} is the superstructure damping. Δ_d is the design displacement from Equation 6.27 and x represents the portion of lateral force carried by superstructure bending back to the abutments.

6.3.3.5 Iterative Design Procedure

For design in the transverse direction of loading, an iterative design procedure will be necessary in many cases incorporating two initial assumptions: the fraction of load carried by superstructure bending back to the abutments, and the displacement profile. The procedure follows the following steps of which Figure 6.9 is a useful reference.

1. Estimate the fraction of lateral force, $\boldsymbol{x}$, carried by the superstructure bending load path. Generally this will be based on experience. In the absence of guidance, assume $\boldsymbol{x} = 0.5$ for restraint at abutments, and $\boldsymbol{x} = 0$ for unrestrained bridge ends.
2. Estimate the initial displacement profile, Δ_i. This will involve choosing a displacement shape and determining the limit-state displacement capacities of the piers as described in Section 6.3.2.2. The displacement shape is then scaled to the critical pier or abutment and the displacement profile obtained. A parabolic or sine-based displacement shape may be assumed for the initial iteration.
3. Determine the SDOF system displacement from Equation 6.27 using the displacement profile from step 2.
4. Determine the effective mass from Equation 6.28, including the appropriate contribution from pier mass (typically 1/3).
5. Determine the yield displacements of all piers (Equation 6.13), and hence their displacement ductility demands (defined as the pier displacement from the displacement profile from step 2 divided by the yield displacement of the pier). This then allows calculation of the pier equivalent viscous damping from Equation 6.22. Note that it is possible that some piers will respond elastically (displacement ductility <1), in which case the pier damping should be taken as $\xi = 0.05$.
6. Determine the ratios of shear force carried by the piers. If it is assumed that all piers have equal flexural reinforcement, and that all piers yield, the shears will be approximately in proportion to the inverse of the pier height. In reference to Figure 6.9, the shear force carried by a pier is given by Equation 6.30. If any of the piers are expected to remain elastic, at less than the yield capacity, then the proportion of force carried by that pier should be reduced from $1/H_i$ to μ_i/H_i, where $\mu_i < 1$. The proportion carried by yielding piers remains unchanged. Note that be definition, and again with reference to Figure 6.9, the shear force carried by the abutments would be given by Equation 6.31.

$$V_i = (1-x)\cdot\sum_{i=1}^{5} F_i \cdot \left(\frac{\frac{1}{H_i}}{\sum_{i=2}^{4}\frac{1}{H_i}}\right) \tag{6.30}$$

$$V_1 + V_5 = x\cdot\sum_{i=1}^{5} F_i \tag{6.31}$$

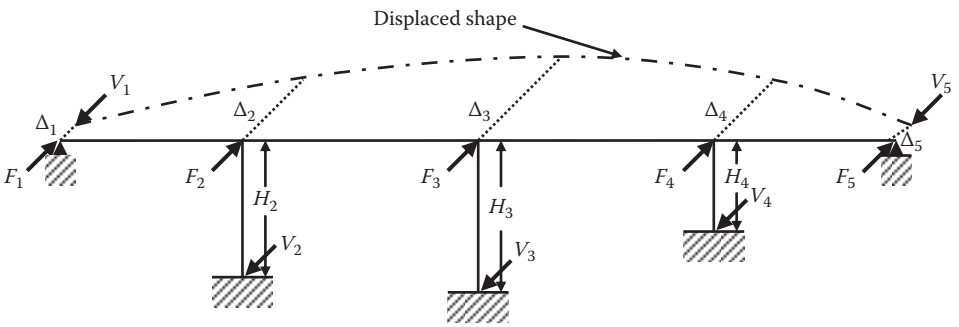

FIGURE 6.9 Bridge under transverse response.

7. Determine system damping, from Equation 6.29. Superstructure damping should be assumed to be 5%. Abutment damping will depend on abutment design and soil properties, but in many cases may also be taken as 5%.
8. Determine effective period, effective stiffness, and total base shear V_{Base} from the design spectrum. This can be done in a step-by-step manner or by direct application of Equation 6.23.
9. Distribute base shear as forces to inertia mass locations using Equation 6.32, which is defined on the basis of force equilibrium between the MDOF and equivalent SDOF systems.

$$F_i = \frac{V_{Base}(m_i\Delta_i)}{\sum(m_i\Delta_i)} \tag{6.32}$$

10. Estimate the effective stiffness for each abutment and pier for the structural analysis model. This will require an estimate of the shears carried by piers and abutments based on the assumption for $\boldsymbol{x}$. With reference to Figure 6.9, the shear forces may be obtained by application of Equations 6.30 and 6.31 where $\Sigma F_i = V_{Base}$. Since the displacement of each pier or abutment, Δ_i is known from step 2, and the shear $\boldsymbol{V}_i$ is known from this step, the effective stiffness of each pier or abutment is known from $K_i = V_i/\Delta_i$. The superstructure translational and torsional stiffness will also be known, and remain constant throughout the analysis iterations.
11. Analyze the structure under the lateral forces F_i to estimate the displacement of the critical pier or abutment. The 2D structural analysis model can be as simple as frame elements to define the superstructure, and springs to define the effective stiffnesses of abutments and piers from step 10.
12. Compare the displacement of the critical pier or abutment from the analysis of step 11 with the limit state displacement obtained in step 2 using the details discussed in Section 6.3.2.2. If the analysis indicates that the displacement of the critical pier or abutment exceeds the design limit, then the assumption for x, the fraction of total inertia force carried by superstructure bending is too high. More force needs to be allocated to the piers, which will increase their effective stiffness and hence the total system effective stiffness. The displacements will thus be reduced. If the displacement is less than the design limit, then x is too low. Revise the estimate for $\boldsymbol{x}$ upward. This process will result in an increase or decrease in the shears carried by the individual piers and hence a change in the pier stiffnesses. Iterate revising the value for x until the displacement of the critical pier or abutment from analysis equals the design limit state value. If the abutment displacement differs from the design assumption, then the abutment stiffness can be adjusted to improve agreement. This will have little effect on pier displacements. However, the influence of higher modes on abutment forces needs to be considered as discussed in Priestley et al. (2007).
13. Repeat steps 1 to 12 by using the value of x, and the displacement profile resulting from step 12 as new estimates for steps 1 and 2 above, and iterate until convergence for x and for the design profile is achieved. The procedure described above generally converges rapidly. It can also be programmed with Matlab, Mathcad, or Excel to proceed through the iterations automatically.

It should be noted that in some cases it will be found that even with $x = 1.0$ the displacement of the critical pier will be less than the design limit. This means that the stiffness of the superstructure is such that it dominates the response. Typically this occurs with short bridges of just a few spans. In such cases, the pier strength will be based on gravity load considerations. Ductile detailing may still be necessary, however, and an analysis using the known stiffnesses of superstructure and piers should be carried out to determine the expected displacements of the piers. For long span and/or tall pier bridges it may be useful to introduce some refinement related to the distributed mass of the pier, and more important, to consider the contribution of higher modes, in analogy to what is done for tall buildings (Adhikari et al., 2010).

6.3.3.6 Capacity Design Effects

The purpose of capacity design is to ensure that undesirable modes of inelastic deformation, such as plastic hinges at unintended locations, or shear failure, cannot occur, and that the influence of higher-mode effects is properly represented. This is achieved by ensuring that the dependable strength of the action (shear, flexure, etc.) at a specific location exceeds the maximum feasible action under seismic response. The general requirement for capacity protection is defined by Equation 6.33 where S_E is the value of the design action being capacity protected, corresponding to the design lateral force distribution found from the DDBD process, ϕ^o is the ratio of overstrength moment capacity to required capacity of the plastic hinges, ω is the amplification of the action being considered, because of higher mode effects, S_D is the design strength of the capacity protected action, and ϕ_S is a strength-reduction factor relating the dependable and design strengths of the action. With bridge structures there are two separate areas to be considered—capacity design related to actions in the piers, and superstructure consideration.

$$\phi_S S_D \geq S_R = \phi^o \omega S_E \tag{6.33}$$

Piers: The primary concern is determining the maximum feasible shear force that can be developed in the piers. With reference to Equation 6.33, it is primarily the overstrength factor ϕ^o that is involved, with dynamic amplification playing no, or at most a lesser part in amplifying the design shear force. Dynamic amplification related to higher-mode effects can, however be significant in the following cases:

- When pier mass is a significant proportion of the total mass contributing to lateral inertia forces on a pier, then higher-mode response resulting from response of the pier as a distributed-mass vertical beam may increase column shears, and even curvature ductility factors, above the level corresponding to the SDOF distribution of design forces, and should be considered.
- The torsional mass inertia of a wide superstructure supported by a cantilever pier may induce a significant second mode response. This will be apparent in a potential variation in the height at which the column moment drops to zero. The position at which this occurs may be above or below the center of superstructure mass, and is best determined by nonlinear time-history analysis. If this is not carried out it is suggested that the maximum shear force be evaluated assuming that the point of zero moment is dropped 15% below the center of superstructure mass, thus corresponding to a 17.6% increase in the capacity design shear force.
- With flexible superstructures higher mode response may increase the response of piers at some distance from the bridge centre. For example, bridges with stiff central piers and flexible outer piers may have increased displacement response because of higher modes. Note that if the bridge is symmetric about its center, the second mode, which is anti-symmetric will have a zero participation factor under transverse excitation, and displacements of the symmetric third mode, which would have the central pier displacing in the opposite direction from the two outer piers will induce small displacements. Because the main effect will be a small increase in the displacement ductility demand of the two outer piers, which will not be critical for design, this effect can generally be ignored.

Superstructure: Both overstrength at plastic hinges and higher mode effects may have a significant influence on the maximum transverse moments developed in the superstructure, and on the maximum abutment reactions. These are discussed separately in the following sections.

a. Overstrength Capacity of Plastic Hinges: The situation with structures with dual seismic load paths is opposite from that occurring with single-load path structures. In the case of bridge structures with part of the inertia load being carried by ductile columns and part by an elastic superstructure, an increase in the strength of the ductile columns resulting from material overstrength will result in an increase in the effective secant stiffness of the columns at design level response. Since the superstructure stiffness remains unchanged at the elastic value, this means that the total

stiffness of the structure has increased, and displacements, as a consequence, will be decreased. The superstructure forces and abutment reactions will thus reduce. It is thus clear that the ϕ^o value corresponding to flexural overstrength at plastic hinges should not be applied when estimating superstructure forces. As discussed in b. below, it is in fact appropriate to use an estimate of plastic hinge capacity lower than the design level in determining the superstructure demands.

b. Higher Mode Effects: It has been found (Alvarez, 2004) that higher mode effects are generally less significant for bridges than with building structures. The width of the superstructure may mean that with monolithic single-column/superstructure designs, the moment at the top of the column may be indeterminate, since the pier/superstructure is essentially a two-mode system. Analyses of typical designs indicate that pier moments at the height of the superstructure center-of-mass will rarely exceed $M_1 = \pm 0.2 M_2$. This value could be used if detailed analyses are not carried out. The principal influence of this uncertainty will be a possible increase in the design shear force in the pier, as already discussed.

   The second region where higher mode effects may be significant are in the superstructure transverse moments, and consequent abutment reactions, which are of course directly related to the superstructure moments in the end spans. Generally superstructure transverse seismic moments are not of great concern, as adequate capacity will normally be provided as a consequence of gravity load design. They should, however, be checked. The higher-mode amplification of superstructure transverse moments is normally not critical for bridges with four spans or less, when span lengths are 50 m (164 ft.) or less (Alvarez, 2004).

c. Estimation of Higher Mode Effects: Although bridges are often highly irregular, they are often comparatively simple in a structural sense, in that they are comprised of comparatively few structural elements. It is thus often feasible to carry out nonlinear time-history analyses to verify the design displacements, and to determine the influence of higher mode effects.

For bridge structures an alternative approach, which is fully compatible with the DDBD philosophy has been investigated (Alvarez, 2004). For this, the structural representation was such that stiffness of members with potential plastic hinges (e.g., piers) was taken as the secant stiffness to peak displacement response, whereas elastic elements (e.g., the superstructure) were modeled by initial-stiffness values. This conforms to the analysis model used to distribute the inertia forces described in Section 6.3.3.5, steps 10 and 11. It was found that combining the higher-mode elastic forces from such analyses with the DDBD inelastic first-mode approach gave an excellent representation of force-envelopes. This procedure has been termed the "efffective modal superposition" (EMS) approach. A specific application to bridges can be found in Adhikari et al. (2010).

6.3.3.7 Curved Bridges

With regard to horizontally curved bridges, there are two options: (1) design of the bridge using geometry as it is presented, or (2) 'unwrapping' of the curved bridge into an equivalent straight bridge whose length is equal to the arc length of the actual geometry. The AASHTO Guide Specifications (AASHTO, 2011) allow for bridges with subtended angles <90° to be designed and analyzed as if they are straight. If the subtended angle is <30°, static analysis is allowed, whereas if the subtended angle is between 30° and 90° elastic dynamic or inelastic time history analysis is required (although still with an equivalent straight geometry).

A recent study has been conducted on bridges with varying support conditions and number of spans (2, 4, and 6 span structures) and subtended angles varying from 15° to 90° in 15° increments. The bridges were all designed as if they were straight using the DDBD approach described in this chapter. Nonlinear time history analysis was then conducted on the resulting designs using both the straight geometry and the actual curved geometry. In all cases, agreement between the target displacement profile and nonlinear time history analysis using the straight geometry was very good. In general, the nonlinear time history analysis of the structures using the curved geometry also agreed with the target displacement profile from the straight geometry, with one exception: bridges that contain some degree of longitudinal restraint

at the abutments. In such a case, superstructure curvature develops arch action in the superstructure generating high axial loads and as a consequence high axial stiffness. In those cases, the response from nonlinear time history analysis indicated displacements much smaller than the target profile. For all other abutment support cases, the influence of plan curvature of the superstructure was small.

This study is ongoing, however, as of the writing of this document, it is suggested that the AASHTO Guide Specification (AASHTO, 2011) limits on plan curvature may be followed with regard to DDBD as long as the bridge longitudinal restraint at the abutments is small (which is often the case).

6.3.3.8 Longitudinal Design

In the longitudinal direction, each pier and abutment usually displaces the same amount. As a consequence, the design displacement for the longitudinal direction will be that of the shortest pier. This leads to a rather straightforward design process and essentially follows that of an SDOF system, with the exception of the calculation of damping and distribution of forces between piers. The example in Section 6.4.2 will demonstrate the design process in the longitudinal direction.

6.3.4 Design of Isolated Bridges

Bridges with partial or full isolation of the superstructure may be readily designed with DDBD. The two primary areas of the design process that are impacted are calculation of the individual pier displacements and equivalent viscous damping, both of which are shown in Figure 6.10.

With regard to calculation of displacements, the displaced shape of pier and isolator system will contain elastic and plastic components because of pier and isolator flexibility (see Figure 6.10). With

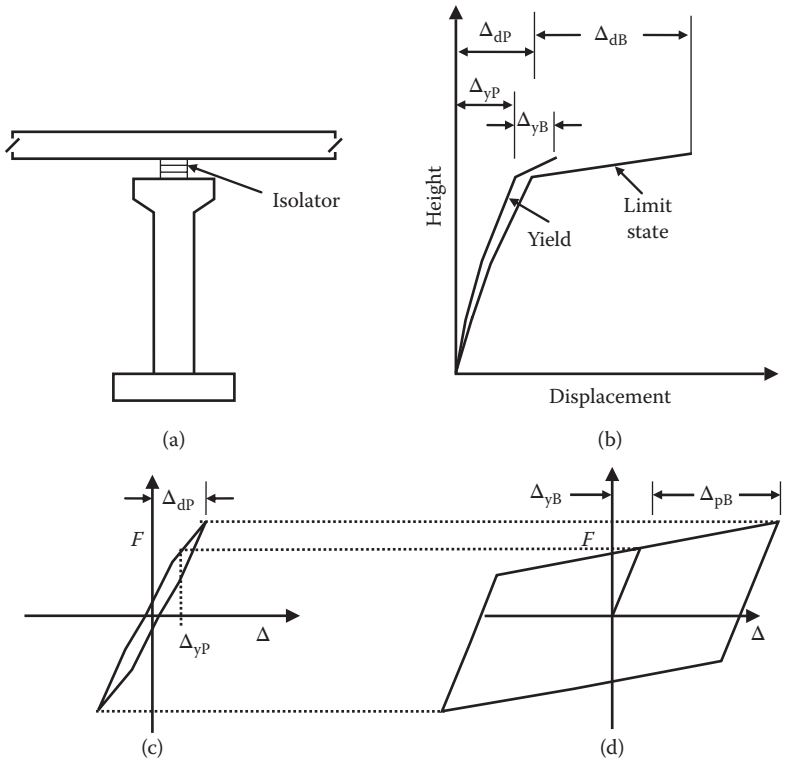

FIGURE 6.10 Damping for a cantilever pier with an isolated deck. (a) Structure. (b) Displacement profiles. (c) Pier. (d) Isolator hysteresis. (From Priestley, M. J. N. et al., *Direct Displacement-Based Seismic Design of Structures*, IUSS Press, Pavia Italy, 2007. With permission.)

regard to equivalent viscous damping, in Equation 6.29 the damping of each pier, ξ_i, must include a component because of isolator damping. That is, before application of Equation 6.29 for the entire bridge system, the damping of each pier-isolator system must be evaluated. The damping of pier and isolator may be weighed according to the work done by each to obtain ξ_i. This is expressed in Equation 6.34 where ξ_P is the pier damping and ξ_B the bearing damping. Design displacements for the pier and bearing are Δ_{dP} and Δ_{dB}, respectively. Application of Equation 6.29 would then follow to obtain the effective damping for the entire bridge system. More details on this topic may be found in Priestley et al. (2007).

$$\xi_i = \frac{\xi_P \Delta_{dP} + \xi_B \Delta_{dB}}{\Delta_{dP} + \Delta_{dB}} \tag{6.34}$$

6.3.5 Cable-Stayed Bridges

The main conceptual issues in designing cable-stayed bridges for seismic consideration are discussed in Calvi et al. (2010); the only aspect that will be addressed here is the application of displacement-based design to the preliminary design in the longitudinal direction to check pier sections and establish connection characteristics.

In highly seismic regions, the tower pier designed for gravity may not provide sufficient stiffness and strength to control the vertical response of the deck under seismic actions.

The vertical response of the deck becomes relevant for the longitudinal seismic response because, as illustrated in Figure 6.11, as the deck displaces longitudinally, the pendulum nature of the response causes portions of the deck to either sag or lift, inducing an important higher mode in the longitudinal response, in which the deck displaces the tops of the towers, with the deck segments located forward accelerating downward, and deck segments behind the towers accelerating upward. Such a longitudinal seismic response can impose significant eccentric forces on the towers. The actual eccentric load that must be carried by the tower piers will depend on the vertical acceleration of the deck, which cannot be easily estimated.

In order to conservatively size the tower pier sections at the conceptual design stage with allowance for vertical deck response, one can consider the extreme scenario (illustrated in Figure 6.11) in which the rising side of the deck slackens the cables completely, such that the cable loads associated with the sagging portion of the deck must be carried by the tower piers.

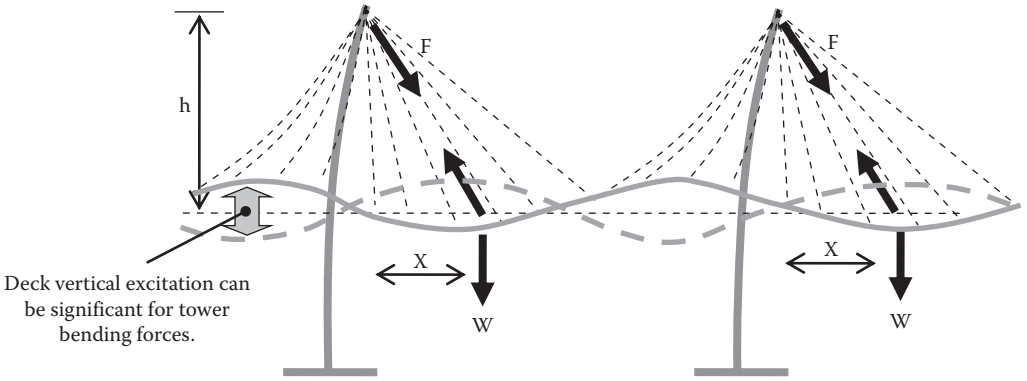

FIGURE 6.11 Qualitative deformed shape of cable-stayed bridge under longitudinal seismic excitation. (From Calvi, G. M. et al., *J. Earthquake Eng.*, 14, ISS8, 1139–1171, 2010. With permission.)

For the deck-to-pier connections, reasonable characteristics can be set in order to suitably limit the seismic response of the deck. Important criteria for the seismic design in the longitudinal direction may include requirements to

- Limit the longitudinal displacements of the deck in order to ease joint requirements. The displacement capacity of movement joints is dependent on manufacturer capabilities. However, a typical movement joint may have a limit of up to 0.5 m, whereas specialist movement joints can be manufactured to sustain over a meter of movement.
- Limit the vertical displacements of the deck by controlling the lateral displacements at the top of the tower piers.
- Limit the curvature demands in the tower piers.

Satisfaction of the last two of these criteria will depend on the excitation of the tower itself in addition to the longitudinal movements of the deck, whereas the first design requirement can be effectively controlled through good selection of the deck-to-pier connections. In order to do this, one can use a direct displacement-based design procedure, such as shown in the flowchart of Figure 6.12 (based on

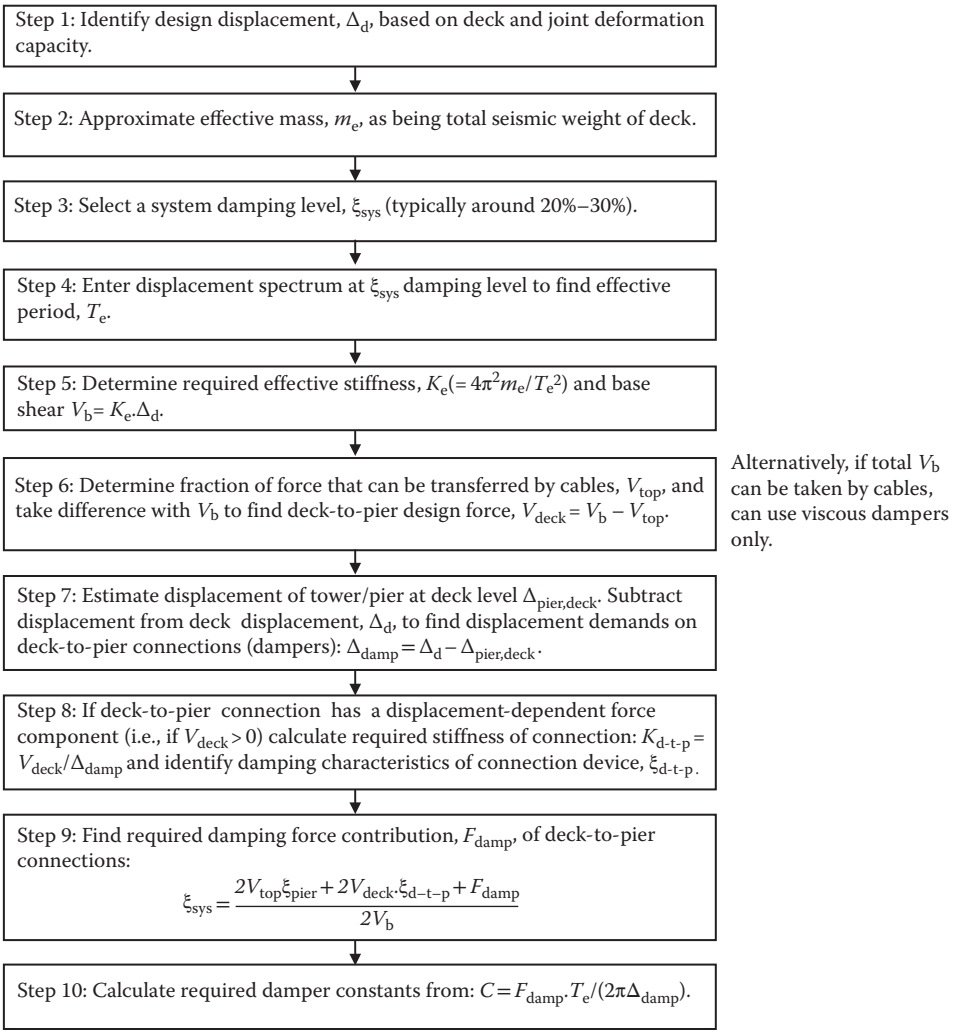

FIGURE 6.12 Displacement-based seismic design procedure for preliminary sizing of deck-to-pier connection characteristics in longitudinal response direction.

Priestley et al., 2007), which is applicable for systems with intermediate type deck-to-pier connections that incorporate viscous dampers, possibly in parallel to elastic displacement-dependent devices (such as rubber bearings).

6.4 Design Examples

6.4.1 Single-Degree-of-Freedom Bridge Pier

A cantilever bridge column that is 10 m (32.8 ft.) tall to the center of the superstructure mass is to be designed for a region of high seismicity (PGA = 0.7 g) using DDBD principles. The bridge is founded on firm ground and the spectral shape for the 5% damping displacement spectrum can be scaled from Figure 6.7d. On the basis of preliminary design, a circular column of 2.0 m (78.74 in.) has been selected, and the reinforcement yield strength is $f_y = 470$ MPa (68.3 ksi). Two conditions are considered: normal ground motion and ground motion with velocity fling effects. The design limit state is represented by the more critical of a displacement ductility of $\mu = 4$, or a drift of $\theta_d = 0.035$. The tributary weight contributing to seismic inertia of the column is 5000 kN (1124 kips). In this example, for simplicity, we ignore strain penetration into the foundation for calculation of the yield displacement. $E_s = 200$ GPa.

Design Displacement: From Equation 6.12a the yield curvature is

$$\phi_y = \frac{2.25 \times \left(\frac{470}{200{,}000}\right)}{2.0} = 0.00264/\text{m, where } E_s = 200 \text{ GPa}$$

Thus from Equation 6.13 the yield displacement is

$$\Delta_y = \frac{0.00264 \times 10^2}{3} = 0.0881 \text{ m (3.47 in.)}$$

Based on the design ductility limit of $\mu = 4$, and the drift limit of $\theta_d = 0.035$, the design displacement is the lesser of

$$\Delta_d = 4 \times 0.0881 = 0.353 \text{ m and } \Delta_d = 0.035 \times 10 = 0.350 \text{ m (13.8 in.)}$$

In this case the two limits produce almost identical results. Since the drift limit governs, the ductility at design displacement is

$$\mu = \frac{0.35}{0.0881} = 3.97$$

Equivalent viscous damping: From Equation 6.22a, the equivalent viscous damping at peak response is

$$\xi_e = 0.05 + \frac{0.444(3.97 - 1)}{3.97\pi} = 0.155 \ (15.5\%)$$

Maximum spectral displacement for 5% damping: The corner period for peak displacement response is $T_c = 4.0$ seconds. Scaling to a PGA of 0.7 seconds from Figure 6.7d, which applies for a PGA of 0.4 g, the corresponding displacement is

$$\Delta_{C,5} = 0.5 \times \frac{0.7}{0.4} = 0.875 \text{ m (34.4 in.)}$$

Design Strength for Normal Ground Motion: Equation 6.23 could be used directly. However, for clarity, the steps leading to Equation 6.23 are taken sequentially. Applying the damping correction factor of Equation 6.8 the corner-period response displacement for 15.5% damping is

$$\Delta_{C,15.5} = 0.875 \times \left(\frac{0.07}{0.02 + 0.155} \right)^{0.5} = 0.553 \text{ m}$$

Thus, by proportion, the effective response period of the bridge is

$$T_e = \frac{4 \times 0.35}{0.553} = 2.53 \text{ sec}$$

From Equation 6.10, with the mass of (5000/g) tones, effective stiffness at peak response is

$$K_e = \frac{4\pi^2 m_e}{T_e^2} = \frac{4\pi^2 5000}{(9.805 \times 2.53^2)} = 3145 \text{ kN/m}$$

Finally, from Equation 6.11, the design base shear force is

$$V_{Base} = K_e \Delta_d = 3145 \times 0.35 = 1100 \text{ kN } (247 \text{ kips})$$

Design Strength for Velocity Pulse Ground Motion: For this case, Equation 6.23 is used directly, with $\alpha = 0.25$:

$$V_{Base} = \frac{4\pi^2 5000}{9.805 \times 4^2} \cdot \frac{0.875^2}{0.35} \cdot \left(\frac{0.07}{0.02 + 0.155} \right)^{2 \times 0.25} = 1741 \text{ kN } (391 \text{ kips})$$

This is 58% higher than for the normal ground condition case.

6.4.2 Multi-Degree-of-Freedom Bridge—Longitudinal

The four-span bridge of Figure 6.13 has a superstructure depth of 2 m (6.56 ft.) and monolithic connections between the piers and superstructure. Superstructure mass averages 190 kN/m (12.7 kip/ft.) (including the weight of an internal cap beam, but not the column weight). We assume that the abutments are free to move longitudinally on frictionless bearings. The design displacements for the 2 m (6.56 ft.) diameter single-column piers are based on a damage control concrete compressive strain limit.

Specified material strengths are $f'_c = 30$ MPa (hence, $f'_{ce} = 1.3 \times 30 = 39$ MPa [5.66 ksi]) and $f_y = f_{yh} = 420$ MPa (hence $f_{ye} = 462$ MPa [67.0 ksi]). The ratio of ultimate to yield strength of the longitudinal reinforcement is 1.35. Longitudinal bar diameter is 40 mm (1.575 in.), with 50 mm (1.97 in.) cover, and the transverse reinforcement is initially selected as 20 mm (0.79 in.) diameter at 100 mm (3.94 in.) spacing

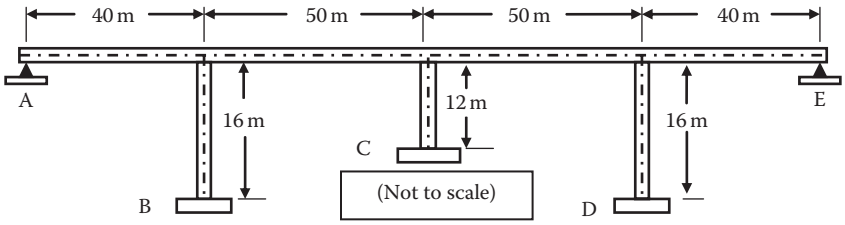

FIGURE 6.13 Four-span bridge.

along the column axis. Small adjustments to the spacing may be made after final design. Reinforcement strains at ultimate stress are 0.10 and 0.12 for longitudinal and transverse reinforcement, respectively.

The design spectra, corresponding to a PGA of 0.6 g are taken from ATC32 (ATC, 1996) for a medium ground condition, and are shown in Figure 6.14. Note that the displacement spectrum is not linear in this example, and there is no corner period.

Design displacement: The displacement of the 12 m central pier will govern.

Step 1: The core diameter is $D' = 2000 - 2 \times 50 + 20 = 1920$ mm. Hence,

$$\rho_v = \frac{4A_b}{D's} = \frac{4 \times 314}{(1920 \times 100)} = 0.00654$$

Step 2: From the design aids shown in Figure 6.15b with $f_{yh}/f'_{ce} = 420/39 = 10.8$, we find $f'_{cc} = 1.23$ $f'_{ce} = 48.0$ MPa (6.96 ksi).

Step 3: The damage-control limit compression strain is

$$\varepsilon_{dc,c} = 0.004 + 1.4\frac{\rho_v f_{yh} \varepsilon_{su}}{f'_{cc}} = 0.004 + \frac{1.4(0.00654 \times 420 \times 0.12)}{48.0} = 0.0136$$

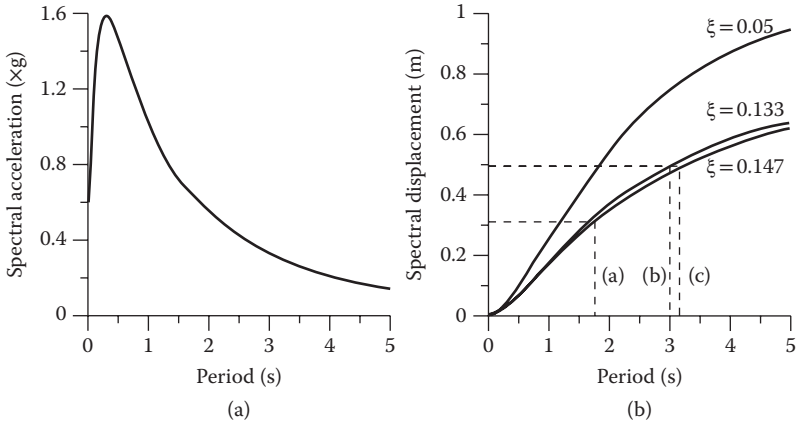

FIGURE 6.14 Design spectra. (a) Acceleration spectrum (5%). (b) Displacement spectra.

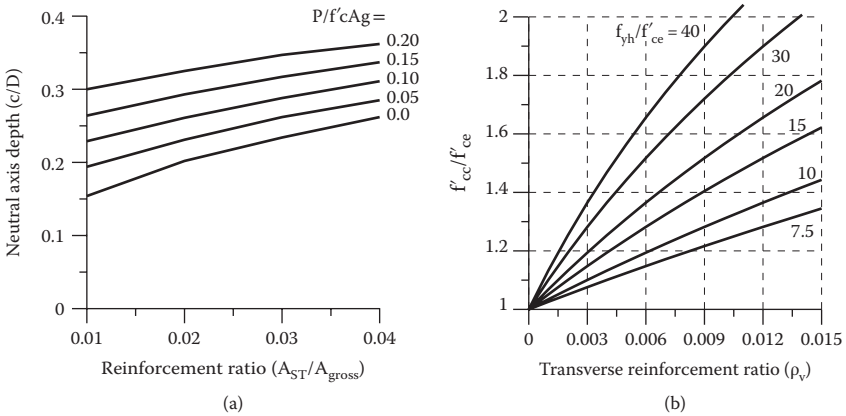

FIGURE 6.15 Design aids for design displacement of circular columns. (a) Neutral axis depth. (b) Confined concrete strength. (From Priestley, M. J. N. et al., *Direct Displacement-Based Seismic Design of Structures*, IUSS Press, Pavia Italy, 2007. With permission.)

Step 4: Column axial force ratio: $P/f'_{ce}A_g = \dfrac{10}{(39\times 3.14)} = 0.0816$

Step 5: We estimate the longitudinal reinforcement ratio as 1.8%. From Figure 6.15b $c/D = 0.240$

Step 6: The damage-control limit-state curvatures are thus from Equations 6.15:

$$\phi_{ls,c} = \frac{\varepsilon_{c,ls}}{c} = \frac{0.0136}{0.48} = 0.0283/\text{m} \leftarrow \text{governs}$$

$$\phi_{ls,s} = \frac{\varepsilon_{s,ls}}{(d-c)} = \frac{0.06}{(1.93-0.48)} = 0.0414/\text{m}$$

Step 7: Plastic Hinge Length: From Equation 6.19:

$$k = 0.2\left(\frac{f_u}{f_{ye}} - 1\right) \leq 0.08 = 0.2\times 0.35 = 0.07:$$

From Equation 6.14, with $d_{bl} = 40$ mm the strain penetration length is

$$L_{SP} = 0.022 f_{ye} d_{bl} = 0.022\times 462\times 40 = 407 \text{ mm} (16 \text{ in.})$$

Hence, with the column in double bending, since it is fixed at the top, L_C = 6.0 m, and $L_P = kL_C + L_{SP} \geq 2L_{SP} = 0.07\times 6 + 0.407 = 0.827$ m (32.6 in.) from Equation 6.18.

Step 8: Design Displacement: The yield curvature is found from Equation 6.12a as

$$\phi_y = \frac{2.25\varepsilon_y}{D} = \frac{2.25\left(\dfrac{462}{200{,}000}\right)}{2.0} = 0.0026/\text{m}$$

Since the column is in double bending, strain penetration applies at both top and bottom, and the effective length for yield displacement is thus $(H + 2L_{SP})$. We assume both the footing and superstructure to be rigid. From Equation 6.13b:

$$\Delta_y = \frac{\phi_y (H + 2L_{SP})^2}{6} = \frac{0.0026 \times 12.814^2}{6} = 0.0712 \text{ m}$$

The design displacement is then

$$\Delta_D = \Delta_y + (\phi_{ls} - \phi_y) L_P H = 0.0712 + (0.0283 - 0.0026) \times 0.827 \times 12 = 0.326\text{m} (12.8 \text{ in.})$$

The corresponding displacement ductility capacity is $\mu_\Delta = 0.326/0.0712 = 4.58$.

The displacement capacity of piers B and D will exceed this, and hence do not need to be calculated.

Yield displacements: The yield displacement of pier C has already been calculated as 0.0712 m (2.8 in.). The yield displacement of piers B and D is

Piers B and D: $\Delta_y = \dfrac{\phi_y (H + 2L_{SP})^2}{6} = \dfrac{0.0026(16 + 2\times 0.407)^2}{6} = 0.123 \text{ m} (4.84 \text{ in.})$

Pier C: $\Delta_y = 0.0712$ m (2.8 in.)

Displacement ductilities

Piers B and D: $\mu_\Delta = 0.326/0.123 = 2.65$

Pier C: $\mu_\Delta = 0.326/0.0712 = 4.58$

Pier damping: From Equation 6.26a

Piers B and D: $\xi_{B,D} = 0.05 + 0.444\left(\frac{\mu - 1}{\mu\pi}\right) = 0.05 + 0.444 \times \frac{1.65}{2.65\pi} = 0.138$

Pier C: $\xi_C = 0.05 + 0.444 \times \frac{3.58}{4.58\pi} = 0.160$

System damping: We chose to have the same flexural reinforcement ratio for all piers. As a consequence the flexural strength of all piers will be essentially the same, with small differences at top and bottom, as a consequence of differences in axial load, and also (smaller) differences between piers as a consequence of different levels of strain-hardening associated with different ductility demands. These can be resolved in the final design stage.

With equal moment capacities, the shears carried by the piers are in inverse proportion to their height. Hence $V_C = 1.333V_A$

$$\xi_{sys} = \frac{\sum_m V_i \xi_i}{\sum_m V_i} = \frac{2 \times 1.0 \times 0.138 + 1 \times 1.333 \times 0.160}{2 + 1.333} = 0.147$$

Spectral reduction factor: From Equation 6.8 the spectral reduction factor, to be applied to the 5% damped displacement spectrum is

$$R_\xi = \left(\frac{0.07}{0.02 + \xi_{sys}}\right)^{0.5} = \left(\frac{0.07}{0.02 + 0.147}\right)^{0.5} = 0.647$$

The displacement spectrum for the 14.7% damping is included in Figure 6.14b.

Effective period: The effective period of response is found entering with a displacement of 0.326 m, and intersecting the spectrum for $\xi_{sys} = 0.147$, as shown by the dashed line, yielding $T_e = 1.761$ seconds.

Effective mass: All of the superstructure mass will participate in the only longitudinal mode of significance. Priestley et al. (1996) recommends that 1/3 of the column mass be added to the mass lumped at the superstructure level. Hence the effective weight is

$$m_e.g = (190\,\text{kN/m}) \times 180\,\text{m} + 0.333(12 + 2 \times 16) \times 73.8\,\text{kN/m} = 35{,}300\,\text{kN}\ (7{,}936\,\text{kips})$$

Effective stiffness: From Equation 6.10:

$$K_e = \frac{4\pi^2 m_e}{T_e^2} = \frac{4\pi^2 \cdot 35.3}{9.805 \times 1.761^2} = 45.9\,\text{MN/m}$$

Base shear force: From Equation 6.11

$$V_{Base} = K_e \Delta_D = 45.9 \times 0.326 = 14.95\text{MN}\ (3360\,\text{kips})$$

This base shear is distributed to the columns in inverse proportion to their heights. Thus

$$V_B = V_D = \frac{14.95}{3.33} = 4.49\,\text{MN} \rightarrow M_B = M_D = 4.49 \times 8 = 35.9\,\text{MNm}\ (318{,}000\,\text{kip.in.})$$

$$V_C = \frac{1.33 \times 14.95}{3.33} = 5.97\,\text{MN} \rightarrow M_C = 5.97 \times 6 = 35.8\,\text{MNm}\ (317{,}000\,\text{kip.in.})$$

P-Δ check: With bridge designs, the *P*-Δ moment should always be checked in accordance with the recommendations of Section 6.3.2.6. From Equation 6.25 the Stability Index is

$$\theta_\Delta = \frac{P\Delta_{max}}{M_D} = \frac{10 \times 0.326}{35.8} = 0.091$$

As this is <0.10, the recommendations of Section 6.3.6.3 indicate that *P*-Δ effects can be ignored.

Moment-curvature analysis indicates that with an axial load of 10 MN, this moment can be provided, at a peak compression strain of 0.0136, by 91,200 mm^2 of flexural reinforcement (2.9%). The neutral axis depth of 540 mm is close to the assumed value of 480 mm, although the hoop spacing may need to be reduced in the final design to provide the required design curvature. The required number of 40 mm dia. bars is 72.6. This might be increased to 74 when the moment capacity of the longer columns is checked, because of their reduced axial load, and lower ductility demand.

6.4.3 Multi-Degree-of-Freedom Bridge—Transverse

The four-span bridge designed for longitudinal response in Section 6.4.2 and shown in Figure 6.13 is now designed for transverse response. As previously noted the bridge is supported on single-column piers, and we assume the support condition corresponds to that depicted in Figure 6.16c. The superstructure is considered to be torsionally flexible, and hence the effective height is taken to the center of the superstructure. This adds 1.0 m (3.28 ft.) to the column heights, which are thus 17 m (55.8 ft.) for columns B and D, and 13 m (42.6 ft.) for column C for transverse design. Superstructure transverse moment of inertia is 40 m^4 (4630 ft.^{4}).

The bridge is restrained by shear keys at the ends, and the abutment structure is required to remain essentially elastic under the earthquake defined by Figure 6.14. An abutment lateral displacement of 40 mm (1.6 in.) is permitted. As this is small compared with the pier displacements, the superstructure and abutment damping levels are not separated, and a value of $\xi = 0.05$ is assumed for the component of lateral force carried by the superstructure. The solution below follows the steps outlined in Section 6.3.3.

Step 1 Estimate fraction of lateral force carried by superstructure bending: A value of $x = 0.5$ is selected as an initial guess for the fraction of lateral inertia force transmitted to the abutments.

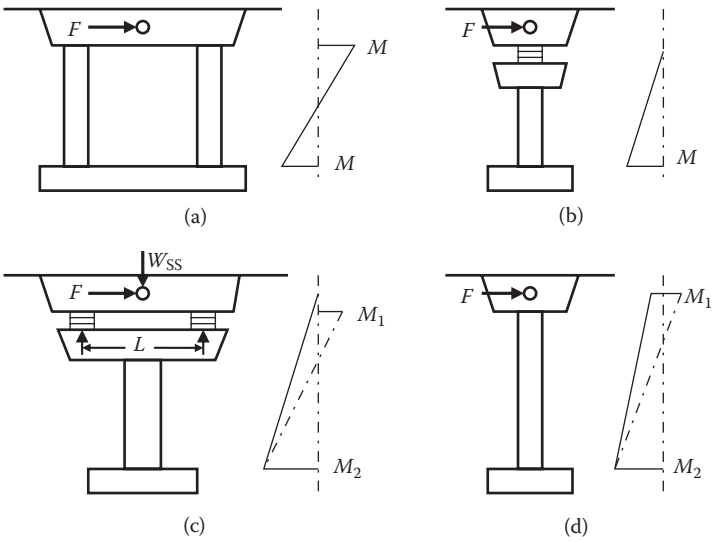

FIGURE 6.16 Transverse response of bridge piers. (a) Multi-column pier. (b) Single column, single. (c) Single column, multiple bearing. (d) Single column, monolithic. (From Priestley, M. J. N. et al., *Direct Displacement-Based Seismic Design of Structures*, IUSS Press, Pavia Italy, 2007. With permission.)

Step 2 Estimate the initial displacement profile: The initial displacement profile is assumed to be parabolic with the displacement at piers B and D equal to 70% of the displacement of pier C. The magnitude of the displacement profile will be determined by the critical abutment or pier displacement. As described in the problem statement, the permitted displacement for abutments A and E is 40 mm. The permitted displacements for piers B, C, and D will be a function of the strain-based damage criteria. From Section 6.4.2, the section yield curvature is given by

$$\phi_y = \frac{2.25\varepsilon_y}{D} = \frac{2.25\left(\frac{462}{200{,}000}\right)}{2.0} = 0.0026/\text{m}$$

whereas the limit state curvature, which is controlled by the concrete compression strain, was given by

$$\phi_{ls,c} = \frac{\varepsilon_{c,ls}}{c} = \frac{0.0136}{0.48} = 0.0283/\text{m}$$

with a strain penetration length given by

$$L_{SP} = 0.022 f_{ye} d_{bl} = 0.022 \times 462 \times 40 = 407 \text{ mm} (16.0 \text{ in.}),$$

the yield displacement for piers B and D is given by

$$\Delta_y = \frac{\phi_y (H + L_{SP})^2}{3} = \frac{0.0026 \times 17.407^2}{3} = 0.263 \text{ m } (10.4 \text{ in.})$$

whereas for pier C, where the height is 13 m, the yield displacement is 0.156 m (6.1 in.). From Equation 6.18, the plastic hinge length for piers B and D is

$$L_P = kL_C + L_{SP} \geq 2L_{SP} = 0.07 \times 17 + 0.407 = 1.597 \text{ m } (62.9 \text{ in.})$$

Similarly, for pier C, the plastic hinge length is 1.317 m (51.9 in.). The strain-based displacements for piers B and D are then obtained as follows:

$$\Delta_D = \Delta_y + (\phi_{ls} - \phi_y) L_P H = 0.263 + (0.0283 - 0.0026) \times 1.597 \times 17 = 0.961 \text{ m } (37.9 \text{ in.})$$

whereas for pier C, the strain-based limit displacement is 0.596 m (23.5 in.). From this example, it is clear that pier C will control the displacement profile as the initial estimate of displacements of piers B and D are 70% of 0.596 m = 0.417 m, which is less than the strain-based displacements for those piers. Although for this example it was not necessary to determine the strain-based displacements for piers B and D as they clearly could not govern the magnitude of the displacement profile, it is likely that in some cases, it will not be immediately evident which pier will govern the profile. For example, if the central pier had been much taller than the two side piers, the side piers would likely govern the overall magnitude of the displacement profile. The initial displacement profile for this example is thus as follows: $\Delta_A = \Delta_E = 0.04$ m; $\Delta_B = \Delta_D = 0.417$ m; $\Delta_C = 0.596$ m.

Step 3 Determine the SDOF system displacement: In order to determine the SDOF system displacement from Equation 6.27, the inertia weight for each abutment and pier must first be defined. The inertia weights are assumed to include the tributary superstructure weight (190 kN/m) and 1/3 of the weight of each pier. For abutments A and E, the inertia weight is $m_A = m_E = 20$ m × 190 kN/m = 3800 kN. For piers B and D, the inertia weight is $m_B = m_D = 45$ m × 190 kN/m + 16/3 × 73.8 kN/m = 8944 kN. For pier C,

the inertia weight is $m_C = 50\text{ m} \times 190\text{ kN/m} + 12/3 \times 73.8\text{ kN/m} = 9795\text{ kN}$. The SDOF system displacement from Equation 6.27 is then

$$\Delta_d = \frac{2\times3800 \times 0.04^2 + 2 \times 8944 \times 0.417^2 + 9795 \times 0.596^2}{2\times3800 \times 0.04 + 2 \times 8944 \times 0.417 + 9795 \times 0.596} = 0.485\,\text{m} \quad (19.1\text{ in.})$$

Step 4 Determine effective mass: From Equation 6.28, the effective mass is

$$m_e = \frac{2 \times 3800 \times 0.04 + 2 \times 8944 \times 0.417 + 9795 \times 0.596}{0.485 \times 9.81} = 2856\text{ tones} \quad (3149\text{ kips})$$

Step 5 Determine pier displacement ductility, and equivalent viscous damping: Pier yield and target displacements were calculated in step 2. Therefore, displacement ductilities for the three piers are

$$\mu_\Delta = \frac{0.417}{0.263} = 1.59\ (\text{Piers B and D}) \qquad \mu_\Delta = \frac{0.596}{0.156} = 3.82\ (\text{Pier C})$$

The equivalent viscous damping for the Piers follows from Equation 6.22a

$$\xi = 0.05 + 0.444 \times \left[\frac{1.59-1}{1.59\pi}\right] = 0.102 \text{ for Piers B and D}$$

$$\xi = 0.05 + 0.444 \times \left[\frac{3.82-1}{3.82\pi}\right] = 0.154 \text{ for Pier C}$$

Step 6 Determine the ratios of shear force carried by the piers: From Equation 6.30, the shear force the piers is given by

$$V = (1-0.5) \times \frac{\frac{1}{17}}{2\times\frac{1}{17}+\frac{1}{13}} \times \sum_{i=1}^{5} F_i = 0.151 \times \sum_{i=1}^{5} F_i \text{ for Piers B and D}$$

$$V = 0.198 \times \sum_{i=1}^{5} F_i \text{ for Pier C}$$

Step 7 Determine system damping: Since the superstructure and abutment damping are not treated separately, Equation 6.29 can be simplified to

$$\xi_e = \frac{0.5\times0.486\times0.05 + 0.5\left(\frac{2\times0.417\times0.102}{17} + \frac{0.596\times0.154}{13}\right)/\left(\frac{2}{17}+\frac{1}{13}\right)}{0.5\times0.486 + 0.5\left(\frac{2\times0.417}{17} + \frac{0.596}{13}\right)/\left(\frac{2}{17} + \frac{1}{13}\right)} = 0$$

Step 8 Determine effective period, stiffness, and design base shear: From Figure 6.14, entering with the target system displacement of 0.485 m and interpolating for a damping of 0.089, the effective period is estimated as $T_e = 2.31$ seconds. The effective stiffness, K_e, is obtained from Equation 6.10 as

$$K_e = \frac{4\pi^2 \times 2856}{2.31^2} = 21{,}183\text{ kN/m}$$

The base shear, from Equation 6.11 is then

$$V_{\text{Base}} = 21183 \times 0.485 = 10,282 \text{ kN } (2312 \text{ kips})$$

Step 9 Distribute base shear force to inertia mass locations: Utilizing Equation 6.32, the base shear force to each of the five inertia mass locations is obtained. For abutments A and E, the applied lateral force is $F = 10,282 \times \dfrac{3800 \times 0.04}{2 \times 3800 \times 0.04 + 2 \times 8944 \times 0.417 + 9795 \times 0.596} = 115 \text{ kN } (25.9 \text{ kips})$.

Similarly, the forces applied at the tops of Piers B and D are each 2820 kN (634 kips), whereas at the top of Pier C it is 4413 kN (992 kips).

Step 10 Estimate abutment and pier effective stiffness: In step 9, the forces applied to each inertia mass location were determined. In step 11, these forces will be applied to a structural analysis model. In this step, the properties for the analysis model will be obtained. In order to accomplish this, the shear forces carried by each abutment and pier must be estimated. From Equation 6.32

$$V_{\text{A}} + V_{\text{E}} = 0.5 \times 10,282 = 5,142 \text{ kN } (1,156 \text{ kips})$$

Therefore, the shear force in each abutment may be estimated as 5142/2 = 2571 kN. From Equation 6.30, the shear force in Piers B and D is given by

$$V = (1 - 0.5) \times 10,282 \times \frac{\dfrac{1}{17}}{2 \times \dfrac{1}{17} + \dfrac{1}{13}} = 1,554 \text{ kN } (349 \text{ kips})$$

Similarly, for Pier C, the force is estimated as 2,033 kN (457 kips). The effective stiffness of each abutment and pier can then be obtained by dividing the shear force in each member by the displacement of each member from step 2. For abutments A and E, the effective stiffness for the analytical model is 2,571/0.04 = 64,300 kN/m. For Piers B and D, the effective stiffness is 1,554/0.417 = 3,730 kN/m, whereas for Pier C, the effective stiffness is 2,033/0.596 = 3,410 kN/m.

Step 11 Analyze the structure under the applied lateral force vector: A structural analysis model incorporating the data from step 10 for abutment and pier stiffness is developed. Applying the lateral force vector from step 9 results in the following abutment and pier displacements: Abutments A and E achieve a displacement of 0.0426 m, Piers B and D achieve a displacement of 0.3826 m, and Pier C achieves a displacement of 0.5724 m.

Step 12 Revise the value of x, if needed: In step 1, it was assumed that the abutments would carry 50% of the applied lateral force. Comparing the displacements from step 11 with those from step 2, which were: $\Delta_{\text{A}} = \Delta_{\text{E}} = 0.04$ m; $\Delta_{\text{B}} = \Delta_{\text{D}} = 0.417$ m; $\Delta_{\text{C}} = 0.596$ m indicates that the assumption of $x = 0.5$ is slightly low as the displacement of the central pier is somewhat less than the target. In order to increase the central pier displacement, the force resisted by the abutment will need to be increased, thus resulting in reduced pier strength and stiffness and hence an increase in the pier displacement. A value of $x = 0.54$ is selected. Past experience has indicated that to speed convergence, a value equal to twice that needed from scaling of the actual to desired displacements is appropriate. For this example, the calculation is shown as

$$x_{\text{new}} = 0.5 + \frac{2 \times (596 - 572)}{572} \times 0.5 = 0.54$$

We then return to step 10 to determine the revised estimate for abutment and pier stiffness. This results in abutment shear forces of 2,776 kN, shear forces in Piers B and D of 1,430 kN, and a shear force of 1,870 kN in Pier C. For abutments A and E, the effective stiffness for the analytical model is then revised to 2,776/0.04 = 69,400 kN/m. For Piers B and D, the effective stiffness is 1,430/0.417 = 3,430 kN/m,

TABLE 6.1 Second Iteration for Example

Step 3	$\Delta_d = 0.477$ m
Step 4	$m_e = 2{,}834$ tones
Step 5	$\mu_\Delta = 1.52$ (Piers B and D); $\mu_\Delta = 3.83$ (Pier C) $\xi = 0.098$ (Piers B and D); $\xi = 0.154$ (Pier C)
Step 6	$V = 0.139 \times \sum_{i=1}^{5} F_i$ (Piers B and D); $V = 0.182 \times \sum_{i=1}^{5} F_i$ (Pier C)
Step 7	$\xi_e = 0.085$
Step 8	$T_e = 2.20$ second; $K_e = 23{,}191$ kN/m; $V_{Base} = 11{,}061$ kN
Step 9	$F_A = F_E = 127$ kN; $F_B = F_D = 2{,}969$ kN; $F_C = 4{,}869$ kN
Step 10	$V_A = V_E = 2{,}987$ kN; $V_B = V_D = 1{,}538$ kN; $V_C = 2{,}012$ kN $K_A = K_E = 74{,}664$ kN/m; $K_B = K_D = 3{,}865$ kN/m; $K_C = 3{,}375$ kN/m
Step 11	$\Delta_A = \Delta_E = 0.039$ m; $\Delta_B = \Delta_D = 0.406$ m; $\Delta_C = 0.613$ m
Step 12	$x = 0.51$ $V_A = V_E = 2{,}821$ kN; $V_B = V_D = 1{,}639$ kN; $V_C = 2{,}143$ kN $K_A = K_E = 70{,}516$ kN/m; $K_B = K_D = 4{,}117$ kN/m; $K_C = 3{,}595$ kN/m $\Delta_A = \Delta_E = 0.040$ m; $\Delta_B = \Delta_D = 0.395$ m; $\Delta_C = 0.595$ m

whereas for Pier C, the effective stiffness is 1,870/0.596 = 3,140 kN/m. The structure is then reanalyzed with the same lateral force vector from step 9 and the displacements compared with the target values. The results from this analysis result in the following displacements: $\Delta_A = \Delta_E = 0.041$m; $\Delta_B = \Delta_D = 0.396$ m; $\Delta_C = 0.593$ m. As the central pier displacement is now much closer to the target value of 0.596 m from step 2, the abutment forces because of superstructure bending have been correctly estimated resulting in a value of $x = 0.54$.

Step 13 Conduct additional iterations: The displacement profile is revised by scaling the profile from step 12 to the target central pier displacement of 0.596 m, whereas keeping the abutment displacements at 0.040 m. The revised displacement profile is then $\Delta_A = \Delta_E = 0.04$ m; $\Delta_B = \Delta_D = 0.398$ m; $\Delta_C = 0.596$ m. The value of $x = 0.54$ is also used in the second iteration. Steps 3 through 12 are then repeated until convergence is reached for the displacement profile and x. The calculations for steps 3 through 12 are shown in Table 6.1. After the second iteration, convergence has been reached for both the value of x and the displaced shape, and the design is complete.

6.5 Summary

This chapter presents an overview of the DDBD approach for the design of bridge structures. The procedure, which has been developed over the course of many years, has been shown to provide the engineer with an approach that allows for control of structural performance under seismic attack. A key feature of DDBD is the role that deformation plays in the design process. The procedure starts with the selection of desired structural performance, expressed as a displacement, and concludes with the required strength and stiffness needed to achieve that level of displacement under the design earthquake. As a consequence, the approach is well suited for performance-based design where design can be achieved for multiple levels of structural performance and seismic hazard. Several examples at the end of the chapter demonstrate the method for single- and multispan bridge structures.

References

AASHTO. 2011. *Guide Specifications for LRFD Seismic Bridge Design*, 2nd Ed., American Association of State Highway and Transportation Officials, Washington, DC.

Adhikari G., Petrini L., and Calvi, G. M. 2010. Application of direct displacement based design to long span bridges. *Bull. Earthquake Eng.*, 8(4), 897–919.

Akkar, S. and Bommer, J. J. 2007. Prediction of elastic displacement response spectra in Europe and the Middle East. *Earthquake Eng. Struct. Dyn.*, 36(10), 1275–1301.

Alvarez, J. C. 2004. *Displacement Based Design of Continuous Concrete Bridges under Transverse Seismic Excitation*. MSc Thesis, Rose School, IUSS, Pavia, p. 99.

ASCE. 2010. *ASCE Standard ASCE/SEI7-10, Minimum Design Loads for Buildings and Other Structures*, American Society of Civil Engineering, Reston, VA.

ATC-32 1996. *Improved Seismic Design Criteria for California Bridges: Provisional Recommendations and Resource Document*, Applied Technology Council, Redwood City, CA, pp. 256 and 365.

Calvi, G. M., Sullivan, T. J., and Villani, A. (2010). Conceptual Seismic Design of Cable-Stayed Bridges. *J. Earthquake Eng.*, 14(8), 1139–1171.

CEN. 2005., Eurocode 8. Design of Structures for Earthquake Resistance—Part 3. *Strengthening and repair of buildings*, EN 1998-3, Comite Europeen de Normalisation, Brussels, Belgium.

Dwairi, H. M., Kowalsky, M. J., and Nau, J. M. 2007. Equivalent Damping in Support of Direct Displacement-Based Design. *J. Earthquake Eng.*, 11(4), 512–530.

Faccioli, E., Paolucci, R., and Rey, J. 2004. Displacement Spectra for Long Periods. *Earthquake Spectra.*, 20(2), 347–376.

Faccioli, E. and Villani, M. 2009. Seismic Hazard Mapping for Italy in Terms of Broadband Displacement Response Spectra. *Earthquake Spectra.*, 25(3), 515–539.

Gasparini, D. A. and Vanmarcke, E. H. 1976. *SIMQKE: A program for artificial motion generation* User's manual and Documentation, Civil Engineering Department, MIT, p.32.

Grant, D. N., Blandon, C. A., and Priestley, M. J. N. 2005. *Modelling Inelastic Response in Direct Displacement-Based Design*, Report 2005/03, IUSS Press, Pavia, p. 104.

Gulkan, P. and Sozen, M. 1974. Inelastic Response of Reinforced Concrete Structures to Earthquake Motions. *ACI J.*, 71(12), 604–610.

ICC. 2006. *International Building Code*, International Code Council, Washington, DC, p. 663.

Jacobsen, L. S. 1930. Steady forced vibrations as influenced by damping. *ASME Trans.*, 52(1), 169–181.

Jacobsen, L. S. 1960. Damping in composite structures. *Proceedings, 2nd World Conference on Earthquake Engineering*, Vol. 2, Tokyo and Kyoto, Japan, 1029–1044.

Paulay, T. and Priestley, M. J. N. 1992. *Seismic Design of Reinforced Concrete and Masonry Buildings*, Wiley, New York, p. 744.

Pennucci, D., Sullivan, T.J., and Calvi, G.M. 2011. Displacement reduction factors for the design of medium and long period structures. *J. Earthquake Eng.*, 15(S1), 1–29.

Petrini, L., Maggi, C., Priestley, M. J. N., and Calvi, G. M. 2008. Experimental Verification of Viscous Damping Modeling for Inelastic Time History Analyzes. *J. Earthquake Eng.*, 12(1), 125–145.

Priestley, M. J. N. and Kowalsky, M. J. 2000. Direct Displacement-Based Seismic Design of Concrete Buildings. *Bull., NZSEE*, 33(4), 421–444.

Priestley, M. J. N. 1997. Displacement-based seismic assessment of reinforced concrete buildings. *J. Earthquake Eng.*, 1(1), 157–192.

Priestley, M. J. N. 1993. Myths and Fallacies in Earthquake Engineering – Conflicts between Design and Reality. *Bull. NZSEE*, 26(3), 329–341.

Priestley, M. J. N., Seible, F., and Calvi, G. M. 1996. *Seismic Design and Retrofit of Bridges*, Wiley, New York, p. 686.

Priestley, M. J. N. 2000. Performance Based Seismic Design. *Keynote Address, 12th World Conference on Earthquake Engineering*, Auckland, Paper No. 2831.

Priestley, M. J. N., Calvi, G. M., and Kowalsky, M. J. 2007. *Direct Displacement-Based Seismic Design of Structures* IUSS Press, Pavia Italy, ISBN 978-88-6198-000-6, p. 740.

Priestley, M. J. N. 2003. *Myths and Fallacies in Earthquake Engineering* (Revisited). The 9th Mallet Milne Lecture, IUSS Press, Pavia, p. 121.

Shibata, A. and Sozen, M. 1976. Substitute Structure Method for Seismic Design in Reinforced Concrete. *ASCE J. Struct. Eng.*, 102(1), 1–18.

Structural Engineers Association of California 1999. *Recommended Lateral Force Requirements and Commentary*, 7th Ed., SEAOC, Sacramento, CA.

7

Seismic Bridge Design Specifications for the United States

Roy A. Imbsen
Imbsen Consulting

7.1 Background

Seismic design of bridges as we know it today in the United States began at California Department of Transportation (Caltrans) immediately after the San Fernando earthquake on February 11, 1971. The first seismic design criteria (SDC) that followed was implemented into Caltrans design practice in 1973 (Imbsen and Gates, 1973). This was a prescriptive design criteria based on a ductile design approach with prescribed ductility factors to allow damage and to avoid collapse. Allowing damage to occur with the formation of plastic hinges in the columns provides a performance level of "life safety." This ductile design approach was selected instead of a more costly and difficult to achieve elastic design. This approach was

formally adopted by AASHTO in 1975 (AASHTO, 1975) with some minor modifications for application to all regions in the United States. These criteria remained in AASHTO until 1990 (AASHTO, 1990) when it was replaced by the ATC-6 Seismic Design Guidelines for Highway Bridges (ATC, 1981) and formally adopted by AASHTO as Division 1-A (AASHTO, 1992). ATC-6 was also adopted by AASHTO in 1983 as a Guide Specifications (AASHTO, 1983), which later became Division 1-A.

After several damaging earthquakes in the 1980s and 1990s, and as more recent relevant research efforts were completed, it became clear that improvements to the seismic practice for bridges should be undertaken. Several efforts culminated in 2003 that prompted the AASHTO T-3 Committee to initiate the development of the AASHTO Guide Specifications for LRFD Seismic Bridge Design (Imbsen, 2007a and 2007b). These efforts included

1. ATC-32 (publication of) Improved SDC for California Bridges (ATC, 1996)
2. Caltrans development of provisional SDC (Caltrans, 1999)
3. Development and implementation of the South Carolina Seismic Design Specifications (SCDOT, 2001)
4. Publication of MCEER/ATC-49 (NCHRP 12-49) Recommended Guidelines (MCEER, 2004)

Thus in 2005, with the T-3 AASHTO Seismic Design Technical Committee's support, work began to identify and consolidate the best practices from these four documents in to a new single document of seismic design specification that was completed in 2007 (I&A, 2005 and 2006; Imbsen, 2007a and 2007b) and submitted to AASHTO T-3 Committee for their technical review and approval. The final document entitled "AASHTO Guide Specifications for LRFD Seismic Bridge Design" was adopted and published by AASHTO, the first edition in 2009, and second in 2011, respectively (AASHTO, 2009 and 2011). Within the context of this chapter, this document will be referred to as *Seismic Guide* (AASHTO, 2011). To assist the reader the sections that follow generally correspond to those in the *Seismic Guide*. The chapters and articles making reference to the *Seismic Guide* are shown in italics.

With the adoption of the *Seismic Guide* there are now two distinct methodologies being used for Seismic design of a bridge, one being the traditional Force-Based Approach (FBA) as used in the AASHTO LRFD Bridge Specification and the second being the Displacement-Based Approach (DBA) as introduced in the *Seismic Guide*. Both methods are based on achieving a ductile design with a performance level of "life safety" for a ground motion having a return period of 975 years.

The FBA with prescribed ductility factors R, to allow damage encompasses many uncertainties and is less reliable than the DBA as used in the *Seismic Guide*. However, the FBA is considered acceptable for the lowest seismic zone since the uncertainties are reduced in this lower seismic zone. Although the use of ductility factors has been eliminated in the *Seismic Guide*, substantially reducing the level of uncertainty, the performance level of "life safety" has not been changed. However a new hazard level was introduced having a 7.5% probability of exceedence in 75 years (i.e., 975-year return period) to replace the 10% probability of exceedence in 50 years (i.e., 475-year return period), as illustrated in Figure 7.1.

This new approach, which eliminates the use of an "R" factor and allows for a ductile response, uses either a simplified implicit displacement procedure or a more rigorous pushover assessment of displacement capacity. The selection of which procedure to use is based on SDCs, similar to the seismic zone approach used in the AASHTO LRFD Bridge Design Specifications. Both the *Seismic Guide* and the LRFD Bridge Specification design procedures include prescriptive detailing for plastic hinging regions and for capacity protection of those elements that should not experience damage. By taking advantage of a substantial amount of laboratory testing and lessons learned from past earthquakes, the detailing and design requirements in the *Seismic Guide* are a significant improvement to seismic bridge design.

Although the practice in seismic design of bridges has traditionally been to comply with code requirements to achieve facilities that do not collapse, the resulting postearthquake damage has been costly and disruptive, and in some instances bridges have been demolished and replaced with new bridges. In retrospect facility owners and users are concerned with economic losses from damage and disruption by the loss of use. The interruption of service in a roadway system and demand for repair services can

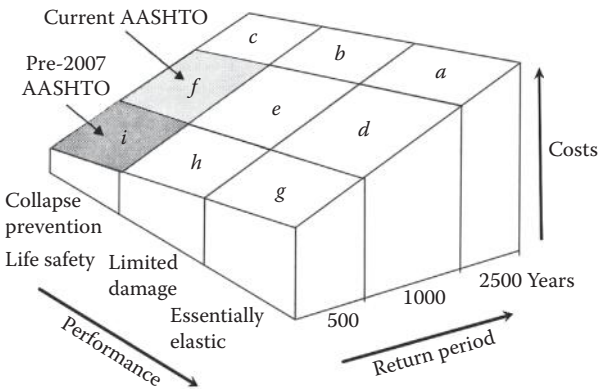

FIGURE 7.1 Cost implications of performance-based design.

have substantial effects on the economic and social well-being of a community as demonstrated in past earthquakes. For example, government-reported loss data from the Kobe and Northridge earthquakes show that total economic losses including loss of use and disruption were ten times greater than the direct costs for repairing damaged structures. These statistics suggest that the ductile design approach for bridges that began shortly after the San Fernando earthquake is being challenged in light of new developments that have surfaced since that time. Minimizing damage using Energy Dissipating Devices (EDD) is being used for critical bridges and is gaining acceptance on the more common bridges in the moderate and high seismic zones.

7.2 Introduction

7.2.1 Development Goals and Key Features of the Seismic Guide

The development of the AASHTO Guide Specifications for LRFD Seismic Bridge Design began with National Cooperative Highway Program (NCHRP) Task 193 in 2003 (I&A, 2005). This NCHRP project was organized to assist the AASHTO T-3 Subcommittee for Seismic Design of Bridges to complete another step toward producing a LRFD seismic design provisions for inclusion into the *AASHTO LRFD Bridge Design Specifications*. The T-3 Subcommittee defined very specific tasks as described in this section that the envisioned were needed to supplement the existing completed efforts (i.e., *AASHTO Division I-A*, MCEER/ATC-49 (*NCHRP 12-49) Recommended Guidelines, SCDOT Specifications, Caltrans Seismic Design Criteria, NYDOT Seismic Intensity Maps*, and *ATC-32*). A primary objective was to develop a specification for AASHTO that was user friendly and could be implemented into practice easily using the same format as that used in AASHTO Division 1-A. The tasks were completed under the guidance of the T-3 Subcommittee (I&A, 2005) and the assistance of their board of reviewers to yield a stand-alone *Seismic Guide* that was evaluated by AASHTO and adopted in 2007 (Imbsen, 2007a and 2007b). This project was completed by Imbsen Consulting under a subcontract with TRC/Imbsen & Associates, Inc. As mentioned above, this contract began with six tasks that were defined by the T-3 AASHTO Committee on Seismic Design of Highway Bridges. The tasks included

1. Review of pertinent documents and information that was available at that time
2. The selection and justification of a seismic hazard to be used and its approval by the T-3 AASHTO Committee
3. Development of an expanded "no-analysis" zone to be incorporated into a DBA
4. Selection and recommendation of a seismic design approach for highway bridges having steel superstructures

5. Recommendation on a procedure to be used for liquefaction design for highway bridges
6. Development of a user friendly specification utilizing the available technology that would easily be implemented in all seismic zones within the United States

Additionally, the new *Seismic Guide* incorporates recent experience, best practices, and research results that are a significant improvement over the traditional FBA. It is expected that the *Seismic Guide* will be revised as future refinements or improvements become available.

Key features of this *Seismic Guide* include

- Adoption of the 7.5 probability of exceedance in the 75 (i.e., 975-year return period) year design life of a bridge for development of a design spectrum.
- Adoption of the NEHRP site classification system that includes site factors for determining response spectrum ordinates.
- Calibration to ensure sufficient conservatism (1.5 safety factor) for minimum support length requirements and ductility capacity. This conservatism is consistent with that needed to accommodate the reserve capacity of the plastic hinging mechanism of the bridge system that could not be accounted for using a numerical solution.
- Establishment of four SDCs for the various seismic hazards within the United States that would not be a significant departure from the current practice having a 500-year return period.
- Development of new imperical equations to determine the ductile displacement capacity of reinforced concrete columns in the low to moderate seismic zones.
- Introduction of global design strategies allowing for three types of bridge structural systems.
  - Type 1-Design a ductile substructure with an essentially elastic superstructure.
  - Type 2-Design an essentially elastic substructure with a ductile superstructure.
  - Type 3-Design an elastic superstructure and substructure with a fusing mechanism at the interface between the superstructure and the substructure.

A performance-based approach, as used in the *Seismic Guide*, aims at providing bridge designers with the capability to achieve as a minimum a "life safety" performance level for the various seismic hazards in the United States.

7.2.2 Ground Motion Hazard

The first initial step to a more comprehensive seismic design approach in the AASHTO 1976 Bridge Design Specifications was to include a USGS map of peak ground acceleration for a 500-year seismic hazard. This map was subsequently updated with the 1983 adoption of ATC-6 as the AASHTO Guide Specification for Seismic Design of Highway Bridges, which became known as Division 1A. The 975-year seismic hazard was also developed by USGS specifically for the *Seismic Guide*. As described in the NCHRP 20-07/193 study, the 975-year return period was justified based on correlation with historical earthquakes in various parts of the United States (I&A, 2006). The 975-year return period was subsequently approved by AASHTO for the *Seismic Guide* then subsequently adopted for the AASHTO LRFD Specifications and the FHWA Retrofitting Manual.

As shown in NCHRP Project 20-07/193 the hazard level for the 2500-year return period corresponds to a shaking level at about the median-plus-one standard deviation level in many parts of the United States. Considering Caltrans' practice, which uses median attenuation models for setting the safety limit state ground motion criteria for ordinary bridges; it can be argued that the 2500-year hazard level is too conservative for ordinary (conventional) bridges. This level of conservatism in the seismic hazard coupled with conservatism in the design specifications led to the AASHTO decision to reject the 2500-year return period as proposed in MCEER/ATC-49 (NCHRP 12-49) and adopting a 975-year return period as proposed in NCHRP 20-07/193.

7.2.3 Flow Charts

The flow charts were developed to provide a means of implementing the *Seismic Guide* into design practice. The two main flow charts entitled "Seismic Design Procedure Flow Chart" as shown in Figures 7.2 and 7.3, guide the engineer in applying the *Seismic Guide*. Subflow charts referenced in the main flow charts cover specific tasks that are required for the seismic design. A typical subflow chart is for example shown in Figure 7.4 "Demand Analysis Flow Chart" provides additional information for the demand analysis task.

The flow chart in Figure 7.2 guides the designer on the applicability of the specifications and the breadth of the design procedure dealing with all the SDCs. Figure 7.3 continues to show the core flow chart of procedures outlined for bridges in SDC B, C, and D. The requirements for single-span bridges and bridges in SDCA are included in the flow chart shown in Figure 7.2. The core flow chart directs the designer to subflow charts as shown in example in Figure 7.4, needed to complete specific tasks defined in the core flow chart. Part of the T-3 review process included six trial bridges typical of those being built in various parts of the United States. The trial bridges were different types with various seismic hazards. All designers involved in conducting the trials remarked on how helpful the flow charts were in applying the new *Seismic Guide*.

7.3 General Requirements

7.3.1 Applicability of *Seismic Guide*

The *Seismic Guide* was developed for the design of new conventional bridges (i.e., slab, beam, girder, and box girder superstructures) to resist the effects of earthquake motions. For other types of construction (e.g., suspension bridges, cable-stayed bridges, truss bridges, arch type, and movable bridges) the owner should specify and/or approve appropriate provisions. The *Seismic Guide* philosophy can be used as a basis for developing a more comprehensive site specific seismic design specification for an essential or critical bridge.

The provisions specified in the *Seismic Guide* are minimum requirements. Additional provisions are needed to achieve higher performance criteria for minimum or no damage as required for essential or critical bridges. These provisions are site/project specific and are generally tailored to a particular structure type.

For these special cases selecting the performance level should be done in consultation with the owner. The three performance levels used in seismic bridge design include

- Life safety (i.e., no collapse)
- Essential
- Critical

Although the *Seismic Guide* is based on a performance of "life safety" the basic principles used may be applied to the higher performance levels.

Designing bridges for "life safety" as mentioned in above paragraph, began at Caltrans in 1973 shortly after the San Fernando earthquake (Imbsen and Gates, 1973). This performance level was selected because it was most practical to meet the ductile design approach developed for the design. Essential Bridges are bridges that should as a minimum be opened to emergency vehicles and for security, defense, or economic purposes once inspected after the design level earthquake. And subsequently open to all traffic within days after the event. Critical bridges are formally designated as critical for a defined local emergency plan and are required to be open to all traffic once inspected after a design level earthquake.

A road map for the successful application of the *Seismic Guide* includes

1. Select a performance level and the global design strategy best suited to achieve the selected performance.
2. Determine the seismic hazard including the ground site effects.

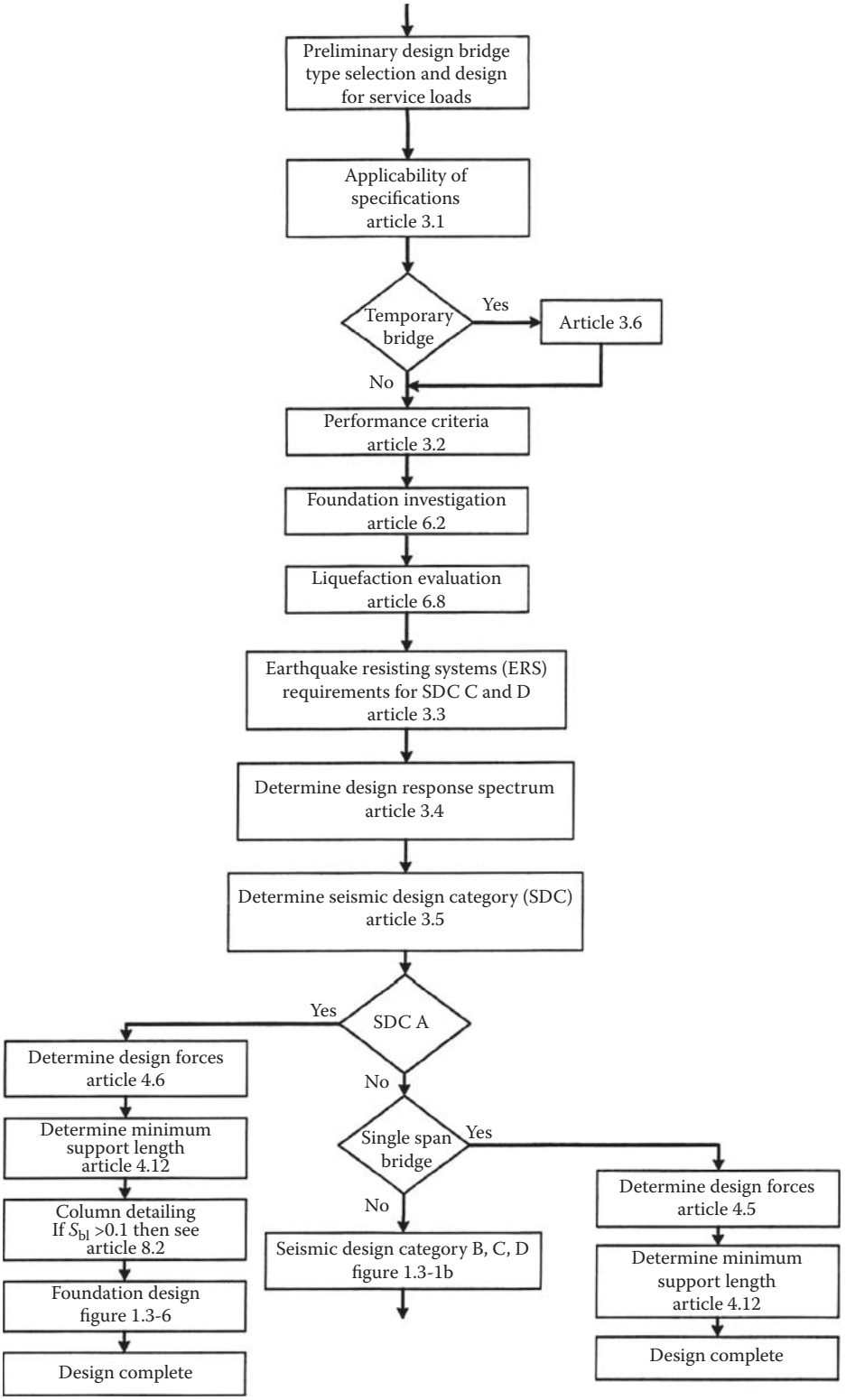

FIGURE 7.2 Seismic design procedure flow chart.

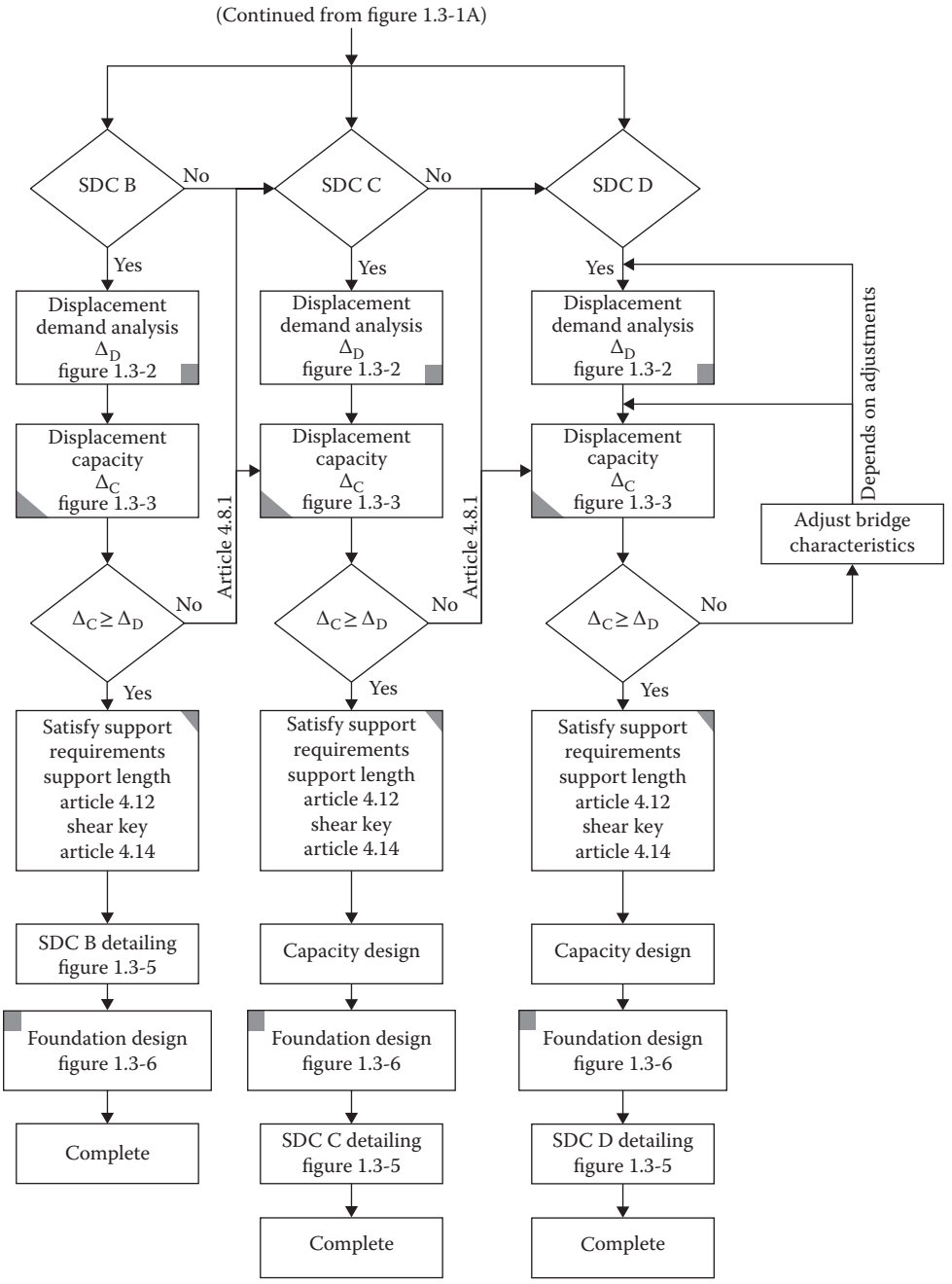

FIGURE 7.3 Seismic design procedure flow chart (continued).

3. Perform a seismic response analysis to determine the displacement and force demands.
4. Design the bridge to meet the imposed displacement demands.
5. Check the load path and provide the displacement capacity and capacity protection principles for the elements that are designed to remain elastic or essentially elastic as needed to achieve the selected performance level.

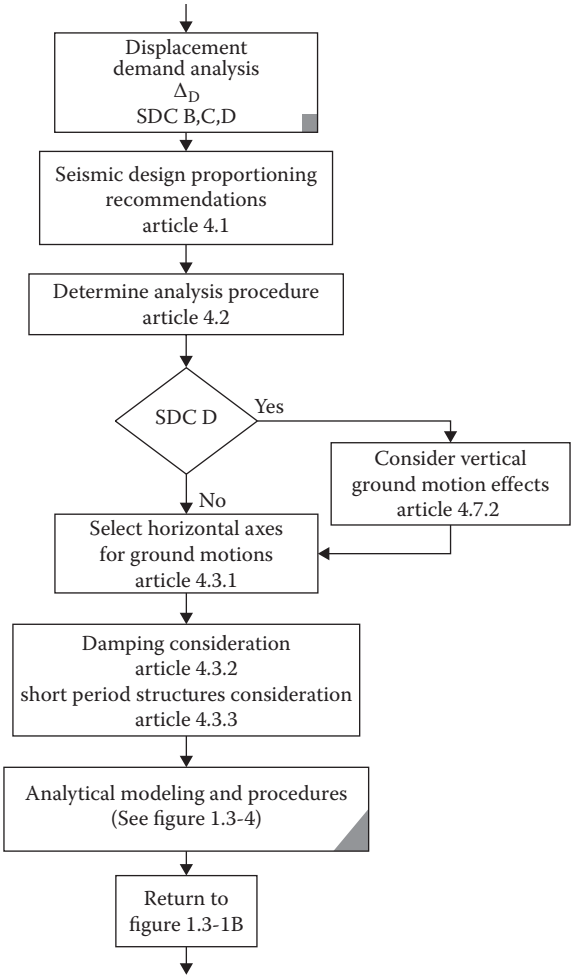

FIGURE 7.4 Demand analysis subflow chart.

7.3.2 Performance Criteria

Bridges are designed for the life safety performance objective considering a seismic hazard corresponding to a 7% probability of exceedance in 75 years. Higher levels of performance, such as the operational objective, may be used with the authorization of the bridge owner. Life safety for the design event infers that the bridge has a low probability of collapse but, may suffer significant damage and significant disruption to service. Partial or complete replacement may be required.

Significant damage level includes permanent offsets and damage consisting of cracking, reinforcement yielding, major spalling of concrete and extensive yielding and local buckling of steel columns, global and local buckling of steel braces, and cracking in the bridge deck slab at shear studs. These conditions may require closure to repair the damages. Partial or complete replacement of columns may be required in some cases. For sites with lateral flow because of liquefaction, significant inelastic deformation is permitted in the piles. Partial or complete replacement of the columns and piles may be necessary if significant lateral flow occurs. If replacement of columns or other components is to be avoided, the design strategy producing minimal or moderate damage such as seismic isolation or the control and reparability design concept should be assessed. Significant disruption to service level includes limited access (reduced lanes, light emergency traffic) on the bridge. Shoring may be required.

7.3.3 Seismic Ground Motion Shaking Hazard

The development of the *Seismic Guide* began in 2003 with T-3 Subcommittee third and final rejection of MCEER/ATC-49 (NCHRP 12-49). The T-3 Subcommittee requested that the Ground Shaking Hazard for the *Seismic Guide* be improved, as mentioned above for Task 2 and as described in more detail in the Methodology Document Task F3-5 AASHTO T-3 Support (Imbsen, 2004). The following issues were addressed:

1. Selection of Return Period and Design Spectrum for a Single Hazard Level, which is more consistent without the hazards used in bridge design addressing a No Collapse Criteria of bridges
2. Range of Applicability for No Analysis or Limited Analysis, consistent with the implementation of a User Friendly Criteria

It was deemed important to focus and examine these issues in detail as achieving consensus on these issues was considered a major milestone in the potential adoption of the *Seismic Guide*.

Since the overall objective of the T-3 Subcommittee was to mitigate the highway systems' vulnerability to seismic damage, it was desirable to lay out a path to consolidate recent research into updated, implementable design guidelines for practicing engineers to use on a national basis.

This task required an assessment of the then current seismic hazard provisions that were included in the following:

1. AASHTO Division 1-A
2. ATC-32
3. Caltrans SDC
4. NCHRP Project 12-49 "Recommended LRFD Guidelines for the Seismic Design of Highway Bridges"
5. South Carolina DOT SDC for highway bridges

The resources sited above were screened to identify portions that should be retained and included in the *Seismic Guide*. The screening and retention of appropriate material took into consideration the following aspects:

1. Research conducted since AASHTO Division 1-A.
2. Ensuring practical and implementable guidelines.
3. Cost-effective use of public funds.
4. Reasonable tolerance of risk.
5. Ease of use by a practicing bridge engineer.
6. Review of comments explaining the reasons why NCHRP 12-49 was not accepted by AASHTO T-3 Committee and other related reference documents.
7. Ensuring that the guidelines are adoptable by AASHTO (based on discussions and reviews with T-3 members and other states).

The objective of Task F3-5 (Imbsen, 2004) was to propose a road map that drew special consideration to the issues highlighted by the AASHTO's T-3 Subcommittee needing improvement or modification.

The ground-shaking hazard prescribed in the *Seismic Guide* is defined in terms of acceleration-response spectra and site coefficients. They are determined in accordance with the general procedure as described in the *Seismic Guide Article 3.4.1* or the site-specific procedure in *Article 3.4.3*.

Using either the general procedure or the site-specific procedure, a decision as to whether the design motion is defined at the ground surface or some other depth needs to be made as an initial step in the design process.

7.3.3.1 Design Spectra Based on General Procedure

Design-response spectra is constructed using response spectral accelerations taken from national ground motion maps and site factors described in *Article 3.4.2* as shown in Figure 7.6. Values of PGA,

S_s and S_1 (see Figure 7.6) may be obtained from ground motion maps shown in the *Seismic Guide*. Alternatively, they may also be obtained using the *Seismic Guide* accompanying CD-ROM, which contains electronic versions of the ground motion maps.

The site coefficients for the ground accelerations F_{pga}, F_a are shown in Table 7.1a for the PGA and S_a, and F_v are shown in Table 7.1b, for S_1. Site Class B (soft rock) is taken to be the reference site category for USGS ground motion site factors. Site Class B rock is therefore the site condition for which the site coefficient factor is 1.0. Site Classes A, C, D, and E have separate sets of site factors for zero-period (F_{pga}), the short-period range (F_a), and the long-period range (F_v), as indicated in Table 7.1a and b. These site factors generally increase as the soil profile becomes softer (in going from Site Class A to E) because of the strongly nonlinear behavior of soil. Except for Site Class A (hard rock), the factors also decrease as the ground motion level increases. For Site Classes C, D, or E, these nonlinear site factors increase the ground motion more in areas having lower rock ground motions than in areas having higher rock ground motions.

In the general procedure, the spectral response parameters are defined using the *USGS/AASHTO Seismic Hazard Maps* produced by the U.S. Geological Survey (USGS) depicting probabilistic ground motion and spectral response for 7% probability of exceedance in 75 years as shown in Figure 7.5 for the Peak Horizontal Acceleration, PGA.

7.3.3.2 Design Spectra Based on Site-Specific Procedures

The objective of the site-specific probabilistic ground-motion analysis, as described in *Article 3.4.3*, is to generate a uniform-hazard acceleration response spectrum considering a 7% probability of exceedance in 75 years for spectral values over the entire period range of interest.

The intent in conducting a site-specific probabilistic ground motion study is to develop ground motions that are more accurate for the local seismic and site conditions than that obtained using the general procedure. Accordingly, such studies should be comprehensive and incorporate current scientific interpretations at a regional scale.

A site-specific procedure shall be used if any of the following apply:

- Soils at the site require site-specific evaluation (i.e., Site Class F soils, *Article 3.4.2.1*); unless a determination is made that the presence of such soils would not result in a significantly higher response of the bridge.
- The bridge is considered to be critical or essential according to *Article 4.2.2* for which a higher degree of confidence of meeting the seismic performance objectives of *Article 3.2* is desired.
- The site is located within 6 miles of a known active fault and its response could be significantly and adversely influenced by near-fault ground motion characteristics.

7.3.4 Seismic Design Categories

In establishing the partitions for the SDCs a key issue raised by the T-3 Committee was establishing the zones between the analysis and no-analysis requirements that were similar to those in AASHTO Division 1-A.

The SDC reflects the variation in Seismic Hazard Level across the country and is used to specify different requirements for methods of analysis, minimum support lengths, column design details, capacity protection, and foundation and abutment design procedures.

The Seismic Hazard Level is defined as a function of the magnitude of the ground surface shaking as expressed by $S_{D1} = F_v S_I$ at the one second period (see Figure 7.4). Each bridge is designed to one of four SDCs, A through D, based on the one second period design spectral acceleration for the design earthquake as shown in Table 7.2.

The design requirements for each of the proposed SDCs are shown in Table 7.3 and described in this section. No detailed seismic structural analysis is required for a single-span bridge or for any bridge in SDC A as shown in Figure 7.2. Specific detailing requirements are applied for SDC A. For single-span

FIGURE 7.5 Peak horizontal acceleration (PGA) for the conterminous United States with 7% probability of exceedance in 75 years.

TABLE 7.1A Values of F_{pga} and F_a as a Function of Site Class and Mapped Peak Ground Acceleration or Short-Period Spectral Acceleration Coefficient

	Mapped Spectral Response Acceleration Coefficient at Short Periods				
Site Class	PGA ≤ 0.10 $S_s \le 0.25$	PGA = 0.20 $S_s = 0.50$	PGA = 0.30 $S_s = 0.75$	PGA = 0.40 $S_s = 1.00$	PGA ≥ 0.50 $S_s \ge 1.25$
A	0.8	0.8	0.8	0.8	0.8
B	1.0	1.0	1.0	1.0	1.0
C	1.2	1.2	1.1	1.0	1.0
D	1.6	1.4	1.2	1.1	1.0
E	2.5	1.7	1.2	0.9	0.9
F	*a*	*a*	*a*	*a*	*a*

Note: Use straight line interpolation for intermediate values of PGA and S_s, where PGA is the peak ground acceleration and S_s the spectral acceleration coefficient at 0.2 second obtained from the ground motion maps.

[a] Site-specific response geotechnical investigation and dynamic site response analyses shall be considered (*Article 3.4.3*).

TABLE 7.1B Values of F_v as a Function of Site Class and Mapped 1 Second Period Spectral Acceleration Coefficient

	Mapped Spectral Response Acceleration Coefficient at 1 Second Periods				
Site Class	$S_1 \le 0.1$	$S_1 = 0.2$	$S_1 = 0.3$	$S_1 = 0.4$	$S_1 \ge 0.5$
A	0.8	0.8	0.8	0.8	0.8
B	1.0	1.0	1.0	1.0	1.0
C	1.7	1.6	1.5	1.4	1.3
D	2.4	2.0	1.8	1.6	1.5
E	3.5	3.2	2.8	2.4	2.4
F	*a*	*a*	*a*	*a*	*a*

Note: Use straight line interpolation for intermediate values of S_1, where S_1 is the spectral acceleration coefficient at 1.0 second obtained from the ground motion maps.

[a] Site-specific geotechnical investigation and dynamic site response analyses shall be performed (*Article 3.4.3*).

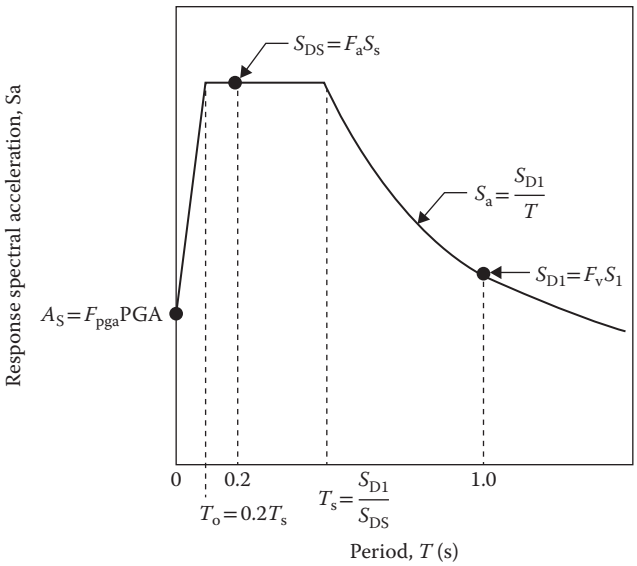

FIGURE 7.6 Design response spectrum, using the three-point method.

TABLE 7.2 Partitions for Seismic Design Categories A, B, C, and D

Value of $S_{D1} = F_v S_1$	SDC
$S_{D1} < 0.15$	A
$0.15 \leq S_{D1} < 0.30$	B
$0.30 \leq S_{D1} < 0.50$	C
$0.50 \leq S_{D1}$	D

bridges, minimum support length requirement shall apply according to *Article 4.12* in the *Seismic Guide*. However, detailed geotechnical analysis of the abutments may be required by the owner for a single-span bridge if there is potential for significant lateral spreading or other forms of abutment instability are possible because of liquefaction. For both single-span bridges and bridges classified as SDC A, the connections must be designed for specified forces in *Article 4.5* and *Article 4.6* respectively, and should also meet minimum support length requirements of *Article 4.12*.

7.3.5 Seismic Design Requirements for SDC A, B, C, and D

Having determined the SDC the specific design requirements for each of the SDC's is shown in Table 7.3 and described below with reference to the applicable article(s) in the *Seismic Guide* for each of these requirements.

7.3.5.1 Global Design Strategies (*Article 1.1, 1.3, 3.3, and 7.2*)

There are three Global Seismic Design Strategies used in the *Seismic Guide*. These are based on the expected behavior characteristics of the bridge system, which include

- Type 1: Ductile Substructure with an Essentially Elastic Superstructure—this category includes conventional plastic hinging in columns, pier walls, and abutments that limit inertial forces by full mobilization of passive soil resistance. Also included are foundations that may limit inertial forces by in-ground hinging, such as pile bents and integral abutments on piles.
- Type 2: Essentially Elastic Substructure with a Ductile Superstructure—this category applies only to steel superstructures where energy dissipation is achieved in the cross frames at the piers.
- Type 3: Elastic Superstructure and Substructure with a fusing mechanism between the two—this category includes seismically isolated structures and structures where supplemental energy dissipation devices, such as dampers, are used to control inertial forces transferred between the superstructure and substructure.

7.3.5.2 Earthquake Resisting Systems Requirements for SDC C & D (*Article 3.3*)

For the purposes of encouraging the use of appropriate systems and of ensuring due consideration of performance for the owner, the ERS and earthquake resisting elements (ERE) are categorized as follows:

- Permissible
- Permissible with owner's approval
- Not recommended for new bridges

These terms, as originally defined in NCHRP 12-49 (MCEER, 2004) apply to both systems and elements. For a system to be in the permissible category, its primary ERE's shall be in the permissible category. If any ERE is not permissible, then the entire system is not permissible.

For SDC C or D, all bridges and their foundations should have a clearly identifiable Earthquake Resisting System (ERS) selected to achieve the life safety criteria. The ERS must provide a reliable and uninterrupted load path for transmitting seismically induced forces into the surrounding soil and

TABLE 7.3 Design Reguirements for Seismic Design Categories A, B, C, and D

Requirements	A	B	C	D
Global Strategy	—	Recommended	Required	Required
Identification ERS	—	Recommended	Required	Required
Support Connections	Required	Required	Required	Required
Support Length	Required	Required	Required	Required
Demand Analysis	—	Required	Required	Required
Implicit Capacity	—	Required	Required	—
Pushover Capacity	—	—	—	Required
Detailing–Ductility	—	SDC B	SDC C	SDC D
Capacity Protection	—	Recommended	Required	Required
P-Δ Effect	—	—	Required	Required
Minimum Lateral Strength	—	Required	Required	Required
Liquefaction Potential	—	Recommended	Required	Required

sufficient means of energy dissipation and/or restraint to reliably control seismically induced displacements. All structural and foundation elements of the bridge should be capable of achieving anticipated displacements consistent with the requirements of the chosen design strategy of seismic resistance and other structural requirements.

7.3.5.3 Support Connections *(Article 4.13)*

Support Connections are required for all four of the SDCs. The connections are required to insure that unseating of the superstructure, which may lead to collapse is prevented. Restraint is used between frames to minimize seismic displacements and reduce the out-of-phase displacements between frames of a multiframe system. Additionally the joints must provide movement for service load conditions (e.g., thermal, shrinkage, imposed live loads). Also the joints should be designed to transmit the seismic inertia loads from the superstructure to the foundation. Shear keys must also be designed strong enough to transmit the inertia loads to the foundation. They, in some cases, may be designed as a fuse mechanism to protect foundation elements from being damaged during a severe earthquake.

7.3.5.4 Support Length *(Article 4.12)*

As shown in Table 7.3 Support Length determination is required in all four SDCs, which is also shown in the flow charts included in Figures 7.2 and 7.3; *Article 4.12* is referenced for the specifications giving the details to follow in meeting the requirements.

Minimum Support Lengths were developed and calibrated to prevent unseating that could lead to collapsed spans. The calculation for a hinge seat length involves four components:

1. Minimum edge distance
2. Other movement attributed to prestress shortening, creep, shrinkage, and thermal expansion or contraction
3. Skew effect
4. Relative hinge displacement

The formulas were originally developed as part of the ATC-6 effort to include the effects of differential ground movements at the supports. The differential ground movements included both rotational and translational effects because of the traveling waves that occur in an earthquake. The formulas were compiled using typical column heights, span lengths, and multiple span frames. The formulas were developed to be conservative to account for the uncertainties in the ground motions and the fact that hinge supports are not expensive to build.

New support length formulas were developed for all the SDCs to be included in the *Seismic Guide* that included the recent research conducted at the University of California Berkeley. However, during the *Seismic Guide* review the T-3 AASHTO Committee elected to retain the original support length formulas for SDC A, B, and C since they were more conservative with the formulas proposed for the *Seismic Guide*. The formula developed for SDC D was included in the *Seismic Guide Article 4.12.3* (DesRoches and Fenves, 1997) (I&A, 2005), because it was considered more appropriate for the higher SDC D to include the latest research finding.

7.3.5.5 Demand Analysis *(Articles 4.3 and 4.4)*

As shown in Table 7.3 Demand Analysis is required for SDC B, C, and D. The flow chart in Figure 7.3 further directs, with the darkened square on the lower right hand corner, the designer to a subflow chart where the specific requirements are given for the SDC B, C, and D. As shown in this flow chart vertical ground motions effects as described in *Article 4.7.2* are required for SDC D. This subflow further directs the designer to the details on modeling procedures and the analysis procedures with the specific reference to the various articles defining the requirements indicated by the darkened triangle.

7.3.5.6 Implicit Capacity *(Article 4.8.1)*

As shown in the Table 7.3 Implicit Capacity determination for displacements is required for SDC B and C. The flow chart shown in Figure 7.3 further directs the designer to a subflow chart that indicates that the displacement capacities are determined using an "implicit procedure" specifically developed for these SDC B and C (Imbsen 2007a and 2007b) to avoid having to conduct a pushover capacity analysis to obtain the displacement capacity in these moderate seismic categories. The development of the implicit procedure is described in Section 7.3.5.7. The requirements for each of these SDCs are described in *Article 4.8.1*

7.3.5.7 Pushover Capacity *(Article 4.8.2)*

As shown in Table 7.3 the pushover capacity determination is only required in SDC D. As indicated in the subflow chart, the displacement capacity determination is described in *Article 4.8.2*. The nonlinear static procedure (NSP) is commonly referred to as "pushover analysis." This procedure is used to determine the most reliable displacement capacities of a structure or frame as it reaches its limit of structural stability or the maximum allowable as defined in the *Seismic Guide Article 4.3.3*. NSP is an incremental linear analysis, which captures the overall nonlinear behavior of the elements, including soil effects, by pushing them laterally to initiate plastic action. Each increment of loading pushes the frame laterally, through all possible stages, until the potential collapse mechanism is achieved.

The analytical model used in the pushover analysis accounts for the redistribution of internal actions as components respond in the nonlinear range. This is expected to provide a more realistic measure of behavior than can be obtained from elastic analysis procedures. This design procedure is a key element in the philosophic development of the *Seismic Guide*. The pushover method of analysis has seen increasing use throughout the 1990s, especially in Caltrans' seismic retrofit program. This analysis method provides additional information on the expected deformation demands of columns and foundations and as such provides the designer with a greater understanding of the expected performance of the bridge. This procedure was successfully applied to the Caltrans 29/580, 980 Viaduct located in Oakland, CA as part of the seismic retrofit program. This was the first application of the performance-based approach used in California and possibly the United States (Imbsen and Liu, 1994).

7.3.5.8 Detailing for Ductility *(Articles 4.10–4.13 and Section 6, 7 and 8)*

As shown in Table 7.3 specific detailing requirements are required for SDC B, C, and D. The flow chart included in Figure 7.3 references *Articles 4.12 and 4.13* of the *Seismic Guide*. Additional guidance on the requirements is given in *Articles 4.10, 4.11*, and *Sections 6, 7, and 8*. Seismic detailing for ductility

increased incrementally for each of the SDC depending on the earthquake hazard intensity as established in the *Seismic Guide*.

7.3.5.9 Capacity Protection *(Sections 4.8–4.14, 7.5–7.7, 8.5–8.16)*

As shown in Table 7.3 the requirements for Capacity Protection includes SDC B, C, and D. Capacity protection is recommended for SDC B and is required for SDC C and D. An adequate margin of strength between the ductile plastic hinging components and nonductile components is required for capacity protection. Desired locations of plastic hinging require specific details and strength for ductile response. The other components are designed to have a sufficient margin of strength to assure that the designated yielding mechanism occurs and undesirable nonductile failure mechanisms (e.g., concrete crushing, shear cracking, elastic buckling, and facture) are prevented from occurring. Included in this section is a requirement that the ultimate compressive axial force, Pu, SDC C, and D be <0.2 fc Ag.

7.3.5.10 *P*-Δ Effect *(Article 4.11.5)*

As shown in Table 7.3 the requirement for *P*–Δ effect is only required in SDC C and D. The subflow chart (*Seismic Guide, Figure 1.3.3*) and described in Seismic Guide *Article 4.11.5* for the evaluation of *P*-Δ Capacity Requirements. Typical highway bridges are designed so that the *P*-Δ effects can be neglected that can be verified by checking the *P*-Δ effect to verify that it is <0.25 M_p. This applies to both reinforced concrete members and steel components. If these conditions are not satisfied the column moment capacity maybe increased, or alternatively a rigorous nonlineal analysis can be conducted.

7.3.5.11 Minimum Lateral Strength *(Article 8.7)*

As shown in Table 3.3 this check is required for all SDCs. These requirements are limited to ductile member design for SDC B, C, and D. The minimum lateral flexural capacity of each column is checked to verify that it has a minimum lateral capacity to resist 0.1 of the tributary load acting on the column.

7.3.5.12 Liquefaction Potential *(Article 6.8)*

As shown in Table 7.3 this check is recommended for SDC B and required for SDC C and D. Liquefaction hazard or the potential for seismically generated pore pressure leading to reduced soil shear strength, slope failures, and associated ground deformations are considered for this requirement. Laboratory and site investigation methods to determine the liquefaction strength of site soils (including SPT and CPT methods) are discussed leading to empirical evaluation procedures commonly used to determine the potential for triggering liquefaction. Screening approaches to assess the need for such evaluations in regions of low seismicity are also described in *Article 6.8* of the *Seismic Guide*.

7.4 Analysis and Design Requirements

This section recommends the method of seismic analysis and design for bridges. Modeling recommendations and requirements are given in the *Seismic Guide Section 4*. The seismic design demand displacements are determined in accordance with the procedures in the *Seismic Guide Section 5*. Material and foundation design requirements are given in *Sections 6, 7, and 8*.

7.4.1 Seismic Demand Determination *(Articles 4.1–4.8)*

The *Seismic Guide* provides guidance on the modeling to distribute the stiffness and mass to capture the response of a bridge subjected to an earthquake. Although many types of modeling, as shown in Figure 7.7, are available in the commercial computer programs, the most popular model typically used

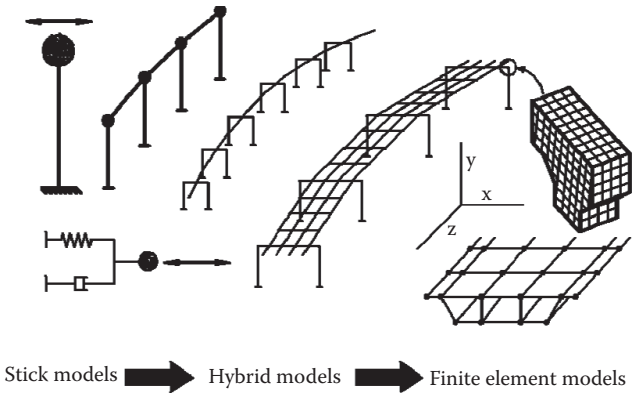

FIGURE 7.7 Bridge models available on commercial computer programs.

is the spline model. Spline models are generally used with nodes at the quarter or fifth points within a span and columns are modeled with nodes at the one-third points. As described in S*ection 6* of the *Seismic Guide* the effects of the foundation can be modeled using one of several different techniques.

As shown in Table 7.3, there is no Demand Analysis required for SDC-A and for single-span bridges. Demand Analysis is required for SDC B, C, and D. The demand analysis techniques include: (1) Equivalent Static, (2) Elastic Dynamic Analysis (EDA), and (3) Nonlinear Time History. The chosen technique depends on the complexity of the bridge and the selected performance category. The most commonly used technique is the Elastic Response Spectrum Dynamic Analysis. The *Seismic Guide* gives guidance on the selection of an appropriate analysis procedure.

7.4.2 Capacity Determination *(Articles 4.9–4.12)*

For design purposes, each structure is typically categorized according to its intended structural seismic response in terms of damage level (i.e., ductility demand). Figure 7.8 shows the test results demonstrating the progression of damage of a ductile reinforced concrete column.

The displacement capacity of a reinforced concrete column such as that shown in the flow chart included in Figure 7.3 for SDC D may be approximated analytically by doing a pushover analysis. This analysis is done to approximate the nonlinear relationship between the applied load, F, and the displacement, Δ, by applying a monotonic loading as shown in Figure 7.9. This procedure was initially presented (Imbsen, 1979) using the capacity of a reinforced concrete column having a capacity defined by the onset of strain hardening in the longitudinal reinforcement.

To demonstrate, consider for example, the calculation of the load versus displacement relationship as a cantilever column is loaded from zero lateral load to the attainment of the ultimate displacement, Δ_u, with a monotonically applied lateral (shear) load, *F*, at the superstructure level as illustrated in Figure 7.9. Ultimate, in this case, corresponds to the attainment of a capacity limit state, which could be rupture of the tension steel, crushing of concrete, or other local failure modes. The range of possible limit states is discussed later in this section. Figure 7.9 illustrates four stages of loading. The first stage corresponds to the undeformed structure. The second stage is the elastic range before yield of the idealized section. The third stage illustrates plastic deformation before attainment of the maximum permissible plastic rotation that corresponds to reaching the first limit state of ultimate displacement. The fourth and final stage corresponds to the beginning of the loss of lateral strength of the column. For example, as longitudinal bars buckle and fracture and as the concrete crushes, the lateral strength of the columns diminishes. A schematic lateral load versus displacement plot for this column is shown in Figure 7.9.

Each stage is described as follows.

Between Stage 0 and 1 the column is elastic and the elastic component of deflection, Δ_e, is

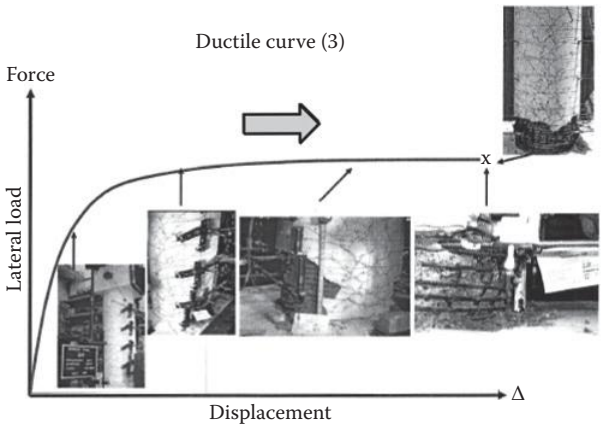

FIGURE 7.8 Photograph showing damage on a ductile reinforced concrete column.

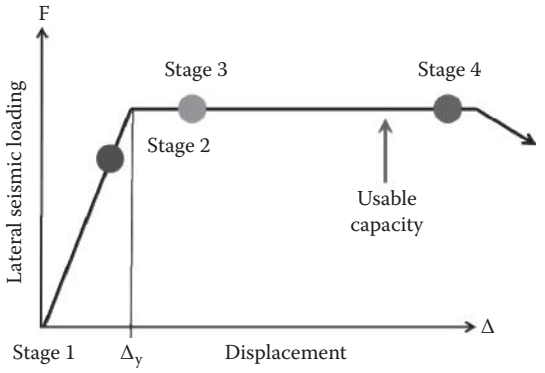

Stages	Description
1	Zero lateral load
2	Just before yielding
3	Just following formation of the plastic hinge
4	Just before plastic hinge capacity-degradation

FIGURE 7.9 Idealized force versus displacement plot.

$$\Delta_e = \frac{FL^3}{3E_eI_{eff}} \tag{7.1}$$

where

L = the length from the fixed end to the free tip (or the inflection point of a fixed-beam-column element)
E_cI_{eff} = the effective flexural stiffness of the member, including cracking effects

When the plastic strength of the member (F_p, M_p) is reached and $\Delta_e = \Delta_{yi}$, the idealized yield displacement is given by

$$\Delta_{yi} = \frac{F_pL^3}{3E_eI_{eff}} = \frac{M_pL^2}{3EI_{eff}} = \frac{1}{3}\phi_{yi}L^2 \tag{7.2}$$

M_p = the plastic moment capacity
ϕ_{yi} = the idealized yield curvature

For the plastic displacement component, Δ_p

$$\Delta_p = \phi_p L_p (L - 0.5 L_p) \tag{7.3}$$

L_p = the analytical equivalent plastic hinge length
ϕ_p = the plastic curvature defined as

$$\phi_p = \phi_u - \phi \tag{7.4}$$

where ϕ_u = the ultimate curvature obtained from a cross-section analysis ϕ_{yi} = the idealized yield curvature.

The total displacement; Δ_u, is given by

$$\Delta_u = \Delta_{yi} + \Delta_p \tag{7.5}$$

where

Δ_{yi} = the elastic component of displacement corresponding to the idealized yield
Δ_p = the plastic component of displacement

The analytical plastic hinge length for columns, L_p, may be taken as the equivalent length of column over which the plastic curvature is assumed constant for estimating the plastic rotation. The plastic displacement of an equivalent cantilever member from the point of maximum moment to the point of contra-flexure may be determined using the plastic rotation and the equivalent cantilever length. The plastic hinging length varies depending on the configuration of the column. A few examples are given below.

For reinforced concrete columns framing into a footing, an integral bent cap, an oversized shaft, cased shaft, or top of pile in a pile bent, the plastic hinge length, L_p in inches, may be determined as

$$L_p = 0.08L + 0.15 f_{ye} d_{bl} \geq 0.3 f_{ye} d_{bl} \tag{7.6}$$

where

L = length of column from point of maximum moment to the point of moment contraflexure (in.)
f_{ye} = expected yield strength of longitudinal column reinforcing steel bars (ksi)
d_{bl} = nominal diameter of longitudinal column reinforcing steel bars (in.)

The first term in Equation 7.6 quantifies the spread of plasticity along the member (i.e., 8% of the cantilever length). The second term quantifies the length of plastic strain penetration into the adjacent element (e.g., footing, cap beam, etc.).

For noncased prismatic drilled shafts, reinforced concrete piles, and prestressed concrete piles, the soil contact tends to distribute the curvatures along the member, and the analytical plastic hinge length, below ground L_p (in.) may be determined as

$$L_p = 0.1H' + D^* \leq 1.5D^* \tag{7.7}$$

where

D* = diameter of circular shafts or cross-section dimension in direction under consideration for oblong shafts (in.)
H' = length of shaft from the ground surface to point of contraflexure above ground (in.)

For members where significant confinement is present hinging region, as with columns with steel jackets or for horizontally isolated flared reinforced concrete columns, the plastic hinge length, L_p in inches, may be determined as

$$L_p = G_f + 0.3 f_{ye} d_{bl} \tag{7.8}$$

where

G_f = gap between the isolated flare or top of jacket and the soffit of the bent cap (in.)
f_{ye} = expected yield strength of longitudinal column reinforcing steel bars (ksi)
d_{bl} = nominal diameter of longitudinal column reinforcing steel bars (in.)

Inelastic action is intended to be restricted to flexural plastic hinges in columns and pier walls and inelastic soil deformation behind abutment walls and wing walls. Details and member proportions shall ensure large ductility capacity, μ_C, under load reversals without significant strength loss with ductility demands ($4.0 \le \mu_D \le 6.0$). This response is anticipated for a bridge in SDC D designed for the life safety Criteria.

For Limited Ductility Response ductility demands are reduced ($\mu_D \le 4.0$). A plastic mechanism as described above for Full-Ductility Structures is required. Intended yielding shall be restricted to locations that are readily accessible for inspection following a design earthquake unless prohibited by the structural configuration. Detailing and proportioning requirements are less than those required for Full-Ductility Structures.

As shown in Table 7.3, there are two methods for determining capacity. The implicit capacity determination for the low to moderate seismic categories (SDC B and C) and the pushover capacity determination for SDC D. The implicit capacity determination was developed as described in NCHRP 20-07/Task 193 (I&A, 2006) to provide a simplified method for determining displacement capacity of reinforced concrete columns in SDCs B and C. This simplified method provides an alternative to do more refined capacity determination using the pushover analysis technique. This simplified method was developed in response to the request made by the T-3 AASHTO Committee to develop a user friendly specification that could be easily implemented into practice. The development of these equations takes advantage of the research conducted by Berry and Eberhard (2003) to develop a procedure to estimate flexural damage in reinforced concrete columns. Their research focused on developing fragility curves for two flexural damage states. The first being concrete cover spalling and the second being buckling of the longitudinal reinforcing steel bars. The equations developed for the *Seismic Guide* Specification included those developed for the lower damage state of concrete spalling. Berry and Eberhard compiled a database, which included physical test results on 253 reinforced concrete columns and 163 spiral reinforced columns were considered in the development of the fragility curves.

To incorporate the test results and the expression for spalling, developed by Berry and Eberhard into the design procedure, a second database was generated. The second database was developed complying with the design requirements given in the *Seismic Guide*. The second database included reinforced concrete columns ranging from 3 to 7 ft. in diameter, heights 20–50 ft. with 1%, 2%, 3%, and 4% reinforcing steel. The designed columns were then evaluated numerically considering three design limit states. Initially the columns were evaluated for yielding of the reinforced steel. The second limit state considered concrete spalling for a concrete cracking strain of 0.005. And for the third limit state the columns were evaluated at a ductility, μ, equal to 4.

Columns for bridges in SDC B were targeted for a drift capacity corresponding to minor damage. Concrete spalling was considered as the limit state for this seismic design of SDC B. The equation shown below appears in *Article 4.8.1* of the *Seismic Guide* as

$$\Delta_C^L = 0.12 H_o \left(-1.27 \ln(x) - 0.32\right) \ge 0.12 H_o \tag{7.9}$$

$$\text{In which}: x = \Lambda \, B_o / H_o \tag{7.10}$$

where

Λ is a fixity factor for the column equal to
$\Lambda = 1$ for fixed-free (pinned on one end)
$\Lambda = 2$ for fixed top and bottom

For a partially fixed connection on one end, interpolation between 1 and 2 is permitted.

B_o = Column width or diameter (ft.) measured parallel to the direction of displacement under
H_o = Height from top of footing to top of the column (i.e., column clear height, ft.)

For SDC C, the drift capacity is targeted to a maximum drift corresponding to moderate damage. The equation shown below also appears in *Article 4.8.1* of the *Seismic Guide* as

$$\Delta_C^L = 0.12 H_o \left(-2.32 \ln(x) - 1.22\right) \geq 0.12 H_o \tag{7.11}$$

Experimental and analytical studies of reinforced concrete columns representing those typically built was considered to develop empirical equations for the displacement capacity in SDC B and C.

Nonlinear Static Pushover Analysis, as defined in Section 7.3.5.7 above, is used to determine the reliable displacement capacities of a structure or frame in SDC D.

Because the analytical model used in the pushover analysis accounts for the redistribution of internal actions as components respond inelastically, pushover analysis is expected to provide a more realistic measure of behavior than can be obtained from elastic demand analysis procedures.

In addition to providing deformability by providing adequate confinement, bridges subject to earthquake ground motion may be susceptible to instability because of *P*-Δ effects. Inadequate strength can result in accumulation of biased structural displacements in one direction causing excessive ductility demand on plastic hinges in the columns, large residual deformations, and possibly collapse. The lateral resistance of a column is therefore limited as shown in Table 7.3, to control the additional displacements that *P*-Δ effects can impose.

P-Δ effects lead to a loss of stiffness and loss in strength once yielding occurs in the columns of a bridge. In severe cases, this can result in the force–displacement relationship having a negative slope once a plastic mechanism is fully developed. The value for Δ given by Equation 7.11 is such that this reduction in strength is limited to 25% of the plastic strength of the pier or bent. The check as shown in Equation 7.12 is preferred to ensure the adequacy of the results obtained using an elastic demand analysis.

$$P_{dl} \Delta_r \leq 0.25 \, M_p \tag{7.12}$$

The displacement of any column or pier in the longitudinal or transverse direction must satisfy.

P-Δ effects may be ignored in the analysis and design of Type 1 structures (see *Article 3.3*) if the following is satisfied:

- For reinforced concrete columns

$$P_{dl} \Delta_r \leq 0.25 \, M_p \tag{7.13}$$

- For steel columns:

$$P_{dl} \Delta_r \leq 0.25 \, M_n \tag{7.14}$$

where

P_{dl} = unfactored dead load acting on the column (kip)
Δ_r = relative lateral offset between the point of contraflexure and the furthest end of the plastic hinge (in.)
M_p = idealized plastic moment capacity of reinforced concrete column based on expected material properties (kip-in.)
M_n = nominal moment capacity of structural steel column based on nominal material properties (kip-in.)

- For a single pile shaft, Δ_r should be taken as

$$\Delta_r = \Delta_D - \Delta_S \tag{7.15}$$

where

Δ_D = displacement demand as determined in accordance with *Article 4.3* (in.) of the *Seismic Guide*
Δ_S = pile shaft displacement at the point of maximum moment developed in ground (in.)

An explicit *P*-Δ check was not required in the previous edition of these specifications but has been introduced herein because two conservative provisions have been relaxed in the *Seismic Guide*. These are

- The shape of the response spectrum (*Figure 3.10.4.1.1* [of the *Seismic Guide*]) has been changed from being proportional to $1/T^{2/3}$ to 1/T. The reason $1/T^{2/3}$ provision in the previous edition was to give conservative estimates of force and displacement in bridges with longer periods (≥1.0 seconds), which, in an indirect way, provided for such effects as *P*-Δ. With the change of the spectrum to being proportional to 1/*T*, an explicit check for *P*-Δ is introduced.
- The flexure resistance factor, ø, for seismic design of columns with high axial loads has been increased from a minimum value of 0.5–0.9 *(Article 5.10.11.4.1b*). Use of a low resistance factor led to additional strength being provided in heavily loaded columns that could be used to offset reductions due to *P*-Δ, in the previous edition. The increased value for ø now permitted in Section 7.5 is a second reason for requiring an explicit check for *P*-Δ.

7.5 Analytical Models and Procedures

7.5.1 General

As shown in Table 7.3, Demand Analysis is required for SDC B, C, and D. This is also shown in the flow charts included in Figures 7.2 and 7.3. Seismic design encompasses demand analysis and displacement capacity verification. The objective of a demand analysis is to estimate the forces and displacements induced by the seismic excitation. A displacement capacity determination of piers and bents is required for SDC B, C, and D to verify that the capacities are greater than the demands.

A complete bridge system may be composed of a single frame and a series of frames separated by expansion joints and/or, articulated construction joints. Individual frame sections are supported on their respective substructures. Substructures consist of piers, single column, or multiple column bents that are supported on their respective foundations.

The seismic response of a bridge includes the development of an analytical model followed by a response analysis of the analytical model to predict the resulting dynamic response for component design. Both the development of the analytical model and the selected analysis procedure are dependent on the seismic hazard, selected seismic design strategy, and the complexity of the bridge. There are various levels or degrees of refinement in the analytical model and analytical procedures that are available to the designer.

The entire bridge ERS for analysis purposes is referred to as the "global" model, whereas an individual bent or column is referred to as a "local" model. The term "global response" describes the overall behavior of the bridge system including the effects of adjacent components, subsystems, or boundary conditions. The term "local response" refers to the behavior of an individual component or subsystem being analyzed to determine, for example, its capacity using a pushover analysis. Both global models and local models are included in the *Seismic Guide* Specifications.

Individual bridge components should have displacement capacities greater than the displacement demands derived from the "global" analysis.

7.5.2 Abutments

As described in the *Seismic Guide* modeling the abutment should reflect the behavior of the abutment in the two horizontal directions. There are two ERS that can be used for the passive pressure of the embankment at the abutment. One ERS includes the abutment contribution and the other does not include the abutment contribution. The active and passive pressure zones in the soil embankment behind the abutment for longitudinal movements are shown in Figure 7.10.

The contribution of the abutment embankment was first recognized in the reconnaissance investigations conducted following the San Fernando earthquake in 1971 (Fung et al., 1971). Simplified methods were developed to account for the contributions by equating the observed residual displacements observed with the passive pressures created in the soils behind the abutments. The Caltrans simplified methods were subsequently confirmed by Romstad and Maronie (Romstad et al., 1996). Since there are some instances where abutment contributions are not included the designer may elect to use the ERS without the abutment contribution as described in the *Seismic Guide* in *Article 5.2.3*.

Case 1: ERS without Abutment Contribution
Case 2: ERS with Abutment Contribution

These same two alternatives are also used for the transverse resistance of the abutments as described in *Article 5.2.4*. Using Case 1, without abutment contribution is used most applicable to the longer bridges or on curved bridges with a small radius. It may also be desirable to not include abutment contribution in the lower seismic zones.

7.5.3 Foundations

The requirement to include soil springs was introduced in the *Seismic Guide* to assist the designer with logical procedure to determine when the effects of the foundation should be included in the seismic response analysis and the modeling methods that can be used for various types of Foundations.

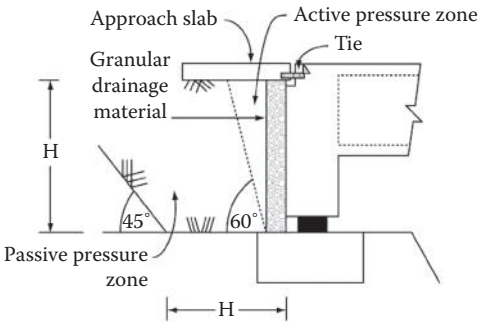

FIGURE 7.10 Abutment passive pressure zone.

Two Foundation Modeling Methods (FMM) are introduced for various foundation types and for various SDCs as described in *Article 5.3.* The various foundation types include: (1) spread footings, (2) pile foundations, and (3) drilled shafts. FMM 1 is less rigorous and typically applicable for the low to moderate seismic zones (i.e., SDC B and C) located in site class A, B, C, and D. The more rigorous FMM 2 method is typically used for SDC D.

7.5.4 Analytical Procedures

The objective of seismic analysis is to assess displacement demands of a bridge and its individual components. Equivalent static analysis and linear EDA are the appropriate analytical tools for estimating the displacement demands for normal bridges.

In specifying the Seismic Design Category (SDC), two principles are followed. First, as the seismic hazard increases, improved modeling and analysis for seismic demands is necessary because the behavior may be sensitive to the maximum demands. Second, as the complexity of the bridge increases, more sophisticated models are required for seismic demand analysis and displacement capacity evaluation. For bridges with a regular configuration, a single-degree-of-freedom model maybe sufficient to represent the seismic response. For these types of bridges, the equivalent static analysis (ESA) (Procedure 1), as described in the *Seismic Guide Article 5.4.2* may be used to establish displacement demands.

For structures that do not satisfy the requirements of regularity for an elastic response spectrum analysis, Procedure 2 EDA, as described in *Article 5.4.3* of the *Seismic Guide,* may be used to determine the displacement demands.

Nonlinear Time History analysis Procedure 3, as described in *Article 5.4.4*, should be used for critical or essential bridges as defined in *Article 4.2.2* and in some cases for Normal Bridges in SDC D using devices for isolation or energy dissipation. In this type of analysis, component capacities are characterized in the mathematical model used for the seismic response analysis.

Inelastic static analysis "Pushover Analysis" is the appropriate analytical tool used to establish the displacement capacities for normal bridges assigned to SDC D as described above in Section 7.4.2.

7.5.5 Mathematical Modeling

For EDA methods, there is an approximation in representing the force–deformation relationship of inelastic structural elements by a single linearized stiffness. For inelastic columns or other inelastic earthquake-resisting elements, the common practice is to use an elastic stiffness for steel elements and a cracked stiffness for reinforced concrete elements. However, the stiffness of seismic isolator units, abutments, and foundation soils are represented by a secant stiffness consistent with the maximum deformation. The designer shall consider the distribution of displacements from an elastic analysis to verify that they are consistent with the inelastic behavior of the earthquake-resisting elements.

In using an EDA for a bridge, the bridge should be modeled as a three-dimensional space frame with joints and nodes selected to realistically model the stiffness and inertia effects of the structure. Each joint or node should have six degrees-of-freedom, three translational and three rotational. The structural mass should be lumped with a minimum of three translational inertia terms at each node.

The mass should take into account structural elements and other relevant loads including, but not limited to, pier caps, abutments, columns, and footings. Other loads such as live loads may be included. Generally, the inertia effects of live loads are not included in the analysis; however, the probability of a large live load being on the bridge during an earthquake should be considered when designing bridges with high live-to-dead load ratios that are located in metropolitan areas where traffic congestion is likely to occur.

7.5.6 Effective Section Properties

Elastic analysis assumes a linear relationship between stiffness and strength. Concrete members display nonlinear response before reaching their idealized yield limit state.

Section properties, flexural stiffness, E_cI_{eff}, shear stiffness parameter $(GA)_{eff}$, and torsional stiffness G_cJ_{eff}, shall reflect the cracking that occurs that before the yield limit state is reached. The effective sections properties are described in *Article 5.6* of the *Seismic Guide*.

7.6 Foundation and Abutment Design

7.6.1 General

This section includes only those foundation and abutment requirements that are specifically related to seismic resistant construction. It assumes compliance with all the basic requirements necessary to provide support for vertical loads and lateral loads other than those because of earthquake motions. These include, but are not limited to, provisions for the extent of foundation investigation, fills, slope stability, bearing and lateral soil pressures, drainage, settlement control, and pile requirements and capacities.

7.6.2 Foundation Investigation

Subsurface investigations, including borings and laboratory soil tests, are conducted to provide pertinent and sufficient information for the determination of the Site Class. To provide the input and site characterization needed to complete all geotechnical aspects of the seismic design, subsurface exploration, laboratory tests, in situ tests, and geophysical tests of the subsurface materials are conducted. The goal of the site characterization for seismic design is to develop the subsurface profile and soil property information required for seismic analyses and design.

Soil parameters generally required for seismic design include

- Initial dynamic shear modulus at small strains or shear wave velocity
  - Equivalent viscous damping ratio
  - Shear modulus reduction and equivalent viscous damping characteristics as a function of shear strain
  - Cyclic shear strength parameters (peak and residual)
- Liquefaction resistance parameters

For Site Class determination, soil should be characterized to a depth of at least 100 ft. using standard penetration tests (SPT), cone penetrometer tests (CPT), or shear wave velocity measurements, unless rock is encountered before 100 ft. The groundwater elevation should be determined. If seasonal groundwater fluctuations occur, the seasonally averaged groundwater elevation should be determined.

Laboratory tests are performed to determine the strength, deformation, and flow characteristics of soil and rock or both, and their suitability for the foundation selected. In areas of higher seismicity (e.g., SDC D), it may be appropriate to conduct special dynamic or cyclic tests to establish the liquefaction potential or stiffness and material damping properties of the soil at some sites, if unusual soils exist or if the foundation is supporting an essential or critical bridge. There are no special seismic foundation investigation requirements for SDC A.

In addition to the normal site investigation, the engineer may require, for SBC B and C, the submission of a report that describes the results of an investigation to determine potential hazards and seismic design requirements related to (1) slope instability, and (2) increase in lateral earth pressure, all as a result of earthquake motions.

The engineer may require, for SDC D, the submission of a written report, which shall include in addition to the potential hazard requirements, a determination of the potential for surface rupture because of faulting or differential ground displacement (lurching), a site specific study to investigate the potential hazards of liquefaction and fill settlement in addition to the influence of cyclic loading on the deformation and strength characteristics of foundation soils.

Spread footings in SDC B shall be proportioned to resist overturning, sliding, flexure, and shear because of the lesser of the following:

- The forces obtained from an elastic linear seismic analysis
- The forces associated with the overstrength plastic moment capacity of the column or wall

Spread footings in SDC C and SDC D shall be proportioned to resist overturning, sliding, flexure, and shear because of the forces associated with the overstrength plastic moment capacity of the column or wall.

7.7 Structural Steel Components

7.7.1 General

The development of Section 7.7, Structural Steel Components, began with the initiation of Task 4 as defined by the AASHTO T-3 Committee on Seismic Design (AASHTO, 1990). The objective of Task 4 was to select the most appropriate seismic design procedure (i.e., displacement or force based) for a bridge with a steel superstructure. The emphasis of this task was to address analysis and design requirements for a bridge composed of steel girders. The seismic design of a bridge system and its components includes two categories:

1. A system with a restrained connection at the interface between the superstructure and the substructure
2. A system with an Energy Dissipation Devices (EDD) between the superstructure and the substructure

The second edition (1998) of the AASHTO LRFD Specifications initially addressed the seismic lateral load distribution and load path to carry the inertia effects of the superstructure deck to the bearings. These specifications required that a clear and a straightforward load path from the superstructure to the substructure should exist. All elements should be designed to stay elastic during an earthquake. Diaphragms and cross frames, lateral bracing, and bearings should be part of the seismic load path. The specifications suggested that if these members were designed to respond in a ductile manner or allow some movements, the damage should be limited. However, the specifications did require that the cross frames and end diaphragms stay elastic during earthquakes.

In an effort to select the most appropriate design procedure for the *Seismic Guide*, two design examples were selected from the work done by Itani and Sedarat (2000) "Seismic Analysis and Design of the AISI LRFD Design Examples of Steel Highway Bridges." This effort was a continuation to the 1996 AISI published Vol. II Chapter 1B of the Highway Structures, Design Handbook, "Four LRFD Design Examples of Steel Highway Bridges" (AISI, 1996). In 1996 these design examples covered the gravity design of the superstructure according to the AASHTO LRFD Bridge Specifications. The main two purposes in examining this report (Itani and Sedarat, 2000) are to

1. Identify the performance objective for seismic design of steel girder structures.
2. Identify and compile the specifications required for proper completion of the steel design process.

The design should show a clear, straightforward load path, as shown in Figure 7.11 within the superstructure, through the bearings or connections to the substructure, within the substructure, and

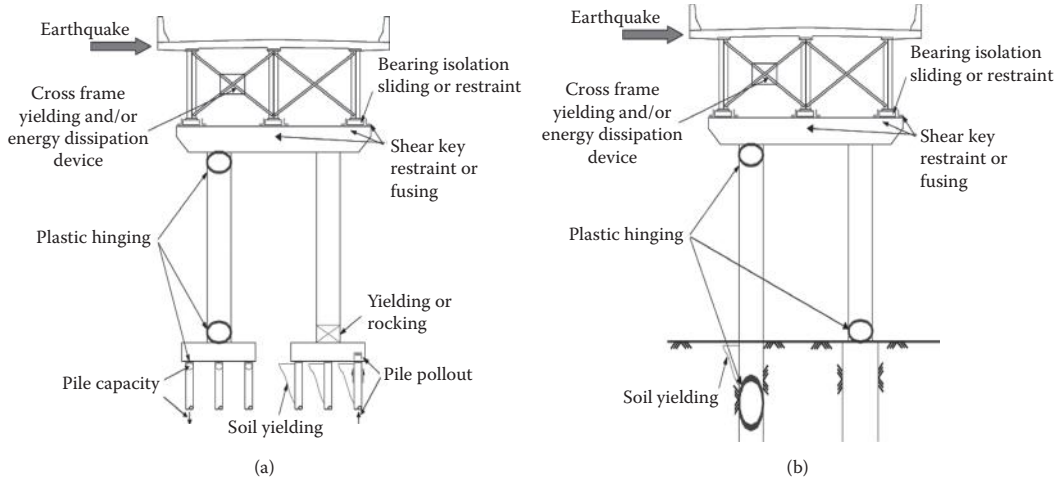

Note: Affected components shown are inclusive to types 1, 2, and 3 and do reflect specific components that are permitted to fuse under type 1, 2, or 3 specified in article 7.2 of the *Seismic Gudie*.

FIGURE 7.11 Seismic load path and affected components. (a) Pile footing. (b) Drilled shaft.

ultimately to the foundation exists: All components and connections should be capable of resisting the imposed seismic load effects consistent with the chosen load path.

The flow of forces in the prescribed load path should be accommodated through all affected components and their connections including, but not limited to, flanges and webs of main beams or girders, cross frames, steel-to-steel connections, slab-to-steel interfaces, and all components of the bearing assembly from bottom flange interface through the anchorage of anchor bolts or similar devices in the substructure. The substructure shall also be designed to transmit the imposed force effects into the soils beneath the foundations. The analysis and design of end diaphragms and cross frames shall include the horizontal supports at an appropriate number of bearings.

The requirements in the *Seismic Guide* apply to bridges with either

- A concrete deck that can provide horizontal diaphragm action
- A horizontal bracing system in the plane of the top flange, which in effect provides diaphragm action

A load path as shown in Figure 7.11 is established to transmit the inertial loads to the foundation based on the stiffness characteristics of the deck, diaphragms, cross frames, and lateral bracing. Unless a more refined analysis is made, an approximate load path shall be assumed as follows:

- The seismic inertia loads in the deck shall be assumed to be transmitted directly to the bearings through end diaphragms or cross frames.
- The development and analysis of the load path through the deck or through the top lateral bracing, if present, must utilize assumed structural actions analogous to those used for the analysis of wind loadings.

7.7.2 Performance Criteria

The intent of this section is to ensure the ductile response of steel bridges during earthquakes. First, effective load paths shall be provided for the entire structure as outlined below. Following the concept of capacity design, the load effect arising from the inelastic deformations of part of the structure shall be properly considered in the design of other elements that are within its load path.

Second, steel substructures should be detailed to ensure stable ductile behavior. Note that the term "substructure" here refers to structural systems exclusive of bearings and articulations. Steel substructures require ductile detailing to provide satisfactory seismic performance.

Most components of steel bridges are not expected to behave in a cyclic inelastic manner during an earthquake. It has however been observed in recent earthquakes that cyclic behavior has occurred in the end diaphragms composed of steel cross bracing. Based on this observation and recent research has led to the inclusion of the Type 2 Global Design Strategy for the design of an essential elastic substructure and a ductile superstructure as shown in Figure 7.13. The provisions of this article are only applicable to the limited number of components (such as specially detailed ductile substructures as shown in Figure 7.12, or ductile steel diaphragms as shown in Figure 7.13) whose stable hysteretic behavior is relied upon to ensure satisfactory bridge seismic performance. The seismic provisions of *Section 7* in the *Seismic Guide* are not applicable to the other steel members expected to remain elastic during seismic response. In most steel bridges, the steel superstructure is expected (or can be designed) to remain elastic.

The engineer should demonstrate a clear, straightforward load path (see Figure 7.11) within the superstructure, through the bearings or connections to the substructure within the substructure, and ultimately to the foundation exists. All components and connections shall be capable of resisting the imposed seismic load effects consistent with the chosen load path.

This section is intended for design of superstructure steel components. Those components are classified into two categories: Ductile and Essentially Elastic. Based on the characteristics of the bridge structure, the designer has one of three options for a seismic design strategy:

1. Type 1—Design a ductile substructure with an essentially elastic superstructure such as concrete substructure, steel substructure, and concrete filled steel pipe substructure.
2. Type 2—Design an essentially elastic substructure with a ductile superstructure.
3. Type 3—Design an elastic superstructure and substructure with a fusing mechanism at the interface between the superstructure and the substructure.

In this section, reference to an essentially elastic component is used where the force demand to the nominal capacity ratio of any member in the superstructure is <1.5.

For Global Design Strategy Type 1 performance criteria design of steel substructures or concrete filled steel pipe substructure of the columns are designed as ductile structural elements using a force reduction factor, R, not >4. The beams, panel zone at the column beam intersections and the connections are designed as essentially elastic elements.

Seismic design forces for individual members and connections of bridges identified as Type 2 are determined by dividing the unreduced elastic forces by the appropriate Response Modification Factor (R) as specified in the *Seismic Guide Article 7.2.2*. These factors shall only be used when all of the design requirements of this section are satisfied. A combination of orthogonal seismic forces equivalent to the

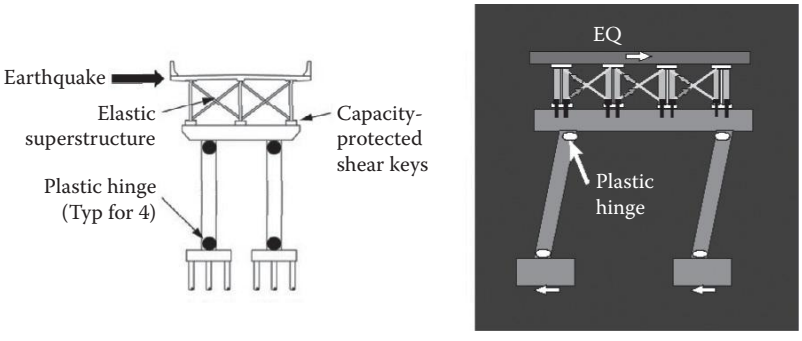

FIGURE 7.12 Ductile substructures (Type 1).

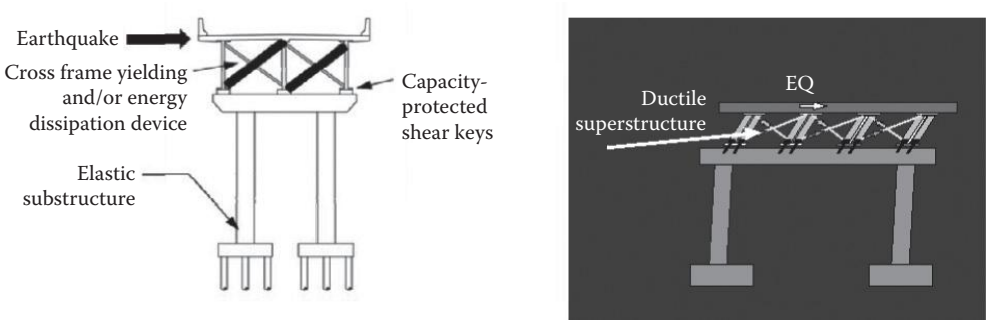

FIGURE 7.13 Ductile superstructures (Type 2).

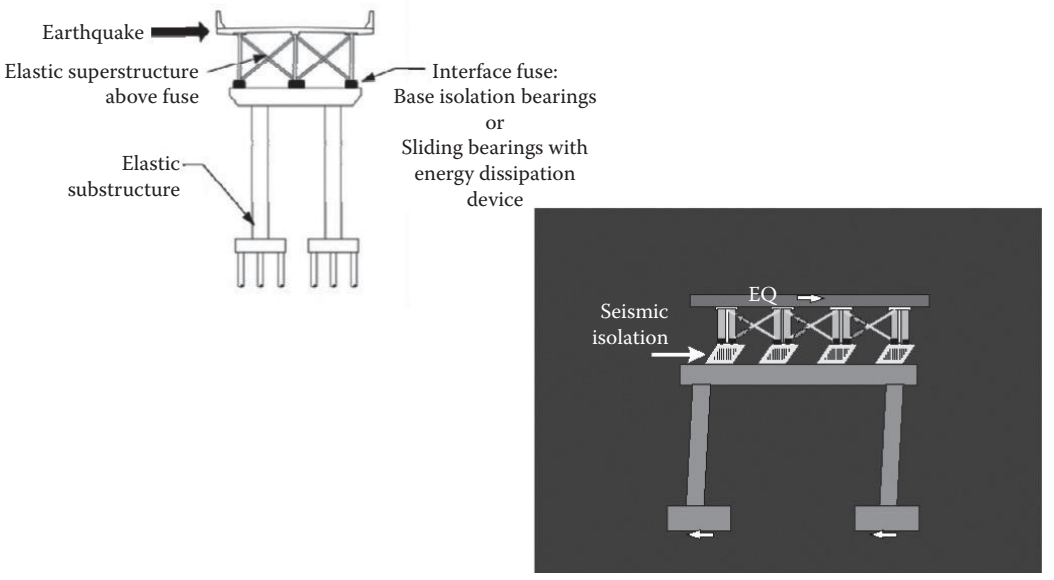

FIGURE 7.14 Fusing mechanism (Type 3).

orthogonal seismic displacement combination specified in *Article 4.4* of the *Seismic Guide* shall be used to obtain the unreduced elastic forces.

For Type 2 structures, the design of the superstructure is accomplished using a force-based approach with an appropriate reduction for ductility. Those factors are used for the design of transverse bracing members, top laterals and bottom laterals. For SDC B, C, or D a reduction factor, *R*, equal to 3 is used for ordinary bracing that is a part of the ERS having ductile end-diaphragms as defined in *Article 7.4.6*. The force reduction factor, *R*, can be increased to 4 for SDC D if the provisions in *Article 7.4.6* are satisfied.

For Type 3 structures (Figure 7.14), the designer shall assess the overstrength capacity for the fusing interface including shear keys and bearings, then design for an essentially elastic superstructure and substructure.

Other framing systems and frames that incorporate special bracing, active control, or other energy absorbing devices, or other types of special ductile superstructure elements shall be designed on the basis of published research results, observed performance in past earthquakes, or special investigation, and provide a level of safety comparable to those in the *AASHTO LRFD Bridge Design Specifications* (AASHTO, 2012).

7.8 Reinforced Concrete Components

7.8.1 General

The development of this section focuses on the sixth task defined by the AASHTO T-3 Committee, as described above in Section 7.2, to develop a user friendly specification utilizing available technology for the design of concrete components. Design and construction of concrete components that include superstructures, columns, piers, footings, and their connections are included in this section.

A vertical support is considered a column if the ratio of the clear height to the maximum plan dimensions is >2.5. For supports with a ratio <2.5, the provisions for piers apply. A pier wall is designed as a pier in its strong direction and a column in its weak direction.

The pile extensions of pile bents as well as drilled shafts and caissons are designed and detailed as columns. The purpose of the design is to ensure that a column is provided with adequate ductility and is forced to yield in flexure and that the potential for a shear, compression failure because of longitudinal bar buckling, or loss of anchorage mode of failure is minimized. The actual ductility demand on a column or pier is a complex function of a number of variables, including

- Earthquake characteristics, including duration, frequency content, and near-field (or pulse) effects
- Design force level
- Periods of vibration of the bridge
- Shape of the inelastic hysteresis loop of the columns, and hence effective hysteretic damping
- Elastic damping coefficient
- Contributions of foundation and soil conditions to structural flexibility
- Spread of plasticity (plastic hinge length) in the column

The damage potential of a column is also related to the ratio of the duration of strong ground shaking to the natural period of vibration of the bridge.

The 1989 Loma Prieta and 1994 Northridge earthquakes confirmed the vulnerability of columns with inadequate transverse reinforcement and inadequate anchorage of longitudinal reinforcement. Additionally it was learned that

- Attention should be given to provide adequate reinforcement for positive moments in the superstructure over monolithic supports.
- Provisions for adequate shear strength in joints between columns and bent caps to resist transverse forces.
- Consideration added reinforcement for torsion, particularly in outrigger-type bent caps.

7.8.2 Seismic Design Category A and Single-Span Bridges

For SDC A the bridge is designed for all nonseismic loads and does not require a seismic demand analysis. There are no seismic design requirements except for limited requirements that are implemented in the design procedures.

As included in the provisions specified in the *Seismic Guide Articles 4.1 and 4.2*, seismic analysis for bridges in SDC A is not generally required. SDC A includes acceleration levels that are ≤0.15. This category is further divided into two groups, one <0.05 and the other between 0.05 and 0.15. These two groupings are used to determine minimum design forces in lieu of conducting a more rigorous analysis. The division of SDC A at an acceleration coefficient of 0.05 recognizes that, in parts of the country with very low seismicity, seismic forces on connections are very small. The minimum support length for bridges in SDC A is covered in the *Seismic Guide Article 4.12*.

A detailed seismic analysis is generally not required for single-span bridges regardless of the SDC. However, the connections between the bridge span and the abutments should be designed both longitudinally and transversely to resist a horizontal seismic force not less than the acceleration coefficient, A_s, times the tributary permanent load except as modified for SDC A. The lateral force is carried into the foundation as illustrated in Figure 7.11. The minimum required support lengths are specified in the *Seismic Guide Article 4.12*.

Requirements for single-span bridges are not as rigorous as for multispan bridges because of their favorable response to seismic loads that have been demonstrated in past earthquakes. As a result, single-span bridges need not be analyzed for seismic loads regardless of the SDC, and design requirements are limited to minimum support lengths and connection forces. Adequate support lengths are required in both the transverse and longitudinal directions. Connection forces are based on the premise that the bridge is very stiff and that the fundamental period of response will be short. This assumption acknowledges the fact that the period of vibration is difficult to calculate because of significant interaction with the abutments.

These reduced requirements are also based on the assumption that there are no vulnerable substructures (i.e., no columns) and that a rigid (or near-rigid) superstructure is in place to distribute the in-plane loads to the abutments. If, however, the superstructure is not able to act as a stiff diaphragm and sustains significant in-plane deformation during horizontal loading, it should be analyzed for these loads and designed accordingly.

Although not specifically covered in the *Seismic Guide*, single-span trusses may be sensitive to in-plane loads and the designer may need to take additional precautions to ensure the safety of truss superstructures.

7.8.3 Seismic Design Category B, C, and D

The design force requirement for SDC B is taken as the lesser of the forces resulting from the overstrength plastic hinging moment capacity or unreduced elastic seismic forces in columns or pier walls. Bridges designed in accordance with SDC B are designed and detailed to achieve a displacement ductility, μ_D, of at least 2.

The design force requirements for SDC C and D are based on forces resulting from the over strength plastic hinging moment capacity or the maximum connection capacity following the capacity design principles as described in the *Seismic Guide Article 4.11*.

The provisions provide a mechanism to permit the use of various seismic resisting systems and elements. Selection of an appropriate ERS for SDC C and D is fundamental to achieving adequate seismic performance as described in *Article 3.5*. To this end, the identification of the lateral-force-resisting concept and the selection of the necessary ERE to facilitate the concept should be accomplished in the conceptual design phase of the project; which includes Type-Selection, Layout, and Global Design Strategy. Seismic performance is typically better in systems with regular configurations and evenly distributed stiffness and strength. Thus configuration constraints, such as skew, unequal pier heights and sharp curves, conflict to some degree, with the preferred systems. For this reason, it is advisable to resolve potential conflicts between configuration, seismic performance, and Global Design Strategy early in the design effort. The classification of ERS and ERE are divided into the categories of (1) permissible, (2) permissible with owner's approval, and (3) not recommended. This is done to encourage consideration of seismic performance that leads to the most desirable outcome based on past experience and observations of earthquake damage, which ensures the best postearthquake serviceability wherever possible. It is not the intention of the *Seismic Guide* to discourage the use of systems that require owner approval. But additional design effort between the designer and owner are required to implement such systems. But, to promote a dialog so that the owner is made aware of the additional design effort is needed and a consensus between the designer and owner is required to implement such systems.

7.8.4 Properties and Applications

The expected concrete compressive strength, f'_{ce}, shall be taken as the most probable long-term concrete strength based upon regional experience and is taken as

$$f'_{ce} \geq 1.3 f'_c \tag{7.16}$$

where f'_c = compressive strength of concrete (ksi)

In view of the fact that an extreme seismic event has a low probability of occurring, the extreme concrete strength is used. This rationale is different than the conservative values used for severe loads. The unconfined concrete compressive strain at the maximum compressive stress ε_{co} shall be taken as equal to 0.002. And the ultimate unconfined compression (spalling) strain ε_{sp} shall be taken as equal to 0.005. Typical values for the ultimate compressive strain, ε_{cu}, range from 0.008 to 0.025, depending on the amount of transverse confinement reinforcement. In normal design practice, ultimate compressive strain values are limited to approximately 0.02. Where in-ground plastic hinging is part of the ERS, the confined concrete of the core should be limited to a maximum compressive strain of 0.008 to limit in-ground damage.

The confined compressive strain, ε_{cc}, and the ultimate compressive strain, ε_{cu}, for confined concrete are computed using Mander's model (Mander et al., 1988a) as shown in Figure 7.15. Mander's stress–strain model for confined concrete is used for determining section response. The stress–strain model for unconfined concrete is also shown in the same figure.

Reinforcing Steel is modeled with a stress–strain relationship that exhibits an initial elastic portion, a yield plateau and a strain hardening range as shown in Figure 7.16. These models vary depending on the bar size and the specified grade of steel.

For SDC B and C the expected material properties are used to determine the section stiffness and over strength properties. The displacement capacities are determined using the Implicit Capacity procedure as described in Section 7.3.5.6. For SDC D the expected material properties are used to determine the section stiffness and over strength the properties as for SDC B and C. Displacement capacities are also determined using the expected material properties in conducting the pushover analysis.

Lessons learned from past earthquakes and research performed during the last four decades has added considerable knowledge on the overall bridge system and the dependency on individual component behavior. Selected key components that are commonly used in bridge construction for increased seismic resistance include

- Circular and rectangular columns
- Columns reinforced with interlocking hoops or spirals

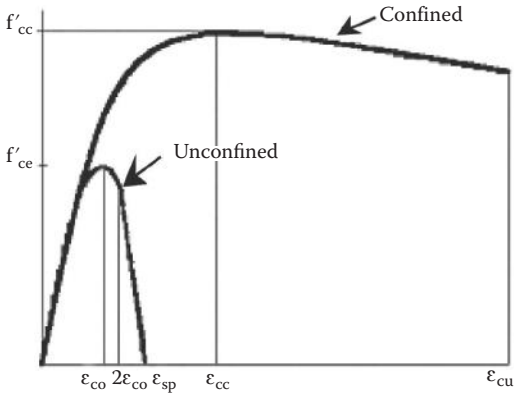

FIGURE 7.15 Concrete stress–strain.

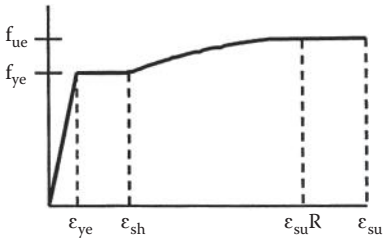

FIGURE 7.16 Reinforcing steel stress–strain model.

- Circular column extending from prismatic and nonprismatic shafts columns
- Pier walls
- Shear keys

Identifying the elastic and postelastic behavior of these components is the state-of-the-art practice used in the Displacement-Based Approach for the *Seismic Guide*. In the last four decades, research has focused on the behavior of bridges following major earthquakes. Investigations of past earthquakes revealed important lessons and led the practice into more in-depth verification of the response of bridge components and the overall ERS of a bridge.

Experience and research has shown that transverse confinement reinforcement in the zones of yielding is the key to the successful performance of ductile reinforced concrete columns during earthquakes. Transverse reinforcement serves to confine the main longitudinal reinforcement and the concrete within the core of the column, thus preventing buckling of the main longitudinal reinforcement and the severe loss of compression strength in the concrete. Additionally, transverse reinforcement is also effective as shear reinforcement and increases the shear capacity critically needed for capacity protection of the column.

Modern bridge design standards that are included in the *Seismic Guide* require minimum transverse confinement reinforcement and sufficient shear reinforcement to resist the shear forces developed by the formation of plastic hinges. Special attention is given to the reinforcement details to ensure that transverse reinforcement remains effective during the cyclic loading that occurs during earthquakes.

Unfortunately, before 1971 the transverse reinforcement placed in most bridge columns was totally inadequate by today's knowledge as incorporated new design provisions. For example, a typical pre1971 AASHTO detail consisted of transverse hoops of half inch diameter steel bars (No. 4 bar) spaced at l2 inches on center. Hoops were lap spliced and without crossties to support rectangular hoops at intermediate points. The column damage suffered during the San Fernando earthquake demonstrated the inadequacy of this detail.

The stress–strain curve for concrete is highly dependent on the confinement of the concrete. There is an appreciable increase in strength and deformation capacity with increased confinement. The ductility requirements in high seismic areas could not have been achieved if concrete strains were limited to 0.003 or 0.004 as they are for service load designs. In reinforced concrete structures, confinement is enhanced with passive resistance by means of closely spaced spiral, hoop or tie reinforcement. When the concrete section is under compression, Poisson's effect will produce lateral expansion as shown in Figure 7.17. The stiffer confining reinforcement restrains this expansion, thereby exerting a confining pressure.

The *Seismic Guide* has very detailed requirements for providing confinement reinforcement in components designed to provide seismic resistance. The most efficient type of confining reinforcement is circular hoops or spiral reinforcement. The rectangular section with square ties and crossties will provide little confinement unless the aspect ratio of the section is <1.5. Adding crossties helps significantly in confining the concrete core with aspect ratios >1.5.

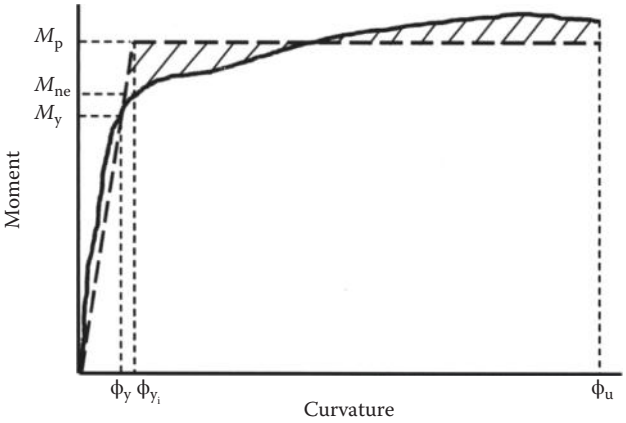

FIGURE 7.17 Moment-curvature model.

Modern design of reinforced concrete columns complies with the following fundamentals:

- Ductility: Ductility is mathematically defined as the ratio of ultimate deformation to the deformation at yield.

  Ductile response of structural components is characterized by several cycles of inelastic deformation without significant degradation of strength or stiffness. The most desirable type of ductile response in bridge systems is sustained hysteric force–deformation cycles that dissipate energy. This type of response can be generated either internally, within the structural members by the formation of flexural plastic hinges, or externally with isolation bearings or external energy dissipation devices. The analytical derived deformations are limited in the specifications so the structure will not exceed its inelastic deformation capacity.

  Ordinary bridges are not designed to respond elastically during the design earthquake because of economic constraints and the uncertainties in predicting seismic demands. This philosophy is based on the relatively low probability that a major earthquake will occur at a given site, within the design life of the bridge and the willingness of the owner to absorb the repair cost at a future date if a major earthquake occurs.
- Predetermined location of damage: Inelastic behavior by design is limited to predetermined locations within the bridge system that are easily inspected and repaired following an earthquake. Continuous column/pile shaft combinations are an exception since inelastic behavior may occur below ground. Preferable locations for inelastic behavior to occur on most bridges include: columns, pier walls, backwalls, wingwalls, seismic isolation and EDD, bearings, shear keys, and steel end-diaphragms.

  Significant inelastic response in concrete superstructures is not desirable because they are difficult to inspect and repair. Furthermore, superstructure damage may prevent the bridge from being repaired to a serviceable condition.
- Plastic Moment Capacity for Ductile Concrete Members for SDCS B C, and D: The moment–curvature relationship shown in Figure 7.18 is departure from the traditional axial-moment interaction as traditionally used for either steel or reinforced concrete. For seismic design, the deformation requirements beyond yield are required using a moment–curvature analysis to calculate the displacement as required for use in the *Seismic Guide*.

  The plastic moment capacity of all ductile concrete members shall be calculated by moment–curvature (M–ϕ) analysis based on the expected material properties. The moment–curvature analysis shall include the axial forces because of dead load together with the axial forces because of overturning as given in *Article 4.11.4*.

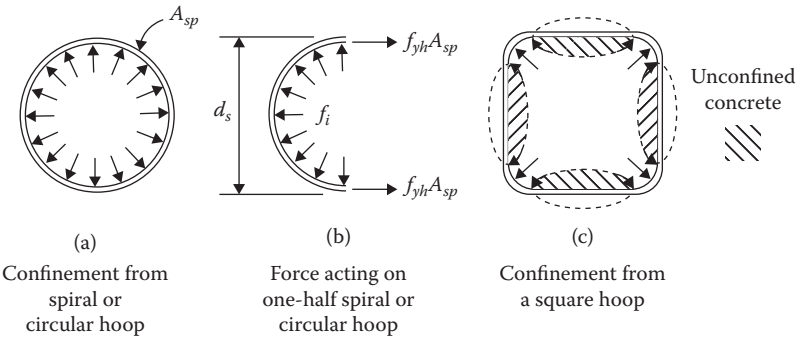

FIGURE 7.18 Poisson's effect on confined columns in compression.

The M–ϕ curve can be idealized with an elastic perfectly plastic response to estimate the plastic moment capacity of a member's cross section. The elastic portion of the idealized curve passes through the point marking the first reinforcing bar yield. The idealized plastic moment capacity is obtained by equating the areas between the actual and the idealized M–ϕ curves beyond the first reinforcing bar yield point as shown in Figure 7.18.

Moment curvature analysis obtains the curvatures associated with a range of moments for a cross section based on the principles of strain compatibility and equilibrium of forces. A moment–curvature analysis based on strain compatibility and nonlinear stress–strain relations can be used to determine plastic limit states. The results from this rational analysis are used to establish the rotational capacity of plastic hinges as well as the associated plastic deformations. The process of using the moment–curvature sectional analysis to determine the lateral load–displacement relationship of a frame, column, or pier is known as a "pushover analysis."

The expected nominal moment capacity, M_{ne}, for essentially elastic response shall be based on the expected concrete and reinforcing steel strengths when the concrete strain reaches a magnitude of 0.003.

In order to determine force demands on capacity-protected members connected to a hinging member, a overstrength magnifier, λ_{mo}, shall be applied to the plastic moment capacity of the hinging member such that

$$M_{po} = \lambda_{mo} M_p \tag{7.17}$$

where

M_p = idealized plastic moment capacity of reinforced concrete member based upon expected material properties (kip-ft.)
M_{po} = overstrength plastic moment capacity (kip-ft.)
λ_{mo} = overstrength magnifier
= 1.2 for ASTM A 706 reinforcement
= 1.4 for ASTM A 615 Grade 60 reinforcement

The ultimate curvature, ϕ_u, is determined as the smaller of

- The ultimate compressive strain, ε_{cu}, of the confined concrete divided by the distance from the plastic neutral axis to the extreme fiber of the confined concrete core.
- The reduced ultimate tensile strain, ε_{su}^{R}, of the reinforcing steel divided by the distance from the plastic neutral axis to the extreme tension fiber of the longitudinal column reinforcement. The reduced strain ε_{su}^{R}, as shown in Figure 7.16 is considered essential in minimizing

the effects of Low Cycle Fatigue of rebars subjected to cycles of high strain values as in the case of an extreme earthquake event.

The overstrength magnifier, λ_{mo}, accounts for

- Material strength variations between the column and adjacent members (e.g., superstructure, bent cap, footings, oversized pile shafts)
- Columns moment capacities greater than the idealized plastic moment capacity

Typical values for the ultimate curvature as given in the *Seismic Guide Article 8.5 Commentary*, ϕ_u, *range from* $0.03/B_o$ *to* $0.08/B_o$ depending on many factors, such as

- The amount of transverse confinement reinforcement provided
- The reduced ultimate tensile strain of the longitudinal column reinforcement
- The magnitude of the axial load
- The shape and dimensions of the column cross section.

The location of the plastic neutral axis is determined based on satisfying the requirements of compatibility and equilibrium of the section using material models such as those outlined in *Seismic Guide, Article 8.4.*

An adequate margin of strength shall be provided between the designated ductile failure mode and nonductile failure modes. Desired locations of plastic hinging shall be identified and detailed for ductile response. Sufficient overstrength shall be provided to assure the desired yielding mechanism occurs and undesirable nonductile failure mechanisms, such as concrete crushing, shear cracking, elastic buckling, and fracture are prevented from forming.

- Detailing: Seismic detailing is exhibited in an elaborate list of requirements in the *Seismic Guide* that are incrementally increased for each seismic category depending on the given earthquake hazard intensity. For the low to moderate seismic hazard with low ductility demands the level of confinement is low. This may be the case for confined but not necessarily for shear. Transverse reinforcement for shear must always be provided. Shear failure in a column can lead to a loss of vertical load carrying capacity. Figures 7.19 and 7.20 show typical transverse arrangement for single-column bent and a multicolumn bent. The increased density of transverse reinforcement is depicted in the plastic hinge zones.

The plastic hinge region is typically taken as the maximum of

- 1.5 sectional dimension in the direction of bending

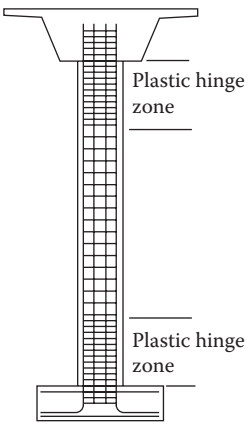

FIGURE 7.19 Single columns lateral reinforcement in plastic hinge zone region.

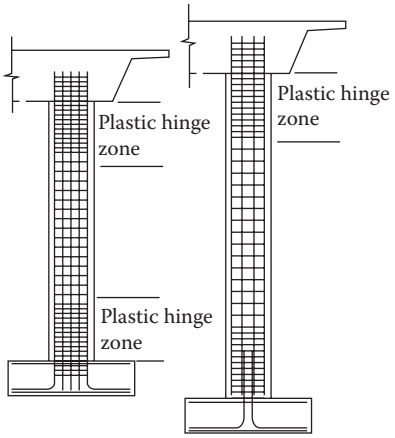

FIGURE 7.20 Multicolumn lateral reinforcement in plastic hinge regions.

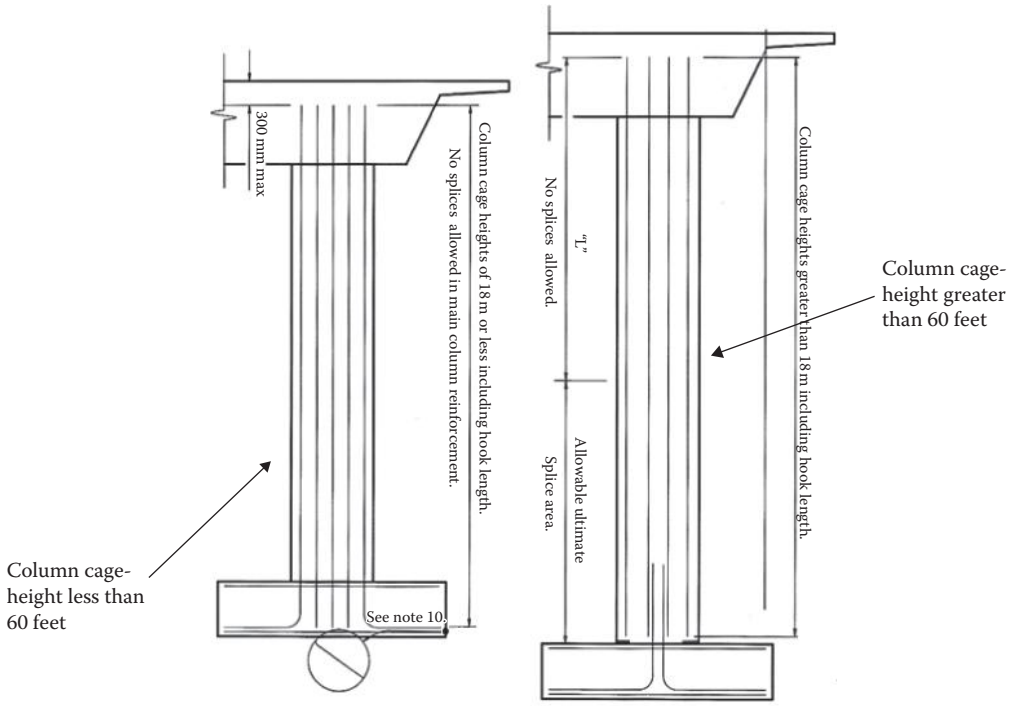

FIGURE 7.21 Longitudinal reinforcement splicing in multicolumn bent.

- The portion of the column where the moment demand exceeds 75% of the maximum plastic moment
- The analytical plastic hinge length

Splicing of column vertical reinforcement is another important detailing issue in high seismic regions. Typically, column cages with height <60 ft. can be constructed with no splicing of

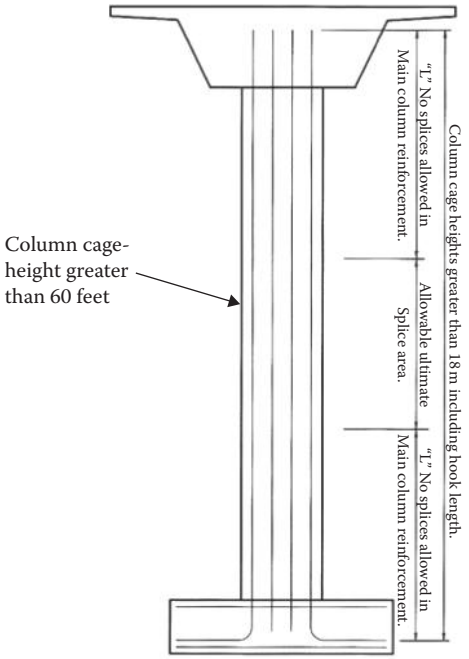

FIGURE 7.22 Longitudinal reinforcement splicing in single-column bent.

longitudinal reinforcement. For column cage reinforcement <60 ft., allowable splice regions depends on the column framing condition considering a single-or multicolumn bent with a typical pin connection to the footing as shown in Figures 7.21 and 7.22.

7.9 Summary

Seismic design of bridges in the United States is currently going through a transition from an FBA to a DBA. The FBA began at Caltrans immediately after the San Fernando earthquake on February 11, 1971. The first SDC that followed was implemented into their design practice in 1973. This was a prescriptive design criteria based on a ductile design approach using plastic hinges that allow damage but avoid collapse. Allowing damage to occur with the formation of plastic hinges in the columns would provide a performance level of "life safety" at a minimal initial construction cost. This was done as an alternative to providing a bridge that would remain elastic at a higher impractical cost with no damage. These new criteria considered: (1) seismic hazard, (2) local ground response, (3) dynamic structural analysis, and (4) ductility reductions for design that are still today the primary four topics within the criteria considered in our most recent design specification.

This approach was formally adopted by AASHTO in 1975 (AASHTO 1975) with some slight modifications for application to all regions in the United States. These modifications included the USGS maps that were available for the PGA at that time for the entire United States. These criteria remained effective until 1990 (AASHTO 1990) when it was replaced by the ATC-6 Seismic Design Guidelines for Highway Bridges (ATC 1981) and formally adopted by AASHTO as Division l-A (AASHTO 1990 and 1992). There were some improvements included in AASHTO Division 1-A, however the ductile design approach with prescribed ductility factors to allow damage remained. This approach encompasses many uncertainties and is less reliable than the DBA as used in the recently developed AASHTO Guide Specifications for LRFD Seismic design of Highway (AASHTO 2011). Although the use of ductility factors has been eliminated,

substantially reducing the level of uncertainly, the performance level of "life safety" has not been changed. Additionally, a new hazard level was introduced of a 7.5% probability of exceedance in 75 years (i.e., 975-year return period) to replace the l0% probability of exceedance in 50 years (i.e., 475-year return period). Although there have been improvements with the adoption of each of these criteria, the four primary topics remain the same with the improvements being made separately within each of these primary topic areas.

Although the practice in seismic design of bridges has traditionally been to comply with code requirements to achieve facilities that do not collapse, the resulting postearthquake damage has been costly and disruptive, and in some instances bridges have been demolished and replaced with new bridges. Facility owners and users are concerned with economic losses from damage and disruption by the loss of use. The interruption of service in a roadway system and demand for repair services can have substantial effects on the economic and social well-being of a community as demonstrated in past earthquakes. For example, government-reported loss data from the Kobe and Northridge earthquakes show that total economic losses including loss of use and disruption were 10 times greater than the direct costs for repairing damaged structures (Imbsen and Mokha).

Seismic isolation was initially used to achieve continued functionality for bridges by retrofitting bridges on critically important transportation lifeline routes. However recent updates to the AASHTO LRFD Bridge Design AASHTO (2009) and *Seismic Guide* recognize the benefits and promote the use of seismic isolation as an initial alternative design strategy for new bridges. Some of these updates include: (l) the addition of the clause in the AASHTO LRFD Bridge Design Specification (*Article 1.3.3*) to substitute the use of "energy-dissipating devices" in place of the "conventional ductile ERS" *Seismic Guide* (2) the addition of seismic isolation as a design strategy (*Article 1.1*) in the *Seismic Guide*, and (3) the updated third edition of the AASHTO Guide Specifications for Seismic Isolation Design (AASHTO 2010) with the updated seismic design hazard as defined in the companion AASHTO Specifications.

Given the recent changes in the AASHTO Specifications and recent technology in seismic isolation, it is now possible to design for continued functionality. Historically major critical lifeline bridges have been retrofitted to achieve continued functionality at cost savings of 30% as compared to conventional retrofits to life safety that does not provide continued functionality. Cost savings have also been realized in using an isolation design strategy for continued functionality for new bridges. Decisions made at Caltrans 40 years ago to use a ductile design approach to achieve a performance level of "life safety" at reduced initial construction costs should be reevaluated in light of the lessons learned from recent earthquakes and the development of recent seismic isolation technology. The performance level of life safety is just not good enough for the current technology; let us raise the standard to Continued Functionality.

References

AASHTO. 1975. AASHTO *Standard Specifications for Highway Bridges* (1973, 12th Edition with Interiums thru 1975). American Association of State Highway and Transportation Officials, Washington, DC.

AASHTO. 1983. *Guide Specifications for Seismic Design of Highway Bridges.* American Association of State Highway and Transportation Officials, Washington, DC.

AASHTO. 1990. AASHTO *Standard Specifications for Highway Bridges* (1989, 14th Edition with Interiums thru 1990). American Association of State Highway and Transportation Officials, Washington, DC.

AASHTO. 1992. *Standard Specifications for Highway Bridges* (15th Edition). American Association of State Highway and Transportation Officials, Washington, DC. AASHTO Guide Specifications for Seismic Design of Highway Bridges, 1983, Division-1A.

AASHTO. 2007b. AASHTO Guide Specifications for LRFD Seismic Design. Prepared by R.A. Imbsen, available online as of Jan 2008, at: http://bridges.transportation.org/sites/bridges/docs/2007%20Ballot%20%20Seismic%Guidelines.pdf.

AASHTO. 2009. *Guide Specifications for LRFD Seismic Bridge Design* (with 2010 Interim Revision, 1st Edition). American Association of State Highway and Transportation Officials, Washington, DC.

AASHTO. 2010. *Guide Specification for Seismic Isolation Design* (3rd Edition). American Association of State Highway and Transportation Officials, Washington, DC.

AASHTO. 2011. *Guide Specifications for LRFD Seismic Bridge Design* (2nd Edition). American Association of State Highway and Transportation Officials, Washington, DC.

AASHTO. 2012. *Customary U.S. Units, 2012*. American Association of State Highway and Transportation Officials, Washington, DC.

AISI. 1996. *Highway Structures Design Handbook (Vol. II Chapter 1B). Four LRFD Design Examples of Steel Highway Bridges*. American Institute of Steel and Iron, Washington, DC.

ATC.1981. *Seismic Design Guidelines for Highway Bridges*. ATC-6, FHWA Report No. FHWA/RD-81/081, Applied Technology Council, Berkeley, CA.

ATC. 1996. *Improved Seismic Design Criteria for California Bridges: Provisional Recommendations*. ATC-32, Applied Technology Council, Redwood City, CA.

Berry, M. and Eberhard, M. 2003. *Estimating Flexural Damage in Reinforced Concrete Columns*. University of Washington, WA.

Caltrans. 1999. *Seismic Design Criteria* (Version 1.0). California Department of Transportation, Sacramento, CA.

DesRoches, R., and Fenves, G. 1997. *New Design and Analysis Procedures for Intermediate Hinges in Multiple-Frame Bridges*. (UCB/EERC 97/12), Earthquake Engineering Research Center, University of California, Berkeley, CA.

Imbsen, R. 1979. *Seismic Design of Highway Bridges Workshop Manual*. Federal Highway Administration, Washington, DC.

Fung, G., LeBeau, R., Klein, E., Belvedere, J., and Goldschmidt, A. 1971. *Field Investigation of Bridge Damage in the San Fernando Earthquake*. State of California, Division of Highways, Bridge Department, Sacramento, CA.

I&A. 2005. *Updating Recommended LRFD Guidelines for Seismic Design of Highway Bridges*. NCHRP (National Cooperative Research Program) 20-07/Task 193 Task 6 Report, Imbsen and Associates, Inc., Sacramento, CA.

I&A. 2006. *Recommended LRFD Guidelines for the Seismic Design of Highway Bridges*. NCHRP 20-07/Task 193 Imbsen/TRC, Sacramento, CA.

Imbsen, R. 2004. *Road-Map for Recommended LRFD Guidelines for the Seismic Design of Highway Bridges*, (Version 2). NCHRP Methodology Document Task F3-5, National Cooperative Research Program, Washington, DC.

Imbsen, R. 2007a. *AASHTO Guide Specifications for Seismic Bridge Design*. Imbsen Consulting, Sacramento, CA.

Imbsen, R. 2007b. *Recommended LRFD Guidelines for the Seismic Design of Highway Bridges*. NCHRP 20-7/Task 193, Addendum for Task 6 Report. Implicit Equations for Displacement Capacity in Seismic Design Category B and C, Imbsen Consulting, Sacramento, CA.

Imbsen, R. and Gates, J. 1973. *Recent Innovations in Seismic Design and Analysis Techniques for Bridge Structures. 42nd Annual Convention*, Structural Engineers of California, Sacramento, CA.

Imbsen, R. and Liu, W. D. 1994. Nonlinear Seismic Evaluation of Steel and Concrete Bridge Structures. *Eleventh International Bridge Conference*, Pittsburgh, PA, June 13–15.

Itani, A. M. and Sedarat, H. 2000. *Seismic Analysis and Design of the. AISI LRFD Design Examples of Steel Highway Bridges*. CCEER 00-8, University of Nevada, Reno, NV.

Mander, J. B., Priestley, M. J. N., and Park, R. 1988a. Theoretical Stress-Strain Model for Confined Concrete. *J. Struct. Eng.*, ASCE, 114(8), 1804–1826.

Mander, J. B., Priestley, M. J. N., and Park, R. 1988b. Observed Stress-Strain Behavior of Confined Concrete. *J. Struct. Eng.*, ASCE, 114(8), 1827–1849.

MCEER. 2004. *Recommended LRFD Guidelines for the Seismic Design of Highway Bridges*. MCEER/ATC-49, Multidisciplinary Center for Earthquake Engineering Research/Applied Technology Council, University at Buffalo, Buffalo, NY.

Romstad, K., Kutter, B., Maroney, B., Vanderbilt, E., Griggs, M., and Chai, Y. H. 1996. *Longitudinal Strength and Stiffness Behavior of Bridge Abutments*. Report No. UCS-STR-96-1, Department of Civil Engineering, University of California, Davis, CA. Report to California Dept. of Transportation, Sacramento, CA.

SCDOT. 2001. *Seismic Design Specifications*. South Carolina Department of Transportation, Columbia, SC.

Further Reading

NHI. 2011a. NHI Course No. 130093, *LRFD Seismic Analysis and Design of Bridges Reference Manual*. Publication No. FHWA-NHI-11-030, National Highway Institute, Washington, DC.

NHI. 2011b. NHI Course No. 130094, *LRFD Seismic Analysis and Design of Transportation, Geotechnical Features and Structural Foundations Reference Manual*. Publication No. FHWA-NHI-11-032, National Highway Institute, Washington, DC.

Relevant Websites

http://bridges.transportation.org/sites/bridges/docs/2007%20Ballot%20%20Seismic%Guidelines.pdf.

8

Seismic Design of Concrete Bridges

Larry Wu
California Department of Transportation

8.1 Introduction

The recent earthquake damage survey indicated that the reinforced concrete bridges, especially, less confined concrete columns, were quite susceptible to damage under strong earthquake ground shaking as discussed in Chapter 2. This chapter presents a seismic design example for a four-span cast-in-place prestressed concrete box girder bridge located in high seismic region. The design is based on two AASHTO Specifications: AASHTO LRFD Bridge Design Specifications, 2012 Edition (LRFD BDS) (AASHTO, 2012) and AASHTO Guild Specifications for LRFD Seismic Bridge Design (LRFD SBD) (AASHTO, 2011). Chapter 7 provides a more detailed discussion on Seismic Design Specifications in the United States.

8.2 Bridge Seismic Design Specifications

8.2.1 AASHTO LRFD Bridge Design Specifications, 2012 Edition (LRFD BDS)

The traditional "Force-Based" design philosophy is embedded into LRFD BDS (AASHTO, 2012). The focus of design is on elastic force demand, F, of bridge components, especially, column elastic moment responses. By introducing the Responses Modification Factor, R, the design force is calculated as $F_D = F/R$. However, the capacity of a bridge component is expressed as the resistance force, that is, F_C. The design criterion is set as $F_D/F_C < 1.0$. The general design cycle is illustrated in Figure 8.1, and typical design procedure is shown in Figure 8.2.

8.2.2 AASHTO Guide Specifications for LRFD Seismic Bridge Design, 2nd Edition (LRFD SBD)

More advanced design philosophy, "Displacement-Based" design procedure, is specified in LRFD SBD (AASHTO, 2011). The objective of this approach is to ensure that the bridge structure system and its components have enough displacement capacity to withstand the deformation imposed by the design earthquake. Using displacements rather than forces as a measurement of earthquake damage allows a structure to fulfill the required functions. In a displacement-based seismic design, the first step is to check the proportion requirements for bridge components and configurations based on the balanced strength and stiffness criteria. Then the displacement demand, Δ_D, is calculated through the appropriate seismic evaluation procedure. However, the displacement capacity, Δ_C, is estimated by inelastic static pushover analysis. The design criterion is set as $\Delta_D/\Delta_C < 1.0$. The design procedure is shown in Figure 8.3.

8.3 Example Bridge Description

8.3.1 Bridge Configuration

A four-span single column bent cast-in-place prestressed concrete box girder bridge, located at Los Angeles area, California, is shown in Figure 8.4. The span lengths are 120 ft, 150 ft, 160 ft, and 130 ft. The column heights are 26 ft, 28 ft, and 30 ft for Bent 2, Bent 3, and Bent 4, respectively. The circular columns are "fixed" at the bottom, supported by pile caps with group of driving concrete piles. The bridge is constructed on Class C site. The typical section is shown in Figure 8.5 (piles not shown).

8.3.2 Bridge Member Size and Reinforcement

Bridge design is inherently an iterative process. In accordance with AASHTO LRFD Specifications (AASHTO, 2012), a complete concrete bridge design usually include three Limit States: Service Limit State, Strength Limit State, and Extreme Limit State. Bridge seismic design is covered by Extreme Limit

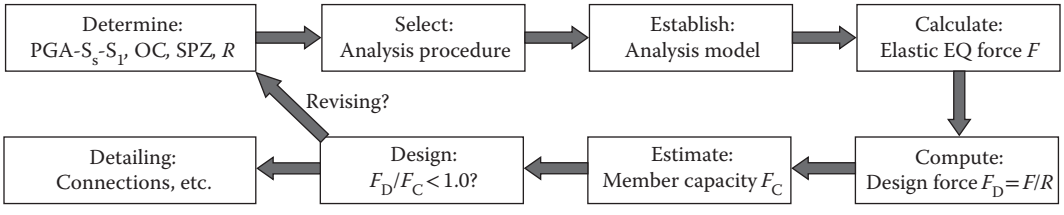

FIGURE 8.1 Force-based bridge seismic design cycle.

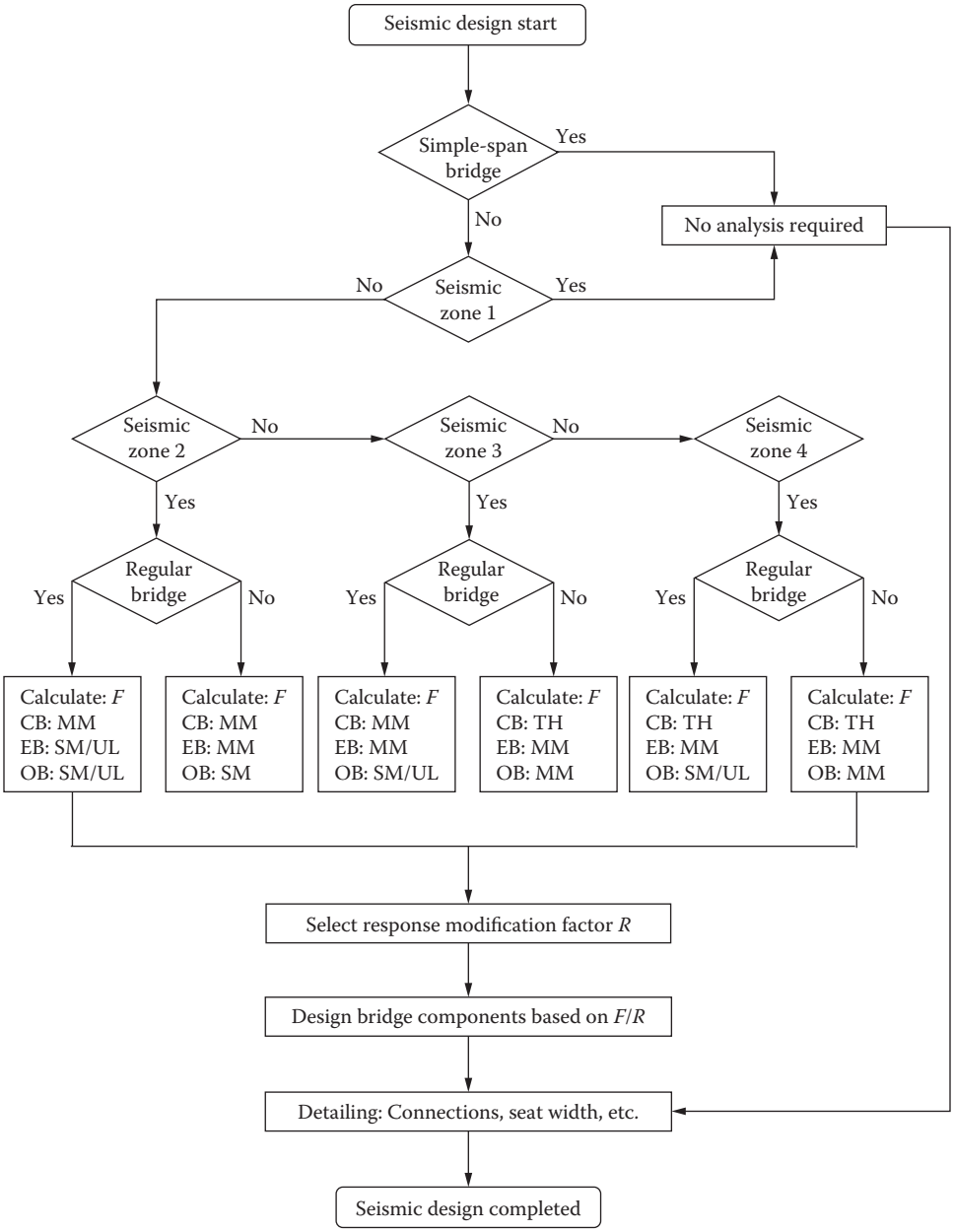

CB: Critical bridge; EB: Essential bridge; OB: Other bridge; SM: Single model spectrum analysis; UL: Uniform load analysis; MM: Multi-model spectrum analysis; TH: Time history analysis;

FIGURE 8.2 Force-based bridge seismic design procedure—LRFD BDS.

State. In general, a bridge is designed to satisfy Service and Strength Limit States first, and then, if necessary, to refine the design of various components to satisfy Extreme Limit States, such as seismic performance requirements. In practice, however, engineers should keep certain seismic requirements in mind even during the Service and Strength Limit States design. This is especially important while selecting the span configuration, column sizes, column reinforcement requirements, and bent cap width.

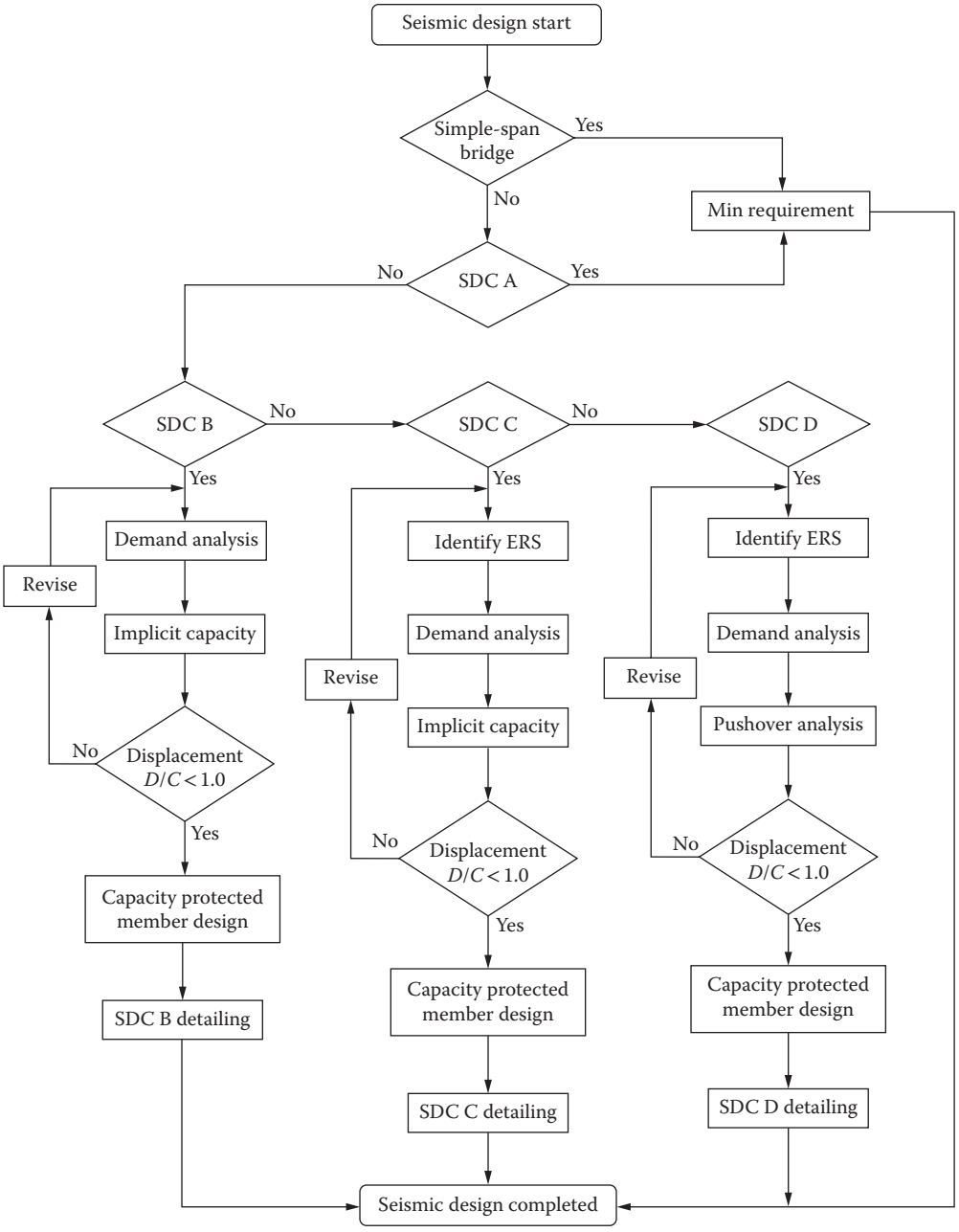

FIGURE 8.3 Displacement-based bridge seismic design procedure—LRFD SBD.

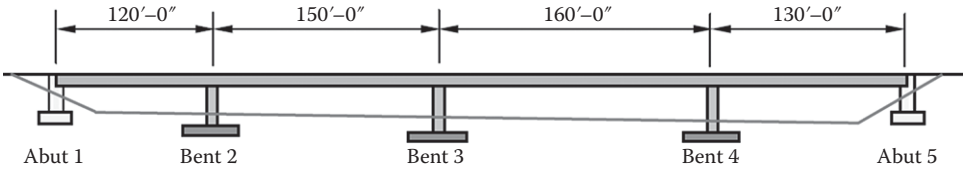

FIGURE 8.4 Bridge layout.

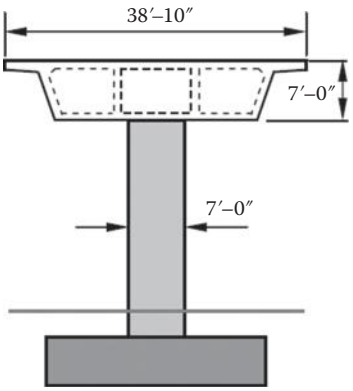

FIGURE 8.5 Bent layout.

TABLE 8.1 Example Bridge-Member Size and Column Reinforcement

Location	Span Length L (ft)	Column Height H_c(ft)	Column Diameter d_c(ft)	Column Main Reinforcement	Col. Trans. Reinforcement	Bent Cap Width B_c (ft)	Structure Depth D (ft)	Deck Width B (ft)
Abut 1							7.0	38.83
Span 1	120.0						7.0	38.83
Bent 2		28.0	7.0	#14 tot 48	#8 bundle @ 8	9.0	7.0	38.83
Span 2	150.0						7.0	38.83
Bent 3		30.0	7.0	#14 tot 48	#8 bundle @ 8	9.0	7.0	38.83
Span 3	160.0						7.0	38.83
Bent 4		32.0	7.0	#14 tot 48	#8 bundle @ 8	9.0	7.0	38.83
Span 4	130.0						7.0	38.83
Abut 5							7.0	38.83

For the example bridge, the member dimensions and reinforcement, determined by Service and Strength Limit States, are listed in Table 8.1.

8.4 Bridge Seismic Design Based on LRFD BDS

8.4.1 Bridge Regularity Check

From LRFD BDS Table 4.7.4.3.1-2, the first step is to check if the bridge meets requirements for a regular bridge. The longest span for this bridge is Span 3, and the shortest span is Span 1. The maximum span length ratio is 1.23, which is less than the allowed maximum of 2.0. The next step is to check the maximum bent stiffness ratio. Through column section analysis, the Effective (or Cracked) Section Moment of Inertia, I_c, are 53.05 ft^4, 54.14 ft^4, and 53.63 ft^4 for Bent 2, Bent 3, and Bent 4, respectively. Correspondingly, the effective stiffnesses for Bent 2, Bent 3, and Bent 4 are 313.2 k/in, 259.8 k/in, and 212.1 k/in. The calculated maximum bent stiffness ratio is 1.48, which is less than the allowed maximum of 4.0. This bridge, therefore, can be classified as a Regular Bridge.

8.4.2 Acceleration Coefficients—PGA, S_s, S_1

In LRFD BDS, the seismic hazard at a bridge site is represented by an acceleration response spectrum configured by three acceleration coefficients: Peak Ground Acceleration Coefficient (PGA), Short-Period (0.2 seconds) Acceleration Coefficient (S_s), and Long-Period (1.0 seconds) Acceleration Coefficient (S_1).

The contours of acceleration coefficients are drafted in LRFD BDS (AASHTO, 2012) Figure 3.10.2.1-1 to Figure 3.10.2.1-21. The maps are based on a uniform risk model of seismic hazard with 7% probability of exceedance in 75 years (approximately 1000-year return period). This example bridge is located at Los Angeles area. From the acceleration coefficient maps, it can be checked out that at the bridge site, PGA = 0.7 (LRFD BDS, Figure 3.10.2.1-4), $S_s = 1.75$ (LRFD BDS, Figure 3.10.2.1-5), $S_1 = 0.75$ (LRFD BDS Figure 3.10.2.1-6).

8.4.3 Site Classification and Site Effects

It is well known that the soil conditions at the bridge site have significant influences on the design acceleration response spectrum. In LRFD BDS, the site conditions are classified into six classes, called A, B, C, D, E, and F, and listed in Table 8.2.

The different site classes have different site effects. These site effects are represented by three site coefficients: F_{pga}, F_a, and F_v. The values of these three coefficients are given in Tables 8.3, 8.4, and 8.5, respectively.

Since the example bridge is constructed on Class C site, it is found from above tables that the site coefficients are: $F_{pga} = 1.0$, $F_a = 1.0$, and $F_v = 1.3$.

TABLE 8.2 Site Classes

Site Class	Soil Type and Profile
A	Hard rock with measured shear wave velocity, $\overline{v}_s > 5000$ ft/s
B	Rock with 2500 ft/sec $< \overline{v}_s < 5000$ ft/s
C	Very dense soil and soil rock with 1200 ft/s $< \overline{v}_s < 2500$ ft/s, or $\overline{N} > 50$ blows/ft, or $\overline{s}_u > 2.0$ ksf
D	Stiff soil with 600 ft/s $< \overline{v}_s < 1200$ ft/s, or 15 blows/ft $< \overline{N} < 50$ blows/ft, or 1.0 ksf $< \overline{s}_u < 2.0$ ksf
E	Soil profile with $\overline{v}_s < 600$ ft/s, or $\overline{N} < 15$ blows/ft, or $\overline{s}_u < 1.0$ ksf, or soft clay with depth > 10 ft
F	Soil requiring site-specific ground motion response evaluation

TABLE 8.3 Value of F_{pga}

Site Class	PGA ≤ 0.10	PGA = 0.20	PGA = 0.30	PGA = 0.40	PGA ≥ 0.50
A	0.8	0.8	0.8	0.8	0.8
B	1.0	1.0	1.0	1.0	1.0
C	1.2	1.2	1.1	1.0	1.0
D	1.6	1.4	1.2	1.0	1.0
E	2.5	1.7	1.2	0.9	0.9
F	Site-specific response investigation and dynamic site response analysis should be considered.				

TABLE 8.4 Value of F_a

Site Class	$S_s \leq 0.25$	$S_s = 0.50$	$S_s = 0.75$	$S_s = 1.00$	$S_s \geq 1.25$
A	0.8	0.8	0.8	0.8	0.8
B	1.0	1.0	1.0	1.0	1.0
C	1.2	1.2	1.1	1.0	1.0
D	1.6	1.4	1.2	1.0	1.0
E	2.5	1.7	1.2	0.9	0.9
F	Site-specific response investigation and dynamic site response analysis should be considered.				

TABLE 8.5 Value of F_v

Site Class	$S_1 \leq 0.1$	$S_1 = 0.2$	$S_1 = 0.3$	$S_1 = 0.4$	$S_1 \geq 0.5$
A	0.8	0.8	0.8	0.8	0.8
B	1.0	1.0	1.0	1.0	1.0
C	1.7	1.6	1.5	1.4	1.3
D	2.4	2.0	1.8	1.6	1.5
E	3.5	3.2	2.8	2.4	2.4
F	Site-specific response investigation and dynamic site response analysis should be considered.				

8.4.4 Design Acceleration Response Spectrum

In LRFD BDS, the design acceleration response spectrum is specified as three segments:

$$C_s = \begin{cases} A_s + (S_{DS} - A_s)\dfrac{T}{T_0} & T \leq T_0 \\ S_{DS} & T_0 \leq T \leq T_s \\ \dfrac{S_{D1}}{T} & T_s \leq T \end{cases} \tag{8.1}$$

in which $T_0 = 0.2T_S$, $T_S = S_{D1}/S_{DS}$, and A_s is the acceleration coefficient at zero period determined by

$$A_s = F_{pga}\text{PGA} \tag{8.2}$$

S_{DS} is the design spectral acceleration coefficient at 0.2 second period determined by

$$S_{DS} = F_a S_s \tag{8.3}$$

S_{D1} is the design spectral acceleration coefficient at 1.0 second period determined by

$$S_{D1} = F_v S_1 \tag{8.4}$$

For the example bridge located at Los Angle area and constructed on Class C site, the design acceleration coefficients at three critical periods are calculated as: $A_s = F_{pga}\text{PGA} = 0.7$, $S_{DS} = F_a S_s = 1.75$, $S_{D1} = F_v S_1 = 0.975$, and turning periods are: $T_S = S_{D1}/S_{DS} = 0.557$ s, $T_0 = 0.2T_S = 0.111$ s. The design acceleration response spectrum is shown in Figure 8.6.

8.4.5 Bridge Operational Categories—OC

Based on social/survival and security/defense requirements, all bridges are classified into three Operational Categories: Critical Bridges (CB), Essential Bridges (EB), and Other Bridges (OB). CB must remain open to all traffic after the design earthquake (1000-year return period event) and must be usable by emergency vehicles and for security/defense purposes immediately after a large earthquake (2500-year return period event). EB, as a minimum, should be open to emergency vehicles and for security/defense purposes immediately after the design earthquake. For the example bridge, it is just a general highway bridge, no any special requirements for opening to traffic after the design earthquake. Therefore, this bridge is classified as Other Bridge.

8.4.6 Seismic Performance Zone—SPZ

Based on the value of Acceleration Coefficient at the bridge site, LRFD BDS specifies four different Seismic Performance Zones listed in Table 8.6. Obviously the example bridge is located in Zone 4 since

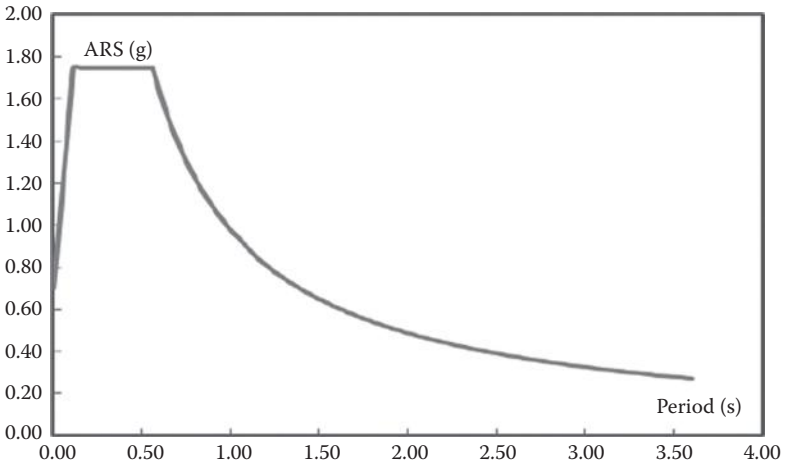

FIGURE 8.6 Seismic response coefficient.

TABLE 8.6 Seismic Performance Zone

Acceleration Coefficient	$S_{D1} \leq 0.15$	$0.15 < S_{D1} \leq 0.30$	$0.30 < S_{D1} \leq 0.50$	$S_{D1} > 0.50$
Seismic Performance Zone	1	2	3	4

$S_{D1} = 0.975 > 0.50$. For bridges located in different seismic zones, the requirements of seismic analysis, design, and detailing will be different, which is shown in Figure 8.2.

8.4.7 Bridge Elastic Seismic Response Analysis

In LRFD BDS, four seismic analysis methods are specified for a multispan girder bridge: Uniform Load Elastic Method (UL), Single-Mode Elastic Method (SM), Multimode Elastic Method (MM), and Time History Analysis (TH). Since the example bridge is classified as a regular nonessential noncritical bridge, the SM is adopted to analyze bridge elastic responses.

It is obvious for this example that the bridge dead load is uniformly distributed along the span because of a constant deck width and depth. However, the stiffnesses at three bents are different because of different column heights, although the column diameter and reinforcement are the same among three columns. Figure 8.7 shows bridge deformation along transverse direction. This deformation is a combination of transition and rotation because of an offset between the center of mass and the center of stiffness. A step-by-step elastic dynamic analysis along bridge transverse direction is summarized in Table 8.7.

A similar step-by-step analysis can be performed along bridge longitudinal direction with only one transition movement. The calculations are listed in Table 8.8.

The next step is to combine the seismic force effects on each of the principal axes of a component resulting from analyses in the two perpendicular directions. Obviously there is no transverse moment response along bridge longitudinal analysis since the bridge is un-skewed. However, there are very small longitudinal moment responses along bridge transverse analysis because of the offset between center of mass and center of stiffness. The two cases of combinations are listed in Table 8.9. It is seen that the control case is the transverse combination.

8.4.8 Response Modification Factor—R

Both experimental model test and field seismic investigation indicate that the columns will behave inelastically during strong seismic shaking and never reach their elastic seismic responses (forces) calculated from dynamic analyses. Therefore, it is uneconomical to design those columns to resist larger

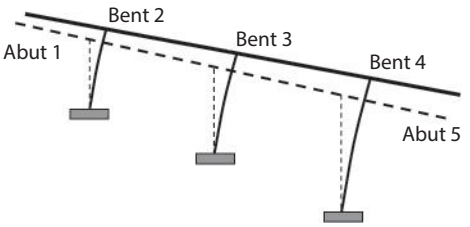

FIGURE 8.7 Single-mode analysis—transverse direction.

TABLE 8.7 Column Seismic Moment Demand Calculation—Transverse Direction

Location	Abut 1	Bent 2	Bent 3	Bent 4	Abut 5	Sum
Column Section Gross I (ft^4)		117.9	117.9	117.9		
Column Section Crack I_c (ft^4)		53.05	54.14	53.63		
Abut/Bent Trans. Stiffness K_T (k/in)	62.6	313.2	259.8	212.1	42.4	890.2
Trans. Self Weight W_T (kips)	713	1,755	1,967	1,870	764.3	7,070
Bent Offset Distance (to Abut 1) D_{A1}(ft)	0.0	120.0	270.0	430.0	560.0	560.0
Trans. Stiffness Offset K_TD_{A1} (k/in-ft)	0.0	37,580	70,159	91,204	23,756	222,659
Trans. Weight Offset W_TD_{A1} (k-ft)	0.0	210,659	531,189	804,138	428,022	1,974,008
Bridge Trans. Vibration Period T (sec)	$T = 0.32(\text{Sum}(W_T)/\text{Sum}(K_T))^{0.5}$					0.902
Acceleration Coefficient C_s	$C_s = S_{D1}/T$ (Since $T > T_s = 0.557$)					1.081
Total Trans. Seismic Force F_T (kips)	$F_T = \text{Sum}(W_T)\ C_s$					7,644
Bridge Center of Mass X_{cM} (ft)	$X_{cM} = \text{Sum}(W_TD_{A1})/\text{Sum}(W_T)$					279.2
Bridge Center of Rigidity X_{cR} (ft)	$X_{cR} = \text{Sum}(K_TD_{A1})/\text{Sum}(K_T)$					250.2
Offset: CL Mass-CL Rigidity, $D_{M\text{-}R}$ (ft)	$D_{M\text{-}R} = X_{cM} - X_{cR}$					29.0
Additional Rotation Moment M_R (k-ft)	$M_R = F_TD_{M\text{-}R}$					221,905
Rotation Stiffness $J_T = K_T(D_{A1} - X_{cM})^2$	4,882,648	7,937,711	22,023	4,822,960	3,344,658	21,010,001
Displacement by F_T, $\Delta_F = F_T/\text{Sum}(K_T)$(in)	8.59	8.59	8.59	8.59	8.59	
Rotation by M_R, $\theta_R = M_R/\text{Sum}(J_T)$ (rad)	0.00088	0.00088	0.00088	0.00088	0.00088	
Additional Displacement by θ_R, Δ_R (in)	–2.64	–1.37	0.21	1.90	3.27	
Total Displacement Demand Δ_D (in)	5.94	7.21	8.80	10.49	11.86	
Trans. Force Demand F_D (kips)	372	2,259	2,286	2,224	503	7,644
Col. Trans. Moment Demand M_T (k-ft)		63,239	58,570	71,172		

TABLE 8.8 Column Seismic Moment Demand Calculation—Longitudinal Direction

Location	Abut 1	Bent 2	Bent 3	Bent 4	Abut 5	Sum
Column Section Gross I (ft^4)		117.9	117.9	117.9		
Column Section Crack I_c (ft^4)		53.05	54.14	53.63		
Abut/Bent Long. Stiffness K_L (k/in)	150.0	1,252.7	1,039.4	848.4	150.0	3,440
Long. Self Weight W_L (kips)	713	1,755	1,967	1,870	764	7,070
Bridge Long. Vibration Period T (sec)	$T = 0.32(\text{Sum}(W_L)/\text{Sum}(K_L))^{0.5}$					0.459
Acceleration Coefficient C_s	$C_s = S_{Ds}$ (Since $T_0 < T < T_s = 0.557$)					1.75
Total Trans. Seismic Force F_L (kips)	$F_L = \text{Sum}(W_L)\ C_s$					12,373
Displacement by F_L, $\Delta_F = F_L/\text{Sum}(K_L)$(in)	3.60	3.60	3.60	3.60	3.60	
Long. Force Demand F_D (kips)	539	4,505	3,738	3,051	539	12,373
Col. Long. Moment Demand M_L (k-ft)		63,068	56,068	48,817		

TABLE 8.9 Column Design Moment—Transverse and Longitudinal Combination

Location	Bent 2	Bent 3	Bent 4
Input Transverse EQ_T: Column Transverse Response $M_{T\text{-}T}$ (k-ft)	63,239	58,570	71,172
Input Transverse EQ_T: Column Longitudinal Response $M_{L\text{-}T}$ (k-ft)	2	0	1
Input Longitudinal EQ_L: Column Transverse Response $M_{T\text{-}L}$ (k-ft)	63,068	56,068	48,817
Input Longitudinal EQ_L: Column Longitudinal Response $M_{L\text{-}L}$ (k-ft)	0	0	0
Trans. Response M_T (k-ft): Max$((1.0M_{T\text{-}T} + 0.3M_{T\text{-}L}), (0.3M_{T\text{-}T} + 1.0M_{T\text{-}L}))$	63,239	58,570	71,172
Long. Response M_L(k-ft): Max$((1.0M_{L\text{-}T} + 0.3M_{L\text{-}L}), (0.3M_{L\text{-}T} + 1.0M_{L\text{-}L}))$	63,068	56,068	48,817
Circle Column Design Moment M_D = Max$(M_T, M_L)/R$ (k-ft)	21,084	22,857	23,724

TABLE 8.10 Response Modification Factor

	Operational Category		
Substructure	Critical	Essential	Other
Wall-type piers—larger dimension	1.5	1.5	2.0
Reinforced concrete pile bent—vertical piles only	1.5	2.0	3.0
Reinforced concrete pile bent—with batter piles	1.5	1.5	2.0
Single-column bent	1.5	2.0	3.0
Multiple column bent	1.5	3.5	5.0
Steel or composite steel and concrete pile bent—vertical piles only	1.5	3.5	5.0
Steel or composite steel and concrete pile bent—with batter piles	1.5	2.0	3.0

earthquakes elastically. In LRFD BDS, a Response Modification Factor, called R-Factor, is introduced to account for the inelastic behavior of bridge components. The design seismic forces are determined by dividing the forces resulting from elastic analysis by the appropriate responses modification factor as specified in Table 8.10.

For the example bridge, which has three single-column bents, neither critical nor essential, from the table above, the R-Factor should be 3.0. Then the design moments for these three columns are just one-third of the corresponding elastic moments, which are listed in the last row of Table 8.9.

8.4.9 Column Moment Capacity and Demand/Capacity Check

The nominal moment capacity, M_n, of a reinforced concrete column with an axial load P can be computed through a standard column section P–M interaction analysis. In LRFD BDS, the factored moment resistance is specified as

$$M_r = \phi_M M_n \tag{8.5}$$

in which ϕ_M is the moment Resistance Factor. In general, $\phi_M = 1.0$ almost in all seismic design codes around world. In LRFD BDS, however, the Resistance Factor is specified as $\phi_M = 0.9$.

For this example bridge, the column cross section is shown in Figure 8.8, and P–M curve is shown in Figure 8.9. The factored moment resistance and moment demand/capacity ratio check are summarized in Table 8.11.

It can be seen that the moment capacities are less than demand approximately 30%, which means the column reinforcement of #14 total 48, from (DL + LL) design, is not enough to resist the design earthquake (PGA = 0.7).

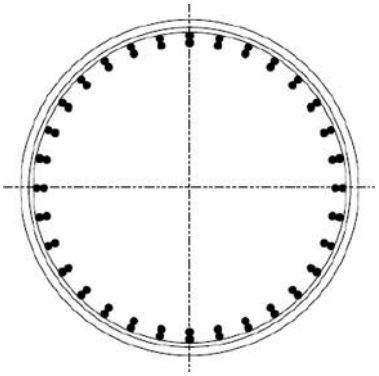

FIGURE 8.8 Column cross section.

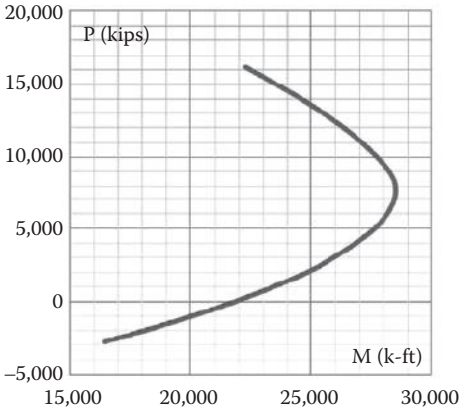

FIGURE 8.9 Column section *P*–*M* curve.

TABLE 8.11 Column Moment Demand/Capacity Check (#14 total 48)

Location	Bent 2	Bent 3	Bent 4
Column section nominal moment capacity M_n (k-ft)	21,048	20,467	20,320
Column axial load P_u (kips)	1,755	1,967	1,870
Concrete compressive strength f'_c(ksi)	4.0	4.0	4.0
Axial load ratio P_u/f'_cA_g (%)	7.92%	8.88%	8.44%
Moment resistance factor ϕ_M	0.9	0.9	0.9
Factored moment resistance $M_r = \phi_M M_n$ (k-ft)	18,133	18,420	18,288
Column moment demand/capacity ratio $r_M = M_D/M_r$	1.162	1.241	1.297

The second iteration is performed with column reinforcement of #11 total 64 (steel ratio 2.87%). The results are summarized in Table 8.12. Still the column at Bent 4 is under designed approximately 16%.

The third iteration is continuously performed with column reinforcement of #11 total 88 (steel ratio 3.94%). The results are summarized in Table 8.13. This time the column at Bent 4 is under designed approximately 3%. In order to keep all moment D/C ratios <1.0, the column reinforcement at Bent 4 needs to increase to #14 total 92 with steel ratio 4.12%, which is over the maximum 4% allowed steel ratio.

TABLE 8.12 Column Moment Demand/Capacity Check (#14 total 64)

Location	Bent 2	Bent 3	Bent 4
Column section crack I_c (ft^4)	62.21	62.48	62.34
Bent trans. stiffness K_T (k/in)	367.3	299.9	246.6
Circle column design moment M_D (k-ft)	22,857	24,473	25,652
Factored moment resistance M_r (k-ft)	21,922	22,167	22,054
Column moment demand/capacity ratio $r_M = M_D/M_r$	1.043	1.104	1.163

TABLE 8.13 Column Moment Demand/Capacity Check (#14 total 88)

Location	Bent 2	Bent 3	Bent 4
Column section crack I_c (ft^4)	66.43	66.79	66.61
Bent trans. stiffness K_T (k/in)	392.2	320.6	263.4
Circle column design moment M_D (k-ft)	25,144	26,995	28,238
Factored moment resistance M_r (k-ft)	27,293	27,472	27,390
Column moment demand/capacity ratio $r_M = M_D/M_r$	0.921	0.983	1.031

8.4.10 *P*-Δ Requirements

Since an excessive displacement may lead to a significant *P*-Δ effects and further result in a structural instability, in LRFD BDS, an additional displacement check is enforced after designing the bridge based on the "Force" requirements. The displacement of any column or pier in longitudinal or transverse direction shall satisfy

$$\Delta P_u < 0.25\phi_M M_n \tag{8.6}$$

in which P_u is the axial load on column, ϕ_M the moment Resistance Factor, M_n the column nominal moment capacity, and Δ the factored column displacement expressed as

$$\Delta = R_d \Delta_e \tag{8.7}$$

in which Δ_e is column elastic displacement response, and R_d is the displacement magnification factor expressed as

$$R_d = \begin{cases} \left(1 - \dfrac{1}{R}\right)\dfrac{1.25T_s}{T} + \dfrac{1}{R} & T < 1.25T_s \\ 1.0 & T \geq 1.25T_s \end{cases} \tag{8.8}$$

where R is the response modification factor, and T_s the characteristic ground motion period. For this example bridge, along transverse direction, $T = 0.759$ seconds (third iteration with #14 total 88 column bars), $T_s = 0.557$ seconds. Because $T > 1.25T_s$, the displacement magnification factor $R_d = 1.0$. A step-by-step *P*-Δ check is summarized in Table 8.14. Obviously, the *P*-Δ effects are insignification for this strong-column bridge.

8.4.11 Foundation Design

In LRFD BDS, the foundation design force is based on column overstrength moment resistance assuming the plastic hinge will form at the bottom of column (top of footing). For a typical pile (with pile cap) foundation surrounded by competent soil, the axial force demand on an individual pile can be calculated by

TABLE 8.14 Column *P*-Δ Effect Check (#14 total 88)

Location	Bent 2	Bent 3	Bent 4
Column elastic displacement Δ_e (in)	6.06	7.41	8.85
Displacement magnification factor R_d (since $T > 1.25T_s$)	1.0	1.0	1.0
Factored column displacement $\Delta = R_d\Delta_e$ (in)	6.06	7.41	8.85
Axial load on top of column P_u (kips)	1,755	1,967	1,870
Factored moment resistance M_r (k-ft)	27,293	27,472	27,390
P-Δ Demand: ΔP_u (k-ft)	886	1,215	1,379
P-Δ Resistance: $0.25M_r$ (k-ft)	6,828	6,868	6,847

TABLE 8.15 Force Demand on Top of Footing with Column Rebar #14 Total 88

	90	75	60.	45.	30.	15	0
Force Demand				Deg.			
$M_{p\text{-}y}$ (k-ft)	39,987	38,625	34,630	28,275	19,994	10,340	0
$M_{p\text{-}x}$ (k-ft)	0	10,340	19,994	28,275	34,630	38,625	39,987
P (kips)	2,142	2,142	2,142	2,142	2,142	2,142	2,142
V_p (kips)	1,333	1,554	1,775	1,996	2,217	2,438	2,659

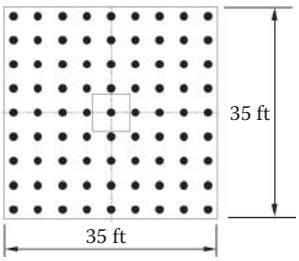

FIGURE 8.10 Footing size and pile layout—LRFD BDS.

$$R_i = \frac{P}{N_p} \pm \frac{M_y c_{x-i}}{I_y} \pm \frac{M_x c_{y-i}}{I_x} \tag{8.9}$$

in which R_i is pile axial force demand (positive means compression force and negative implies tension force), P the total vertical load on pile foundation, N_p the total number of piles under pile cap, I_x and I_y the effective moment of inertia of pile group, $c_{x\text{-}i}$ and $c_{y\text{-}i}$ the distances from neutral axis to the pile, M_x and M_y the moment demands on bottom of pile cap taken as

$$M_x = \phi_F\left(M_{p-x}^{col} + V_{p-x}^{col} D_F\right); \quad M_y = \phi_F\left(M_{p-y}^{col} + V_{p-y}^{col} D_F\right) \tag{8.10}$$

where $\phi_F = 1.3$ is the overstrength factor, M_{p-x}^{col} and M_{p-y}^{col} the column plastic moment capacities, V_{p-x}^{col} and V_{p-y}^{col} the column shear forces associated with column plastic moments, and D_F the pile cap depth.

For the example bridge, 70-ton driving concrete piles are used to support bent foundations. Under service load condition, pile compression and tension capacities are 140 kips and 70 kips. However, under seismic load condition, the capacities can be doubled. Taking Bent 3 footing design as an example, Table 8.15 lists the force demands acting on top of footing.

Based on Equation 8.9, the footing design is performed and the required footing size and pile layout is shown in Figure 8.10. The required footing depth is 7.0 ft, and total 81 piles are needed to resist the column plastic hinge forces.

8.5 Bridge Seismic Design Based on LRFD SBD

8.5.1 Balanced Stiffness Check

A similar procedure as in designing bridges based on LRFD BDS is followed here. The first step in LRFD SBD is to check the balanced stiffness requirements. For a bridge with constant deck width and depth, the balanced stiffness requirements include: (1) any two bents within a frame or any two columns within a bent, the smaller effective bent or column stiffness cannot be less than a half of the larger effective bent or column stiffness; (2) adjacent bents within a frame or adjacent columns within a bent, the smaller effective bent or column stiffness cannot be less than three-quarter of the larger effective bent or column stiffness. For this example bridge, the member size and column reinforcement are listed in Table 8.1. Based on a column reinforcement of #14 total 48 bars, the balanced stiffness check is listed in Table 8.16. It can be seen that the minimum stiffness ratio between any two bents is 0.68 > 0.5, and the minimum stiffness ratio between any adjacent bents is 0.82 > 0.75. The balanced stiffness requirements are satisfied.

8.5.2 Design Acceleration Response Spectrum

Both LRFD BDS and LRFD SBD specify same procedure to configure the design acceleration response spectrum. Only difference is that instead of C_s in LRFD BDS, S_a is used in LRFD SBD. So the design acceleration response spectrum is expressed as

$$S_a = \begin{cases} A_s + (S_{DS} - A_s)\dfrac{T}{T_0} & T \le T_0 \\ S_{DS} & T_0 \le T \le T_s \\ \dfrac{S_{D1}}{T} & T_s \le T \end{cases} \tag{8.11}$$

The definitions of all parameters are the same as in Equation 8.1. Input earthquake acceleration response spectrum, shown in Figure 8.6, is also used to design the example bridge based on LRFD SBD.

8.5.3 Seismic Design Category—SDC

Different ground shaking levels imply different seismic risks. In LRFD BDS, four Seismic Performance Zones (Table 8.6) are specified to distinguish these risks and to enforce different design requirements. Correspondingly, in LRFD SBD, four Seismic Design Categories, called SDC A, SDC B, SDC C, and SDC D, shown in Table 8.17, are established also based on the values of seismic acceleration coefficient at 1.0 second period. The SDC reflects the variation in seismic risk and is used to permit different

TABLE 8.16 Balanced Stiffness—Transverse

Location	Cracked Section I_c (ft^4)	Column Height H_c (ft)	Column Stiffness K_c(k/in)	Column Stiffness Ratio K_{ci}/K_{c2}	Column Stiffness Ratio K_{ci}/K_{c3}	Column Stiffness Ratio K_{ci}/K_{c4}	Required Minimum Stiffness Ratio K_{ci}/K_{cj}
Bent 2	53.05	26.0	313.2	1.00	1.21	1.43	0.5
Bent 3	54.14	28.0	259.8	0.83	1.00	1.23	0.5
Bent 4	53.63	30.0	212.1	0.68	0.82	1.00	0.5

TABLE 8.17 Seismic Design Category

Acceleration Coefficient	$S_{D1} \leq 0.15$	$0.15 < S_{D1} \leq 0.30$	$0.30 < S_{D1} \leq 0.50$	$S_{D1} > 0.50$
SDC	A	B	C	D

TABLE 8.18 Required Analysis Procedures

	Regular Bridge		Not Regular Bridge	
SDC	Simple Span	Multispan (< 7)	Simple Span	Multispan
A	Not Required	Not required	Not required	Not required
B, C, D	Not Required	Procedures 1 or 2	Not required	Procedure 2

TABLE 8.19 Bent Elastic Displacement Responses—Transverse and Longitudinal Combination

Location	Bent 2	Bent 3	Bent 4
Input Transverse EQ_T: Bent Transverse Response $\Delta_{T\text{-}T}$ (in)	7.21	8.80	10.49
Input Transverse EQ_T: Bent Longitudinal Response $\Delta_{L\text{-}T}$ (k-ft)	0	0	0
Input Longitudinal EQ_L: Column Transverse Response $\Delta_{T\text{-}L}$ (k-ft)	3.60	3.60	3.60
Input Longitudinal EQ_L: Column Longitudinal Response $\Delta_{L\text{-}L}$ (k-ft)	0	0	0
Trans. Response $\Delta_{e\text{-}T}$ (k-ft): Max$((1.0\Delta_{T\text{-}T} + 0.3\Delta_{T\text{-}L}), (0.3\Delta_{T\text{-}T} + 1.0\Delta_{T\text{-}L}))$	7.21	8.80	10.49
Long. Response $\Delta_{e\text{-}L}$(k-ft): Max$((1.0\Delta_{L\text{-}T} + 0.3M_{L\text{-}L}), (0.3\Delta_{L\text{-}T} + 1.0\Delta_{L\text{-}L}))$	3.60	3.60	3.60

requirements for methods of analysis, minimum support lengths, column design details, and foundation and abutment design procedures. The detail requirements for all four SDCs are provided in LRFD SBD Section 5.3. For the example bridge, the SDC is classified as SDC D since $S_{D1} = 0.975 > 0.5$.

8.5.4 Bridge Seismic Response Analysis

In LRFD SBD, three seismic analysis procedures are specified: Equivalent Static Analysis (Procedure 1), Elastic Dynamic Analysis (Procedure 2), and Nonlinear Time History Analysis (Procedure 3). The procedure requirements for different bridge classifications and different seismic design categories are listed in Table 8.18.

Since the example bridge is classified as a regular multispan bridge with SDC D requirements, the Procedure 1, Equivalent Static Analysis, is used to analyses bridge seismic responses.

The calculation steps are the same as shown in Table 8.7 (transverse) and Table 8.8 (longitudinal). The focus now is on column/bent displacement responses. Table 8.19 lists displacement responses at all three bents and displacement combinations along two orthogonal directions.

Obviously, the bridge responses under strong seismic shaking should not be purely elastic after columns and other components yielding. In "Force-Based" design, a force reduction factor, R, is applied to the elastic force responses to estimate the design force demands. Similar, in "Displacement-Based" design (LRFD SBD), a displacement modification factor, R_d, is introduced to estimate the design displacement demands. The formula to calculate this factor is given in Equation 8.12.

$$R_d = \begin{cases} \left(1 - \dfrac{1}{\mu_D}\right)\dfrac{1.25T_s}{T} + \dfrac{1}{\mu_D} & T < 1.25T_s \\ 1.0 & T \geq 1.25T_s \end{cases} \tag{8.12}$$

TABLE 8.20 Bent Design Displacement Demand

Location		Bent 2	Bent 3	Bent 4
Transverse	T (seconds)	0.902		
	$1.25T_s$ (seconds)	0.696		
	$\Delta_{e\text{-}T}$ (in)	7.21	8.80	10.49
	Δ_y (in) (see Table 8.21)	2.28	2.60	2.97
	$\mu_D = \Delta_{e\text{-}T}/\Delta_y$	3.17	3.38	3.53
	R_d (second) ($T > 1.25T_s$)	1.00	1.00	1.00
	$\Delta_T = R_d\,\Delta_{e\text{-}T}$ (in)	7.21	8.80	10.49
Longitudinal	T (second)	0.459		
	$1.25T_s$ (second)	0.696		
	$\Delta_{e\text{-}L}$ (in)	3.60	3.60	3.60
	Δ_y (in) (see Table 8.22)	1.14	1.30	1.49
	$\mu_D = \Delta_{e\text{-}L}/\Delta_y$	3.16	2.78	2.42
	R_d (second) ($T < 1.25T_s$)	1.354	1.331	1.304
	$\Delta_L = R_d\,\Delta_{e\text{-}L}$ (in)	4.87	4.78	4.69

where $\mu_D = \Delta_e/\Delta_y$, is column displacement ductility demand, Δ_e is column elastic displacement response and Δ_y is column yield displacement.

For the example bridge, along both transverse and longitudinal directions, the design displacements are calculated in Table 8.20.

8.5.5 Bent Displacement Capacity Evaluation

In LRFD SBD, a so-called "pushover" analysis is specified to evaluate bridge displacement capacity if a bridge is designed for SDC D. As the name implies, the pushover analysis is a process of pushing bridge horizontally, with a prescribed loading pattern, incrementally, until the bridge reaches an unstable condition. This incremental linear analysis should capture the overall nonlinear behavior of various bridge components by pushing them to initiate inelastic action. At each incremental step, the pushing force and representative displacement are monitored, and a pushover curve can be plotted to illustrate the progression of bridge inelastic deformation until collapse.

The bridge displacement capacity evaluation through pushover analysis starts from material ultimate strain capacity, further to section ultimate curvature capacity, then advance to plastic hinge ultimate rotation capacity, continue to member ultimate deformation capacity, and finally end up to bridge global ultimate displacement capacity.

For a cantilever column, the local displacement capacity can be estimated by "section analysis" and concentrated plasticity approach. Through the section analysis, a Moment–Curvature relationship can be established for any particular member cross section. When the concrete reaches the ultimate compressive strain ε_{cu} or the steel reaches the ultimate tensile strain ε_{su}, the corresponding curvature is called section ultimate curvature ϕ_u. A typical moment–curvature curve is plotted in Figure 8.11.

The plastic deformation of a member can be evaluated by distributed plasticity approach or by concentrated plasticity approach. Based on the extensive cyclic tests of cantilever reinforced concrete columns, it was found that the plastic rotation of a reinforced concrete column under lateral load action is concentrated at very limited region close to column bottom. Within this region, a significant plastic curvature is developed, and this curvature can be idealized as a constant ϕ_p, as shown in Figure 8.12 for a typical cantilever column. According to concentrated plastic hinge assumption, the plastic rotation is calculated by

$$\theta_p = L_p\phi_p = L_p\left(\phi_u - \phi_y\right) \tag{8.13}$$

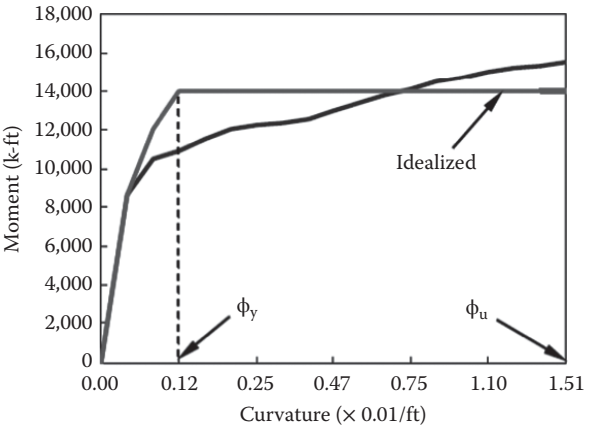

FIGURE 8.11 Typical moment–curvature.

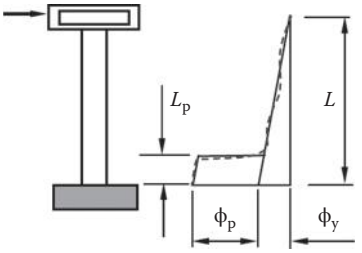

FIGURE 8.12 Idealized curvature distribution.

in which ϕ_y and ϕ_u are yield curvature and ultimate curvature respectively, and L_p the idealized plastic hinge length expressed as

$$L_p = 0.08L + 0.15 f_{ye} d_{bl} \geq 0.3 f_{ye} d_{bl} \tag{8.14}$$

where f_{ye} is the expected yield strength of longitudinal column reinforcing steel (ksi), d_{bl} the nominal diameter of longitudinal column rebar (in), and L the length of column from point of maximum moment to the point of moment contraflexure (in)

The total displacement capacity including the yield displacement and the plastic displacement

$$\Delta_C = \Delta_y + \Delta_p \tag{8.15}$$

where the yield displacement is

$$\Delta_y = \frac{L^2}{3}\phi_y \tag{8.16}$$

and the plastic displacement is

$$\Delta_p = \theta_p\left(L - \frac{L_p}{2}\right) \tag{8.17}$$

For the example bridge with column reinforcement of #14 total 48, the displacement capacity evaluations are summarized in Tables 8.21 and 8.22.

TABLE 8.21 Bent Displacement Capacity—Transverse Direction

Location	Bent 2	Bent 3	Bent 4
Column section yield curvature ϕ_y (1/ft)	0.00073	0.00072	0.00072
Column section ultimate curvature ϕ_u (1/ft)	0.00816	0.00802	0.00809
Column section plastic curvature $\phi_p = (\phi_u - \phi_y)$ (1/ft)	0.00744	0.00730	0.00736
Column longitudinal rebar diameter d_{bl} (in)	1.693	1.693	1.693
Column rebar expected yield strength f_{ye} (ksi)	68.0	68.0	68.0
Column length (Height) L (in)	336.0	360.0	384.0
Column plastic hinge length $L_p = 0.08L + 0.15f_{ye}d_{bl}$ (in)	44.15	46.07	47.99
Column yield displacement $\Delta_y = L^2\phi_y/3$ (in)	2.28	2.60	2.97
Column plastic displacement $\Delta_p = L_p(\phi_u - \phi_y)(L - L_p/2)$ (in)	8.59	9.44	10.6
Total displacement capacity $\Delta_C = (\Delta_y + \Delta_p)$ (in)	10.87	12.05	13.57

TABLE 8.22 Bent Displacement Capacity—Longitudinal Direction

Location	Bent 2	Bent 3	Bent 4
Column section yield curvature ϕ_y (1/ft)	0.00073	0.00072	0.00072
Column section ultimate curvature ϕ_u (1/ft)	0.00816	0.00802	0.00809
Column section plastic curvature $\phi_p = (\phi_u - \phi_y)$ (1/ft)	0.00744	0.00730	0.00736
Column longitudinal rebar diameter d_{bl} (in)	1.693	1.693	1.693
Column rebar expected yield strength f_{ye} (ksi)	68.0	68.0	68.0
Half column length (height) L (in)	168.0	180.0	192.0
Half column plastic hinge length $L_p = 0.08L + 0.15f_{ye}d_{bl}$ (in)	30.71	31.67	32.63
Half column yield displacement $\Delta_y = L^2\phi_y/3$ (in)	0.57	0.65	0.74
Half column plastic displacement $\Delta_p = L_p(\phi_u - \phi_y)(L - L_p/2)$ (in)	2.90	3.16	3.52
Total displacement capacity $\Delta_C = 2(\Delta_y + \Delta_p)$ (in)	6.95	7.63	8.52

8.5.6 Bent Displacement Demand/Capacity Check

In LRFD SBD, three displacement requirements have to be satisfied. The basic requirement is to control the design displacement at each bent along both transverse and longitudinal directions less than the corresponding bent displacement capacity. The second requirement is to limit column ductility demand less than the allowed maximum limit. The third requirement is to limit column P-Δ effect within the allowable range.

For the example bridge, Table 8.23 summarizes all checks for these three displacement requirements. It is clear that all requirements are satisfied. The maximum displacement D/C ratio is only 0.77 at Bent 4 along transverse direction. The maximum displacement ductility demand is 4.27 at Bent 2 along longitudinal direction. The P-Δ effects are insignification for this strong-column bridge.

8.5.7 Column Shear Design

In LRFD SBD, column shear design includes four steps: (1) determine shear demand, (2) determine column plastic hinge region, (3) compute shear capacity both inside plastic hinge zone and outside plastic hinge zone, and (4) check shear demand/capacity ratio inside and outside plastic hinge zone.

The shear demand, V_u, in SDC D, shall be determined based on the force associated with column overstrength moment M_{po} defined as

$$M_{po} = \lambda_{mo} M_p \tag{8.18}$$

TABLE 8.23 Bent Displacement Demand/Capacity Check

Location			Bent 2	Bent 3	Bent 4
$r = \Delta_D/\Delta_C < 1.0$	Transverse	$\Delta_{D\text{-}T}$ (in)	7.21	8.80	10.49
		$\Delta_{C\text{-}T}$ (in)	10.87	12.05	13.57
		$r_T = \Delta_{D\text{-}T}/\Delta_{C\text{-}T}$	0.66	0.73	0.77
	Longitudinal	$\Delta_{D\text{-}L}$ (in)	4.87	4.78	4.69
		$\Delta_{C\text{-}L}$ (in)	6.95	7.63	8.52
		$r_L = \Delta_{D\text{-}L}/\Delta_{C\text{-}L}$	0.70	0.63	0.55
$\mu_D = \Delta_D/\Delta_y < 5.0$	Transverse	$\Delta_{D\text{-}T}$ (in)	7.21	8.80	10.49
		$\Delta_{y\text{-}T}$ (in)	2.28	2.60	2.97
		$\mu_{D\text{-}T} = \Delta_{D\text{-}T}/\Delta_{y\text{-}T}$	3.17	3.38	3.53
	Longitudinal	$\Delta_{D\text{-}L}$ (in)	4.87	4.78	4.69
		$\Delta_{y\text{-}L}$ (in)	1.14	1.30	1.49
		$\mu_{D\text{-}L} = \Delta_{D\text{-}L}/\Delta_{y\text{-}L}$	4.27	3.68	3.15
$P_{DL}\Delta_D < 0.25M_p$	Transverse	$M_{p\text{-}T}$ (k-ft)	22,360	22,737	22,565
		$P_{DL}\Delta_{D\text{-}T}$ (k-ft)	1,055	1,442	1,635
		$0.25M_{p\text{-}T}$ (k-ft)	5,590	5,684	5,641
	Longitudinal	$M_{p\text{-}L}$ (k-ft)	22,360	22,737	22,565
		$P_{DL}\Delta_{D\text{-}L}$ (k-ft)	712	783	731
		$0.25M_{p\text{-}L}$ (k-ft)	5,590	5,684	5,641

TABLE 8.24 Bent/Column Shear Force Demand

Location		Bent 2	Bent 3	Bent 4
Transverse	$M_{p\text{-}T}$ (k-ft)	22,360	22,737	22,565
	λ_{po} (ASTM A 706 Rebar)	1.20	1.20	1.20
	$M_{po\text{-}T} = \lambda_{po}M_{p\text{-}T}$ (k-ft)	26,832	27,284	27,078
	$H_{c\text{-}T}$ (ft) (fix-free)	28.0	30.0	32.0
	$V_{u\text{-}T} = M_{po\text{-}T}/H_{c\text{-}T}$ (kips)	958	909	846
Longitudinal	$M_{p\text{-}L}$ (k-ft)	22,360	22,737	22,565
	λ_{po} (ASTM A 706 Rebar)	1.20	1.20	1.20
	$M_{po\text{-}L} = \lambda_{po}M_{p\text{-}L}$ (k-ft)	26,832	27,284	27,078
	$H_{c\text{-}L}$ (ft) (fix-fix)	14.0	15.0	16.0
	$V_{u\text{-}L} = M_{po\text{-}L}/H_{c\text{-}L}$ (kips)	1,917	1,819	1,692

where λ_{mo} is the overstrength magnifier with the value $\lambda_{mo} = 1.2$ for ASTM A 706 rebar or $\lambda_{mo} = 1.4$ for ASTM A 615 Grade 60 rebar, and M_p is the idealized plastic moment capacity based on expected material properties.

For the example bridge, ASTM A 706 rebar is used in all three columns. Along bridge transverse direction, the column can be modeled as a "fix-free" condition. Along bridge longitudinal direction, the column should be modeled as a "fix-fix" condition. Column shear force demands along both directions are calculated in Table 8.24.

The plastic hinge region, L_{pr}, shall be taken as the larger of: (1) 1.5 times the gross cross-sectional dimension of bending, (2) the region of column where the moment demand exceed 75% of the maximum plastic moment, and (3) the analytical plastic hinge length L_p.

For the example bridge, the plastic hinge regions for all three columns are determined in Table 8.25.

Column shear capacity includes concrete shear capacity and transverse reinforcing steel shear capacity. The design shear strength should be calculated as

$$V_r = \phi_s V_n \tag{8.19}$$

TABLE 8.25 Column Plastic Hinge Region

Location		Bent 2	Bent 3	Bent 4
Transverse	1.5 $d_{c\text{-}T}$ (in)	126.0	126.0	126.0
	75% moment region	84.0	90.0	96.0
	$L_{p\text{-}T}$ (in)	44.15	46.07	47.99
	$L_{pr\text{-}T}$ (in)	126.0	126.0	126.0
Longitudinal	1.5 $d_{c\text{-}L}$ (in)	126.0	126.0	126.0
	75% moment region	42.0	45.0	48.0
	$L_{p\text{-}L}$ (in)	30.71	31.67	32.63
	$L_{pr\text{-}L}$ (in)	126.0	126.0	126.0

where $\phi_s = 0.9$ is the shear resistance factor, V_n is nominal shear capacity expressed as

$$V_n = V_s + V_c \tag{8.20}$$

in which V_s is transverse reinforcing steel shear capacity and V_c concrete shear capacity.

For a circular column with circular hoops, the shear capacity by steel hoops is computed by

$$V_s = \frac{\pi}{2}\left(\frac{nA_{sp}F_{yh}D'}{s}\right) \le 0.25\sqrt{f'_c}A_e \tag{8.21}$$

where n is number of individual interlocking hoop core sections, A_{sp} the area of hoop rebar, f_{yh} the yield strength of hoop rebar, D' the column core diameter, s the spacing of hoop rebar, f'_c the nominal concrete compressive strength, $A_e = 0.8\,A_g$ is column effective area, and A_g is column gross area.

The shear capacity by concrete within plastic hinge region is calculated by

$$V_c = v_c A_e \tag{8.22}$$

$$v_c = \begin{cases} 0.032\alpha'\left(1 + P_u / 2A_g\right)\sqrt{f'_c} \le \min\left(0.11\sqrt{f'_c},\ 0.047\alpha'\sqrt{f'_c}\right) & \text{if } P_u > 0 \\ 0.0 & \text{if } P_u < 0 \end{cases} \tag{8.23}$$

with shear stress adjustment factor

$$\alpha' = f_s/0.15 + 3.67 - \mu_D \tag{8.24}$$

here $f_s = \rho_s f_{yh} \le 0.35$ and $\rho_s = 4A_{sp}/sD'$ is shear steel ratio.

For concrete shear capacity outside plastic hinge region, only change is $\alpha' = 3.0$.

For the example bridge, the detail shear capacity calculations are listed in Tables 8.26 and 8.27 for the segments inside plastic hinge region. A similar calculation can be performed for the segments outside plastic hinge region.

The last step for column shear design is to check shear demand/capacity ratio. Table 8.28 lists all three column shear design results. The maximum shear D/C ratio is 0.871 at Bent 2 column, which is the shortest column.

8.5.8 Foundation Design

The foundation design procedure in LRFD SBD is the same as in LRFD BDS. Equation 8.9 is used to calculate pile compression and tension forces. However, the overstrength factor ϕ_F (λ_{mo}) in Equation 8.10 is not 1.3 but 1.2. In evaluating column plastic moment, the expected material properties are used.

TABLE 8.26 Column Steel Shear Capacity

Location		Bent 2	Bent 3	Bent 4
Transverse	$d_{c\text{-}T}$ (in)	84.0	84.0	84.0
	D' (in)	79.0	79.0	79.0
	s (in)	8.0	8.0	8.0
	A_{sp} (in^2) (#8 bundle)	1.58	1.58	1.58
	f_{yh} (ksi)	60.0	60.0	60.0
	N	1	1	1
	$V_{s\text{-}T} = (\pi/2)(nA_{sh}f_{yh}D'/s)$ (kips)	1,471	1,471	1,471
Longitudinal	$V_{s\text{-}L} = (\pi/2)(nA_{sh}f_{yh}D'/s)$ (kips)	1,471	1,471	1,471

TABLE 8.27 Column Concrete Shear Capacity

Location		Bent 2	Bent 3	Bent 4
Transverse	A_g (in^2)	5,542	5,542	5,542
	$A_e = 0.8A_g$ (in^2)	4,433	4,433	4,433
	P_u (kips)	1,755	1,967	1,870
	f'_c (ksi)	4.0	4.0	4.0
	$\rho_s = 4A_{sh}/(sD')$	0.01	0.01	0.01
	$f_s = \rho_s f_{yh} < 0.35$	0.35	0.35	0.35
	$\mu_D = \Delta_D/\Delta_y$	3.17	3.38	3.53
	$\alpha' = f_s/0.15 + 3.67 - \mu_D$	2.84	2.63	2.47
	$v_{c1} = 0.032\alpha'(1 + P_u/2A_g)(f'_c)^{0.5}$ (ksi)	0.210	0.198	0.185
	$v_{c2} = 0.11(f'_c)^{0.5}$ (ksi)	0.220	0.220	0.220
	$v_{c3} = 0.047\alpha'(f'_c)^{0.5}$ (ksi)	0.267	0.247	0.232
	$v_c = \min(v_{c1}, v_{c2}, v_{c3})$ (ksi)	0.210	0.198	0.185
	$V_{c\text{-}T} = v_c A_e$ (kips)	932	878	820
Longitudinal	$\mu_D = \Delta_D/\Delta_y$	1.58	1.38	1.21
	$\alpha' = f_s/0.15 + 3.67 - \mu_D$	4.42	4.62	4.79
	$v_{c1} = 0.032\alpha'(1 + P_u/2A_g)(f'_c)^{0.5}$ (ksi)	0.283	0.296	0.307
	$v_{c2} = 0.11(f'_c)^{0.5}$ (ksi)	0.220	0.220	0.220
	$v_{c3} = 0.047\alpha'(f'_c)^{0.5}$ (ksi)	0.415	0.434	0.450
	$v_c = \min(v_{c1}, v_{c2}, v_{c3})$ (ksi)	0.220	0.220	0.220
	$V_{c\text{-}L} = v_c A_e$ (kips)	975	975	975

TABLE 8.28 Column Shear Demand/Capacity Ratio-$r_{v\text{-}T}$ and $r_{v\text{-}L}$

Location		Bent 2	Bent 3	Bent 4
Transverse	$V_{u\text{-}T}$ (kips)	958	909	846
	ϕ_s	0.90	0.90	0.90
	$V_{s\text{-}T}$ (kips)	1,471	1,471	1,471
	$V_{c\text{-}T}$ (kips)	932	878	820
	$V_{n\text{-}T} = \phi_s(V_{s\text{-}T} + V_{c\text{-}T})$ (kips)	2,163	2,113	2,061
	$r_{v\text{-}T} = V_{u\text{-}T}/V_{n\text{-}T}$	0.443	0.430	0.411
Longitudinal	$V_{u\text{-}L}$ (kips)	1,917	1,819	1,692
	ϕ_s	0.90	0.90	0.90
	$V_{s\text{-}L}$ (kips)	1,471	1,471	1,471
	$V_{c\text{-}L}$ (kips)	975	975	975
	$V_{n\text{-}L} = \phi_s(V_{s\text{-}L} + V_{c\text{-}L})$ (kips)	2,201	2,201	2,201
	$r_{v\text{-}L} = V_{u\text{-}L}/V_{n\text{-}L}$	0.871	0.826	0.769

TABLE 8.29 Force Demand on Top of Footing with Column Rebar #14 Total 48

	90	75	60	45	30	15	0
Force Demand	Deg.						
$M_{p\text{-}y}$ (k-ft)	26,485	25,582	22,937	18,728	13,242	6,855	0
$M_{p\text{-}x}$ (k-ft)	0	6,855	13,242	18,728	22,937	25,582	26,485
P (kips)	2,142	2,142	2,142	2,142	2,142	2,142	2,142
V_p (kips)	883	1,028	1,173	1,319	1,464	1,609	1,755

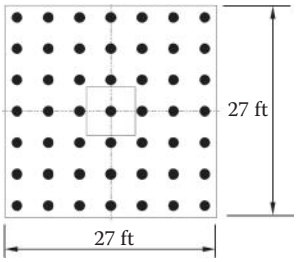

FIGURE 8.13 Footing size and pile layout—LRFD SBD.

For the example bridge at Bent 3 footing, the force demands from column plastic hinge are listed in Table 8.29 for the column with #14 total 48 longitudinal reinforcing bars.

Based on Equation 8.9, the footing design is performed and the required footing size and pile layout is shown in Figure 8.13. The required footing depth is 6.0 ft, and total 49 piles are needed to resist the column plastic hinge forces.

8.6 Summary

A bridge seismic design example is briefly presented in this chapter. Both current AASHTO Bridge Design Specifications (AASHTO, 2012) and Guide Specifications for LRFD Seismic Bridge Design (AASHTO, 2011) are used to design this bridge. The focus is on bridge column and foundation design. The design results indicate that under the same earthquake input, if the "Force-Based" design is adopted, the required column main bars are up to #14 total 92 with a steel ratio of 4.12% (over the up-limit of 4.0%); whereas the "Displacement-Based" design requires only #14 total 48 with a steel ratio of 2.15%. The reason leading to this significant different reinforcing is the "Response Modification Factor (R-Factor)." In "Force-Based" design, R-Factor is a constant, not related to seismic intensity or column ductility. For the example bridge, the input earthquake has a PGA of 0.7 g, and peak acceleration of 1.75 g. The column displacement ductility is over 4.0. The R-Factor is only 3.0 for this noncritical nonessential single-column bent bridge, although the bridge is located at Seismic Performance Zone 4. Since the foundation design is based on "Capacity-Design" principle, the "Force-Based" design requires 35 ft × 35 ft × 7 ft footing size with total 81 driving concrete piles (70-ton capacity); whereas the "Displacement-Based" design only requires 27 ft × 27 ft × 6 ft footing size and total 49 driving concrete piles. It may conclude that the "R-Factor" in "Force-Based" design needs to be further adjusted based on Seismic Performance Zone or column ductility, otherwise this method is too conservative for bridge seismic design in high intensity seismic region.

References

AASHTO. 2011. *ASHTO Guild Specifications for LRFD Seismic Bridge Design* (2nd Edition). American Association of State Highway and Transportation Officials, Washington DC.

AASHTO. 2012. *AASHTO LRFD Bridge Design Specifications*, Customary US Units, 2012. American Association of State Highway and Transportation Officials, Washington DC.

9

Seismic Design of Steel Bridges

Chia-Ming Uang
University of California at San Diego

Michel Bruneau
University at Buffalo

Keh-Chyuan Tsai
National Taiwan University

9.1 Introduction

AASHTO provides two publications for the seismic design of steel bridges: the LRFD Bridge Design Specifications (AASHTO, 2012) and the Guide Specifications for LRFD Seismic Bridge Design (AASHTO, 2011). The seismic provisions in the LRFD Bridge Design Specifications, hereafter referred to as the LRFD Specifications, are based on the recommended guidelines in the ATC-6 report published in 1981 (ATC, 1981). The ATC study was initiated by the aftermath of the 1971 San Fernando earthquake that caused significant damages to reinforced concrete bridges. Since bridge substructures are typically made of reinforced concrete in high seismic regions in North America, the LRFD Specifications have been mainly focused on reinforced concrete bridges and the coverage of steel bridges is limited.

Recent earthquakes have shown that steel bridges can be seismically vulnerable to damages. For example, extensive damage to steel bridges was reported after the 1995 Hyogoken-Nanbu Earthquake in Japan (e.g., Bruneau et al., 1996). In the United States, both the 1989 Loma Prieta and 1994 Northridge Earthquakes also revealed the vulnerability of slab-on-steel-girder bridge superstructures if they are not designed and detailed to resist the seismic motions (Robert, 1992; Astaneh-Asl et al., 1994; Bruneau et al., 1995; Itani et al., 2012). Lessons learned from these recent earthquakes resulted in a series of efforts to conduct research and to develop design guidelines for steel bridge structures. Such efforts not only resulted in new design provisions for slab-on-steel girder bridge superstructures in the 2012 edition of the LRFD Specifications, but also, more significantly, culminated in the publication of the Guide Specifications for LRFD Seismic Bridge Design, hereafter referred to as the Guide Specifications

(AASHTO, 2011); the first edition was published in 2009. This publication, which provides extensive coverage for seismic design of steel bridges, is the product of an effort made by the National Cooperative Highway Research Program (NCHRP) to combine its development (ATC and MCEER, 2003), Caltrans publications (ATC, 1996; Caltrans, 2001, 2006), and South Carolina's publication (South Carolina, 2001).

Seismic design provisions contained in the LRFD Specifications are based on *R* factor-based force design procedure. The Guide Specifications, however, are based on a displacement-based design procedure. But since this procedure is mainly developed for concrete structures, for structural steel design the Guide Specifications refer the designer to the *R* factor-based force design procedure in the LRFD Specifications. Therefore, in Section 9.3 of this chapter a brief presentation of the underlying concept for the force-based design procedure is presented first to introduce two important concepts: ductility design and capacity design.

This chapter focuses on concepts and detailing requirements that can help ensure a desirable ductile behavior for steel bridges. Other bridge vulnerabilities common to all types of bridges, such as bearing failure, span collapses because of insufficient seat-width or absence of seismic restrainers, soil liquefactions, and so on, are not addressed in this chapter.

9.2 Basic Seismic Design Philosophy

According to the LRFD Specifications (AASHTO, 2012), the fundamental principles for the development of seismic provisions for bridges are as follows:

1. Small to moderate earthquakes should be resisted within the elastic range of the structural components without significant damage.
2. Realistic seismic ground motion intensities and forces are used in the design procedures.
3. Exposure to shaking from large earthquakes should not cause collapse of all or part of the bridge. Where possible, damage that does occur should be readily detectable and accessible for inspection and repair.

The LRFD Specifications define the design earthquake as that having a 7% probability of exceedance in 75 years (i.e., a 1000-year return period). The Specifications target the so-called Life Safety performance objective, which implies that the bridge thus designed has a low probability of collapse but may suffer significant damage and that significant disruption to service is possible. For steel bridges, damage may include extensive yielding and local buckling of steel columns, buckling and rupture of braces, and so on.

Based on the importance of the bridge, the LRFD Specifications also define three operational categories: critical bridges, essential bridges, and others. Essential bridges and critical bridges are respectively defined as those that must, as a minimum, remain open to emergency vehicles and for security/defense purposes, and be open to all traffic, after the 1000-year return period earthquake. In the latter case, the AASHTO suggests that critical bridges should also remain open to emergency traffic after the 2500-year return period event. Various clauses in the specifications contribute to ensuring that these performance criteria are implicitly met, although these may require the engineer to exercise considerable judgment. The special requirements imposed on essential and critical bridges are beyond the scope of this chapter.

The seismic provisions contained in the AASHTO Specifications are applicable to conventional bridges that include those with slab, beam, box girder, or truss superstructures, and single- or multiple-column piers, wall-type piers, or pile-bent substructures.

9.3 Force-Based *R*-Factor Seismic Design Procedure

9.3.1 Response Modification Factor, *R*

Since bridges that are designed and detailed in accordance with the LRFD Specifications may suffer damage but should have low probability of collapse because of seismically induced ground shaking, bridges thus designed are not expected to remain elastic during a design earthquake for economical reasons.

Instead, the LRFD Specifications use a Response Modification Factor, R, to reduce the elastic seismic design forces for designing different parts of the bridge structure. The Specifications also assume that inelastic action (i.e., structural damage) is confined to the substructure only.

The origin of this force-based, R-factor design procedure can be traced back to the ATC 3-06 document (1978) for building design. Since the seismic design provisions in the LRFD Specifications for steel structure design are directly related to the R factor, it is worthwhile to examine the physical meaning of this R factor.

Figure 9.1 shows the typical response envelope of a structure. Based on the fundamental period of the structure, the designer first calculates the elastic design base shear, C_e (see point E in the figure). In LRFD Specifications, C_e is then reduced by a factor R to a design seismic force level C_s at point S.

$$C_s = \frac{C_e}{R} \tag{9.1}$$

Point S is the first significant yield point beyond which the structure will respond inelastically. In other words, under lateral loads, a structure designed based on this reduced seismic force level first responds elastically, followed by an inelastic response as the lateral forces are increased beyond that level. The redundancy that is built into the system together with the ductility allows a series of plastic hinges to form in the structure, leading to a yielding mechanism at the strength level C_y.

Idealizing the actual structural response curve by an elasto-perfectly plastic curve, the system ductility factor, μ_s, can be defined as

$$\mu_s = \frac{\Delta_u}{\Delta_y} \tag{9.2}$$

Then the system ductility reduction factor, $R\mu$, can be defined as

$$R_\mu = \frac{C_e}{C_y} \tag{9.3}$$

The R_μ factor accounts for the reduction of the seismic force level from C_e to C_y. Such a force reduction is possible because ductility, which is measured by the ductility factor μ ($= \Delta_u/\Delta_y$), is built into the structural system. The ductility capacity is achieved by meeting stringent ductility detailing requirements for structural components that are expected to yield during a design earthquake. For single-degree-of-freedom systems, relationships between μ and R_μ have been proposed (e.g., Newmark and Hall, 1982). The reserve strength that exists between the yield level (C_y) and the first significant yield level (C_s) is defined as the system overstrength factor, Ω:

$$\Omega = \frac{C_y}{C_s} \tag{9.4}$$

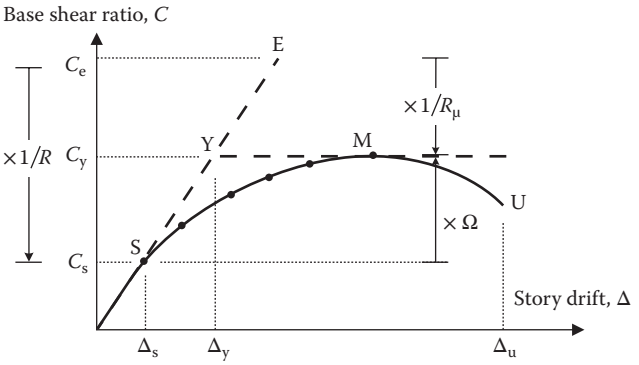

FIGURE 9.1 Concept of response modification factor, R.

This system reserve strength is contributed mainly by the redundancy (or internal force redistribution) of the structure. That is, once the first plastic hinge is formed at the force level C_s, the redundancy of the structure would allow more plastic hinges to form in other designated locations before the ultimate strength, C_y, is reached. Other factors that contribute to the system overstrength include code requirements for multiple loading combinations, code minimum requirements regarding proportioning and detailing, material strength higher than that specified in the design, strain hardening, member oversize, and so on.

Based on the definition of the above terms, the Response Modification Factor, R, for use with strength design can be derived as follows (Uang, 1991):

$$R = \frac{C_e}{C_s} = \frac{C_e}{C_y}\left(\frac{C_y}{C_s}\right) = R_\mu \Omega \tag{9.5}$$

The LRFD Specifications require that inelastic hinging occur in the substructure columns where they can be readily inspected and repaired. Table 9.1 shows the values of R assigned to different substructures. The table shows that the R value ranges from 3 to 5 for steel substructures. A multiple column bent with well detailed columns has a high value (= 5) of R because of its good ductility capacity and redundancy. A low R value (= 3) is assigned to single columns because of a lack of redundancy. (The Guide Specifications specify an R value of no larger than 4 for both single- and multiple-column bents.)

Although modern seismic codes for building and bridge designs both use the R-factor design procedure, there is one major difference. For building design (ASCE, 2010), the R factor is applied at the system level. That is, components designated to yield during the design earthquake share the same R value, and other components are proportioned by the capacity design procedure to ensure that these components remain in the elastic range. For bridge design, however, the R factor is applied at the component level. Therefore, different R values are specified to different parts of the same structure.

9.3.2 Ductility Design

Using an R factor larger than one implies that the ductility demand must be met by designing those structural components with detailing requirement to allow ductile response. The ductility capacity of a steel member is generally limited by the development of instability limit states. Considering an I-shaped flexural member for example, instability can be caused by one or more of the following three limit states: flange local buckling, web local buckling, and lateral-torsional buckling. The ductility capacity in each limit state is a function of the slenderness ratio, λ. For flange local buckling, λ is the flange width-thickness ratio ($b_f/2t_f$). Figure 9.2 shows the effect of λ on the strength and deformation capacity.

TABLE 9.1 Response Modification Factor, R, for Substructures

Substructure	R
Reinforced concrete pile bents	
• vertical piles only	3.0
• with batter piles	2.0
Single columns	3.0
Steel or composite steel and concrete pile bents	
• vertical piles only	5.0
• with batter piles	3.0
Multiple column bents	5.0

Source: Data from AASHTO, *LRFD Bridge Design Specifications,* American Association of State Highway and Transportation Officials, Washington, DC, 2012.

Note: For "Other" bridges; R values are lower for Critical and Essential bridges.

When the member's cross section is seismically compact (i.e., $\lambda \le \lambda_p$), the member can reach its plastic moment (M_p) capacity. More significantly, the member has high ductility (see Curve 1). Curve 3 represents the response of a member with a slender section. The member would buckle in the elastic range; both its strength and deformation capacity are inadequate for seismic design.

Note that repeated cyclic loading will also trigger buckling after a number of cycles of inelastic response, even though the width-thickness ratio is less than the λ_p limits specified in Table 9.4. Figure 9.3 compares the cyclic response of two such beams with different flange width-thickness ratios (Tsai and Popov, 1989). The strength of the beam having a larger width-thickness ratio degrades faster

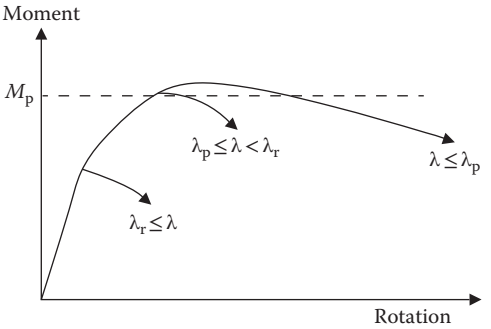

FIGURE 9.2 Effect of slenderness ratio on strength and deformation capacity of a flexural member. (Adapted from Yura, J. A. et al., *J. of Struct. Div.*, ASCE, 104(ST9), 1355–1370, 1978.)

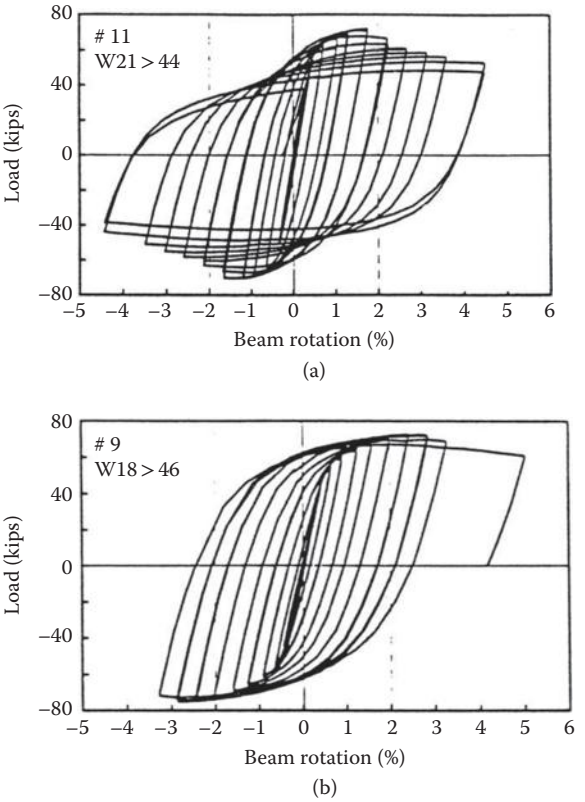

FIGURE 9.3 Effect of beam flange width–thickness ratio on strength degradation: (a) $b_f/2t_f = 7.2$; (b) $b_f/2t_f = 5.0$.

under cyclic loading as local buckling develops. This justifies the need for more stringent slenderness requirements in seismic design than those permitted for plastic design.

9.3.3 Capacity Design

In addition to ductility design, capacity design is another equally important concept for seismic design of structures. Recall that the LRFD Specifications require that inelastic action be confined to the substructure. For example, steel columns (or "deformation-controlled" elements) in a multiple column bent are to be designed for an R value of 5 with plastic hinges forming at the column ends. Thus, those components not participating as part of the primary energy-dissipating system should be "capacity protected." These components include the superstructure, joints and cap beam, spread footings, pile caps, and foundations. Two methods are provided in the LRFD Specifications to determine the seismic force demand of these "force-controlled" elements. The lesser of the force demand is then used for the design of these elements.

The first method is to use a reduced R value to determine the required seismic force. Table 9.2 shows that a value of R equal to 1.0 is to be used to design the connection between the column and cap beam or footing; an $R = 1.0$ means that the unreduced elastic earthquake load is to be used in capacity design. An even more conservative value (0.8) is to be used to design the connection between the abutment and superstructure.

The design seismic forces determined from the above method can be conservative. Recall from Figure 9.1 that the substructure (e.g., columns in a multiple-column bent) is designed for a high value of R (= 5). Once plastic hinges form at both ends of the columns, the ultimate strength of the bent at point M in Figure 9.1 can be easily established from a plastic analysis. For bridges in high seismic regions, the required seismic forces for the components that need to be capacity protected correspond to the maximum forces capable of being developed by plastic hinging of the columns. To demonstrate this concept, refer to the simple moment frame shown in Figure 9.4. Plastic hinges are expected to form at the column ends.

TABLE 9.2 Response Modification Factor, R, for Connections

Connection	R
Columns, piers, or pile bents to cap beam or superstructure	1.0
Columns or piers to foundations	1.0
Superstructure to abutment	0.8

Source: Data from AASHTO, *LRFD Bridge Design Specifications,* American Association of State Highway and Transportation Officials, Washington, DC, 2012.

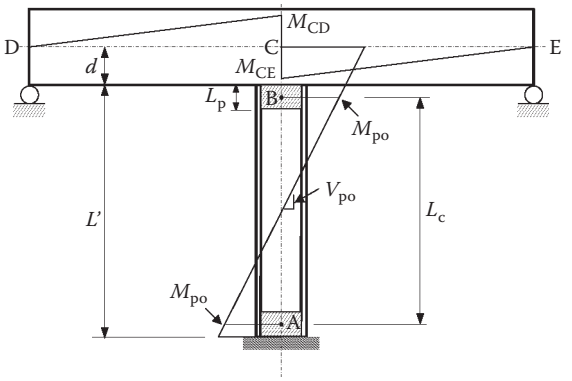

FIGURE 9.4 Capacity design using moment overstrength concept.

TABLE 9.3 Steel Grades and R_y Values

ASTM Designation	A709 Gr. 36[a]	A709 Gr. 50, 50W; A992	A500 Gr. B	A501	A53 Gr. B
Min. Yield Stress, F_y (ksi)	36	50	46	36	35
R_y	1.5	1.1	1.4	1.4	1.5

[a] For SDC B only, others for SDC C and D.

The corresponding seismic moment diagram is also shown. The plastic hinge length is designated as L_p. For design purposes, assume a point plastic hinge at the center of the plastic hinge length (points A and B in the figure). The expected maximum moment to be developed at the plastic hinge is defined as the overstrength moment capacity, M_{po}:

$$M_{po} = \lambda_{mo} M_n \tag{9.6}$$

In the above equation, λ_{mo} is the overstrength factor taken as 1.25 per the LRFD Specifications and 1.2 per the Guide Specifications to account for the effect of cyclic strain hardening. M_n is the nominal moment strength based on the expected yield stress, F_{ye}:

$$F_{ye} = R_y F_y \tag{9.7}$$

where R_y is the yield stress adjustment factor, and F_y the minimum specified yield stress.

Table 9.3 lists permissible AASHTO M270 (equivalent to ASTM A709) steel grades and their R_y values. These include grades with a minimum yield strength ranging from 36 to 100 ksi. These steels meet the AASHTO Standards for the mandatory notch toughness and weldability requirements and hence are prequalified for use in welded bridges. For ductile elements that are designed to yield, steels must be capable of developing a satisfactory hysteretic energy during earthquakes.

Once M_{po} is established at points A and B, the slope of the column moment diagram represents the overstrength column shear:

$$V_{po} = \frac{2M_{po}}{L_c} \tag{9.8}$$

Extrapolating the column moment diagram to the centroid of the cap beam (point C) gives the moment at that location:

$$M_c = V_{po}\left(\frac{L'}{2} + d\right) = M_{po} + V_{po}\left(\frac{L_p}{2} + d\right) \tag{9.9}$$

This moment is then distributed to the left and right sides of the cap beam based on their relative flexural stiffness.

9.4 AASHTO LRFD Specifications versus Guide Specifications

Both the LRFD Specifications and Guide Specifications use a 1000-year design earthquake to target the life safety performance objective for seismic design of conventional bridges, and both consider ductility and capacity design concepts. For seismic design, each bridge shall be assigned to one of the four seismic zones (1 to 4) in the LRFD Specifications; the seismic zone is established based on the horizontal response spectral acceleration coefficient (S_{D1}) at 1.0 second period of the bridge. The Guide Specifications rename these four seismic zones as Seismic Design Categories (SDC) A to D.

The LRFD Specifications specify that plastic hinges be formed only at locations in the substructure columns where they can be readily inspected and repaired. The 2012 edition of the LRFD Specifications provides additional requirements for slab-on-steel-girder bridges. This type of bridges shall be designed as either of the two types. In Type 1, design an elastic superstructure and a ductile substructure. Both the superstructure and substructure are to remain elastic and a fusing mechanism (e.g., base isolation or shearing off of anchor bolts) is provided at the interface in Type 2 design.

For higher seismic design categories (C and D), the Guide Specifications require that a clearly identifiable earthquake resisting system (ERS) be selected. A clear load path shall be provided and the bridge needs to be designed based on one of the three Global Seismic Design Strategies. Types 1 and 3 correspond to Types 1 and 2 in the LRFD Specifications, where the superstructure is to remain essentially elastic and the substructure can be designed to be either ductile or essentially elastic. A Type 2 ERS is created for steel superstructures. In this category, the substructure remains essentially elastic but the superstructure is ductile; the ductility is achieved by ductile elements in the pier cross-frames. Note that the Guide Specifications define "essentially elastic" as that when the force demand to the nominal capacity ratio of a member or connection is <1.5, where the nominal capacity is based on an expected yield stress, F_{ye}, and a resistance factor, ϕ, of 1.0.

The Guide Specifications provide a list of "permissible" ERSs and earthquake-resisting elements (EREs). For Type 1 bridges, the ductile steel substructure includes single columns, ductile moment-resisting frames, concrete-filled steel pipes, or ductile concentrically braced steel frames. For Type 2 bridges, ductile end diaphragms are permissible but require owner's approval for using it.

9.5 Type 1 Seismic Steel Substructures

9.5.1 General

The Guide Specifications provide information on the seismic design of Type 1 construction with essentially elastic superstructures and ductile substructures for SDC C and D. Both beams and columns are constructed of steel I-shaped sections with their webs in a common plane.

Columns are subjected to both axial load and moment and should be designed as a beam-column in accordance with the LRFD Specifications. These Specifications do not provide ductility requirements, but the Guide Specifications do. To control local buckling, see Table 9.4 for the limiting width-thickness ratios for both the ductile and essentially elastic components.

To control global buckling of ductile members, the Guide Specifications classify a column as either axial compression load dominant or flexural moment dominant. A column is flexural moment dominant when

$$\frac{P_u}{P_n} < \frac{M_u}{M_n} \tag{9.10}$$

where P_u and M_u are the factored axial load and moment acting on the column, whereas P_n and $M_n$are the nominal axial and flexural strengths based on the expected yield stress. In such case the member slenderness, λ_b, defined below cannot be larger than the limiting λ_{bp} value listed in Table 9.5.

$$\lambda_b = \frac{L}{r_y} \tag{9.11}$$

where L = unsupported length of the member, and r_y = radius of gyration about minor axis. Otherwise, the column is classified as axial load dominant and the member slenderness, λ_c, cannot exceed λ_{cp} listed in Table 9.5:

$$\lambda_c = \frac{KL}{r_y \pi}\sqrt{\frac{F_y}{E}} \tag{9.12}$$

TABLE 9.4 Limiting Width–Thickness Ratios for Local Buckling Control

Description of Element	Width-Thickness Ratio	Essentially Elastic (λ_r)	Ductile (λ_p)
Flange of I-shaped section in flexure	b/t	$0.56\sqrt{\frac{E}{F_y}}$	$0.30\sqrt{\frac{E}{F_y}}$
Web of I-shaped section in flexure or combined flexure and axial compression	h/t_w	$5.70\sqrt{\frac{E}{F_y}}\left(1-\frac{0.74P_u}{\phi_b P_y}\right)$	for $P_u \le 0.125\,\phi_b P_y$: $3.14\sqrt{\frac{E}{F_y}}\left(1-\frac{1.54P_u}{\phi_b P_y}\right)$ for $P_u > 0.125\,\phi_b P$: $1.12\sqrt{\frac{E}{F_y}}\left(2.33-\frac{P_u}{\phi_b P_y}\right) \ge 1.49\sqrt{\frac{E}{F_y}}$
Round HSS in axial compression or flexure	D/t	$\frac{0.09E}{F_y}$	$0.44\sqrt{\frac{kE}{F_y}}$
Rectangular HSS in axial compression and/or flexure compression	b/t	$1.40\sqrt{\frac{E}{F_y}}$	$0.64\sqrt{\frac{E}{F_y}}$

Note: $\phi_b = 0.9$.

TABLE 9.5 Limiting Slenderness Ratios for Lateral Buckling Control

	Essentially Elastic Member	Ductile Member
λ_{cp} when Axial Compression Load Dominant: $\frac{P_u}{P_n} \ge \frac{M_u}{M_n}$	1.50	0.75
λ_{bp} when Flexural Moment Dominant: $\frac{P_u}{P_n} < \frac{M_u}{M_n}$	$4.40\sqrt{\frac{E}{F_y}}$	$\frac{0.086E}{F_y}$

9.5.2 Ductile Moment-Resisting Frames

This category includes single-column structures, single-tier frame bents, or multitier frame bents. The prevailing philosophy in the seismic design of ductile frames in buildings is to force plastic hinging to occur in beams rather than in columns (i.e., a strong-column-weak-beam design) in order to better distribute hysteretic energy and inelastic deformations along the building height and to avoid soft-story type failure mechanisms (AISC, 2010b). This requires seismically compact sections with stringent lateral bracing for the beams. However, such a constraint is not realistic for steel bridges, nor is it generally desirable. Steel bridges frequently have deep beams that are not typically compact sections, and that are much stiffer flexurally than their supporting steel columns. Moreover, bridge structures in North America are generally "single-story" (single-tier) structures, and all the hysteretic energy dissipation is concentrated in this single story. With the exception of multitier frame bents, therefore, the strong-beam-weak-column design philosophy is adopted for bridge design. The beams, panel zones, and connections are capacity protected, that is, they need to be designed as essentially elastic elements.

9.5.2.1 Single-Column Bents

For single-column bents, a value R equal to 3.0 can be used (see Table 9.1). A plastic hinge is expected to form at the bottom end of the column. In addition to satisfying the slenderness requirements for both local buckling (Table 9.4) and member global buckling (Table 9.5), lateral support should also be

provided at the plastic hinge region. When lateral bracing is through the column flanges, each flange lateral support needs to be designed for a force equal 2% of the yield strength of one flange area. When it is not practical to provide lateral support, the column maximum slenderness, KL/r, shall be limited to 60, and transverse moments produced by the forces otherwise resisted by the lateral bracing shall be included in the seismic load combinations.

9.5.2.2 Single-Tier Ductile Moment Frames

For single-tier ductile moment frames, the Guide Specifications specify an R value of no > 4. (Note from Table 9.1 that a value of 5 for R can be used per the LRFD Specifications.) Plastic hinges are expected to form at both top and bottom ends of each column (see Figure 9.5). In the figure, the plastic hinge length (L_p) can be taken as the maximum of 1/8 of the clear height (L') of the steel column and 1.5 times the gross cross-sectional dimension in the direction of bending. The overstrength moment of the plastic hinge, M_{po}, is computed as shown in Equation 9.6. For an I-shaped column section bent about strong axis and with an axial load P_u, the reduced plastic moment capacity is

$$M_{nx} = 1.18 M_{px}\left(1 - \frac{P_u}{AF_{ye}}\right) \le M_{px} \tag{9.13}$$

where $M_{px} = Z_x F_{ye}$ and Z_x = plastic sectional modulus. The column needs to be designed as a beam-column. To ensure ductility, the Guide Specifications limit the factored axial compression because of seismic load and permanent loads to $0.2A_gF_y$.

To design the cap beam, first extrapolate the column seismic moment diagram to the centroid of the cap beam, where moments at points C and F in Figure 9.5 are established by using Equation 9.9. The moment and corresponding shear represent the effect of earthquake load, which needs to be combined with the gravity load effect for cap beam design.

Complete-joint-penetration groove welds shall be specified for the column-to-beam (or beam-to-column) connections. For building applications, AISC 341 allows limited yielding (AISC, 2010b). For bridge design, the Guide Specifications require the panel zone to remain essentially elastic. The required shear force in the panel zone is (see Figure 9.6)

$$V_{u(pz)} = P_f = \frac{M_{cf}}{d_c - t_{cf}} \tag{9.14}$$

where M_{cf} is the column moment at the beam face (see Figure 9.5), and P_f is the column flange force at the beam face. The design shear strength is

$$V_{n(pz)} = CV_p = C\left(0.58 R_y F_{yw} D t_w\right) \tag{9.15}$$

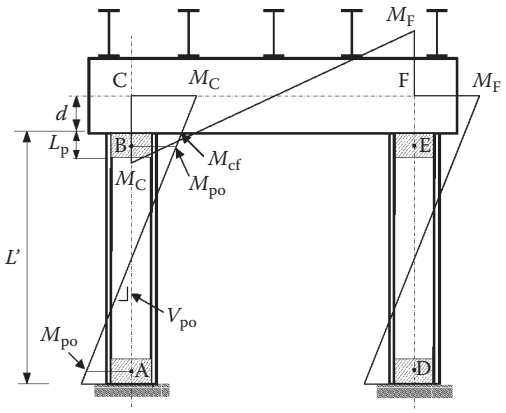

FIGURE 9.5 Internal forces for capacity design.

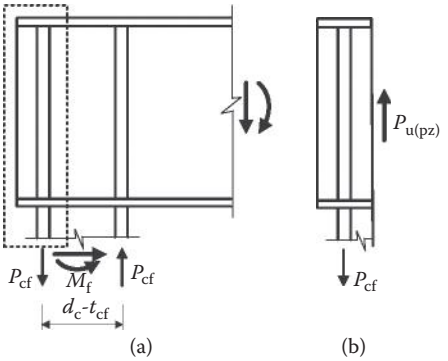

FIGURE 9.6 Column-to-beam panel zone shear force: (a) column-to-cap beam moment connection; (b) freebody for panel shear.

where C is the ratio of shear-buckling strength to the shear yield strength defined in the LRFD Specifications. Note that since the Guide Specifications define "essentially elastic" as that when the demand-capacity ratio is <1.5, where the capacity is calculated based on F_{ye}, it is expected that a panel zone thus designed may still experience limited yielding or buckling. It is prudent to keep the demand-capacity ratio below 1.0 if the design intent is to keep the panel zone to remain elastic.

When the panel zone design shear strength is insufficient, doubler plates that are attached to the panel zone by welding can be used for building applications (AISC, 2010b). For bridge applications, however, welding doubler plates to the beam web may cause fatigue problem. In such case, it is preferable to specify a thicker beam web to increase the panel zone shear strength. Continuity plates need to be provided on both sides of the panel zone. The combined width needs to be at least 0.8 times the column flange width. These continuity plates need to be designed as bearing stiffeners with a concentrated load of P_f calculated from Equation 9.14.

9.5.2.3 Column-to-Beam Connections

Widespread brittle fractures of welded moment connections in building moment frames that were observed following the 1994 Northridge, California Earthquake have raised great concerns. Shortly after the Northridge earthquake, the SAC Joint Venture initiated a comprehensive study of the seismic performance of steel moment frames. Funded by the Federal Emergency Management Agency (FEMA), SAC developed guidelines for structural engineers, building officials, and other interested parties for the evaluation, repair, modification, and design of welded steel moment frame structures in seismic regions (FEMA, 2000). Together with other research activities, moment connection types that have been prequalified for building construction can be found in AISC 358 (AISC, 2010a). AWS D1.8 (AWS, 2009) provides requirements for welding. Although bridge designers are encouraged to become familiar with these documents, it should be noted that these provisions and prequalified moment connections have been developed for building applications assuming plastic hinging in the beam and no axial force exists in the beam. Since plastic hinging is expected in the columns for bridge applications, the effect of axial load needs to be evaluated.

9.5.2.4 Multitier Ductile Moment Frames

For taller moment-resisting frames, adding intermediate beams that do not support gravity loads below the top beam can increase the lateral stiffness of the frame (see Figure 9.7). In such case, enforcing strong beam-weak column design may produce the "weak-story" failure mechanism in which all column plastic hinging occurs in one tier with greater local ductility demands. The global plastic mechanism shown in Figure 9.7 requires column plastic hinging at top and bottom ends only in addition to plastic hinging of intermediate beams at their ends. The capacity design principles mentioned earlier for

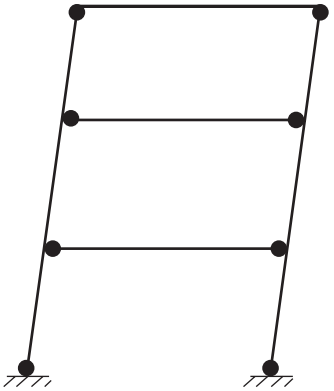

FIGURE 9.7 Acceptable plastic mechanism for multipier bent. (Adapted from AASHTO, Guide Specifications for LRFD Seismic Bridge Design, American Association of State Highway and Transportation Officials, Washington, DC, 2011.)

single-tier moment-resisting frames can be modified to achieve such design. For example, to ensure a strong-column-weak intermediate beam condition, the following needs to be satisfied at each column-intermediate beam connection (see Figure 9.7):

$$\sum M_{pc}^{*} = M_{pc(top)}^{*} + M_{pc(bottom)}^{*} \geq M_{pb}^{*} \tag{9.16}$$

M_{pb}^{*} represents the seismic moment demand of the intermediate beam imposed to the connection at column centerline. It can be computed by extrapolating the overstrength moment capacity of the intermediate beam to the column centerline. $M_{pc(top)}^{*}$ and $M_{pc(bottom)}^{*}$ are the column plastic moment capacities above and below the connection, which can be computed by using Equation 9.13.

9.5.3 Braced Frames

Compared to moment-resisting frames, braced frames have considerable lateral strength and stiffness. Depending on the geometry, a braced frame can be classified as either a concentrically braced frame (CBF) or an eccentrically braced frame (EBF). A CBF relies on tensile yielding and compression buckling of the diagonal braces to dissipate energy. A CBF is further divided into an Ordinary CBF (OCBF) or a Special CBF (SCBF), depending on whether stringent ductility and capacity requirements are met. Recently, a new type of braced frame called buckling-restrained braced frame (BRBF) has also been developed in which braces would not buckle globally (see Section 9.9.2). Alternatively, in an EBF, a short segment of the beam called link is designed to yield primarily in shear. For building design, the R values are provided in ASCE 7 (2010), and AISC 341 (2010b) provides detailed design procedures for all these braced systems. The background information on the development of the design provisions and design examples can be found in Bruneau et al. (2011).

9.5.3.1 Concentrically Braced Frames

In a CBF system, the working lines of members essentially meet at a common point (see Figure 9.8). Diagonal brace members in a CBF are expected to undergo large inelastic deformation during a severe earthquake. Properly proportioned and detailed brace members can sustain these inelastic deformations and dissipate hysteretic energy in a more stable manner through successive cycles of compression buckling and tension yielding. Columns and beams are capacity protected to remain essentially elastic, thus maintaining the gravity load-carrying capacity during a major earthquake. According to AISC 341 for building applications, a CBF can be designed as either a SCBF or an OCBF. SCBFs are

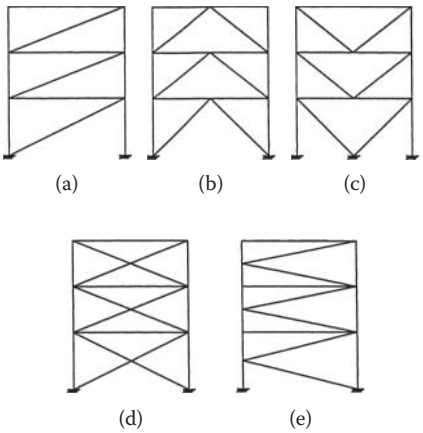

FIGURE 9.8 Typical concentric bracing configurations: (a) diagonal braced; (b) inverted V-braced; (c) V-braced; (d) X-braced; (e) K-braced.

expected to withstand significant inelastic deformations during a major earthquake. A large value of R (= 6) is assigned to the SCBF system, but more stringent ductility detailing requirements need to be satisfied. OCBFs are designed to higher levels of design seismic forces (R = 3¼) to minimize the extent of inelastic deformations; the use of it in high seismic regions is also restricted (ASCE, 2010). However, if an earthquake greater than that considered for design occurs, structures with SCBF could be greatly advantaged over the OCBF, in spite of the higher design force level considered in the latter case.

Although the Guide Specifications specify an R value of 4 for single- or multiple-column bents, no value is provided for a ductile CBF when it is used in Type 1 construction. According to the ATC-49 report (ATC and MCEER, 2003), which is the source document for the Guide Specifications, a value of 3 is specified for ductile CBFs.

9.5.3.1.1 Bracing Configuration

Braces designed to yield in tension and buckle in compression in a ductile CBF (or SCBF) are treated as permissible EREs per the Guide Specifications. CBFs exhibit the best seismic performance when both yielding in tension and inelastic buckling in compression of their diagonal members contribute significantly to the total hysteretic energy dissipation. To provide redundancy and to balance the tensile and compressive strengths in an SCBF system, AISC 341 requires that at least 30% but not more than 70% of the total seismic force be resisted by tension braces. This requirement will rule out the configuration shown in Figure 9.8a. But this redundancy requirement can be waived if the bracing members are substantially oversized to provide essentially elastic seismic response.

9.5.3.1.2 Bracing Members

Tests have shown that, after buckling, an axially loaded member rapidly loses compressive strength under repeated inelastic load reversals and does not return to its original straight position (see Figure 9.9). The energy absorption capability of a brace in compression depends on its member effective slenderness ratio (KL/r) and its resistance to local buckling. Since they are subjected to more stringent detailing requirements, The Guide Specifications limit KL/r to 120. A more stringent limit was specified in the past editions of AISC 341. But the latest edition (2010) relaxes the KL/r limit to 200 for braces in SCBF because slender braces designed for compression strength behave well because of the overstrength inherent in their tension capacity. Also, the postbuckling cyclic fracture life of bracing members generally increases with an increase in slenderness ratio. An upper limit (200) is provided to preclude dynamic effects associated with extremely slender braces.

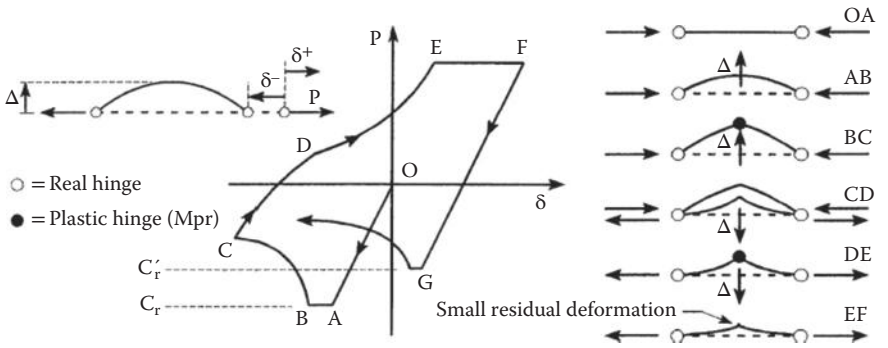

FIGURE 9.9 Cyclic response of a brace.

The plastic hinge that forms at midspan of a buckled brace may lead to severe local buckling. Large cyclic plastic strains that develop in the plastic hinge are likely to initiate fracture because of low-cycle fatigue. Therefore, the width-thickness ratio of stiffened or unstiffened elements of the brace section for SCBFs must be limited to the values of λ_p specified in Table 9.4. The limiting λ_r values can be used for brace sections of OCBFs. Taking the rectangular or square hollow structural section (HSS) for example, the Guide Specifications require that the *b/t* ratio be limited to $0.64\sqrt{E/F_y}$ and $1.40\sqrt{E/F_y}$ for SCBF and OCBF, respectively. AISC 341 sets the corresponding limits to $0.55\sqrt{E/F_y}$ and $0.64\sqrt{E/F_y}$ instead. Given that the limits in the Guide Specifications were taken from the Recommended LRFD Guidelines for the Seismic Design of Highway Bridges (ATC and MCEER, 2003), which reflected values implemented in earlier editions of the AISC Seismic Provisions, it is prudent to use the more conservative AISC limits for bridge design.

9.5.3.1.3 Bracing Connections

The gusset connection needs to be capacity protected. End connections of the brace can be designed as either rigid or pin connection. For either of the end connection type, test results showed that the hysteresis responses are similar for a given *KL/r* (Popov and Black, 1981). When the brace is pin-connected and the brace is designed to buckle out of plane, it is suggested that the brace be terminated on the gusset a minimum of two times the gusset thickness from a line about which the gusset plate can bend unrestrained by the column or beam joints (AISC, 2010b). This condition is illustrated in Figure 9.10. The gusset connection needs to be designed for the AISC expected bracing strength increased by 10%. The expected brace strength in tension is $1.1R_yF_yA_g$, and the expected brace strength in compression is

$$C = \min\left\{R_yF_yA_g,\ 1.14F_{cre}A_g\right\} \times 1.1 \tag{9.17}$$

where F_{cre} is the brace buckling stress based on F_{ye}. The Guide Specifications provide design requirements to check gusset connection on tensile rupture of the effective net section, block shear rupture, compression, and edge buckling. To ensure ductile failure mode, the only acceptable failure mode of gusset plates is yielding on the gross section.

The effect of end fixity should be considered in determining the critical buckling axis. For example, if rigid end conditions are used for in-plane buckling and pinned connections are used for out-of-plane buckling, a *K* value of 0.85 can be used for in-plane buckling. When analysis indicates that the brace will buckle in the plane of the braced frame, the design flexural strength of the connection should be equal to or >1.1 times the expected flexural strength ($= 1.1R_yF_yZ$) of the brace.

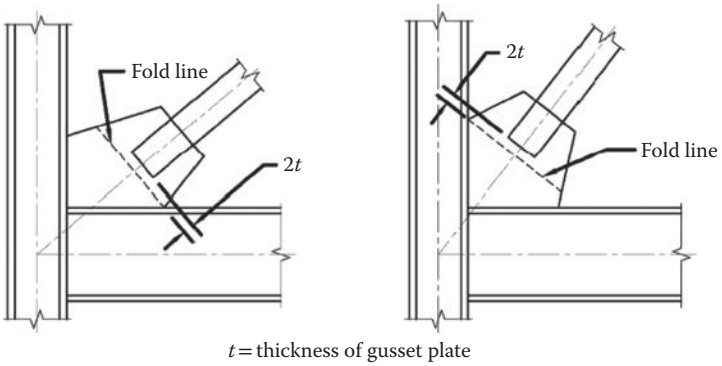

FIGURE 9.10 Plastic hinge and free length of gusset plate. (From ANSI/AISC 360-10. American Institute of Steel Construction, Chicago, Illinois, 2010. With permission.)

9.5.3.1.4 Beams and Columns

Based on the capacity design principle, columns in a CBF must be designed to remain essentially elastic when all braces have reached their expected tension or compression capacities. The Guide Specifications require that the limiting width-thickness ratios of these members satisfy the λ_r requirement in Table 9.4. For columns in an SCBF, however, it is prudent that λ_p be met, a requirement that is used in AISC 341.

9.5.3.1.5 Special Requirements for Brace Configuration

Because braces meet at the midspan of beams in V-type and Inverted-V-type braced frames (see Figure 9.8b and c), the vertical force resulting from the unequal compression and tension strengths of the braces can have a considerable impact on the cyclic behavior. Therefore, when this type of brace configuration is considered for SCBFs, AISC 341 requires that

1. A beam that is intersected by braces be continuous between columns.
2. A beam that is intersected by braces be designed to support the effects of all the prescribed tributary gravity loads assuming that the bracing is not present.
3. A beam that is intersected by braces be designed to resist the prescribed force effects incorporating an unbalanced vertical seismic force. This unbalanced seismic load shall be substituted for the seismic force effect in the load combinations, and is the maximum unbalanced vertical force applied to the beam by the braces. The force in tensile brace is assumed to have yielded and reached $R_y P_y$. To maximize the unbalanced vertical force, the brace in compression is assumed to have buckled and its strength has degraded to 0.3 $P_{n.}$
4. The top and bottom flanges of the beam at the point of intersection of braces shall be adequately braced.

Figure 9.8e features a K-braced frame with two braces intersect the column at mid-height. Once the compression brace buckles, the unbalanced horizontal force may jeopardize the gravity load carrying capacity of the column. Therefore, K-braced frames should not be used as an earthquake-resisting system (ERS).

9.5.3.2 Eccentrically Braced Frames

An EBF is a system of columns, beams, and braces in which at least one end of each bracing member connects to a beam at a short distance from its beam-to-column connection or from its adjacent beam-to-brace connection (see Figure 9.11). The short segment of the beam between the brace connection and the column or between brace connections is called the link. Links in a properly designed EBF system will yield primarily

in shear in a ductile manner (AISC, 2010b; Bruneau et al., 2011). Therefore, an EBF system possesses high stiffness in the elastic range and excellent ductility capacity in the inelastic range (Popov et al., 1989). The high elastic stiffness is provided by the braces and the high ductility capacity is achieved by transmitting one brace force to another brace or to a column through shear and bending in the link. Following the capacity design concept, buckling of braces and beams outside of the link can be prevented by designing these members to remain elastic, whereas resisting forces associated with the fully yielded and strain hardened links.

If the link is part of the cap beam for bridge applications, plastic hinging of the link would lead to vertical beam movement (see Figure 9.12). Therefore, the Guide Specifications do not recommend that EBF be used as an ERS for conventional bridges. When implemented in a way to avoid this problem, however, the EBF concept has been used for the seismic retrofit (Itani et al., 1998) and new construction (Nader et al., 2000; McDaniel et al., 2003; Buckle et al., 2005) of long-span bridges in the United States. Figure 9.13 shows one example, where built-up I-shaped links were used to connect four shafts of the tower in the Self-Anchored Suspension Span of the New San Francisco-Oakland Bay Bridge. The tow shear links are designed to satisfy the following criteria: (1) supply the tower with the required lateral stiffness for service load conditions, (2) remain almost elastic during a functional evaluation earthquake, (3) yield in shear during a safety evaluation earthquake, thus dissipating energy and limiting the damage in the tower shafts, and (4) facilitate replacement after a safety evaluation earthquake, if necessary, by using bolted connections between the links and shafts (Nader and Maroney, 2007).

All of the original research on EBF was conducted for building applications; the beams in such EBF applications were typically W-shapes, and lateral bracing had to be provided at the ends of the link to ensure their stability during large inelastic deformations (AISC, 2010b). However, for most bridge applications, EBFs would be used in locations where lateral bracing of the link cannot be achieved. In such cases, links with built-up box sections can be used, because such built-up box cross sections are not susceptible to lateral-torsional buckling. EBFs having such links and without lateral bracing of the link beams perform in a ductile manner, provided the specified section compactness requirements are met (Berman and Bruneau, 2007, 2008a, 2008b). Note that HSS sections cannot be used for such links because

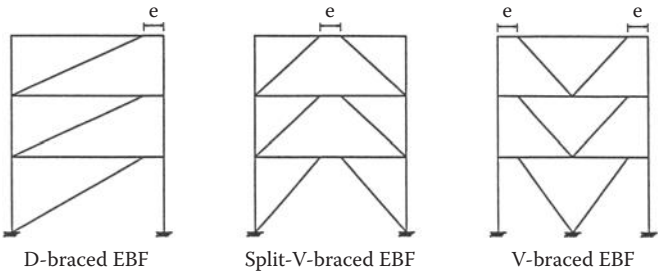

FIGURE 9.11 Typical eccentric bracing configurations.

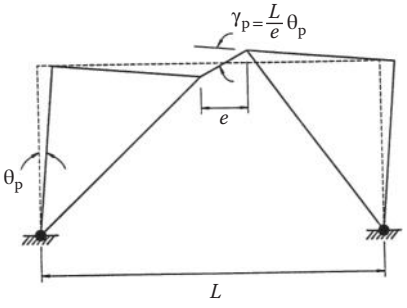

FIGURE 9.12 Yielding mechanism of an eccentric braced frame.

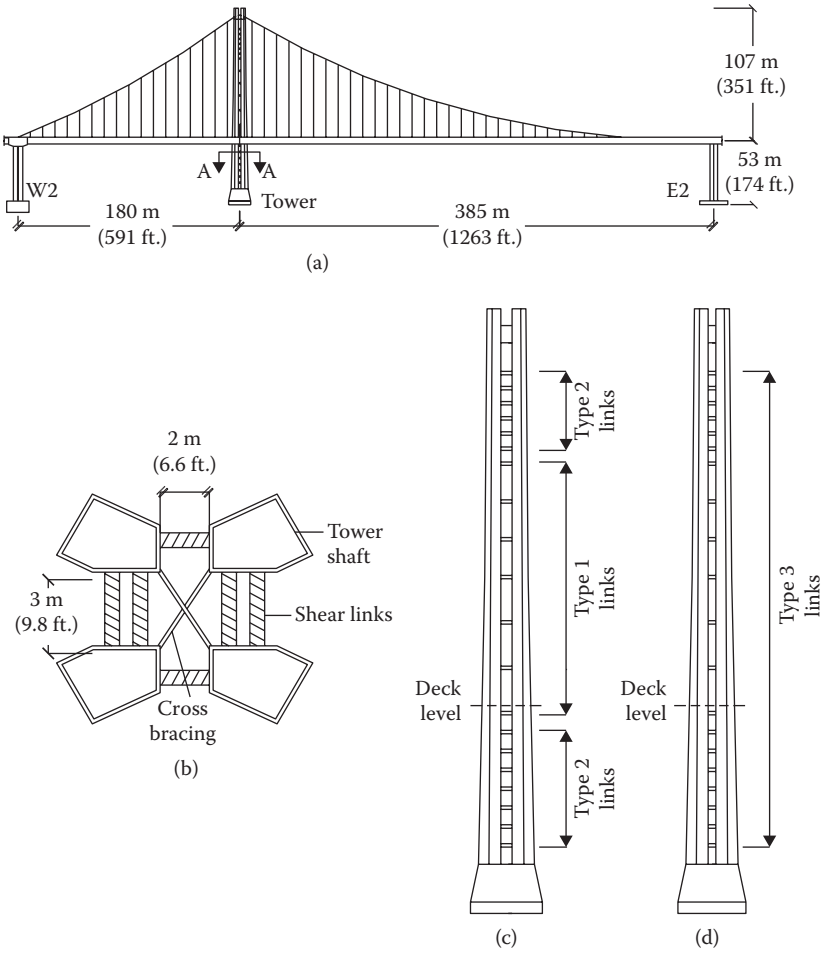

FIGURE 9.13 The new San Francisco-Oakland Bay Bridge self-anchored suspension span.

of concerns about their low cycle fatigue life under large inelastic deformations (see Bruneau et al., 2011). Also note that extremely tall and narrow boxes may not be adequate, as they can experience lateral-torsional buckling (i.e., buckle about their weak axis); to prevent this undesirable behavior, links of built-up box sections should be sized such that $I_y > 0.67I_x$, where I_y, is the link's moment of inertia about an axis in the plane of the EBF, and I_x is the moment of inertia about an axis perpendicular to that plane.

External intermediate stiffeners, as in Figure 9.14, were considered in the experimental and analytical work of Berman and Bruneau (2006; 2008a; 2008b); these were welded to both the webs and the flanges. However, because such stiffeners have no benefit on flange buckling, AISC 341 and CSA S16 do not require them to be connected to the flange. This suggests that intermediate stiffeners could be fabricated inside the built-up box section (which may be desirable for architectural appeal or other reasons). EBF having built-up box links have been used for the towers of the temporary structure designed to support and provide seismic resistance to the deck of the self-anchored suspension segment of the East Span of the San-Francisco-Oakland Bay Bridge during its construction (see Figure 9.15).

AASHTO does not provide design provisions for EBFs. The designer can refer to AISC 341 instead, which includes the design requirements for sizing links, placing of intermediate stiffeners, lateral bracing for I-shaped links, link deformation check, and capacity design to ensure that other parts of the structure remains elastic.

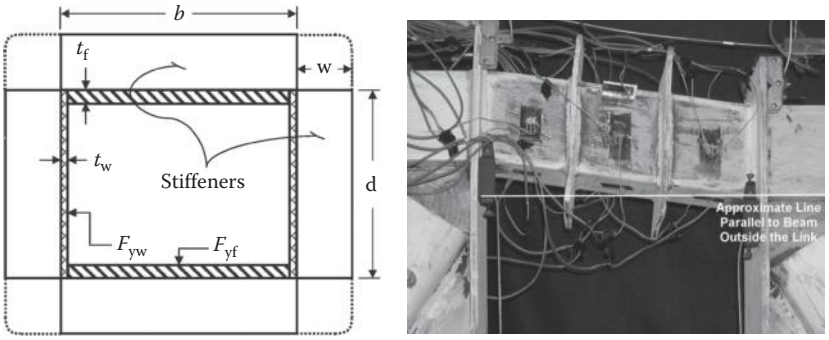

FIGURE 9.14 (a) Generic built-up box cross section with exterior stiffeners; (b) deformed link at 0.123 rads rotation (From Berman, J. and Bruneau, M., *Technical Report MCEER-05-0004*, Multidisciplinary Center for Earthquake Engineering Research, State University of New York at Buffalo, NY, 2005, courtesy of MCEER, University at Buffalo.)

FIGURE 9.15 EBF tower for temporary support structure of new self-anchored suspension Bay Bridge. (Courtesy of Klohn Crippen Berger.)

9.6 Type 2 Seismic Steel Structures: Slab-on-Steel-Girder Bridge Superstructures

9.6.1 Load Path

For years steel girder bridges were generally considered to perform well in earthquakes and, thus, seismic codes did not require explicit design of bridge superstructures. This was based on the assumption that the superstructure needs to be designed for gravity load, which, by default, should provide sufficient lateral strength. Recent earthquakes, however, showed the vulnerability of this type of bridges if a seismic load path is not clearly provided, analyzed, and designed (Itani et al. 2012). Typical damages included unseated longitudinal girders, and failure of composite slab shear connectors, end cross-frames and their connections, bearings, and so on (Robert, 1992; Astaneh-Asl et al. 1994; Bruneau et al. 1995).

To provide a load path, the inertia force from the deck needs to be transferred to the support cross-frames; shear connectors are typically needed for this purpose. Failure of shear connectors at these most critical locations will cause the deck to slip on the top flange of the girder, and thus, alter the load path.

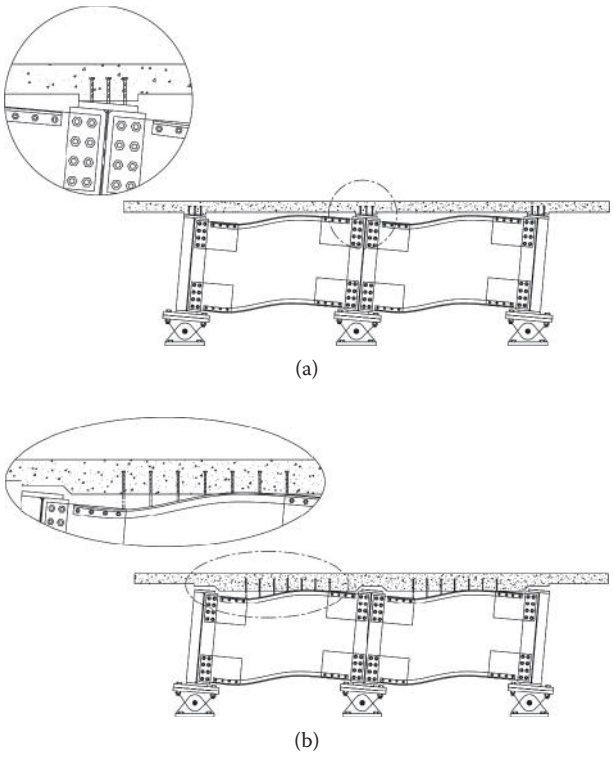

FIGURE 9.16 Kinematics of a support cross-frame showing shear connectors in combined tension and shear: (a) shear connectors on girder top flanges; (b) shear connectors on top chords. (From Itani, A. M. et al., Paper T155-3, Structural Engineering World Wide, 2010. With permission.)

Figure 9.16 shows the kinematics of a support cross-frame with shear connectors on the girder top flange or top chord. It shows that the connectors are subjected to combined axial and shear forces. The LRFD Specifications provide design equations for headed shear connector subjected to both shear and axial force. Once sufficient shear connectors are provided to transfer the slab inertia force, the seismic force has to be transferred through the end diaphragms to the supports. Since end diaphragms serve as part of the load path, two design approaches result: design end diaphragms to either remain elastic or serve as the ductile ERSs to dissipate energy. The LRFD Specifications require that the superstructure remain elastic. Therefore, the support cross-frames also need to be designed to remain elastic.

9.6.2 Type 2 Earthquake-Resisting System

An alternate design approach is provided in the Guide Specifications. Recognizing that end diaphragms are key links along the load path, it may be possible, in some cases, to prevent damage from developing in the nonductile substructure (i.e., piers, foundation, and bearings) by replacing the steel diaphragms over abutments and piers with specially designed ductile diaphragms calibrated to yield before the strength of the substructure is reached (Sarraf and Bruneau, 1998a). This objective is schematically illustrated in Figure 9.17 for slab-on-girder bridges and in Figure 9.18 for deck-truss bridges. In the latter case, however, ductile diaphragms must be inserted in the last lower lateral panels before the supports in addition to the end-diaphragms. In deck-truss bridges, seismically induced inertia forces in the transverse direction at deck level act with a sizable eccentricity with respect to the truss reaction supports, and the entire superstructure (top and lower lateral bracings, end and interior cross-frames bracings, and other lateral-load resisting components) are mobilized to transfer these forces from deck to supports.

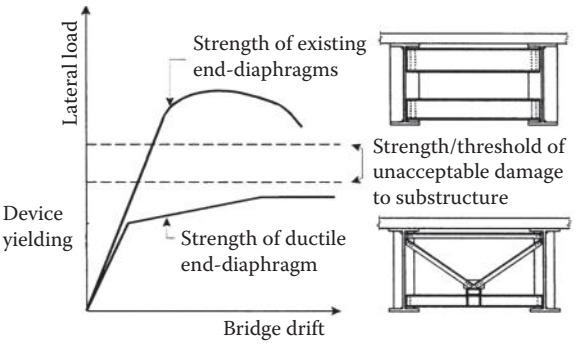

FIGURE 9.17 Schematic illustration of the ductile end-diaphragm concept.

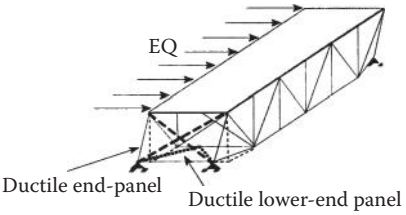

FIGURE 9.18 Ductile diaphragm retrofit concept in a deck-truss.

The ductile end-diaphragm concept has been substantially validated experimentally (Zahrai and Bruneau, 1999a, 1999b; Sarraf and Bruneau, 2002; Carden et al., 2006a, 2006b), and has been included in the Guide Specifications. The response modification factor, R, to be considered in design of the ductile end-diaphragm is given by

$$R = \left(\frac{\mu + \dfrac{K_{DED}}{K_{SUB}}}{1 + \dfrac{K_{DED}}{K_{SUB}}} \right) \leq 4 \tag{9.18}$$

where μ = displacement ductility capacity of the end diaphragm (≤ 4), K_{DED} = stiffness of ductile end diaphragm, and K_{SUB} = stiffness of superstructure.

Although conceptually simple, the implementation of ductile diaphragms in existing bridges requires consideration of many strength, stiffness, and drift constraints germane to the type of steel bridge investigated. For example, for slab-on-girder bridges, because girders with bearing stiffeners at the supports can contribute nonnegligibly to the lateral strength of the bridges, stiff ductile diaphragms are preferred. Tests (Zahrai and Bruneau, 1999b) confirmed that stiff welded ductile diaphragms are indeed more effective than bolted alternatives. Substructure-to-superstructure relative stiffness is also important to ensure a satisfactory implementation (Alfawakhiri and Bruneau, 2000, 2001). As for deck-trusses, both upper and lower limits are imposed on the ductile diaphragm stiffness to satisfy maximum drifts and ductility requirements, and a systematic solution strategy is often necessary to achieve an acceptable retrofit (Sarraf and Bruneau, 1998a, 1998b).

Several types of systems capable of stable passive seismic energy dissipation could serve as ductile diaphragms. For example, special concentrically braced frame (SCBF), EBF, and BRBF can be used; design provisions in AISC 341 can be used for this purpose. In addition, shear panel systems (SPS) (Fehling et al., 1992; Nakashima, 1995) and steel triangular-plate added damping and stiffness devices (TADAS) (Tsai et al., 1993) have also received a particular attention. Examples of how these systems would be implemented in the end-diaphragms of a typical 40 m span slab-on-girder bridge are shown in Figure 9.19. Similar conceptual implementations in deck-trusses are shown in Figure 9.20. Kanaji et al. (2005) have used buckling restrained braces to create a ductile cross-frame system as part of the seismic retrofit of the third-longest cantilever truss span in the world, located in Osaka in Japan.

Celik and Bruneau (2009, 2011) expanded the ductile diaphragm concept to make it dissipate hysteretic energy under both transverse and longitudinal seismic excitations. This has been achieved using the buckling restrained braces layout schematically illustrated in Figure 9.21.

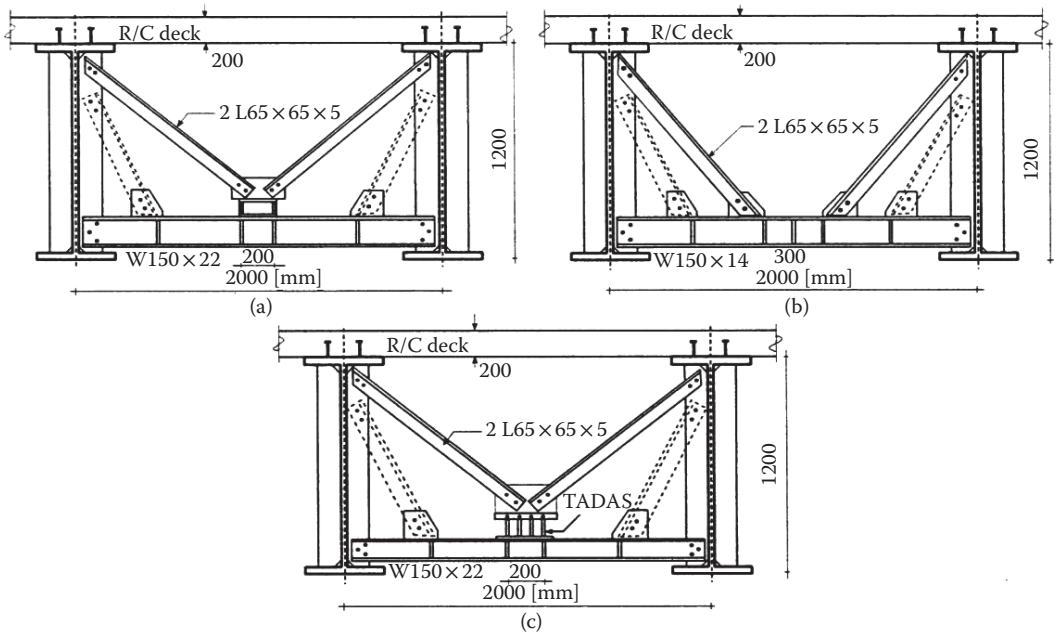

FIGURE 9.19 Ductile end diaphragm in a typical 40 m-span bridge (a) SPS; (b) EBF; (c) TADAS. (Other unbraced girders not shown; dotted members only if required for jacking purposes for nonseismic reasons).

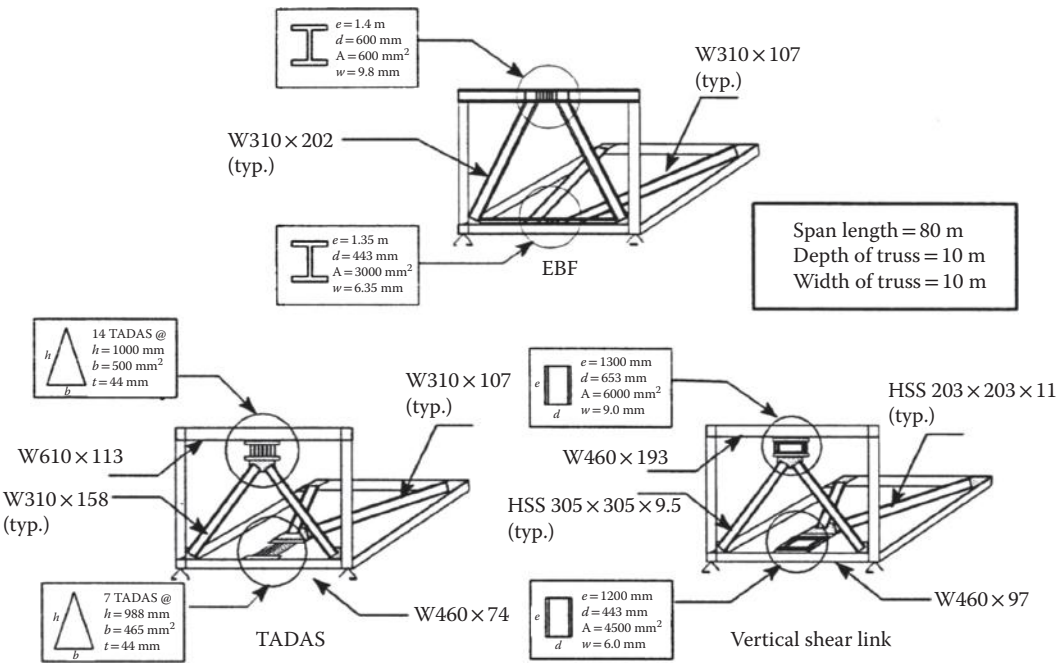

FIGURE 9.20 Examples of ductile retrofit systems at span end of deck-trusses.

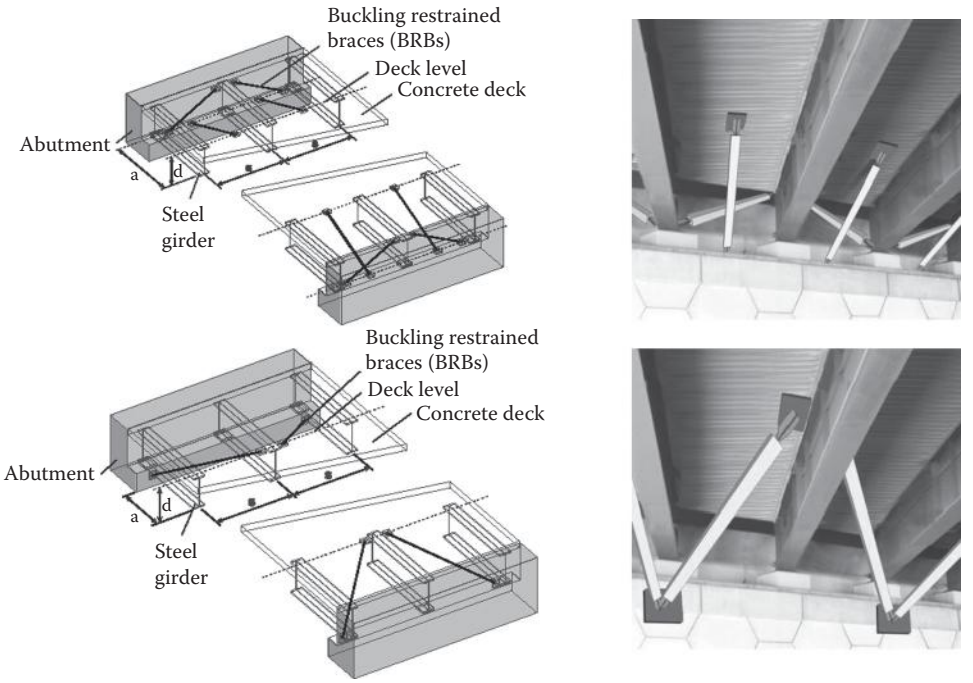

FIGURE 9.21 Ductile end diaphragms alternatives using BRBs. (From Celik, O.C. and Bruneau, M., *Technical Report MCEER-07-0003*, MCEER, University at Buffalo, Buffalo, NY, 2007, courtesy of MCEER, University at Buffalo.)

9.7 Stiffened Steel Box Pier Design

When space limitations dictate the use of smaller-size bridge piers, steel box or circular sections gain an advantage over the reinforced concrete alternative. For circular or unstiffened box sections, the ductile detailing provisions of AISC 341 (2010b) or CHBDC (2009) shall apply, including the diameter-to-thickness or width-to-thickness limits. For box column of large dimensions, however, it is also possible to stiffen the wall plates by adding longitudinal and transverse stiffeners inside the section.

Design provisions for stiffened box column are not covered in either the AASHTO or AISC design specifications. But the design and construction of this type of bridge piers has been common in Japan for more than 30 years (see Chapter 12 for details).

9.8 Concrete Filled Steel Tube Piers

Concrete-filled steel columns have been used in buildings (e.g., Bauer, 1988; Taranath, 1988; Webb and Peyton, 1990; Viest et al., 1997; Seilie and Hooper, 2005; Leon and Lange, 2006), and earlier in nonbuilding applications, as pylons for hydroelectric lines in Switzerland (Vogeli, 1950), as concrete-filled steel piers in bridges (see Kerensky and Dallard, 1968 for early example) and as piles in many applications (Gerwick, 1995). Concrete-filled composite columns offer the following advantages:

1. The steel can provide some confinement of the concrete and permit development of the full composite capacity, with stable inelastic behavior and energy dissipation.
2. All the concrete in the member can contribute to strength and ductility of the member as concrete breaching and spalling does not occur.
3. The steel shell can act as formwork for the concrete.
4. Construction may be accelerated if the steel shell alone can provide resistance to dead load.
5. The steel components can be fabricated off-site in a controlled environment.

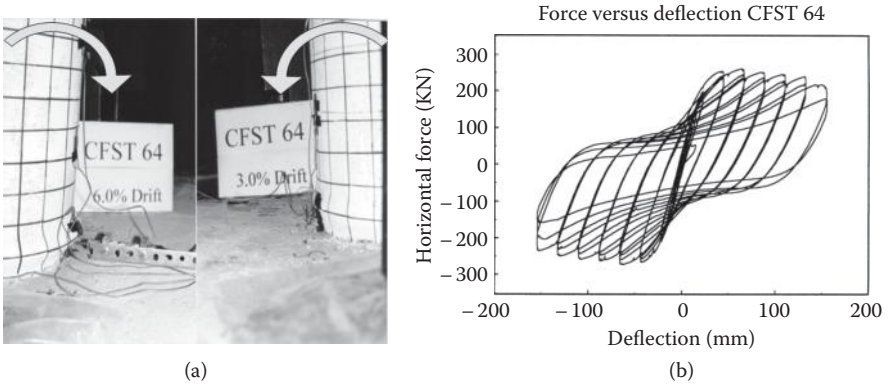

FIGURE 9.22 Cyclic inelastic response of concrete-filled steel tubes. (From Marson, J. and Bruneau, M., *Ottawa Carleton Earthquake Engineering Research Centre Report OCEERC 00-22,* Ottawa, Ontario, Canada, December, 398, 2000.)

6. The concrete core delays local buckling of the steel shell, and prevents its inward buckling, also enhancing ductility.
7. Reinforcing bars in the type of applications considered here are unnecessary in the concrete.
8. The final aesthetics are architecturally pleasing.

Within some detailing constraints, concrete-filled members can also exhibit satisfactory seismic performance (Hajjar, 2000; Tort and Hajjar, 2004; Marson and Bruneau, 2004). Typical cyclic inelastic behavior is shown in Figure 9.22, which demonstrates ductile behavior, with some strength and stiffness degradation because of local buckling upon repeated cycling, as exhibited by pinching of the hysteretic curves. Local buckling can be controlled by limits on the tube diameter-thickness ratio (D/t). For seismic applications, design equations in the AASHTO LRFD Specifications and the CSA Standard for the Design of Steel Structures (CSA, 2009) were developed by Bruneau and Marson (2004). Their derivation is also presented in Bruneau et al. (2011). Also note that an additional advantage of concrete-filled tubes is their superior blast resistance, which makes them attractive from a multihazard design perspective (Fujikura et al., 2008, Fouche and Bruneau, 2010).

It has been demonstrated that the design strengths of concrete-filled tube provided in the LRFD Specifications are conservative. Although this is acceptable for nonseismic applications, it is not if concrete-filled tube is used as the ductile substructure. Therefore, the Guide Specifications use the Bruneau and Marson (2004) equations that more realistically predict the plastic moment of such columns for capacity design.

9.9 Alternative Schemes

9.9.1 Introduction

Beyond the approaches and procedures provided in design specifications, a number of alternative schemes and strategies have been considered by engineers to achieve satisfactory seismic performance, either for new bridges or as part of retrofit strategies. Some of these ideas are summarized in this section.

9.9.2 Buckling-Restrained Braces

CBFs presented in Section 9.5.3.1 are widely used for building construction. This type of framing system has high lateral stiffness. Figure 9.9 shows the typical cyclic response of a conventional brace. For seismic applications, however, diagonal braces are expected to buckle in compression and yield in tension.

Because a plastic hinge will form at the midspan of the brace, high curvature demand under cyclic loading also has a tendency to rupture the brace. The hysteresis loop is severely pinched because of global buckling, and the energy dissipation is limited. Note that the compressive strength is less than that in tension.

To provide a more reliable source of energy dissipation, the concept of Buckling-Restrained Brace (BRB) was first developed in Japan in the early 1970s. Extensive research was since conducted in Japan and a variety of BRBs have been developed. But it was not until after the Kobe Earthquake in 1995 that Japanese designers started to incorporate BRBs in the so-called "damage-tolerant" seismic design of multistory buildings (Wada et al., 2004). But the design practice in Japan has been to treat BRBs as hysteretic dampers and dynamic analysis is needed. See Uang and Nakashima (2004) and Xie (2005) for the development of BRBs.

The BRB concept was introduced to North America after the Northridge Earthquake in 1994. Nippon Steel first marketed its BRBs as the "Unbonded Brace." In the meantime, the engineering community in California led an effort to develop an *R*-factor-based equivalent lateral force design procedure such that, in design, BRBs can be treated as conventional members in a static analysis (Sabelli and Lopez, 2004). This development was very significant in that it simplified the design process and allowed BRB frames to be codified and gain wide acceptance by the design profession in a short time. BRBs have been used for both new construction and seismic retrofit of existing buildings (Tajirian et al., 2003).

BRBs are conceived to avoid global buckling of the brace such that a full and stable hysteresis loop can be developed to dissipate energy (see Figure 9.23). A variety of BRBs have been developed, but their concept is similar. Figure 9.24 demonstrates an example of this concept. In this example, a yielding steel core, usually of lower strength steel and high ductility, is encased in a steel tube with mortar infill. Unlike a steel-concrete composite member, however, some unbonding materials or an air gap is provided to isolate the yielding steel core and the surrounding buckling-restraining mechanism to prevent composite action. The ends of the yielding steel core are strengthened for connection to the other part of the structure (see Figure 9.25). In selecting and designing the unbonding mechanism, the Poisson effect of the yielding steel core under compression needs to be properly considered. Although a properly designed BRB will not buckle globally, steel core do experience higher-mode buckling (or "micro-buckling"). The buckled steel core would then be in touch with the buckling-restraining mechanism and some compressive load would be transferred

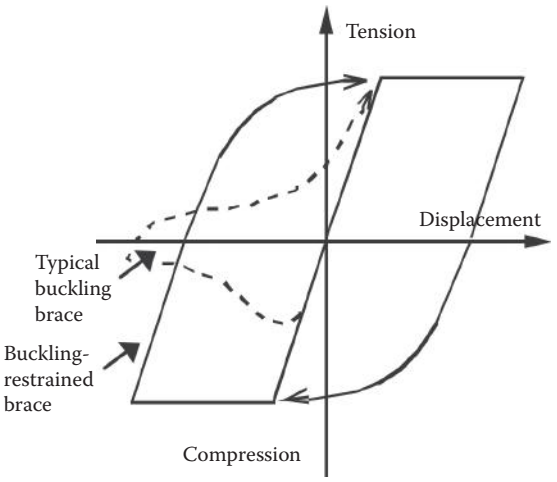

FIGURE 9.23 Behavior of conventional brace versus buckling-restrained brace. (From Clark, P. et al., *Proceedings of 69th Annual Convention, SEAOC,* Sacramento, CA, 1999. With permission.)

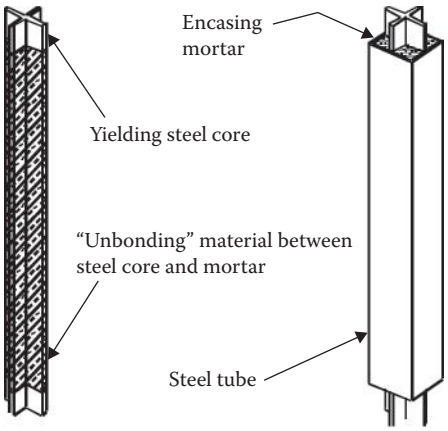

FIGURE 9.24 Concept of a type of buckling-restrained brace. (From Clark, P. et al., *Proceedings of 69th Annual Convention, SEAOC,* Sacramento, CA, 1999. With permission.)

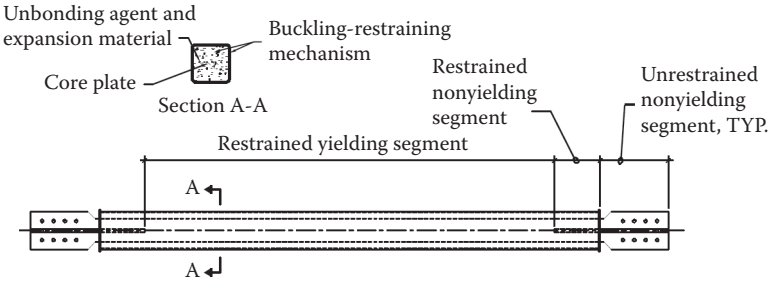

FIGURE 9.25 Components of buckling-restrained brace. (From Wada, A. et al., *Development of Unbonded Brace,* Nippon Steel Corporation Building Construction and Urban Development Division, Tokyo, Japan, 1998. With permission.)

and resisted by the latter. Therefore, the maximum compressive load developed in a BRB is generally higher than the maximum tensile load under cyclic loading. This increased compressive load needs to be considered in capacity design of surrounding gusset connections and framing members.

Figure 9.26 shows some BRB cross sections that have been proposed. Cases a through d use mortar or concrete as part of the buckling-restraining mechanism. Case a is the most popular section; the flat steel bar can be replaced by a cruciform section like that shown in Figure 9.24 if a high capacity is needed. Cases e through h are the so-called "steel-only" BRBs as mortar or concrete is not used. In all cases, the buckling-restraining mechanism needs to be properly designed such that global buckling of the brace is avoided (Matsui et al., 2009). The BRB end connections can be either bolted or true pin. Gusset connection also needs to be properly designed to avoid buckling. A typical hysteresis response of the BRB is shown in Figure 9.27.

Damage control design using BRBs has been extended to two long-span bridges in Japan after the Kobe Earthquake, one for seismic retrofit and one for new construction. For bridge application, the following are the desirable characteristics of the BRB (Usami et al., 2005):

1. Stable hysteretic response and high energy dissipation capacity
2. Large deformation capacity
3. High low-cycle fatigue strength

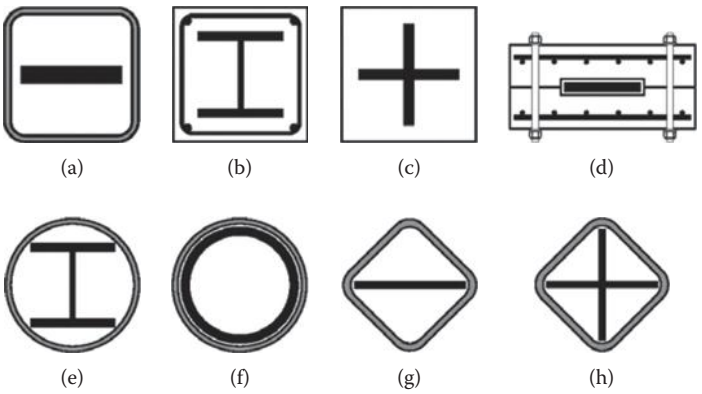

FIGURE 9.26 Cross sections of various buckling-restrained braces. (From Wada, A. et al., *Development of Unbonded Brace,* Nippon Steel Corporation Building Construction and Urban Development Division, Tokyo, Japan, 1998. With permission.)

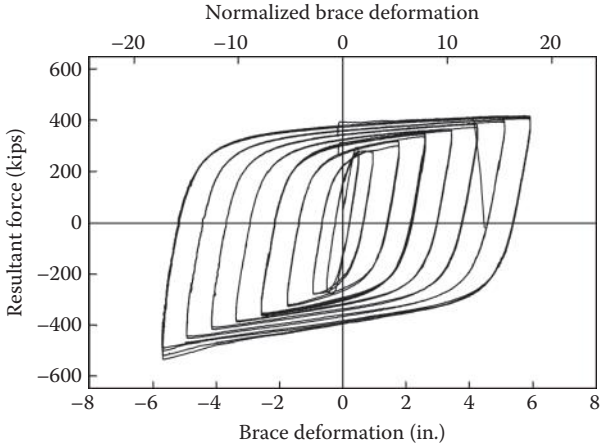

FIGURE 9.27 Typical BRB cyclic response.

4. High durability, including climate resistance
5. Low cost in fabrication and construction
6. Ease of replacement

The Minato Bridge, which was constructed in 1974 and experienced some damage in the 1995 Kobe Earthquake, is a 980 m long cantilever truss bridge (see Figure 9.28). Seismic retrofit of this bridge, completed in 2007, included the introduction of a sliding base isolation underneath the bridge deck and replacing some existing truss members by BRBs. The selection of the BRB locations was based on the high strain energy ratios of the truss members as identified from modal analysis (Kanaji et al., 2006). BRBs that are appropriate for building applications needed to be modified to make them lighter and suitable for connecting to the existing gussets. Figure 9.29 shows that each diagonal brace in the tower is composed of two parallel "steel-only" BRBs with low yield core steel (F_y = 33 ksi); the cross section of the steel core is in a cruciform shape (see Figure 9.30). Reduced-scale BRB testing was conducted to verify the performance. It was reported that the BRBs had excellent low-cycle fatigue strength, and that the equivalent viscous damping ratio exceeded 30%.

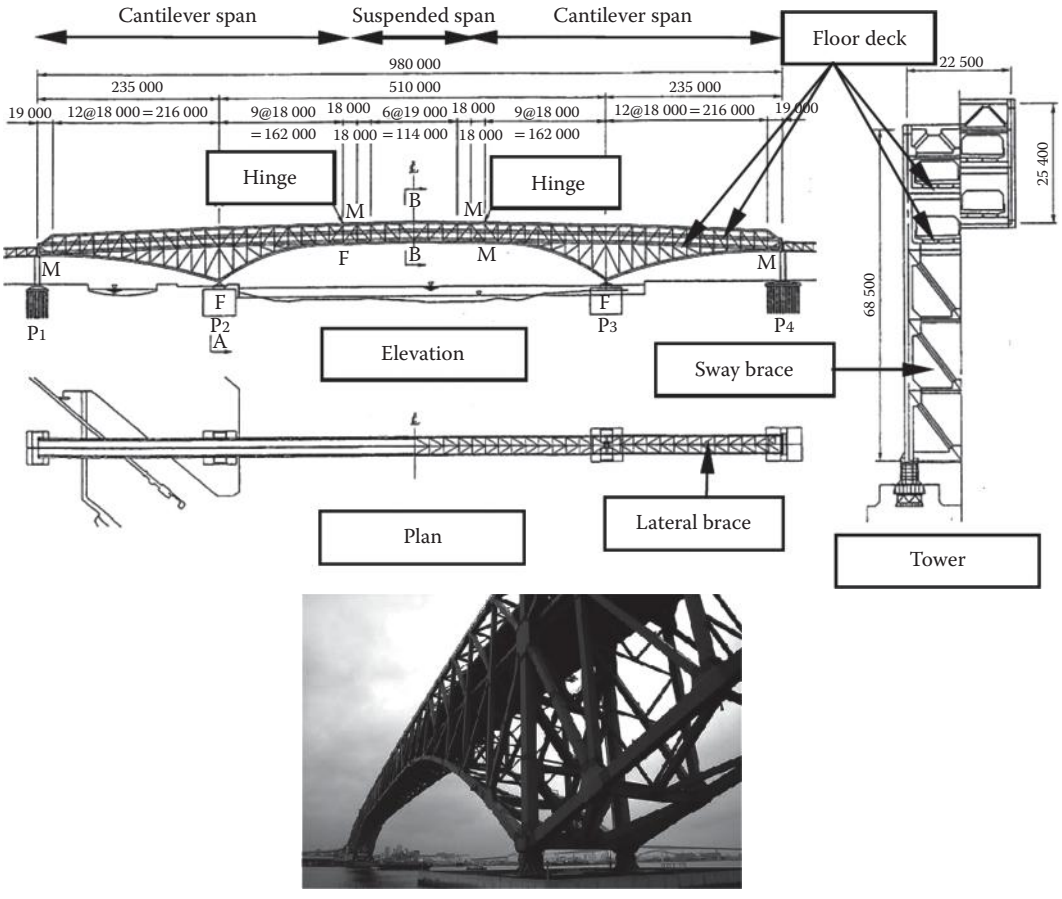

FIGURE 9.28 Minato Bridge retrofitted with BRBs. (Courtesy of H.B. Ge, Meijo University.)

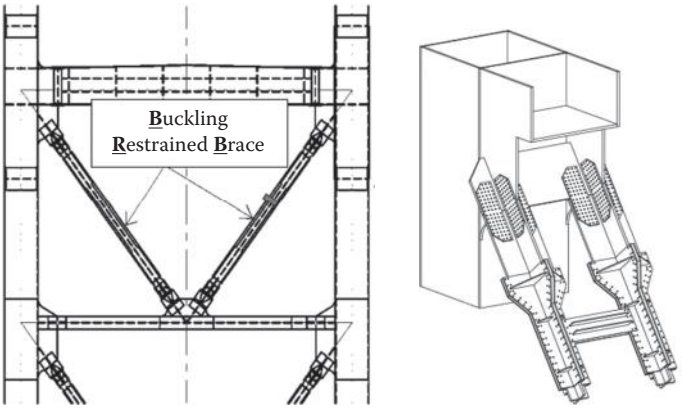

FIGURE 9.29 Steel-only BRBs in Minato Bridge towers. (a) Tower BRBs; (b) Brace end connections. (Courtesy of H.B. Ge, Meijo University.)

The Owatari Bridge was the first new bridge in Japan that used BRBs to enhance its seismic performance; the bridge was constructed in 2004 (see Figure 9.31). BRBs were placed in the piers, main truss diagonals, and sway bracings (Ge et al., 2008).

BRBs have also been used in the ductile diaphragms in Japan (see Figure 9.32). A similar concept to use BRBs as ductile end diaphragms for bi-directional earthquake excitation was also proposed by Celik and Burneau (2009).

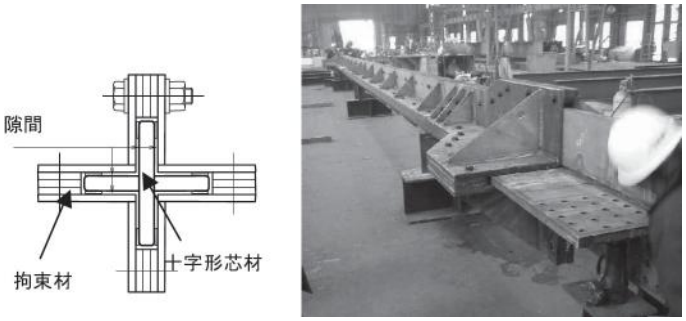

(a) (b)

FIGURE 9.30 Steel-only BRBs in Minato Bridge towers. (a) BRB cross section; (b) BRB fabrication. (Courtesy of H.B. Ge, Meijo University.)

FIGURE 9.31 Owatari Bridge in Japan. (Courtesy of H.B. Ge, Meijo University.)

FIGURE 9.32 BRBs used as ductile diaphragm. (Courtesy of H.B. Ge, Meijo University.)

In the United States, the Foresthill Road Bridge located in Northern California was the first bridge that incorporated BRBs (Reno and Pohl, 2010). This 3-span steel truss bridge was built in the early 1970s and measures 2428 ft. from one side to the other. At more than 730 ft. above the American River, it is the fourth highest bridge in the United States and the ninth highest bridge in the world (Figure 9.3). One important design objective to retrofit this bridge was to limit the seismic forces on the longitudinal abutment anchors of the bridge, both to protect the anchorages themselves and protect the surrounding truss members. Based on detailed analysis, the design team determined that using BRBs achieved the performance objectives and allowed for repairable damage after a maximum credible event. This was achieved by confining the inelastic demands to sacrificial link-plates that will fail at a prescribed strain and then allow the BRBs to engage. The link plates can easily be replaced and, once the BRBs begin yielding, they will perform in a stable inelastic, ductile behavior that allows large energy dissipation. The final configuration, with BRBs located longitudinally at the truss bottom chord connections to the abutments, was an effective and economical way to meet the design objectives.

9.9.3 Rocking Bridge Towers

Temporary uplifting of a column or tower leg from its base in an overturning motion is known are rocking. This phenomenon has long been studied, analytically and experimentally, for a number of applications (e.g., Housner, 1963; Meek, 1975; Psycharis, 1982; Kelley and Tsztoo, 1977; Priestley et. al., 1978; Toranzo et al., 2009; Midorikawa et al., 2003; Pollino and Bruneau, 2007, 2010a, 2010b; Eatherton et al., 2008, 2009).

Examples of bridges in which rocking of the piers during earthquakes has been allowed to achieve satisfactory seismic resistance include the South Rangitikei Rail Bridge, in New Zealand, designed and constructed in the 1970s (Priestley et al., 1996) and the North Approach of the Lions' Gate Bridge, in Vancouver, British Columbia (Dowdell and Hamersley, 2000). The benefits of allowing partial uplift of bridge piers has been also recognized and adopted for the retrofit of the Carquinez Bridge (Jones et al., 1997), the Golden Gate Bridge (Ingham et al., 1997), and the San Mateo-Hayward Bridge (Prucz et al., 1997), all in California. Note that pier E17 of the San Francisco-Oakland Bay Bridge rocked during the Loma Prieta earthquake (Housner, 1990).

The hysteretic curves obtained from a controlled-rocking system are "flag-shaped," as shown in Figure 9.33 for the case of a 2-legged bridge pier free to rock and having elasto-plastic BRBs at their base to provide energy dissipation (Pollino and Bruneau, 2007). Equations that describe this behavior are presented in Bruneau et al. (2011). The BRBs in such applications would be implemented vertically such that they do not transfer horizontal shear at the base of the pier. Note that only a half-cycle of hysteretic energy dissipation is shown in Figure 9.33; by symmetry, the curve repeats itself for displacement in the other direction. Also note that transition from first to second cycle response curve occurs when the BRBs yield in compression and carry a portion of the weight after the system comes to rest upon completion of the first cycle (Pollino and Bruneau, 2007).

Pollino and Bruneau (2007, 2010a, 2010b) formulated a rocking design procedure for bridge piers and verified its adequacy by shake table testing of tall specimens, with and without energy dissipating devices at their base, subjected to multidirectional earthquake excitations (Figure 9.34). Nonlinear time-history analyses are recommended to validate such designs, particularly when interaction with other piers and abutments (through the bridge deck) plays an important role.

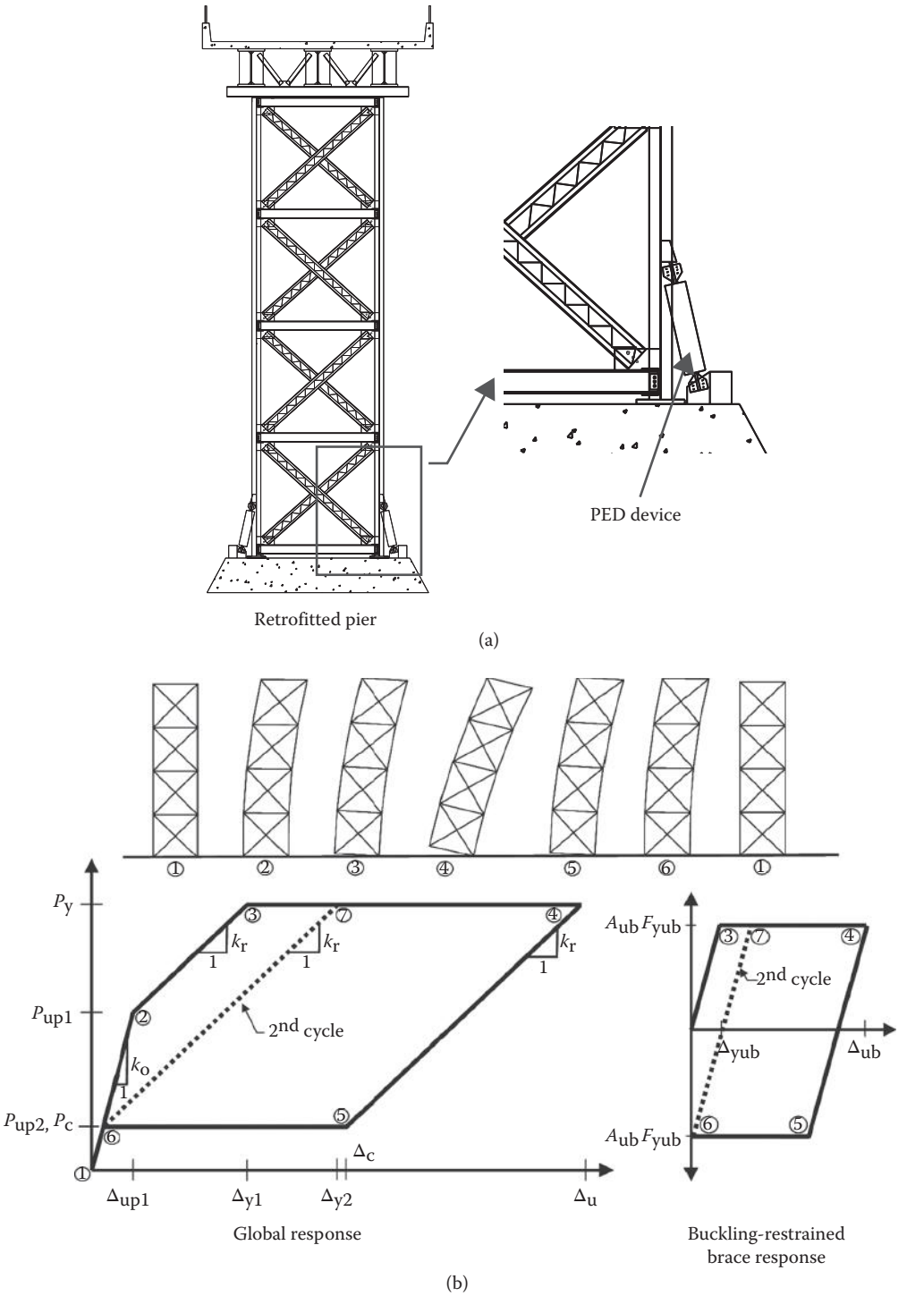

FIGURE 9.33 Controlled rocking of bridge tower: (a) schematic and location of energy dissipation device adjacent to columns free to uplift; (b) hysteretic behavior. (From Pollino, M., and Bruneau, M., Report No. MCEER-04-0011, Multidisciplinary Center for Earthquake Engineering Research, State University of New York at Buffalo, Buffalo, NY, 2004. With permission.)

(a)

(b)

(c)

FIGURE 9.34 Seismic retrofit of Foresthill Bridge with BRBs: (a) aerial view; (b) BRB installation; (c) bolted end connection. (Courtesy of M.L. Reno, Quincy Engineering.)

References

AASHTO. 2011. *Guide Specifications for LRFD Seismic Bridge Design*, 1st Edition. American Association of State Highway and Transportation Officials, Washington, DC.

AASHTO. 2012. *LRFD Bridge Design Specifications*, Customary U.S. Unit, 2012. American Association of State Highway and Transportation Officials, Washington, DC.

AISC. 2010a. Prequalified Connections for Special and Intermediate Steel Moment Frames for Seismic Applications. *ANSI/AISC 358-10*. American Institute of Steel Construction, Chicago, IL.

AISC. 2010b. Seismic Provisions for Structural Steel Buildings. *ANSI/AISC 341-10*. American Institute of Steel Construction, Chicago, IL.

Alfawakhiri F. and Bruneau, M. 2000. Flexibility of Superstructures and Supports in the Seismic Analysis of Simple Bridges. *Earthquake Eng. Struct. Dyn.*, 29(5), 711–729.

Alfawakhiri, F. and Bruneau, M. 2001. Local versus Global Ductility Demands in Simple Bridges. *J. Struct. Eng.*, ASCE, 127(5), 554–560.

ASCE. 2010. Minimum Design Loads for Buildings and Other Structures. *ANSI/ASCE 7-10*. American Society of Civil Engineers, Reston, VA.

Astaneh-Asl, A., Bolt, B., McMullin, K. M., Donikian, R. R., Modjtahedi, D., and Cho, S. W. 1994. Seismic performance of steel bridges during the 1994 Northridge earthquake. *Report No. UCB/CE-STEEL 94/01*. University of California, Berkeley, CA.

ATC. 1978. Tentative Provisions for the Development of Seismic Regulations for Buildings. *Report No. ATC-3-06*. Applied Technology Council, Redwood City, CA.

ATC. 1981. Seismic Design Guidelines. For. Highway Bridges. *Report No. ATC-6*. Applied Technology Council, Redwood City, CA.

ATC. 1996. Improved Seismic Design. Criteria for California Bridges: Provisional Recommendations. *Report No. ATC-32*. Applied Technology Council, Redwood City, CA.

ATC and MCEER. 2003. Recommended LRFD Guidelines for the Seismic Design of Highway Bridges. *Report No. ATC-49/NCHRP 12-49*. Applied Technology Council, Redwood City, CA.

AWS. 2009. Structural Welding Code–Seismic Supplement. *D1.8/D1.8M*, Doral. American Welding Society, FL.

Bauer, C. J. 1988. New standards for innovative composite construction' *Constr. Specifier*, 04, 84–89.

Berman, J. and Bruneau, M. 2005. Approaches for the Seismic Retrofit of Braced Steel Bridge Piers and Proof-of-Concept Testing of an Eccentrically Braced Frame with Tubular Link. *Technical Report MCEER-05-0004*, Multidisciplinary Center for Earthquake Engineering Research, State University of New York at Buffalo, Buffalo, NY.

Berman, J. and Bruneau, M. 2006. Further Development of Tubular Eccentrically Braced Frame Links for the Seismic Retrofit of Braced Steel Truss Bridge Piers. *Technical Report MCEER-06-0006*, Multidisciplinary Center for Earthquake Engineering Research, State University of New York at Buffalo, Buffalo, NY.

Berman, J. and Bruneau, M. 2007. Experimental and Analytical Investigation of Tubular Links for Eccentrically Braced Frames. *Eng. Struct. J.*, 29(8), 1929–1938.

Berman, J. and Bruneau, M. 2008a. Tubular Links for Eccentrically Braced Frames, I: Finite Element Parametric Study. *J. Struct. Eng.*, ASCE, 134(5), 692–701.

Berman, J. and Bruneau, M. 2008b. Tubular Links for Eccentrically Braced Frames, II: Experimental Verification. *J. Struct. Eng.*, ASCE, 134(5), 702–712.

Bruneau, M. and Marson, J. 2004. Seismic Design of Concrete-Filled Circular Steel Bridge Piers. *J. Bridge Eng.*, ASCE, 9(1), 24–34.

Bruneau, M., Uang., C.M., and Sabelli, R. 2011. *Ductile Design of Steel Structures*, 2nd Edition, McGraw-Hill, New York, NY, 921.

Bruneau, M., Wilson, J. C., and Tremblay, R. 1996. Performance of Steel Bridges during the 1995 Hyogo-Ken Nanbu (Kobe, Japan) Earthquake. *Canadian J. Civil Eng.*, 23(3), 678–713.

Buckle, I., Dusicka, P., and Itani, A. 2005. Development of Built-Up Shear Links as Energy Dissipators for the Seismic Protection of Long-Span Bridges. *Bridge Struct.: Assessment, Design and Construc.*, 1(1), 19–27.

Caltrans. 2001. *Guide Specifications for Seismic Design of. Steel Bridges*. California Department of Transportation, Sacramento, CA.

Caltrans. 2006. *Seismic Design Criteria*. California Department of Transportation, Sacramento, CA.

Carden, L., Itani, A., and Buckle, I. 2006a. Seismic Performance of Steel Girder Bridges with Ductile End Cross Frames using Single Angle X-Braces. *J. Struct. Eng.*, ASCE, 132(3), 329–337.

Carden, L. Itani, A., and Buckle, I. 2006b. Seismic Performance of Steel Girder Bridges with Ductile Cross Frames using Buckling Restrained Braces. *J. Struct. Eng. J.*, ASCE, 132(1), 338–345.

Celik, O. and Bruneau, M. 2009. Seismic Behavior of Bidirectional-resistant Ductile End Diaphragms with Buckling Restrained Braces in Straight Steel Bridges. *Eng. Struct.*, 31(2), 380–393.

Celik, O. and Bruneau, M. 2011. Skewed Slab-on-Girder Steel Bridge Superstructures with Bidirectional-Ductile End Diaphragms. *J. Bridge Eng.*, ASCE, 16(2), 207–218.

Celik, O. C. and Bruneau, M. 2007. Seismic Behavior of Bidirectional-Resistant Ductile End Diaphragms with Unbonded Braces in Straight or Skewed Steel Bridges. *Technical Report MCEER-07-0003*, MCEER, University at Buffalo, Buffalo, NY.

Clark, P., Aiken, I., Kasai, K., Ko, E., and Kimura, I. 1999. Design Procedures for Buildings Incorporating Hysteretic Damping Devices. *Proceedings of 69th Annual Convention*, SEAOC, Sacramento, CA.

CSA. 2009. Design of Steel Structures. *CAN/CSA S16-09*. Canadian Standards Association, Mississauga, ON, Canada.

Dowdell, D. and Hamersley, B. 2000. Lions' Gate Bridge North Approach—Seismic Retrofit. *Behaviour Steel Structures in Seismic Areas: Proc., Third International Conference*, STESSA 2000, Montreal, Canada, August 21–24, A.A. Balkema, Rotterdam, The Netherlands, pp. 319–326.

Eatherton, M., Hajjar, J. F., Deierlein, G. G., Krawinkler, H., Billington, S., and Ma, X. 2008. Controlled Rocking of Steel-Framed Buildings with Replaceable Energy-Dissipating Fuses. *Proc., 14th World Conference on Earthquake Engineering*, Beijing, China.

Eatherton, M., Hajjar, J. F., Deierlein, G. G., Ma, X., Billington, S., and Krawinkler, H. 2009. Steel-Framed Rocking Structural Systems for Moderate Seismic Zones. *Proceedings ASCE/SEI Structures Congress*, ASCE, Reston, VA.

Fehling, E., Pauli, W., and Bouwkamp, J. G. 1992. Use of Vertical Shear-Links in Eccentrically Braced Frames. *Proc., 10th World Conf. on Earthquake Engrg., Madrid*, 9, 4475–4479.

FEMA. 2000. Recommended Seismic Design Criteria for New Steel Moment-Frame Buildings. *Report No. FEMA-350*. Federal Emergency Management Agency, Washington, DC.

Fouche, P. and Bruneau, M. 2010. Non-Linear Analysis of Multi-Hazard Performance of Concrete Filled Steel Tubes Bridge Piers. *Proc., 8th International Conference on Short and Medium Span Bridges*, Niagara Falls, Ontario, Canada.

Fujikura, S., Bruneau, M., and Lopez-Garcia, D. 2008. Experimental Investigation of Multihazard Resistant Bridge Piers having Concrete-Filled Steel Tube under Blast Loading. *J. Bridge Eng.*, ASCE, 13(6), 586–594.

Ge, H. B., Luo, X. Q., and Usami, T. 2008. Damage Control Design of Bridge in Japan. *Proc., Tenth International Symposium on Structural Engineering for Young Experts*, Changsha, China.

Gerwick, B. C. 1995. In the Wet. *Civil Engineering*, ASCE, Reston, VA.

Hajjar, J. F. 2000. Concrete-Filled Steel Tube Columns under Earthquake Loads. *Progress in Struct. Eng. Materials*, 2(1), 72–82.

Housner, G. 1963. The Behavior of Inverted Pendulum Structures during Earthquakes. *Bull. Seismol. Society of America*, 53(2), 403–417.

Housner, G. 1990. Chairman, The Governor's Board of Inquiry on the 1989 Loma Prieta Earthquake. *Competing Against Time*. Office of Planning and Research, State of California.

Ingham, T., Rodriguez, S., Nadar, M., Taucer, F., and Seim, C. 1997. Seismic Retrofit of the Golden Gate Bridge. *Proc. National Seismic Conference on Bridges and Highways: Progress in Research and Practice*, San Diego, CA.

Itani, A. M., Douglas, B. M., and El-Fass, S. 1998. Cyclic Behavior of Shear Links in Retrofitted Richmond-San Rafael Bridge Towers. *Paper T155-3, Structural Engineering World Wide,* San Francisco, CA.

Itani, A. M., Monzon, E. V., and Grubb, M. A. 2012. AASHTO LRFD Provisions for the Seismic Design of Steel Plate Girder Bridges. *Eng. J.*, AISC, 49(3), 109–114.

Jones, M., Holloway, L., Toan, V., and Hinman, J. 1997. Seismic Retrofit of the 1927 Carquinez Bridge by a Displacement Capacity Approach. *Proceedings of Second National Seismic Conference on Bridges and Highways*, Progress in Research and Practice, Sacramento, CA.

Kanaji, H., Kitazawa, M., and Suzuki, N. 2005. Seismic Retrofit Strategy using Damage Control Design Concept and the Response Reduction Effect for a Long-span Truss Bridge. *Proc., of US-Japan Bridge Workshop*, Tsukuba, Japan.

Kanaji, H., Fujino, Y., Watanabe, E., and Suzuki, N. 2006. Seismic Retrofit of A Long-Span Truss Bridge Applying Damage Control Strategy. *Proceedings of International Association for Bridge and Structural Engineering Conference*, Copenhagen, Denmark.

Kelley, J. and Tsztoo, D. 1977. Earthquake Simulation Testing of a Stepping Frame with Energy-Absorbing Devices. *Report No. EERC 77-17*, Earthquake Engineering Research Center, University of California, Berkeley, CA.

Kerensky, O. and Dallard, N. 1968. The four-level interchange between M4 and M5 motorways at Almodsbury. *Proc. Inst. Civ. Eng. Struct. Build.,* 40, 295–322.

Leon, R. T. and Lange, J. (eds.) 2006. *Composite Construction in Steel and Concrete V*. ASCE, New York, NY, p. 765.

Marson, J. and Bruneau, M. 2000. Cyclic Testing of Concrete-Filled Circular Steel Tube Bridge Columns having Encased Fixed Based Detail. *Ottawa Carleton Earthquake Engineering Research Centre report OCEERC 00-22*, Ottawa, Ontario, Canada, December, 398.

Marson, J. and Bruneau, M. 2004. Cyclic Testing of Concrete-Filled Circular Steel Bridge Piers Having Encased Fixed-Base Detail. *J. Bridge Eng.*, ASCE, 9(1), 14–23.

Matsui, R., Takeuchi, T., and Hajjar, J. F. 2009. Local Buckling Failure Conditions for Buckling Restrained Braces. *6th International Conference on Urban Earthquake Engineering*, Tokyo, Japan.

McDaniel, C., Uang, C. M., and Seible, F. 2003. Cyclic Testing of Built-up Steel Shear Links for the New Bay Bridge. *J. Struct. Eng.*, ASCE, 129(6), 801–809.

Meek, J. W. 1975. Effects of Foundation Tipping on Dynamic Response. *J. Struct. Division*, ASCE, 101(ST7), 1297–1311.

Midorikawa, M., Azuhata, T., Ishihara, T., and Wada, A. 2003. Shaking Table Tests on Rocking Structural Systems Installed Yielding Base Plates in Steel Frames. STESSA 2003: *Proc., Behaviour of Steel Structures in Seismic Areas*, June 9–12, Naples, Italy, A.A. Balkema, Rotterdam, The Netherlands, pp. 449–454.

Nader, M., Manzanarez, R. l., and Maroney, B. 2000. Seismic design strategy of the new East Bay Bridge suspension span. *Paper No. 0911, 12th World Conference on Earthquake Engineering*, Auckland, New Zealand.

Nader, M. and Maroney, B. 2007. The New San Francisco-Oakland Bay Bridge Eastern Span. *Structures*, NCSEA/CASE/SEI.

Nakashima, M. 1995. Strain-Hardening Behavior of Shear Panels Made of Low-Yield Steel. I: Test. *J. Struct. Eng.*, ASCE, 121(12), 1742–1749.

Newmark, N. M. and Hall, W. J. 1982. *Earthquake Spectra and Design*, Earthquake Engineering Research Institute, Oakland, CA.

Pollino, M. and Bruneau, M. 2007. Seismic Retrofit of Bridge Steel Truss Piers Using a Controlled Rocking Approach. *J. Bridge Eng.*, ASCE, 12(5), 600–610.

Pollino, M. and Bruneau, M. 2010a. Bi-Directional Behavior and Design of Controlled Rocking 4-Legged Bridge Steel Truss Piers. *J. Struct. Eng.*, ASCE, 136(12), 1512–1522.

Pollino, M. and Bruneau, M. 2010b. Seismic Testing of a Bridge Truss Pier Designed for Controlled Rocking. *J. Struct. Eng.*, ASCE, 136(12), 1523–1532.

Popov, E. P. and Black, W. 1981. Steel Struts under Severe Cyclic Loading. *J. of Struct. Div.*, ASCE, 90(ST2), 223–256.

Popov, E. P., Engelhardt, M. D., and Ricles, J. M. 1989. Eccentrically Braced Frames: U.S. Practice. *AISC.,* 26(2), 66–80.

Priestley, M. J. N., Evison, R. J., and Carr, A. J. 1978. Seismic Response of Structures Free to Rock on Their Foundations. *Bull. New Zealand National Society for Earthquake Eng.*, 11(3), 141–150.

Priestley, M. J. N., Seible, F., and Calvi, G. M. 1996. *Seismic Design and Retrofit of Bridges*, John Wiley & Sons, New York, NY.

Prucz, Z., Conway, W. B., Schade, J. E., and Ouyang, Y. 1997. Seismic Retrofit Concepts and Details for Long-span Steel Bridges. *Proc. 2nd National Seismic Conference on Bridges and Highways*, Progress in Research and Practice, Sacramento, CA.

Psycharis, I. N. 1982. *Dynamic Behavior of Rocking Structures Allowed to Uplift*. Ph.D. Dissertation, California Institute of Technology, Pasadena, CA.

Reno, M. L. and Pohl, M. N. 2010. Seismic Retrofit of California's Auburn-Foresthill Bridge. *J. Transportation Board*, TRB, 2201/2010, 83–94.

Robert, J. E. 1992. Sharing California's Seismic Lessons. *Modern Steel Construction*, American Institute of Steel Construction, Chicago, IL, pp. 32–37.

Sabelli, R. and Lopez, W. 2004. Design of Buckling-Restrained Braced Frames. *Modern Steel Construction*, 44(3), 67–73.

Sarraf, M. and Bruneau, M. 1998a. Ductile Seismic Retrofit of Steel Deck-Truss Bridges: Strategy and Modeling. *J. Struct. Eng.*, ASCE, 124(11), 1253–1262.

Sarraf, M. and Bruneau, M. 1998b. Ductile Seismic Retrofit of Steel Deck-Truss Bridges: Design Applications. *J. Struct. Eng.*, ASCE, 124(11), 1263–1271.

Sarraf, M. and Bruneau, M. 2002. Seismic Performance of a Ductile Retrofitted Deck-Truss Bridge. *Proc., 7th U.S. National Conference on Earthquake Engineering*, Boston, on CD-ROM.

Seilie, I. F. and Hooper, J. D. 2005. Steel Plate Shear Walls: Practical Design and Construction. *Modern Steel Construction*, AISC.

South Carolina DOT. 2001. *Seismic Design Specifications for Highway Bridges*. South Carolina Department of Transportation, Columbia, SC.

Tajirian, F. F., Aiken, I. D., and Kimura, I. 2003. Application of Buckling-Restrained Braces in the United States. *Proc., 8th World Seminar on Seismic Isolation, Energy Dissipation and Active Vibration Control of Structures*, Yerevan, Armenia.

Taranath, B. S. 2012. *Structural Analysis and Design of Tall Buildings*, CRC Press, Boca Raton, FL.

Toranzo, L. A., Restrepo, J. I., Mander, J. B., and Carr, A. J. 2009. Ductile End-Diaphragms for Seismic Retrofit of Slab-on-Girder Steel Bridges. *J. Earthquake. Eng.*, 13(6), 882–898.

Tort, C. and Hajjar, J. F. 2004. Damage Assessment of Rectangular Concrete-Filled Steel Tubes for Performance-Based Design. *Earthquake Spectra*, EERI, 20(4), 1317–1348.

Tsai, K. C., Chen, H. W., Hong, C. P., and Su, Y. F. 1993. Design of Steel Triangular Plate Energy Absorbers for Seismic-Resistant Construction. *Earthquake Spectra*, 9(3), 505–528.

Tsai, K. C. and Popov E. P. 1989. Performance of Large Seismic Steel Moment Connections under Cyclic Loads. *Eng. J.*, AISC, 26(2), 51–60.

Uang, C. M. 1991. Establishing R (or R_w) and C_d Factors for Building Seismic Provisions. *J. Struct. Eng.*, ASCE, 117(1), 19–28.

Uang, C. M. and Nakashima, M. 2004. Steel Buckling-Restrained Braced Frames. (Chapter 16) in *Earthquake Engineering from Engineering Seismology to Performance-Based Engineering.* Y. Bozorgnia and V. V. Bertero (eds.), CRC Press, Boca Raton, FL.

Usami, T., Lu, Z., and Ge, H. 2005. A Seismic Upgrading Method for Steel Arch Bridges Using Buckling-Restrained Braces. *Earthquake Eng. Struct. Dyn.*, 34(4–5), 471–496.

Viest, I. M., Colaco, J. P., Furlong, R. W., Griffis, L. G., Leon, R. T., and Wyllie, L. A., Jr. (1997). *Composite Construction Design for Buildings*, ASCE and McGraw-Hill, New York, NY.

Vogeli, R. 1950. 'New Transmission Lines with Concrete Filled Steel Tube Towers. *Proc.*, *Int. Conf. Large Electric Systems*, 2, 223.

Wada, A., Huang, Y., and Bertero, V. V. 2004. Innovative strategies in earthquake engineering. (Chapter 10) in *Earthquake Engineering: From Engineering Seismology to Performance-Based Engineering*, Bozorgnia, Y. and Bertero, V.V. (eds.), CRC Press, Boca Raton, FL.

Wada, A., Saeki, E., Takeuchi, T., and Watanabe, A. 1998. *Development of Unbonded Brace*. Nippon Steel Corporation Building Construction and Urban Development Division, Tokyo, Japan.

Webb, J. and Peyton, J. M. 1990. 'Composite Concrete-Filled Steel Tube Columns. *Proc.*, *2nd Natl. Structures Conf.*, The Institution of Engineers, Adelaide, Australia, pp. 181–185.

Xie, Q. 2005. State of the Art of Buckling-Restrained Braces in Asia. *J. Constructional Steel Research*, 61(6), 727–748.

Yura, J. A., Galambos, T. V., and Ravindra, M. K. 1978. The Bending Resistance of Steel Beams. *J. of Struct. Div*., ASCE, 104(ST9), 1355–1370.

Zahrai, S. M. and Bruneau, M. 1999a. Ductile End-Diaphragms for Seismic Retrofit of Slab-on-Girder Steel Bridges. *J. Struct. Eng.*, ASCE, 125(1), 71–80.

Zahrai, S. M. and Bruneau, M. 1999b. Cyclic Testing of Ductile End Diaphragms for Slab-on-Girder Steel Bridges. *J. Struct. Eng.*, ASCE, 125(9), 987–996.

10

Seismic Design of Thin-Walled Steel and CFT Piers

Yoshiaki Goto

Nagoya Institute of Technology

10.1 Introduction

For elevated highway bridges in urban areas shown in Figure 10.1, thin-walled hollow steel piers and concrete-filled tubular (CFT) piers are often preferred to reinforced concrete (RC piers) piers in Japan, because those piers make it possible to reduce cross-sectional size as well as construction period. Before the 1995 Kobe earthquake (Hyogo-ken Nanbu earthquake), thin-walled hollow steel piers were common. Although some of these piers had concrete infill to prevent the local deformation of hollow tube caused by vehicle collision, the effect of the concrete infill was ignored in seismic design. Prior to the Kobe earthquake, thin-walled hollow piers were designed only for the Level 1 moderate earthquake with high probability of occurrence. In this design, the so-called seismic coefficient method based on linear static analysis was employed within the frame work of allowable stress design (ASD), and no damage was permitted in piers (Japan Road Association, 1980). Owing to the small lateral seismic design force for the Level 1 earthquake, some thin-walled hollow steel piers were seriously damaged during the Kobe earthquake. From the lessons learned from the Kobe earthquake, the revised seismic design specifications (Japan Road Association, 1996, 2002b, 2012b) introduced the concept of two-level seismic design. In this design, in addition to the conventional ASD for the Level 1 earthquake, the

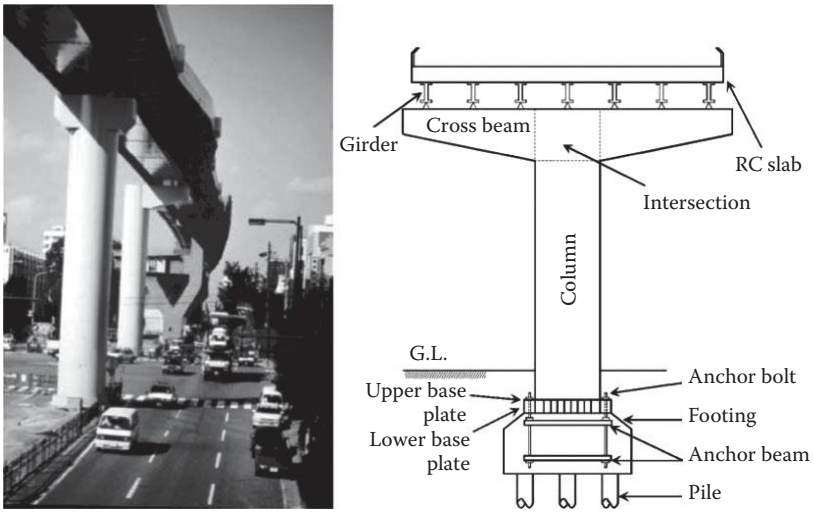

FIGURE 10.1 Thin-walled steel bridge piers.

dynamic performance of the steel and CFT piers is required to be checked for the Level 2 earthquake ground motions that represent those of major earthquakes such as the Kobe earthquake. For the performance check of piers under the Level 2 earthquake ground motions, nonlinear dynamic analysis has to be carried out to account for the plastification of members. It was recommended first in the 1996 design specifications (Japan Road Association, 1996) to use CFT piers in order to enhance the seismic performance of hollow piers under the Level 2 earthquake.

In this chapter, first, the types of thin-walled steel and CFT bridge piers are explained. Second, the damages observed for thin-walled hollow steel piers during the Kobe earthquake are explained. Third, the structural parameters that affect the seismic behavior of steel piers are discussed in relation with their limitations specified by the Japanese design code. Fourth, the current design method for the Level 2 earthquake is explained and discussed. Fifth, some of the recent research achievements for thin-walled steel piers and CFT piers are outlined. These achievements are chiefly concerned with the future development of an advanced seismic design where the coupling of multidirectional strong ground motions predicted by scenario earthquakes is considered.

10.2 Types of Piers

Cross-sectional shapes of thin-walled hollow steel bridge piers are of two types, rectangular and circular. The columns of rectangular piers (Figure 10.2a) are composed of four longitudinally stiffened panels. In addition, diaphragms or transverse stiffeners are installed inside the hollow rectangular columns in order to prevent the cross-sectional deformations. There are slits in the diaphragms, transverse stiffeners, and upper base plate where the longitudinal stiffeners penetrate. This detail is necessary to avoid weld lines crossing that tends to cause metal fracture under cyclic loading. The longitudinal stiffeners are continuous from the top to the bottom of steel columns and the lower ends of the stiffeners are welded to the lower base plate. The columns of circular piers (Figure 10.2b) are usually stiffened only by diaphragms. It is rare to install longitudinal stiffeners inside the circular columns. Thin-walled stiffened rectangular piers are preferred to thin-walled circular piers due to the following two reasons in Japan. One reason is that the cross-section of the columns of the rectangular piers is more efficient than that of the circular piers within the framework of the conventional seismic design practice in Japan, where the safety of bridges is checked against the unidirectional seismic accelerations applied in the longitudinal direction and that in the transverse direction independently (see Figure 10.2). The other reason is that

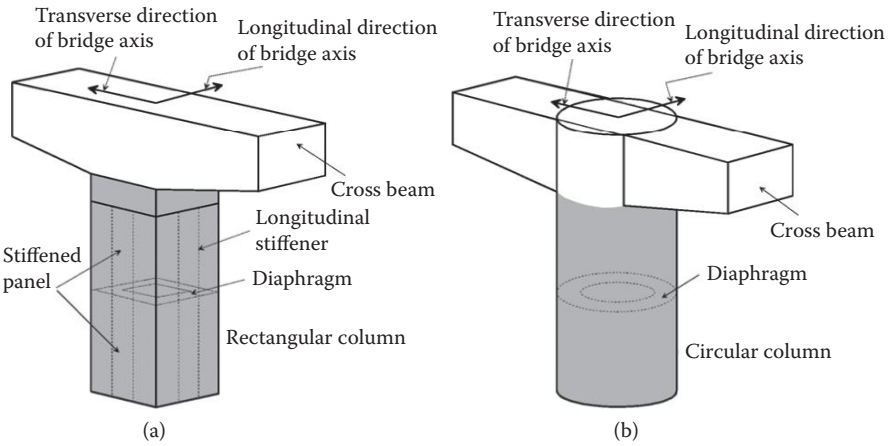

FIGURE 10.2 Types of steel bridge piers: (a) Rectangular steel pier; (b) Circular steel pier.

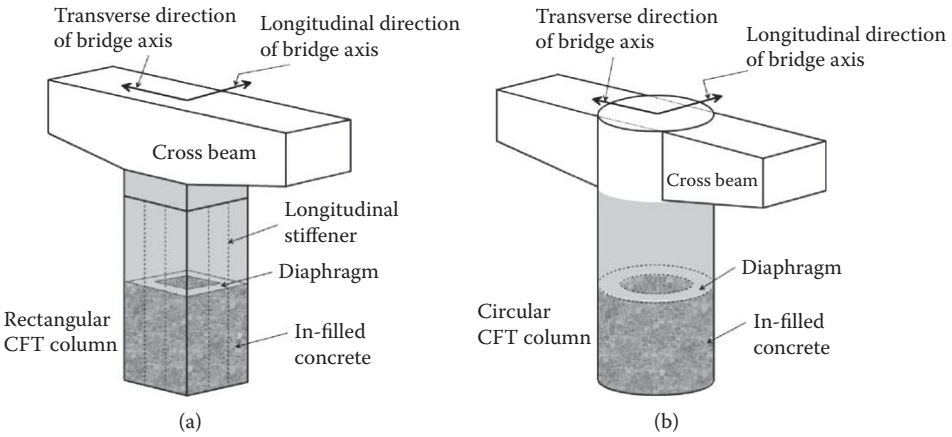

FIGURE 10.3 Types of thin-walled CFT bridge piers: (a) Rectangular CFT pier; (b) Circular CFT pier.

it is easier and less expensive to manufacture welded connections between a rectangular column and a cross-beam with box section because of their geometrical conformity (see Figure 10.2a). Except for the circular piers intended for aesthetic purposes, circular piers are primarily used for horizontally curved girder bridges where the piers exhibit bidirectional behavior because of the curved shape of girders even under the unidirectional horizontal seismic accelerations used for design. In case when columns with variable cross-section are used for piers, plastification is usually permitted only at the base panels of the columns referred to as control panel until the piers reach their ultimate states. This is to prevent the variable cross-sectional columns from losing their seismic performance due to the plastification at the upper cross-sections before they fully exhibit their expected seismic performance.

To enhance the seismic performance of thin-walled rectangular and circular steel piers, the internal hollow spaces of their columns are filled with concrete (Figure 10.3). These piers with in-filled concrete are referred to as CFT piers. Concrete is cast up to an appropriate height such that local buckling will not occur at the hollow section above the concrete-filled section. It is desirable to install a horizontal diaphragm inside the steel tube and cast concrete up to the location of this diaphragm. The diaphragm effectively transfers the axial compressive force from the steel tube to the in-filled concrete. The strength and ductility enhancement in CFT piers is primarily due to the composite action and local buckling restraint caused by the confined in-filled concrete. The details of this mechanism are explained later in Section 10.6.3. The strength enhancement in CFT piers, however, sometimes results in high tensile stress concentration

and accumulation of plastic strains, thus resulting in metal fracture (Public Work Research Institute of Japan, 1997–2000) in the outer steel tube before CFT piers attain their enhanced strength and ductility. Therefore, it is very important to proportion the steel tube, stiffeners, and diaphragms in order to prevent this kind of premature failure. It should be noted that thin-walled steel piers before the Kobe earthquake had concrete infill. However, this was used to prevent the local deformations of hollow steel tubes caused by vehicle collision. The effect of concrete infill was not reflected in the seismic design of piers.

The thin-walled and CFT piers mainly discussed herein are single cantilever piers with fixed base.

10.3 Damages in 1995 Kobe Earthquake

After the Kobe earthquake, damages of 355 steel piers were investigated (Editorial Committee for the Report on the Hanshin-Awaji Earthquake Disaster, 1996). The steel piers were roughly classified into 3 categories according to the difference of the design codes on which they were based. They were based on either of the 1980 specifications, the 1973 specifications, or the other specifications in and before 1964. Severe damages are observed in 3% of the 355 piers. The severely damaged piers were mostly based on the design specifications before 1964. Two rectangular piers collapsed as shown in Figure 10.4. The direct cause of this collapse is considered to be the metal fracture at the welded corners of the rectangular column cross-section. However, local buckling deformations of stiffened panels might have some large influence on the stress and strain concentration that caused the fracture at the corners. As a matter of fact, there had been no specifications for the stability design of stiffened panels before 1972. Furthermore, longitudinal stiffeners installed inside the hollow rectangular columns were observed to be discontinuous for one of the two collapsed piers. It should be noted that CFT piers were not common at the time of the Kobe earthquake as mentioned in Section 10.2.

A major damage pattern observed for the steel piers was the local buckling in columns (Figures 10.5 and 10.6), regardless of the categories of steel piers. Many of the local buckling deformations were observed at the transition point of plate thickness (Figures 10.5a and 10.6a), the hollow section just above the

(a)

(b)

FIGURE 10.4 Collapsed thin-walled steel piers: (a) Collapsed rectangular pier at Iwaya Viaduct; (b) Collapsed rectangular pier at Tateishi Viaduct.

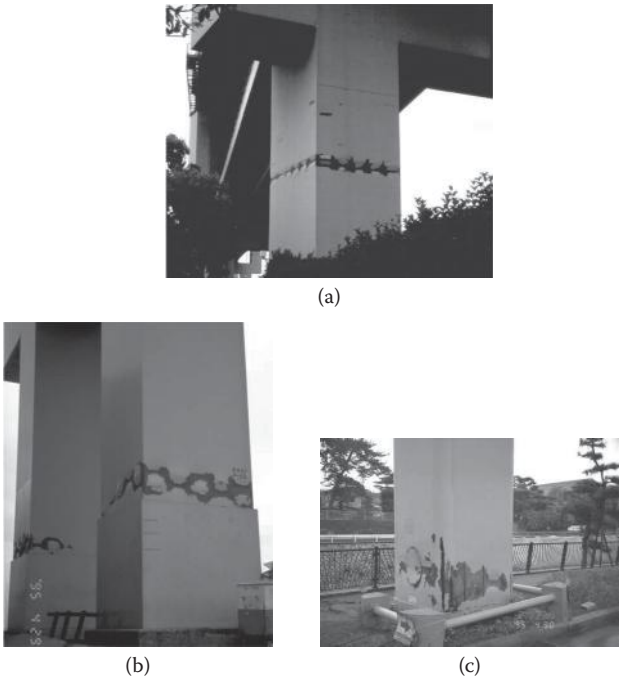

(a) (b) (c)

FIGURE 10.5 Local buckling deformations of rectangular columns: (a) Local buckling at transition point of plate thickness; (b) Local buckling just above concrete-filled section; (c) Local buckling initiated from manhole.

(a) (b)

FIGURE 10.6 Local buckling deformations of circular columns: (a) Local buckling at transition point of plate thickness (b) Local buckling just above concrete-filled section.

concrete-filled section (Figures 10.5b and 10.6b), and the location of manholes where longitudinal stiffeners were discontinuous (Figure 10.5c). The circular columns in the steel piers mostly exhibited a local buckling deformation pattern referred to as elephant bulge (Figure 10.6). This damage is considered to be caused not by the vertical seismic excitations but mainly by the horizontal seismic forces. The local buckling deformation resulted in strain concentration that sometimes led to metal fracture (Figure 10.7). Metal fracture was also observed in some welds. In the case of frame-type bridge piers, metal fracture occurred at a corner of beam-to-column connection (Figure 10.8). In addition, shear buckling deformations were observed in some cross beams (Figure 10.9). This type of damage is not so harmful, unless bearings that support girders are placed on the beams. Instead, it is considered to be beneficial in terms of energy dissipation.

At the base of steel piers, elongation of anchor bolts (Figure 10.10) and fracture in welds at the connection between the upper base plate and the panel plates were observed.

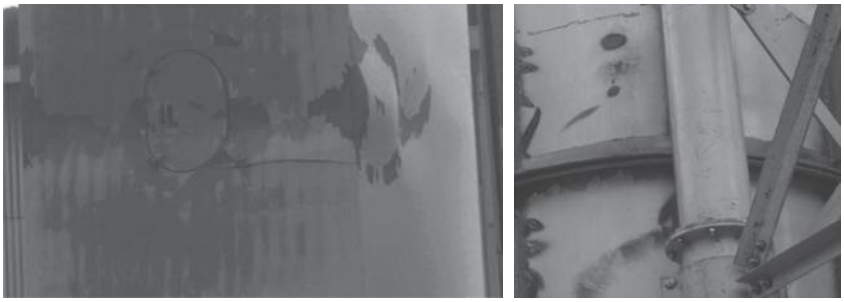

(a) (b)

FIGURE 10.7 Metal fracture caused by buckling deformation: (a) Horizontal crack near buckling bulge initiated from manhole of rectangular column; (b) Horizontal crack at elephant foot bulge of circular column.

FIGURE 10.8 Metal fracture at corner of beam-to-column connection.

FIGURE 10.9 Shear buckling of thin-walled steel cross beam in frame-type pier.

Before the Kobe earthquake, steel bridge piers were only designed for Level 1 earthquakes with relatively small lateral seismic coefficient ranging from 0.2 to 0.3 (Japan Road Association, 1980). This value corresponds to the seismic acceleration of 200–300 gal in structures. The seismic coefficient was multiplied to dead loads to calculate seismic design horizontal forces. The response stresses caused by the seismic design horizontal forces in structures were calculated by linear static analysis. The safety of the structures was checked within the frame work of the ASD such that no damage occurs in piers

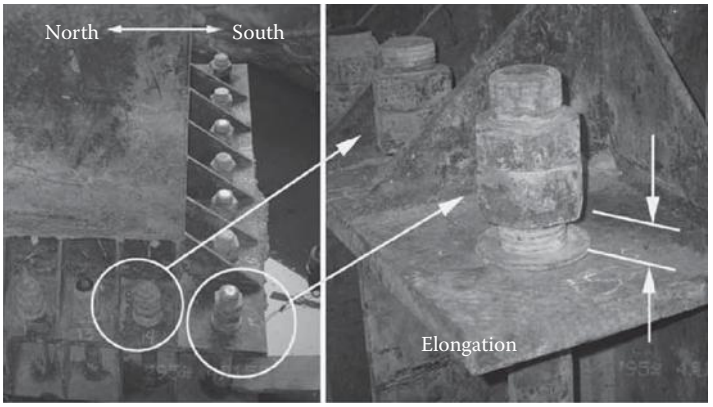

FIGURE 10.10 Plastic elongation of anchor bolts.

under the response stresses. However, there were no considerations in the seismic design for their behavior under Level 2 earthquake ground motions like those of the Kobe earthquake, where the horizontal seismic acceleration amounted to 1500–2000 gal in structures. Despite the fact that the seismic force calculated for a Level 1 earthquake is much smaller than that of the Kobe earthquake, the damages of the steel piers were relatively small due to their superior ductility, compared with those of RC piers. This implies that the thin-walled steel piers designed properly for the Level 2 earthquake are expected to exhibit excellent seismic performance.

10.4 Structural Parameters

10.4.1 Thin-Walled Rectangular Steel Piers

The columns of the thin-walled rectangular steel piers shown in Figure 10.2a and 10.11c are composed of 4 longitudinally stiffened plates (panels). In addition, diaphragms or transverse stiffeners are installed inside the hollow rectangular columns. It was in 1972 that a design method for thin-walled stiffened plates was first presented in the Japanese design specifications (Japan Road Association, 1972). Most of the structural parameters that are used now were introduced at that time.

Stability and ductility of thin-walled rectangular steel piers are considered to be influenced by the following 6 independent parameters as defined below.

$$\alpha = a/b_f \tag{10.1}$$

$$n \tag{10.2}$$

$$R_R = \{b_f/(nt)\}\sqrt{(\sigma_y/E)\cdot 12(1-\nu^2)/(\pi^2 k_R)} \tag{10.3}$$

$$R_s = (h_r/t_r)\sqrt{(\sigma_{sy}/E)\cdot 12(1-\nu^2)/(\pi^2 k_s)} \tag{10.4}$$

$$\gamma = (EI_r)/(b_f D) = (Et_r h_r^3/3)/\{Eb_f t^3/12(1-\nu^2)\} = 4(1-\nu^2)t_r h_r^3/(b_f t^3) \tag{10.5}$$

$$\gamma_t = (EI_t)/(b_f D) = (EI_t)/\{Eb_f t^3/12(1-\nu^2)\} \tag{10.6}$$

$$\overline{\lambda} = \sqrt{P_y / P_{cr}} \tag{10.7}$$

The above parameters given by Equations 10.1 through 10.7 are defined for the control flange panels where the plastification is permitted. The biaxial principal axes of the rectangular columns generally coincide with the longitudinal and transverse directions of a bridge. In the conventional seismic design of bridge piers, the performance of bridge piers are checked under unidirectional seismic forces applied in the longitudinal and transverse directions of the bridge independently. Therefore, under the longitudinal seismic force, the panels parallel to the transverse direction become flange panels, whereas the panels parallel to the longitudinal direction become flange panels under the transverse seismic force. The control flange panels of columns are usually located between the upper base plate and the lowest diaphragm or the lowest transverse stiffener (Figure 10.11). Some details of the above parameters are explained in the following.

α is the aspect ratio of the control flange panel where a = the distance between the upper base plate and the lowest diaphragm or the lowest transverse stiffener and b_f = width of the flange panel; n is the number of

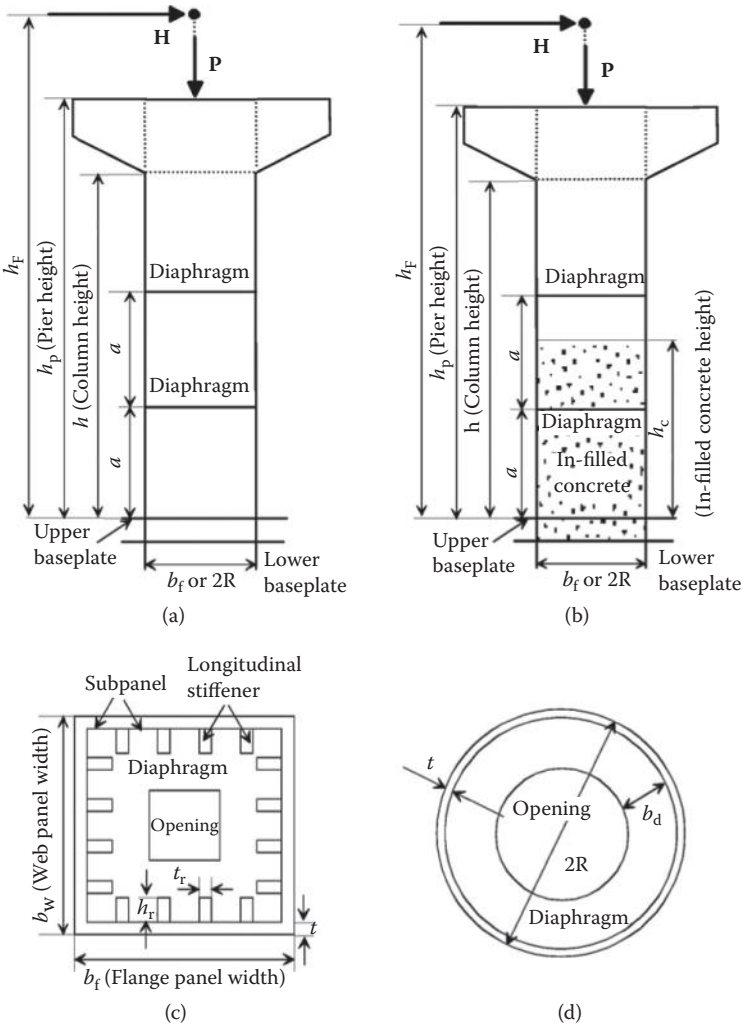

FIGURE 10.11 Definition of geometrical variables for thin-walled steel and CFT piers: (a) Thin-walled hollow steel pier; (b) CFT cpier; (c) Cross-section of square column; (d) Cross-section of circular column.

subpanels per one flange panel. A subpanel is defined as a strip plate between adjacent longitudinal stiffeners. (n−1) is the number of longitudinal stiffeners per one panel; R_R is the width-to-thickness ratio parameter of the subpanel, where b/n = width, t = thickness, and σ_y = yield stress, respectively, of the subpanel; E = Young's modulus and ν = Poisson's ratio, respectively, of steel; and k_R = plate buckling coefficient of a subpanel. For k_R, $k_R = 4.0$ is assumed as the minimum value for a rectangular plate with 4 edges simply supported.

R_s is the width-to-thickness ratio parameter of a longitudinal stiffener where h_r = width, t_r = thickness, σ_{sy} = yield stress, and k_s = plate buckling coefficient, respectively, of a longitudinal stiffener. For k_s, $k_s = 0.43$ is assumed as the minimum value for a stiffener plate model with one free longitudinal edge and three simply supported edges.

γ is the relative flexural rigidity of a longitudinal stiffener where EI_r = flexural rigidity of a longitudinal stiffener and D = flexural rigidity of a flange panel plate to which the stiffener is attached. The cross-sectional second moment of inertia I_r for the longitudinal stiffener is evaluated in terms of the strong axis defined at the point welded to the panel.

γ_t is the relative flexural rigidity of a diaphragm or a transverse stiffener, where EI_t = flexural rigidity of a diaphragm or a transverse stiffener. The cross-sectional second moment of inertia I_t for the diaphragm or the transverse stiffener is evaluated in terms of the strong axis defined at the point welded to the panel.

$\bar{\lambda}$ is the effective slenderness ratio parameter of a pier. The height of a pier denoted as h_p (Figure 10.11) is the distance between the upper base plate and the upper surface of the cross-beam. P_{cr} is the elastic buckling strength of a pier for the sway mode in the direction of applied seismic force. P_y denotes the yield strength of the control cross section of a pier column, as given by

$$P_y = \sigma_y A_\Sigma + \sigma_{sy} A_{\Sigma s} \tag{10.8}$$

where A_Σ = total cross-sectional area of 4 panel plates and $A_{\Sigma s}$ = total cross-sectional area of longitudinal stiffeners.

In addition to the structural parameters shown in Equations 10.1 through 10.7, overall width-to-thickness ratio parameter R_F for a stiffened flange panel is used. In this case, the materials of a longitudinal stiffeners and subpanels are assumed to be the same, that is, $\sigma_{sy} = \sigma_y$. R_F defined below is derived by transforming a stiffened flange panel into an equivalent orthotropic plate.

$$R_F = (b_r/t)\sqrt{(\sigma_y/E)\cdot 12(1-\nu^2)/(\pi^2 k_F)} \tag{10.9}$$

where the buckling coefficient k_F of a stiffened panel is given by

$$k_F = \left\{(1+\alpha^2)^2 + n\gamma\right\} \Big/ \left\{\alpha^2(1+n\delta_r)\right\} \text{ for } \alpha \le (1+n\gamma)^{1/4} \tag{10.10}$$

$$k_F = 2(1+\sqrt{1+n\gamma}\,)/(1+n\delta_r) \text{ for } \alpha > (1+n\gamma)^{1/4} \tag{10.11}$$

where

$$\delta_r = h_r t_r/(b_f t) \tag{10.12}$$

The structural parameters α, n, R_R, R_S, γ, γ_t, $\bar{\lambda}$, and R_F defined by Equations 10.1 through 10.7 and Equation 10.9 have been used in the Japanese design specifications (Japan Road Association, 1972, 1980, 1996, 2002a, 2002b, 2012a). In the newly revised seismic design specifications (Japan Road Association, 2012b), two more parameters of b_w/b_f and $l_{ef}/(b_f+b_w)$ are introduced (Okada et al.,

2010). b_w / b_f denotes the aspect ratio of the control cross-section of a rectangular pier where b_f = width of control flange panel and b_w = width of web panel. l_{ef} denotes the effective length of a pier, as given by

$$l_{ef} = \pi\sqrt{EI_c / P_{cr}} \tag{10.13}$$

where EI_c is the flexural rigidity of the control cross-section of the pier. The control cross-section corresponds to the column section at the location of the control flange panels.

Apart from the structural parameters used in the Japanese design specifications, slenderness ratio parameter $\bar{\lambda}_s$ for a longitudinal stiffener is often used in conjunction with R_R to express the strength and ductility of longitudinally stiffened panels. $\bar{\lambda}_s$ is defined as follows (Usami et al., 1995).

$$\bar{\lambda}_s = \frac{1}{\sqrt{Q}}\frac{a}{r_s}\frac{1}{\pi}\sqrt{\frac{\sigma_{sy}}{E}} \tag{10.14}$$

where r_s is the strong axis radius of gyration of T-shaped cross-sectional area composed of one longitudinal stiffener and a segment of the attached panel plate with the length of b/n. The axis of gyration is defined at the centroid of the T-shaped cross-sectional area. Q is given by

$$Q = \left(\beta - \sqrt{\beta^2 - 4R_R}\right) / (2R_R) \le 1.0 \tag{10.15}$$

where

$$\beta = 1.33R_R + 0.868 \tag{10.16}$$

10.4.2 Thin-Walled Circular Steel Piers

Similar to the columns of thin-walled rectangular steel piers, diaphragms are usually installed inside the hollow columns thin-walled circular hollow columns to prevent the excessive cross-sectional deformations that reduce the strength and ductility of piers (Figure 10.2b and Figure 10.11d). However, normally, longitudinal stiffeners are not used, being different from thin-walled rectangular steel piers. In order to provide sufficient in-plane stiffness to the diaphragms, requirements for their thickness t_d and width b_d are given in terms of the radius R of circular piers as $b_d \ge R/10 + 70$ (mm) and $t_d \ge b_d / 17$ (Part II: Steel bridges) (Japan Road Association, 2002a, 2012a). In addition, the interval of the diaphragms in the longitudinal direction of the columns is required to be smaller than $6R$.

The stability and ductility of thin-walled circular steel piers with diaphragms that satisfy the above requirements are governed by the following two parameters (Japan Road Association, 2002b, 2012b) defined for their control sections where plastification is permitted.

$$R_t = (R/t)(\sigma_y/E)\sqrt{3(1-\nu^2)} \tag{10.17}$$

$$\bar{\lambda} = \sqrt{P_y/P_{cr}} \tag{10.18}$$

R_t is the radius-to-thickness ratio parameter, where R and t are the radius and the thickness, respectively, of a thin-walled circular column. $\bar{\lambda}$ is the effective slenderness ratio parameter of a pier. P_{cr} is the elastic buckling strength. P_y is the yield strength of the control cross-section of a column, as given by

$$P_y = \sigma_y \pi \{R^2 - (R-t)^2\} \tag{10.19}$$

10.4.3 CFT Piers

The structural parameters of the outer steel tubes of CFT piers (Figure 10.3 and Figure 10.11b) are the same as those shown for the hollow rectangular and circular steel piers discussed in Sections 10.4.1 and 10.4.2. In addition to the above, the ratio σ_c/σ_y between the compressive strength of in-filled concrete and the yield stress of steel tube is an important parameter for CFT piers. However, Japanese seismic design specifications (Japan Road Association, 2002b) recommends to use a specified low strength concrete of $\sigma_c = 18 N/mm^2$ to avoid an extreme strength enhancement of composite section. The ratio h_c/h_F between the in-filled concrete height h_c and the height h_F of a point in superstructure where the resultant seismic horizontal inertia force H acts is another important structural parameter of CFT piers (Figure 10.11). Both of the heights are measured from the upper base plate of the piers.

10.5 Seismic Design Specifications in Japan

10.5.1 Parameter Limitations and Structural Details

In the Japanese design specifications of highway bridges (Japan Road Association, 2002a, 2012), limitations are set to some of the structural parameters of the columns in thin-walled hollow steel piers and CFT piers in order to enhance the ductility of piers. In addition, some structural details are specified to avoid fracture of the steel. Herein, the limitations of the structural parameters as well as structural details are explained.

10.5.1.1 Thin-Walled Rectangular Steel Piers

Upper limits are set to the width-to-thickness ratio parameters of the subpanels R_R and longitudinal stiffeners R_s, respectively, defined by Equations 10.3 and 10.4 as $R_R \leq 0.5$ and $R_s \leq 0.7$ (Part II; Steel bridges) (Japan Road Association, 2002a). This is to enhance the ductility of the rectangular steel piers by limiting the minimum thicknesses of the subpanels and stiffeners such that excessive local buckling deformations will not occur.

For the relative flexural rigidity of longitudinal stiffeners γ defined by Equation 10.5, the lower limit γ_{req} referred to as required relative flexural rigidity is specified in order to prevent the occurrence of unfavorable overall panel buckling prior to the subpanel buckling (Figure 10.12). This provision is also to keep the stiffened panels within small buckling deformations. The required relative flexural rigidity γ_{req} is determined from the condition that the overall strength of a stiffened panel coincides with the sum of the strengths of subpanels that are assumed to be simply supported by rigid longitudinal stiffeners. In order to evaluate the buckling strength of the overall panel, the stiffening conditions by diaphragms or transverse stiffeners have to be classified into two cases.

First where rigid diaphragms or rigid transverse stiffeners are installed at short intervals so that the overall panel buckles in a single half-wave mode between the adjacent diaphragms or the adjacent transverse stiffeners. In this case, the relative flexural rigidity of the diaphragms or transverse stiffeners γ_t and the aspect ratio of the overall panel α have to satisfy the following condition.

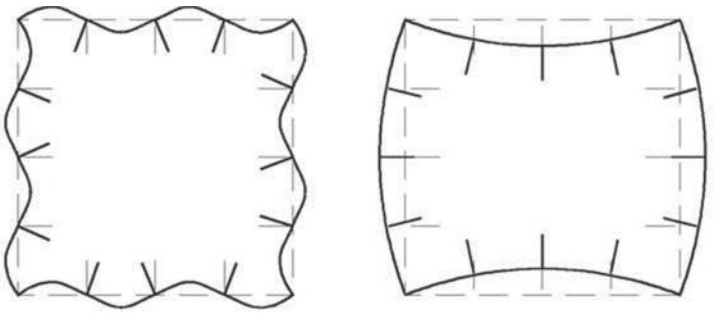

(1) Subpanel buckling (2) Overall panel buckling

(a)

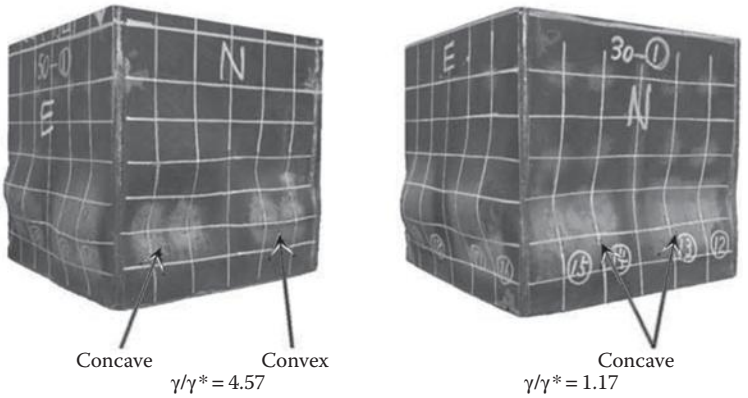

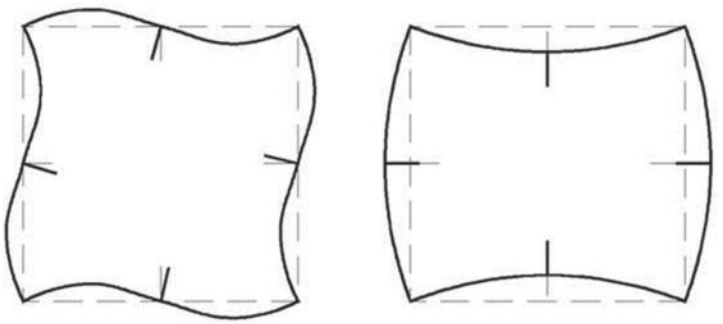

(1) Subpanel buckling (2) Overall panel buckling

(b)

FIGURE 10.12 Subpanel buckling and overall panel buckling of thin-walled rectangular column: (a) Cross sectional deformation of column with multiple stiffeners; (b) Cross sectional deformation of column with single stiffener.

$$\gamma_t \geq \gamma_{treq} = (1 + n\gamma_{req})/(4\alpha^3) \text{ and } a/b = \alpha \leq \alpha_0 = (1 + n\gamma)^{1/4} \quad (10.20a,b)$$

where γ_{treq} is referred to as required relative flexural rigidity of the diaphragms or transverse stiffeners. α_0 denotes an aspect ratio where the elastic buckling of the overall panel occurs in a single half-wave mode and the buckling strength becomes minimum. Under the condition of Equations 10.20a and 10.20b, γ_{req} is given as

$$\gamma_{req} = 4\alpha^2 n(t_0/t)^2(1+n\delta_r) - (\alpha^2+1)^2/n \text{ for } t/t_0 \geq 1.0 \tag{10.21}$$

$$\gamma_{req} = 4\alpha^2 n(1+n\delta_r) - (\alpha^2+1)^2/n \text{ for } t/t_0 < 1.0 \tag{10.22}$$

Second, where the panels are stiffened by not so rigid transverse stiffeners (diaphragms) or the intervals of the transverse stiffeners are long. This case is the complementary set of Equations 10.20a and 10.20b expressed as

$$\gamma_t < \gamma_{treq} \text{ or } \alpha > (1+n\gamma)^{1/4} \tag{10.23}$$

Under the condition of Equations 10.23, the effect of diaphragms or transverse stiffeners are ignored in the calculation of the overall panel strength and γ_{req} is given as

$$\gamma_{req} = \left[\left\{2n^2(t_0/t)^2(1+n\delta_r)-1\right\}^2 - 1\right]/n \text{ for } t/t_0 \geq 1.0 \tag{10.24}$$

$$\gamma_{req} = \left[\left\{2n^2(1+n\delta_r)-1\right\}^2 - 1\right]/n \text{ for } t/t_0 < 1.0 \tag{10.25}$$

For thin-walled steel piers, diaphragms are mostly installed at an interval smaller than the pier width b, that is, $\alpha = a/b \leq 1.0$. Therefore, the case specified by Equation 10.23 is very rare.

In Equations 10.21, 10.22, 10.24, and 10.25, δ_r (see Equation 10.12) has to satisfy $\delta_r \geq 1/(10n)$. This is to prevent the cross section of the longitudinal stiffeners from becoming very small. t_0 is the so-called critical plate thickness of subpanels beyond which yielding occurs prior to buckling. The equation to calculate t_0 was revised in the 1980 specifications (Japan Road Association, 1980) in accordance with the revision of the compression strength curve for steel plate element. According to this specifications, the strength of subpanels is assumed to be governed by yielding when $R_R \leq 0.5$, being different from the 1972 specifications (Japan Road Association, 1972) where the strength of subpanels was assumed to be governed by yielding when $R_R \leq 0.7$. Therefore, t_0 is now given as follows:

$$t_0 = (b_f/n)\sqrt{\left(\sigma_y/E\right)\cdot 12\left(1-\nu^2\right)/\left(4\pi^2\right)}\Big/0.5 \tag{10.26}$$

The required stiffness ratios for longitudinal stiffeners γ_{req} expressed by Equations 10.21 and 10.24 correspond to the minimum rations for the case where yielding occurs in subpanels before the overall panel buckling occurs. In this case, the required relative flexural rigidity γ_{req} is reduced to account for the reduction in strength of subpanels because of yielding. Therefore, there is no guarantee that the overall panel buckling is prevented in the plastic range even when $\gamma \geq \gamma_{req}$ is satisfied. As a matter of fact, alternate loading experiments and numerical analyses showed that longitudinal stiffeners with γ_{req} are not rigid enough to prevent the overall panel buckling (Usami et al., 1992; Goto et al., 2007). In view of this fact, the allowable strains to calculate the allowable horizontal displacement or the allowable curvature of steel piers under the Level 2 earthquake are specified by using γ_{req} defined by Equation 10.22 or Equation 10.25, regardless of the value of t/t_0 (Japan Road Association, 2002b). γ_{req} defined by Equation 10.22 or 10.25 is specifically referred to as optimum stiffness ratio that is expressed as γ^*. γ^* ignores the reduction in the strength of the subpanels due to yielding. In this way, longitudinal stiffeners of thin-walled steel piers designed after the Kobe earthquake usually satisfy the condition $\gamma \geq \gamma^*$. However, $\gamma \geq \gamma^*$ is still insufficient to prevent the overall panel buckling as can be seen in Figure 10.12b. From a precise numerical analysis under a bidirectional horizontal cyclic load, Goto et al. (2007) showed that $\gamma \geq 2\gamma^*$ is most preferable for square piers with the longitudinal stiffeners of $R_s = 0.7$ that is specified as a upper limit of the width-to-thickness ratio parameter of the longitudinal stiffeners. The piers with the stiffeners of $R_s = 0.7$ attain the utmost performance so far as $\gamma \geq 2\gamma^*$ is satisfied. Usami et al. (1992) recommended to use the stiffeners with $\gamma \geq 3\gamma^*$. This recommendation was proposed, based

on a unidirectional cyclic loading experiment. However, under more versatile bidirectional cyclic loading, the performance of piers with $\gamma = 3\gamma^*$ is not improved, compared to piers with $\gamma = 2\gamma^*$, as long as $R_s = 0.7$ is adopted. This is because of the local buckling of longitudinal stiffeners caused by the cyclic bidirectional loading. In order to improve the performance of the piers by using the stiffeners with high bending rigidity of $\gamma \geq 3\gamma^*$, it is essential to increase the thickness of the stiffeners such that $R_s \leq 0.6$ is satisfied.

The longitudinal stiffeners are recommended to be continuous from the top to the lower base plate of the steel piers. The strength and ductility of the steel piers were observed to be lost because of the discontinuity of the longitudinal stiffeners in the Kobe earthquake. In order to keep the longitudinal stiffeners continuous, slits are made in the diaphragms, transverse stiffeners, and upper base plate where the longitudinal stiffeners penetrate. The above details are to avoid weld line crossing that tends to cause metal fracture under cyclic loading (low cycle fatigue).

In the seismic design practice based on Japanese seismic design specifications (Japan Road Association, 2012b), 6 structural parameters with their ranges specified as $0.3 \leq R_F \leq 0.5$, $0.3 \leq R_R \leq 0.5$, $\gamma \geq \gamma^*$, $0.2 \leq \bar{\lambda} \leq 0.5$, $2.5 \leq l_{ef}/\left(b_f + b_w\right) \leq 9.0$, and $0.5 \leq b_w/b_f \leq 2.0$ are used to express the allowable strains for the control panels of the columns in the hollow rectangular steel piers. Therefore, the rectangular steel piers are usually proportioned within these ranges. There are no limitations in α and n. However, $\alpha = 0.4$–1.2 and $n = 4$–6 are usually used.

Apart from structural parameters, the behavior of hollow steel piers are governed by the axial force ratio defined by P/P_y, where P is the axial compressive force under dead load. The ductility of thin-walled steel piers decreases with the increase in P/P_y. In design practice, $P/P_y \leq 0.5$ is usually adopted because the allowable strains are specified only for this range in the design specifications.

In order to prevent fracture at the corner welds of rectangular cross-sections (Figure 10.4), three possible structural details are proposed for rectangular piers (Japan Road Association, 2002b). The first is to use a corner plate to reinforce four corners. The second is to avoid corner welding by rounding off the corners. The third is to apply full penetration groove welding or partial penetration groove welding by K groove to the corner welding and to use quality guaranteed steel materials that provide the required mechanical characteristics along the plate thickness.

10.5.1.2 Thin-Walled Circular Steel Piers

For thin-walled circular members, R_t is specified as $R_t \leq 0.091$ in the design specifications (Part II: Steel bridges) (Japan Road Association, 2002a) such that yielding occurs before local buckling. This is to ensure the ductility of the thin-walled circular members. However, based on the damages of the circular steel piers observed in the Kobe earthquake along with those in the experiments, more strict limitation of $R_t \leq 0.08$ is recommended in the seismic design specifications to be used for the columns of thin-walled circular steel piers (Japan Road Association, 2002b).

In design practice, $0.03 \leq R_t \leq 0.08$ and $0.2 \leq \bar{\lambda} \leq 0.4$ are generally adopted for circular piers under $P/P_y \leq 0.2$, because limiting strains for the thin-walled circular columns are shown in these ranges. In addition, uniform wall thickness is normally adopted in the longitudinal direction of thin-walled hollow circular columns, in view of the fact that serious local buckling damage occurred at the transition point of the stepped thickness in the Kobe earthquake.

10.5.1.3 CFT Piers

Parameter limitations for the outer steel tube of CFT piers are not clearly mentioned. However, the structural parameters of $0.3 \leq R_F \leq 0.7$, $0.3 \leq R_R \leq 0.7$, $0.2 \leq \bar{\lambda} \leq 0.5$, $\gamma/\gamma_{req} \geq 1.0$, $2.5 \leq l_{ef}/(b_f + b_w) \leq 9.0$, and $0.5 \leq b_w/b_f \leq 2.0$ are used to express the allowable strain for the control panels of the rectangular stiffened outer steel tube under $P/P_y \leq 0.2$. In the case of a larger axial force ratio in the range of $0.2 < P/P_y \leq 0.5$, the parameter range for R_R is more restrictive as $0.3 \leq R_R \leq 0.5$. For the circular outer

steel tube, $0.03 \le R_t \le 0.12$ and $0.2 \le \bar{\lambda} \le 0.4$ are used under $P/P_y \le 0.2$. Therefore, the above parameter limitations are generally adopted in the seismic design practice. The upper limits of R_F, R_R, and R_t are eased for the outer steel tubes of CFT piers, compared with those of hollow steel piers. This is due to the buckling restraining mechanism of CFT piers. However, the limitation of the axial force ratio P/P_y for circular CFT piers is the same as that for hollow piers. Specifically, the limitation of P/P_y for circular CFT piers is very restrictive. This is simply because of the lack of experimental data in the range of $0.2 < P/P_y$ for circular CFT piers. It was shown by Goto et al. (2010a, 2010b, 2011) and Ghosh et al., (2011) that the magnitude of P/P_y less affects the local buckling deformation of circular CFT piers, being different from hollow piers where a large axial force ratio accelerates the progress of local buckling deformation and reduces their ductility under alternate horizontal loads. Therefore, it is necessary to specify more appropriate liming values of P/P_y in order to make full use of the excellent performance of CFT piers under high axial force ratio.

For rectangular thin-walled steel cross sections in the CFT columns, stress and strain concentrations occur at the corners are caused by the outward local buckling mode of the four stiffened panels. This is because the inward deformation is restrained by the in-filled concrete. Therefore, in order to prevent the fracture at the corner weld, it will be desirable to employ any of the structural details for the corners explained in Section 10.5.1.1.

A diaphragm is recommended to be installed at the location of the upper surface of the in-filled concrete. This diaphragm plays an important role in transmitting the compressive stress from its outer steel tube to the in-filled concrete, as explained later in Section 10.6.3. In-filled concrete height ratio h_c/h_F has to be determined such that the failure of the hollow section will not occur before the failure of the concrete-filled section. For this purpose, the following requirement has to be satisfied.

$$h_c/h_F > 1 - M_{s0}/M_a \tag{10.27}$$

where h_c is the in-filled concrete height measured from the upper base plate of a pier; h_F the height from the upper base plate to the acting point of the resultant horizontal seismic inertia force H in a superstructure (Figure 10.11); M_a an allowable bending moment of the composite section at the base of a CFT pier under the compressive axial force P as explained later in Section 10.5.2.2; M_{s0} a limiting bending moment of the hollow section calculated by $M_{s0} = (\sigma_{s0} - P/A)Z_g$; σ_{s0} either of the two values, that is, the yield stress of steel or the stress obtained by multiplying 1.7 to the allowable stress of a steel plate considering local buckling; and Z_g the section modulus of the hollow section. Low strength in-filled concrete of 18 N/mm^2 is recommended to prevent the strength of the CFT section from becoming considerably larger than that of the hollow steel section.

10.5.2 Verification of Seismic Performance

10.5.2.1 Concept

According to the Japanese seismic design specifications for highway bridges (Japan Road Association, 2002b), required seismic performance of piers has to be ensured by using two levels of design earthquake ground motions, referred to as Level 1 and Level 2 earthquakes. The Level 1 earthquake corresponds to a moderate earthquake with high probability of occurrence, whereas the Level 2 earthquake corresponds to the two types of major earthquakes with less probability of occurrence, that is, Type I and Type II. The Level 2-Type I earthquake is a plate boundary-type earthquake with a large magnitude and a long duration time like the 2011 Tohoku earthquake. The Level 2-Type II earthquake is an inland-type earthquake with a pulse-like record, such as the 1995 Kobe earthquake. Unidirectional design seismic acceleration waves are determined, based on the aforementioned earthquakes, and the required

TABLE 10.1 Seismic Performance Levels

		Post-earthquake Serviceability and Reparability	
Performance Level	Safety	Serviceability	Reparability
Seismic performance 1 (no essential damage)	Prevent unseating	Maintain serviceability	Minimal repair
Seismic performance 2 (limited damage)	Prevent unseating	Immediate restoration of serviceability is possible	Reparable in short term
Seismic performance 3 (no critical damage)	Prevent unseating	—	—

TABLE 10.2 Seismic Demands for Performance

		Level 2 Earthquake (Major Earthquake with Less Probability of Occurrence)	
Classification of Bridge Types	Level 1 Earthquake (Moderate Earthquake with High Probability of Occurrence)	Type I (Plate Boundary Type Earthquake with a Large Magnitude)	Type II (Inland Direct Strike Type Earthquake)
Bridge-Type A (bridges of standard importance)	Seismic performance 1	Seismic performance 3	Seismic performance 3
Bridge-Type B (bridges of high importance)	Seismic performance 1	Seismic performance 2	Seismic performance 2

performance of bridges is verified under the design unidirectional seismic waves in the longitudinal and transverse directions of bridges independently.

Under the Level 1 earthquake ground motion, the performance of piers has to be verified within the framework of the ASD by the so-called seismic coefficient method employing linear static analysis and no damage is permitted in piers. Under the Level 2 earthquake ground motions, damages are allowed in piers, depending on the importance of the superstructures supported by the piers. For the bridges of standard importance (Type A Bridge), no critical damage that causes unseating of the superstructures is allowed in piers. This is to ensure the safety of bridges. For bridges of high importance (Type B Bridge), damage is limited within a level that enables immediate postearthquake serviceability and short-term reparability. Therefore, postearthquake serviceability and reparability in addition to safety have to be verified for these bridges. The performance verification under the Level 2 earthquake is made based on the response obtained by nonlinear dynamic analysis. Three levels of seismic performances defined in terms of safety, postearthquake serviceability, and reparability are shown in Table 10.1. The seismic performances required for the aforementioned two types of bridges are summarized in Table 10.2. In what follows, the verification method for safety, postearthquake serviceability, and reparability are explained, focusing on the case of the Level 2 earthquake ground motions.

10.5.2.2 Verification for Safety

The safety of bridge piers is verified by the condition that the average value of the dynamic responses of piers under Level 2 earthquake ground motions is within the specified allowable value. As the dynamic response of the piers, either the sway displacement of the piers or the curvature of columns in the piers is used for safety verification. For the respective quantities, allowable sway displacement δ_a and allowable curvature ϕ_a are specified.

The allowable sway displacement δ_a is defined as an ultimate displacement δ_u at the peak of an envelope curve of the hysteretic horizontal force–horizontal displacement (Figure 10.13a). This hystretic relation is obtained by a displacement-controlled alternate loading with increasing amplitude. The reason why the peak force point is selected as an ultimate point to evaluate the allowable displacement δ_a is that the peak point corresponds to transition point from stability state to instability state. Since δ_u is not so much

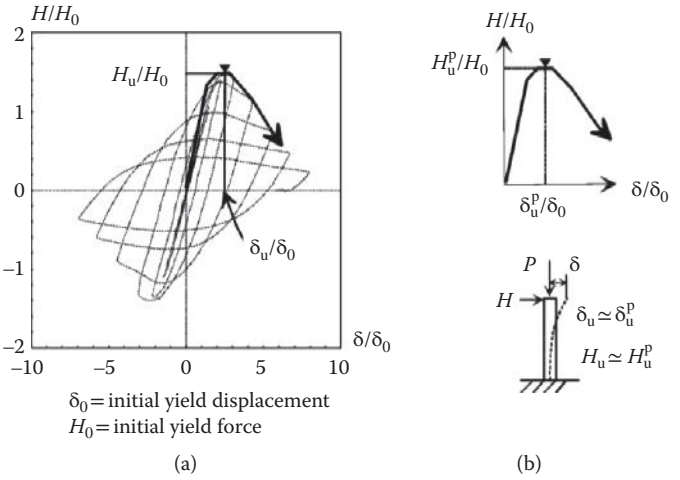

FIGURE 10.13 Definition of allowable displacement and its calculation by pushover analysis: (a) Cyclic loading experiment; (b) Pushover analysis.

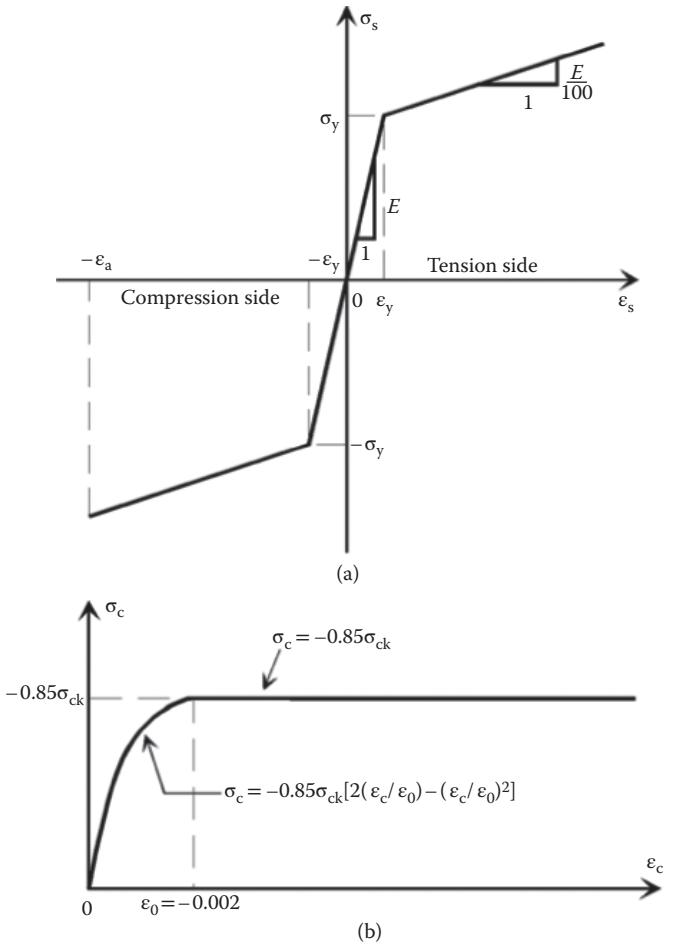

FIGURE 10.14 Stress–strain relations for steel and in-filled concrete: (a) Stress-stain curve of steel; (b) Stress–strain curve of concrete.

influenced by load history, δ_u can be approximated by δ_u^p that is identified as a displacement at the peak of horizontal force–horizontal displacement curve (Figure 10.13b) obtained by the pushover analysis.

In the current design, the responsive sway displacement δ of the piers is calculated by the so-called $M-\phi$ model. The $M-\phi$ model is formulated under the Bernoulli–Euler beam assumption, based on the stress–strain relations for steel and concrete shown in Figure 10.14a and b. Concrete is assumed not to resist tensile stress. An allowable curvature of ϕ_a is determined by the pushover analysis as a curvature when the extreme fiber strain evaluated on the compression side of the steel cross section of the column reaches an allowable strain ε_a specified in the seismic design specifications. Bending moment at $\phi = \phi_a$ is referred to as allowable bending moment, denoted as M_a. Details of ε_a are explained later in this section. The allowable sway displacement δ_a of the piers is identified by the pushover analysis as a sway displacement when the curvature ϕ of the column reaches the allowable curvature ϕ_a.

In the seismic design specifications, the allowable strain ε_a normalized by the yield strain ε_y is defined below for the steel columns of hollow steel piers and CFT piers classified according to the shape of cross sections.

(Thin-walled hollow steel piers)

Rectangular steel cross section:

$$\frac{\varepsilon_a}{\varepsilon_y} = \left[\frac{\left(1.58 - \frac{P}{P_y}\right)^{3.16} \times (1.68 - R_R)^{2.48} \times (0.65 - R_F)^{0.41} \times \left\{ 23.87 - \frac{l_{ef}}{(b_f + b_w)} \right\}^{2.9} \times \left\{ 2\alpha \Big/ \left(1 + b_w / b_f\right) \right\}^{0.3}}{2500\left(P/P_y + 1.0\right) \times \left(b_w / b_f\right)^{0.17}} + 0.5 \right] \tag{10.28}$$

$$\text{Circular steel cross section: } \varepsilon_a/\varepsilon_y = 20 - 140R_t \tag{10.29}$$

(CFT piers)

$$\text{Rectangular steel cross section: } \varepsilon_a/\varepsilon_y = 7 \tag{10.30}$$

$$\text{Circular steel cross section: } \varepsilon_a/\varepsilon_y = 5 \tag{10.31}$$

The above formulas, to evaluate the allowable strain ε_a, were empirically determined by curve-fitting the allowable strain data experimentally obtained for various types of pier specimens. In the experiment, the allowable strain ε_a is calculated by the $M-\phi$ column model as an extreme fiber strain on the compression side of the column cross section when the horizontal displacement of the $M-\phi$ column model reaches the allowable displacement δ_a obtained in the alternate loading test (Figure 10.13d). It

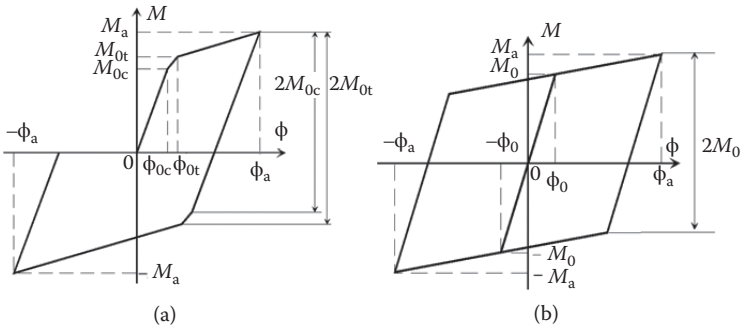

FIGURE 10.15 Hysteretic $M-\phi$ models for thin-walled steel and CFT columns: (a) thin-walled circular steel column; (b) thin-walled rectangular steel column and CFT column.

should be noted that the use of Equations 10.28 through 10.31 are limited to the hollow steel piers or the CFT piers that satisfy the parameter limitations shown in Sections 10.5.1.1 through 10.5.1.3.

The response sway displacement or the response curvature of the columns in the steel piers under the Level 2 earthquake ground motions is calculated by the dynamic time-history analysis, using the M–ϕ model. The constitutive bending moment–curvature (M–ϕ) relation in this model is represented by the kinematic hardening model. The skeleton curves for thin-walled circular hollow columns are expressed by a tri-linear curve, shown in Figure 10.15a, while those for the thin-walled rectangular hollow columns and CFT columns are expressed by a bilinear curve, shown in Figure 10.15b. In Figure 10.15a, (M_{0c}, ϕ_{0c}) denotes a point when an extreme fiber strain at the middle surface of the thin-walled steel sections reaches the yield point on the compression side. (M_{0t}, ϕ_{0t}) denotes a similar yield point on the tension side. In Figure 10.15b, (M_0, ϕ_0) is determined as a point when an extreme fiber strain at the middle surface of the thin-walled steel cross sections first reaches the yield point either on the compression side or on the tension side.

The safety of piers is verified by checking that either the response displacement or the response curvature under the Level 2 earthquake ground motions is within the corresponding allowable value.

In addition to the displacement check or the curvature check mentioned above, it is recommended to carry out an approximate strength check for the allowable horizontal force H_a of the piers by the following equation.

$$H_a = M_a/h_F \geq 0.4c_z(W_U + 0.5W_P) \tag{10.32}$$

where M_a = allowable bending moment at the bottom section of a column (Section 10.5.2.2), h_F = height measured from the bottom of the column to the acting point of the resultant horizontal seismic inertia force in a superstructure, c_z = area modification factor that takes a value ranging from 0.7 to 1.0, depending on the frequency of major earthquake occurrence in the corresponding area, W_U = weight of a superstructure supported by the pier, and W_P = weight of the pier.

The strength check by Equation 10.32 is intended to prevent the strength of piers from becoming small by the current deformation check method.

10.5.2.3 Verification for Postearthquake Serviceability and Reparability

Postearthquake serviceability and reparability corresponding to the seismic performance 2 defined in Table 10.1 are verified by the condition that the residual horizontal displacement δ_R of a pier at the height of h_F is smaller than $h_F/100$, where h_F is the height measured from the upper base plate to the point where the resultant horizontal seismic inertia force of a superstructure acts. δ_R is approximately estimated by the following formula, based on the maximum displacement of the M–ϕ pier model obtained by the dynamic response analysis under the Level 2 earthquake ground motions.

$$\delta_R = C_R(\delta_m/\delta_0 - 1)(1-r)\delta_0 \tag{10.33}$$

where δ_m = maximum response horizontal displacement of a pier under the Level 2 earthquake ground motions, δ_0 = yield displacement when curvature of a column first reaches ϕ_{0c} for the thin-walled hollow rectangular steel pier and the CFT pier or ϕ_0 for the thin-walled hollow circular pier. $C_R = 0.45$ for both the thin-walled hollow steel pier and the CFT pier, $r = 0.2$ for the hollow pier, and $r = 0.1$ for the CFT pier.

10.5.2.4 Future Revisions Needed

There still remains some room to be revised in the current seismic design for thin-walled steel and CFT piers. Herein, two points are discussed. One is on the improvement of the accuracy of the safety verification method by placing more proper emphasis on the strength-based method. The other is on an advanced seismic design considering the coupling of the more realistic multidirectional components of regional earthquake ground motions predicted for earthquake scenarios.

The current safety verification method for Level 2 earthquakes lays emphasis more on the deformation-based method than on the strength-based method. That is, the safety of a pier is examined whether the response sway displacement of a pier or the response curvature of a column in a pier calculated by nonlinear dynamic analysis is within an allowable value. The allowable sway displacement and the allowable curvature is taken as the values at the peak force point of the envelope of a hysteretic horizontal force–sway displacement curve of the pier obtained under an alternative horizontal load as shown in Figure 10.13a. These allowable values are usually calculated by the pushover analysis, assuming that the displacement and curvature up to the peak horizontal force point are less influenced by load history. However, in reality, it often happens that displacement and curvature up to the peak horizontal force point are strongly influenced by the load histories applied to the pier. Therefore, the pushover analysis sometimes overestimates or underestimates the allowable sway displacement and curvature improperly. In contrast, the peak value of the horizontal force, that is, the strength of a pier is less influenced by load history. This is because the material strength of steel is almost constant irrespective of the load history. So far as the allowable limit state of the thin-walled steel piers is defined by the peak point of the horizontal force–sway displacement curves as in the current seismic design, it will be more appropriate to introduce some rational strength-based method into their safety verification in addition to the conventional deformation-based method. Later in Section 10.6.4, it will be demonstrated that the accuracy of the strength-based method is superior specifically in the safety verification under bidirectional horizontal seismic accelerations.

Recent development of earthquake engineering has made it possible to predict multidirectional components of regional earthquake ground motions by numerical simulation, considering earthquake scenarios. As a result, the safety of important bridges such as elevated highway bridges in urban areas is often required to be verified under the coupling of these multidirectional components of earthquake ground motions. However, in the current seismic design specifications for the Level 2 earthquake, the performance of piers is checked for the unidirectional horizontal seismic accelerations applied in the longitudinal and the transverse directions of bridges independently. In this way, the allowable limit states of piers specified in the current design code are intended for the case under unidirectional seismic accelerations and these limit states cannot be directly applied to the safety check under the coupling of multidirectional components of seismic accelerations. Therefore, it is an urgent necessity to revise the current seismic design code to specify the allowable limit states of piers under the coupling of multidirectional earthquake ground motions. A recent research achievement concerning the safety verification under the coupling of multidirectional seismic accelerations is explained in Section 10.6.4.

10.6 Recent Research Achievements Toward an Advanced Seismic Design

10.6.1 General

Extensive efforts have been made to establish an advanced seismic design of elevated highway bridges since the 1995 Kobe earthquake. Unfortunately, considerable part of the research achievements have not yet been directly reflected on the current seismic design specifications. Herein, some recent research achievements for thin-walled steel and CFT piers are outlined. First, the recent development of advanced and accurate numerical models for thin-walled steel piers and CFT piers are explained along with the related experiments. Second, the effectiveness of the advanced numerical models is demonstrated by showing how the controversial issue regarding the upgrading mechanism of CFT piers was solved by the analysis using the advanced model. Third, a criterion to identify the ultimate state of piers under bidirectional horizontal ground motions is discussed by using the advanced numerical models. This is to propose an advanced seismic design method that lays more emphasis on the strength check, in view

of the application to the seismic design considering the coupling of the multidirectional strong ground motions predicted by scenario earthquakes.

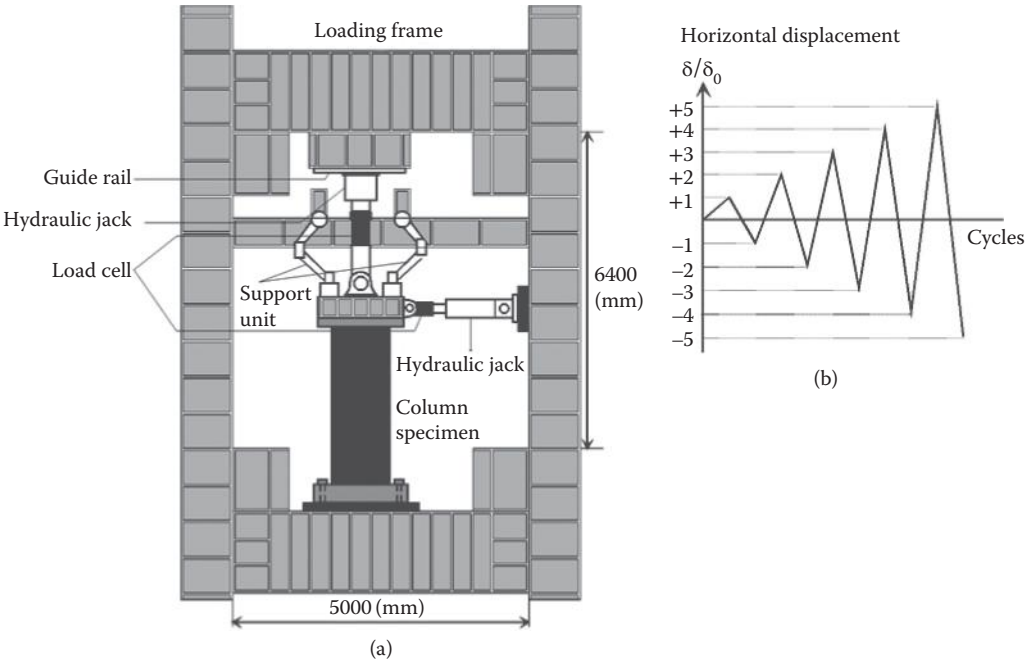

FIGURE 10.16 Unidirectional cyclic loading experiment on columns: (a) Cyclic loading system; (b) Uni-directional loading pattern. (From Public Work Research Institute of Japan, *Report of cooperative research on limit state seismic design for bridge piers*, I-VIII and summary, Public Work Research Institute of Japan, 1997–2000.)

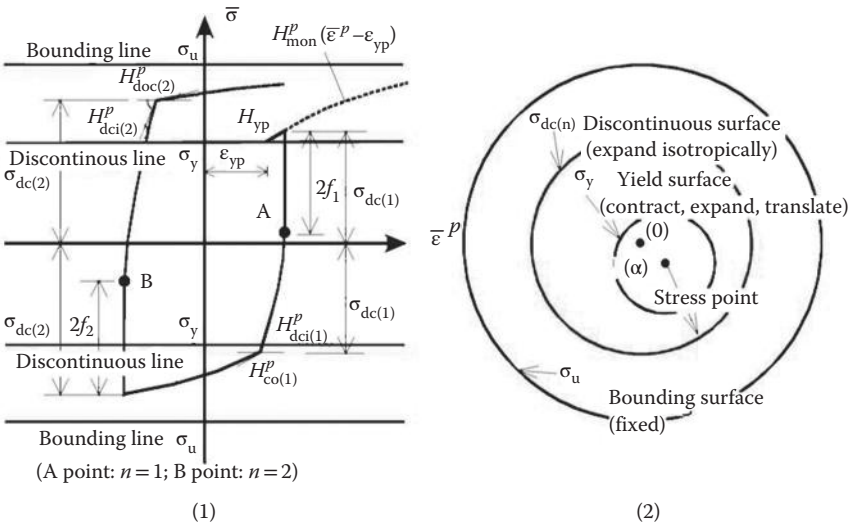

FIGURE 10.17 3-surface model for structural steel. (Adapted from Goto, Y. et al., *J. Struct. Eng.*, ASCE, 124(11), 1290–1301, 1998; Goto, Y. et al., *J. Struct. Eng.*, ASCE, 132(10), 1621–1631, 2006.)

10.6.2 Seismic Experiment and Development of Advanced Seismic Analysis

Immediately after the 1995 Kobe earthquake, a lot of unidirectional cyclic loading experiments shown in Figure 10.16 were carried out on 1/3 scale models to assess the strength and ductility of thin-walled hollow steel and CFT piers in view of the damages caused by the earthquake (Public Work Research Institute of Japan, 1997–2000). From these experiments, it was observed that the ultimate behavior of thin-walled hollow steel piers is governed by the behavior of columns, such as the local buckling of individual plate elements or shell elements and the cyclic metal plasticity of material steel. Based on these experimental observations, accurate versatile numerical models (Goto et al., 1998; Usami and Ge, 1998) were developed. These numerical models are FE models expressed by geometrically and materially nonlinear shell elements. Specifically, the FE models include accurate cyclic metal plasticity models, such as

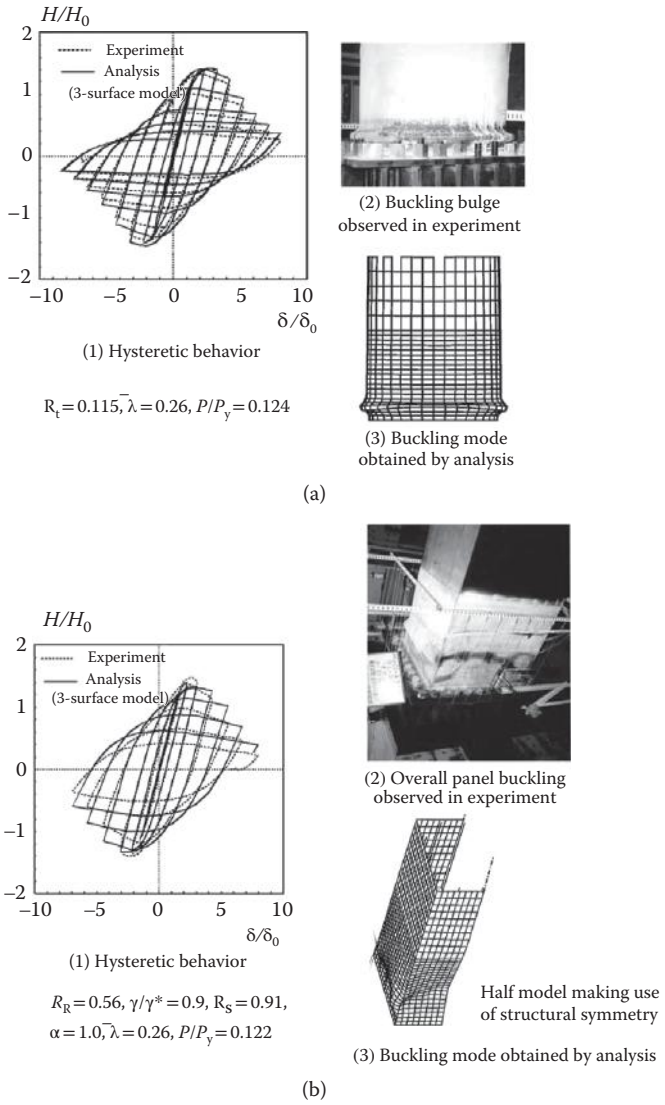

FIGURE 10.18 Behavior of thin-walled steel columns under unidirectional cyclic loading: (a) Circular steel column specimen (NO.8); (b) Square steel column specimen (NO.2).

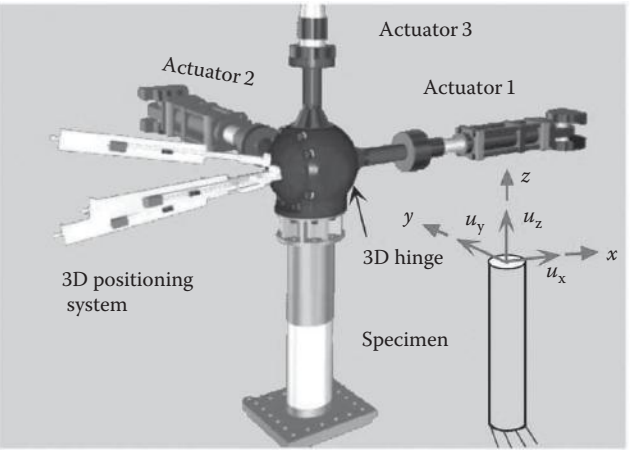

FIGURE 10.19 3D loading and measuring system. (Courtesy of Nagoya Institute of Technology, Japan.)

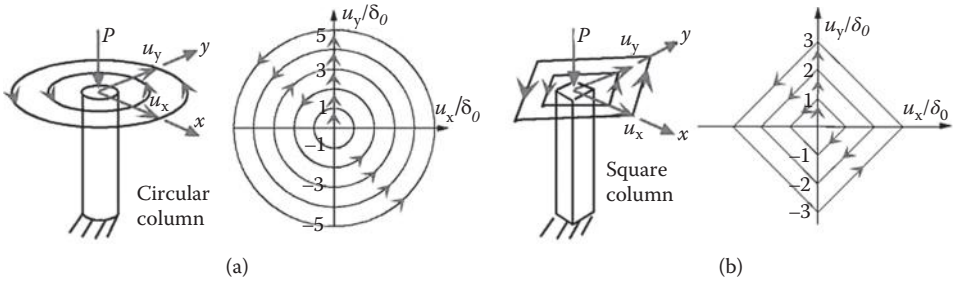

FIGURE 10.20 Bidirectional loading patterns: (a) Circular loading for circular column; (b) Diamond loading for square column.

the 3-surface model (Goto et al., 1998, 2006) and the modified 2-surface model (Shen et al., 1995). The 3-surface model was developed primarily for steel columns where equivalent plastic strains often exceed 100% under large alternate loading. This constitutive model precisely takes into account the important characteristic of cyclic steel plasticity such as existence of yield plateau, contraction or expansion of elastic range, and cyclic strain hardening. To express these characteristics, the 3-surface model uses three surfaces, that is, a yield surface, a discontinuous surface, and a bounding surface (see Figure 10.17). The ultimate hysteretic behavior and deformation of thin-walled steel piers can be simulated accurately by the FE models with the 3-surface constitutive model (see Figure 10.18).

In view of the importance to examine the more realistic ultimate behavior of columns under the coupling of two horizontal seismic accelerations, fully computerized 3D loading system (Figure 10.19) was developed in 2002 at Nagoya Institute of Technology in Japan (Obata and Goto, 2002, 2007). With this loading system, a bidirectional cyclic loading test and a bidirectional pseudo-dynamic test were conducted on thin-walled steel columns. By the calibration based on these bidirectional experimental results, the 3-surface cyclic plasticity model for steel was further improved (Goto et al., 2006). As a result, the bidirectional hysteretic behavior and time-history responses of thin-walled steel columns have become able to be analyzed accurately by the FE models (Goto et al., 2006, 2007, 2009a, 2009b). The computed hysteretic behaviors of circular and rectangular thin-walled steel piers under the bidirectional loading patterns shown in Figure 10.20 are compared to the corresponding experimental results in Figures 10.21 and 10.22.

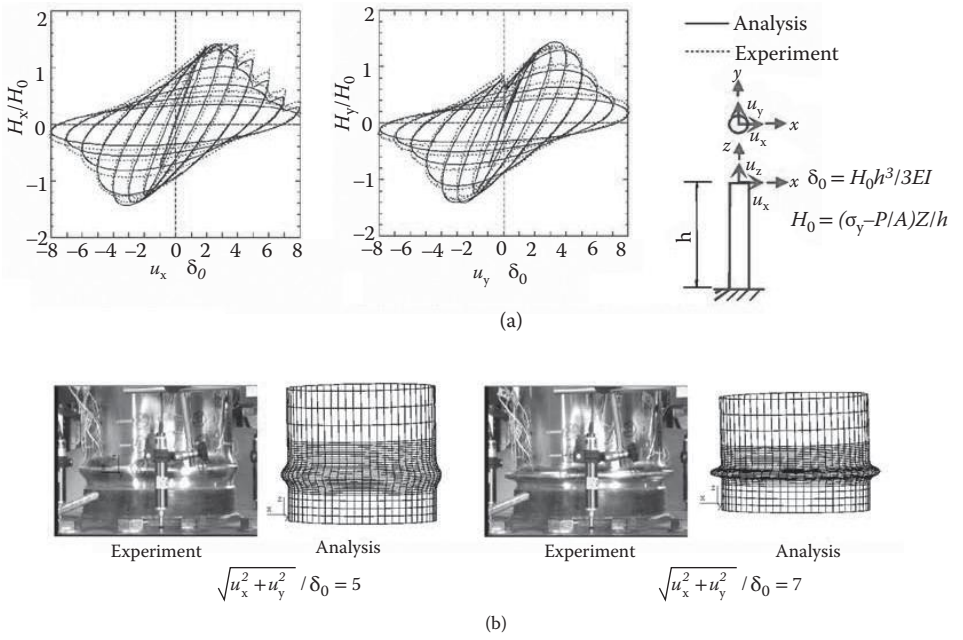

FIGURE 10.21 Behavior of thin-walled circular column under circular loading: (a) Hysteretic behaviour in x and y direction (PT-4.5-3); (b) Local buckling at lower part of column (PT-4.5-3).

Owing to the numerical difficulty caused by the complicated interaction between a thin-walled steel tube and an in-filled concrete under cyclic loading, most of the numerical models presented so far for CFT columns are simplified models based on the beam theories referred to as moment–curvature model (Japan Road Association, 2002b), concentrated plasticity model, and distributed plasticity model (Susantha et al., 2001). These models, however, cannot directly take into account the cyclic local buckling behavior of steel tube, the interface action between steel tube and in-filled concrete, and the confinement of concrete infill. In order to improve these problems associated with the existing models, an advanced numerical model for CFT columns has been developed quite recently (Goto et al., 2010a, 2010b, 2011, 2013). In this model, the outer steel tube and the in-filled concrete are represented by nonlinear shell and solid elements, respectively. To express the material behavior, the 3-surface cyclic plasticity model used for steel tube, whereas the concrete damaged plasticity model (Lee and Fenves, 1998) combined with the discrete crack model (Chen, 1982) is used for in-filled concrete. Contact with friction behavior based on the Coulomb model is considered for the interface modeling between steel tube and in-filled concrete. The above numerical model for CFT piers can directly take into account the local buckling behavior of steel tube, the steel-concrete interface interaction, and the confinement of concrete infill. As a result, the pinching hysteretic curve characteristic to CFT columns was analyzed accurately for the first time by the proposed numerical model as shown in Figure 10.23. Furthermore, the analysis with the advanced model succeeded in identifying the mechanism of how the ductility of CFT piers is enhanced. This mechanism will be explained later in Sections 10.6.3.

The pseudo dynamic test (Obata and Goto, 2007; Goto et al., 2009a, 2009b) may be used as an economical alternative to the shaking table test. However, it is hard to evaluate quantitatively the errors included in the pseudo-dynamic test, such as those existent in the control of actuators and those caused by the frictions at the pinned connections of actuators. Furthermore, dynamic effects such as the strain rate sensitivity of material cannot be appropriately considered in the pseudo-dynamic test. Therefore, a shaking table

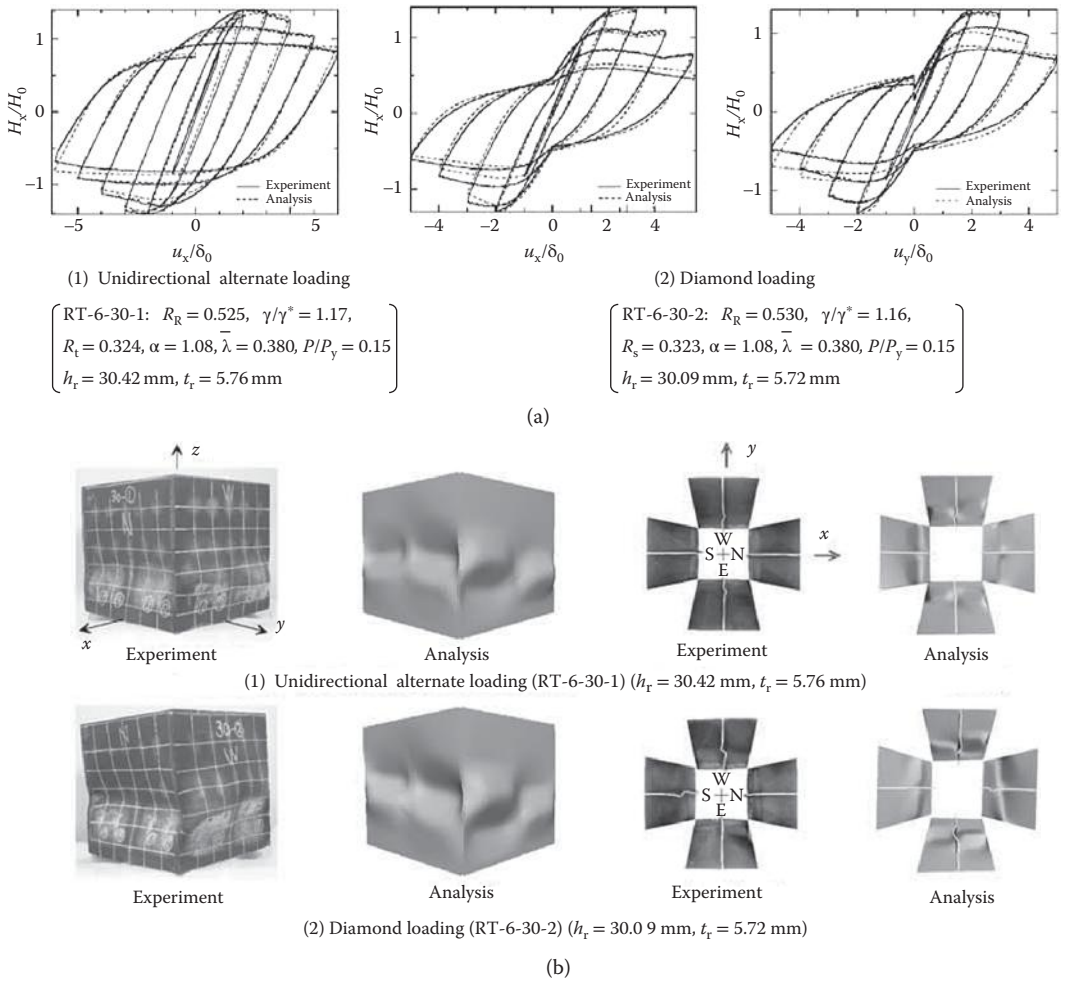

FIGURE 10.22 Behavior of thin-walled square columns under diamond loading: (a) Hysteretic behavior; (b) Buckling deformation at lower part of columns (Final stage).

test was recently conducted by the author in cooperation with Tongji University in China to examine the dynamic behavior of steel and CFT columns with circular cross-sections (see Figure 10.24) (Osada et al., 2010, 2011; Ebisawa et al., 2011; Goto et al., 2013). In this test, 1/8 scale single pier specimens with a mass fixed at the top were used. The steel tubes utilized for the thin-walled steel column and CFT column specimens are the same in terms of material and geometry. The in-filled concrete of the CFT column specimens is cast up to the location of the horizontal diaphragm.

An input acceleration wave for the shaking table test was created, based on the longitudinal (LG)-component of Tsugaru observed at Tsugaru Bridge during the 1983 Nihonkai-chubu earthquake. First, the LG-component of Tsugaru was first magnified by 300%. The axial force ratio P/P_y of the columns in the scaled pier specimens under dead load is the same as that of the actual piers. Therefore, the natural period of the 1/8 scale specimens is $\sqrt{1/8}$ of the actual piers. Then, second, the time axis of the input acceleration component was shortened by multiplying $\sqrt{1/8}$, such that the magnitude of the response acceleration spectrum of the scaled specimens corresponds with that of the actual piers under the LG component of 300% Tsugaru.

The test results for the hollow steel and CFT column specimens under the horizontal acceleration are compared in Figure 10.25 with the numerical results in terms of the time history responses of the

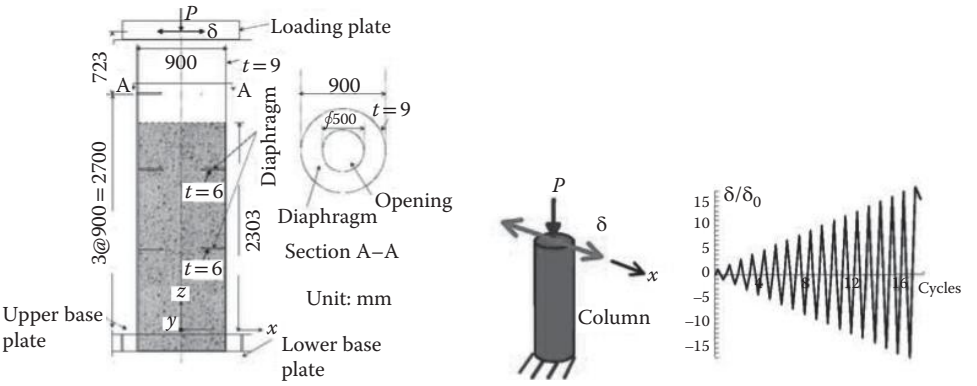

$R_t = 0.123$, $\bar{\lambda} = 0.268$

$\sigma_c = 27.93$MPa $(P/\sigma_y A_s = 0.114)$

$\sigma_c = 21.46$MPa $(P/\sigma_y A_s = 0.199)$

(a)

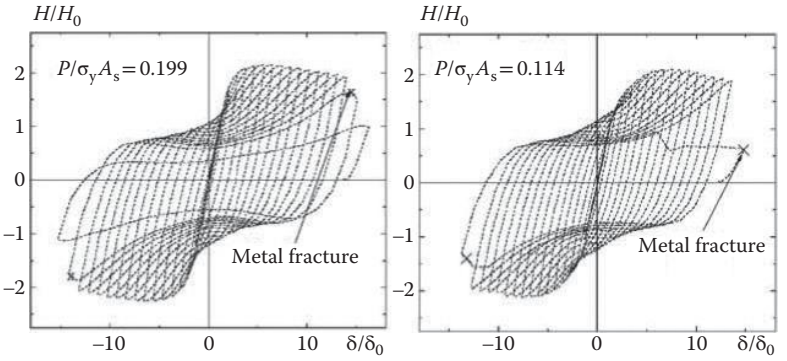

(b)

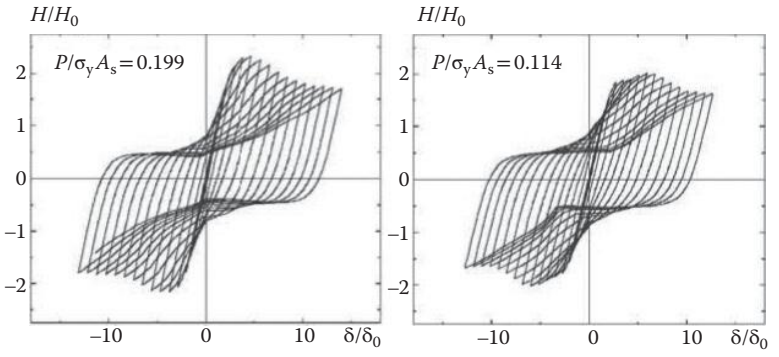

(c)

FIGURE 10.23 Behavior of CFT columns under unidirectional alternate loading: (a) Specimen and unidirectional alternate loading pattern; (b) Experiment; (c) Analysis.

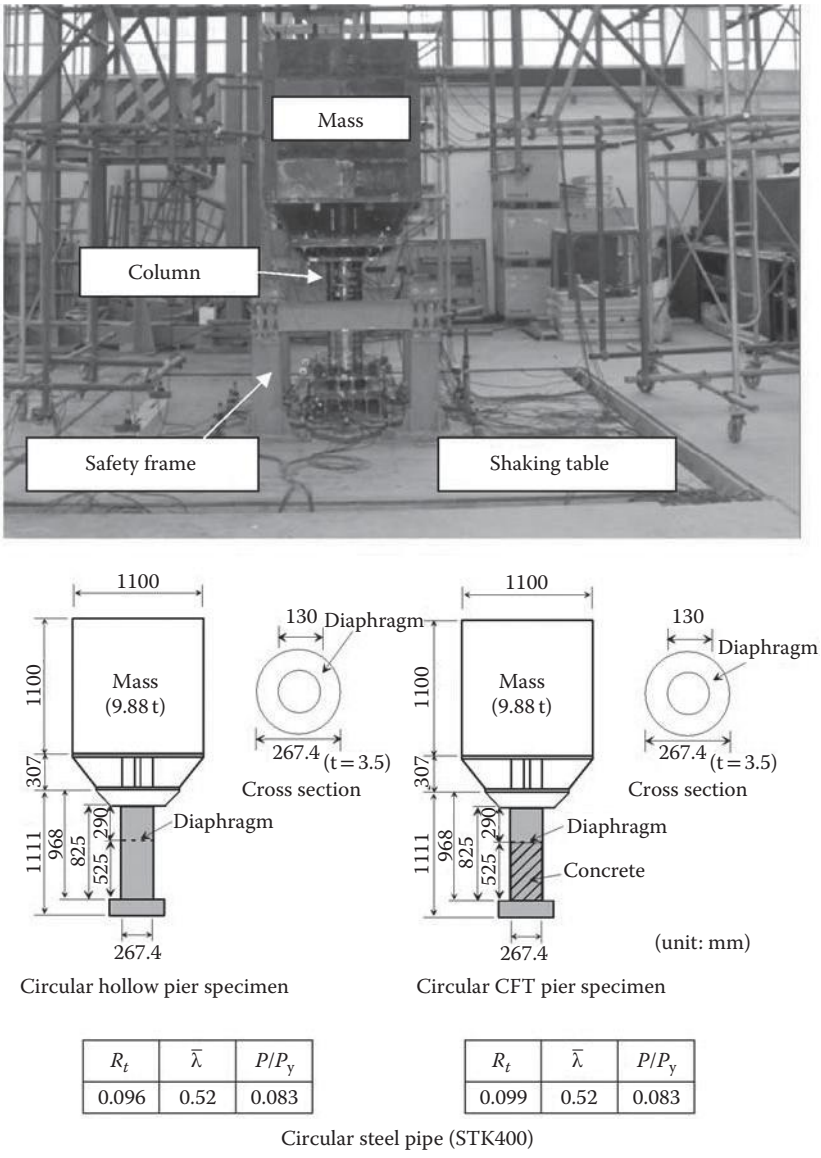

R_t	$\bar{\lambda}$	P/P_y
0.096	0.52	0.083

R_t	$\bar{\lambda}$	P/P_y
0.099	0.52	0.083

Circular steel pipe (STK400)

FIGURE 10.24 Shaking table test on thin-walled steel and CFT columns. (Courtesy of Tongji University, China.)

horizontal displacement component and the horizontal restoring force component at the top of the column model. It should be noted that the hollow column collapsed in the experiment, whereas the damage of the CFT column specimen was very small. Therefore, 450% of the LG-component of Tsugaru was again applied to the specimen after the 300% of Tsugaru had been applied. As can be seen from Figure 10.25, there is a good coincidence between the analytical and experimental results in spite of the fact that the numerical model ignores the effect of the strain rate sensitivity in materials. This is probably because high strain rate occurs in a very limited area of the column specimen and it has only a small effect on the hysteretic behavior. The above result implies that strain rate sensitivity can be ignored in the seismic analysis of circular steel columns.

For comparison of the seismic behavior between the hollow steel column and the CFT column, the progress of local buckling deformations of the steel tube and the time-history responses of the oscillation center of sway displacement at the top of column specimens are shown in Figures 10.26 and 10.27,

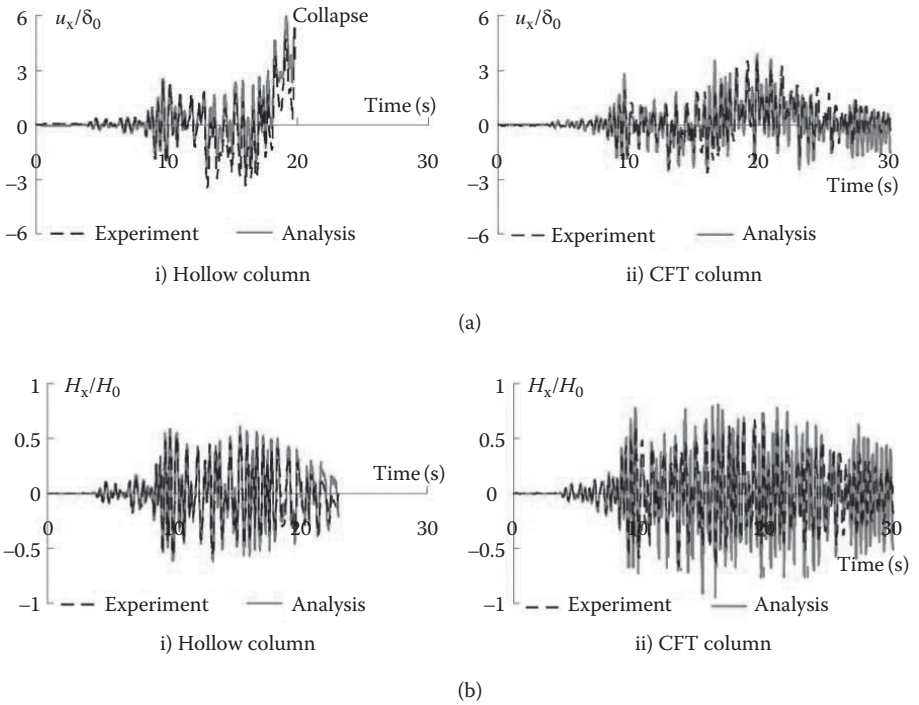

FIGURE 10.25 Time history responses of thin-walled circular steel and CFT column specimens under 300% of LG component of Tsugaru: (a) Time history responses of horizontal displacement component; (b) Time history responses of horizontal restoring force component.

respectively. It should be noted from the results of the CFT column specimen in Figure 10.26 that the local buckling deformation of steel tube under 450% of the LG-component of Tsugaru was illustrated such that the change of local buckling deformation pattern can be more clearly identified. In Figure 10.26, the results obtained by the FE models are also shown. It is observed equally for the results of the experiment and analysis shown in Figure 10.26 that the local buckling deformation of the hollow column specimen monotonically increases on one side of the steel tube and this local buckling deformation leads to the collapse of the column. In contrast, the local buckling deformation of the CFT column specimen that once appeared on one side of the steel tube disappeared and, then, it appeared on the other side of the column at the same time. In this way, the repetition of the appearance and the disappearance of local bucking deformations occurred on both sides of the steel tube under seismic acceleration. As a result, the local buckling deformation of the CFT column increased very slowly, compared with that of the hollow column in spite of the fact that the input acceleration wave with a higher magnitude was applied to the CFT column. Regarding the residual sway displacement, the plastic sway displacement of the CFT column specimen that occurred in the positive direction during the principal part of the input acceleration gradually decreased during the subsequent input acceleration with relatively small amplitude. Finally, the residual sway displacement of the CFT column specimen became very small (see Figure 10.27). The above behavior of the CFT column specimen to reduce the residual displacement is different from that of the so-called self-centering columns (Palermo et al., 2007) in that the oscillation center for the latter case always remains at the original location. In the present shaking table test, there may be some possibility that the residual displacement of the CFT column specimen happened to be reduced by the property of the input acceleration wave. However, it is shown by numerical analysis that the residual displacements of the CFT column specimen were reduced similarly under different kind of seismic accelerations. Therefore, it is considered that the reduction in the residual displacement of the CFT column specimen is affected to a certain extent by the local buckling restraining mechanism where the progress of the local

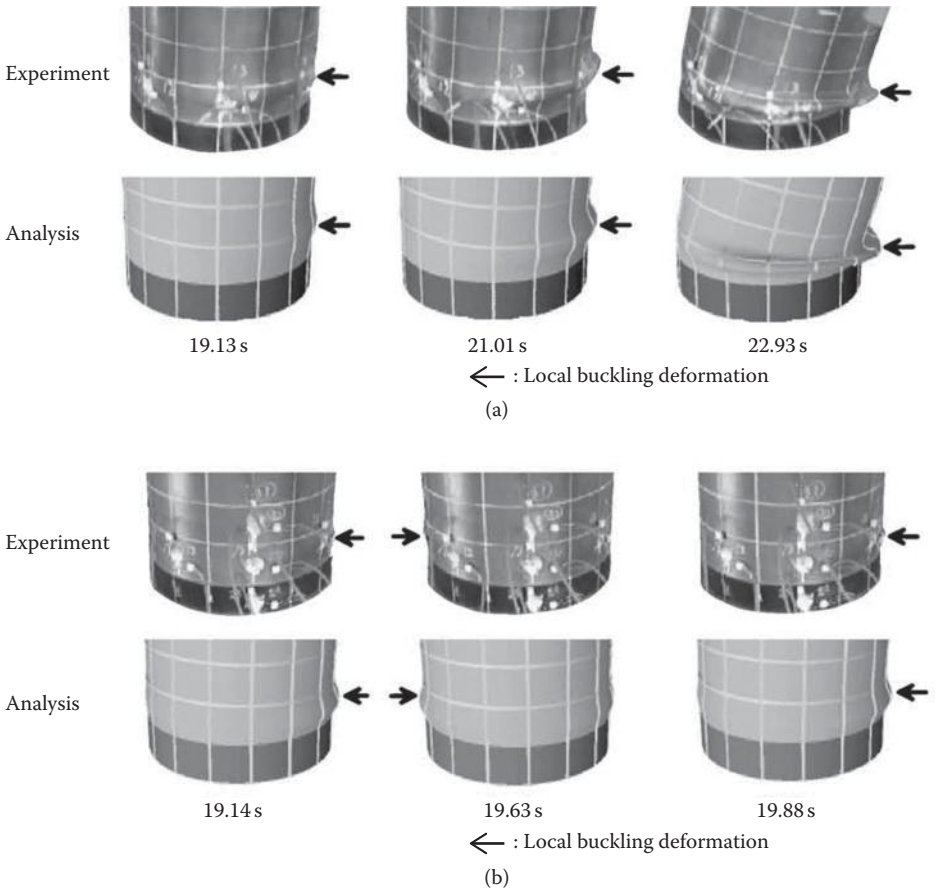

FIGURE 10.26 Progress and restoration of local buckling deformation of steel tubes of hollow and CFT columns under unidirectional horizontal seismic acceleration: (a) Hollow column specimen under 300% of LG component of Tsugaru; (b) CFT column specimen under 450% of LG component of Tsugaru.

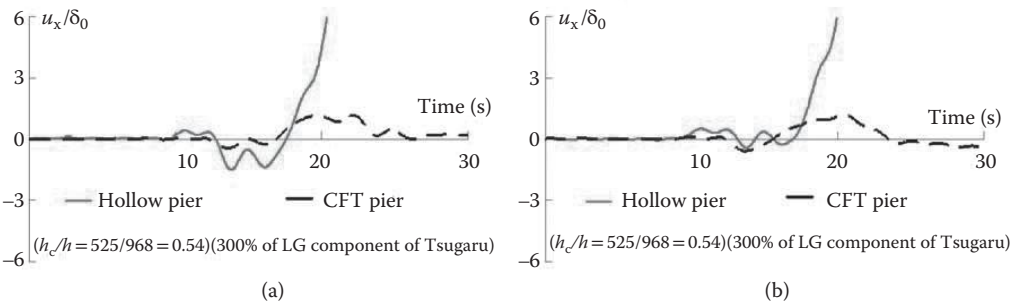

FIGURE 10.27 Time-history responses of oscillation center of sway displacements at the top of CFT and hollow circular column specimens under 300% of LG acceleration component of Tsugaru: (a) Experiment; (b) Analysis.

buckling deformation is restrained under the loading, unloading, and reverse loading process because of the seismic acceleration (Goto et al., 2012; Goto et al., 2013). This local buckling restoring mechanism of CFT columns will be explained later in Section 10.6.3, based on the numerical results.

It can also be seen from Figures 10.25, 10.26 and 10.27 that the proposed numerical model well simulates the nonlinear dynamic behavior of the steel and CFT column specimens under seismic accelerations. It

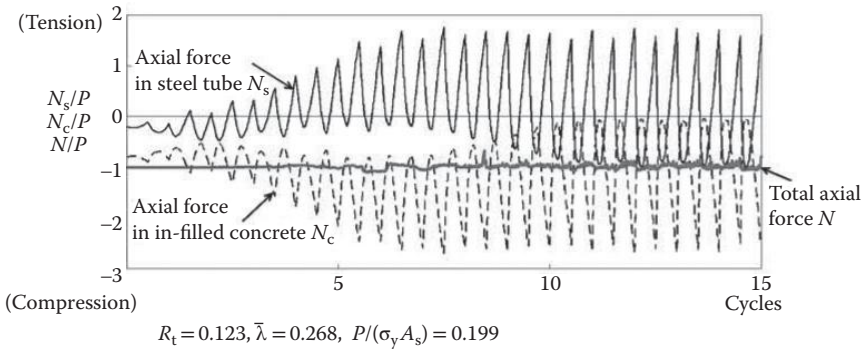

FIGURE 10.28 Axial force sharing ratio between steel tube and in-filled concrete of circular CFT column under unidirectional alternate horizontal loading.

is demonstrated in this section that the numerical models developed for steel and CFT columns are very accurate. However, it is still costly and time-consuming to use them for ordinary seismic design. At present, these models may be used for accurate numerical simulations as an alternative to experiments. The models explained herein, however, will be conveniently used in the advanced seismic design in the next generation where the numerical simulation of peta-scale will be common.

10.6.3 Assessment of Upgraded Performance of CFT Piers by Advanced Model

It is well known from experimental observations that the strength, ductility, and energy dissipation capacity of thin-walled steel piers are considerably improved by filling with concrete the internal hollow space of steel columns with diaphragms (Public Work Research Institute of Japan, 1997–2000). The strength enhancement of CFT piers is mainly because of the composite action of steel and concrete in columns, whereas their ductility and energy dissipation capacity are enhanced by the local buckling restraint in the outer steel tube of columns. However, there has been an argument regarding the mechanism of how the local buckling of the outer tube is restrained. Some researchers insisted that the in-filled concrete resists against the inward local buckling deformation of the steel tube and this will enhance the local buckling strength (Kitada, 1998). However, from the experimental observations, others opposed to the above insistence by saying that the local buckling mode of hollow circular tube is a so-called elephant foot bulge mostly with outward deformation as shown in Figure 10.6, and that the resistance of the in-filled concrete against the outward buckling deformation is less effective. Goto et al. (2010a) proposed a hypothesis that a main cause of the local buckling restraint is attributed to the phenomenon that the axial force on the steel tube gradually changes from compression to tension under alternate loading and this tensile force restrain the progress of the local buckling deformation. To examine this hypothesis, the axial force sharing ratio between steel tube and in-filled concrete at the column base was calculated by using the advanced numerical model (Goto et al., 2010a, 2010b, 2013) for circular and rectangular CFT columns under alternate unidirectional horizontal displacement with increasing amplitude applied at the top of the columns. Focusing on the circular CFT column under the compressive vertical force of $P = 0.199\sigma_y A_s$ (Figure 10.23), it is shown in Figure 10.28 how the axial force sharing ratio changes with the increase of loading cycles. In this figure, the total axial force of the CFT column is denoted as N, whereas the axial forces acting on the in-filled concrete and steel tube are denoted as N_c and N_s, respectively. Theoretically, the sum of N_c and N_s coincides with N. At the column base, N is equal to the constant vertical compressive force $-P = -0.199\sigma_y A_s$, N_c, N_s, and N are normalized by P in Figure 10.28. As can be seen from Figure 10.28, at the initial stage, both the concrete core and steel tube carry compressive forces, the sum of which is equal to $-P$. However, with the increase in the cycles of the alternating horizontal displacement, the center of the oscillating axial force N_s in steel tube gradually changes from compression

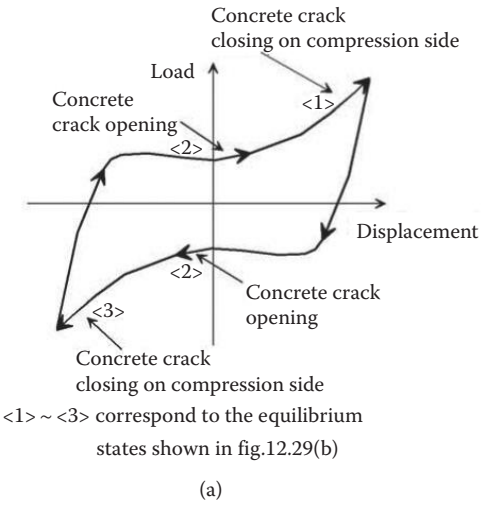

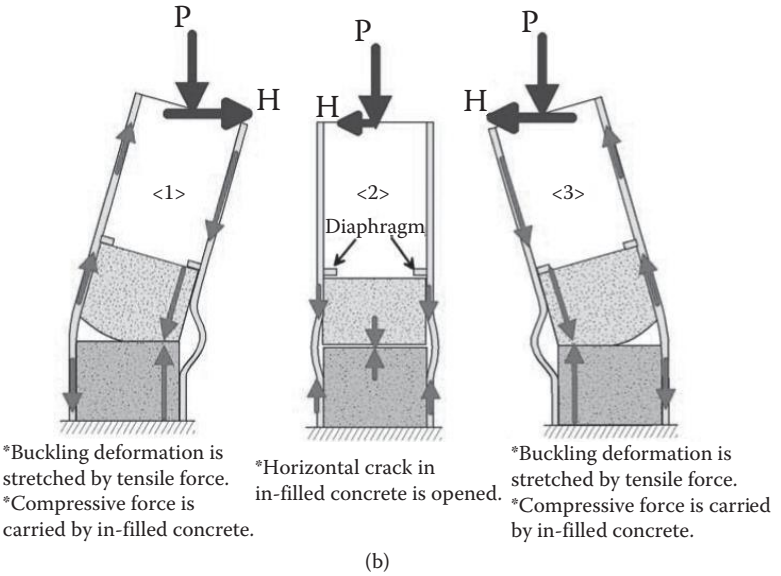

FIGURE 10.29 Mechanism of buckling restraint and pinching hysteretic behavior of CFT column: (a) Typical pinching hysteretic curve; (b) Force distribution in steel tube and in-filled concrete.

to tension and the maximum tension value of N_s amounts to 170% of P. However, the center of the oscillating axial force N_c acting on the in-filled concrete moves further to the compressive direction and the maximum value of N_c amounts to 270% of $-P$. However, the relation of $N_c + N_s = -P$ is maintained. In this way, thin-walled CFT columns under alternate loading with increasing horizontal displacement amplitude exhibit a remarkable phenomenon that the center of the oscillating axial force N_s in steel tube changes from compression to tension with the increase in loading cycles. Therefore, regarding the axial force N_s acting on steel tube, the magnitude of the maximum tensile force exceeds that of the compressive force. This mechanism is schematically explained in Figure 10.29, based on the calculated results by the advanced numerical model. According to Figure 10.29, local buckling first occurs in the steel tube and the compressive rigidity of the steel tube decreases. At the same time, dilatation occurs in the in-filled concrete at the compression side because of its plastification under alternate loading. Therefore, most part of the compressive force once carried by the steel tube is transferred by the diaphragm to the in-filled

concrete. The increased compressive force N_c acting on the in-filled concrete does not crush the concrete because the compressive strength of the in-filled concrete is enhanced by the confinement from the steel tube. On the other hand, the steel tube carries the tensile axial force that cannot be resisted by the in-filled concrete because of the horizontal cracks. Therefore, the magnitude of the tensile force that acts on the tension side of the steel tube section exceeds that of the compressive force under alternate loading and this increased tensile force stretches and restores to some extent the local buckling deformation that appeared once on the compression side of the steel tube at states <1> and <3>, as schematically shown in Figure 10.29.

From the above buckling restraining mechanism of CFT columns where the most part of the compressive axial force is carried by the confined in-filled concrete, the magnitude of the axial force ratio of $P/(\sigma_y A_s)$ is considered to less affect the local buckling deformation of the steel tube (Ghosh et al., 2011). This is different from hollow columns where large axial force accelerates the progress of the local buckling deformation and reduces the ductility of the columns under alternate horizontal load.

The advanced numerical model can also be used to explain the characteristic pinching hysteretic behavior of CFT columns shown in Figure 10.23. This behavior becomes obvious after the initiation of horizontal cracks in the in-filled concrete and the local buckling of the steel tube. When the horizontal displacement decreases in the unloading process from state <1> in Figure 10.29, the horizontal cracks closed in the compression side open because of the decrease in the compressive force of concrete at state <2>. As a result, the bending stiffness of the in-filled concrete is reduced and the slope of the hysteretic curve becomes smaller. However, when the displacement increases from <2> to <3> in the reverse direction, the horizontal cracks, once opened, close again on the compression side and the column regains its stiffness.

10.6.4 Safety Verification of Thin-Walled Hollow Steel Piers under Bidirectional Horizontal Seismic Accelerations

It is an urgent necessity to develop an advanced safety verification method for the multidirectional strong ground motions because there arise many requests nowadays to check the safety of important bridges under the multidirectional strong ground motions predicted by scenario earthquakes.

Among the multidirectional components of ground motions, the vertical component has only a limited effect on the seismic performance of elevated bridges except for the case where the magnitude of the vertical acceleration is extraordinarily large. This is because the resonance between the vertical ground motion and the flexural vibration of the bridge girders seldom occurs. The predominant period of vertical ground motion is much smaller than the period of lower order flexural vibration mode of girders. Therefore, it will be sufficient for practical purposes to consider just the coupling of bidirectional components of seismic horizontal ground motions in order to evaluate the ultimate states of bridge piers. Herein, a safety verification method presented by Goto et al. (2009a, 2009b) for thin-walled hollow steel columns is explained in some detail.

The conventional Japanese seismic design specifications for highway bridges (Japan Road Association, 2002b) adopt a criterion that the ultimate state of a column under unidirectional horizontal seismic acceleration is reached at the limit point of the horizontal restoring force-horizontal displacement curve, as explained in Section 10.5.2.2. This is because the limit point is a transition point from stability state to instability state. However, there is no such criterion to specify the ultimate state of a column under bidirectional seismic horizontal forces. Herein, a criterion is proposed as follows within the framework of the elastic-plastic stability theory such that the criterion under bidirectional forces is consistent with the conventional unidirectional criterion of limit load instability. The elastic-plastic stability theory classifies the equilibrium state of the column as stable, critical, or unstable according to whether the 2nd variation of the external work $\Delta^2 W$ defined by the following equation is positive, zero, or negative, respectively.

$$\Delta^2 W = \Delta H_x \Delta u_x + \Delta H_y \Delta u_y = \sqrt{\Delta H_x^2 + \Delta H_y^2}\sqrt{\Delta u_x^2 + \Delta u_y^2}\cos\theta \tag{10.34}$$

where $(\Delta u_x, \Delta u_y)$ denotes an arbitrary incremental horizontal displacement vector at the top of a column from the equilibrium state and $(\Delta H_x, \Delta H_y)$ is the resulting incremental horizontal restoring force vector

that acts at the top of the column; θ is an angle between these two incremental vectors. The ultimate state of the column under bidirectional seismic loads can be identified by a zero-crossing point of $\Delta^2 W$ from positive to negative. Needless to say, this identification method is also valid for a unidirectional load.

For design applications, the possibility of using two types of ultimate interaction curves is examined to express the ultimate state of thin-walled steel columns. One is an interaction curve expressed in terms of the two horizontal restoring force components at the top of the columns. The other is an interaction curve expressed by the two horizontal displacement components. These interaction curves are derived by the so-called pushover analysis. Circular columns exhibit homogenous behavior in the horizontal directions and the shape of the ultimate interaction curves is circular. Therefore, a pushover analysis in one direction is enough to identify the circular interaction curves. However, rectangular columns exhibit orthotropic behavior and the shape of the interaction curves is biaxially symmetric (Figure 10.30). This implies that pushover analyses in multidirections from 0 to 45° are necessary to identify the ultimate interaction curves. For practical applications, the ultimate interaction curves expressed in terms of horizontal restoring force components (H_x, H_y) and horizontal displacement components (u_x, u_y), respectively, at the top of columns are assumed to be expressed by the following equations.

$$\text{(Circular column)}\ (H_x / H_u^P)^2 + (H_y / H_u^P)^2 = 1 \tag{10.35}$$

$$(u_x / \delta_u^P)^2 + (u_y / \delta_u^P)^2 = 1 \tag{10.36}$$

$$\text{(Rectangular column)}\ \left|H_x / H_{xu}^P\right|^{\alpha_H} + \left|H_y / H_{yu}^P\right|^{\beta_H} = 1 \tag{10.37}$$

$$\left|u_x / \delta_{xu}^P\right|^{\alpha_u} + \left|u_y / \delta_{yu}^P\right|^{\beta_u} = 1 \tag{10.38}$$

where (δ_u^P, H_u^P) is the peak point of the horizontal force-horizontal displacement relation calculated by the pushover analysis for circular columns. $(\delta_{xu}^P, H_{xu}^P)$ and $(\delta_{yu}^P, H_{yu}^P)$ are the peak points obtained by the pushover analysis in the x and y directions, respectively, of rectangular columns. The x and y axes are

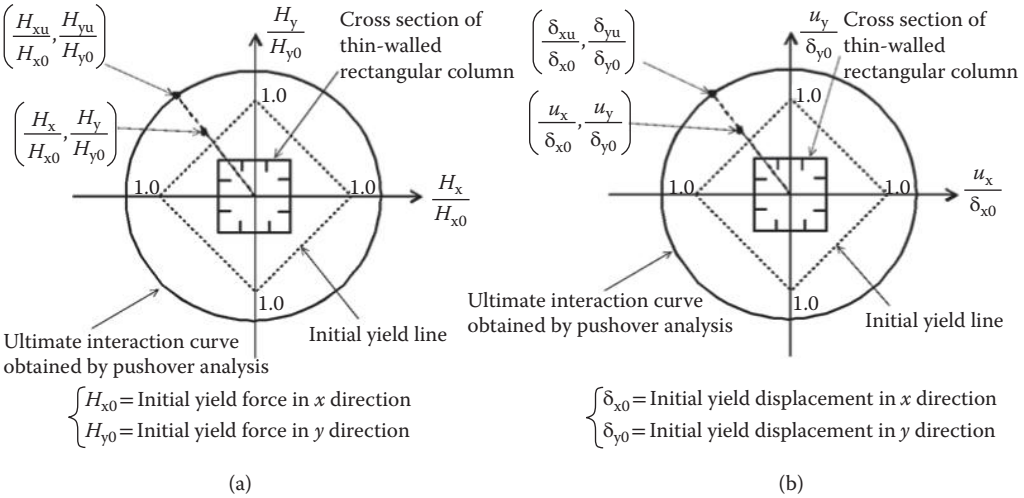

FIGURE 10.30 Ultimate interaction curves for thin-walled rectangular columns: (a) Interaction curve expressed in terms of horizontal restoring force components; (b) Interaction curve expressed in terms of horizontal displacement components.

coincident with the axes of biaxial symmetry of the rectangular cross section. The constants (α_H, β_H) and (α_u, β_u) are determined such that Equations 10.37 and 10.38 best fit the ultimate horizontal restoring force components and displacement components, respectively, obtained by the pushover analysis to multidirections. In the case of square cross sections, $H^P_{xu} = H^P_{yu}$, $\delta^P_{xu} = \delta^P_{yu}$, $\alpha_H = \beta_H$, and $\alpha_u = \beta_u$ hold in Equations 10.37 and 10.38. Therefore, pushover analyses in two horizontal directions are at least necessary to identify the unknown constants. As the two directions for the pushover analysis, *x* or *y* axis and one diagonal axis, respectively, of the square cross-sections are selected. Assuming that (δ^P_u, H^P_u) and $(\delta^P_{diau}, H^P_{diau})$ are the peak points of the pushover analysis in the *x* or *y* direction and the diagonal direction, respectively, the interaction equations for square columns are expressed as

$$\text{(Square column)} \quad \left|H_x/H^P_u\right|^{\alpha_H} + \left|H_y/H^P_u\right|^{\alpha_H} = 1 \tag{10.39}$$

$$\left|u_x/\delta^P_u\right|^{\alpha_u} + \left|u_y/\delta^P_u\right|^{\alpha_u} = 1 \tag{10.40}$$

where

$$\alpha_H = \log 2/\{(\log 2)/2 - \log(H^P_{diau}/H^P_u)\} \tag{10.41}$$

$$\alpha_u = \log 2/\{(\log 2)/2 - \log(\delta^P_{diau}/\delta^P_u)\} \tag{10.42}$$

The validity of the ultimate interaction curves is examined by comparing the results of nonlinear dynamic FE analyses on several types of thin-walled circular and square hollow column models under various bidirectional seismic accelerations. These bidirectional seismic accelerations are those observed during major earthquakes. In Figure 10.31, the maximum responses of horizontal restoring force components and lateral displacement components calculated for two types of square columns up to the instability state are marked with filled circles on $H_x/H^P_u - H_y/H^P_u$ and $u_x/\delta^P_u - u_y/\delta^P_u$ planes, respectively, in comparison with the corresponding ultimate interaction curves. When instability does not occur in the columns throughout the time-history analysis, the maximum responses are marked with empty circles. The instability state is identified by the criterion based on Equation 10.34. It should be noted in

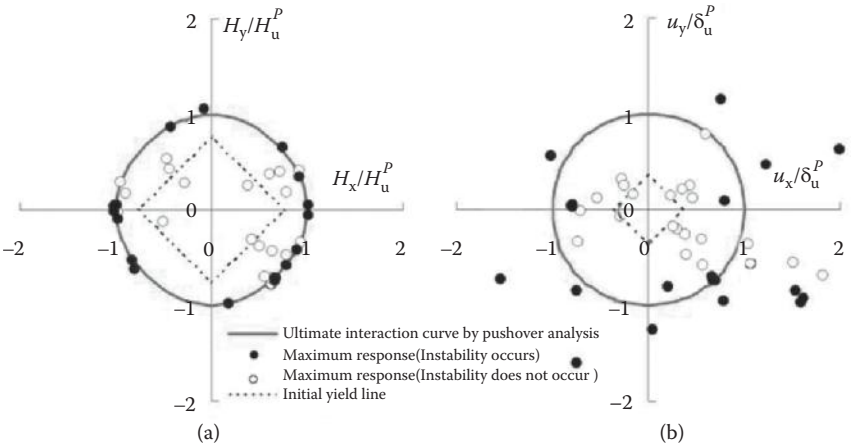

FIGURE 10.31 Ultimate interaction curves and maximum responses of thin-walled square steel columns under various bidirectional horizontal seismic accelerations: (a) Horizontal restoring force components; (b) Horizontal displacement components.

Figure 10.31 that the ultimate interaction curves for the two square columns almost coincide with each other because the nondimentionalized quantities are used to express the interaction curves.

From Figure 10.31a, it is observed for the ultimate interaction curves of square columns defined in terms of the two horizontal restoring force components that the filled circles are located very close to the ultimate interaction curves and the empty circles are mostly inside these curves, regardless of the types of columns and earthquake ground motions. A similar tendency is also observed for circular columns. These results suggest that the interaction curve expressed by the two horizontal restoring force components, as given by Equation 10.35 or 10.39, well approximates the ultimate states of columns under bidirectional seismic accelerations. The various load histories given by the earthquake ground motions little affect the ultimate states of columns expressed by the two horizontal restoring force components. The ultimate states of columns expressed by the force interaction curves obtained by the pushover analysis are considered to be moderately conservative, compared to those identified by the dynamic time-history analysis. This is because the restoring forces under earthquake ground motions may increase due to the cyclic strain hardening phenomenon of steel in the plastic range (Cofie and Krawinkler, 1985). Therefore, there will be a good reason to use Equations 10.35, 10.37, and 10.39 for design purpose.

In contrast, as can be seen from Figure 10.31b, the ultimate interaction curves expressed in terms of two lateral displacement components, as given by Equation 10.40, do not accurately predict the ultimate states of columns under bidirectional seismic accelerations. The displacements at the ultimate states are strongly affected by the load history applied to the columns. This fact implies that the accuracy of the conventional displacement check (see Section 10.5.2.2) is questionable, at least under bidirectional seismic accelerations. Furthermore, it will be necessary to examine the accuracy of using the deformation-based quantities, such as curvature and strain, to express the ultimate states of thin-walled steel columns defined as the point of limit load instability.

Considering the above results, the interaction curves expressed by the two horizontal restoring force components are recommended for general use for the safety check of thin-walled steel columns. The empirical equations to generally predict H_u^P and H_{diau}^P that are used for Equations 10.35, 10.39, and 10.41 are derived as follows for columns with uniform cross-sections in terms of the parameters explained in Section 10.4.

$$\text{(Circular column)}\ \frac{H_u^P}{H_0} = \left\{ \frac{C_1}{R_t^{\bar{a}} \bar{\lambda}'^{\bar{b}} (1 + P/P_y)^{\bar{c}}} + C_2 \right\} \left(1 - \frac{P}{P_y} \right)^{-1} \tag{10.43}$$

TABLE 10.3A Constants for Prediction Equations of H_u^P and H_{diau}^P: For Thin-Walled Circular Steel Piers

Steel Type	$\bar{a}$	$\bar{b}$	$\bar{c}$	C_1	C_2
SM490	0.575	0.339	3.090	0.123	0.814
SS400	0.139	0.064	0.591	1.060	−2.500

TABLE 10.3B Constants for Prediction Equations of H_u^P and H_{diau}^P: For Thin-Walled Square Steel Piers Made of SM490 Steel

Loading Direction	$\bar{a}$	$\bar{b}$	$\bar{c}$	$\bar{d}$	$\bar{e}$	C_1	C_2
H_u^P (x, y axis)	8.71×10^{-4}	1.70×10^{-3}	1.65×10^{-4}	2.38×10^{-3}	2.47×10^{-2}	4.01×10	-3.90×10
H_{diau}^P (Diagonal)	1.86×10^{-3}	1.68×10^{-3}	3.31×10^{-4}	3.64×10^{-3}	3.36×10^{-2}	2.69×10	-2.59×10

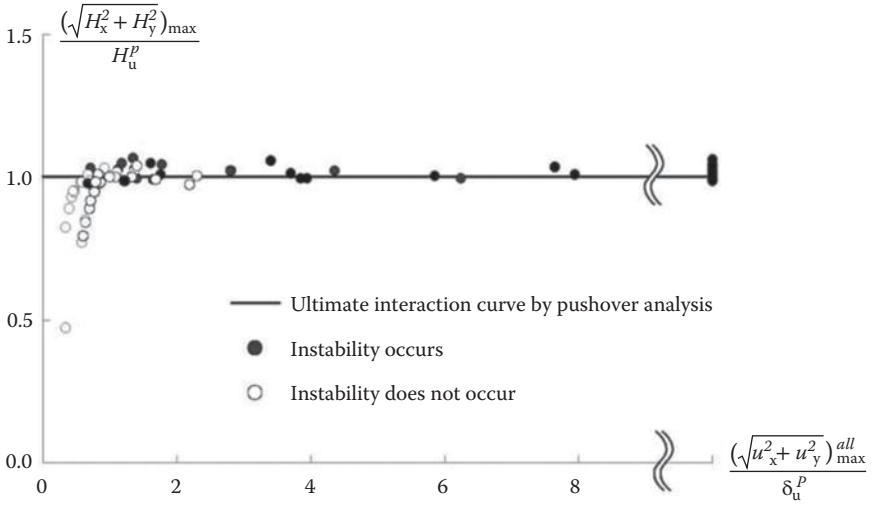

FIGURE 10.32 Instability and maximum response sway displacements of thin-walled circular steel columns near ultimate interaction curves.

$$\text{(Square column)}\ \frac{H_u^P \text{ or } H_{diau}^P}{H_0} = \left\{\frac{C_1}{R_R^{\bar{a}}\bar{\lambda}_s^{\bar{b}}\alpha^{\bar{c}}\bar{\lambda}'^{\bar{d}}(1+P/P_y)^{\bar{e}}} + C_2\right\}\left(1-\frac{P}{P_y}\right)^{-1} \tag{10.44}$$

Equation 10.43 is applicable to the ranges of $0.04 \le R_t \le 0.12$, $0.28 \le \bar{\lambda}' \le 0.50$ and $0.10 \le P/P_y \le 0.3$, whereas Equation 10.44 is applicable to the ranges of $0.3 \le R_R \le 0.65$, $0.4 \le \bar{\lambda}_s \le 0.75$, $0.2 \le \bar{\lambda}' \le 0.55$, $0.5 \le \alpha \le 1.0$ and $0.075 \le P/P_y \le 0.3$. In Equations 10.43 and 10.44, H_0 is the initial yield horizontal force as given by $H_0 = (\sigma_y - P/A)Z/h$, where A = cross-sectional area, Z = section modulus, and h = height, respectively, of a thin-walled steel column. $\bar{\lambda}'$ is the slenderness ratio parameter of a column defined by $\sqrt{P_y/P'_{cr}}$ where P'_{cr} is the buckling strength of the column with a height of h (Figure 10.33b). The constants in Equations 10.43 and 10.44 are summarized in Table 10.3.

Based on the dynamic response analysis under various bidirectional seismic waves, it is examined how the columns behave when the horizontal restoring force approaches the ultimate interaction curve expressed by the two horizontal restoring force components. For this purpose, the relation between the maximum response resultant restoring force $\left(\sqrt{H_x^2+H_y^2}\right)_{max}\Big/H_u^P$ and the maximum response resultant displacement $\left(\sqrt{u_x^2+u_y^2}\right)_{max}^{all}\Big/\delta_u^P$, respectively, at the top of columns are plotted for two types of circular columns (see Figure 10.32). For the case when instability occurs in the columns, $\left(\sqrt{H_x^2+H_y^2}\right)_{max}\Big/H_u^P$ is identified as the maximum response resultant force before the first instability state occurs. The values so identified are plotted with filled circles. However, for the case when instability does not occur in the columns, the maximum response resultant restoring forces throughout the analysis are plotted as $\left(\sqrt{H_x^2+H_y^2}\right)_{max}\Big/H_u^P$ with open circles. $\left(\sqrt{u_x^2+u_y^2}\right)_{max}^{all}\Big/\delta_u^P$ is taken as the maximum response resultant displacement throughout the analysis, regardless of whether instability occurs in the columns or not. It can be seen from Figure 10.32 that $\left(\sqrt{u_x^2+u_y^2}\right)_{max}^{all}\Big/\delta_u^P$ gradually increases with the increase of $\left(\sqrt{H_x^2+H_y^2}\right)_{max}\Big/H_u^P$ when columns are stable. However, if $\left(\sqrt{H_x^2+H_y^2}\right)_{max}\Big/H_u^P$ further increases and almost touches the line of unity, that is, the location of the ultimate interaction curves, the columns become unstable and $\left(\sqrt{u_x^2+u_y^2}\right)_{max}^{all}\Big/\delta_u^P$ increases drastically under small increase in $\left(\sqrt{H_x^2+H_y^2}\right)_{max}\Big/H_u^P$. A similar phenomenon is also observed for square columns (Goto and Ebisawa, 2010c). The response property of the columns shown in Figure 10.32 strongly supports the validity of adopting the interaction curve expressed in terms

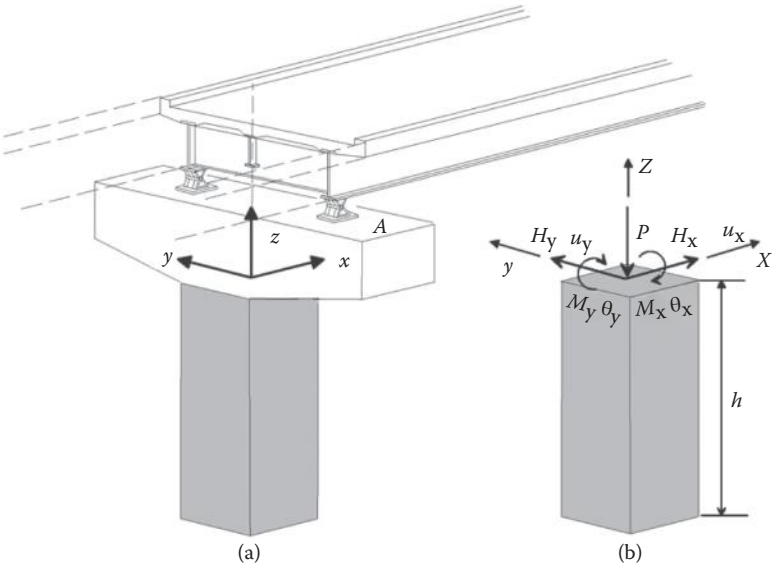

FIGURE 10.33 Force and moment components acting at the top of column of elevated bridge under bidirectional horizontal seismic accelerations: (a) Elevated bridge; (b) Forces and moments acting at top of column.

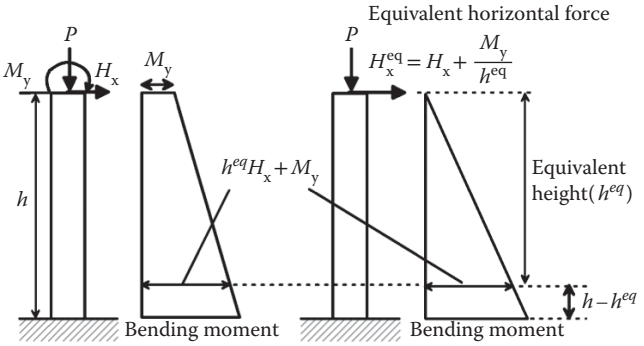

FIGURE 10.34 Conversion of column-top moment to equivalent horizontal force.

of bidirectional horizontal restoring force components to specify the ultimate states of columns under arbitrary bidirectional seismic accelerations.

The superstructure of elevated girder bridges is usually supported by more than two bearings located on the upper surface of the cross-beam that is rigidly connected to the top of the column (see Figure 10.33a). Therefore, it is necessary to consider the effect of biaxial horizontal bending moment components acting at the top of the column in addition to the biaxial horizontal force components and the dead load (Figure 10.33b). Herein, the ultimate interaction curves (Equations 10.35 and 10.39), expressed in terms of the bidirectional horizontal restoring force components, are modified to account for the effect of the biaxial restoring moment components (M_x, M_y) (Goto and Ebisawa, 2010c). From the investigation based on numerical analysis, it was shown that equivalent horizontal restoring force components (H_x^{eq}, H_y^{eq}) that include the effect of the bending moment components can be expressed as

$$H_x^{eq} = H_x + M_y / h_x^{eq}\,;\; H_y^{eq} = H_y - M_x / h_y^{eq} \tag{10.45a,b}$$

where h_x^{eq} and h_y^{eq} are defined as equivalent heights. For square and circular columns, h_x^{eq} coincides with h_y^{eq}. Therefore, h_x^{eq} and h_y^{eq} are expressed as h^{eq} for these columns. By substituting Equations 10.45a and

TABLE 10.4 Constants of Prediction Equation for Equivalent Pier Height h_{eq} for Columns Made of SM490 Steel

Piers	$\bar{a}$	$\bar{b}$	$\bar{c}$	$\bar{d}$	$\bar{e}$	C_1	C_2
Circular	−0.1471	0.0010	0.0207	—	—	1.3625	−0.0477
Square	−0.0217	0.0679	0.1336	−0.0088	0.1210	1.7908	−0.9226

10.45b into Equations 10.35 and 10.39, the ultimate interaction equations for circular and square columns are finally derived as follows:

$$\text{(Circular steel column)} \left\{(H_x + M_y/h^{eq})/H_u^P\right\}^2 + \left\{(H_y - M_x/h^{eq})/H_u^P\right\}^2 = 1 \tag{10.46}$$

$$\text{(Square steel column)} \left|\left\{(H_x + M_y/h^{eq})/H_u^P\right\}\right|^{\alpha_H} + \left|\left\{(H_y - M_x/h^{eq})/H_u^P\right\}\right|^{\alpha_H} = 1 \tag{10.47}$$

From Equation 10.45a, it may be interpreted that a column under in-plane horizontal restoring force H_x and restoring moment M_y reaches its ultimate state when the bending moment at the height of $h - h^{eq}$ reaches the ultimate bending capacity of a column section. This interpretation is schematically shown in Figure 10.34. It should be noted that h^{eq} is always smaller than the height h of a column. The above fact coincides with the experimental observation that local buckling occurs slightly above the column base because of the local buckling restraint at the base of the column. h^{eq} is empirically expressed by the following equation.

$$\text{(Circular column)} \frac{h_{eq}}{h} = \left\{\frac{C_1}{R_t^{\bar{a}}\bar{\lambda}'^{\bar{b}}(1+P/P_y)^{\bar{c}}} + C_2\right\} \tag{10.48}$$

$$\text{(Square column)} \frac{h^{eq}}{h} = \left(\frac{C_1}{R_R^{\bar{a}}\bar{\lambda}_s^{\bar{b}}\alpha^{\bar{c}}\bar{\lambda}'^{\bar{d}}\left(1+P/P_y\right)^{\bar{e}}} + C_2\right) \tag{10.49}$$

where the constants of Equations 10.48 and 10.49 are shown in Table 10.4.

In the strength-based method, the safety of thin-walled bridge piers is checked by whether the maximum responses of the biaxial equivalent horizontal restoring force components acting at the top of columns are within the corresponding ultimate interaction curves given by Equation 10.46 or 10.47.

In order to obtain the responses of the biaxial horizontal force components and the biaxial horizontal moment components at the top of columns (Figure 10.33b), it is necessary to carry out nonlinear dynamic response analysis on an entire elevated bridge system model under bidirectional horizontal seismic accelerations. For this purpose, piers and superstructures may be represented by nonlinear 3D beam elements for the present until computers come to have enough capability to carry out numerical analysis by using the advanced column models shown in Section 10.6.2.

In addition to the safety check, it should be reminded that the serviceability and reparability of piers after the earthquake have to be checked, based on the criterion expressed in terms of residual deformation such as the one shown in Section 10.5.2.3.

10.7 Summary and Concluding Remarks

In this chapter, seismic behavior and design of thin-walled steel piers and CFT piers are explained. First, the damages of the thin-walled hollow steel and piers that were observed during the 1995 Kobe earthquake are discussed. Then, the current seismic design specification after the Kobe earthquake is explained. Finally, some of the recent research achievements are outlined. These achievements are concerned with

the future development of an advanced seismic design where advanced FE models are employed to check directly the performance of bridges under the coupling of the realistic multidirectional components of seismic ground motions. Among the recent research achievements, three important achievements are introduced. One is on the advanced FE models developed for thin-walled steel piers and CFT piers under bidirectional horizontal seismic forces. Another is on a unique buckling restraining mechanism of CFT piers that plays an important role to enhance their strength and ductility. This mechanism was newly elucidated by the advanced FE model, bidirectional cyclic loading test and shaking table test. The other is on a strength-based safety verification method for thin-walled hollow steel piers under bidirectional horizontal seismic accelerations. However, a safety verification method for CFT piers is not included here because the related research is now underway.

CFT piers are generally superior to thin-walled hollow steel piers in terms of their seismic performances, such as safety and postearthquake serviceability. However, the enhanced strength of CFT piers sometimes causes metal fracture in the columns before the piers fully attain their superior strength and ductility. Therefore, the future research need is to establish some rational verification method or structural details to prevent metal fracture. For this purpose, the above-mentioned advanced FE models are expected to provide useful information of local stress and strain concentrations that cause the fractures.

During the 2011 Tohoku earthquake, several elevated highway bridges supported by thin-walled steel piers were subjected to severe ground motions in Sendai, Miyagi prefecture. These piers were designed, based on the seismic design specifications (Japan Road Association, 1996) after the Kobe earthquake. Fortunately, the steel piers were free from damage. However, some of the laminated rubber bearings were seriously damaged. Rubber bearings came to be frequently used for bridges after the Kobe earthquake. Until the Tohoku earthquake, serious damage to the rubber bearings had never been experienced, although several major earthquakes occurred in Japan after the Kobe earthquake. In the current seismic design, the rubber bearings are designed not to be damaged before plastification occurs in the piers. Therefore, the failure of the rubber bearings is against the current seismic design scenario. The causes of this failure have to be examined extensively and reflected in the design of rubber bearings if necessary.

Notations

The following notations are used in this chapter.

A = cross-sectional area of a thin-walled steel pier
A_Σ = total cross-sectional area of four panel plates
$A_{\Sigma s}$ = total cross-sectional area of longitudinal stiffeners
A_s = cross-sectional area of steel section of a CFT pier
a = length of a panel
b_f = width of a flange panel plate
b_w = width of a web panel plate
$\overline{a}, \overline{b}, \overline{c}, \overline{d}, \overline{e}$ = constants of prediction equations for H_u^P and H_{diau}^P
b_d = width of a ring diaphragm
C_1, C_2 = constants of prediction equations for H_u^P and H_{diau}^P
C_R = modification factor in the equation to calculate horizontal earthquake force
c_z = area modification factor in the formula
$D = Et^3/12(1-\nu^2)$ = flexural rigidity of a panel plate
E = Young's modulus of steel
EI_c = flexural rigidity of the control section of a pier
EI_t = flexural rigidity of a diaphragm or a transverse stiffener
EI_r = flexural rigidity of a longitudinal stiffener
H = horizontal inertia force acting at the top of a pier

$H_0 = (\sigma_y - P/A)Z/h$ = horizontal yield strength of a pier
$H_a = M_a / h_F$ = horizontal strength of a pier
H_u^P = peak horizontal force of a pier by pushover analysis
H_{diau}^P = peak horizontal force of a pier in diagonal direction by pushover analysis
H_{xu}^P = peak horizontal force of a rectangular pier in x direction by pushover analysis
H_{yu}^P = peak horizontal force of a rectangular pier in y direction by pushover analysis
$(\sqrt{H_x^2 + H_y^2})_{max}$ = maximum restoring force before the first instability point of a pier
(H_x, H_y) = bidirectional horizontal restoring force components of a pier
(H_x^{eq}, H_y^{eq}) = equivalent horizontal restoring force components of a pier
h = height of a column measured from the upper base plate to the lower surface of a cross-beam
h_c = in-filled concrete height of CFT pier
h_F = height from the upper base plate to the acting point of the horizontal seismic inertia force resultant H in superstructure
h_p = height of a pier measured from the upper base plate to the upper surface of a cross-beam
h^{eq} = equivalent height when $h_x^{eq} = h_y^{eq}$
h_x^{eq} = equivalent height to convert M_y into equivalent horizontal force in x direction
h_y^{eq} = equivalent height to convert M_x into equivalent horizontal force in y direction
h_F = height from the bottom of a pier to a point in superstructure where seismic inertia force acts
h_r = width of a longitudinal stiffener
k_F = plate buckling coefficient of a stiffened panel
k_R = plate buckling coefficient of a subpanel
k_s = plate buckling coefficient of a longitudinal stiffener
l_{ef} = effective length of a pier
M = bending moment of a pier
M_a = allowable bending moment at the bottom of a pier
M_{s0} = limiting bending moment of hollow section just above concrete-filled section
M_0 = yield bending moment
M_{0c} = yield bending moment of a pier on compression side
M_{0t} = yield bending moment of a pier on tension side
(M_x, M_y) = biaxial restoring moment components of a pier
N = axial force of a pier
N_c = axial force acting on the concrete section of a CFT pier
N_s = axial force acting on the steel section of a CFT pier
n = number of spaces between longitudinal stiffeners per one panel
P = vertical load (dead load) acting on the top of a pier
P_{cr} = elastic buckling strength of a pier with height of h_p
P'_{cr} = elastic buckling strength of a column with height of h
P_y = compressive yield strength of a pier
R = radius of cross-section of a circular pier
R_F = width-to-thickness ratio parameter of a stiffened subpanel
R_R = width-to-thickness ratio parameter of a subpanel between longitudinal stiffeners
R_t = radius-to-thickness ratio parameter of thin-walled circular pier
R_s = width-to-thickness ratio parameter of a longitudinal stiffener
r = ratio between the primary stiffness and the secondary stiffness of a pier
t = thickness of a panel plate or a thin-walled circular cross-section
t_d = thickness of a ring diaphragm for thin-walled circular pier
t_r = thickness of a longitudinal stiffener
t_0 = critical thickness of a subpanel beyond which yielding occurs before buckling

u = horizontal displacement at the top of a pier
(u_x, u_y) = horizontal displacement components of a pier
$(\sqrt{u_x^2 + u_y^2})_{\max}^{all}$ = maximum response displacement throughout the analysis
W_P = weight of a pier
W_U = weight of superstructure supported by a pier
Z = section modulus of thin-walled steel pier at the base
Z_g = section modulus of hollow section just above concrete-filled section of a CFT pier
α = b/a = aspect ratio of a panel
α_0 = aspect ratio of a stiffened panel where buckling strength becomes minimum in half-wave mode
α_H, β_H = constants of ultimate force interaction curve
α_u, β_u = constants of ultimate displacement interaction curve
$\Delta^2 W$ = 2nd variation of external work
$(\Delta u_x, \Delta u_y)$ = horizontal components of incremental displacement at the top of a pier
$(\Delta H_x, \Delta H_y)$ = horizontal components of incremental restoring force a pier
δ_0 = yield displacement of a pier
δ_{x0} = yield displacement of a rectangular pier in x direction
δ_{y0} = yield displacement of a rectangular pier in y direction
δ_a = allowable lateral displacement of a pier
δ_m = maximum lateral displacement of a pier under Level 2 earthquake
δ_R residual lateral displacement of a pier
δ_r = cross-sectional area ratio between one longitudinal stiffener and one panel plate
δ_u = lateral displacement at the peak of the envelope of hysteretic curves of a pier
δ_u^p =lateral displacement of a pier at the peak force by pushover analysis
δ_{diau}^p = lateral displacement of a square pier at the peak force in diagonal direction
δ_{xu}^p = lateral displacement of a rectangular pier at the peak force point in x direction
δ_{yu}^p = lateral displacement of a rectangular pier at the peak force point in y direction
ε_a = allowable strain of steel section of a pier
ε_y = yield strain of steel section of a pier
θ = angle between the vectors of $(\Delta u_x, \Delta u_y)$ and $(\Delta H_x, \Delta H_y)$
$\gamma = (E_s I_r / bD)$ = relative flexural rigidity of a longitudinal stiffener
$\gamma_t = (E_{st} I_t / bD)$ = relative flexural rigidity of diaphragms or transverse stiffeners
γ_{req} = required relative flexural rigidity of a longitudinal stiffener
γ^* = optimum stiffness ratio of a longitudinal stiffener
γ_{treq} = required relative flexural rigidity of a diaphragm or a transverse stiffener
$\bar{\lambda} = \sqrt{P_y / P_{cr}}$ = effective slenderness ratio parameter of a pier with the height of h_p
$\bar{\lambda}' = \sqrt{P_y / P'_{cr}}$ = effective slenderness ratio parameter of a column with the height of h
$\bar{\lambda}_s$ = slenderness ratio parameter of a longitudinal stiffener
ν = Poisson's ratio of steel
σ_c = compressive strength of concrete
σ_y = yield stress of a panel plate
σ_{sy} = yield stress of a longitudinal stiffener
σ_{s0} = yield stress of the material or stress obtained by multiplying 1.7 to the allowable stress to local buckling
ϕ = curvature of a pier
ϕ_a = allowable curvature of a pier
ϕ_0 = yield curvature of a pier
ϕ_{0c} = yield curvature of a pier on compression side
ϕ_{0t} = yield curvature of a pier on tension side

References

Chen W. F. 1982. *Plasticity in reinforced concrete*. McGraw-Hill, Inc, USA.

Cofie, N. G., and Krawinkler, H. 1985. Uniaxial cyclic stress-strain behavior of structural steel. *J. Eng. Mech.*, ASCE, 111(9), 1105–1120.

Ebisawa T., Goto, Y., Osada, N., Lu, W., and Lu, X. 2011. Bi-directional shaking table test on circular CFT piers and FEM analysis. *Proceedings of 66th Annual meeting,* Japan Society of Civil Engineers, (JSCE), I-206, pp. 411–412 (in Japanese).

Editorial Committee for the Report on the Hanshin-Awaji Earthquake Disaster. 1996. *Report on the Hanshin-Awaji earthquake disaster*. Damage to civil engineering structures: Bridge structures, Japan Society of Civil Engineers (JSCE), Maruzen, Inc., Tokyo, Japan (in Japanese).

Ghosh, P. K., Goto, Y., and Seki, K. 2011. Effect of axial load on strength and ductility of thin-walled circular CFT columns. *Proceedings of The 2011 World Congress on Advances in Structural Engineering and Mechanics(ASEM'11)*, Seoul, Korea, pp. 5460–5471.

Goto, Y., Ebisawa, T., and Lu, X. 2013. Local buckling restraining behavior of thin-walled circular CFT columns under seismic load. *J. Struct. Eng.*, ASCE, 10.1061/(ASCE) ST.1943–541X,0000904, posted ahead of print.

Goto, Y., Jiang, K., and Obata, M. 2006. Stability and ductility of thin-walled circular steel columns under cyclic bidirectional loading, *J. Struct. Eng.*, ASCE, 132(10), 1621–1631.

Goto, Y., Jiang, K., and Obata, M. 2007. Hysteretic behavior of thin-walled stiffened rectangular steel columns under cyclic bi-directional loading. Doboku Gakkai Ronbunshuu A. *Proc. of JSCE*, 63(1), 122–141 (in Japanese).

Goto, Y., Koyama, R., Fujii, Y., and Obata, M. 2009a. Ultimate state of thin-walled rectangular steel columns under bi-directional seismic excitations, Doboku Gakkai Ronbunshuu A. *Proc.of JSCE*, 65(1), 61–80 (in Japanese).

Goto, Y., Muraki, M., and Obata, M. 2009b. Ultimate state of thin-walled circular steel columns under bidirectional seismic accelerations. *J. Struct. Eng*, ASCE, 135(12), 1481–1490.

Goto, Y., Ghosh, P. K., and Kawanishi, N. 2010a. Nonlinear finite element analysis for hysteretic behavior of thin-walled circular columns with in-filled concrete. *J. Struct. Eng.*, ASCE, 136 (11), 1413–1422.

Goto, Y., Mizuno, K., Ghosh, P. K., and Fujii, Y. 2010b. FEM analysis for hysteretic behavior of thin-walled stiffened rectangular steel columns with in-filled concrete, Doboku Gakkai Ronbunshuu A. *Proc. Of JSCE*, 66(4), 816–835 (in Japanese).

Goto, Y., and Ebisawa, T. 2010c. Ultimate state of thin-walled stiffened square steel bridge piers subject to bi-directional horizontal seismic forces and moments. *Proc. 9th Pacific Steel Conference*, 1222–1229.

Goto, Y., Mizuno, K., and Ghosh, P. K. 2011. Nonlinear finite element analysis for cyclic behavior of thin-walled stiffened rectangular steel columns with in-filled concrete. *J. Struct. Eng.*, ASCE, 138(5), 571–584.

Goto, Y., Wang, Q.Y., and Obata, M. 1998. FEM analysis for hysteretic behavior of thin-walled columns. *J. Struct. Eng.*, ASCE, 124(11), 1290–1301.

Japan Road Association. 1972. *Design specifications for highway bridges and commentary*, Part I: Common part, Part II: Steel bridges, Japan Road Association, Tokyo, Japan (in Japanese).

Japan Road Association. 1980. *Design specifications for highway bridges*, Part I: Common part, Part II: Steel bridges, Part III: Concrete bridges, Part IV: Seismic design, Japan Road Association, Tokyo, Japan (in Japanese).

Japan Road Association. 1996. *Design specifications for highway bridges*, Part I: Common part, Part II: Steel bridges, Part III: Concrete bridges, Part IV: Seismic design, Japan Road Association, Tokyo, Japan (in Japanese).

Japan Road Association. 2002a. *Design specifications for highway bridges and commentary*, Part I: Common part, Part II: Steel bridges, Japan Road Association, Tokyo, Japan (in Japanese).

Japan Road Association. 2002b. *Specifications for highway bridges*, IV: Seismic design, Japan Road Association, Tokyo, Japan.

Japan Road Association. 2012a. *Design specifications for highway bridges and commentary*, Part I: Common part, Part II: Steel bridges, Japan Road Association, Tokyo, Japan (in Japanese).

Japan Road Association. 2012b. *Specifications for highway bridges and commentary*, Part I: Common part, IV: Seismic design, Japan Road Association, Tokyo, Japan (in Japanese).

Kitada, T. 1998. Ultimate strength and ductility of state-of-the-art concrete-filled steel bridge piers in Japan, *Eng. Struct.*, 26(4–6), 347–354.

Lee, J., and Fenves, G. L. 1998. Plastic-damage model for cyclic loading of concrete structures, *J. Eng. Mech.*, ASCE, 124(8), 892–900.

Obata, M., and Goto, Y. 2002. Multi-directional pseudo-dynamic experiment of steel bridge piers, *Proc. of ICASS02*, 1, 171–178.

Obata, M., and Goto, Y. 2007. Development of multidirectional structural pseudo dynamic test. *J. Struct. Eng.*, ASCE, 133(5), 628–645.

Okada, S., Ono, K., Taniue, H., Tokunaga, M., and Mishimura, N. 2010. Seismic performance of stiffened steel members with rectangular section under high compressive axial force, Doboku Gakkai Ronbunshuu A, *Proc. of JSCE*, 66(3), 576–595 (in Japanese).

Osada, N., Goto, Y., Ebisawa T., Lu, X., and Lu, W. 2010. Bi-directional shaking table test on thin-walled steel piers and FEM analysis, *Proceedings of 65th Annual meeting*. Japan Society of Civil Engineers, (JSCE), I-22, pp. 43–44 (in Japanese).

Osada, N., Goto, Y., Ebisawa T., Lu, W., and Lu, X. 2011. Bi-directional shaking table test on thin-walled circular steel piers and their safety verification method. *Proceedings of 665th Annual meeting*, Japan Society of Civil Engineers, (JSCE), I-201, pp. 401–402 (in Japanese).

Palermo, A., Pampanin, S., and Marriot, D. 2007. Design, modeling, and experimental response of seismic resistant bridge piers with post-tensioned dissipating connections. *J. Struct. Eng.*, ASCE, 133(11), 1648–1661.

Public work research institute of Japan. 1997–2000. *Report of cooperative research on limit state seismic design for bridge piers*, I-VIII and summary.

Shen,C., Mamaghani, I. H. P., Mizuno, E., and Usami, T. 1995. Cyclic Behavior of Structural Steels. II: Theory. *J. Eng. Mech., ASCE*, 121(11), 1165–1172.

Susantha, K. A. S., Ge, H. B. and Usami, T. 2001. Cyclic analysis and capacity prediction of concrete-filled steel box columns. *Earthquake Eng. Struct. Dyn.*, 31(2), 195–216.

Usami, T., and Ge, H. B. B. 1998. Cyclic behavior of thin-walled steel structures-numerical analysis. *Thin-Walled Struct.*, 32(1–3), 41–80.

Usami, T., Mizutani, S., Aoki, T., and Itoh, Y. 1992. Steel and concrete-filled steel compression members under cyclic loading. In: *Stability and ductility of steel structures under cyclic loading*, Fukumoto, Y. and Lee, G. (Eds.), CRC, Boca Raton, pp. 123–138.

Usami, T., Susuki, M., Mamaghani, I. H. M., and Ge, H. B. 1995. A proposal for check of ultimate earthquake resistance of partially concrete filleddteelbridhepiers, *J. Struct. Mech. Earthquake Eng. Proc. Of JSCE*, 525/I-33, 69–82 (in Japanese).

11

Seismic Design of Cable-Supported Bridges

Jian Ren Tao
HNTB Corporation

Semyon Treyger
HNTB Corporation

11.1 Introduction

Cable supported bridges commonly refer to suspension bridges and cable-stayed bridges where the superstructure load is supported and transferred by cables in the longitudinal direction of the bridge. They are the most challenging bridge types to span long distance and difficult crossings. The main purpose of this chapter is to present the general procedure and special issues in seismic design of cable-supported bridges including suspension bridges and cable-stayed bridges. General design considerations for cable supported bridges are presented in Chapters 9 to 11 of *Bridge Engineering Handbook, Second Edition: Superstructure Design*.

Cable supported bridges are often (intuitively) linked to long-span bridges. This is no longer true. In the United States a long-span suspension bridge is defined as one where the length of the span is ≥ 400 ft. (122 m) (ASCE-SSPB, 1996). By this definition many modern cable supported bridges are not

qualified as long-span bridges. When lower cost is no longer the top priority, the record span length of cable supported bridges is broken at the two fronts. On one hand the longest span length record is being broken swiftly and constantly. For example, a new record of longest span length of 1018 m created by Stonecutters Cable-Stayed Bridge was broken even before its completion by Su Tong Cable-Stayed Bridge with main span length of 1088 m. On the other hand, however, the record of the shortest span length for cable supported bridges is also constantly renewed. It is now a common practice in Asia that the aesthetics standards are far more important than economic considerations for the landmark structures; cable supported roadway bridges have been designed and constructed in span range, where other types of bridges may be more suitable and cost-effective. Based on this discussion, the content of this chapter is limited to long-span cable supported bridges.

There are many cable supported bridges, suspension bridges in particular, that were designed and constructed at the time when there were none or little consideration for seismic loadings. These bridges are still serving in major transportation links although they have long passed their "retirement" age, and there is no hope for them to take a rest in foreseeable future. In this case, the seismic performance of these bridges is of great concern. Actually, seismic retrofit design of existing aging cable supported bridges is much more challenging than designing a new bridge. Sound understanding of seismic vulnerabilities and viable retrofit measures for existing bridges will assist engineers to better design new cable supported bridges. Seismic retrofit of existing cable supported bridge will also be discussed in this chapter. Seismic design of cable-supported bridges is a complex and difficult subject and is still evolving. It is neither possible nor necessary to provide in-depth coverage for every aspect in this short chapter. The intention, therefore, is only to present an introduction to the subject, or to cast a brick to attract jade.

11.2 Seismic Performance in Past Earthquakes

The overall performance of cable supported bridges is quite satisfactory. Incidents of collapse of cable supported bridges are very rare. The notable case of such catastrophe is the spectacular collapse of the first Tacoma Narrows Bridge because of aeroelastic flutter on November 7, 1940 (Gimsing and Georgakis, 2012). In another case the Silver Bridge, an eyebar-chain suspension bridge built in 1928 over the Ohio River, collapsed on December 15, 1967 while it was full of rush-hour traffic, resulting in the deaths of 46 people. Investigation of the wreckage pointed to the cause of the collapse being the failure of a single eyebar in a suspension chain, because of a small defect 0.1 in. (2.5 mm) deep (Seim, 2008). Analysis showed that the bridge was carrying much heavier loads than it had originally been designed for and was poorly maintained. Cable supported bridge failure directly caused by earthquakes has not yet been reported.

As of September 2012, there are approximately 57 long-span suspension bridges and 44 cable-stayed bridges in the United States, and a few more are currently under design or under construction. Most of the 57 suspension bridges were designed and built before recent advances in earthquake engineering, and by virtue of their age, had little or no seismic resistant design features. Of considerable surprising and engineering significance, these bridges performed very well during past strong earthquakes. The famous San Francisco Golden Gate Bridge is one of them. The Golden Gate Bridge was built in 1937 and was originally designed to withstand an equivalent lateral force of only 7.5% of gravity. The bridge experienced the 1989 Loma Prieta earthquake and was not damaged at all. The epicenter of the magnitude 7.1 event was approximately 100 km from the bridge. Another well-known suspension bridge in the vicinity is the West Span of San Francisco-Oakland Bay Bridge (SFOBB) (lower portion of Figure 11.1). Comparable to the levels specified in the 1930 Uniform Building Code for buildings, the bridge was designed for only 10% gravity (g) earthquake accelerations (Raab and Wood, 1941; Manzanarez and Nader, 2000). During the 1989 Loma Prieta earthquake the suspension spans of SFOBB suffered no structural damages either, whereas the adjacent East Spans (upper portion of Figure 11.1), a multiple-span of simply supported steel truss bridge, was damaged and caused the closure of this important transportation link. A few bridges of other types in the San Francisco Bay Area were also damaged and collapsed during the same earthquake. The Vincent Thomas Bridge is a 1500 ft. (460 m) long suspension

bridge, crossing the Los Angeles Harbor of California. The bridge was opened in 1963 and has been stricken by several strong earthquakes ever since and has suffered no damage at all.

The historic Wheeling suspension bridge over the Ohio River is one of the 57 long-span suspension bridges in operation in the United States. The bridge was designed and constructed in 1849 by Charles Ellet, Jr., who rightfully may be considered the father of the modern American suspension bridge. Despite the fact that the bridge was not designed to carry today's live loads and seismic loads, the bridge has served as a vital link across the Ohio River for nearly one and a half century. Although the bridge has not been experienced with any strong earthquakes yet, the seismic analysis showed that even earthquakes of magnitude of 7.0 will not cause damage of the main cables and the suspenders posing any threat of catastrophic failure to the bridge (Spyrakos et al., 1999).

So far, there have been no cases of long suspension bridges stricken by severe earthquakes in other parts of the world, but in at least two cases, relatively short suspension bridges have suffered extensive damage. The Arakawa Bridge (Japan, main span 90 m, side spans 52 m) had one tower cracked during the great Kanto earthquake of 1923. The Gosho Bridge (Japan, double span, 124 m per span) had one anchor block-shifted 20 cm, the saddle on the top of the right span moved toward the left span, and the upper chord of the stiffening girder buckled during the Fukui earthquake of 1948 (Castellani, 1987). China now has the most fast growing numbers of cable supported bridges in the world. China is also a country confronting earthquakes as the major natural disasters. However, there are no reported incidents of earthquake-induced damages or failures suffered by cable supported bridges in China. The satisfactory seismic performance may be attributed to the fact that most of the cable supported bridges in China are relatively young; the first cable supported bridge is Nanpu cable-stayed bridge built in 1988 in Shanghai. And they have been designed and constructed using modern technology and materials.

The Akashi-Kaikyo Suspension Bridge was under construction during the 1995 Hyogoken-Nanbu (Kobe) Earthquake. The epicenter of the earthquake (of magnitude of 7.2) was very close to the construction site of the bridge. When the earthquake occurred, all the cable strands were erected and cable squeezing work was in progress. The partially constructed bridge suffered no damages except for the permanent displacement of the main towers (HSBA, 1998). The center span length was lengthened by approximately 1 m due to movement of ground.

Compared to suspension bridges, cable-stayed bridges are relatively new and are thus considered as modern bridges. Although no cable-stayed bridges collapsed during past earthquakes, it seems that cable-stayed bridges have suffered more earthquake-induced damages than suspension bridges. And surprisingly, a few cable-stayed bridges that suffered most damages were designed according to state-of-the-art seismic design practice. Among them is Higashi-Kobe Bridge suffered significant damages

FIGURE 11.1 San Francisco–Oakland Bay Bridge (opened in 1936).

during the 1995 Hyogoken-Nanbu Earthquake and led to complete closure of the Wangan route (Wilson, 2003). Higashi-Kobe Bridge (see Figure 11.2a) is a three-span continuous all-steel double-deck cable-stayed bridge. The total length of the bridge is 885 m, including a center span of 485 m and two side spans of 200 m. The damages include: (1) all connections between the girder and the pendulum supports, wind shoe, and dampers at west end pier were completely severed; (2) the tension in the cable caused the end of the girder at west end pier to uplift approximately 0.5 m; (3) shear-induced buckling in the cross-beams and compression buckling occurred in one leg of the west end pier; (4) shear-induced buckling also occurred in other piers; and (5) the wind shoe at east end pier was damaged. The damage to this new bridge, although neither severe nor extensive as the damage to many older ones in the vicinity, had a major impact on Kobe's transportation systems in the months following the earthquake.

The cable supported bridge that suffered the most significant damages during earthquakes is probably the Chi-Lu Cable Stayed Bridge in Taiwan (Figure 11.2b) (Buckle et al., 2000). On September 21, 1999, the nearly completed prestressed concrete cable-stayed bridge was shaken by the Chi-Chi Earthquake, a magnitude of 7.6. The site of the bridge is located near the epicenter of the earthquake (approximately 10 km). The observed significant damages include: (1) formation of transverse plastic hinges in the pylon at top of the pile cap and above the deck-pylon connection; (2) formation of plastic hinges in concrete box deck at the deck-pylon connection; (3) shear cracking at the cap beam of anchor piers; (4) pounding damage at the end span; (5) tension cracking in the bent columns at the end span supports; and (6) anchorage failure of one stay cable. Although the bridge was still under construction when hit by the strong earthquake, the fundamental structural system was very close to its final condition, the unfinished construction items included erection of precast overhang panels for three cast-in-place segments near center tower and the final stay cable adjustment. Therefore, this case should have more implication than that of Akashi-Kaikyo Bridge that was hit by earthquake with absence of stiffening girder. Based on its span length, the Chi-Lu Bridge is barely qualified as a long-span bridge. In addition both pylon and deck are made of concrete and the fundamental vibration periods of the bridge fall in the range of predominant period of the ground motion.

From statistic point of view, the seismic performance of cable supported bridges may be summarized as follows:

- Cable supported bridges generally perform better than other types of bridges.
- Earth-anchored suspension bridges perform better than self-anchored cable-stayed bridges.
- Cable supported bridges with longer span length perform better than those with shorter span length.
- Cable supported bridges constructed from steel perform better than those constructed from concrete.

(a) (b)

FIGURE 11.2 Cable-stayed bridges damaged during earthquakes. (a) Higashi-Kobe Bridge (opened in 1992). (b) Chi-Lu Cable-Stayed Bridge (opened in 2004).

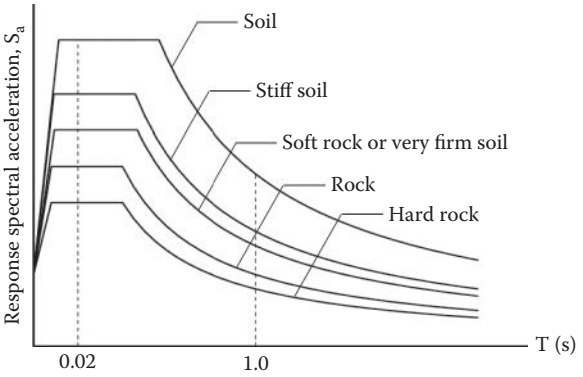

FIGURE 11.3 Typical design response spectra.

The observed seismic performance of cable supported bridges may be better understood by comparing their fundamental vibration period with their design earthquake response spectrum. Figure 11.3 shows a typical design response spectrum adopted in the United States (AASHTO, 2012). The design response spectra used in different regions of the world are look alike. Long-span cable supported bridges fall within the long-period portion of the response spectrum that is on the right side of the plateau where the response is inversely proportional to the period, *T*. The longer the period is, the lower the responses are. Maybe this further provides general understanding for seismic performance of long-span cable supported bridges.

11.3 Seismic Vulnerabilities

Although cable supported bridges demonstrate better global seismic performance as compared to other types of bridges, they are definitely not immune to strong earthquakes. Many bridge engineers believe that the existing long-span cable supported bridges have not yet been tested by "big" earthquakes. Therefore, a good understanding of potential seismic vulnerability in existing cable supported bridges is not only critical for engineers to develop effective retrofit schemes, but also beneficial in assisting them in designing new cable supported bridges. Seismic vulnerability of cable supported bridges in the United States are not revealed directly by the records of damages occurred during past earthquakes, they are demonstrated, or predicted, by computer models using artificial earthquakes.

During 1989 Loma Prieta Earthquake, the West Span of SFOBB did not suffer any damages. However, because it is on the same lifeline link with a closely adjacent truss bridge, East Spans of SFOBB that collapsed during the earthquake, the twin suspension bridge ignited curiosities and drew attentions and concerns. Thus, the 1989 Loma Prieta Earthquake triggered a serious and extensive investigation of seismic performance of existing suspension bridges in the United States. The study started with suspension bridges on the west coast, including the Golden Gate Bridge, West Span of SFOBB, and the Vincent Thomas Bridge. This investigation was later extended to include suspension bridges on the East Coast and central part of the United States.

11.3.1 Suspension Bridges

Although these existing suspension bridges were designed with none or little seismic resistance, they were examined by using most credible earthquake (MCE) events and sophisticated nonlinear analyses. Collapse or global failure of existing suspension bridges during fictitious earthquakes is very unlikely, but extensive damages may occur because of component vulnerabilities. The seismic vulnerability found in components of existing long-span suspension bridges in the United States can be summarized as follows.

11.3.1.1 Bridge Towers

Towers, as primary load carrying members, were designed to carry mainly the gravity load, live load, and wind load and in some cases limited lateral load as earthquake load. Towers of most existing suspension bridges in the United States were constructed from steel, and they are very flexible with long vibration period. Because seismic load considered was an equivalent lateral load of only 7.5%–10% of the gravity, for bridges with sufficient long-span length, the lateral design of towers was usually governed by wind load. Owing to conservatism preserved in the original design (allowable stress design), force capacity may be still adequate even reexamined using MCEs, but due to large displacement and P-Δ effects, foundation uplift may occur after tension yield of hold-down bolts, as the result towers rock when one side of the base of the shaft separates from the pier and shifts the load to the other side and cause the subsequent concentration of strain in the contact area. The tower shaft, multicellular in cross-section, will be overstressed in compression, particularly at the base. The plates of the tower cells are noncompact and are susceptible to buckling. The buckling in exterior cell will occur first and will most likely propagate inward into the tower shaft thus jeopardizing the integrity of the primary gravity load carrying element. This type of vulnerability was predicted for the Golden Gate Bridge (Nader and Ingham, 1996; Rodriguez and Ingham, 1996), West Span of SFOBB Bridge (Ketchum and Waggoner, 1995), and the Vincent Thomas Bridge (Ingham et al., 1997) in events of MCE. Compressive buckling of same nature actually occurred on lower leg of the end pier of Higashi-Kobe Bridge during the 1995 Hyogoken-Nanbu Earthquake because of longitudinal sway of the bridge (Wilson, 2003), and indirectly verified that the predicted vulnerability of steel towers of aforementioned suspension bridges is very realistic. The effective retrofit measure would be the addition of vertical stiffeners to those noncompact plates of the tower cells to reduce the width-to-thickness ratio.

The concrete pedestals supporting the steel tower shafts are under high demands due to both overall shaking and local wall flexure, and may result in tension crack and spall of concrete cover. The retrofit of the lightly reinforced concrete pedestals includes strengthening with prestressed tendons.

11.3.1.2 Stiffening Girders

Stiffening girders are probably the most vulnerable components of the existing suspension bridges in the United States. Stiffening girders are in form of steel trusses in older bridges and steel box girders in newer bridges. Under dead load, it is presumably stress free. The members of the stiffening girder were mainly designed for carrying live load and wind load. Therefore, if a lateral earthquake load greatly exceeds the wind load, extensive damages may occur in the stiffening truss. The most vulnerable elements in the stiffening truss are the lateral braces and their connections. Some components are built-up members, which are composed of several load-carrying elements stitched together with either lattices (thin bars), or perforated cover plates. These types of members, especially lattice members, lose their ability to carry compressive loads soon after the buckling limit has been reached. For Golden Gate Bridge, nearly half of the top lateral braces are required to be replaced and their connections to be strengthened (Rodriguez and Ingham, 1996), and the scope of seismic retrofit completed for the stiffening trusses of the West Span of SFOBB is far more extensive (Caltrans, 2013; Chapter 15). It can be expected that in addition to strengthening the laterals and their connections, the wind connections at the end of the span will need alternation.

11.3.1.3 Suspension Systems

Suspension system includes main cable, suspenders, cable bands, and saddles. The suspension system is the component that is least susceptible to seismic vulnerability. Generally, the main cable was design using safety factor of 2.2 against breaking (by limiting stress of dead plus live load below 45% of the ultimate strength). The dimensioning of the cables is not governed by strength; instead it is governed by consideration of reducing cable relaxation (Gimsing and Georgakis, 2012). In addition, the allowable stress design is very conservative and thus results in great reserved strength. Owing to its flexibility,

cables can accommodate large movements between supports. Typically, approximately 10%–20% of the total load on a main cable is live load and 80%–90% is dead load. Cables are thus sensitive to dead load, but not to traffic load (Buckland, 2003). Cables are not sensitive to seismic load either. Results of studies show that the increase in cable force because of seismic force is only approximately 10% of that because of dead load. Based on the 1987 Whittier Narrows earthquake records and structural seismic analysis of the Vincent Thomas Bridge, it was found that the "additional" cable tension because of seismic load was 10% the initial dead load in the backstay, but only 3% in the side spans and <2% in the main span (Liu et al., 2000). Owing to large deflection and increase of difference in cable angle between main span and side spans, longitudinal shear may cause tower cable saddle connection to slip. Connections of tower and cable saddles of the Golden Gate Bridge are susceptible to such potential vulnerability and required retrofit includes strengthening and immobilizing saddle/cable rollers (GGBHTD, 2011). Similar design conservatism and strength reserves are imbedded in suspenders, too. The design of suspenders is generally controlled by fatigue load. Suspenders may go slack during earthquakes and was considered by some researchers as not detrimental (Ketchum and Waggoner, 1995). Actually, this phenomenon has not been studied enough and its engineering implication is not clear and thus remains as a valid concern. In new bridge designs it is now a common practice to ensure that the accidental loss of one suspender (or stay cable) would not trigger progressive failure of the bridge. Such investigation, however, has not been performed for existing cable supported bridges in event of MCE, and there is lack of information to make a general conclusion as whether progressive failure because of loss of one suspender poses a realistic threat to the seismic safety of the existing cable supported bridges.

11.3.1.4 Foundations

Liquefaction is one of the potential vulnerabilities and shall be prevented. Liquefaction is the direct cause for bridge collapse and severe damages in past earthquakes. Liquefiable soil must be treated by mitigation techniques such as densification, stone columns, or displacement piles. Most of the suspension bridges in the United States are founded on either large pile foundations or large caisson foundations. Despite the fact that there was no or little seismic force considered in the original design, as long as scour and soil liquefaction is not a concern the foundations are found to be adequate even by the current most stringent seismic design standards. For an example, the Brooklyn Bridge in New York was built almost 130 years ago. After rigorous examination, it has been concluded that its caisson foundations do not require retrofitting under the 2500-year seismic design event (Yegian et al., 2008). Foundation retrofit is very expensive and when it becomes unavoidable, bridge replacement option is perhaps more economical and practical.

11.3.1.5 Wind Connections and Expansion Joints

The inelastic seismic analysis reveals that the expansion joints and the wind locks are the most vulnerable elements of existing suspension bridges. During an earthquake event, the stiffening girder will displace as a pendulum hanging from the suspenders resulting in large displacements in both longitudinal and transverse direction. In case of the Golden Gate Bridge when subjected to an event of MCE, the relative longitudinal displacement between the center span and the tower is approximately ±1.30 m. This relative displacement exceeds the 0.46 m capacity of the existing expansion joints and wind locks. Tremendous impact force would damage the wind locks (Rodriguez and Ingham, 1996). Similar problem was reported for almost all the existing suspension bridges in the United States. Damage to joints and wind connections will likely occur even for an operating level earthquake (OBE) event (ASCE-SSPB, 1996). The vulnerability predicted by computer models has been indirectly confirmed by observations of earthquake-induced damages on some modern bridges. In case of Higashi-Kobe Bridge, wind shoe at one of the end piers was completely damaged during the 1995 Hyogoken-Nanbu Earthquake (Wilson, 2003). Strengthening the connections to take the required force, even possible, would greatly contribute to the tower stresses and displacement. A better approach is to weaken the connection by replacing the existing steel pins that link the stiffening girder to the towers. The new pins will act as structural fuses

with a capacity high enough to take the wind and breaking loads, but they would fail early during an earthquake. Dampers between the truss spans and the towers will also be installed to reduce the relative displacements. Such approach was not only adopted for retrofitting the Golden Gate Bridge and other historical suspension bridges, but was also applied in some of the new cable supported bridge designed and constructed using modern technology (Combault and Teyssandier, 2005).

11.3.2 Cable-Stayed Bridges

There are similarities between cable-stayed bridges and suspension bridges, such as being flexible and having relatively long vibration period. Towers, piers, and foundations of cable-stayed bridges, therefore, share same component vulnerabilities as mentioned above for suspension bridges. Likewise, the stays are the least vulnerable components in cable-stayed bridges. Owing to the bracing effects by stays, towers of cable-stayed bridge are more redundant and stable compared to towers of suspension bridges. However, towers and piers of most modern cable-stayed bridges are made of concrete and are more vulnerable to shear and flexural damages and also are less ductile.

There are two major differences between cable-stayed bridges and earth anchored suspension bridges: (1) dead load stress: in cable-stayed bridges the deck is subjected to axial compression because of inclined stays and large locked-in stresses because of construction, whereas in suspension bridges the deck is nearly stress free; (2) construction method: most of the cable-stayed bridges are constructed using balanced cantilever method, the load imposed on partially erected deck, stays and the pylon during erection are more severe than those encountered by the bridge after completion. For instance, in allowable stress design, allowable stresses for stay cables are 56% minimum ultimate tensile strength (MUTS) (PTI, 2007) during construction and 45% MUTS for service load after bridge completion. Being able to withstand construction load that is of greater intensity, the towers, stays, and the bridge deck of cable-stayed bridges have more reserved strength for service loadings. Generally speaking, cable-stayed bridges are more vulnerable during construction and are less vulnerable after completion. In most cases the increase of tension in stay cables due to seismic load is in the order of 10%. This increase in tension may be insignificant for stay cables, because like the main cables in suspension bridges, stay cables are designed using a safety factor of 2.2, but may be of concerns to connections. Connections are commonly designed for either maximum service load demand in stay cables or the yield strength (instead of MUTS) of the connected stay cables, and thus have less reserve in their strength. Therefore connections are more sensitive to seismic loadings.

One of the possible vulnerabilities is that the deck may experience uplift problems during service load and more likely the earthquake loadings. The uplift problem is more pronounced for situation where the side span is short (less than half of the main span length). During the 1995 Hyogoken-Nanbu Earthquake, uplift of deck was found on Higashi-Kobe Bridge (Wilson, 2003) that was only less than 3 years old at that time and was designed using state-of-the-art seismic code.

There are more variations in shape of tower for cable-stayed bridges than for suspension bridges. And concrete towers and bridge decks are more often adopted in cable-stayed bridges. In case of concrete deck with single pole of pylon, the deck is usually monolithically connected with the tower. Such examples are Sunshine Skyway Bridge, Second Cross over the Panama Canal, and Chi-Lu Bridge (Buckle et al., 2000). This is certainly a unique tower-deck connection for cable-stayed bridges. The associated potential problem is that a flexural hinge may occur at both tower and the deck at the location of tower deck connection, such as Chi-Lu Bridge in Chi-Chi Earthquake. Likewise at the tower location, the deck segment is subjected to the largest compression and moment and is thus vulnerable to flexural failure.

11.3.3 Bridges during Construction

For bridges under construction, the relatively short duration of construction (compared to their design life) does not necessarily lead to relatively lower seismic hazards. Actually a study (Wilson and Keith,

2007) shows that probability of cable-stayed bridges subjected to earthquake-induced damages during construction using balanced cantilever method is much higher than when the bridge is completed and in service. During construction, the bridge is put into a very precarious and vulnerable position, and relatively small to moderate earthquake ground motions with a much more frequent rate of occurrence than the design-level ground motions for the full bridge may actually impose significant seismic loads on the partially completed bridge. However, since during construction, the partially erected cable-stayed bridges are also susceptible to instability because of aerodynamic effects of wind load, and temporary bracing (such as buffeting cables) will have to be used during construction. Because it is very unlikely that design earthquake and design wind load will take place at the same time, the stabilizing structure for controlling wind vibration can be designed and served as temporary retrofitting of the bridge for earthquake loading during construction, as well. It is generally accepted that the bridge shall be designed to resist an equivalent static load of 0.10 g for configurations occurring under the assumed construction sequence (Caltrans, 2002).

There are two particular construction periods for cable-stayed bridges when the bridge is in its most vulnerable state, one is the final stages of superstructure extension, before the closure of the side and main spans; and another critical stage exists in between the span closure and before completion of final stay cable adjustment. The first case is readily recognizable, but the second scenario is not so apparent. Immediately after the closure, the bridge seemingly takes its final shape but its internal forces locked-in during balanced cantilever construction basically remains the same. During construction, certain stays, portions of pylon, and superstructure are heavily loaded and may be already in the proximity of their nominal strength. The final stay cable adjustment, therefore, is to put the bridge into the final designed profile, and more importantly is to redistribute internal forces to reach a desirable state where stays and all structure members have sufficient reserved strength for future service and earthquake loads.

When the Chi-Lu Cable Stayed Bridge in Taiwan was hit by the 1999 Chi-Chi earthquake (Buckle et al., 2000), its final stay cable adjustment was just commenced. In other words, the bridge was in the vulnerable period of transition from construction state to fully completed state. It is speculated that two factors that may have contributed to the formation of deck hinge are (1) the precast overhang segments were not installed at the location of tower deck connection and thus created a weak section; (2) the final stay-cable adjustment had not been completed and thus the locked-in moment at the location during cantilever construction had not been alleviated. By the same token that the locked-in moment had accumulated at tower immediately above the deck because of unbalanced stay cable forces and thus leave little reserve in strength for subsequent earthquake loading. It is advisable, therefore, the locked-in stress shall be intentionally kept as minimum during construction, although the final stay cable adjustment is inevitable.

11.4 Conceptual Seismic Design

The first step in designing a new bridge is the "type selection." There are many factors leading to the final selection of a particular bridge type. If the bridge is located in earthquake zone, it is logical that seismic performance should become one of the criteria for type selection. However, this is seldom the case. Selection is about comparisons. Because there is lack of rigorous method of directly comparing seismic performance of different bridge types, seismic design or consideration often begins after the main bridge type is determined (based on other criteria), and its role is to confirm, or in most cases to ensure that the selected bridge type is viable.

In case of seismic retrofit design of an existing cable supported bridge, the design process includes investigation, diagnose, and design. Generally speaking, seismic retrofit design is much more challenging than new design, because the design options are limited because of various constraints set by existing conditions of the bridge and requirements set by owners to preserve the architectural appearance of a historical bridge. The most difficult task is probably the determination of the actual "as-built" conditions of the bridge. Problems associated with information gathering process include locating the

drawings for both original design and for changes made to the bridge over time; determining exactly what materials were actually used in construction and what their remaining strength values are; and perhaps the hardest part is the finding of the accumulated damages and deteriorations in the aged structure. Problems associated with corrosion are sometimes hidden behind paint or they are not in accessible locations. Nondestructive testing techniques may be used to determine the real status of the bridge. Only after such an investigation has been performed and the real structure has been identified, will it make sense to study a retrofitting problem for the structure (ASCE-SSPB, 1996).

In either new design or retrofit, it is very important for designers to (1) understand the seismic response characteristics of cable supported bridges; (2) design to prevent failure (or collapse); and (3) design to eliminate the potential component vulnerabilities as stated in Section 11.3.

11.4.1 Response Characteristics

In the long-span range, cable supported bridges are generally favored for their aesthetically pleasant appearance. From seismic response stand point of view, the long-span cable supported bridges have the following unique characteristics:

1. Long vibration period—Most of the long-span cable supported bridges have fundamental vibration period in the range of approximately 2–8 seconds. It results in: (1) their force response level is relatively low compared to bridges with much shorter vibration periods, because they fall in the lower right part of the typical design earthquake response spectrum; (2) their displacement response is considerably large and makes P-Δ effect more pronounced.
2. Low damping—The superstructure and cables possess little material damping and it takes longer time for the vibration to decay once it started. Ambient vibration tests and forced vibration tests (Yan and Lao, 2000) have shown that the damping ratio of cable-stayed bridges is in the range of 1%–2%. Data acquired during earthquake from instrumented bridge (Ingham et al., 1997) revealed that the damping ratio of suspension bridge is in the range of 1.5%–2.0%. This is much lower than that of commonly adopted 5% critical damping for seismic analysis of bridges. Recorded data of bridges excited by wind also have shown that as long as the structure remains elastic, there is no obvious increase in damping with increased vibration amplitude (ASCE-SSPB, 1996).
3. Complex vibration modes—Because the major structural elements, tower, cable, and deck, have significantly different vibration periods and mode shapes interacting with each other, the vibration modes of the bridge is densely distributed and highly coupled. Due to geometric nonlinearity of cables and stays, the vibration modes and their frequencies are amplitude dependent. The vibration modes and periods obtained from modal analysis can only be verified by micro ambient vibration tests. These modes will change significantly with shifting frequencies during moderate and large vibration when subjected to external force, wind, and earthquakes in particular.
4. Sensitive to multisupport ground motions—The distance between supports is relatively long, and the seismic ground motions may be very different at each support and this may affect the response behavior of the bridge. The difference in ground motions at different supports are resulted from two sources, namely the variation in soil condition and the difference in arrival time of seismic wave between bridge supports.
5. Large expansion joints—Long-span cable supported bridges require large gaps to allow movements because of thermal, service load, and earthquake load effects. This poses another challenge to design engineers. In case of new Self-anchored Suspension Bridge of SFOBB, the movement at end span expansion for the main self-anchored suspension bridge during events of design earthquakes is approximately 2.5 m (closing plus opening). In the longitudinal direction of the Rion-Antirion Bridge, the deck is free to accommodate all thermal and tectonic movements and the

joints are designed to accommodate 2.5 m displacements under service conditions and movements up to 5.0 m under an extreme seismic event (Combault and Teyssandier, 2005).

6. Great importance—Most of the cable supported bridges are considered relatively more important. This is because (1) they often serve as part of a key or lifeline transportation link; (2) they require significantly larger initial investment. Being more important, the design life is also longer. In the United States, the design life for ordinary bridges is 75 years, whereas for important bridges it is 100 years. Consequently, the important and long lasting cable supported bridges are subjected to more stringent performance and design criteria. This feature, although purely social related rather than structure related, has posed an ever-increasing challenge to bridge engineers.

11.4.2 Seismic Design Strategies

There are several design strategies for improving the resistance of a bridge to seismic hazards. The seismic hazards currently known include ground shaking, fault rupture (FR), soil liquefaction, and lateral or vertical ground movements. Approaches to improve the resistance of a bridge to these hazards include (1) strengthening; (2) enhancing ductility (displacement allowance); (3) providing redundancy; (4) tuning or rearticulating; (5) seismic isolation; and (6) energy dissipation. These strategies are generally used in combinations, depending on the bridge and seismic hazard, to reduce the risk of failure at the most optimum cost to the owner (Imbsen, 2001). This chapter will focus primarily on retrofit design for purpose of presentation; however, same strategies may also be applied to new bridge design.

11.4.2.1 Strengthening

It is generally required that superstructure, including lateral bracings, shall remain essentially elastic under events of design earthquakes, and the connections of main load carrying members shall be designed as capacity-protected elements. For these components, a brute force approach is taken, that is, to strengthen the member to an acceptable level of force demand-to-capacity ratio. In order for these members to have sufficiently adequate strength, the demand shall be determined using most adverse conditions. For instance, the load case for determining the maximum force at stay cable connections shall include loss of one adjacent stay cable.

11.4.2.2 Enhance Ductility

For substructures, such as towers, pylons, and piers, strengthening is difficult to achieve, because increasing strength may not enhance safety, nor necessarily reduce damage (Priestley, 2000). In fact, strengthening of substructure leads to an increase in fundamental frequencies and consequently to higher seismic force demands. It has been realized that better seismic performance is achieved by adequate ductility (displacement capacity) instead of force capacity. Long-span cable supported bridges often possess large displacement capacity. This is mainly because of their global flexibility and geometry nonlinearity, not ductility, that is, inelastic displacement capacity. Because inelastic response is inevitable, ductility is critical to prevent bridge collapse. Steel members subjected to high axial compression combined with flexural bending will often buckle at strains near the yield strain of the material, eliminating, or severely compromising the ability of the member to form a stable plastic hinge. In this case, ductility can be improved by lateral stiffening. Stiffeners applied to the component plates can prevent buckling until beyond yield, making the member moderately ductile (Seim and Ingham, 2000). For concrete members, ductile performance is achieved by lateral confinement. Chi-Lu cable-stayed bridge suffered extensive damages during the 1999 Chi-Chi earthquake (Buckle et al. 2000), including two flexural hinges on single pole tower (one above deck and one on the top of pile cap); one flexural hinge on the superstructure and broken stay cable at end pier. Nevertheless the bridge did not collapse owing to the fact that the tower was designed with sufficient ductility,

using design approach analogous to state-of-the-art seismic design codes adopted in California, United States.

11.4.2.3 Provision of Redundancy

The first and foremost rule of thumb is to provide redundancy for the bridge. Redundancy is achieved by providing alternate load path. This is because the random nature of earthquakes and our inability of accurately predicting the bridge response. The biggest uncertainty lies in the prediction of ground motions. Seismologists repeatedly state that ground motions, however parameterized, may differ readily by a factor of two or more for a given exposure level or design event. The solution to this uncertainty is to design ductility and redundancy and toughness (ASCE-SSPB, 1996). It is relevant to examine the Rokko Island Bridge that was severely damaged during the 1995 Hyogoken-Nanbu earthquake. The Rokko Island Bridge is a double-deck steel arch bridge and was completed in 1990 (Wilson, 2003). During the earthquake, the south end of the arch fell off the steel pivot bearings and was shifted 3.1 m eastward, leaving the east arch unsupported by the pier. Complete collapse of the bridge was luckily prevented by the lower cross-beam landing on a settlement jacking block. The jacking block acted as shear key in this case and provided a crucial redundant load path in the lateral direction, although this was not originally intended for. The alternative load path can be provided by shear keys, catch blocks, restrainers, or others. These devices are not expensive and are relatively easy to design and install.

11.4.2.4 Multiple Articulations

Long-span cable supported bridges are required to resist high wind loads, both static and aerodynamic. The requirements for wind performance and seismic performance may be incompatible. For instance, wind performance criteria require stiffer structure, whereas seismic designs often call for flexible bridges. In such a situation rearticulation is a good strategy. Such strategy was applied to the Golden Gate Bridge, West Span of SFOBB, Rion-Antirion Bridge, and will be applied to the New Gerald Desmond Cable-Stayed Bridge that is currently under design. During service load conditions, the stiffening trusses are connected to towers by rigid structural elements and form required load path for wind and live loads. During earthquakes the connection members will fuse off and allow relative displacement in between the towers and the stiffening trusses. This change in articulation will activate the viscous dampers installed at the same locations. The viscous dampers will dissipate energy and reduce the relative displacement between the connected parts. Similar technique was also adopted for the Vincent Thomas Bridge but with a slightly different form. As shown in the Figure 11.4, a hinge was inserted in each side span stiffening truss (Baker et al., 1998; Seim and Ingham, 2000). Each hinge consists of a new pin in the top chord, with new diagonal members framing into it. The bottom chord was cut between the new diagonal members and a fuse element and a damper were placed in the cut, in parallel with the pin. The fuse element

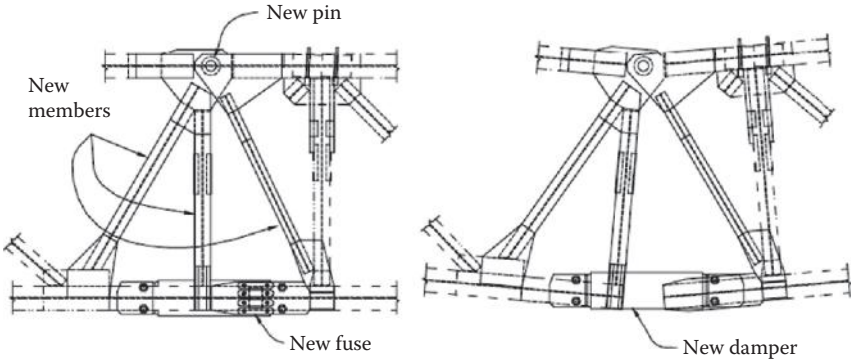

FIGURE 11.4 Rearticulating the stiffening girder. (From Seim, C., and Ingham, T. J., *Proceedings of Structures Congress* ASCE, Washington, DC, 2000.)

is strong enough to carry live and other service loads but it has a capacity less than that of the bottom chord. During an earthquake the fuse will rupture, protecting the chord against overstress. After the fuse element has ruptured the entire stiffening truss (and the side span) can rotate about the pin. The rotation activates the damper, further reducing forces throughout the side span. This retrofit contains elements of rearticulation and damping of the structure. The rearticulating not only provides a mechanism to activate the damper, but also directly eliminates deformation-induced loads in the structure.

11.4.2.5 Base Isolation

To reduce force demands to substructures and foundations, seismic isolation is a good measure being widely used for bridge and building structure. Seismic isolation is often used in combination with viscous dampers. To reduce the adverse inertia force impact on the main bridge, the approach structure of cable supported bridge is often isolated by using isolation sliding bearings, such as what was installed atop the new steel support towers at the Pylon N2 support and at Bent N11 of the Golden Gate Bridge (GGBHTD, 2011), and the Antirion Approach Viaduct of Rion-Antirion Bridges (Infanti and Castellano, 2004). The available sliding bearings for bridge are elastomeric and spherical sliding bearings.

Another form of seismic isolation is foundation uplifting and rocking. Several suspension bridges built in the United States have been diagnosed to have potential foundation rocking at towers when subjected to design earthquakes, although there was no such intention during original design. Seismic retrofit studies show that it is desirable to allow the tower base or the foundation base to rock and uplift during the earthquake. The towers uplift when the dead load is shifted from one shaft to the other (rotation about the longitudinal axis of the bridge). However, the towers rock when one side of the base of the shaft separated from the pier and shifts the load to the other side. Retrofitting the towers by anchoring them to the reinforced concrete pedestals was found to induce higher stresses and did not have any significant advantage in reducing the seismic forces in other locations of the bridge. Towers rock works like a fuse that limits the maximum transverse moment at the base to the uplift moment (equal to the dead load multiplied by the width of the tower base over two). Another advantage in allowing the towers and foundation to rock is the inherent shift in the period of vibration (Nader and Ingham, 1996).

11.4.2.6 Energy Dissipation

To improve the seismic performance of structures by increasing damping using dampers has been proved to be most efficient and cost-effective. Commonly used damper devices are friction devices, metallic hysteresis devices, and fluid viscous dampers (Murphy and Collins, 2004). Friction devices range in complexity from very simple slotted-bolt connections with sliding surfaces to more complex devices. The simple slotted-hole devices have the distinct advantages of being very low cost, and the installation into the existing truss members would be relatively simple. Metallic hysteresis devices, using the inelastic energy dissipation capability of a highly ductile metallic element to dampen motion, are probably the most intensively investigated damping systems for civil structures. One of the most widely known configurations is the so-called added damping and stiffness (ADAS) device (Hanson et al., 1993), including multiplex X-shaped plates designed for inelastic flexure. Other types included steel tube energy absorbing devices and steel shear links. Steel tube energy absorbing devices rely on the axial yielding of steel tubes, whereas steel shear links rely on shear yielding of web to provide the damping. In general, dampers are used to achieve two different objectives, namely to reduce displacements and to reduce force demand.

In the first approach, large damping devices (such as high capacity fluid viscous dampers) are implemented in between towers and stiffening trusses or in between end piers and stiffening trusses or both, and their main purpose is to reduce gross relative displacements between major components, rather than to reduce member forces or dissipate energy. Actually the energy dissipated by large fluid viscous dampers at isolated locations was found to be insignificant (Manzanarez and Nader, 2000; Nader and Ingham, 1996). Several suspension bridges in western United States have been recently retrofitted using the first approach. New cable supported bridges built in other parts of the world have also been implemented with various fluid viscous dampers to enhance their seismic performance.

In the second case, the design scheme consists of installing relatively small damping devices (such as friction and metallic hysteresis devices) at key locations distributed throughout the suspended span to dampen seismic forces from many different vibrational modes while keeping localized deflections small. It was found that the chords and lateral members in stiffening truss were best suited to small damper installation, because of the higher stress levels experienced during seismic events and also because of the ease of installation in these locations. For the dampers placed within the truss chord members, those nearer the midspan experienced higher displacements and overall dissipated more energy than those chord dampers placed near the towers and anchorages. In the case of the dampers located in the lateral truss members, the opposite was true. The dampers nearest to the ends of the spans were subjected to higher displacements, whereas those located near the midspan were not activated as often (Murphy and Collins, 2004). Some suspension bridges in eastern and central United States are currently under consideration for using the second approach for seismic retrofitting.

In some applications the two objectives, namely reduce both displacement and force demand, are to be achieved simultaneously by implementation of shear links distributed in between slender tower shafts. Shear links have been extensively used in building structures and recently gained momentum of being introduced to cable supported bridges in the United States. The new self-anchored suspension bridge of SFOBB is the largest self-anchored suspension span in the world. Its 160 m tall single tower consists of four steel shafts connected with intermittent steel shear links distributed along its height on both longitudinal and transverse directions (Tang and Manzanarez, 2001). The use of shear links for tall bridge towers was also attempted during conceptual design for the New Gerald Desmond Bridge, a three-span cable-stayed bridge at Port of Long Beach of California. The shear links used on bridges are significantly larger than those used for buildings. The prototype of these shear links have been successfully tested in university laboratories (McDaniel et al., 2003), but have never been tested by real earthquakes.

11.5 Special Design Issues

The general seismic design for a new bridge can be outlined as follows:

1. Develop policy and planning (importance of the bridge and its design life).
2. Identify seismic hazard.
3. Develop performance and design criteria.
4. Investigate geotechnical and earthquake input ground motions.
5. Proceed with modeling, analysis, and design.

The procedure for seismic design of an existing cable supported bridge is slightly different:

1. Develop policy and planning (importance of bridge and its remaining service life).
2. Identify seismic hazard.
3. Develop performance and design criteria.
4. Investigate geotechnical and earthquake input ground motions.
5. Investigate as-designed and as-built condition of the bridge.
6. Develop computer model and verify it using ambient vibration tests.
7. Assess seismic vulnerability.
8. Proceed with retrofit modeling, analysis, and design.

The listed items, rather than their sequence of execution, are of greater importance. Obviously, there are interactions between different design stages and iterations are necessary. Each of the design items actually represents a special issue or topic and can be discussed in great depth. Some of these issues are explored in the following sections.

11.5.1 Bridge Designation and Service Life

Seismic design of bridges begins with determination of their importance and design life, or their remaining life in case of seismic retrofit. Although importance of the bridge governs its seismic performance criteria and design criteria, it is certainly not a pure technical issue. It has a lot to do with policy making and consideration of social and financial consequences, and thus mainly determined by the owner. The ground acceleration hazard is usually expressed as a percent probability of exceedance for the life-span of the bridge, that is the return period. In the United States, the design life is 75 years for short and medium span bridges and 100 years for longer span bridges. In reality, however, many of the existing highway bridges have exceeded their design service life, and for various causes, the life-spans of bridges continue to increase. The oldest long-span suspension bridge in the United States, the Wheeling Suspension Bridge in West Virginia (ASCE-SSPB, 1996), was 159 years old as of 2013 and there is no sign that its long service life will be terminated soon. The most impressive statistic resulting from research conducted since the 1989 Loma Prieta earthquake is the conclusion that retrofitting the existing suspension bridges in the United States would be more cost-effective than replacing them. This indicates that most of the cable supported bridges are going to last much longer than was originally designed for. In determination of the seismic hazard and ground motions, what useful life should be ascribed to such bridges? Should such bridges be assumed to last forever? If a structure is to have a design life of 100 years, it would be desirable to have earthquake-occurrence statistics over a period several times that long in order to establish the probability of occurrence of a major earthquake in the vicinity of the structure during its planned life (Clough and Penzien, 2003).

11.5.2 Seismic Hazard and Performance Criteria

Performance criteria are project specific and are relevant to potential seismic hazard. The site-specific seismic hazard is represented by three levels of ground motions, and for each level of ground motion the seismic performance expectations vary depending on the bridge designation and its importance. The seismic design approach has been shifted from force-based design to performance-based design. Performance-based and displacement-based are considered to be synonymous (Priestley, 2000). The performance criteria define the anticipated functionalities and permissible damage levels. Obviously, the establishment of seismic performance criteria is the most critical step in seismic design. For all long-span bridges in California, the general seismic performance criteria listed in Table 11.1 are used as a first guideline followed by the development of project specific performance criteria and design criteria on how these performance criteria can be quantified and met (Gates, 1993; Seible, 2000).

The alternative definitions for Functional Evaluation Earthquake (FEE) and Safety Evaluation Earthquake (SEE) are OBE and MCE, respectively. OBE is the earthquake for which a structure is designed to remain operational, with damage being readily repairable following the event. MCE is defined as the largest earthquake that appears capable of occurring under the known tectonic framework for a specific fault or seismic source, as based on geologic and seismic data. In terms of seismic hazard OBE may be comparable to FEE, but MCE is definitely much larger than SEE.

Once the importance of a bridge in a system is known, then proper bridge performance criteria can be developed. For long-span bridges, seismic performance criteria, with respect to service and damage levels, are typically established for two types of seismic events: FEE and SEE. In several cases in the eastern United States, the two levels have been associated with two different recurrence periods, most commonly 500 and 2500 years, although no formal consensus has yet developed (ASCE-SSPB, 1996). In addition to response under FEE and SEE, for bridges crossing potential active faults require a third level, namely FR, to be considered. Because the Palos Verde Fault passes through the main span of the Vincent Thomas Suspension Bridge, the bridge was also analyzed for a rupture of the fault beneath it. Specifically a "maximum credible" FR of 2.7 m was applied as a relative displacement between the bridge towers (with longitudinal and transverse components, because the fault is at an angle to the bridge) over

TABLE 11.1 Caltrans Seismic Performance Criteria

Seismic Hazard	Performance Criteria		
	Ordinary Bridge	Important Bridge	Life Line Bridge
Ground Motion	Minimum Performance Level	Limited Performance Level	Full Performance Level
FEE	• Immediate full service (I) • Repairable damage within 90 days • Allow lane closures outside peak hours • Minor concrete spalling, joint damage, and limited secondary steel members buckling	• Immediate full service (II) • Repairable damage within 30 days • Repairs will require minimum interference with the flow of traffic • Minor concrete spalling, joint damage, and limited secondary steel members buckling	• Immediate full service (III) • Minimal damage • Essentially elastic • Minor concrete cracking • Minor buckling in secondary steel members
SEE	• No Collapse (I) • Significant damage with a high probability of repair • Maintain vertical load carrying capacity and a minimum lateral system capacity • Damage may require full closure for public traffic • Repair will require complete evaluation	• Limited service • Intermediate repairable damage • Light emergency vehicles within hours • Reduced public traffic lanes within days • Lateral system capacity is relatively reduced • Repair within a year	• Immediate full service (I) • Minor repairable damage • Lateral system capacity slightly effected • Minor concrete spalling, joint damage and limited secondary steel members buckling • Lane closure outside peak hours only • Repair within 90 days
FR	• No Collapse (II) • Extensive damage with low probability of repair • Maintain residual capacity for probable vertical and lateral service load only	Not Applicable	Not Applicable

Definitions:
FEE: The Functional Evaluation Earthquake (FEE) shall be based on the spectra for a 285–300 year return equal hazard event. This (FEE) corresponds to 60% probability the ground motion not being exceeded during the useful life of the bridge.
SEE: The Safety Evaluation Earthquake (SEE) shall be based on the target response spectra for a 1000–2000 year return period equal hazard event. This (SEE) corresponds to 85% probability the ground motion not being exceeded during the useful life of the bridge.
FR: For Fault Rupture (FR) assessment, consult your geotechnical engineer.

Source: Adapted from Seible, F. Proceedings of the 12th World Conference of Earthquake Engineering, Oakland, New Zealand, 2000.

a duration of 10 seconds (Ingham et al., 1997). The conclusion was that the FR was too slow to excite the structure dynamically. The only effect of the FR was to open the expansion joints and lift the main span of the bridge several feet. Another bridge that has known active faults underneath the structure is the Akashi-Kaikyo Bridge in Japan (HSBA, 1998). Obviously there is not enough information on how bridges respond to FR.

It is noticeable that immediate full service after SEE is required by Caltrans seismic performance criteria guidelines for all the lifeline cable supported bridges. How practical are these criteria remains questionable. In fact, the stringent criteria are somewhat relaxed in fully developed seismic performance criteria adopted by the bridge owners. For the Golden Gate Bridge, the performance criteria

for seismic retrofit require that bridge to be open to traffic within 24 hours of MCE, and to be fully operational within one month (Rodriguez and Ingham, 1996). For the New East Spans of SFOBB, in another case, the performance criteria require that after a SEE, the life line including the self-anchored suspension bridge shall provide full service almost immediately (Manzanarez and Nader, 2000). Here "almost" is an indefinite term and as modification to "immediate." For seismic retrofit of the Manhattan Bridge (Fanjiang et al., 2001), the traffic access to the bridge and the approaches following the SEE shall be limited within 48 hours for emergency/defense vehicles and within months for general traffic. After the FEE, the access shall be immediate to all traffic with an allowance of a few hours for inspection. Despite that whether a few hours are sufficient for inspecting an important long-span cable supported bridge remains questionable, allowance of time for inspection is no doubt very prudent. From both technical and practical point of view, there are a couple of aspects that should be considered when making such explicit time limit in performance criteria.

- The minimum time required to inspect an important long-span bridge after a safety level earthquake event and make the assessment that the bridge is safe to open
- The minimum time required for development of retrofit design and to repair the minor damage

Detailed procedure and requirements for post-earthquake inspection and repairing of structural elements anticipated to damage during earthquakes shall be covered in bridge maintenance manual. Considering inspection and repair, it is relevant to cite an incident occurred on the East Spans of SFOBB. A routine inspection during a construction-related closure in September 2009 revealed a crack in a critical 65 ft. long eyebar component of the existing main eastern span (Reid, 2010). The crack was found in one of eight bars sharing the same load and was not present 2 years earlier. Discovery of this crack by itself warranted an immediate bridge closure. Additional components to distribute the load around the crack were promptly designed and fabricated overnight. The repair was completed in approximately 72 hours and the bridge was reopened a day before the original estimate, resulting in only minimal impact to traffic (Carlsen, 2009). On October 27, 2009, during the evening commute, parts of the September emergency repair, a crossbar and two tension rods, collapsed onto the upper deck roadway. One car and a delivery truck were struck by or collided with the 2.25 tons of debris. The bridge was closed to traffic in both directions for six days. The failure of the repair was caused by two design defects: first, the tie rods closely fit the holes in the cross-pieces over the saddles and second, wind caused vibrations in the rods, which in turn caused wear and bending at the through holes, eventually causing a rod fracture. The catastrophic dropping of the cross-piece was caused by a lack of structural attachment to the saddle, being retained only by tack welds, friction, and the tension of the tie rods. Although this incident is not seismic related, it has two important implications: (1) it takes time to understand the damage occurred and to find the right solution and (2) rush to solution under great pressure of reopening the bridge may lead to catastrophic failure and caused longer closure to the bridge.

The damage to the new long-span steel bridges in Kobe area (Wilson, 2003) has already provided an alert to the structural engineering community as to what can happen to even new designs and valuable lessons on both techniques and time frames for restoring these moderately damaged bridges to operational status. There is also the conclusion that the time required for repair work greatly exceeded what is currently thought of as an acceptable limit for closure of a major new transportation route. In the United States, seismic performance criteria would require that, ideally, there be little or no interruption of traffic on such major lifeline routes.

Most of the long-span cable supported bridges are connected to approach spans with relatively shorter span length. As a result the main span and the approach span fall in different categories. The performance criteria for both main span and approach spans, however, must be consistent. For instance, in order for the main span bridge to remain open after MCE events, the approach spans shall only suffer minor repairable damage. Being relatively stiffer and having their fundamental vibration periods fall within short period range of the design response spectrum (Figure 11.3), approach spans, existing structures in particular, are actually more vulnerable for seismic damage, and it is much

more challenge to design approach structures to meet the high-level seismic performance criteria. When determining performance criteria for the cable supported bridges, therefore, the design engineers shall be mindful that the performance of the entire transportation link is actually controlled by the approaches.

11.5.3 Design Criteria

Performance criteria set permissible damage level for design earthquakes, whereas design criteria specify or quantify the damage. In addition, design criteria must provide the technical guidelines to achieve the performance objectives. No damage is defined for structural members as the nominal capacity. Minimal damage implies essentially elastic performance characterized by narrow cracking in concrete, minor inelastic response without apparent permanent deformations. Repairable damage means the damage can be repaired with a minimum risk of losing functionality, characterized by spalling of concrete cover and limited yielding of steel. Significant damage consists of concrete cracking, reinforcement yielding, major spalling of concrete, and deformations in minor bridge components that may require closure of the bridge to repair or replace. To achieve the performance objectives, the estimated displacement demands under design earthquakes shall not exceed the structure's global displacement capacity and the local displacement capacity of any its individual components. Table 11.2 lists a quantitative strain and displacement ductility limit corresponding to the two damage levels for concrete bridges (Duan and Chen, 2003).

Towers and end piers are the most critical bridge elements from seismic design standpoint; they are the only primary elements of long-span cable supported bridges may be designed to yield and form plastic hinges during SEE. Owing to their importance, cable supported bridges are commonly categorized as limited ductility structure. This means that although the strain and ductility demand is limited as shown in Table 11.2, the detailing and proportioning shall be in conformance with full-ductility requirements as defined in ATC-32 (ATC, 1996). It implies that efforts have to be made to reserve sufficient ductility capacity in order to cover great uncertainties in both prediction of demand and capacity of the structure. Representation of plastic hinge in concrete column or pylon structures is a great simplification of the complex inelastic behavior. The multilinear elasto-plastic moment-curvature curves for two orthogonal axes are traditionally used in modeling without considering biaxial bending effects. This may lead to an overestimation of plastic deformation capacity of the structures, that is, the displacement capacity. It is often assumed (or hoped) by design engineers that the error may be negligible if the peak responses in the two orthogonal directions do not occur at the same time. Other source of overestimation of deformation capacity may be attributed to the assumption of confined concrete model. It is often assumed that sufficient confinement can be achieved in designing new concrete members. As a result, Mander's confined concrete model (Paulay and Priestley, 1997) is used to generate capacity curves indiscriminately. Columns and towers of

TABLE 11.2 Damage Levels, Strain, and Ductility

	Strain				Ductility	
Damage Level	Concrete		Steel		Curvature μ_φ	Displacement μ_Δ
Repairable	Larger	0.005 $2\epsilon_{cu}/3$	Larger	0.008 $2\epsilon_{cu}/3$	4–6	2–4
Minimal	Larger	0.004 ϵ_{cu}	Larger	0.003 $1.5\epsilon_y$	2–4	1–2

Notes: ϵ_{cu} is ultimate concrete compression strain depending of confinement; ϵ_y yield strain of steel, ϵ_{sh} hardening strain of steel, $\mu\varphi$ curvature ductility defined as ratio of ultimate curvature to yield curvature, and μ_Δ displacement ductility defined ratio of ultimate displacement to yield displacement.

Source: Adapted from Duan, L., and Chen, W., *Marine Georesources and Geotechnology*, 21(3–4), 2003.

cable supported bridges are usually elements of significant geometrical dimension, and often with noncircular shape for aesthetical considerations. Large dimension, noncircular, and hollow sections greatly limit the confinement effects from lateral reinforcement as anticipated for much smaller circular sections. Failure to recognize this difference will certainly lead to overestimation of the curvature and displacement capacity of the critical members.

For steel bridges, structural components shall be generally designed to ensure that inelastic deformation occur only in the specially detailed ductile substructure elements. Inelastic behavior in the form of controlled damage may be permitted in some of the superstructure (secondary) components such as the end cross-frames or diaphragms, shear keys, and bearings. For all primary components elastic buckling shall be precluded, and for components expected to behave inelastically, initial yielding and inelastic buckling are expected but fracture failure modes shall be prevented by adequate lateral stiffening. All connections and joints of main load-carrying members shall preferably be designed to remain essentially elastic. Generally, seismic design criteria for steel structures vary quite noticeably depending on specific project.

Minimal damage to foundation, including pile foundation and caisson foundation, is permitted during SEE. For pile foundations, the design of the pile-caps is based on capacity design principles. Although under design load conditions only the pier is expected to form plastic hinges with the piles barely approaching yield, the pile-cap is designed to handle over-strength moments from both the pier and the piles (Abbas and Manzanarez, 2001). Anchorage blocks of earth-anchored suspension bridges are normally required to sustain no damage during SEE.

Suspension system, including cables, suspenders, and saddles, is probably the only structural group that is still designed using traditional allowable stress method. Saddles are allowed to reach the yield strength, whereas cables, suspenders must be kept well within their elastic range under SEE, with force demand less than one half of their breaking strength. All connections are designed for the yield strength of the connected components. It is notable that connections for suspension system are not designed as capacity protected structural elements. This is because suspenders and stay cable are usually designed with large factor of safety (for reason as mentioned earlier in Section 11.3.1.3) and thus have ample strength reserves. Minimum factor of safety of 4.0 are commonly adopted for suspenders for service loads based upon ultimate catalog breaking strength. This factor of safety includes the loss of efficiency because of bend over cable bands. To design connections for forces greater than the breaking strength of the rope or stay cable is neither practical nor economical. The required robust or additional safety of the connections is achieved by requiring that the bridge shall remain stable and repairable under conditions involving accidental loss or breakage of any one suspender rope or stay cable. Progressive failure triggered by break of one stay cable or one suspender shall be prevented. There are incidents of broken suspenders and stay-cables (Yanev, 2008); however the effect of these failures has been localized by redundancy. In 1981 one of the diagonal stays of the Brooklyn Bridge broke because of corrosion and killed a pedestrian. All suspenders and stays were subsequently replaced. A suspender broke at the first Bosporus Bridge in 2004 and a stay cable was burned by lightning at the Rion-Antirion Bridge in 2006, neither one causing significant traffic interruptions. Suspender and stay replacement is recognized as a periodic necessity. The suspenders of the Manhattan Bridge have been replaced at least once and will be replaced again under a pending contract (Yanev, 2008). It may be relevant to point out that there is growing tendency of increasing spacing of suspenders or stay cables for various considerations. The increased distance between suspenders affects primarily their own behavior as well as that of the bridge superstructure. As the spacing of suspenders or stays increase, the size of suspenders or stays and their connections will also increase, so does the risk of progressive failure because of accidental loss of a single suspender or stay. The cables themselves are also influenced in at least two ways. The cable bands that improve the behavior of broken wires and the compaction of the cable are reduced. Consequently they transit greater concentrated loads and bending moments to the cable.

Loss of tension (or slack) in stay cables during earthquakes is considered detrimental, because it can lead to unseating of the strand's anchorages and introduce great impact force to connections when slacken stays are reengaged. Because the behavior of stay cables with little or no tension has not been

fully understood yet, it is prudent to prevent cable from slackening under any circumstances. A common practice is to require that the stays have minimum of 10% design dead load tension under SEE events (PLB, 2012). This can be achieved by increasing the initial tension in stays. On the other hand, the increase in initial stay cable forces may cause chain reactions affecting other structural components and shall be carefully examined.

For expansion joints, only minimal damage is permitted for cases where immediate full service of the bridge is required after the design earthquake, and significant damage is allowed for other cases. Minimal damage implies damage can be temporarily bridged with steel plates, and significant damage requires closure to repair.

Long-span cable supported bridges usually serve as vital transportation links and thus have high volume of vehicles. The probability that those bridges are struck by design earthquakes while carrying heavy or even congested live load is realistically very high. For instance the 1989 Loma Prieta earthquake occurred during evening rush hours. Having recognized that it is necessary to consider both inertia and gravity effect of vehicles when assessing the seismic performance, AASHTO LRFD requires that partial live load with earthquakes should be considered, and the percentage of live load to be used shall be determined on a project-specific basis (AASHTO, 2012). The Manhattan Bridge in New York City is one of most congested bridges in the world, including 800 trains per day (Fanjiang et al., 2001), and it is necessary to consider inertia and gravity effects of trains and road vehicles when assessing the seismic performance of the bridge. For traditional suspension bridges with heavy stiffening girders, road way live load is very small comparing to the dead load, and it may be acceptable to neglect the live load. For modern cable supported bridge with streamlined steel box girders in particular, however, the ratio of live load to dead load is much higher, and the effects of live load should perhaps be considered. For Self-Anchored-Suspension Bridge in the New East Span of SFOBB (currently under construction and is scheduled to open in September, 2013), the project-design criteria (Caltrans, 2002) mandates a reduced live load, corresponding to estimated peak hour traffic predictions for the year 2025, to be considered for combination with seismic demands. In addressing the live load effects, design criteria shall provide guidance for applying the most critical live load configuration for seismic demand calculation.

More detailed project-specific design criteria are needed for long-span cable supported bridges because of the following little or limited coverage in the current bridge codes (ASCE-SSPB, 1996): (1) suspension system; (2) detailing requirements for large-size concrete or steel members; (3) the special performance objectives of lifeline bridges; (4) extensive provisions for retrofitting existing steel bridges; (5) seismic devices, such as passive, active, or hybrid protective systems; (6) criteria for nonlinear dynamic analysis for cable supported bridge design or retrofit projects. For better presentation, design criteria for viscous dampers and shear links are covered in separate sections of the chapter. An example of project-specific design criteria is presented in the succeed sections. For a more detailed look at seismic design criteria for long-span cable supported bridges, reference should be made to the project-design criteria for recently designed cable supported bridges in the United States (WADOT, 2000; Caltrans, 2002; PLB, 2012). These documents are available in public domains.

11.5.4 Input Ground Motion

Because input ground motion has tremendous influences on all the design outcomes and greatest impact on construction cost, its selection is probably the most important design item among all. Unfortunately, it is also the most difficult design task to which we have the lowest confidence. Input ground motion used in many cable supported bridge designs to date have been developed by performing probabilistic and deterministic seismic hazard assessments to determine "target" spectra for rock motions, synthesizing spectrum compatible "control" histories of rock motions representative of the site, adjusting these motions for wave passage, and incoherency effects using either analytically derived transfer functions or semi-empirical coherency functions to determine rock motions at each bridge support, readjusting these motions for spectrum compatibility, and then using these motions to drive the bridge model

(if the bridge is founded directly on rock) or soil-foundation-structure interaction (SFSI) models of the foundations (if required). The tacit assumption has been made that spectrum compatible motions are adequate to determine damage (ASCE-SSPB, 1996).

Ground motions are by nature inherently random and variable. Owing to lack of records of strong ground motions in the vicinity of the bridge site, it has now become a common practice to derive artificial and spectra compatible earthquake records for cable supported long-span bridges. The design response spectra are project specific, and they must reflect the magnitude, the fault distance (intensity), and the frequency contents of the design earthquake to be expected for the bridge. Besides intensity and frequency content, duration of the earthquake is another important feature, especially for structures with long vibration periods. One approach to generating an appropriate ground-motion record has been to modify and distort an actual earthquake record so that it represents an event of different magnitude and distance. For an example, the intensity of motion may be adjusted by means of simple amplitude scaling factor, the frequency content may be modified by a change of time scale, and the duration of the earthquake may be changed by truncating or duplicating portion of the record (Clough and Penzien, 2003). Input ground motions in the form of acceleration, velocity, and displacement time histories are almost exclusively used to perform nonlinear time-history analysis for cable supported bridges. The development of input motions must be coordinated with the geotechnical and seismological aspects of a project. Specific issues identified as important are briefly discussed as follows.

- Near-fault effects—Pulse effect is one of the most prominent attributes of near-fault ground motions. Many recordings from recent earthquake events have provided evidence that ground motion record near FR is characterized by a limited number of obvious pulses with very high energy input, this pulse often contains large long-period (2s-8s) content, and this phenomenon often appeared in horizontal and vertical ground motions. Results of recent study have indicated that pulse-type near-fault ground motions will impose more severe damage potential to structures with long fundamental period (Jia and Qu, 2008), and it contributed largely to the significant damage occurred on Chi-Lu Cable-Stayed Bridge during the 1999 Chi-Chi earthquake (Chang et al., 2004).
- Spatial variable ground motions—Owing to their relatively long spans, variation in soil condition and difference in arrival time of seismic wave between bridge supports are large enough to warrant consideration of spatially variable ground motions. The spatial variation results from several effects: extended source effect (mixing waves types and source directions); attenuation effect (variable distance to the FR); wave passage effect (nonvertical wave propagation, the difference of the arrival of the seismic waves to different parts of the bridge because of its length); and spatial coherency effect (scattering and 3-D wave propagation effects). These effects are quantified by generating multiple-support artificial ground motions. The extended source effect and attenuation effect is insignificant and negligible in most cases. The spatial coherency effect is obtained when generating the ground motion at each support by adding random shifts to the phase angles of the reference time history. Traveling wave effects were considered by giving a shift in time to each time history. The shift is based on the assumption that the ground motions propagate parallel to the axis of the bridge at shear wave speed in the rock (Fanjiang et al., 2001). Does multiple support ground input tend to increase the response of the bridge or tend to reduce it? This topic attracted great amount of attention and generated numerous publications, and there are different and even contradictory answers to the above question. Some of these results obtained by different investigators are listed herein for purpose of discussion. Karmakar et al. (2012) conducted studies on the Vincent Thomas Bridge by nonlinear time-history analysis using spectrum-compatible spatial variable ground motions, and found that in some locations, the response of the stiffening girder increased, whereas in other locations the girder response dropped compared to that obtained from using uniform ground motions. Similar response redistribution was also found for typical suspension bridges under nonuniform seismic motions (Ettouney et al., 2001; Harichandran et al., 1996;

Dusseau et al., 1991). Nazmy, at al. (2004) also performed a rigorous nonlinear seismic-response analysis of the as-built bridge and the retrofitted bridge for the Vincent Thomas Suspension Bridge and found that for suspension bridges, the multiple-support excitation imposes relative displacements between the towers and the anchorage blocks, which induce both quasi-static and dynamic stresses and displacements. Due to the high degree of flexibility of suspension bridges, the out-of-phase motions usually give only a minor increase, or even sometimes a decrease, in the stresses in the structure. However, the demands on the expansion joints are generally larger with multiple-support excitation. Quite contrarily, however, Liu et al. (2000) reported that long-span structures with closely coupled vibration modes are particularly sensitive to the out-of-phase component of the ground acceleration input, and primary structural responses in the towers or piers could be underestimated by 30% ~ 40% if the out-of-phase acceleration were to be ignored. This finding was based on their seismic evaluation of the Golden Gate Suspension Bridge. And it may be of interest to cite a completely opposite conclusion made by some experts on exactly the same bridge: the overall effects of multiple-support time-history analysis has been found to result in significant reduction in demand, compared to that obtained by linear uniform base excitation analysis. In the analysis of the Golden Gate Bridge, with the foundations supported on rock, effects of multiple-support excitations (including wave passage, extended source, and ray path coherency) were found to be small when compared with analysis using rigid base excitations (ASCE-SSPB, 1996). According to Murphy and Collins (2004) "The inclusion of spatial variations in the ground motions had a large effect on the response, in some cases greatly increasing the demands on the truss members. However, as this effect is sensitive to the magnitude and configuration of the displacement time histories, which are difficult to know accurately, there is some uncertainty in these results." Obviously, this complex subject has not been fully understood yet, and a comprehensive literature review is beyond the scope of the chapter. From a practical point of view, however, the engineering implications of the topic are tentatively presented as follows:

  - The response of the bridge under multiple-support ground motions is generally different from those excited by identical support ground motion, because multiple-support ground motions may excite vibration modes not captured by using uniform support ground motions, and vice versa. The relative deviation is more severe for longer spans.
  - Because vibration modes for long-span cable supported bridges are closely spaced, and there is no single major mode that dominates the response of the bridge. Therefore, it is desirable to include as many vibration modes as possible. However, both uniform ground motions and variable ground motions are highly idealized and simplified representation of real ground motions. A particular ground motion is just one sample and the stochastic characteristics of true ground motions can only be represented by large number of such samples. The above argument leads to the conclusion that both spatially uniform and variable support motions shall both be used to generate better response envelopes that are most important to design engineers.

- Minimum suites of different input time histories required—The common practice in United States is to use three suites of spectrum-compatible time histories (Lam, 2008a and 2008b). Each suite contains three time histories; two horizontal and one vertical. Because SFOBB is located in between two major active faults, namely the San Andreas Fault and the Hayward Fault, six suites of synthetic seismic ground motions (Manzanarez and Nader, 2000), three for each fault, were developed and used to determine the structural deformation, strength demands and drifts. Studies on certain projects (Lam and Law, 2000), support using of seven sets of spectrum-compatible time histories. This can lead to statistically stable solutions within say 10% error.
- Spectrum compatible motions—Spectrum-compatible motions are favored because they provide envelopes of response maxima when the structural response remains linear, that is, when it is undamaged, but not when significant nonlinearities are expected. This issue is most important when significant response nonlinearities are expected in an earthquake for which the bridge

is expected to remain functional (ASCE-SSPB, 1996). Resolution of this issue would, probably, require the analysis of a particular bridge, under several different sets of modestly spectrum compatible ground motions, representative of actual motions at the site, using bridge models that explicitly account for all important nonlinear behavior modes. Little is known on this subject and more research is required.

11.5.5 Viscous Dampers

In cases where viscous dampers are to be implemented, the validity of the intended strategy rests on the following: (1) the existence of supplemental damper devices suitable for use in cable supported bridges; (2) the best suited locations for installation of dampers; (3) adequate capacity and characteristic damper parameters; (4) suitable auxiliary element or fuse restrainers if in case needed; and (5) successful laboratory testing to prequalify damper manufactures for bidding on the project. For new bridges, dampers are usually installed at the expansion joints on the end piers or at towers in between deck and tower legs. In placing and connecting the dampers, it is important not to leave an alternate load path that would enable the forces to bypass the dampers (Murphy and Collins, 2004). Comprehensive parametrical studies are required to determine the best damper configuration and parameters that define damper force in function (Equation 11.1):

$$F = CV^{n} \tag{11.1}$$

where V is the velocity, and the constant C shall be tuned to achieve a specified trigger force at a velocity threshold. Optimal exponent, n, is case dependent. For instance, linear dampers ($n = 1.0$) were found to be most suitable for the Vincent Thomas Bridge. This is in contrast to the damper retrofit for the Golden Gate Bridge, where dampers with an exponent of one-half ($n = 0.5$) were shown to be more efficient than linear dampers (Ingham et al., 1997). Experiences gained from past applications on cable supported bridges are especially valuable. Presented below are considerations on some special issues that may be of practical implications to practicing engineers.

- Factor of safety for fluid viscous damper—Once seismic demand are known, choice of manufactured damper capacity is solely dependent on a predetermined factor of safety. A proper safety margin rests on realistic estimate of the risks. It must be realized that dampers are susceptible to damage and thus may result in undesirable failure, such as the failure occurred at the Higashi-Kobe Bridge during the 1995 Hyogoken-Nanbu earthquake. The cause of the failure of the damper was later diagnosed as seismic force being underestimated. Despite the fact that the bridge was designed using most stringent and advanced seismic design method and was completed <3 years before being damaged, the damper capacity was proved to be inadequate. This indicates that there is great deal of uncertainty in determining the maximum velocity and thus the maximum damper force. The uncertainty may be resulted from multiple sources: (1) as pointed out earlier, the use of synthetic spectrum compatible ground motion time histories do not necessarily result envelopes of response maxima for nonlinear structures; (2) variation in velocity response is much greater than displacement response. It is quite possible that two different ground input time histories may produce similar displacement amplitude but quite different maximal velocities (can be easily off by a factor of two). Because force in viscous dampers is the function of piston velocity, its accurate prediction relies on accurate prediction of velocity, and numerically it is generally true that the accuracy in calculating velocity is one order lower than that in estimating displacement. Owing to greater uncertainty in predicting maximal damper force, the followings are advisable: (1) a factor of safety of 2.0 is appropriate for fluid viscous dampers; (2) more than three (preferably seven) suites of input ground motions shall be used to produce better envelopes of velocity response maxima; (3) the time step, Δt, used in the time-history analysis shall be small enough in

order to include sufficient high frequency contents to which the dampers are very sensitive; and (4) it may be beneficial to use a group of multiple parallel dampers with smaller capacity rather than a single unit with larger capacity.

- Design of fuse restrainer—Owing to lack of static stiffness, fluid viscous dampers are often installed with fuse restrainers in order to maintain stability of the structure. Fuse restrainer must have adequate stiffness and strength to resist various service loadings, including live load, wind load, and temperature variation, and to prevent dampers from being activated under these loads. During design earthquake events, however, fuse restraint should fail and thus activate the dampers. The fuse or failure mechanism may be simple, but its realization could be very intricate and is dependent on many factors that should be carefully considered. For instance, dampers in longitudinal direction are usually located near expansion joints at the end of the bridge. For long-span bridges, the thermal movement resulted from uniform temperature rise or fall could be quite large, and in some cases the temperature movement at the expansion joints could be larger than those resulted from functional earthquakes. It seems that the fuse restraints shall be able to "distinguish" the load induced by temperature from those induced by earthquakes. In addition to thermal and other transient load effects, actual failure of fuse restraints is greatly influenced by all the permanent forces accumulated during construction and service load conditions. For instance, if fuse restrainers are not installed stress free under total dead load, the locked-in construction force in them and subsequent changes because of long-term effects shall be taken into account in determining a proper force threshold for them to yield. Neglecting force history could lead to two undesirable scenarios: fuse restrainers will either fail prematurely or remain functional during design earthquakes when they are supposed to fail.
- Replace or repair of fuse elements—In some applications the bridge superstructure is supported on frictionless sliding bearings and is laterally restrained mainly by fuses. After design earthquakes, all the fuse restrainers are inactive and need to be restored. Under such condition, the superstructure has no or very little lateral stiffness because fluid viscous dampers do not have static stiffness, and consequently deck can swing and is unstable. Obviously, the performance criterion, immediate full service, cannot be met. Before the bridge can be open to traffic again, all or some of the fuse restraints need to be repaired first to stabilize the deck. In addition, superstructure may be twisted or misaligned with approach spans because of earthquake and needs to be jacked back to its original position. Designer should provide available mechanism for future jacking. Fuse restraints used on the Vincent Thomas Bridge were installed on the lower chord of the stiffening truss. Failure of fuse element will lead to formation of the hinge on the upper chord and the truss will rotate out of its original position (Figure 11.4). In order to repair or replace the damaged fuse restraint, the truss needs to be jacked upward and probably apart, too. Therefore, it has to be figured out at the time of design as how to access and replace the fuse restrainers and how long will it take to reopen the bridge.
- Testing of dampers and fuse restraints—It is generally required by bridge owners that the proposed fluid viscous dampers and associated fuses restrainers shall be prequalified by laboratory testing. For dampers used for retrofitting the Golden Gate Bridge, a test program was conducted at UC Berkeley in the United States (Rodriguez and Ingham, 1996). The program included cyclic testing of 445 kN dampers with a peak velocity of 50 cm/s and a stroke of ±15 cm. For the Rion-Antirion Bridge, the damper prototype tests were performed at the UC San Diego in the United States, whereas the fuse restraints tests were carried out at the FIP Industrial Testing Laboratory in Italy (Infanti and Castellano, 2004). The full-scale test of the prototype damper was characterized by a 3220 kN reaction at the maximum velocity of 160 cm/s and a stroke of ±90 cm. It is noted that the tests for fuse restrainers and fluid viscous dampers were carried out separately. The simplification of testing may be acceptable for this particular case, but should not be taken as a general approach. In cases where one unit consists of multiple dampers and fuse restrainers, interaction between dampers and fuses

could be very important for actual performance of the damper system. Within one group fuse restraints may be arranged in a symmetrical manner in relation to the dampers, but because of complex seismic response, they may not necessarily fail or fuse-off simultaneously. This will introduce adverse vibration modes and dampers will be activated separately and loaded with uneven forces. Consequently, progressive failure of fluid viscous dampers in the same unit may occur. In this case, results obtained by independently testing a typical damper and a typical fuse restraint have little implication to real behavior of the damper unit.

11.5.6 Shear Links

As an alternative energy dissipation device, shear links are very attractive because of their unique advantages of high efficiency, large capacity, and lower initial and maintenance cost. Steel shear links thus have been extensively used in building structures and have been recently introduced to applications to long-span bridges. Because shear links used for bridges are significantly larger than those of used for building structures, they are often made from built-up steel plate sections of various grades that are not available in rolled shapes. Although the design of shear links is case specific, there are challenging design issues and requirements that are common in different applications, such as effects of overstrength of steel because of cyclic hardening; large inelastic rotation capacity imposed on shear links and design of capacity protected connections between shear links and the major structural elements. Key aspects of design, modeling, and testing of steel plate shear links are presented in the included design example. For more detailed information, reference can be made to the papers of Dusicka et al. (2010) and McDaniel et al. (2003).

11.6 Seismic Analysis

Seismic design of cable-supported bridges heavily relies on analysis. To understand and predict the response behavior of the bridge under seismic loadings, both global and local models are required. The global models are developed to capture the overall linear and nonlinear seismic response of the bridge under multisupport ground motions. The local models are needed for detailed evaluation of both the demands and capacities. For important structural components, the local models are first used to explore the complicated inelastic behavior of the components and then lead to simplified representations of the elastic and inelastic mechanical properties of critical components that could then be incorporated into the global model. For instance, local nonlinear moment-curvature analysis leads to simplified plastic hinge representation of column or beam elements in inelastic flexural zones. Another example is the numerical simulation of hysteretic behavior of steel plate shear links. As presented in the included example (Section 11.7), the inelastic and cyclic hardening behavior of the steel plate shear links are captured by sophisticated nonlinear 3-D finite element analysis, and the knowledge gained from the local models are used to develop a highly simplified yet accurate truss analogy model to be implemented into the global model. The conventional approach to SFSI modeling as discussed in Chapter 14 is another such instance, where isolated foundations are analyzed with surrounding soils. The resulted response characteristics are then simplified as either foundation impedance or equivalent foundation soil springs to be used by global models.

The complexity involved with these models varies depending on their purposes. During preliminary design stage, for instance, a simplified elastic global model suffices, because in this stage it is more important for engineers to quickly grasp the basic behavior of the structure in consideration. In simplified models for the main bridge spans, foundation representation, portions of approach structure used as boundary frames, membrane effects of concrete deck, and local connection details may be neglected. Relatively larger mesh size is used as further simplification. Good judgment is essential for making wise choices as to what extent the model can be simplified. Simplified models are also best suited for parametric

studies. In cases where energy dissipation devices are required, extensive parametric studies are required to optimize their configuration and performance parameters. In more advanced or final design phases, however, the detailed models are preferable to most accurately predict the behavior of the structure.

To demonstrate that bridges meet all design criteria, various global analyses, each serves for a specific purpose, are needed. In performance-based approach, adequacy (or vulnerability) is assessed by comparing deformation demands with deformation capacities. To determine the deformation demands would require time-history analysis using global model with all important geometric and material nonlinearities. Whereas to calculate the deformation capacities would require either stand alone or global pushover analysis.

Seismic analysis of cable supported bridges is not really an independent subject, because the related theoretical background, modeling approaches, and analysis techniques are basically the same as those applied on various other structures, and the detailed and systematical descriptions can be found in Chapters 3 through 5. What is presented in this section, therefore, is focused on a few topics that may be of special interest to practicing engineers. Modeling and analysis of shear links are included in the provided example in Section 11.7.

11.6.1 Modeling of Damping

From dynamic analysis point of view, a structural system is fully defined when its physical properties (mass, stiffness, and damping) are known. In most cases, it is relatively easy to evaluate the structural mass and stiffness, but to fully understand energy-loss mechanism and then to express structural damping in proper and convenient mathematical form is rather difficult. For this reason, the damping in most structural system must be evaluated by experimental methods. The simplest and mostly adopted energy-loss mechanism is the viscous-damping, which leads to a convenient form of the structural equation of motions. By introducing normal-coordinate system and assuming orthogonal damping, the damping forces are uncoupled and are expressed in modal damping ratios (Clough and Penzien, 2003). It can be easily proved that the modal damping ratios are the most effective measures of the damping in the system when the analysis is to be carried out by mode-super-position method. When for nonlinear system the dynamic response is to be obtained by step-by-step integration, the damping matrix will be needed in explicit form. One of these explicit expressions, the Rayleigh damping, is discussed in Chapter 3.

In many applications it is desirable to use damping ratios that can be either constant over the whole structure or locally varying between components (element groups). This can be done by using a different form of damping: strain energy proportional damping (Kawashima et al., 1993). This method has been implemented into ADINA program (ADINA, 2011), where two types of strain energy proportional damping will be allowed. In the first type, energy damping ratios applicable to the whole structure are input. In the second type, the energy damping ratios are allowed to vary between different element groups.

As pointed out previously, cable supported bridges are characterized as lightly damped structural system and should not be artificially "over-damped" in seismic analysis. Using current design practice of the internal material damping of 5% modal damping for cable supported bridges is too high. Available data obtained from the ambient vibration and wind vibration surveys reveals that damping ratio for cable supported bridges is in the range of 1%–2%. System identification results of data collected at the Vincent Thomas Suspension Bridge during the 1987 Whittier earthquake show a nearly constant damping ratio of 2% for period range between 2 and 7 seconds. The period range of strongest shake is 0.5–2.5 seconds. The damping ratios of modes in this period range are between 1.5% and 2.0% (Ingham et al., 1997). The assumption, that damping will increase as vibration amplitude grows, has not been really tested. As long as the bridge remains elastic, the damping will remain as the same. When damages occur or there is energy dissipating devices, other types of damping mechanisms, such as hysteretic damping and Coulomb damping, will be formed within the structural system. In foundations there are material and radiation damping. Radiation damping will be dependent on the dimensions of the foundations and the equivalent radius of the soil contact area. Some past studies have shown that for horizontal and

vertical translational motions, the radiation damping is in the order of 10% or greater of critical damping. For rocking and twisting motions, however, the radiation damping is quite small and in the order of 2% of critical damping (ASCE-SSPB, 1996). If inelastic elements, such as plastic hinges, and hysteretic soil springs, and gap elements (allowing for both separation and rocking), have already been explicitly modeled, Rayleigh damping shall not be increased, because extra damping has already been included by these inelastic elements. Additional damping because of energy dissipating devices shall be modeled using concentrated dampers or inelastic springs or combined. In case where damping plays a decisive role as determining pass or fail of the design, conservative approach shall be taken in choosing proper damping values to be used, because damping is the structural property we know the least.

11.6.2 Modeling of Superstructure

With state-of-the-art FE modeling techniques, modeling of superstructures of bridges has become very straightforward and does not warrant detailed descriptions. There is one point about the selection of complexity of superstructure model, however, may be of practical implications and thus discussed briefly herein.

Superstructure decks, despite their different types, can be modeled using combinations of beam elements, truss elements and sometimes membrane, plate, or shell elements. Solid or brick elements are rarely used. Connections between elements can vary from pin connections, full moment connections to full rigid connections. The models comprise of line elements (beam and truss) are often referred to as simplified model. In simplified models, composite action in between primary load carrying members, such as truss and girders, and the concrete deck is not considered. In these cases, deck stiffness is completely neglected and deck inertia is modeled by lumped masses. If further simplification is deemed necessary, the whole superstructure is represented by a single or multiple spines. In contrast to simplified models, detailed models truthfully capture both the geometry and stiffness characteristics of the superstructure. Detailed models use both line elements and plate elements. In detailed models, relative distances between major elements are maintained; concrete deck is explicitly modeled and rigidly connected with line elements to reflect the composite effects. The detailed models are able to predict bridge behavior in both longitudinal and transverse directions. Obviously, using a simplified model reduces the total number of degrees of freedom significantly and simplifies the analysis. Thus simplified models are mostly used and preferred. On the other hand, using a detailed superstructure model requires considerably more effort to do the modeling, analysis and postprocessing of the results. Consequently, detailed models are less frequently used. Figure 11.5 shows detail superstructure model used in conceptual design of the Gerald Desmond Cable-Stayed Bridge.

Both simplified and detailed models were used to analyze the seismic behavior of the Vincent Thomas Bridge. The response of the bridge to the 1994 Northridge earthquake was recorded by accelerometers that were placed on the bridge. This measured response provides excellent opportunity to verify the computer models used. The computed periods of some of the fundamental modes

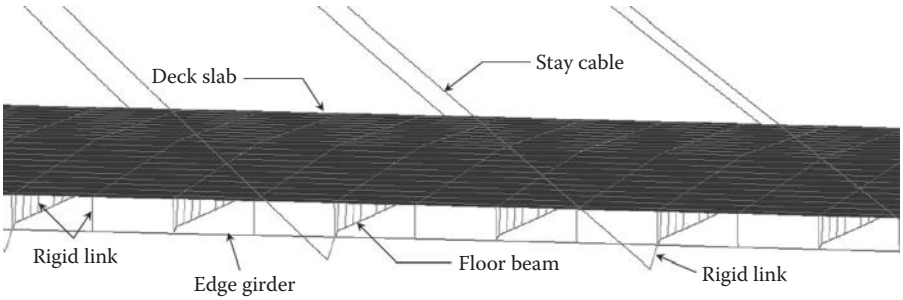

FIGURE 11.5 Detailed superstructure FE model.

are compared with the periods determined from the motions of the bridge, recorded during the Northridge earthquake, by system identification techniques. In those cases where a comparison is possible, the agreement between the computed and measured periods is quite good for the detailed model; whereas the agreement between computed and measured periods for the simplified model is not as good as that for the detailed model. The difference in the results probably arises from the fact that the simplified model is not capable of capturing the partial-composite behavior of the suspended structure. The use of both simplified and detailed models, as described in this chapter, is a practical approach for design. The simplified model proved ideal for parametric studies and the optimization of designs, whereas the detailed model most faithfully reproduced the behavior of the structure (Ingham et al. 1997).

11.6.3 Modeling of Cables and Suspenders

11.6.3.1 Modeling of Main Cables and Suspenders

Main cable of suspension bridges is the major load carrying element having near zero-flexural stiffness and very high axial tensile stresses. These two conditions lead to two different treatments of the nonlinear behavior, one often termed the stress stiffening effect, the other referred to as the large displacement effect. It has been found that in some cases the large displacement nonlinearity does not have a significant impact on results. Thus, the dynamic analysis considering stress-stiffening effect only is adequate (Murphy and Collins, 2004). Because advanced analysis technology considering both sources of nonlinearity is readily available and highly efficient, both stress-stiffening effects and large displacement effects can be considered simultaneously for most applications. The main cable is commonly modeled using 3-D truss elements with elastic material properties. Initial tension force is needed to enforce stress-stiffening effects onto truss members to keep the system stable. In some programs, initial force is input using initial strains. Sag effects and large displacement effects are included using large displacement formulation that updates structural stiffness and solves equilibrium equations of motion based on deformed geometry of the structure. As an important check, the geometry of the main cable and the stiffening girder under total dead load shall be in close agreement of the geometry as shown in the design drawings. Iterations may be required to update initial strains and thus improve the accuracy. A main cable takes the form of catenary under its own weight. For most engineering applications, the catenary can be replaced by a parabolic curve and will only result negligible difference. The parabolic simplification is also applicable to the case where main cables are subjected to nearly uniform tension forces coming from closely spaced suspenders. Although main cables are basically tension only members, at some locations, such as near tower saddles, bending stress can be higher enough to warrant special considerations. In this case, 3-D beam elements can be used in lieu of 3-D truss elements.

Modeling of suspenders is relatively more straightforward. For each suspender a single 3-D tension-only truss element between joints is good enough. Initial strain can be calculated based on initial tension under total dead load. In this case, the initial strains are required to achieve dead load profile as shown on the drawings for the stiffening girder.

11.6.3.2 Modeling of Stays

The nonlinear behavior of stays of cable-stayed bridges is essentially the same as that of main cables of suspension bridge. Because of its low stiffness in bending, a stay can only balance its own weight by taking the form of catenary. Because there are no concentrated loads in between supports of the stay, parabolic is almost an exact representation of the stay geometry. There are two commonly used methods of modeling stays. The first one is identical to that used for modeling the main cables for suspension bridges and the other is the method of linearization using equivalent modulus. In the first approach, each stay is modeled using multiple truss elements, even though there are no point loadings within the span. The sag effects are automatically taking into account by presence of the intermediate joints; and

stress-stiffening effects are activated by inputting initial strains. For most of the situation, using 6–10 equally spaced segments per stay will produce results with sufficient accuracy.

In the second approach, each stay is modeled using single-truss element. The nonlinear stiffness behavior is taken into account by linearizing the cable stiffness using the concept of an equivalent modulus of elasticity (Ernst Equation [Walther, 1988]) as

$$E_{eq} = \frac{E}{\left[\frac{(WL)^2 AE}{12T^3}\right] + 1} \tag{11.2}$$

where E_{eq} is equivalent modulus of elasticity; T tension in the stay; E modulus of elasticity of the steel; W stay weight per unit length; s length of the chord; and L horizontal span (s = cos α); and α angle between horizontal plane and the chord. The modulus E_{eq} defined in Equation 11.2 is only valid for a single value of tension T. If the stay tension increased from T_i to T_j, then equivalent secant modulus of elasticity suitable for any force ranging in between T_i and T_j can be expressed as (Equation 11.3)

$$E_{eq} = \frac{E}{1 + \left[\frac{(WL)^2 (T_i + T_j) AE}{24 T_i^2 T_j^2}\right]} \tag{11.3}$$

For bridges where tension variation in stays is small compared to the dead load, structures can be analyzed with satisfactory accuracy by linear calculation. In other cases, the first method for modeling stays is preferred. Special attention is required when performing seismic analysis, because the largest variation in cable tension could occur during earthquakes, and cable slack under such condition is a general concern. It is of interest to point out that in case where stays are modeled using equivalent secant modulus of elasticity, they are more likely to "slack" under seismic loads. It implies that cable slack resulted in nonlinear time-history analysis is not necessarily a real physical phenomenon. The false alarm is actually given by numerical or modeling problems.

11.6.4 Soil-Structural-Foundation Interaction

For cable supported bridges, the effect of soil-structure-foundation interaction (SFSI) shall be considered in design. SFSI analysis performed using detailed local model will generate added foundation masses, and various foundation springs and dampers to be integrated into the global model. Generally, foundation compliance will lengthen a fixed-based structural model period. Foundation damping will dissipate energy and hence will lower the structural response. Foundation compliance and damping tends to reduce forces, but increase displacement. Soft soils at water crossing sites can amplify ground shaking (Lam, 2008a). Long-span cable supported bridges are particularly sensitive to large displacement under such condition, and SFSI effects should not be neglected. Research results show that for the Vincent-Thomas Bridge, SFSI greatly affects the bridge vibrations. When SFSI is included, there are increments in the deck displacements of 250%–200% with respect to the case of no SFSI (Liu et al., 2000). Additional soil mass on pile or caisson shall be considered. Soil springs shall be developed for both upper bound and lower bound conditions. Effects of foundation scour and soil liquefaction are not included in upper bound soil condition, but are considered in developing lower bound soils springs. For piles group effects shall also be considered. SFSI is one of the most popular topics in structural engineering and detailed information is presented in Chapter 14.

11.6.5 Static Analysis

It may be a little odd to discuss about static analysis under the big title of "seismic analysis," but it is absolutely necessary and will be beneficial. Actually, the static condition of the structure is the very first step of the time

history of the response and an indivisible part of the entire seismic analysis. More importantly, response of a nonlinear structure is history specific, different initial conditions will lead to significantly different behavior. Seismic behavior of bridge could not be correctly predicted without knowing its static condition first. Besides, the model used in seismic analysis is exactly the same one used for static loadings. Unfortunately, the static analysis has not received enough attention and thus deserves a special treatment here.

Static analyses include dead load analysis and live load analysis. For concrete bridges, dead load analysis should also consider long-term effects of creep and shrinkage. To produce meaningful design data, a global model accurately reflecting the dead load condition of the bridge is essential. Dead load condition is the condition in which the completed bridge is in its final geometry as shown in design drawings with all dead and superimposed dead load (SDL) applied. It is the end of the construction and the beginning of the service life. The first important calibration of the model it to compare the reactions obtained with the number resulted from bridge weight take-off. Weight take-off is usually done by hand and is very tedious, especially for steel structures with abundant stiffeners and connections. Nevertheless, it yields useful information more than just the weight. By analyzing the composition of the weight or comparing the unit weight per linear foot or per square feet with those gained from similar designs, engineers can make a quick judgment as whether the design is reasonable. It is a common practice that the bridge weight take-off is carried out at several milestone design stages. The total reaction obtained from the computer model will generally differ from that of calculated by hand, and $\pm 3.0\%$ difference is considered acceptable.

Cable supported bridges are usually constructed in stages. Cable-stayed bridges are typically constructed using balanced cantilever method, and during the process the partially erected bridge components are subjected to loads resulted from the subsequent construction steps and boundary conditions that largely differ from those imposed on the completed bridge. Therefore, cable-stayed bridges are built with locked-in girder stress. The magnitude of the locked-in girder stress is dependent on detailed construction scheme and specific construction equipment adopted. Large locked-in force is detrimental, because it takes away a significant portion of component strength reserved for future loadings. To accurately record the total accumulated stress would require a detailed step-by-step construction stage analysis. Although it would be ideal that the global model resulted from a complete construction staging analysis is used as the base model for seismic analyses, it is not absolutely necessary. When designing a new bridge, detailed construction sequence is not yet known. In these cases, it is sufficient to assume a commonly adopted construction method defined by a few critical construction steps to be used as the design basis. And the dead load analysis shall capture the influence of construction-induced stresses in the major construction stages. An alternative of tracking initial forces is to define desirable target tension forces for stay cables and associated target longitudinal moment for bridge deck for the contractor to meet. Of course these targets must be reasonable and achievable by using available construction technology.

Although it has become apparent that locked-in girder stresses should be considered for cable-stayed bridges, it is still arguable as whether locked-in girder stresses should also be considered for suspension bridges. Over the past one and a half century, remarkable progress has been made in design and construction of suspension bridges. The theory of suspension bridges has evolved from Rankine theory, to elastic theory, 3-S deflection theories and finally today's nonlinear finite deformation theory. Nevertheless, the modern theory of suspension bridges has kept one of the fundamental assumptions rooted in its origin: under the total dead load on the bridge, the cable is parabolic and the stiffening girder is unstressed at mean temperature. The assumption implies that zero stress in the stiffening girder can be achieved by taking a specific erection sequence: lift stiffening girder in segments and hang them freely from the main cables, and then connect all joints after SDL is applied. In reality this ideal erection sequence is never strictly followed. For stability and practical considerations the stiffening girder is connected before SDL is applied. This is particularly true for modern suspension bridges where the streamlined steel box girder segments are connected by butt weld before applying the SDL. For truss-type stiffening girders corrective actions may be used to release the locked-in girder stress

because of erection process. Even with the best attention and adjustment, it is unavoidable that there will be a stress residing in the stiffening girder because of erection process. Two case studies have shown that the locked-in girder stresses because of applied SDL in suspension bridges are too significant to be ignored (Tao and Zong, 2007). For designing new bridges, the condition when the SDL is applied onto the bridge has to be clearly defined before carrying out the detailed designs. If the intended erection process will cause the stiffening girder to be stressed under SDL, the locked-in stress has to be quantified and included in the design. For rehabilitating an existing suspension bridge, it is essential to first determine whether there is locked-in stress in the stiffening girder because of SDL. If present, this stress must be included in developing new retrofit schemes, especially when the stiffening girder is expected to carry additional loads.

Once dead load analysis is validated, live load analysis can be carried out using the same global model. Live load shall be considered for combination with seismic demands in accordance with AASHTO LRFD Bridge Design Specifications (AASHTO, 2012). The loading factor γ_{EQ} to be used is project specific. In designing the new Gerald Desmond Bridge, for instance, factor γ_{EQ} is taken as 0.17 (PLB, 2012). For long-span cable supported bridges, deflected shape (rather than force) due to live load may have more effects on seismic response of the structure, because of P-Δ effects and geometry nonlinearity. Therefore it is important to use load pattern that will result most unfavorable deformation for towers and superstructure.

For bridges with significant geometry and material nonlinearity, their responses, either static or dynamic, are sensitive and dependent on both initial conditions and loading histories, and the principle of linear superposition does not apply. It implies that live load shall be applied after total dead load is applied. Likewise, seismic time-history analysis shall be based on the initial conditions because of all relevant static load effects.

11.6.6 Modal and Spectrum Analysis

Modal analysis is very important for understanding of the dynamic behavior of the bridge. The extracted periods and modal shapes will be used in spectrum analysis. Besides, results grained from modal analysis can be used to further verify the validity of the model. In case of seismic retrofit of an existing bridge, the calculated periods shall be compared with results obtained through an ambient vibration survey. Source of discrepancy shall be resolved. In case of designing a new bridge, modal analysis results can be checked using empirical formulas. For suspension bridges, the frequency of the first asymmetrical vibration mode for stiffening girder can be calculated as (Fan, 1996) (Equation 11.4)

$$f_b = \frac{0.3\left(\frac{E_c A}{W}\right)^{0.5}}{L} \tag{11.4}$$

where E_c is the modulus of elasticity of the main cable, A_c the metallic cross-section area of the main cable, W the mass per unit length of the stiffening girder, and L the length of the center span. Because E_cA and L are readily available and straightforward, the accuracy of frequency resulted from this formula mainly relies on W. If the computer model has already been calibrated using results of weight take-off, the comparison shall be very close. Similar empirical formula can be found for cable-stayed bridges, too.

In current design practice, results from spectrum analysis are no longer used to directly calculate demands for cable supported bridges. Nonetheless, spectrum analysis is still favored by many design engineers and is used to establish an initial probabilistic estimate of seismic demands, to eliminate modeling problems prior to the time-history analysis, and to establish the importance of various dynamic modes on seismic response (Ketchum and Waggoner, 1995). Sufficient vibration modes shall be included in the response spectrum analysis to capture >90% mass participation. In the spectrum analysis, 400 modes were used for the West Span of SFOBB in order to capture 90% of the bridge mass. The most appropriate modal combination is the Complete Quadratic Combination (CQC) method,

which accounts for the participation factors of individual mode shapes and the fact that the maximum response of the various modes does not occur at the same time and in the same direction.

11.6.7 Pushover Analysis

Pushover analysis is needed for two purposes: (1) to investigate the potential failure mechanism and (2) to assess the displacement or ductility capacity of the structure. For cable supported bridges, such analysis is required for towers and end bents. Local detailed analysis, such as moment-curvature analysis, must be carried out first to establish local force/displacement relationship to be implemented into the model used in pushover analysis. Pushover analysis is more straightforward for simple structures where the dominant deflection modes are easily identified. For cable supported bridges, however, to determine deformation pattern to be used in the pushover analysis proved to be a difficult task. The complication involves: (1) there may be no single mode that dominates the response of the bridge and (2) during an earthquake the inertia load vector on a structure varies continuously, whereas in a pushover analysis the load vector remains constant. Although it is required that calculated displacement demand shall be compared with the inelastic displacement capacity, there is lack of general approach for cable supported bridges as how should their global inelastic displacement capacity be evaluated. The problem may be solved by performing more than just one pushover analyses. A tedious but effective method is to examine the demand time history obtained for a particular variable in consideration and observe the deformed shapes of the tower corresponding to response peaks and select the most representative deformed shape to be used in pushover analysis. For the main tower of self-anchored suspension span of SFOBB, as an example, pushover analysis was performed using three load patterns in order to bind the expected lateral behavior (Nader et al., 2001). These three load patterns are: (1) the shape of the first mode, (2) the deformed shape of the tower at a time step corresponding to maximum drift in the global time-history analysis, and (3) a uniform load vector. For conceptual design of the Gerald Desmond Cable-Stayed Bridge, as another example, pushover analysis was performed on shear link tower in both longitudinal and transverse directions using three load patterns: (1) the shape of the first lateral mode, (2) the shape of the second lateral mode, and (3) a uniform load vector.

11.6.8 Nonlinear Time-History Analysis

In total displacement formulation, by neglecting mass or damping coupling between the bridge and the ground, the equations of motion used for time-history analysis of the bridge can be expressed as (Clough and Penzien, 2003)

$$m\ddot{v}^{t} + c\dot{v}^{t} + kv^{t} = -k_{s}v_{g} \tag{11.5}$$

where m, c, and k are the mass, damping and stiffness matrices of the bridge, $\mathbf{v}^t$ the total displacement vector, $\mathbf{v}_g$ the ground displacement vector, and where k_s the stiffness matrix coupling the bridge and the ground degrees of freedom. The ground displacements are applied at the ground nodes. The analysis of the structure is performed in the time domain by step-by-step integration of the equations of motion. Different numerical integration schemes are available. One of the commonly used algorithms is the Newmark-β method, with full Newton iteration at each time step. Because analyses for cable supported bridges are geometrically nonlinear, stiffness matrices are calculated at each time step using most current deformed configuration. To filter out high-frequency modes that have negligible contribution to the total response, a basic time step can be selected as $\Delta t = T_{\text{highest}}/4$, where Δt is the time step used in the integration and T_{highest} is the vibration period of the highest vibration mode to be included. The numerical integration algorithm implemented in ADINA will reduce the time step automatically as

needed to capture any nonlinear response of the structure or to accelerate the convergence. Test runs are necessary to ensure correct results. Diverge problem is often encountered. The problem may be purely numerical related, and can be solved by selecting proper integration scheme and converge criteria. It is more often that a diverging problem indicates hidden modeling problems. It is also possible, in case where the bridge model is bug free; the diverging problem or sudden crash of program execution is an indication that a failure mechanism has formed and the structure has become unstable. It takes experience, good judgment and comprehensive checking to distinguish between numerical problems and physical problems.

Results of nonlinear analysis heavily rely on the initial conditions of the structure. When the bridge is struck by an earthquake, there exist many possible initial conditions depending on DL, live load, and ambient temperature. Initial conditions that may have significant influence on the whole bridge or certain critical components shall be considered. Consequently, multiple time-history runs are required for each set of input ground motion. It must not be forgotten that although the computations are carried out in a deterministic manner, the seismic response of the bridge is by nature a random process, and more samples will result better envelopes to be used in design. Chapter 5 provides a more detailed discussion on seismic random response analysis.

11.7 Design Example—Cable-Stayed Bridge with Shear Links

This section presents the preliminary design and analyses of a three-span cable-stayed bridge implemented with steel shear links. The conceptual design was used by the owner as the base line design to solicit for final design and construction for the Gerald Desmond Bridge Replacement Project. The winning design scheme is very similar but with one major difference, that is the steel shear links are replaced by fluid viscous dampers. Despite that the original design was not adopted, it offers unique features on design of steel plate shear links for concrete towers of long-span cable-stayed bridges, and the knowledge and experiences gained from it may be of practical implications and can be applied elsewhere for future application. A presentation of complete design aspects and analysis is beyond the scope and length limit of the chapter, therefore only selected results, with focus on design and analysis of steel shear link related issues, are provided.

11.7.1 Project Description

The Port of Long Beach (Port), California, in cooperation with the California Department of Transportation (Caltrans), proposes replacement of the existing Gerald Desmond Bridge, which connects State Route (SR) 710 to Terminal Island, in the City of Long Beach, California. The Gerald Desmond Bridge Replacement Project, hereinafter referred as Project, is needed to improve the existing traffic flows, replace the physically deteriorated existing structure, and increase the vertical clearance

FIGURE 11.6 Rendering of the proposed new Gerald Desmond Bridge.

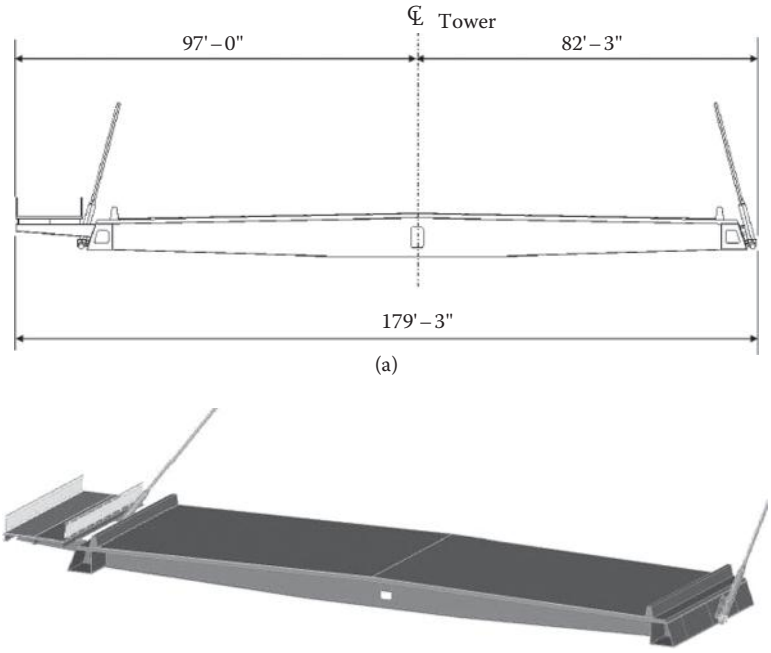

FIGURE 11.7 Proposed steel concrete composite deck: (a) Typical section; (b) 3-D view of typical deck segment.

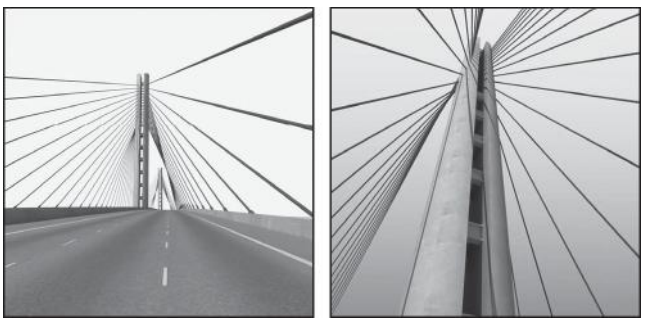

FIGURE 11.8 Rendering of shear link tower: (a) Global view; (b) tower head details.

across the navigation channel. Parson/HNTB Joint Venture is hired by Port to provide the preliminary engineering services for the Project.

The proposed new Gerald Desmond Bridge, as shown in Figure 11.6, consists of three major structures: (1) main span bridge across the navigation channel; (2) high approaches; and (3) low approaches and connecting ramps. The proposed main span bridge is a cable-stayed structure with steel composite deck and concrete substructure in which steel shear links are distributed in both longitudinal and transverse directions to enhance the seismic performance of the bridge. The proposed approach spans comprise of segmental concrete box girders. Main span bridge has a center channel span of 1000 ft. with two side spans of 500 ft., resulting in a main span bridge structure length of 2000 ft.; (Figure 11.7). The bridge structure will carry six lanes of traffic, four 10 ft. wide shoulders, and an integrated Class I bikeway.

The superstructure deck is a steel–concrete composite ladder beam with prefabricated steel box edge girders and prefabricated steel I-girder floor beams spaced at 17 ft. The edge girder is fabricated with inclined exterior web to anchor the stay cables and floor beam stub to accept bolted connections to the

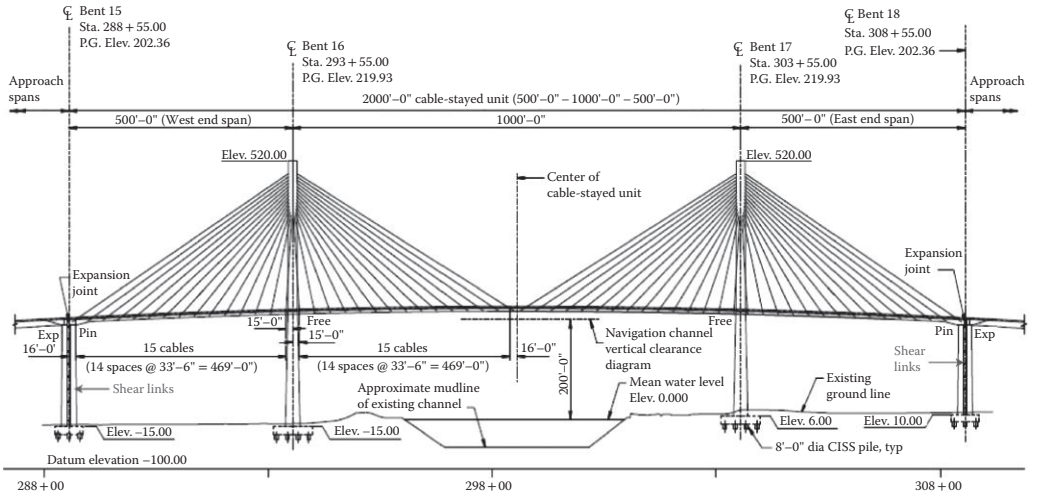

FIGURE 11.9 Main span elevation.

floor beam. The deck slab is formed from lightweight concrete precast panels integrated by cast-in-situ closure pours connecting edge girders, longitudinal stringers, and floor beams using shear studs (Figure 11.8). The steel beam-girder grillage at the end bents is filled with concrete as counterweight to resist uplift of the superstructure. The deck is longitudinally prestressed with high strength posttensioning bars. Stay cables are arranged in two splayed planes in a semi-harp pattern and are spaced at 33.5 ft. centers longitudinally. The deck is designed to be floating vertically as well as longitudinally at the main towers, whereas bumpers create a transverse support between the deck and the tower. At the end bents, the deck is pin-supported.

The single mast concrete towers (Figure 11.9) are composed of two semicircular concrete shafts spaced at 6.5 ft. apart transversely and connected by steel beams or shear links as seismic fuses and energy dissipaters. The shear links, which are replaceable, will deform beyond elastic range to dissipate energy during a major earthquake, whereas the concrete shafts will remain intact (Figure 11.10). In addition to the shear links, there are tension ties corresponding to each set of stay cables, as well as diaphragms at three levels. The end bents comprise of two tapering concrete ladder piers support both the main span bridge and the approach bridge. The seismic design strategy proposed for end bents is similar to what is used for the main towers: Each ladder pier consists of two semicircular hollow shafts spaced at 6.5 ft. apart longitudinally and connected by shear links. Foundations comprise of 8 ft. diameter cast in steel shell (CISS) piles. All piles are spaced at 3.0D. Each tower is supported on a pile cap with an array of 4 × 5 piles and each end bent shaft is supported on a pile cap with an array of 3 × 3 piles. Extensive parametric study and design iterations lead to the optimal tower and end bent geometry and shear link configuration as shown in Figure 11.9. For more design details about the proposed main span bridge, see Project Report Bridge Plans published at Port web site: www.polb.com/bridge.

11.7.2 Design of Steel Plate Shear Links

Two types of plate shear links (Figures 11.11 and 11.12) were proposed for laboratory testing. Only one of them will remain for final design, and the selection will be made based on the test results. Shear Link Type A and Shear Link Type B are both built-up steel plate girders and share the following common features:

1. There is no elastic zone. The links are deformable over the entire span.
2. The cross-sections are uniform and all the parts are made of the same steel.

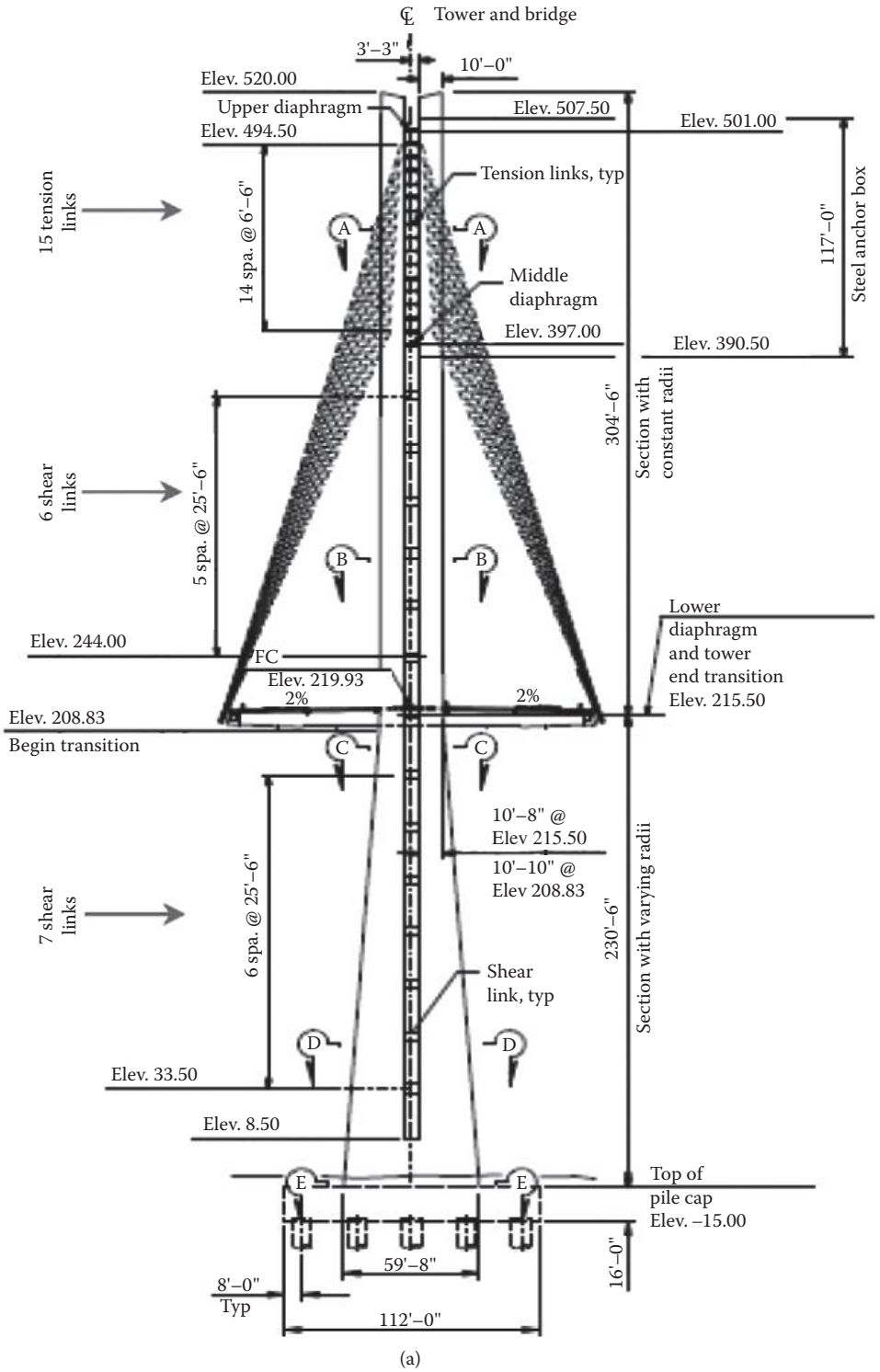

(a)

FIGURE 11.10 Concrete substructure with shear links. (a) Tower elevation.

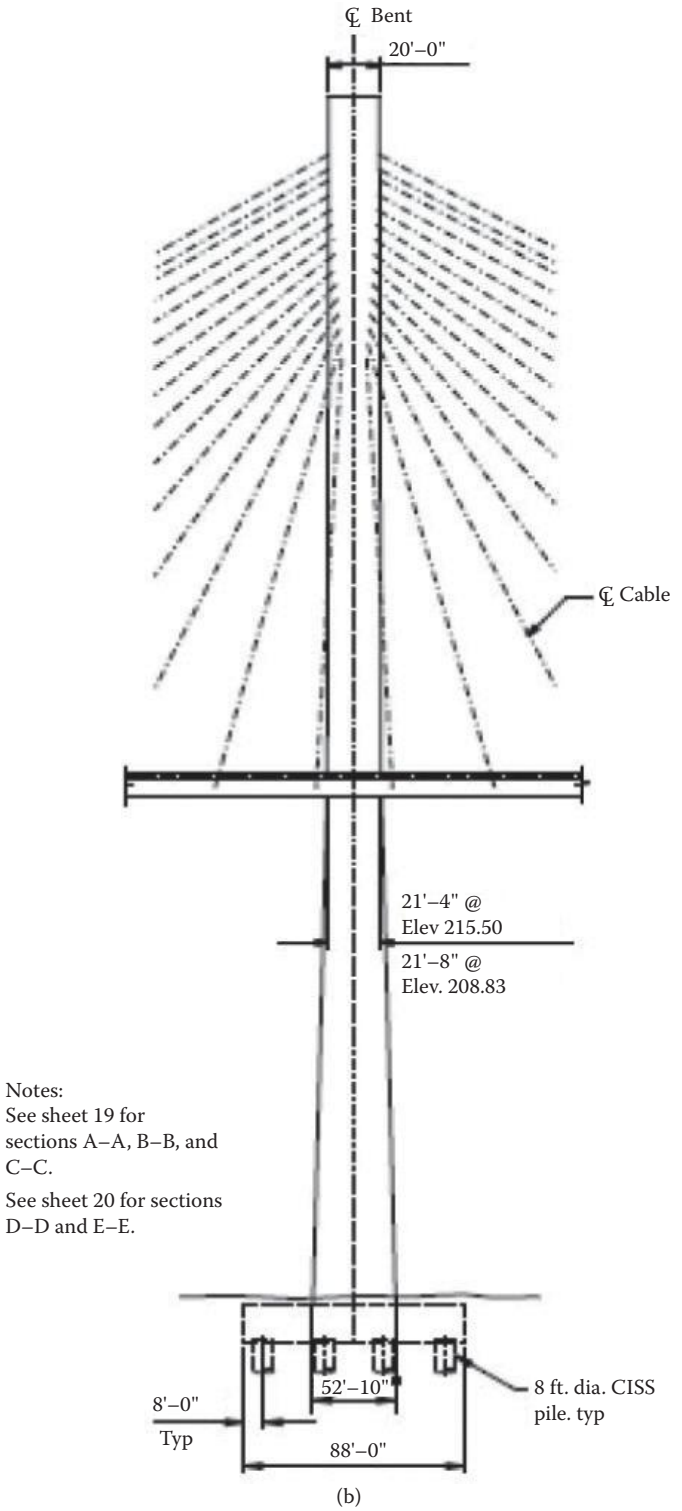

FIGURE 11.10 (*Continued*) Concrete substructure with shear links. (b) Tower side view.

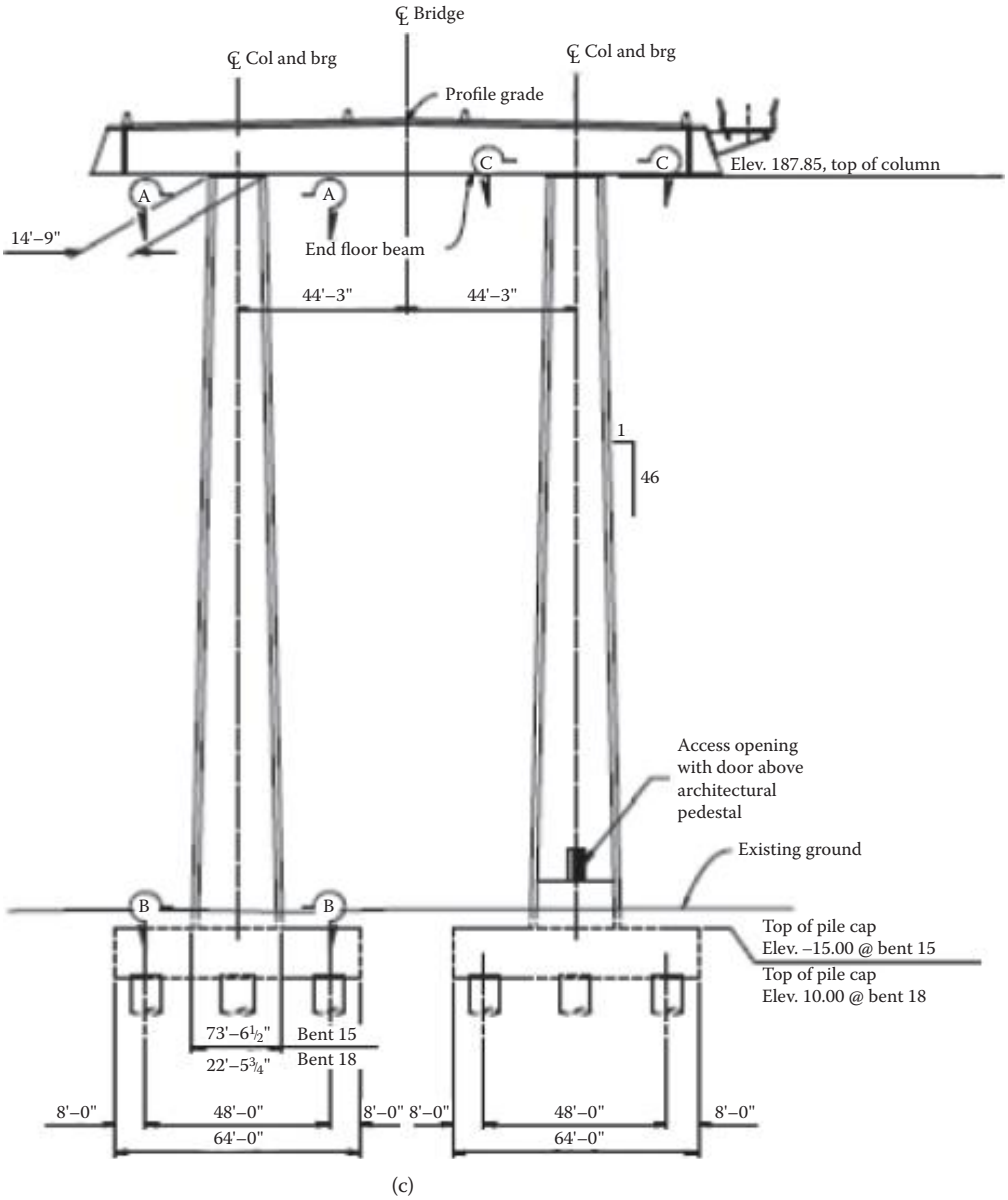

(c)

FIGURE 11.10 (*Continued*) Concrete substructure with shear links. (c) End bent elevation.

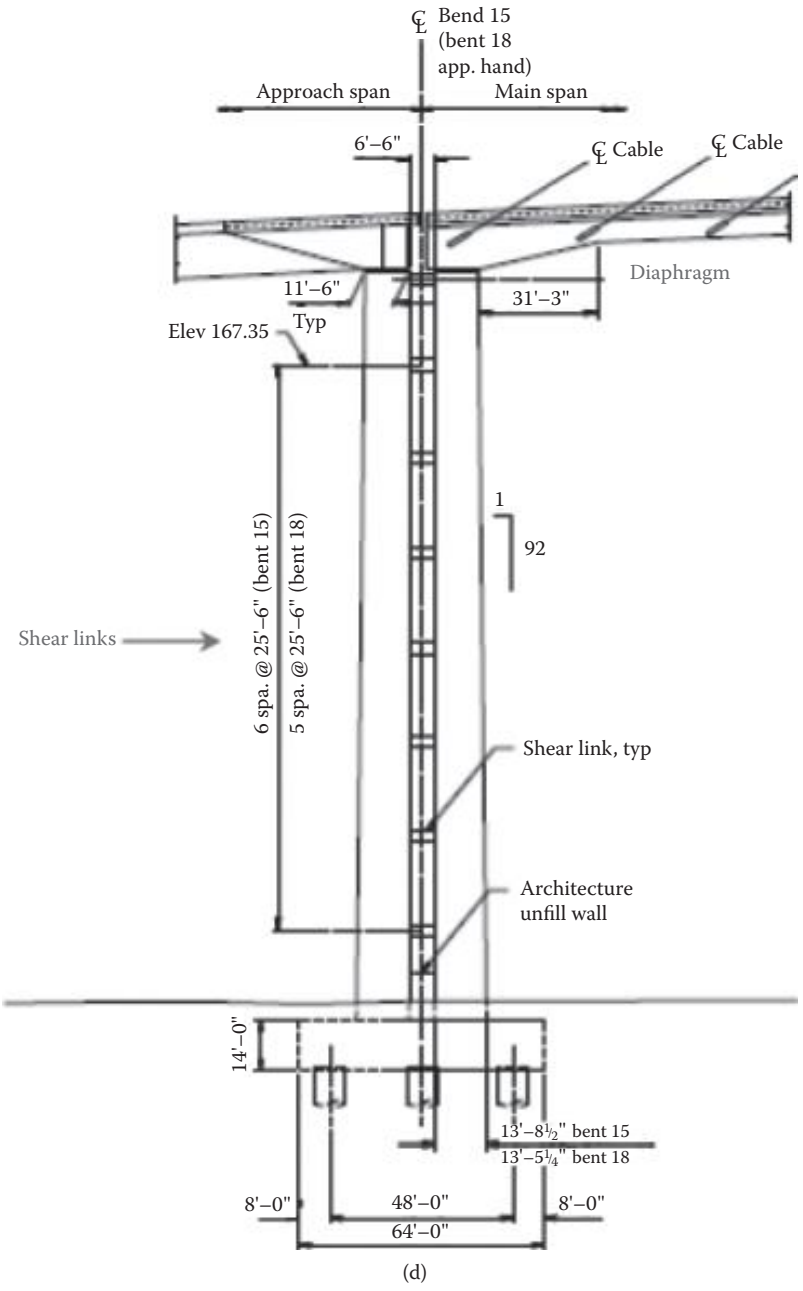

(d)

FIGURE 11.10 (*Continued*) Concrete substructure with shear links. (d) End bent side view.

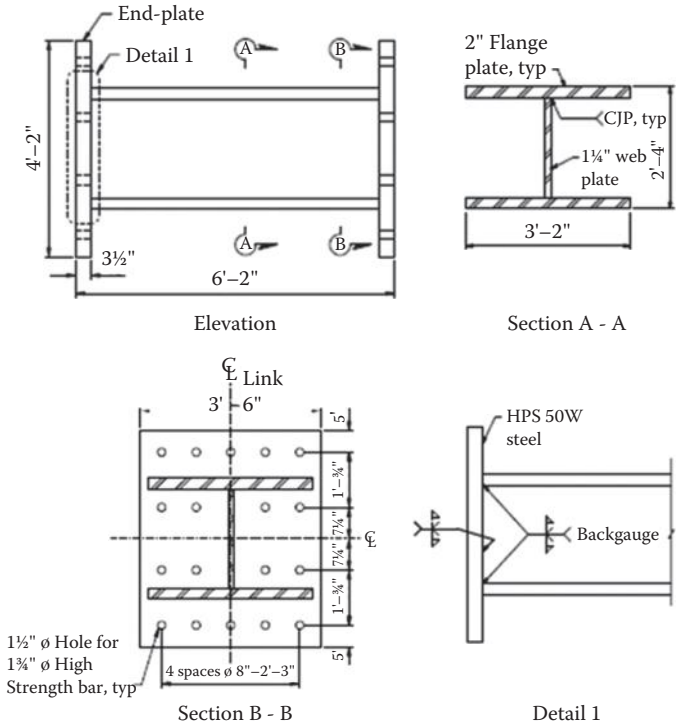

FIGURE 11.11 Steel shear link Type A.

TABLE 11.3 Tensile Test Results of A36LC Steel

Plate	Yield Strength (ksi)	Tensile Strength (ksi)	Elongation (% in 8 in.)	Charpy V-Notch (J) at −20° C
1	42.4	60.5	25.9	Average 355 >> 27 (by AISC)
2	41.1	61.0	25.0	

TABLE 11.4 Summary of Design Parameters

Link Type	Vp (kips)	Mp (kip-in.)	Link Length, e (in.)		bf/(2tf)		h/tw	
			Design	AISC	Design	AISC	Design	AISC
			<	1.6Mp/Vp	<	0.38(E/Fy)1/2	<	1.49(E/Fy)1/2
A	734	87,965	67	192	9.5	10.13	19.2	39.72
B	730	96,431	67	211	9.5	10.13	23.56	39.72

3. The links are connected to concrete tower shafts using end-plate moment connections with post-tensioned bars.

The major difference between them is that Shear Link Type A has an unstiffened web plate, whereas Shear Link Type B has a web plate stiffened with horizontal stiffeners. Owing to its low yield strength and high ductility and toughness, Nucor A36 Low Carbon Steel (A36LC) has been chosen as the base material for the link beams (flange and web). The tensile test results as reported in mill test report from Nucor are presented in Table 11.3. Cyclic axial and shear strain material test of A36LC steel was conducted at University of Washington, Seattle (UWS). The actual yield strength of the steel as delivered is found to be 40.8 ksi, and cyclic overstrength factors (ratio of maximum stress to yield stress) are

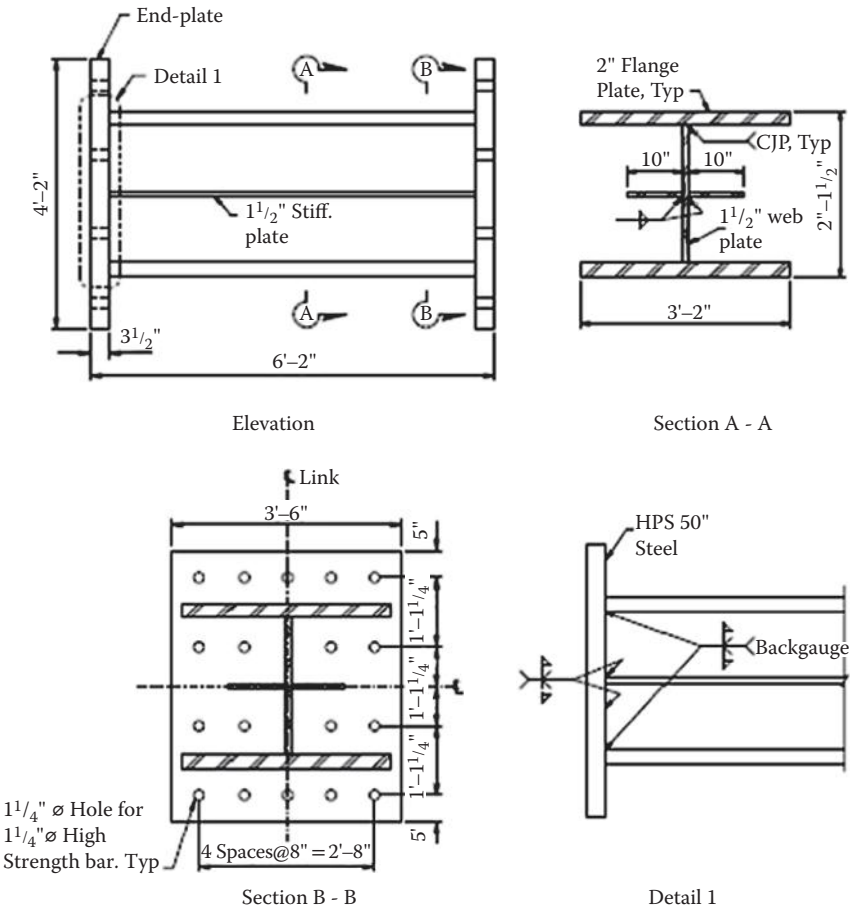

FIGURE 11.12 Steel shear link Type B.

found to be 2.01 for axial stress and 1.88 for shear stress, respectively. For more details of cyclic strain hardening characteristics of A36LC steel, reference can be made to report prepared by Berman (2009). The shear links are designed in accordance with the AISC Seismic Provisions (AISC, 2005). The design parameters are summarized in Table 11.4. Based on experimental evidence, the inelastic response of a link is strongly influenced by the length of the link, e, as related to the ratio M_p (plastic moment)/V_p (plastic shear) of the link cross-section. When the link length is smaller than 1.6 M_p/V_p, shear yielding will dominate the inelastic response. If the link length is >2.6 M_p/V_p, flexural yielding will dominate the inelastic response. For link lengths intermediate between these values, the inelastic response will occur through some combination of shear and flexural yielding. The inelastic deformation (equivalent to energy dissipation) capacity of links is generally greatest for shear yielding links, and smallest for flexural yielding links. The link lengths of both types (see Table 11.4) are significantly smaller than 1.6 M_p/V_p, and are categorized as short shear link.

Owing to its better through-thickness properties, Grade HPS 50W steel is chosen for end-plates. End-plates as designed are anticipated to remain essentially elastic. All welds, including welds at T-joint between link beam and end-plates, will be made in shop in strict conformance with a welding procedure specifications (WPS) developed by Robert E. Shaw for this particular work.

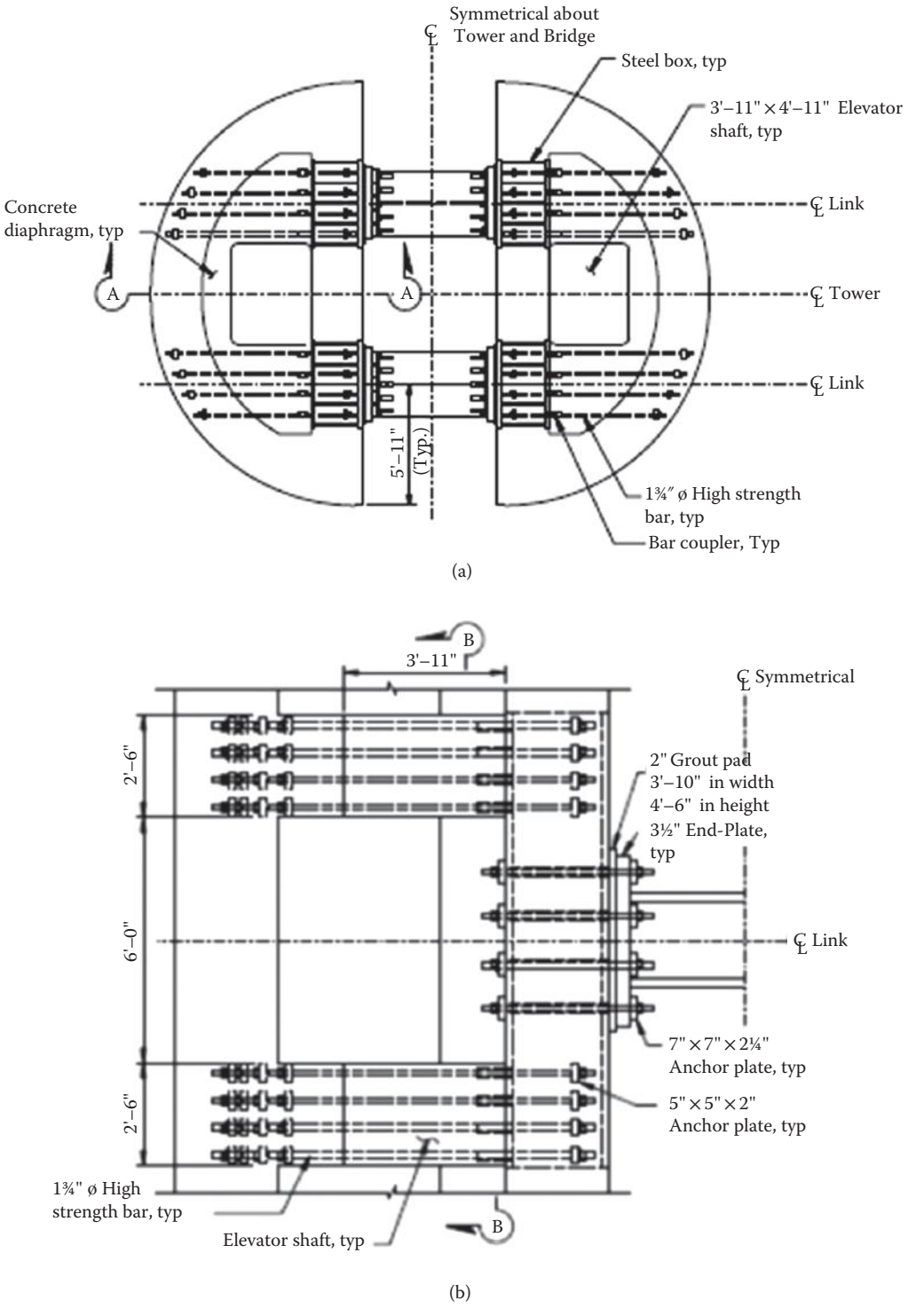

FIGURE 11.13 Shear link connection: (a) Connection plan view (upper link) and (b) Connection section A—A (upper link).

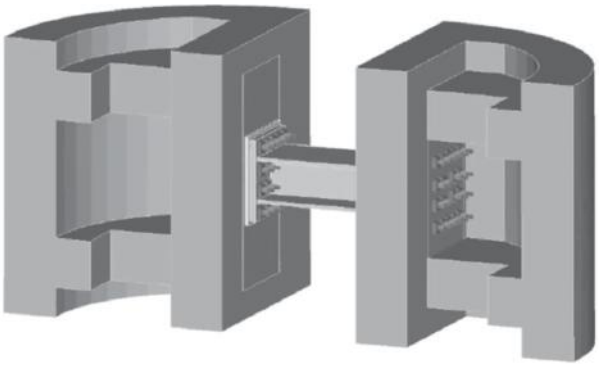

(c)

FIGURE 11.13 *(Continued)* Shear link connection: (c) 3-D view of connection section A—A (upper link).

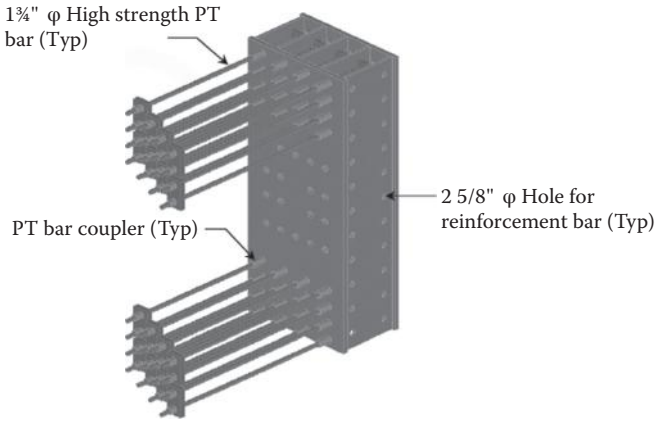

FIGURE 11.14 3-D view of upper link anchor box.

11.7.3 Design of Shear Link Connections

The link beam is directly connected to steel anchor boxes that are embedded inside the straight wall of the concrete shaft of the tower and end piers (Figures 11.13 and 11.14). Both longitudinal and transverse reinforcement of the tower shaft are continuous at the box location. The top and the bottom portions of the steel anchor box, as shown in Figures 11.13b and 11.14, are clamped to the concrete diaphragms using high strength posttensioning bars to form a rigid frame. The steel anchor box and its connection with the concrete shaft are adequately designed to remain elastic under all loading conditions. Figure 11.13c is a 3-D view of a typical upper shear link beam with its connections.

The link beam assembly shall be connected to the steel anchor box in such a way that no significant axial force can develop in the link beam during installation. One and three-quarter inch diameter posttensioned bars are stressed up to 280 kips each at installation. In the design, different bolt spacing is used for Shear Link Type A and Shear Link Type B to optimize their performance and to satisfy the minimum space requirement for stressing. For possible laboratory testing, however, the exact same bolt pattern and spacing may be specified for both types so that only one set of connecting fixtures is needed.

TABLE 11.5 Seismic Performance Criteria

Structural Components	Performance Criteria in Terms of Damage Level	
	FEE	SEE
Piles/drilled shafts	No damage	Minimal damage
Pile caps	No damage	Capacity protected[a]
Approach bridge columns and abutments (above pile caps)	Minimal damage	Moderate damage
Main span bridge towers and end bents (above pile caps)	No damage	Minimal damage
Energy-dissipation shear links	Minimal damage	Significant damage
Superstructure	No damage	Minimal damage
Approach bridge abutment backwalls	Minimal damage	Significant damage
Bearings, hinges, and shear keys	No damage	Moderate damage
Expansion joints	Minimal damage	Significant damage, without collapse of joint
Cable systems (structural elements)	No damage	No damage
Cable systems (nonstructural elements)	No damage	Minimal damage

[a] With force capacity greater than over-strength forces generated from columns, towers, and piles.

Nonshrink high-strength fiber reinforced grout is intended to ease the field fit up and enhance better contact between end-plate of the link beam and the face plate of the steel anchor box. The fibers improve the integrity of the grout, and the grout container prevents the grout from failing out of the joint under cyclic loading.

11.7.4 Seismic Performance and Design Criteria

Main span bridge is categorized as a nonstandard, ordinary bridge. The structure design service life is 100 years, and its seismic design shall consider both SEE and FEE. SEE corresponds to a mean return period of 1000 years, representing approximately a 10% probability of occurrence in 100 years. FEE is defined as an earthquake that has a return period of 100 years, representing approximately a 60% probability of occurrence in 100 years.

According to project-design criteria, structural components shall be designed to the following performance level (Table 11.5) under both SEE and FEE events. For allowable concrete and reinforcement strain values corresponding to minimal and moderate (repairable) damage, refer to Table 11.2.

The steel shear links connecting the two tower shafts and end pier shafts are fundamental to the seismic performance of the bridge. They are essentially the ductile "weak" beams of a tall frame, with the two tower (or pier) shafts creating the "strong" columns. In order for shear links to perform as expected, the design criteria further specify the following:

1. Shear links shall have a minimum plastic rotation capacity of 0.08 radians.
2. Connections of shear links to towers and end piers shall be designed as capacity-protected components and shall be detailed to facilitate their removal and replacement after a major seismic event. An over-strength factor of 2.20 shall be used when designing shear link capacity protected components.
3. All loading combinations not including seismic loads shall not exceed the nominal yield strength of the energy dissipating shear links.

Neither unstiffened shear links nor horizontally stiffened shear links have been used in major infrastructures so far. Likewise, the proposed design of connecting short steel links with concrete columns using posttensioning bars is the first of its type. Therefore, it is required by Port and Caltrans that the proposed shear links, if selected for the final design, have to be proved by a full-scale laboratory testing. The acceptance

criterion is set forth as following: For given loading protocol (see Test Loading Protocol in Section 11.7.9), the test specimen must sustain the required link rotation angle of 0.08 radians for at least one complete loading cycle before the link shear strength dropping below the nominal link shear strength. Designer has made considerable effort in planning the test, such as to set up test goals and requirements and to select an appropriate test loading protocol. Suggestions and recommendations in this regard are also presented in this example.

11.7.5 Analysis of Steel Plate Shear Links

Detailed finite element analyses have been performed using proprietary comprehensive finite element system ADINA (ADINA, 2011) to predict the behavior of the shear links as designed, and to make sure that all the design criteria are met. The analytical work performed is presented below in three groups (1) modeling of A36LC steel material; (2) response of shear links under monotonic loading; and (3) response of shear links under cyclic loading.

11.7.5.1 Modeling of A36LC Steel Material

Resistance of steel will increase when subjected to alternating inelastic strains. This phenomenon is referred to as cyclic strain hardening. Different steels have different cyclic strain hardening characteristics and can only be obtained through experiments. The first step in modeling shear links, therefore, is to establish an appropriate material model that will adequately capture the material behavior of A36LC steel obtained in cyclic load test performed at UWS. For this purpose, ADINA plastic-cyclic material model has been chosen because it is suitable for modeling cyclic inelasticity. This material model is based on

1. The von Mises yield criterion
2. A flow rule using the von Mises yield function
3. An isotropic and/or kinematic hardening rule suitable for use in modeling cyclic plasticity

The plastic-cyclic material model differs from the plastic-bilinear and plastic-multilinear material models because the isotropic and kinematic hardening rules are different. The plastic-cyclic material model is more general and it includes the plastic-bilinear and plastic-multilinear models as special

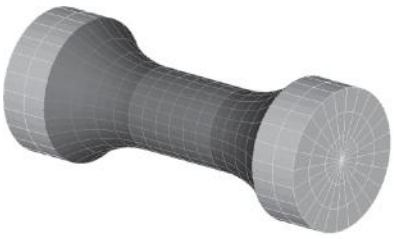

(a)

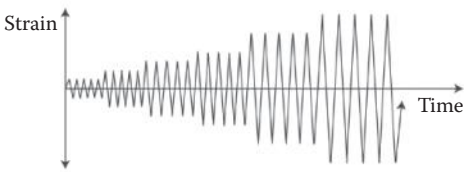

Increasing strain amplitude loading

(b)

FIGURE 11.15 ADINA model for cyclic tension-compression load test. (a) 3-D FE model of specimen. (b) Loading history.

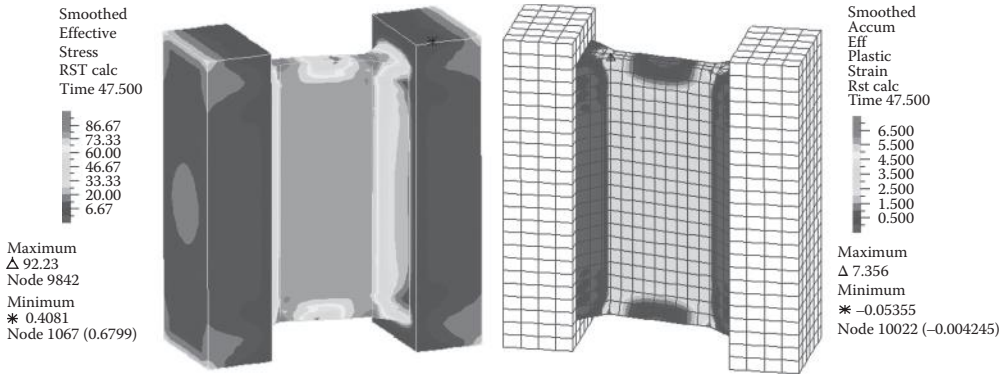

FIGURE 11.16 ADINA model for cyclic shear test.

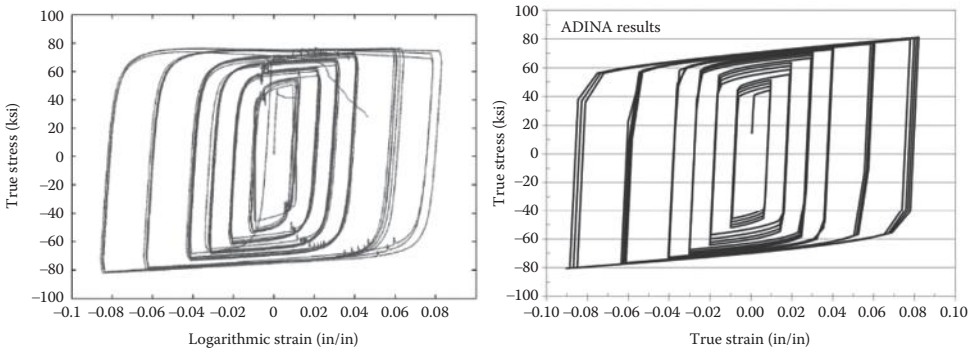

FIGURE 11.17 Cyclic tension-compression behavior of A36LC steel.

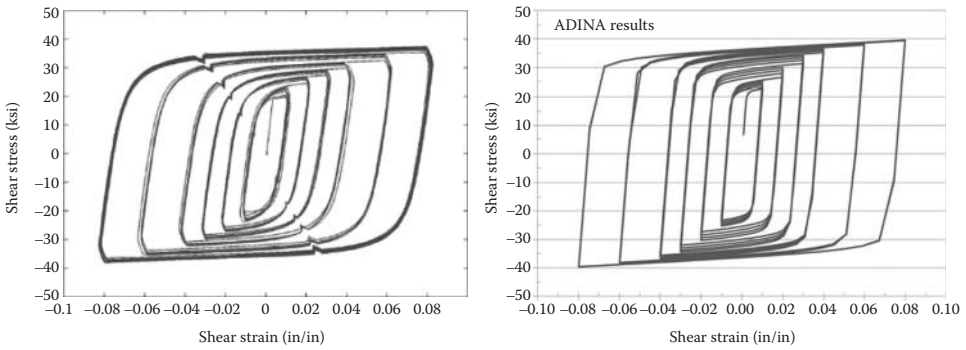

FIGURE 11.18 Cyclic shear behavior of A36LC steel.

cases when suitable material constants are chosen. The material model can be used with the truss, 3-D solid, 3-D shell, and Hermitian beam elements, and it can be applied with small displacement/small strain, large displacement/small strain, and large displacement/large strain formulations. For theoretical background and complete description of plastic-cyclic material model, see ADINA 8.7 User Manual (ADINA, 2011). The parameters of the material model are determined using the testing data. The material test conducted at UWS consists of two parts: cyclic tension-compression test and cyclic shear test. Both tests have been numerically simulated using ADINA as verification of the material model. The obtained results are presented and compared with the testing data in Figures 11.17 and 11.18.

Shown on Figure 11.15 are 3-D finite element representation of the specimen and the loading history applied in both laboratory test and numerical simulations. The middle uniform section of the tension-compression specimen is a 0.5 in. diameter cylinder of 0.625 in. long. The shear specimen consists of two plates fixed onto three rails, namely the middle and the edge rails. In laboratory test setup the two edge rails are fixed and the middle one is connected to the actuator. In numerical simulation, however, only one plate needs to be modeled because of symmetry, with one rail fixed and another free to move up-and-down (Figure 11.16). The deformable section of the shear plate is 0.1875 in. thick and 3.25 in. deep. The loading history used for shear test is identical to that of used for tension-compression test.

It can be seen from the above figures that ADINA material model captures the overall plastic-cyclic characteristics of A36LC steel material. Figure 11.16 shows band plots of effective stress and accumulated plastic strain distribution in shear specimen modeled. It is noted that the stress distribution in deformable section of the plate is fairly uniform and the average effective stress is as high as 80 ksi (nearly twice of its yield strength). This is in good agreement with measured results during tests. The accumulated effective plastic strain is a positive parameter indicating damage level in the material. The higher the accumulated effective plastic strain the material can reach before failure, the more ductile is the material. The maximum accumulated effective plastic strain calculated for shear specimen is approximately 7.3, and this number has been used as threshold for material rupture in the subsequent FEM analyses for shear links. It is also noticed (Figures 11.17 and 11.18) that the numerical results show more pronounced Bauschinger effects. The material model may be further improved by more refined calibration of parameters. For engineering applications, however, the degree of the accuracy is considered satisfactory.

11.7.5.2 Response of Shear Links under Monotonic Loading

Both Shear Link Type A and Shear Link Type B are analyzed without including end-plates and connections. This is equivalent to assuming infinitely rigid connection zones. The links are modeled using 27-node 3-D solid elements and ADINA plastic-cyclic material. For webs the element used is divided into two layers in the through-thickness direction, whereas for flanges where the stress and strain gradient is relatively high the element adopted is divided into 6 layers in through-thickness direction. Large displacement and large strain formulation option is selected for all the analysis, and numerical integration order of 5 is specified for all elements to enhance the accuracy. Based on results of convergence study, the finite element meshing scheme as shown in Figure 11.19 is found to be adequate. At one end of the link the cross-section is fully restrained, and at the other end of the section is forced to displace transversely in the plane of the web. The moving face is kept in parallel with the fixed one and is free to move in perpendicular direction to prevent axial force from being generated. Initial geometry imperfection is also included by applying the 1st shear buckling mode shape to the model with modal

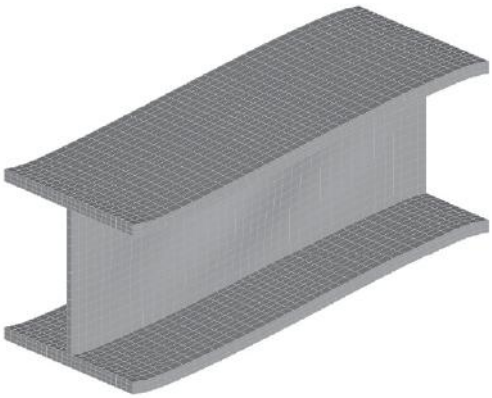

FIGURE 11.19 Out-of-plane deformation in web of shear link Type A.

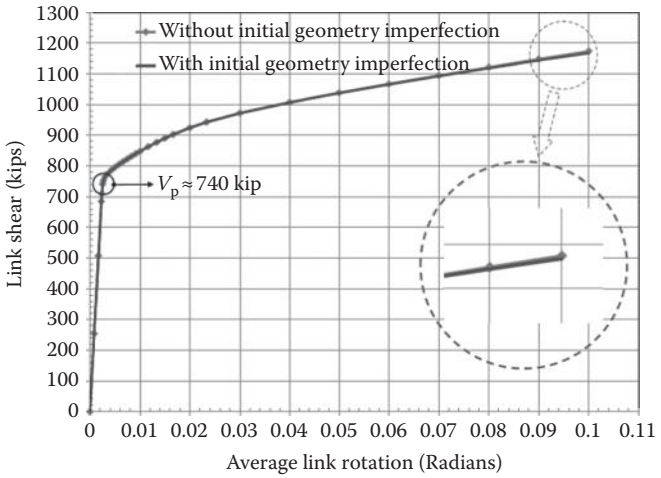

FIGURE 11.20 Response of shear link Type A under monotonic loading.

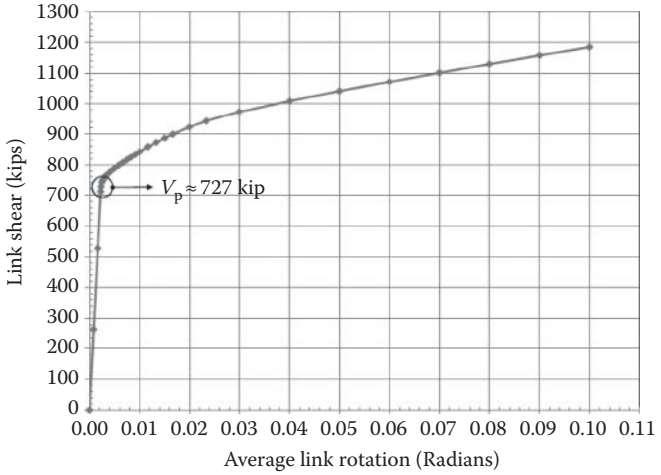

FIGURE 11.21 Response of shear link Type B under monotonic loading.

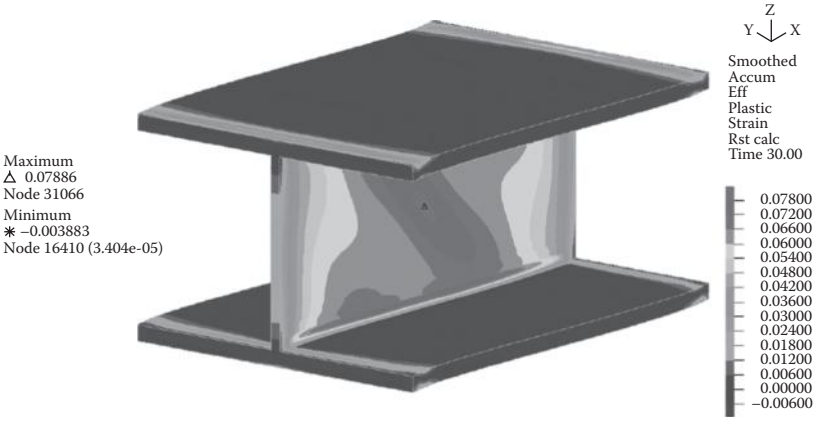

FIGURE 11.22 Effective plastic strain distribution in shear link Type A.

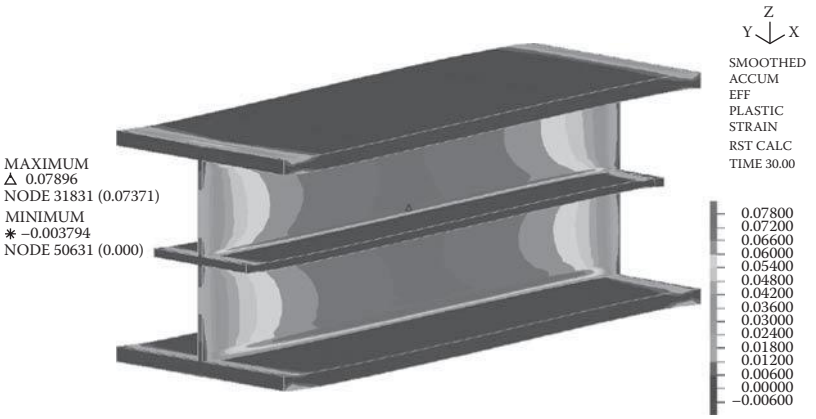

FIGURE 11.23 Effective plastic strain distribution in shear link Type B.

displacement amplitude being scaled to one-thousandth of the link length. In all the analyses, however, welds and residual stresses are not considered.

The selected numerical results of shear links subjected to monotonic displacement loading are presented in Figures 11.20 through 11.23. The analytical results as shown lead to the followings main observations:

- The nominal shear capacity obtained in FEM analysis (Figures 11.20 and 11.21), 740 kip for Shear Link Type A and 727 kip for Shear Link Type B, is very close to what predicted using AISC formula, 734 kip for Shear Link Type A and 730 kip for Shear Link Type B.
- Out-of-plane web deformation observed in Shear Link Type A (Figure 11.19) has negligible effect on its shear strength (Figure 11.20).
- In absence of out-of-plane web deformation, the location of highest stress and strain demand in Shear Link Type A is near the heat affected zone of the weld between web and flanges. Once out-of-plane web deformation occurs, the point of peak strain will shift toward the mid-web area because of tension field action (Figure 11.22). The points of the peak strain indicate location of initial cracking in the web.
- For Shear Link Type B high stress and strain is found to be located near the heat affected zone of the weld between web and flange and the weld between web and the horizontal stiffener (Figure 11.23).
- By AISC definition of link length, both link Type A and link Type B are considered extremely short, and shear yielding should dominate. Nevertheless, significant amount of flange yielding is observable for both types of links at the location near the T-joint between flanges and the end-plates. This indicates another critical location where potential cracks may develop.

11.7.5.3 Response of Shear Links under Cyclic Loading

The loading history used in the analysis is summarized in Table 11.6 and illustrated in Figure 11.24. The deformation history is a variation of that used for testing link-to-column connections proposed in AISC Seismic Provisions (AISC, 2005).

Because the maximum link rotation during SEE events predicted by the time-history analysis (see Section 11.7.8) is <0.03 radians, it is decided that the AISC loading protocol shall be followed until link rotation reaches 0.04 radians. For rotation demand exceeding 0.04 radians, the loading cycle continues at increments of 0.02 radians, with one cycle at each increment.

TABLE 11.6 Loading History for Link Analysis

Load Step	Link Rotation Amplitude (Radian)	Number of Cycles
1	0.00375	6
2	0.00500	6
3	0.00750	6
4	0.01000	6
5	0.01500	4
6	0.02000	4
7	0.03000	2
8	0.04000	1
9	0.06000	1
10	0.08000	1
11	0.10000	1
12	0.12000	1

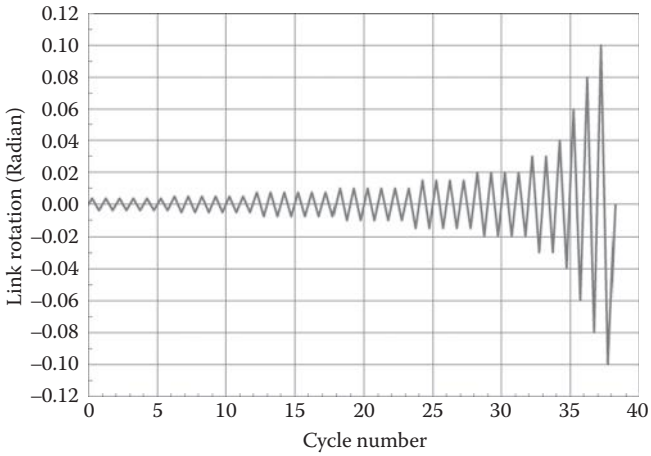

FIGURE 11.24 Loading history for link analysis.

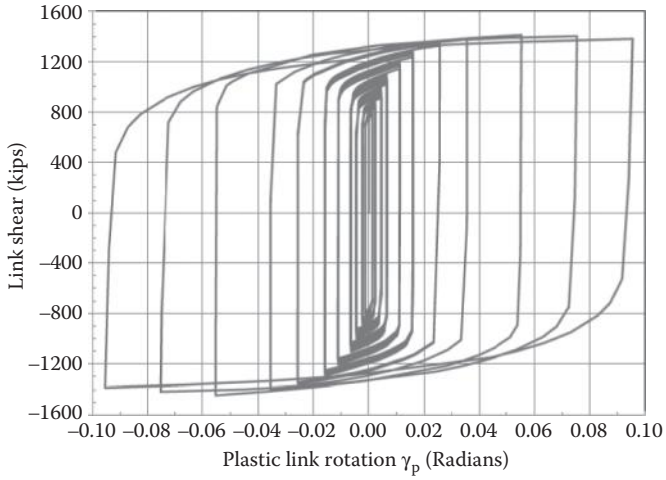

FIGURE 11.25 Shear force versus plastic link rotation for shear link Type A.

FIGURE 11.26 Effective stress distribution in shear link Type A.

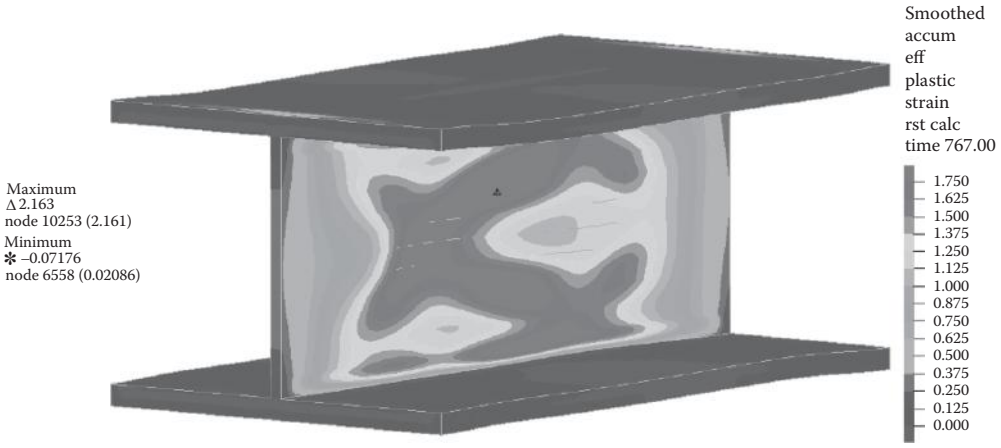

FIGURE 11.27 Accumulated effective plastic strain in shear link Type A.

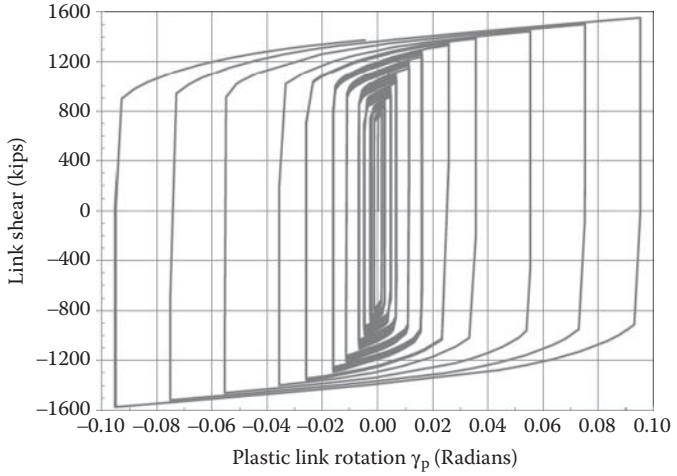

FIGURE 11.28 Shear force versus plastic link rotation for shear link Type B.

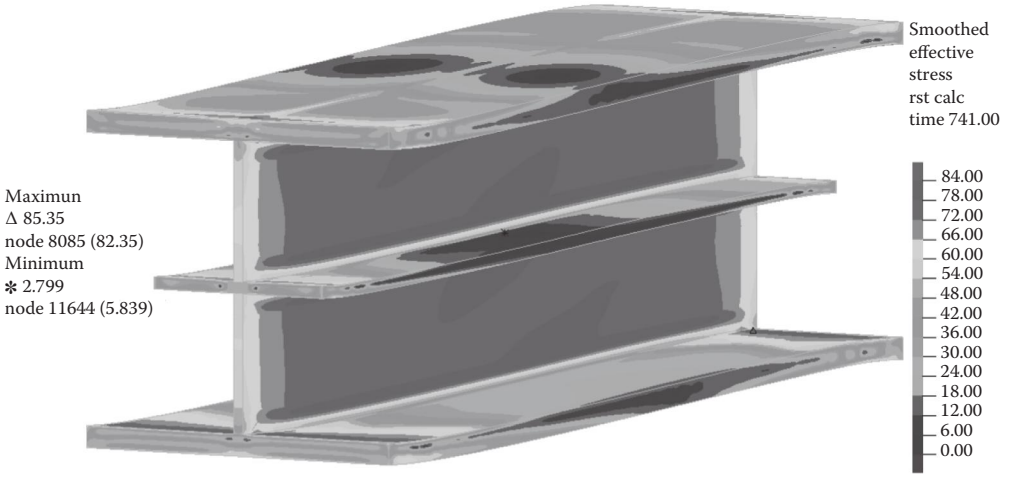

FIGURE 11.29 Effective stress distribution in shear link Type B.

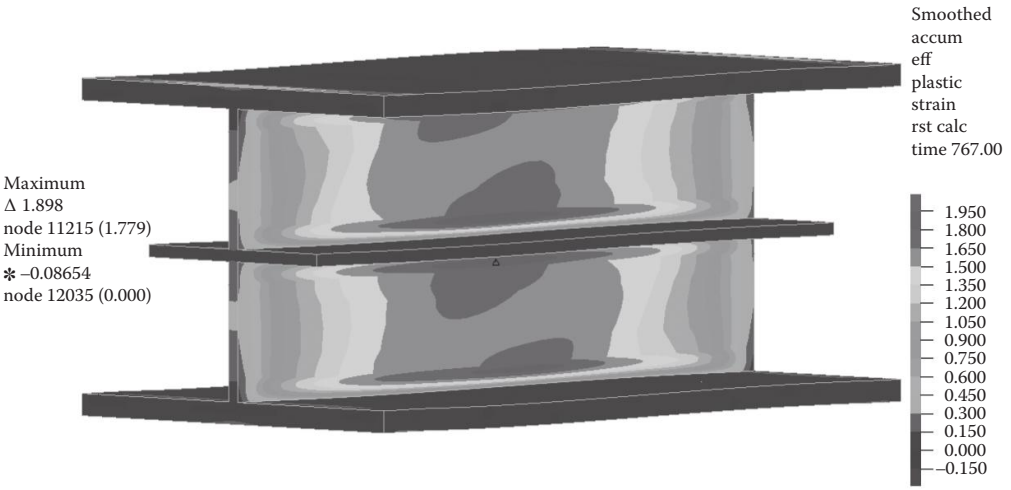

FIGURE 11.30 Accumulated effective plastic strain in shear link Type B.

The hysteretic force–deformation characteristics, band plots of effective stress and accumulated plastic strain of shear links are shown in Figures 11.25 through 11.30. Findings are briefly summarized below.

1. Under the specified loading sequence, both links are capable of sustaining a plastic rotation of 0.08 radians or greater, because the accumulated plastic strain is well below the threshold value for material rupture.
2. The overstrength factors are 1.96 for Shear Link Type A and 2.15 for Shear Link Type B, respectively.
3. The unstiffened web of Shear Link Type A will buckle in shear at plastic rotation of approximately 0.06 radians. The postbuckling response of the link, however, remains stable without significant degradation.

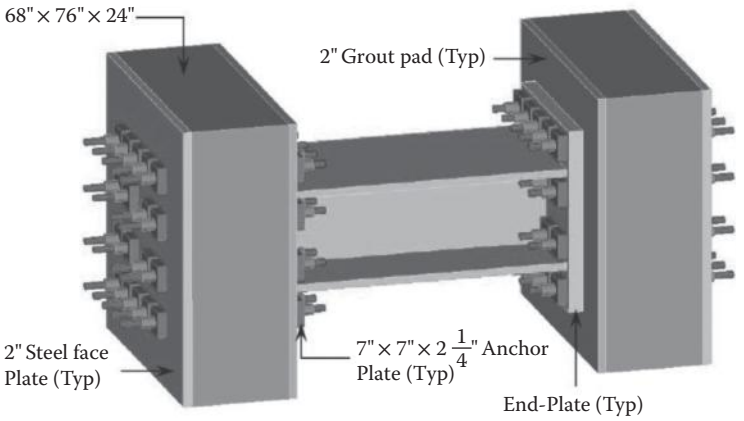

FIGURE 11.31 Computer model for shear link Type A with connections.

4. The stiffened web of Shear Link Type B shows no signs of shear buckling. The stable web leads to lower and more uniformed distribution of plastic shear deformation but higher overstrength.
5. The stress and plastic strain demand are relatively higher in the region where the web intersects with flanges and horizontal stiffeners (in case of Shear Link Type B).

As mentioned above that ADINA plastic-cyclic material model used shows more pronounced Bauschinger effects, and the postyielding stiffness is larger than that of measured in the material test, it is speculated, therefore, the predicted overstrength factors could be slightly higher, too. This will render the design on the conservative side.

Having less heat affected zones, stable postbuckling web performance and relatively lower over strength factor, Shear Link Type A has become an attractive and promising design option.

11.7.6 Analysis of Shear Link Connections

The behavior of the local posttensioned anchorage zone, performance of posttensioning bars, in particular, may have some direct effects on the performance of the links, and thus becomes the focus of the study. The computer model is shown on Figure 11.31 for Shear Link Type A. The computer model used for Shear Link Type B is similar. It should be noted that the design of connections has been constantly improved through the process and the updated design (as shown in the latest design plans) may not be exactly same as what is adopted in the computer model for connections. The results obtained for performance of high strength posttensioning bars, however, are considered still relevant and applicable in principle.

Because the focus is on the performance of posttensioning bars, a relatively coarser meshing scheme is employed for links. The hysteretic force–deformation curves obtained using coarser meshing are almost the same as those resulted from fine meshing, therefore the new meshing scheme is considered satisfactory. To apply cyclic displacement loading, the following boundary conditions are imposed:

1. 1¾ in. diameter posttensioned bars are rigidly connected onto the surfaces of the anchorage plates and there is no bonding in between the bars and concrete.
2. Contact surfaces with zero initial gap size are introduced in between the following pairs of surfaces: anchor plate and end-plate, anchor plate and face plate, end-plate and grout pad and grout pad and concrete block. A friction coefficient of 0.55 is used for both steel on grout and steel on steel.

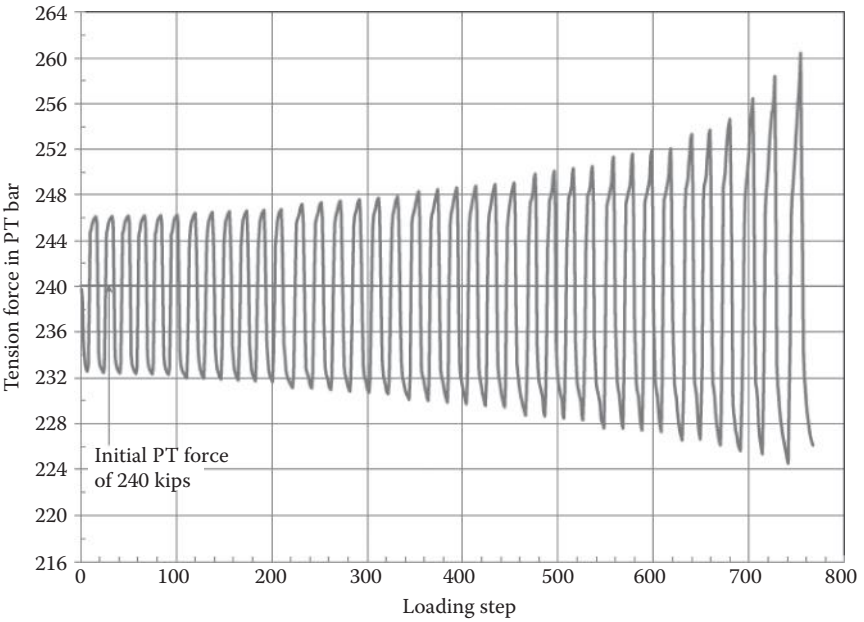

FIGURE 11.32 Force in top middle PT bar of shear link Type A.

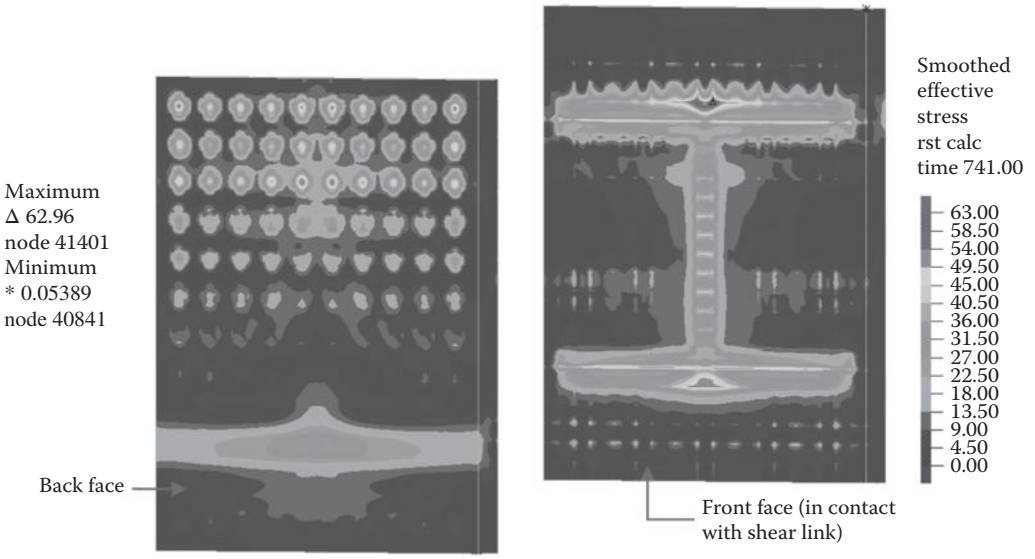

FIGURE 11.33 Effective stress on end-plates of shear link Type A.

3. One of the two concrete blocks is fixed. The fixity is imposed onto the top and bottom and two side faces.
4. The other concrete block is allowed to move up and down in parallel to the fixed one without being restrained in longitudinal direction.

The loading history used in the analysis is the same as that used for individual links described above. No initial geometrical imperfection is considered. The effective pretension in the bar, after all losses in

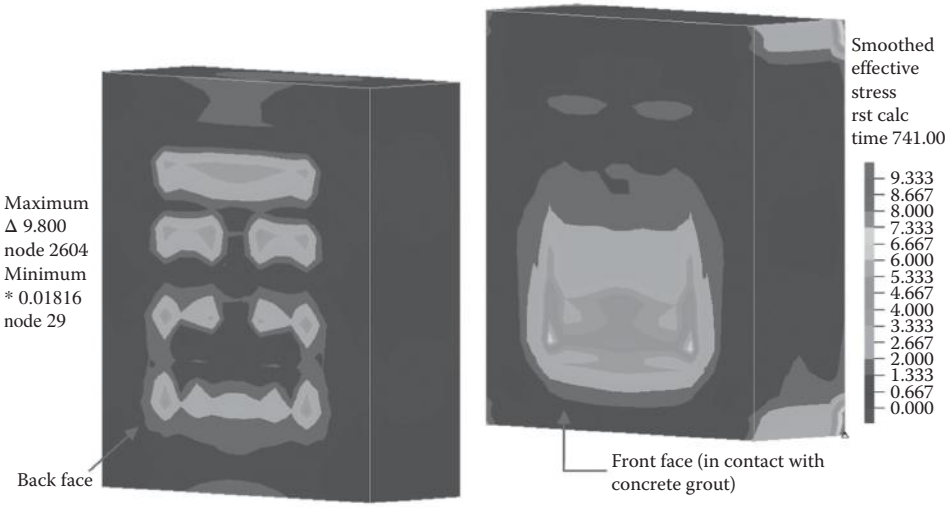

FIGURE 11.34 Effective stress on concrete blocks of shear link Type A.

prestress occur, is assumed to be 240 kips each. Shear links and end-plates are modeled using ADINA plastic-cyclic material, whereas others are all modeled as elastic elements. Large displacement and large strain formulation is used.

The overall force–deformation behavior of both shear links is basically the same as those of captured in analyses of individual links, and the results are omitted to avoid repetition.

It is found that the tension forces in PT bars among the same row only differ by a few kips and the middle bar at top (or bottom) row has the maximum tension force. The time-history of tension force of this bar is plotted in Figure 11.32. It is of interest to note that the tension force amplitude in 1¾ in. diameter posttensioning bars only increased approximately 20 kips, whereas shear force in the link has almost doubled. Further analyses results show that this is not sensitive to the magnitude of initial prestressing force in PT bars. This implies that even under the extreme condition where bars are stressed to the maximum allowable pretension of 280 kips ($0.70Af_{pu}$) each at installation and with zero prestress losses, the maximum tension force in bars will still be kept well below the maximum allowable jacking force of 320 kips ($0.80Af_{pu}$). Because shear force in steel shear links grows much faster than tension force in posttensioning bars, it is anticipated that shear links will fail in shear before the posttensioning bars reach their elastic limit. This indicates that all the posttensioning bars will remain elastic.

The end-plates respond in inelastic range (Figure 11.33), but there is no plastic hinges formed. The yielded fibers close to the surfaces also undergo cyclic strain hardening just as the link web and flanges, so stresses much higher than the yield strength of the steel are observed. The stress distribution on the face of concrete block in contact with grout pad (Figure 11.34) suggests that the end-plate is almost completely lifted off, and it exhibits "thick" plate behavior as described in Kennedy model (Murray and Sumner, 2003; Kennedy et al., 1981) for end-plate moment connections. Shear Link B is modeled with its connections exactly the same way, and their response is very similar to that of Shear Link Type A.

11.7.7 Truss Analogy of Shear Link Beams

The detailed FEM model is very useful in determining both strength and plastic rotation capacity of shear links, but is neither practical nor necessary to be used in global model of the bridge, because it will lead to a model that is too big to run and to postprocessing the results. To solve this problem an alternative method, truss analogy of link beam, was proposed. It captures the fundamental behavior

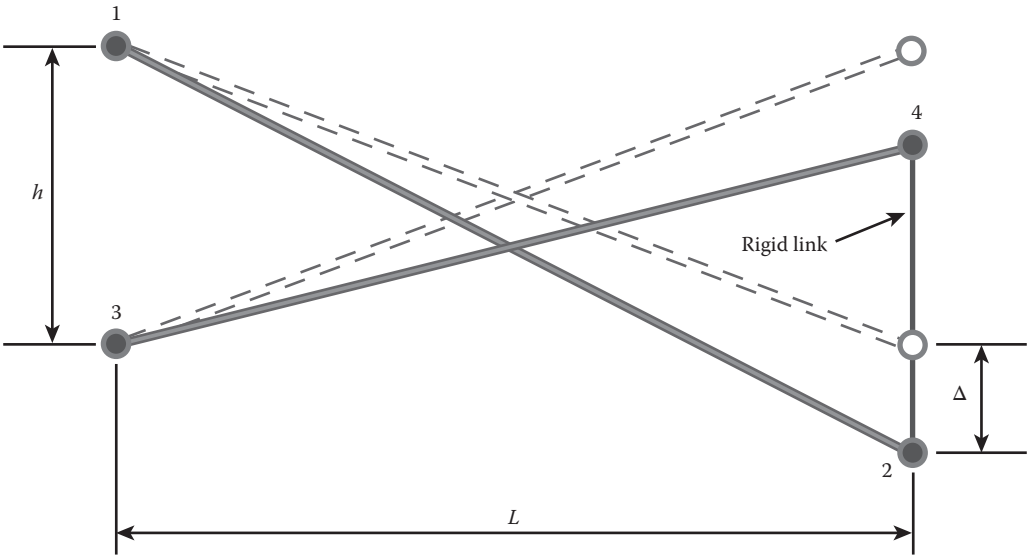

FIGURE 11.35 Truss model for link beam Type A—shear behavior.

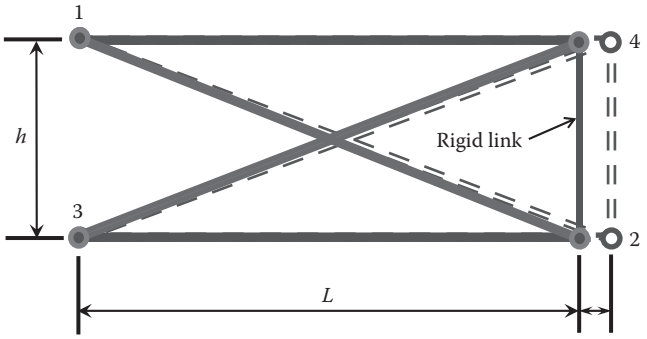

FIGURE 11.36 Truss model for link beam Type A—axial behavior.

of shear link beam, particularly the shear over-strength because of cyclic hardening of steel. It is relatively simple and can be used in a global bridge model. The methodology is illustrated below using link beam Type-A.

Step 1: Build a Model by a Pair of Diagonal Rods—The two rods have exactly the same material and section area. As shown in Figure 11.35, L (equals 67 in.) is the deformable length of link beam Type-A, and h (equals 25 in.) is approximately the height of the web. It is possible that a different value can be chosen for h. The modulus of elasticity E (equals 28,928 ksi) is the same as that used for A36LC steel. Nodes 1 and 3 are restrained, and nodes 2 and 4 are rigidly connected and are free to move.

Step 2: Determine the Equivalent Section Area of Diagonal Rods—A vertical displacement of Δ is imposed on to both the truss model and its companion finite element model (Figure 11.19). And the equivalent section area of the rod is computed by equating the total vertical reactions obtained from the two different models. In this analysis, both models are treated as linear elastic. The calculated section area for the rod is $A = 46.58$ in^2. When this step is

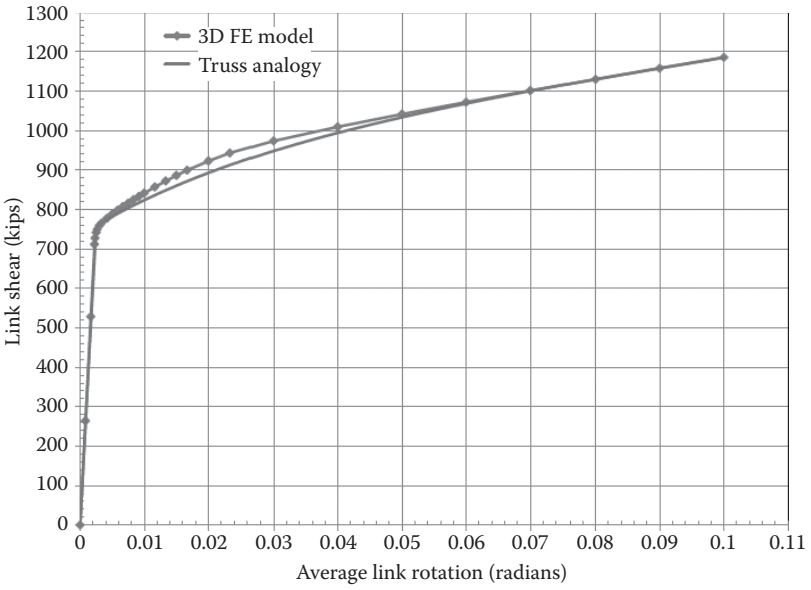

FIGURE 11.37 Comparison between truss model and FEM model—monolithic loading.

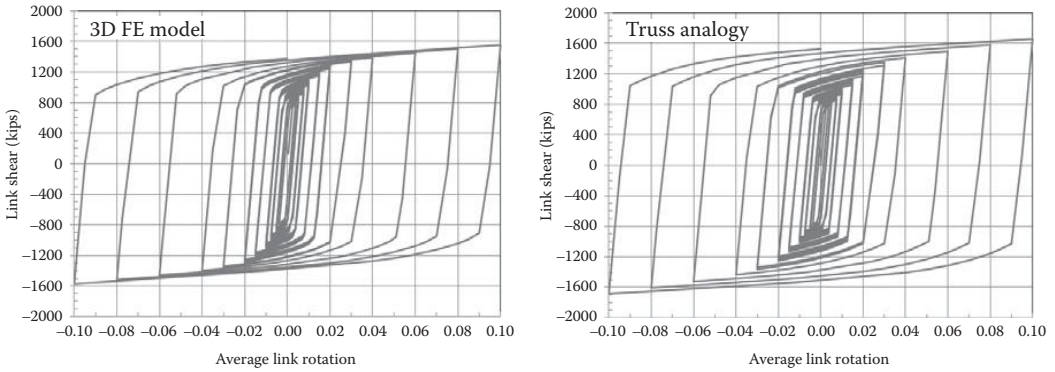

FIGURE 11.38 Comparison between truss model and FEM model—cyclic loading

completed, the truss model should be considered elastically equivalent to that of the finite element model. Of course, this is in the vertical plane only. To include the transverse stiffness of the link beam, a truss laid in the horizontal plane can be created by using the same procedure.

Step 3: Determine the Equivalent Section Area for Added Chords—So far, the truss analogy model only simulates the shear behavior of the link beam. If axial response of the link beam is not trival, the truss analogy model can be easily modified to have proper axial stiffness equivalent to that of the link beam. This is accomplished by adding top and bottom chords and connected with the diagonals as shown in Figure 11.36. Then a horizontal displacement of Δ is imposed on to both the truss model and the finite element model. And the equivalent section area of the chords is computed by equating the total horizontal (axial) reactions obtained from the two different models. In this analysis, both models are treated as linear elastic. The calculated section area for the top and the bottom chord is A

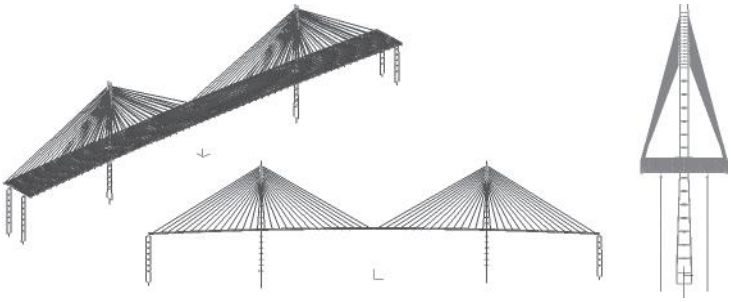

FIGURE 11.39 FEM model of main span bridge.

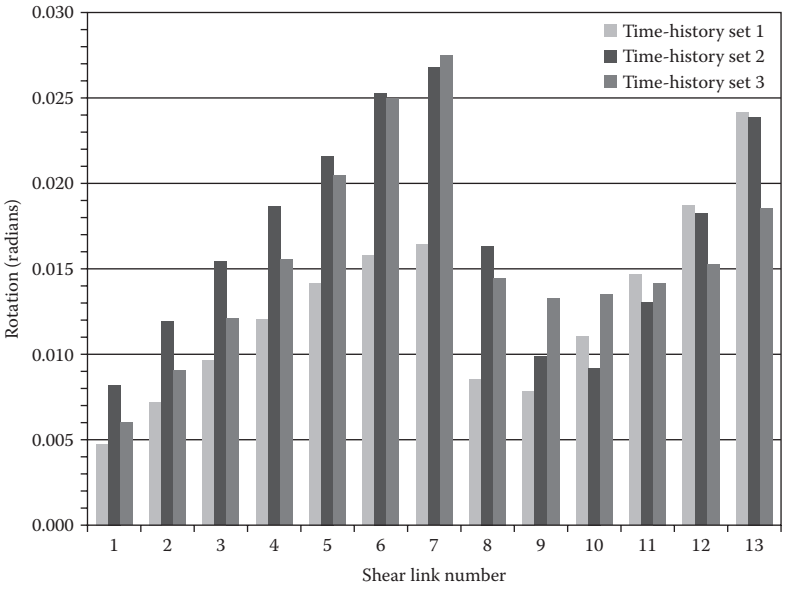

FIGURE 11.40 Demand of shear link rotation—Tower 16.

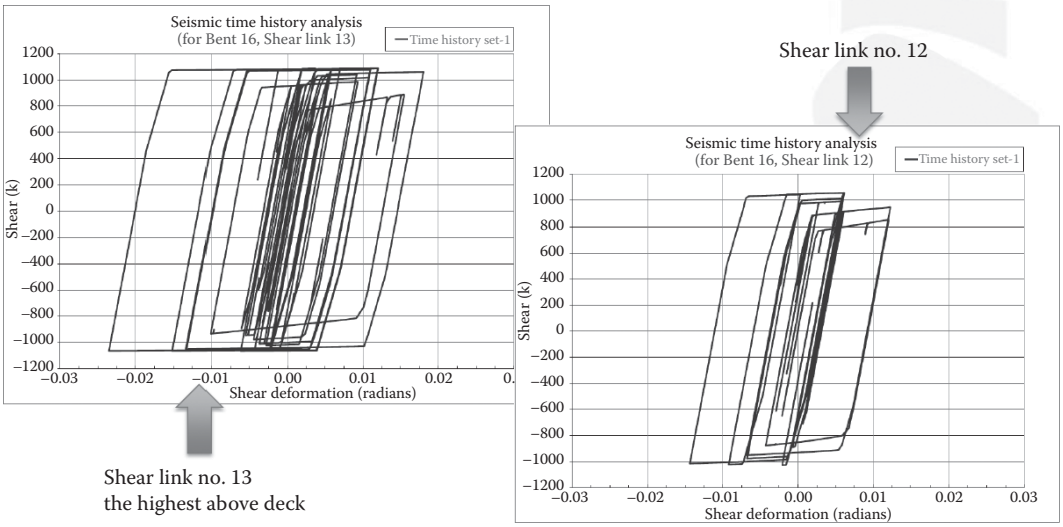

FIGURE 11.41 Hysteretic response of shear links above deck—Tower 16.

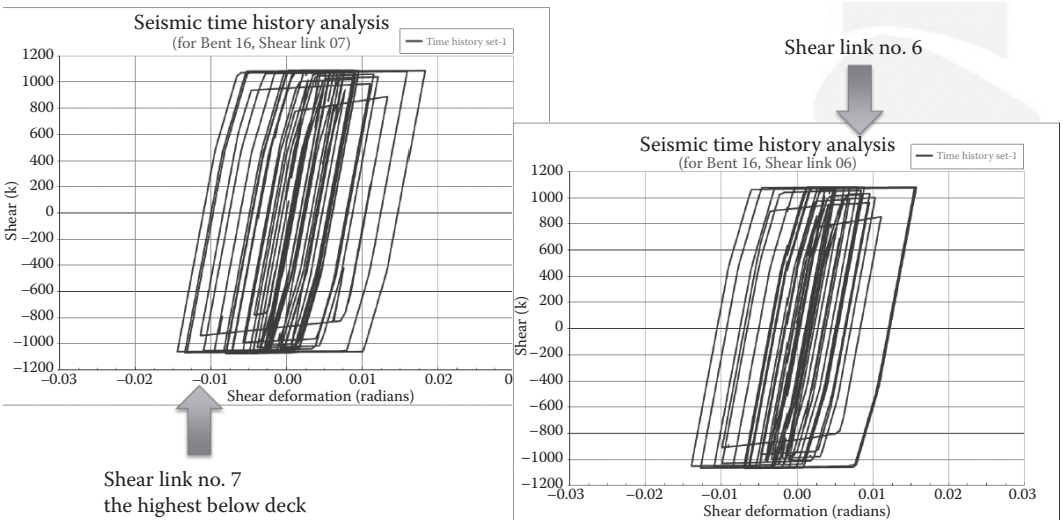

FIGURE 11.42 Hysteretic response of shear links below deck—Tower 16.

= 46.92 in^2. Now the truss model is elastically equivalent to FEM model in both shear and axial actions.

Step 4: Use ADINA Plastic-Cyclic Material Model—To make the truss model also equivalent to the FEM model in inelastic ranges, the last step is to replace the elastic material used in the previous steps by ADINA plastic-cyclic material model with exactly the same material parameters calibrated using test data and used in the FEM model analysis.

Comparisons between truss analogy model and FEM model are made for both monolithic loading and cyclic loading cases and are presented in Figures 11.37 and 11.38. It can be seen that although the match is not perfect, the results obtained using truss analogy captured the characteristic cyclic strain hardening and shear over-strength of the link beam reasonably well, and are thus considered satisfactory for engineering application at this design stage.

11.7.8 Time-History Analysis of Main Span Bridge

The plastic cyclic response characteristics of shear links are implemented into global model of main span bridge using truss analogy method as presented above (Figure 11.39). In the preliminary design stage SFSI is not considered, the piers and towers are fixed at the top of pile footings. Except for shear links, other structural components are all modeled using elastic elements. Effective section properties are used for concrete towers and end piers. Large displacement option is adopted to take into account geometrical nonlinearity of stay cables. Time-history analyses are performed by applying three sets of SEE ground motions (provided by EMI). Using variable ground motion inputs at multiple supports is not considered for this study.

The selected seismic responses of shear links are presented in Figures 11.40 through 11.43. Results are shown for one tower (Bent 16) only; responses of the other tower are very similar. For all three sets of ground motions, concrete tower shafts remain as elastic.

Rotation demand for shear links along the height of tower is plotted in Figure 11.40. Link No. 1 is at the bottom and Link No. 13 is at the top. Link No. 7 is the highest shear link below the deck. Typical hysteretic force–deformation response curves are presented in Figure 11.41 and Figure 11.42 for selected shear links. Time-history of link rotation of Shear Link No. 7 is shown in Figure 11.43.

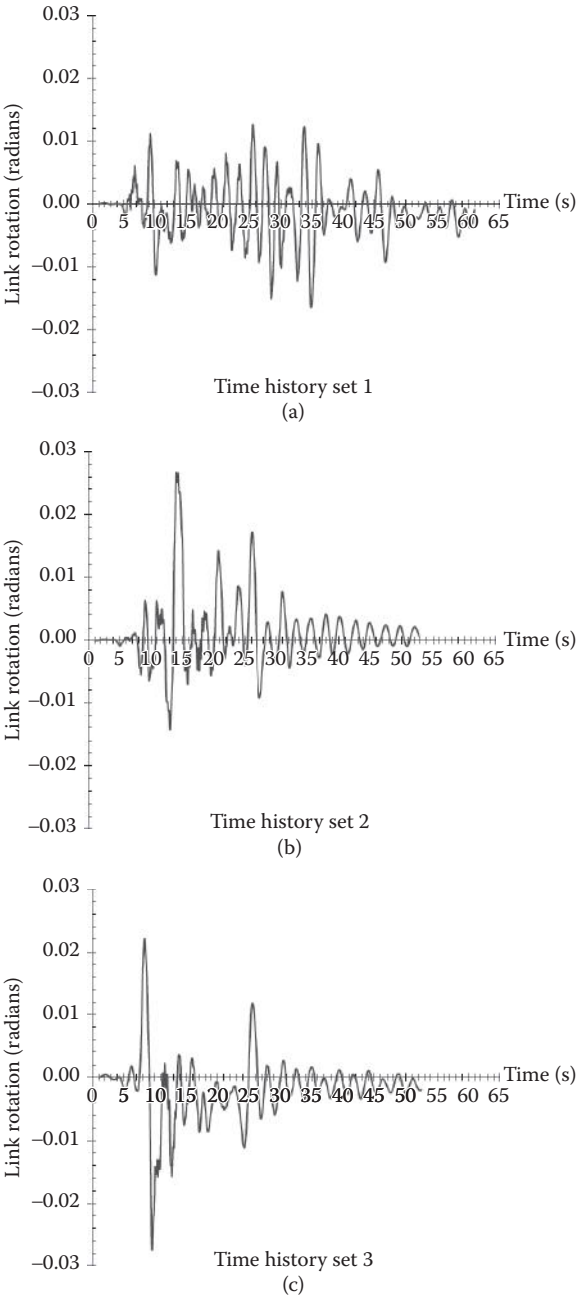

FIGURE 11.43 Deformation time-history of shear link no. 7—Tower 16.

Summary of Analysis Results—Based on the analysis results, the performance of shear links can be summarized as below.

1. All links, from top to bottom, yield in shear and dissipate energy.
2. The maximum rotation demand is <0.03 radians.
3. The maximum shear force at links recorded by time-history analysis is approximately 1100 kips.

4. Residual deformation of shear links is insignificant. The time-history analyses are terminated at the end of the input ground motions. It is anticipated that if time-history analyses are carried further to let the free vibration to decay, the actual permanent deformation of shear links should be smaller than as shown in Figure 11.43.

Discussion on Analysis Results—Extensive analyses have been performed to ensure a sound design and to minimize the risk of premature link failure in either laboratory testing or actual applications. Being interactive with the analyses process, the design of both the link and the connection has been optimized. However, the performance of the links may be controlled by a number of important response aspects that are not fully predictable by the analysis. These factors are as follows:

1. The behavior of the welds—Among all the welds, the welding at the T-joint of link and end-plate is probably the most critical one
2. The postyield web buckling—Predicted by the analysis, the link with unstiffened web will buckle in shear at fairly large plastic rotation and its postbuckling behavior is stable and ductile, and the link is still able to reach the target link rotation of 0.08 radians with <8% drop in peak link force. Nevertheless, this needs to be verified by the test.
3. Performance of posttensioning bars, high-strength fiber grout, and concrete filled inside the steel boxes—Although the analysis results are favorable, there may be unknown factors having adverse impact on link performance. Connections between short steel shear links and concrete columns, using posttensioning bars, has not yet been successfully proved neither in field application nor in laboratory testing.

All of these questions and doubts can only be satisfactorily addressed through a laboratory testing.

11.7.9 Recommendations for Shear Link Laboratory Testing

If the shear links as proposed herein are adopted for the final design, their adequacy has to be successfully proved by a full-scale laboratory testing before fabrication and construction. This is a primary requirement imposed by Port and Caltrans. Designer has made considerable efforts in planning the test, such as to set up test goals and requirements and to select an appropriate test loading protocol. Suggestions and recommendations in this regard are provided in the following sections.

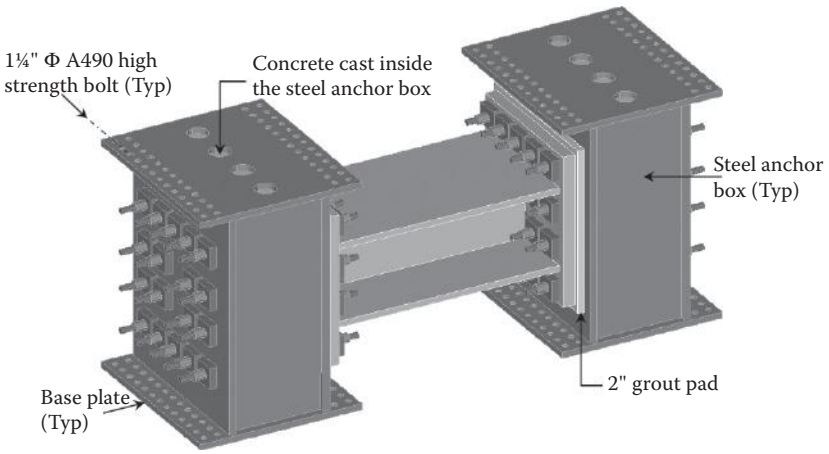

FIGURE 11.44 Shear link with local connection zones.

11.7.9.1 Test Goals and Requirements

The primary objective of this test is to evaluate the link force and deformation capacities for both Shear Link Type A and Shear Link Type B together with their connections. The "connections" used in this section is referring to the portion of the steel anchor box in between the two adjacent concrete diaphragms, including posttensioning bars directly connected to the link beam and the concrete cast inside the steel anchor box (Figure 11.44). With added base plates the steel anchor boxes can be fixed onto the test frame using high-strength bolts. In this case slip-critical connections are required. The appropriate boundary conditions and deformation history will be applied to the steel anchor boxes through the test frame. Being cut out from the surrounding concrete, the steel anchor box reduces from a two-way slab to a column (or deep beam). This is a reasonable simplification and will lead to relatively conservative results.

For the shear link specimen as shown in Figure 11.44, the structural laboratories shall design their own loading mechanism and required test frames and fixtures in accordance with the Test Requirements as discussed below. The structural laboratories may propose to use local connection blocks with different configurations as they deem appropriate.

In addition to verifying the design link rotation capacity of 0.08 radians, the ultimate link rotation capacity may be determined by incrementally increasing the load (see Loading Protocol) to failure. The test results will be used for the following purposes:

1. To assess whether the links and connections as designed are in full conformance with project-design criteria
2. To determine which link type, unstiffened or stiffened using horizontal stiffeners, is superior and will be recommended for the final design
3. To verify and calibrate the analytical model

At a minimum, two steel anchor boxes and two prototype shear links connected with end-plates using complete joint penetration groove weld, one for each type, will be fabricated in shop and shipped to the selected structural laboratory for cyclic load test.

11.7.9.2 Link Behavior to Be Investigated

Specifically, the test is to find the following:

1. Ultimate rotation capacity of the links. The maximum rotation capacity is defined as the maximum amplitude of rotation angle that the link has sustained for at least one full cycle before the link shear strength dropping below the nominal link shear strength.
2. Overstrength factor (ratio of maximum shear capacity to plastic shear) of the links.
3. Response behavior of link beam under cyclic loadings.
4. Response behavior of welds under cyclic loadings.
5. Failure mode of the links.

TABLE 11.7 Link Test Loading Sequence Phase I

Load Step	Link Rotation Amplitude (Radian)	Number of Cycles
1	0.00375	1
2	0.03000	1
3	0.01000	1
4	0.00750	1
5	0.00500	2
6	0.00375	1
7	0.01500	1
8	0.01000	1
9	0.00500	1
10	0.00375	2

TABLE 11.8 Link Test Loading Sequence Phase II

Load Step	Link Rotation Amplitude (Radian)	Number of Cycles
11	0.00375	4
12	0.00500	3
13	0.00750	3
14	0.01000	4
15	0.01500	3
16	0.02000	1
17	0.03000	1

TABLE 11.9 Link Test Loading Sequence Phase III

Load Step	Link Rotation Amplitude (Radian)	Number of Cycles
18	0.04000	1
19	0.06000	1
20	0.08000	1
21	0.10000	1
22	0.12000	1

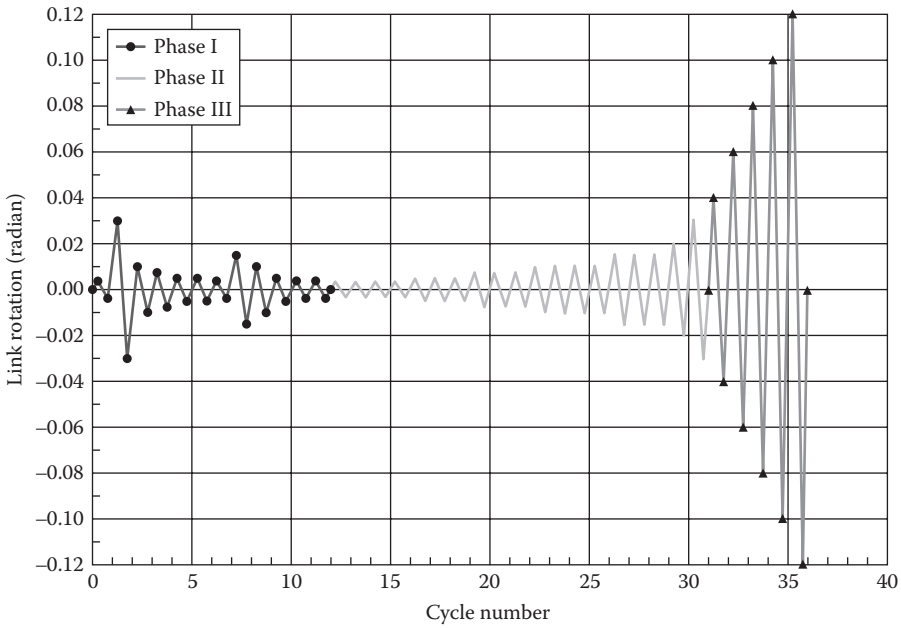

FIGURE 11.45 Loading history for shear link test.

6. Maximum tension force in posttensioned bars.
7. Performance of connection assemblage, including concrete grout and in-fill concrete.
8. Shear link replaceability.

11.7.9.3 Test Requirements

The test shall be performed in accordance with the following requirements:

1. The full-scale test shall be conducted under displacement controlled mode using the given quasi-static loading sequence (see Loading Protocol).
2. Concrete blocks and high-strength fiber grout pads shall be included to represent the local anchorage zone.
3. One and three-quarter inch diameter posttensioning bars shall be stressed to 280 kips each. The minimum effective tension force in the bars shall be 240 kips. The PT ducts shall not be grouted. The effective prestressing force in bars shall be checked and adjusted, if necessary, before the commencement of the test.
4. During testing, axial force in the link shall not exceed 2% of the link shear force.
5. During the test the two steel anchor boxes shall be kept parallel to each other. The tolerance for out-of-parallelism is 5% of the target link rotation amplitude of the current loading cycle.
6. The posttensioning bars shall not be reused.

The structural laboratory shall be capable of conducting the required full-scale shear link test including: provision of loading mechanism, specimen setup, instrumentation installation, testing of the instrumentation, acquisition, and interpretation of the data.

11.7.9.4 Test Loading Protocol

The quasi-static loading protocol to be used for the link test consists of three distinctive phases as summarized in Tables 11.7 through 11.9 and illustrated in Figure 11.45. It is a deviation from the loading protocol for testing link-to-column connections proposed in AISC Seismic Provisions (AISC, 2005), and it is also different from what used in the shear link tests for SFOBB (McDaniel et al., 2003).

The first and the second phase of the loading history reflect the actual cumulative link rotation demands under design earthquake loadings. Each of them represents a complete deformation history resulted from design SEE event in terms of the maximum link rotation and the total number of inelastic cycles. In Phase I the deformation sequence closely follows the response time history, which contains large velocity pulses, whereas in Phase II the deformation sequence is arranged in the order of increasing rotation amplitude.

In Phase III the loading cycle continues at increments of 0.02 radians, with one cycle at each increment until link failure occurs. The link is considered as failed when its shear strength has dropped below its nominal link shear strength. If in case the link failure does not occur when the actuator has reached its maximum capacity (of either force or stroke), the loading cycle shall be kept at the constant rotation amplitude that corresponding to the maximum capacity of the actuator and be repeated until link failure occurs.

Although the proposed loading protocol for shear link laboratory testing differs in order of different amplitudes, it is actually equivalent to that of used in shear link analysis in terms of intensity and accumulative plastic rotations. Having three distinctive loading stages, however, it offers advantage of checking the extent of damage the shear link will experience during each phase. This extra information is helpful in assessing whether the shear link shall be replaced after a major design seismic event.

11.8 Summary

Seismic design of bridges is complicated and challenging, and it requires multidisciplinary team work. Generally, we know bridges better than earthquakes; and we know structures better than soils. We have the lowest confidence on the most critical item, the input ground motion used in designs. This is the fundamental fact. Acknowledging the limits in our knowledge will help us to make good engineering judgment. The ultimate test for our seismic design is no doubt the earthquake itself. Mistakes made in design and construction have been and will continuously be brought out by damages and failures caused by earthquakes. And the recorded input ground motions at bridge supports and the response history of various bridge components during strong earthquakes will be invaluable. Instrumentation needs to be

integrated with either new designs or retrofit designs. Whenever possible, bridge engineers shall persuade the bridge owner to make this rewarding investment.

References

AASHTO. 2012. *AASHTO LRFD Bridge Design Specifications, US Customary Units 2012.* American Association of State Highway and Transportation Officials, Washington, DC.

Abbas, S. and Manzanarez, R. 2001. The Skyway Structures—Design of the New San Francisco – Oakland Bay Bridge East Span. *Proceedings of the 2001 Structures Congress*, ASCE, Washington, DC.

ADINA. 2011. *ADINA Theory and Modeling Guide: ARD 10-7*. ADINA R & D, Inc., Watertown, MA.

AISC. 2005. American Institute of Steel Construction, Inc. *Seismic Provisions for Structural Steel Buildings* (Including Supplement No. 1). American Institute of Steel Construction, Chicago, IL.

ASCE-SSPB. 1996. Subcommittee on Seismic Performance of Bridges. *Seismic Evaluation and Retrofitting of U.S. Long-Span Suspension Bridges*. Subcommittee on Seismic Performance of Bridges, Structures Congress in Chicago, IL.

ATC. 1996. *Advanced Technology Council, Improved Seismic Design Criteria for California Bridges: Provisional Recommendations*. ATC-32 Report, Applied Technology Council, Redwood City, CA.

Baker, G., Ingham, T., and Heathcote, D. 1998. Seismic Retrofit of Vincent Thomas Suspension Bridge. *Transport. Research Record*, 1624, Transportation Research Board, Washington, DC.

Berman, J. W. 2009. Testing of Nucor A36 Low Carbon Steel under Cyclic Axial an Shear Strain. *Report to HNTB Corporation*, Department of Civil and Environmental Engineering, University of Washington, Seattle, WA.

Buckland, P. G. 2003. Increasing the Load Capacity of Suspension Bridges. *J. Bridge Eng.*, 8(5), 288–296.

Buckle, I. G., Chang, K. C., and Hwang, J. S. 2000. *Bridge Damage, the Chi-Chi Taiwan Earthquake of September 21, 1999: Reconnaissance Report*. MCEER Publication, University at Buffalo, Buffalo, NY.

Caltrans. 2002. *San Francisco-Oakland Bay Bridge East Span Seismic Safety Project: Self-Anchored Suspension Bridge Design Criteria*. Prepared by T.Y.Lin International/Moffatt & Nichol Engineers Joint Venture, July, California Department of Transportation, Sacramento, CA.

Caltrans. 2013. *Seismic Retrofit Program*. California Department of Transportation, http://www.dot.ca.gov/hq/paffairs/about/retrofit.htm (accessed January 21, 2013).

Carlsen R. 2009. Unexpected Bay Bridge Crack Slightly Delays Reopening. ENR: Engineering News Record, September 9, https://enr.construction.com

Castellani A. 1987. Safety Margins of Suspension Bridges under Seismic Conditions. *J. Struct. Eng.*, 113(7), 1600–1616.

Chang, K. C., Mo, Y. L., Chen, C. C., Lai, L. C., and Chou, C. C. 2004. Lessons Learned from the Damaged Chi-Lu Cable-Stayed Bridge. *J. Bridge Eng.*, 9(4), 343–352.

Clough, R. W. and Penzien, J. 2003. *Dynamic of Structures* (3rd Edition), Computers and Structures, Inc., Berkeley, CA.

Combault, J. and Teyssandier, J. P. 2005. The Rion-Antirion Bridge Concept, Design and Construction. *Proceedings of Structures Congress*, ASCE, Washington, DC.

Duan, L. and Chen, W. 2003. Basic Design Criteria for Bridges Crossing Open Sea and Bay Area. *Marine Georesources and Geotechnology*, 21(3–4), 289–305.

Dusicka, P., Itani, A. M., and Buckle, I. G. 2010. Cyclic Behavior of Steel Links of Various Grades of Plate Steel. *J. Struct. Eng.*, 136(4), 370–378.

Dusseau, R. A., Dubaisi, H., and Zaher, S. 1991. Nonuniform Seismic Motion of Long-Span Pipeline Suspension Bridges. *J. Transport. Eng.*, 117(2), 242–256.

Ettouney, M., Hapij, A., and Gajer, R. 2001. Frequency-Domain Analysis of Long-Span Bridges Subjected to Nonuniform Seismic Motions. *J. Bridge Eng.*, 6(6), 577–586.

Fan, L. C. 1996. *Seismic Design of Bridge*. Tongji University Press, Shanghai, China (in Chinese).

Fanjiang, G-N., Gajer, R. B., and Ye, Q. 2001. Seismic Evaluation and Retrofit of the Manhattan Bridge. *Proceedings of the 2001 Structures Congress*, ASCE, Washington, DC.

Gates, J. 1993. *Caltrans Seismic Performance Criteria Directive Memo*, California Department of Transportation, Sacramento, CA.

GGBHTD. 2011. *Overview of Golden Gate Bridge Seismic Retrofit Construction Project*. Golden Gate Bridge Highway and Transportation District, San Francisco, CA.

Gimsing, N. and Georgakis, C. T. 2012. *Cable Supported Bridges* (3rd Edition), John Wiley & Sons, New York, NY.

Hanson, R. D., Aiken, I. D., Nims, D. K., Richter, P. J., and Bachman, R. E. 1993. State-of-the-art and state-of-the-practice in seismic energy dissipation. *ATC-17-1*, ATC, Redwood City, CA, pp. 449–471.

Harichandran, R. S., Hawwari, A., and Sweidan, B. N. 1996. Response of Long-Span Bridges to Spatially Varying Ground Motion. *J. Struct. Eng.*, 122(5), 476–484.

HSBA. 1998. *The Akashi-Kaikyo Bridge*. Honshu-Shikoku Bridge Authority, Japan.

Imbsen, R. A. 2001. Use of Isolation for Seismic Retrofitting Bridges. *J. Bridge Eng.*, 6(6), 425–438.

Infanti, S. and Castellano, M. G. 2004. Rion-Antirion Bridge: Design and Full-Scale Testing of the Seismic Protection Devices. *Proceedings of 13th World Conference on Earthquake Engineering*, Paper No. 2174, Vancouver, B.C., Canada.

Ingham, T. J., Rodriguez, S., and Nader, M. 1997. Nonlinear Analysis of the Vincent Thomas Bridge for Seismic Retrofit. *J. Comp. Struct.*, 64(5/6), 1221–1238.

Jia, J. F. and Ou, J. P. 2008. Seismic Analyses of Long-Span Cable-Stayed Bridges Subjected to Near-Fault Pulse-Type Ground Motions. *Proceedings of the 14th World Conference on Earthquake Engineering*, Beijing, China.

Karmakar, D., Ray-Chaudhuri, S., and Shinozuka, M. 2012. Seismic Response Evaluation of Retrofitted Vincent Thomas Bridge under Spartially Variable Ground Motions. *J. Soil Dyn. Earthquake Eng.*, 42, 119–127.

Kawashima, K., Nagashima, H., and Iwasaki, H. 1993. Evaluation of Modal Damping Ratio Based on Strain Energy Proportional Damping Method. *Proceedings Transactions of Structural Engineering*, Japan Society of Civil Engineers, Vol. 40A, pp. 953–965.

Kennedy, N. A., Vinnakota, S., and Sherbourne, A. N. 1981. The Split-Tee Analogy in Bolted Splices and Beam-Column Connections. *Proceedings of the International Conference: Joints in Structural Steelwork*, Teesside Polytechnic, Middlesbrough, Cleveland, England.

Ketchum, M. A. and Waggoner, F. 1995. Seismic Analysis of the West Bay Suspension Spans of the San Francisco-Oakland Bay Bridge. *Proceedings of National Seismic Conference on Bridges and Highways*, San Diego, CA, Federal Highway Administration, Washington, DC.

Lam, I. P. and Law, H. 2000. Soil Structure Interaction of Bridges for Seismic Analysis. *Technical Report MCEER-00-008*, University at Buffalo, Buffalo, NY.

Lam, I. P. 2008a. Lessons on Geotechnical Aspects from Recent Major Long-Span Bridge Design and Retrofit Projects. *MCEER Report*, University at Buffalo, Buffalo, NY.

Lam, I. P. 2008b. Lessons from Recent Projects involving Time History Analyses. *MCEER Report*, University at Buffalo, Buffalo, NY.

Liu, W. D., Kartoum, A., Chang, K., and Imbsen R. 2000. Seismic Performance and Design Considerations of Long Span Suspension Bridges. *Data Utilization Report CSMIP/00-03 (OSMS 00-05)*, California Strong Motion Instrumentation Program, Sacramento, CA.

Manzanarez, R. and Nader, M. 2000. Design of the New San Francisco—Oakland Bay Bridge. *Proceedings of Structures Congress 2000*, ASCE, Washington, DC.

McDaniel, C. C., Uang, C., and Seible, F. 2003. Cyclic Testing of Built-Up Steel Shear Links for the New Bay Bridge. *J. Struct. Eng.*, 129(6), 801–809.

Murphy, T. P. and Collins K. R. 2004. Retrofitting Suspension Bridges Using Distributed Dampers. *J. Struct. Eng.*, 130(10), 1466–1474.

Murray, T. M. and Sumner, E. A. 2003. Extended End-Plate Moment Connection – Seismic and Wind Applications. *Part 4 of AISC Steel Design Guide* (2nd Edition). American Institute of Steel Construction, Chicago, IL.

Nader, M., Abbas, S., and Ingham, T. 2001. Seismic Safety Design of the New San Francisco—Oakland Bay Bridge. *Proceedings of the 2001 Structures Congress*, ASCE, Washington, DC.

Nader, M. N. and Ingham, T. J. 1996. Seismic Retrofit of the Towers of the Golden Gate Bridge. *Proceedings of the 11th World Conference on Earthquake Engineering*, Acapulco, Mexico, Elsevier Science Ltd., London, UK.

Nazmy, A. S., Abdel, A. M., and Masri, S. F. 2004. Seismic Retrofit of the Vincent-Thomas Suspension Bridge. *Emirates. Eng. Research*, 9(2), 35–43.

Paulay, T. and Priestley, M. J. N. 1997. *Seismic Design of Reinforced Concrete and Masonry Buildings.* John Wiley & Sons, New York, NY.

PLB. 2012. Port of Long Beach of California. *Gerald Desmond Bridge Replacement Project—Structural Design Criteria*, Exhibit 2-13-A, Port of Long Beach, Long Beach, CA.

Priestley, M. J. N. 2000. Performance Based Seismic Design. *Proceedings of the 12th World Conference of Earthquake Engineering*, Oakland, New Zealand, A. A. Balkema, Leiden, the Netherlands.

PTI. 2007. *Post-Tensioning Institute, Recommendations for Stay Cable Design, Testing and Installation* (5th Edition). Post-Tensioning Institute, Phoenix, AZ.

Raab, N. C. and Wood H. C. 1941. Earthquake Stress in the San Francisco-Oakland Bay Bridge. *ASCE Transactions*, Paper No. 2123, 106, 1363–1390.

Reid, R. L. 2010. Damaged Eyebar Section Replaced on San Francisco-Oakland Bay Bridge. *Civil Eng.*, ASCE, 80(4), 8–23.

Rodriguez, S. and Ingham, T. J. 1996. Seismic Protective Systems for the Stiffening Truss of the Golden Gate Bridge. *Proceedings of the 11th World Conference on Earthquake Engineering*, Acapulco, Mexico, Elsevier Science Ltd., London, UK.

Seible, F. 2000. Long Span Bridges in California—Seismic Design and Retrofit Issues. *Proceedings of the 12th World Conference of Earthquake Engineering*, Oakland, New Zealand.

Seim, C. and Ingham, T. J. 2000. Innovative Seismic Retrofit of Steel Bridges – Some Examples. *Proceedings of Structures Congress* ASCE, Washington, DC.

Seim, C. 2008. Why Bridges Have Failed Throughout History. *Civil Engineering*, 78(5), 64–71, 84–87.

Spyrakos, C. C., Kemp, E. L., and Venkatareddy, R. 1999. Validated Analysis of Wheeling Suspension Bridge. *J. Bridge Eng.*, 4(1), 1–7.

Tang, M. C. and Manzanarez, R. 2001. San Francisco-Oakland Bay Bridge Design Concepts and Alternatives. *Proceedings of the 2001 Structures Congress* 2001, ASCE, Washington, DC.

Tao, J. R. and Zong, T. 2007. Influence of Locked-in Girder Stress on the Design of Suspension Bridges, *Bridge Design, Construction and Maintenance, (Proceedings of the Construction and Maintenance Conference, Beijing, China)*, Institution of Civil Engineers, London, UK.

WADOT. 2000. Washington State Department of Transportation. *Structural Design Criteria for Tacoma Narrows Parallel Suspension Bridge*, Prepared by PTG/HNTB Tacoma Narrows Joint Venture, Washington State Department of Transportation, Olympia, WA.

Walther, R., Houriet, B., Lsler, W., and Moia, P. 1988. *Cable-Stayed Bridges*. Thomas Telford, London, UK.

Wilson, J. C. 2003. Repair of New Long-Span Bridges Damaged by the 1995 Kobe Earthquake. *J. Performance of Constructed Facilities*, 17(4), 196–205.

Wilson J. C. and Keith, H. 2007. Sesimic Vulnerability and Mitigation during Construction of Cable-Stayed Bridges. *J. Bridge Eng.*, 12(3), 364–372.

Yan, G. M. and Lao, Y. C. 2000. *Modern Cable-Stayed Bridges*. Southwest Jiaotong University Press, Emeishan, China (in Chinese).

Yanev, B. 2008. *Suspension Bridge Cables: 200 Years of Empiricism, Analysis and Management.* Bridge Inspection & Management, New York City Department of Transportation, New York, NY.

12

Seismic Isolation Design for Bridges

Roy A. Imbsen
Imbsen Consulting

Larry Wu
California Department of Transportation

12.1 Introduction

The acceptable performance of bridges for the traditional force-based seismic design approach is to absorb and dissipate energy by the formulation of plastic hinges in a stable manner to prevent collapse during an earthquake. Specially detailed plastic hinge regions of the supporting ductile columns are capable of absorbing energy through many cycles of the dynamic response of the earthquake. Plastic hinge regions of concentrated damage have been repaired or replaced after earthquakes. The rationale of allowing damage as long as "life safety" is preserved is for economic considerations. This traditional design approach of allowing plastic hinges is not acceptable for bridges on critical life line routes.

Seismic isolation, an acceptable alternative, can be used to avoid having damage to bridge structures and may be achieved at lower initial construction costs. Seismic isolation was initially used to retrofit several important bridges located on the critically important transportation lifeline routes. More recently, seismic isolation has been used on noncritical bridges because of construction cost savings with reduced seismic forces on foundations.

The current AASHTO LRFD Bridge Design Specifications (AASHTO LRFD) (AASHTO, 2012) and the Guide Specifications for LRFD Seismic Bridge Design (Seismic Guide) (AASHTO, 2011) recognize the benefits and promote the use of seismic isolation as an alternative design strategy for new bridges. Some of recent updates include: (1) the addition of the clause in the "AASHTO LRFD" (Article 1.3.3) to substitute the use of "energy-dissipating devices" in place of the "conventional ductile earthquake resisting system" (AASHTO, 2012), (2) the addition of seismic isolation as a design strategy (Article 1.1) in the "Seismic Guide" (AASHTO, 2011) and (3) the third edition of the "AASHTO Guide Specifications for Seismic Isolation Design (Isolation Guide)" with the updated seismic design hazard as defined in the companion AASHTO Specifications mentioned above.

Given these recent changes in the AASHTO Specifications and recent technology in seismic isolation, it is now possible to design bridges for continued functionality as described in Chapter 7. Historically, major critical lifeline bridges have been retrofitted to achieve continued functionality at cost savings of 30% as compared to conventional retrofits to a life safety performance level that does not provide continued functionality. Cost savings have also been realized in using an isolation design strategy for continued functionality for new bridges. The ductile design approach to achieve a performance level of "life safety" at reduced initial construction costs should be reevaluated in light of the lessons learned from recent earthquakes and the development of recent seismic isolation technology. Because the performance level of life safety can be improved with the technology that we currently have, we should raise the standard to continued functionality.

12.1.1 Continued Functionality

Recent studies in the United States and Japan have called for improving the seismic resilience of cities. The aim is for key facilities and infrastructure systems to have the ability to maintain their functionality following large earthquakes. At a minimum, a society needs resiliency to quickly recover from a major seismic event. The facilities and infrastructure system critical to the continued functioning of a city should be designed to enable return to service with minimal or no loss of use. The biggest obstacle to implementing designs for continued functionality is the pressure to design bridge projects to satisfy the minimum code requirements for the minimum initial cost. Thus, a more long-term view is needed that considers structural damage, and disruption costs to communities from the loss of functionality of key infrastructure systems as documented in the U.S. Department of Transportation report on the Northridge Earthquake, January 17, 1994 (USDOT, 2002).

12.1.2 Seismic Isolation for Continued Functionality

For nearly 20 years, seismic isolation design technology has been used to maintain the functionality of important bridges designed for performance objectives that were substantially beyond the minimum AASHTO requirements. One of the first major critical bridges to implement Friction Pendulum technology was the Benicia-Martinez Bridge in California. This bridge as shown in Figure 12.1 is located on a critical route of I-680 between San Francisco and the Travis Military Airport designated as an alternative to the San Francisco Airport. Another example shown in Figure 12.2 is the critically important bridge, the I-40 Bridge across the Mississippi River in Memphis Tennessee, on the main east west corridor across the United States. This bridge was designed to provide continued functionality.

The damage to bridges as witnessed in past earthquakes is primarily because of their lack of ductility and/or inability to deform to the displacements imposed during an earthquake. The "Seismic Guide" (AASHTO, 2011) suggests three possible global seismic design strategies as described in Section 3.3 to consider at the beginning of the design process, one of which is seismic isolation. Because both the

FIGURE 12.1 Retrofitted Benicia-Martinez Bridge, California.

FIGURE 12.2 Retrofitted I-40 Mississippi River Bridge, Memphis, Tennessee.

"Isolation Guide" and the Seismic Guide utilize a displacement-based approach to provide a given level of seismic performance, the designer should consider seismic isolation at the outset of the design process and compare the demands, capacities, and performance of the seismically isolated and nonisolated bridge designs.

Isolation bearings can be used to design and retrofit bridges to avoid structural damage during the most severe earthquake. The primary goal in a seismic isolation strategy is to decouple a structure from the earthquake ground motions. This strategy has been used for various bridge systems where the inertia effects of the vibrating superstructure are separated from the substructure at the interface between superstructure and substructure. This reduces the forces transmitted to the substructure columns, piers, and foundations. The earthquake energy is absorbed by heat in the isolation bearing that provides protection for the substructure (see Figure 12.3).

The isolation systems currently being used for bridges are classified as hysteretic energy dissipating, which are passive energy dissipating systems. The behavior is modeled mathematically as force versus displacement loops of hysteric energy dissipation systems (Constantinou et al., 1998).

This chapter is devoted to the developments and applications of seismic isolation design for bridge structures. Following a brief presentation of current AASHTO LFRD (AASHTO, 2012) and the Seismic Guide (AASHTO, 2011) and the Isolation Guide (AASHTO, 2010), the state of the practice and implementation of seismic isolations are discussed. The basic concepts, modeling and analysis methods, testing, and evaluation are then addressed. A design example is given for illustration purposes. Procurement for construction is also described for practical application.

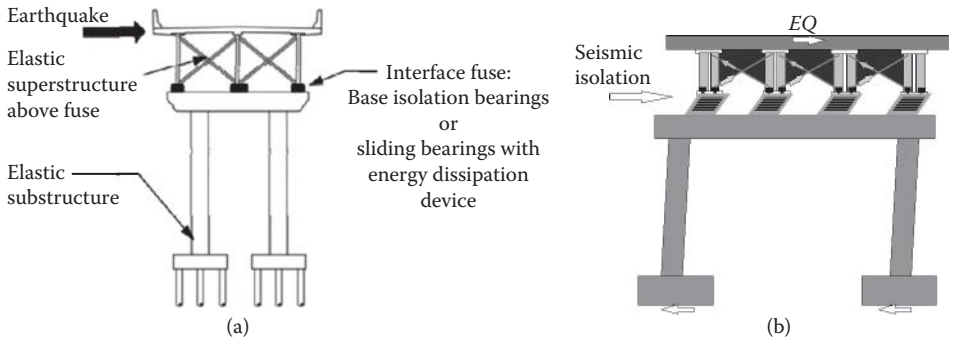

FIGURE 12.3 Global design strategy—Type 3 seismic isolation.

12.2 AASHTO Specifications and Guide Specifications

12.2.1 Background

AASHTO requirements for seismic design of bridges are described in the following three documents: (1) AASHTO LRFD (AASHTO, 2012), (2) Seismic Guide (AASHTO, 2011), and (3) Isolation Guide (AASHTO, 2010). The AASHTO LRFD is based on the traditional force-based method. Using this approach, the elastic demand forces are divided by a prescribed response modification factor "*R*" to obtain the forces in yielding members as shown in Figure 12.4. As mentioned above inherent in this approach is damage in the plastic hinge regions (see Figures 12.5 and 12.6a). Note there is an increase in damage as the displacement and ductility demand increase. The Seismic Guide is based on the displacement-based method considering the strain limitation of the materials in determining the displacement capacities for each of the ductile components.

The Isolation Guide (AASHTO, 2010) uses displacement-based approach with inelastic deformation occurring in the isolators instead of the plastic hinges as shown in Figure 12.6b. In summary, earthquake resistant design of bridges may be accomplished in one of two ways:

1. Increase the capacity of the bridge
   a. Strength
   b. Displacement
2. Reduce demand
   a. Ductility (i.e., formulation of plastic hinge)
   b. Energy dissipation devices (e.g., isolations, damping)

In calibrating the Seismic Guide (AASHTO, 2011), it became apparent that increased performance could be achieved using isolation (see Figure 12.6b).

12.2.2 AASHTO Guide Specifications for LRFD Seismic Bridge Design

The Seismic Guide (AASHTO, 2011) was developed specifically for bridges, using a displacement-based approach with design factors calibrated to prevent collapse and to reflect both the ductility and inherent reserve capacity to deform under imposed seismic displacements. Initially seismic isolation was used as a means of retrofitting existing bridges to decrease their vulnerability to collapse during an earthquake but, seismic isolation is now used to improve the seismic performance of new bridges.

As shown in Figure 12.7, the designated shaded region "f" of the schematic diagram is the calibration point for Collapse Prevention at a 1000-year return period. It should be noted that this is a change

from the previous AASHTO Specification for 500 year hazard with Collapse Prevention as shown in the region designated "c" in the figure.

There are several factors of safety included in the actual bridge design process that must also be examined to align the safety requirements, as specified in the Guide Specification for the calculation of displacement requirements for the support widths, with the strength (i.e., force) of the ductile reinforced columns

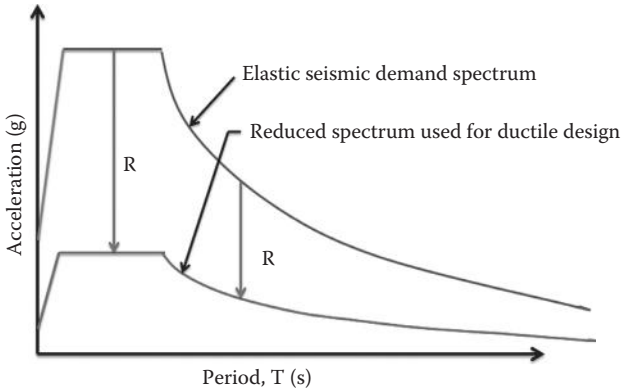

FIGURE 12.4 Response modification factor "*R*" for ductile design.

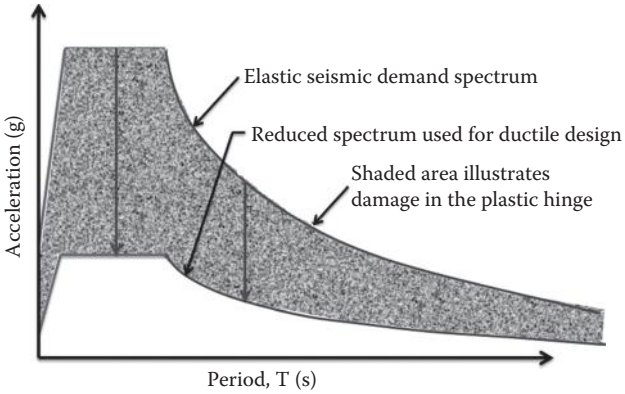

FIGURE 12.5 State of practice for life safety performance.

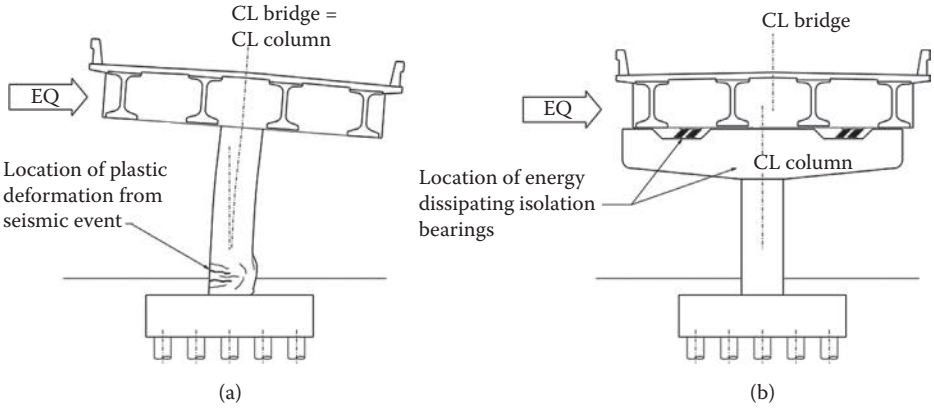

FIGURE 12.6 Bridges with plastic hinging and isolation. (a) Nonisolated structure. (b) Isolated structure.

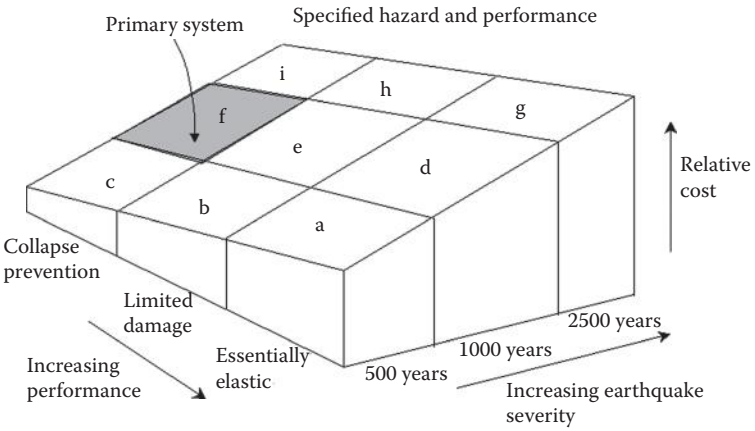

FIGURE 12.7 Calibration objectives with life safety performance and 974-year hazard.

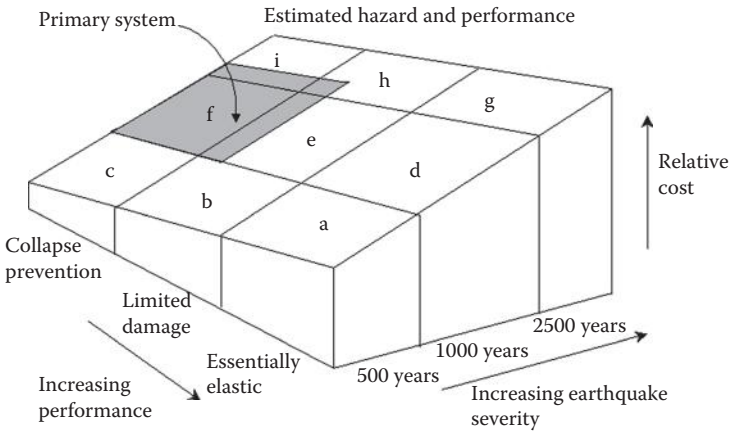

FIGURE 12.8 Calibration objectives with estimated added conservatism.

(see Figure 12.7). The design process begins with the estimation of the plastic hinging moment and force capacity of this "key" component. This estimation includes the following sources of conservatism:

- Computational versus experimental displacement capacity of components
- Effective damping above the 5% assumed for the design spectra
- Dynamic strain rate effect
- Pushover technique governed by the first plastic hinge to reach ultimate capacity

These sources of conservatism each have a factor of at least 1.2 and for some the factor varies up to 1.5. It can be conservatively estimated that the combined effect is a factor of safety of 1.5. Thus having established the combined effect for strength, the formulas developed to compute support width were multiplied by a factor of 1.5. This can be considered as an increase above the calibration point as indicated both by the performance moving into the Limited Damage Range and the Earthquake Hazard increasing to 1400–1500 year return period as indicated by the shaded area beyond block "f" (see Figure 12.8). Thus, there is additional inherent safety in collapse prevention inherent in the conservatism of the design process.

The Seismic Guide suggests three global design strategies. One of these strategies is seismic isolation. Using seismic isolation the performance can be extended into the elastic range with no damage (see Figure 12.9). Going into the elastic range with a longer period reduces the inertia forces transferred to

the substructure, which reduces the substructure and foundations costs as shown by the lower plane in Figure 12.9 labeled "Isolation Applied." This illustrates the path between the Seismic Guide and the use of isolation as described in the Isolation Guide. This leads to the obvious question "Why not use isolation for new bridge design?" A comparison between life-safety and continued functionality are listed in Table 12.1.

This table illustrates the differences between using the ductile design approach with anticipated damage and using isolation to achieve continued functionality.

To further illustrate the benefits of using seismic isolation, consider the elastic design demand spectrum shown in Figure 12.4 with the reduction "*R*" for ductility, and also Figure 12.5 with the elastic design spectrum and the damage zone in reducing the spectrum to the design level. Shown in Figure 12.10 is the same elastic design demand spectrum with the design capacity enveloping this elastic

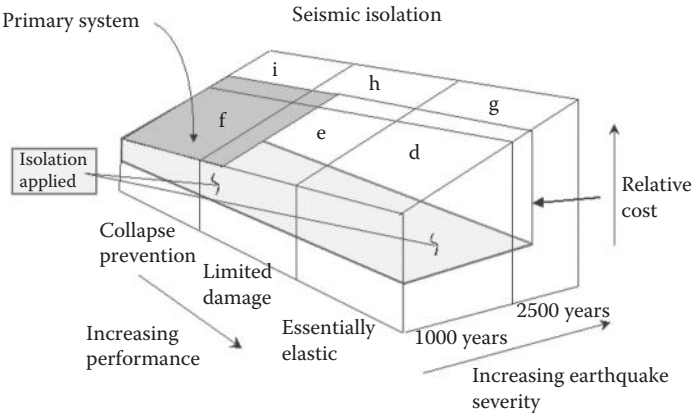

FIGURE 12.9 Illustration of the increased performance using seismic isolation.

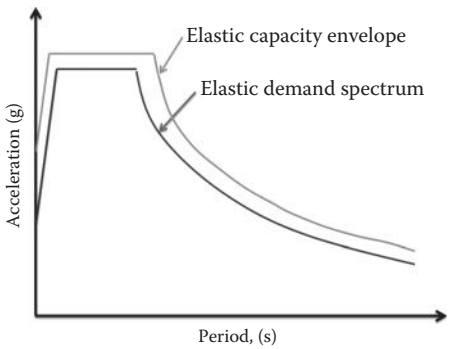

FIGURE 12.10 Design spectrum and capacity envelope for continued functionality.

TABLE 12.1 Comparison between Life-Safety and Continued Functionality

Life Safety	Continued Functionality
• Ductile design (i.e., $R > 1$) with anticipated damage	• Reliably elastic (i.e., $R < 1$) no structural damage
• Initial construction with plastic hinging	• Initial construction with isolation
• Energy absorbed with crushing concrete and steel yielding (low reliability)	• Energy absorbed with isolation devices requiring added displacement capacity (high reliability)
• Repair or replacement	• No structural damage
• Potential for an extended loss of service and revenue	• Minimum or no lost service and revenue and continued functionality
• Design elastic–plastic	• Design reliably elastic

demand design spectrum with the design spectrum. The capacity can be achieved in one or two ways, either by designing the structure to resist the seismic demand elastically without forming a plastic hinge or by using isolation and designing elastically.

A typical example of using isolation for a single column is shown in Figure 12.6b. In this case, seismic isolation bearings are used to separate the superstructure from the substructure by adding a cap member to the substructure column and the addition of the bearings as shown in the figure.

12.3 Current State of Practice

12.3.1 Typical Isolations

There are currently three types of seismic isolation systems used in the United States that include

- Lead Core Rubber (LCR) by Dynamic Isolation Systems, Inc. and Seismic Energy Products, Inc.
- EradiQuake by R.J. Watson, Inc.
- Friction Pendulum by Earthquake Protection Systems, Inc.

LCR—These bearings are manufactured by the Dynamic Isolation Systems, Inc. and Seismic Energy Products, Inc. The LCR is a lead rubber bearing with a lead core (see Figure 12.11).

These bearings are available in circular, square, and rectangular shapes. As shown in the figure, the bearing is composed of an energy dissipating lead core, with internal rubber layers separated by steel reinforcing plates that are encased in a rubber cover. The rubber layers and lead core together provide the initial stiffness required to resist the lateral effects of service loads. During a seismic event the layered steel plates deform forcing the lead core to yield and absorb energy.

EradiQuake—This bearing is manufactured by R.J. Watson, Inc. (see Figure 12.12) The EradiQuake bearing is a sliding bearing having a PTFE interfaced with a flat sliding plate to provide the horizontal

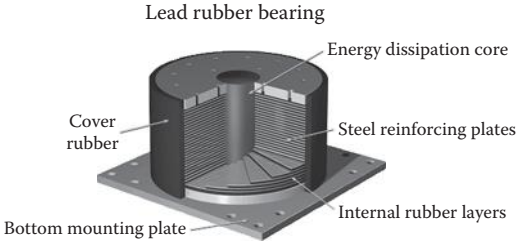

FIGURE 12.11 Lead core rubber (LCR) bearing.

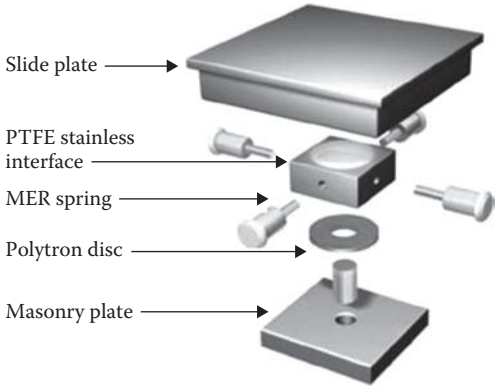

FIGURE 12.12 EradiQuake bearing.

movements in any direction. The Polytron Disc provides for the multirotational capabilities of the bearing. The MER spring provides the recentering capabilities and contributes to the energy dissipating of the system. Energy is also dissipated by friction at the Teflon/Stainless interface.

Triple Pendulum—This bearing is a multispherical sliding bearing (see Figure 12.13). This bearing has four concave surfaces upon which sliding can occur as shown in the figure. These concave surfaces are interfaced with slides that have a self-lubricating bearing material. Each of the four surfaces has separate sliding regimes that can be tuned to provide the most optimal behavior of isolators and energy dissipation.

The Triple Pendulum bearing shown in Figure 12.13 incorporates three pendulums in one bearing, each with properties selected to optimize the structure's response for different earthquake strengths and frequencies. The properties of each of the bearing's three pendulums are chosen to become sequentially active at different earthquake strengths as shown in the plot for the Triple Pendulum bearing included in Figure 12.14. Its predecessor, the single pendulum bearing, is also shown in Figure 12.14. The Triple Pendulum bearing is a new innovation in seismic isolation that provides better performance at lower bearing costs and reduced construction costs.

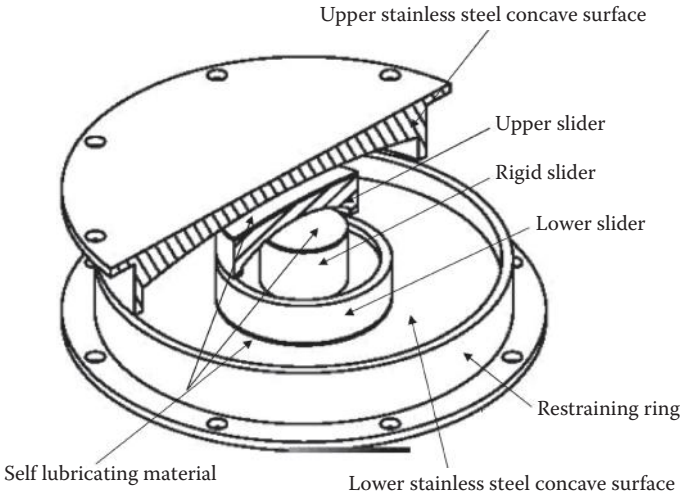

FIGURE 12.13 Triple pendulum bearing.

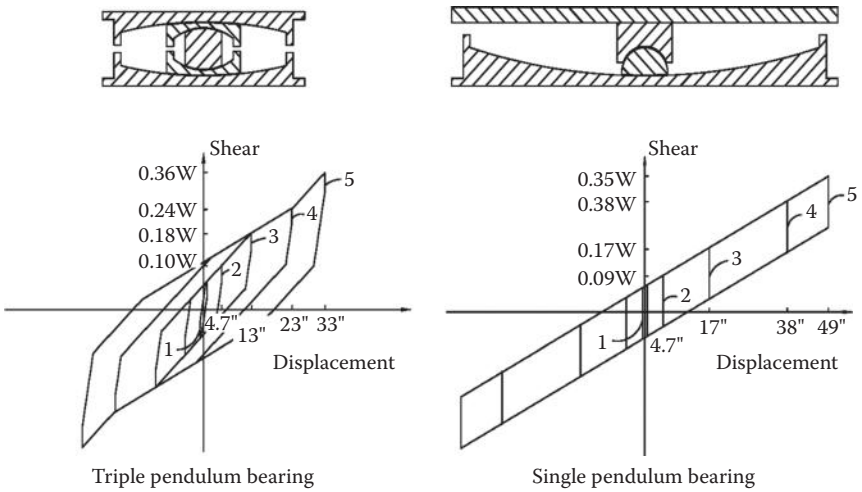

FIGURE 12.14 Comparison of triple pendulum and single pendulum bearings.

A spherical friction bearing is selected for the bearing design example in Section 12.6. This example illustrates how seismic isolation is used on a four-span continuous cast-in-place prestressed box girder bridge.

12.3.2 Bridges with Seismic Isolation Bearings

The Lead Rubber Bearings were used on the AirTrain Light Rail structure (Imbsen, 2001) going to the JFK Airport in New York City (see Figure 12.15a). This seven mile elevated rail line is supported on the bearings (see Figure 12.15b).

EradiQuake bearings were installed on the Castleton-on-Hudson Bridge shown in Figure 12.16a as the part of the bridge retrofit. EradiQuake bearing installation is shown in Figure 12.16b.

Two bridges have been selected to illustrate how seismic isolation, Friction Pendulum Bearing (FPB), can be used to increase the seismic protection of bridges. The bridges are Benicia-Martinez Bridge located in the Bay Area of San Francisco, California (see Figure 12.1), and the I-40 Mississippi River Bridge in Memphis, Tennessee (see Figure 12.2).

The Benicia-Martinez Bridge was the first of the eight toll bridges in California for which detailed seismic evaluations were carried out to develop retrofit schemes and construction costs (Imbsen, 2001).

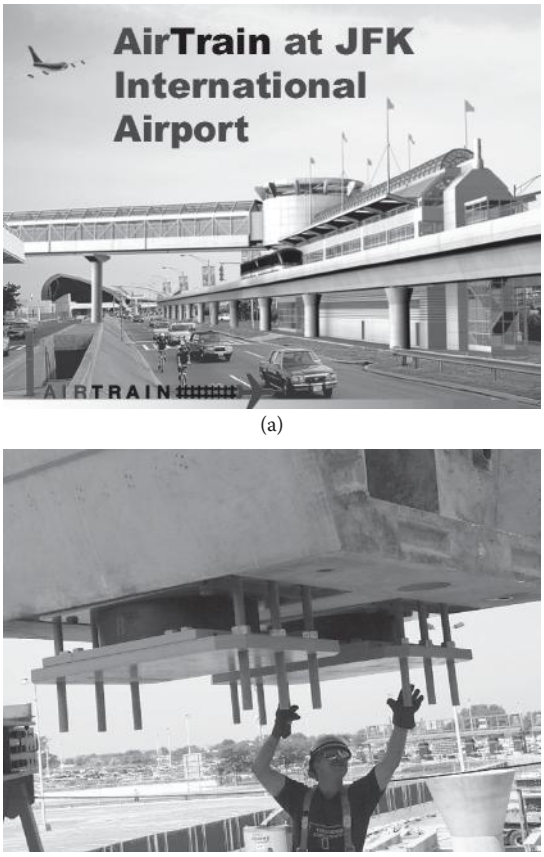

(a)

(b)

FIGURE 12.15 AirTrain structure at JFK airport. (a) AirTrain. (b) Isolation bearings.

(a) (b)

FIGURE 12.16 Castelton-on-Hudson Bridge. (a) Bridge overview. (b) EradiQuake bearing installation.

FIGURE 12.17 Friction pendulum bearing (FPB).

This bridge was considered to be a critical link for the regional economic activities and was classified as an important bridge having the following performance requirements:

- The bridge should remain essentially elastic under the Functional Evaluation Earthquake defined as having a 40% probability of occurring during the useful life of the bridge.
- The bridge should provide service to normal traffic almost immediately following the Safety Evaluation Earthquake. Any damage incurred should be repairable with limited loss of service, that is, short closure time.

A detailed seismic investigation of the bridge was conducted showing that the truss, bearings, and nonductile hollow concrete piers were seismically deficient and very vulnerable to damage for both the Functional and Safety Evaluation Earthquakes. Two retrofit strategies for the main truss spans were proposed. First strategy used the more conventional strengthening approach and the second used isolation. The FPB shown in Figure 12.17 was selected with a total displacement of 53 inches in each direction and a vertical load capacity of 5000 kips.

This bearing holds the record for the world's largest bearing. The construction costs using the isolation design were 30% less than that of the more conventional retrofit.

The second application is for the I-40 Mississippi River Bridge (Imbsen, 2001). The main river crossing includes two tied-arch spans (2 at 900 ft) and five steel box girder spans (2 at 330 ft and 3 at 400 ft) (see Figure 12.2).

This crossing is a critical lifeline serving the two states on either side of the river and is a critical link for national transportation system. It is located at the southeastern edge of the New Madrid seismic

zone. Seismic performance goals were determined by the owners, the states of Tennessee, and Arkansas, in conjunction with the Federal Highway Administration (FHWA), to be a vital link that must remain operational following a Contingency Level earthquake having a 2% PE in 50 years (i.e., 2500-year return period). Several alternative seismic design strategies were reviewed with the final selection being isolation using the FPB as shown in Figure 12.18 for the tied-arch truss.

This bearing has a vertical load carrying capacity of 20,000 kips, which was a record at the time this bridge was built. Similar FPBs were used for the five steel box girder spans. A modular joint was required to accommodate both the transverse and longitudinal movements associated with the isolation strategy (see Figure 12.19).

For the I-40 Bridge, the construction costs for the main river crossing were 30% less using isolation, as compared to a more conventional retrofit of using ductile column design along with member strengthening.

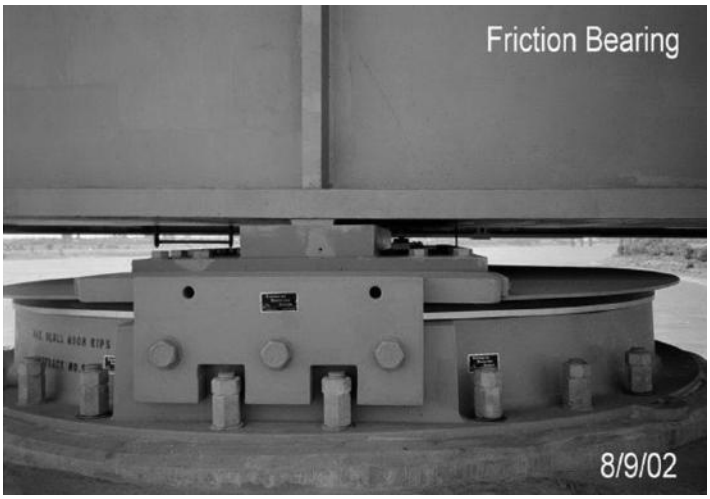

FIGURE 12.18 Friction pendulum bearing (FPB).

FIGURE 12.19 Modular joint installation.

12.3.3 Remarks

Seismic isolation has now progressed to a mature technology. It has a significant range of applications, which includes upgrading the seismic resistance of existing bridges and designing new bridges. There are currently three types of seismic isolation bearings being used in the United States from which to choose, depending upon the type of bridge, seismic hazard, and desired performance. The manufacturers of the proprietary bearings listed above all comply with the Isolation Guide (AASHTO, 2010). This specification is performance based requiring each manufacturer to conduct: (1) system tests, (2) prototype tests, and (3) quality tests to insure that their manufactured products meet the requirements of each application. All manufacturers have engineering support to provide assistance in selecting the isolation design parameters for their bearings. Seismic isolation, when properly applied, reduces the lateral seismic forces in the substructure and foundation resulting in a cost savings with improved performance.

12.4 Design Requirements and Procedures

12.4.1 General Requirements

There are two interrelated parts in designing seismic isolation devices for bridge applications. First, isolation bearings must be designed for all nonseismic loads as specified in AASHTO LRFD (AASHTO, 2012). In addition, isolation bearings are designed to satisfy seismic requirements and to safely support the vertical loads during a seismic event. Chapter 1 of Part 3 provides detailed design information on bearings under nonseismic loads. This section describes the second part of the design requirements.

One of the main tasks of seismic design is to determine the maximum displacement for providing adequate clearance, and required properties for performance verification tests of an isolation system resulting from seismic loads.

The second main task is to determine the seismic design force for connections between the superstructure and substructure at isolation bearings. For seismic zones 2, 3, and 4, the seismic design force at each bearing shall be determined as

$$F_A = K_{eff} d_t \tag{12.1}$$

where K_{eff} is effective stiffness and d_t is total design displacement.

Columns and piers shall be designed for the maximum force that may be developed in the isolators. The foundation design forces need not exceed the elastic force nor the forces resulting from plastic hinging of the column.

12.4.2 Other Requirements

It is important to check displacements of the isolation system resulting from nonseismic lateral load combination and to provide adequate rigidity to resist frequently occurring wind, thermal, and braking loads. To prevent cumulative displacement and to accommodate isolator installation imperfection, the period and its corresponding to the restoring force alone shall meet the following requirements:

$$T_r < 6 \text{ sec} \tag{12.2}$$

$$F_{dt} > \begin{cases} F_{0.5\,dt} \\ W/80 \\ 1.05\,F_f \end{cases} \tag{12.3}$$

where T_r is the period corresponding to its tangent stiffness based on the restoring force alone at any displacement, Δ, up to its total design displacement, d_t; F_{dt} is the restoring force at d_t; $F_{0.5dt}$ is the restoring force at 0.5 dt; W is weight of structure supported by the bearing and F_f is the static friction force.

Isolation systems in a laterally undeformed state are required to support the minimum three times unfactored dead and live loads. A system should also be stable under 1.2 times the dead load and any vertical load due to seismic live load plus overturning at a horizontal displacement equal to the offset displacement plus the larger of (1) 1.1 dt, for maximum earthquake (2) 2 dt for Seismic Zones 1 and 2 for 1000-year earthquake, or (3) 1.5 dt for Seismic Zones 3 and 4 for 1000-year earthquake.

Isolation systems shall provide rotation capacity to resist the effects of dead load, live load, and construction misalignments at a minimum of 0.005 rad. The design rotation capacity of the isolator shall exceed the maximum seismic rotation demand. The designer should consider the following in selecting an isolation system:

- Service loads and movements
- Sliding system has larger axial load capacity
- Available height and space
- Displacement demands
- Temperatures

12.4.3 Analysis Procedures

The Isolation Guide (AASHTO, 2010) permits the simplified method, single and multimodal spectral methods to be used for seismic isolation design based on two basic assumptions: the energy dissipation in the isolation system can be expressed as equivalent viscous damping and stiffness of isolation systems as effective linear stiffness. For isolated systems where effective damping ratios > 30% of critical and/or effective periods larger than 3 seconds, a nonlinear time-history analysis is required.

12.4.3.1 Simplified Method

The simplified method of analysis is applicable to isolated bridges that respond predominantly as a single degree of freedom system without coupling of displacement in orthogonal directions. The equivalent static seismic force is determined by

$$F = C_{smd} W \tag{12.4}$$

$$C_{smd} = \frac{C_{sm}}{B_L} = \frac{S_{D1}}{T_{eff} B_L} < \frac{S_{DS}}{B_L} \tag{12.5}$$

$$B_L = \left(\frac{\xi}{0.05} \right)^{0.3} \tag{12.6}$$

$$T_{eff} = 2\pi \sqrt{\frac{W}{K_{eff} g}} \tag{12.7}$$

$$K_{eff} = \sum\nolimits_j K_{effj} \tag{12.8}$$

$$K_{effj} = \frac{k_{sub} k_{eff}}{k_{sub} + k_{eff}} \tag{12.9}$$

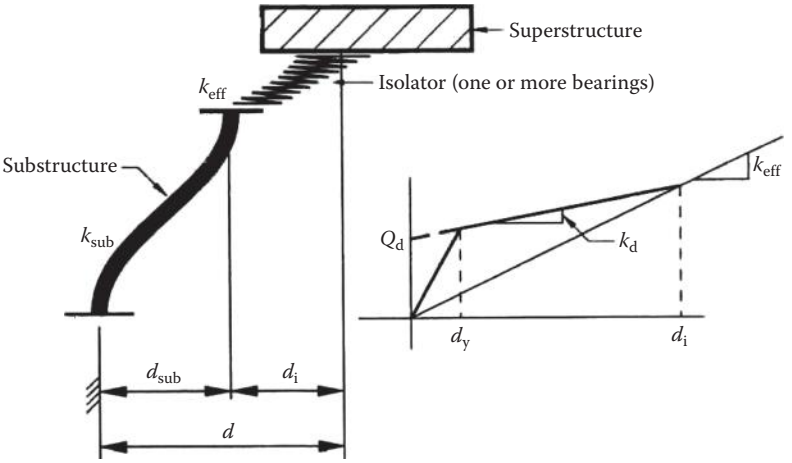

FIGURE 12.20 Lateral load response of isolated bridge.

$$\xi = \frac{\text{Total Dissipated Energy}}{2\pi \sum_j \left(K_{effj} d^2\right)} \tag{12.10}$$

$$d = \left(\frac{g}{4\pi^2}\right)\left(\frac{S_{D1} T_{eff}}{B_L}\right) \tag{12.11}$$

where, B_L is damping coefficient for the long-period range of the design response spectrum; ξ is equivalent viscous damping ratio; W is total vertical load for design of the isolated system ($DL + LL_s$); S_{D1} is acceleration coefficient; T_{eff} is effective period (second); K_{eff} is effective stiffness; k_{eff} and k_{sub} are stiffness for the isolator and substructure unit, respectively (see Figure 12.20); g is acceleration because of gravity; d is displacement of isolated bridge.

12.4.3.2 Single-Mode Spectral Method

The method is appropriate for isolated bridges that respond predominantly as a single degree of freedom system without coupling of displacement in orthogonal directions. In this procedure, equivalent elastic properties, that is, effective linear stiffness is calculated at the design displacement and used to represent the stiffness of the nonlinear isolators. Equivalent static force is given by the product of the elastic seismic force coefficient and dead load W of the superstructure supported by isolation bearings. Analysis shall be performed independently for the two orthogonal axes and combined as specified in the LRFD Seismic Guide (AASHTO, 2011).

12.4.3.3 Multimode Spectral Method

This procedure is the same as specified in the LRFD Seismic Guide (2011) using the 5% damping ground motion response spectra with the following modifications:

1. The isolation bearings are represented by their effective stiffness values.
2. The response spectrum is modified to incorporate the effect of higher damping of the isolated system. This results in a reduction of the response spectra values for the isolated modes. For all the other modes, the 5% damping response spectra should be used.

A typical modified response spectrum is shown in Figure 12.21.

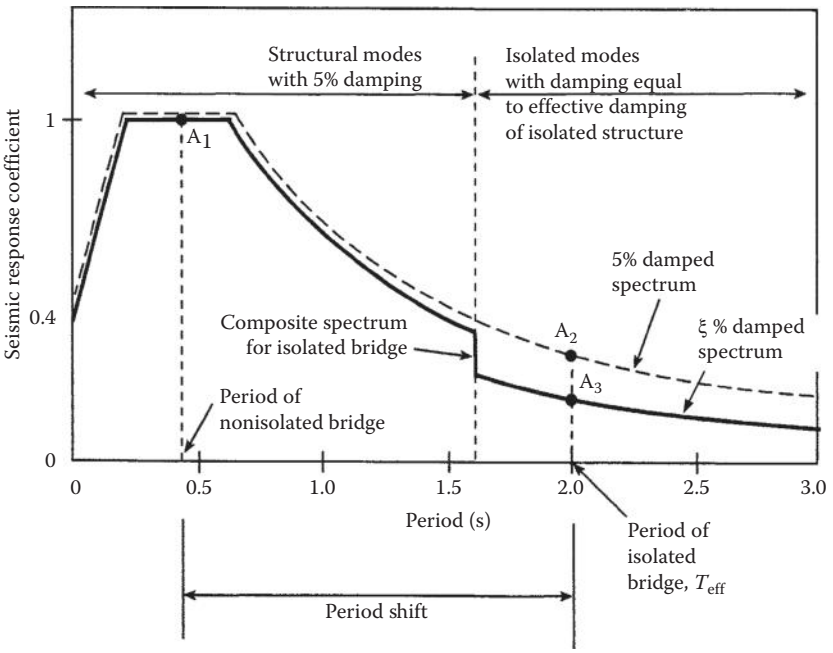

FIGURE 12.21 Modified design response spectrum for isolated bridge.

12.4.3.4 Time-History Analysis

As mentioned earlier, time-history analysis is required for isolation systems with high damping ratio (>30%) and/or effective periods larger than 3 seconds. The isolation systems shall be modeled using nonlinear force-deformation characteristics of the isolators obtained from tests. At least three sets of ground acceleration time histories compromising three orthogonal components shall be used in analysis. Each set shall be simultaneously applied to the model. The maximum response shall be used for the design if ground motion time-history analyses are performed. The average value of the response may be used for the design if seven or more ground motion time-history analyses are performed.

12.5 Testing and Evaluation

The seismic design specification is a performance-based specification. Each of three types of isolation bearings described above has its own main features and must comply with the design and testing requirements set forth in the Isolation Guide. The testing protocol as provided in the Isolation Guide (AASHTO, 2010) began with the first edition of the Isolation Guide (AASHTO, 1991). However, the first edition of the Isolation Guide (AASHTO, 1991) only addressed the application of elastomeric bearings to be used for seismic isolation. The required testing for the elastomeric bearing did not include the design and testing procedures for sliding bearings. The second edition of the Isolation Guide (AASHTO, 1999) was a significant modification to the 1991 Isolation Guide as discussed below. Additional contributions were made in connection with the Highway Innovation Technology Evaluation Center (HITEC) as the "Guidelines for the Testing Seismic Isolation and Energy Dissipating Devices" (HITEC, 1996) were developed. These guidelines were compiled by a team of experts from State Transportation Departments, university researchers, private industry, and the Federal Highway Administration.

12.5.1 HITEC

The HITEC evaluation program began in January 1994 in a cooperative program between FHWA, Caltrans, and HITEC to perform a full-scale dynamic testing and evaluation program of the systems available at that time. The systems included both isolation and damping devices. Testing was performed on 11 systems including both domestic and international manufacturers. A test plan was developed by a panel from State Transportation Departments, university researchers and private industry (Ghasemi, 1999). The objectives of the evaluation program include

- Implementing a program of full-scale dynamic testing sufficient to characterize the fundamental properties and performance characteristics of the devices evaluated
- Providing guidance on the selection, use, and design of seismic isolation and energy dissipation devices for different levels of performance
- Helping with the development of suggested guide specifications for the use of seismic isolation and energy dissipation devices in new bridges and retrofit project

This program examined the important properties and performance characteristics of all systems—stability, range, capacity, resilience, resistance to service and dynamic loads, energy dissipation, functionality in extreme environments, resistance to aging and creep, predictability of response, fatigue and wear, and size effects.

These properties provide engineers with critical information on the suitability of these devices for specific applications. Furthermore, the program addresses the ability of the vendor or manufacturer to provide a quality system and to understand and predict system response.

The testing program developed by HITEC was to increase the confidence level of the bridge community to promote the use of seismic isolation and damping devices for a cost effective to protect bridges from severe earthquake damage. The testing protocol in the Isolation Guide began with the recommendations from HITEC Report (HITEC, 2002).

The purposes of these tests as described in the report are to provide information on

- A benchmark of the pseudo-static response of a virgin seismic isolator
- Dynamic response of a seismic isolator
- Influence of the axial pressure on the pseudo-static and dynamic response of a seismic isolator
- Dependence of the pseudo-static response of a seismic isolator to bidirectional loading
- Restoring force capacity of a seismic isolator
- Simulation of the service life displacement history of a seismic isolator
- Pseudo-static response of a seismic isolator following repeated large-displacement cyclic testing
- Pseudo-static response of a seismic isolator for displacements in excess of the rated displacement
- Response of a seismic isolator over the range of extreme temperatures
- Response of a seismic isolator that includes a sacrificial restraint
- Response of a seismic isolator to a predetermined earthquake history
- Response of a seismic isolator following exposure to environmental conditions representative of its potential application in a bridge structure
- Response of a seismic isolator to tension force at the rated displacement

12.5.2 AASHTO

The second edition of the Isolation Guide (AASHTO, 1999) included a number of modifications. A newly formed AASHTO T-3 Seismic Design Technical Committee was assigned the task of modifying the 1991 Isolation Guide. At that time, this new Isolation Guide was considered to be the state-of-the-art seismic isolation design and testing requirements available worldwide for design of seismically isolated structures. Although developed for seismic isolation of bridges, these Guide Specifications were used in the design of many important and critical seismically isolated structures worldwide. In 2010 AASHTO

updated this document to reflect the current state of practice in the design of seismically isolated bridges. A key requirement of the Isolation Guide is that any seismic isolation system must meet the following requirements before their use:

- System characterization tests
- Prototype tests
- Quality-control tests

Because the Isolation Guide is a performance-based specification, tests must be performed to substantiate both the properties of the individual isolator and the system.

12.5.2.1 System Characterization Tests

The "System Characterization Tests" specified in Article 13.1 in the Isolation Guide describes those requirements. These tests are required when a new isolation bearing is developed either by an existing bearing manufacturer or a new manufacturer. Tests also include load-temperature tests and wear and fatigue testing as described in Articles 13.1.1 and 13.1.2, respectively. The low-temperature test is conducted to verify that the properties of the isolator do not change within a specified range at the low temperatures. Wear or travel and fatigue tests are required to account for movements resulting from both imposed thermal displacement and live load rotations for at least 30 years. Tests are performed at the design contact pressure for a given temperature range and a minimum rate of application as given in Article 13.1.2 of the Isolation Guide.

Determination of the system characteristics seismic isolation systems are designed assuming that the energy dissipation of the system can be expressed in terms of the equivalent viscous damping, and stiffness can be represented by an effective linear stiffness. This assumption can be verified by conducting cyclic load tests on an individual isolator unit as described in Article 13.3 of the Isolation Guide. The energy dissipated for an isolator is the area within hysteresis loop. Using the results of these tests the following characteristics can be determined:

- System adequacy
- Incremental force capacity
- Maximum measured force
- Maximum measured displacement
- Average effective stiffness
- Minimum effective stiffness
- Minimum energy dissipated per cycle
- Stability under vertical load
- Specimen deterioration

12.5.2.2 Prototype Tests

Prototype tests are performed to verify that the properties used in the design and analysis are the same as the test results. Tests are performed on the full size specimens of each type used in the design. Tests should include all components used in the isolation system. A sequence of tests are performed for a prescribed number of cycles at a vertical load and in some cases a portion of live load that includes the total dead load for the following:

- Thermal
- Wind and braking: preseismic test
- Seismic
- Wind and braking: postseismic test
- Seismic performance verification
- Stability

The prototype testing also includes determination on loading rate dependency using dynamic testing at a prescribed rate to check variability on the characteristic strength Q_d and effective stiffness K_{eff}.

12.5.2.3 Quality-Control Tests

Quality-control testing is conducted on every bearing. The following tests are conducted for all bearing types:

- Compression capacity
- Combined compression and shear
- Posttest acceptance criteria
  - Elastomeric bearings
    - Lack of rubber-to-steel bond
    - Laminate placement fault
    - Surface cracks on the rubber
    - Permanent deformation
  - Sliding bearings
    - Lack of bearing-liner-to-metal bond
    - Scarring of stainless steel plate
    - Permanent deformation
    - Leakage

12.5.3 Recommended Bridge-Bearing Seismic Isolation Tests

Seismic isolation bearings must have adequate strength to safely support the maximum structure loads that occur during severe earthquakes. Also, verifying the dynamic bearing properties used in design requires that bearings be tested at the natural vibration period of the isolation system ("real time testing"). Quality Control real time tests verify the dynamic bearing properties when vertically loaded at the average bearing dead plus reduced seismic live load. Bearing Capacity Tests on two prototype bearings verify that the bearings will avoid instability and collapse during a maximum credible earthquake event. Real Time Property Tests on two prototype bearings measure the dynamic properties for the full range of loads and displacements applicable in the design. The Energy Capacity Test verifies the bearing's ability to dissipate the earthquake's energy under realistic seismic loading conditions. The tests specified below use the load and displacement definitions of the Isolation Guide (AASHTO, 2010), as applicable to each bearing size and type. It is important that the Isolation Guide Article 13.1 System Characterization Tests are performed in addition to the tests specified below.

12.5.3.1 Real Time Property Tests

These property tests are performed on two bearings of each type, and are used to measure the dynamic properties of a bearing over the range of loads and displacements used in the design. These tests are conducted at the isolated structure period $T_{eff,}$ in order to characterize the dynamic stiffness and damping properties, and energy dissipation capacities at a rate of energy input representative of seismic conditions. Modeling of the bearing properties in the design and analysis of the structure is based on the measured bearing properties from the Real Time Property Tests. The Real Time Property tests should be performed as specified below on the same two prototype bearings in the order listed in Table 12.2. All force-deflection loops shall show a positive incremental force-carrying capacity for all incremental displacements away from the bearing's center position. Bearings shall have no structural damage as a result of these tests, but may not be used for construction.

TABLE 12.2 Real Time Property Tests

Applied vertical bearing load Average test load sustained within +/−10% of listed value. Minimum and maximum loads within +/−30% of listed value	Lateral displacement cycles, imposed at +/−the displacements listed. Displacements are the minimum positive and negative displacement amplitudes for each cycle. Cycles are applied continuously	Maximum test duration for total number of cycles listed
Average ($DL + LL_s$)	3 cycles at TDD	3 T_{eff}
Average ($DL + LL_s$)	20 cycles at +/−1 inch	40 seconds
Average ($DL + LL_s$)	150% TDD, 75% TDD, 25% TDD	3 T_{eff}
50% Max ($DL + LL_s + OT$)	150% TDD, 75% TDD, 25% TDD	3 T_{eff}
Max ($DL + LL_s$)	150% TDD, 75% TDD, 25% TDD	3 T_{eff}
1.2 Max ($DL + LL_s + OT$)	150% TDD, 75% TDD, 25% TDD	3 T_{eff}

12.5.3.2 Bearing Capacity Tests

Bearing Capacity Tests are intended to ensure that the bearings will exhibit safe structural behavior during the combined loadings that occur during maximum credible earthquake shaking, when considering the effects of both lateral and vertical ground shaking. Vertical earthquake shaking effects have caused the collapse of many bridges and the structural failure of seismic isolation bearings, but are often ignored by bridge designers when implementing a minimum code design. Also, every year earthquakes occur that are stronger than the code defined design earthquakes. Because maintaining stability in the bearings is critical to avoiding collapse of an isolated bridge, it is very important that the bearings have the strength and stability necessary to withstand maximum credible earthquake shaking without structural bearing failures. These Bearing Capacity Tests check for significant structural degradation caused by the maximum combined vertical and shear loads, and anticipated earthquake energy input. To control lateral seismic displacements, the bearing should maintain a positive incremental lateral stiffness when laterally loaded to the maximum shear load and displacement, whereas supporting the maximum vertical loads. If a positive incremental lateral stiffness is not maintained, bearing displacements larger than the calculated design displacement will occur, which may cause isolation system instability and bridge collapse. The uplift capacity tests check that bearings can safely accommodate short duration uplift displacements or tension loads, and afterwards maintain their lateral strength and stiffness when loaded again at the design compression loading. Each test should be performed in the order listed below on each of two bearings of each type. Bearings must be able to complete the tests in the order shown and meet the acceptance criteria as specified for each test. Bearings may be damaged as a result of these tests. The capacity tested bearings may not be used for construction.

12.5.3.3 Energy Dissipation Capacity Test

The bearing is vertically loaded at the Max ($DL + LL_s$) compression load then 5 lateral displacement cycles are consecutively imposed at displacements not < +/− TDD displacement. The total duration of the five cycles of lateral loading should not be more than $5T_{eff.}$ The EDC used in design should not be more than the average EDC measured for the five cycles.

12.5.3.3.1 Design Uplift Displacement or Tension Load

Bearings that may undergo uplift displacement shall be tested to simulate the maximum seismic uplift displacement. Bearings that may be subject to tension loading shall be tested for the maximum tension load. Starting at the center un-displaced position, the Max ($DL + LL$) compression load is applied and the bearing is displaced to +TDD, then the maximum MCE uplift displacement or tension load is imposed and the bearing is displaced back to the center position, then the Max ($DL + LL$) load is reapplied and the bearing is displaced to −TDD, and then back to the starting position. The uplift displacement or

tension load, and lateral displacement movements, shall not result in a permanent loss of the bearing compression, tension, or lateral load capacities.

12.5.3.3.2 Positive Lateral Stiffness

The bearing is vertically loaded at the Max ($DL + LL + OT$) compression load, then one complete lateral displacement cycle is imposed at not < +/−1.25 TDD displacement. The force-deflection plot shall have a positive incremental force-resisting capacity for all increases in lateral displacement away from center. At the 1.25 TDD displacement, the applied vertical load shall not be less than the Max ($DL + LL + OT$) compression load.

12.5.3.3.3 Maximum Combined Compression and Shear Loads

At a vertical load not <1.3 ($DL + LL + OT$), a lateral load of not <1.3 (k_{max} TDD) shall be applied and sustained for 5 seconds. The lateral and vertical displacements shall not increase more than 3% during the 5 seconds of sustained loads. The bearing shall demonstrate no loss of vertical or lateral load carrying capacity as a result of this test. The 1.3 vertical load factor provides for a reserve vertical strength capacity to safely accommodate vertical earthquake shaking effects. The 1.3 lateral load factor provides for a reserve lateral shear strength capacity to safely accommodate an earthquake stronger than the minimum code specified design earthquake.

12.5.3.4 Tests Performed at Reduced Test Rates or on Reduced Scale Bearings

Seismic isolation bearings are sometimes tested very slowly, imposing the code specified lateral cyclic displacements at a "quasi-static" rate. Quasi-static tests are adequate for testing a bearing's strength, but misrepresent the ability of a bearing to dissipate the earthquake's energy within the realistic time duration of an earthquake. If the Energy Dissipation Capacity Test cannot be performed on full-scale bearings as specified, the EDC used in design may be calculated from the results of slower velocity tests performed on full-scale bearings, adjusted according to slow velocity and real time tests performed on reduced-scale bearings. Reduced-scale bearings must be of the same type and exactly of the same materials, and not smaller than one-quarter scale. Reduced-scale bearings are tested for 5 cycles in real time at the reduced-scale TDD. The reduced scale 5 cycle slow test is performed at the same test cycle period that is used to test the full-scale bearings, and then the test is performed at the real time $5T_{eff}$ for the reduced-scale bearings. The reduced-scale bearing vertical load shall not be less than one-eighth of the full-scale vertical load. The reduced-scale TDD shall not be less than one-quarter of the full-scale TDD. The reduced-scale T_{eff} shall not be less than one-half of the full scale T_{eff}. The EDC used in design shall be calculated as

$$\text{EDC (used in design)} = \text{EDC (full} - \text{scale slow)}\left[\frac{\text{EDC (reduced} - \text{scale real time)}}{\text{EDC (reduced} - \text{scale slow)}}\right]^2$$

If the slow velocity Energy Dissipation Capacity test is not performed on full-scale bearings, or if reduced-scale real time tests are not performed, then the value of ξ (equivalent viscous damping ratio) used in design shall not exceed 0.05. If the Combined Design Compression and Shear, or Positive Lateral Stiffness, or Uplift Displacement, or Tension Load tests are not performed as specified on the prototype bearings, then the bearing's ultimate vertical strength capacity must be at least three times the Max ($DL + LL + OT$), and the F (seismic force) used to design the upper structure shall be at least twice the F value calculated from a structural evaluation based on the calculated elastic properties of the bearings. If the Real Time Property Tests are not performed as specified on the prototype bearings, then the value of ξ used in design shall not exceed 0.05, and the F used in the structure design shall not be taken as less than twice the F value as calculated from the elastic properties of the full size bearings.

TABLE 12.3 Quality Control Tests

Applied vertical bearing load Minimum and maximum loads within +/−30% of load value. Average test load sustained within +/−10% of load value	Lateral displacement cycles, imposed at +/−the displacements listed. Displacements are the minimum positive and negative displacement amplitudes for each cycle. Cycles are applied continuously	Maximum test duration for total number of cycles listed
Average ($DL + LL_s$)	3 cycles at TDD	3 T_{eff}

12.5.3.5 Quality-Control Tests

Quality-control tests are performed on 100% of all bearings, as specified below. Each bearing's effective stiffness, effective damping, and restoring force stiffness values, shall be within the tolerances established for the quality-control tests of production bearings as listed in Table 12.3. All force-deflection loops shall show a positive incremental force-carrying capacity for all incremental displacements away from the bearing's centered, un-displaced position. Bearings shall not be damaged as a result of this test.

12.5.3.6 Comparison with AASHTO Minimum Bearing Tests and Design Requirements

The above tests are performed at higher vertical loads than the Isolation Guide Article 13.2 Prototype Tests, and the 15.2, 17.2, and 18.5 Quality-Control Tests. The Isolation Guide Article 13.2.2 Prototype Tests are performed at the average dead load only, not including live load, or seismic overturning load, or vertical earthquake load. In practice, bearings supporting longer than average bridge span will support a higher than the average dead load. The Isolation Guide Article 13.2.2.6 Stability test for maximum vertical load uses reduced live load LL_s, and has no load for vertical earthquake shaking. The Isolation Guide design live load is LL, and LL_s is an arbitrarily reduced live load. Inadequate bearing vertical load capacity causes bearing damage, reduced lateral bearing stiffness, and increased lateral displacements, which can cause bearing and total bridge collapse. Seismic isolation bearings should safely maintain stability under the maximum vertical loads including full design live loads, and vertical earthquake shaking effects. It is important to recognize that although seismic isolation has been proven as a seismic design approach, there are no industry standards for the materials, manufacturing, or testing methods for the bearings. An isolated bridge designed according to the current Isolation Guide, but using bearings procured through low bid without industry standards for bearing materials, manufacturing, and testing methods, is very dangerous. Achieving seismic isolation designs that avoid bearing damage and collapse depends on using a bearing manufacturer with proven bearing materials, manufacturing, and testing methods, and also performing bearing tests as recommended above. These tests represent a recommended 20 year technical update to the Isolation Guide Article 13.2 Prototype tests that is needed for performing tests at realistic maximum vertical loads and dynamic lateral loading conditions. The above recommended tests should replace the tests specified in Articles 13.2, 15.2, 17.2, and 18.5, of the Isolation Guide (AASHTO, 2010).

12.6 Design Examples

12.6.1 Introduction

This section presents a seismic isolation example of a four-span continuous cast-in-place prestressed box Girder Bridge. Fourteen examples of precast concrete girder and steel I-girder bridges are developed to demonstrate the application of isolation for varying seismic hazard, site classification, isolator type in NCHRP Project 20-7/262 Report (Buckle et al., 2012). These examples illustrate the application of isolation to various bridges and isolators for different seismic hazards.

12.6.2 Bridge Descriptions and Seismic Hazard

An isomeric view of a four-span continuous cast-in-place prestressed box girder bridge with two-column bents is shown in Figure 12.22. As shown the span lengths are 90, 120, 130, and 100 ft long. A Typical Section is shown in Figure 12.23. As shown in the figure, the bridge carries three traffic lanes and superstructure width of 58.67 ft, and depth is 5.5 ft. The column diameter is 5.5 ft, and the column heights are 24, 26, and 24 ft at Bent 2, Bent 3, and Bent 4, respectively. All columns are fixed at the bottom. The spherical friction isolation bearings are installed at top of columns.

The ARS design spectrum is shown in Figure 12.24. The peak ground acceleration at the bridge site is 0.5g. The site is classified as Type D. The design spectral acceleration coefficient at 0.2 second period is $S_{DS} = 1.25g$, and the design spectral acceleration coefficient at 1.0 second period is $S_{D1} = 0.63g$.

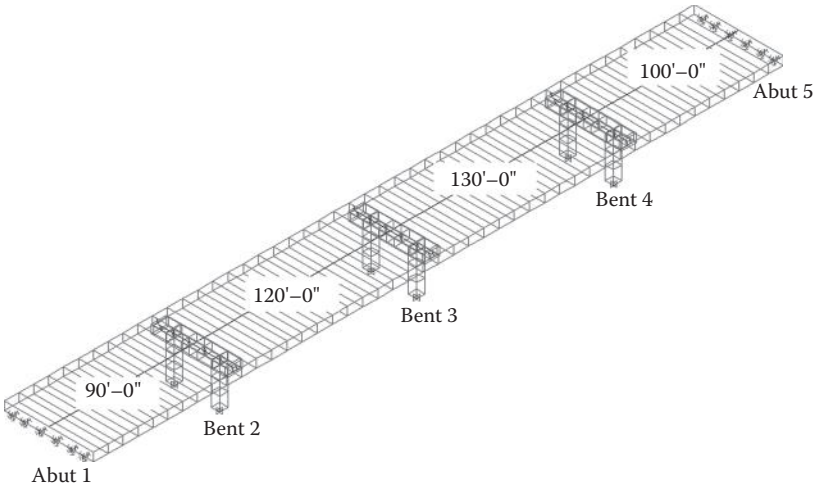

FIGURE 12.22 Bridge layout: four-span two-column bent bridge.

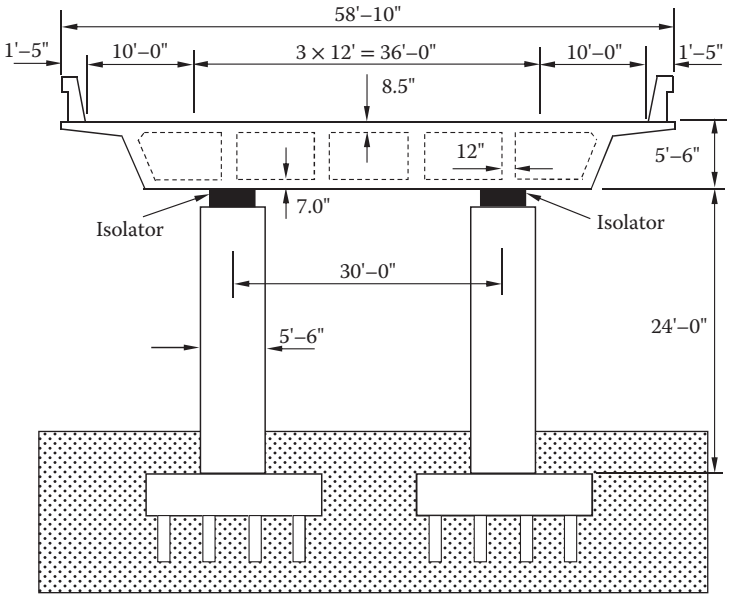

FIGURE 12.23 Typical section: two-column bent.

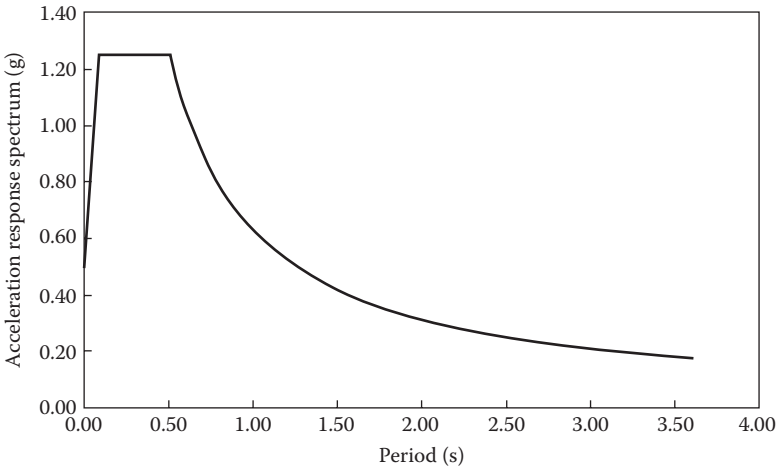

FIGURE 12.24 Acceleration response spectrum.

12.6.3 Design Requirements

Perform the following design calculations in accordance with the Isolation Guide (AASHTO, 2010), the Seismic Guide (AASHTO, 2011), and the AASHTO LRFD (AASHTO, 2012):

- Longitudinal bridge response analysis—simplified method
- Transverse bridge response analysis—simplified method
- Response combination
- Isolator design
- Substructure design

12.6.4 Longitudinal Bridge Response Analysis—Simplified Method

The effective weights on abutments and bents are calculated through the design for Service Limit States and Strength Limit States. The abutment longitudinal stiffness is determined according to Caltrans Seismic Design Criteria (SDC) (Caltrans, 2010). The bent/column longitudinal stiffness is determined by assuming a cantilever deflection. Table 12.4 lists the effective weight and effective stiffness.

Because the required isolator properties are calculated at the design displacement, whereas this displacement is not known at the beginning of an analysis, the iteration process has to be performed. As listed in Table 12.5, the initial system displacement is set as to $d = 10S_{D1} = 6.30$ in, the calculated displacement is $d = 8.00$ in, which has 21.3% difference. Then, as listed in Table 12.6, the second iteration starts at the displacement $d = 8.00$ in, and the updated displacement is $d = 8.96$ in, which has 12% difference. Table 12.7 summarizes the results after six iterations.

12.6.5 Transverse Bridge Response Analysis—Simplified Method

Because the center of mass and the center of stiffness are not coincident with one another, the bridge vibration along transverse direction includes two parts: rotation and translation. The bridge rotation is calculated in Table 12.8. It can be seen that the rotation is very small for this bridge.

The uniform transverse responses can be calculated similar to the longitudinal responses. Table 12.9 listed the effective weight and effective stiffness for transverse analysis. The iteration results are listed in Tables 12.10 and 12.11. Table 12.12 summarizes the results after six iterations.

TABLE 12.4 Effective Weight and Substructure Effective Stiffness—Longitudinal Analysis

Location	Abutment 1	Bent 2	Bent 3	Bent 4	Abutment 5	Sum
Effective weight $W_{\text{eff-j}}$ (kips)	540.0	2140.0	2310.0	2380.0	600.0	7970.0
Substructure stiffness $K_{\text{sub-j}}$ (k/in)	1225.0	438.8	346.6	442.5	1225.0	

TABLE 12.5 Bridge Longitudinal Response Analysis—First Iteration

Location	Abutment 1	Bent 2	Bent 3	Bent 4	Abutment 5	Sum
Initial system displacement d (in)	$d = 10S_{D1}$					**6.30**
System characteristic strength Q_d (kips)	$Q_d = 0.07W$					557.9
System postyield stiffness K_d (k/in)	$K_d = Q_d/d$					88.6
Characteristic strength $Q_{d\text{-}j}$ (kips)	$Q_{d\text{-}j} = Q_d(W_j/W)$					
	37.8	149.8	161.7	166.6	42.0	
Postyield stiffness $K_{d\text{-}j}$ (k/in)	$K_{d\text{-}j} = K_d(W_j/W)$					
	6.0	23.8	25.7	26.4	6.7	
Stiffness coefficient α_j	$\alpha_j = (K_{d\text{-}j}d + Q_{d\text{-}j})/(K_{sub\text{-}j}d - Q_{d\text{-}j})$					
	0.0098	0.11146	0.1600	0.1271	0.0109	
Effective stiffness $K_{eff\text{-}j}$ (k/in)	$K_{eff\text{-}j} = \alpha_j K_{sub\text{-}j}/(1 + \alpha_j)$					
	11.9	45.1	47.8	49.9	13.3	
Isolator displacement $d_{isol\text{-}j}$ (in)	$d_{isol\text{-}j} = d/(1 + \alpha_j)$					
	6.24	5.65	5.43	5.59	6.23	
Isolator stiffness $K_{isol\text{-}j}$ (k/in)	$K_{isol\text{-}j} = Q_{d\text{-}j}/d_{isol\text{-}j} + K_{d\text{-}j}$					
	12.1	50.3	55.4	56.3	13.4	
Substructure displacement $d_{sub\text{-}j}$ (in)	$D_{sub\text{-}j} = d - d_{isol\text{-}j}$					
	0.06	0.65	0.87	0.71	0.07	
Effective period T_{eff} (sec)	$T_{eff} = 0.32([\Sigma(W_{eff\text{-}j})/\Sigma(K_{eff\text{-}j})]^{0.5}$					2.20
Effective damping ξ_{eff}	$\xi_{eff} = 2\Sigma(Q_{d\text{-}j}\, d_{isol\text{-}j})/\pi\Sigma[K_{eff\text{-}j}(d_{isol\text{-}j} + d_{sub\text{-}j})^2]$					0.30
Damping factor B_L	$B_L = (\xi_{eff}/0.05)^{0.3}$ if $\xi_{eff} < 0.3$; $B_L = 1.7$ if $\xi_{eff} > 0.3$					1.70
System displacement d (in)	$d = 9.79S_{D1}T_{eff}/B_L$					**8.00**

TABLE 12.6 Bridge Longitudinal Response Analysis—Second Iteration

Location	Abutment 1	Bent 2	Bent 3	Bent 4	Abutment 5	Sum
Initial system displacement d (in)	$d = 9.79S_{D1}T_{eff}/B_L$					**8.00**
System characteristic strength Q_d (kips)	$Q_d = 0.07W$					557.9
System postyield stiffness K_d (k/in)	$K_d = Q_d/d$					69.8
Characteristic strength $Q_{d\text{-}j}$ (kips)	$Q_{d\text{-}j} = Q_d(W_j/W)$					
	37.8	149.8	161.7	166.6	42.0	
Postyield stiffness $K_{d\text{-}j}$ (k/in)	$K_{d\text{-}j} = K_d(W_j/W)$					
	4.7	18.7	20.2	20.8	5.3	
Stiffness coefficient α_j	$\alpha_j = (K_{d\text{-}j}d + Q_{d\text{-}j})/(K_{sub\text{-}j}d - Q_{d\text{-}j})$					
	0.0077	0.0892	0.1239	0.0988	0.0086	
Effective stiffness $K_{eff\text{-}j}$ (k/in)	$K_{eff\text{-}j} = \alpha_j K_{sub\text{-}j}/(1 + \alpha_j)$					
	9.4	35.9	38.2	39.8	10.5	

(*Continued*)

TABLE 12.6 Bridge Longitudinal Response Analysis—Second Iteration (*Continued*)

Location	Abutment 1	Bent 2	Bent 3	Bent 4	Abutment 5	Sum
Isolator displacement $d_{isol\text{-}j}$ (in)	$d_{isol\text{-}j} = d/(1+\alpha_j)$					
	7.93	7.34	7.11	7.28	7.93	
Isolator stiffness $K_{isol\text{-}j}$ (k/in)	$K_{isol\text{-}j} = Q_{d\text{-}j}/d_{isol\text{-}j} + K_{d\text{-}j}$					
	9.5	39.1	43.0	43.7	10.6	
Substructure displacement $d_{sub\text{-}j}$ (in)	$D_{sub\text{-}j} = d - d_{isol\text{-}j}$					
	0.06	0.65	0.88	0.72	0.07	
Effective period T_{eff} (sec)	$T_{eff} = 0.32([\Sigma(W_{eff\text{-}j})/\Sigma(K_{eff\text{-}j})]^{0.5}$					2.47
Effective damping ξ_{eff}	$\xi_{eff} = 2\Sigma(Q_{d\text{-}j}\, d_{isol\text{-}j})/\pi\Sigma[K_{eff\text{-}j}(d_{isol\text{-}j} + d_{sub\text{-}j})^2]$					0.30
Damping factor B_L	$B_L = (\xi_{eff}/0.05)^{0.3}$ if $\xi_{eff} < 0.3$; $B_L = 1.7$ if $\xi_{eff} > 0.3$					1.70
System displacement d (in)	$d = 9.79 S_{D1} T_{eff}/B_L$					**8.96**

TABLE 12.7 Summary of 6th Iteration Results—Longitudinal Analysis

Iteration No.	1	2	3	4	5	6
Effective period T_{eff} (sec)	2.20	2.47	2.61	2.68	2.71	2.73
Effective damping ξ_{eff}	0.30	0.30	0.30	0.30	0.31	0.31
System displacement d (in)	8.00	8.96	9.46	9.72	9.84	9.90

TABLE 12.8 Transverse Displacement by Rotation

Location	Abutment 1	Bent 2	Bent 3	Bent 4	Abutment 5	Sum
Effective weight $W_{eff\text{-}j}$ (kips)	540.0	2,140.0	2,310.0	2,380.0	600.0	7,970.0
Isolator effective stiffness $K_{isol\text{-}j}$ (k/in)	7.60	29.1	31.0	32.3	8.4	99.98
Distance to abutment 1 $D_{A1\text{-}j}$ (ft)	0.0	90.0	210.0	340.0	440.0	
Transverse stiffness offset KF_j (kips)	$KF_j = K_{eff\text{-}j}\, D_{A1\text{-}j}$					
	0.0	31,434	78,223	131,622	44,413	285,692
Transverse weight offset WF_j (k-ft)	$WF_j = W_{eff\text{-}j}\, D_{A1\text{-}j}$					
	0.0	192,600	485,100	809,200	264,000	1,750,900
Bridge center of rigidity X_{CR} (ft)	$X_{CR} = \Sigma KF_j/\Sigma K_{eff\text{-}j}$					219.65
Bridge center of mass X_{CM} (ft)	$X_{CM} = \Sigma WF_j/\Sigma W_{eff\text{-}j}$					219.69
Rotation resistance J_R (k-ft)	$J_R = \Sigma[(D_{A1\text{-}j} - X_{CM})^2 K_{eff\text{-}j}]$					1,733,182
Rotation angle θ_R	$\theta_R = (\Sigma F_{sub\text{-}j})(X_{CM} - X_{CR})/J_R]$					0.000002
Transverse displacement $d_{R\text{-}j}$ (in)	$d_{R\text{-}j} = \theta_R(D_{A1\text{-}j} - X_{CR})$					
	−0.0007	−0.0004	0.0000	0.0004	0.0007	

TABLE 12.9 Effective Weight and Substructure Effective Stiffness—Transverse Analysis

Location	Abutment 1	Bent 2	Bent 3	Bent 4	Abutment 5	Sum
Effective weight $W_{eff\text{-}j}$ (kips)	540.0	2140.0	2310.0	2380.0	600.0	7970.0
Substructure stiffness $K_{sub\text{-}j}$ (k/in)	219.4	438.8	346.6	442.5	221.3	

TABLE 12.10 Bridge Transverse Response Analysis—First Iteration

Location	Abutment 1	Bent 2	Bent 3	Bent 4	Abutment 5	Sum
Initial system displacement d (in)	$d = 10S_{D1}$					**6.30**
System characteristic strength Q_d (kips)	$Q_d = 0.07W$					557.9
System postyield stiffness K_d (k/in)	$K_d = Q_d$ /d					88.6
Characteristic strength $Q_{d\text{-}j}$ (kips)	$Q_{d\text{-}j} = Q_d(W_j/W)$					
	37.8	149.8	161.7	166.6	42.0	
Postyield stiffness $K_{d\text{-}j}$ (k/in)	$K_{d\text{-}j} = K_d(W_j/W)$					
	6.0	23.8	25.7	26.4	6.7	
Stiffness coefficient α_j	$\alpha_j = (K_{d\text{-}j}d + Q_{d\text{-}j})/(K_{sub\text{-}j}d - Q_{d\text{-}j})$					
	0.0562	0.1146	0.1600	0.1271	0.0621	
Effective stiffness $K_{eff\text{-}j}$ (k/in)	$K_{eff\text{-}j} = \alpha_j K_{sub\text{-}j}/(1 + \alpha_j)$					
	11.7	45.1	47.8	49.9	12.9	
Isolator displacement $d_{isol\text{-}j}$ (in)	$d_{isol\text{-}j} = d/(1 + \alpha_j)$					
	5.96	5.65	5.54	5.59	5.93	
Isolator stiffness $K_{isol\text{-}j}$ (k/in)	$K_{isol\text{-}j} = Q_{d\text{-}j}/d_{isol\text{-}j} + K_{d\text{-}j}$					
	12.3	50.3	55.4	56.3	13.7	
Substructure displacement $d_{sub\text{-}j}$ (in)	$D_{sub\text{-}j} = d - d_{isol\text{-}j}$					
	0.34	0.65	0.87	0.71	0.37	
Effective Period T_{eff} (sec)	$T_{eff} = 0.32([\Sigma(W_{eff\text{-}j})/\Sigma(K_{eff\text{-}j})]^{0.5}$					2.21
Effective damping ξ_{eff}	$\xi_{eff} = 2\Sigma(Q_{d\text{-}j}\, d_{isol\text{-}j})/\pi\Sigma[K_{eff\text{-}j}(d_{isol\text{-}j} + d_{sub\text{-}j})^2]$					0.30
Damping factor B_L	$B_L = (\xi_{eff}/0.05)^{0.3}$ if $\xi_{eff} < 0.3$; $B_L = 1.7$ if $\xi_{eff} > 0.3$					1.70
System displacement d (in)	$d = 9.79S_{D1}T_{eff}/B_L$					**7.96**

TABLE 12.11 Bridge Transverse Response Analysis—Second Iteration

Location	Abutment 1	Bent 2	Bent 3	Bent 4	Abutment 5	Sum
Initial system displacement d (in)	$d = 9.79S_{D1}T_{eff}/B_L$					**7.96**
System characteristic strength Q_d (kips)	$Q_d = 0.07W$					557.9
System postyield stiffness K_d (k/in)	$K_d = Q_d/d$					70.1
Characteristic strength $Q_{d\text{-}j}$ (kips)	$Q_{d\text{-}j} = Q_d(W_j/W)$					
	37.8	149.8	161.7	166.6	42.0	
Postyield stiffness $K_{d\text{-}j}$ (k/in)	$K_{d\text{-}j} = K_d(W_j/W)$					
	4.8	18.8	20.3	20.9	5.3	
Stiffness coefficient α_j	$\alpha_j = (K_{d\text{-}j}d + Q_{d\text{-}j})/(K_{sub\text{-}j}d - Q_{d\text{-}j})$					
	0.0443	0.0897	0.1246	0.0994	0.0489	
Effective stiffness $K_{eff\text{-}j}$ (k/in)	$K_{eff\text{-}j} = \alpha_j K_{sub\text{-}j}/(1 + \alpha_j)$					
	9.3	36.1	38.4	40.0	10.3	
Isolator displacement $d_{isol\text{-}j}$ (in)	$d_{isol\text{-}j} = d/(1 + \alpha_j)$					
	7.62	7.30	7.07	7.24	7.58	
Isolator stiffness $K_{isol\text{-}j}$ (k/in)	$K_{isol\text{-}j} = Q_{d\text{-}j}/d_{isol\text{-}j} + K_{d\text{-}j}$					
	9.7	39.3	43.2	44.0	10.8	
Substructure displacement $d_{sub\text{-}j}$ (in)	$D_{sub\text{-}j} = d - d_{isol\text{-}j}$					
	0.34	0.65	0.88	0.72	0.37	
Effective period T_{eff} (sec)	$T_{eff} = 0.32([\Sigma(W_{eff\text{-}j})/\Sigma(K_{eff\text{-}j})]^{0.5}$					2.47
Effective damping ξ_{eff}	$\xi_{eff} = 2\Sigma(Q_{d\text{-}j}\, d_{isol\text{-}j})/\pi\Sigma[K_{eff\text{-}j}(d_{isol\text{-}j} + d_{sub\text{-}j})^2]$					0.30
Damping factor B_L	$B_L = (\xi_{eff}/0.05)^{0.3}$ if $\xi_{eff} < 0.3$; $B_L = 1.7$ if $\xi_{eff} > 0.3$					1.7
System displacement d (in)	$d = 9.79S_{D1}T_{eff}/B_L$					**8.95**

TABLE 12.12 Summary of 6th Iteration Results—Transverse Analysis

Iteration No.	1	2	3	4	5	6
Effective period T_{eff} (sec)	2.21	2.47	2.61	2.68	2.72	2.73
Effective damping ξ_{eff}	0.30	0.30	0.31	0.31	0.31	0.31
System displacement d (in)	7.96	8.95	9.47	9.73	9.86	9.92

TABLE 12.13 Response Combination—Isolator Design Displacement

Load Cases	Combination Rule	Abutment 1	Bent 2	Bent 3	Bent 4	Abutment 5
Longitudinal EQ input (in)	Long. displacement u_L	9.89	9.29	9.06	9.23	9.88
	Trans. displacement v_L	0.00	0.00	0.00	0.00	0.00
Transverse EQ input (in)	Long. displacement u_T	0.00	0.00	0.00	0.00	0.00
	Trans. displacement v_T	9.63	9.31	9.08	9.25	9.60
Load case 1 (in)	$u_1 = u_L + 0.3u_T$	9.89	9.29	9.06	9.23	9.88
	$v_1 = v_L + 0.3v_T$	2.89	2.79	2.72	2.77	2.88
	$R_1 = (u_1^2 + v_1^2)^{0.5}$	10.30	9.70	9.46	9.63	10.29
Load case 2 (in)	$u_2 = 0.3u_L + u_T$	2.97	2.79	2.72	2.77	2.97
	$v_2 = 0.3v_L + v_T$	9.63	9.31	9.08	9.25	9.60
	$R_2 = (u_2^2 + v_2^2)^{0.5}$	10.08	9.72	9.48	9.65	10.05
Isolator design Displacement d_t(in)	$d_t = \text{Max}(R_1 + R_2)$	**10.30**	**9.72**	**9.48**	**9.65**	**10.29**

12.6.6 Response Combinations

According to the combination rule specified in the Guide Specifications (AASHTO, 2011), the displacement combinations are listed in Table 12.13, and the shear force combinations are listed in Table 12.14.

12.6.7 Isolation Bearing Design

The design of Spherical Friction Bearing is presented as an example. This type of bearing has an articulated slider to permit rotation and a spherical sliding interface. The required design parameters are listed in Table 12.15, in which $Q_{d\text{-}j}$ and $K_{d\text{-}j}$ are the maximum values of the final longitudinal and transverse iteration.

Based on the design requirements listed above, the size of bearing is determined in Table 12.16. It can be seen that the required overall diameter of isolator is approximately 4.6 ft at Bents and 3.8 ft at Abutments. Because the column diameter is 5.5 ft, the required isolator of diameter 4.6 ft can be installed at the top of columns without a problem. For abutment seat, a 4.0 ft seat width should be enough to install the isolators on the top of seat.

12.6.8 Substructure Design

For an isolated bridge, the substructure including columns and footings should remain essentially elastic during the design earthquake event. The design force demand is the maximum force allowed to be transferred by the isolator. Table 12.17 lists the design of column main reinforcement and shear reinforcement. It is seen that the minimum 1% steel ratio for column main reinforcement is satisfied.

For footing design, the column elastic moment, and shear are transferred to the bottom of footing. Then the axial deal loads including footing and cover soil weight are added to the moment and shear actions. The pile tension and compression loads can be determined by balancing all axial, moment and shear actions. For all three bents, the required column footing size is 16' × 16' × 4', and the required total of 70 ton piles are 16.

TABLE 12.14 Response Combination—Substructure Design Shear Force

Load Cases	Combination Rule	Abutment 1	Bent 2	Bent 3	Bent 4	Abutment 5
Longitudinal EQ input (kips)	Long. force U_L	37.68	144.83	154.46	160.53	41.86
	Trans. force V_L	0.00	0.00	0.00	0.00	0.00
Transverse EQ input (kips)	Long. force U_T	0.00	0.00	0.00	0.00	0.00
	Trans. force V_T	37.16	144.84	154.47	160.54	41.22
Load case 1 (kips)	$U_1 = U_L + 0.3U_T$	37.68	144.83	154.46	160.53	41.86
	$V_1 = V_L + 0.3V_T$	11.15	43.45	46.34	48.16	12.36
	$R_1 = (U_1^2 + V_1^2)^{0.5}$	39.30	151.21	161.26	167.60	43.64
Load case 2 (kips)	$U_2 = 0.3U_L + U_T$	11.30	43.45	46.34	48.16	12.56
	$V_2 = 0.3V_L + V_T$	37.16	144.84	154.47	160.54	41.22
	$R_2 = (U_2^2 + V_2^2)^{0.5}$	38.84	151.22	161.27	167.61	43.09
Substructure design Force F_t (kips)	$F_t = \text{Max}(R_1 + R_2)$	**39.30**	**151.22**	**161.27**	**167.61**	**43.64**

TABLE 12.15 Bearing Design Parameters

Design Parameters	Calculation	Abutment 1	Bent 2	Bent 3	Bent 4	Abutment 5
Characteristic strength Q_d (2 bearings per bent) (kips)	$Q_d = Q_{d\text{-}j}/2$	18.90	74.90	80.85	83.30	21.00
Minimum postyield stiffness K_d (2 bearings per bent) (k/in)	$K_d = K_{d\text{-}j}/2$	1.90	7.51	8.11	8.35	2.11
Design displacement d_t (in)	d_t (see above)	10.30	9.72	9.48	9.65	10.29
Design dead load P_{DL} (kips)	P_{DL} (DL analysis)	270	1070	1155	1190	300
Design live load P_{LL} (kips)	P_{LL} (LL analysis)	181	717	774	797	201

TABLE 12.16 Design Isolation Bearing

Location	Abutment 1	Bent 2	Bent 3	Bent 4	Abutment 5
Required radius of curvature R (in)	$R = P_{DL}/K_d$				
	142.47	142.47	142.47	142.47	142.47
Required coefficient of friction μ	$\mu = Q_d/P_{DL}$				
	0.07	0.07	0.07	0.07	0.07
Select 15GF teflon as sliding surface (μ = 0.1008) Allowable bearing pressure σ_c (psi)	3000	3000	3000	3000	3000
Required contact area A_c (in^2)	$A_c = P_{DL}/\sigma_c$				
	90.00	356.67	385.00	396.67	100.00
Required disk diameter d_d (in)	$d_d = (4A_c/\pi)^{0.5}$				
	10.70	21.31	22.14	22.47	11.28
Required isolator diameter L_{chord} (in)	$L_{chord} = 2(1.5d_t + d_d/2)$				
	41.62	50.47	50.58	51.43	42.17
Required overall isolator width B (ft)	$B = L_{chord} + 2s$ (s = 2.0")				
	3.80	4.54	4.55	4.62	3.85
Required rise of concave surface h (in)	$h = (L_{chord})^2/8R$				
	1.52	2.24	2.24	2.32	1.56
Required throat thickness t (in)	$t = 0.5\{[4(P_{DL} + P_{LL})/(\pi\sigma_b)]^{0.5}\text{-}d_d\}$) assume $\sigma_b = \sigma_c$				
	1.56	3.11	3.24	3.28	1.65
Required isolator height H (in)	$H = h + t + 3"$				
	6.08	8.35	8.48	8.61	6.21

TABLE 12.17 Column Design

Design Parameters	Calculation	Bent 2	Bent 3	Bent 4
Design force at top of column V_D (kips)	$V_D = F_t$	151.22	161.27	167.61
Design moment at bottom of column M_D (k-ft)	$M_D = V_D H_c$	3692	4193	4023
Main reinforce: assume 1% steel ratio A_{s0} (in^2)	$A_{s0} = 0.01(\pi d_c^2/4)$	34.21	34.21	34.21
Design main reinforce: #10 total 28, A_s (in^2)	$A_s = 28 \times 1.27$	35.56	35.56	35.56
Nominal moment capacity M_C (k-ft)	M_C by P-M Analysis	6430	6554	6606
Moment demand/capacity ratio R_M	$R_M = M_D/M_C$	0.56	0.64	0.61
Design shear reinforce: #6@6, A_v (in^2/ft)	$A_v = 0.44 \times 12/6$	0.88	0.88	0.88
Column shear capacity V_C (kips)	V_C By SDC 3.6	921	921	921
Shear demand/capacity ratio R_V	$R_V = V_D/V_C$	0.16	0.18	0.18

12.7 Procurement for Construction

The procurement process begins with the designer's selection of an isolation bearing. There are three isolation bearings currently available: (1) EradiQuake, (2) Lead Rubber, and (3) Friction Pendulum. Having made the decision to use an isolation strategy for a bridge the designer, with or without the assistance of a bearing manufacturer, must conduct a dynamic analysis to determine the required displacement capacity, effective period and damping for the given hazard and performance requirement. Having the seismic demands and service load requirements, the designer can proceed with the isolation design by selecting the most appropriate isolation bearing to be used. Having selected the bearings, the designer can proceed with the design with or without the assistance of the bearing manufacturer(s) to develop the seismic requirements to be included in the contract drawings. These will include the required bearing load capacities, displacement capacities, maximum and minimum effective stiffness, and maximum effective damping at the design displacement.

At this point, the designer should decide the method of procurement to use. There are two possible alternatives for the final selection of the seismic bearing. The selection can be made by either owner/designer or the contractor as shown in the flow chart (Figure 12.25).

Following the owner/designer selection, the designer can go sole source with the bearings specified on the contract drawings. This approach has been used on several projects in States of Alaska, California, Washington, and Tennessee. In this case, the owner may select to furnish the bearings or to have the contractor furnish the bearings. The advantage of this path is that the bearing can be prototype tested early in the design process to verify that the bearing corresponded with the design.

In the owner/designer selection process, another approach, "competitive early source selection" has been used successfully to allow all the bearing manufacturers to compete in early stages of the design process. Bridge bearings are key components in a bridge for service load conditions and especially for seismic loads and should be selected in the early stages of the design process. This process has been used successfully in California for several years and more recently in the State of Washington.

The competitive early source process begins with an invitation to selected qualified manufacturers of seismic isolation bearings to responds to request to supply bearing for a given bridge project. The request should include a bridge description and/or a general plan, the seismic hazard, the required performance, the required prototype and quality control testing and a schedule for prototype testing and production of completed bearings. The objectives of seismic isolation system and the basis for the evaluation and selection should also be described.

Then the manufacturer's response should include a description of their proposed design solution using their isolation bearings and provide a guaranteed price for each of the bearings used in their solution. A description of their testing protocol and equipment should also be in their response.

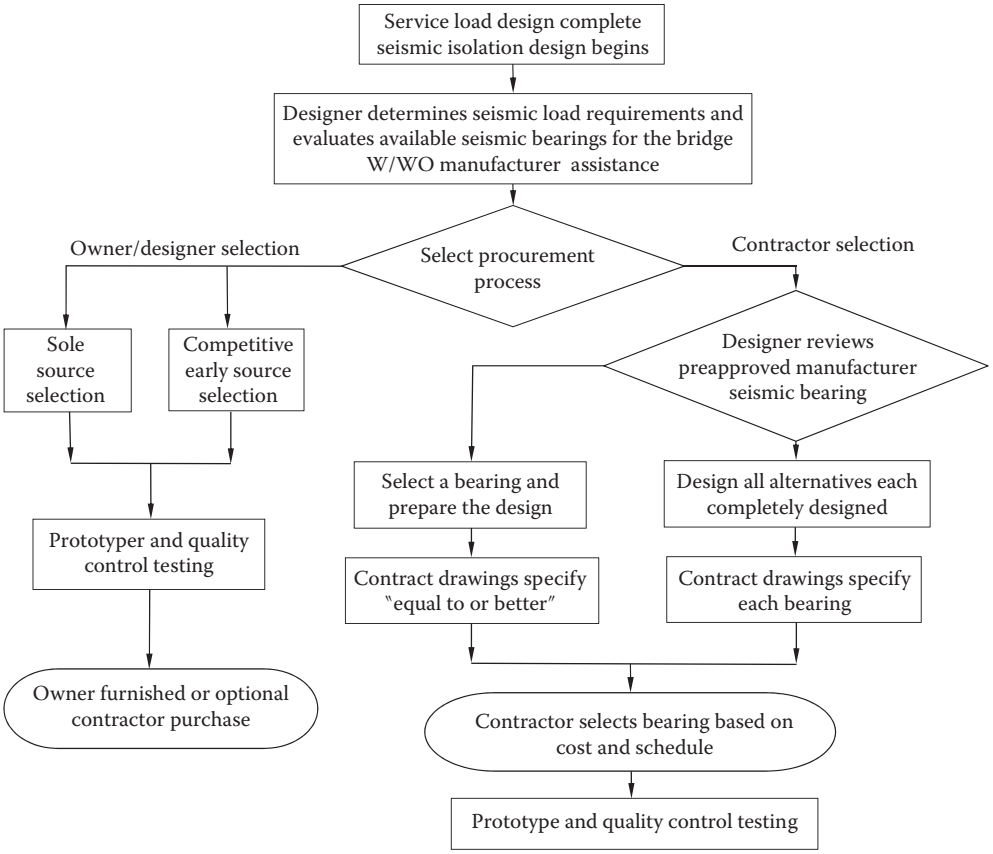

FIGURE 12.25 Bearing procurement process.

The evaluation of the manufacturer's response conducted by the owner/designer should include the manufacturer's demonstration of their technical ability to meet the requirements of the project, the seismic performance of the bridge, the testing and production schedules and the bearing unit costs. As shown in Figure 12.25, the "competitive early source selection" also has the advantage of having tests conducted early in the design process.

The benefits to the owner/designer selection include

- Bearing properties are known early in the design process
- Teaming with the manufacturer to incorporate their experience and knowledge early in the design process
- Selection is made by the designer

Following the contractor selection, the designer may proceed with the preapproved manufacturers bearings (see Figure 12.25). The designer can select one from possible alternatives and proceed with the design. The election will be based on load capacity, displacement capacity, thermal requirements, and clearance requirements. This selected bearing is shown in the contract documents with a clause that other isolation bearing will be consider with "equal to or better" properties. Instead of choosing to include a single example bearing, the designer may design all preapproved bearings or simply specify the design requirements along with designation for each of bearing of in the contract documents. Final selection of isolation bearing will be made by the contactor based on the least cost. However, the designer must specify the prototype and production-bearing test program and tolerance required for the bearings during the tests.

The disadvantage of allowing contractor select bearing type is that the manufacturer must perform the prototype testing after the design is completed. If the contractor selected bearing does not pass the prototype testing this could cause in a delay in the project schedule.

12.8 Summary

The acceptance of seismic isolation for design of new bridges and retrofit of existing bridges has increased significantly during last two decades. An attempt has been made to introduce basic concepts of seismic isolation, state-of-the-art and state-of-the-practice in bridge application, design methods, testing and evaluation, and procurement considerations. A design example is given to illustrate how seismic isolation is used on a four-span continuous cast-in-place prestressed box girder bridge. Because seismic isolation technologies and advances are being made constantly, engineers are encouraged to consider realistic prototype testing results being made available to the design community on seismic isolation for various bridge projects, and significant improvement in code developments.

References

AASHTO. 1991. *Guide Specifications for Seismic Isolation Design*, American Association of State Highway and Transportation Officials, Washington, DC.

AASHTO. 1999. *Guide Specifications for Seismic Isolation Design* (Second Edition), American Association of State Highway and Transportation Officials, Washington, DC.

AASHTO. 2010. *Guide Specifications for Seismic Isolation Design* (Third Edition), American Association of State Highway and Transportation Officials, Washington, DC.

AASHTO. 2011. *Guide Specifications for LRFD Seismic Bridge Design* (2nd Edition), American Association of State Highway and Transportation Officials, Washington, DC.

AASHTO. 2012. *AASHTO LRFD Bridge Design Specifications* (Customary U.S. Units), American Association of State Highway and Transportation Officials, Washington, DC.

Buckle, I, Al-Ani, M., and Monzon, E. 2012. *AASHTO Subcommittee On Bridges and Structures,* Agenda Item T3—Attachment A— Appendix B, Design Examples, July 8th–12th, Austin, TX.

Caltrans. 2010. *Seismic Design Criteria*, *Version 1.6.* California Department of Transportation, Sacramento, CA.

Constantinou, M. C., Soong T. T., and Dargush G. F. 1998. *Passive Energy Dissipation Systems for Structural Design and Retrofit*. Mongraph Series, MCEER, University at Buffalo, State University of New York, Buffalo, NY.

Ghasemi, H. 1999. Seismic Protection of Bridges. *Public Roads*, U.S. Department of Transportation, Federal Highway Administration, Washington, DC, Vol. 62(5).

HITEC. 1996. *Guidelines for the Testing of Seismic Isolation and Energy Dissipating Devices*. *CERF Report HITEC 96-02*, Highway Innovative Technology Evaluation Center, Washington, DC.

HITEC. 2002. *Guidelines for the Testing of Large Seismic Isolator and Energy Dissipation Devices*. *CERF Report HITEC 40600*, Highway Innovative Technology Evaluation Center, Washington, DC.

Imbsen, R. 2001. Use of Isolation for Seismic Retrofitting Bridges. *J. Bridge Eng.*, New York City Bridge Conference, 6(Special Issue), 425–438.

USDOT. 2002. *Effects of Catastrophic Events on Transportation System Management and Operations,* Northridge Earthquake—January 17, 1994, U.S. Department of Transportation, Washington, DC.

13

Seismic Retrofit Technology

Kevin I. Keady
California Department of Transportation

Fadel Alameddine

Thomas E. Sardo
California Department of Transportation
Parsons Group

13.1 Introduction

The primary philosophy and performance criteria for retrofitting bridges are to prevent the structure from reaching the collapse limit state for the design earthquake. Upon completion of the seismic analysis and the vulnerability study for existing bridges, the engineer must develop a retrofit strategy to achieve the required design criteria. Depending on the importance of structures, there are two levels of retrofit. For ordinary structures, a lower level of retrofit may be implemented. The purpose of this level of retrofit is to prevent collapse. With this level of retrofit, repairable damage is generally expected after a moderate earthquake. Following a major earthquake, significant damage is expected, and replacement of structures may be necessary. For important structures, a higher level of retrofit could be required at a considerably higher cost. The purpose of this level of retrofit is not only to prevent collapse but also to provide serviceability after a major earthquake.

There are two basic retrofit philosophies for a concrete girder bridge. The first is to force plastic hinging into the columns and keep the superstructure elastic. This is desirable because columns can be more easily inspected, retrofitted, and repaired than in superstructures. The second is to allow plastic hinging in the superstructure provided that ductility levels are relatively low and the vertical shear load carrying capacity is maintained across the hinge. This is desirable when preventing hinging in the superstructure is either prohibitively expensive or not possible. In other words, this strategy is permissible provided that the hinge in the superstructure does not lead to collapse. To be conservative, the contribution of concrete should be ignored and the steel stirrups need to be sufficient to carry one and a half times the dead load shear reaction if hinging is allowed in the superstructure.

There are two basic retrofit philosophies for steel girder bridges. The first is to let the end cross frames and/or bearings fail and take retrofit measures to ensure that the spans do not drop off their seats and

collapse. In this scenario, the end cross frames and/or bearings act as a "fuse" by failing at a relatively small seismic force and thus protecting the substructure from being subjected to any potential larger seismic force. This may be the preferred strategy if the fusing force is low enough such that the substructure can survive with little or no retrofit. The second philosophy is to make sure that the end cross frames and/or bearings do not fail. This implies that the end cross frames and/or bearings transfer the full seismic force to the substructure and retrofitting of the substructure may be required. The substructure retrofit includes the bent caps, columns or pier walls, and foundations. In both philosophies, a superstructure retrofit is generally required, although the extent is typically greater with the fixed bearing scheme.

The purpose of this chapter is to briefly discuss potential vulnerabilities to girder bridge components and suggest practical retrofit solutions and details. For each bridge component, the potential vulnerabilities are introduced and retrofit concepts are presented along with specific design considerations. Chapter 2 provides an extensive discussion about earthquake damage to bridges. Chapter 14 discusses the retrofit strategy for several important bridges. For a more detailed seismic bridge retrofit, references are made to Caltrans MTD 20-4 (Caltrans 2010a) and FHWA-HRT-06-32 (FHWA 2006).

13.2 Analysis Techniques for Bridge Retrofit

For ordinary bridges, a dynamic modal response spectrum analysis is usually performed under the design earthquake. The modal responses are combined using the complete quadratic combination (CQC) method. The resulting orthogonal responses are then combined using the "30 Percent Rule." Two cases are considered when combining orthogonal seismic forces. Case 1 is the sum of forces due to transverse loading plus 30% of forces due to longitudinal loading. Case 2 is the sum of forces due to longitudinal loading plus 30% of forces due to transverse loading.

A proper analysis should consider abutment springs and truss-like restrainer elements. The soil foundation structure interaction should be considered when deemed important. Effective properties of all members should be used. Typically, two dynamic models are utilized to bind the assumed nonlinear response of the bridge: a "tension model" and a "compression model." As the bridge opens up at its joints, it pulls on the restrainers. In contrast, as the bridge closes up at its joints and its superstructure elements go into compression.

For more important bridges, a nonlinear time history analysis is often required. This analysis can be of uniform support excitation or of multiple support excitation, depending on the length of the bridge and the variability of the subsurface condition.

The design earthquake loading depends on the type of evaluation that is considered for the subject bridge. Table 13.1 shows the seismic performance criteria for the design and evaluation of bridges developed by the California Department of Transportation (2010b). The Safety Evaluation response spectrum is obtained using

1. Deterministic ground motion assessment using maximum credible earthquake
2. Probabilistically assessed ground motion with a long return period

TABLE 13.1 Seismic Performance Criteria

Ground Motion at Site	Minimum Performance Level	Important Bridge Performance Level
Functional Evaluation	Immediate service level repairable damage	Immediate service level minimal damage
Safety Evaluation	Limited service level significant damage	Limited service level repairable damage

TABLE 13.2 Strain Limits

	Significant Damage	Repairable Damage	Minimal Damage
Concrete strain limit ε_c	ε_{cu}	$2/3(\varepsilon_{cu})$	the greater of $1/3(\varepsilon_{cu})$ or 0.004
Grade 430 bar #29 to #57 Steel strain limit ε_s	0.09	0.06	0.03
Grade 280 bar #29 to #57 Steel strain limit ε_s	0.12	0.08	0.03
Grade 430 bar #10 to #25 Steel strain limit ε_s	0.12	0.08	0.03
Grade 280 bar #10 to #25 Steel strain limit ε_s	0.16	0.10	0.03
Structural Steel	ε_{sh}	Larger of 0.008 and $2/3(\varepsilon_{sh})$	Lager of 0.003 and $1.5\varepsilon_y$

The functional evaluation response spectrum is derived using probabilistically assessed ground motions that have a 60% probability of not being exceeded during the useful life of the bridge. A separate functional evaluation is usually required only for important bridges.

With the above-prescribed input earthquake loading and using an elastic dynamic multimodal response spectrum analysis, the displacement demand can be computed. The displacement capacity of various bents may then be calculated using two-dimensional or three-dimensional nonlinear static pushover analysis with strain limits associated with expected damage at plastic hinge locations (Chapters 5 and 6). When performing a pushover analysis for a concrete bridge, a concrete stress–strain model that considers effects of transverse confinement such as Mander's model and a steel stress–strain curve are used for considering material nonlinearity (Mander, Priestley, and Park 1988). Limiting the concrete compressive strain to a magnitude smaller than the confined concrete ultimate compressive strain and the steel strain to a magnitude smaller than steel rupture strain results in lesser curvature of the cross section under consideration. Smaller curvatures are usually associated with smaller cracks in the plastic hinge region.

Table 13.2 shows the general guidelines on strain limits that can be considered for a target level of damage in a plastic hinge zone. These limits are applied for the ultimate concrete strain ε_{cu} and the ultimate strain in the reinforcing steel $\varepsilon_{su.}$ The ultimate concrete strain can be computed using a concrete confinement model such as Mander's model. For a poorly confined concrete section, the difference between minimal damage and significant damage becomes insignificant. With displacement demands and displacement capacities estimated, the demand-to-capacity (*D*/*C*) ratios can be computed showing adequacy or inadequacy of the subject bridge. The *D*/C ratios for shear, seat width, and piles should also be checked. The initial modeling assumptions, such as abutment stiffness, and so on used in the diagnostic model are then verified. If necessary, the model is rerun with revised assumptions, and then checked again. This process is repeated until results converge with the assumed modeling parameters. The *D*/*C* ratios provide the basis for the development of the bridge retrofit strategy. Figure 13.1 shows a typical procedure to develop the retrofit strategy (FHWA 2006).

13.3 Superstructure Retrofits

Superstructures can be categorized into two different categories: concrete and steel. After the 1971 San Fernando, California Earthquake, the primary failure leading to bridge collapse was identified as unseating of superstructures at the expansion joints and abutments, a problem shared by both types of superstructures. Other potential problems that may exist with steel superstructures is weak cross bracing and/or diaphragms. Concrete bridge superstructures have the potential to form plastic hinges during a longitudinal seismic response, which is largely dependent upon the amount of reinforcement used and the way it is detailed.

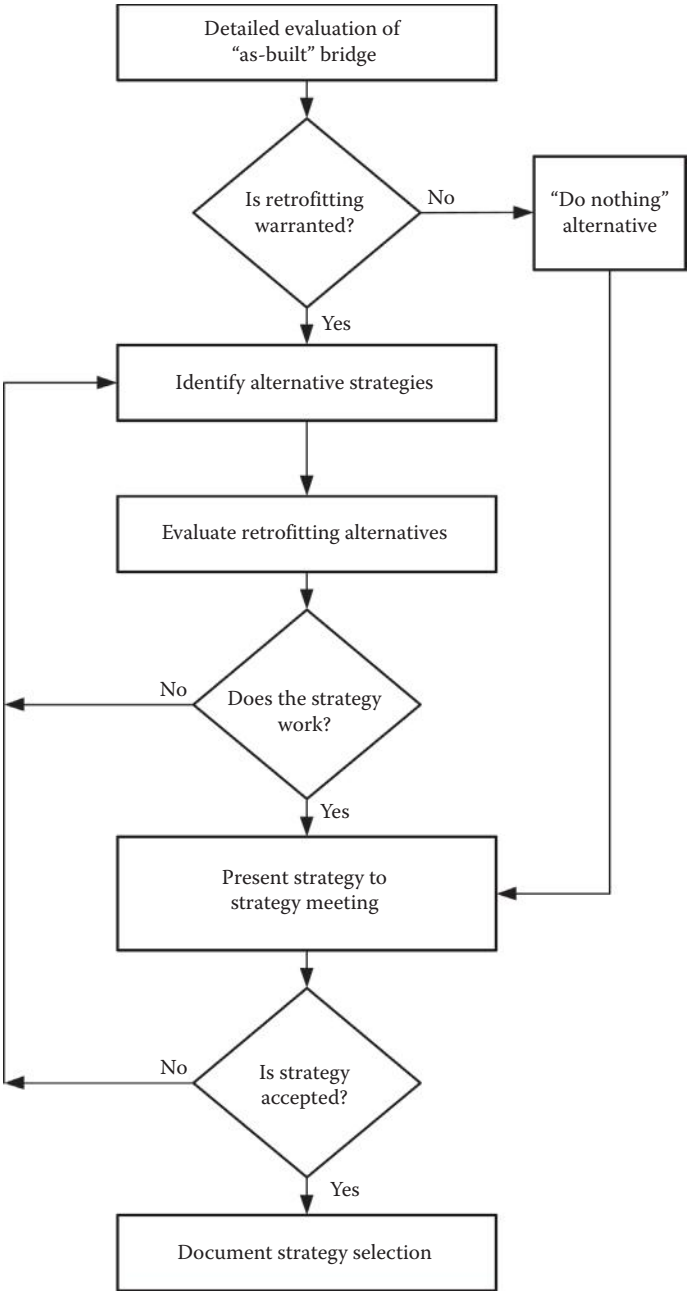

FIGURE 13.1 Retrofit strategy development flowchart.

13.3.1 Expansion Joints and Hinges

During an earthquake, adjacent bridge frames will often vibrate out of phase, causing two types of displacement problems. The first type is a localized damage caused by the frames pounding together at the hinges. Generally, this localized damage will not cause bridge collapse and is therefore not a major concern. The second type occurs when the hinge joint separates, possibly allowing the adjacent spans to

become unseated if the movement is too large. Suspended spans (i.e., two hinges within one span) are especially vulnerable to becoming unseated (Figure 13.2).

13.3.1.1 Simply Supported Girders

The most common problem for simply supported structures is girders falling off their seats due to a longitudinal response (Chapter 2). If the seismic force on the structure is large enough to fail the bearings, then the superstructure becomes vulnerable to unseating at the supports.

There are several ways of retrofitting simply supported steel girders and/or precast concrete girders. The most common and traditional way is to use cable restrainers, since the theory is fundamentally the same for both types of girders. For more about cable restrainers, refer to Section 13.3.1.3. Care should be taken when designing the cables to intrude as little as possible on the vertical clearance between the girders and the roadway. The cable retrofit solution for simply supported girders can be combined with a cap seat extension if expected longitudinal displacements are larger than the available seat width.

Another possible solution for steel girders is to make the girders continuous over the bents by tying the webs together with splice plates (Figure 13.3). The splice plate should be designed to support factored dead load shears assuming the girder becomes unseated. The splice plate is bolted to the girder webs and has slotted or oversized holes to allow for temperature movement. This retrofit solution usually works for most regular and straight structures, but not for most irregular structures. Any situation where the opposing girders do not line up will not work. For example, bridges that vary in width or are bifurcated may have different numbers of girders on opposite sides of the hinge. Bridges that are curved may have the girders at the same location but are kinked with respect to each other. In addition, many structures may have physical restrictions such as utilities, bracing, diaphragms, stiffeners, and so on, which need to be relocated in order for this strategy to work.

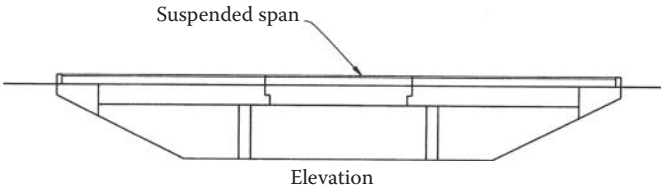

FIGURE 13.2 Suspended span.

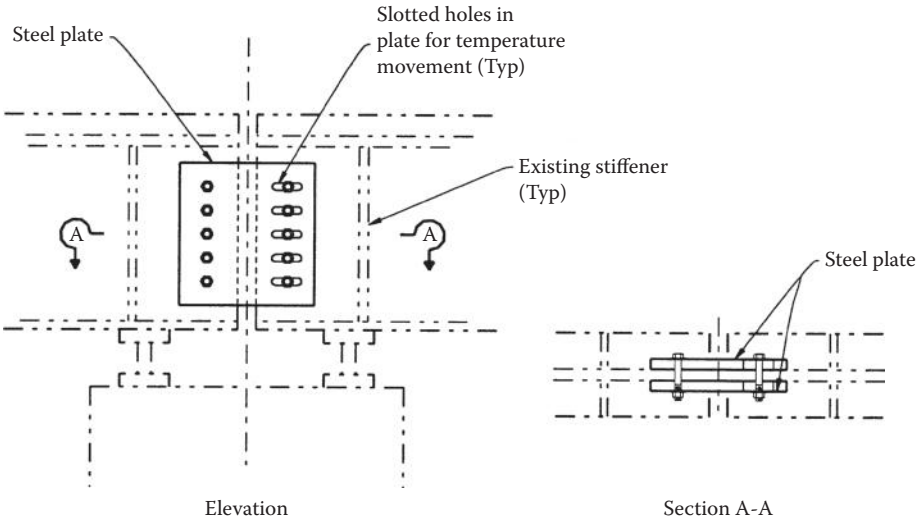

FIGURE 13.3 Steel girder hinge plate retrofit.

13.3.1.2 Continuous Girders with In-Span Hinges

For continuous steel girders, the hinges are typically placed near the point of zero moment that is roughly at 20% of the span length. These hinges can be either seat type as shown in Figure 13.4 or hanger type as shown in Figure 13.5. The hanger-type hinges are usually designed for vertical dead and live loads. These loads are typically larger than forces that can be imparted onto the hanger bar from a longitudinal earthquake event, and thus retrofitting the hanger bar is generally unnecessary. Hanger-type hinges typically have more seismic resistance than seat-type hinges but may still be subjected to seismic damage. Hanger bars are tension members that are vulnerable to differential transverse displacement on either side of the hinge. The differential displacement between the girders causes the hanger bars to go into bending plus tension. These hinges often have steel bars or angles that bear against the opposite web, or lugs attached to the flanges, which are designed to keep the girders aligned transversely for wind forces. These devices are usually structurally inadequate and are too short to be effective with even moderate seismic shaking. Consideration should be given to replacing them or adding supplemental transverse restrainers (Caltrans 2010a). Cross bracing or diaphragms on both sides of the hinge may have to be improved in conjunction with the transverse restrainer.

It can generally be assumed that any seat-type hinge used with steel girders will need additional transverse, longitudinal, and vertical restraint in even moderately severe seismic areas (Caltrans 2010a).

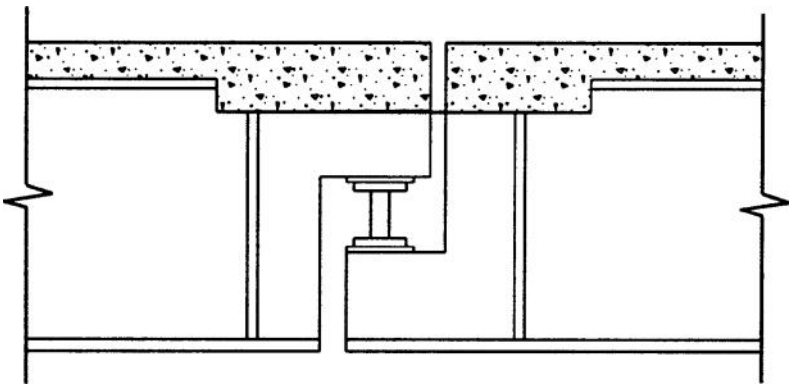

FIGURE 13.4 Seat type hinge.

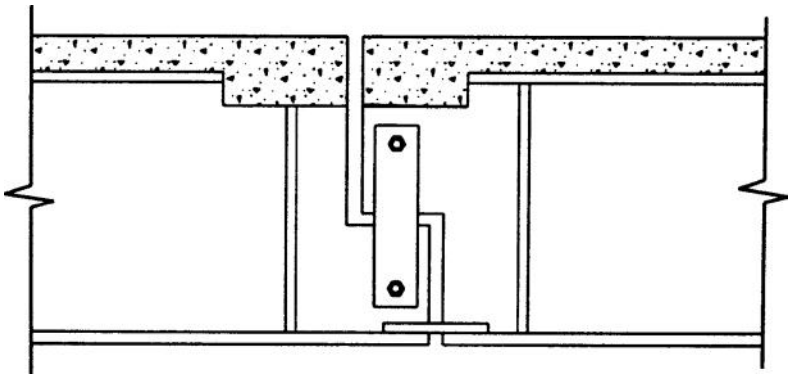

FIGURE 13.5 Hanger type hinge.

Continuous concrete box girders typically have in-span-type hinges. These hinge seats are typically 6 to 8 in. (150 to 200 mm), while some are even less on many of the older bridges. Because of the localized damage that occurs at hinges (i.e., spalling of the concrete, etc.), the actual length of hinge seat available is much less than the original design. Therefore, a means of providing a larger hinge seat and/or tying the frames together is necessary.

13.3.1.3 Restrainers

Restrainers are used to tie the longitudinal frames together, limiting the relative displacements from frame to frame and to provide a load path across the joint. The main purpose is to prevent the frames from falling off their supports. There are two basic types of restrainers: cables and rods. The choice between cables and rods is rather arbitrary, but some factors to consider may be structure period, flexibility, strength of hinge/bent diaphragm, tensile capacity of the superstructure, and, to some degree, the geometry of the superstructure. Hinge restrainers can be designed in accordance with Caltrans Bridge Design Aid 14-1 (Caltrans 2008).

There are various types of longitudinal cable-restraining devices as shown in Figures 13.6 to 13.8. Cable-restraining units, such as the ones shown in Figures 13.6 and 13.7, generally have an advantage over high-strength rods because of the flexibility with its usage for varying types of superstructures. For simply supported girders, cables may be anchored to a bracket mounted to the underside of the girder flange and wrapped around the bent cap and again anchored as shown in Figure 13.9. This is the preferred method. Another possibility is to have the cables anchored to a bracket mounted to the bottom flange and simply attached to an opposing bracket on the other side of the hinge, as shown in Figure 13.10. The latter example is generally used for shorter bridges with a larger seat area at the bent

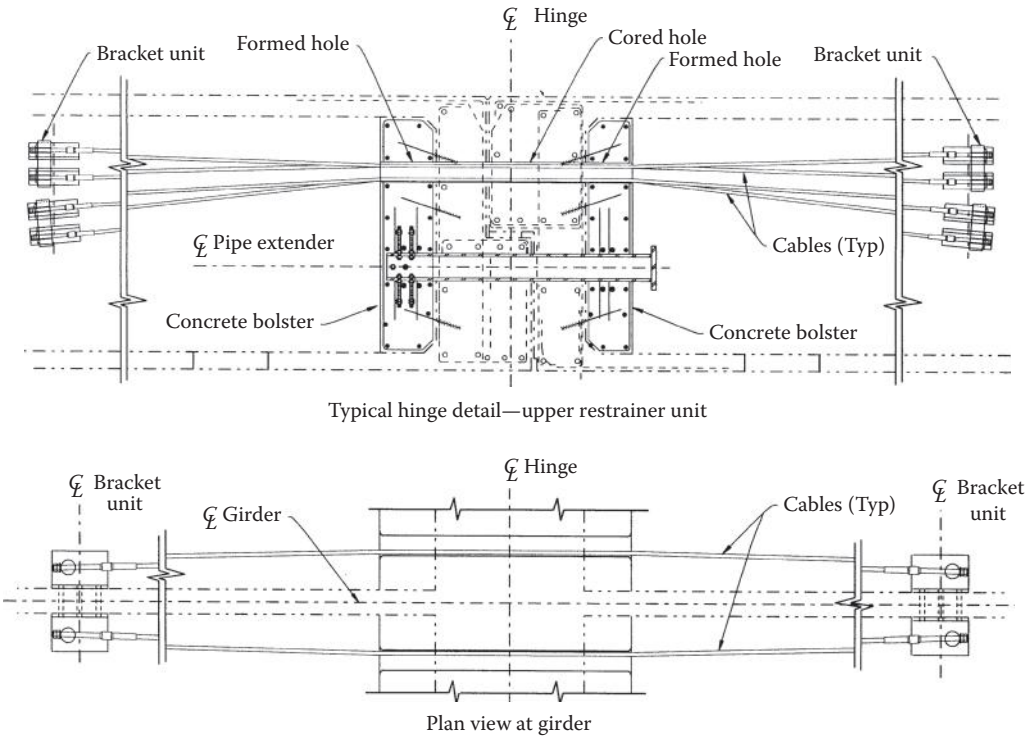

FIGURE 13.6 Type 1 hinge restrainer.

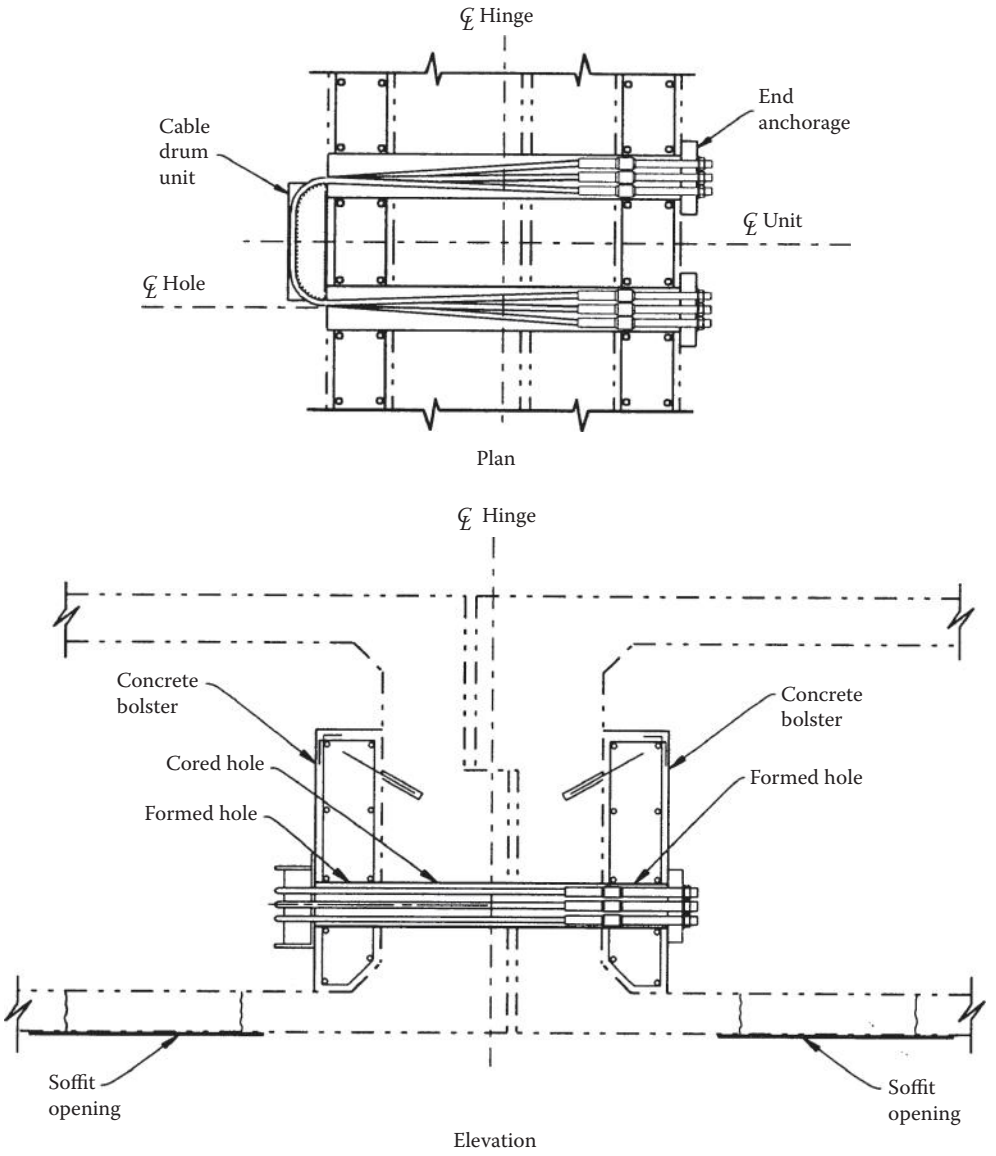

FIGURE 13.7 C-1 hinge restrainer.

cap or in situations where vertical clearances may be limited. Moreover, cables have the advantage of using a variety of lengths, since the anchorage devices can be mounted anywhere along the girders, whether it be steel or concrete, in addition to being anchored to the nearest bent cap or opposite side of the hinge diaphragm. For example, if the restrainer is relatively short, this may shorten the period, possibly increasing the demand to the adjacent bridge frames. Therefore, for this example, it may be desirable to lengthen the restrainer, keeping the force levels to within the capacities of the adjacent segments (Caltrans 2008). On the other hand, if the restrainer is too long, unseating can occur, and an additional means of extending the seat length becomes necessary.

High-strength rods are another option for restricting the longitudinal displacements and can be used with short seats without the need for seat extenders. Unlike cables, where high-strength rods are used, shear keys or pipes are generally used in conjunction since rods can be sheared with transverse movements

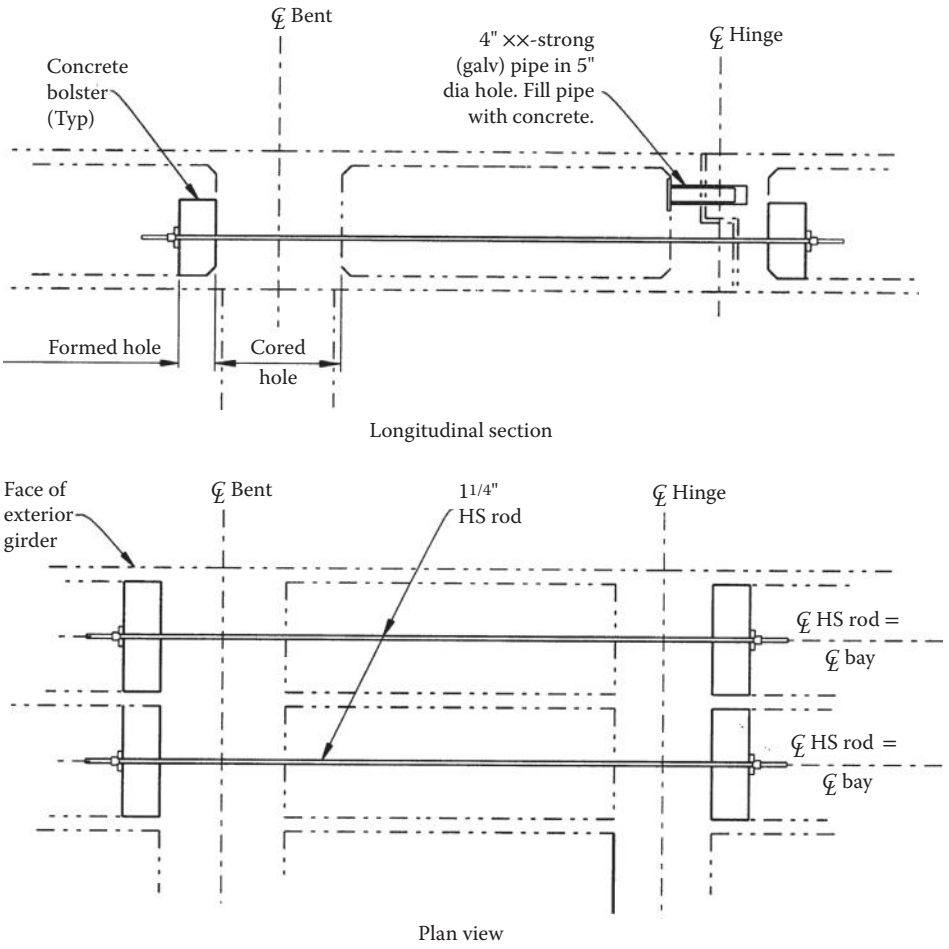

FIGURE 13.8 HS rod restrainer.

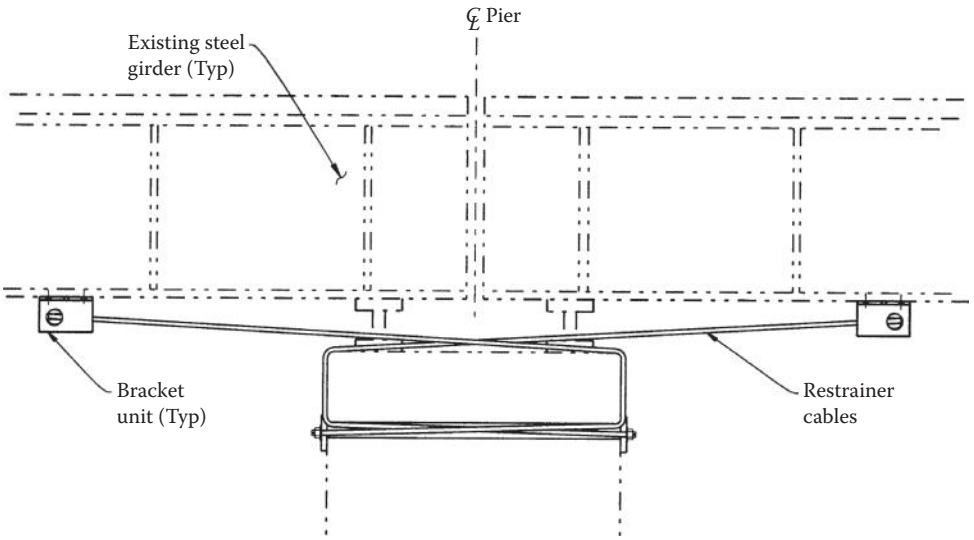

FIGURE 13.9 Cable restrainer through bent cap.

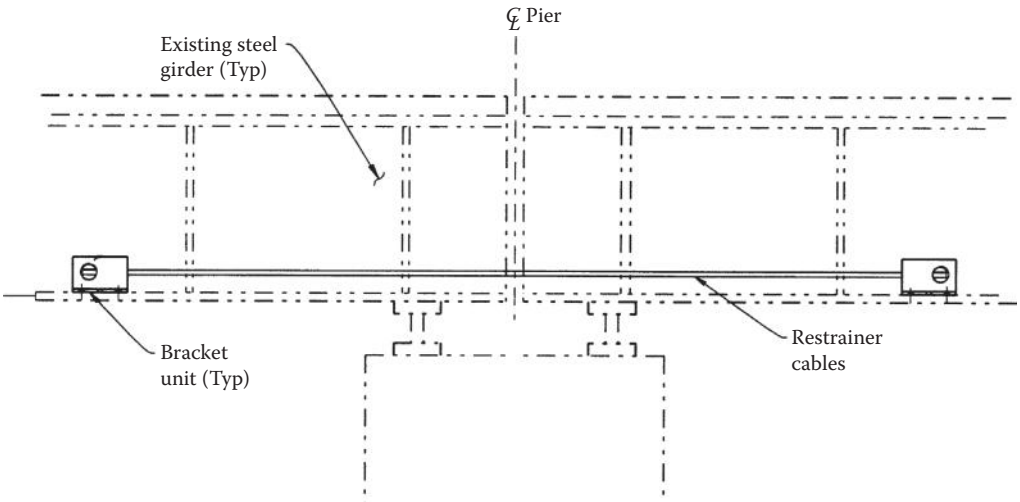

FIGURE 13.10 Girder to girder cable restrainer.

at hinge joints. Geometry may be a limiting factor when using high strength rods. For example, if a box girder bridge is shallow, it may not be possible to install a long rod through a narrow access opening. For both cables and rods, the designer needs to consider symmetry when locating restraining devices.

13.3.1.4 Pipe Seat Extenders

When a longer restraining device is preferred, increased longitudinal displacements will result and may cause unseating. It is therefore necessary to incorporate pipe seat extenders to be used in conjunction with longer restrainers when unseating will result. An 8 in. (200 mm), XX strong pipe is used for the pipe seat extender that is placed in a 10 in. (250 mm) cored (and formed) hole (Figure 13.11). A 10 in. (250 mm) cored hole allows vertical jacking if elastomeric pads are present and replacement is required after the pad fails. Longitudinal restraining devices (namely, cables and rods) must be strain compatible with the seismic deflections imposed upon the hinge joint. In other words, if the longitudinal restrainers were too short, the device would have long yielded before the pipe seat extender was mobilized, deeming the longitudinal restrainers useless. To limit the amount of cored holes in the diaphragm, the restrainer cables can be placed through the pipes as shown in Figure 13.12. The pipes are not only used for vertical load carrying capacity but can also be used successfully as transverse shear keys.

13.3.2 Steel Bracing and Diaphragms

Lateral stiffening between steel girders typically consists of some type of cross bracing system or channel diaphragm. These lateral bracing systems are usually designed to resist wind loads, construction loads, and centrifugal force from live loads and seismic loads. The seismic loads prescribed by older codes were a fraction of current code seismic loads and, in some cases, may not have controlled bracing design. In fact, in many cases, the lateral bracing system is not able to withstand the "fusing" forces of the bearing capacity and/or shear key capacity. As a result, bracing systems may tend to buckle and, if channel diaphragms are not full depth of the girder, the webs could cripple. In general, the ideal solution is to add additional sets of bracing, stiffeners, and/or full-depth channel diaphragms as close to the bearings as physically possible.

Retrofit solutions chosen depend on space restrictions. New bracing or diaphragms must be placed as to not interfere with existing bracing, utilities, stiffeners, and cable restrainers and leave enough access for maintenance engineers to inspect the bearings. Skewed bents further complicate space restrictions. When choosing a retrofit solution, the engineer must keep in mind that the retrofit will be constructed

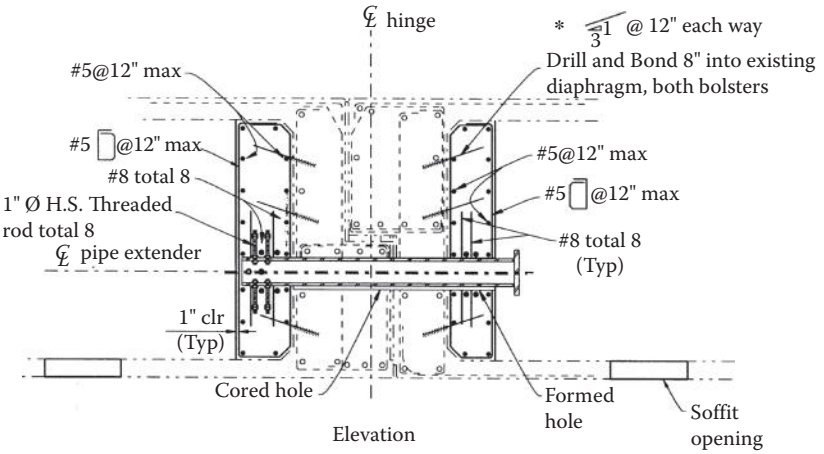

FIGURE 13.11 Pipe seat extender.

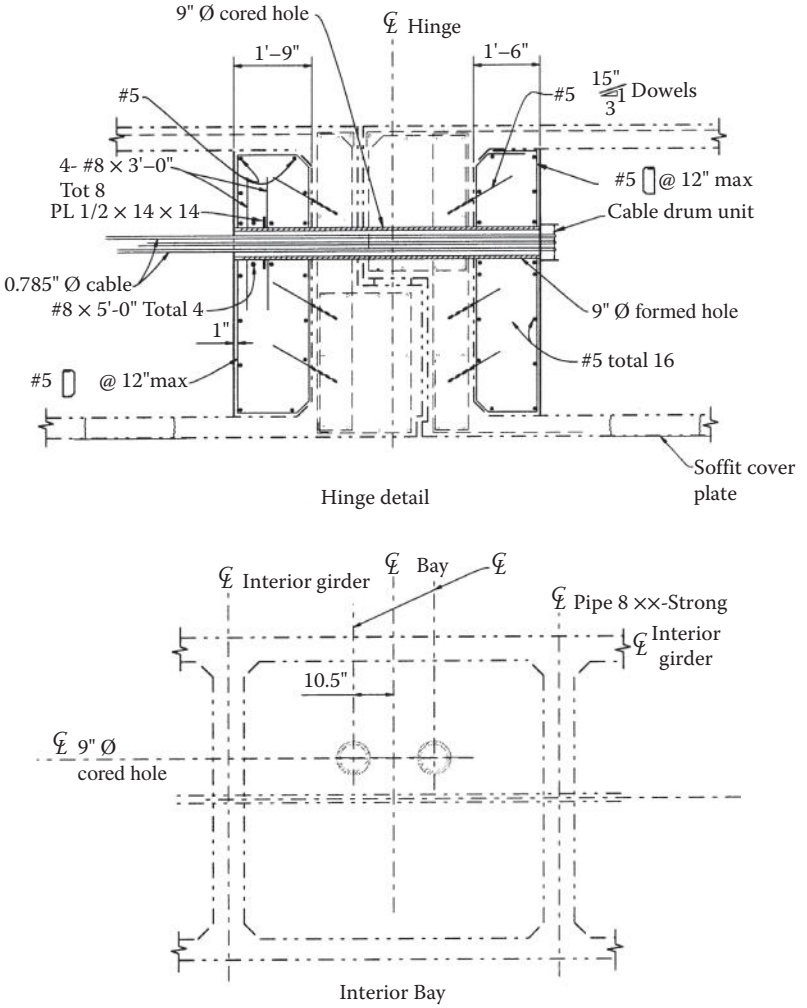

FIGURE 13.12 Restrainers/pipe seat extender.

while the structure is carrying traffic. Stresses in a bracing member tend to cycle under live load, which makes it difficult for the engineer to assess actual member stresses. As a result, any retrofit solution that requires removing and replacing existing members is not recommended. In addition, careful consideration should be given to bolted versus welded connections. As previously mentioned, structures are under live loads during the retrofit operation and thus members are subjected to cyclic stresses. It may be difficult to achieve a good quality weld when connecting to a constantly moving member. The bolted connections should be designed as bearing connections for seismic loading.

13.3.3 Concrete Edge Beams

Edge beams are used to enhance the longitudinal capacity of a concrete bridge. These beams link consecutive bents together outside the existing box structure. In the United States, edge beams have been used to retrofit double-deck structures with long outriggers.

In a single-level bridge structure, outriggers are vulnerable in torsion under longitudinal excitation. Two retrofit alternatives are possible. The first alternative is to strengthen the outrigger cap while maintaining torsional and flexural fixity to the top of the column. The second alternative is to pin the top of the column; thus reducing the torsional demand on the vulnerable outrigger cap. Using the second alternative, the column bottom fixity needs to be ensured by means of a full footing retrofit.

In a double-deck structure, pinning the connection between the lower-level outrigger cap and the column is not possible since fixity at that location is needed to provide a lateral support to the upper deck. In situations where the lower deck is supported on a long outrigger cap, the torsional softening of that outrigger may lead to loss of lateral restraint for the upper-deck column. This weakness can be remedied by using edge beams to provide longitudinal lateral restraint. The edge beams need to be stiff and strong enough to ensure plastic hinging in the column and reduce torsional demand on the lower deck outrigger cap.

13.4 Substructure Retrofits

Most earthquake damage to bridge structures occurs at the substructure. There are many types of retrofit schemes to increase the seismic capacity of existing bridges, and no one scheme is necessarily more correct than another. One type of retrofit scheme may be to encase the columns and add an overlay to footings. Another might be to attract forces into the abutments and out of the columns and footings. This section discusses some different concepts to increase the capacities of individual members of the substructure.

13.4.1 Concrete Columns

Bridge columns constructed in the United States prior to 1971 are generally deficient in shear, flexure, and/or lateral confinement. Stirrups used were typically #4 bar spaced at 12 in. (#13 bars spaced at 300 mm) on center for the entire column length including the regions of potential plastic hinging. Typically, the footings were constructed with footing dowels, or starter bars, with the longitudinal column reinforcement lapped onto the dowels. As the force levels in the column approach yield, the lap splice begins to slip. At the onset of yielding, the lap splice degrades into a pin-type condition and, within the first few cycles of inelastic bending, the load-carrying capacity degrades significantly. This condition can be used to allow a "pin" to form and avoid costly footing repairs. Various methods have been successfully used to both enhance the shear capacity and ductility by increasing the lateral confinement of the plastic hinge zone for bridge columns with poor transverse reinforcement details. Following is a list of these different types and their advantages and/or disadvantages.

13.4.1.1 Column Casings

The major functions of the column casing types listed below is to enhance the ductility, shear, and/or flexural capacity of an existing reinforced concrete column and, in some cases, limit the radial dilating strain within the plastic hinge zone. Because of the lap splice detail employed in older columns, one

of the issues facing column retrofitting is to maintain fixity at the column base. The lateral confining pressure developed by the casing is capable of limiting the radial dilating strain of the column, enough to "clamp" the splice together, preventing any slippage from occurring. Tests have shown that if the radial dilating strains are limited to less than 0.001, the lap splice remains fixed and is capable of developing the full plastic moment capacity of the section (Priestley and Seible 1991). Contrary to limiting the radial strains, is to permit these strains to take place (i.e., radial dilating strains greater than 0.001), allowing a "pin" to form while providing adequate confinement throughout the plastic hinge region.

13.4.1.1.1 Steel Casings

There are three types of retrofit schemes that are currently employed to correct the problems of existing columns through the use of steel jacketing. The first type is typically known as a Class F type of column casing retrofit as shown in Figure 13.13. This type of casing is fully grouted and is placed in the full height of the column. It is primarily used for a column that is deficient in shear and flexure. It limits the radial dilating strain to less than 0.001, effectively fixing the lap splice from slipping. The lateral confining pressure for design is taken as 300 psi (2.068 MPa) and, when calculated for a 0.5 in. (13 mm) thick steel casing with A36 steel, it is equivalent to a #8 bar (#25 bar) at a spacing of about 1.5 in. (38 mm) It can therefore be seen that the confinement, as well as the shear, is greatly enhanced. The allowable displacement ductility ratio for a class F column casing is typically 6, allowing up to 8 in isolated locations. It has been tested well beyond this range; however, the allowable ductility ratio is reduced to prohibit fracturing of the longitudinal bars and also limit the level of load to the footing.

The second type of casing is a Class P type and is only a partial height casing; therefore, it does not help a column that is deficient in shear. As can be seen from Figure 13.13, the main difference between a Class F and a Class P type column casing is the layer of polyethylene between the grout and the column. This permits the column to dilate outward, allowing the strain to exceed 0.001, forming a pin at the base of the column. It should be noted that the casing is still required in this condition to aid in confining the column. The limit of this type of retrofit is typically taken as 1.5 times the columns diameter or to where the maximum moment has decreased to 75%.

The third type of steel column casing is a combination of the first two and, hence, known as a *Class P/F*, also shown in Figure 13.13. It is used like a Class P casing, but for a column with a shear deficiency.

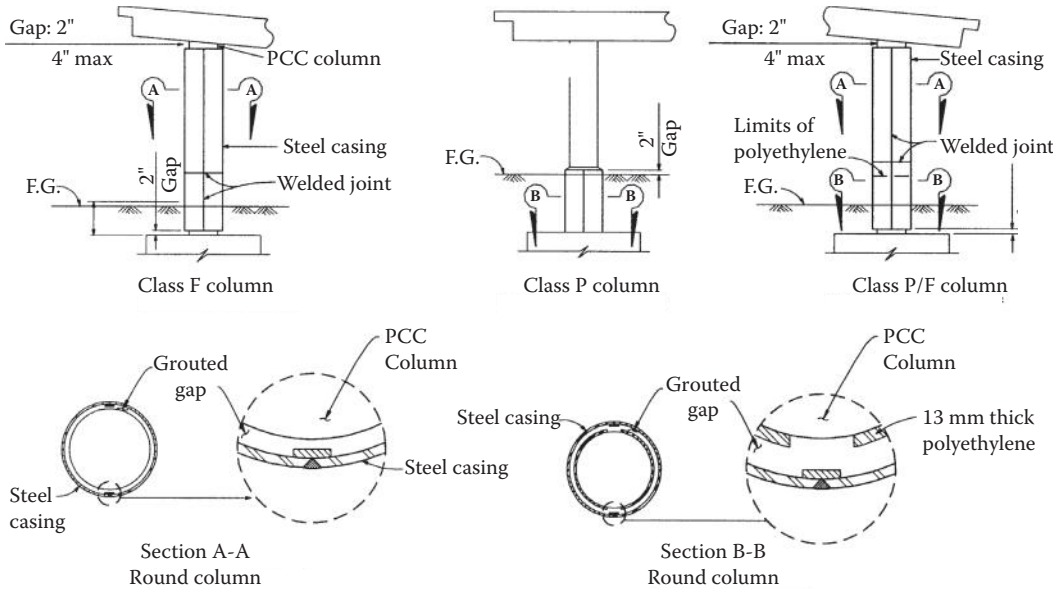

FIGURE 13.13 Steel column casings.

All of these casings can be circular (for circular or square columns) or oblong (for rectangular columns). If a rectangular column is deficient in shear only, it is sometimes permitted to use flat steel plates if the horizontal clearances are limited and it is not possible to fit an oblong column in place. For aesthetic purposes, the Class P casing may be extended to full height in highly visible areas. It can be unsightly if an oblong casing is only of partial height. It is important to mention that the purpose of the 2 in. (50 mm) gap at the ends of the column is to prevent the casing from bearing against the supporting member acting as compression reinforcement, increasing the flexural capacity of the column. This would potentially increase the moments and shears into the footing and/or bent cap under large seismic loads. Figure 13.14 shows a completed steel jacket retrofit.

13.4.1.1.2 Concrete Casings

When retrofitting an unusually shaped column without changing the aesthetic features of the column's geometry, a concrete casing may be considered as an alternative. Existing columns are retrofitted by placing hoops around the outer portion of the column and then drilling and bonding bars into the column to enclose the hoops. The reinforcement is then encased with concrete, thus, maintaining the original shape of the column. The design of a concrete jacket follows the requirements of a new column. Although this method increases the shear and flexural capacities of the column and provides additional confinement without sacrificing aesthetics, it is labor intensive and therefore can be costly. Figure 13.15 shows confining reinforcement in a concrete casing retrofit.

13.4.1.1.3 Fiber-Reinforced Plastic (FRP) Composite Casings

Recently, there has been significant research and development using advanced composites—Fiber-reinforced plastic (FRP) in bridge design and retrofit. Similar to steel casings, advanced composite casings increase the confinement and shear capacity of existing concrete bridge columns. This type of

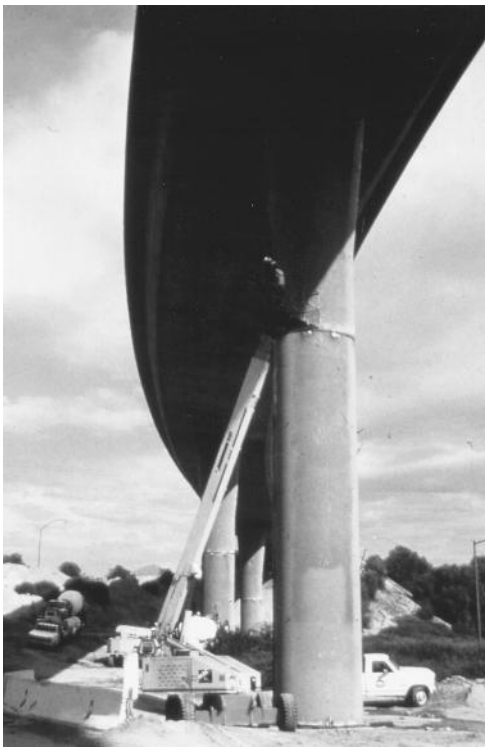

FIGURE 13.14 Steel casing retrofit.

FIGURE 13.15 Confining reinforcement in a concrete casing.

column retrofit (Figure 13.16) has proved to be competitive with steel casings when enhancing column shear capacity and may also provide an economic means of strengthening bridge columns. However, currently, composites are not economical when limiting lap splice slippage inside expected plastic hinge zones. The advantage of using some types of composite casings is that the material can be wrapped to the column without changing its geometric shape. This is important when aesthetics are important or lateral clearances at roadways are limited.

13.4.1.1.4 Wire Wrap Casings

Another type of system approved by the California Department of Transportation is a "wire wrap" system. It consists of a prestressing strand hand wrapped onto a column, wedges are then placed between the strand and the column, effectively prestressing the strand and actively confining the column, as shown in Figure 13.17. The advantage of this type of system is that, like the advanced composites, it can be wrapped to any column without changing the geometric shape. Its basic disadvantage is that it is labor intensive and currently can only be applied to circular columns.

13.4.1.2 In-Fill Walls

Reinforced concrete in-fill walls may also be used as an alternative for multicolumn bridge bents, as shown in Figure 13.18. This has two distinct advantages: it increases the load-carrying capacity of the columns in the transverse direction and limits the transverse displacements. By limiting the displacements transversely, the potential for plastic hinge formation in the bent cap is eliminated. Therefore, cost may prove to be less than some other retrofit alternatives mentioned earlier. It is important to note that the in-fill wall is not effective in the longitudinal capacity of bridge bents with little or no skew.

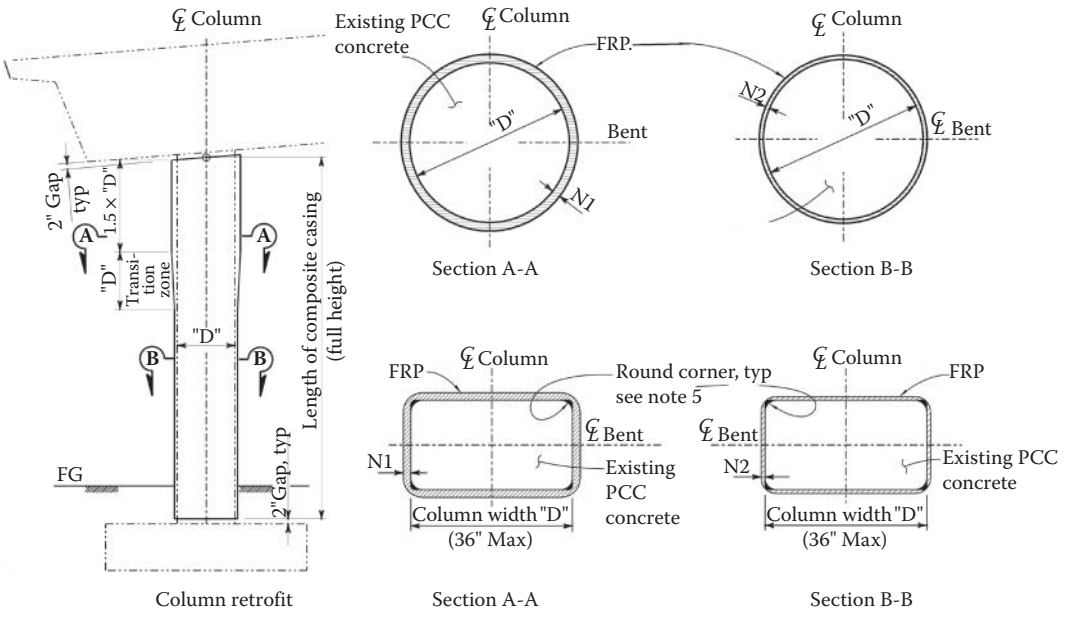

E-glass FRP system		
Round column, number of layers (Min)		
Column diameter	N1	N2
12"	4	2
24"	7	4
36"	11	6
48"	14	7
60"	17	9
72" Max	21	11

Carbon FRP system		
Round column, number of layers (Min)		
Column diameter	N1	N2
12"	3	3
24"	6	3
36"	8	4
48"	11	6
60"	14	7
72" Max	16	8

E-glass FRP system		
Rectangular column, number of layers (Min)		
Column width	N1	N2
12"	6	3
18"	8	4
24"	11	6
30"	13	7
36" Max	16	8

Carbon FRP system		
Rectangular column, number of layers (Min)		
Column width	N1	N2
12"	4	3
18"	6	3
24"	8	4
30"	10	5
36" Max	12	6

FIGURE 13.16 Advanced composite column casing.

13.4.1.3 Link Beams

Link beams are used to enhance the transverse capacity of a concrete bent. The placement of a link beam over a certain height above ground level determines its function.

A link beam can be placed just below the soffit level and acts as a substitute to a deficient existing bent cap. The main function of this kind of a link beam is to protect the existing superstructure and force hinging in the column.

In other cases, a link beam is placed somewhere between the ground level and the soffit level in order to tune the transverse stiffness of a particular bent. This type of retrofit can be encountered in situations

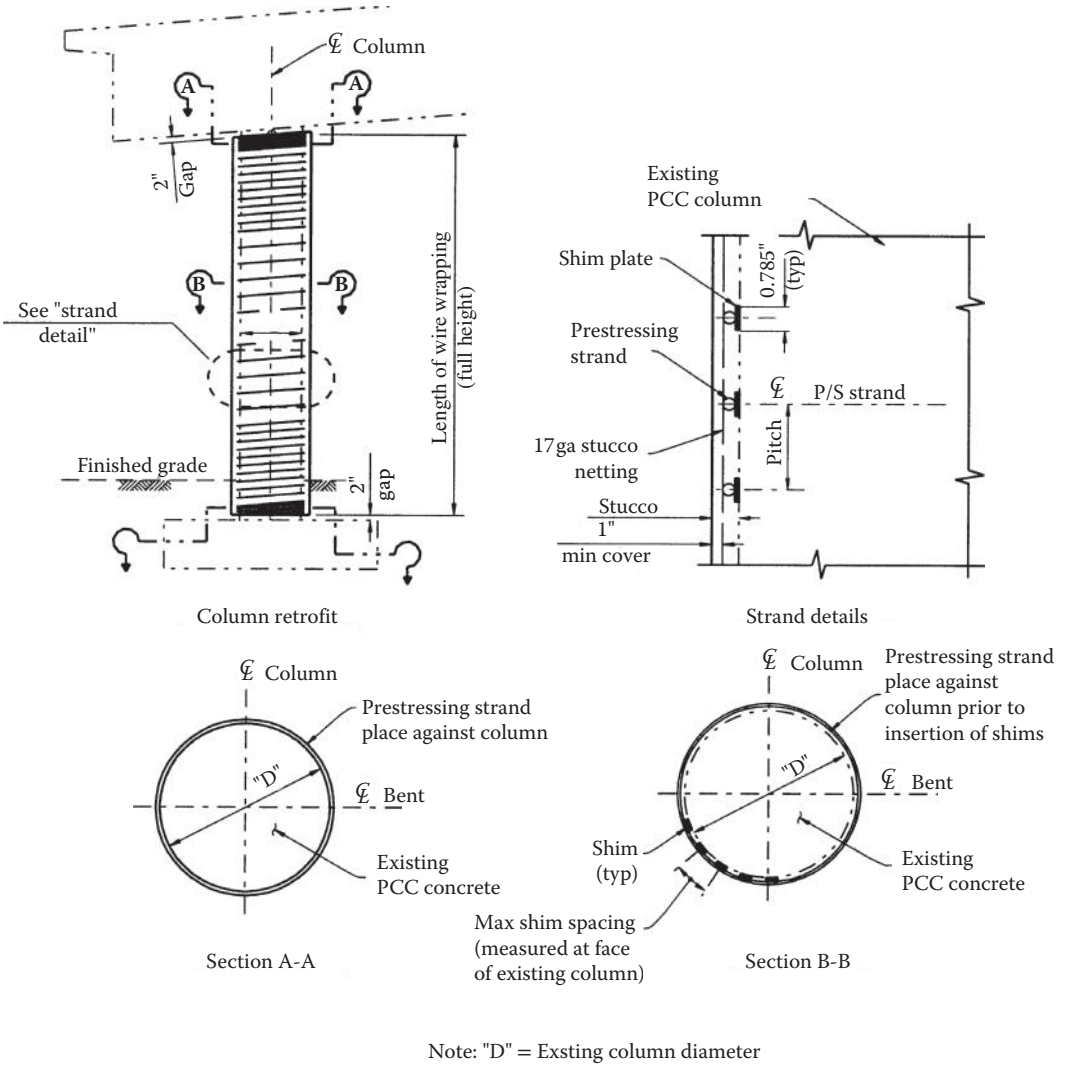

FIGURE 13.17 Column wire wrap.

where a box superstructure is supported on bents with drastically unequal stiffnesses. In this case, the center of mass and the center of rigidity of the structure are further apart. This eccentricity causes additional displacement on the outer bents, which can lead to severe concentrated ductility demands on just a few bents of the subject bridge. This behavior is not commonly preferred in seismically resistant structures, and the use of link beams in this case can reduce the eccentricity between the center of mass and the center of rigidity. This structural tuning is important in equally distributing and reducing the net ductility demands on all the columns of the retrofitted bridge.

13.4.2 Pier Walls

Until recently, pier walls were assumed to be more vulnerable to seismic attack than columns. However, extensive research performed at the University of California, Irvine has proved otherwise.[6] Pier walls, nevertheless, are not without their problems. The details encompass poor confinement and lap splices, similar to that of pre-1971 bridge columns. Pier walls are typically designed and analyzed as a shear wall about the strong axis and as a column about the weak axis. The shear strength of pier walls in the strong direction

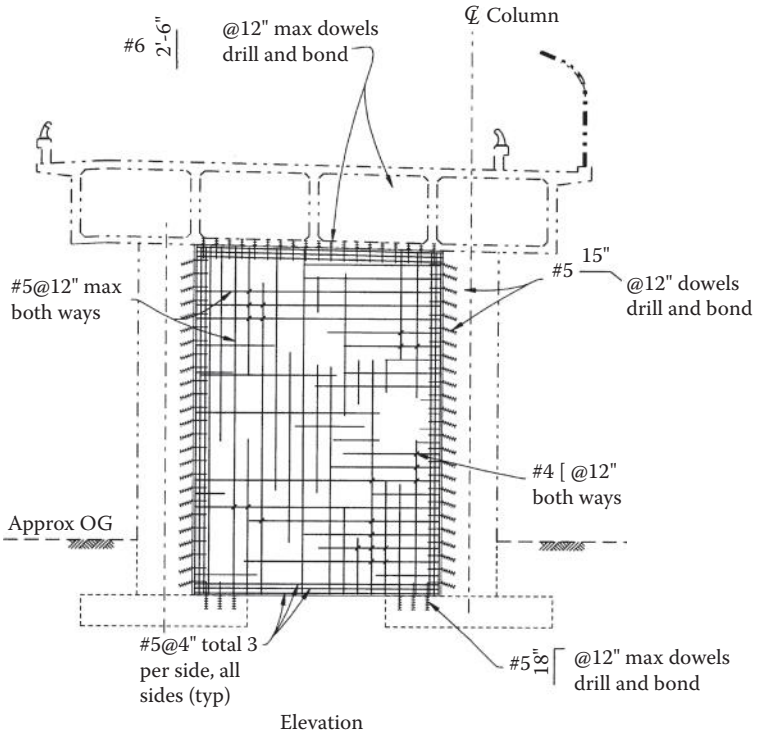

FIGURE 13.18 In-fill wall.

is usually not a concern and one can expect a shear stress of about $0.21\sqrt{f_c'}$ ksi $\left(0.25\sqrt{f_c'}\ \text{MPa}\right)$. For the weak direction, the allowable demand displacement ductility ratio in existing pier walls is 4.0. Similar to columns, many older pier walls were also built with a lap splice at the bottom. If the lap splice is long enough, fixity will be maintained and the full plastic moment can be developed. Tests conducted at the University of California at Irvine have shown that lap splices that are 28 times the diameter of the longitudinal bar are adequate (Haroun et al., 1993). However, a lap splice detail with as little as 16 bar diameters will behave in the same manner as that of a column with an inadequate lap splice and may slip, forming a pin condition. Because of the inherent flexibility of pier walls about its weak axis, the method of retrofit for this type of lap splice is a plate with a height 2 times the length of the splice, placed at the bottom of the wall. The plate thickness is not as critical as the bolt spacing. It is generally recommended that the plate be 1 in. (25 mm) thick with a bolt spacing equal to that of the spacing of the main reinforcement, only staggered, and not to exceed 14 in. (355 mm). If additional confinement is required for the longer lap splice, the plate height may be equal to the lap splice length.

13.4.3 Steel Bents

Most steel bents encountered in older typical bridges can be divided in two groups. One group contains trestle bents typically found in bridges spanning canyons, and the second group contains open-section, built-up steel columns. The built-up columns are typically I-shaped sections, which consist of angles and plates bolted or riveted together. The second group is often found on small bridges or elevated viaducts.

Trestle steel bents are commonly supported on pedestals resting on rock or relatively dense foundation. In general, the truss members in these bents have very large slenderness ratios that lead to very early elastic buckling under low-magnitude earthquake loading. Retrofitting of this type of bent consists basically of balancing between member strengthening and enhancing the tensile capacity of the foundation and keeping connection capacities larger than member capacities. In many situations, foundation

retrofit is not needed where bent height is not large and a stable rocking behavior of the bent can be achieved. Strengthening of the members can be obtained by increasing the cross-sectional area of the truss members or reducing the unsupported length of the members.

Figure 13.19 shows the retrofit of Castro Canyon Bridge in Monterey County, California. The bent retrofit consists of member strengthening and the addition of a reinforced concrete block around the bent to pedestal connection. In this bridge, the pedestals were deeply embedded in the soil, which added to the uplift capacity of the foundation.

For very tall trestle bents, foundation tie-downs, in addition to member strengthening, might be needed in order to sustain large overturning moments. Existing anchor bolts for base plates supported on top of pedestals are usually deficient. Replacement of these older bolts with high-strength bolts or the addition of new bolts can be done to ensure an adequate connection capable of developing tension and shear strength. The addition of new bolts can be achieved by coring through the existing base plate and pedestal or by enlarging the pedestal with a concrete jacket surrounding the perimeter bolts. The use of sleeved anchor bolts is desirable to induce some flexibility into the base connection.

The second group of steel bents contains open-section, built-up columns. These members may fail due to yielding, local buckling, or lateral torsional buckling. For members containing single I-shaped section, lateral torsional buckling typically governs. Retrofit of this type of columns consists of enclosing the section by bolting channel sections to the flanges. Figure 13.20 shows this type of retrofit. Installation of these channels is made possible by providing access through slotted holes. These holes are later covered by tack welding plates or left open. For larger members with an open section as seen in Figure 13.21, retrofit consists of altering the existing cross section to a multicell box section.

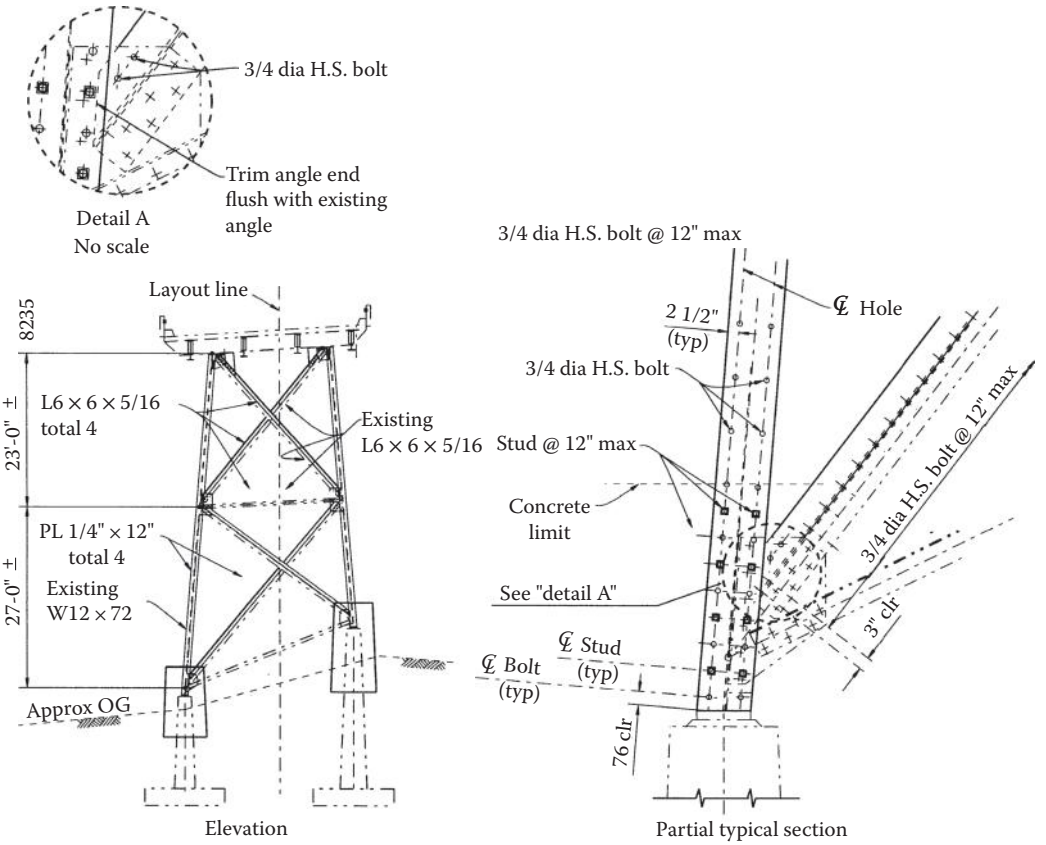

FIGURE 13.19 Trestle bent retrofit.

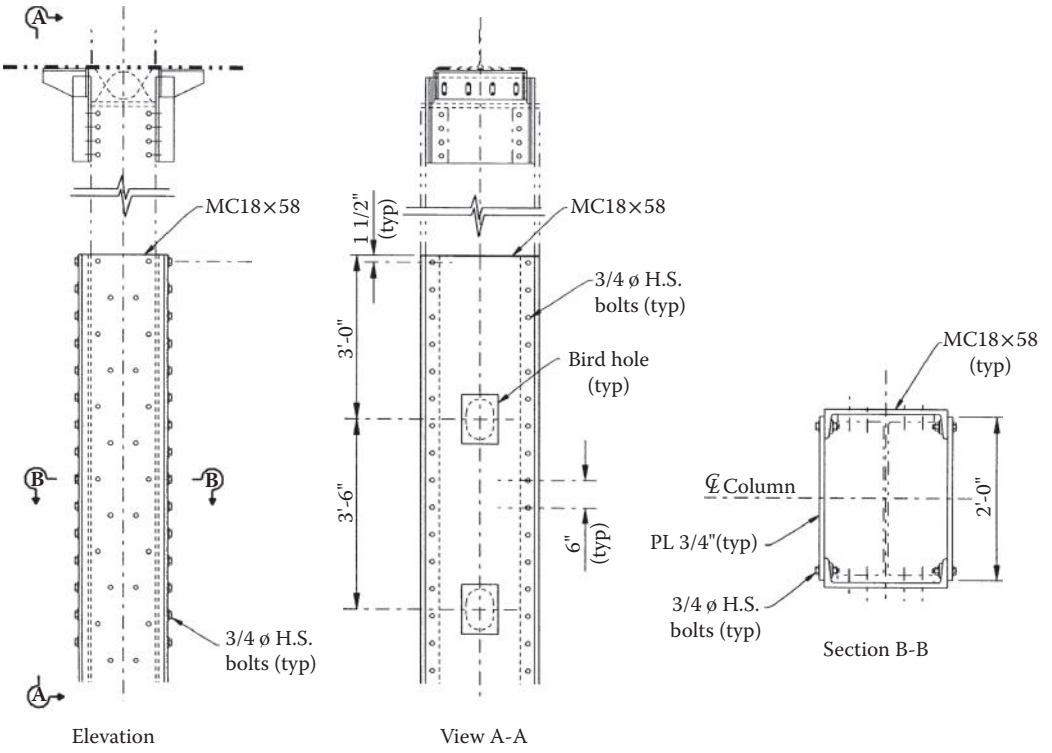

FIGURE 13.20 I-Shape steel column retrofit.

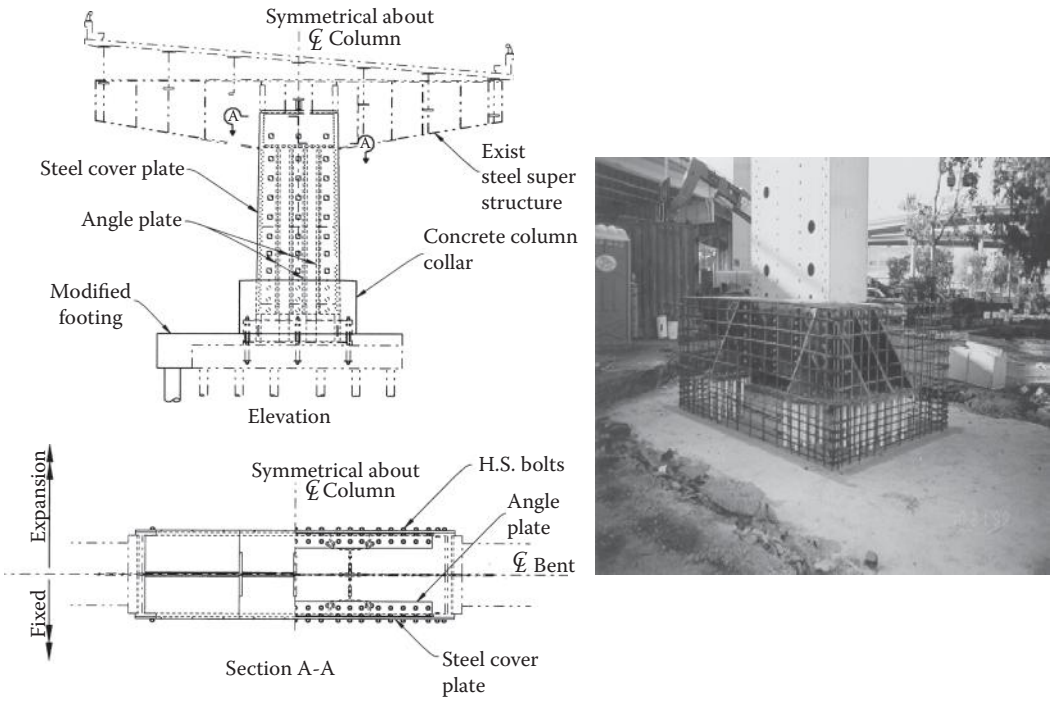

FIGURE 13.21 Open section steel column retrofit.

The seismic behavior of a multicell box is quite superior to an open section of a single box. These advantages include better torsional resistance and a more ductile inelastic behavior. In a multicell box, the outside plates sustain the largest deformation. This permits the inside plates to remain elastic in order to carry the gravity load and prevent collapse during an earthquake. To maintain an adequate load path, the column base connection and the supporting foundation should be retrofitted to ensure the development of the plastic hinge just above the base connection. This requires providing a grillage to the column base as seen in Figure 13.21 and a footing retrofit to ensure complete load path.

13.4.4 Bearing Retrofit

Bridge bearings have historically been one of the most vulnerable components in resisting earthquakes. Steel rocker bearings in particular have performed poorly and have been damaged by relatively minor seismic shaking. Replacement of any type of bearings should be considered if failure will result in collapse of the superstructure. Bearing retrofits generally consist of replacing steel rocker type bearings with elastomeric bearings. In some cases, where a higher level of serviceability is required, base isolation bearings may be used as a replacement for steel bearings. For more information on base isolation, see detailed discussion in Chapter 11. Elastomeric bearings are preferred over steel rockers because the bridge deck will only settle a small amount when the bearings fail, whereas the deck will settle several inches when rockers fail. Elastomeric bearings also have more of a base isolation effect than steel rockers. Both types of bearings may need catchers, seat extenders, or some other means of providing additional support to prevent the loss of a span. Although elastomeric bearings perform better than steel rockers, it is usually acceptable to leave the existing rockers in place since bearing replacement is more expensive than installing catchers to prevent collapse during an earthquake.

13.4.5 Shear Key Retrofit

The engineer needs to consider the ramifications of a shear key retrofit. The as-built shear keys may have been designed to "fuse" at a certain force level. This fusing will limit the amount of force transmitted to the substructure. Thus, if the shear keys are retrofitted and designed to be strong enough to develop the plastic capacity of the substructure, this may require a more expensive substructure retrofit. In many cases, it is rational to let the keys fail to limit forces to the substructure and effectively isolate the superstructure. Also note that superstructure lateral bracing system retrofits will also have to be increased to handle increased forces from a shear key retrofit. In many cases, the fusing force of the existing shear keys is large enough to require a substructure retrofit. In these situations, new or modified shear keys should be constructed to be compatible with the plastic capacity of the retrofitted substructure. There are other situations that may require a shear key retrofit. Transverse movements may be large enough so that the external girder displaces beyond the edge of the bent cap and loses vertical support. For a multiple-girder bridge, it is likely that the side of the bridge may be severely damaged and the use of a shoulder or lane will be lost, but traffic can be routed over a portion of the bridge with few or no emergency repairs. This is considered an acceptable risk. On the other hand, if the superstructure of a two- or three-girder bridge is displaced transversely so that one line of girders loses its support, the entire bridge may collapse. Adequate transverse restraint, commonly in the form of shear keys, should be provided.

13.4.6 Cap Beam Retrofit

There are several potential modes of failure associated with bent caps. Depending on the type of bent cap, these vulnerabilities could include bearing failures, shear key failures, inadequate seat widths, and cap beam failures. Table 13.3 lists several types of bent caps and potential vulnerabilities.

Cap beam modes of failure may include flexure, shear, torsion, and joint shear. Prior to the 1989 Loma Prieta Earthquake, California, there was very little emphasis placed on reinforcement detailing of bent cap beams for lateral seismic loads in the vicinity of columns. As a result, cap beams supported on

TABLE 13.3 Potential Bent Cap Vulnerabilities

	Cap Beam							
Cap Type	Bearings	Shear Keys	Seat Width	Moment	Shear	Torsion	Joint Shear	Bolted Cap/Col Connection
Concrete Drop Cap-Single Column Bent	X	X	X				X	
Concrete Drop Cap-Multi Column Bents	X	X	X	X	X		X	
Integral Concrete Cap-Single Column Bent							X	
Integral Concrete Cap-Multi Column Bent				X	X	X	X	
Inverted T-Simple Support for Dead Load, Continuous for Live Load-Single Col. Bent		X					X	
Inverted T-Simple Support for Dead Load, Continuous for Live Load-Multi Col. Bent		X					X	
Inverted T-Simple Support for Both Dead Load Live Load-Single Column Bent	X	X	X				X	
Inverted T-Simple Support for Both Dead Load and Live Load-Multiple Column Bent	X	X	X	X	X	X	X	
Steel Bent Cap-Single Column Bent	X	X	X					X
Steel Bent Cap-Multi Column Bent	X	X	X					X
Integral Outrigger Bent						X	X	
Integral C Bent						X	X	

multiple columns were not designed and detailed to handle the increased moment and shear demands that result from lateral transverse framing action. In addition, the beam/column joint is typically not capable of developing the plastic capacity of the column and thus fails in joint shear. For cap beams supported by single columns, although they do not have framing action in the transverse direction and are not subjected to moment and shear demands that are in addition to factored vertical loads, joint shear must still be considered as a result of longitudinal seismic response. In these situations, retrofit of the superstructure is not common since single-column bents are typically fixed to the footing and fixity at top of the column is not necessary.

Retrofit solutions that address moment and shear deficiencies typically include adding a bolster to the existing cap as shown in Figure 13.22. Additional negative and positive moment steel can be placed on the top and bottom faces of the bolsters, as required, to force plastic hinging into the columns. These bolsters also contain additional shear stirrups and steel dowels to ensure a good bond with the existing cap for composite action. Prestressing can also be included in the bolsters. In fact, prestressing has proven to be an effective method to enhance an existing cap's moment, shear, and joint shear capacity. This is particularly true for bent caps that are integral with the superstructure.

Special consideration should be given to the detailing of bolsters. The engineer needs to consider bar hook lengths and bending radii to make sure that the stirrups will fit into the bolsters. Although the philosophy is to keep the superstructure elastic and take all inelastic action in the columns, realistically, the cap beams will have some yield penetration. Thus, the new bolster should be detailed to provide adequate confinement for the cap to guarantee ductile behavior. This suggests that bolsters should not be just doweled onto the existing bent cap. There should be a continuous or positive connection between the bolsters through the existing cap. This can be achieved by coring through the existing cap. The hole pattern should be laid out to miss the cap's existing top and bottom steel. It is generally difficult to miss existing shear stirrups so the engineer should be conservative when designing the new

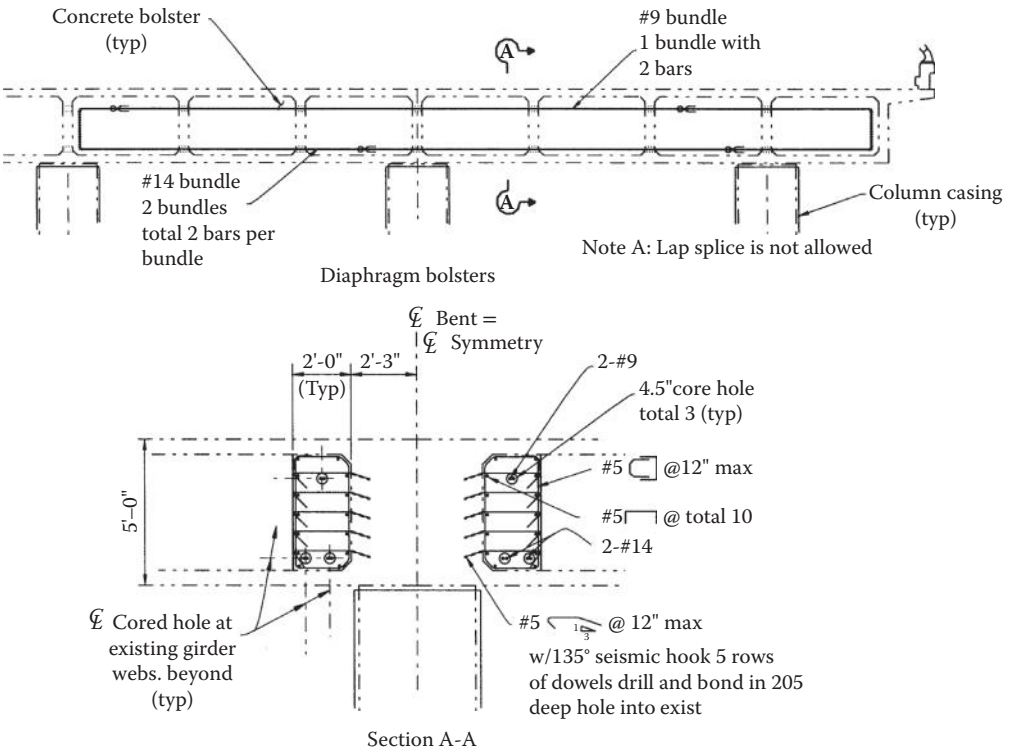

FIGURE 13.22 Bent cap retrofit.

stirrups by not depending on the existing shear steel. The steel running through the existing cap that connects the new bolsters can be continuous stirrups or high-strength rods, which may or may not be prestressed.

The cap retrofit is much easier with an exposed cap but can be done with integral caps. In order to add prestressing or new positive and negative steel and add dowels to make sure that the bolsters in adjacent bays are continuous or monolithic, the existing girders have to be cored. Care must be taken to avoid the main girder steel and/or prestressing steel.

Torsion should be investigated in situations where the superstructure, cap beam, and column are monolithic. In these situations, longitudinal loads are transferred from the superstructure into the columns through torsion of the cap beam. Superstructures supported on cap beams with bearings are unlikely to cause torsional problems. Torsion is mainly a problem in outriggers connected to columns with top fixed ends. However, torsion can also exist in bent cap beams susceptible to softening due to longitudinal displacements. This softening is initiated when top or especially bottom longitudinal reinforcement in the superstructure is not sufficient to sustain flexural demands due to the applied plastic moment of the column. Retrofit solutions should ensure adequate members' strength along the load path from superstructure to column foundation.

In the case of an outrigger, the cap beam nominal torsional yield capacity should be greater than the column flexural plastic moment capacity. Torsion reinforcement should be provided in addition to reinforcement required to resist shear, flexure, and axial forces. Torsion reinforcement consists of closed stirrups, closed ties, or spirals combined with transverse reinforcement for shear, and longitudinal bars combined with flexural reinforcement. Lap spliced stirrups are considered ineffective in outriggers, leading to a premature torsional failure. In such cases, closed stirrups should not be made up of pairs of U-stirrups lapping one another. Where necessary, mechanical couplers or welding should be used to develop the full capacity of torsion bars. When plastic hinging cannot be avoided in the superstructure, the concrete should be considered ineffective in carrying any shear or torsion. Regardless of where plastic hinging occurs, the outrigger should be proportioned such that the ultimate torsional moment does not exceed four times the cracking torque. Prestressing cannot be considered effective in torsion unless bonded in the member. Unbonded reinforcement, however, can be used to supply axial load to satisfy shear friction demands to connect outrigger caps to columns and superstructure. Bonded tendons should not be specified in caps where torsional yielding will occur. Designers must consider effects of the axial load in caps due to transverse column plastic hinging when satisfying shear and torsion demands.

13.4.7 Abutments

Abutments are generally classified into two types: seat type and monolithic. The monolithic type of abutment is commonly used for shorter-span bridges, whereas longer-span bridges typically use a seat type. Contrary to the seat type abutment, the monolithic abutment has the potential for heavy damage. This is largely due to the fact that the designer has more control through the backwall design. The backwall behaves as a fuse to limit any damage to the piles. However, since this damage is not a collapse mechanism, it is therefore considered to be acceptable damage. Additionally, the monolithic abutment has proven itself to perform very well in moderate earthquakes, sustaining little or no damage. Some typical problems encountered in older bridges are as follows:

- Insufficient seat length for seat-type abutments
- Large gallery, or gap, between the backwall and superstructure's end diaphragm
- Insufficient longitudinal and/or transverse shear capacity
- Weak end diaphragms at monolithic abutments

Following are some of the more common types of retrofits used to remedy the abutment problems mentioned above.

13.4.7.1 Seat Extenders and Catchers

Seat extenders at abutments and drop caps generally consist of additional concrete scabbed onto the existing face (Figures 13.23 and 13.24). The seat extenders attached to an existing abutment or a bent cap face shoud be designed like a corbel. When designing the connecting steel between the new seat extender and the existing concrete, shear friction for vertical loads should be considered. Tensile forces caused by friction should also be considered when the girder moves in the longitudinal direction and pulls the new concrete away from the existing bent cap or abutment. Compression strut and bearing loads under the girder also need to be considered. Note that the face of the existing concrete should be intentionally roughened before the new concrete is placed to ensure a good bond.

If bearing failure results in the superstructure dropping 6 in. (150 mm) or more, catchers could be added to minimize the drop. Catchers generally are designed to limit the superstructure drop to 2 in. (50 mm) and can provide additional seat width. In other words, catchers are basically seat extenders that are detailed to reduce the amount the superstructure is allowed to drop. The design procedure is similar for both seat extenders and catchers. In some cases, an elastomeric bearing pad is placed on top of the catcher to provide a landing spot for the girder after bearing failure. The friction factor for concrete on an elastomeric pad is less than that for concrete on concrete so the tension force in the corbel could possibly be reduced. One special consideration for catchers is to make sure to leave enough room to access the bearing for inspection and replacement. Figure 13.25 shows a catcher beam for a steel girder bridge.

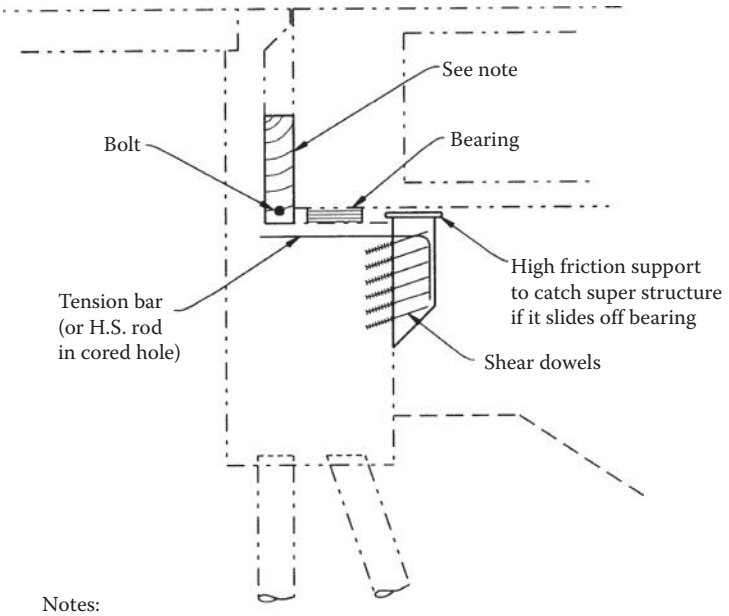

Notes:

Gap filler to mobilize backwall and embankment soil.
Filler can be as follows:

(A) Steel or harwood strips inserted by slipping them horizontally in the space above seat and rotating to vertical. Bolt together.

(B) Fill space with concrete through top. The use of polystyrene between new concrete and bridge structure requires traffic control.

Hardwood filler (option A) shown in sketch above.

FIGURE 13.23 Seat extender at abutment.

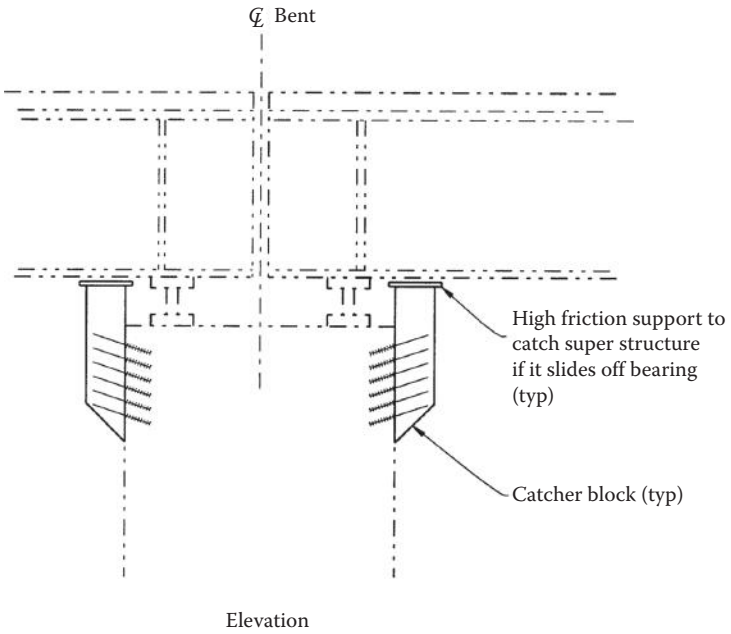

FIGURE 13.24 Seat extender at bent cap.

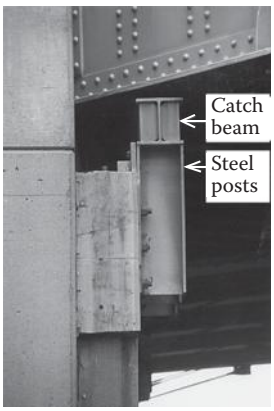

FIGURE 13.25 Catcher beam for steel girder bridge.

13.4.7.2 Fill Galleries with Timber, Concrete, or Steel

Some seat type abutments have a gallery, or a large gap, between the superstructures end diaphragm and the backwall. It is important to realize that the columns must undergo large deformations before the soil can be mobilized behind the abutment if this gap is not filled. Therefore, as a means of retrofit, the gallery is filled with concrete, steel, or timber as shown in Figure 13.26 to engage the backwall and, hence, the soil. However, timber is a potential fire hazard and in some parts of the United States may be susceptible to termite attack. When filling this gap, the designer should specify the expected thermal movements rather than the required thickness. This prevents any problems that may surface if the backwall is not poured straight.

13.4.7.3 L Brackets on Superstructure Soffit

Similar in theory to filling the gallery behind the backwall is adding steel angles (or brackets) to the flanges of steel I-girders as shown in Figure 13.27. These brackets act as "bumpers" that transfer the longitudinal reaction from the superstructure into the abutment, and then into the soil.

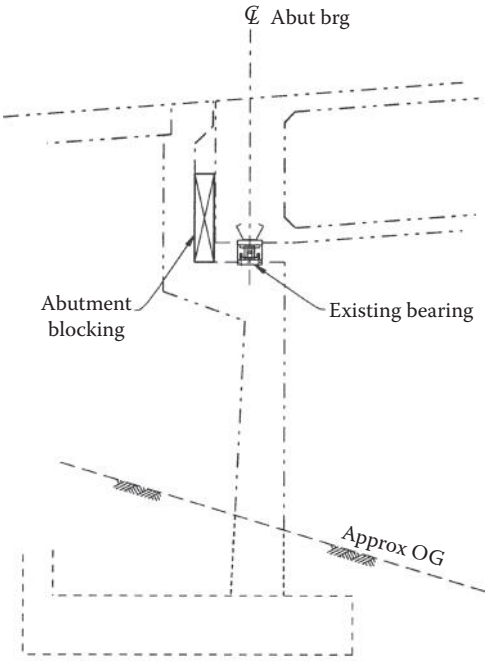

FIGURE 13.26 Abutment blocking.

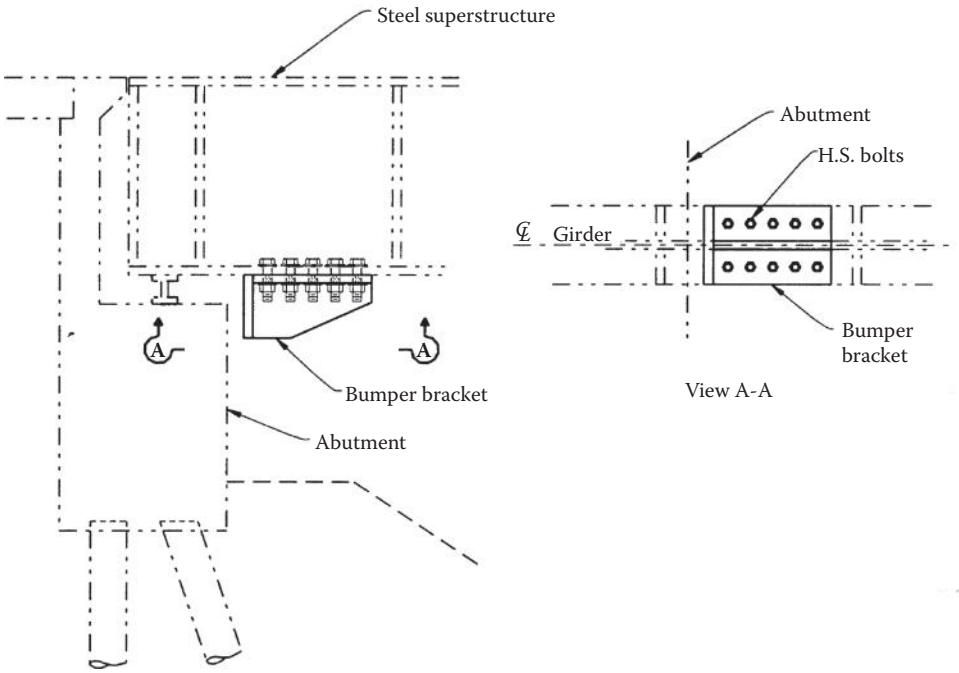

FIGURE 13.27 Bumper bracket at abutment.

13.4.7.4 Shear Keys, Large CIDH Piles, Anchor Slabs, and Vertical Pipes

For shorter-span bridges, an effective retrofit scheme is to attract the forces away from the columns and footings and into the abutments. This usually means modifying and/or strengthening the abutment thereby "locking up" the abutment, limiting the displacements and hence, attracting most of the loads. Although this type of retrofit is more effective in taking the load out of columns for shorter span structures, the abutments still may require strengthening, in addition to retrofitting the columns, for longer-span bridges.

Methods that are intended to mobilize the abutment and the soil behind the abutments may consist of vertical pipes, anchor piles, seismic anchor slabs, or shear keys as shown in Figures 13.28 and 13.29. For heavily skewed or curved bridges, anchor piles or vertical pipes are generally the preferred method due to the added complication from geometry. For instance, as the bridge rotates away from the abutment, there is nothing to resist this movement. By adding an anchor pile at the acute corners of the abutment, the rotation is prohibited and the anchor pile then picks up the load.

13.4.8 Foundations

Older footings have many vulnerabilities that can lead to failure. The following is a list of major weaknesses encountered in older footings:

- Lack of top mat reinforcement and shear reinforcement
- Inadequate development of tension pile capacity
- Inadequate size for development of column plastic moment

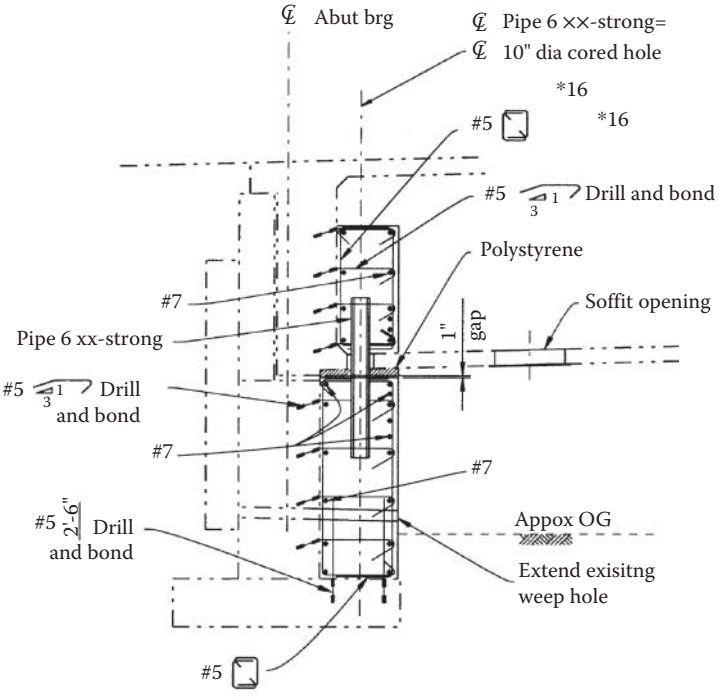

FIGURE 13.28 Vertical pipe at abutment.

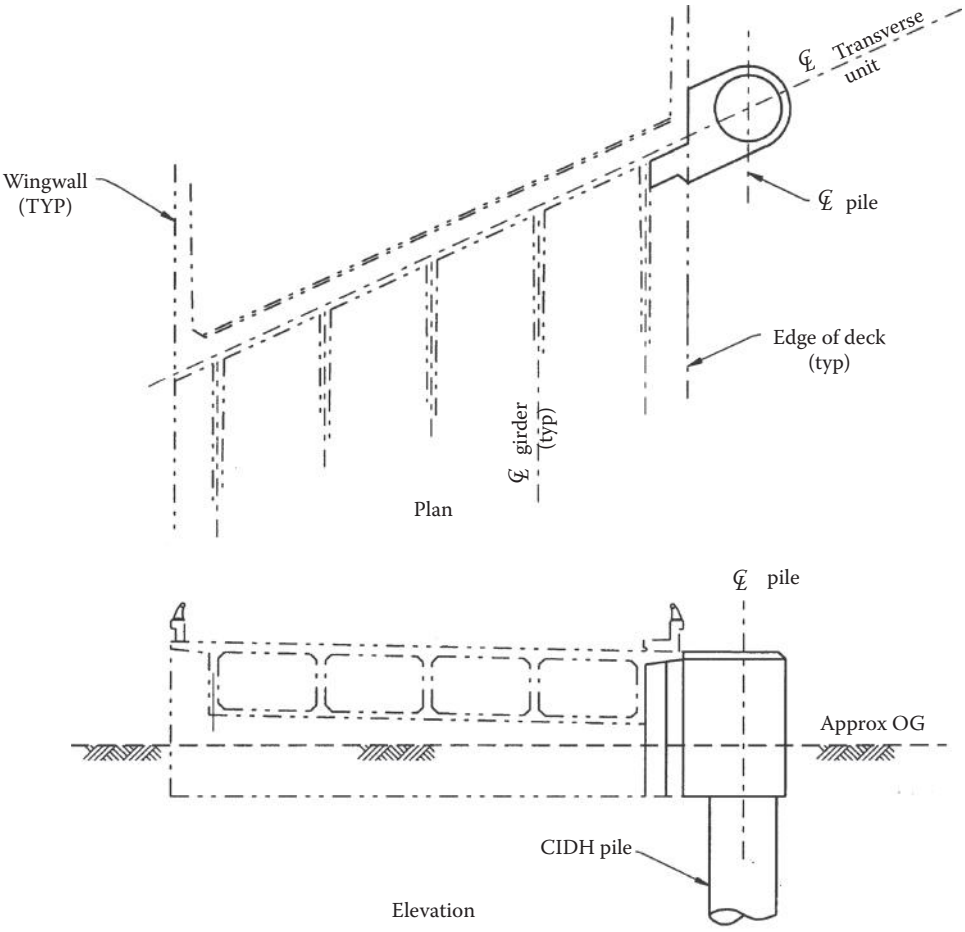

FIGURE 13.29 Anchor pile at abutment.

Footings can be divided into two categories:

1. Spread footings resting on relatively dense material or footings resting on piles with weak tension connection to the footing cap. This latter group is treated similarly to spread footings since a strategy can be considered to ignore the supporting piles in tension.
2. Footings with piles that act in tension and compression.

In general, retrofit of footings supporting columns with a class P type casing is not needed. If a column has been retrofitted with a class F casing, retrofit of footings is needed to develop the ultimate demand forces from the column. Typically, complete retrofit of one bent per frame including the column and the footing is recommended. Note that retrofit strategies for multicolumn bents can often be limited to columns because of common pin connections to footings. Footing retrofit is usually avoided on multicolumn bridges by allowing pins at column bases as often as possible. Pins can be induced by allowing lap splices in main column bars to slip or by allowing continuous main column bars to cause shear cracking in the footing.

For spread footings supporting low- to medium-height single columns, rocking behavior of the bent should be investigated for stability and the footing capacity can be compared against the resulting forces from the rocking analysis. These forces can be of lesser magnitude than forces induced by column plastic hinging. Typically, retrofits for this case consists of adding an overlay to enhance the footing shear

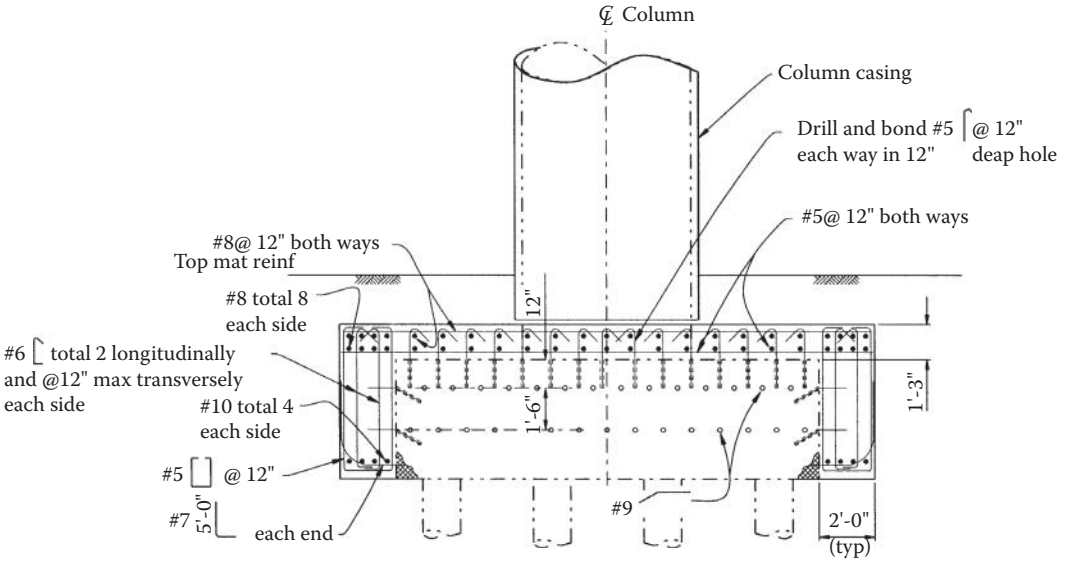

FIGURE 13.30 Widening footing retrofit.

capacity or even widening of the footing to gain larger footprint for stability and increase of the flexural moment capacity. The new concrete is securely attached to the old footing. This is done by chipping away at the concrete around the existing reinforcement and welding or mechanically coupling the new reinforcement to the existing bars. Holes are then drilled and the dowels are bonded between the faces of the existing and new concrete as shown in Figure 13.30.

For spread footings supporting a tall single column, rocking behavior of the bent can lead to instability and some additional piles might be needed to provide stability to the tall bent. Columns retrofitted with a type F casing will induce increased shear and increased tension demands on the top fiber of existing footings. These demands typically will require adding a top mat of reinforcement to the footing (Figure 13.30). The top mat is tied to the existing footing with dowels and concrete is placed over the new piles and reinforcement. Where high compression capacity piles are added, reinforcement with an extension hook is welded or mechanically coupled to the existing bottom reinforcement. The hook acts to confine the concrete where the perimeter piles are under compression demand.

When tension capacity is needed, the use of standard tension/compression piles is preferred to the use of tie-downs. In strong seismic events, large movements in footings are associated with tie-downs. Generally, tie-downs cannot be prestressed to reduce movements without overloading existing piles and compression. The tie-downs movements are probably not a serious problem with short columns where P-Δ effect are minimal. Also, tie-downs should be avoided where ground water could affect the quality of installation.

For pile cap footings, the ability of existing piles to cause tension on top fiber of the footing where no reinforcement is present can lead to footing failure. Therefore, adding a top overlay in conjunction with footing widening might be necessary.

In sites where soft soil exists, the use of larger piles of diameters 24 in. (600 mm) and above may be deemed necessary. These larger piles may induce high flexural demands requiring additional capacity from the bottom reinforcement. In this situation, prestressing of the footing becomes an alternative solution since it enhances the footing flexural capacity in addition to confining the concrete where perimeter piles act in compression (Figure 13.31). This retrofit is seldom used and is considered as a last recourse.

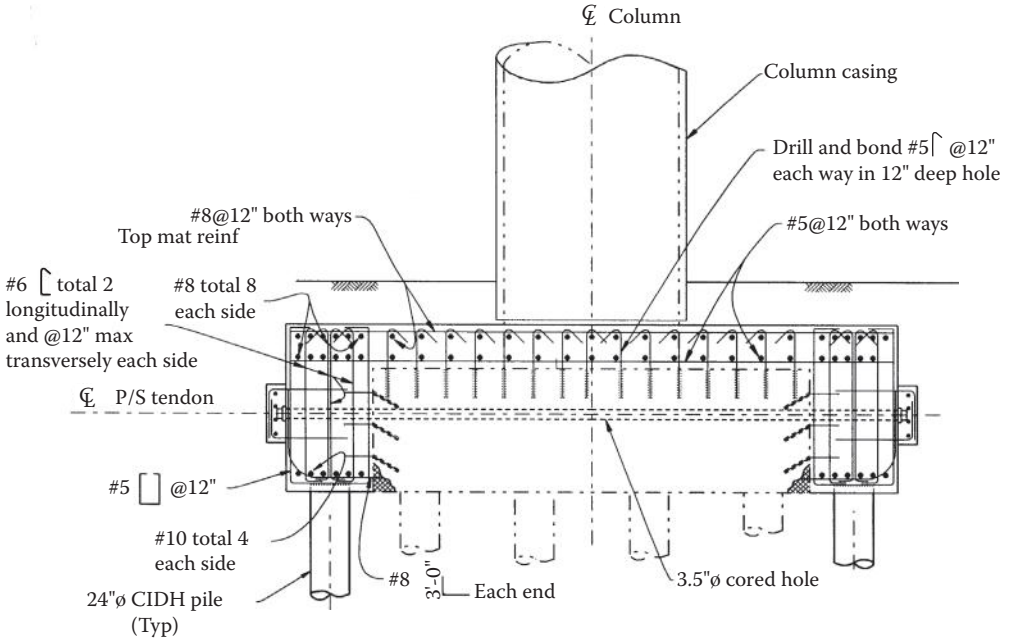

FIGURE 13.31 Footing retrofit using prestressing.

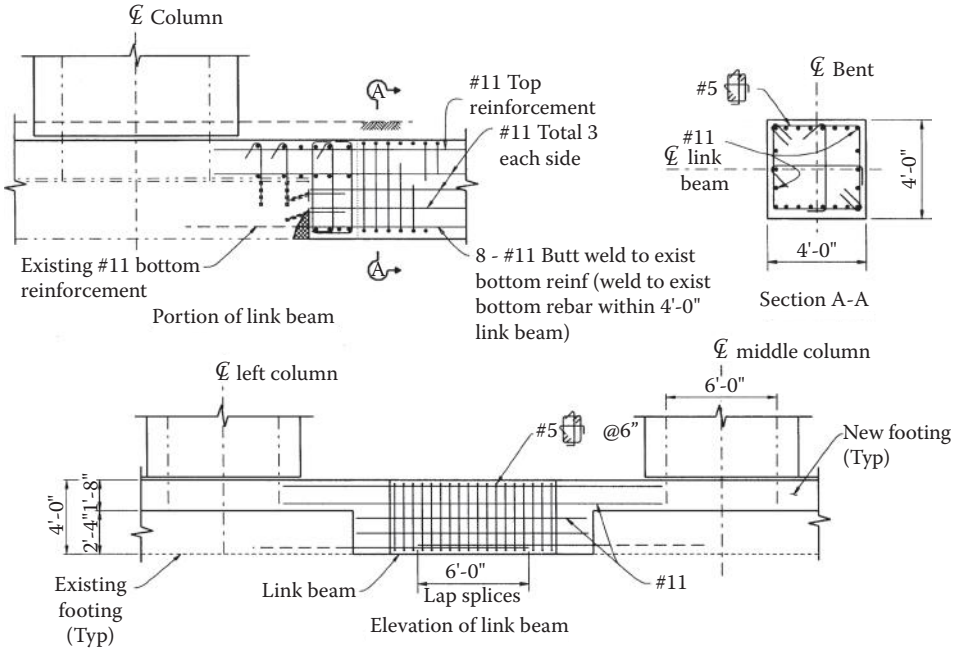

FIGURE 13.32 Link beam footing retrofit.

A rare but interesting situation occurs when a tall, multicolumn bent has pinned connections to the superstructure instead of the usual monolithic connections and is resting on relatively small spread footings. This type of bent is quite vulnerable under large overturning moments and the use of link beams, as shown in Figure 13.32, is considered economical and sufficient to provide adequate stability and load transfer mechanism in a seismic event.

13.5 Summary

The seismic-resistant retrofit design of bridges has been evolving dramatically since the 1989 Loma Perita Earthquake. Many of the retrofit concepts and details discussed in this chapter have emerged as a result of research efforts and evaluation of bridge behavior in past earthquakes. This practice has been successfully tested in relatively moderate earthquakes but has not yet seen the severe test of a large magnitude earthquake. The basic philosophy of current seismic retrofit technology in the United States is to prevent collapse by providing sufficient seat for displacement to take place or by allowing ductility in the supporting members. The greatest challenge to this basic philosophy will be the next big earthquake. This will serve as the utmost test to current predictions of earthquake demands on bridge structures.

References

Caltrans. 2008. *Bridge Design Aids (BDA) 14-1: Hinge Restrainer Design Method*, California Department of Transportation, Sacramento, CA.

Caltrans. 2010a. *Memo To Designers (MTD) 20-4: Seismic Retrofit Guidelines For Bridges In California*, California Department of Transportation, Sacramento, CA.

Caltrans. 2010b. *Bridge Memo to Designers (MTD) 20-1:- Seismic Design Methodology*, California Department of Transportation, Sacramento, CA.

FHWA. 2006. *Seismic Retrofitting Manual For Highway Structures: Part 1 – Bridges, FHWA-HRT-06-032*, Federal Highway Administration, U.S. Department of Transportation, Turner-Fairbank Highway Research Center, 6300 Georgetown Pike, McLean, VA.

Haroun, M. A., Pardoen, G. C., Shepherd, R., Haggag, H. A., Kazanjy, R. P. 1993. *Cyclic Behavior of Bridge Pier Walls for Retrofit*, CA 92717-2175, Department of Civil and Environmental Engineering, University of California, Irvine, Irvine, CA.

Mander, J. B., Priestley, M. J. N., and Park, R. 1988. "Theoretical Stress-Strain Model for Confined Concrete," *Journal of Structural Engineering*, ASCE, 114(8), 1804–1826.

Priestley, M. J. N. and Seible, F. 1991. *Seismic Assessment and Retrofit of Bridges*, *SSRP-91/03*, July, Department of Applied Mechanics and Engineering Sciences, University of California, San Diego, La Jolla, CA.

14

Soil–Foundation–Structure Interaction

Wen-Shou Tseng
Paul C. Rizzo Associates, Inc.

Joseph Penzien
International Civil Engineering Consultants, Inc.

14.1 Introduction

Prior to the 1971 San Fernando, California earthquake, nearly all damages to bridges during earthquakes were caused by ground failures, such as liquefaction, differential settlement, slides, and/or spreading; little damage was caused by seismically induced vibrations. Vibratory response considerations had been limited primarily to wind excitations of large bridges, the great importance of which was made apparent by the failure of the Tacoma Narrows suspension bridge in the early 1940s, and to moving-loads and impact excitations of smaller bridges.

The importance of designing bridges to withstand the vibratory response produced during earthquakes was revealed by the 1971 San Fernando earthquake, during which many bridge structures collapsed. Similar bridge failures occurred during the 1989 Loma Prieta and 1994 Northridge, California earthquakes, and the 1995 Kobe, Japan earthquake. As a result of these experiences, much has been done recently to improve provisions in seismic design codes, advance modeling and analysis procedures, and

develop more effective detail designs, all aimed at insuring that newly designed and retrofitted bridges will perform satisfactorily during future earthquakes.

Unfortunately, many of the existing older bridges in the United States and other countries, which are located in regions of moderate to high seismic intensity, have serious deficiencies that threaten life safety during future earthquakes. Because of this threat, aggressive actions have been taken in California, and elsewhere, to retrofit such unsafe bridges, bringing their expected performances during future earthquakes to an acceptable level. To meet this goal, retrofit measures have been applied to the superstructures, piers, abutments, and foundations.

It is because of this most recent experience that the importance of coupled soil–foundation–structure interaction (SFSI) on the dynamic response of bridge structures during earthquakes has been fully realized. In treating this problem, two different methods have been used: (1) the "elasto-dynamic" method developed and practiced in the nuclear power industry for large foundations, and (2) the so-called "empirical *p–y*" method developed and practiced in the offshore oil industry for pile foundations. Each method has its own strong and weak characteristics, which generally are opposite to those of the other, thus restricting their proper use to different types of bridge foundation. By combining the models of these two methods in series form, a hybrid method is reported herein that makes use of the strong features of both methods, while minimizing their weak features. While this hybrid method may need some further development and validation at this time, it is fundamentally sound; thus, it is expected to become a standard procedure in treating seismic SFSI of large bridges supported on different types of foundation.

The subsequent sections of this chapter discuss all aspects of treating seismic SFSI by the "elasto-dynamic," "empirical *p–y*," and "hybrid" methods, including generating seismic inputs, characterizing soil-foundation systems, conducting force/deformation demand analyses using the substructuring approach, performing force/deformation capacity evaluations, and judging overall bridge performance. The last section presents the latest development of SFSI.

14.2 Description of SFSI Problems

The broad problem of assessing the response of an engineered structure interacting with its supporting soil or rock medium (hereafter called soil medium for simplicity) under static and/or dynamic loadings will be referred herein as the "soil–structure interaction (SSI)" problem. For a building that generally has its superstructure above ground fully integrated with its substructure below, reference to the SSI problem is appropriate when describing the problem of interaction between the complete system and its supporting soil medium. However, for a long bridge structure, consisting of a super structure supported on multiple piers and abutments having independent and often distinct foundation systems, which in turn are supported on the soil medium, the broader problem of assessing interaction in this case is more appropriately and descriptively referred to as the "soil–foundation–structure interaction (SFSI)" problem. For convenience, the SFSI problem can be separated into two subproblems, namely, a "soil–foundation interaction (SFI)" problem and a "foundation–structure interaction (FSI)" problem. Within the context of SFSI, the SFI part of the total problem is the one to be emphasized, since, once it is solved, the FSI part of the total problem can be solved following conventional structural response analysis procedures. Because the interaction between soil and a bridge's foundations makes up the core of an SFSI problem, it is useful to review the different types of bridge foundations that may be encountered in dealing with this problem.

14.2.1 Bridge Foundation Types

From the perspective of SFSI, the foundation types commonly used for supporting bridge piers can be classified in accordance with their soil-support configurations into four general types, namely, (1) spread footings, (2) caissons, (3) large-diameter shafts, and (4) slender-pile groups. These types as described separately below are shown in Figure 14.1.

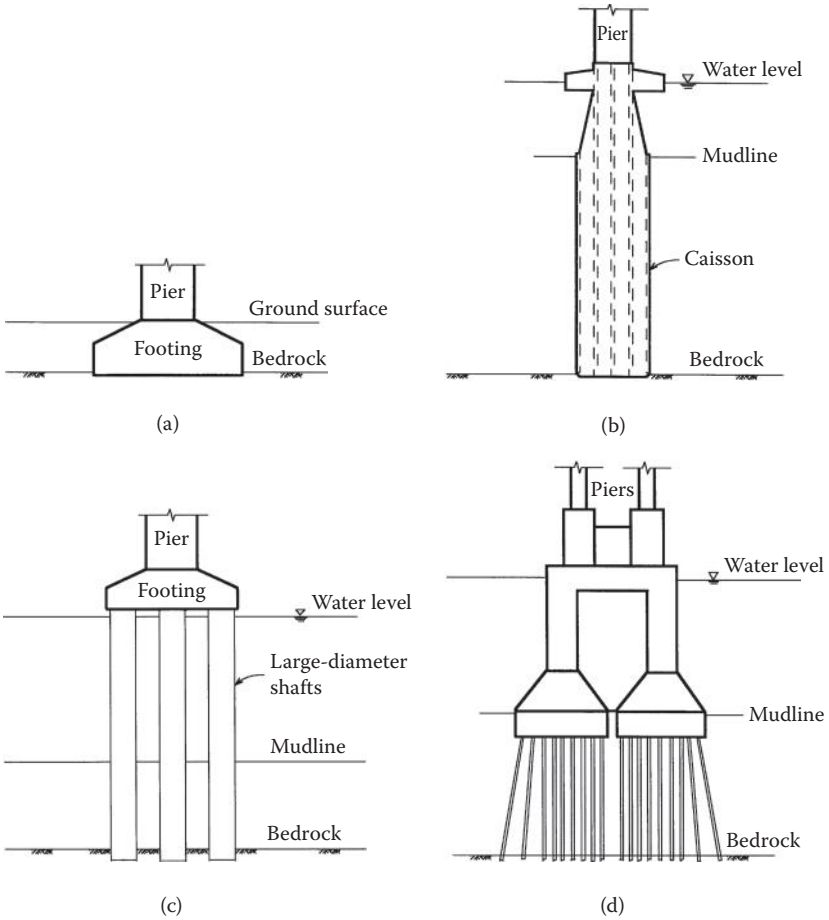

FIGURE 14.1 Bridge foundation types: (a) spread footing; (b) caisson; (c) large-diameter shafts; and (d) slender-pile group.

14.2.1.1 Spread Footings

Spread footings bearing directly on soil or rock are used to distribute the concentrated forces and moments in bridge piers and/or abutments over sufficient areas to allow the underlying soil strata to support such loads within allowable soil bearing pressure limits. Of these loads, lateral forces are resisted by a combination of friction on the foundation bottom surface and passive soil pressure on its embedded vertical face. Spread footings are usually used on competent soils or rock that have high allowable bearing pressures. These foundations may be of several forms, such as (1) isolated footings, each supporting a single column or wall pier, (2) combined footings, each supporting two or more closely spaced bridge columns, and (3) pedestals that are commonly used for supporting steel bridge columns where it is desirable to terminate the structural steel above grade for corrosion protection. Spread footings are generally designed to support the superimposed forces and moments without uplifting or sliding. As such, inelastic action of the soils supporting the footings is usually not significant.

14.2.1.2 Caissons

Caissons are large structural foundations, usually in water, that permit dewatering to provide a dry condition for excavation and construction of the bridge's foundations. They can take many forms to suit specific site conditions and can be constructed of reinforced concrete, steel, or composite steel and

concrete. Most caissons are in the form of a large cellular rectangular box or cylindrical shell structure with a sealed base. They extend up from deep firm soil or rock-bearing strata to above mudline where they support the bridge piers. The cellular spaces within the caissons are usually flooded and filled with sand to some depth for greater stability. Caisson foundations are commonly used at deep water sites having deep soft soils. Transfer of the imposed forces and moments from a single pier takes place by direct bearing of the caisson base on its supporting soil or rock stratum and by passive resistance of the side soils over the embedded vertical face of the caisson. Since the soil-bearing area and the structural rigidity of a caisson is very large, the transfer of forces from the caisson to the surrounding soil usually involves negligible inelastic action at the soil/caisson interface.

14.2.1.3 Large-Diameter Shafts

These foundations consist of one or more large-diameter, usually in the range of 4 to 12 ft. (1.2 to 3.6 m), reinforced-concrete cast-in-drilled hole (CIDH) or concrete cast-in-steel-shell (CISS) piles. Such shafts are embedded in the soils to sufficient depths to reach firm soil strata or rock where a high degree of fixity can be achieved, thus allowing the forces and moments imposed on the shafts to be safely transferred to the embedment soils within allowable soil-bearing pressure limits and/or allowable foundation displacement limits. The development of large-diameter drilling equipment has made this type of foundation economically feasible; thus, its use has become increasingly popular. In actual applications, the shafts often extend above ground surface or mudline to form a single pier or a multiple-shaft pier foundation. Because of their larger expected lateral displacements as compared to those of a large caisson, a moderate level of local soil nonlinearities is expected to occur at the soil/shaft interfaces, especially near the ground surface or mudline. Such nonlinearities may have to be considered in design.

14.2.1.4 Slender-Pile Groups

Slender piles refer to those piles having a diameter or cross-section dimensions less than 2 ft. (0.6 m). These piles are usually installed in a group and provided with a rigid cap to form the foundation of a bridge pier. Piles are used to extend the supporting foundations (pile caps) of a bridge down through poor soils to more competent soil or rock. A pile's resistance to a vertical load may be essentially by point bearing when it is placed through very poor soils to a firm soil stratum or rock, or by friction in case of piles that do not achieve point bearing. In real situations, the vertical resistance is usually achieved by a combination of point bearing and side friction. Resistance to lateral loads is achieved by a combination of soil passive pressure on the pile cap, soil resistance around the piles, and flexural resistance of the piles. The uplift capacity of a pile is generally governed by the soil friction or cohesion acting on the perimeter of the pile. Piles may be installed by driving or by casting in drilled holes. Driven piles may be timber piles, concrete piles with or without prestress, steel piles in the form of pipe sections, or steel piles in the form of structural shapes (e.g., H shape). Cast-in-drilled-hole piles are reinforced-concrete piles installed with or without steel casings. Because of their relatively small cross-section dimensions, soil resistance to large pile loads usually develops large local soil nonlinearities that must be considered in design. Furthermore, since slender piles are normally installed in a group, mutual interactions among piles will reduce overall group stiffness and capacity. The amounts of these reductions depend on the pile-to-pile spacing and the degree of soil nonlinearity developed in resisting the loads.

14.2.2 Definition of the SFSI Problem

For a bridge subjected to externally applied static and/or dynamic loadings on the above-ground portion of the structure, the SFSI problem involves evaluation of the structural performance (demand/capacity ratio) of the bridge under the applied loadings taking into account the effect of SFI. Since in this case the ground has no initial motion prior to loading, the effect of SFI is to provide the

foundation-structure system with a flexible boundary condition at the soil–foundation interface location when static loading is applied and a compliant boundary condition when dynamic loading is applied. The SFI problem in this case therefore involves (1) evaluation of the soil–foundation interface boundary flexibility or compliance conditions for each bridge foundation, (2) determination of the effects of these boundary conditions on the bridge's overall structural response (e.g., force, moment, or deformation) demands, and (3) evaluation of the resistance capacity of each soil–foundation system that can be compared with the corresponding response demand in assessing performance. That part of determining the soil–foundation interface boundary flexibilities or compliances will be referred to subsequently in a gross term as the "foundation stiffness or impedance problem;" that part of determining the bridge's structural response as affected by the soil–foundation boundary flexibilities or compliances will be referred to as the "foundation–structure interaction problem;" and that part of determining the resistance capacity of the soil–foundation system will be referred to as the "foundation capacity problem."

For a bridge structure subjected to seismic conditions, dynamic loadings are imposed on the structure. These loadings, which originate with motions of the soil medium, are transmitted to the structure through its foundations; therefore, the overall SFSI problem in this case involves, in addition to the foundation impedance, foundation–structure interaction, and foundation capacity problems described above, the evaluation of (1) the soil forces acting on the foundations as induced by the seismic ground motions, referred to subsequently as the "seismic driving forces," and (2) the effects of the free-field, ground-motion-induced soil deformations on the soil–foundation boundary compliances and on the capacity of the soil–foundation systems. In order to evaluate the seismic driving forces on the foundations and the effects of the free-field ground deformations on compliances and capacities of the soil–foundation systems, it is necessary to determine the variations of the free-field motion within the ground regions that interact with the foundations. This problem of determining the free-field ground-motion variations will be referred to herein as the "free-field site response problem." As shown later, the problem of evaluating the seismic driving forces on the foundations is equivalent to determining the "effective or scattered foundation input motions" induced by the free-field soil motions. This problem is referred to herein as the "foundation scattering problem."

Thus, the overall SFSI problem for a bridge subjected to externally applied static and/or dynamic loadings can be separated into the evaluation of (1) foundation stiffnesses or impedances, (2) foundation–structure interactions, and (3) foundation capacities. For a bridge subjected to seismic ground motion excitations, the SFSI problem involves two additional steps, namely, the evaluation of free-field site response and foundation scattering. When solving the total SFSI problem, the effects of the nonzero soil deformation state induced by the free-field seismic ground motions should be evaluated in all five steps mentioned above.

14.2.3 Demand versus Capacity Evaluations

As described previously, assessing the seismic performance of a bridge system requires evaluation of SFSI involving two parts. One part is the evaluation of the effects of SFSI on the seismic-response demands within the system; the other part is the evaluation of the seismic force and/or deformation capacities within the system. Ideally, a well-developed methodology should be one that is capable of solving these two parts of the problem concurrently in one step using a unified suitable model for the system. Unfortunately, to date, such a unified method has not yet been developed. Because of the complexities of a real problem and the different emphases usually demanded of the solutions for the two parts, different solution strategies and methods of analysis are warranted for solving these two parts of the overall SFSI problem. To be more specific, evaluation on the demand side of the problem is concerned with the overall SFSI system behavior that is controlled by the mass, damping (energy dissipation), and stiffness properties, or collectively, the impedance properties, of the entire system; and, the solution must satisfy the global system's dynamic equilibrium and compatibility conditions. This system behavior is

not sensitive, however, to approximations made on local element behavior; thus, its evaluation does not require sophisticated characterizations of the detailed constitutive relations of its local elements. For this reason, evaluation of demand has often been carried out using a linear or equivalent linear analysis procedure. On the contrary, evaluation of capacity must be concerned with the extreme behavior of local elements or subsystems; therefore, it must place emphasis on the detailed constitutive behaviors of the local elements or subsystems when deformed up to near-failure levels. Since only local behaviors are of concern, the evaluation does not have to fully satisfy the system's global equilibrium and compatibility conditions. For this reason, evaluation of capacity is often obtained by conducting nonlinear analyses of detailed local models of elements or subsystems or by testing of local members, connections, or subassemblages, subjected to simple pseudo-static loading conditions.

Because of the distinct differences between effective demand and capacity analyses as described above, the analysis procedures presented subsequently differentiate between these two parts of the overall SFSI problem.

14.3 Current State of the Practice

The evaluation of SFSI effects on bridges located in regions of high seismicity has not received as much attention as for other critical engineered structures, such as dams, nuclear facilities, and offshore structures. In the past, the evaluation of SFSI effects for bridges has, in most cases, been regarded as a part of the bridge foundation design problem. As such, emphasis has been placed on the evaluation of load-resisting capacities of various foundation systems with relatively little attention having been given to the evaluation of SFSI effects on seismic-response demands within the complete bridge system. Only recently have formal SSI analysis methodologies and procedures been developed and applied in other industries and been adopted and applied to seismic performance evaluations of bridges (Mylonakis et al. 1997), especially large important bridges (Lam and Law 1996; Tseng 1996).

Even though the SFSI problems for bridges pose their own distinct features (e.g., multiple independent foundations of different types supported in highly variable soil conditions ranging from soft to very soft), the current practice is to adopt, with minor modifications, the same methodologies and procedures developed and practiced in other industries, most notably, the nuclear power and offshore oil industries. Depending upon the foundation type and its soil support condition, the procedures currently being used in evaluating SFSI effects on bridges can broadly be classified into two main methods, namely, the so-called "elasto-dynamic" method that has been developed and practiced in the nuclear power industry for large foundations, and the so-called "empirical p–y" method that has been developed and practiced in the offshore oil industry for pile foundations. The bases and applicabilities of these two methods are described separately below.

14.3.1 Elasto-Dynamic Method

This method is based on the well-established elasto-dynamic theory of wave propagation in a linear elastic, viscoelastic, or constant-hysteresis-damped elastic half-space soil medium. The fundamental element of this method is the constitutive relation between an applied harmonic point load and the corresponding dynamic response displacements within the medium called *the dynamic Green's functions*. Since these functions apply only to a linear elastic, visoelastic, or constant-hysteresis-damped elastic medium, they are valid only for linear SFSI problems. Since application of the elasto-dynamic method of analysis uses only mass, stiffness, and damping properties of an SFSI system, this method is suitable only for global-system response-analysis applications. However, by adopting the same equivalent linearization procedure as that used in the seismic analysis of free-field soil response, for example, that used in the computer program SHAKE (Schnabel et al. 1972), the method has been extended to one that can accommodate global soil nonlinearities, that is, those nonlinearities induced in the free-field soil medium by the free-field seismic waves (Tseng and Hadjian 1991).

Application of the elasto-dynamic theory to dynamic SFSI started with the need for solving machine-foundation vibration problems (Richart et al. 1970). Along with other rapid advances in earthquake engineering in the 1970s, application of this theory was extended to solving seismic SSI problems for building structures, especially those of nuclear power plants (Veletsos et al. 1971; Kausel and Roesset 1974; Wong and Luco 1976). Such applications were enhanced by concurrent advances in analysis techniques for treating soil dynamics, including development of the complex-modulus representation of dynamic soil properties and use of the equivalent linearization technique for treating ground-motion-induced soil nonlinearities (Seed and Idriss 1970; Schnabel et al. 1972; Waas 1972; and Lysmer et al. 1975). These developments were further enhanced by the extensive model calibration and methodology validation and refinement efforts carried out in a comprehensive large-scale SSI field experimental program undertaken by the Electric Power Research Institute (EPRI) in the 1980s (Tang 1989). All of these efforts contributed to advancing the elasto-dynamic method of SSI analysis currently being practiced in the nuclear power industry (Tseng and Hadjian 1991).

Because the elasto-dynamic method of analysis is capable of incorporating mass, stiffness, and damping characteristics of each soil, foundation, and structure subsystem of the overall SFSI system, it is capable of capturing the dynamic interactions between the soil and foundation subsystems and between the foundations and structure subsystem; thus, it is suitable for seismic demand analyses. However, since the method does not explicitly incorporate strength characteristics of the SFSI system, it is not suitable for capacity evaluations.

As previously mentioned in Section 14.2.1, there are four types of foundation commonly used for bridges, namely, (1) spread footings, (2) caissons, (3) large-diameter shafts, and (4) slender-pile groups. Since only small local soil nonlinearities are induced at the soil–foundation interfaces of spread footings and caissons, application of the elasto-dynamic method of seismic demand analysis of the complete SFSI system is valid. However, the validity of applying this method to large-diameter shaft foundations depends on the diameter of the shafts and on the amplitude of the imposed loadings. When the shaft diameter is large so that the load amplitudes produce only small local soil nonlinearities, the method is reasonably valid. However, when the shaft diameter is relatively small, the larger-amplitude loadings will produce local soil nonlinearities sufficiently large to require that the method be modified as discussed subsequently. Application of the elasto-dynamic method to slender-pile groups is usually invalid because of the large local soil nonlinearities that develop near the pile boundaries. Only for very low-amplitude loadings can the method be used for such foundations.

14.3.2 Empirical "*P–Y*" Method

This method was originally developed for the evaluation of pile-foundation response due to lateral loads (Matlock and Reese 1961; Matlock 1970; Reese et al. 1974) applied externally to offshore structures. As used, it characterizes the lateral soil resistance per unit length of pile, p, as a function of the lateral displacement, y. The "p–y" relation is generally developed on the basis of an empirical curve that reflects the nonlinear resistance of the local soil surrounding the pile at a specified depth (see Figure 14.2). Construction of the curve depends mainly on soil material strength parameters, for example, the friction angle, ϕ, for sands and cohesion, c, for clays at the specified depth. For shallow soil depths where soil surface effects become important, construction of these curves also depends on the local soil failure mechanisms, such as failure by a passive soil resistance wedge. Typical "p–y" curves developed for a pile at different soil depths are shown in Figure 14.3. Once the set of "p–y" curves representing the soil resistances at discrete values of depth along the length of the pile has been constructed, evaluation of pile response under a specified set of lateral loads is accomplished by solving the problem of a beam supported laterally on discrete nonlinear springs. The validity and applicability of this method are based on model calibrations and correlations with field experimental results (Matlock 1970; Reese et al. 1974; and others).

On the basis of the same model considerations used in developing the "p–y" curves for lateral response analysis of piles, the method has been extended to treating the axial resistance of soils to piles per unit

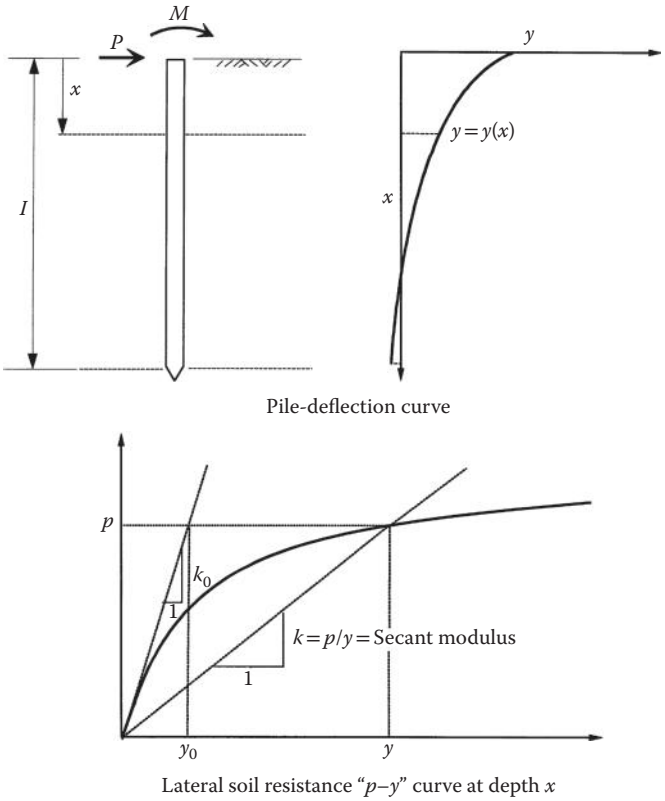

FIGURE 14.2 Empirical *p–y* curves and secant modulus.

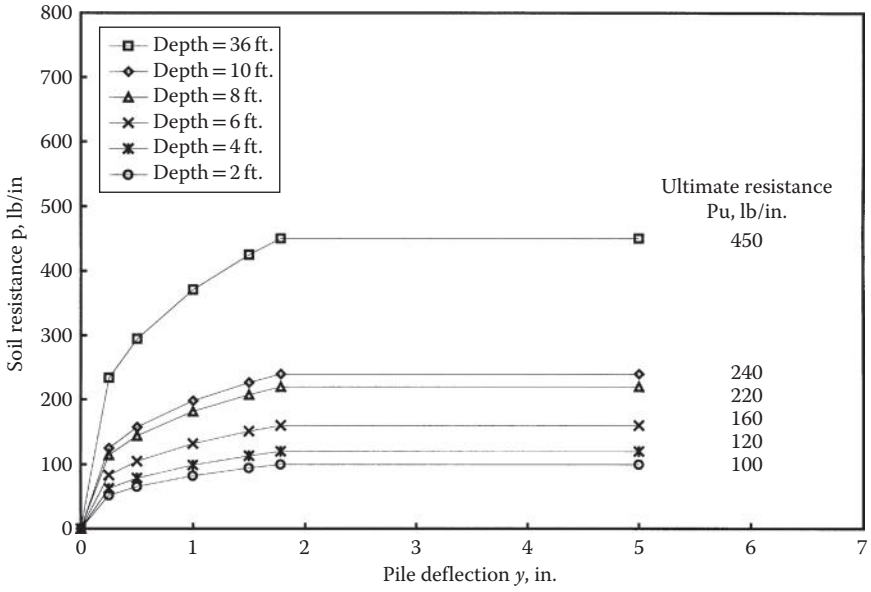

FIGURE 14.3 Typical *p–y* curves for a pile at different depths.

length of pile, *t*, as a nonlinear function of the corresponding axial displacement, *z*, resulting in the so-called axial "*t–z*" curve, and treating the axial resistance of the soils at the pile tip, *Q*, as a nonlinear function of the pile tip axial displacement, *d*, resulting in the so-called "*Q–d*" curve. Again, the construction of the "*t–z*" and "*Q–d*" curves for a soil-supported pile is based on empirical curvilinear forms and the soil strength parameters as functions of depth. Utilizing the set of "*p–y*," "*t–z*," and "*Q–d*" curves developed for a pile foundation, the response of the pile subjected to general three-dimensional (3-D) loadings applied at the pile head can be solved using the model of a 3-D beam supported on discrete sets of nonlinear lateral "*p–y*," axial "*t–z*," and axial "*Q–d*" springs. The method as described above for solving a soil-supported pile foundation subjected to applied loadings at the pile head is referred herein as the empirical "*p–y*" method, even though it involves not just the lateral "*p–y*" curves but also the axial "*t–z*" and "*Q–d*" curves for characterizing the soil resistances.

Since this method depends primarily on soil-resistance strength parameters and does not incorporate soil mass, stiffness, and damping characteristics, it is, strictly speaking, only applicable for capacity evaluations of slender-pile foundations and is not suitable for seismic demand evaluations because, as mentioned previously, a demand evaluation for an SFSI system requires the incorporation of the mass, stiffness, and damping properties of each of the constituent parts, namely, the soil, foundation, and structure subsystems.

Even though the "*p–y*" method is strictly not suited to demand analyses, it is current practice in performing seismic-demand evaluations for bridges supported on slender-pile group foundations to make use of the empirical nonlinear "*p–y*," "*t–z*," and "*Q–d*" curves in developing a set of equivalent-linear lateral and axial soil springs attached to each pile at discrete elevations in the foundation. The soil-pile systems developed in this manner are then coupled with the remaining bridge structure to form the complete SFSI system for use in a seismic demand analysis. The initial stiffnesses of the equivalent-linear "*p–y*," "*t–z*," and "*Q–d*" soil springs are based on secant moduli of the nonlinear "*p–y*," "*t–y*," and "*Q–d*" curves, respectively, at preselected levels of lateral and axial pile displacements, as shown schematically in Figure 14.2. After completing the initial demand analysis, the amplitudes of pile displacement are compared with the corresponding preselected amplitudes to check on their mutual compatibilities. If incompatibilities exist, the initial set of equivalent-linear stiffnesses is adjusted and a second demand analysis is performed. Such iterations continue until reasonable compatibility is achieved. Since soil inertia and damping properties are not included in the above-described demand-analysis procedure, it must be considered as being approximate; however, it is reasonably valid when the nonlinearities in the soil resistances become so large that the inelastic components of soil deformations adjacent to piles are much larger than the corresponding elastic components. This condition is true for a slender-pile group foundation subjected to relatively large amplitude pile-head displacements. However, for a large-diameter shaft foundation, having larger soil bearing areas and higher shaft stiffnesses, the inelastic components of soil deformations may be of the same order or even smaller than the elastic components; in which case, application of the empirical "*p–y*" method for a demand analysis as described previously can result in substantial errors.

14.4 Seismic Inputs to SFSI System

The first step in conducting a seismic performance evaluation of a bridge structure is to define the seismic input to the coupled soil–foundation–structure system. In a design situation, this input is defined in terms of the expected free-field motions in the soil region surrounding each bridge foundation. It is evident that to precisely characterize such motions is practically unachievable within the present state of knowledge of seismic ground motions. Therefore, it is necessary to use a rather simplistic approach in generating such motions for design purposes. The procedure most commonly used for designing a large bridge is to (1) generate a three-component (two horizontal and vertical) set of accelerograms representing the free-field ground motion at a "control point" selected for the bridge site, and (2) characterize the spatial variations of the free-field motions within each soil region of interest relative to the control motions.

The control point is usually selected at the surface of bedrock (or surface of a firm soil stratum in case of a deep soil site), referred to herein as "rock outcrop," at the location of a selected reference pier; and the free-field seismic wave environment within the local soil region of each foundation is assumed to be composed of vertically propagating plane shear (*S*) waves for the horizontal motions and vertically propagating plane compression (*P*) waves for the vertical motions. For a bridge site consisting of relatively soft top soil deposits overlying competent soil strata or rock, the assumption of vertically propagating plane waves over the depth of the foundations is reasonably valid as confirmed by actual field downhole array recordings (Chang et. al 1989).

The design ground motion for a bridge is normally specified in terms of a set of parameter values developed for the selected control point, which include a set of target acceleration response spectra (ARS) and a set of associated ground motion parameters for the design earthquake, namely (1) magnitude, (2) source-to-site distance, (3) peak ground (rock-outcrop) acceleration (PGA), velocity (PGV), and displacement (PGD), and (4) duration of strong shaking. For large important bridges, these parameter values are usually established through regional seismic investigations coupled with site-specific seismic hazard and ground motion studies; whereas, for small bridges, it is customary to establish these values based on generic seismic study results such as contours of regional PGA values and standard ARS curves for different general classes of site soil conditions.

For a long bridge supported on multiple piers that are in turn supported on multiple foundations spaced relatively far apart, the spatial variations of ground motions among the local soil regions of the foundations need also be defined in the seismic input. On the basis of the results of analyses using actual earthquake ground motion recordings obtained from strong motion instrument arrays, such as the El Centro differential array in California and the SMART-1 array in Taiwan, the spatial variations of free-field seismic motions have been characterized using two parameters, namely, (1) apparent horizontal wave propagation velocity (speed and direction) that controls the first-order spatial variations of ground motion due to the seismic wave passage effect and (2) a set of horizontal and vertical ground-motion "coherency functions" that quantifies the second-order ground-motion variations due to scattering and complex 3-D wave propagation (Abrahamson 1992). Thus, in addition to the design ground motion parameter values specified for the control motion, characterizing the design seismic inputs to long bridges needs to include the two additional parameters mentioned above, namely, (1) apparent horizontal wave velocity and (2) ground motion coherency functions; therefore, the seismic input motions developed for the various pier-foundation locations need to be compatible with the values specified for these two additional parameters.

Having specified the design seismic ground-motion parameters, the steps required in establishing the pier-foundation location-specific seismic input motions for a particular bridge are as follows: (1) develop a three-component (two horizontal and vertical) set of free-field rock-outcrop motion time histories that are compatible with the design target ARS and associated design ground motion parameters applicable at a selected single control-point location at the bridge site (these motions are referred to herein simply as the "response-spectrum-compatible time histories" of control motion), (2) generate response-spectrum-compatible time histories of free-field rock-outcrop motions at each bridge pier-support location such that their coherencies relative to the corresponding components of the response-spectrum-compatible motions at the control-point and at other pier-support locations are compatible with the wave passage parameters and the coherency functions specified for the site (these motions are referred to herein as "response-spectrum-and-coherency-compatible motions), and (3) carry out free-field site-response analyses for each pier-support location to obtain the time histories of free-field soil motions at specified discrete elevations over the full depth of each foundation using the corresponding response-spectrum-and-coherency-compatible free-field rock-outcrop motions as inputs.

In the following sections, procedures are presented for generating the set of response-spectrum-compatible rock-outcrop time histories of motion at the control-point location and for generating the sets of response-spectrum-and-coherency-compatible rock-outcrop time histories of motion at all pier-support locations, and guidelines are given for performing free-field site-response analyses.

14.4.1 Free-Field Rock-Outcrop Motions at Control-Point Location

Given a prescribed set of target ARS and a set of associated design ground motion parameters for a bridge site as described previously, the objective herein is to develop a three-component set of time histories of control motion that (1) provides a reasonable match to the corresponding target ARS and (2) has time-history characteristics reasonably compatible with the other specified associated ground motion parameter values. In the past, several different procedures have been used for developing rock-outcrop time histories of motion compatible with a prescribed set of target ARS. These procedures are summarized as follows:

1. Response-Spectrum Compatibility Time-History Adjustment Method (Gasparini and Vanmarcke 1976; Silva and Lee 1987; Lilhanand and Tseng 1988; Bolt and Gregor 1993)—This method as generally practiced starts by selecting a suitable three-component set of initial or "starting" accelerograms and proceeds to adjust each of them iteratively, using either a time-domain (Lilhanand and Tseng 1988; Abrahamson 1992a) or a frequency-domain (Gasparini and Vanmarcke 1976; Silva and Lee 1987; Bolt and Gregor 1993) procedure, to achieve compatibility with the specified target ARS and other associated parameter values. The time-domain adjustment procedure usually produces only small local adjustments to the selected starting time histories, thereby producing response-spectrum-compatible time histories closely resembling the initial motions. The general "phasing" of the seismic waves in the starting time history is largely maintained while achieving close compatibility with the target ARS: minor changes do occur, however, in the phase relationships. The frequency domain procedure as commonly used retains the phase relationships of an initial motion, but does not always provide as close a fit to the target spectrum as does the time-domain procedure. Also, the motion produced by the frequency-domain procedure shows greater visual differences from the initial motion.
2. Source-to-Site Numerical Model Time-History Simulation Method (Papageorgiou and Aki 1983; Silva and Lee 1987; Bolt 1987; Boore and Akinson 1987; Sommerville and Helmberger 1990)—This method generally starts by constructing a numerical model to represent the controlling-earthquake source and source-to-site transmission and scattering functions and then accelerograms are synthesized for the site using numerical simulations based on various plausible fault-rupture scenarios. Because of the large number of time-history simulations required in order to achieve a "stable" average ARS for the ensemble, this method is generally not practical for developing a complete set of time histories to be used directly; rather it is generally used to supplement a set of actual recorded accelerograms, in developing site-specific target response spectra and associated ground motion parameter values.
3. Multiple Actual Recorded Time-History Scaling Method (NRC 1989; ICBO 2012)—This method starts by selecting multiple three-component sets (generally ≥ 7) of actual recorded accelerograms that are subsequently scaled in such a way that the average of their response spectral ordinates over the specified frequency (or period) range of interest matches the target ARS. Experience in applying this method shows that its success depends very much on the selection of time histories. Because of the lack of suitable recorded time histories, individual accelerograms often have to be scaled up or down by large multiplication factors, thus raising questions about the appropriateness of such scaling. Experience also indicates that, unless a large ensemble of time histories (typically > 20) is selected, it is generally difficult to achieve matching of the target ARS over the entire spectral frequency (or period) range of interest.
4. Connecting Accelerogram Segments Method (Seed and Idriss 1969a)—This method produces a synthetic time history by connecting together segments of a number of actual recorded accelerograms in such a way that the ARS of the resulting time history fits the target ARS reasonably well. It generally requires producing a number of synthetic time histories to achieve acceptable matching of the target spectrum over the entire frequency (or period) range of interest.

At the present time, Method 1 is considered most suitable and practical for bridge engineering applications. In particular, the time-domain time-history adjustment procedure that produces only local time-history disturbances has been applied widely in recent applications. This method, as developed by Lilhanand and Tseng (1988), which is based on earlier work by Kaul (1978), is described below.

The time-domain procedure for time-history adjustment is based on the inherent definition of a response spectrum and the recognition that the times of occurrence of the response spectral values for the specified discrete frequencies and damping values are not significantly altered by adjustments of the time history in the neighborhoods of these times. Thus, each adjustment, which is made by adding a small perturbation, $\delta a(t)$, to the selected initial or starting acceleration time history, $a(t)$, is carried out in an iterative manner such that, for each iteration, i, an adjusted acceleration time history, $a_i(t)$, is obtained from the pervious acceleration time history, $a_{(i-1)}(t)$, using the relation

$$a_i(t) = a_{(i-1)}(t) + \delta a_i(t) \tag{14.1}$$

The small local adjustment, $\delta a_i(t)$, is determined by solving the integral equation

$$\delta R_i\left(\omega_j \beta_k\right) = \int_0^{t_{jk}} \delta a_i(\tau) h_{jk}\left(t_{jk} - \tau\right) d\tau \tag{14.2}$$

which expresses the small change in the acceleration response value $\delta R_i(\omega_j, \beta_k)$ for frequency ω_j and damping β_k resulting from the local time-history adjustment $\delta a_i(t)$. This equation makes use of the acceleration unit-impulse response function $h_{jk}(t)$ for a single degree-of-freedom oscillator having a natural frequency ω_j and a damping ratio β_k. Quantity t_{jk} in the integral represents the time at which its corresponding spectral value occurs, and τ is a time lag.

By expressing $\delta a_i(t)$ as a linear combination of impulse response functions with unknown coefficients, the above integral equation can be transformed into a system of linear algebraic equations that can easily be solved for the unknown coefficients. Since the unit-impulse response functions decay rapidly due to damping, they produce only localized perturbations on the acceleration time history. By repeatedly applying the above adjustment, the desired degree of matching between the response spectra of the modified motions and the corresponding target spectra is achieved, while, in doing so, the general characteristics of the starting time history selected for adjustment are preserved.

Since this method of time-history modification produces only local disturbances to the starting time history, the time-history phasing characteristics (wave sequence or pattern) in the starting time history are largely maintained. It is therefore important that the starting time history be selected carefully. Each three-component set of starting accelerograms for a given bridge site should preferably be a set recorded during a past seismic event that has (1) a source mechanism similar to that of the controlling design earthquake, (2) a magnitude within about ±0.5 of the target controlling earthquake magnitude, and (3) a closest source-to-site distance within 10 km of the target source-to-site distance. The selected recorded accelerograms should have their PGA, PGV, and PGD values and their strong shaking durations within a range of ±25% of the target values specified for the bridge site and they should represent free-field surface recordings on rock, rock-like, or a stiff soil site; no recordings on a soft site should be used. For a close-in controlling seismic event, for example, within about 10 km of the site, the selected accelerograms should contain a definite velocity pulse or the so-called "fling." When such recordings are not available, Method 2 described previously can be used to generate a starting set of time histories having an appropriate fling or to modify the starting set of recorded motions to include the desired directional velocity pulse.

Having selected a three-component set of starting time histories, the horizontal components should be transformed into their principal components and the corresponding principal directions should be evaluated (Penzien and Watabe 1974). These principal components should then be made response-spectrum compatible using the time-domain adjustment procedure described above or the standard

frequency-domain adjustment procedure (Silva and Lee 1987; Hao et al. 1989; Bolt and Gregor 1993). Using the latter procedure, only the Fourier amplitude spectrum, not the phase spectrum, is adjusted iteratively.

The target ARS are in general identical for the two horizontal principal components of motion; however, a distinct target spectrum is specified for the vertical component. In such cases, the adjusted response-spectrum-compatible horizontal components can be oriented horizontally along any two orthogonal coordinate axes in the horizontal plane considered suitable for structural analysis applications. However, for bridge projects that control seismic events with close-in seismic sources, the two horizontal target response spectra representing motions along a specified set of orthogonal axes are somewhat different, especially in the low-frequency (long period) range; thus, the response-spectrum-compatible time histories must have the same definitive orientation. In this case, the generated three-component set of response-spectrum-compatible time histories should be used in conjunction with their orientation. The application of this three-component set of motions in a different coordinate orientation requires transforming the motions to the new coordinate system. It should be noted that such a transformation of the components will generally result in time histories that are not fully compatible with the original target response spectra. Thus, if response-spectrum compatibility is desired in a specific coordinate orientation (such as in the longitudinal and transverse directions of the bridge), target response spectra in the specific orientation should be generated first and then a three-component set of fully response-spectrum-compatible time histories should be generated for this specific coordinate system.

As an example, a three-component set of response-spectrum-compatible time-histories of control motion, generated using the time-domain time-history adjustment procedure, is shown in Figure 14.4.

14.4.2 Free-Field Rock-Outcrop Motions at Bridge Pier-Support Locations

As mentioned previously, characterization of the spatial variations of ground motions for engineering purposes is based on a set of wave passage parameters and ground motion coherency functions. The wave passage parameters currently used are the apparent horizontal seismic wave speed, V, and its direction angle θ relative to an axis normal to the longitudinal axis of the bridge. Studies of strong- and weak-motion array data including those in California, Taiwan, and Japan show that the apparent horizontal speed of S-waves in the direction of propagation is typically in the 2–3 km/s range (Chang et al. 1986; Abrahamson 1992b). In applications, the apparent wave-velocity vector showing speed and direction must be projected along the bridge axis giving the apparent wave speed in that direction as expressed by

$$V_{\text{bridge}} = \frac{V}{\sin\theta} \tag{14.3}$$

To be realistic, when θ becomes small, a minimum angle for θ, say 30°, should be used in order to account for waves arriving in directions different from the specified direction.

The spatial coherency of the free-field components of motion in a single direction at various locations on the ground surface has been parameterized by a complex coherency function defined by the relation

$$\Gamma_{ij}(i\omega) = \frac{S_{ij}(i\omega)}{\sqrt{S_{ii}(\omega)}\sqrt{S_{jj}(\omega)}}\ i, j = 1, 2, ..., n \text{ locations} \tag{14.4}$$

in which $S_{ij}(i\omega)$ is the smoothed complex cross-power spectral density function and $S_{ii}(\omega)$ and $S_{jj}(\omega)$ are the smoothed real power-spectral density (PSD) functions of the components of motion at locations i and j. The notation $i\omega$ in the above equation is used to indicate that the coefficients $S_{ij}(i\omega)$ are complex valued (contain both real and imaginary parts) and are dependent upon excitation frequency ω. On the

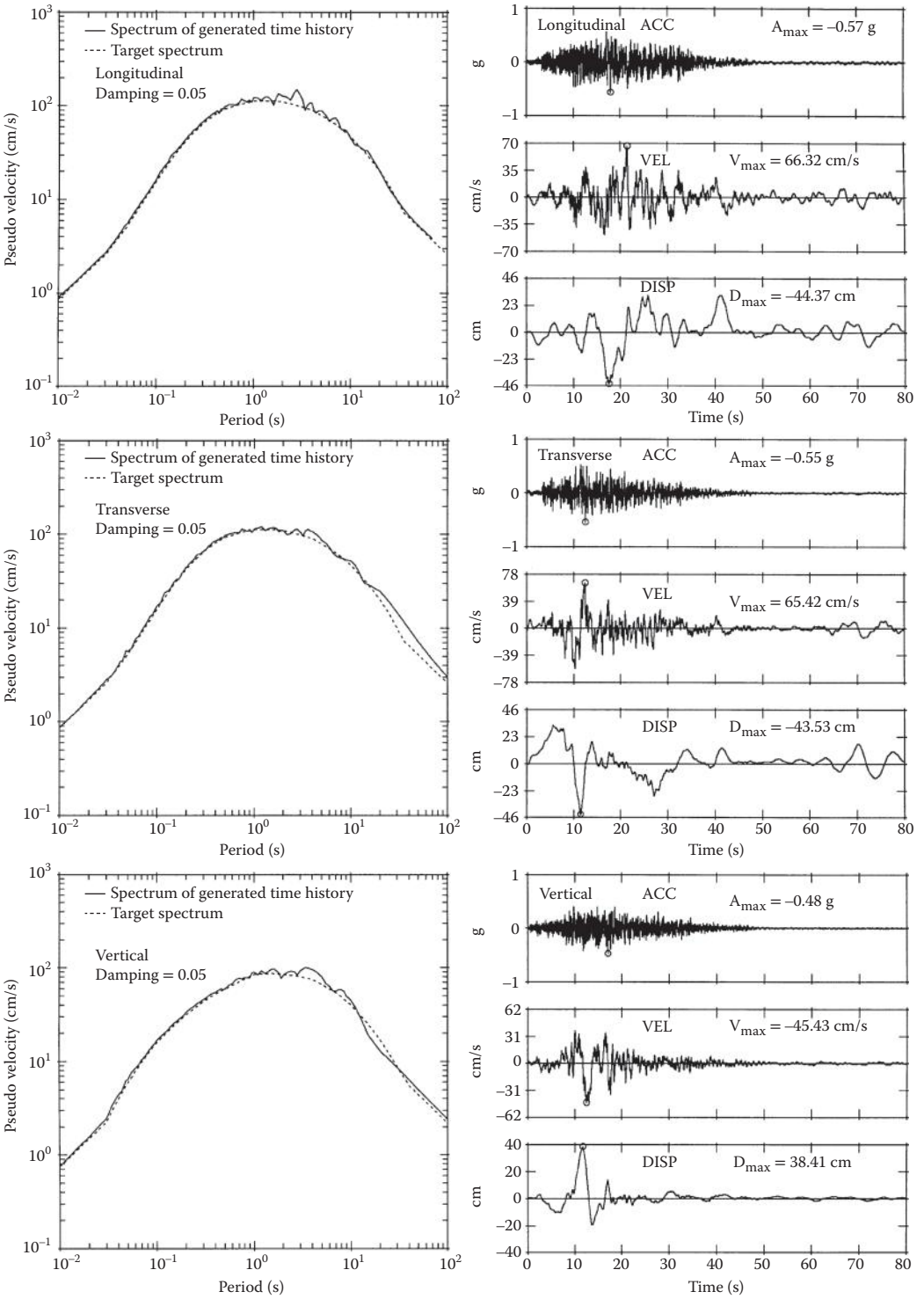

FIGURE 14.4 Examples of a three-component set of response spectrum compatible time histories of control motion.

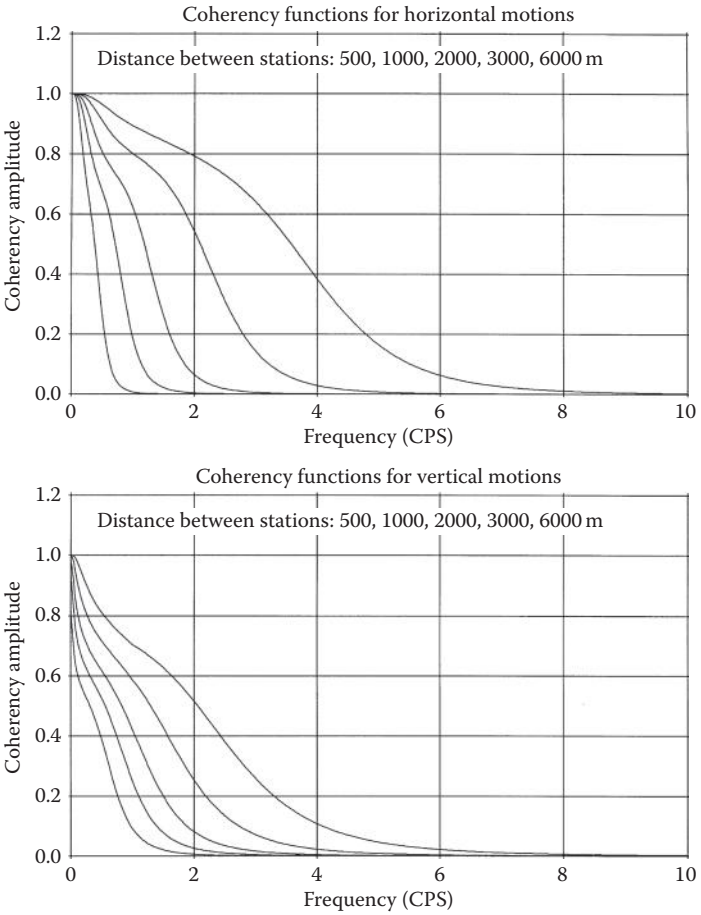

FIGURE 14.5 Example of coherency functions of frequency at discrete separation distances.

basis of the analyses of strong motion array data, a set of generic coherency functions for the horizontal and vertical ground motions has been developed (Abrahamson et al. 1991). These functions for discrete separation distances between locations *i* and *j* are plotted against frequency in Figure 14.5.

Given a three-component set of response-spectrum-compatible time histories of rock-outcrop motions developed for the selected control-point location and a specified set of wave-passage parameters and "target" coherency functions as described above, response-spectrum-compatible and coherency-compatible multiple-support rock-outcrop motions applicable to each pier-support location of the bridge can be generated using the procedure presented below. This procedure is based on the "marching method" developed by Hao et al. (1989), and extended by Tseng et al. (1993).

Neglecting, for the time being, ground motion attenuation along the bridge axis, the components of rock-outcrop motions at all pier-support locations in a specific direction have PSD functions that are common with the PSD function $S_o(\omega)$ specified for the control motion, that is,

$$S_{ii}(\omega) = S_{jj}(\omega) = S_o(\omega) = \left|u_o(i\omega)\right|^2 \tag{14.5}$$

where $u_o(i\omega)$ is the Fourier transform of the corresponding component of control motion, $u_o(t)$. By substituting Equation 14.5 into Equation 14.4, one obtains

$$S_{ij}(i\omega) = \Gamma_{ij}(i\omega) S_o(\omega) \tag{14.6}$$

which can be rewritten in a matrix form for all pier-support locations as follows:

$$S(i\omega) = \Gamma(i\omega) S_o(\omega) \tag{14.7}$$

Since, by definition, the coherency matrix $\Gamma(i\omega)$ is an Hermitian matrix, it can be decomposed into a complex conjugate pair of lower and upper triangular matrices $\boldsymbol{L}(i\omega)$ and $\boldsymbol{L}^*(i\omega)^T$ as expressed by

$$\Gamma(i\omega) = L(i\omega)\mathrm{L}^*(i\omega)^T \tag{14.8}$$

in which the symbol * denotes complex conjugate. In proceeding, let

$$\boldsymbol{u}(i\omega) = \boldsymbol{L}(i\omega)\,\eta_{\phi_i}(i\omega) u_o(i\omega) \tag{14.9}$$

in which $\boldsymbol{u}(\omega)$ is a vector containing components of motion $u_i(\omega)$ for locations, $i = 1, 2,..., n$; and $\eta_{\phi_i}(i\omega) = \{e^{i\phi_i(\omega)}\}$ is a vector containing unit-amplitude components having random phase angles $\phi_i(\omega)$. If $\phi_i(\omega)$ and $\phi_j(\omega)$ are uniformly-distributed random phase angles, the relations

$$E[\eta_{\phi_i}(i\omega)\eta^*_{\phi_j}(i\omega)] = 0, \text{ if } i \neq j \tag{14.10}$$

$$E[\eta_{\phi_i}(i\omega)\eta^*_{\phi_j}(i\omega)] = 1, \text{ if } i = j$$

is satisfied, where the symbol $E[]$ represents ensemble average. It can easily be shown that the ensemble of motions generated using Equation 14.9 satisfies Equation 14.7. Thus, if the rock-outcrop motions at all pier-support locations are generated from the corresponding motions at the control-point location using Equation 14.9, the resulting motions at all locations will satisfy, on an ensemble basis, the coherency functions specified for the site. Since the matrix $\boldsymbol{L}(i\omega)$ in Equation 14.9 is a lower triangular matrix having its diagonal elements equal to unity, the generation of coherency-compatible motions at all pier locations can be achieved by "marching" from one pier location to the next in a sequential manner starting with the control-pier location.

In generating the coherency-compatible motions using Equation 14.9, the phase-angle shifts at various pier locations due to the single plane-wave passage at the constant speed V_{bridge} defined by Equation 14.3 can be incorporated into the term $\eta_{\phi_i}(i\omega)$. Since the motions at the control-point location are response-spectrum-compatible, the coherency-compatible motions generated at all other pier locations using the above-described procedure will be approximately response-spectrum compatible. However, an improvement on their response-spectrum compatibility is generally required, which can be done by adjusting their Fourier amplitudes but keeping their Fourier phase angles unchanged. By keeping these angles unchanged, the coherencies among the adjusted motions are not affected. Consequently, the adjusted motions are not only response-spectrum compatible but also coherency compatible.

In generating the response-spectrum-compatible and coherency-compatible motions at all pier locations by the procedure described above, the ground motion attenuation effect has been ignored. For a long bridge located close-in to the controlling seismic source, attenuation of motion with distance away from the control-pier location should be considered. This can be achieved by scaling the generated motions at various pier locations by appropriate scaling factors determined from an appropriate ground motion attenuation relation. The acceleration time histories generated for all pier locations should be integrated to obtain their corresponding velocity and displacement time histories, which should be checked to ensure against having numerically-generated baseline drifts. Relative displacement time-histories between the control-pier location and successive pier locations should also be checked to ensure that they are reasonable. The rock outcrop motions finally obtained should then be used in an

appropriate site response analyses to develop the corresponding free-field soil motions required in conducting the SFSI analyses for each pier location.

14.4.3 Free-Field Soil Motions

As previously mentioned, the seismic inputs to large bridges are defined in terms of the expected free-field soil motions at discrete elevations over the entire depth of each foundation. Such motions must be evaluated through location-specific site-response analyses using the corresponding previously-described rock-outcrop free-field motions as inputs to appropriately-defined soil/bedrock models. Usually, as mentioned previously, these models are based on the assumption that the horizontal and vertical free-field soil motions are produced by upward/downward propagation of one-dimensional shear and compression waves, respectively, as caused by the upward propagation of incident waves in the underlying rock or firm soil formation. Consistent with these types of motion, it is assumed that the local soil medium surrounding each foundation consists of uniform horizontal layers of infinite lateral extent. Wave reflections and refractions will occur at all interfaces of adjacent layers, including the soil/bedrock interface, and reflections of the waves will occur at the soil surface. Computer program SHAKE (Schnabel et al. 1972; Idriss and Sun 1992) is most commonly used to carry out the above-described one-dimensional type of site-response analysis. For a long bridge having a widely varying soil profile from end to end, such site response analyses must be repeated for different soil columns representative of the changing profile.

The cyclic free-field soil deformations produced at a particular bridge site by a maximum expected earthquake are usually of the nonlinear hysteretic form. Since the SHAKE computer program treats a linear system, the soil column being analyzed must be modeled in an equivalent linearized manner. To obtain the equivalent linearized form, the soil parameters in the model are modified after each consecutive linear time-history response analysis is complete, which continues until convergence to strain-compatible parameters is reached.

For generating horizontal free-field motions produced by vertically propagating shear waves, the needed equivalent-linear soil parameters are the shear modulus G and the hysteretic damping ratio β. These parameters, as prepared by Vucetic and Dobry (1991) for clay and by Sun et al. (1988) and by the Electric Power Research Institute (EPRI) for sand, are plotted in Figures 14.6 and 14.7, respectively, as functions of shear strain γ. The shear modulus is plotted in its nondimensional form G/G_{max}, where G_{max} is the in situ shear modulus at very low strains ($\gamma \leq 10^{-4}\%$). The shear modulus G must be obtained from cyclic shear tests, while G_{max} can be obtained using $G_{max} = \rho V_s^2$ in which ρ is the mass density of the soil and V_s is the in situ shear wave velocity obtained by field measurement. If shear wave velocities are not available, G_{max} can be estimated using published empirical formulas that correlate shear wave velocity or shear modulus with blow counts and/or other soil parameters (Hardin and Black 1968; Seed and Idriss 1970; Hardin and Drevnich 1972; Hardin 1978; Seed et al. 1984; and Dickenson 1994). To obtain the equivalent linearized values of G/G_{max} and β following each consecutive time-history response analysis, values are taken from the G/G_{max} versus γ and β versus γ relations at the effective shear strain level defined as $\gamma_{eff} = \alpha\gamma_{max}$ in which γ_{max} is the maximum shear strain reached in the last analysis and α is the effective strain factor. In the past, α has usually been assigned the value 0.65; however, other values have been proposed (e.g., Idriss and Sun 1992). The equivalent-linear time-history response analyses are performed in an iterative manner, with soil parameter adjustments being made after each analysis, until the effective shear strain converges to essentially the same value as used in the previous iteration (Seed and Idriss 1969b). This normally takes 4 to 8 iterations to reach 90% to 95% of full convergence when the effective shear strains do not exceed 1% to 2%. When the maximum strain exceeds 2%, a nonlinear site response analysis is more appropriate. Computer programs available for this purpose are DESRA (Lee and Finn 1978), DYNAFLOW (Prevost 1989), DYNAID (Prevost 1993), and SUMDES (Li et al. 1992).

For generating vertical free-field motions produced by vertically propagating compression waves, the needed soil parameters are the low-strain constrained elastic modulus $E_p = \rho V_p^2$, where V_p is

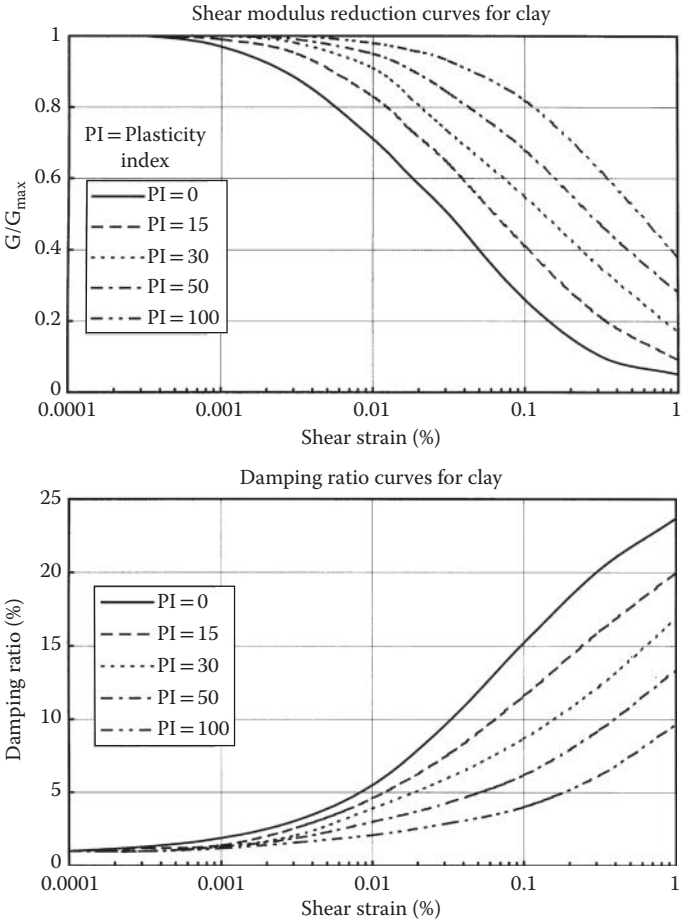

FIGURE 14.6 Equivalent linear shear modulus and hysteretic damping ratio as functions of shear strain for clay. (From Vucetic, M. and Dobry, R., *J. Geotech. Eng. ASCE*, 117(1), 89–107, 1991. With permission.)

the compression wave velocity, and the corresponding damping ratio. The variations of these soil parameters with compressive strain have not as yet been well established. At the present time, vertical site response analyses have generally been carried out using the low-strain constrained elastic moduli, E_p, directly and the strain-compatible damping ratios obtained from the horizontal response analyses, but limited to a maximum value of 10%, without any further strain-compatibility iterations. For soils submerged in water, the value of E_p should not be less than the compression wave velocity of water.

Having generated acceleration free-field time histories of motion using the SHAKE computer program, the corresponding velocity and displacement time histories should be obtained through single and double integrations of the acceleration time histories. When unrealistic drifts appear in the displacement time histories, appropriate corrections should be applied. If such drifts appear in a straight line manner, it usually indicates that the durations specified for Fourier transforming the recorded accelerograms are too short; thus, increasing these durations will usually correct the problem. If the baseline drifts depart significantly from a simple straight line, this tends to indicate that the analysis results may be unreliable, in which case, they should be carefully checked before being used. Time histories of free-field relative displacement between pairs of pier locations should also be generated and then be checked to judge the reasonableness of the results obtained.

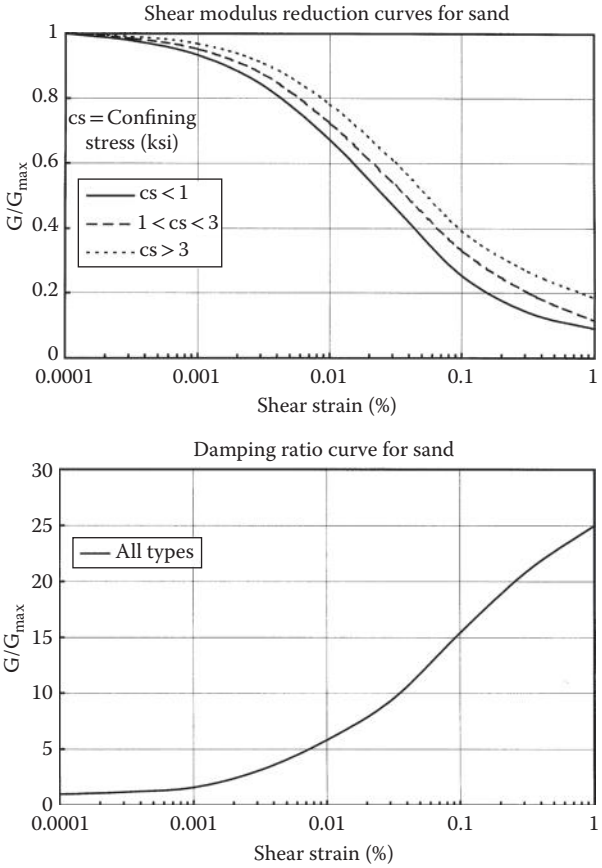

FIGURE 14.7 Equivalent linear shear modulus and hysteretic damping ratio as functions of shear strain for sand. (From Sun, J. I. et al., Reort No. UBC/EERC-88/15, Earthquake Engineer Research Center, University Of California, Berkeley, 1988.)

14.5 Characterization of Soil–Foundation System

The core of the dynamic SFSI problem for a bridge is the interaction between its structure–foundation system and the supporting soil medium, which, for analysis purposes, can be considered to be a full half-space. The fundamental step in solving this problem is to characterize the constitutive relations between the dynamic forces acting on each foundation of the bridge at its interface boundary with the soil and the corresponding foundation motions, expressed in terms of the displacements, velocities, and accelerations. Such forces are called herein the "soil–foundation interaction forces." For a bridge subjected to externally applied loadings, such as dead, live, wind, and wave loadings, these soil–foundation interaction forces are functions of the foundation motions only; however, for a bridge subjected to seismic loadings, they are functions of the free-field soil motions as well.

Let h be the total number of degrees of freedom (DOF) of the bridge's foundations as defined at their soil/foundation interface boundaries; $\boldsymbol{u}_h(t)$, $\dot{\boldsymbol{u}}_h(t)$, and $\ddot{\boldsymbol{u}}_h(t)$ be the corresponding foundation displacement, velocity, and acceleration vectors, respectively; and, $\overline{\boldsymbol{u}}_h(t)$, $\dot{\overline{\boldsymbol{u}}}_h(t)$, and $\ddot{\overline{\boldsymbol{u}}}_h(t)$ be the free-field soil displacement, velocity, and acceleration vectors in the h DOF, respectively; and let $\boldsymbol{f}_h(t)$ be the corresponding soil–foundation interaction force vector. Using these notations, characterization of the soil–foundation interaction forces under seismic conditions can be expressed in the general vectorial functional form

$$f_h(t) = \mathfrak{I}_h(\boldsymbol{u}_h(t), \dot{\boldsymbol{u}}_h(t), \ddot{\boldsymbol{u}}_h(t), \overline{\boldsymbol{u}}_h(t)\, \dot{\overline{\boldsymbol{u}}}_h(t), \ddot{\overline{\boldsymbol{u}}}_h(t)) \tag{14.11}$$

Since the soils in the local region immediately surrounding each foundation may behave nonlinearly under imposed foundation loadings, the form of $\mathfrak{I}_h$ is, in general, a nonlinear function of displacements $\boldsymbol{u}_h(t)$ and $\overline{\boldsymbol{u}}_h(t)$ and their corresponding velocities and accelerations.

For a capacity evaluation, the nonlinear form of $\mathfrak{I}_h$ should be retained and used directly for determining the soil–foundation interaction forces as functions of the foundation and soil displacements. Evaluation of this form should be based on a suitable nonlinear model for the soil medium coupled with appropriate boundary conditions, subjected to imposed loadings that are usually much simplified compared to the actual induced loadings. This part of the evaluation is discussed further in Section 14.8.

For a demand evaluation, the nonlinear form of $\mathfrak{I}_h$ is often linearized and then transformed to the frequency domain. Letting $\boldsymbol{u}_h(i\omega)$, $\dot{\boldsymbol{u}}_h(i\omega)$, $\ddot{\boldsymbol{u}}_h(i\omega)$, $\overline{\boldsymbol{u}}_h(i\omega)$, $\dot{\overline{\boldsymbol{u}}}_h(i\omega)$, $\ddot{\overline{\boldsymbol{u}}}_h(i\omega)$, and $f_h(i\omega)$ be the Fourier transform of $\boldsymbol{u}_h(t)$, $\dot{\boldsymbol{u}}_h(t)$, $\ddot{\boldsymbol{u}}_h(t)$, $\overline{\boldsymbol{u}}_h(t)$, $\dot{\overline{\boldsymbol{u}}}_h(t)$, $\ddot{\overline{\boldsymbol{u}}}_h(t)$, and $f_h(t)$, respectively, and making use of the relations

$$\dot{\boldsymbol{u}}_h(i\omega) = i\omega \boldsymbol{u}_h(i\omega); \ddot{\boldsymbol{u}}_h(i\omega) = -\omega^2 \boldsymbol{u}_h(i\omega) \tag{14.12}$$

and

$$\dot{\overline{\boldsymbol{u}}}_h(i\omega) = i\omega \overline{\boldsymbol{u}}_h(i\omega); \ \ddot{\overline{\boldsymbol{u}}}_h(i\omega) = -\omega^2 \overline{\boldsymbol{u}}_h(i\omega)$$

Equation 14.11 can be cast into the more convenient form

$$f_h(i\omega) = \mathfrak{I}_h(\boldsymbol{u}_h(i\omega), \overline{\boldsymbol{u}}_h(i\omega)) \tag{14.13}$$

To characterize the linear functional form of $\mathfrak{I}_h$, it is necessary to solve the dynamic boundary-value problem for a half-space soil medium subjected to force boundary conditions prescribed at the soil/foundation interfaces. This problem is referred to herein as the "soil impedance" problem, which is a part of the foundation impedance problem referred to earlier in Section 14.2.2.

In the linearized form, Equation 14.13 can be expressed as

$$\boldsymbol{f}_h(i\omega) = \boldsymbol{G}_{hh}(i\omega)\{\boldsymbol{u}_h(i\omega) - \overline{\boldsymbol{u}}_h(i\omega)\} \tag{14.14}$$

in which $\boldsymbol{f}_h(i\omega)$ represents the force vector acting on the soil medium by the foundation and the matrix $\boldsymbol{G}_{hh}(i\omega)$ is a complex, frequency-dependent coefficient matrix called herein the "soil impedance matrix."

Define a force vector $\overline{\boldsymbol{f}}_h(i\omega)$ by the relation

$$\overline{\boldsymbol{f}}_h(i\omega) = \boldsymbol{G}_{hh}(i\omega)\,\overline{\boldsymbol{u}}_h(i\omega) \tag{14.15}$$

This force vector represents the internal dynamic forces acting on the bridge's foundations at their soil/foundation interface boundaries resulting from the free-field soil motions when the foundations are held fixed, that is, $\boldsymbol{u}_h(i\omega) = \boldsymbol{0}$. The force vector $\overline{\boldsymbol{f}}_h(i\omega)$ as defined in Equation 14.15 is the "seismic driving force" vector mentioned previously in Section 14.2.2. Depending upon the type of bridge foundation, the characterization of the soil impedance matrix $\boldsymbol{G}_{hh}(i\omega)$ and associated free-field soil input motion vector for demand analysis purposes may be established utilizing different soil models as described below.

14.5.1 Elasto-Dynamic Model

As mentioned in Section 14.3.1, for a large bridge foundation such as a large spread footing, caisson, or single or multiple shafts having very large diameters, for which the nonlinearities occurring in the local soil region immediately adjacent to the foundation are small, the soil impedance matrix

$\boldsymbol{G}_{hh}(i\omega)$ can be evaluated utilizing the dynamic Green's functions (dynamic displacements of the soil medium due to harmonic point-load excitations) obtained from the solution of a dynamic boundary-value problem of a linear damped-elastic half-space soil medium subjected to harmonic point loads applied at each of the h DOF on the soil/foundation interface boundaries. Such solutions have been obtained in an analytical form for a linear damped-elastic continuum half-space soil medium by Apsel (1979). Because of complexities in the analytical solution, dynamic Green's functions have only been obtained for foundations having relatively simple soil/foundation interface geometries, for example, rectangular, cylindrical, or spherical soil/foundation interface geometries, supported in simple soil media. In practical applications, the dynamic Green's functions are often obtained in numerical forms based on a finite element discretization of the half-space soil medium and a corresponding discretization of the soil/foundation interface boundaries using a computer program such as SASSI (Lysmer et al. 1981), which has the capability of properly simulating the wave radiation boundary conditions at the far field of the half-space soil medium. The use of finite-element soil models to evaluate the dynamic Green's functions in numerical form has the advantage that foundations having arbitrary soil/foundation interface geometries can be easily handled; it, however, suffers from the disadvantage that the highest frequency, that is, cut-off frequency, of motion for which a reliable solution can be obtained is limited by the size of the finite element used for modeling the soil medium.

Having evaluated the dynamic Green's functions using the procedure described above, the desired soil impedance matrix can then be obtained by inverting, frequency-by-frequency, the "soil compliance matrix," which is the matrix of Green's function values evaluated for each specified frequency ω. Because the dynamic Green's functions are complex valued and frequency dependent, the coefficients of the resulting soil impedance matrix are also complex valued and frequency dependent. The real parts of the soil-impedance coefficients represent the dynamic stiffnesses of the soil medium that also incorporate the soil inertia effects; the imaginary parts of the coefficients represent the energy losses resulting from both soil material damping and radiation of stress waves into the far-field soil medium. Thus, the soil impedance matrix as developed reflects the overall dynamic characteristics of the soil medium as related to the motion of the foundation at the soil/foundation interfaces.

Because of the presence of the foundation excavation cavities in the soil medium, the vector of free-field soil motions prescribed at the soil/foundation interface boundaries has to be derived from the seismic input motions of the free-field soil medium without the foundation excavation cavities as described in Section 14.4. The derivation of the motion vector requires the solution of a dynamic boundary-value problem for the free-field half-space soil medium having foundation excavation cavities subjected to a specified seismic wave input such that the resulting solution satisfies the stress-free conditions at the surfaces of the foundation excavation cavities. Thus, the resulting seismic response motions reflect the effects of seismic wave scattering due to the presence of the cavities. These motions are, therefore, referred to herein as the "scattered free-field soil input motions."

The effects of seismic wave scattering depend on the relative relation between the characteristic dimension, f, of the foundation and the specific seismic input wave length, λ, of interest, where $\lambda = 2\pi V_s/\omega$ or $2\pi V_p/\omega$ for vertically propagating plane shear or compression waves, respectively; V_s and V_p are, as defined previously, the shear and compression wave velocities of the soil medium respectively. If the input seismic wave length λ is much longer than the characteristic length f, the effect of wave scattering will be negligible; on the other hand, when $\lambda \leq f$, the effect of wave scattering will be significant. Since the wave length λ is a function of the frequency of input motion, the effect of wave scattering is also frequency dependent. Thus, it is evident that the effect of wave scattering is much more important for a large bridge foundation, such as a large caisson or a group of very-large-diameter shafts, than for a small foundation having a small

characteristic dimension, such as a slender-pile group; it can also be readily deduced that the scattering effect is more significant for foundations supported in soft soil sites than in stiff soil sites.

The characterization of the soil impedance matrix utilizing an elasto-dynamic model of the soil medium as described above requires soil material characterization constants that include (1) mass density, ρ, (2) shear and constrained elastic moduli, G and E_p (or shear and compression wave velocities, V_s and V_p), and (3) constant-hysteresis damping ratio, β. As discussed previously in Section 14.4.3, the soil shear modulus decreases, while the soil hysteresis damping ratio increases as functions of soil shear strains induced in the free-field soil medium due to the seismic input motions. The effects of these so-called "global soil nonlinearities" can be easily incorporated into the soil impedance matrix based on an elasto-dynamic model by using the free-field-motion-induced strain-compatible soil shear moduli and damping ratios as the soil material constants in the evaluation of the dynamic Green's functions. For convenience of later discussions, the soil impedance matrix, $\boldsymbol{G}_{hh}(i\omega)$, characterized using an elasto-dynamic model will be denoted by the symbol.

14.5.2 Empirical "*P–Y*" Model

As discussed in Section 14.3.2, for a slender-pile group foundation for which soil nonlinearities occurring in the local soil regions immediately adjacent to the piles dominate the behavior of the foundation under loadings, the characterization of the soil resistances to pile deflections has often relied on empirically derived "*p–y*" curves for lateral resistance and "*t–z*" and "*Q–d*" curves for axial resistance. For such a foundation, the characterization of the soil impedance matrix needed for demand analysis purposes can be made by using the secant moduli derived from the nonlinear "*p–y*", "*t–z*," and "*Q–d*" curves, as indicated schematically in Figure 14.2. Since the development of these empirical curves has been based upon static or pseudo-static test results, it does not incorporate the soil inertia and material damping effects. Thus, the resulting soil impedance matrix developed from the secant moduli of the "*p–y*," "*t–z*," and "*Q–d*" curves reflects only the static soil stiffnesses but not the soil inertia and soil material damping characteristics. Hence, the soil impedance matrix so obtained is a real-valued constant coefficient matrix applicable at the zero frequency ($\omega = 0$); it, however, is a function of the foundation displacement amplitude. This matrix is designated herein as to differentiate it from the soil impedance matrix defined previously. Thus, Equation 14.14 in this case is given by

$$\boldsymbol{f}_h(i\omega) = \boldsymbol{G}_{hh}(i\omega)\{\boldsymbol{u}_h(i\omega) - \overline{\boldsymbol{u}}_h(i\omega)\} \tag{14.16}$$

where $G^s_{hh}(0)$ depends on the amplitudes of the relative displacement vector $\Delta\boldsymbol{u}_h(i\omega)$ defined by

$$\Delta\boldsymbol{u}_h(i\omega) = \boldsymbol{u}_h(i\omega) - \overline{\boldsymbol{u}}_h(i\omega) \tag{14.17}$$

As mentioned previously in Section 3.2, the construction of the "*p–y*," "*t–z*," and "*Q–d*" curves depends only on the strength parameters but not the stiffness parameters of the soil medium; thus, the effects of global soil nonlinearities on the dynamic stiffnesses of the soil medium, as caused by soil-shear-modulus decrease and soil-damping increase as functions of free-field-motion-induced soil shear strains, cannot be incorporated into the soil impedance matrix developed from these curves. Furthermore, since these curves are developed on the basis of results from field tests in which there are no free-field ground-motion-induced soil deformations, the effects of such global soil nonlinearities on the soil strength characterization parameters and hence the "*p–y*," "*t–z*," and "*Q–d*" curves cannot be incorporated.

Because of the small cross-sectional dimensions of slender piles, the seismic wave scattering effect due to the presence of pile cavities is usually negligible; thus, the scattered free-field soil input motions

$\overline{u}_h(i\omega)$ in this case are often taken to be the same as the free-field soil motions when the cavities are not present.

14.5.3 Hybrid Model

From the discussions in the above two sections, it is clear that characterization of the soil–foundation interaction forces for demand analysis purposes can be achieved using either an elasto-dynamic model or an empirical "*p–y*" model for the soil medium, each of which has its own merits and deficiencies. The elasto-dynamic model is capable of incorporating soil inertia, damping (material and radiation), and stiffness characteristics; and, it can incorporate the effects of global soil nonlinearities induced by the free-field soil motions in an equivalent linearized manner. However, it suffers from the deficiency that it does not allow for easy incorporation of the effects of local soil nonlinearities. On the contrary, the empirical "*p–y*" model can properly capture the effects of local soil nonlinearities in an equivalent linearized form; but, it suffers from the deficiencies of not being able to properly simulate soil inertia and damping effects, and it cannot treat the effects of global soil nonlinearities. Since the capabilities of the two models are mutually complimentary, it is logical to combine the elasto-dynamic model with the empirical "*p–y*" model in a series form such that the combined model has the desired capabilities of both models. This combined model is referred to herein as the "hybrid model."

To develop the hybrid model, let the relative displacement vector, $\Delta \boldsymbol{u}_h(i\omega)$, between the foundation displacement vector $\boldsymbol{u}_h(i\omega)$ and the scattered free-field soil input displacement vector, as defined by Equation 14.17, be decomposed into a component representing the relative displacements at the soil/foundation interface boundary resulting from the elastic deformation of the global soil medium outside of the soil/foundation interface, designated as $\Delta \boldsymbol{u}_h{}^e(i\omega)$, and a component representing the relative displacements at the same boundary resulting from the inelastic deformations of the local soil regions adjacent the foundation, designated as $\Delta \boldsymbol{u}_h{}^i(i\omega)$; thus,

$$\Delta u_h(i\omega) = \Delta u_h^i(i\omega) + \Delta u_h^e \tag{14.18}$$

Let $\boldsymbol{f}_h{}^e(i\omega)$ represent the elastic force vector that can be characterized in terms of the elastic relative-displacement vector $\Delta \boldsymbol{u}_h{}^e(i\omega)$ using the elasto-dynamic model, in which case

$$f_h^e(i\omega) = \boldsymbol{G}_{hh}^e(i\omega)\Delta \boldsymbol{u}_h^e(i\omega) \tag{14.19}$$

where $\boldsymbol{G}_{hh}{}^e(i\omega)$ is the soil impedance matrix as defined previously in Section 14.5.1, which can be evaluated using an elasto-dynamic model. Let $\boldsymbol{f}_h{}^i(i\omega)$ represent the inelastic force vector that is assumed to be related to $\Delta \boldsymbol{u}_h{}^i(i\omega)$ by the relation

$$f_h^i(i\omega) = \boldsymbol{G}_{hh}^i(i\omega)\Delta \boldsymbol{u}_h^i(i\omega) \tag{14.20}$$

The characterization of the matrix $\boldsymbol{G}_{hh}^i(i\omega)$ can be accomplished by utilizing the soil secant stiffness matrix $\boldsymbol{G}_{hh}^s(o)$ developed from the empirical "*p–y*" model by the procedure discussed below.

Solving Equations 14.19 and 14.20 for $\Delta \boldsymbol{u}_h^e(i\omega)$ and $\Delta \boldsymbol{u}_h^i(i\omega)$ respectively, substituting these relative displacement vectors into Equation 14.18, and making use of the force continuity condition that $\boldsymbol{f}_h^e(i\omega) = \boldsymbol{f}_h^i(i\omega)$, since the elasto-dynamic model and the inelastic local model are in series, one obtains

$$f_h(i\omega) = \left\{ \left[\boldsymbol{G}_{hh}^i(i\omega) \right]^{-1} + \left[\boldsymbol{G}_{hh}^e(i\omega) \right]^{-1} \right\}^{-1} \Delta \boldsymbol{u}_h(i\omega) \tag{14.21}$$

Comparing Equation 14.14 with Equation 14.21, one finds that, by using the hybrid model, the soil impedance matrix is given by

$$\boldsymbol{G}_{hh}(i\omega)=\left\{\left[\boldsymbol{G}^{i}_{hh}(i\omega)\right]^{-1}+\left[\boldsymbol{G}^{e}_{hh}(i\omega)\right]^{-1}\right\}^{-1} \tag{14.22}$$

Since the soil impedance matrix $\boldsymbol{G}^{s}_{hh}(i\omega)$ is formed by the static secant moduli of the nonlinear "*p*–*y*," "*t*–*z*," and "*Q*–*d*" curves when $\omega = 0$, Equation 14.22 becomes

$$\boldsymbol{G}^{s}_{hh}(0)=\left\{\left[\boldsymbol{G}^{i}_{hh}(0)\right]^{-1}+\left[\boldsymbol{G}^{e}_{hh}(0)\right]^{-1}\right\}^{-1} \tag{14.23}$$

where $G^{s}_{hh}(0)$ is the soil stiffness matrix derived from the secant moduli of the nonlinear "*p*–*y*," "*t*–*z*," and "*Q*–*d*" curves. Solving Equation 14.23, for $G^{i}_{hh}(0)$ gives

$$\boldsymbol{G}^{i}_{hh}(0)=\left\{\left[\boldsymbol{G}^{s}_{hh}(0)\right]^{-1}-\left[\boldsymbol{G}^{e}_{hh}(0)\right]^{-1}\right\}^{-1} \tag{14.24}$$

Thus, Equation 14.22 can be expressed in the form

$$\boldsymbol{G}_{hh}(i\omega)=\left\{\left[\boldsymbol{G}^{i}_{hh}(0)\right]^{-1}+\left[\boldsymbol{G}^{e}_{hh}(i\omega)\right]^{-1}\right\}^{-1} \tag{14.25}$$

From Equation 14.25, it is evident that when $\Delta\boldsymbol{u}_{h}{}^{i}(i\omega) << \Delta\boldsymbol{u}_{h}{}^{e}(i\omega)$, $\boldsymbol{G}_{hh}(i\omega) \rightarrow \boldsymbol{G}^{e}_{hh}(i\omega)$; however, when $\Delta\boldsymbol{u}_{h}{}^{i}(i\omega) >> \Delta\boldsymbol{u}_{h}{}^{e}(i\omega)$, $\boldsymbol{G}_{hh}(i\omega) \rightarrow \boldsymbol{G}^{i}_{hh}(0) \rightarrow \boldsymbol{G}^{s}_{hh}(0)$. Thus, the hybrid model represented by this equation converges to the elasto-dynamic model when the local inelastic soil deformations are relatively small, as for the case of a large footing, caisson, or very-large-diameter shaft foundation; whereas, it converges to the empirical "*p*–*y*" model when the local inelastic soil deformations are relatively much larger as for the case of a slender-pile group foundation. For a moderately-large-diameter shaft foundation, the local inelastic and global elastic soil deformations may approach a comparable magnitude; in which case, the use of a hybrid model to develop the soil impedance matrix as described above can properly represent both the global elasto-dynamic and local inelastic soil behaviors.

As local soil nonlinearities are induced by the relative displacements between the foundation and the scattered free-field soil input motions, they do not affect the scattering of free-field soil motions due to the stress-free conditions present at the surface of the foundation cavities. Therefore, in applying the hybrid model described above, the scattered free-field soil input motion vector $\overline{\boldsymbol{u}}_{h}(i\omega)$ should still be derived using the elasto-dynamic model described in Section 14.5.1.

14.6 Demand Analysis Procedures

14.6.1 Equations of Motion

The seismic response of a complete bridge system involves interactions between the structure and its supporting foundations and between the foundations and their surrounding soil media. To develop the equations of motion governing the response of this system in discrete (finite element) form, let *s* denote the number of DOF in the structure, excluding its *f* DOF at the structure/foundation interface locations, and let *g* denote the number of DOF in the foundations, also excluding the *f* DOF but including the *h* DOF at all soil/foundation interfaces as defined in Section 14.5. Corresponding with those DOF, let vectors $\boldsymbol{u}_{s}(t)$, $\boldsymbol{u}_{f}(t)$, and $\boldsymbol{u}_{g}(t)$ contain the total-displacement time histories of motion at the DOF *s*, *f*, and *g* respectively.

14.6.1.1 Linear Modeling

Since the soil medium surrounding all foundations is continuous and of infinite extent, a rigorous model of a complete bridge system must contain stiffness and damping coefficients that are dependent upon

the excitation (or response) frequencies. Such being the case, the corresponding equations of motion of the complete system having n DOF ($n = s + f + g$) must rigorously be represented in the frequency domain.

Considering the coupled structure–foundation system as a free–free (no boundary constraints) system having externally applied forces $-\boldsymbol{f}_h(t)$ acting in the h DOF, its equations of motion can be expressed in the frequency-domain form

$$\begin{bmatrix} \boldsymbol{D}_{ss}(i\omega) & \boldsymbol{D}_{sf}(i\omega) & 0 \\ \boldsymbol{D}_{sf}^T(i\omega) & \boldsymbol{D}_{ff}(i\omega) & \boldsymbol{D}_{fg}(i\omega) \\ 0 & \boldsymbol{D}_{sf}^T(i\omega) & \boldsymbol{D}_{gg}(i\omega) \end{bmatrix} \begin{Bmatrix} \boldsymbol{u}_s(i\omega) \\ \boldsymbol{u}_f(i\omega) \\ \boldsymbol{u}_g(i\omega) \end{Bmatrix} = \begin{Bmatrix} 0 \\ 0 \\ \boldsymbol{f}_g(i\omega) \end{Bmatrix} \tag{14.26}$$

in which $\boldsymbol{u}_s(i\omega)$, $\boldsymbol{u}_f(i\omega)$, $\boldsymbol{u}_g(i\omega)$, and $\boldsymbol{f}_g(i\omega)$ are the Fourier transforms of vectors $\boldsymbol{u}_s(t)$, $\boldsymbol{u}_f(t)$, $\boldsymbol{u}_g(t)$, and $\boldsymbol{f}_g(t)$ respectively; and matrices, $i, j = s, f, g$, are the corresponding impedance (dynamic stiffness) matrices. The g components in vectors $\boldsymbol{u}_g(i\omega)$ and $\boldsymbol{f}_g(i\omega)$ are ordered such that their last h components make up vectors $\boldsymbol{u}_h(i\omega)$ and $-\boldsymbol{f}_h(i\omega)$, respectively, with all other components being equal to zero.

For a viscously-damped linear structure–foundation system, the impedance matrices $\boldsymbol{D}_{ij}(i\omega)$ are of the form

$$\boldsymbol{D}_{ij}(i\omega) = \boldsymbol{K}_{ij} + i\omega\boldsymbol{C}_{ij} - \omega^2\boldsymbol{M}_{ij} \quad i, j = s, f, g \tag{14.27}$$

in which $\boldsymbol{K}_{ij}$, $\boldsymbol{C}_{ij}$, and $\boldsymbol{M}_{ij}$ are the standard stiffness, damping, and mass matrices respectively, which would appear in the system's equations of motion if expressed in the time domain. For a constant-hysteresis-damped linear system, the impedance matrices are given by

$$\boldsymbol{D}_{ij}(i\omega) = \boldsymbol{K}_{ij}^* - \omega^2\boldsymbol{M}_{ij} \quad i, j = s, f, g \tag{14.28}$$

in which $\boldsymbol{K}_{ij}^*$ is a complex stiffness matrix obtained by assembling individual finite-element matrices $\boldsymbol{K}^{*(m)}$ of the form

$$K^{*(m)} \equiv \left\{1 - 2(\beta^{(m)})^2 + 2i\beta^{(m)}\sqrt{1-(\beta^{(m)})^2}\right\}\boldsymbol{K}^{(m)} \doteq (1 + 2i\beta^{(m)})\boldsymbol{K}^{(m)} \tag{14.29}$$

where $\boldsymbol{K}^{(m)}$ denotes the standard elastic stiffness matrix for finite element m as used in the assembly process to obtain matrix $\boldsymbol{K}_{ij}$ and $\beta^{(m)}$ is a damping ratio specified appropriately for the material used in finite element m (Clough and Penzien 1993).

The hysteretic form of damping represented in Equation 14.28 is the more appropriate form to use for two reasons: (1) it is easy to accommodate different damping ratios for the different materials used in the system, and (2) the resulting modal damping is independent of excitation (or response) frequency ω, consistent with test evidence showing that real damping is indeed essentially independent of this frequency. As noted by the form of Equation 14.27, viscous damping is dependent upon frequency ω, contrary to test results; thus, preference should definitely be given to the use of hysteretic damping for linear systems that can be solved in the frequency domain. Hysteretic damping is unfortunately incompatible with solutions in the time domain.

Vector $-\boldsymbol{f}_h(i\omega)$, which makes up the last h components in force vector $\boldsymbol{f}_g(i\omega)$ appearing in Equation 14.26, represents, as defined in Section 14.5, the internal soil–foundation interaction forces at the soil/foundation interfaces when the entire coupled soil-foundation-structure system is responding to the free-field soil input motions. Therefore, to solve the SFSI problem, this vector must be characterized in

terms of the foundation displacement vector $\boldsymbol{u}_h(i\omega)$ and the free-field soil displacement vector. As discussed previously in Section 14.5, for demand analysis purposes, this vector can be linearized to the form

$$-\boldsymbol{f}_h(i\omega) = \boldsymbol{G}_{hh}(i\omega)\left\{\overline{\boldsymbol{u}}_h(i\omega) - \boldsymbol{u}_h(i\omega)\right\} \tag{14.30}$$

in which $-\boldsymbol{f}_h(i\omega)$ represents the force vector acting on the foundations from the soil medium and $\boldsymbol{G}_{hh}(i\omega)$ is the soil impedance matrix that is complex valued and frequency dependent.

Substituting Equation 14.30 into Equation 14.26, the equations of motion of the complete bridge system become

$$\begin{bmatrix} \boldsymbol{D}_{ss}(i\omega) & \boldsymbol{D}_{sf}(i\omega) & 0 \\ \boldsymbol{D}_{sf}^T(i\omega) & \boldsymbol{D}_{ff}(i\omega) & \boldsymbol{D}_{fg}(i\omega) \\ 0 & \boldsymbol{D}_{fg}^T(i\omega) & [\boldsymbol{D}_{gg}(i\omega) + \boldsymbol{G}_{gg}(i\omega)] \end{bmatrix} \begin{Bmatrix} \boldsymbol{u}_s(i\omega) \\ \boldsymbol{u}_f(i\omega) \\ \boldsymbol{u}_g(i\omega) \end{Bmatrix} = \begin{Bmatrix} 0 \\ 0 \\ \overline{\boldsymbol{f}}_g(i\omega) \end{Bmatrix} \tag{14.31}$$

in which

$$\boldsymbol{G}_{gg}(i\omega) = \begin{bmatrix} 0 & 0 \\ 0 & \boldsymbol{G}_{hh}(i\omega) \end{bmatrix}; \quad \overline{\boldsymbol{f}}_g(i\omega) = \begin{Bmatrix} 0 \\ \overline{\boldsymbol{f}}_h(i\omega) \end{Bmatrix} \tag{14.32}$$

Vector $\overline{\boldsymbol{f}}_h(i\omega)$ is the free-field soil "seismic driving force" vector defined by Equation 14.15, in which the free-field soil displacements in vector $\overline{\boldsymbol{u}}_h(i\omega)$ result from scattering of incident seismic waves propagating to the bridge site as explained previously in Section 14.5.

14.6.1.2 Nonlinear Modeling

When large nonlinearities develop in the structure–foundation subsystem during a seismic event, evaluation of its performance requires nonlinear modeling and analysis in the time domain. In this case, the standard linear equations of motion of the complete system as expressed by

$$\begin{bmatrix} \boldsymbol{M}_{ss} & \boldsymbol{M}_{sf} & 0 \\ \boldsymbol{M}_{sf}^T & \boldsymbol{M}_{ff} & \boldsymbol{M}_{fg} \\ 0 & \boldsymbol{M}_{fg}^T & \boldsymbol{M}_{gg} \end{bmatrix} \begin{Bmatrix} \ddot{\boldsymbol{u}}_s(t) \\ \ddot{\boldsymbol{u}}_f(t) \\ \ddot{\boldsymbol{u}}_g(t) \end{Bmatrix} + \begin{bmatrix} \boldsymbol{C}_{ss} & \boldsymbol{C}_{sf} & 0 \\ \boldsymbol{C}_{sf}^T & \boldsymbol{C}_{ff} & \boldsymbol{C}_{fg} \\ 0 & \boldsymbol{C}_{fg}^T & \boldsymbol{C}_{gg} \end{bmatrix} \begin{Bmatrix} \dot{\boldsymbol{u}}_s(t) \\ \dot{\boldsymbol{u}}_f(t) \\ \dot{\boldsymbol{u}}_g(t) \end{Bmatrix} + \begin{bmatrix} \boldsymbol{K}_{ss} & \boldsymbol{K}_{sf} & 0 \\ \boldsymbol{K}_{sf}^T & \boldsymbol{K}_{ff} & \boldsymbol{K}_{fg} \\ 0 & \boldsymbol{K}_{fg}^T & \boldsymbol{K}_{gg} \end{bmatrix} \begin{Bmatrix} \boldsymbol{u}_s(t) \\ \boldsymbol{u}_f(t) \\ \boldsymbol{u}_g(t) \end{Bmatrix} = \begin{Bmatrix} 0 \\ 0 \\ \boldsymbol{f}_g(t) \end{Bmatrix} \tag{14.33}$$

must be modified appropriately to characterize the nonlinearities for use in a step-by-step numerical solution. Usually, it is the third term on the left-hand side of this equation that must be modified to represent the nonlinear-hysteric force-deformation behavior taking place in the individual finite elements of the system. The second term in this equation, representing viscous damping forces, is usually retained in its linear form with the full viscous damping matrix $\boldsymbol{C}$ being expressed in the Rayleigh form

$$\boldsymbol{C} = \alpha_R \boldsymbol{M} + \beta_R \boldsymbol{K} \tag{14.34}$$

in which $\boldsymbol{M}$ and $\boldsymbol{K}$ are the full mass and elastic-stiffness matrices shown in Equation 14.33 and α_R and β_R are constants assigned numerical values that will limit the modal damping ratios to levels within acceptable bounds over a range of modal frequencies dominating the seismic response.

For a time-domain solution of Equation 14.33 in its modified nonlinear form, all parameters in the equation must be real (no imaginary parts) and frequency independent. It remains therefore to modify the soil impedance matrix $\boldsymbol{G}_{hh}(i\omega)$ so that when introduced into Equation 14.30, the inverse Fourier transform of $-\boldsymbol{f}_h(i\omega)$ to the time domain will yield a vector $-\boldsymbol{f}_h(t)$ having no frequency-dependent parameters. To accomplish this objective, separate $\boldsymbol{G}_{hh}(i\omega)$ into its real and imaginary parts in accordance with

$$\boldsymbol{G}_{hh}(i\omega) = \boldsymbol{G}_{hh}^{R}(\omega) + i\boldsymbol{G}_{hh}^{I}(\omega) \tag{14.35}$$

in which $\boldsymbol{G}_{hh}^{R}(\omega)$ and $\boldsymbol{G}_{hh}^{I}(\omega)$ are real functions of ω. Then approximate these functions using the relations

$$\boldsymbol{G}_{hh}^{R}(\omega) \doteq \overline{\boldsymbol{K}}_{hh} - \omega^2 \overline{\boldsymbol{M}}_{hh};\ \boldsymbol{G}_{hh}^{I}(\omega) \doteq \omega \overline{\boldsymbol{C}}_{hh} \tag{14.36}$$

where the real constants in matrices $\overline{\boldsymbol{K}}_{hh}$, $\overline{\boldsymbol{M}}_{hh}$, and $\overline{\boldsymbol{C}}_{hh}$ are assigned numerical values to provide best fits to the individual frequency-dependent functions in matrices $\boldsymbol{G}_{hh}^{R}(\omega)$ and $\boldsymbol{G}_{hh}^{I}(\omega)$ and over the frequency range of major influence on seismic response. Typically, applying these best fits to the range $0 < \omega < 4\pi$ rad/s, corresponding to the range $0 < f < 2$ Hz, where $f = \omega/2\pi$, is adequate for most large bridges. In this fitting process, it is sufficient to treat $\overline{\boldsymbol{M}}_{hh}$ as a diagonal matrix, thus affecting only the diagonal functions in matrix $\boldsymbol{G}_{hh}^{R}(\omega)$. The reason for selecting the particular frequency-dependent forms of Equations. 14.36 is that when they are substituted into Equation 14.35, which in turn is substituted into Equation 14.30, the resulting expression for $\boldsymbol{f}_h(i\omega)$ can be Fourier transformed to the time domain yielding

$$-\boldsymbol{f}_h(t) = \overline{\boldsymbol{K}}_{hh}\left\{\overline{\boldsymbol{u}}_h(t) - \boldsymbol{u}_h(t)\right\} + \overline{\boldsymbol{C}}_{hh}\left\{\dot{\overline{\boldsymbol{u}}}_h(t) - \dot{\boldsymbol{u}}_h(t)\right\} + \overline{\boldsymbol{M}}_{hh}\left\{\ddot{\overline{\boldsymbol{u}}}_h(t) - \ddot{\boldsymbol{u}}_h(t)\right\} \tag{14.37}$$

Substituting $-\boldsymbol{f}_h(t)$ given by this equation for the last h components in vector $\boldsymbol{f}_g(t)$, with all other components in $\boldsymbol{f}_g(t)$ being equal to zero, and then substituting the resulting vector $\boldsymbol{f}_g(t)$ into Equation 14.33 gives

$$\begin{bmatrix} M_{ss} & M_{sf} & 0 \\ M_{sf}^T & M_{ff} & M_{fg} \\ 0 & M_{fg}^T & [M_{gg} + \overline{M}_{gg} \end{bmatrix} \begin{Bmatrix} \ddot{u}_s(t) \\ \ddot{u}_f(t) \\ \ddot{u}_g(t) \end{Bmatrix} + \begin{bmatrix} C_{ss} & C_{sf} & 0 \\ C_{sf}^T & C_{ff} & C_{fg} \\ 0 & C_{fg}^T & [C_{gg} + \overline{C}_{gg} \end{bmatrix} \begin{Bmatrix} \dot{u}_s(t) \\ \dot{u}_f(t) \\ \dot{u}_g(t) \end{Bmatrix} +$$
$$\begin{bmatrix} K_{ss} & K_{sf} & 0 \\ K_{sf}^T & K_{ff} & K_{fg} \\ 0 & K_{fg}^T & K_{gg} + \overline{K}_{gg} \end{bmatrix} \begin{Bmatrix} u_s(t) \\ u_f(t) \\ u_g(t) \end{Bmatrix} = \begin{Bmatrix} 0 \\ 0 \\ \overline{K}_{gg}\overline{u}_g(t) + \overline{C}_{gg}\dot{\overline{u}}_g(t) + \overline{M}_{gg}\ddot{\overline{u}}_g(t) \end{Bmatrix} \tag{14.38}$$

in which

$$\overline{\boldsymbol{M}}_{gg} = \begin{bmatrix} 0 & 0 \\ 0 & \overline{\boldsymbol{M}}_{hh} \end{bmatrix};\ \overline{\boldsymbol{K}}_{gg} = \begin{bmatrix} 0 & 0 \\ 0 & \overline{\boldsymbol{K}}_{hh} \end{bmatrix};\ \overline{\boldsymbol{C}}_{gg} = \begin{bmatrix} 0 & 0 \\ 0 & \overline{\boldsymbol{C}}_{hh} \end{bmatrix} \tag{14.39}$$

showing that no frequency-dependent parameters remain in the equations of motion, thus allowing the standard time-domain solution procedure to be used for solving them. Usually, the terms $\overline{\boldsymbol{C}}_{gg}\ \dot{\overline{\boldsymbol{u}}}_g(t)$ and $\overline{\boldsymbol{M}}_{gg}\ \ddot{\overline{\boldsymbol{u}}}_g(t)$ on the right-hand side of Equation 14.38 have small effects on the solution of this equation; however, the importance of their contributions should be checked. Having modified the third term on the left-hand side of Equation 14.38 to its nonlinear hysteretic form, the complete set of coupled equations can be solved for displacements $\boldsymbol{u}_s(t)$, $\boldsymbol{u}_f(t)$, and $\boldsymbol{u}_g(t)$ using standard step-by-step numerical integration procedures.

14.6.2 Solution Procedures

14.6.2.1 One-Step Direct Approach

In this approach, the equations of motion are solved directly in their coupled form. If the system is treated as being fully linear (or equivalent linear), the solution can be carried out in the frequency domain using Equation 14.31. In doing so, the complete set of complex algebraic equations are solved

separately for discrete values of ω over the frequency range of interest yielding the corresponding sets of displacement vectors $\boldsymbol{u}_s(i\omega)$, $\boldsymbol{u}_f(i\omega)$, and $\boldsymbol{u}_g(i\omega)$. Having obtained these vectors for the discrete values of ω, they are inverse Fourier transformed to the time domain giving vectors $\boldsymbol{u}_s(t)$, $\boldsymbol{u}_f(t)$, and $\boldsymbol{u}_g(t)$. The corresponding time histories of internal forces and/or deformations in the system can then be obtained directly using standard finite-element procedures.

If the structure–foundation subsystem is modeled as a nonlinear system, the solution can be carried out in the time domain using Equation 14.38. In this case, the coupled nonlinear equations of motion are solved using standard step-by-step numerical integration procedures.

This one-step direct approach is simple and straight forward to implement for a structural system supported on a single foundation, such as a building. However, for a long multiple-span bridge supported on many independent foundations, a very large system of equations and an associated very large number of seismic free-field inputs in vector $\overline{\boldsymbol{u}}_g(i\omega)$s result, making the solution computationally impractical, especially when large nonlinearities are present in the equations of motion. In this case, it is desirable to simplify the problem by finding separate solutions to a set of smaller problems and then combine the solutions in steps so as to achieve the desired end result. The multiple-step substructuring approach described subsequently is ideally suited for this purpose.

14.6.2.2 Multiple-Step Substructuring Approach

For long bridges supported on multiple foundations, the support-separation distances are sufficiently large so that each foundation subsystem can be treated as being independent of the others; therefore, the soil impedance matrix for each foundation will be uncoupled from those of the other foundations. In this case, to simplify the overall problem, each foundation subsystem can be analyzed separately to obtain a boundary impedance matrix called the "foundation impedance matrix" and a consistent boundary force vector called the "foundation driving-force vector," both of which are associated with the DOF at its structure/foundation interface. Having obtained the foundation impedance matrix and the associated driving force vector for each foundation subsystem, all such matrices and vectors can be combined into the equations of motion for the total structure as a free-free system, resulting in $(s + f)$ DOF present in the structure–foundation subsystem rather than the $(s + f + g)$ DOF present in the complete soil–structure–foundation system. This reduced set of equations having $(s + f)$ DOF can be solved much more efficiently than solving the equations for the complete system having $(s + f + g)$ DOF as required by the one-step direct approach.

Referring to Equation 14.31, it is seen that the linear equations of motion for each independent foundation system "j" can be expressed in the frequency-domain form

$$\begin{bmatrix} \boldsymbol{D}_{ff}^{j}(i\omega) & \boldsymbol{D}_{fg}^{j}(i\omega) \\ \boldsymbol{D}_{fg}^{j}(i\omega)^{T} & [\boldsymbol{D}_{gg}^{j}(i\omega)+\boldsymbol{G}_{gg}^{j}(i\omega)] \end{bmatrix} \begin{Bmatrix} \boldsymbol{u}_{f}^{j}(i\omega) \\ \boldsymbol{u}_{g}^{j}(i\omega) \end{Bmatrix} = \begin{Bmatrix} 0 \\ \overline{\boldsymbol{f}}_{g}^{j}(i\omega) \end{Bmatrix} \tag{14.40}$$

in which

$$\overline{\boldsymbol{f}}_{g}^{j}(i\omega) = \boldsymbol{G}_{gg}^{j}(i\omega)\overline{\boldsymbol{u}}_{g}^{j}(i\omega) \tag{14.41}$$

Solving the second of Equation 14.40 $\boldsymbol{u}_g^j(i\omega)$ for gives

$$\boldsymbol{u}_{g}^{j}(i\omega) = \left[\boldsymbol{D}_{gg}^{j}(i\omega)+\boldsymbol{G}_{gg}^{j}(i\omega)\right]^{-1}\left[-\boldsymbol{D}_{fg}^{j}(i\omega)^{T}\boldsymbol{u}_{f}^{j}(i\omega)+\overline{\boldsymbol{f}}_{g}^{j}(i\omega)\right] \tag{14.42}$$

Substituting this equation into the first of Equation 14.40 yields

$$\left[\boldsymbol{D}_{ff}^{j}(i\omega)+\boldsymbol{F}_{ff}^{j}(i\omega)\right]\boldsymbol{u}_{f}^{j}(i\omega)=\overline{\boldsymbol{f}}_{f}^{j}(i\omega) \tag{14.43}$$

where

$$\boldsymbol{F}_{ff}^{j}(i\omega)\equiv-\boldsymbol{D}_{fg}^{j}(i\omega)[\boldsymbol{D}_{gg}^{j}(i\omega)+\boldsymbol{G}_{gg}^{j}(i\omega)]^{-1}\boldsymbol{D}_{fg}^{j}(i\omega)^{T} \tag{14.44}$$

$$\overline{\boldsymbol{f}}_{f}^{j}(i\omega)\equiv-\boldsymbol{D}_{fg}^{j}(i\omega)[\boldsymbol{D}_{gg}^{j}(i\omega)+\boldsymbol{G}_{gg}^{j}(i\omega)]^{-1}\overline{\boldsymbol{f}}_{g}^{j}(i\omega) \tag{14.45}$$

Matrix and $\boldsymbol{F}_{ff}^{j}(i\omega)$ vector $\overline{\boldsymbol{f}}_{f}^{j}(i\omega)$ will be referred to herein as the "foundation impedance" matrix and its associated "foundation driving-force" vector $\overline{\boldsymbol{u}}_{f}^{j}(i\omega)$, respectively, for the jth foundation. For convenience, a foundation-motion vector is now defined as given by

$$\overline{\boldsymbol{u}}_{f}^{j}(i\omega)\equiv\boldsymbol{F}_{ff}^{j}(i\omega)^{-1}\overline{\boldsymbol{f}}_{f}^{j}(i\omega) \tag{14.46}$$

so that the driving-force vector $\overline{\boldsymbol{f}}_{f}^{j}(i\omega)$ can be expressed in the form

$$\overline{\boldsymbol{f}}_{f}^{j}(i\omega)=\boldsymbol{F}_{ff}^{j}(i\omega)\overline{\boldsymbol{u}}_{f}^{j}(i\omega) \tag{14.47}$$

The motion vector $\overline{\boldsymbol{u}}_{f}^{j}(i\omega)$ given by Equation 14.46 is referred to subsequently as the "effective (scattered) foundation input motion" vector. Conceptually, this is the vector of foundation motions that, when multiplied by the foundation impedance matrix $\boldsymbol{F}_{ff}^{j}(i\omega)$, yields the foundation driving-force vector $\overline{\boldsymbol{f}}_{f}^{j}(i\omega)$ resulting from the prescribed scattered free-field soil input motions contained in vector $\overline{\boldsymbol{u}}_{g}^{j}(i\omega)$.

Combining Equations 14.43 for all foundation subsystems with the equations of motion for the complete free-free structure subsystem yields the desired reduced matrix equation of motion for the entire structure–foundation system in the linear form

$$\begin{bmatrix}\boldsymbol{D}_{ss}(i\omega) & \boldsymbol{D}_{sf}(i\omega)\\ \boldsymbol{D}_{sf}(i\omega)^{T} & [\boldsymbol{D}_{ff}^{s}(i\omega)+\boldsymbol{F}_{ff}(i\omega)]\end{bmatrix}\begin{Bmatrix}\boldsymbol{u}_{s}(i\omega)\\ \boldsymbol{u}_{f}(i\omega)\end{Bmatrix}=\begin{Bmatrix}0\\ \overline{\boldsymbol{f}}_{f}(i\omega)\end{Bmatrix} \tag{14.48}$$

in which $\boldsymbol{D}_{ss}(i\omega)$ and $\boldsymbol{D}_{sf}(i\omega)$ are given by Equations 14.27 and 14.28 directly, $\boldsymbol{D}_{ff}^{s}(i\omega)$ is that part of $\boldsymbol{D}_{ff}(i\omega)$ given by these same equations as contributed by the structure only, and

$$\overline{\boldsymbol{f}}_{f}(i\omega)=\boldsymbol{F}_{ff}(i\omega)\overline{\boldsymbol{u}}_{f}(i\omega) \tag{14.49}$$

The solution of Equation 14.48 for discrete values of ω over the frequency range of interest gives the desired solutions for $\boldsymbol{u}_{s}(i\omega)$ and $\boldsymbol{u}_{f}(i\omega)$. To obtain the corresponding solution $\boldsymbol{u}_{g}^{j}(i\omega)$ for each foundation subsystem j, a back substitution is required. This is done by substituting the solution $\boldsymbol{u}_{f}^{j}(i\omega)$ for each foundation subsystem j into Equation 14.42 and computing the corresponding response motions in vector $\boldsymbol{u}_{g}^{j}(i\omega)$. This step is called the "foundation feed-back" analysis.

When large nonlinearities develop in the structure during a seismic event, the reduced equations of motion representing the coupled structure–foundation system must be expressed in the time domain. To do so, consider the structure alone as a free–free linear system having externally applied forces $\boldsymbol{f}_{f}(t)$ acting in the f DOF. The equations of motion for this system can be expressed in the frequency domain form

$$\begin{bmatrix} \boldsymbol{D}_{ss}(i\omega) & \boldsymbol{D}_{sf}(i\omega) \\ \boldsymbol{D}_{sf}(i\omega)^T & \boldsymbol{D}_{ff}^{s}(i\omega) \end{bmatrix} \begin{Bmatrix} \boldsymbol{u}_s(i\omega) \\ \boldsymbol{u}_f(i\omega) \end{Bmatrix} = \begin{Bmatrix} 0 \\ \boldsymbol{f}_f(i\omega) \end{Bmatrix} \tag{14.50}$$

in which $\boldsymbol{f}_f(i\omega)$ is the Fourier transform of vector $\boldsymbol{f}_f(t)$. If Equation 14.50 is to represent the coupled structure–foundation system, then $\boldsymbol{f}_f(i\omega)$ must satisfy the relation

$$\boldsymbol{f}_f(i\omega) = \boldsymbol{F}_{ff}(i\omega)\left\{\bar{\boldsymbol{u}}_f(i\omega) - \boldsymbol{u}_f(i\omega)\right\} \tag{14.51}$$

in which matrix $\boldsymbol{F}_{ff}(i\omega)$ is an assembly of the individual foundation impedance matrices $\boldsymbol{F}_{ff}^{j}(i\omega)$ given by Equation 14.44 for all values of j and vector $\bar{\mathrm{u}}_f(i\omega)$ is the corresponding complete foundation-motion vector containing all individual vectors $\bar{\mathrm{u}}_f^{j}(i\omega)$ given by Equation 14.46.

Equation 14.50 can be converted to the time-domain form

$$\begin{bmatrix} \boldsymbol{M}_{ss} & \boldsymbol{M}_{sf} \\ \boldsymbol{M}_{sf}^T & \boldsymbol{M}_{ff}^{s} \end{bmatrix} \begin{Bmatrix} \ddot{\boldsymbol{u}}_s(t) \\ \ddot{\boldsymbol{u}}_f(t) \end{Bmatrix} + \begin{bmatrix} \boldsymbol{C}_{ss} & \boldsymbol{C}_{sf} \\ \boldsymbol{C}_{sf}^T & \boldsymbol{C}_{ff}^{s} \end{bmatrix} \begin{Bmatrix} \dot{\boldsymbol{u}}_s(t) \\ \dot{\boldsymbol{u}}_f(t) \end{Bmatrix} + \begin{bmatrix} \boldsymbol{K}_{ss} & \boldsymbol{K}_{sf} \\ \boldsymbol{K}_{sf}^T & \boldsymbol{K}_{ff}^{s} \end{bmatrix} \begin{Bmatrix} \boldsymbol{u}_s(t) \\ \boldsymbol{u}_f(t) \end{Bmatrix} = \begin{Bmatrix} 0 \\ \boldsymbol{f}_f(t) \end{Bmatrix} \tag{14.52}$$

in which $\boldsymbol{K}_{ff}^{s}$, $\boldsymbol{C}_{ff}^{s}$, and $\boldsymbol{M}_{ff}^{s}$ are the standard stiffness, damping, and mass matrices contributed by the structure only (no contributions from the foundation) and $\boldsymbol{f}_f(t)$ is the inverse Fourier transform of $\boldsymbol{f}_f(i\omega)$ given by Equation 14.51. In order for $\boldsymbol{f}_f(t)$ to have no frequency-dependent parameters, as required by a time-domain solution, matrix $\mathbf{F}_{ff}(i\omega)$ should be separated into its real and imaginary parts in accordance with

$$\boldsymbol{F}_{ff}(i\omega) = \boldsymbol{F}_{ff}^{R}(\omega) + i\boldsymbol{F}_{ff}^{I}(\omega) \tag{14.53}$$

in which $\mathrm{F}_{ff}^{R}(\omega)$ and $\mathrm{F}_{ff}^{I}(\omega)$ can be approximated using the relations

$$\boldsymbol{F}_{ff}^{R}(\omega) \doteq \bar{\boldsymbol{K}}_{ff} - \omega^2\boldsymbol{M}_{ff}; \boldsymbol{F}_{ff}^{I}(\omega) \doteq \omega\bar{\boldsymbol{C}}_{ff} \tag{14.54}$$

where the real constants in matrices $\bar{\boldsymbol{K}}_{ff}$, $\bar{\boldsymbol{M}}_{ff}$, and $\bar{\mathrm{C}}_{ff}$ are assigned numerical values to provide best fits to the individual frequency-dependent functions in matrices $\boldsymbol{F}_{ff}^{R}(\omega)$ and $\boldsymbol{F}_{ff}^{I}(\omega)$ over the frequency range of major influence on seismic response; usually the range $0 < \omega < 4\pi$ rad/s is adequate for large bridges. In this fitting process, it is sufficient to treat $\bar{\boldsymbol{M}}_{ff}$ as a diagonal matrix, thus, affecting only the diagonal functions in matrix $\boldsymbol{F}_{ff}^{R}(\omega)$.

Substituting Equation 14.54 into Equation 14.53 and the resulting Equation 14.53 into Equation 14.51, this latter equation can be inverse Fourier transformed giving

$$\boldsymbol{f}_f(t) = \bar{\boldsymbol{K}}_{ff}\left\{\bar{\boldsymbol{u}}_f(t) - \boldsymbol{u}_f(t)\right\} + \bar{\boldsymbol{C}}_{ff}\left\{\dot{\bar{\boldsymbol{u}}}_f(t) - \dot{\boldsymbol{u}}_f(t)\right\} + \bar{\boldsymbol{M}}_{ff}\left\{\ddot{\bar{\boldsymbol{u}}}_f(t) - \ddot{\boldsymbol{u}}_f(t)\right\} \tag{14.55}$$

which when introduced into Equation 14.50 yields the desired reduced linear equations of motion in the time-domain form

$$\begin{bmatrix} \boldsymbol{M}_{ss} & \boldsymbol{M}_{ff} \\ \boldsymbol{M}_{sf}^T & [\boldsymbol{M}_{ff}^{S} + \bar{\boldsymbol{M}}_{ff}] \end{bmatrix} \begin{Bmatrix} \ddot{\boldsymbol{u}}_s(t) \\ \ddot{\boldsymbol{u}}_f(t) \end{Bmatrix} + \begin{bmatrix} \boldsymbol{C}_{ss} & \boldsymbol{C}_{sf} \\ \boldsymbol{C}_{sf}^T & [\boldsymbol{C}_{ff}^{s} + \bar{\boldsymbol{C}}_{ff}] \end{bmatrix} \begin{Bmatrix} \dot{\boldsymbol{u}}_s(t) \\ \dot{\boldsymbol{u}}_f(t) \end{Bmatrix} + \begin{bmatrix} \boldsymbol{K}_{ss} & \boldsymbol{K}_{sf} \\ \boldsymbol{K}_{sf}^T & [\boldsymbol{K}_{ff}^{s} + \bar{\boldsymbol{K}}_{ff}] \end{bmatrix} \begin{Bmatrix} \boldsymbol{u}_s(t) \\ \boldsymbol{u}_f(t) \end{Bmatrix} = \begin{bmatrix} 0 \\ \bar{\boldsymbol{K}}_{ff}\bar{\boldsymbol{u}}_f(t) + \bar{\boldsymbol{C}}_{ff}\dot{\bar{\boldsymbol{u}}}_f(t) + \bar{\boldsymbol{M}}_{ff}\ddot{\bar{\boldsymbol{u}}}_f(t) \end{bmatrix} \tag{14.56}$$

showing that no frequency-dependent parameters remain in the equations of motion, thus satisfying the time-domain solution requirement. Again, as explained previously, the full viscous damping matrix in this equation is usually expressed in the Rayleigh form given by Equation 14.34 in which constants α_R and β_R are assigned numerical values to limit the modal damping ratios to levels within acceptable bounds over the range of frequencies dominating seismic response. As explained previously for Equation 14.38, the damping and mass terms on the right-hand side of Equation 14.56 usually have small effects on the solution; however, their importance should be checked.

Having modified the third term on the left-hand side of Equation 14.56 to its nonlinear hysteretic form, the complete set of coupled equations can be solved for displacements $\boldsymbol{u}_s(t)$ and $\boldsymbol{u}_f(t)$ using standard step-by-step numerical integration procedures.

To obtain the corresponding $\boldsymbol{u}_g^j(i\omega)$ for each foundation subsystem j, the previously defined "foundation feed-back analyses" must be performed. To do so, each subvector $\boldsymbol{u}_f^j(t)$ contained in vector$\mathbf{u}_f(t)$, must be Fourier transformed to obtain $\boldsymbol{u}_f^j(i\omega)$. Having these subvectors for all values of j, each one can be substituted separately into Equation 14.42 giving the corresponding subvector $\boldsymbol{u}_g^j(i\omega)$. Inverse Fourier transforming each of these subvectors yields the corresponding vectors $\boldsymbol{u}_f^j(t)$ for all values of j.

14.7 Demand Analysis Examples

This section presents the results of three example solutions to illustrate applications of the demand analysis procedures described in the previous section, in particular, the multiple-step substructuring approach. These examples have been chosen from actual situations to illustrate application of the three methods of soil–foundation modeling (1) the elasto-dynamic method, (2) the empirical "p–y" method, and (3) the hybrid method.

14.7.1 Caisson Foundation

The first example is chosen to illustrate application of the elasto-dynamic method of modeling and analysis to a deeply embedded caisson foundation of a large San Francisco bay-crossing bridge. The foundation considered is a large reinforced concrete cellular caisson, 80 ft. (24.4 m) long, 176 ft. (53.6 m) wide, and 282 ft. (86.0 m) tall, located at a deep soil site and filled with water. The configuration of the caisson and its supporting soil profile and properties are shown in Figure 14.8. The soil properties are the shear-strain-compatible equivalent-linear properties obtained from free-field site response analyses using SHAKE with the seismic input motions prescribed at bedrock surface in the form of rock outcrop motion. Thus, these properties have incorporated stiffness degradation effects due to global soil nonlinearities induced in the free-field by the selected seismic input.

Since the caisson is deeply embedded and has large horizontal dimensions, the local soil nonlinearities that develop near the soil/caisson interface are relatively small; therefore, they were neglected in the demand analysis. The soil–caisson system was modeled using the elasto-dynamic method, that is, the system was modeled by an elastic foundation structure embedded in a damped-elastic soil medium having the properties shown in Figure 14.8. This model, developed using the finite-element SASSI computer program for one-quarter of the soil–caisson system, is shown in Figure 14.8. Using this model, the foundation impedance matrix, that is defined by Equation 14.44, and its associated effective (scattered) foundation input motion vector, that is, $\boldsymbol{F}_{ff}^j(i\omega)$ defined by Equation 14.46, were evaluated consistent with the free-field seismic input using SASSI. The foundation impedance matrix associated with the 6 DOF of the node located at the top of the caisson El. 40 ft. (12.2 m) was computed following the procedure described in Section 6. The individual impedance functions in this matrix are shown in Figure 14.9. The amplitudes of the transfer functions for longitudinal response motions of the caisson relative to the corresponding seismic input motion, as computed for several elevations, are shown in Figure 14.10. The 5%-damped ARS computed for these motions are also shown in Figure 14.10 where they can be

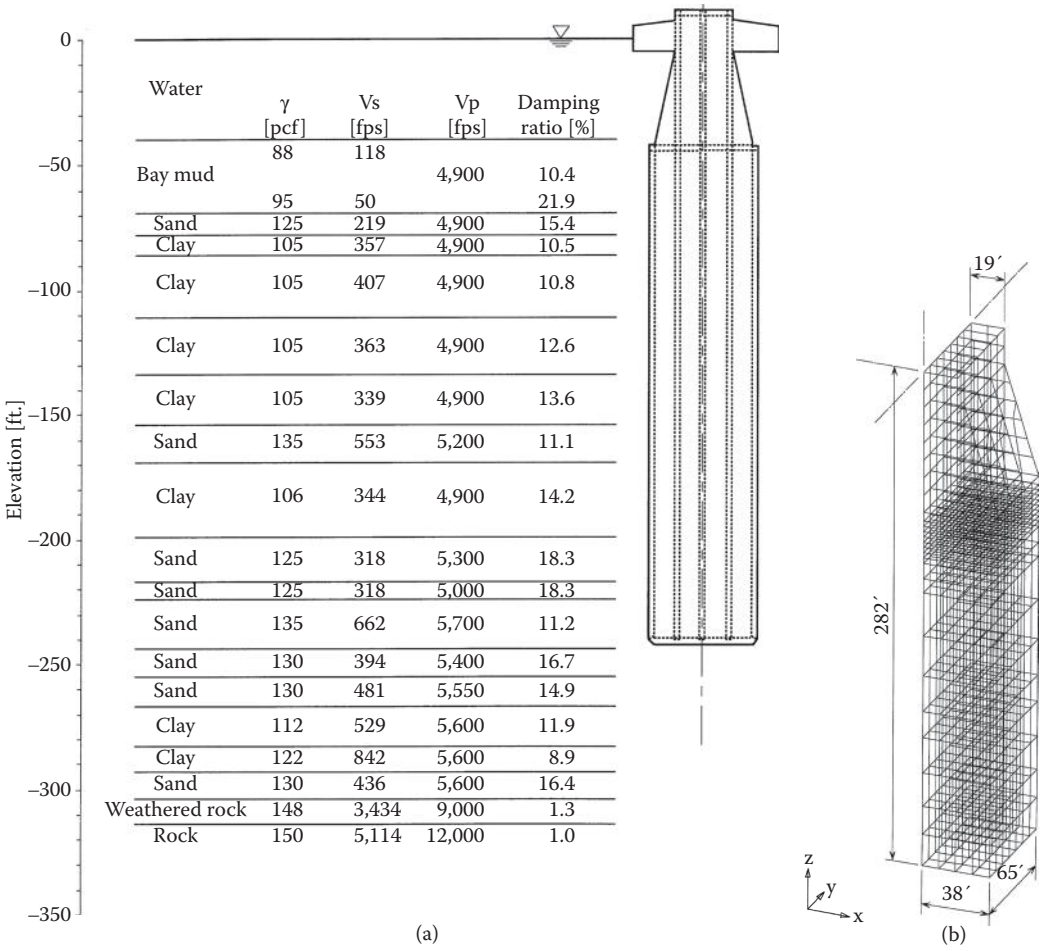

	γ [pcf]	Vs [fps]	Vp [fps]	Damping ratio [%]
Water				
	88	118		
Bay mud			4,900	10.4
	95	50		21.9
Sand	125	219	4,900	15.4
Clay	105	357	4,900	10.5
Clay	105	407	4,900	10.8
Clay	105	363	4,900	12.6
Clay	105	339	4,900	13.6
Sand	135	553	5,200	11.1
Clay	106	344	4,900	14.2
Sand	125	318	5,300	18.3
Sand	125	318	5,000	18.3
Sand	135	662	5,700	11.2
Sand	130	394	5,400	16.7
Sand	130	481	5,550	14.9
Clay	112	529	5,600	11.9
Clay	122	842	5,600	8.9
Sand	130	436	5,600	16.4
Weathered rock	148	3,434	9,000	1.3
Rock	150	5,114	12,000	1.0

FIGURE 14.8 Configuration and soil profile and properties of the cassion foundation at its SASSI half-model.

compared with the 5%-damped response spectra for the corresponding seismic input motion prescribed at bedrock level and the corresponding free-field soil motion at the mudline elevation.

As indicated in Figure 14.10, the soil–caisson interaction system alone, without pier tower and super structure of the bridge being present, has characteristic translational and rocking mode frequencies of 0.7 and 1.4 Hz (periods 1.4 and 0.7 s), respectively. The longitudinal scattered foundation motion associated with the foundation impedance matrix mentioned above is the motion represented by the response spectrum for El. 40 ft. (12.2 m) as shown in Figure 14.10.

The response spectra shown in Figure 14.10 indicate that, because of the 0.7 s translational period of the soil–caisson system, the scattered foundation motion at the top of the caisson where the bridge's pier tower would be supported, exhibits substantial amplifications in the neighborhood of this period. In the period range longer than 2.0 s, in which the bridge system's major natural vibration frequencies are located, the spectral values for the scattered foundation input motion are seen to be smaller than the corresponding values for the free-field mudline motion. The above results point out the importance of properly modeling both the stiffness and the inertial properties of the soil–caisson system so that the resulting scattered foundation motions to be used as input to the foundation–structure system will appropriately represent the actual dynamic characteristics of the soil–caisson interaction system.

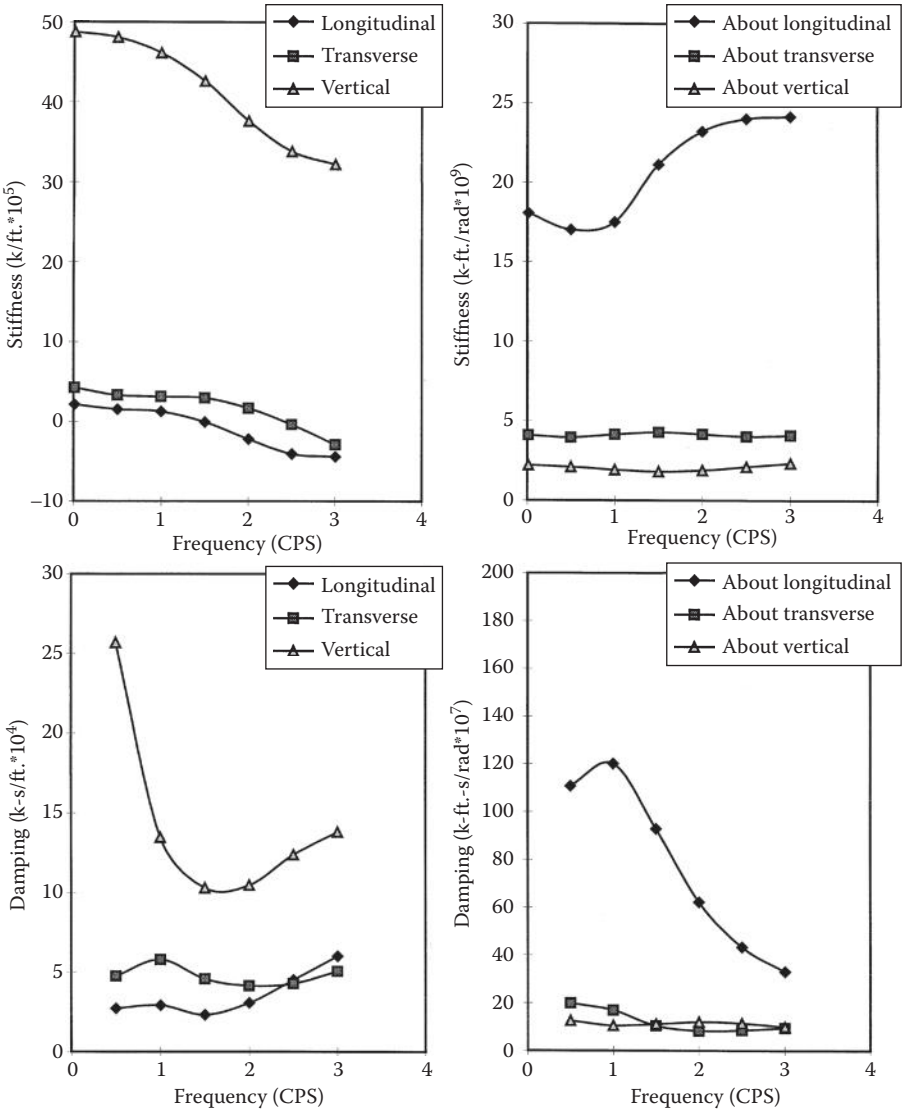

FIGURE 14.9 Foundation impedance functions at the top of the caisson considered.

14.7.2 Slender-Pile-Group Foundation

The second example is to illustrate the application of the empirical "*p–y*" method in a demand analysis of a slender-pile-group foundation constructed at a deep soil site. The pile-group foundation selected is one of 78 pier foundations of a long water-crossing steel truss bridge. The foundation is constructed of two 24 ft. (7.32 m)–diameter, bell-shaped precast reinforced concrete pilecaps, which are linked together by a deep cross beam, as shown in Figure 14.11. Each bell-shaped pilecap is supported on a group of 28 steel 14BP89 H-pipes, giving a total of 56 piles supporting the combined two-bell pilecap. The piles in the outer ring and in the adjacent inner ring are battered at an angle of 4 to 1 and 6 to 1, respectively, leaving the remaining piles as vertical piles. The top ends of all piles are embedded with sufficient lengths into the concrete that fills the interior space of the bell-shaped pilecaps such that these piles can be considered as fixed-head piles. The piles penetrate deep into the supporting soil medium to an

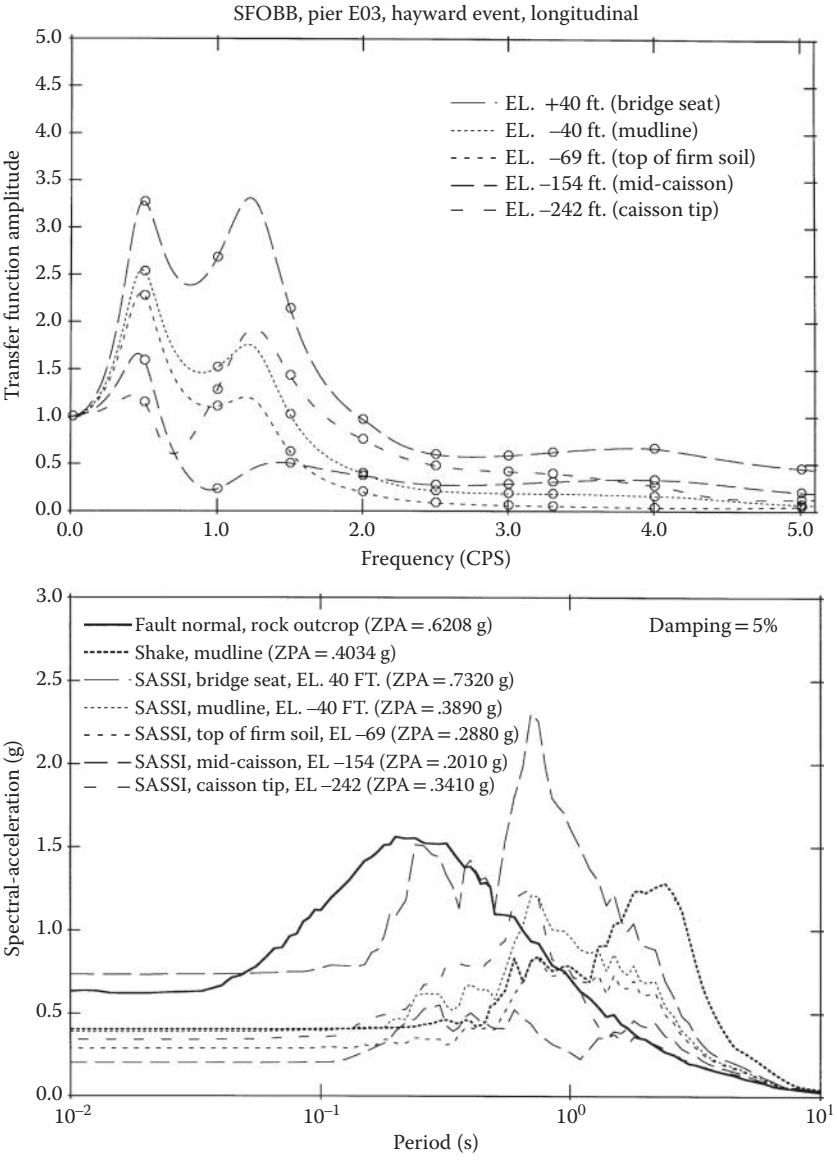

FIGURE 14.10 Transfer function amplitudes and 5% damped response spectra for scattered foundation motions of the caisson at several elevations.

average depth of 147 ft. (44.8 m) below the mudline, where they encounter a thick dense sand layer. The soil profile and properties at this foundation location are shown in Figure 14.12. As indicated in this figure, the top 55 ft. (16.8 m) of the site soil is composed of a 35 ft. (10.7 m) layer of soft bay mud overlying a 20 ft. (6.1 m) layer of loose silty sand.

Because of the soft top soil layers and the slender piles used, the foundation under seismic excitations is expected to undergo relatively large foundation lateral displacements relative to the free-field soil. Thus, large local soil nonlinearities are expected to occur at the soil/pile interfaces. To model the nonlinear soil resistances to the piles' lateral and axial deflections, the empirically derived lateral "*p–y*" and axial "*t–z*," and the pile-tip "*Q–d*" curves for each pile were used. Typical "*p–y*" and "*t–z*" curves developed for the piles are shown in Figure 14.13. Using the nonlinear "*p–y*," "*t–z*," and "*Q–d*" curves

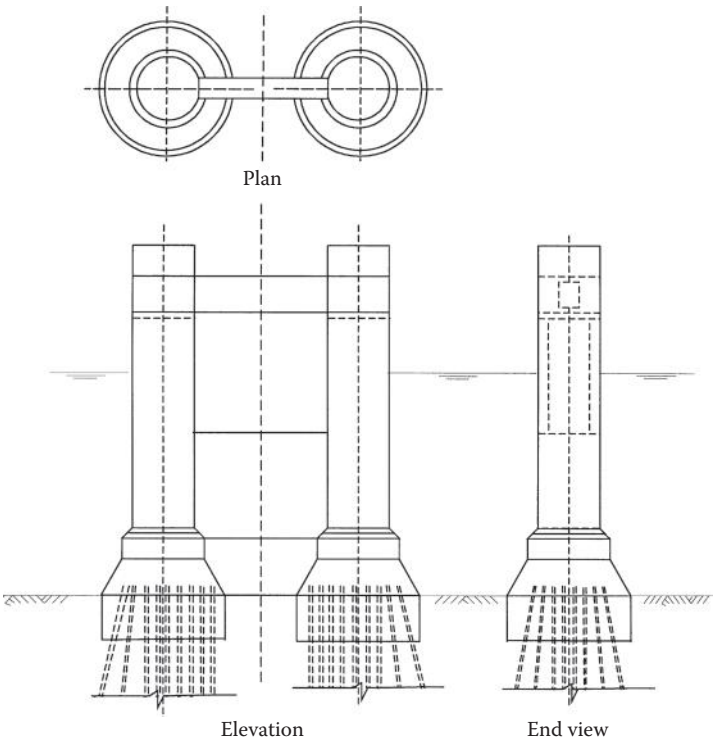

FIGURE 14.11 Configuration of the slender-pile group foundation considered.

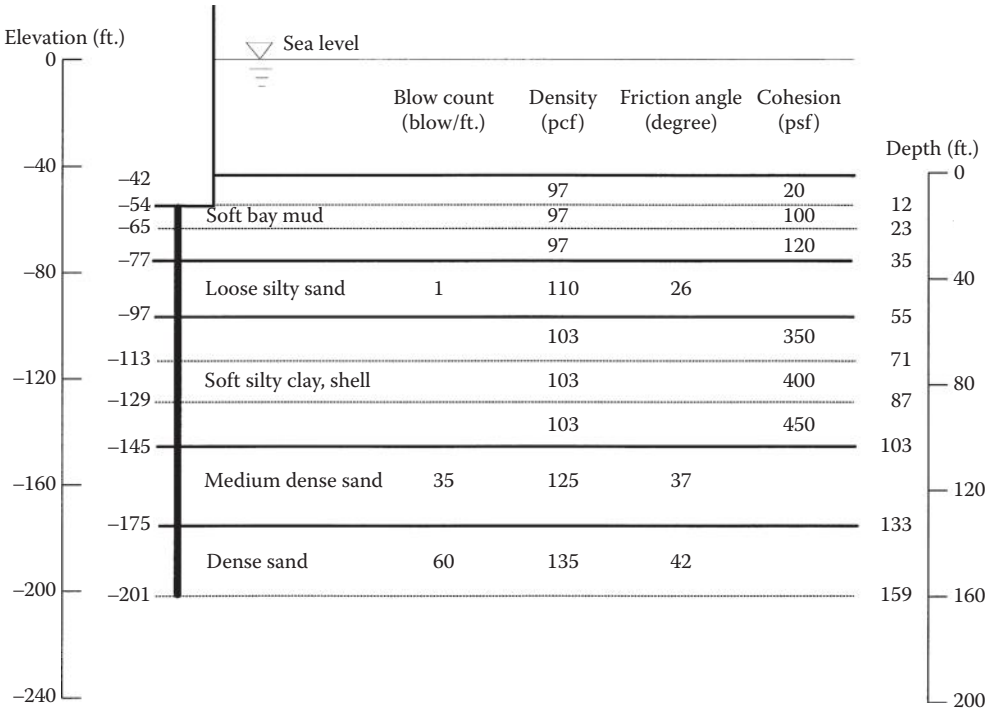

FIGURE 14.12 Soil profile and properties at the slender-pile group foundation considered.

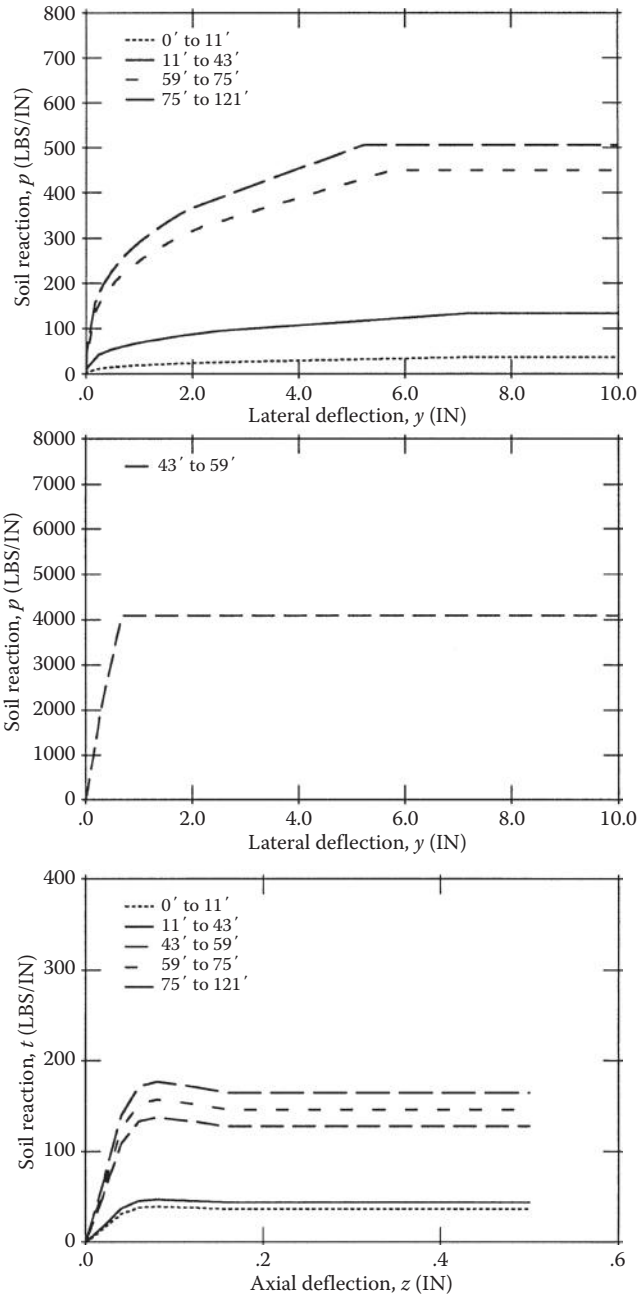

FIGURE 14.13 Typical p–y and t–z curves for the piles of the slender-pile group foundation considered.

developed, evaluation of the foundation impedance matrix, $\boldsymbol{F}_{ff}^{f}(i\omega)$, and the associated scattered foundation input motion vector, $\overline{\boldsymbol{u}}_f(i\omega)$, were obtained following the procedures described below:

1. Determine the pile-group deflected shape using a nonlinear analysis program such as GROUP (Reese et al., 1990), LPIPE (Reese and Wang 2010), and APILE2 (Reese and Wang 1990), as appropriate, under an applied set of monotonically increasing axial and lateral forces and an overturning moment.
2. Select target levels of axial and lateral deflections at each selected soil depth corresponding to a selected target level of pilecap displacement and determine the corresponding secant moduli from the applicable nonlinear "*p–y*," "*t–z*," and "*Q–d*" curves.
3. Develop a model of a group of elastic beams supported on elastic axial and lateral soil springs for the pile group using the elastic properties of the piles and the secant moduli of the soil resistances obtained in Step 2 above.
4. Compute the foundation impedance matrix and associated scattered foundation input motion vector for the model developed in Step 3 using Equations 14.44 and 14.46.

Since the "*p–y*," "*t–z*," and "Q-d" curves represent pseudo-static force-deflection relations, the resulting foundation impedance matrix computed by the above procedure is a real (not complex) frequency-independent pseudo-static stiffness matrix, that is, $\boldsymbol{F}_{ff}^{j}(i\omega) = \boldsymbol{F}_{ff}^{j}(0)$. For the pile group foundation considered in this example, the beam-on-elastic-spring model shown schematically in Figure 14.14 was used. The foundation stiffness matrix is associated with the 6 DOF of the nodal point located at the bottom center of the pilecap is shown in Figure 14.14. The scattered foundation motions in the longitudinal, transverse, and vertical directions associated with this foundation stiffness matrix are represented by their 5%-damped ARS shown in Figure 14.15. These spectra can be compared with the corresponding spectra for the seismic input motion prescribed at the pile-tip elevation and the free-field mudline motions computed from free-field site response analyses using SHAKE. As shown in Figure 14.15, the spectral values for the scattered pilecap motions, which would be used as input to the foundation/structure system, are lower than the spectral values for the free-field mudline motions. This result is to be expected for two reasons: (1) the soft top soil layers present at the site are not capable of

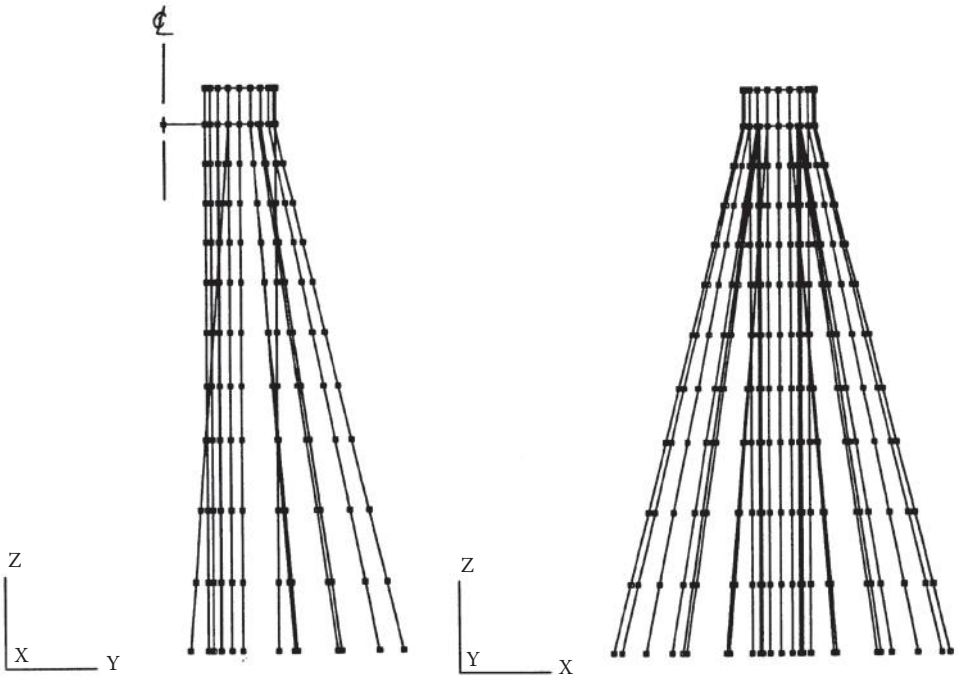

FIGURE 14.14 Beam-on-elastic-foundation half-model for the slender-pile group foundation considered.

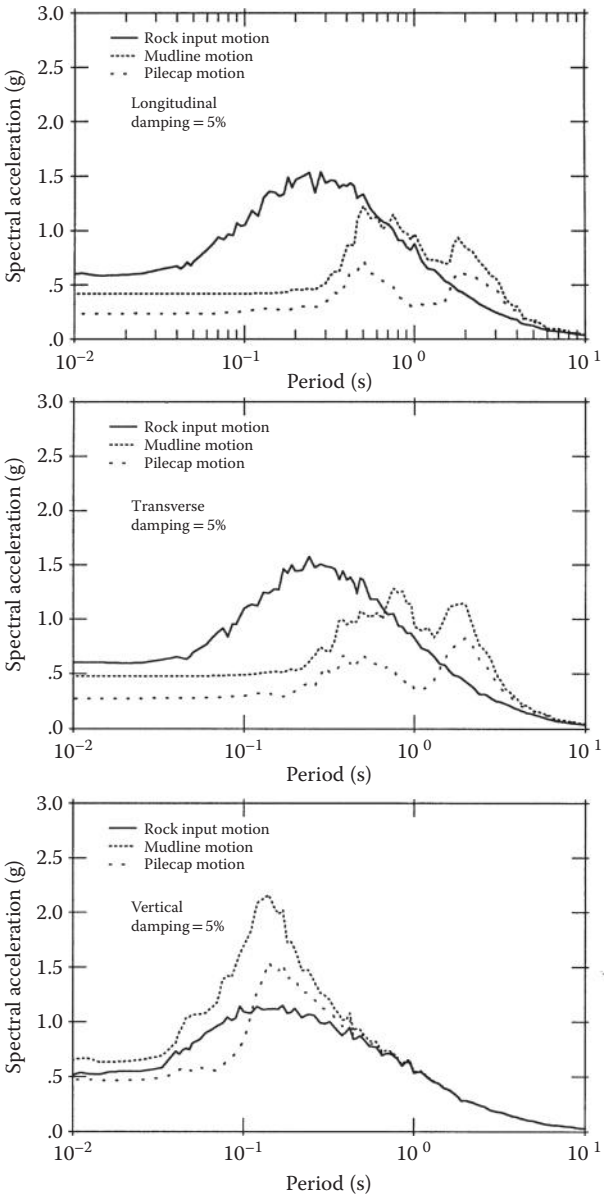

FIGURE 14.15 Comparisons of 5% damped response spectra for the rock input, mudline, and scattered pile cap motions in longitudinal, transverse, and vertical directions.

driving the pile group foundation, and (2) the battered piles, acting with the vertical piles resist lateral loads primarily through stiff axial truss action; in which case, the effective input motions at the pilecap are controlled more by the free-field soil motions at depth, where more competent soil resistances are present, than by the soil motions near surface.

14.7.3 Large-Diameter Shaft Foundation

The third example is to illustrate application of the demand analysis procedure using the hybrid method of modeling. This method is preferred for a foundation constructed of a group of large-diameter CISS

or CIDH shafts. Because of the large horizontal dimensions and substantial masses associated with the shafts in this type of foundation, the dynamic interaction of the shafts with the surrounding soil medium is more appropriately modeled and analyzed using the elasto-dynamic method; however, because the shafts resist loadings in a manner like piles, the local soil nonlinearities present in the soil–shaft interface regions near the ground surface where soft soils are usually present may be sufficiently large that they should be explicitly considered using a method such as the empirical "*p–y*" method.

The foundation selected for this example is composed of two 10.5 ft. (3.2 m) diameter shafts 150-ft. (45.7 m) long, each consisting of a steel shell of wall thickness 1.375 in. (34.9 mm) filled with concrete. These two shafts are designed to be used as seismic retrofit shear piles for adding lateral stiffnesses and lateral load-resistance capacities to the H-pile-group foundation considered in the second example discussed previously. The two shafts are to be linked to the existing pile group at the pilecap through a pilecap extension that permits the shafts to resist only horizontal shear loads acting on the pilecap, not axial loads and overturning moments. These shear piles have been designed to resist seismic horizontal shear loads acting on the pile head up to 3,000 kips (13,344 KN) each.

To determine the foundation impedance matrix and the scattered pilecap motion vector associated with the horizontal displacements of the shafts at the pilecap, a SASSI model of one-half

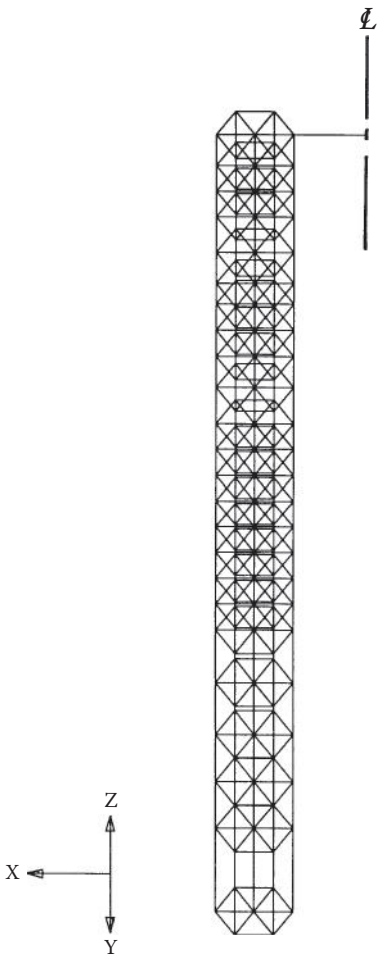

FIGURE 14.16 SASSI half-model of the large-diameter shaft foundation considered.

TABLE 14.1 Strain-Compatible Soil Properties for the Large-Diameter Shaft Foundation

			Unit Wt.	Shear Wave		Compressing Wave	
EL ft. (m)	Depth; ft. (m)	Thickness; ft. (m)	$\frac{K}{ft.^3}\left(\frac{KN}{m^3}\right)$	Velocity $\frac{ft.}{s}\left(\frac{m}{s}\right)$	Damping Ratio	Velocity $\frac{ft.}{s}\left(\frac{m}{s}\right)$	Damping Ratio
−50 (−15.2)	0 (0.0)	10 (3.05)	0.096 (15.1)	202.1 (61.6)	0.10	4,800 (1,463)	0.09
−60 (−18.3)	10 (3.05)	10(3.05)	0.096 (15.1)	207.5 (63.3)	0.15	5,000 (1,524)	0,10
−70 (−21.3)	20 (6.10)	10(3.05)	0.096 (15.1)	217.7 (66,4)	0.17	5,000 (1,524)	0,10
−80 (−24.4)	30 (9.15)	20 (6.10)	0.110 (17.3)	137.5 (41,9)	0.25	4,300 (1,311)	0,10
−100 (−30.5)	50 (15.2)	10(3.05)	0.096 (15.1)	215.7 (65.8)	0.20	4,800 (1,463)	0.10
−110 (−33.5)	60 (18.3)	20 (6.10)	0.096 (15.1)	218.4 (66.6)	0.20	4,300 (1,311)	0.10
−130 (−39.6)	80 (24.4)	20 (6.10)	0.096 (15.1)	233.0 (71.0)	0.20	4,900 (1,494)	0.10
−150 (−45.7)	100 (30.5)	20 (6.10)	0.120(18.8)	420.4(123.2)	0.20	5,500 (1,677)	0.10
−170 (−51.8)	120 (36.6)	10 (3.05)	0.120 (18.8)	501.0 (152.7)	0.19	6,000 (1,829)	0.10
−180 (−54.9)	130 (39.6)	10 (3.05)	0.120 (18.8)	532.7 (162.4)	0.19	5,800 (1,768)	0.10
−190 (−57.9)	140 (42.7)	20 (6.10)	0.125 (19.6)	607.2 (135,1)	0.18	5,800 (1,768)	0.10
−210 (−64.0)	160 (48.8)	20 (6.10)	0.128 (20.1)	806.9 (246.0)	0.16	5,800 (1,768)	0.10
−230 (−70.1)	180 (54.9)	10(3.05)	0.133 (20.9)	1,374.4 (419.0)	0.11	6,400 (1,951)	0.10
−240 (−78.2)	190 (57.9)	5 (1.52)	0.140 (21.9)	2,844.9 (367.3)	0.02	12,000 (3,658)	0.02
−245 (−74.7)	195 (59.5)	halfspace	0.145 (22.8)	6,387.2 (1,947.3)	0.01	12,000 (3,658)	0.01

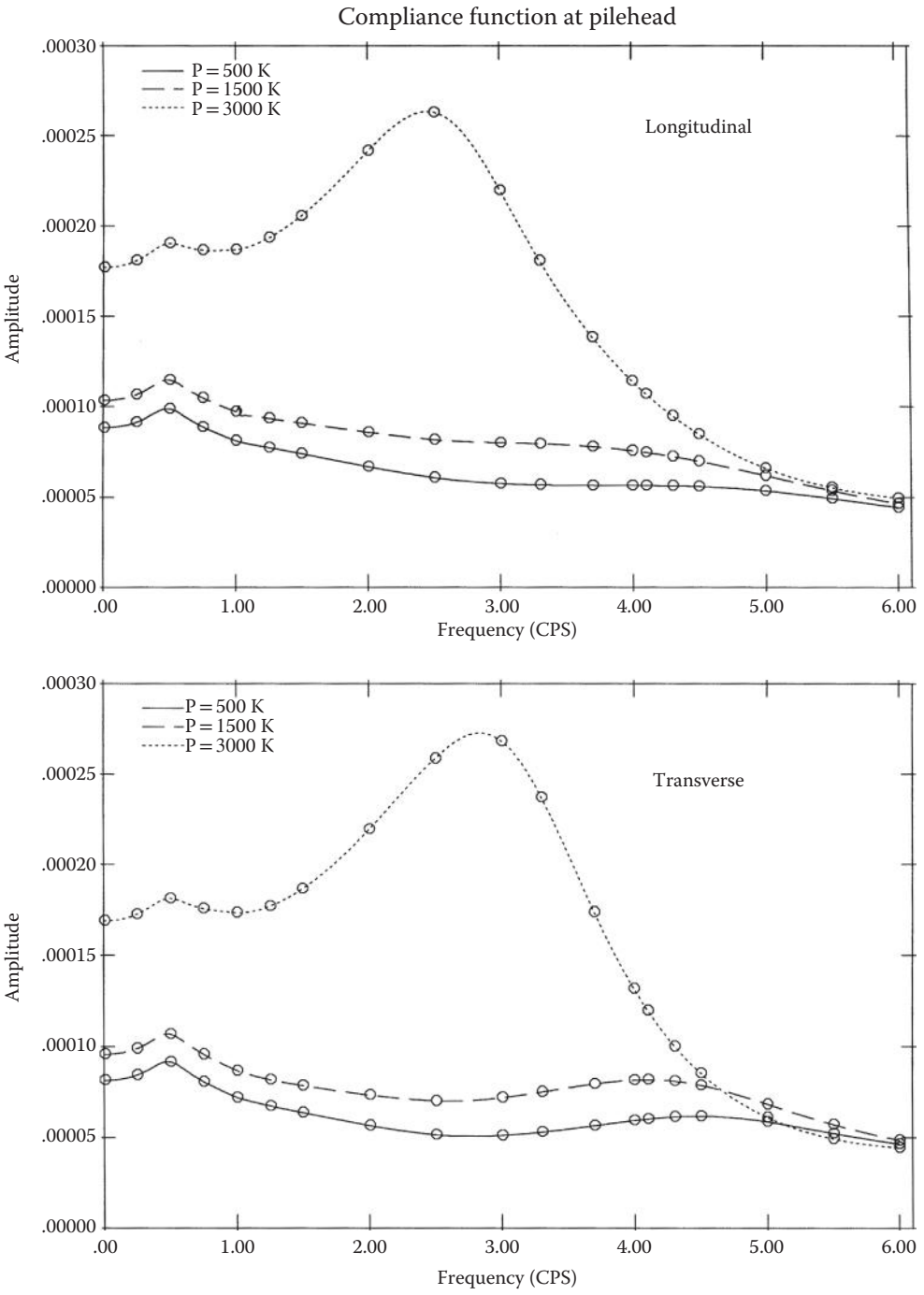

FIGURE 14.17 Foundation compliance functions at discrete values of shear load applied at the top of the shaft foundation.

of the soil-shaft system is developed as shown in Figure 14.16. The soil properties used in this model are the strain-compatible properties shown in Table 14.1, which were obtained from the free-field site response analyses using SHAKE; thus, the effects of global soil nonlinearities induced in the free-field soil by the design seismic input have been incorporated. To model the local soil nonlinearities occurring near the soil–shaft interface, 3-D (two lateral and one axial) soil springs are used to connect the beam elements representing the shafts to the soil nodes located at the boundary of the soil–shaft interfaces. The stiffnesses of these springs are derived in such a manner that they match the secant moduli of the empirical "*p–y*," "*t–z*," and "*Q–d*" curves developed for the shafts, as described previously in Section 14.5.3. Using the complete hybrid model shown in Figure 14.16, foundation compliances as functions of frequency were developed for harmonic pile-head shear loads varying from 500 (2,224) to 3,000 kips (13,334 KN). The results obtained are shown in Figure 14.17. It is seen that by incorporating local soil nonlinearities using the hybrid method, the resulting foundation compliance coefficients are not only frequency dependent due to the soil and shaft inertias and soil layering effects as captured by the elasto-dynamic method, but they are also load-/deflection-amplitude dependent due to the local soil nonlinearities, as captured by the empirical "*p–y*" method. The shear load-deflection curves obtained at the pile-head in the low frequency

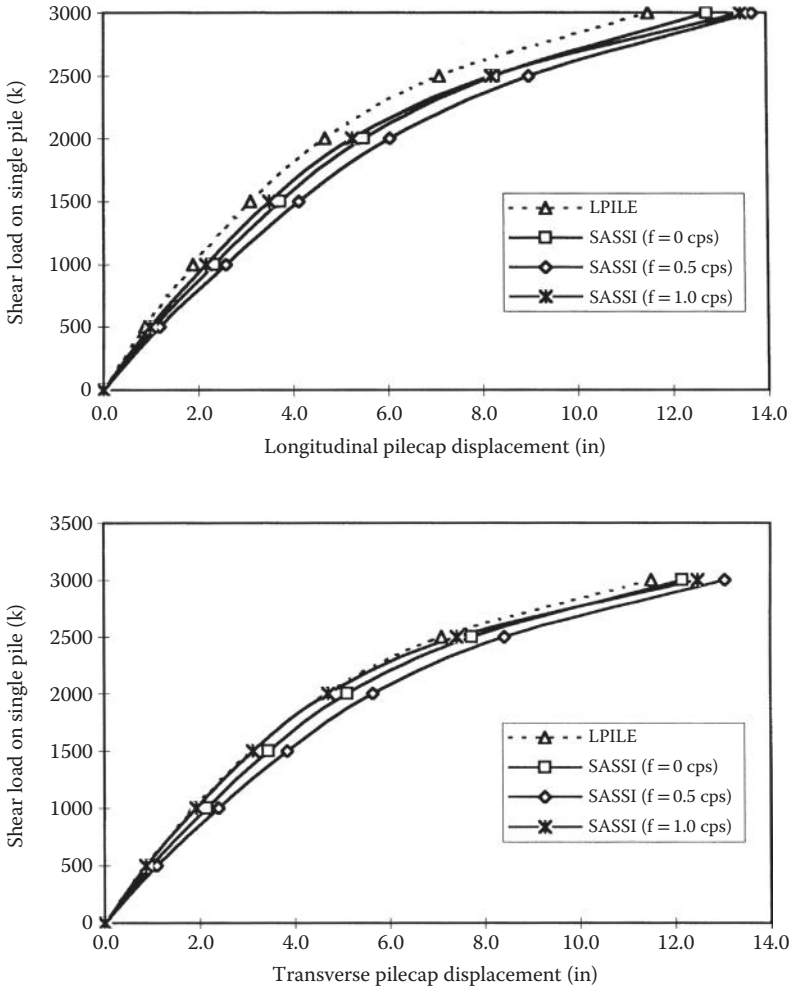

FIGURE 14.18 Typical shear load–deflection curves at several forcing frequencies.

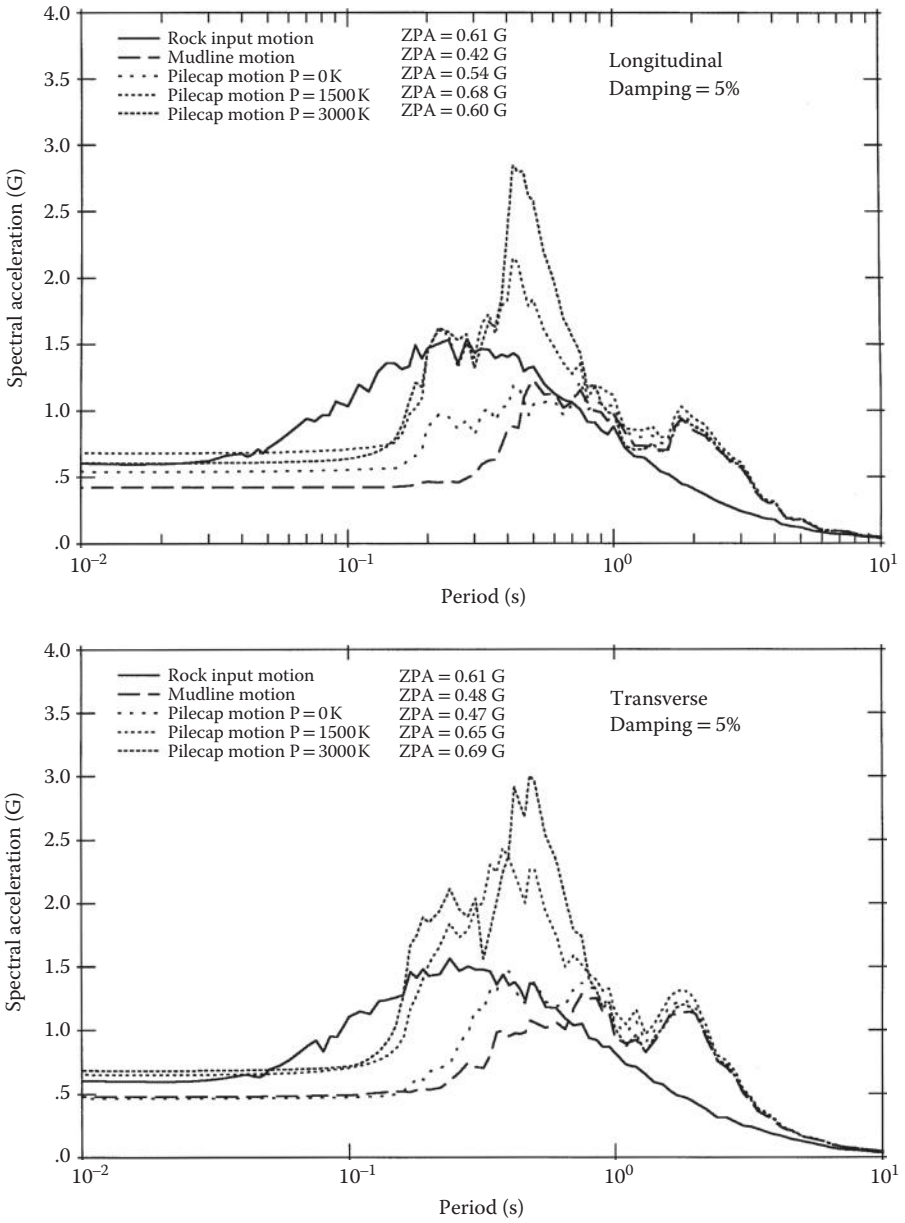

FIGURE 14.19 Comparisons of 5% damped response spectra for the longitudinal and transverse rock input, mudline, and scattered pile cap motions for the shaft foundations at several shear load levels.

range (≤1.0 Hz) are shown in Figure 14.18. The deflection curve for zero frequency, that is, the static loading case, compares well with that obtained from a nonlinear analysis using LPILE (Reese et al. 1989), as indicated in Figure 14.18.

Subjecting the foundation to the design seismic input motions prescribed at the pile-tip elevation and the corresponding free-field soil motions over its full depth, scattered foundation motions in the longitudinal and transverse directions of the bridge at the bottom center of the pile cap were obtained as shown in terms of their 5%-damped ARS in Figure 14.19, where they can be compared with the corresponding response spectra for the seismic input motions and the free-field mudline motions. It

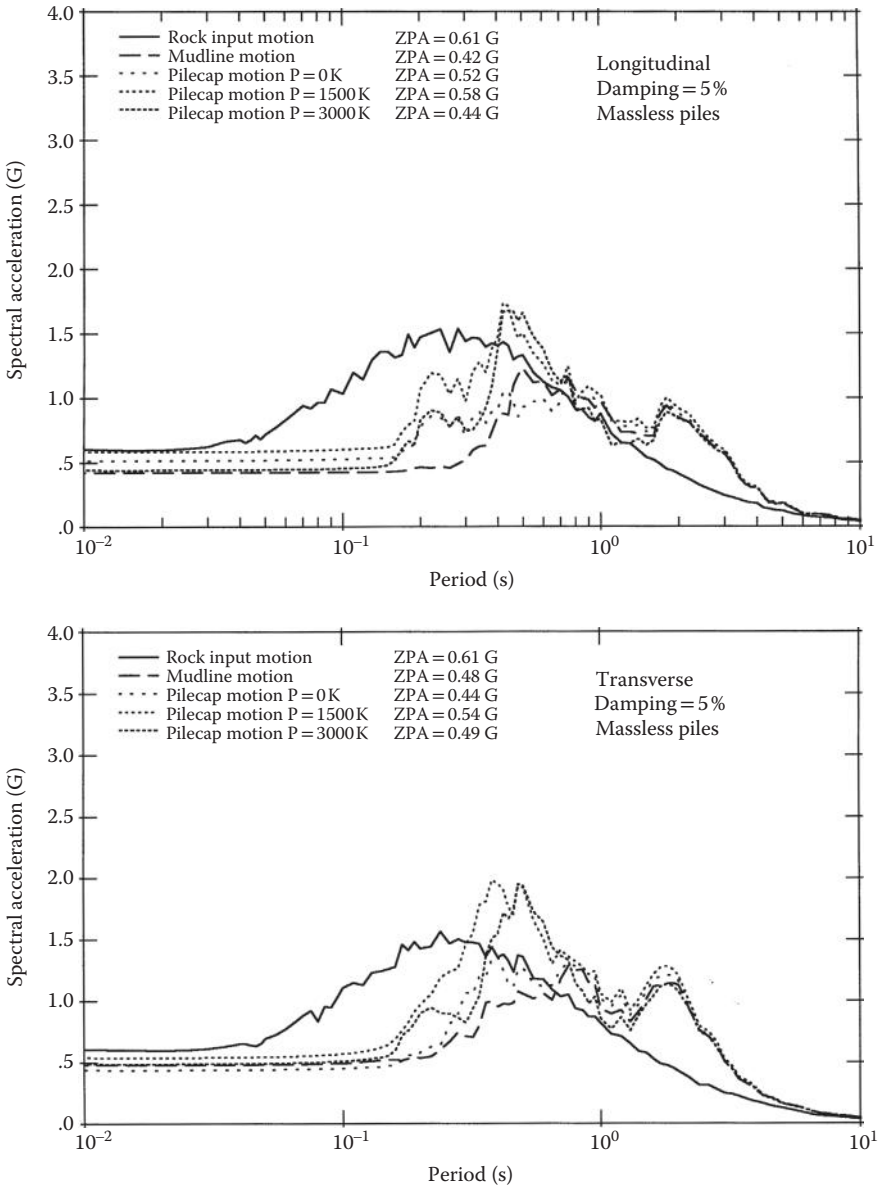

FIGURE 14.20 Comparisons of 5% damped response spectra for the longitudinal and transverse rock input, mudline, and scattered pile cap motions for the shaft foundation without masses in the shafts.

is seen that, because of the substantial masses of the shafts, the spectral amplitudes of the scattered motions are higher than those of the free-field mudline motions for frequencies in the neighborhood of the soil–shaft system frequencies. Thus, for large-diameter shaft foundations constructed in deep soft soil sites, it is important that the soil and shaft inertias be properly included in the soil–foundation interaction analysis. Neglecting the shaft masses will result in underestimating the scattered pilecap motions in the longitudinal and transverse directions of the bridge, as represented in Figure 14.20.

14.8 Capacity Evaluations

The objective of the capacity evaluation is to determine the most probable levels of seismic resistance of the various elements, components, and subsystems of the bridge. The resistance capacities provided by this evaluation, along with the corresponding demands, provide the basis for judging seismic performance of the complete bridge system during future earthquakes. In the domain of SFSI as discussed here, the capacity evaluation focuses on soil–foundation systems.

For a bridge subjected to static loadings, the soil–foundation capacities of interest are the load resistances and the associated foundation deflections and settlements. Their evaluation constitutes the bulk of the traditional foundation design problem. When the bridge is subjected to oscillatory dynamic loadings, including seismic, the static capacities mentioned above are, alone, insufficient in the process of judging soil–foundation performance. In this case, it is necessary to assess entire load-deflection relationships, including their cyclic energy dissipation characteristics, up to load and/or deformation limits approaching failure conditions in the soil–foundation system. Because of the complexity of this assessment, the capacity evaluation must be simplified in order to make it practical. This is usually done by treating each soil–foundation system independently and by subjecting it to simplified pseudo-static monotonic and/or cyclic deformation-controlled step-by-step patterns of loading, referred to herein as the "pushover" analysis.

Because near-failure behavior of a soil–foundation system is involved in the capacity evaluation, it necessarily involves postelastic nonlinear behavior in the system's constituent components, including the foundation's structural elements and connections and its surrounding soil medium. Thus, ideally, a realistic evaluation of the capacities should be based on in situ tests conducted on prototypical foundation systems. Practical limitations, however, generally do not allow the conduct of such comprehensive tests. It is usually necessary, therefore, to rely solely upon a combination of analysis and limited-scope in situ or laboratory tests of selected critical components. These tests are performed either to provide the critical data needed for a capacity analysis or to confirm the adequacy and reliability of the results obtained from such analysis. Indicator-pile tests that have often been performed for a bridge project is an example of limited-scope testing.

In a typical "pushover" analysis, the foundation's structural components are represented by appropriate nonlinear finite elements capable of representing the near-failure nonlinear features, such as plastic hinging, ductile or brittle shearing, tensile or compressive yielding and fracturing, local and global buckling, and stiffness and capacity degradations due to P-Δ effects; and, the surrounding soil medium is usually represented either by nonlinear finite elements capable of modeling the postelastic constitutive behavior of the material or by empirically-derived generalized nonlinear soil springs such as those developed from the "*p–y*," "*t–z*," and "*Q–d*" curves used for pile foundations. Ideally, the soil–foundation model used should also be able to properly represent the important nonlinear behaviors that could develop at the soil–foundation interfaces, such as slippage, debonding, and gapping. After the model has been developed, it is then subjected to a set of suitable pushover loading programs that simulate the loading conditions imposed on the soil–foundation system by the bridge pier at its interface with the foundation.

Conducting a step-by-step pushover analysis of the model described above, one can identify load and deformation levels associated with the various failures modes in the soil–foundation system. Then, load and deformation limits can be set beyond which the performance goals set for the bridge will no longer be met. These limits can be considered the capacity limits of the foundation system.

Because large uncertainties usually exist in a capacity evaluation, the capacity limits obtained therefrom should be reduced using appropriate capacity reduction ϕ-factors. Each reduction factor adopted should adequately cover the lower limit of capacity resulting from the uncertainties. The reduced capacity limits established in this manner become the allowable capacity limits for use in comparing with the corresponding demands obtained through the demand analysis.

14.9 Recent Advances

14.9.1 Shallow Foundations

In recent years there has been considerable interest in developing nonlinear analysis procedures and considering nonlinear SFSI response in design of shallow foundations (Gajan et al. 2003; Thomas et al. 2005; Kutter et al. 2006; Raychowdhury 2008; Orense et al. 2010). Nonlinear SFSI response of shallow foundation has great potential to dissipate significant amounts of earthquake energy, resulting in a substantial reduction of force demand in the structure, if potential consequences such as excessive tilting, settlement, or bearing failure are controlled within acceptable limits.

Procedures to analyze and predict highly nonlinear moment-rotation, shear-sliding, and axial load-settlement behavior of shallow foundations have been developed. Two approaches that have been developed to date, namely, beam-on-nonlinear-Winkler-foundation (BNWF) and macro-element methods, are presented in the following subsections.

14.9.1.1 Beam-on-Nonlinear-Winkler-Foundation Method

The beam-on-nonlinear-Winkler-foundation (BNWF) method is developed to capture the sliding, settling, and rocking behavior of a shallow foundation response during an earthquake. The development of the BNWF method originates from Winkler's early representation of the physical soil medium using a system of discrete, closely spaced, independent linear elastic springs as shown in Figure 14.21. The soil–foundation interface is assumed to be an assembly of discrete, nonlinear elements composed of springs, dashpots, and gap elements. A major challenge of this approach is the determination of constitutive modeling of nonlinear springs, dashpots, and gap elements. Different experimental data have been collected and used to compare with the numerical solution predicted using a mesh of nonlinear Winkler springs and gap elements (Kutter et al. 2006).

Although nonlinear spring models are extensively used, there is no commonly accepted analytical procedure for developing static, cyclic, and dynamic spring resistance curves from experimental data. The following guidelines (Kutter et al. 2006; Raychowdhury 2008) may be used in applying the BNWF modeling:

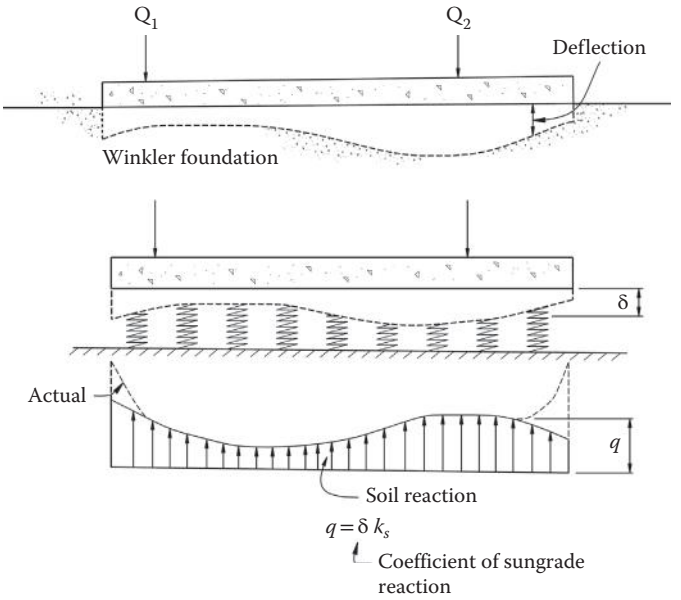

FIGURE 14.21 Winkler-foundation concept.

- Spring backbone curves similar to those typically used for modeling soil-pile response can be taken as a baseline and further modified to model shallow foundation response.
- General shape of the moment-rotation, settlement-rotation and shear-sliding curves shall be developed based on experiments involving footing aspect ratios, structure models, static and dynamic loading, sand and clay tests, and a range of bounding factors to account for uncertainty.
- The moment–rotational (M-θ) response of foundations resting on clayey soil results in a more pinched behavior and a highly U-shaped settlement-rotation (s–θ) history. The end spring resistance functions should be carefully selected to capture U-shaped behavior. ATC-40 (ATC 1996) end spring amplifications reasonably account for the increased stiffness at the edges of the foundation, provided the proper length of the increased stiffness zone is selected.
- The *M*-θ and *s*-θ responses are most sensitive to the selection of bearing-pressure distribution and magnitude. A parabolic shape is more reasonable for footings on sands, while an inverse parabolic shape with higher edge-spring resistances is more reasonable for footing on clay. The *M*-θ and *s*-θ responses are least sensitive to magnitude of tension capacity provided in the springs.
- The overall response is highly sensitive to the amount of sliding occurring. A more suitable estimate of interface friction related to the critical-state friction angle should be used.

14.9.1.2 Macro-Element Method

The macro-element method is developed to simulate the load-displacement behavior of shallow foundations under various loading conditions (Nova and Montrasio 1991; Cassidy et al. 2002; Cremer et al. 2001 and 2002; Chatzigogos et al. 2007). The macro-element constitutive model, based on plasticity theory,

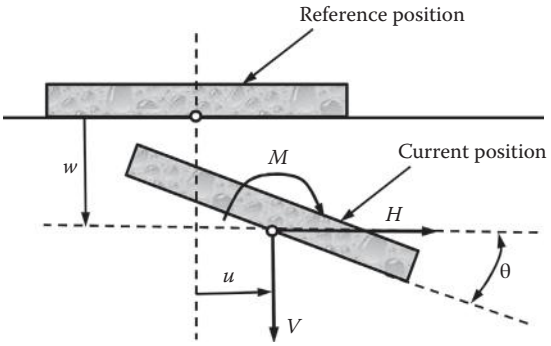

FIGURE 14.22 A macro-element model.

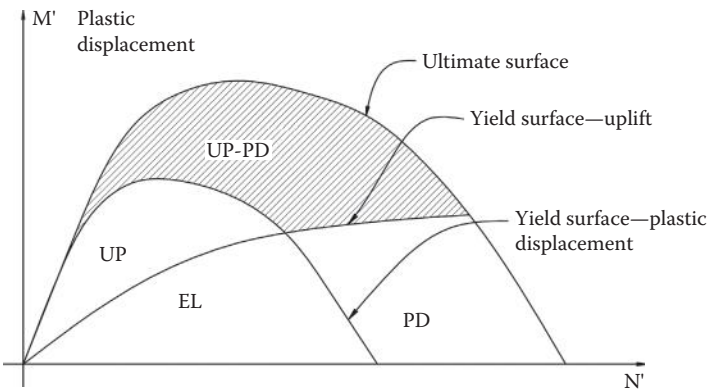

FIGURE 14.23 Constitutive models of a macro-element.

considers the foundation and the soil as a macro-element for which the loadings act as generalized stress variables while the displacements are the corresponding generalized strain variables as shown in Figure 14.22. The concept of macro-element provides an alternative simplified approach, which reduces the size of the problem significantly while preserving the essential features of the dynamic response of the system.

A major challenge of this method is the proper application and selection of plasticity-based constitutive modeling of the macro-element. In order to model uplift and of soil yielding, three elements need to be developed as shown in Figure 14.23: (1) ultimate surface, (2) yield surface with hardening laws, and (3) the flow rules.

Cassidy–Byr ne–Houlsby Model

This model is based on the work-hardening plasticity theory. It was developed to predict the behavior of rigid circular footings on sand when subjected to combined static vertical, horizontal, and moment loading (Cassidy et al. 2002). The models are applicable to footings on sand, but those published to date are largely limited to monotonic loading.

Cremer–Pecker–Davenne Model

This model considers material nonlinearities of soil (yielding of soil under the foundation) and geometrical nonlinearities at soil–foundation interface (uplift at the soil–foundation interface). It is developed to simulate the behavior of shallow foundations on cohesive soil. Model parameters are identified by using finite-element analysis simulations of the soil–foundation system under various types of cyclic loading paths (Cremer et al. 2001 and 2002).

Chatzigogos–Pecker–Salencon Model

This model is based on multi-mechanism plasticity formalisms to treat the two basic nonlinearities (soil yielding and footing uplifting) simultaneously. The Eurocode 8 equation for strip footings on homogeneous soils can be extended, with minor modifications, to the case of circular footings on soils with a vertical cohesion gradient (Chatzigogos et al. 2007).

14.9.2 Larger-Scale Experimental Testing

A research program has recently been developed to study soil–foundation–structure interaction using the NEES infrastructure in the United States (Gajan et al. 2003; Wood et al. 2004; Thomas et al. 2005; Dryden and Fenves 2009; Moss et al. 2011). Complementary shaking table, centrifuge, field, and laboratory specimens have been designed and tested since 2004. Comprehensive computational models have been developed to interpret the response of the individual experiments, to relate the test specimen response to the performance of the prototype system, and to understand the limitations of the boundary conditions inherent to each of the experiments. Centrifuge tests of individual bridge bents are used to evaluate the nonlinear response of the soil and foundation system. Field tests of individual bridge bents are used to evaluate the linear response of the soil, foundation, and structure in situ. Shaking table tests of a two-span model are used to evaluate the nonlinear response of the structure subjected to bidirectional, incoherent support motion. And, static tests of bents and individual columns are used to evaluate size effects and strength degradation in shear under cyclic loads. Computational simulations play a central role in interpreting the response behavior of the individual experiments, relating the test specimen response to the performance of the prototype system, and understanding the limitations of the boundary conditions inherent to each individual experiment.

14.10 Concluding Statements

The previous sections of this chapter discuss the various elements of a modern state-of-the-art SFSI seismic analysis for large important bridges. These elements include (1) generating the site-specific rock-outcrop motions and corresponding free-field soil motions, (2) modeling and analysis of individual

soil–foundation systems to establish foundation impedances and scattered motions, (3) determining SFSI using the substructuring method of analyses, and (4) assessing overall bridge performance by comparing force/deformation demands with corresponding capacities. Without retracing the details of these elements, certain points are worthy of special emphasis as follows:

- Best-estimate rock and soil properties should be used in the generation of free-field seismic motions, with full recognition of the variations (randomness) and uncertainties (lack of knowledge) involved.
- Likewise, best-estimate material properties should be used in modeling the foundations, piers, abutments, and superstructure, also recognizing the variations and uncertainties involved.
- In view of the above-mentioned variations and uncertainties, sensitivity analyses should be conducted to provide a sound basis for judging the overall seismic performance.
- Considering the current state of development, one should clearly differentiate between the requirements of a seismic force/deformation demand analysis and the corresponding capacity evaluation. The former is concerned with global system behavior; thus, it must satisfy only global dynamic equilibrium and compatibility. The latter, however, places emphasis on the behavior of local elements, components, and subsystems, requiring that equilibrium and compatibility be satisfied only at the local level within both the elastic and postelastic ranges of deformation.
- In conducting a demand analysis, equivalent-linear modeling, coupled with the substructuring method of analysis, has the advantages that (1) the results are more controllable and predictable, (2) the uncertainties in system parameters can easily be evaluated separately, and (3) the SFSI responses can be assessed at stages. These advantages lead to a high level of confidence in the results when the nonlinearities are relatively weak. However, when strong nonlinearities are present, nonlinear time-history analyses should be carried out in an iterative manner so that system response is consistent with the nonlinearities.
- When strong nonlinearities are present in the overall structural system, usually in the piers and superstructure, multiple sets of seismic inputs should be used separately to conduct the demand analyses; since, such nonlinearities cause relatively large dispersions of the maximum values of critical response.
- The "elasto-dynamic" method of treating SFSI is valid for foundations having large horizontal dimensions, such as large spread footings and caissons; while the "empirical *p–y*" method is valid only for slender-pile foundations subjected to large-amplitude deflections. For foundations intermediate between these two classes, for example, those using large-diameter shafts, both of these methods are deficient in predicting SFSI behavior. In this case, the "hybrid" method of modeling has definitive advantages, including its ability to treat all classes of foundations with reasonable validity.
- The "*p–y*" method of treating SFSI in both demand analyses and capacity evaluations needs further development, refinement, and validation through test results, particularly with regard to establishing realistic *p–y*, *t–z*, and *Q–d* curves. For seismic applications, changes in the characteristics of these curves, due to global soil nonlinearities induced by the free-field ground motions, should be assessed.
- The "hybrid" method of treating SFSI, while being fundamentally sound, also needs further development, refinement, and test validation to make it fully acceptable for bridge applications.
- Systematic research and development efforts, involving laboratory and field tests and analytical correlation studies, are required to advance the SFSI analysis methodologies for treating bridge foundations.

The state of the art of SFSI analysis of large bridge structures has been rapidly changing in recent years; a trend that undoubtedly will continue on into the future. The reader is therefore encouraged to take note of new developments as they appear in future publications.

Acknowledgment

The authors wish to express their sincere thanks and appreciation to Joseph P. Nicoletti and Abbas Abghari for their contributions to Sections 14.2, and 14.4, and Lian Duan for his contribution to Sections 14.9, respectively.

References

Abrahamson, N. A. 1992a. "Non-Stationary Spectral Matching", *Seismol. Research Letter*, 63(1), 30.

Abrahamson, N. A. 1992b. "Spatial Variation of Earthquake Ground Motion for Application to Soil-Structure Interaction," *Report No. TR-100463*, March, Electric Power Research Institute, Palo Alto, CA.

Abrahamson, N. A., Schneider, J. F., and Stepp, J. C. 1991. "Empirical Spatial Coherency Functions for Application to Soil-Structure Interaction Analyses", *Earthquake Spectra*, 7(1), 1–28.

Apsel, R. J. 1979. "Dynamic Green's Function for Layered Media and Applications to Boundary Value Problems", *Ph.D. Thesis*, University of California, San Diego, CA.

ATC. 1996. *Seismic Evaluation and Retrofit of Concrete Buildings (ATC-40)*, Volume 1, Applied Technology Council, Redwood City, CA.

Bolt, B. A. (Editor) 1987. *Seismic Strong Motion Synthetics*, New York Academic Press, New York, NY.

Bolt, B. A. and Gregor, N. J. 1993. "Synthesized Strong Ground Motions for the Seismic Condition Assessment of Eastern Portion of the San Francisco Bay Bridge", *Report No. EERC 93-12*, Earthquake Engineering Research Center, University of California, Berkeley, CA.

Boore, D. and Akinson, G. 1987. "Stochastic Prediction of Ground Motion and Spectral Response Parameters at Hard-Rock Sites in Eastern North America", *Bulletin of the Seismological Society of America*, 77, 440–467.

Cassidy, M. J., Byrne, B. W., and Houlsby, G. T. 2002. "Modelling the Behaviour of Circular Footings Under Combined Loading on Loose Carbonate Sand," *Géotechnique*, 52(10), 705–712.

Chang, C. Y., Power, M. S., Idriss, I. M., Sommerville, P. G., Silva, W., and Chen, P. C. 1986. "Engineering Characterization of Ground Motion, Task II; Observation Data on Spatial Variations of Earthquake ground Motion", *NUREG/CR-3805*, Vol. 3, U.S. Nuclear Regulatory Commission, Washington, DC.

Chang, C. Y., Tseng, W. S., Tang, Y. K., and Power, M. S. 1989. "Variations of Earthquake Ground Motions with Depth and Its Effects on Soil-Structure Interaction," *Proc. Second Department of Energy Natural Phenomena Hazards Mitigation Conference*, October 3–5, Knoxville, TN.

Chatzigogos, C. T., Pecker, A., and Salencon, J. 2007. "A Macro-Element For Dynamic Soil-Structure Interaction Analyses Of Shallow Foundations," The *4th International Conference on Earthquake Geotechnical Engineering*, June 25–28, Thessalonki, Greece.

Clough, R. W. and Penzien, J. 1993. *Dynamics of Structures*, Second Edition, McGraw-Hill, Inc., New York, NY.

Cremer, C., Pecker, A., and Davenne, L. 2001. "Cyclic Macro - Element of Soil - Structure Interaction: Material and Geometrical Non-Linearities," *International Journal of Numerical and Analytical Methods in Geomechanics,* 25(13), 1257–1284.

Cremer, C., Pecker, A., and Davenne, L. 2002. "Modelling of Non Linear Dynamic Behaviour of A Shallow Foundation with Macro-Element," *Journal of Earthquake Engineering*, 6(2), 175–212.

Dickenson, S. E. 1994. "Dynamic Response of Soft and Deep Cohesive Soils During the Loma Prieta Earthquake of October 17, 1989," *Ph.D. Dissertation*, University of California, Berkeley, CA.

Dryden, M. and Fenves, G. L. 2009. "The Integration of Experimental and Simulation Data in the Study of Reinforced Concrete Bridge Systems Including Soil-Foundation-Structure Interaction," *PEER Report 2009/03*, Pacific Earthquake Engineering Research Center, University of California, Berkeley, CA.

Gajan, S., Phalen, J. D., and Kutter, B. L. 2003. "Soil-Foundation-Structure Interaction: Shallow Foundations," Centrifuge Data Report For SSG02, *Report No.Ucd/Cgmdr-03/01,* University of California, Davis, CA.

Gasparini, D. and Vanmarcke, E. H. 1976. *SIMQKE: A program for Artificial Motion Generation*, Department of Civil Engineering, Massachusetts Institute of Technology, Cambridge, MA.

Hao, H., Oliviera, C. S., and Penzien, J. 1989. "Multiple-Station Ground Motion Processing and Simulation Based on SMART-1 Array Data," *Nuclear Engineering and Design*, 3(6), 2229–2244.

Hardin, B. O. 1978. "The Nature of Stress-Strain Behavior for Soils," *Proc. ASEC Geotech. Eng. Div. Specialty Conference on Earthquake Eng. and Soil Dyn*., 1, 3–90.

Hardin, B. O. and Black, W. L. 1968. "Vibration Modulus of Normally Consolidated Clay," *Journal of Soil Mechanics and Foundation Division*, ASCE, 94(2), 353–369.

Hardin, B. O. and Drnevich, V. 1972. "Shear Modulus and Damping in Soils: Design Equations and Curves," *Journal of Soil Mechanics and Foundations Division*, ASCE, 98(7), 667–691.

ICBO. 2012. International Building Code, International Conference of Building Officials, Whittier, CA.

Idriss, I. M. and Sun, J. I. 1992. *User's Manual for SHAKE 91*, Center for Geotechnical Modeling, University of California, Davis, CA.

Kaul, M. K. 1978. "Spectrum-Consistent Time-History Generation," *Journal of Engineering Mechanics Division*, ASCE, 104(4), 781–788.

Kausel, E. and Roësset, J. M. 1974. "Soil-Structure Interaction Problems for Nuclear Containment Structures," *Proc. ASCE Power Division Specialty Conference*, August, Denver, CO.

Kutter, B. L., Martin, G., Hutchinson, T. et al. 2006. "Workshop on Modeling of Nonlinear Cyclic Load-Deformation Behavior of Shallow Foundation," *PEER Report 2005/14*, Pacific Earthquake Engineering Research Center, University of California, Berkeley, CA.

Lam, I. P. and Law, H. 1996. "Soil-Foundation-Structure Interaction - Analytical Considerations by Empirical p-y Method," *Proc. 4th Caltrans Seismic Research Workshop*, July 9–11, Sacramento, CA.

Lee, M. K. W. and Finn, W. D. L. 1978. "DESRA-2: Dynamic Effective Stress Response Analysis of Soil Deposits with Energy Transmitting Boundary Including Assessment of Liquification Potential," *Report No. 38*, Soil Mechanics Series, Dept. of Civil Engineering, University of British Columbia, Vancouver, Canada.

Li, X. S., Wang, Z. L., and Shen, C. K. 1992. "SUMDES, a Nonlinear Procedure for Response Analysis of Horizontally-Layered Sites, Subjected to Multi-directional Earthquake Loading," Department of Civil Engineering, University of California, Davis, CA.

Lilhanand, K. and Tseng, W. S. 1988. "Development and Application of Realistic Earthquake Time Histories Compatible with Multiple-Damping Design Response Spectra," *Proc. 9th World Conference of Earthquake Engineers*, August 2–9, Tokyo-Kyoto, Japan.

Lysmer, J., Udaka, T., Tsai, C. F., and Seed, H. B. 1975. "FLUSH - A Computer Program for Approximate 3-D Analysis of Soil-Structure Interaction," *Report No. EERC 75–30*, Earthquake Engineering Research Center, University of California, Berkeley, CA.

Lysmer, J., Tabatabaie-Raissai, M., Tajirian, F., Vahdani, S., and Ostadan, F. 1981. "SASSI-A System for Analysis of Soil-Structure Interaction", *Report No. UCB/GT/81-02*, Department of Civil Engineering, University of California, Berkeley, CA.

Matlock, H. 1970. "Correlations for Design of Laterally Loaded Piles in Soft Clay," *Proc. Offshore Technology Conference*, Paper No. OTC1204, April 22–24, Dallas, TX.

Matlock, H. and Reese, L. C. 1961. "Foundation Analysis of Offshore Pile Supported Structures," *Proc. 5th Int. Conf. on Soil Mech. and Found. Eng.*, Paris, France, July 17–22.

Moss, R. E. S., Kuo, S., and Crosariol, V. 2011. "Shake Table Testing of Seismic Soil-Foundation-Structure-Interaction." *ASCE Geofrontiers Conference*, March Dallas, TX.

Mylonakis, G., Nikolaou, A., and Gazetas, G. 1997. "Soil-Pile-Bridge Seismic Interaction: Kinematic and Inertia Effects. Part I: Soft Soil," *Earthquake Engineering & Structural Dynamics*, 26(3), 337–359.

Nova, R. and Montrasio, L. 1991. "Settlements of shallow foundations on sand," *Géotechnique*, 41(2), 243–256.

NRC. 1989. "*Standard Review Plan*", Section 3.71., Revision 2, August, US Nuclear Regulatory Commission, Washington, DC.

Orense, R. P., Chouw, N., and Pender, M. J. 2010. *Soil-Foundation-Structure Interaction*, CRC Press, Leiden, The Netherlands.

Papageorgiou, A. S., and Aki, K. 1983. "A Specific Barrier Model to the Quantitative Description of Inhomogeneous Faulting and the Prediction of Strong Motion," *Bulletin of the Seismological Society of America*, 73, 693–722 and 953–978.

Penzien, J. and Watabe, M. 1974. "Characteristics of 3-Dimensional Earthquake Ground Motions," *Earthquake Engineering & Structural Dynamics*, 3(4), 365–373.

Prevost, J. H. 1993. "DYNAFLOW: A Nonlinear Transient Finite Element Analysis Program," Department of Civil Engineering and Operations Research, Princeton University, Preinceton, NJ.

Prevost, J. H. 1989. "DYNAID: A Computer Program for Nonlinear Seismic Site Response Analysis," *Report No. NCEER-89-0025*, National Center for Earthquake Engineering Research, Buffalo, New York, NY.

Raychowdhury, P. 2008. "***N***onlinear Winkler-Based Shallow Foundation Model for Performance Assessment of Seismically Loaded Structures," *PhD. Dissertations*, University of California, San Diego, CA.

Reese, L. C., Awoshirka, K., Lam, P. H. F., and Wang, S. T. 1990. Documentation of Computer Program GROUP - Analysis of a Group of Piles Subjected to Axial and Lateral Loading, Ensoft, Inc., Austin, TX.

Reese, L. C., Cox, W. R., and Koop, F. D. 1974. "Analysis of Laterally Loaded Piles in Sand," *Proc. Offshore Technology Conference*, Paper No. OTC2080, May 6–8, Dallas, TX.

Reese, L. C. and Wang, S. T. 1997. Documentation of Computer Program LPILE - A Program for Analysis of Piles and Drilled Shafts Under Lateral Loads, Ensoft, Inc., Austin, Texas, 1989, Latest Update, Version 6.0, 2010.

Reese, L. C. and Wang, S. T. 1990. Documentation of Computer Program APILEZ - Analysis of Load Versus Settlement for an Axially Loaded Deep Foundation, Ensoft, Inc., Austin, TX.

Richart, F. E., Hall, J. R. Jr., and Woods, R. D. 1970. *Vibrations of Soils and Foundations*, Prentice-Hall, Englewood Cliffs, NJ.

Schnabel, P. B., Lysmer, J., and Seed, H. B. 1972. "SHAKE - A Computer Program for Earthquake Response Analysis of Horizontally Layered Sites," *Report No. EERC 72–12*, Earthquake Engineering Research Center, University of California, Berkeley, CA.

Seed, H. B. and Idriss, I. M. 1969a. "Rock Motion Accelerograms for High-Magnitude Earthquakes," *Report No. EERC 69-7*, Earthquake Engineering Research Center, University of California, Berkeley, CA.

Seed, H. B. and Idriss, I. M. 1969b. "Influence of Soil Conditions on Ground Motions During Earthquakes," *Journal of the Soil Mechanics and Foundations Division*, 95(SM1), 99–138.

Seed, H. B. and Idriss, I. M. 1970. "Soil Moduli and Damping Factors for Dynamic Response Analysis," *Report No. EERC 70–10*, Earthquake Engineering Research Center, University of California, Berkeley, CA.

Seed, H. B., Wong, R. T., Idriss, I. M., and Tokimatsu, K. 1984. "Moduli and Damping Factors for Dynamic Analyses of Cohesionless Soils," *Report No. UCB/EERC-84/14*, Earthquake Engineering Research Center, University of California, Berkeley, CA.

Silva, W. J. and Lee, K. 1987. WES RASCAL Code for Synthesizing Earthquake Ground Motions," *State-of-the-Art for Assessing Earthquake Hazards in United States, Report 24*, Army Engineers Waterway Experimental Station, Miscellaneous Paper 5-73-1, Vicksburg, MS.

Sommerville, P. G. and Helmberger, D. V. 1990. "Modeling Earthquake Ground Motion at Close Distance," *Proc. EPRI/Stanford/USGS Workshop on Modeling Earthquake Ground Motion at Close Distances*, August 23, Palo Alto, CA.

Sun, J. I., Golesorkhi, R., and Seed, H. B. 1988. "Dynamic Moduli and Damping Ratios for Cohesive Soils," *Report No. UBC/EERC-88/15*, Earthquake Engineer Research Center, University of California, Berkeley, CA.

Tang, Y. K. 1989. "Proceedings: EPRI/NRC/TPC Workshop on Seismic Soil-Structure Interaction Analysis Techniques Using Data from Lotung Taiwan," *EPRI NP-6154*, Electric Power Research Institute, Palo Alto, CA. March.

Thomas, J. M., Gajan, S., and Kutter, B. L. 2005. "Soil-Foundation-Structure Interaction: Shallow Foundations. Centrifuge Data Report For The Ssg04 Test Series," *Report No. Ucd/Cgmdr-05/02,* University of California, Davis, CA.

Tseng, W. S. 1996. "Soil-Foundation-Structure Interaction Analysis by the Elasto-Dynamic Method," *Proc. 4th Caltrans Seismic Research Workshop*, Sacramento, CA, July 9–11.

Tseng, W. S. and Hadjian, A. H. 1991. "Guidelines for Soil-Structure Interaction Analysis," *EPRI NP-7395*, Electric Power Research Institute, Palo Alto, CA, October.

Tseng, W. S., Lilhanand, K., and Yang, M. S. 1993. "Generation of Multiple-Station Response-Spectra-and-Coherency-Compatible Earthquake Ground Motions for Engineering Applications," *Proc. 12th Int. Conference on Struct. Mech. in Reactor Technology*, Paper No. K01/3, August 15–20, Stuttgard, Germany.

Veletsos, A. S. and Wei, Y. T. 1971. "Lateral and Rocking Vibration of Footings," *Journal of the Soil Mechanics and Foundations Division*, ASCE, 97(SM9), 1227–1249.

Vucetic, M. and Dobry, R. 1991. "Effects of Soil Plasticity on Cyclic Response," *Journal of Geotechnical Engineering*, ASCE, 117(1), 89–107.

Waas, G. 1972. "Analysis Method for Footing Vibrations through Layered Media," *Ph.D. Dissertation*, University of California, Berkeley, CA.

Wong, H. L. and Luco, J. E. 1976. "Dynamic Response of Rigid Foundations of Arbitrary Shape," *Earthquake Engineering & Structural Dynamics*, 4(6), 587–597.

Wood, S. L., Anagnos, T., Arduino, A. et al. 2004. Using NEES To Investigate Soil-Foundation-Structure Interaction, *13th World Conference on Earthquake Engineering*, Paper No. 2344, August 1–6. Vancouver, B.C., Canada.

15

Seismic Design Practice in California

Mark Yashinsky
California Department of Transportation

Lian Duan
California Department of Transportation

15.1 Introduction

15.1.1 AASHTO Seismic Guidelines and Caltrans SDC

The American Association of State Highway and Transportation Officials (AASHTO) published the first edition of the Guide Specifications for Seismic Bridge Design in 2009 (AASHTO 2009) and the second edition in 2011 (AASHTO 2011). Seismic design is divided into four categories. Bridges in areas of low historic seismicity are identified as Category A and require a minimum seismic design. Bridges in areas of high seismicity (such as California) are in Category D and require a capacity-based seismic design.

The California Department of Transportation (Caltrans) publishes its own *Seismic Design Criteria* (SDC) (Caltrans 2013) along with the *Guide Specifications for Seismic Design of Steel Bridges* (Steel Guide) (Caltrans 2014). Caltrans SDC and Steel Guide are based on required seismic performance criteria, a displacement-based approach, and a capacity design concept. The seismic criteria in the SDC are similar to the seismic criteria in the AASHTO Guide Specifications for Category D. The main difference is that the Caltrans SDC and Steel Guide are based on a displacement-based approach, while the AASHTO Guide Specifications are mostly based on force-based response reduction factors and are mostly directed at short- to medium-span bridges. Also, unlike the AASHTO Guide Specifications, the Caltrans SDC and Steel Guide are codes that must be followed for all new bridges designed in California. In additional to the SDC and Steel Guide, Caltrans has additional seismic design guidance

materials in Section 20 of the Memo to Designers (MTD Caltrans 2010a). Example problems and specific procedures are provided in Section 14 of Bridge Design Aids (BDA) (Caltrans 2008a, 2008b, 2008c, 2008d, and 2011). More information can be found on Caltrans Office of Earthquake Engineering website at http://www.dot.ca.gov/hq/esc/earthquake_engineering/.

This chapter first presents the historical development of seismic design criteria, seismic bridge design methodologies and concepts in general, and then discusses effective details for the seismic design of highway bridges used in Caltrans practice.

15.1.2 Historical Development of Seismic Design Criteria

After the 1933 Long Beach Earthquake, California began designing bridges for a small lateral earthquake force. Bridge damage during the 1971 San Fernando Earthquake prompted Caltrans to develop comprehensive seismic design criteria. Highway bridges in California were typically designed using a single-level, force-based design approach based on a "no-collapse" design philosophy. Seismic loads were determined on the basis of a set of soil conditions and a suite of four site-based standard Acceleration Response Spectra (ARS). Structures were analyzed using the three-dimensional elastic dynamic multimodal response spectrum method. Structural components were designed using a reduction *Z*-factor (Caltrans 1990) to reduce seismic forces for ductility and risk. Minimum transverse reinforcement confinements were required.

All bridges built after 1971 were designed using this new procedure, which was included as an addendum to the AASHTO Standard Specifications for Highway Bridges. The Applied Technology Council (ATC) wrote a comprehensive report on the new Caltrans Bridge Criteria, which was published as ATC-6 (ATC 1981). Bridges designed using the new seismic criteria performed well during subsequent earthquakes. Unfortunately, California had an existing inventory of several thousand bridges that were designed before the new criteria had been developed. A retrofit program to prevent unseating of older bridges was initiated in the late 1970s, but the vulnerability of the columns was not addressed until the 1987 Whittier Narrows Earthquake almost caused the collapse of a bridge column on the I-605/I-5 overcrossing. Research and retrofit programs to strengthen poorly reinforced bridge columns had begun, but it had not progressed sufficiently when the 1989 Loma Prieta Earthquake occurred.

The 1989 Loma Prieta Earthquake alerted the California legislature and the governor of the vulnerability of older bridges, and a comprehensive retrofit program was initiated. Additional bridge damage during the 1994 Northridge earthquake accelerated and increased the scope of the retrofit program. Research and testing conducted for the retrofit program was used to improve bridge seismic design in California. The ATC-32, developed as a comprehensive report (ATC 1996) on the new Caltrans Bridge Criteria, was published in 1996. The Federal Highway Administration (FHWA) required all states to adopt ATC-6.

Retrofit procedures for existing bridges were provided in Caltrans Memo to Designers 20-4 (Caltrans 2010c) and used during the retrofit program. About 85% of highway bridges in California are cast-in-place (CIP), posttensioned, concrete box girder bridges. Therefore, Caltrans seismic criteria are directed toward this type of structure. In 1999, Caltrans published the performance and displacement-based seismic design criteria (SDC), which focuses mainly on standard concrete bridges (Caltrans 1999a), with the current version 1.7 (Caltrans 2013a). In 2001, Caltrans published the Guide Specifications for Seismic Design of Steel Bridges (Caltrans 2001) and will publish the 2nd Edition in 2014 (Caltrans 2014). Significant advances in earthquake engineering have been made during the last 20 years.

For "important" bridges, performance-based, project-specific criteria are required to be developed. The performance-based criteria usually require a two-level design. The first level of design is to ensure the performance (service) of a bridge in earthquake events that have a relatively small

magnitude but may occur several times during the life of the bridge. The second level of design is to achieve the performance (no collapse) of a bridge under a severe earthquake that has only a small probability of occurring during the useful life of the bridge. The performance-based criteria should include guidelines for development of site-specific ground motion estimates, capacity design to preclude brittle failure modes, rational procedures for joint shear design in concrete, and the definition of limit states for various performance objectives. Several criteria (Caltrans 1997 and 1999b; IAI 1995) have been developed and implemented for the design and retrofitting of important bridges by California bridge engineers.

Caltrans has been continuing to conduct research and develop new seismic criteria. Seismic hazards such as near-fault ground motion, vertical accelerations, surface faulting, liquefaction, lateral spreading, and tsunami run-up have been identified and methods for determining these hazards at the bridge site and designing for them have been developed. Procedures for designing for joint shear, for shear keys, for different foundations, and for different kinds of bridges, ductile steel end diaphragms have been developed in updates to the SDC and Steel Guide, in the various sections of Memo to Designers (MTD), in Caltrans BDA, in Standard Bridge Details, and in other Caltrans Documents. MTD 20-11 (Caltrans 1999c) provides rules for new seismic criteria developed for California and for developing project-specific seismic criteria. Research is continuing on seismic hazards, mainly through the Pacific Earthquake Engineering Research Center (PEER), and on structural and geotechnical issues through yearly research proposals submitted to the Structure and Geotechnical Research Technical Advisory Panels (STAP/GTAP).

15.2 Seismic Design Procedure and Performance Criteria

15.2.1 Bridge Categories

Bridges are divided into two categories for seismic design. Bridges are considered *nonstandard* if they have an irregular geometry, unusual framing (multilevel, variable width, bifurcating, or highly horizontally curved superstructures, different structure types, outriggers, unbalanced mass and/or stiffness, high skew), or unusual geologic conditions (soft soil, moderate-to-high liquefaction potential, and proximity to an earthquake fault) (Caltrans 2010b). Bridges that do not meet the nonstandard criteria are considered *standard* and can be designed using Caltrans SDC. Bridges that are slightly nonstandard (such as precast girder bridges) can be designed using the SDC as long as the connections are carefully designed to simulate the behavior of CIP box girder bridges. Bridges that have large differences in stiffness between columns and bents, unusual shapes such as arch bridges, or are in liquefiable or soft soil are considered nonstandard and must be designed using project-specific seismic design criteria.

Another category is for *ordinary* and *important* bridges. A bridge is classified as *important* when it meets one of the following:

- Required to provide postearthquake life safety, such as access to emergency facilities
- Time for restoration of functionality after closure would create a major economic impact
- Formally designated as critical by a local emergency plan

A bridge is classified as "ordinary" when it is not **c**lassified as an important bridge.

Almost all bridges in California are considered *ordinary* and are designed not to collapse for the Design Seismic Hazards at the bridge site. Occasionally a bridge is too expensive to be economically replaced or it is on a "disaster recovery" route and may be designed using enhanced project-specific seismic criteria. Very rarely is a bridge identified as being *important* and is designed to remain in service for smaller earthquakes and to be repairable for larger earthquakes.

TABLE 15.1 Performance Criteria for California Bridges

Bridge Category	Seismic Hazard Evaluation Level	Postearthquake Damage Level	Postearthquake Service Level
Important	Functional	*Minimal*	*Immediate*
	Safety	*Repairable*	*Limited*
Ordinary	Safety	*Significant*	*No Collapse*

Definitions:

Functional Level Evaluation: A project-specific hazard level will be developed in consultation with the Seismic Safety Peer Review Panel as defined in MTD20-16. Ordinary Bridges are not designed for Functional Evaluation Seismic Hazards.

Safety Level Evaluation: For Ordinary Bridges, this is the "Design Earthquake" as defined below. For Important Bridges, the safety evaluation ground motion has a return period of approximately 1000–2000 years.

Design Earthquake is the collection of seismic hazards at the bridge site used in the design of bridges. The "Design Earthquake" consists of the Design Spectrum as defined in the SDC Version 1.5 Appendix B and may include other seismic hazards such as liquefaction, lateral spreading, surface faulting, and tsunami.

Damage Levels:

- *Minimal:* Essentially elastic performance.
- *Repairable:* Damage that can be repaired with a minimum risk of losing functionality.
- *Significant:* A minimum risk of collapse, but damage that could require closure to repair.

Service Levels:

- *Immediate:* Full access to normal traffic is available almost immediately following the earthquake.
- *Limited:* Limited access (e.g., reduced lanes, light emergency traffic) is possible within days of the earthquake. Full service is restorable within months.
- *No Collapse:* There may be no access following the earthquake.

15.2.2 Seismic Performance Criteria

Caltrans Memo to Designers 20-1 (Caltrans 2010b) provides seismic performance criteria for important and ordinary bridges, as shown in Table 15.1.

The Design Earthquake for Ordinary Bridges is the larger of the deterministically derived and probabilistically derived (with 5% in 50 years probability of exceedance) seismic hazards at the bridge site. The ground motion design spectra are the envelopes of the deterministic ground motion, the probabilistic ground motion, and ground motion 12 km from a *M*6.5 earthquake (minimum ground motion).

15.3 Seismic Design Criteria

15.3.1 General Provisions (Displacement-Based Design)

Bridge engineers calculate displacements for bridges with fuses that limit the amount of force during earthquakes. These fuses are usually ductile columns that form plastic hinges and undergo large rotations during earthquakes. The displacement demand due to the earthquake is compared to the displacement capacity of the structure. If the displacement capacity exceeds the displacement demand and several other criteria are met, then the bridge is usually considered satisfactory.

For ordinary bridges, structural members are identified as either ductile or capacity-protected members. A ductile member is a member that is intentionally well designed to deform inelastically for several cycles without significant degradation of the strength or stiffness under the design earthquake. On the other hand, a capacity-protected member is a member that is expected to behave essentially elastic. The preferable ductile members on most bridges should be limited to predetermined locations within the bridge that can be easily inspected and repaired following an earthquake and may include columns,

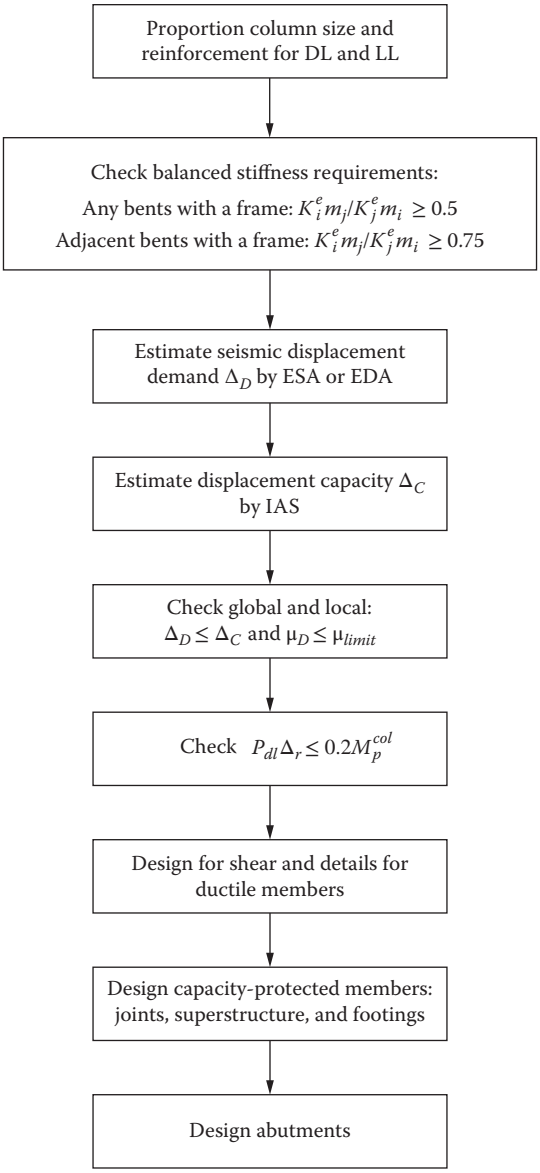

FIGURE 15.1 Caltrans seismic design procedure for ordinary standard bridges.

pier walls, backwalls, wingwalls, seismic isolation and damping devices, bearings, shear keys, and steel end diaphragms.

A displacement-based seismic design has long been espoused by Nigel Priestley (Priestley, Calvi, and Kowalsky 2007) and is discussed in more detail in Chapter 6. A similar procedure has been used in seismic bridge design in California since 1994. Figure 15.1 shows the design flowchart for the ordinary standard bridges.

15.3.1.1 Seismic Loads

For ordinary bridges, safety-evaluation ground motion is presented by the design response spectrum (DRS), the envelope of a deterministic and probabilistic spectrum. Figure 15.2 shows a set of the horizontal DRS. When the bridge site peak rock acceleration is 0.6 g or greater, an equivalent static

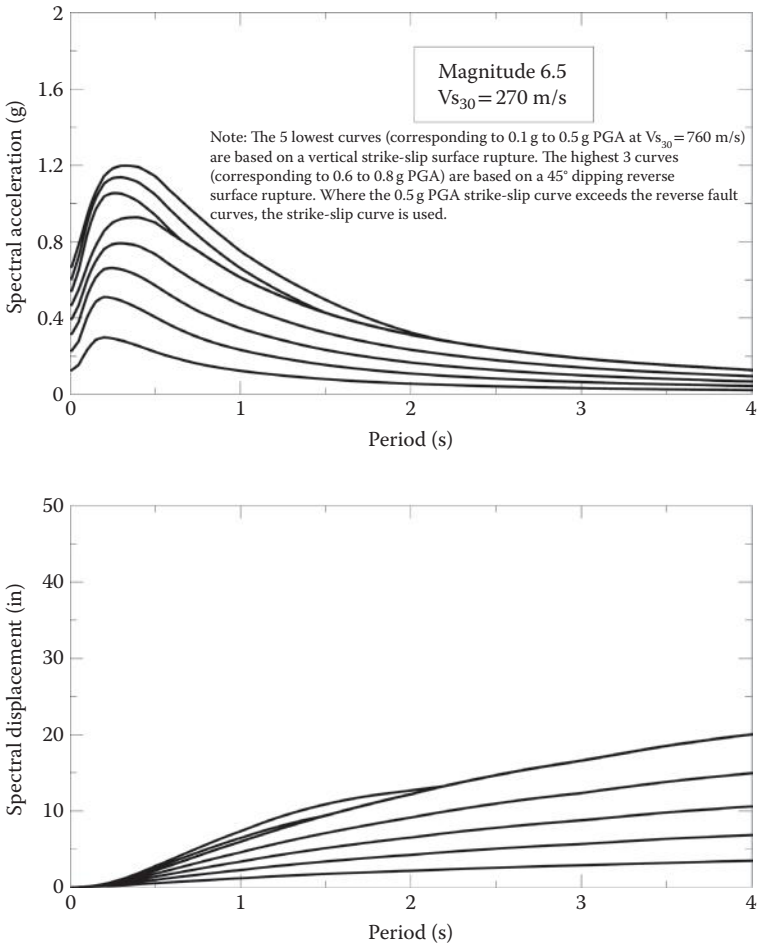

FIGURE 15.2 Spectral accelration and displacement for $V_{30} = 270$ m/s ($M = 6.5$).

vertical uniform load equal to 25% of the dead load shall be applied upward and downward to the superstructure to estimate the effects of vertical acceleration.

For structures within 16 miles (25 km) from an active fault, the spectral ordinates of the appropriate standard response spectrum curves shall be modified by a near-fault adjustment factor as shown in Figure 15.3.

15.3.1.2 Global Displacement

The displacements of the global bridge system and the frame should satisfy the following requirement:

$$\Delta_D \leq \Delta_C \tag{15.1}$$

where Δ_D is the displacement demand determined by the global analysis, the stand-alone analysis, or the larger of the two, if both types of analyses are necessary; Δ_C is the displacement capacity when any plastic hinge capacity reaches its ultimate capacity.

15.3.1.3 Local Displacement Ductility Capacity

To ensure the dependable ductile behavior of all columns regardless of seismic demand, a minimum local displacement ductility capacity of $\mu_c = \Delta_c/\Delta_Y \geq 3$ is required, and target local ductility of $\mu_c \geq 4$ is

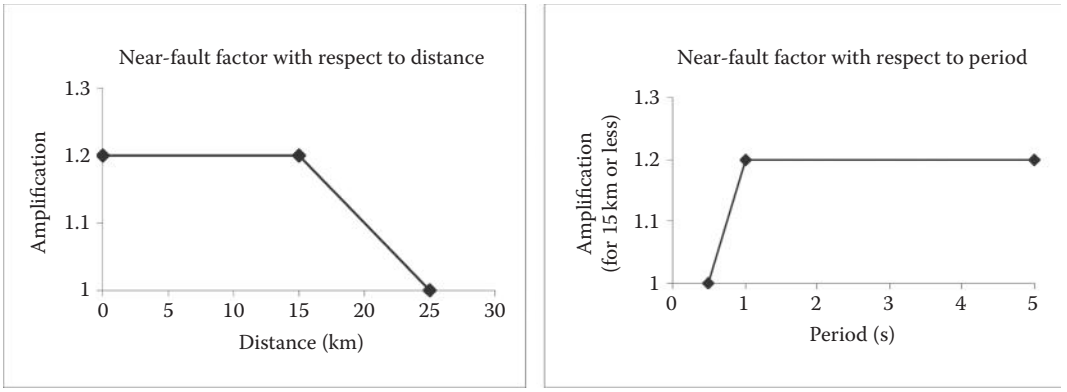

FIGURE 15.3 Near-fault adjustment factor.

recommended. The local displacement ductility capacity should be calculated for an equivalent member that approximates a fixed-base cantilever element.

15.3.1.4 Target Displacement Ductility Demand

The engineers are encouraged to limit displacement ductility demands, defined as $\mu_D = \Delta_D/\Delta_Y$, to the following limits that were calibrated to laboratory tests:

- Single-column bents supported on fixed foundation $\mu_D \leq 4$
- Multicolumn bents supported on fixed or pinned footings $\mu_D \leq 5$
- Pier walls (weak direction) supported on fixed or pinned footings $\mu_D \leq 5$
- Pier walls (strong direction) supported on fixed or pinned footings $\mu_D \leq 1$

15.3.1.5 Force

The forces in a capacity-protected member should satisfy the following requirement:

$$F_D \leq F_C \tag{15.2}$$

where F_D is the force demand determined by the joint-force equilibrium considering the plastic hinging capacity of the ductile component multiplied by 1.2 of an overstrength factor; F_C is the force capacity limit specified in SDC (Caltrans 2013) for concrete members and Steel Guide (Caltrans 2014) for steel members.

15.3.1.6 *P*-Δ Effects

The *P*-Δ effects tend to increase the displacement and decrease lateral load-carrying capacity of a bridge column. These effects can typically be ignored if the moment ($P_{dl}\Delta_r$) is less than or equal to 20% of the column plastic moment, that is,

$$P_{dl}\Delta_r \leq 0.2\, M_p^{col} \tag{15.3}$$

where Δ_r is the relative offset between the point of contra-flexure and the base of the plastic hinge and P_{dl} is the tributary dead load applied at the center of gravity of the bridge column.

15.3.1.7 Minimum Lateral Strength

Although providing ductile detailing is essential for achieving the expected performance requirements, each column shall be designed to have a minimum lateral flexural capacity to resist a lateral force of $0.1P_{dl}$ where P_{dl} is the tributary dead load applied at the center gravity of the superstructure.

15.3.2 Seismic Demand Analysis

Although bridges are expected to have a nonlinear response during earthquakes, they are usually modeled and analyzed as linear elastic systems. There are a couple of reasons for this. Newmark (1972) observed that the maximum displacement of long-period linear and nonlinear systems is about the same. Therefore, Caltrans requires bridges to have a period greater than 0.7 s so the maximum displacement can be obtained from a linear analysis.

Recent studies have shown that the maximum displacement of linear and nonlinear systems can be very different when subjected to near-fault motion. Moreover, about 50% of bridges in California can be subject to near-fault ground motion. However, difficulties in routinely performing nonlinear analyses have resulted in linear elastic seismic demand analyses still being accepted for standard ordinary bridges.

For ordinary standard bridges, the following methods are recommended to estimate the displacement demands.

15.3.2.1 Equivalent Static Analysis (ESA)

The ESA method specified in Caltrans SDC (Caltrans 2013) can be used to estimate the displacement demands for simpler structures that have balanced spans, similar bent stiffness, and low skew, and seismic response is primarily captured by the fundamental mode of vibration. In the ESA method, the fundamental period is determined using tributary mass and stiffness at each bent. The applied seismic force is the product of the period-dependent ARS coefficient and the tributary weight.

The displacement can be obtained using the relationship between stiffness, mass, and displacement shown in Equations (3.4) and (3.5). The demands from the transverse and longitudinal analysis are combined into two cases (Case 1 = 100% transverse + 30% longitudinal) (Case 2 = 30% transverse + 100% longitudinal).

$$\text{Stiffness}(K) = \frac{\text{Force}(F)}{\text{Displacement}(\Delta)} \tag{15.4}$$

$$\Delta = \frac{F}{K} = \frac{\text{Weight} \times \text{Spectral\_Acceleration}}{\text{Stiffness}} \tag{15.5}$$

15.3.2.2 Elastic Dynamic Analysis (EDA)

The EDA method may be used for more complicated structures. The EDA is linear elastic multimode spectral analysis with the appropriate response spectrum and with an adequate number of modes considered to capture a minimum of 90% mass participation. A minimum of three elements per column and four elements per superstructure span should be used. The complete quadratic combination (CQC) method is recommended to combine EDA modal results.

15.3.2.3 Global and Stand-Alone Analysis

The global analysis specified in Caltrans SDC (Caltrans 2013) is an elastic dynamic analysis that considers the entire bridge modeled from abutment to abutment. It is often used to determine displacement demands on multiframe structures. The stand-alone analysis is an elastic dynamic analysis that considers only one individual frame. To avoid having individual frames dependent on the strength and stiffness of adjacent frames, the separate stand-alone model for each frame must meet all requirements of the SDC.

15.3.2.4 Effective Stiffness

In both ESA and EDA methods, the effective stiffness of the components should be used in order to obtain realistic evaluation for the structure's period and displacement demands. The effective stiffness

of ductile components should represent the component's actual secant stiffness near yield. The effective stiffness should include the effects of concrete cracking, reinforcement, and axial load for concrete components; residual stresses, out of straightness, and axial load for steel components; and the restraints of the surrounding soil for pile.

For ductile concrete column members, effective moments of inertia, I_{eff}, should be based on cracked section properties and can be determined from the initial slope of the M-ϕ curve between the origin and the point designating first yield of tensile reinforcement. The torsional moment of inertia of concrete column J_{eff} may be taken as 0.2 time J_{gross}. For capacity-protected concrete members, I_{eff} should be based on their level of cracking. For a conventionally reinforced concrete box girder superstructure, I_{eff} can be estimated between 0.5 and 0.75 times I_{gross}, moment of inertia of a gross section. For prestressed concrete superstructures, I_{eff} is assumed to be the same as I_{gross} because prestressing steel limits the cracking of concrete superstructures.

For built-up steel members, effective section properties developed by Duan, Reno, and Lynch (2000) may be used.

15.3.2.5 Near-Fault Effects

Methods for analyzing bridges for other seismic hazards have also been developed. Bridges over faults have their foundations offset in the appropriate directions. The resulting displacements at the top of the columns are added to ground-shaking displacements. Bridges on liquefied soil are modeled with a reduced soil stiffness. Bridges on lateral spreading soil are designed to resist the lateral spreading force provided by the geotechnical engineer. The response spectra are increased for near-fault and basin effects. The dead load is increased by 25% and applied uniformly (up and down) along the superstructure to design for vertical acceleration. Bridges along the coast are subjected to a time history of tsunami waves or the geotechnical engineer can provide the resulting moments and forces on the bridge. More information on these procedures can be obtained from Section 20 of Caltrans MTD and the SDC.

15.3.3 Seismic Capacity Analysis

15.3.3.1 Moment–Curvature Analysis

The main purpose of moment–curvature analysis is to study the section behavior and to provide basic input data for the pushover analysis.

For a reinforced concrete member, the cross section is divided into a proper number of concrete and steel layers or filaments representing the concrete and reinforcing steel. Each concrete and steel layer or filament is assigned its corresponding stress–strain relationships. Confined and unconfined stress–strain relationships are used for the core concrete and for cover concrete respectively.

For a structural steel member, the section is divided into steel layers or filaments and a typical steel stress–strain relationship is used for tension and compact compression elements, and an equivalent stress–strain relationship with reduced yield stress and strain can be used for a noncompact compression element.

Although calculating the seismic demand can be done with a linear elastic model, a more sophisticated analysis is required to determine a bridge's seismic capacity. A moment–curvature analysis is performed on the bridge columns and the resulting curvature at yield, and the ultimate load is used to determine the columns' displacement capacity. In the equation shown below for calculating the total displacement capacity (Δ_C), the first quantity is the elastic displacement (Δ_y) due to curvature along the column, while the second quantity is the plastic displacement (Δ_p) due to curvature along the plastic hinge length (see Figure 15.4).

$$\Delta_c = \left[0.33L^2\right]\phi_y + \left[(L)L_p - 0.5L_p^2\left(\phi_u - \phi_y\right)\right] \tag{15.6}$$

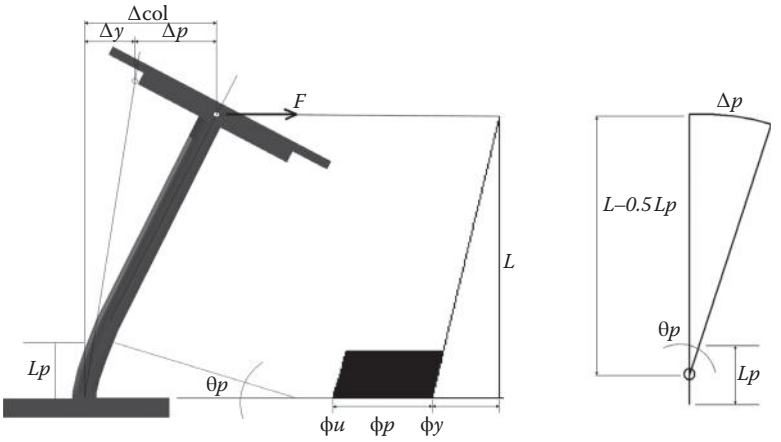

FIGURE 15.4 Displacement capacity derived from moment–curvature distribution of a column.

15.3.3.2 Inelastic Static Analysis (ISA)—Pushover Analysis

Inelastic static analysis (ISA), commonly referred to as the "pushover analysis," is usually used to determine the displacement capacity of a bent, frame, or the whole bridge. The expected material properties should be used to model structural members. IAS is a static, nonlinear procedure in which the magnitude of lateral loading is incrementally increased with a certain predefined pattern, until the potential collapse mechanism is achieved.

The simplest method, elastic-plastic hinge analysis, may be used to obtain an upper-bound solution. The most accurate method, distributed plasticity analysis, can be used to obtain a better solution. Refined plastic hinge analysis is an alternative that can reasonably achieve both computational efficiency and accuracy.

In Figure 15.5, we can see that the capacity of a two-column bent is reached when the capacity of the first plastic hinge is exhausted (Δ_C). In general, we say the seismic displacement capacity is reached when there is a significant drop in a member or system's lateral load-carrying ability. Note that the seismic demand is shown on the same graph to allow the engineer to clearly see whether the structure in safe for earthquakes.

15.3.4 Design Requirements

15.3.4.1 Minimum Seat Width

To prevent unseating of superstructures at hinges, piers, and abutments, the seat width should be available to accommodate the anticipated thermal movement, prestressing shortening, concrete creep and shrinkage, and the relative longitudinal earthquake displacement, and should not exceed the following minimum seat requirements (Caltrans 2013):

$$N_{\min} = \text{larger of} \begin{cases} \Delta_{ps} + \Delta_{cr+sh} + \Delta_{temp} + \Delta_{eq} + 100(\text{mm}) \\ 600 \text{ mm (For seat width at hinges)} \\ 760 \text{ mm (For seat width at abutments)} \end{cases} \tag{15.7}$$

where Δ_{ps}, Δ_{cr+sh}, Δ_{temp}, and Δ_{eq} are relative displacements due to prestressing, concrete creep and shrinkage, temperature, and earthquake respectively (mm).

15.3.4.2 CIP Concrete Box Girder Bridges

The first step is to check that the displacement capacity of the columns, bents, and so on is greater than the displacement demand with a pushover analysis as described in the last section. Then the columns are checked to make sure that the nominal shear capacity is greater than the shear demand.

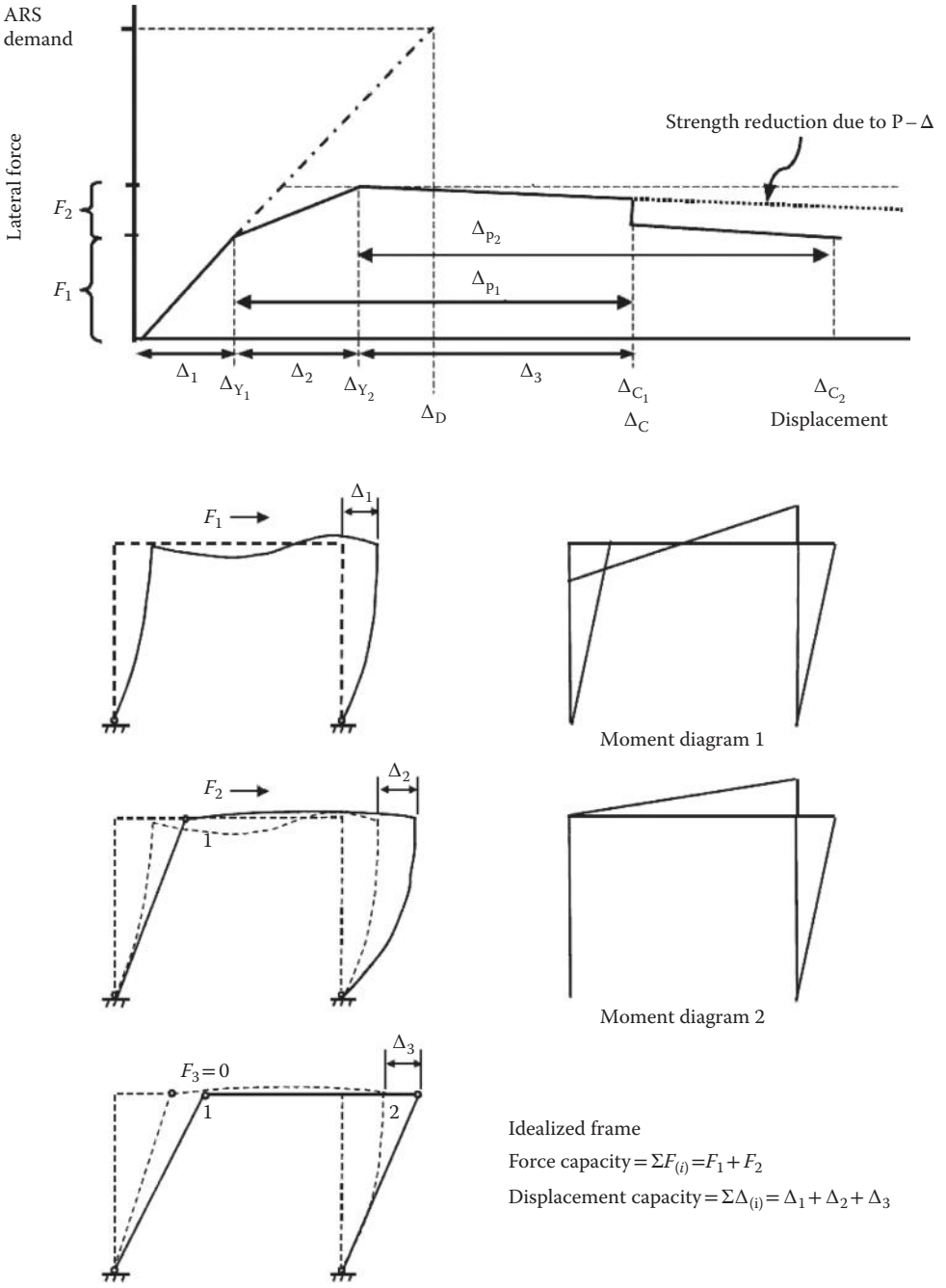

FIGURE 15.5 Pushover analysis for a two-column bent.

15.3.4.2.1 Shear Design

The cantilever column shown in Figure 15.6 is pushed by the force V_p that causes the column to form a plastic hinge $V_p = M_p/L$. However, to address variations in material properties and other uncertainties in member strengths, we make the shear demand equal to $V_o = 1.2V_p$, which is called the overstrength factor.

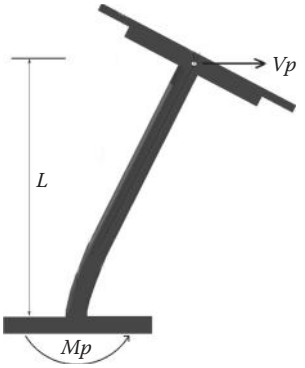

FIGURE 15.6 Determining the shear demand for a cantilever column.

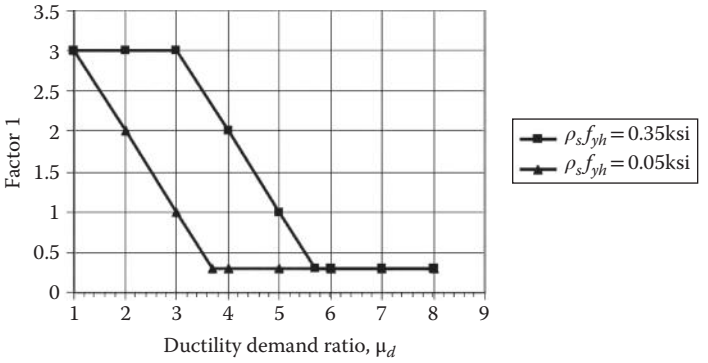

FIGURE 15.7 Concrete shear factor 1.

Bridge columns are designed to meet the following requirement:

$$\phi V_n \geq V_o \tag{15.8}$$

where V_n is the nominal shear capacity of the column plastic zone and ϕ is the resistance factor = 0.90.

$$V_n = V_c + V_s \tag{15.9}$$

$$V_c = (\text{factor 1})(\text{factor 2})\sqrt{f_c'} \tag{15.10}$$

$$V_s = \frac{A_v f_{yh} D}{s}(\text{factor 1})(\text{factor 2})\sqrt{f_c'} \tag{15.11}$$

where V_c is the shear strength of the concrete that is dependent on the damage in the plastic hinge region (factor 1) and the axial load (factor 2) as shown in Figure 15.7. V_s is the shear strength provided by the transverse reinforcement.

A_v is the area of the shear reinforcement; f_{yh} is the yield strength of the shear reinforcement; s is the spacing of the shear reinforcement; D is the column diameter; and $\sqrt{f_c'}$ is the concrete compressive strength.

$$\text{Factor 2} = \begin{cases} 1 + \dfrac{P_c}{2000A_g} < 1.5 & \text{(English Units)} \\ 1 + \dfrac{P_c}{13.8A_g} < 1.5 & \text{(Metric Units)} \end{cases}$$

where P_c is axial load in lb (N) and A_g is the cross-section area in in.^{2} (mm^2).

15.3.4.2.2 Limiting Longitudinal Reinforcement Ratios

The ratio of the longitudinal reinforcement to the gross cross section of the compression members should not be less than 0.01 and 0.005 for columns and pier walls respectively, and not more than 0.04.

15.3.4.2.3 Plastic Hinge Region

The plastic hinge region for ductile members is defined as the larger of the following:

- 1.5 (The cross-sectional dimension in the direction of bending)
- Region where the moment exceeds 75% of the maximum plastic moment, M_p^{col}
- 0.25 (Length of column from the point of maximum moment to the point of contra-flexure)

15.3.4.2.4 Transverse Reinforcement in Plastic Hinge Regions

For confinement in plastic hinge regions, in terms of the volumetric ratio, ρ_s for columns with circular and interlocking core sections, $\rho_s = 4A_{bh}/D's$, should be designed to ensure members meet the performance requirements.

The maximum spacing (s) for lateral reinforcement in the plastic end regions should not exceed the smallest of (1) 20% of the least dimension of the cross section for columns and one-half of the least cross-section dimension of piers, (2) six times the nominal diameter of the longitudinal reinforcement, and (3) 200 mm.

15.3.4.2.5 Joint Proportion and Reinforcement

- Moment-resisting integral connections should be designed to resist the overstrength capacity M_p^{col} and associated shear.
- The principal tension stress p_t and compression stress p_c should not exceed $1.0\sqrt{f_c'}$ (Mpa) and 0.25 f_c', respectively. The bent cap width required for the joint shear transfer shall not be less than the cross-section dimension of the column in the direction of bending plus 600 mm.
- When the principal tension stress $p_t \le 0.29\sqrt{f_c'}$ (MPa), for circular columns, or columns with intersecting spirals, the volumetric ratio of transverse reinforcement in the form of spirals or hoops to be continued into the cap or footing, ρ_s should not be less than

$$0.29\sqrt{f_c'} / f_{yh}$$

- When the principal tension stress $p_t > 0.29\sqrt{f_c'}$, the additional reinforcement should be provided and well distributed within $D/2$ from the face of column as specified in Caltrans SDC (Caltrans 2013).

Figure 15.8 shows a three-dimensional (3-D) representation of the knee-joint shear reinforcement layout.

15.3.4.3 Structural Steel

15.3.4.3.1 Limiting Width-to-Thickness Ratios

For capacity-protected components, the width–thickness ratios of compression elements should not exceed the limiting value λ_r as specified in Caltrans Guide Specification (Caltrans 2014). For ductile

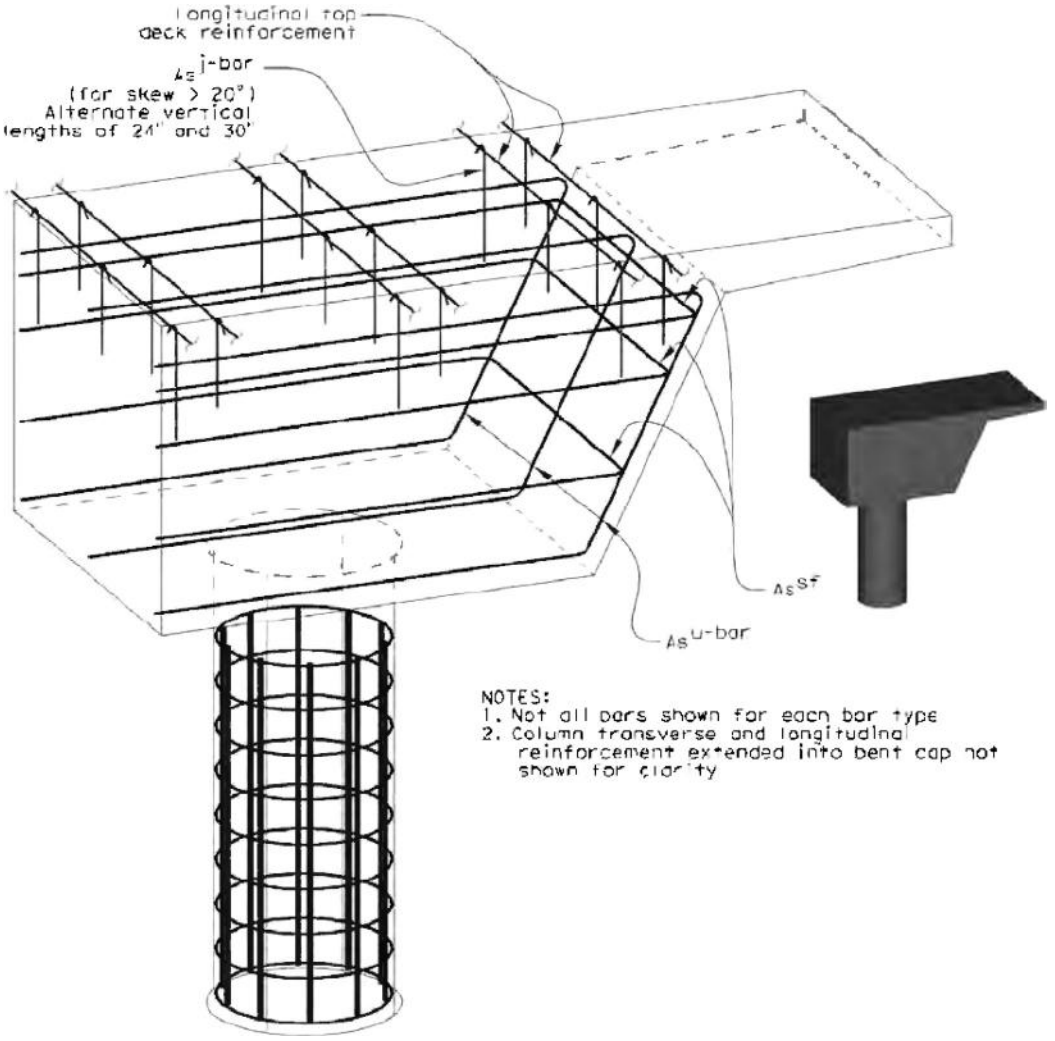

FIGURE 15.8 Knee-joint shear reinforcement layout.

components, width–thickness ratios should not exceed the λ_p as specified in Caltrans Guide Specification (Caltrans 2014). Welds located in the expected inelastic region of ductile components are preferably complete penetration welds. Partial penetration groove welds are not recommended in these regions. If the fillet welds are the only practical solution for an inelastic region, quality control (QC) and quality assurance (QA) inspection procedures for the Fracture Critical Members should be followed.

15.3.4.3.2 Limiting Slenderness Ratio

The slenderness parameter λ_c for compression members and λ_b for flexural members should not exceed the limiting values, λ_{cp} and λ_{bp}, respectively, as specified in the Guide Specifications (Caltrans 2014).

15.3.4.3.3 Limiting Axial Load Ratio

High axial load in columns usually results in the early deterioration of strength and ductility.

The ratio of factored axial compression due to seismic load and permanent loads to yield strength ($A_g F_y$) for columns in ductile moment-resisting frames and single-column structures should not exceed 0.3.

15.3.4.3.4 Shear Connectors

Shear connectors should be provided on the flanges of girders, end-cross frames, or diaphragms to transfer seismic loads from the concrete deck to the abutments or pier supports. The cross frames or diaphragms at the end of each span are the main components to transfer the lateral seismic loads from the deck down to the bearing locations.

15.3.5 Design Requirements for Other Types of Bridges

Caltrans Office of Earthquake Engineering has begun developing seismic details and procedures for precast girder and other types of bridges in order to meet the Department's goal of accelerated bridge construction (ABC) and to move toward the next generation of bridges (NGB). These bridges may have a capacity-protected design similar to the CIP box girder bridge or in some cases they may be allowed free rotation (with pinned connections between the superstructure and substructure) or even free translation between column and superstructure joints (with isolation bearings and shear keys).

In Figure 15.9 (from the AASHTO Guide Specifications), Caltrans capacity-protected seismic design would be like "1" in the longitudinal direction and "3" in the transverse direction. However, a precast girder system could use "2" or "4" in the longitudinal direction and "4" or "5" (for a shorter bridge) in the transverse direction. These are not the only possible earthquake resistant systems. Caltrans is working to make slab bridges, precast bridges, steel bridges, arch bridges, modular bridges, and other types

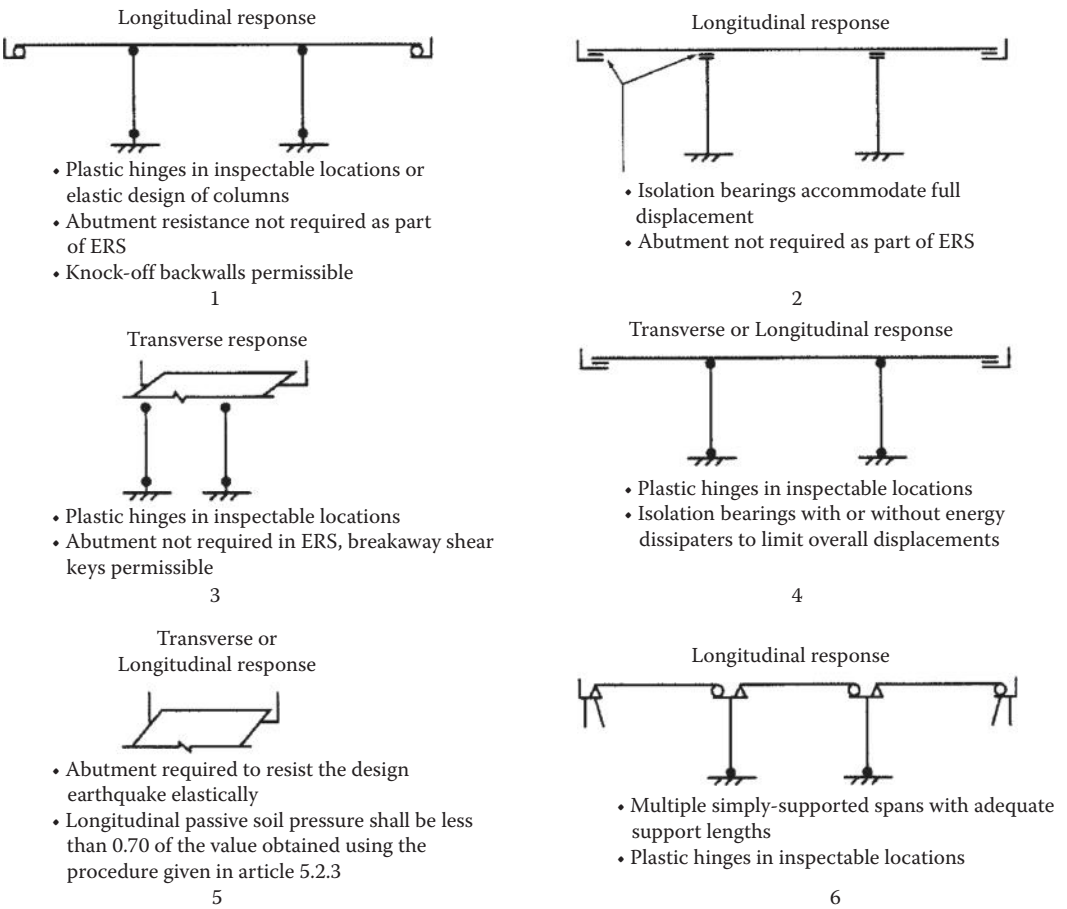

FIGURE 15.9 Earthquake-resistant systems from AASHTO seismic guidelines.

of bridges that have reliable earthquake performance. These systems have different degrees of fixity between adjacent elements and may require new earthquake-resisting elements.

For instance, a precast girder bridge can be designed like a CIP bridge with continuous positive and negative reinforcement in the superstructure, the bent cap, and the column, all going through the joint (Figure 15.10).

However, a shorter precast girder bridge can be designed to resist earthquakes with abutment shear keys and a backwall, and a longer precast girder bridge can be designed with isolation bearings and shear keys at the bents (Figure 15.11).

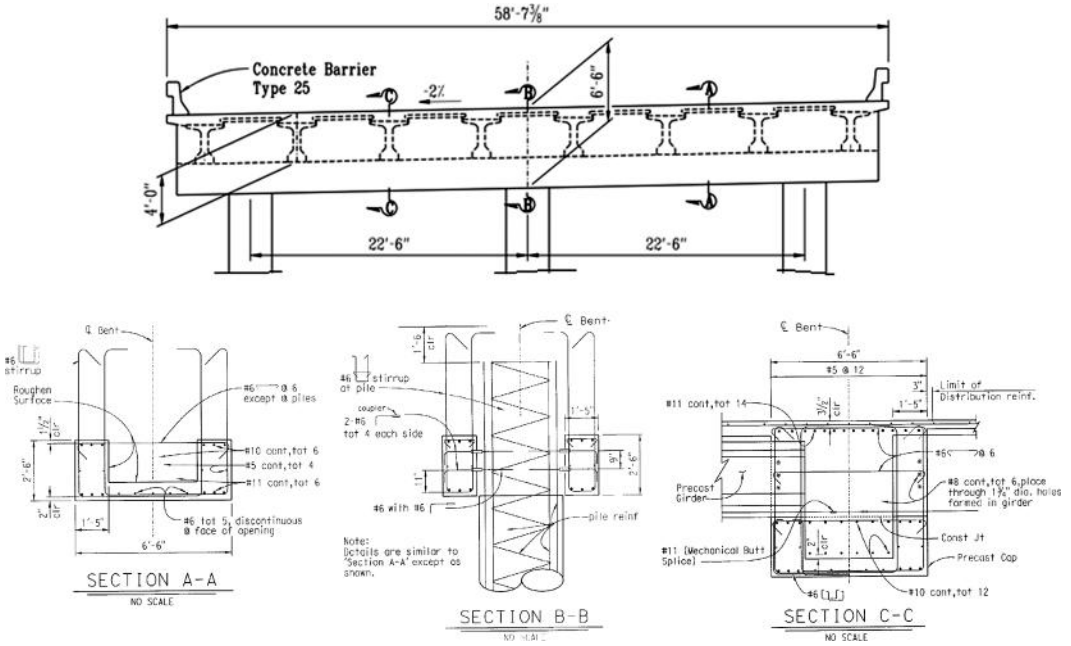

FIGURE 15.10 Precast girder bridge designed like Caltrans CIP Box Girder Bridge.

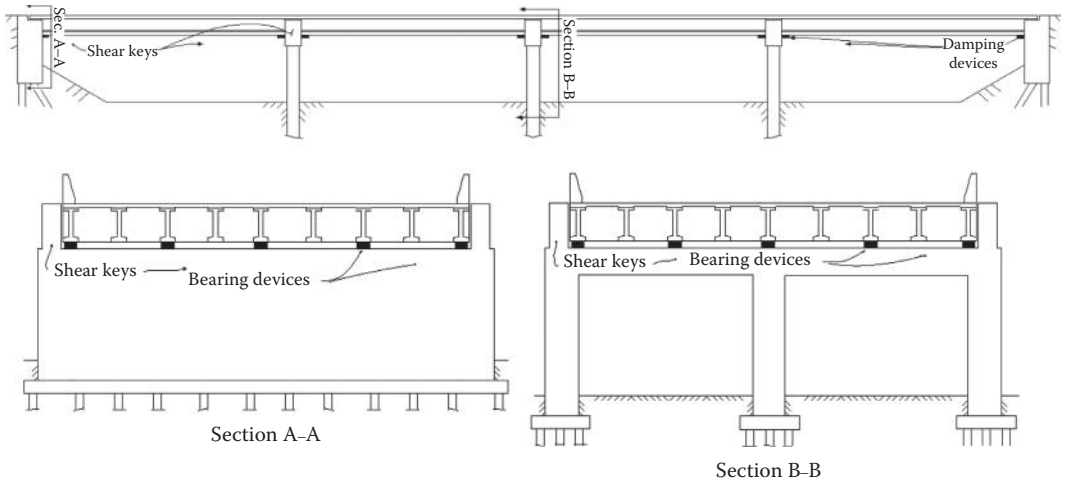

FIGURE 15.11 Long precast girder bridge designed with isolation bearings and shear keys.

15.4 Project-Specific Seismic Design Criteria

Nonstandard bridges, important bridges, and big bridge projects are required to develop their own seismic criteria. The project-specific criteria address the specific hazard, performance criteria, analysis methods, and acceptance criteria. Nonstandard bridges such as arch and truss bridges are not addressed in Caltrans SDC and require a seismic strategy to prevent collapse. Even projects with CIP posttensioned, box girder bridges may get their own seismic criteria if they are part of an expensive interchange. Moreover, interchanges include ramps and connectors with short-radius curves, high skews, and varying height columns that require project-specific criteria. Bridges supported by liquefiable soil or over a fault require project-specific criteria. Even standard, ordinary bridges that are part of a new expressway may get project-specific ground motion. Long-span bridges usually represent an important investment and so bridge owners are willing to spend extra money to prevent severe damage in regions of frequently occurring large earthquakes. The columns of tall bridges are difficult to shore and repair and so the owner may want them to remain essentially elastic in regions of frequent large earthquakes.

Suspension and cable-stayed bridges require specific seismic criteria to ensure that the cable anchors are stronger than the cables and that one or more cables can break while continuing to support the bridge deck. The towers of suspension and cable-stayed bridges usually require special fuses since it is unwise to allow damage to the only load-bearing members on a long-span structure. Moreover, long-span bridges carry large inertia forces and require special earthquake devices. Shock transmission devices allow slow-temperature movements at expansion joints but they lockup during earthquakes, preventing shorter hinges from unseating. A variety of damping devices can be designed to absorb energy at smaller displacements, thus preventing the need for enormous foundations and substructures that would only attract larger loads. Isolation devices in combination with shear keys would support the superstructure during smaller earthquakes but would isolate the substructure for damaging forces during larger earthquakes.

A good example of project-specific design criteria is the one developed for San Francisco-Oakland Bay Bridge (SFOBB) East Span Replacement Project. The current bridge has the largest daily traffic in the United States (280,000 vehicles) and so the designers were anxious to keep the replacement bridge in service. The new bridge is composed of a long skyway made up of precast girder segments on ductile columns with very strong foundations and a self-anchored suspension bridge at the west end of the structure. The bridge was designed to resist two levels of earthquake: a functional evaluation earthquake (FEE) with a 92-year return period and minimal damage and a safety evaluation earthquake (SEE) with a 1500-year return period and repairable damage.

To achieve this project criterion (Caltrans 1999b), the bridge was designed as a limited-ductility structure. For the SEE, the skyway potion will have repairable damage to the plastic hinge region of the piers and the tower will have damage to modular shear links that can be replaced after the earthquake (Figure 15.12).

15.5 Seismic Retrofit Practice

Since the 1971 San Fernando earthquake struck the Los Angeles area, Caltrans has been engaged in an ongoing bridge seismic safety retrofit program. The state's bridge earthquake retrofit program involves approximately 2,200 structures and a cost of more than $8 billion in construction (Caltrans 2013b).

The seismic retrofit strategies include (1) strengthening the existing bridge columns by jacketing with a steel casing or fiber reinforced polymer (FRP) composite casing; (2) giving footings more support by placing additional pilings in the ground or by using steel tie-down rods to better anchor the footings to the ground; (3) making bridge abutments larger; and (4) installing restrainers and hinge sear extensions. This section briefly describes retrofit practice for Ordinary Standard bridges and several large bridges.

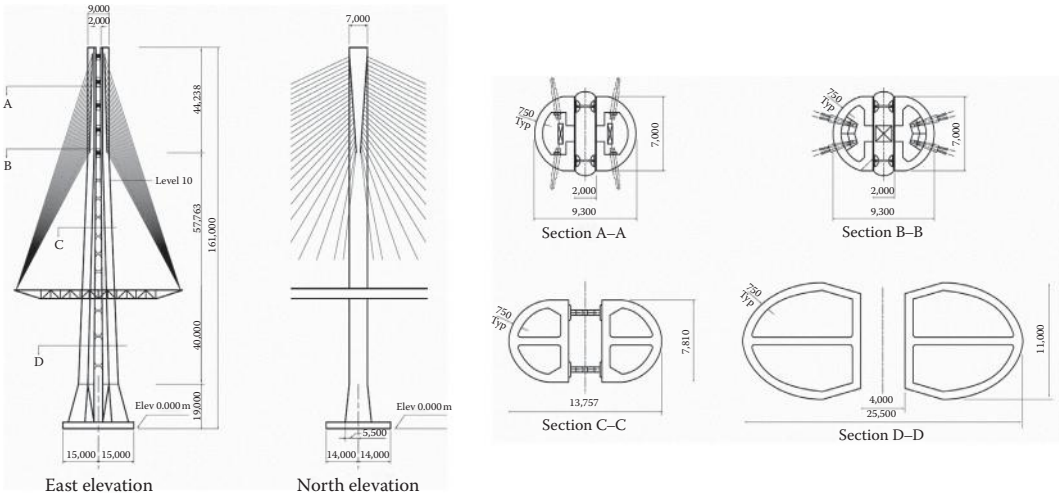

FIGURE 15.12 Single tower for East Bay Bridge with shear link.

FIGURE 15.13 The Interstate 5/Route 52 Interchange and Ardath Overcrossing in San Diego.

15.5.1 Standard Bridges

The seismic criteria for ordinary standard bridge retrofits are provided in Caltrans Memos to Designers 20-4 (Caltrans 2010c). Existing bridges cannot meet all the requirements in Caltrans SDC such as the providing columns and bents of about equal stiffness. Therefore, the guiding principal for retrofits is to prevent collapse.

15.5.1.1 Cast-in-Place Girder Bridge: Ardath Overcrossing

Ardath Overcrossing is on Interstate 5/Route 52 Interchange in San Diego, California (Figure 15.13), built in 1966. This overcrossing is a reinforced concrete box girder bridge with a "Y" shape (in plan) composed of four frames.

The west alignment consists of three continuous spans and a cantilever span supported on a skewed abutment and three skewed two-column bents (Abutment 1 and Bents 2–4).

The north alignment consists of four continuous spans and a cantilever span supported by four single-column bents and an abutment (Bents 7AL–10AL and Abutment 11AL).

The south alignment consists of five continuous spans and a cantilever span supported by five single-column bents and an abutment (Bents 7R3–11R3 and Abutment 12R3).

The central frame connects the west, north, and south alignments at three hinges and has a two-column bent and two single-column bents (Bent 5, Bent 6AL, and Bent 6R3).

The three abutments have short seats and rocker bearings. The three hinges have 16 in. (40.6-cm) seats and elastomeric bearing pads. Other structural details are in Table 15.2 (El-Azazy, Alameddine, and Hipley 1999). The soil is loose-to-slightly-compacted silt and fine sand overlaying dense sands with no groundwater. The bridge is within 0.8 km of the $M_w = 7.0$ Rose Canyon Fault, and the bridge site has a PGA of 0.7 g. The goal of this retrofit was to prevent bridge collapse and minimize the amount of foundation work because of the heavy traffic and underground utilities. The main vulnerabilities were short hinge and abutment seats, inadequate lap splices, poor confinement at the bottom of columns, and under-reinforced foundations.

A 3-D multimodal EDA was performed on the as-built bridge. The displacement demand over the yield–displacement ratio at the bents for Case 1 and Case 2 (Case 1 = 100% transverse + 30% longitudinal, Case 2 = 30% transverse + 100% longitudinal) are listed in Table 15.2. The columns were retrofitted with a Class F casing to allow a plastic hinge to form at the base of the column, or with a Class P/F column casing to allow a pin to form.

Since the columns had inadequate transverse reinforcement, full-height steel shells were provided. Because of problems with busy roads, railroads, and utilities near the foundations, the engineers were selective about which footings would get additional piles. Several retrofit models were created with pinned and fixed-column bases representing columns that were designed to develop small and large bottom moments during an earthquake. The model that best protected the structure while eliminating footing work at difficult locations was then selected as the retrofit.

Since the columns at Bent 2 had only a small amount of longitudinal reinforcement, a Class F column casing was selected, because the small plastic moment could be handled by the existing foundation.

The columns at Bents 3, 4, and 5 were retrofitted with Class P/F casings to reduce the bottom moment and eliminate the need for footing work on Interstate 5. Bents 6AL and 6R3 were provided with class F casings. Bent 6AL had a large footing that could handle the moment with an overlay, whereas Bent 6R3 required additional piles. Since these footings were in the median of the freeway, the footing work could proceed with little disruption to traffic.

Bent 8AL was selected to support the north alignment with a fixed column and piles, whereas Bents 9AL and 10AL were allowed to rock with Class F casings and footing overlays. This decision eliminated the need to drive piles next to the railroad and at a difficult location at Bent 10AL.

Class P/F casings were provided at Bents 9R3 and 11R3 to avoid footing work under the Route 52 alignment and in an embankment. Bents 7R3 and 10R3 were retrofitted with Class F casings and piles. Bent 8R3 was retrofitted with a Class F casing and a footing overlay, but no piles were required because of its large footing dimensions.

The out-of-phase displacement of adjacent frames at the hinges was calculated. All the hinges had displacements larger than the 40.6-cm hinge seats and were retrofitted with pipe-seat extenders and cable restrainers. Similarly, pedestals were built in front of the abutments to allow larger superstructure movements.

This retrofit was designed to provide support for the superstructure, confinement and shear strength for the columns, and additional strength to the foundations so that the bridge could survive the Maximum Credible Earthquake (MCE) on the Rose Canyon Fault. However, after the MCE, the bridge could sustain damage that may require repairs or even replacement.

TABLE 15.2 Structural Details and Retrofit Strategy

Col.	Column Ht ft. (m)	Column Diameter ft. (m)	Footing ft. (m)	Displacement Demand Ratio		Retrofit Strategy
				Case 1	Case 2	
2L	33 (10.1)	6 (1.83)	4 × 15 × 17 (1.2 × 4.6 × 5.2) with piles	3.26	4.05	Class F with no footing work
2R	33 (10.1)	6 (1.83)	4 × 15 × 17 (1.2 × 4.6 × 5.2) with piles	3.60	4.20	Class F with no footing work
3L	73 (22.3)	6 (1.83)	4.25 × 15 × 27 (1.3 × 4.7 × 8.2) with piles	2.48	2.62	Class P/F with no footing work
3R	73 (22.3)	6 (1.83)	4.25 × 15 × 27 (1.3 × 4.7 × 8.2) with piles	2.71	2.72	Class P/F with no footing work
4L	67 (20.4)	6 (1.83)	4.25 × 15 × 27 (1.3 × 4.7 × 8.2) with piles	3.63	3.60	Class P/F with no footing work
4R	67 (20.4)	6 (1.83)	4.25 × 15 × 27 (1.3 × 4.7 ×8.2) with piles	3.88	3.73	Class P/F with no footing work
5L	58 (17.7)	6 (1.83)	4.25 × 15 × 27 (1.3 × 4.7 × 7.0) with piles	4.84	4.29	Class P/F with no footing work
5R	58 (17.7)	6 (1.83)	4.25 × 15 × 27 (1.3 × 4.7 × 7.0) with piles	4.08	4.20	Class P/F with no footing work
6AL	55 (16.8)	6 × 15 (1.83 × 4.57) oval	5.25" × 21 × 43 (1.6 × 6.4 × 13.1) with piles	4.19	5.23	Class F with footing widening and overlay
7AL	57 (17.4)	6 (1.83)	3.75 × 15 × 27 (1.1 × 4.7 × 8.2) with piles	1.58	1.87	Class F with footing overlay
8AL	60 (18.3)	6 × 15 (1.83 × 4.57) oval	5.25" × 21 × 53 (1.6 × 6.4 × 16.2) with piles	3.81	3.47	Class F with widening, overlay, and piles
9AL	65 (19.8)	6 (1.83)	3.75 × 15 × 27 (1.1 × 4.7 × 8.2) spread footings	1.33	1.02	Class F with footing overlay
10AL	70 (21.4)	6 (1.83)	3.75 × 15 × 27 (1.1 × 4.7 × 8.2) spread footings	1.91	1.40	Class F with footing overlay
6R3	55 (16.8)	6 × 10 (1.83 × 3.05) oval	4 × 18 × 28 with piles	3.14	4.16	Class F with widening, overlay, and piles
7R3	60 (18.3)	6 (1.83)	4.25 × 18 × 28 (1.2 × 5.5 × 8.5) with piles	2.04	2.29	Class F with widening, overlay, and piles
8R3	65 (19.8)	6"× 10 (1.83 × 3.05) oval	4 × 18 × 33 (1.2 × 5.5 × 10.1) with piles	3.59	3.65	Class F with footing overlay
9R3	33 (10.1)	6 × 10 (1.83 × 3.05) oval	5 × 15 × 38 (1.5 × 4.6 × 11.6) with piles	7.28	6.83	Class P/F with no footing work
10R3	35 (10.7)	6 (1.83)	4 × 18 × 28 (1.2 × 5.5 × 8.5) with piles	2.25	3.05	Class F with widening, overlay, and piles
11R3	65 (19.8)	6 (1.83)	4.25 × 18 × 28 (1.3 × 5.5 × 8.5) with piles	1.01	1.37	Class P/F with no footing work

All piles are 16-inch-diameter cast-in-drilled-hole piles.

FIGURE 15.14 The Sierra point overhead.

15.5.1.2 Steel Girder Bridge: Sierra Point Overhead

This bridge, built in 1957, carries Highway 101 over railroad tracks in South San Francisco (Figure 15.14). It is a 10-span steel girder bridge, with girders supported by steel floor beams. One end of each girder is bolted to a floor beam stiffener, and the other end is attached to a rocker bearing on top of a short seat on the floor beam. The floor beams are supported by 2–4 nonductile reinforced concrete columns. Steel bearings sit atop the columns and are welded to the floor beams. The columns are supported by under-reinforced spread footings on stiff clay. The bridge abutments are on a 60° skew parallel to the railroad tracks, but the bents have no skew. This interesting configuration results in some floor beams being supported by the abutments.

The bridge site has a 0.4 g PGA and is about 16 km from the $M_w = 8.0$ San Andreas Fault. The weak columns and poorly reinforced footings leave the bridge vulnerable to the earthquakes that frequently strike the San Francisco Bay Area. However, the proximity of the railroad limited the retrofit options. Therefore, this bridge was retrofitted with isolation bearings in 1985, making it the first isolated bridge in the United States. All the bearings at the columns and at the abutments were replaced by lead/rubber bearings, which were designed so that the seismic forces would be less than the capacity of the columns and footings. These lead/rubber bearings were rectangular, but round lead/rubber bearings are now used in other bridges because they provide much better performance, particularly for bridges that must move in all directions. To prevent the rocker-supported end of the steel girders from becoming unseated, 0.9 in. (2.2-cm) steel tie rods were used to connect them to the bolted girders on the other side of the floor beams.

After the retrofit, the bridge was instrumented with strong-motion accelerometers above and below the isolators. The epicenter of the 1989 Loma Prieta earthquake was about 100 km from the bridge site, and the measured acceleration at the bridge was 0.29 g above the isolators and 0.31 g below the isolators (parallel to the bridge). These two accelerations were about the same, which shows that the lead core did not yield during the earthquake and the bridge behaved elastically with no damage.

15.5.2 Nonstandard Bridges

15.5.2.1 Concrete Arch Bridge: Bixby Creek Bridge

The Bixby Creek Bridge is a 715 ft. (218-m) long, reinforced concrete arch bridge built in 1932. The simple-span T-girder superstructure is supported on split-column bents, two 331 ft. (101-m) arch rings, and two massive towers (Figure 15.15).

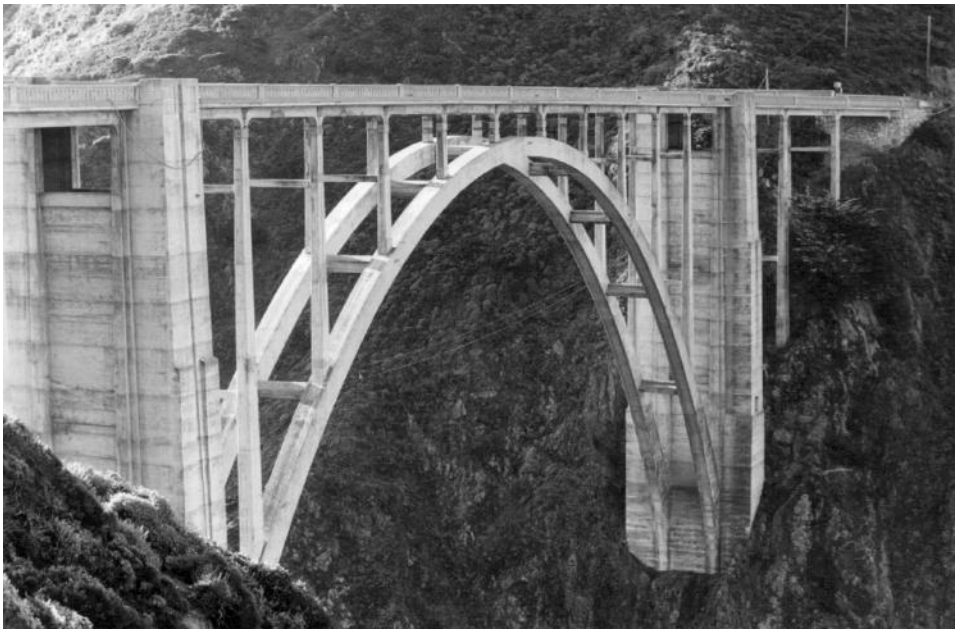

FIGURE 15.15 The Bixby Creek Bridge before retrofitting.

This bridge is within 1.85–2.5 miles (3–4 km) of the $M_w = 7.5$ San Gregorio Fault. The major vulnerability of this bridge is the fragile spandrel columns. To protect them, the bridge deck was posttensioned and attached to massive concrete blocks that were built at the two abutments, as shown in part (a) of Figure 15.16. These blocks move transversely and longitudinally for service loads but will engage large pile caps during an earthquake. The superstructure was further stiffened by making it continuous and adding stiff edge beams.

Transverse movement was also limited by the addition of shear panels at the arch crown. Thus, transverse movement that could have broken the shorter spandrel columns was limited by in-plane bending of the stiffened deck, anchorage at the ends of the bridge, and shear panels at the crown. The towers were strengthened by concrete ribs, a vertical shear panel in their hollow interior, and prestressing cables that anchor the tower into bedrock. The original intent was to fiber-wrap the spandrel columns, but there was some concern about the aesthetics of this historical bridge, so concrete casings were used. This retrofit method of making the superstructure act as the primary load path was repeated with many of California's reinforced concrete arch bridges.

15.5.2.2 Movable Bridge: Sacramento River Bridge

The Sacramento River Bridge at Rio Vista, built in 1958, is a steel through-truss bridge with a 318 ft. (100 m) main lift span supported by 187 ft. (57 m) tall steel towers. The towers are anchored to massive concrete piers (Figure 15.17). A 750-kip (3336 kN) counterweight hangs from cables at each tower to help raise and lower the main span. The approach spans are supported on reinforced concrete two-column bents and seat-type abutments. The entire bridge is on piles that extend through loose material into dense sands and stiff clay.

This bridge is 7 km from the $M_w = 6.75$ Coast Range/Sierra Nevada Boundary Zone fault. Site-specific response spectra were developed and used to create three sets of spectra-compatible time histories. The bridge was analyzed with the main span at deck level and the counterweights restrained by rails at the top of the towers. An ESA was performed on the as-built bridge and nonlinear time-history analyses

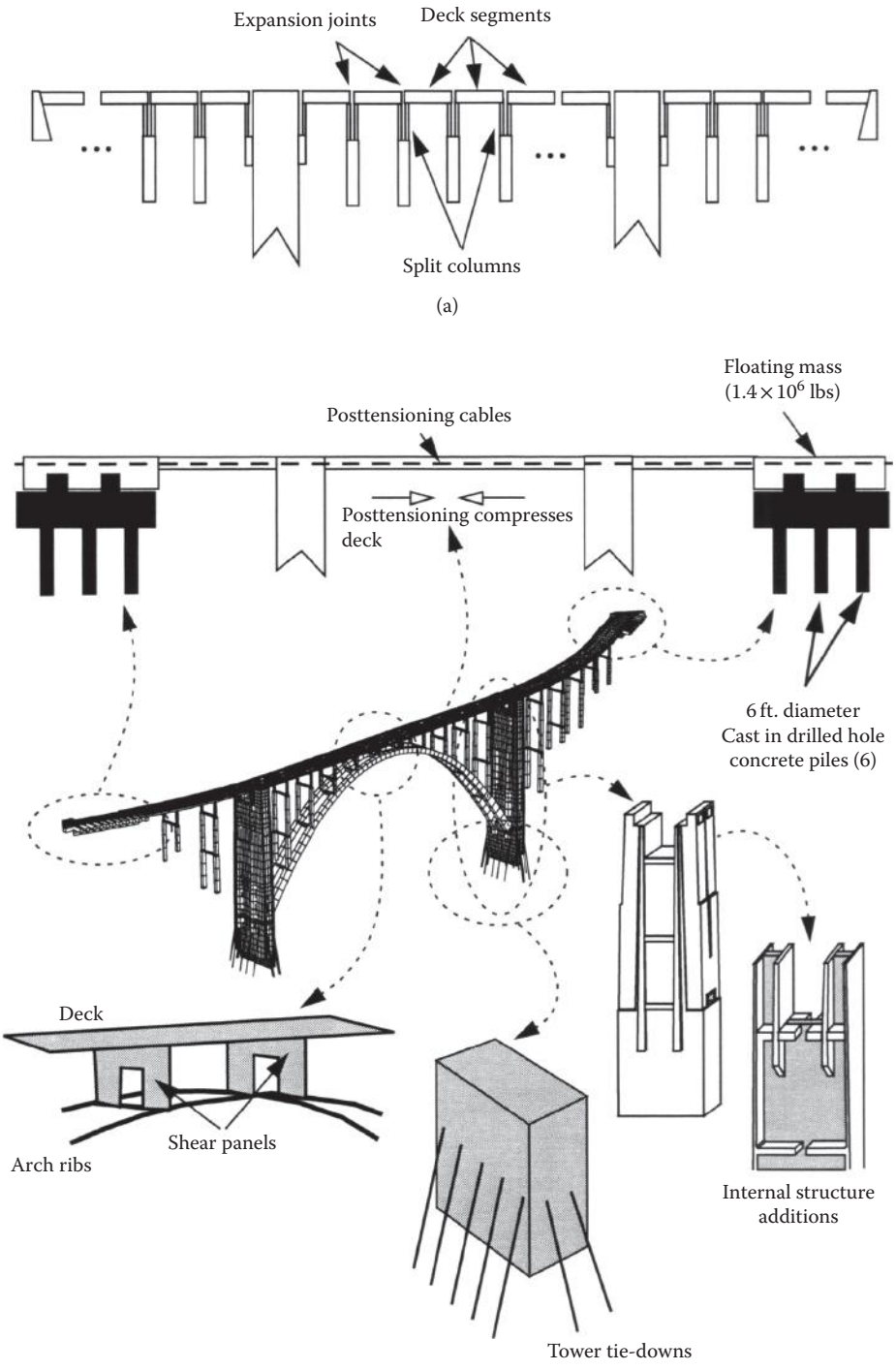

FIGURE 15.16 Retrofit of Bixby Creek Bridge. (From McCallen, D. et al., *UCRL-ID-134419*, June, Lawrence Livermore National Laboratory, Livermore, CA, 1999. With permission.)

FIGURE 15.17 The Sacramento River Bridge at Rio Vista.

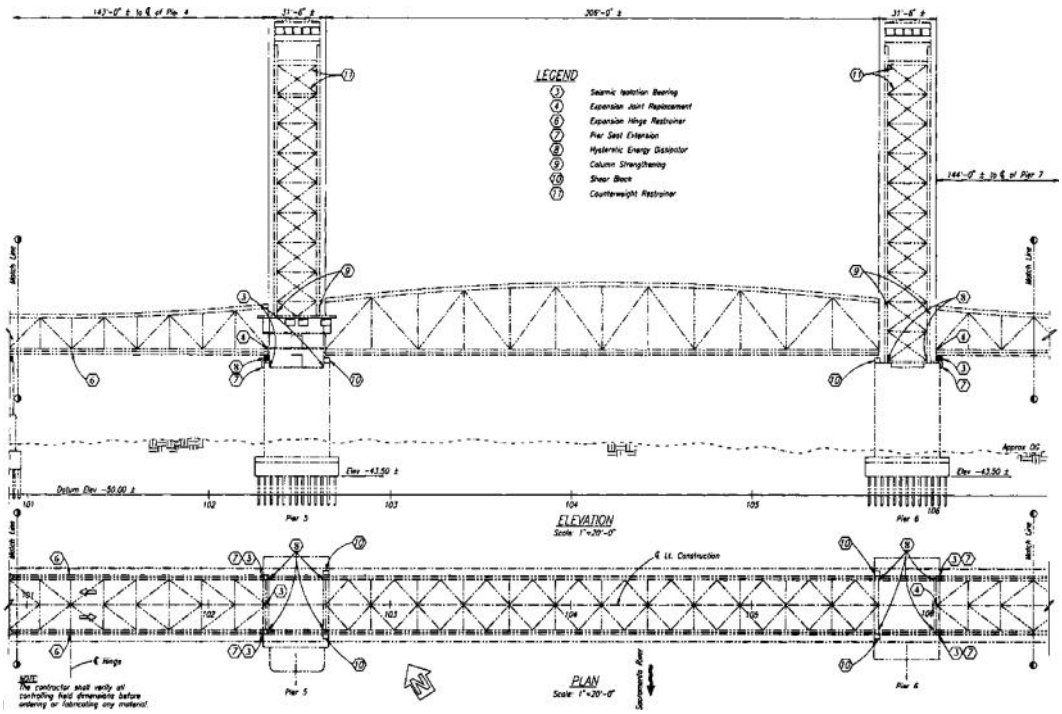

FIGURE 15.18 Seismic retrofit plan drawing for the Sacramento River Bridge at Rio Vista. (From Uzarski, J., *Proceedings from the Second U. S. Seminar on the Seismic Design, Evaluation, and Retrofit of Steel Bridges, UCB/CEE-Steel-96/09.* Department of Civil and Environmental Engineering, University of California, Berkeley, CA, 1996. With permission.)

were performed on the towers. Pushover analyses were performed on the tower and the piers to obtain capacities. The following vulnerabilities were found:

1. Shear failure of steel-bearing anchor bolts at the abutments and two-column bents (these bents are not visible in Figure 15.17).
2. Flexural yielding of anchor bolt-bearing plates at the bottom of the towers, resulting in rocking and large displacement of the towers.

3. Shear failure of the link beam between the two-column bents, resulting in large displacements and possible collapse.

To prevent this damage, the east and west truss spans were isolated by replacing the steel bearings at each bent with lead/rubber isolation bearings and by replacing the existing expansion joints at the abutments and the towers with expansion joints capable of 30 cm of movement (Figure 15.18).

At the towers, the existing anchor plates were replaced, to force the anchor bolts to yield to tension. Hydraulic dampers were added to connect the concrete piers to the tower legs to control uplift of the towers after the yielding of the anchor bolts. To prevent a soft-story response at the bottom of the towers, the steel legs were reinforced by flange plates.

Analysis showed that the retrofitted bridge model had acceptable displacement demands at the towers and at the tops of the two-column bents (these bents are not shown in Figure 15.18).

15.5.2.3 San Francisco-Oakland Bay Bridge West Span

The San Francisco-Oakland Bay Bridge (SFOBB), a main connection of San Francisco Bay, is one of the most important bridges in the United States. The bridge has the upper and lower concrete decks carrying five lanes in each direction and provides service to over 280,000 vehicles daily. The West Span (Figure 15.19) of 10,122 ft. (3,085.2 m) includes three continuous truss spans of 389 ft. + 95 ft. + 377 ft. (118.6 m + 29.0 m + 114.9 m) and the twin suspension bridges arranged end to end around a center anchorage. The twin bridges (Figure 15.20) have main spans of 2,310 ft. (704.1 m) and back spans of 1,160 ft. (353.6 m) and are virtually identical. The double-deck stiffening truss is made up of built-up members, laced members, and some rolled sections.

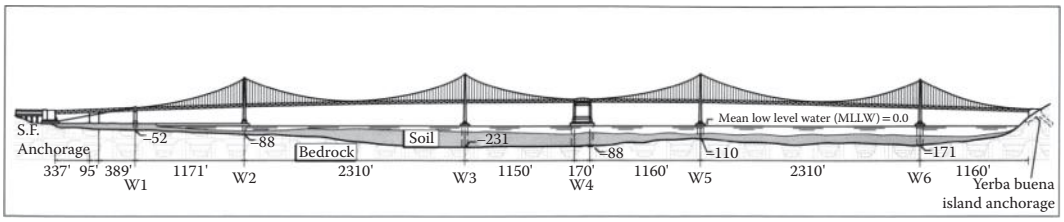

FIGURE 15.19 Overview of San Francisco-Oakland Bay Bridge—West Span.

(a) (b)

FIGURE 15.20 San Francisco-Oakland Bay Bridge West Span under retrofit construction.

All the towers are similar, except that Towers W2 and W6 are about 420 ft. (128.0 m) tall, while Towers W3 and W5 are about 470 ft. (143.3 m). The tower legs are cellular in cross section, made up of 1 in. (25.4 mm) thick vertical web plates connected along their edges with angles. Tower W2 is supported by a gravity concrete pier that was constructed in a sheet-pile cofferdam 90 ft. (27.4 m) below water. Towers W3, W5, and W6 are supported by cellular, hollow, reinforced concrete caissons that extend from 110 ft. (33.5 m) to 230 ft. (70.1 m) below water level. Pier W4 is actually a central anchorage for the twin, end-to-end suspension bridges and supported by a hollow cross-section caisson of 92 ft. × 197 ft. (28.0 m × 60.0 m), which is formed using fifty-five 15 ft. (4.6 m) diameter by 5/16 in. (8 mm) thick steel cylinders. It extends 220 ft. (67.1 m) below water and 280 ft. (85.3 m) above water. It was the largest pier in the world at the time of its construction. All the caissons were socketed into the underlying bedrock.

The seismic retrofit of SFOBB West Span (Figure 15.20) was the top priority of the California Department of Transportation. The seismic retrofit design of SFOBB west spans was performed by considering both the safety evaluation earthquake (FEE), which has a mean return period in the range of 1,000–2,000 years, and the functionality evaluation earthquake (FEE), which has a mean return period of 300 years with a 40% probability of exceedance during the expected life of the bridge.

The West Span was seismically retrofitted in 2004 to improve operational and safety standards to the greatest extent possible and to achieve the project-specific, performance-based seismic design criteria (Caltrans 1997, Reno and Pohll 1998). The retrofit project not only opened under the original engineer's estimate but was also constructed and closed out for less than the engineer's estimate plus contingencies. This was a remarkable feat for complicated steel retrofit work, such as that encountered on the San Francisco-Oakland Bay Bridge West Span Retrofit.

The superstructure retrofit includes the following:

- Adding cable ties at mid span of both suspension bridge main spans to help control longitudinal movement.
- Strengthening of the floor beam to vertical connection with tie-rods and additional plates.
- Strengthening of the stiffening truss chords and diagonals by the addition of plates and the replacement of lacings with perforated plates and/or additional plates (Figure 15.21).
- Adding a new upper deck lateral bracing system using a tube section in a chevron configuration.
- Replacing the complete lower deck lateral bracing system with ductile members.
- Strengthening gusset connections by replacing rivets with high-strength bolts and by adding edge stiffeners.

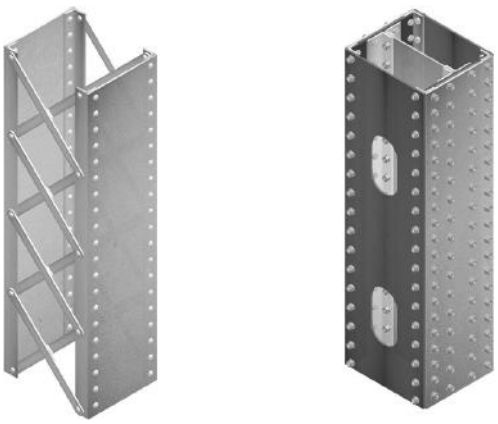

FIGURE 15.21 Stiffening truss member retrofit.

- Modifying the truss-to-tower connection to allow greater relative longitudinal movement and installing total 96 viscous dampers between each chord and the tower or the anchorage (Figure 15.22).
- Installing the friction pendulum isolation bearings for the Continuous Trusses to reduce substructure loading.

The tower retrofit (Figure 15.23) includes the following:

- Installing new anchor bolts to resist uplift forces and installing internal pipe shear keys at the base.
- Strengthening the cable saddle connection to the top of the tower.
- Strengthening gusset connections by replacing rivets with high-strength bolts and by adding additional plates.
- Adding new longitudinal and transverse stiffeners to strut and diagonal plates.
- Installing new plates for tower legs.

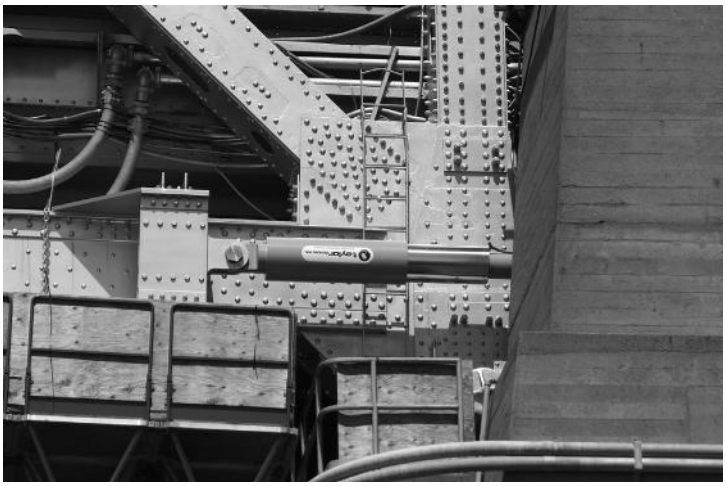

FIGURE 15.22 Suspension span dampers.

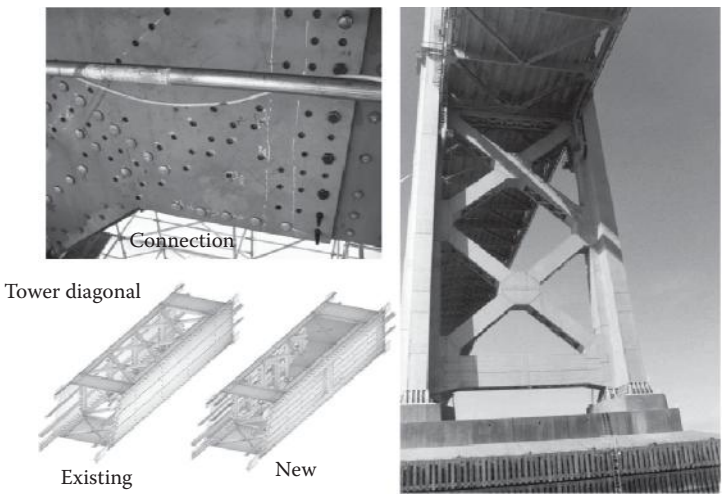

FIGURE 15.23 Suspension span tower retrofit.


FIGURE 15.24 Pier W4—central anchorage retrofit.

The pier and foundations retrofit includes the following:

- Strengthening of Pier W1, Bents A and B foundations, and Pier W4 (Figure 15.24) by providing either a concrete or steel jacket around the foundation.
- Drilling and grouting vertical high-strength rods to the full height of the foundation for Pier W2.
- Adding concrete jackets, drilling and grouting high-strength rods vertically, and prestressing horizontally through the pedestals for Piers W2, W3, W5, and W6.

15.6 Summary

Bridge Seismic Criteria was developed in California following the 1971 San Fernando Earthquake and gradually found its way into the national seismic guideline through the efforts of AASHTO. These two criteria are coming together through AASHTO's T3 Committee. However, Caltrans will continue to develop its own seismic criteria for the foreseeable future.

The main elements of Caltrans Seismic Design Criteria are the use of ductile elements with adjacent elements that are designed with overstrength factors to ensure plastic hinging occurs in the expected ductile elements. In order for this design philosophy to work, ample confinement reinforcement for concrete members, ample continuity of reinforcement, ample seats, and providing as uniform a structure as possible are required.

The latest efforts have been to codify these procedures, to extend them to different types of bridges, to bring them to ABC, and to use them to address a variety of seismic hazards including liquefaction, lateral spreading, surface faulting, near-fault effects, tsunami, and so on.

Tsunami maps are being developed along California's coast, liquefaction maps are being developed by the California Geological Survey, bridges on active faults are being identified, and new ARS Tools are being put on the Internet to automatically notify engineers and management when damaging earthquakes occur.

Caltrans SDC is currently at Version 1.7 and Guide is at the Second Edition, and continues to grow with new versions coming out every year or two. The latest advances have been in designing better column-to-superstructure connections, especially for knee joints. Much work has been going on to design more reliable shear keys, to obtain better analytical models for abutments and pile caps, and so on.

All of these advances come from Caltrans research program; from lessons learned by going out and studying bridge behavior following earthquakes; from discussions with the professors and researchers all over the world; and through attending workshops, conferences, and meetings with bridge engineers from other states.

Defining Terms

AASHTO American Association of State Highway and Transportation Officials
ARS Acceleration Response Spectra
Bearing An element used to support bridge girders on bent or abutment seats.
Bent (or pier) An intermediate support under the superstructure.
Box Girder A superstructure composed of two or more girders, top and bottom horizontal diaphragms, and transverse vertical diaphragms.
Cable-Stayed Bridge A bridge having one or more towers strung with taut, diagonal cables supporting the bridge deck. The cables are placed parallel to one another in a harp configuration, or they can radiate outward in a fan configuration.
Cap A horizontal element that joins vertical elements together. A bent cap connects the tops of the columns. A pile cap connects the tops of the piles. A dropped bent cap sits below the girders, whereas an integral bent cap is part of the superstructure.
Capacity The amount of strain, curvature, and displacement an element can undergo before it loses its ability to resist a load.
CIDH Pile A pile formed by dropping a steel cage into a hole and filling it with concrete.
CISS cast-in-steel-shell Similar to a CIDH Pile but with a steel shell that was driven into the ground.
Confinement Transverse reinforcement such as spirals, hoops, stirrups, and so on, that support longitudinal reinforcement and concrete.
CQC Complete quadratic combination—a way of summing the contribution of different modes of vibration.
Damping We typically see damping in the reduction of amplitude of a vibrating body over time. Usually, damping refers to resistance to velocity "c," but it is also used to refer to anything that absorbs energy during an earthquake.
Deck The horizontal riding surface on a bridge.
Demand The amount of strain, curvature, and displacement an element undergoes due to an earthquake.
Design Earthquake The seismic hazards that a structure is designed to resist.
Ductility The ability of a structural element to deform without breaking.
Embankment Soil on two sides of a road or other obstacles to provide a ramp on and off of a bridge.
Expansion Joint A transverse joint that accommodates superstructure expansion and contraction.
Fault Crossing A bridge that is over an earthquake fault.
Faults Boundary between tectonic plates that can slowly slip (causing creep) or suddenly rupture (causing an earthquake).
FHWA Federal Highway Administration
Interchange Elevated structures at intersections of highways that allow drivers to continue or change direction without stopping.
Isolation Devices with small lateral stiffness used to reduce the inertia force below the device.
Key An element that limits superstructure movement.
Knee Joint The connection to the bent cap for columns that are too close to the end of the bent cap.
Lateral Bracing Transverse elements between girders to prevent out-of-plane displacements caused by wind and seismic loads.
Lateral Spreading Tendency for loose soil to move after it liquefies.
Liquefaction Tendency for the pore pressure in loose soil to increase during earthquakes, resulting in loss of bearing capacity, reduction of soil stiffness, soil movement, and so on.
LRFD Load and Resistance Factor Design, the current state-of-practice for bridge design.
Magnitude Measurement of the size of earthquakes.

Movable Bridge A water crossing that moves to allow the passage of boats underneath.
Near-Fault Effects Enhancement to ground shaking close to the fault.
Ordinary Bridges Bridges that do not justify the considerable expense to keep them in service following earthquakes.
Outrigger When a support cannot be placed directly under a superstructure because of an obstacle, an outrigger bent is used to straddle the obstacle.
Overcrossing A bridge that carries roads or city streets over a highway.
Overhead A bridge that carries a road over a railroad.
PGA Peak ground acceleration.
Pier This is the same as a bent, which is defined above.
Pier Wall A solid, reinforced-concrete bent whose height is less than 2.5 times its width. Pier walls are often placed in rivers to ensure the smooth flow of water. Pier walls act in flexure in the longitudinal direction, and they act in shear in the transverse direction.
Pile Shaft A large-diameter pile that directly supports the bent cap.
Plastic Hinge Location on an element where yielding and deformation can occur without breaking.
Restrainer A steel rod, steel cable, rubber-impregnated chain, or similar device that prevents a superstructure from becoming unseated during an earthquake.
SDC Seismic design criteria.
SDOF Single degree of freedom.
Shear Key A concrete element that resists forces up to a certain point and then fails in shear.
Skew The angle between the centerline of the superstructure and a horizontal line perpendicular to the abutments or bents.
Slab Bridge A solid reinforced-concrete superstructure supported over two or more bents.
Soffit The underside of the superstructure.
Standard Bridges Well-designed box girder bridge with good reinforcement details and no unusual hazards.
Stiffener A horizontal or vertical plate that is bolted or welded to steel bridge members, like girder webs, to prevent buckling.
Substructure Elements such as piers, abutments, and foundations that support the superstructure.
Superstructure The bridge elements supported by the substructure.
Suspension Bridge A bridge constructed by draping steel cable over two towers and firmly anchoring the cable at the bridge approaches.
Truss Bridge Bridge designed with a top chord in compression and a bottom chord in tension to conserve weight and to span long distances.
Undercrossing A bridge carrying a highway over a road or city street.
Underpass A bridge carrying a railroad over a highway, road, or city street.
Viaduct A very long elevated structure that carries vehicles over a series of obstacles including city streets, railroad yards, and rivers.
Wingwall An earth-retaining structure attached to each side of an abutment.

References

AASHTO. 2009. *Guide Specifications for LRFD Seismic Bridge Design, 1st Edition*, American Association of State Highway and Transportation Officials, Washington, DC.
AASHTO. 2011. *ASHTO Guild Specifications for LRFD Seismic Bridge Design, 2nd edition*, American Association of State Highway and Transportation Officials, Washington, DC.
ATC. 1981. *ATC-6 Seismic Design Guideline for Highway Bridges*. FHWA Contract No. DOT-FH-11-9295. Applied Technology Council, Berkeley, CA.

ATC. 1996. ***ATC-32*** *Improved Seismic Design Criteria for California Bridges: Provisional Recommendations*. Applied Technology Council, Redwood City, CA.

Caltrans. 1990. *Bridge Design Specifications*, California Department of Transportation, Sacramento, CA.

Caltrans. 1997. *San Francisco - Oakland Bay Bridge West Spans Seismic Retrofit Design Criteria*, Edited by Duan, L., California Department of Transportation, Sacramento, CA.

Caltrans. 1999a. *Seismic Design Criteria, Version 1.1* California Department of Transportation, Sacramento, CA.

Caltrans. 1999b. *San Francisco-Oakland Bay Bridge East Span Seismic Safety Project Design Criteria, Version 7*, Prepared by TY Lin/Moffatt & Nichol Engineers, California Department of Transportation, Sacramento, CA.

Caltrans. 1999c. *Bridge Memo to Designers (20-11)—Establishing Bridge Seismic Design Criteria*, California Department of Transportation, Sacramento, CA.

Caltrans. 2001. *Guide Specifications for Seismic Design of Steel Bridges, 1st Edition*, California Department of Transportation, Sacramento, CA.

Caltrans. 2008a. *Bridge Design Aids (14-1)—Hinge Restrainer Design Method*, California Department of Transportation, Sacramento, CA.

Caltrans. 2008b. *Bridge Design Aids (14-3)—Fiber Reinforced Polymer (FRP) Composites Column Casing Systems*, California Department of Transportation, Sacramento, CA.

Caltrans. 2008c. *Bridge Design Aids (14-4)—Joint Shear Modeling Guidelines for Existing Structures*, California Department of Transportation, Sacramento, CA.

Caltrans. 2008d. *Bridge Design Aids (14-5)—Example Seismic Retrofit Details*, California Department of Transportation, Sacramento, CA.

Caltrans. 2010a. *Bridge Memo to Designers Section 20—Seismic*, California Department of Transportation, Sacramento, CA.

Caltrans. 2010b. *Bridge Memo to Designers (20-1)—Seismic Design Methodology*, California Department of Transportation, Sacramento, CA.

Caltrans. 2010c. *Bridge Memo to Designers (20-4)—Seismic Retrofit Guidelines for Bridges in California*, California Department of Transportation, Sacramento, CA.

Caltrans. 2011. *Bridge Design Aids (14-2)—Steel Column Casing Design and Details*, California Department of Transportation, Sacramento, CA.

Caltrans. 2013a. *Seismic Design Criteria, Version 1.7*, California Department of Transportation, Sacramento, CA.

Caltrans. 2013b. *Seismic Retrofit Program*. http://www.dot.ca.gov/hq/paffairs/about/retrofit.htm (accessed June 20, 2013).

Caltrans. 2014. *Guide Specifications for Seismic Design of Steel Bridges, 2nd Edition*, California Department of Transportation, Sacramento, CA.

Duan, L., M. Reno, and J. Lynch. 2000. "Section Properties for Latticed Members of San Francisco-Oakland Bay Bridge," *Journal of Bridge Engineering*, ASCE 5(2), 156–164.

El-Azazy, S., F. Alameddine, and P. Hipley. 1999. "The seismic retrofit and instrumentation of Ardath Road Overcrossing," *ASCE Fifth Lifeline Conference Proceedings*. American Society of Civil Engineers, New York, NY.

IAI. 1995. *Benicia-Martinez Bridge Seismic Retrofit—Main Truss Spans Final Retrofit Strategy Report*, Imbsen and Association Inc., Sacramento, CA.

McCallen, D., C. Noble, and M. Hoehler. June, 1999. *"The Seismic Response of Concrete Arch Bridges: With Focus on the Bixby Creek Bridge, Carmel, California*," UCRL-ID-134419, Lawrence Livermore National Laboratory, Livermore, CA.

Newmark, N.M. and E. Rosenblueth. 1972. *Fundamentals of Earthquake Engineering*, Prentice-Hall, Englewood Cliffs, NJ.

Priestley, M.N.J., G.M. Calvi, and M.J. Kowalsky. 2007. *Displacement Based Seismic Design of Structures*, Fondazione EUCENTRE, IUSS Press, Pavia, Italy.

Reno, M. and M. Pohll. 1998. "Seismic Retrofit of San Francisco–Oakland Bay Bridge West Span," *Transportation Research Record: Journal of the Transportation Research Board*, 1624, 73–81.

Uzarski, J. 1996. "Seismic evaluation and retrofit of Sacramento River Bridge at Rio Vista," *Proceedings from the Second U. S. Seminar on the Seismic Design, Evaluation, and Retrofit of Steel Bridges, UCB/CEE-Steel-96/09*. Department of Civil and Environmental Engineering, University of California, Berkeley, CA.

Further Reading

Priestley, M.N.J., F. Seible, and G.M. Calvi. 1996. *Seismic Design of Bridge Structures*. Wiley, New York, NY.

Relevant Websites

http://www.dot.ca.gov/hq/esc/earthquake_engineering/.

16

Seismic Design Practice in China

Kehai Wang
Research Institute of Highway

Qian Li
Research Institute of Highway

Han Wei
Research Institute of Highway

Yue Li
Research Institute of Highway

16.1 Introduction

China is located between the Circum-Pacific Seismic Belt and the Eurasian Seismic Belt, extruded by the Pacific Plate, the Indian Plate and the Philippine Sea Plate, with intensive distribution of earthquake fault. Chinese Taipei is located on the Circum-Pacific Seismic Belt; several provinces such as Xizang, Xinjiang, Yunnan, Sichuan, and Qinghai are located on the Eurasian Seismic Belt. Dozens of major earthquakes have occurred in Chinese history. Bridge damage during the 1976 Tangshan Earthquake prompted Chinese engineers to develop highway bridge seismic design criteria. Learned from the past earthquakes and foreign experiences, *Specifications of Earthquake Resistant Design for Highway Engineering (Interim)* (China-MOC, 1977) was published in 1977. *Specifications of Earthquake Resistant Design for Highway Engineering, JTJ 004-89* (China-MOC, 1989) (hereafter referred to as *89 Specifications*) was formally promulgated in 1989, *Guidelines for Seismic Design of Highway Bridges, JTG/T B02-01-2008* (China-MOT, 2008) (hereafter referred as to *08 Guidelines*) was promulgated in 2008, and the new version of *Specifications of Earthquake Resistant Design for Highway Engineering* and *Guidelines of Seismic Performance Evaluation for Highway Bridges* (hereafter referred to as *Evaluation Guidelines*) are currently under development and are expected to be published in 2012.

In this chapter, several historical major earthquakes and damage to bridges are firstly presented, and then the 1976 Tangshan Earthquake and the 2008 Wenchuan Earthquake are presented in detail. The development of bridge seismic design in China is briefly described. The main contents of the *08 Guidelines* are presented. The principles and evaluation methods specified in the draft of *Evaluation Guidelines* are also discussed. Finally, the seismic retrofit of the Nanjing Yangtze River Bridge is presented.

16.2 Earthquake Damage to Bridges

16.2.1 Bridge Damage in Chinese Historical Earthquakes

Since 1949, more than 30 major earthquakes with the magnitude larger than M7.0 had occurred in China (including Taiwan Area), most of which were in densely populated areas (see Table 16.1 [Wang, 2007] and Figure 16.1). Many bridges suffered substantial damage in the destructive earthquakes. The damage of bridges in the Xingtai Earthquake, the Tonghai Earthquake, the Luhuo Earthquake, the Haicheng Earthquake, the Lancang Gengma Earthquake, the Chi-Chi Earthquake, and the Yushu Earthquake are briefly described below. The information of the Tangshan Earthquake and the Wenchuan Earthquake will be introduced in detail in Section 16.2.2 and 16.2.3, respectively.

Two major earthquakes, with magnitudes of M6.8 and M7.2 and the epicentral intensity degrees of 9 and 10 occurred in a row in Xingtai City, Hebei Province, China, in March, 1966. In the earthquakes, the bridge collapse and traffic disruption were caused by cracked, sank, and uplifted ground, and flooding water and erupted sand. Figure 16.2 shows the collapsed Houxinzhuang Bridge over Luyang River because of ground movement. It was the first destructive earthquake that occurred in the densely populated areas in China since 1949. After this earthquake, Chinese government and engineers began the research programs on earthquake prediction, and the guidelines named "Prevention-oriented" was established, marking that the Chinese earthquake prevention and disaster mitigation work entered a

TABLE 16.1 Major Earthquakes with the Magnitude Larger than M7.0 in China Since 1949

No.	Dates	Epicenter	Description
1	1/1/1955	Kangding, Sichuan Province	Magnitude: M7.5
2	4/15/1955	Wuqia, Xinjiang Uygur Autonomous Region	Magnitude: M7.0
3	3/8~3/29/1966	Xingtai, Hebei Province	Earthquake with the magnitude larger than M6.0 occurred 5 times in a row, the biggest magnitude: M7.2
4	1/5/1970	Tonghai, Yunnan Province	Magnitude: M7.7
5	2/3/1973	Luhuo, Sichuan Province	Magnitude: M7.9
6	5/11/1974	Zhaotong, Yunnan Province	Magnitude: M7.1
7	2/4/1975	Haicheng, Liaoning Province	Magnitude: M7.3
8	5/29/1976	Longlin, Yunnan Province	Two major earthquakes occurred, the magnitude of which is M7.3 and M7.4, respectively
9	7/28/1976	Tangshan, Hebei Province	Magnitude: M7.8
10	8/16/1976 8/23/1976	Songpan, Sichuan Province	Magnitude: M7.2
11	11/6/1988	Lancang and Gengma,Yunnan Province	Magnitude: M7.6/M7.2
12	9/21/1999	Chi-Chi, Taiwan	Magnitude: M7.6
13	5/12/2008	Wenchuan, Sichuan Province	Magnitude: M8.0
14	4/14/2010	Yushu, Qinghai Province	Magnitude: M7.1

FIGURE 16.1 Major earthquake in China with the magnitude larger than M7.0 since 1949.

FIGURE 16.2 Houxinzhuang Bridge over Luyang River collapsed in the 1966 Xingtai Earthquake.

new phase. The 1966 Xingtai Earthquake is a milestone of Chinese earthquake disaster reduction work, and also a significant sign that Northern China entered an earthquake active period.

A major earthquake with a magnitude of M7.7 occurred in the Tonghai City, Yunnan Province, on January 5, 1970, the focal depth was 13 km, and the epicentral intensity reached 10°. According to the phenomenon that roads and bridges seriously collapsed along the fault, engineers realized surface dislocation did great harm to highway infrastructures. In this earthquake, the large scale of the landslide along the Puyuan Road made most of the roadbed completely buried and caused traffic disruption

and difficult to repair after the earthquake; on the other side, many stone arch bridges in the high intensity areas performed well. After this earthquake, the first national earthquake conference was held in Beijing on January 17, 1970, on which one important decision was made to establish the China Earthquake Administration. From then on, all Chinese earthquake research and earthquake disaster reduction works have been developing in an organized and systematic manner under the leadership of the China Earthquake Administration.

A major earthquake with a magnitude of M7.9 occurred in the Luhuo County, Sichuan Province, on February 3, 1973. In this earthquake, 1 bridge severely damaged, 9 bridges suffered minor damage, such as cracks and railings fall, and 25 culverts damaged at different levels. The severely damaged bridge was the Hongqi Bridge near the Xiongji Ridge, which was a stone arch bridge with one span of 8 m and grouting masonry pebbles, the abutment, which was made from pebbles with straight joint, abutments were torn off the skewback and slide to the river with a distance of 80 cm, leading to uselessness after the earthquake. Figure 16.3 shows bridges damaged in the 1973 Luhuo earthquake.

A major earthquake with a magnitude of M7.3 occurred in Haicheng City, Liaoning Province, on February 4, 1975, the focal depth was 16.21 km, and the epicentral intensity reached 9° (IOG, 1983). In this earthquake, 154 bridges were damaged or even collapsed, 846 bridges suffered minor damage or no damage. Among the severe damaged bridges, 4 spans of Panshan Bridge built in 1971 (Figure 16.4a), 2 spans of the approach of Tianzhuangtai Liaohe Arch Bridge with 8 continuous span collapsed (Figure 16.4b); Qikou Gunzipao Arch Bridge with 3 continuous spans was severely damaged; Yingkou Xigushu Dongfanghong Bridge with 2 continuous spans sank, and was severely damaged. The three arch bridges mentioned above located in severe liquefaction sites, the severe damage of which were related to the bank slip or sank.

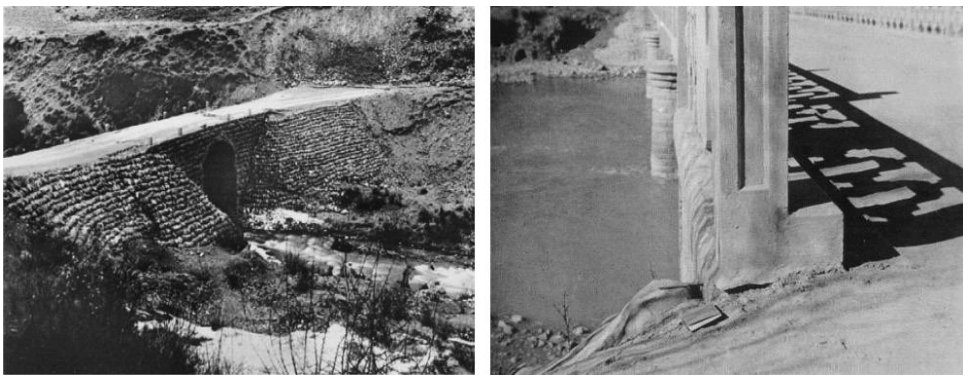

FIGURE 16.3 Bridges damaged in the 1973 Luhuo Earthquake.

FIGURE 16.4 Bridges damaged in the 1975 Haicheng Earthquake.

Two major earthquakes of magnitudes of M7.6 and M7.2 with an interval of 13 minutes and an epicentral distance of 63 km occurred in Lancang and Gengma County, Yunnan Province on November 6, 1988. In the areas with intensity between 7 and 9°, many bridges are subject to different degrees of damage (Wang and Yang, 1993). A stone arch bridge with good foundations, along roads near Shihuiyao, located in the areas with intensity of 9°, suffered severe damage, the vault cracked approximately 20 m, with the width reached 1–3 cm. The Hongxing Bridge along Mengsheng to Tujie highway, a reinforced concrete double-curved arch bridge with poor foundations, heaved 2–3 cm at the central section because of sank and ripped foundations. The Shuangjiang Mengmeng River Bridge located in the areas with intensity of 7°, a reinforced concrete double-curved arch bridge, with poor construction quality and poor foundations, horizontally cracked with 3–5 cm, the vault of the bridge sank by 3–5 cm. The Mengsheng Stone Arch Bridge, with good foundations and good construction quality, suffered slight damage in the earthquake.

The Chi-Chi Earthquake with a magnitude of M7.6 occurred in Taiwan on September 21, 1999, the focal depth was 7.5 km. Bridges were severely damaged by the surface dislocation. Among 987 surveyed bridges along the provincial, county, and regional roads, 2.56% severely damaged and 17.8% slight or moderate damaged. Nine bridges' piers inclined leading to severely crack or decks fell, they are: Caotunwu Bridge (Figure 16.5), Dongshi Shiwei Bridge (Figure 16.6), Mingzhu Bridge, Tongtou Bridge, Changgeng Bridge, Taizhong Yijiang Bridge, Pifeng Bridge, Longmen Bridge, and Jilu Bridge (Figure 16.7). According to the postearthquake survey, most of the damaged bridges located around the causative fault named Chelongpu fault, and the main types of damaged bridges included: simply supported I-beam bridge, continuous box-type bridge, and continuous I-beam bridge (Zheng et al., 1999; Wang, 2007).

A major earthquake with a magnitude of M7.1 occurred in Yushu County, Qinghai Province, on April 14, 2010, the focal depth was 33 km. According to the postearthquake survey, the main damage of bridges included: decks dislocation (Figure 16.8), bearing failure, and shear keys failure (Figure 16.9), and severe pier crack was not found in the disaster areas.

16.2.2 Bridge Damage in Tangshan Earthquake

The Tangshan Earthquake occurred on July 28, 1976, with a magnitude of M7.8, the epicenter located in the southeast of Tangshan City, the focal depth was 11 km. There was an obvious earthquake fault across the city. The intensity of urban areas reached 11°. Buildings in the whole city almost completely collapsed, and the damage was extremely serious. It was a rare urban earthquake disaster in human history. As occurred in the early morning, more than 240,000 people were killed and approximately 160,000 wounded. Earthquake caused such heavy losses, mainly because Tangshan City was designated at 6° preearthquake and as a result no earthquake protection was implemented. That is an extremely painful lesson.

Postearthquake investigation showed that bridges widely collapsed or suffered serious damage in the areas of 9–11°; in the areas of 8°, most were subject to different levels of damage, few severely damaged, and several collapsed; in the areas of 7°, a small number of bridges was severely damaged, the majority suffered moderate damage or minor damage (see Figures 16.10 through 16.14 [Liu, 1986; Fan, 1997]). Results of 130 highway girder bridges surveyed in the areas of 7–11° are shown in Table 16.2, from which, 72 bridges suffered moderate damage and needed to be retrofit; the number was more than half.

In the Tangshan Earthquake, in addition to superstructures unseated, pier inclined, crack or even failure, the most prominent damage was the sliding of abutment and bank. There were 24 bridges subject to this damage. Among the 18 collapsed bridges, 15 collapsed mainly because of different levels of bank slope sliding and foundation failure; the remaining 3 mainly because of piers fracture, bearing failure, beam collision, and large relative displacement of adjacent piers.

照片烏溪 1　北邊遠受損橋梁，靠近橋台連續 7 座墩柱受損致橋面下陷傾斜

(a)

照片烏溪 5 墩柱發生非常嚴重之剪力破壞。

(b)

照片烏溪 3　連續兩跨橋面掉落河床

(c)

FIGURE 16.5 Wuxi Bridge.

FIGURE 16.6 Shiwei Bridge fell down.

FIGURE 16.7 Concrete spalling of towers of a cable bridge.

FIGURE 16.8 One bridge on the provincial road, decks dislocation in longitudinal and transverse direction.

FIGURE 16.9 Batang 1st Bridge, bearing failure, decks dislocation, shear keys failure.

FIGURE 16.10 Shahe Highway Bridge, pier collapsed, decks fell, decks moved toward the river center (9°).

Among 32 arch bridges surveyed after the earthquake, 6 collapsed accounting for 18.75%, 2 severely damaged accounting for 6.25%, 8 moderately damaged accounting for 25%, 6 slightly damaged accounting for 18.75%, and 10 basically intact accounting for 31.25%. Lessons learned from postearthquake survey can be summarized as follows:

1. The most important factor affecting the seismic performance of arch bridges is the foundation conditions. In the Tangshan Earthquake, a lot of single-span stone arch bridges, double-curved arch bridges, and masonry arch bridges with poor ductility located in the areas of 8°, suffered slight damage or even maintained basically intact because of good ground conditions; but single-span arch bridges located on poor foundation and multispan arch bridges with flexible piles/piers suffered severe damage, such as damage of spandrel arch and spandrel structure, crack on arch crown and arch springing, uplift of arch ring or even collapse (Figures 16.15 through 16.17).
2. In the moderate-intensity earthquakes, the main arch ribs can be basically intact, but the spandrel structures are easy to fail.

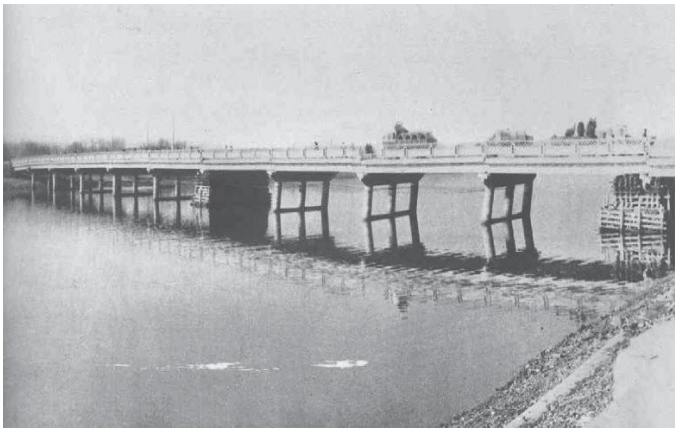

(a)

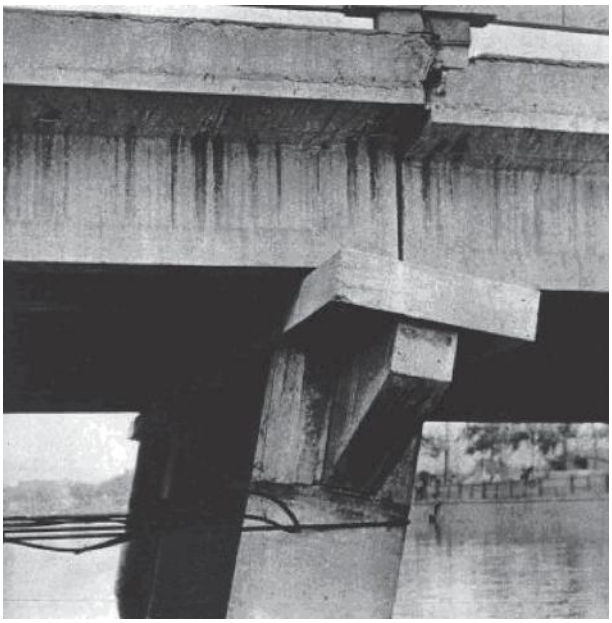

(b)

FIGURE 16.11 Jiyunhe Highway Bridge in Chagu Tianjin, pier inclined, pier top and decks unhitch (10°).

3. Multispan arch bridges suffered more serious damage than single-span arch bridges under the same conditions. When one span of the multispan arch bridge collapses, more spans would also collapse by the chain reaction (He, 1989).
4. The extent of earthquake damage of multispan arch bridges was related to pier height, span number, and span length. The higher of piers, the more spans, the longer of span, the more severe damage of bridges would be suffered.

16.2.3 Bridge Damage in Wenchuan Earthquake

The Wenchuan Earthquake with a magnitude of M8.0 occurred on May 12, 2008, the epicenter located at Yingxiu town, Wenchuan County, the focal depth was 14 km, and was a shallow earthquake, whose effects spread to most regions of China including Sichuan, Gansu, and Shaanxi provinces, and even

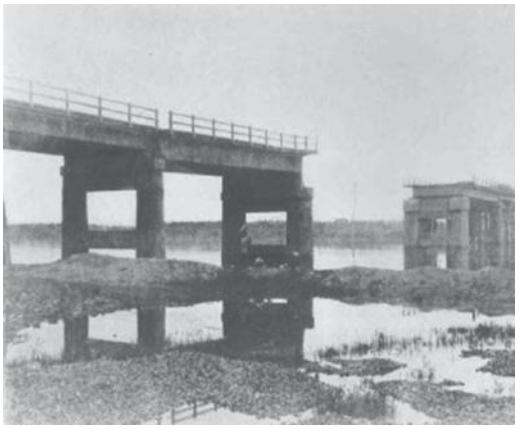

(a)

(b)

FIGURE 16.12 Lutai Bridge in Chagu Tianjin, the middle 54 m tied arch fell, each pier has a clear comparative subsidence, concrete beam extrusion, collision.

overseas. It was the most destructive earthquake that occurred in densely populated areas since 1949; economical losses caused by the earthquake disaster exceeded the 1976 Tangshan Earthquake. The affected areas were mainly in the mountainous region, leading to more destructive secondary disaster such as landslip, rolling stones, and Barrier Lake. Infrastructures along expressways, national and provincial highways, and rural roads suffered damage at various levels, leading to highways connected Wenchuan County, Maoxian County, Beichuan County, and Qingchuan County were completely disrupted, bringing great difficulties to the relief work (China-MOC, DOT of Sichuan, Gansu, Shanxi, 2009).

Among the 2154 surveyed bridges along national and provincial highways, 401 suffered apparent damage, 52 of which failed completely, 70 suffered severely damage, and 279 suffered moderate damage. Most of bridges that suffered serious damage or complete failure are located on highways around Yingxiu and Beichuan. The proportions of different damage level are shown in Table 16.3.

Seventy-three bridges along national highways and expressways from Dujiangyan city to Yingxiu town, mainly suffered damage such as collapse, decks dislocation, shear keys failure, and piers crushing. Shoujiang Bridge (Figure 16.18), Guxigou Bridge, Mengzigou Bridge, Baishuixi Bridge, Yuzixi Bridge, and Xinfangzi Bridge suffered severe damage, such as girder dislocation, bearing sliding, shear keys failure, and decks subsidence; the fifth unit of Baihua Bridge collapsed, the rest were subject to severe damage, resulting in uselessness (Figure 16.19). The first span of Yingxiu Minjiang Bridge was buried by landslip on the left bank. Miaoziping Minjiang Bridge suffered damage such as one span fell, girder

(a)

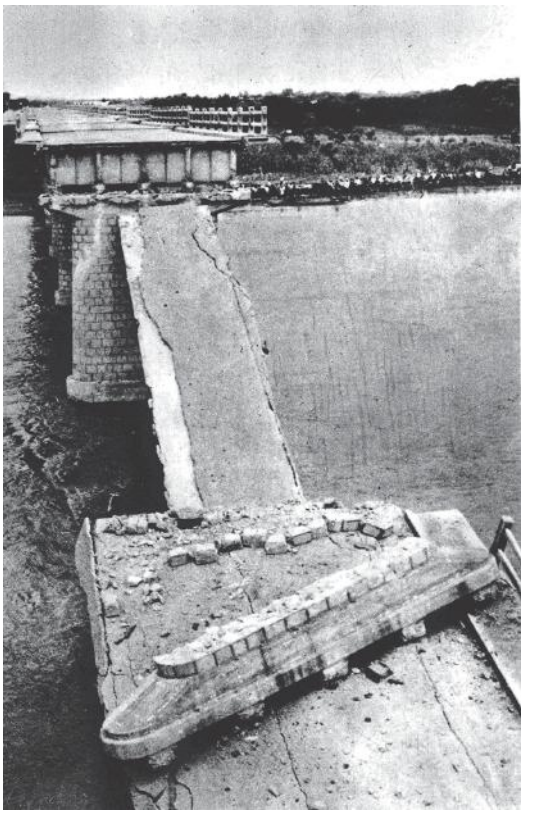

(b)

FIGURE 16.13 Qian'an County Luan River Bridge, two spans fell (8°).

FIGURE 16.14 Luanhe Highway River Bridge in Luan County, spans from 2 to 24 fell (8°).

TABLE 16.2 Damage of Highway Girder Bridges in Areas of 7–11°

Damage Category	Numbers	Ratio (%)
Collapse	18	13.86
Severe damage	20	15.36
Moderate damage	34	26.15
Slight damage	25	19.23
No damage	33	25.38

(a)

(b)

FIGURE 16.15 A single span double-curved bridge collapsed.

dislocation in longitudinal and transverse directions, and shear keys failure. Yingxiu Shunhe Bridge crossing the main fault completely collapsed because of shear failure of piers.

Fifty-five bridges, most simply supported concrete beam bridges located on the main fault along highway from Yingxiu town to Wenchuan County, were severely damaged because of their closer distances to the epicenter and high intensity of 9–11°. K26 + 773 Shunhe Bridge, Yiwanshui Bridge (Figure 16.20), and Chediguan Bridge (Figure 16.21) were buried or smashed by landslide; and other bridges suffered damage such as shear failure of piers and girder dislocation.

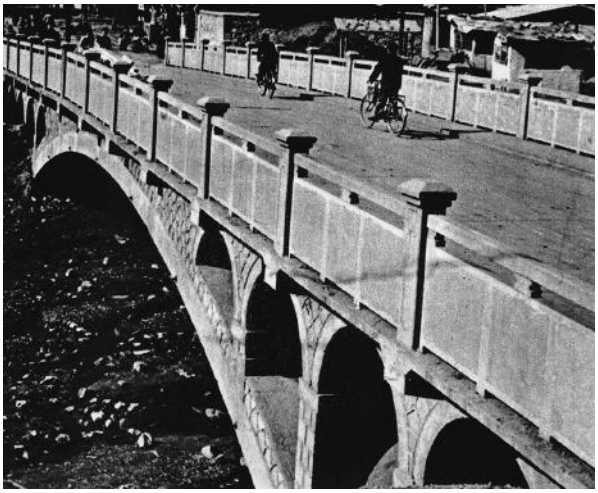

FIGURE 16.16 A single span double-curved bridge with good foundations intact.

FIGURE 16.17 Seven spans stone arch bridge, arch ring cracked, the joint between the spandrel and main pier dislocated.

TABLE 16.3 Proportions of Different Damage Level of Highway Bridges

Damage category	Numbers	Ratio (%)
Complete failure	52	2.41
Severe damage	70	3.25
Moderate damage	279	12.95
Slight damage	1009	46.84
Intact	744	34.54

FIGURE 16.18 Shoujiang Bridge.

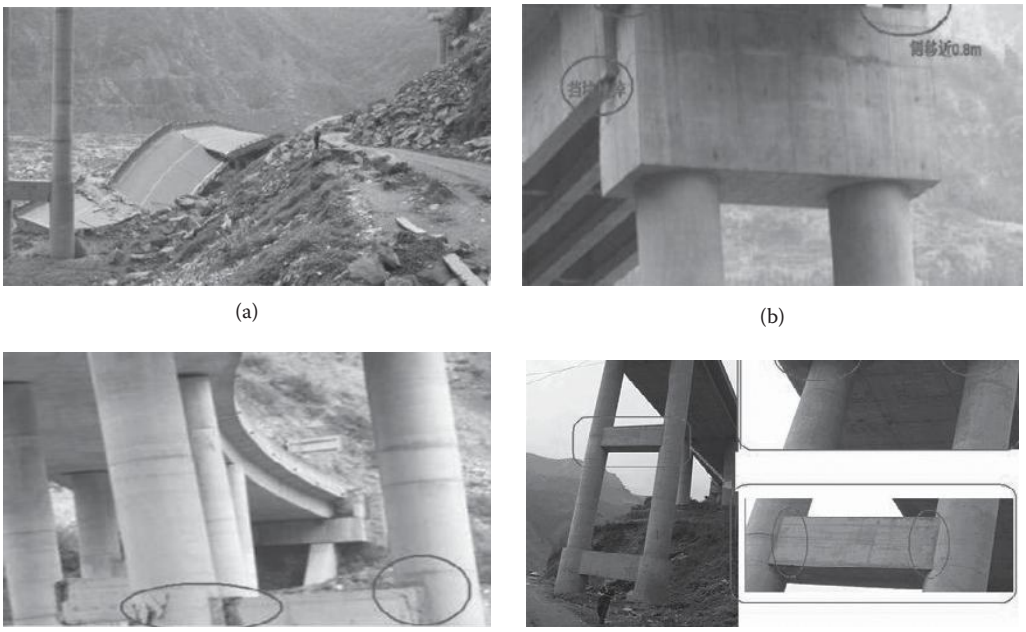

FIGURE 16.19 Baihua Bridge: (a) the fifth unit on the curved part collapsed; (b) shear keys failure, beam dislocated in transverse direction; (c) pier-tie beam joint failure; (d) tie beam crack, bearing failure.

FIGURE 16.20 Yiwanshui Bridge collapsed by stone hitting.

FIGURE 16.21 Chediguan Bridge, 1-3 span collapse by stone hitting.

FIGURE 16.22 Mianyang Airport Terminal Bridge, pier shear failure.

Local bridges in Dujiangyan City, Mianzhu City, Shifang City also suffered various degrees of damage. The piers of Mianzhu Huilan Overpass suffered shear failures, one span of Gaoyuan Bridge in Dujiangyan city collapsed; Mianyang Airport Terminal Bridge suffered damage such as shear failure of piers (Figure 16.22) and girder dislocation.

Bridges mentioned above paragraphs were mainly beam bridges, arch bridges also suffered various degrees of damage in the earthquake. A small amount of bridges completely collapsed, such as Jingtianba Bridge (Figure 16.23), Chenjiaba Bridge, Hongdong Bridge (Figure 16.24), and Xiaoyudong Bridge (Figure 16.25); the majority showed good seismic performance. Many arch bridges, especially small and medium-span stone bridges located on hard sitebehaved well, such as Shuangqiaogou Bridge, Danzha Bridge, the First Yuzixi Bridge (Old Bridge), the Second Yuzixi Bridge (Old Bridge), and so on. The single-span stone arch bridge shown in Figure 16.26, near the demolished Baihua Bridge, maintained basically intact during the earthquake. The first Yuzixi Bridge under construction, which was simply supported skewed T-beam bridge, suffered damage such as girder dislocation, piers inclined, span buried, but the old bridge (Figure 16.27) nearby suffered slight damage such as fence falling and remaining traffic after the earthquake. The double-curved arch bridge, such as Qianjin Bridge (Figure 16.28), Menggu Bridge, Xiaohezi Bridge, Sigou Bridge, and so on also showed good performance.

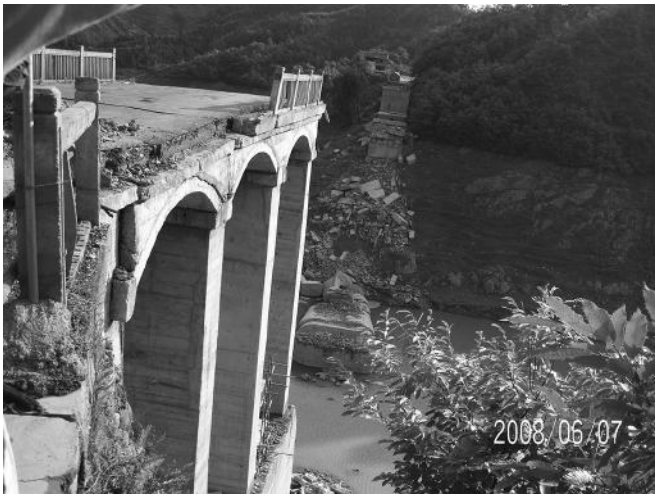

FIGURE 16.23 Jingtianba Bridge collapsed.

FIGURE 16.24 Hongdong Bridge collapsed.

FIGURE 16.25 Xiaoyudong Bridge, damaged severely.

FIGURE 16.26 Stone arch bridge near Baihua Bridge, intact.

FIGURE 16.27 First Yuzixi Bridge (Old bridge), intact.

FIGURE 16.28 Qianjin Bridge built in 1980, intact.

Lessons for seismic design of bridges learned from the Wenchuan Earthquake are summarized as follows:

1. Site selection is very important for road traffic. There were a large number of bridges collapsed by earthquake-induced landslide in the Wenchuan Earthquake.
2. More attention should be paid to the conceptual design and structural measures, providing multiple defense lines for structural safety.
3. More attention should be paid to the relationship between the bridge axis (longitudinal direction) and the seismic wave propagation direction. Bridge design engineers and geotechnical engineers should work together to achieve the alignment of the bridge axis to the direction of the seismic wave propagation as perpendicular as possible, but should not be parallel to each other.
4. Avoid horizontally curved, sloped, and skewed alignments for bridges as much as possible, and assure harmonious arrangement of structure, that is uniform distribution of the structural stiffness and mass. When curved, sloped, and skewed scheme is difficult to avoid, special seismic design considerations should be considered.
5. The importance of bridges are not only related to the importance of the linked roadway, but also the function of bridges in the disaster relief work.
6. Seismic design for bridges is necessary and efficient. A large number of earthquake phenomena show that: most bridges without seismic design consideration collapsed, but bridges with seismic resistance design basically achieved the goal of "no collapse in large earthquakes." Although there are certain issues that need to be improved in Chinese seismic design code, *89 Specifications*, but from a practical point of view, most of the highway bridges designed according to *89 Specifications* pass through the test of earthquakes, achieving the goal of "no collapse in large earthquakes."

16.3 Development of Bridge Seismic Design

16.3.1 Bridge Seismic Design Methods

Based on lessons learned from earthquakes, bridge seismic design method has been continuously improved from the initial single-index control of strength to the double-indices control of strength and displacement, and now to multitarget control of structural performance. To sum up, bridge seismic design methods mainly include: strength-based design, ductility-based design, displacement-based design, and performance-based design.

In the past, the strength-based design method was adopted in Chinese *89 Specifications* and *Specifications of Earthquake Resistant Design of Railway Engineering, GBJ 111-87* (China-MOR, 1987). Compared to the interim version issued in 1977, the main adjustments in the *89 Specifications* are as follows (Yang et al., 1989). (1) The method of improving intensity was abandoned, as an alternative the important factor was adopted to adjust the seismic force, in which the calculation of seismic forces was relatively more reasonable. (2) In the 1975 Haicheng Earthquake and the 1976 Tangshan Earthquake, the phenomenon of soil liquefaction, such as sand blasting and water oozing not only occurred in the sandy soil areas, but also in the sand loam areas. According to this experience, the blow count of standard penetration adjusted by the seismic shear stress was adopted as the liquefaction discriminant index, and then the liquefaction discriminant formula was established. (3) A lot of bridges collapsed by the holistic movement to river center of abutments and backfilling of abutments in the Haicheng Earthquake and the Tangshan Earthquake, the sliding mechanism of the abutment was studied, the abutment seismic soil pressure calculation equation in the liquefaction areas was established, and then adopted by the *89 Specifications*.

One lesson learned from structures performance in actual earthquakes is that as long as the structure maintains its initial strength or its strength does not drop sharply because of the increasing inelastic deformation, the structure will survive and the repair cost will not be too high. With increasing attention on ductility design for bridges in the worldwide, as a part of seismic design of highway engineering, *08 Guidelines* was published in 2008 with adopting the ductility design method. Compared to the *89 Specifications*, the main adjustments are as follows: (1) a two-stage design method was applied with the first phase of the elastic design and the second phase of ductility design to ensure sufficient ductility of structure, and improving the single-index control of strength to double-indices control of strength and displacement; (2) the concept of the comprehensive influence coefficient was abolished; (3) the seismic isolation design provisions were added; (4) the new design acceleration response spectrum were improved in several aspects, such as extending spectrum period, adding site coefficient, damping adjustment coefficient, and vertical acceleration response spectrum and so on. The details will be introduced in Section 16.4.

16.3.2 Development of Seismic Design Specifications of Highway Bridges

Before the Xingtai Earthquake from 1949 to 1966, the earthquake resistant engineering was at the initial stage in China. In the mid 1950s, earthquake engineering began to be involved in the national plan. Around 1956, the first *Seismic Intensity Zoning Map of China* was published (Wang and Dai, 2010). Based on the seismic design code of the former Soviet Union, the first *Building design code in earthquake district* (draft) of China was completed in 1959 (Wang and Dai, 2010), which proposed the calculation method of seismic excitation based on the spectrum theory. The primary object of this draft was mainly for building constructions, although highway engineering was included. In terms of the seismic excitation, the calculation method was nearly the same as the code of the former Soviet Union. After the Xingtai Earthquake, from 1966 to 1976 the earthquake resistant engineering was at the foundation stage in China. At this stage, a series of great earthquakes occurred in the Xingtai City of Hebei Province in 1966, the Tonghai County of Yunnan Province in 1970, the Luhuo County of

Sichuan Province in 1973, and the Haicheng City of Liaoning Province in 1975, which brought a huge loss to life and property. Because of the frequent earthquakes, the National Construction Commission published the *Temporary Provisions for Seismic Design of Buildings in Beijing and Tianjin Regions* (China-NCC, 1968) in 1968 in order to ensure the safety of infrastructures in Beijing and Tianjin. In the early 1970s, more than 100 prototype vibration tests in fields and scaled experimental model tests in laboratories on various types of bridges were performed in China. In 1997, the Ministry of Communications organized and developed the specifications of earthquake resistant design for highway engineering, and published the *Specifications of earthquake resistant design for highway engineering (Interim)* (China-MOC, 1977).

After the Tangshan Earthquake in 1976, the earthquake resistant engineering was at the development stage in China. Extensive earthquake damage data collected from the Tangshan Earthquake and the comprehensive research of seismic theory greatly promoted the revisions and enhancements of seismic design standards for engineering structures. The Tangshan Earthquake was an important milestone in the development of bridge seismic research in China. After the Tangshan Earthquake, research institutions investigated a great amount of bridges in fields, providing fundamental data for analyzing seismic performance of different bridge structures and studying the reasonable seismic design methods. Based on the experience of seismic design after 1975, and the seismic damage investigation for the Tangshan Earthquake in 1976, the Ministry of Communication developed the *Specifications of earthquake resistant design for highway engineering (Interim)*, and issued *89 Specifications* in 1989. Since then, the applicability of *89 Specifications* was expanded to whole highway engineering including bridges, tunnels, subgrades, and retaining walls.

After 1990s, the earthquake resistant engineering stepped up to a new development stage in China. The *Law of the people's republic of China on precautions against earthquake and relief of disaster* (China-NPC, 1998) was formally promulgated and came into force on March 1, 1998, putting Chinese disaster prevention and mitigation work on a legal track. At this stage, because of the construction requirement of highway and the development of anti-seismic technology in domestic and overseas, the Ministry of Transport organized the further modification of the *89 Specifications*. The modified specifications are composed by the compulsory *Specification of earthquake resistant for highway engineering* (to be published) and the recommendatory *08 Guidelines*. And the former is being composed and the latter has been published in 2008.

16.4 Guidelines for Seismic Design of Highway Bridges (2008)

16.4.1 Fundamental Principles of Seismic Design

The *89 Specifications* was formally promulgated and came into force on January 1, 1990. By 2008, in the past 20 years, a series of major earthquakes occurred including the 1989 Loma Prieta Earthquake and the 1994 Northridge Earthquake in the United States, the 1995 Kobe Earthquake (Hyogoken-Nanbu Earthquake), the 1999 Turkey Earthquake, and so on. In these earthquakes, the serious damage of bridges made engineers improve the seismic design methods. In 2008, the Ministry of Transport published the *08 Guidelines*. The *08 Guidelines* has major breakthroughs in many ways and bring in line with international seismic design standards and practice for highway bridges. There are essential differences between the *08 Guidelines* and the previous two specifications in design principles and methods. Compared with the *89 Specifications*, the new contents of *08 Guidelines* mainly include in seismic fortification criterion, design method, seismic excitation and seismic isolation, reduction design, and so on.

It has a long history that the three seismic fortification goals named "no damage (operational) in minor earthquakes, repairable in moderate earthquakes, no collapse in large earthquakes" are taken as seismic design principle for structures. But the seismic design of highway bridges in previous specifications is only based on one of the three. In the *08 Guidelines*, the seismic design principle with two levels

TABLE 16.4 Definitions of Seismic Fortification Categories of Bridges

Seismic Fortification Category	Definitions
A	Grand bridges with single span over 150 m
B	Bridges with single span within 150 m on express way and class I highway Grand bridges and great bridges with single span within 150 m on class II highway
C	Medium and small bridges on class II highway, grand bridges and great bridges with single span within 150 m on class III and IV highway
D	Medium bridges and small bridges on class III and IV highway

TABLE 16.5 Seismic Fortification Goals of Bridges

	Seismic Fortification Goal	
Seismic Design Category	Seismic Excitation E1	Seismic Excitation E2
A	In earthquakes with approximately 475 years return period, remain usable without damage or repair	In earthquakes with approximately 2000 years return period, remain usable without or with simple repair under partial slightly damage
B	In earthquakes with approximately 75–100 years return period, remain usable without damage or repair	In earthquakes with approximately 1000–2000 years return period, should not collapse or suffer serious structural damage, remain usable for emergent traffic after being temporary reinforced
C	In earthquakes with approximately 50 years return period, remain usable without damage or repair	In earthquakes with approximately 1000 years return period, should not collapse or suffer serious structural damage, remain usable for emergent traffic after being temporary reinforced
D	In earthquakes with approximately 25 years return period, remain usable without damage or repair	—

and two stages of design was introduced and the seismic design method only based on strength is modified to control by double indices of strength and deformation. In the light of importance, maintainability, and role in earthquake relief work, and so on, highway bridges are divided into four categories with A, B, C, and D in the *08 Guidelines* (see Table 16.4). The value of seismic excitation is modified by the importance coefficient C_i. Corresponding to each level of seismic excitation, the seismic fortification goal of different categories of bridges is specified as listed in Table 16.5. From Table 16.5, it can be seen that in minor earthquake B and C categories should be in the elastic state and be designed based on strength, in large earthquake B and C categories should be "no collapse," which would be assured by checking both of the strength and deformation. If achieving in minor and large earthquakes, the objective of seismic protection in moderate earthquake implies satisfaction.

In the *89 Specifications* and the former interim version, the comprehensive influence coefficient C_z was introduced to make up the difference between the elastic calculation results and the actual inelastic seismic response. Because the principle of fortification according to earthquake levels was adopted in the *08 Guidelines*, the comprehensive influence coefficient in the *89 Specifications* was abolished. Only the seismic design of bridge structures becomes more distinct and definite.

16.4.2 Seismic Excitation

In the *08 Guidelines*, the acceleration response spectrum mainly reflects prolonging the period of response spectrum and introducing site coefficient, damping adjustment coefficient, vertical acceleration response spectrum, and so on.

The site soils are classified into 4 categories by average shear wave velocity of soils and thickness of covering soil, and the maximum of acceleration response spectrum was adjusted by the site condition. The site coefficient C_s in the *08 Guidelines* is shown in Table 16.6.

Adjusted by the coefficients of site, damping and structural importance, the maximum value of horizontal acceleration response spectrum S_{max} shall be determined by the Equation 16.1:

$$S_{max} = 2.25\, C_i\, C_s\, C_d\, A \tag{16.1}$$

where C_s is structure importance factor; C_s site coefficient; C_d adjustment damping coefficient of seismic acceleration response spectrum; A horizontal seismic acceleration peak value.

The horizontal acceleration response spectrum with 0.05 damping ratio is determined by the Equation 16.2 (Figure 16.29):

$$S = \begin{cases} S_{max}(5.5T + 0.45), & T < 0.1s \\ S_{max}, & 0.1s \le T \le T_g \\ S_{max}(T_g / T), & T > T_g \end{cases} \tag{16.2}$$

where T_g is characteristic period of sites(s); T natural vibration period of structure(s).

In most seismic design codes, vertical seismic excitation is usually determined by horizontal response spectrum multiplied by a factor of 1/2–2/3. This is based on a fact that the spectrum figures in the two directions are similar. After statistically analyzing 448 horizontal seismic waves and 230 vertical seismic waves, researchers got the total mean characteristic of the vertical and horizontal response spectra ratio, and found the ratio had some relevance with site conditions, and the relation between the ratio

TABLE 16.6 Site Coefficient C_s

Fortification Intensity	6°	7°		8°		9°
Category of Site Soil	0.05 g	0.1 g	0.15 g	0.2 g	0.3 g	0.4 g
I	1.2	1.0	0.9	0.9	0.9	0.9
II	1.0	1.0	1.0	1.0	1.0	1.0
III	1.1	1.3	1.2	1.2	1.0	1.0
IV	1.2	1.4	1.3	1.3	1.0	0.9

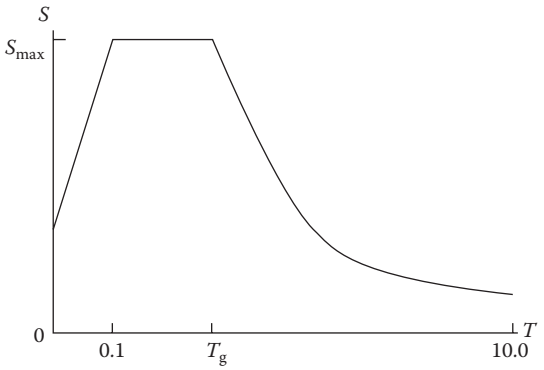

FIGURE 16.29 Horizontal acceleration response spectrum.

and distance was not obvious. The *08 Guidelines* adopted the research findings mentioned above and introduced the vertical and horizontal response spectra ratio *R*, which is determined by the Equations 16.3 and 16.4.

$$\text{Rock site } R = 0.65 \tag{16.3}$$

$$\text{Soil site}: R = \begin{cases} 1.0 & T < 0.1s \\ 1.0 - 2.5(T - 0.1) & 0.1s \le T < 0.3s \\ 0.5 & T \ge 0.3s \end{cases} \tag{16.4}$$

where T is natural vibration period of structure (s).

In addition, when considering seismic excitation in three orthogonal directions using response spectrum method, the *08 Guidelines* specifies that the maximum response E_X in X direction, E_Y in Y direction and E_Z in Z direction should be calculated separately and the total maximum seismic response could be determined by the Equations 16.5:

$$E = \sqrt{E_X^2 + E_Y^2 + E_Z^2} \tag{16.5}$$

16.4.3 Dynamic Response Analysis Method

In the *08 Guidelines*, the dynamic response analysis methods include the response spectrum method, power spectrum method, and time history method. Applicable analysis methods are recommended (Table 16.7) to catch dynamic response characteristics for different bridges based on their complexities and irregularities. The regular and irregular bridges are mainly classified by span number, geometry, mass distribution, stiffness distribution, geological conditions in site, and so on.

For regular bridges, the seismic response is mainly based on the first mode and analyzed by the simplified formula recommended in the *08 Guidelines*. Thus, in the two levels of seismic excitation, all the dynamic response of regular bridges can be calculated by the simplified single-mode response spectrum method. At the high seismic excitation level (E2), for irregular bridges only the nonlinear time history method can be used, and for regular bridges the modified factor method can be used to consider the elastic-plastic effect based on the elastic response.

16.4.4 Ductility-Based Design Approach for Concrete Bridges

The ductility-based seismic design theory has been developed for approximately 50 years. The ductility-based seismic design approach has been introduced in the foreign seismic design codes. In the *08 Guidelines*, the terms of ductility-based seismic design, capacity protection principle, and ductility-based construction detail design are introduced to increase the inelastic deformation capacity on the condition of no significant change of the initial strength. Thus collapse of structures is avoided in large earthquakes.

TABLE 16.7 Recommended Seismic Analysis Method

Seismic Performance Level	Category B		Category C		Category D	
	Regular	Irregular	Regular	Irregular	Regular	Irregular
E1	SM/MM	MM/TH	SM/MM	MM/TH	SM/MM	MM
E2	SM/MM	TH	SM/MM	TH	—	—

Note: TH is linear and nonlinear time history method; SM single-mode response spectrum or power spectrum method; MM multimodes response spectrum or power spectrum method.

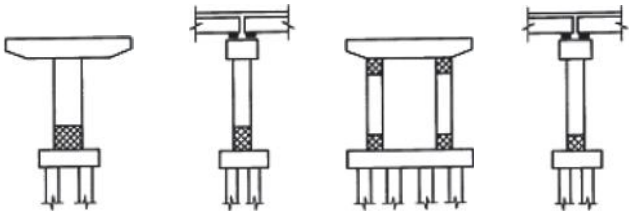

FIGURE 16.30 Distributions of plastic hinges on girder bridge piers (shadow parts represent plastic hinge regions).

For concrete girder bridges, plastic hinges are usually expected to locate on piers or columns. Piers of reinforced concrete bridges shall be designed as ductile components that could dissipate seismic energy by inelastic deformation. The distributions of the plastic hinges on reinforced concrete girder bridges are shown in Figure 16.30. In the longitudinal direction, the plastic hinges are located at the bottom of piers on continuous girder bridges, simply supported girder bridges, and at two ends of piers on continuous rigid frame bridges. In the transverse direction, the plastic hinges are located at the bottom of single-column piers and at two ends of double- and multicolumn piers.

Foundation, bent cap, superstructure, and joint should be designed as capacity protected members, whose moment, shear force, and axial force should correspond to the ultimate moment (considering the over-strength coefficient) of piers, namely based on the capacity protected principle.

1. Check for shear force demands (design value) and capacities of ductile piers in the longitudinal and transverse directions
   For ductile piers, the shear force demands in the longitudinal and transverse directions are determined by the Equations 16.6 through 16.9.
   A. Shear force demand in the longitudinal direction V_{c0}
      When potential plastic hinge at the bottom of ductile piers:

$$V_{c0} = \phi^0 \frac{M_{zc}^x}{H_n} \tag{16.6}$$

      When potential plastic hinges at the top and bottom of ductile piers:

$$V_{c0} = \phi^0 \frac{M_{zc}^x + M_{zc}^s}{H_n} \tag{16.7}$$

   B. Shear force demand in the transverse direction V_{c0}
      When potential plastic hinge at the bottom of ductile piers:

$$V_{c0} = \phi^0 \frac{M_{hc}^x}{H_n} \tag{16.8}$$

      Potential plastic hinges at the top and bottom of ductile piers:

$$V_{c0} = \phi^0 \frac{M_{hc}^x + M_{hc}^s}{H_n} \tag{16.9}$$

      Where M_{zc}^s, M_{zc}^x is moment on the top and bottom of columns corresponding to the ultimate flexural capacity in longitudinal direction based on the designed reinforcement, the standard material strengths, and the most unfavorable axial force (kN·m).

M_{hc}^{s}, M_{hc}^{x} is moment on the top and bottom of columns corresponding to the ultimate bending capacity in transverse direction based on the designed reinforcement, the standard material strengths, and the most unfavorable axial force (kN·m).
H_n is clear height of pier, or vertical height from centroid of the superstructure to the bottom of pier for the single column pier in transverse direction (m).
ϕ^0 is over-strength coefficient of the ultimate bending capacity, $\phi^0 = 1.2$

2. Moment demand of the bent cap of ductile pier M_{p0} (Equations 16.10):

$$M_{p0} = \phi^0 M_{hc}^{s} + M_G \tag{16.10}$$

Where M_G is moment induced by gravity (kN·m).

3. Shear force demand of the bent cap of ductile pier V_{c0} (Equation 16.11):

$$V_{c0} = \phi^0 \frac{M_{pc}^{R} + M_{pc}^{L}}{L_0} \tag{16.11}$$

where M_{pc}^{L}, M_{pc}^{R} is bending capacity of the right and left bent cap utilizing designed reinforcement and standard material properties, respectively (kN·m); L_0 clear span of bent cap (m).

4. Force demands in foundations: In the longitudinal and transverse directions, the moment, shear and axial force demands in the foundation should be calculated based on the ultimate moment (magnified by the over-strength coefficient ϕ^0), shear force and the most unfavorable axial force at the expected plastic hinge regions (see Figure 16.31, Equation 16.12).

$$M_{c0} = \phi^0 M_{hc}^{x}, \; M_{c0}^{l} = \phi^0 M_{zc}^{x} \tag{16.12}$$

where M_{zc}^{x}, M_{hc}^{x} is moment on the bottom of columns corresponding to the ultimate bending capacity in longitudinal and transverse directions, respectively (kN·m).

In Figure 16.31, V_{c0}, V_{c0}^{l} are the design shear force value of the plastic hinge on the bottom of piers in the longitudinal and transverse direction, respectively; P_{min}, P_{max} are the maximum and minimum axial force at the plastic hinge region of columns in the transverse direction, respectively.

At the high seismic excitation level (E2), the shear strength of the plastic hinge region in the longitudinal and transverse directions is given by Equation 16.13:

$$V_{c0} \le \phi\left(0.0023\sqrt{f_c' A_e} + V_s\right) \tag{16.13}$$

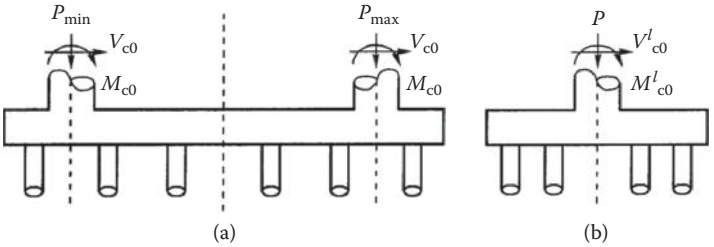

FIGURE 16.31 Schematic plan of design loads in foundations.

where V_{c0} is design shear force (kN); f_c' standard compressive strength of concrete (MPa); V_s shear capacity of stirrups (kN).

$$V_s = 0.1\frac{A_k b}{S_k} f_y \le 0.067\sqrt{f_c' A_e}$$

where A_e is area of confined concrete core (cm^2); A_k total area of stirrups on one cross-section (cm^2); S_k stirrups space (cm); f_{yh} design value of tensile strength of stirrups (MPa); b width of piers in the calculation direction (cm); and ϕ reduction factor of shear strength, $\phi = 0.85$.

Equation 16.13 is introduced from the *Caltrans Seismic Design Criteria Version 1.1* (Caltrans, 2000) by simplifying some factors, which is relatively conservative.

In addition to checking strength, the deformation capacity of piers should be checked by the equation 16.14. Namely, at the high seismic excitation level (E2), the rotation capacity of the plastic hinge region in longitudinal and transverse direction should satisfy (Equation 16.14)

$$\theta_p \le \theta_u \tag{16.14}$$

where θ_p is plastic rotation of the potential plastic hinge under seismic excitation E2; θ_u ultimate facultative plastic rotation of the potential plastic hinge, calculate by equivalent yield curvature of section, curvature at ultimate damage state, equivalent length of plastic hinge, and ductility safety coefficient.

For regular bridges, the displacement on the top of piers may be checked.

To provide effective constraint for concrete at plastic hinge region, improve ductility and shear resistant strength, and prevent buckling of longitudinal reinforcement, the distribution and minimum ratio of transverse reinforcement at the plastic hinge region are specified in the *08 Guidelines*. In which, the minimum ratio of transverse reinforcement $\rho_{s,min}$ is given by Equation 16.15a and b.

For circular section

$$\rho_{s,min} = \left[0.14\eta_k + 5.84(\eta_k - 0.1)(\rho_t - 0.01) + 0.028\right]\frac{f_c'}{f_{yh}} \ge 0.004 \tag{16.15a}$$

For rectangular section

$$\rho_{s,min} = \left[0.1\eta_k + 4.17(\eta_k - 0.1)(\rho_t - 0.01) + 0.02\right]\frac{f_c'}{f_{yh}} \ge 0.004 \tag{16.15b}$$

where η_k is axial compression ratio; ρ_t reinforce ratio in longitudinal direction; f_c' standard compressive strength of concrete (MPa); f_{yh} design value of tensile strength of stirrups (MPa).

16.4.5 Seismic Isolation and Energy Dissipation Design

Considering the development of bridge construction and application of the seismic isolation technology, some principles and provisions for isolation bridges are introduced in the *08 Guidelines*. The bridge meeting one of the following conditions can utilize the seismic isolation technology.

1. Piers are very rigid and natural vibration period is relatively short.
2. Pier heights are distinctly different.
3. The characteristics of the site expected ground motions is clear and the energy focuses in high-frequency band.

When one of the following conditions exists, it should not utilize the seismic isolation technology.

1. The site may be failed in earthquake.
2. The stiffness of substructures is relatively small and the natural vibration period is relatively long.
3. The site has soft soil.
4. The negative reaction may appear in the bearing.

Same as bridges without seismic isolation device, bridges utilized with seismic isolation device should be designed and checked in the low and high seismic excitation levels. And piers, abutment, and foundation should still be designed and checked based on the capacity protection principle. Meanwhile, in addition to test the product quality and normal service performance, it should check the shear strain and stability of seismic isolation device under seismic excitation.

16.5 Guidelines of Seismic Performance Evaluation for Highway Bridges

Highway bridges have been designed and built based on different seismic design specifications in China. Hundreds of thousands of highway bridges have been built in the past 20 years. To maintain bridge safety in the national highway transportation system, *Evaluation Guidelines* is under development to guide the seismic performance evaluation of highway bridges. *Evaluation Guidelines* includes five parts namely Chapter I General, Chapter II Terms and Symbols, Chapter III Basic Demand and Procedures for Seismic Performance Evaluation of Bridges, Chapter IV First Level of Seismic Performance Evaluation of Bridges, and Chapter V Second Level of Seismic Performance Evaluation of Bridges. The *Evaluation Guidelines* is under final review and shall be published in 2012.

16.5.1 Seismic Fortification Criterion of Existing Bridges

Unlike the *08 Guidelines* and the *89 Specifications*, the *Evaluation Guidelines* divides the existing bridges into two categories: critical and general bridges whose seismic performance demands are different, even designed at the same time (see Tables 16.8 and 16.9). Moreover in the *Evaluation Guidelines*, four seismic excitation levels (P1–P4) are introduced, providing more accurate description of the critical and general bridges, and theirs corresponding seismic performance objectives.

TABLE 16.8 Seismic Performance Levels of Critical Bridges

	General Condition		
Seismic Level	SL1	SL2	SL3
Seismic excitation level P1 (100-year return period event)	PL3	PL3	PL3
Seismic excitation level P2 (500-year return period event)	PL1	PL2	PL2
Seismic excitation level P3 (1000-year return period event)	PL0	PL1	—
Seismic excitation level P4 (2000-year return period event)	PL0	PL0	PL1

TABLE 16.9 Seismic Performance Levels of General Bridges

	General Condition		
Seismic Level	SL1	SL2	SL3
Seismic excitation level P1 (100-year return period event)	PL2	PL3	PL3
Seismic excitation level P2 (500-year return period event)	PL0	PL1	PL1

It permits that damage occurs on bridges in earthquakes, and for the existing bridges the permitted damage degrees gets along with succeeding service life and importance of the bridges. The succeeding service life of bridges is indirectly divided and based on the corresponding seismic design code.

1. SL1: bridges constructed before 1990, designed by the 1977 interim specification or without seismic design, moreover the succeeding service life exceeds 15 years.
2. SL2: bridges designed by the *89 Specifications* from 1990 to 2008.
3. SL3: bridges required to evaluate the seismic performance for special reasons and designed by the *08 Guidelines*.

The seismic performance of existing bridges is divided into four levels referred to the *08 Guidelines* and *Seismic Retrofitting Manual for Highway Structures: Part 1-Bridges (2006)* (Buckle et al., 2006) as follows:

1. Seismic performance level PL0: No demand.
2. Seismic performance level PL1: in minor earthquake bridges suffer serious damage, yet not collapse, the safety of lives can be guaranteed; bridges probably require removal and replacement after large earthquakes.
3. Seismic performance level PL2: bridges suffer moderate damage, usable by emergency vehicles after detailed check, clear and temporary reinforcement, any damage is repairable in earthquake.
4. Seismic performance level PL3: No damage or only little damage occurs, and is usable without requirement after detailed check, no effect on the passing of all vehicles, damage in earthquake can be repaired without interrupting traffic.

16.5.2 Seismic Performance Evaluation Approach of Highway Bridges

Taking into account vulnerability, seismic risk, and geologic hazard, the seismic performance evaluation of existing bridges is divided into two levels (seen in Figure 16.32). The first level is mainly on evaluating macro factors, structural measures, and details. The second level is mainly on comprehensively evaluation by seismic analysis and checking, combined with the effect of structural details.

Taking into account geological hazard risk of sites, the first level includes four factors, preventing girder falling performance, horizontal supporting capacity of bearings, construction details of piers, and geological hazard risk of sites.

- Evaluation of preventing girder falling performance. The possibility of girder falling is judged by comprehensively evaluating the factors of supporting width at the end of girder, integrity of superstructures, and displacement limiting measures, and so on.
- Evaluation of bearing horizontal supporting capacity. The procedure of using additional dead loads for initial evaluation specified in *Seismic Retrofitting Manual for Highway Structures: Part 1-Bridges (2006)* (Buckle et al., 2006) is recommended.
- Evaluation of construction details of piers. The seismic capacity provided by strength and ductile construction details is evaluated from the minimum ratio of transverse reinforcement, ratio of longitudinal reinforcement, joint, and anchorage of reinforcement.
- Evaluation of geological hazard risk of sites. Liquefaction, settlement and hazard of ground fault are evaluated initially based on site datum.

For bridges located in regions with higher risk of geological hazard, the effect of sites should be considered in the second evaluation level. Additionally, for a batch of bridges, all bridges should be evaluated at the first level. Based on the evaluation results, taken into account the importance, seismic risk and expected service lifetime, the bridges evaluated at the second level are selected.

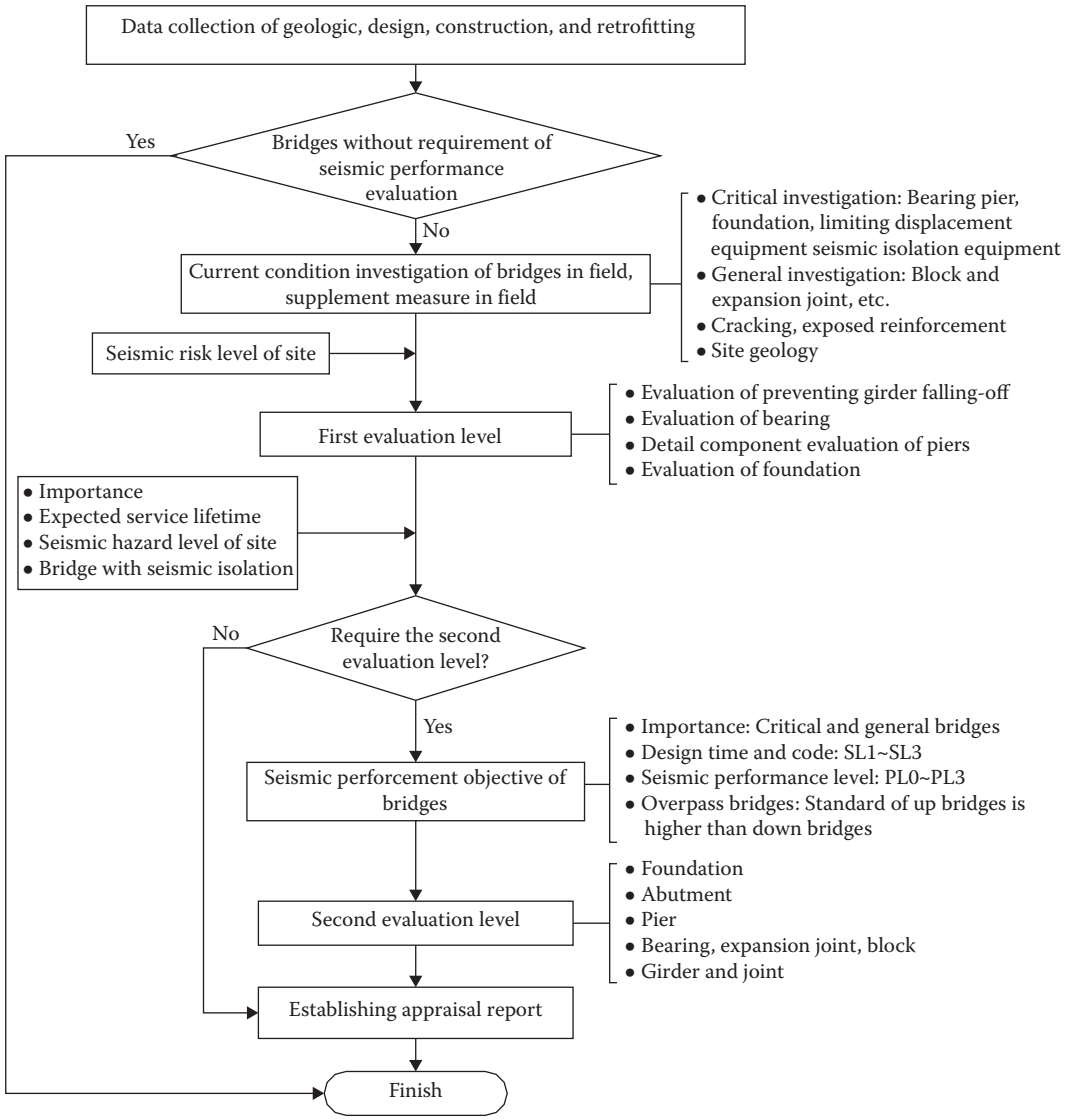

FIGURE 16.32 Basic procedure of seismic performance evaluation.

In the second evaluation level, the detail seismic performance of critical members within the seismic load-path in a bridge should be evaluated, which mainly include the following components: abutments, piers, girders and joints, bearings, expansion joints and shear keys, foundations, and seismic isolation devices. In the second evaluation level, the demand/capacity ratio approach is introduced to evaluate the seismic performance of members.

In the second evaluation level, the acceleration response spectrum of the *08 Guidelines* is referenced, and the difference between the two guidelines lies in the importance coefficient C_i of the *08 Guidelines* is replaced by the seismic excitation adjustment coefficient R_i. The seismic excitation adjustment coefficient R_i is defined as the acceleration peak ratio between ground motion with different return period and the design ground motion (see Table 16.10). The objective of R_i is to clarify the characteristic of seismic excitation level and prevent from repeatedly multiplying the importance coefficient in the design

process. In addition, the near field effect on the dynamic response of structures is considered in the *Evaluation Guidelines*.

In the *08 Guidelines*, the analysis method is determined by bridge regularity and seismic excitation levels. Although in the *Evaluation Guidelines*, the analysis method is determined by bridge regularity and demand of seismic performance, and when demand aimed at seismic performance level PL1 and PL2, the linear response spectrum method is used in the first evaluation level for all bridges. Only when the above analysis results reflect the damage of members, the nonlinear dynamic time-history method is applicable. The details are as follows:

1. Evaluation of regular bridges corresponding to seismic performance PL3: linear single-degree and multidegree freedom response spectrum method
2. Evaluation of irregular bridges corresponding to seismic performance PL3: linear multidegree freedom response spectrum method, linear dynamic time-history method
3. Evaluation of regular bridges corresponding to seismic performance PL1 and PL2: linear single-degree and multidegree freedom response spectrum method, nonlinear dynamic time-history method
4. Evaluation of irregular bridges corresponding to seismic performance PL1 and PL2: linear multidegree freedom response spectrum method, nonlinear dynamic time-history method

16.6 Seismic Retrofit Practice for Highway Bridges

In China, one of the most classical retrofitting practice of highway bridges is the retrofitting of the Nanjing Yangtze Bridge. The Nanjing Yangtze Bridge is a grand bridge for highway and railway, which was constructed in 1960s, and opened to traffic in 1968 (Figure 16.33). The bridge is located at the middle and lower reaches of the Yangtze River, which falls in a moderate seismic active region. At the initial design stage, in order to resist earthquakes with 6°, only lateral force resisting capacity of piers supporting fixed bearing of continuous girder was checked, but resistance demand for higher intensity earthquakes was not considered. After the 1966 Xingtai Earthquake, the 1975 Haicheng Earthquake and

TABLE 16.10 R_i Corresponding to Seismic Excitation Level

Seismic Excitation Level	P1 (100-year return period)	P2 (500-year return period)	P3 (1000-year return period)	P4 (2000-year return period)
E_X	0.5	1.0	1.3	1.7

FIGURE 16.33 Nanjing Yangtze Bridge.

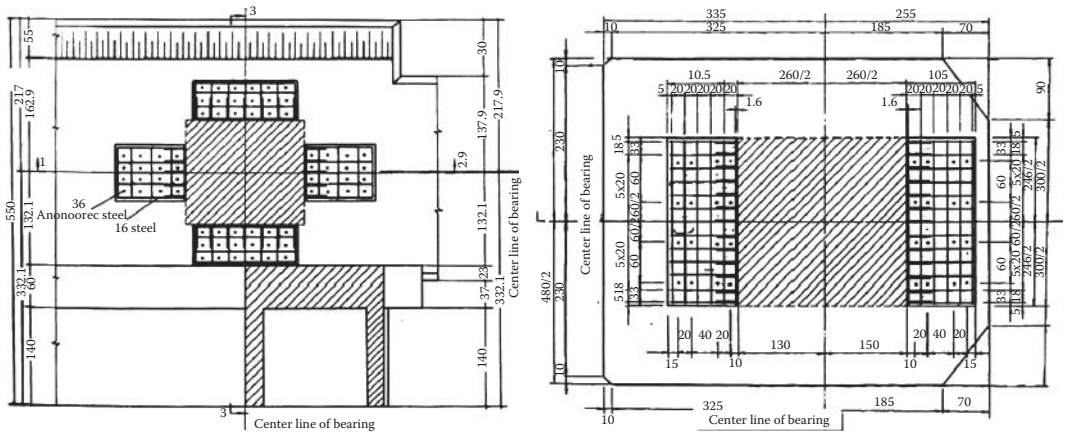

FIGURE 16.34 Bearing, retrofitting of shear keys: (a) fixing bearing; (b) movable bearing.

the 1976 Tangshan Earthquake, more attention was paid to the seismic safety of the Nanjing Yangtze Bridge. The retrofit was the first sample in China. From 1977 to 1994, the bearing, preventing girder falling measures and liquefiable soil were reinforced.

The following parts cannot satisfy the requirement of resistance under earthquakes with 7°: connection bolts between girders and the top of bearings, anchor bolts between the bottom of bearings and piers, bearing welding joint of prestressing concrete highway approach bridges with 32 m spans, no preventing girder falling measures in simply supported railway approach bridges, weak transverse stiffness in the main arch and subsidence risk in the spandrel arch of highway double-arch bridge, the sliding of high backfill soil, and so on.

1. Under the earthquake with 7°, shear stress of anchor bolts in the steel girder bearings and connection bolts at the top of steel girder bearing has exceeded the permission value. In the condition of keeping the format and number, the old of bolts was replaced.
2. Considering bearing types and corresponding stress, shear keys were retrofitted in four ways. For fixing bearing, reinforced concrete block and anchor bolts were installed on both sides in the longitudinal and transverse direction, with bottom and lateral steel plates (Figure 16.34a). For movable bearing, reinforced concrete block and anchor bolts were installed only on both sides in the transverse direction (Figure 16.34b).

   To resist larger horizontal seismic excitation, the reinforced concrete shear keys besides fixing bearings at the middle of the continuous girder were jointed together by U-shape steel shell in longitudinal and transverse directions to reduce the plane dimension and number of shear keys. The inner side steel plate of the shell was weld with the bottom plate of bearings to assure the shear keys bear force together in longitudinal and transverse directions. Bolts were put on both sides of shear keys in longitudinal and transverse direction. The shear keys were packed with reinforced concrete. Epoxy resin mortar was filled in bolt holes.

   For the other bearings, bolts were put on both sides of shear keys in longitudinal and transverse directions (fixing bearing), or only in transverse direction (movable bearing).
3. The scheme of putting connection at the end of girder in the longitude direction and shear keys in the transverse direction was introduced to prevent the girder falling.

   Shear keys in the transverse direction were put on both sides of inner girders. Formed steel supporting beams crossed through girder bottom, inside transverse shear keys made from angle irons were connected with the two supporting beams; outside transverse shear keys made from angle irons were connected with the flange of the supporting beams.

Longitudinal link was put on the root of diaphragm at girder ends, two section steel crossed through the bottom of diaphragm, the flanges extended from section steel ends were connected with four vertical angle irons.

Longitudinal link and transverse shear keys were separated from the girder by hard wood and the space between the wood and the girder should not be less than 10 mm.

4. For movable bearings in the prestressing reinforced concrete highway approach bridges, a steel plate was weld on each side of dental plates and the length of weld was prolonged (Figure 16.35a). For fixing the bearing with lower height, unequal-leg steel angle were weld on dental plates; three stiffening plates were weld on the steel angles (Figure 16.35b).
5. To improve the transverse stiffness and its integrity of main arch in the double-curved arch highway bridges, reinforced concrete draft rod were installed between arches (Figure 16.36). To prevent the spandrel arch falling, transverse shear keys were put on two sides of the cap beam.
6. In the retrofitting process of the Nanjing Yangtze Bridge, because the local liquefaction around the vibrating-impacting bore might be harmful to the existing piers by using vibroflotation construction method, the approach of compaction sand pile was applied in the light of many buildings in the region around the approaching bridge and small construction area.

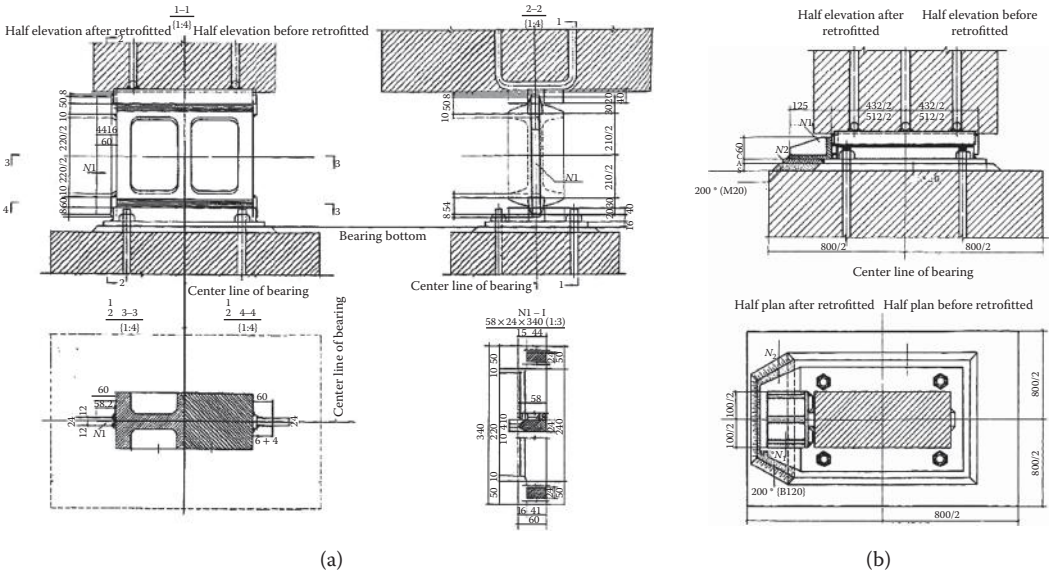

FIGURE 16.35 Retrofitting of bearing in prestressing reinforced concrete highway approach bridges: (a) movable bearing; (b) fixing bearing.

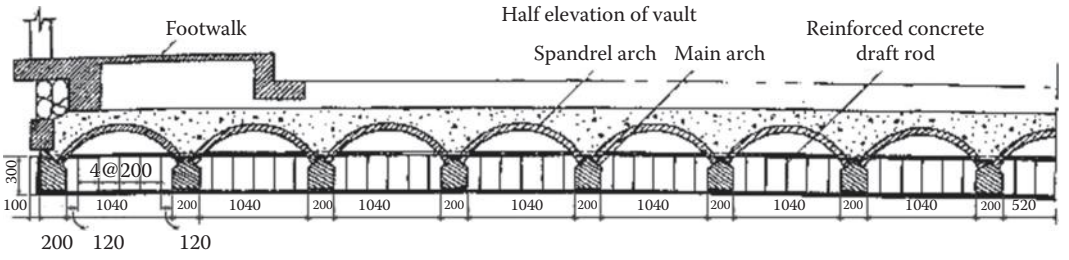

FIGURE 16.36 Retrofitting of highway double-curved arch bridges.

Terms

Seismic fortification criterion—Measure of requirements for seismic resistance, determined by the earthquake intensity and the importance of highway bridges.

Seismic fortification intensity—Seismic intensity approved by national authorities as a region's standard on earthquake resistance protection. Generally, this standard can be equal to the basic seismic intensity specified in *Seismic ground motion parameter zonation map of China*, in which the return period is 475 years, that is 10% probability of exceedance in 50 years.

Seismic performance evaluation—By examining the structural design, construction quality, and current status, based on the stipulated requirements for seismic resistance protection, evaluate the seismic performance and safety of structure under seismic excitation of corresponding resistance level.

Seismic measure—The seismic design contents beside computation of seismic excitation and resistance, including details of seismic measures.

Details of seismic measures—According to seismic conceptual design principles, the detail requirements of structural and nonstructural components generally do not need the calculation.

Design basic acceleration of ground motion—The design value of seismic acceleration whose return period is 475 years.

Characteristic period—The period corresponding to starting point of descending section on the acceleration response spectrum used by seismic design, determined by the seismic environment, and site classification.

Seismic excitation E1—Seismic excitation whose return period is shorter specified in the *08 Guidelines*, corresponding to the first fortification level.

Seismic excitation E2—Seismic excitation whose return period is longer specified in the *08 Guidelines*, corresponding to the second fortification level.

Notations

η_k = axial compression ratio

θ_p = plastic rotation of the potential plastic hinge under seismic excitation *E2*

θ_u = ultimate facultative plastic rotation of the potential plastic hinge, calculate by equivalent yield curvature of section, curvature at ultimate damage state, equivalent length of plastic hinge, and ductility safety coefficient

ρ_t = reinforce ratio in longitudinal direction

Φ = reduction factor of shear strength, $\phi = 0.85$

ϕ^0 = over-strength coefficient of bending capacity of cross-section, $\phi^0 = 1.2$

A = horizontal seismic acceleration peak value

A_e = area of confined concrete core (cm^2)

A_k = total areas of stirrups on one cross-section (cm^2)

b = width of piers in the calculation direction (cm)

C_d = adjustment damping coefficient of seismic acceleration response spectrum

C_i = structure importance factor

C_s = site coefficient

E = total max earthquake response in the computation direction.

E_X = maximum earthquake response in the computation direction under *X*-direction seismic excitation.

E_Y = maximum earthquake response in the computation direction under *Y*-direction seismic excitation.

E_Z = maximum earthquake response in the computation direction under Z-direction seismic excitation.
f'_c = standard compressive strength of concrete (MPa)
f_{yh} = design value of tensile strength of stirrups (MPa)
H_n = clear height of pier, or vertical height from centroid of the superstructure to the bottom of pier for the single-column pier in transverse direction (m)
L_0 = clear span of bent cap (m)
M_G = moment induced by gravity (kN·m)
M^s_{hc}, M^x_{hc} = moment on the top and bottom of columns corresponding to the ultimate flexural capacity in transverse direction based on the designed reinforcement, the standard material strengths, and the most unfavorable axial force (kN·m)
M^L_{pc}, M^R_{pc} = bending capacity of the right and left bent cap utilizing designed reinforcement and standard material properties, respectively (kN·m)
M^s_{zc}, M^x_{zc} = moment on the top and bottom of columns corresponding to the ultimate flexural capacity in longitudinal direction based on the designed reinforcement, the standard material strengths, and the most unfavorable axial force (kN·m)
R_i = adjustment coefficient of seismic excitation that is the ratio of the peak acceleration value corresponding to different return period and peak acceleration value of basic design earthquake ground motion
S = horizontal design acceleration response spectrum
S_k = stirrups space (cm)
S_{max} = maximum value of horizontal design acceleration response spectrum
T = natural vibration period of structure(s)
T_g = characteristic period of sites(s)
V_{c0} = design shear force (kN)
V_s = shear capacity of stirrups (kN)

References

Buckle, I., Friedland, I., Mander, J. et. al. 2006. *Seismic Retrofitting Manual for Highway Structures Part 1 Bridges (FHWA-HRT-06-032)*. U.S. Department of Transportation Federal Highway Administration, Washington, DC.

Caltrans. 2000. *Seismic Design Criteria* (Version 1.1). California Department of Transportation, Sacramento, CA.

China-MOC. 1977. *Specifications of Earthquake Resistant Design for Highway Engineering (Interim)*. China Ministry of Communication, China Communications Press, Beijing, China (in Chinese).

China-MOC. 1989. *Specifications of Earthquake Resistant Design for Highway Engineering, Standard of the China Ministry of Communication, JTJ 004-89*. China Ministry of Communication, China Communications Press, Beijing, China (in Chinese).

China-MOC, DOT of Sichuan, Gansu, Shanxi. 2009. *Collective Drawings of Highway Infrastructures in Wenchuan Earthquake*. China Ministry of Communication, China Communications Press, Beijing, China (in Chinese).

China-MOR. 1987. *Specifications of Earthquake Resistant Design of Railway Engineering, China Standard GBJ 111-87*. China Ministry of Railways, China Planning Press, Beijing (in Chinese).

China-MOT. 2008. *Guidelines for Seismic Design of Highway Bridges, Recommended Standard of China Ministry of Transport, JTG/T B02-01-2008*. China Ministry of Transport, China Communications Press, Beijing, China (in Chinese).

China-NCC. 1968. *Temporary Provisions for Seismic Design of Buildings in Beijing and Tianjin Regions*. China National Construction Committee, China (in Chinese).

China-NPC. 1998. *Law of the People's Republic of China on Precautions Against Earthquake and Relief of Disaster*. China National People's Congress, China Legal Publishing House, Beijing (in Chinese).

Fan, L. 1997. *Bridge Seismic*. Tongji University Press, Shanghai, China (in Chinese).

He, D. 1989. Seismic Computation of Multi-Span Arch Bridge. *World Information on Earthquake Engineering*, 4 (in Chinese).

IOG. 1983. *Collective Drawings of Eight Chinese Earthquake*. Institute of Geology, China Earthquake Administration, Seismological Press, Beijing, China (in Chinese).

Liu, H. 1986. *The Great Tangshen Earthquake*. Seismological Press, Beijing, China (in Chinese).

Wang, K. 2007. *Seismic Research on Bridge*s. China Railway Publishing House, Beijing, China (in Chinese).

Wang, X., and Yang, J. 1993. *Lifeline and Special Buildings Damaged in Lancang-Gengma Earthquake. J Seismol. Res*, 10(4), 425–429 (in Chinese).

Wang, Y., and Dai, G. 2010. *Evolution and Present Updating of Code for Seismic Design of Buildings. J. Building Struct.*, 31(6), 7–16 (in Chinese).

Yang, F., Huang, Y., Liu, J., and Yong, Z. 1989. *Introduction of Seismic Design of Highway Engineering. Highway*, 9(1), 11–17 (in Chinese).

Zheng J. T., Shi, M., Lu, L. et al. 1999. *Damages Investigation of Bridge Systems in Ji-Ji Earthquake*. Workshop on damage investigate of 1999 Ji-Ji earthquake, B23-B46 (in Chinese).

17

Seismic Design Practice in Italy

Gian Michele Calvi
IUSS Pavia and Eucentre Foundation

Paolo Emilio Pinto
Sapienza University of Rome

Paolo Franchin
Sapienza University of Rome

17.1 Introduction

17.1.1 Seismicity of Italy

The Italian seismic history is well documented since the year 217 BC, as presented in (CPTI, 2004) and critically discussed in (Stucchi et al., 2004); however, the first seismic design provisions were issued in 1909 after the great Messina Straits earthquake and their application was limited to the zones close to the strait.

The hazard maps were revised several times to essentially include the new areas hit by specific earthquakes. A more rational seismic hazard map, based on a combination of a probabilistic seismic hazard assessment and on the intensities obtained from isoseismal maps of earthquakes that occurred in the previous 800 years, was developed in 1984, following the 1976 Friuli and the 1980 Irpinia–Basilicata earthquakes.

Only in 2003, a seismic zoning that covered the entire country, based on studies of probabilistic seismic hazard assessment (PSHA), was adopted, requiring to account for seismic action everywhere, although with different probability of occurrence.

Finally, in 2008 (Stucchi et al., 2011), a full PSHA became the code reference for seismic design of structures.

An important consideration to develop this map was that, while earthquakes with magnitude exceeding M_w7.5 have never been reported in the country, M_w6 events have had in the past 1000 years an average return period of 12 years and even moderate or small events can cause significant damage,

particularly to the historical heritage (the damage distribution caused by earthquakes with M_w greater or smaller than 5 is shown in Figure 17.1). As a consequence, low-energy events cannot be ignored.

The earthquake source model (Meletti et al., 2008) used for the development of the hazard map is shown in Figure 17.2. Thirty-six seismic source zones covering the most seismically active areas are identified, with a description of the main parameters of each one of them, including an estimate of the main seismogenic layer (in terms of mean depth of the main earthquakes) and the predominant focal mechanism. This earthquake source model is based on the earthquake catalogue presented in (CPTI, 2004) and (Stucchi et al., 2004); it contains the events depicted in Figure 17.3.

Considering maximum magnitudes suggested by historical, seismological, and geological knowledge (in any case adopting $M_{wMAX} \geq 6.14$) and applying different sets of attenuation models, the PSHA study was completed in terms of PGA classes of 0.025 g on a grid of points at 0.05° (approximately 11,000 points at about 6 km). The PGA median values at 10% probability of exceedance in 50 years, computed on firm ground ($V_{S30} > 800$ m/s) are shown in Figure 17.4.

The study was then expanded considering PGA values calculated for several probabilities of exceedance in 50 years and spectral accelerations for varied spectral periods and exceedance probabilities. Nine levels of probability of exceedance in 50 years were considered: 2, 5, 10, 22, 30, 39, 50, 63, and 81%, while the spectral accelerations values were computed for the ten periods: 0.10, 0.15, 0.2, 0.3, 0.4, 0.5, 0.75, 1.0, 1.5, and 2 s, for each probability of exceedance.

The values of these more than 250 parameters were computed for each grid point: these data represent today the seismic hazard database of Italy and are available on webGIS application (the application is at: http://esse1-gis.mi.ingv.it/s1_en.php) (Martinelli and Meletti, 2008). In a simple and fast way, the user may obtain hazard curves and uniform hazard spectra for the location of interest.

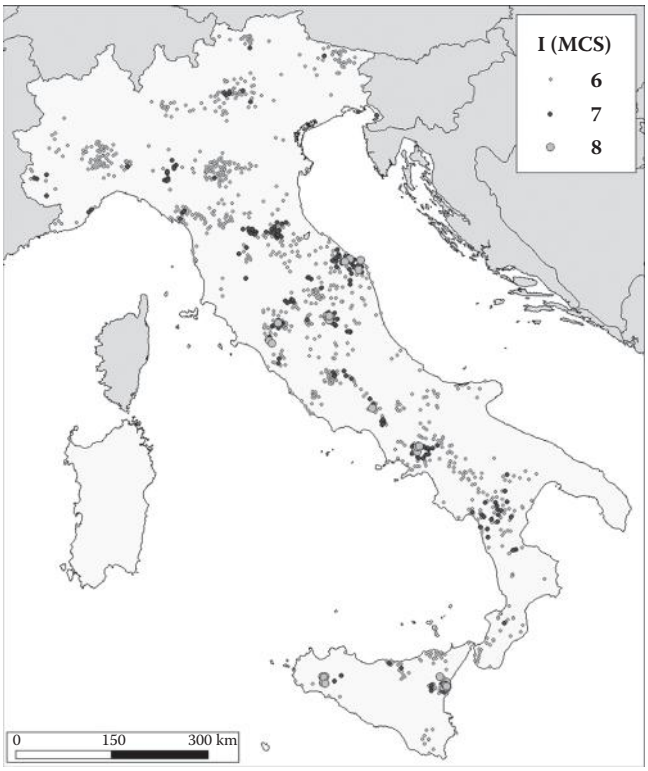

FIGURE 17.1 Damaged localities for well-documented earthquakes after 1950 and $M_w < 5.0$, according to the macroseismic database DBMI11. (Courtesy of C. Meletti, http://emidius.mi.ingv.it/DBMI11.)

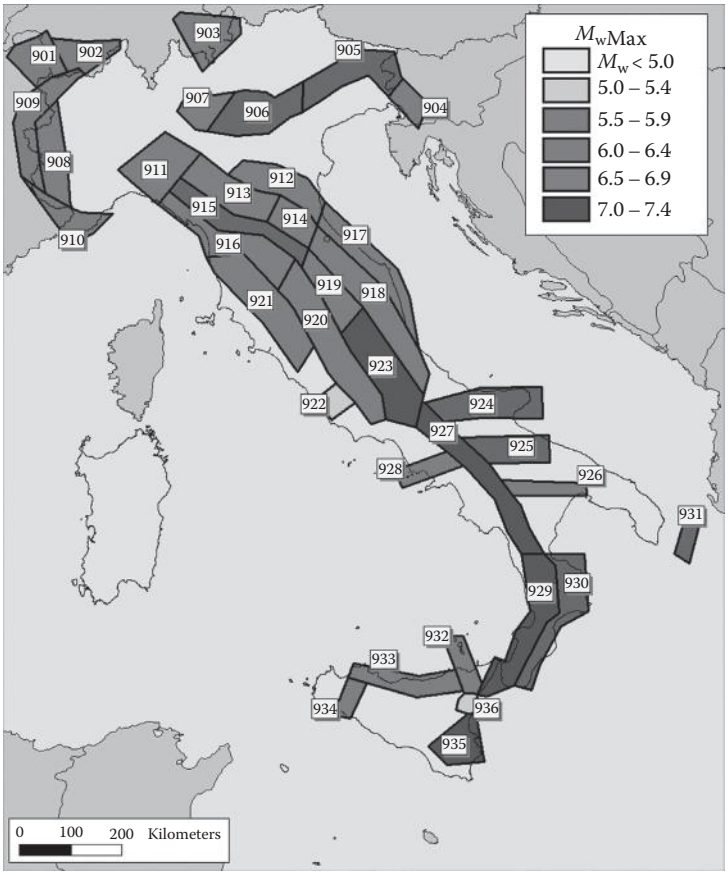

FIGURE 17.2 Source zone model. The colors represent the maximum observed magnitude in the earthquake catalogue or in the faults database DISS. (From Meletti, C., F. et al., *Tectonophysics*, 450(1), 85–108, 2008, http://diss.rm.ingv.it/, With permission.)

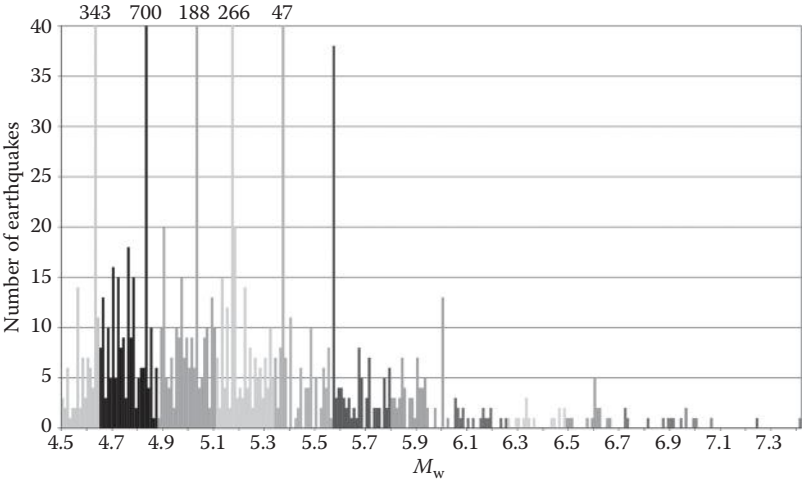

FIGURE 17.3 Number of earthquakes in CPTI04 catalogue per 0.01 magnitude value. The shades represent the different 0.23-unit-wide magnitude bins adopted for determining the seismicity rates. (Courtesy of C. Meletti.)

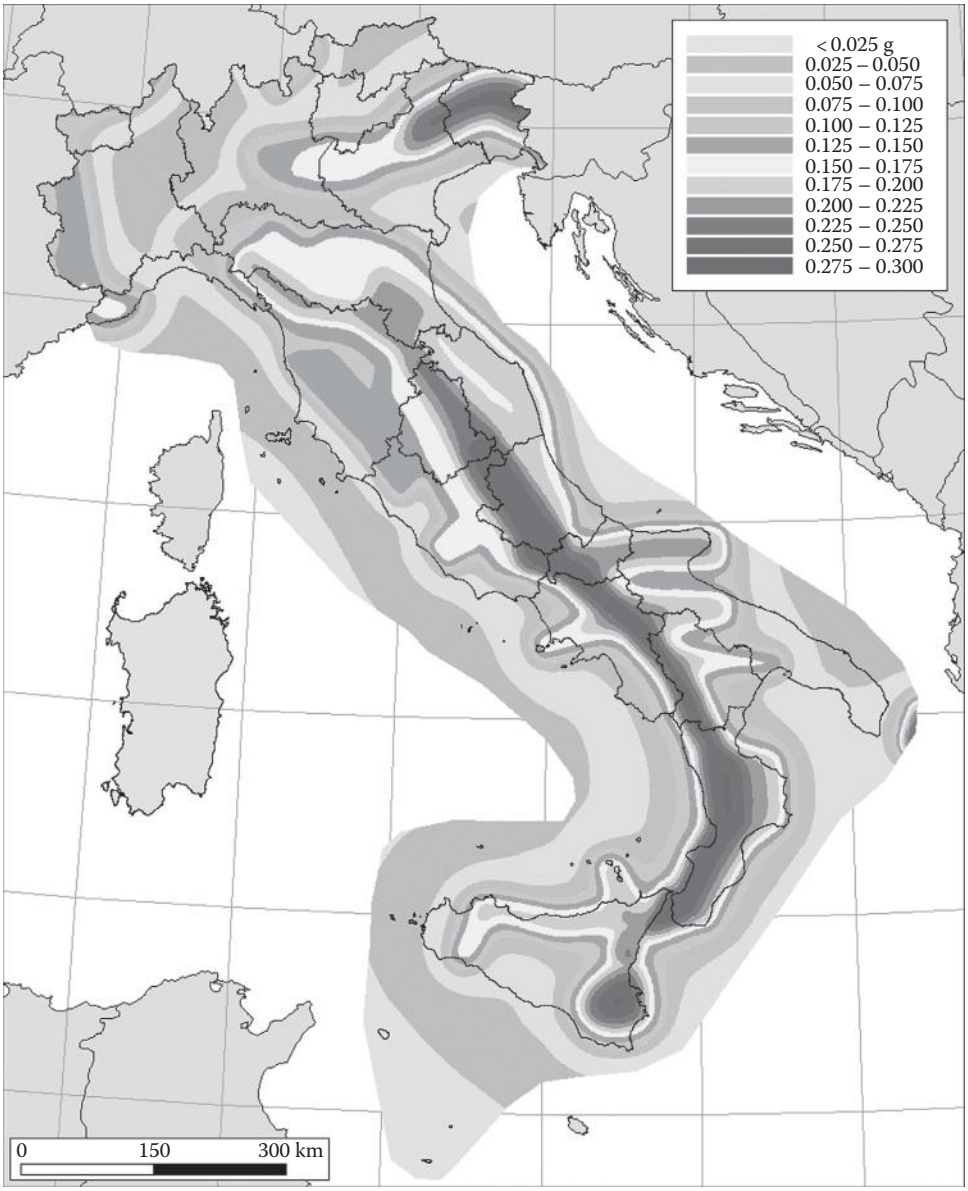

FIGURE 17.4 The reference seismic hazard map of Italy, in terms of PGA with 10% probability of exceedance in 50 years, computed on hard ground ($V_{S30} > 800$ m/s).

As discussed in Section 17.2, the seismic code refers to these site-dependent (rather than zone-dependent) uniform hazard spectra to derive design spectra.

Seismic hazard maps obtained from similar PSHA studies have been recently derived in terms of the spectral displacement demand at long periods of vibration (i.e., 10 s) rather than the PGA at short periods. An example is shown in Figure 17.5, where it appears that the correlation between the two parameters is not very strong. This kind of map has not yet been considered by seismic design codes, nor extensively applied in practice, but appear to be very relevant and promising, particularly for long period of vibration structures, such as bridges often are. In addition, they are of fundamental relevance in the context of displacement-based design, addressed in Chapter 7 of this volume.

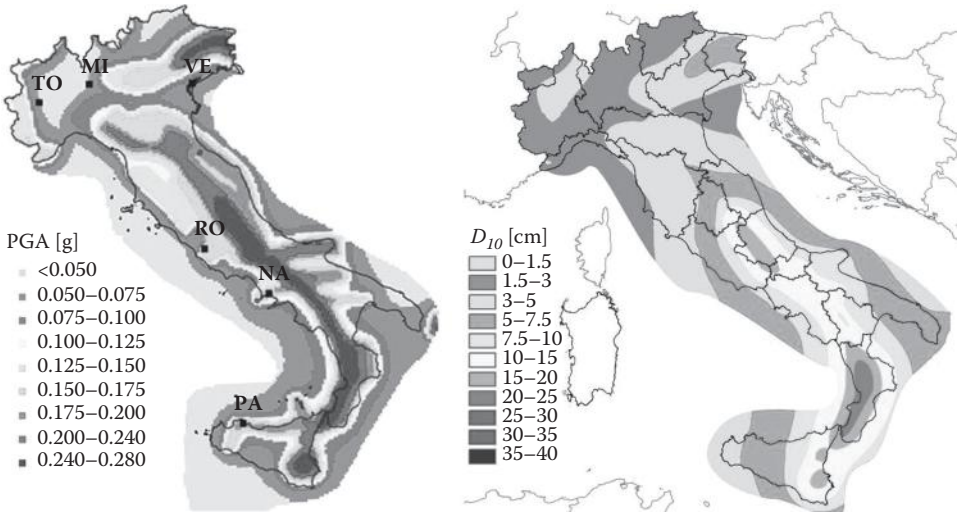

FIGURE 17.5 Comparison of the long period (10 s) spectral displacement map with the *PGA* map obtained for the same probability of exceedance (10% in 50 years) on firm ground. (From Faccioli, E. and M Villani, *Earthquake Spectra,* 25(3), 515–539, 2009.)

17.1.2 Damage to Bridges in Recent Earthquakes

17.1.2.1 General Aspects

In the last 40 years, four major earthquakes have hit the country, in Friuli (1976, M_w 6.4), Irpinia (1980, M_w 6.9), Umbria and Marche (1997, M_w 6.1), and L'Aquila (2009, M_w 6.3). No evidence of damage to bridges and viaducts has been reported in the literature for the first three events listed; although this may be simply due to scarce attention paid to detailed reports; it has to be noted as well that the most common bridge types in Italy are reputed to have adequate capacities to resist horizontal actions even when these have not been explicitly considered. This generally applies to viaducts of moderate height and specifically to abutments, foundations and single-stem piers, and continuous or simply supported spans.

The damage to bridges and viaducts during the 2009 L'Aquila earthquake confirmed that the weak link of this bridge typology remains the pier-deck and abutment-deck connections, whose decisive importance was almost ignored in the code prescription in force in the 1970s, when a large part of the bridges of the Italian road network was built.

The damage resulting from the L'Aquila earthquake (Calvi et al., 2009) is the main subject of discussion in this section, a damage that could have been much more severe, had the ground motion been characterized by larger spectral displacements. These would have engaged to a greater extent the exposed weakness of the support devices; fortunately the relatively small magnitude of the event limited the area hit by a strong ground motion.

Even considering the limited extent of the damage, it is clear that there is the need for an accurate, structure-specific assessment of the critical connections, applying the latest seismic performance criteria and knowledge on the seismic hazard, to plan for some upgrade, not limited to the area affected by this last earthquake.

This obviously applies to a greater extent to the great variety of bridge typologies present in all Italian regions and not referable to continuous or simply supported multispan viaducts.

A very specific class of bridges that requires special studies is that of masonry arch bridges, typical of the nineteenth century railway. Some damage to this structural type has been reported after the Umbria–Marche earthquake (Resemini and Lagomarsino, 2004).

FIGURE 17.6 Typical viaduct of the "Autostrada dei Parchi."

17.1.2.2 The Highway Network in the Area Struck by the L'Aquila Earthquake

The area affected by the April 6, 2009 event is crossed by two highways, planned in the 1960s and constructed in about 20 years, with portions opened to traffic in 1969 and reaching completion in 1993. The actual configuration represents the faster east–west connection in central Italy.

Bridges and viaducts in both highways are mostly of the same type, being simply-supported prestressed beams with a cast-in-place RC slab, supported on single-stem cantilever piers with polygonal or rectangular hollow-core section (see Figure 17.6 for a typical example). Most of the span lengths are between 35 m (114.8 ft.) and 45 m (147.6 ft.). Bearings are predominantly of the cast-iron mechanical type (hinges and rollers). In the parts of more recent construction, the bridge type evolved into a continuous prestressed box girder with circular hollow-core piers.

17.1.2.3 Assessment of the Expected Performance

The rather uniform and simple bridge type has made it feasible to perform some approximate assessment of the seismic capacity, in terms of ground motion intensity, of the bridges and viaducts in the area, allowing the evaluation of the expected performance under a seismic action with prescribed return period (Calvi et al., 2009).

Typical hollow rectangular pier sections, pier height varying between 10 m (32.8 ft.) and 45 m (147.6 ft.) and reasonable superstructure deck and pier cap masses [corresponding to spans of about 40 m (131.2 ft.)] were considered, together with standard material properties. The pier reinforcement was then determined through a simulated design according to the code in force at the time of construction and to the corresponding common practice.

Under nonseismic actions, a minimum reinforcement equal to 0.8% of the concrete section was found to be adequate for all piers under nonseismic actions, while 12 mm (0.47 in.) bars at 200 mm (7.87 in.) spacing resulted for shear design.

The results of seismic nonlinear analysis indicated that peak ground accelerations (PGA) of about 0.25 g in the transverse direction would have induced some shear collapse in piers shorter than about 20 m (65.6 ft.). In all other cases, in the transverse and longitudinal direction, much larger PGA would be required to induce flexural or shear failure in a pier.

It is thus evident that the pier strength capacities have to be deemed adequate even for the accelerations recorded in the epicentral area. This suggests that major damage to the piers should not be expected, also considering the quite conservative procedure employed to assess the seismic capacity and the assumption on the bearing capacity, assumed to be able to transmit the full inertia forces from the superstructure. Actually, the inadequacy of these devices would lead to their premature failure that will possibly protect the piers limiting the transmitted shear force. Such failures, however, may also result in uncontrolled kinematic mechanisms, with random permanent displacements of the superstructure associated with traffic interruption, and in the extreme case of loss of support.

17.1.2.4 Observed Performance

A total of 10 viaducts showed some degree of damage, affecting about 250 spans. The type of damage, as expected, was limited to bearings failures with more or less severe consequences in terms of hindrance to traffic at the superstructure joints. A single case of settlement of the backfill of an abutment was observed. In one case, some significant residual flexural cracks were reported in some piers.

Figures 17.7 and 17.8 illustrate some typical situations involving bearings failure, showing roller dislocation, up to complete expulsion, with damage to the concrete-supporting blocks, and significant permanent displacements. The latter, in turn, have often resulted in relative displacements and breaking of deck joints, as shown in Figure 17.9.

The maximum spectral displacement demands recorded in the area are in general less than 100 mm (4.0 in.). It is evident that larger displacement demands would have resulted in a much more significant damage potential as previously discussed.

17.1.2.5 Emergency Repair Interventions

The highway bridge engineers reacted promptly to the emergency, surveying all bridges for damage, fixing all situations that posed a safety threat, and reopening the highways to traffic within a very short period of time, while effectively communicating with the media with traffic information.

Typical repairs and retrofits are to install temporary supports after jacking of the superstructure and removal of the damaged steel bearings as shown in Figure 17.10, within one day.

In the case where through flexural cracks were detected, an FRP wrapping of the piers was immediately completed, as shown in Figure 17.11.

FIGURE 17.7 Damage to movable bearings: caused by prevailingly lateral displacement, with elements of the bearing in direct contact in an unstable configuration after expulsion of the rollers (left); due to a prevailingly longitudinal displacement, with displacement of the roller out of the seat without complete expulsion (right).

FIGURE 17.8 Abutment damage: roller expulsion and damage to the concrete.

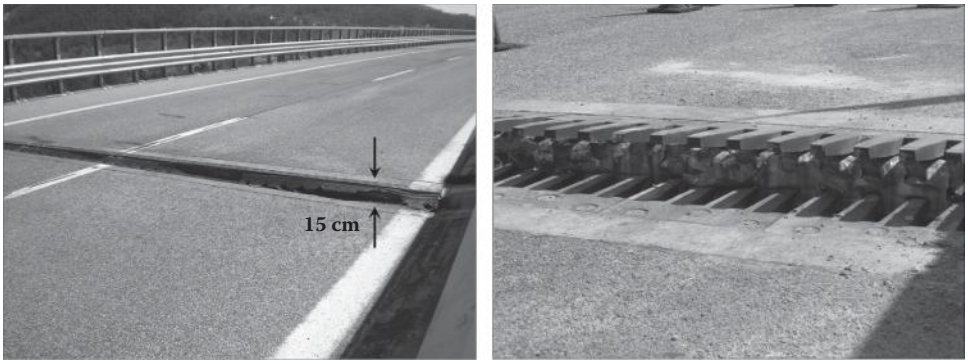

FIGURE 17.9 Consequences of bearings failures at the deck slab level: rubber expansion joints (left) and abutment steel joints (right).

FIGURE 17.10 Lifting of the deck (left) and installation of temporary steel-neoprene supports (right).

FIGURE 17.11 FRP strengthening of some circular piers with through flexural cracks.

17.1.3 Historical Development of Bridge Construction and of Normative Documents in Italy

The vast majority of the bridges on Italian highway systems were built during the two decades from 1955 to 1975, after which construction of new highways was interrupted by law, considering the program as sufficiently developed and diverting the national budget to other priorities. This post-WWII construction, starting with the main North–South A1 highway, represented a quantum leap in the design and the construction technology in Italy, due to the severe difficulties posed by the morphology of the territory, specifically in the Bologna–Firenze portion that crosses the Apennine range. This was the time of the systematic adoption of the prestressing technology and the construction of large-span arch bridges (Figure 17.12, top left), built with huge cradles (Figure 17.12, top right), and frame bridges with unusually high piers (Figure 17.12, bottom).

Major bridges such as these can still be regarded as works of architectural values, though they by no means represent a large portion of the highway bridge inventory. The rest of the bridges, running on less mountainous terrain, are of rather uniform type of simply supported spans, with prestressed beams and cast-in-place deck slab, with span length in the 30 m (98.4 ft.) to 40 m (131.2 ft.) range, and piers that were either of the single stem or frame types (an example is the viaduct already shown in Figure 17.6).

In the late 1980s construction resumed, without the systematic character of the previous period and at a smaller scale, to fill some important gaps that had emerged in the meantime. The bridge types of this period are substantially unchanged, though the quality of construction has considerably improved. It should be mentioned that, during all this period, in parallel with highway construction, the National Road Society (ANAS) has kept upgrading the network of state roads, enlarging sections and rectifying portions, with the necessary erection of new bridges.

FIGURE 17.12 Bridges from the 1950s and 1960s: RC arch bridge on the Firenze–Bologna portion of the A1 highway (top, left); Formwork for the casting of a multispan RC arch on the Firenze–Bologna portion of the A1 highway (top, right); The "Sfalassà" viaduct, 1968–1973 (bottom, left); The "Italia" viaduct (bottom, right).

Throughout the described process, the national design code did not evolve significantly. The safety format remained firmly anchored to the allowable stress design until early 2000, and changes, with regard to bridges, were mainly in terms of traffic loads, whose intensity increased over time.

Seismic design criteria in particular completely missed the international progress, simply consisting in the application of nominal "equivalent" static horizontal forces with no consideration regarding ductile behavior. The maximum value of these forces, in the area of higher seismicity, was just 10% of the weight. Further, the continuous and substantial variation in the definition of the seismic zones has resulted in many cases in a discontinuous level of seismic protection for bridges even along the same highway.

The year 2008 has marked a turning point in the code (MI, 2008), with the mandatory adoption of the limit-state format, and, most importantly, the introduction of a quite refined new description of the seismic action based on the latest hazard characterization presented in Section 17.1.1, and associated modern design criteria (see Section 17.2). This event culminated a period that started in 2003 when, after an earthquake, a draft of a modern code (PCM, 2003) in line with the Euroodes (CEN, 2005a, 2005b and 2005c) was put forward to be used discretionally in parallel with the previous one, together with the obligation for all public bodies to perform a seismic assessment of their strategic structures. The latter obligation, of course, also involved all bridge structures. The completion of this program will take several years and, at the moment, it is being carried out for those portions of the highway network that are also subject to functional upgrading.

17.2 Current Seismic Design Code

17.2.1 Performance Requirements

The current structural design code considers four general performance levels (limit states):

1. Operational (SLO): the structure is undamaged and fully operative after the earthquake.
2. Damage (SLD): the structure undergoes a limited amount of structural, nonstructural and content damage, not compromising its strength and stiffness and remaining immediately usable after the earthquake, with the exception of some equipment.
3. Life safety (SLV): the structure undergoes significant damage to structural and nonstructural elements, as well as content, to the point that repair may not be economic, but must retain some lateral stiffness and strength and a significant portion of its vertical load-bearing capacity.
4. Collapse (SLC): the structure experiences severe unrepairable damage, but retains a margin against vertical loads and a lower one against horizontal actions.

The performance requirements are that the above performance levels should not be exceeded for associated seismic intensity levels, specified in terms of the average return period as a function of the bridge importance. The latter is determined on the basis of the functional importance of the bridge within the road network, in terms of emergency management and economic consequence of the failure, as well as on the structural relevance. The fundamental parameter expressing the importance of the bridge is the *reference life* V_R, which can vary, for example, from 50 years for an ordinary structure on a local road, to 100 years for an ordinary structure on a highway, to 200 years for bridges on strategic arteries of the network.

The seismic intensity levels are specified, as already mentioned, in terms of average return periods, which are reported in Table 17.1, that are related to probabilities of exceedance P_{VR} of the associated performance levels during V_R.

In the case of bridges, the SLV performance level only needs to be verified. Its definition is also particularized to bridges, stating that the structure must be designed so as to confine the damage to either specifically designed locations of the piers or in dissipative devices at the piers–deck interface. The code explicitly states that the scope of seismic design of bridges is limited to girder and arch bridges, therefore excluding cable stayed and suspension bridges.

TABLE 17.1 Target Exceedance Probabilities and Corresponding Average Return Periods for the Four Performance Levels in the Code, for Three Different Values of the Reference Life V_R

Performance Level	P_{VR}	T_R ($V_R = 50$)	T_R ($V_R = 100$)	T_R ($V_R = 200$)
SLO	0.81	30	60	120
SLD	0.63	50	101	201
SLV	0.10	475	949	1898
SLC	0.05	975	1950	2475

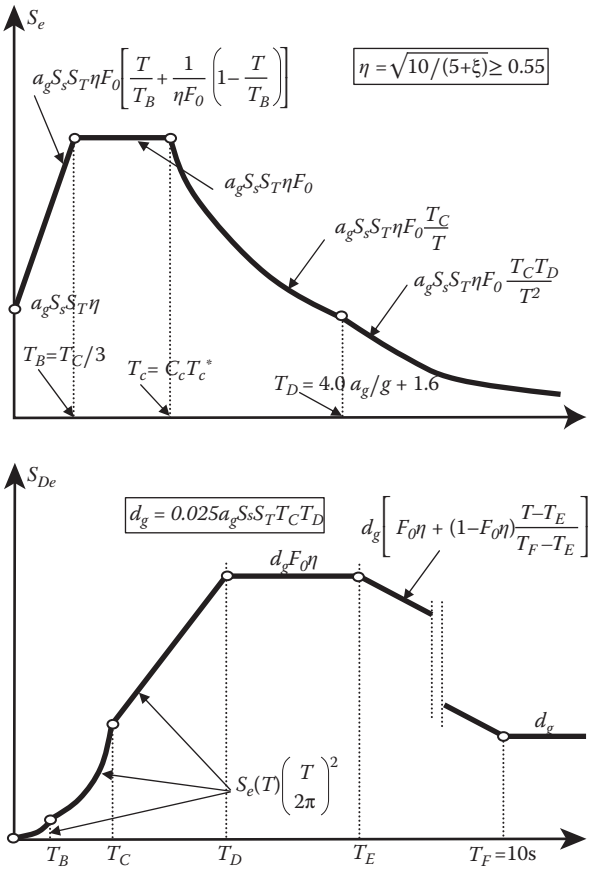

FIGURE 17.13 Acceleration and displacement spectral shapes according to the current seismic design code.

As far as the seismic intensity is concerned, in the code the concept of seismic zonation has been superseded by a refined site-dependent description of the seismic action in terms of the whole response spectrum for different soils/topography and for several return periods, between 30 and 2475 years (see Section 17.1.1). To facilitate practical application, the code retained the standard Eurocode spectral shapes, which have been fit to local uniform hazard spectra. The spectral shapes for acceleration and displacements are shown together with their functional form in Figure 17.13. The shapes are parameterized by the peak ground acceleration (PGA) on rock/stiff soil a_g, the amplification factor F_0 (ratio of plateau acceleration to PGA) and the corner period on rock, T_C^*. The code provides these three parameters on a 0.05° by 0.05° geographical grid. Tables 17.2 and 17.3 report the values of the soil and topography amplification factors, by corresponding category.

TABLE 17.2 Soil Categories and Corresponding Elastic Response Spectrum Parameters in the Code

Soil	Brief Description	V_{S30} (m/s)	S_S	C_C
A	Rock outcrop, stiff soil	>800	1.0	1.0
B	Weathered rock, very dense sand or gravel, very stiff clay	360–800	$1.0 \le 1.4 - 0.4F_0\frac{a_g}{g} \le 1.2$	$1.1\left(T_C^*\right)^{-0.2}$
C	Dense sand or gravel, stiff clay	180–360	$1.0 \le 1.7 - 0.6F_0\frac{a_g}{g} \le 1.5$	$1.05\left(T_C^*\right)^{-0.33}$
D	Loose to medium dense sand or gravel, soft to firm clay	<180	$0.9 \le 2.4 - 1.5F_0\frac{a_g}{g} \le 1.8$	$1.25\left(T_C^*\right)^{-0.5}$
E	No more than 20 m of soil C or D over a stiffer stratum		$1.0 \le 2.0 - 1.1F_0\frac{a_g}{g} \le 1.6$	$1.15\left(T_C^*\right)^{-0.4}$
S1	Deposits with at least 8 m of high plasticity clay or 3 m of organic clay/silt	<100	Ad-hoc studies required	
S2	Liquefaction-susceptible soils			

TABLE 17.3 Topographical Amplification Parameter as a Function of Topography

Class	Topography	Structure Location	S_T
T1	Flatland (i < 15°)		1.0
T2	Slope (i > 15°)	On top	1.2
T3	Heights with narrow crest and slopes with 15°< i < 30°	On the crest	1.2
T4	Heights with narrow crest and slopes with i > 30°	On the crest	1.4

Figure 17.14 shows an example of a site on the Bologna–Firenze portion of the main North–South highway. The top-left plot shows the acceleration and displacement response spectra for two bridges at the same site, with reference lives of 50 years and 200 years, respectively. The remaining plots show the variation of the three parameters a_g, F_0 and T_C^* with the return period T_R. Note that F_0 remains virtually constant around 2.4.

One aspect of the specification of the seismic action particularly relevant to bridges is the spatial variability of the intensity along the bridge axis. The code states that its effect shall be considered when significant, and in particular when the soil conditions under the supports would require different response spectra. As an approximation, it is suggested to sum the dynamic component of the total response, evaluated using response spectrum analysis with the most severe spectrum, to the static component, evaluated by imposing patterns of differential displacements. When motions at the supports can be considered as independent (differences in geotechnical conditions or orography), the differential displacement is expressed as follows:

$$d_{ij,\max} = 1.25\sqrt{d_{g,i}^2 + d_{g,j}^2} \tag{17.1}$$

where $d_{g,i}$ and $d_{g,j}$ are the peak ground displacements (PGD) at support i and j respectively (see Figure 17.13). The code then provides expressions for the differential displacement in cases where discontinuities in the orography and soil category are minor, as a function of the distance between supports. These, however, usually result in equally minor effects that can be neglected.

17.2.2 Design Alternatives

As already mentioned, the main alternatives facing the designer are whether to go for a traditional design in which energy dissipation occurs in the piers, or to go for an isolation scheme, whereby all or some of the piers are connected to the deck via mechanical devices. There seems to be a clear tendency

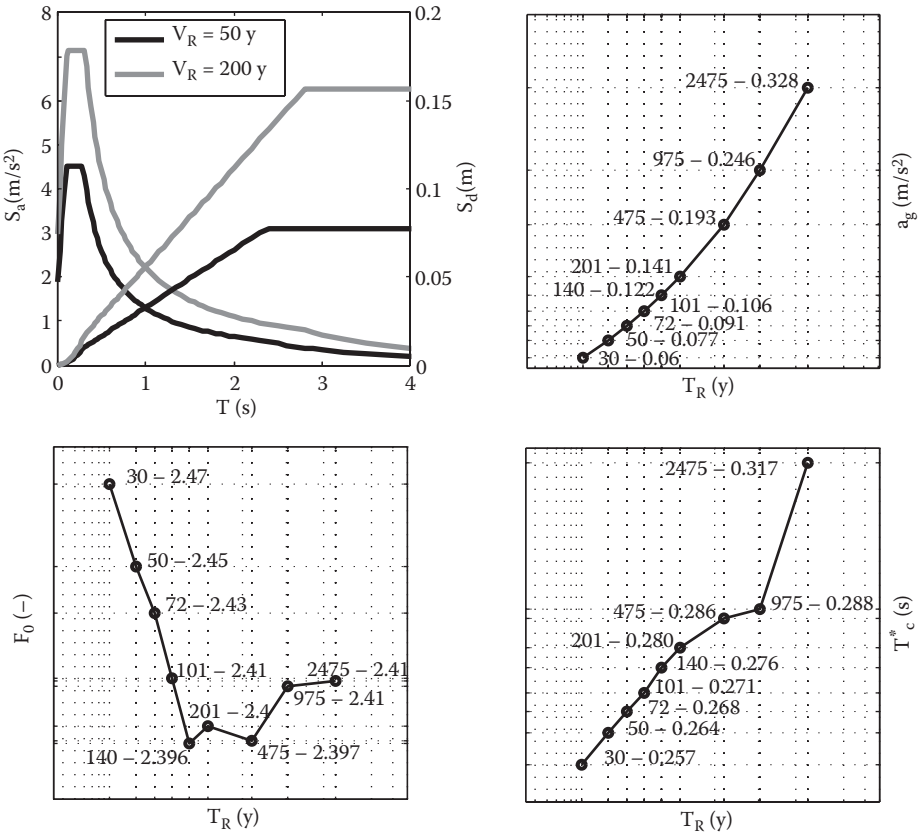

FIGURE 17.14 Variability of the design seismic action for the SLV limit state as a function of the reference life of the bridge: acceleration and displacement response spectra for two value of V_R(top, left), variation of a_g, F_0, and T_C^* versus T_R.

toward an increased use of isolation solutions. The next sections briefly describe code provisions for both cases. Within traditional design, a choice is offered by the code between two different target ductility levels, denominated High and Low. Designing for the second one yields structures that perform better by exhibiting lower damage at the SLV intensity level, at the expense of slightly higher initial cost. In general, however, for both levels of target ductility, the design criteria for bridges result in quite low ductility demands, as compared to those accepted for buildings. The underlying philosophy is justified on the one hand by the critical importance of bridges in the overall infrastructural system of the country, and on the other, by the minor incidence of bridges and viaducts on the overall cost of highways in Italy.

17.2.3 Traditional Design: Force-Reduction Factors

The traditional design is a force-based approach, that is, one where strength is designed to action effects derived from the elastic spectrum divided by a force-reduction factor q, and the ductility implied by the force-reduction is ensured through compliance with capacity design and detailing rules. All verifications are in terms of strength, with no explicit check on displacement or ductility, with the only exception of the seating length.

The maximum values q_0 for the force-reduction factor are reported in Table 17.4.

TABLE 17.4 Maximum Values q_0 of the Force-Reduction Factor. The Factor $\lambda = 1$, for $\alpha \geq 3$, $\lambda = \sqrt{\alpha/3}$, for $3 \geq \alpha \geq 1$, Where $\alpha = L/H$ Is the Shear–Span Ratio

Element	High Ductility	Low Ductility
RC vertical piers	3.5λ	1.5
RC inclined piers	2.1λ	1.2
Steel vertical piers	3.5	1.5
Steel inclined piers	2.0	1.2
Steel piers with concentric bracings	2.5	1.5
Steel piers with eccentric bracings	3.5	–
Abutments rigidly connected with the deck	1.5	1.5
Buried abutments (rigidly moving with soil) or abutments flexibly connected with the deck	1.0	1.0
Arches	2.0	1.2

For RC piers, these values are reduced as a function of the normalized axial force $\nu = N_{Ed}/A_c f_{ck} < 0.6$ according to:

$$q_0(\nu) = \begin{cases} q_0 & \nu < 0.3 \\ q_0 - \left(\dfrac{\nu}{0.3} - 1\right)(q_0 - 1) & 0.3 \leq \nu < 0.6 \end{cases} \tag{17.2}$$

It is well known that the concept of a global force-reduction factor is based on the assumption that energy dissipation is approximately uniform throughout the structure. When the structure satisfies this requirement, it is called *regular*. This is seldom the case for bridges, where in fact piers' geometry is dictated by the soil profile and by reasons of visual uniformity, resulting in different ductility demands. This lack of uniformity is penalized by a reduction of the factor q, starting from q_0, as a function of the ratio, over all piers, between the maximum and the minimum values of the ratio $\rho = qM_{Ed}/M_{Rd}$ of the pier strength required for elastic behavior to the actual provided pier strength (as a proxy of ductility demand):

$$q = q_0(\nu)K_R = q_0(\nu)\frac{2}{\rho_{\max}/\rho_{\min}} \geq 1, \quad \text{for } \frac{\rho_{\max}}{\rho_{\min}} > 2 \tag{17.3}$$

When $\rho_{\max}/\rho_{\min} \leq 2$, the bridge is still called *regular*.

This reduction rule is the main design criterion leading to the low ductility demand mentioned at the end of the previous section.

17.2.4 Capacity Design and Detailing Rules

Failure modes other than flexural failure in the critical zones (those intended to be dissipative) in the piers, such as, for example, shear failure, bearing failure, bending failure outside critical zones, and foundation failure must be prevented from occurring by amplifying the corresponding design action through an *overstrength factor* γ_{Rd}. This factor is evaluated as follows:

$$\gamma_{Rd} = 0.7 + 0.2q \geq 1 \tag{17.4}$$

which gives values between 1 and 1.4, for the maximum allowed value of $q = 3.5$. This formula allows for differentiating the capacity design protection for bridges of high and low target ductility.

For RC piers, γ_{Rd} is modified as a function of the normalized axial force v according to

$$\gamma_{Rd}(\nu) = \begin{cases} \gamma_{Rd} & \nu < 0.1 \\ \gamma_{Rd}\left[1 + 2(\nu - 0.1)^2\right] & 0.1 \leq \nu < 0.6 \end{cases} \tag{17.5}$$

Action effects transmitted by flat sliders and elastomeric bearing devices must be increased by $\gamma_{Rd} = 1.3$.

The code then prescribes minimum reinforcement for achieving local ductility in the dissipative zones of the piers. In particular, no confinement reinforcement is required for low normalized axial forces ($\nu \leq 0.08$), or for thin-wall sections (hollow-box or double-tee), provided $\nu \leq 0.2$ and the curvature ductility capacity is not lower than 12 with concrete strain not exceeding 3.5‰. In all other cases, the minimum mechanical reinforcement ratio for confinement is given as a function of cross-section shape:

- Rectangular sections $\omega_{wd,r} = 0.33\left(A_c / A_{cc}\right)\nu - 0.7 \geq 0.12$, with A_c and A_{cc} the gross and core concrete area respectively, and $\omega_{wd,r} = \left(A_{sw}/bs\right) f_{yd} / f_{cd}$ where b is the section dimension orthogonal to the stirrup arms.
- Circular sections $\omega_{wd,c} = 1.4\omega_{wd,r}$, with $\omega_{wd,c} = 4\left(A_{sp}/D_{sp}s\right) f_{yd} / f_{cd}$ where A_{sp} and D_{sp} are the area and diameter of the spiral reinforcement respectively.

This confinement reinforcement is extended for the larger of the section height or the distance between the section of maximum moment and the section where the moment has decreased by 20%. For a further equal length, the code requires a gradually decreasing confinement reinforcement, not lower than half of the amount in the critical zone. In the critical zone, each longitudinal bar must be restrained by stirrups or ties of area:

$$\frac{A_t}{s} = \sum A_s \frac{f_{ys}}{1.6 f_{yt}} \tag{17.6}$$

where f_{ys} and f_{yt} are the yield strength of the longitudinal bars and ties/stirrups respectively.

17.2.5 Verifications

Piers must be checked for axial force and biaxial bending, as well as shear force. In the critical section, the following condition must be verified:

$$\left(\frac{M_{Ed,y}}{M_{Rd,y}\left(N_{Ed}\right)}\right)^{\alpha} + \left(\frac{M_{Ed,z}}{M_{Rd,z}\left(N_{Ed}\right)}\right)^{\alpha} \leq 1.0 \tag{17.7}$$

where the exponent α depends on the cross-section shape, while y and z denote the cross-section axes. Outside the critical zone, the following condition must be verified:

$$\left(\frac{\gamma_{Rd} M_{Ed,y}}{M_{Rd,y}\left(N_{Ed}\right)}\right)^{\alpha} + \left(\frac{\gamma_{Rd} M_{Ed,z}}{M_{Rd,z}\left(N_{Ed}\right)}\right)^{\alpha} \leq 1.0 \tag{17.8}$$

For what concerns the shear force, the verification takes the form

$$V_{gr} = \min\left(qV_{Ed};\ \gamma_{Rd}\frac{M_{Rd,top}\left(N_{Ed}\right) + M_{Rd,bot}\left(N_{Ed}\right)}{L_V}\right) \leq \frac{V_{Rd}}{\gamma_{Bd}} \tag{17.9}$$

where the additional protection factor against brittle failure is given by

$$\gamma_{Bd} = 1.25 + 1 - \frac{qV_{Ed}}{V_{gr}} \leq 1.25 \tag{17.10}$$

The shear strength V_{Rd} must be evaluated as for nonseismic situations, as the minimum of steel-failure- and concrete-failure-related strengths:

$$V_{Rd,s} = 0.9d\frac{A_{sw}}{s}(\cot\theta + \cot\alpha)\sin\alpha \tag{17.11}$$

$$V_{Rd,c} = 0.9db_w\alpha_c\left(0.5f_{cd}\right)\frac{\cot\theta + \cot\alpha}{1+\cot^2\theta} \tag{17.12}$$

where $1 \le \cot\theta \le 2.5$, and α_c is a coefficient accounting for the beneficial effect of compressive axial force in the member.

The superstructure must be designed with no damage at the SLV performance level. Usually strength verifications are not necessary in the longitudinal direction for straight bridges. In the transverse direction, the shear transmitted at the pier's top is calculated as follows:

$$V_{gr} = V_{Ed}\frac{\gamma_{Rd}M_{Rd}\left(N_{Ed}\right)}{M_{Ed}} \le qV_{Ed} \tag{17.13}$$

If the pier frames into the superstructure, $M_{gr} = \gamma_{Rd}M_{Rd}\left(N_{Ed}\right)$.

Fixed bearings must be designed to the same capacity design action as in Equation (17.13). Sliding bearings must retain their full functionality under the maximum displacements, evaluated as follows:

$$d_E = \mu_d d_{Ed} \quad \text{with } \mu_d = \begin{cases} q & T \ge T_C \\ 1+(q-1)T_C/T \le 5q-4 & T < T_C \end{cases} \tag{17.14}$$

Where relative displacement can occur between deck and the piers, a minimum length to prevent unseating failure must be provided equal to

$$l_s = l_m + d_{ij} + d_E \tag{17.15}$$

where $l_m \ge 400$ mm (15.7 in.) is the length required to place the bearing device and d_{ij} is the relative displacement between the bases of the piers. When this length cannot be provided, seismic restrainers must be put in place, capable of resisting a force equal to

$$F_d = 1.5S\frac{a_g}{g}W \tag{17.16}$$

where W is the tributary weight of the deck.

Abutments must be designed with no damage at the SLV performance level. In a way of simplification, it is accepted to carry out the verification independently for the two orthogonal plan directions.

Action effects can be obtained from a separate model of the abutment when this is connected to the deck via sliding bearings. The friction action from the bearings, however, must be accounted for in the verifications, amplified by a factor of 1.3. In all other cases, the abutment should be included in the same model as the bridge, whereby SSI is accounted for. The action effects on the abutment must be computed using a force-reduction factor $q = 1.5$. For the analysis in the transverse direction, interaction with the backfill and foundation soil can be disregarded and the acceleration can be taken equal to a_g.

17.2.6 Seismic Isolation and Energy Dissipation

Mechanical devices employed in seismic isolation allow relative displacements and dissipate energy; these are classified as *seismic isolation bearings*, with vertical load-bearing function, and *auxiliary devices*, which do not support vertical loads. The code states that all devices must be provided with a higher level of protection with respect to the substructures (piers and abutments)—and superstructure. This increased protection is obtained by verifying that the devices remain fully functional under displacements d_2 induced by a seismic intensity level with return period corresponding to the SLC (collapse) performance level. The substructure and superstructure must remain elastic under the SLV intensity level. For the purpose of strength verifications of the super structure, the action effects can be divided by a force-reduction factor of $q = 1.5$.

Emphasis is placed on the variability of the mechanical properties of the devices. These can change as a function of the following:

- Maximum deformation
- Deformation velocity
- Axial force
- Temperature
- Cumulative wear due to repeated displacement excursions
- Inherent variability within any production batch

The code requires that analysis is carried out with all combinations of upper- and lower-bound properties for the devices, and that verifications must be carried out for the most unfavorable action effect.

Devices to be used in Italy must first be qualified according to a standardized test procedure (*qualification* test). For each new isolated structure, 20% of the devices to be installed must be checked for conformity to the qualified typology (a less demanding *acceptance* test). Both qualification and acceptance testing procedures basically follow the European Standard EN15129 (CEN, 2005b), which is referenced by Eurocode 8 Part 2 (CEN, 2005a) as well.

17.2.7 Methods of Analysis and Modeling Issues

Regarding the methods of analysis, the chapter of the code on seismic design of bridges makes reference to the previous chapter on buildings. In general, for traditionally designed bridges, all four methods including linear static, nonlinear static, linear dynamic, and nonlinear static modeling, can be adopted, while nonlinear static (NLS) analysis is explicitly excluded for seismically isolated ones.

In practice, however, the applicability of the linear static (LS) analysis is limited to bridges obeying strict conditions of simplicity and regularity, hence the reference method is linear dynamic (LD) analysis, that can be implemented as either modal analysis with response spectrum or time-history analysis.

For nonisolated bridges, linear analysis can be applied without restriction, given that irregular behavior translates into smaller values of the force-reduction factor, eventually leading to elastic design ($q \approx 1$).

For isolated bridges, linear analysis can be applied when linear modeling of the devices is admitted. Devices can be modeled linearly when:

- The equivalent linear stiffness k_{esi}, defined as the secant stiffness of the device at the reference displacement d_1 (induced by the SLV intensity level), is at least 50% of the secant stiffness at $0.2d_1$.
- The equivalent viscous damping ratio $\xi_{esi} = \sum E_{Di} \Big/ \left(2\pi K_{eff} d_1^2\right)$ is lower than 30% (E_{Di} being the energy dissipated in the ith isolator in one cycle at displacement amplitude d_1, $K_{eff} = \sum 1 \Big/ \left(1/k_{esi} + 1/k_{subi}\right)$ is the sum of the composite stiffnesses of each isolator and the corresponding substructure and d_1 is the displacement at $T_{eff} = 2\pi\sqrt{M_D / K_{eff}}$).
- The force-displacement law does not change more than 10% for variations of the deformation velocity within a ±30% range around the design velocity.
- The force increment in the isolation devices corresponding to an increase of the displacement from 0.5 d_1 to d_1 is larger than $0.025N_{Ed}$.

The above procedure implicitly assumes that the deformation of the substructure is negligible with respect to that of the isolators. This is the case for stiff piers. When adopting the seismic isolation solution in presence of flexible piers, one can either resort to nonlinear dynamic analysis or use weighted modal damping.

When linear analysis is applicable, if the analysis is of the modal type all modes with participating mass ratio (PMR) larger than 5% must be included and a minimum total PMR of 85% must be reached.

For seismically isolated bridges, the elastic spectrum must be reduced by

$$\eta = \sqrt{\frac{10}{5+\xi_{esi}}} \tag{17.17}$$

for all periods $T > 0.8T_{is}$ where T_{is} is the isolation period. This reduction, for linear time-history analysis, must be achieved either by using modal decomposition and applying the reduction mode-wise, or by suitably modifying the damping matrix.

For linear analysis, or for nonlinear analysis with simplified constitutive laws (e.g., concentrated plasticity), the code provides indications on the reduction of members' stiffness. For traditional nonisolated bridges, piers that are expected to develop a plastic hinge at the base should be assigned a reduced stiffness proportional to the secant-to-yield stiffness:

$$E_c I_{eff} = 1.2\frac{M_{Rd}}{\phi_y} \tag{17.18}$$

where the 20% increase is meant to account for the noncracked higher portion of the pier.

RC decks should also be assigned a reduced torsional stiffness, between 30% and 50% for hollow-box cross sections and down to zero for open sections or simple slabs.

Coming to nonlinear dynamic (NLD) analysis, the code does not provide additional provisions specific to bridges. The only indications regard the criteria for selecting a suite of input ground motion time series. The latter can either be recorded natural motions or synthetic ones. In all the cases, they must satisfy some spectrum-compatibility conditions:

- The average elastic 5%-damped spectrum of synthetic time series should not be lower than 10% of the target spectrum anywhere in the periods ranging between 0.15 s and 2.0 s or $2T$; the upper limit becomes $1.2T_{is}$ for isolated structures. The duration of synthetic time series should reflect the dominant macro-seismic parameters for the site, with a stationary portion not shorter than 10 s.
- Among synthetic motions, time series produced by seismological models are permitted under the condition that properties of the source and the propagation path are adequately documented.
- Geotechnical systems, and hence, for example, bridges such as integral abutment bridges, can be analyzed only with recorded natural motions.
- Recorded motions should be selected with reference to the dominant macro-seismic parameters and should approximate the target spectra in the range of periods of interest.

It is apparent how the criteria for selecting recorded motions are more flexible than those for synthetic ones. More generally, as it is common to many international codes, the guidance given for NLD analysis is quite limited and, as a result, the designer must take responsibility and justify the modeling choices and the judgment of the results. In particular, it is worth noting how the acceptable ductility limits are not specified. The only indication about verifications is that the average of the maximum responses can be used if at least seven motions are considered.

Finally, a mention in passing should be given to a clause stating that the "nonlinear dynamic analysis shall be compared to a modal analysis with response spectrum, in order the check the differences in terms of global forces at the base of the piers." This statement is clearly a residual from a time when confidence in analysis of nonlinear type was still limited. In any case, the code does not tell how to judge discrepancies.

For bridges, all analysis types must be carried out with the two horizontal and the vertical components of the seismic action acting simultaneously on the bridge.

Notably, the code does not even mention the particular relevance of the spatial variability of ground motion in the evaluation of the devices' displacements in seismically isolated bridges.

17.3 Seismic Retrofit Practice

17.3.1 Introduction

Starting with a first decree from the Civil Protection Department (PCM, 2003), the activity on the seismic assessment as well as on the upgrade of existing roadway bridges has significantly increased. This activity is essentially carried out by two main actors, the National Highway Administration (ANAS) and the private concessionaires managing the pay-toll highways. Assessment is carried out by ANAS on a larger scale, with the ultimate goal of having a nation-wide knowledge of the safety of all its bridges, for use in future upgrading programs. Private concessionaires, on the other hand, carry out seismic assessment and retrofit as part of the functional upgrades (e.g., platform widening) that are committed to perform as part of their concession agreement with the state. Both activities are essentially carried out according to guidelines prepared by the authors (the latest version in [Pinto et al., 2009]), which have been later introduced in the current seismic code.

17.3.2 Code and Guidelines

For the first time the current code, issued in 2008, contains a chapter dealing with the assessment and retrofit of existing structures: this chapter follows closely the European normative (CEN, 2005c), similar to what is done for the design of new structures, described in Section 17.2. Recognizing the still evolutive state of knowledge on the matter, the mandatory part of the norm is relatively short and contains only the general principles and application rules, while most prescriptions and indications are left to an auxiliary document (MI, 2009), again similar to the Annexes of the Eurocodes.

As for new structures, the theoretical framework is performance based, with the performance levels described in Section 17.2. For existing structures, however, only the SLV performance level needs to be mandatorily verified. Further, the format for assessment is explicitly *displacement based*, requiring formal verification of displacement capacity for ductile failure modes, complemented with strength verifications for brittle failure modes (e.g., shear, foundations). The seismic action is thus described by the elastic, unreduced response spectrum. Nonlinear analysis is the reference method, with linear dynamic analysis allowed only when so-called regularity condition is satisfied (which ensures that displacements predicted by linear analysis are a good approximation of those obtainable through a nonlinear one). The condition is expressed as follows:

$$\frac{\rho_{\max}}{\rho_{\min}} \le 2.5 \tag{17.19}$$

where $\rho = M_{Ed}/M_{Rd} \cong \theta_{Ed}/\theta_y$ is a measure of ductility and the above ratio is computed considering all $\rho \ge 2$.

The second important feature of the framework is the way *knowledge* on the structure is dealt with. On the basis of a quantitative assessment of the combined available data on geometry, construction details, and material properties, knowledge is discretized in three levels, to which values of a so-called *confidence factor* are attached, and used to reduce mean material strengths.

Specific indications for existing bridges are scarce, consisting of an indication that, given the fact that structures are normally exposed and hence easy to be inspected, the maximum knowledge level should be pursued, along with capacity formulas for the ductile and brittle failure modes.

The ultimate (collapse) drift of a bridge pier $\theta = \delta/L_s$ is given by the expression

$$\theta_u(N) = \theta_y(N) + \left[\phi_u(N) - \phi_y(N)\right] L_p \left(1 - \frac{0.5 L_p}{L_S}\right) \tag{17.20}$$

where $\theta_y(N) = \phi_y(N) L_S/3$ with L_s is the shear span of the pier. Yield and ultimate curvatures $\phi_y(N)$ and $\phi_u(N)$ as a function of axial force N must be obtained from sectional analysis.

The ultimate shear strength is given by the expression (Kowalsky and Priestley, 2000)

$$V_u = 0.8A_c k(\mu_d)\sqrt{f_c} + N\frac{h-x}{2L_S} + \frac{A_{sw}}{s} f_y z \tag{17.21}$$

where $k(\mu_d)$ is a displacement-ductility-dependent factor that reduces shear strength.

17.3.3 Typologies of Intervention

As indicated above, the seismic upgrading decision comes in parallel with the necessity of widening the platform.

There are two cases: pay-toll highways already have separate ways, each one comprising generally two regular lanes plus an emergency one, while state highways almost always consist of a single way carrying traffic in both directions, with narrow or nonexistent emergency lanes. The approach to widening is correspondingly different.

In the first case, represented with an example in Figure 17.15 (left), the longitudinal scheme is preserved and additions are placed on the sides and connected to the existing deck, supported on pier extensions that are designed similar to the existing ones. The old superstructure is typically made up of prestressed I-beams with cast-in-place RC slab, while the new one is most frequently of the mixed steel-concrete type. Connections of the new concrete with the old one, so as to achieve a monolithic behavior, are realized at the level of the foundation mat and of the pier transverse beams (with patterns of bars drilled into the existing structure and bonded with epoxy resins), as well as at the level of the deck slab.

Figure 17.15 (middle and right) represents state highway viaducts. In the first example, a single-stem pier (with solid circular cross section) is carrying a shared simply-supported prestressed deck with two traffic lanes in opposite directions. In this case, the old deck is replaced with a new, larger, composite steel-concrete deck continuous over the piers, and the construction of a new parallel viaduct with the same deck typology. In the second example, the dimension of the portal pier is such as to allow for the replacement of the old superstructure (which carried two traffic lanes in each direction) with two separate superstructures with the same number of lanes, but larger lane width, and an emergency lane. The structural intervention on the pier consists of the addition of two lateral extensions at the cap level, and of a strengthening of the foundation. Also, in this case the new deck is a continuous mixed steel-concrete beam.

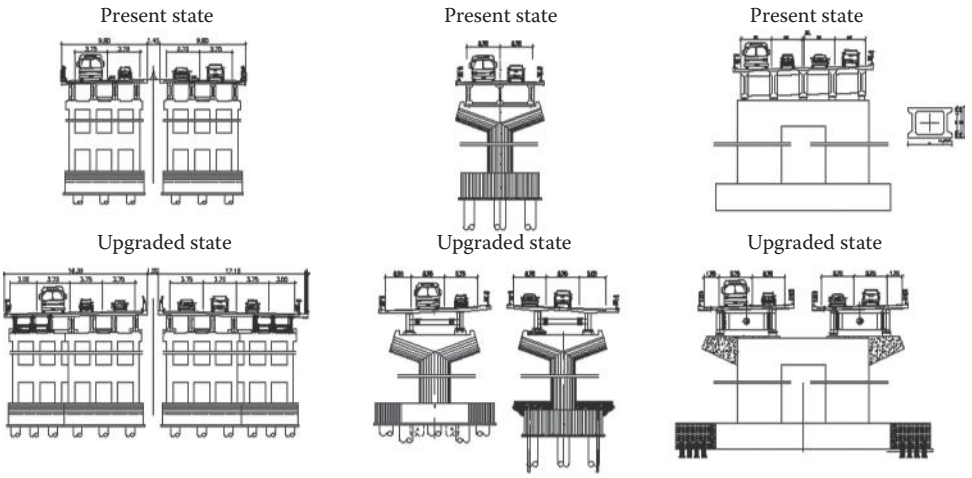

FIGURE 17.15 Situations arising in practice: widening of an existing deck (left), replacement of deck (middle), replacement of a single deck with separate decks for each direction (right). (Adapted from Pinto, P.E. and Franchin, P., *Journal of Earthquake Engineering,* 14(8), 1221–1252, 2010.)

17.4 Illustration of Selected Designs

All the bridges illustrated in this section belong to the same portion of the main North–South A1 highway in Italy. This old highway built in the 1960s is being upgraded either by widening the existing platform along the same axis or by modifying the route with larger curvature radii and smaller gradients. Seismic design was carried out prior to the release of the latest code in 2008, but the concessionaire decided to follow the general prescriptions of Eurocode 8 Parts 1 and 2, and later of the draft code issued in 2003 (PCM, 2003), for the upgrade works of this highway portion.

The first two selected bridges represent rather special examples of uncommon structural configuration and share the construction material, which is prestressed concrete. Lately, this choice has been tending to be confined to these kind of special bridges, while ordinary ones, even with important span lengths, are preferably built with composite steel-concrete girders with concrete piers. The last selected bridge exemplifies this typology.

17.4.1 Bridge over the Reno River

The A1 crosses the Reno River near Bologna at the foot of the Apennine range. The Reno crossing consists of two twin bridges that only slightly differ for the horizontal curve radius of 1400.0 m (4593 ft.) versus 1350.0 m (4429 ft.), and has a single-cell posttensioned concrete box girder, continuous for nine spans, with a total length of 32.75 + 5 × 45.0 + 90.0 + 135.0 + 90.0 = 574.50 m (107.4 + 5 × 147.6 + 295.3 + 442.9 + 295.3 = 1884.8 ft.) (Figure 17.16, top).

The box girder has a constant depth of 4.50 m (14.8 ft.) with a total deck width of 15.70 m (41.5 ft.) (Figure 17.16, bottom). The lateral slabs cantilever with a span of about 3.70 m, with a small variation close to the "Firenze" abutment to maintain a constant curvature radius of the box girder, which is incrementally launched from the opposite abutment.

Piers 1 to 6 have a concrete box cross section with overall dimensions of 9.0 × 3.0 m (29.5 × 9.8 ft.), with corner radius of 0.75 m (2.5 ft.), and constant wall thickness of 0.3 m. The heights of the piers vary from 10.0 m (32.8 ft.) of pier 1 to 13.50 m (44.3 ft.) of pier 6. Foundations are direct with a mat of 9.0 × 14.0 × 2.0 m (29.5 × 45.9 × 6.6 ft.) resting on consolidated ground (jet-grouting).

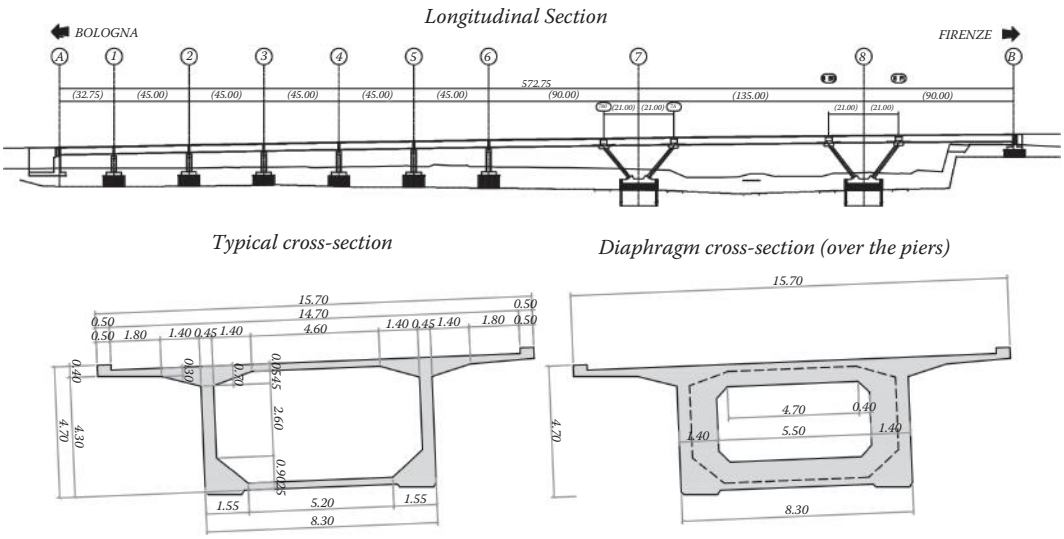

FIGURE 17.16 Viaduct over the Reno River on the A1 North–South highway: longitudinal section (top) typical cross sections (bottom).

The last two piers, number 7 and 8, are V-shaped with composite steel-concrete pylons inclined at 42° from the vertical (Figures 17.17 and 17.18). Each of the four pylons making up the pier is made up of concrete-filled tubes of 1.80 × 3.50 m (5.9 × 11.5 ft.) with 16 mm thickness. The foundations are again direct on consolidated ground, with a circular mat of 20.0 m diameter and variable thickness (from 2.50 m [8.2 ft.] to 3.00 m [9.8 ft.] in the central portion). The pylon connection with the foundation ensures flexural continuity. The pylons frame is also into the superstructure. As a result, piers 7 and 8 constitute a fixed point for the deck in the longitudinal direction. The superstructure is free to move on two flat sliders on each of the remaining piers, with a transverse restrainer provided at the center of the box girder.

The prescribed construction material properties are a minimum concrete cylinder strength of 35 MPa (5 ksi) (no less than 28 MPa (4 ksi) at posttensioning) for the deck, and 28 MPa (4 ksi) and 32 MPa (4.6 ksi), for piers 1 to 6 and piers 7 to 8, respectively. Steel grade is Italian FeB44k [B430 with a 430 MPa (62 ksi) characteristic yield stress] for ordinary reinforcement, and minimum ultimate tensile strength 1860 MPa (270 ksi) for prestressing reinforcement.

FIGURE 17.17 Viaduct over the Reno River on the A1 North–South highway: view of the completed viaduct at the river crossing (left) and view during the construction of the steel launching nose (right). (Courtesy of SPEA-Società Autostrade SpA, Italy.)

FIGURE 17.18 Viaduct over the Reno River on the A1 North–South highway: inclined composite steel-concrete pylons, positioning of the steel pipes (left) and concrete pouring (right). (Courtesy of SPEA-Società Autostrade SpA, Italy.)

As already mentioned, as far as the seismic design criteria are concerned, the bridge had been designed before the enforcement of the last design code and the associated hazard maps. Given its importance, however, the site seismicity had been determined with a site-specific hazard characterization, leading to a design PGA of 0.17g and a suite of natural ground motions recorded in the Apennine environment during the 1997 Umbria–Marche earthquakes. These records have been employed for the purpose of the linear response history analysis used for seismic design. Mass and initial stiffness proportional Rayleigh damping had been used with coefficients set for a 5% damping ratio at the first two vibration modes. The first mode, with a period of $T_1 = 1.19$ s, is longitudinal, while the second one, with a period of $T_2 = 0.81$ s, is transversal.

The target performance was elastic response at the design level earthquake.

17.4.2 Viaduct over the Aglio Creek

The bridge over the Aglio creek is a five-spans "Dywidag" frame, with the continuous variable-depth box girder built by balanced cantilever from the piers and solidarization at midspan (Figure 17.19). The total length is 77.0 + 3 × 148.0 + 77.0 = 598 m (252.6 + 3 × 385.6 + 252.6 = 1962.0 ft.). The bridge is horizontally curved with variable radius of minimum value 1000.0 m (3280 ft.).

The posttensioned concrete superstructure has depth variable according to a sine profile, from a maximum of 7.50 m (24.6 ft.) over the piers to a minimum of 3.0 m (9.8 ft.) at midspan. The deck slab width is equal to 19.70 m (64.6 ft.). The upper deck slab has a parabolically varying thickness from 0.65 m (26 in.) over the 0.60 m (24 in.) thick webs, down to 0.25 m (10 in.) at the slab midspan and the free edges of the cantilevers. The bottom slab thickness varies from 1.10 m (3.6 ft.) over the piers to 0.25m (10 in.) at the bridge midspan.

Piers' heights vary from 38.50 m (126.3 ft.) to 78.00 m (255.9 ft.). The bottom portion has a box section with wall thickness varying from 0.6 m (24 in.) to 1.20 m (48 in.), and external dimensions of 10.0 × 11.0 m (32.8 × 36.1 m). The upper portion, of height 20.0 m (65.6 ft.) for all piers, has a reduced open cross section made up of four blades stemming from the lower box section vertices (see Figure 17.19). Each blade has external dimensions of 1.20 × 4.25 m (3.9 × 13.9 ft.), with rounded corners.

Abutments consist of a two-cell, box-section stem of height about 10.0 m (32.8 ft.), and a rear wall continuing up to 14.0 m (45.9 ft.). The deck is supported on a pair of flat-sliders at the abutments, one

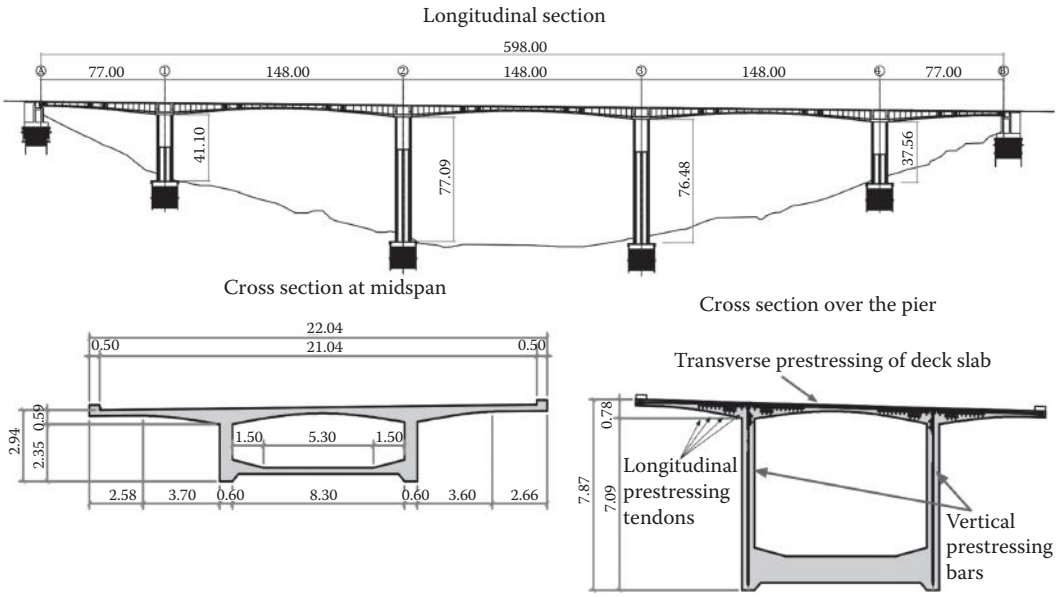

FIGURE 17.19 Viaduct over the Aglio creek on the A1 North–South highway: longitudinal section (top) and sample cross-sections (bottom). (Courtesy of SPEA-Società Autostrade SpA, Italy.)

FIGURE 17.20 Viaduct over the Aglio creek on the A1 North–South highway: view from abutment B (left) and cantilever construction from the piers (right). (Courtesy of SPEA-Società Autostrade SpA, Italy.)

of which is unidirectional to restrain transverse displacements. Shock absorbers are provided to resist longitudinal impulsive actions from earthquakes and braking forces.

Foundations, for both piers and abutments, are of the caisson type, with a diameter of 16.0 m (52.5 ft.) and depth variable between 20.0 m (65.6 ft.) and 35.0 m (114.8 ft.). The circular mat at the top of the caisson has a thickness of 3.0 m (9.8 ft.).

Prestressing of the posttensioned type is employed extensively. In particular, the deck according to the construction method is posttensioned with two orders of cables, one used during construction (Figure 17.20) with new cables added with each deck segment, and the second at the bottom chord put in tension after solidarization at midspan. Notably, prestressing is also used for the upper deck slab, the diaphragms and the webs, the latter posttensioned with vertical ϕ36 bars.

The prescribed construction materials properties are a minimum concrete cylinder strength of 45 MPa (6.5 ksi) (no less than 28 MPa [4 ksi] at post-tensioning) for the deck, and 32 MPa (4.6 ksi) and 45 MPa (6.5 ksi), for the blades and the lower portions of the piers, respectively. The minimum concrete strength for foundations and abutments is 28 Mpa (4 ksi). Steel grade is Italian FeB44k (B430 with a 430 MPa [62 ksi] characteristic yield stress) for ordinary reinforcement, and minimum ultimate tensile strength 1860 MPa (270 ksi) for prestressing reinforcement.

Seismic design criteria are the same as for the bridge over the Reno River. The site-specific hazard characterization led to a design PGA of 0.19 g and the same suite was employed for the purpose of the linear response history. Again, mass and initial stiffness proportional Rayleigh damping was used with coefficients set for a 5% damping ratio at the first two vibration modes. The first and second mode, with period $T_1 = 1.85$ s and $T_2 = 1.33$ s, are both transversal.

17.4.3 Rioveggio Interchange

One of the bridges making up the interchange in Rioveggio between the A1 highway and State Road 325 is shown in Figures 17.21 and 17.22. The bridge has a composite steel-concrete dual-girder deck continuous over the piers, of the curved plan for a total length (along the axis) equal to $31.30 + 2 \times 40 + 3 \times 36 + 27.85 = 247.15$ m ($102.7 + 2 \times 131.2 + 3 \times 118.1 + 91.4 = 810.8$ ft.). The concrete slab has a constant width of 12.50 m (41.0 ft.) carrying traffic lanes for 10.50 m (34.5 ft.). The cross section is an open box section, made torsionally rigid with lower chord bracings and transverse diaphragms at 4.0 m (13.1 ft.) intervals. The total section depth is 2.0 m (6.6 ft.), of which 0.3 m (12 in.) is the concrete

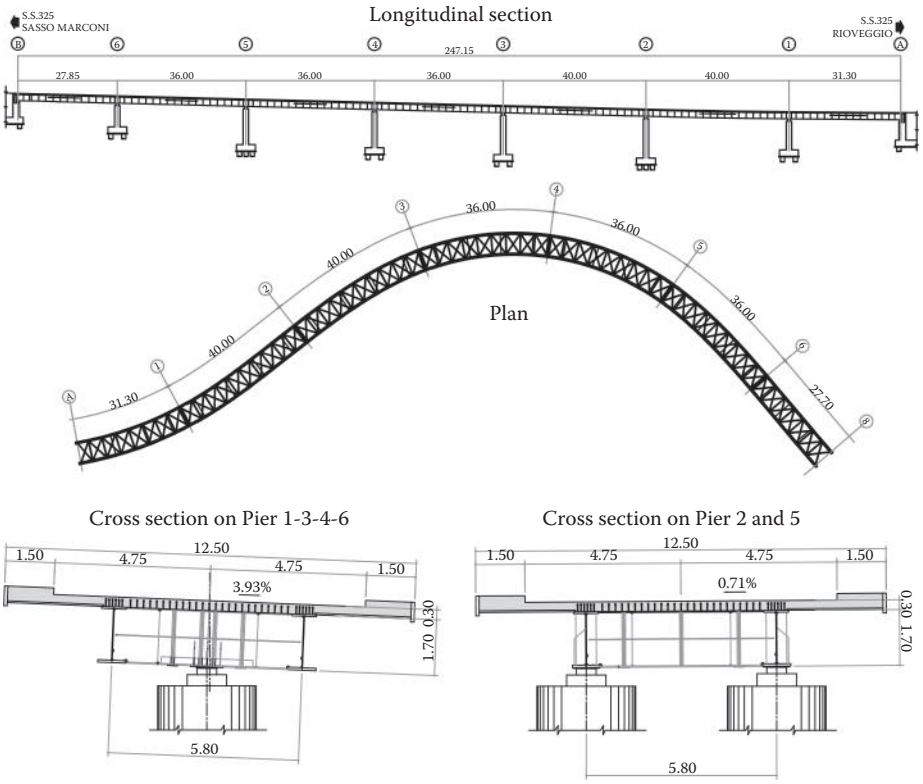

FIGURE 17.21 Rioveggio interchange on the A1 North–South highway: Longitudinal section (top), plan view at the level of the top and bottom horizontal bracings (middle) and cross sections (bottom). Top bracings are needed for the construction phase only. Note the stiffened-plate diaphragms at the supports. Diaphragms elsewhere are made of braces. (Courtesy of SPEA-Società Autostrade SpA, Italy.)

FIGURE 17.22 Rioveggio interchange on the A1 North–South highway: view of steel girders during construction. (Courtesy of SPEA-Società Autostrade SpA, Italy.)

slab, cast in situ over 5.0 cm (2 in.) thick predalles. The spacing between the two steel girders is 5.80 m (19.0 ft.). Transverse diaphragms at the piers and abutments are made of stiffened plates. Joints between the 27 girder segments of lengths varying between 10.125 m (33.2 ft.) and 12.50 m (41.0 ft.) are welded, while diaphragm braces are jointed with high-precision shear-only connections.

The bridge is seismically isolated by means of high-damping rubber bearings. To reduce torsional effects piers 1–3–4–6 are made of single RC stem and support a single isolator device, while piers 2 and 5 are made of two stems with one device each.

The prescribed construction materials properties are as follows: Fe510 corrosion-protected steel for both standard profiles and the plates of the built-up steel girders, having thicknesses t up to 75.0 mm, which has a design yield stress of $fd = 355.0$ MPa (51.5 ksi) for $t \leq 40.0$ mm (1.57 in.) and $fd = 315.0$ MPa (45.7 ksi) for $t > 40.0$mm (1.57 in.); steel St37-3K for the shear connectors; minimum concrete cylinder strength of 32 MPa (4.6 ksi) for the superstructure, and 28 MPa (4.0 ksi) and 25 MPa (3.6 ksi), for the piers/abutments and foundations, respectively. Steel grade is Italian FeB44k (B430 with a 430 MPa [62 ksi] characteristic yield stress) for ordinary reinforcement.

Seismic design has been carried out in compliance with the 2003 draft code (PCM, 2003). Design PGA was taken equal to 0.15g times an importance factor $\gamma_I = 1.3$. The soil was attributed to class B to which corresponds an amplification factor $S = 1.25$ constant over the spectrum. The ordinates of the response spectrum were reduced by $\eta = 0.82$ to account for an equivalent damping factor of 10% of the isolators. The design was carried out on the basis of the results of modal analysis with response spectrum, with two orthogonal components of the seismic action (directional combination with the "100/30" rule). The first four modes were considered for response analysis, yielding a cumulative participation mass ratio in both plan directions between 80% and 85%.

RC piers' stiffness was not reduced for cracking.

17.4.4 Other Bridges

The following pictures in Figures 17.23 through 17.25 illustrate two more examples of recent completion of the composite steel-concrete type, with deck continuous over the piers.

FIGURE 17.23 Viaduct in Morbegno on State Road 38 of the Stelvio Pass. (Courtesy of GP Ingegneria Srl, Italy.)

FIGURE 17.24 Viaduct in Morbegno on State Road 38 of the Stelvio Pass. (Courtesy of GP Ingegneria Srl, Italy.)

FIGURE 17.25 Viaducts over the Bollone creek on A1 North–South Highway. (Courtesy of SPEA-Società Autostrade SpA, Italy.)

References

Calvi, G.M., P.E. Pinto, P. Franchin, and R. Marnetto. 2009. The highway network in the area struck by the event, *Seismic Design (Progettazione Sismica)*, 03/English, 173–178.

CEN. 2005a. EN1998-2 Design of Structures for Earthquake Resistance Part 2 Bridges, European Committee for Standardization, Brussels, Belgium.

CEN. 2005b. PREN15129 Anti-seismic devices, European Committee for Standardization. Brussels, Belgium.

CEN. 2005c. EN1998-3 Design of Structures for Earthquake Resistance Part 3 Assessment and retrofitting of buildings, European Committee for Standardization, Brussels, Belgium.

CPTI working group. 2004. Parametric Catalogue of Italian Earthquakes (in Italian), version 2004 (CPTI04), INGV, Bologna.

Faccioli, E. and M Villani. 2009. Seismic Hazard Mapping for Italy in Terms of Broadband Displacement Response Spectra, *Earthquake Spectra,* 25(3), 515–539.

Kowalsky, M.J. and M.J.N. Priestley. 2000. Improved Analytical Model for Shear Strength of Circular Reinforced Concrete Columns in Seismic Regions, *ACI Structural Journal*, 97(3), 388–396.

Martinelli, F. and C. Meletti. 2008. A webGIS Application for Rendering Seismic Hazard Data in Italy, *Seismological Research Letters*, 79(1), 68–78.

Meletti, C., F. Galadini, G. Valensise, M. Stucchi, R. Basili, S. Barba, G. Vannucci, and E. Boschi. 2008. A Seismic Source Model for the Seismic Hazard Assessment of the Italian Territory, *Tectonophysics*, 450(1), 85–108.

MI Italian Ministry of Infrastructures. 2008. "New Technical Norms for Constructions" (in Italian), DM14/1/2008, Rome, Italy.

MI Italian Ministry of Infrastructures. 2009. "Commentary to the New Technical Norms for Constructions" (in Italian), DM1/2/2009, Rome, Italy.

PCM Italian Presidency of the Council of Ministers. 2003. "First Elements Regarding Criteria for Seismic Classification of the National Territory and Technical Norms for the Construction in Seismic Zones" (in Italian), OPCM3274/2003, Rome, Italy.

Pinto, P.E. and P. Franchin. 2010. Issues in the Upgrade of Italian Highway Structures, *Journal of Earthquake Engineering*, 14(8), 1221–1252.

Pinto, P.E., P. Franchin, and A. Lupoi. 2009. Seismic assessment and strengthening of existing bridges (in Italian), IUSSpress, Pavia, Italy.

Resemini, S. and S. Lagomarsino. 2004. On the seismic vulnerability of masonry arch bridges (in Italian), Proc. of XI National Congress "Earthquake Engineering in Italy," Genova, Italy.

Stucchi, M., C. Meletti, V. Montaldo, H. Crowley, G.M. Calvi, and E. Boschi. 2011. Seismic Hazard Assessment (2003–2009) for the Italian Building Code, *Bulletin of Seismological Society of America*, 101(4), 1885–1911.

Stucchi, M., P. Albini, C. Mirto, and A. Rebez. 2004. Assessing the Completeness of Italian Historical Earthquake Data. *Annals of Geophysics*, 47(2–3), 659–673.

Further Reading

fib International Federation of Structural Concrete. 2007. Seismic bridge design and retrofit – structural solutions, Bulletin 39, Lausanne, Switzerland.

Relevant Websites

The website of the main Italian highway concessionaire "Autostrade per l'Italia", with an overview of ongoing projects: http://www.autostrade.it/en/opere/interventi_incorso.html?initPos=2.

The seismic hazard database of Italy, available on a webGIS application: http://esse1-gis.mi.ingv.it/s1_en.php.

Information on Italian earthquakes, starting with the series of events that hit the Emilia region since May 20th, 2012 (the text of this chapter had already been completed when this earthquake struck): www.eqclearinghouse.it (some damage to bridges at: http://www.eqclearinghouse.org/2012-05-20-italy/2012/06/01/field-teams-finale-emilia-viaduct-29-05-2012/).

The 2008 Italian Technical Norms for Constructions (in Italian), from the site of the Ministry of Infrastructures: http://www.cslp.it/cslp/index.php?option=com_content&task=view&id=66&Itemid=20.

The 2004 Parametric Catalogue of Italian Earthquakes (in Italian), from the site of INGV: http://emidius.mi.ingv.it/CPTI04/.

18

Seismic Design Practice in Japan

Shigeki Unjoh
Public Works Research Institute, Japan

18.1 Introduction

Japan is one of the most seismically disastrous countries in the world and has often suffered significant damage from large earthquakes. The earthquake disaster prevention technology for highway bridges has been developed on the basis of such extensive damage experiences since the 1923 Kanto earthquake. Various provisions for designing bridges have been developed to mitigate damage due to the instability of soils such as soil liquefaction and the insufficient strength and ductility of structural members. Furthermore, design detailing including unseating prevention devices was introduced to prevent the total collapse of bridges against a large earthquake exceeding the design level. With development and improvement of seismic design provisions, damage to highway bridges caused by the earthquakes had been decreasing dramatically in recent years.

However, the Hyogo-ken nanbu (Kobe) earthquake of January 17, 1995, caused extensive damage to highway bridges. Collapse and near collapse of superstructures occurred at nine sites, and other destructive damage occurred at 16 sites (MOC, 1995a). Figure 18.1 shows one of the shocking collapses of viaducts. The bridge with length of over 635 m (2083 ft.) collapsed. The earthquake revealed that a number

FIGURE 18.1 Collapse of viaduct during the 1995 Hyogo-ken nanbu earthquake.

of critical issues must be revised in the seismic design and seismic retrofit of bridges (Kawashima, 1995; Kawashima and Unjoh, 1997). On the basis of the lessons learned from the Kobe earthquake through the various research and investigation, the seismic design methods were significantly revised in 1996 as the *Seismic Design Specifications for Highway Bridges* (JRA, 1996). The intensive earthquake ground motion observed during the Kobe earthquake has been considered in the design as well as the capacity and ductility design concepts. After that, the seismic design specifications were revised in 2002 by employing the performance-based design concept (JRA, 2002). The seismic design specifications are continuously being updated with the introduction of the recent bridge construction technology that was issued in 2012.

This chapter presents technical developments for seismic design and seismic retrofit of highway bridges in Japan. The history of the earthquake damage and development of the seismic design methods is described first. The damage caused by the 1995 Hyogo-ken nanbu earthquake and the lessons learned from the earthquake are then described. The current Seismic Design Specifications for Highway Bridges (JRA, 2002), which introduced the performance-based seismic design concept, is described. The seismic performance levels and design methods as well as the ductility design methods for reinforced concrete piers, steel piers, foundations, and bearing supports are described. Furthermore, the history of the past seismic retrofit practices is described. The seismic retrofit program after the 1995 Hyogo-ken nanbu earthquake is described with emphasis on the seismic retrofit of reinforced concrete piers. Finally, the effectiveness of the implementation of seismic retrofit through the past recent earthquakes is presented.

18.2 History of Earthquake Damage and Development of Seismic Design Methods

One year after the 1923 Great Kanto earthquake, consideration of the seismic effect in the design of highway bridges was initiated. The Civil Engineering Bureau of the Ministry of Interior (MOI) issued "The Method of Seismic Design of Abutments and Piers" in 1924. The seismic design method has been developed and improved through extensive experiences in a number of past earthquakes and with progress of technical developments in earthquake engineering. Table 18.1 summarizes the history of seismic design provisions for highway bridges.

TABLE 18.1 History of Seismic Design Provisions for Highway Bridges

		1926 Details of Road Structure (draft), Road Law, MIA	1939 Design Specifications of Steel Highway Bridges (draft), MIA	1956 Design Specifications of Steel Highway Bridges, MOC	1964 Design Specifications of Substructures (Pile Foundations), MOC	1964 Design Specifications of Steel Highway Bridges, MOC	1966 Design Specifications of Substructures (Survey and Design), MOC	1968 Design Specifications of Substructures (Piers and Direct Foundations), MOC	1970 Design Specifications of Substructures (Caisson Foundations), MOC	1971 Specifications for Seismic Design of Highway Bridges, MOC	1972 Design Specifications of Substructures (Cast-in-place Piles), MOC	1975 Design Specifications of Substructures (Pile Foundations), MOC	1980 Design Specifications of Highway Bridges, MOC	1990 Design Specifications of Highway Bridges, MOC	1996 Design Specifications of Highway Bridges, MOC	2002 Design Specifications of Highway Bridges, MLIT
Seismic loads	Level 1: Seismic coefficient (kh(g)) and seismic design spectra (Sa) for elastic design	Largest seismic loads	kh = 0.2 Varied dependent on the site	kh = 0.1–0.35 Varied dependent on the site and ground condition						kh = 0.1–0.3 Standardization dependent on zone, ground condition, and structural response characteristics				kh = 0.1–0.3 Integration of seismic coefficient method		
	Level 2: Seismic coefficient (kh(g)) and seismic design spectra (Sa) for ductility design													kh = 0.7–1.0 Plate boundry type large earthquake (Type I)	kh1 = 0.7–1.0, kh2 = 1.5–2.0 Plate boudnary type large earthquake (Type I), inland type earthquake (Type II)	
	Dynamic earth pressure	Equations proposed by Mononobe and Okabe were supposed to be used.					Provision of dynamic earth pressure								Provision of dynamic earth pressure for ductility design	
	Dynamic hydraulic pressure	Less effect on piers except high piers in deep water.						Provision of hydraulic pressure		Provision of dynamic hydraulic pressure						
Reinforced concrete column	Bending moment at bottom	Supposed to be designed in a similar way provided in current design method						Provisions of definite design method (allowable stress and analytical method)								
	Shear	Less effect on RC piers except those with smaller section area such as RC frame and hollow section						Provisions of definite design method (allowable stress and analytical method)					Provisions of definite design method check of shear strength		Reduction of allowable shear stress	
	Re-bar arrangement details: termination of main reinforcement at mid-height												Elongation of anchorage length of terminated reinforcement at mid-height and decrease of allowable shear stress		Shear strength and ductility enhancement (confinement details)	
	Ductility capacity							Less effect on RC piers with larger section area					Primitive ductility check methods	Detailed ductility check method	Improvemnet of ductility design method	
Steel column	Bending and shear					Based on allowable stress design method										
	Ductility capacity														Provision of ductility design method	
Foundations	Footing						Provisions of effective width and (designed as a cantilever plate)						Provisions of effective width and check of shear strength			
	Pile foundation		Bearing capacity in vertical direction condition was supposed to be checked.		Provisions of definite design method (Bearing capacity in vertical and horizontal directions)						Provisions of definite design method condition (foundation on slope, consolidation settlement, lateral movement)					
	Direct foundation		Stability (overturning and sliding) was supposed to be checked.				Provisions of definite design method (bearing capacity, stability analysis)									
	Caisson foundation				Supposed to be designed in a similar way provided in Design Specification of Caisson Foundation of 1969				Provisions of definite design method							
	Ductility capacity														Check of ductility capacity for pile and caisson foundations	
Soil liquefaction									Provisions of soil layers of which bearing capacity shall be ignored in seismic design				Provisions of evaluation method of soil liquefaction and the treatment in seismic design	Consideration of effect of fine sand content	Revision of evaluation method of soil liquefaction for level 2 earthquake design method against liquefaction-induced lateral spreading	
Bearing support	Bearing support		Provisions of design method for steel bearing supports (bearing, roller, anchor bolt)						Provision of transmitting method of seismic load at bearing						Revision of design method for level 2 earthquake	
	Unseating prevention devices							Provisions of bearings seat length S	Provisions of stopper at movable bearings, unseating prevention devices (seat length S, connection of adjacent girders)				Provisions of stopper at movable bearings, unseating prevention devices (seat length S, girder length SE, and devices)		Provision of enhanced unseating prevention devices	
Seismic isolation	Isolation bearings and Isolation design methods													Initiation of application of Menshin design	Provision of seismic isolation design using LRB and HDR	

In particular, the seismic design method was integrated and upgraded by compiling the "Specifications for Seismic Design of Highway Bridges" in 1971. The design method for soil liquefaction and unseating prevention devices was introduced in the specifications. It was revised in 1980 and integrated as "Part V: Seismic Design" in "Design Specifications of Highway Bridges." The primitive check method for ductility of reinforced concrete piers was included in the reference of the specifications. It was further revised in 1990 and ductility check of reinforced concrete piers, soil liquefaction, dynamic response analysis, and design detailing were induced. It should be noted here that the detailed ductility check method for reinforced concrete piers was first introduced in the 1990 Specifications.

However, the Hyogo-ken nanbu earthquake (M7.3) of January 17, 1995, exactly one year after the 1994 Northridge earthquake in California, caused destructive damage to highway bridges as described earlier. After the earthquake, the "Committee for Investigation on the Damage of Highway Bridges Caused by the Hyogo-ken nanbu Earthquake" was established in the Ministry of Construction (MOC) to investigate the damage and to identify the factors that caused the damage.

On February 27, 1995, the Committee approved the *Guide Specifications for Reconstruction and Repair of Highway Bridges Which Suffered Damage due to the Hyogo-ken nanbe Earthquake*, (MOC, 1995b) and the MOC announced on the same day that the reconstruction and repair of the highway bridges that suffered damage during the Hyogo-ken nanbu earthquake should be made according to the Guide Specifications. It was decided by the MOC on May 25, 1995, that the Guide Specifications should be tentatively used in all sections of Japan as emergency measures for seismic design of new highway bridges and seismic strengthening of existing highway bridges until the Design Specifications of Highway Bridges were revised (JRA, 1995).

In May 1995, the "Special Sub-Committee for Seismic Countermeasures for Highway Bridges" was established in the "Bridge Committee," Japan Road Association (JRA), to draft the revision of the Design Specifications of Highway Bridges. The new Design Specifications of Highway Bridges was approved by the Bridges Committee, and issued by the MOC on November 1, 1996 (JRA, 1996; Kawashima, Nakano, Nishikawa, et al., 1997). The specifications were revised on the basis of the lessons learned from the Hyogo-ken nanbu earthquake and the various research and investigation. The intensive earthquake ground motion with a short distance from the inland earthquakes with a magnitude of 7, as the Hyogo-ken nanbu earthquake had been, was added as one of the target design ground motions.

After that, research and investigations have continuously been made to update the design specification of highway bridges. The new design specifications of highway bridges were issued by the Ministry of Land, Infrastructure, Transport and Tourism (MLIT) on December 27, 2001, and were published with commentary from JRA in March 2002 (JRA, 2002; Unjoh, Nakatani, Tamura, et al., 2002). The revised specifications were targeted to employ the performance-based design concept and to enhance the durability of bridge structures for long-term use, along with inclusions of improved knowledge on the bridge design and construction methods after the 1996 Specifications.

The 2011 Great East Japan earthquake with moment magnitude of M_w 9.0 occurred on March 11, 2011. Destructive damage was caused by strong shaking and tsunami that occurred along the Pacific coast of east Japan. In particular, a huge tsunami attacked the coastal area and approximately 20,000 people were killed or missing, and 130,000 houses totally collapsed due to the devastating earthquake. Because of the extremely wide fault zone with an area of 500 km × 200 km (310 miles × 124 miles), numerous aftershocks occurred in sequence. Eight hundred and forty aftershocks with a magnitude of M4.0 or greater occurred; the largest aftershock with M7.6 was observed 60 days after the main shock. The aftershocks significantly affected the progress of the damage and caused a delay in the recovery works. In spite of such strong shaking, the damage to highway bridges was not significant and the bridges in general withstood such strong shaking well. This is because of the continuous improvement of seismic design methods and the continuous implementation of seismic retrofit for existing vulnerable bridges. On the other hand, several bridges in the coast line were washed away by the effect of strong tsunami. Research and investigations on the effect of tsunami on the bridges are now being urgently conducted.

18.3 Damage Due to the 1995 Hyogo-ken Nanbu Earthquake

The 1995 Hyogo-ken nanbu earthquake was the first earthquake that hit an urban area in Japan. Although the magnitude of the earthquake was moderate (M7.3), the ground motion was much larger than considered in the design specifications. It occurred very close to the Kobe City with shallow focal depth.

Damage occurred at highway bridges on Routes 2, 43, 171, and 176 of the National Highway, Route 3 (Kobe Line), and Route 5 (Bay Shore Line) of the Hanshin Expressway, and the Meishin and Chugoku Expressways. Damage was investigated for all bridges on National Highways and Expressways in the area where destructive damage occurred. The total number of piers surveyed reached 3396 (MOC, 1995a). Most of the damaged bridges were designed according to the 1964 Design Specifications or older ones. Although the seismic design methods had been improved and amended several times since 1924, only a requirement for lateral force coefficient that was used in static allowable stress design was provided in the 1964 Design Specifications or older ones.

Figure 18.2 compares the damage of piers (bridges) dependent on the applied design specifications. The degree of the damage was classified as A_s (collapse), A (near collapse), B (moderate damage), C (damage of secondary members), and D (minor or no damage). It should be noted in this comparison that the intensity of ground shaking in terms of response spectra was not the same for all of the surveyed piers. Keeping in mind such difference in ground motion, it is apparent from Figure 18.2 that about 9% of the piers based on pre-1980 design specifications suffered A_s or A damage, while no such damage was developed in the piers designs based on post-1980 design specifications.

Although the damage was more in the bridges designed according to the older design specifications, it was assumed that essential revision was required even in the recent design specifications to prevent damage against destructive earthquakes such as the Hyogo-ken nanbu earthquake. The main modifications were as follows:

1. Increase lateral capacity and ductility of all structural components in which seismic force is predominant so that ductility of a total bridge system is enhanced. For this purpose, it was required to upgrade the "Check of Ductility of Reinforced Concrete Piers," which has been in use since 1990, to a "Ductility Design Method," and to apply the Ductility Design Method to all structural components.
2. Include the ground motion observed at Kobe during the earthquake as a design force in the Ductility Design Method.

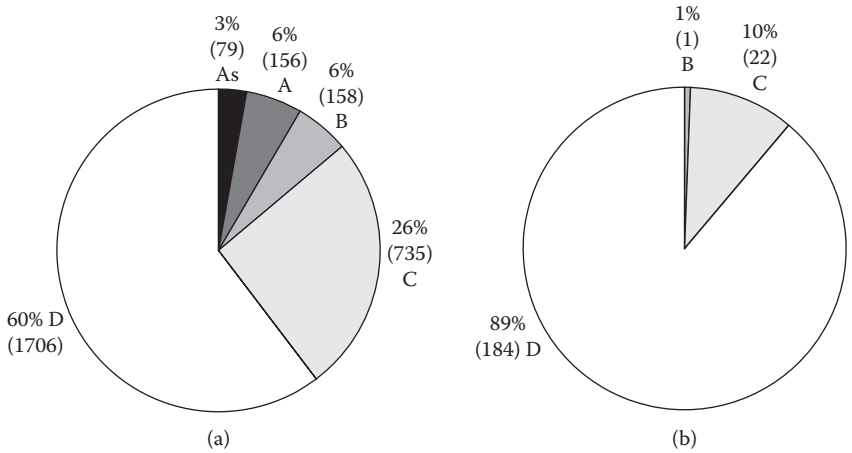

FIGURE 18.2 Comparison of the damage degree depending on applied design specifications (*As*: collapse, *A*: near collapse, *B*: moderate damage, *C*: damage of secondary members, *D*: minor or no damage). (a) Pre-1980 Design Specifications. (b) Post-1980 Design Specifications.

3. Specify input ground motions in terms of acceleration response spectra for dynamic response analysis more actively.
4. Increase tie reinforcements to introduce intermediate ties for increasing confinement and then ductility of piers. It was decided not to terminate longitudinal reinforcements at midheight to prevent premature shear failure, in principle.
5. Adopt multispan continuous bridges for increasing number of indeterminates of the total bridge system.
6. Adopt rubber bearings for absorbing lateral displacement between a superstructure and substructures and to consider correct mechanism of force transfer from a superstructure to substructures.
7. Include the Menshin (seismic isolation) design.
8. Increase strength, ductility, and the energy dissipation capacity of unseating prevention devices.
9. Consider the effect of lateral spreading associated with soil liquefaction in the design of foundations at the site vulnerable to lateral spreading.

The 1995 Hyogo-ken nanbu earthquake had a large impact on the earthquake disaster prevention measures in various fields. On the basis of the above lessons, Part V: Seismic Design of the Design Specifications of Highway Bridges (JRA) was totally revised in 1996, and the design procedure moved from the traditional elastic seismic coefficient methods with allowable stress approach to the ductility design method. Major revision of the 1996 Design Specifications was the introduction of the explicit two-level seismic design consisting of the seismic coefficient method and the ductility design method. Table 18.2 shows the seismic performance matrix provided in the 1996 Design Specifications. The bridges are categorized into two groups depending on their importance; standard bridges (Type A bridges) and important bridges (Type B bridges). The seismic performance level (SPL) is selected depending on the importance of bridges. For moderate ground motions induced in the earthquakes with a high probability of occurrence, both A and B bridges should behave in an elastic manner without essential structural damage (SPL 1). For extreme ground motions induced in earthquakes with a low probability of occurrence, Type A bridges should prevent critical failure (SPL 3), whereas Type B bridges should perform with limited damage (SPL2).

In the Ductility Design Method, two types of ground motions are considered. The first are the ground motions that could be induced in plate-boundary-type earthquakes with a magnitude of about 8. The ground motion at Tokyo in the 1923 Kanto earthquake was a typical target of this type of ground motion. The second is the ground motion developed in earthquakes with magnitudes of about 7 to 7.3 at very short distance. Obviously the ground motions at Kobe in the Hyogo-ken nanbu earthquake was a typical target of this type of ground motion. The first and the second ground motions were called Type I and Type II ground motions respectively. The recurrence time of Type II ground motion is generally longer than that of Type I ground motion.

The fact that lack of near-filed strong motion records prevented serious evaluation of the validity of recent seismic design codes is important. The Hyogo-ken nanbu earthquake revealed that the history

TABLE 18.2 Seismic Performance Matrix (Design Ground Motion and Seismic Performance Level)

Types of Design Ground Motions		Standard Bridges (Type A)	Important Bridges (Type B)
Level 1 earthquake: ground motions with a high probability of occurrence		SPL 1: Prevent damage	
Level 2 earthquake: ground motions with a low probability of occurrence	Interplate earthquakes (Type-I)	SPL 3: Prevent critical damage	SPL 2: Limited damage for function recovery
	Inland earthquakes (Type-II)		

Note: SPL: Seismic Performance Level

of strong motion recording is very short, and that no near-field records have yet been measured by an earthquake with a magnitude on the order of 8. It is therefore essential to have sufficient redundancy and ductility in a total bridge system.

18.4 2002 Seismic Design Specifications of Highway Bridges

18.4.1 Performance-Based Design Specifications

For the purpose of responding to the international harmonization of design codes and flexible applications of newly developed structures and construction methods, the JRA Design Specifications were revised on the basis of the performance design concept in 2002 (JRA, 1995). The performance-based design concept is that the performance requirements and the verification policies are clearly specified. The 2002 Design Specifications employed such style to specify both the requirements and the acceptable solutions including detailed performance verification methods. Most of the design methods and detailing specified in the 1996 Design Specifications were placed as one of the acceptable solutions that satisfied the requirements. For example, the analysis method to evaluate the response against loads is placed as one of the verification methods or acceptable solutions. Therefore, designers can propose new ideas or select other design methods with necessary verification data. In future, the acceptable solutions will be increased and widened with an increase in the verification data of new ideas on materials, structures, and construction methods.

18.4.2 Basic Principle of Seismic Design

Figure 18.3 shows the performance-based code structure of the 2002 Design Specifications. The static and dynamic verification methods of the seismic performance as well as the evaluation methods of the strength and ductility capacity of bridge components are placed as the verification methods and the acceptable solutions, which can be modified by the designers with the verifications data.

The same seismic performance matrix as that specified in 1996 Specifications, as shown in Table 18.2, was provided in the 2002 Design Specifications. Two levels of ground motions such as moderate ground motions induced in earthquakes with a high probability of occurrence (Level 1 earthquake) and intensive ground motions induced in earthquakes with a low probability of occurrence (Level 2 earthquake) are considered.

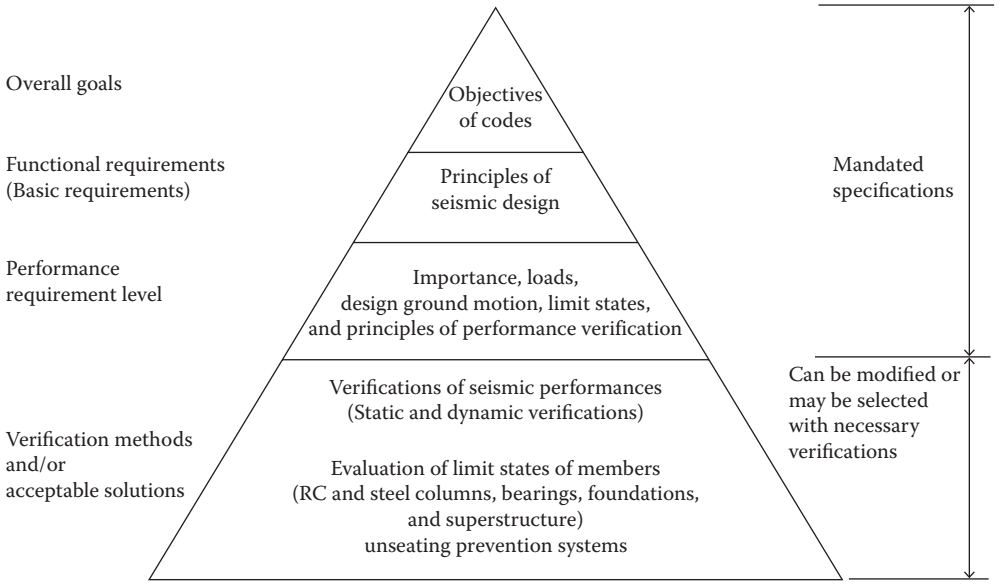

FIGURE 18.3 Code structure of 2002 JRA Seismic Design Specifications.

TABLE 18.3 Key Issues of Seismic Performance

			Repairability	
SPL	Safety	Functionability	Short Term	Long Term
SPL 1 Prevent damage	Safety against unseating of superstructure	Same function as before earthquake	No need of repair for function recovery	Simple repair
SPL 2 Limited damage for function recovery	Safety against unseating of superstructure	Early function recovery can be made	Function recovery can be made by temporary repair	Relatively easy permanent repair work can be made
SPL 3 Prevent critical damage	Safety against unseating of superstructure	–	–	–

Depending on the importance of the bridge, the target performance is selected from three categories of (1) SPL 1: prevent damage, (2) SPL 2: limited damage for function recovery, and (3) SPL 3: prevent critical damage. Table 18.3 shows key issues to consider the target seismic performances including safety, functionality, and reparability. Safety is the capability to prevent collapse of bridges and not to affect drivers seriously. Functionality is the capability to be used soon even if the bridge has been damaged during earthquakes. Repairability is the capability to be repaired easily after the earthquakes. Repairability includes short-term function recovery and long-term permanent repair.

18.4.3 Design Ground Motions

Design ground motions are specified as follows:

$$S = c_Z \cdot c_D \cdot S_0 \tag{18.1}$$

$$S_I = c_Z \cdot c_D \cdot S_{I0} \tag{18.2}$$

$$S_{II} = c_Z \cdot c_D \cdot S_{II0} \tag{18.3}$$

where S = acceleration response spectrum for level 1 earthquake, S_I and S_{II} = acceleration response spectra for Type I and Type II ground motions of level 2 earthquake, S_0 = standard acceleration response spectrum for level 1 earthquake, S_{I0} and S_{II0} = standard acceleration response spectrum for Type I and Type II ground motions of level 2 earthquake, respectively, c_Z = modification coefficient for zone, and c_D = modification coefficient for damping ratio h given as follows:

$$c_D = \frac{1.5}{40h+1} + 0.5 \tag{18.4}$$

Table 18.4 and Figure 18.4 show the standard acceleration response spectra (damping ratio $h = 0.05$) for level 1 earthquake, and Type I and Type II ground motions of level 2 earthquake.

The site-specific design ground motions are considered if the ground motion can be appropriately estimated on the basis of the information on the earthquake including past history and the location and detailed condition of the active faults and ground conditions including the transmitting condition from the faults to the construction sites. The site-specific design ground motion is necessary to be developed on the basis of accurate information on the earthquake faults and ground conditions as well as the verified evaluation methodology of the fault-induced ground motions. However, the area to get such detailed information in Japan is very limited so far. Therefore, continuous investigations and research are needed on this issue.

TABLE 18.4 Standard Acceleration Response Spectra

Ground Type	S_0 (gal) with Natural Period T(s)		
	(a) Level 1 Earthquake: S_0		
Class I	$S_o = 431T^{1/3}$ ($S_o \geqq 160$) for $T < 0.1$	$S_o = 200$ for $0.1 \leqq T \leqq 1.1$	$S_o = 220/T$ for $1.1 < T$
Class II	$S_o = 427T^{1/3}$ ($S_o \geqq 200$) for $T < 0.2$	$S_o = 250$ for $0.2 \leqq T \leqq 1.3$	$S_o = 325/T$ for $1.3 < T$
Class III	$S_o = 430T^{1/3}$ ($S_o \geqq 240$) for $T < 0.34$	$S_o = 300$ for $0.34 \leqq T \leqq 1.5$	$S_o = 450/T$ for $1.5 < T$
	(b) Level 2 Earthquake (Type I Ground Motions): S_{I0}		
Ground Type	S_{I0} (gal) with Natural Period T(s)		
Class I	$S_{I0} = 700$ for $T \leqq 1.4$		$S_{I0} = 980/T$ for $1.4 < T$
Class II	$S_{I0} = 1505T^{1/3}$ ($S_o \geqq 700$) for $T < 0.18$	$S_{I0} = 850$ for $0.18 \leqq T \leqq 1.6$	$S_{I0} = 1306T$ for $1.6 < T$
Class III	$S_{I0} = 1511T^{1/3}$ ($S_0 \geqq 700$) for $T < 0.29$	$S_{I0} = 1000$ for $0.29 \leqq T \leqq 2.0$	$S_{I0} = 2000/T$ for $2.0 < T$
	(c) Level 2 Earthquake (Type II Ground Motions): S_{II0}		
Ground Type	S_{II0} (gal) with Natural Period T(s)		
Class I	$S_{II0} = 4463T^{2/3}$ for $T < 0.3$	$S_{II0} = 2000$ for $0.3 \leqq T \leqq 0.7$	$S_{II0} = 1104/T^{5/3}$ for $0.7 < T$
Class II	$S_{II0} = 3224T^{2/3}$ for $T < 0.4$	$S_{II0} = 1750$ for $0.4 \leqq T \leqq 1.2$	$S_{II0} = 2371/T^{5/3}$ for $1.2 < T$
Class III	$S_{II0} = 2381T^{2/3}$ for $T < 0.5$	$S_{II0} = 1500$ for $0.5 \leqq T \leqq 1.5$	$S_{II0} = 2948/T^{5/3}$ for $1.5 < T$

18.4.4 Seismic Performance Verification

18.4.4.1 Seismic Performance Level and Limit States

To achieve the required performance in the design, it is necessary to select and determine the limit states of highway bridges that satisfy the corresponding seismic performance levels. For example, the basic principles to determine the limit state for SPL 2 is as follows: (1) plastic hinges should be developed only at expected portions and the capacity of plastic hinges should be determined so that the damaged members can be repaired relatively easily and quickly without replacement of main members, (2) location of plastic hinges should be selected at portions where appropriate energy absorption is made and where the repair can be made relatively easily, (3) considering structural conditions, the members with plastic hinges should be appropriately arranged and the limit states of the members with plastic hinges should be determined appropriately. Figure 18.5 shows general ideas on the arrangement of the location of plastic hinges and the limit states of the members for ordinary bridges. The examples of bridges with single-column piers, Menshin (seismic isolation) bridges, bridges with wall-type piers, and rigid frame bridges are shown.

18.4.4.2 Verification Methods of Seismic Performance

Figure 18.5 shows the flowchart of seismic design of highway bridges. It is the fundamental policy of the verification of seismic performance that the response of the bridge structures against design earthquake ground motions should not exceed the specified limit states.

Table 18.5 shows the applicable verification methods of seismic performance. In the seismic design of highway bridges, it is important to provide the strength and ductility capacities to appropriately resist the intensive earthquakes. The verification methods are based on the static analysis and dynamic analysis. In the 2002 Design Specifications, seismic coefficient method, ductility design method, and dynamic analysis are specified and these design methods are selected on the basis of the complexity of the dynamic response characteristics of highway bridges.

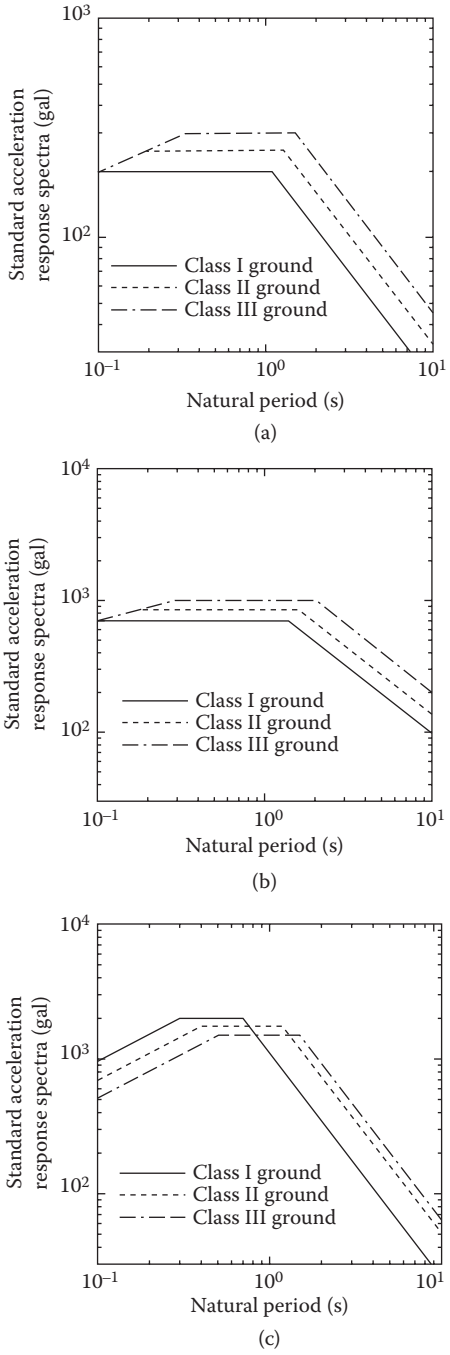

FIGURE 18.4 Standard acceleration response spectra (Class I Ground: stiff ground, Class II Ground: medium ground, Class III Ground: soft ground). (a) Level 1 Earthquake: S_0. (b) Level 2 Earthquake (Type I Ground Motions): S_{I0}. (c) Level 2 Earthquake (Type II Ground Motions): S_{II0}.

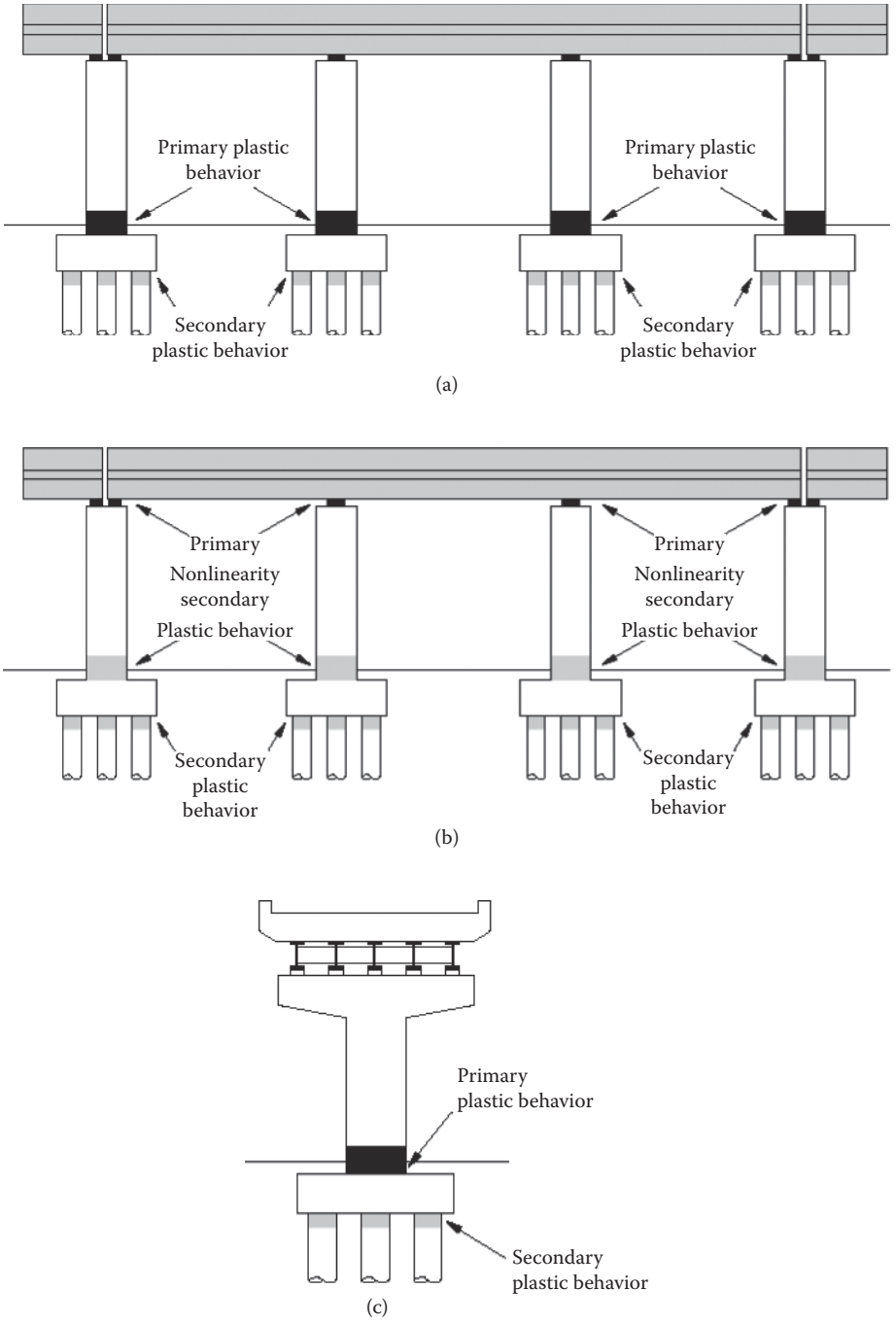

FIGURE 18.5 Examples of designed locations of primary plastic hinges or primary nonlinearity. (a) Bridges with single-column piers (in longitudinal direction to the bridge axis). (b) Menshin bridges (in longitudinal direction to the bridge axis). (c) Bridges with single-column piers (in transverse direction to the bridge axis).

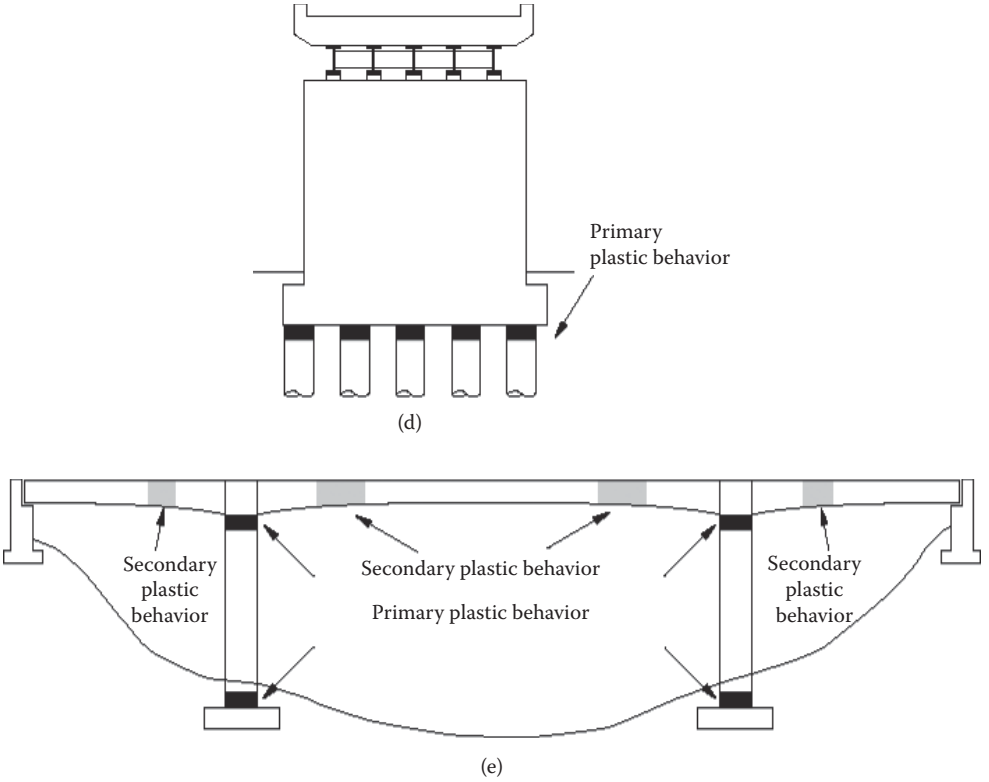

FIGURE 18.5 (Continued) Examples of designed locations of primary plastic hinges or primary nonlinearity. (d) Bridges with wall-type piers (in transverse direction to the bridge axis). (e) Rigid frame bridges (in longitudinal direction to the bridge axis).

TABLE 18.5 Applicable Verification Methods of Seismic Performance Depending on Earthquake Response Characteristics of Bridge Structures

Dynamic Characteristics SPL to be Verified	Bridges with Simple Configuration	Bridges with Multiplastic Hinges and without Verification of Applicability of Energy Constant Rule	Bridges with Limited Application of Static Analysis	
			With Multimode Response	Bridges with Complicated Configuration
SPL 1	Static verification	Static verification	Dynamic verification	Dynamic verification
SPL 2/SPL 3		Dynamic verification		
Example of bridges	Bridges other than right columns	1. Bridges with rubber bearings to distribute inertia force of superstructures 2. Seismically isolated bridges 3. Rigid frame bridges 4. Bridges with steel columns	1. Bridges with long natural period 2. Bridge with high piers	1. Cable-stayed bridges, suspension bridges 2. Arch bridges 3. Curved bridges

The static verification methods including the seismic coefficient method and the ductility design method are applicable for the bridges with simple configuration and single predominant mode. The dynamic verification method is applied for bridges with a complex configuration, that is, for such cases where the applicability of the static verification methods is limited. In the 2002 Design Specifications, the applicability of the dynamic analysis is widened and the dynamic verification method is expected to be mainly used for the seismic design with appropriate design consideration. The general conditions to employ the dynamic analytical method include the following cases:

1. Principal mode shapes that contribute to bridge response are different from the ones assumed in the static verification methods.
2. More than two modes significantly contribute to bridge response.
3. Primary plastic hinges form at more than two locations.
4. Locations of the development of primary plastic hinges are difficult to estimate because of complex structural configuration.
5. Applicability of the static analytical method based on the equal energy principle to estimate the nonlinear response is not yet verified.

18.4.5 Design Methods

Bridges are designed by both the seismic coefficient method and the ductility design method when the static analytical method is applicable as shown in Figure 18.6. In the seismic coefficient method, a lateral force coefficient ranging from 0.2 to 0.3 has been used based on the allowable stress design approach.

In the ductility design method, assuming that a principal plastic hinge is formed at the bottom of pier as shown in Figure 18.5a and d and applying the equal energy principle, a bridge is designed so that the following requirement is satisfied.

$$k_{hc} \cdot W \leq P_a \tag{18.5}$$

where

$$k_{hc} = c_S \cdot c_z \cdot k_{hc0} \tag{18.6}$$

$$c_S = \frac{1}{\sqrt{2\mu_a - 1}} \tag{18.7}$$

$$W = W_U + c_P W_P \tag{18.8}$$

where k_{hc} = lateral force coefficient, W = equivalent weight, P_a = lateral capacity of a pier, c_S = modification coefficient for nonlinear response characteristics, c_Z = modification coefficient for zone, which is 0.7, 0.85, and l.0 depending on the zone, k_{hc0} = standard lateral force coefficient, μ_a = allowable displacement ductility factor of a pier, W_U = weight of a part of a superstructure supported by a pier, W_P = weight of a pier, and c_P = coefficient depending on the type of failure mode of a pier. c_P is 0.5 for a pier in which either flexural failure or shear failure is developed after flexural cracks, and 1.0 for a pier in which shear failure is developed. The lateral capacity of a pier, P_a, is defined as a lateral force at the gravity center of a superstructure.

For Type B bridges, residual displacement developed at a pier after an earthquake must be checked as

$$\delta_R \leq \delta_{Ra} \tag{18.9}$$

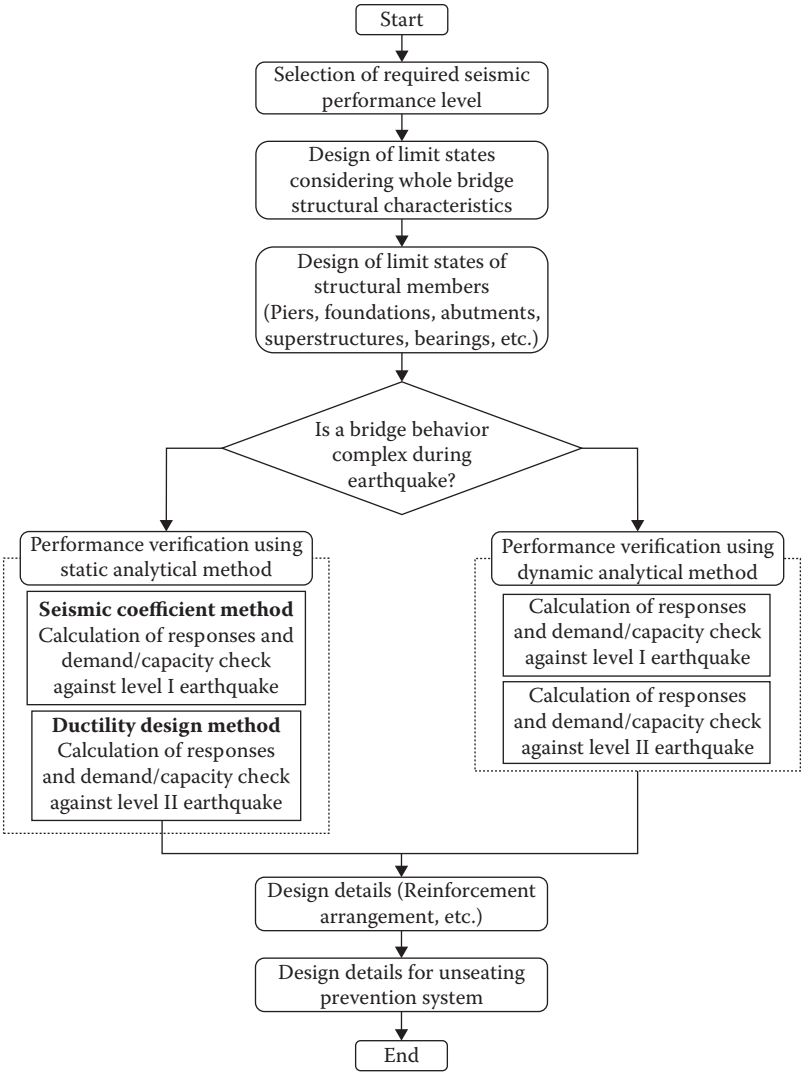

FIGURE 18.6 Flowchart of seismic design.

where

$$\delta_R = c_R(\mu_r - 1)(1-r)\delta_y \tag{18.10}$$

$$\mu_r = \frac{1}{2}\left\{\left(\frac{c_z k_{hc0} W}{P_a}\right)^2 + 1\right\} \tag{18.11}$$

where δ_R = residual displacement of a pier after an earthquake, δ_{Ra} = allowable residual displacement of a pier, r = bilinear factor defined as a ratio between the first stiffness (yield stiffness) and the second stiffness (post-yield stiffness) of a pier, c_R = coefficient depending on the bilinear factor r, μ_r = response ductility factor of a pier, and δ_y = yield displacement of a pier. δ_{Ra} should be 1/100 of the distance between the bottom of a pier and the gravity center of a superstructure.

18.4.6 Design Seismic Force

Table 18.6 shows standard lateral force coefficients k_{hc0} in Equation 18.6 for Type I and Type II ground motions. Type I ground motions have been used since 1990 (1990 Design Specifications), while Type II ground motions were introduced in the 1996 Design Specifications just after the Hyogo-ken nanbu earthquake. It should be noted here that k_{hc0} at stiff site (Class I Ground) has been assumed to be smaller than k_{hc0} at moderate (Class II Ground) and soft soil (Class III Ground) sites in Type I ground motions. Type I ground motions were essentially estimated from an attenuation equation for response spectra that were derived from a statistical analysis of 394 components of strong motion records. Type II ground motions were determined by simply taking envelopes of response accelerations of major strong motions recorded at Kobe during the Hyogo-ken nanbu earthquake.

Although the acceleration response spectral intensity at short natural period is higher in Type II ground motions than in the Type I ground motions, the duration of extreme accelerations excursion is longer in Type I ground motions than in Type II ground motions. As will be described later, such a difference in the duration has been taken into account to evaluate the allowable displacement ductility factor of a reinforced concrete pier considering the effect of number of cyclic loadings.

18.4.7 Ductility Design of Reinforced Concrete Piers

18.4.7.1 Evaluation of Failure Mode and Lateral Capacity

In the ductility design of reinforced concrete piers, the failure mode of the pier is evaluated as the first step. Failure modes are categorized into three types based on the flexural and shear capacities of the pier as follows:

$$\left\{\begin{array}{ll} P_u \leq P_s & \text{- bending failure} \\ P_s < P_u \leq P_{s0} & \text{- bending to shear failure} \\ P_{s0} < P_u & \text{- shear failure} \end{array}\right\} \tag{18.12}$$

where P_u = bending capacity, P_s = shear capacity in consideration of the effect of cyclic loading, and P_{s0} = shear capacity without consideration of the effect of cyclic loading. The lateral capacity of the reinforced concrete piers is determined according to the failure mode as follows:

TABLE 18.6 Standard Lateral Force Coefficient k_{hc0} for Ductility Design Method

Ground Type	Lateral Force Coefficient k_{hc0}		
	(a) Level 2 Earthquake (Type I Ground Motions)		
Class I	$k_{hc0} = 0.7$ for $T \leqq 1.4$		$k_{hc0} = 0.876T^{-2/3}$ for $1.4 < T$
Class II	$k_{hc0} = 1.51T^{1/3}$ ($k_{hc0} \geqq 0.7$) for $T < 0.18$	$k_{hc0} = 0.85$ for $0.18 \leqq T \leqq 1.6$	$k_{hc0} = 1.16T^{-2/3}$ for $1.6 < T$
Class III	$k_{hc0} = 1.51T^{1/3}$($k_{hc0} \geqq 0.7$) for $T < 0.29$	$k_{hc0} = 1.0$ for $0.29 \leqq T \leqq 2.0$	$k_{hc0} = 1.59T^{-2/3}$ for $2.0 < T$
	(b) Level 2 Earthquake (Type II Ground Motions)		
Ground Type	Lateral Force Coefficient k_{hc0}		
Class I	$k_{hc0} = 4.46T^{2/3}$ for $T \leqq 0.3$	$k_{hc0} = 2.00$ for $0.3 \leqq T \leqq 0.7$	$k_{hc0} = 1.24T^{-4/3}$ for $T > 0.7$
Class II	$k_{hc0} = 3.22T^{2/3}$ for $T < 0.4$	$k_{hc0} = 1.75$ for $0.4 \leqq T \leqq 1.2$	$k_{hc0} = 2.23T^{-4/3}$ for $1.2 < T$
Class III	$k_{hc0} = 2.38T^{2/3}$ for $T < 0.5$	$k_{hc0} = 1.5$ for $0.5 \leqq T \leqq 1.5$	$k_{hc0} = 2.57T^{-4/3}$ for $1.5 < T$

$$P_a = \begin{cases} P_u & \text{- bending failure } (P_c < P_u) \\ P_u & \text{- bending to shear failure} \\ P_{s0} & \text{- shear failure} \end{cases} \tag{18.13}$$

where P_c = bending capacity to develop crack.

18.4.7.2 Displacement Ductility Factor

The allowable displacement ductility factor of a pier, μ_a, in Equation 18.7 is dependent on the failure mode and that for a pier with the bending failure is evaluated as follows:

$$\mu_a = 1 + \frac{\delta_u - \delta_y}{\alpha \delta_y} \tag{18.14}$$

where α = safety factor, δ_y = yield displacement of a pier, and δ_u = ultimate displacement of a pier. Along with the lateral capacity of a pier, P_a, in Equation 18.5, δ_y and δ_u are defined at the gravity center of a superstructure. For a reinforced concrete single pier, as shown in Figure 18.5a and d, the ultimate displacement, δ_u, is evaluated as follows:

$$\delta_u = \delta_y + \left(\phi_u - \phi_y\right) L_p \left(h - \frac{L_p}{2}\right) \tag{18.15}$$

where ϕ_y = yield curvature of a pier at the bottom, ϕ_u = ultimate curvature of a pier at the bottom, h = height of a pier, and L_P = plastic hinge length of a pier. The plastic hinge length is given as follows:

$$L_p = 0.2h - 0.1D \quad (0.1D \le L_p \le 0.5D) \tag{18.16}$$

where D is the width or the diameter of a pier.
The yield curvature ϕ_y and ultimate curvature ϕ_u in Equation 18.15 are evaluated assuming stress–strain relations of reinforcements and concrete as shown in Figure 18.7. The stress σ_c ~ strain ε_c relation of concrete with lateral confinement is assumed to be as follows:

$$\sigma_c = \begin{cases} E_c \varepsilon_c \left[1 - \frac{1}{n}\left(\frac{\varepsilon_c}{\varepsilon_{cc}}\right)^{n-1}\right] & \varepsilon_c \le \varepsilon_{cc} \\ \sigma_{cc} - E_{des}\left(\varepsilon_c - \varepsilon_{cc}\right) & \varepsilon_{cc} < \varepsilon_c \le \varepsilon_{cu} \end{cases} \tag{18.17}$$

$$n = \frac{E_c \varepsilon_{cc}}{E_c \varepsilon_{cc} - \sigma_{cc}} \tag{18.18}$$

where σ_{cc} = maximum strength of the confined concrete, E_c = elastic modules of the concrete, ε_{cc} = strain at maximum strength, and E_{des} = gradient at descending branch. In Equation 18.17, σ_{cc}, ε_{cc}, and E_{des} are determined as

$$\sigma_{cc} = \sigma_{ck} + 3.8\alpha\rho_s\sigma_{sy} \tag{18.19}$$

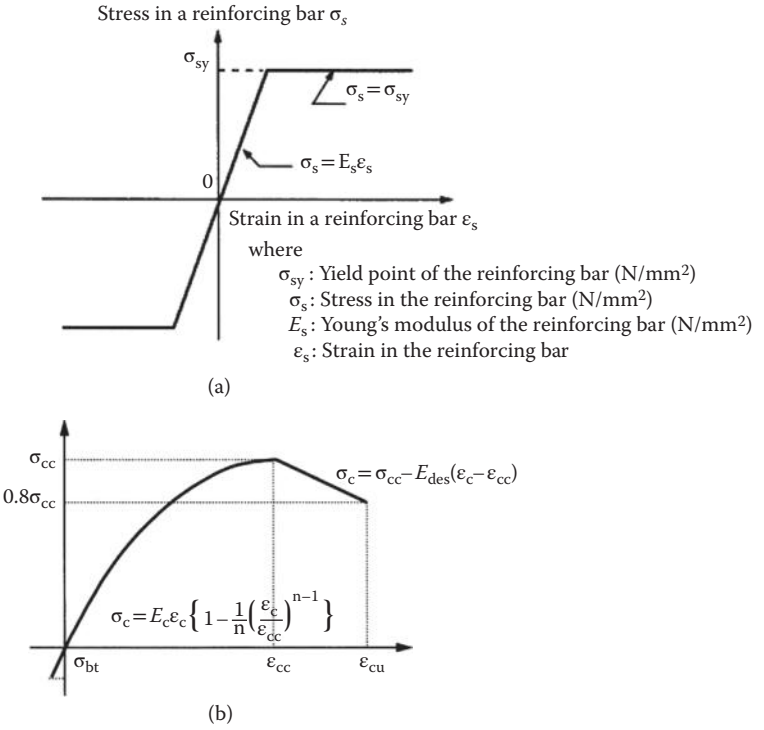

FIGURE 18.7 Stress and strain relations of reinforcing bars and confined concrete. (a) Reinforcing bars. (b) Concrete.

$$\varepsilon_{cc} = 0.002 + 0.033\beta\frac{\rho_s\sigma_{sy}}{\sigma_{ck}} \tag{18.20}$$

$$E_{des} = 11.2\frac{\sigma_{ck}^2}{\rho_s\sigma_{ck}} \tag{18.21}$$

where σ_{ck} = design strength of the concrete, σ_{sy} = yield strength of reinforcements, α and β = coefficients depending on the shape of a pier (α =1.0 and β =1.0 for a circular pier, and α = 0.2 and β = 0.4 for a rectangular pier), and ρ_s = tie reinforcement ratio defined as follows:

$$\rho_s = \frac{4A_h}{sd} \le 0.018 \tag{18.22}$$

where A_h = sectional area of tie reinforcement, s = space of tie reinforcements, and d = effective height of section.

The ultimate curvature, ϕ_u, is defined as a curvature when the concrete strain train, ε_c, at longitudinal reinforcing bars in compression reaches an ultimate strain, ε_{cu}, defined as follows:

$$\varepsilon_{cu} = \begin{cases} \varepsilon_{cc} & \text{for Type I ground motion} \\ \varepsilon_{cc} + \dfrac{0.2\sigma_{cc}}{E_{des}} & \text{for Type II ground motion} \end{cases} \tag{18.23}$$

TABLE 18.7 Safety Factor α

Types of Bridges	Type I Ground Motions	Type II Ground Motions
Type B	3.0	1.5
Type A	2.4	1.2

where ε_{cc} and σ_{cc} = strain and stress of the confined concrete at maximum strength. It is important to note that the ultimate strain, ε_{cu}, depends on the types of ground motions; ε_{cu} for Type II ground motions is larger than that for Type I ground motions. On the basis of a loading test, it is known that a certain level of failure in a pier such as a sudden decrease of lateral capacity occurs at smaller lateral displacement in a pier subjected to a loading hysteresis with more number of load reversals. To reflect such a fact, it was decided that the ultimate strain, ε_{cu}, should be evaluated by Equation 18.23, depending on the type of ground motions. Therefore, the allowable ductility factor, μ_a, depends on the type of ground motions; μ_a is larger for a pier subjected to Type II ground motions than a pier subjected to Type I ground motions.

It should be noted that the safety factor α in Equation 18.14 depends on the type of bridges as well as the type of ground motions as shown in Table 18.7. This is to preserve higher seismic safety in the important bridges, and to take account of the difference of recurrent time between Type I and Type II ground motions. The displacement ductility factors for piers with bending to shear failure and shear failure should be 1.0 to prevent brittle failure.

18.4.7.3 Shear Capacity

Shear capacity of reinforced concrete piers is evaluated by a conventional method as follows:

$$P_s = S_c + S_s \tag{18.24}$$

$$S_c = c_c c_e c_{pt} \tau_c bd \tag{18.25}$$

$$S_s = \frac{A_w \sigma_{sy} d(\sin\theta + \cos\theta)}{1.15a} \tag{18.26}$$

where P_s = shear capacity, S_c = shear capacity shared by concrete, S_s = shear capacity shared by shear reinforcements, τ_c = shear stress capacity shared by concrete, c_c = modification factor for cyclic loading (0.6 for Type I ground motions, 0.8 for Type II ground motions), c_e = modification factor for scale effect of effective height of section, c_{pt} = modification factor for longitudinal reinforcement ratio, b, d = width and effective height of section, Aw = sectional area of shear reinforcement, σ_{sy} = yield strength of shear reinforcement, θ = angle between the vertical axis and shear reinforcement, and a = space of shear reinforcements.

The modification factor on scale effect of effective width, c_e, was based on the experimental study of loading tests of beams with various effective heights and was introduced from the 1996 Design Specifications. Table 18.8 shows the modification factor on the scale effect.

18.4.7.4 Arrangement of Reinforcement

Figure 18.8 shows the suggested arrangement of tie reinforcements for various shapes of the section. Tie reinforcements should be deformed bars with a diameter equal to or larger than 13 mm (0.51 in.), and it should be placed in most bridges at a distance of not more than 150 mm (5.9 in.). In special cases, such as bridges with pier height more than 30 m, the distance of tie reinforcement may be

TABLE 18.8 Modification Factor on Scale Effect for Shear Capacity Shared by Concrete

Effective Height of Section d (m)	Coefficient ce
$d \leqq 1$	1.0
$d = 3$	0.7
$d = 5$	0.6
$d \geqq 10$	0.5

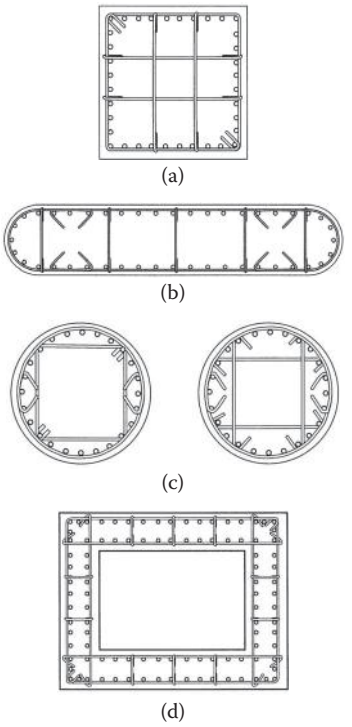

FIGURE 18.8 Confinement of core concrete by tie reinforcement. (a) Square section. (b) Semisquare section. (c) Circular section. (d) Hollow section.

increased at height so that the pier strength does not sharply decrease at the section. Intermediate ties should also be provided with the same distance as the ties to confine the concrete. Space of the intermediate ties should be less than 1 m (39 in.).

18.4.7.5 Two-Column Bent

To determine the ultimate strength and ductility factor for two-column bents, it is modeled as the frame model with plastic hinges at the both end of the lateral cap beam and columns as shown in Figure 18.9. Each elastic frame member has the yield stiffness that is obtained on the basis of the axial load by the dead load of the superstructure and the column. The plastic hinge is assumed to be placed at the end part of a cap beam and the top and bottom part of each column. The plastic hinges are modeled as spring elements with bilinear moment–curvature relation. The location of plastic hinges is half the distance of the plastic hinge length off from the end edge of each member, where the plastic hinge length L_p is assumed to be that given in Equation 18.16.

When the two-column bent is subjected to the lateral force in the transverse direction, the axial force developed in the beam and columns is affected by the applied lateral force. Therefore, the horizontal

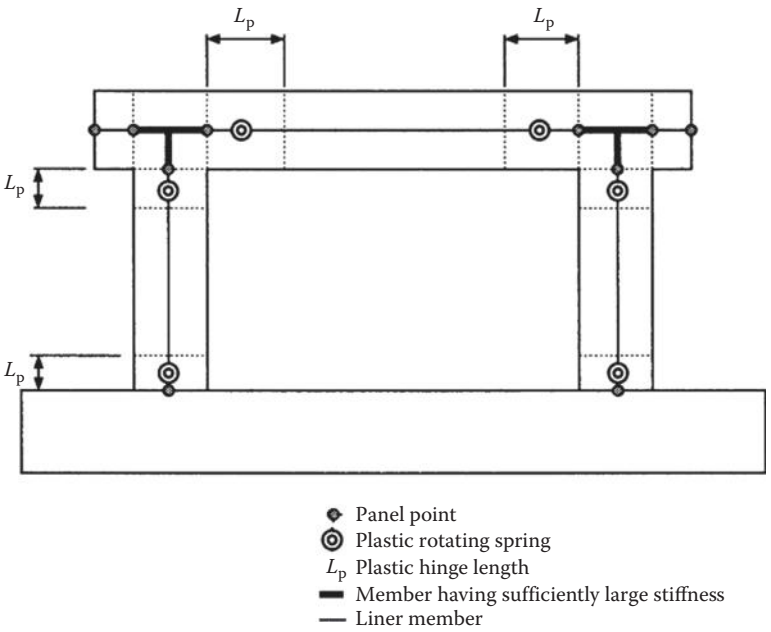

FIGURE 18.9 Analytical idealization of two-column bents.

force–displacement relation is obtained through the static pushover analysis considering the axial force N –moment M interaction relation. The ultimate state of each plastic hinge is obtained by the ultimate plastic angle θ_{pu} as follows:

$$\theta_{pu} = \left(\frac{\phi_u}{\phi_y} - 1\right) L_p \phi_y \tag{18.27}$$

where ϕ_u = ultimate curvature and ϕ_y = yield curvature.

The ultimate state of the whole two-bent column is determined so that all four plastic hinges developed reach the ultimate plastic angle or the largest plastic angle in four plastic hinges reaches twice the ultimate plastic angle of the hinge.

18.4.8 Ductility Design of Steel Piers

18.4.8.1 Failure Mode

To improve seismic performance of a steel pier, it is important to avoid specific brittle failure modes. Figure 18.10 shows typical brittle failure modes for rectangular and circular steel piers that were found during the1995 Hyogo-ken nanbu earthquake. Since the earthquake, extensive research and testing have been carried out on the design details of hollow steel piers in order to enhance their ductility. The following are the basic concepts to avoid such brittle failure modes and to improve the seismic performance of steel piers:

1. Fill the steel column with concrete
2. Improve structural parameters related to buckling strength
   a. Decrease the width-thickness ratio of stiffened plates of rectangular piers or the diameter-thickness ratio of steel pipes
   b. Increase the stiffness of stiffeners
   c. Reduce the diaphragm spacing

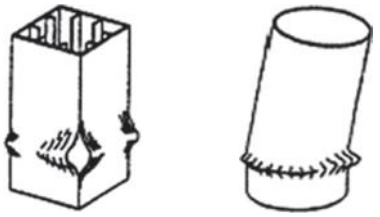

FIGURE 18.10 Typical brittle failure modes of steel piers. (a) Fracture of corners. (b) Elephant knee buckling.

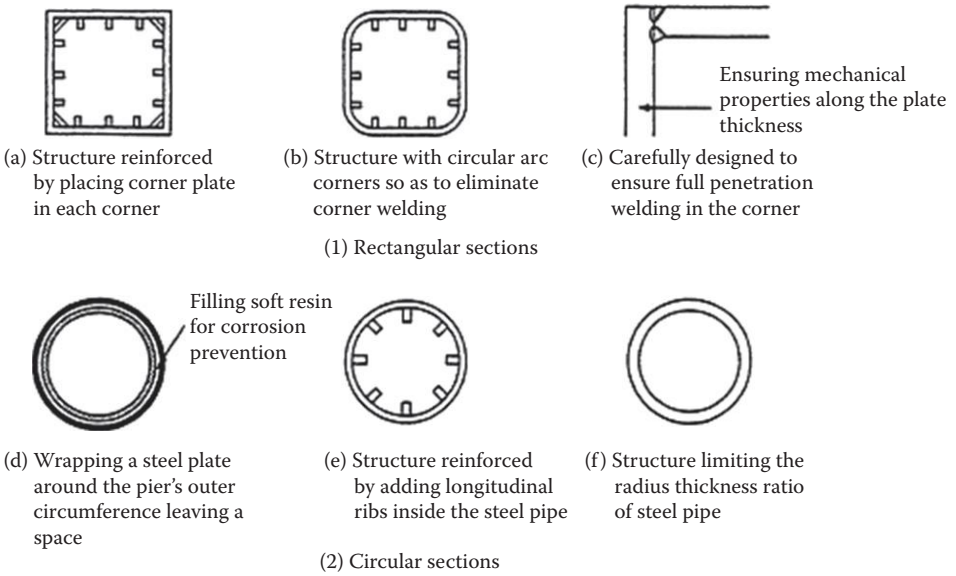

FIGURE 18.11 Examples of structural details for preventing brittle failure.

   d. Strengthen corners using the corner plates
3. Improve the welding section at the corners of the rectangular section
4. Eliminate the welding section at the corners by using round corners.

As a result, structural details shown in Figure 18.11 are proved to be effective in preventing brittle failures and increasing the horizontal strength as well as ductility as follows:

1. Steel piers with rectangular sections
   a. A structure using a corner plate to reinforce the corner.
   b. A structure that eliminates corner welding by rounding off the corner part in a circular arc.
   c. A structure that applies full penetration groove welding in the corner, and uses quality guaranteed steel materials to provide the required mechanical characteristics along the plate thickness.
2. Steel piers with circular sections
   d. A structure wrapping a steel plate around the pier's outer circumference leaving a space about one-half of the thickness of host material.
   e. A structure reinforcing the steel pipe with longitudinal ribs.
   f. A structure limiting the radius–thickness ratio of steel pipes.

Item (a) in the above represents a structure that retains the angle in the corner with use of a closed section even if considerable deformation develops, resulting in a possibility to prevent cracks in welded

corner. Item (b) intends to prevent rupture destruction in the corner by eliminating the corner welding. Item (c) aims at preventing ruptures originating in the welded part by using a welding joint that allows sufficient penetration in the corner welding, along with preventing the steel plate in the corner from splitting by tensile forces along the plate thickness.

Item (d) intends to prevent the concentration of deformation or cracks by dispersing the deformation through multistage propagation of the buckling waves, as the local buckling deformation contacts the outer steel plate when it exceeds a given deformation level. Item (e) is to prevent lantern buckling caused by vertical ribs, along with the concentration of the deformation. Item (f) can prevent cracks caused by concentrated local deformation, and increasing ductility of the steel pipe by limiting its radius thickness ratio. On the basis of the experimental study, item (a) for the rectangular section, and items (d), (e), and (f) for the circular section are effective in preventing brittle failures in addition to increasing the ductility. Lowering the width–thickness ratio of the stiffening plate and increasing its stiffness can also improve the ductility of a pier with a rectangular section.

18.4.8.2 Design Procedure

Seismic performance of steel piers considering the nonlinear behavior is fundamentally verified by using a dynamic analytical method. The maximum response of a steel pier against a level 2 earthquake obtained from the dynamic analysis should not exceed its allowable displacement. In addition, the residual displacement calculated by substituting the maximum response displacement at the height of the gravity center of the superstructure into Equation 18.9 should not exceed the allowable residual displacement. The bilinear factor, r, of the postyield secondary stiffness to the first yield stiffness used in the calculation of the residual displacement is given in Equation 18.10. The allowable displacement of a steel pier is generally determined in accordance with the results of cyclic loading tests for specimens having structural details similar to those of real piers. Allowable residual displacement is 1/100 of the distance between the bottom of a pier to the gravity center of the superstructure.

To obtain the response by using dynamic analytical methods, nonlinear hysteretic model of a steel pier is necessary and the following models are shown in the 2002 Design Specifications.

For a hollow steel pier, a bilinear model with secondary stiffness of $E/100$ is used for the stress–strain curve of the steel plate as shown in Figure 18.12a, where E is the Young's modulus of steel. The use of a bilinear model with secondary stiffness is based on consideration of the effect of strain hardening in steel and the consistency between the analytical and experimental values of the maximum horizontal force of a steel pier. Depending on the sectional shape of a steel pier, the allowable strain, ε_a, corresponding to he allowable displacement is calculated by:

$$\text{For a rectangular section}: \varepsilon_a = 20 - 25R_F \tag{18.28}$$

$$\text{For a circular section}: \varepsilon_a = 20 - 140R_t \tag{18.29}$$

where R_F = width–thickness ratio for a steel section with plastic behavior and R_t = radius–thickness ratio for a steel section with plastic behavior. Figure 8.12b shows the moment–curvature model of the section of a hollow steel pier.

On the other hand, for a steel pier with concrete filling, the same stress–strain curve of steel is used as shown in Figure 18.12a and that of concrete is shown in Figure 18.13a. Depending on the sectional shape of a steel pier, the allowable strain, ε_a, corresponding to the allowable displacement is specified as follows:

$$\text{For a rectangular section}: \varepsilon_a = 7 \tag{18.30}$$

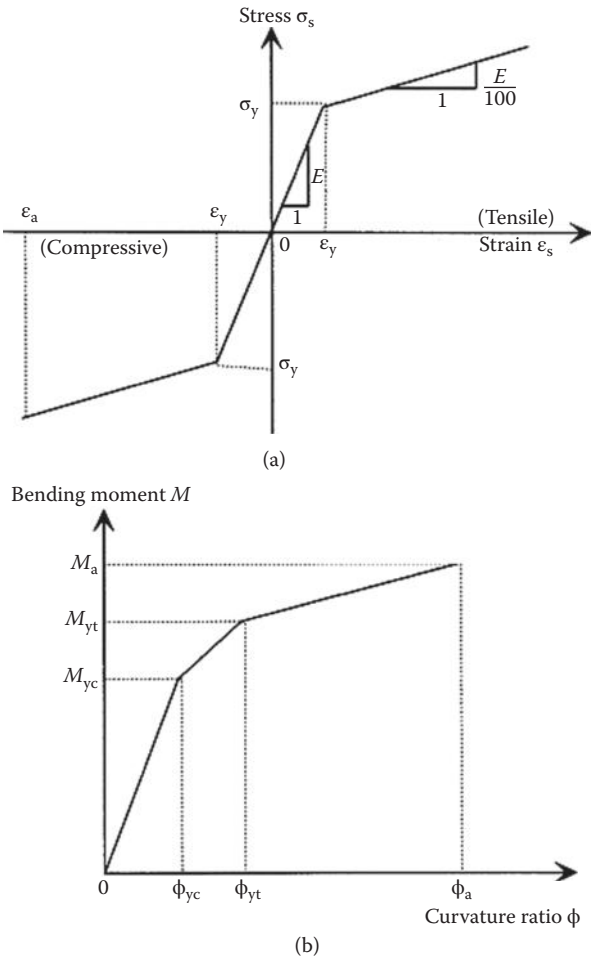

FIGURE 18.12 Mathematical model for a hollow steel pier. (a) Stress–strain curve of steel. (b) M-ϕ relation for plastic behavior.

$$\text{For a circular section} : \varepsilon_a = 5 \tag{18.31}$$

18.4.9 Menshin (Seismic Isolation) Design

18.4.9.1 Basic Principle

Implementation of Menshin bridges should be carefully chosen from the point of view not only of seismic performance but also of function for traffic and maintenance, based on the advantage and disadvantage of increasing natural period. The Menshin design should not be adopted under the following conditions:

1. Sites vulnerable to loss of bearing capacity due to soil liquefaction and lateral spreading
2. Bridges supported by flexible columns
3. Soft soil sites where potential resonance with surrounding soils could be developed by increasing the fundamental natural period
4. Bridges with uplift force at bearings

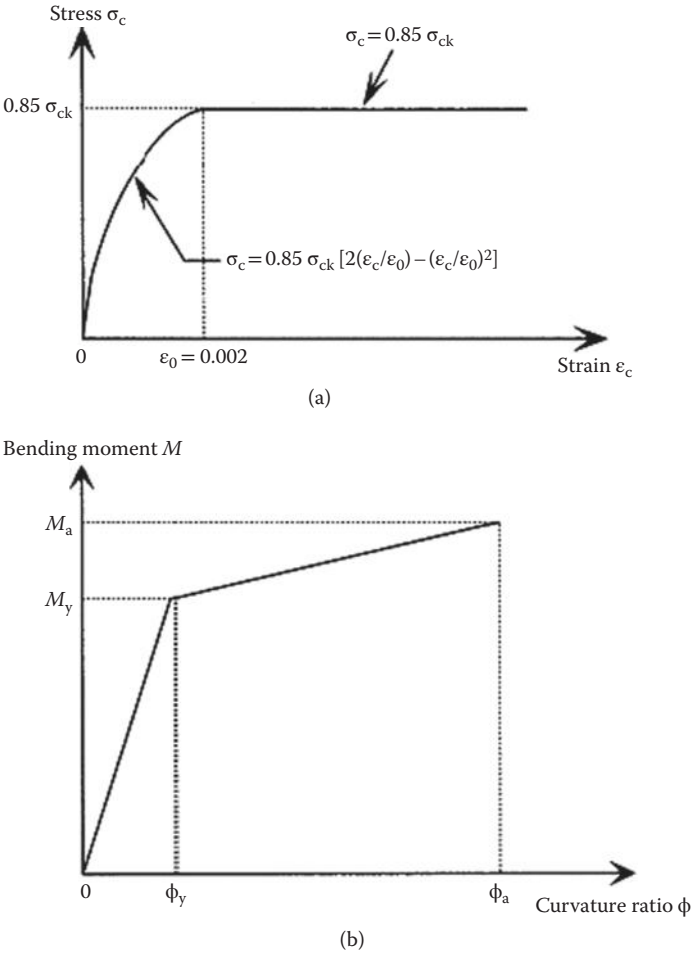

FIGURE 18.13 Mathematical model for a steel pier with concrete filling. (a) Stress–strain curve of concrete. (b) M-ϕ relation for plastic behavior.

It is suggested that the design be made with an emphasis on increasing the energy-dissipating capability and a distribution of lateral force to as many substructures as possible. In order to not concentrate the hysteretic deformation at piers, but at isolation bearings, the fundamental natural period of a Menshin bridge should be about two times or longer than the fundamental natural period of the same bridge supported by conventional fixed bearings. It should be noted that further elongation of the natural period aiming to decrease the lateral force is not recommended.

18.4.9.2 Design Procedure

Verification of seismic performance of a Menshin bridge is done on the basis of the dynamic analytical methods. Menshin devices (isolation bearings) are modeled as a nonlinear member having inelastic hysteretic property or an equivalent linear member having equivalent stiffness and damping ratio. Figure 18.14 shows a typical inelastic model of Menshin devices. Parameters for these nonlinear models are determined on the basis of the cyclic loading tests of Menshin devices used. The equivalent stiffness K_B and equivalent damping ratio h_B of a Menshin device for the equivalent linear model as shown in Figure 18.15 are evaluated as follows:

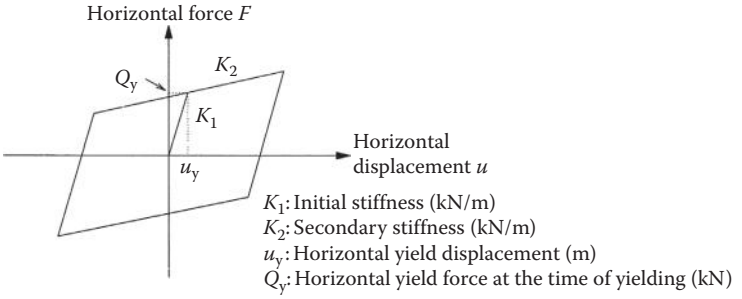

FIGURE 18.14 Inelastic hysteretic of Menshin (seismic isolation) devices.

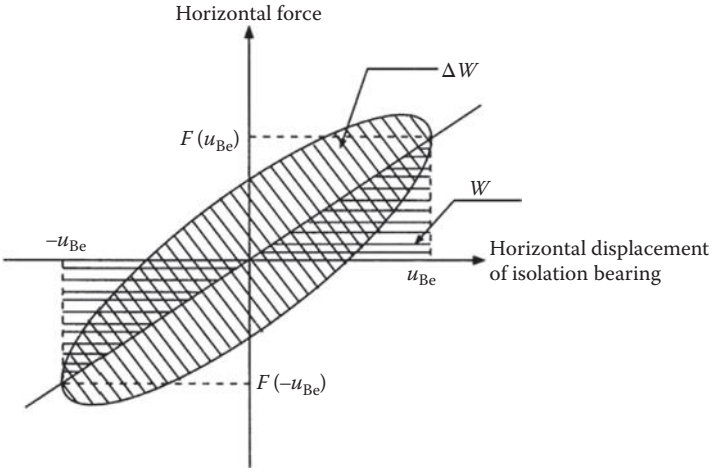

FIGURE 18.15 Equivalent stiffness and damping ratio of Menshin (seismic isolation) devices.

$$K_B = \frac{F(u_{Be}) - F(-u_{Be})}{2u_{Be}} \tag{18.32}$$

$$h_B = \frac{\Delta W}{2\pi W} \tag{18.33}$$

$$u_{Be} = c_B u_B \tag{18.34}$$

where $F(u)$ = restoring force of a device at a displacement u, u_{Be} = effective design displacement of a device, ΔW = energy dissipated per cycle, W = elastic strain energy, c_B = coefficient to evaluate the effective displacement (= 0.7), and u_B = design displacement of a device.

The responses of bridge members and Menshin devices are checked with their allowable capacity. In order to concentrate the inelastic deformation in the Menshin devices, the allowable displacement ductility factor of a pier μ_m is evaluated by:

$$\mu_m = 1 + \frac{\delta_u - \delta_y}{\alpha_m \delta_y} \tag{18.35}$$

where α_m is a safety factor used in Menshin design, and is given as

$$\alpha_m = 2\alpha \tag{18.36}$$

where α is the safety factor in the conventional design as shown in Table 18.7. Equation 18.35 means that the allowable displacement ductility factor of a pier in the Menshin design should be smaller than that in the conventional design. The reason for the smaller allowable ductility factor in the Menshin design is to limit the hysteretic displacement of a pier at the plastic hinge zone so that principle hysteretic behavior develops at the Menshin devices as shown in Figure 18.5b.

Simple devices that can resist extreme earthquakes have to be used. Currently, lead rubber bearings (LRB) and high damping rubber bearings (HDR) have been used as typical Menshin devices. The Menshin devices have to be anchored to superstructures and substructures with bolts, and should be replaceable. The clearance has to be provided between the deck and the abutment or between adjacent decks.

18.4.10 Design of Foundations

In the seismic design of a foundation, a lateral force equivalent to the ultimate lateral capacity of a pier, P_u, is assumed to be a design force as

$$k_{hp} = c_{df} \frac{P_u}{W} \tag{18.37}$$

where k_{hp} = lateral force coefficient for a foundation, c_{df} = modification coefficient (= 1.1), and W = equivalent weight by Equation 18.8. The foundation is designed so that the response subjected to the design force is less than the yield displacement of foundations. Because the inspection and repair for the foundations are not generally easy, the damage of foundations should be limited as much as possible. On the other hand, because the lateral capacity of a wall-type pier is very large in the transverse direction, the lateral seismic force evaluated by Equation 18.37 becomes, in most cases, excessive. Therefore, if a foundation has sufficiently large lateral capacity compared with the lateral seismic force, the foundation can be designed assuming a plastic hinge at the foundation and surrounding soils as shown in Figure 18.5c.

For a pile foundation, a foundation should be so idealized that a rigid footing is supported by piles that are supported by soils. The flexural strength of a pier defined by Equation 18.37 should be applied as a seismic force to foundations at the bottom of the footing together with the dead weight of the superstructure, pier, and soils on the footing. Figure 18.16 shows the idealized nonlinear model of a pile foundation. The nonlinearity of soils and piles is considered in the analysis.

The safety of the foundation should be checked so that (1) the foundation does not reach its yield point, (2) if the primary nonlinearity is developed in the foundations, the response displacement is less than the displacement ductility limit, and (3) the displacement developed in the foundation is less than the allowable limit. The allowable ductility and allowable limit of displacement are noted as 4 in. displacement ductility, 40 cm (15.7 in.) in horizontal displacement, and 0.025 rad in rotation angle, respectively. For a caisson type foundation, the foundation should be modeled as a reinforced concrete column that is supported by soil spring and the safety is checked in the same way as that for pile foundations.

18.4.11 Design against Soil Liquefaction and Liquefaction-Induced Lateral Spreading

18.4.11.1 Estimation of Liquefaction Potential

Since the 1995 Hyogo-ken nanbu earthquake caused liquefaction even at coarse sand or gravel layers, which had been regarded invulnerable to liquefaction, a gravel layer was included in the soil layers that require liquefaction potential estimation. Soil layers that satisfy the following conditions are estimated to be potential liquefaction layers:

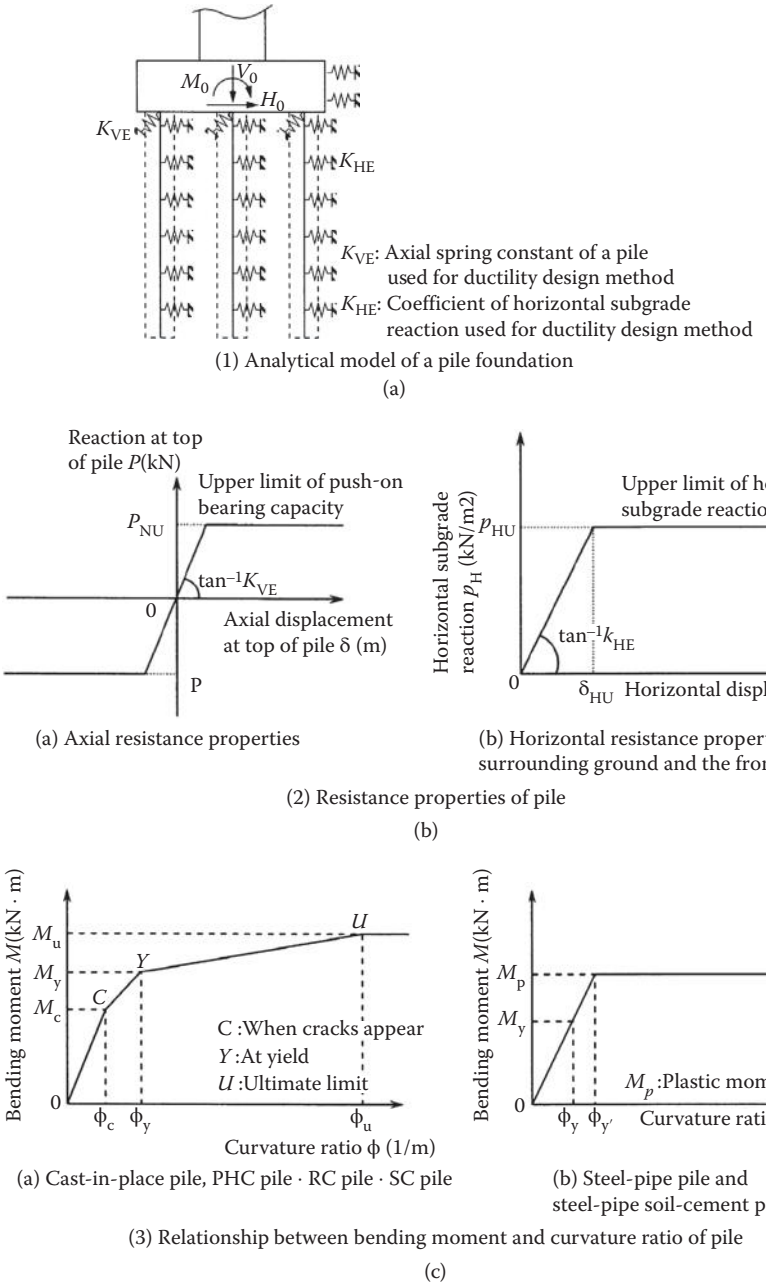

FIGURE 18.16 Idealized nonlinear model of a pile foundation.

1. Saturated soil layer that is located within 20 m under the ground surface and in which groundwater level is less than 10 m deep.
2. Soil layer in which fine particle content ratio *FC* is equal or less than 35% or the plasticity index I_P is equal to or less than 15.
3. Soil layer in which mean grain size D_{50} is equal to or less than 10 mm and 10% grain size D_{10} is equal to or less than 1 mm.

Liquefaction potential is estimated by the safety factor against liquefaction F_L as

$$F_L = \frac{R}{L} \tag{18.38}$$

where F_L = liquefaction resistant ratio, R = dynamic shear strength ratio, and L = shear–stress ratio during an earthquake. The dynamic shear strength ratio R may be expressed as

$$R = c_W R_L \tag{18.39}$$

where c_W = corrective coefficient for ground motion characteristics (1.0 for Type I ground motions, 1.0–2.0 for Type II ground motions), and R_L = cyclic triaxial strength ratio. The cyclic triaxial strength ratio was estimated by laboratory tests with undisturbed samples by in situ freezing method.

The shear–stress ratio during an earthquake may be expressed as

$$L = r_d k_{hg} \frac{\sigma_v}{\sigma'_v} \tag{18.40}$$

where r_d = modification factor for shear–stress ratio with depth, k_{hg} = seismic coefficient for the evaluation of liquefaction potential, σ_v = total loading pressure, and σ'_v = effective loading pressure.

It should be noted here that the design seismic coefficient for the evaluation of liquefaction potential k_{hg} is ranging from 0.3 to 0.4 for Type I ground motions, and from 0.6 to 0.8 for Type II ground motions.

18.4.11.2 Design Treatment of Liquefaction for Bridge Foundations

When liquefaction occurs, the strength and the bearing capacity of a surrounding soil decrease. In the seismic design of highway bridges, soil constants of a sandy soil layer, which is evaluated to be liquefied, reduce according to the F_L value. The reduced soil constants are calculated by multiplying the coefficient D_E in Table 18.9 to the soil constants estimated on an assumption that the soil layer does not liquefy.

18.4.11.3 Design Treatment of Liquefaction-Induced Ground Flow for Bridge Foundations

Consideration of the influence of liquefaction-induced ground flow was included since the 1996 Design Specifications. The case in which the ground flow that may affect the bridge seismic performance is likely to occur is generally that the ground is judged to be liquefiable and is exposed to unbalanced earth pressure, for example, the ground behind a seaside protection wall. The effect of liquefaction-induced ground flow is considered as the static force acting on a structure. This method ensures that the surface soil is of the nonliquefiable and liquefiable layers, and the forces equivalent to the passive earth

TABLE 18.9 Reduction Coefficient D_E for Soil Constants due to Soil Liquefaction

Range of F_L	Depth from the Present Ground Surface x (m)	Dynamic Shear Strength Ratio R			
		$R \leqq 0.3$		$0.3 < R$	
		Level 1	Level 2	Level 1	Level 2
$F_L \leqq 1/3$	$0 \leqq x \leqq 10$	1/6	0	1/3	1/6
	$10 < x \leqq 20$	2/3	1/3	2/3	1/3
$1/3 < F_L \leqq 2/3$	$0 \leqq x \leqq 10$	2/3	1/3	1	2/3
	$10 < x \leqq 20$	1	2/3	1	2/3
$2/3 < F_L \leqq 1$	$0 \leqq x \leqq 10$	1	2/3	1	1
	$10 < x \leqq 20$	1	1	1	1

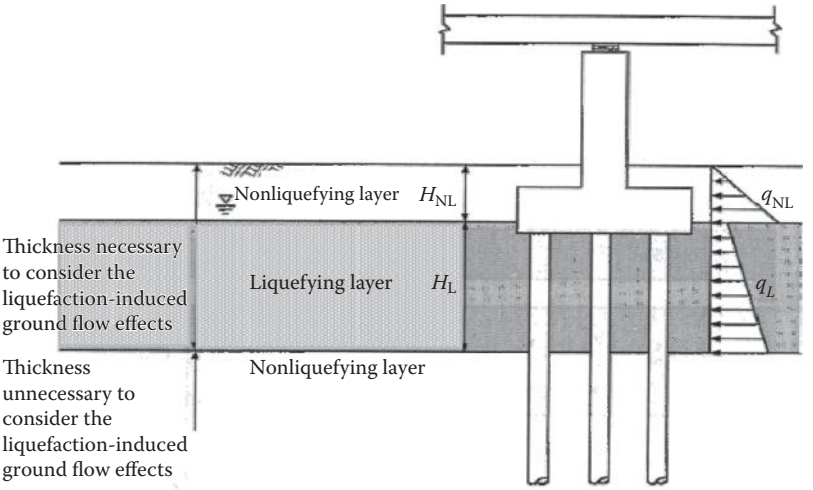

FIGURE 18.17 Idealized model for calculating lateral force due to lateral spreading.

pressure and 30% of the overburden pressures are applied to the foundation in the nonliquefiable layer and liquefiable layer, respectively.

The seismic safety of a foundation is checked by confirming the displacement at the top of the foundation caused by ground flow does not exceed an allowable value, in which a foundation and the ground are idealized as shown in Figure 18.17. The allowable displacement of a foundation may be taken as two times the yield displacement of a foundation. In this process, the inertia force of the structure need not necessary be considered simultaneously, because the liquefaction-induced ground flow may take place after the principal ground motion.

18.4.12 Design of Bearing Supports

The bearings are classified into two groups: Type A bearings resisting the seismic force of level 1 earthquake, and Type B bearings resisting the seismic force of level 2 earthquake. Seismic performance of Type B bearings is much higher than that of Type A bearings. In Type A bearings, a displacement-limiting device, which is described later, has to be coinstalled in both longitudinal and transverse directions, while it is not required in Type B bearings. Because of the importance of bearings as one of the main structural components, Type B bearings should be used in Menshin bridges.

Figure 18.18 shows the design forces for the bearing supports. The uplift force applied to the bearing supports is specified as

$$R_U = R_D - \sqrt{R_{HEQ}^2 + R_{VEQ}^2} \tag{18.41}$$

where R_U = design uplift force applied to the bearing support, R_D = dead load of superstructure, and R_{HEQ} and R_{VEQ} are vertical reactions caused by the horizontal seismic force and vertical force respectively.

18.4.13 Unseating Prevention Systems

Unseating prevention measures are required for highway bridges. The unseating prevention systems consists of enough seat length, a falling-down prevention device, a displacement-limiting device, and a settlement prevention device. The basic requirements are as follows:

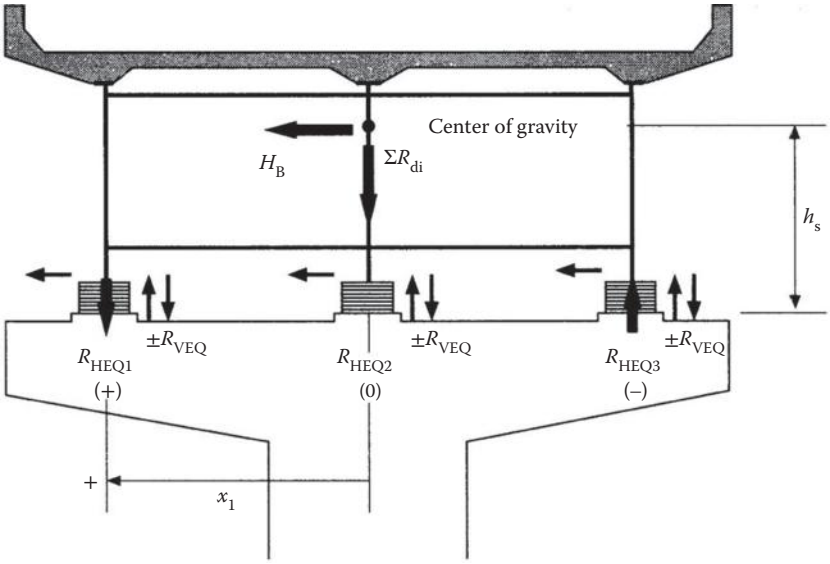

FIGURE 18.18 Design forces for bearing supports.

1. The unseating prevention systems have to be so designed that unseating of a superstructure from its supports can be prevented as much as possible even if unpredictable failures of the structural members occur.
2. Enough seat length must be provided and a falling-down prevention device must be installed at the ends of the superstructures against longitudinal response. If Type A bearings are used, a displacement-limiting device has to be further installed at not only the ends of a superstructure but at each intermediate support in a continuous bridge.
3. If Type A bearings are used, a displacement-limiting device is required at each support against transverse response. The displacement-limiting device is generally not required if Type B bearings are used. But, even if Type B bearings are adopted, it is required in skewed bridges, curved bridges, bridges supported by columns with narrow crest, bridges supported by few bearings per pier, and bridges constructed at sites vulnerable to lateral spreading associated with soil liquefaction.

The seat length S_E is evaluated a as

$$S_E = u_R + u_G \geq S_{EM} \tag{18.42}$$

$$S_{EM} = 0.7 + 0.005l \tag{18.43}$$

$$u_G = \varepsilon_G L \tag{18.44}$$

where u_R = relative displacement (m) developed between a superstructure and a substructure subjected to a seismic force equivalent to the lateral force coefficient *khc* by Equation 18.6, u_G = relative displacement of ground along the bridge axis, S_{EM} = minimum seat length (m), ε_G = ground strain induced during an earthquake along the bridge axis, which is 0.0025, 0.00375, and 0.005 for Class I, II and III sites respectively, L= distance that contributes to the relative displacement of ground (m), and l = span length (m). If two adjacent decks are supported by a pier, the larger span length should be l in evaluating the seat length.

TABLE 18.10 Modification Coefficient for Clearance c_B

$\triangle T/T_1$	c_B
$0 \leqq \triangle T/T_1 < 0.1$	1
$0.1 \leqq \triangle T/T_1 < 0.8$	$\sqrt{2}$
$0.8 \leqq \triangle T/T_1 \leqq 1.0$	1

In addition to the above requirements, the following considerations have to be made.

1. To prevent collisions between a deck and an abutment or between two adjacent decks, enough clearance must be provided. The clearance between those structural components S_B is evaluated as

$$S_B = \begin{cases} u_S + L_A & \text{between a deck and an abutment} \\ c_B u_S + L_A & \text{between two adjacent decks} \end{cases} \tag{18.45}$$

   where u_S = relative displacement developed between adjacent structural components at level 2 earthquake, L_A = redundancy of a clearance (generally ± 1.5 cm), and c_B = modification coefficient for clearance as shown in Table 18.10. The modification coefficient c_B was determined on the basis of an analysis of the relative displacement response spectra. It depends on a difference of natural periods $\Delta T = T_1 - T_2$ ($T_1 > T_2$), where T_1 and T_2 represent the natural period of two adjacent bridge systems.
2. The clearance at an expansion joint L_E is evaluated as

$$S_B = \begin{cases} \delta_R + L_A & \text{between a deck and an abutment} \\ c_B \delta_R + L_A & \text{between two adjacent decks} \end{cases} \tag{18.46}$$

   where δ_y = relative displacement developed between adjacent structural components at level 1 earthquake and L_A = redundancy of a clearance (generally ± 1.5 cm).

18.5 Seismic Retrofit Practices for Highway Bridges

18.5.1 Seismic Retrofit before the 1995 Hyogo-ken Nanbu Earthquake

The MLIT has carried out seismic vulnerability evaluation of existing highway bridges five times throughout the country since 1971 as part of the comprehensive earthquake disaster prevention measures for highway facilities (Kawashima and Unjoh, 1990; Kawashima, Unjoh, and Mukai, 1994; Unjoh, Terayama, Adachi, and Hoshikuma, 1997). Seismic retrofit for vulnerable bridges had been successively done on the basis of the seismic evaluations. Table 18.11 shows the history of past seismic evaluations.

The first seismic evaluation was done in 1971 to promote the earthquake disaster prevention measures for highway facilities. The significant damage of bridges caused by the San Fernando Earthquake, United States, in February 1971, triggered the seismic evaluation. Bridges with span lengths equal to or longer than 5 m (16.4 ft.) on all sections of national expressways and national highways, and sections of other local highways, were evaluated. Attention was paid to detect deterioration such as cracks of reinforced concrete structures, tilting, sliding, settlement, and scouring of foundations. Approximately 18,000 bridges in total were evaluated and approximately 3,200 bridges were found to require retrofit.

Following the first seismic evaluation, it had been subsequently done in 1976, 1979, 1986, and 1991 with gradually expanding highways and evaluation items. The seismic evaluation in 1986 was done with an increase in social needs to insure the seismic safety of highway traffic after the damage caused by

TABLE 18.11 Past Seismic Evaluations for Highway Bridges

Year	Highways Evaluated	Evaluation Items	Number of Bridges		
			Evaluated	Require Retrofit	Retrofitted
1971	All sections of national expressways and national highways, and sections of the others (bridge length ≧ 5 m)	① Deterioration ② Bearing seat length S for bridges supported by bent piles	18,000	3,200	1,500
1976	All sections of national expressways and national highways, and sections of the others (bridge length ≧ 15 m or overpass bridges)	① Deterioration of substructures, bearing supports and girders/slabs ② Bearing seat length S and devices for preventing falling-off of superstructure	25,000	7,000	2,500
1979	All sections of national expressways, national highways and principal local highways, and sections of the others (bridge length ≧ 15 m or overpass bridges)	① Deterioration of substructures and bearing supports ② Devices for preventing falling-off of superstructure ③ Effect of liquefaction ④ Bearing capacity of soils and piles ⑤ Strength of RC piers ⑥ Vulnerable foundations (bent pile and RC frame on two independent caisson foundations)	35,000	16,000	13,000
1986	All sections of national expressways, national highways and principal local highways, and sections of the others (bridge length ≧ 15 m or overpass bridges)	① Deterioration of substructures, bearing supports and concrete girders ② Devices for preventing falling-off of superstructure ③ Effect of soil liquefaction ④ Strength of RC piers (bottom of piers and termination zone of main reinforcement) ⑤ Bearing capacity of piles ⑥ Vulnerable foundations (bent piles and RC frame on two independent caisson foundations)	40,000	11,800	8,000
1991	All sections of national expressways, national highways and principal local highways, and sections of the others (bridge length 15 m or overpass bridges)	① Deterioration of substructures, bearing supports and concrete girders ② Devices for preventing falling-off of superstructure ③ Effect of soil liquefaction ④ Strength of RC piers (piers and termination zone of main reinforcement) ⑤ Vulnerable foundations (bent piles and RC frame or two independent caisson foundations)	60,000	18,000	7,000 (As of the end of 1994)

Note: Number of bridges evaluated, number of bridges that required retrofit, and number of bridges retrofitted in the above are approximate numbers.

the 1982 Urakawa-oki earthquake and the 1983 Nihon-kai-chubu earthquake. The bridges with span lengths equal to or longer than 15 m on all sections of national expressways, national highways and principal local highways, and sections of others, and overpasses were evaluated. The evaluation items included deterioration, unseating prevention devices, strength of substructures, and stability of foundations. Approximately 40,000 bridges in total were evaluated and approximately 11,800 bridges were found to require retrofit. In the 1991 seismic evaluation, the highways to be evaluated were expanding from the evaluation in 1986. Approximately 60,000 bridges in total were evaluated and approximately 18,000 bridges were found to require retrofit. Through a series of seismic evaluations, approximately 32,000 bridges in total were retrofitted by the end of 1994.

Emphasis had been placed on installing unseating prevention devices in the past seismic retrofit. Because the installation of the unseating prevention devices was being completed, it had become important to promote the strengthening of substructures with inadequate strength, lateral stiffness, and ductility.

18.5.2 Seismic Retrofit Program after the 1995 Hyogo-ken Nanbu Earthquake

For increasing seismic safety of the bridge structures that suffered damage by the 1995 Hyogo-ken nanbu earthquake, various new drastic changes were introduced in the new design codes and seismic retrofit for bridge structures.

Because the damage was mainly to single reinforced concrete piers/columns with a relatively small concrete section, the seismic retrofit program had been initiated for those columns, which were designed by the pre-1980 Design Specifications, at extremely important bridges such as bridges on expressways, urban expressways, and designated highway bridges, and also double deckers and overcrossings, and so on, which significantly affected highway functions once damaged. It was a three-year program since 1995 and approximately 30,000 piers were evaluated and retrofitted by the end of the fiscal year 1997. Unseating devices were also installed for these extremely important bridges. After the three-year program, the speed to promote the seismic retrofit works became a little slow, but the work steadily continued. In general, the retrofit for bridges with easy construction condition sites had been completed, but the bridges with the difficult construction condition sites were left to be retrofitted.

18.5.3 Three-Year (2005–2007) Seismic Retrofit Program

The MLIT carried out a three-year program of seismic retrofit of existing bridge structures in the fiscal years 2005–2007. The objectives of this program were to promote the seismic retrofit and to complete the improvement for important emergency routes rapidly. The program was initiated by the damage caused by the 2004 Niigata-ken-chuetsu earthquake and the 2005 Fukuoka-ken-seiho-oki earthquake; also, due to the anticipated occurrence of large-scale earthquakes in the pacific plate boundaries including Tokai, Tonankai, and Nankai regions. The period of the program was limited to three years and the retrofit works were to be done considering the effectiveness and efficiency of road networks.

The target bridges in the program were those designed according to the pre-1980 Design Specifications. The following bridges were given high priority to be retrofitted on the basis of the past earthquake damage experiences.

1. Retrofit for columns
   a. Single reinforced concrete column bents with termination of longitudinal reinforcing bars at midheight.
   b. Steel single column bents.
   c. Reinforced concrete column bents with fixed bearing condition at continuous girder bridges and with termination of longitudinal reinforcing bars at midheight.
2. Unseating prevention devices

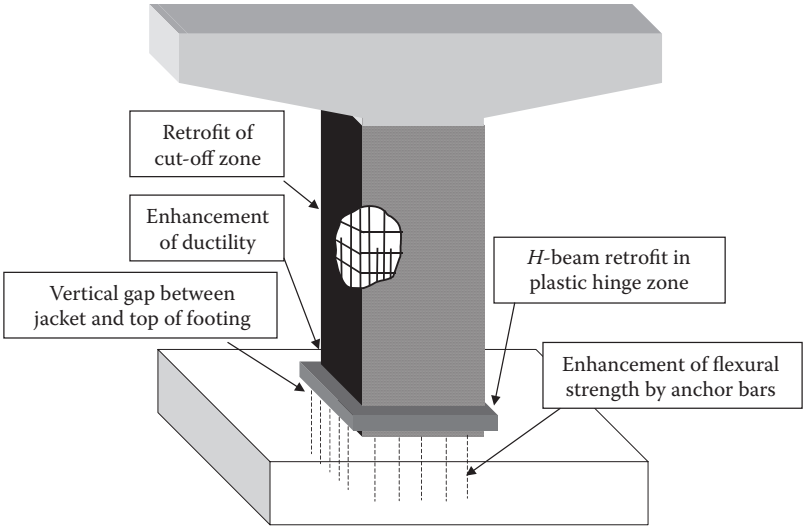

FIGURE 18.19 Seismic retrofit of reinforced concrete piers by steel jacketing with controlled increase of flexural strength.

a. Simply-supported girder bridges except a single-span bridge with abutments at both ends.
b. Continuous girder bridges with vulnerability potential of lateral spreading induced by soil liquefaction.

The main purpose of the seismic retrofit of reinforced concrete columns is to increase their shear strength, in particular for the columns with termination of longitudinal reinforcements at midheight without enough anchorage length. This enhances the ductility of columns because premature shear failure can be avoided.

However, if only the ductility of columns is enhanced, residual displacement developed at columns after an earthquake may increase. Therefore, the flexural strength should be increased at the same time. On the other hand, the increase in flexural strength of columns causes an increase in the seismic force transferred from columns to foundations. It was found from an analysis of various types of foundations that the effect of increasing seismic force on foundations may not be significant if the increasing rate of the flexural strength of columns is less than around 2. It is therefore suggested to increase the flexural strength of columns within this limit so that it does not cause serious damage to foundations. For such requirements, seismic strengthening by steel jackets with controlled increase of flexural strength was suggested. This uses steel jackets surrounding the existing columns as shown in Figure 18.19 (JRA, 1995). Epoxy resin or shrinkage-compensation mortar is injected between the concrete surface and the steel jacket. A small gap is provided at the bottom of columns between the steel jacket and the top of footing. This prevents an excessive increase in the flexural strength. To increase the flexural strength of columns in a controlled manner, anchor bolts are provided at the bottom of the steel jacket. They are drilled into the footing. By selecting an appropriate number and size of the anchor bolts, the degree of increase of the flexural strength of columns may be controlled. A gap is required to introduce the flexural failure at the bottom of columns. Columns with a rectangular section also have H-beams installed around them at the lower end of the jacket. This prevents the bulging of longitudinal bars and keeps the confining effect of the jacket.

Conventional reinforced concrete jacketing methods are also suggested for the retrofit of reinforced concrete piers, especially for the piers that require an increase in strength. It should be noted here that an increase in the strength of the pier should carefully be designed in consideration with the strength of foundations and footings.

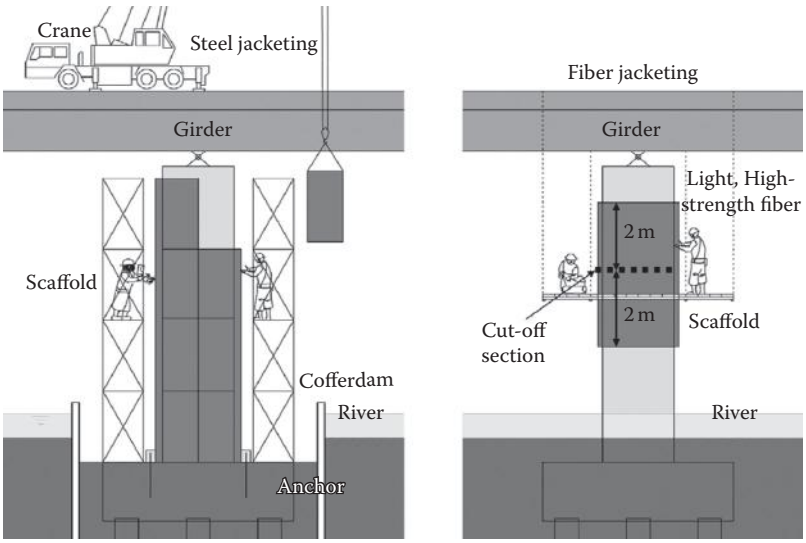

FIGURE 18.20 Comparison of construction methods for steel jacketing and fiber sheet jacketing for river crossing bridges.

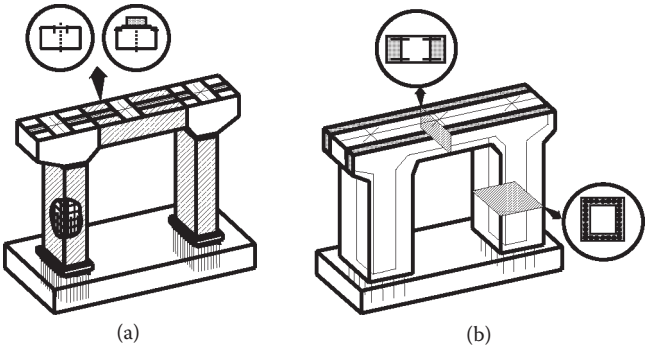

FIGURE 18.21 Seismic retrofit of two-column bents.

Also, retrofit measures of midheight section of columns were also used to prevent brittle shear failure at the section. Steel jacketing or sheet jacketing using carbon fiber sheets or aramid fiber sheets were applied to improve the shear and bending strength at the section as shown in Figure 18.20. These sheet materials are light weight and so can be applied with relatively easy construction conditions without the requirement for heavy construction machines.

During the Hyogo-ken nanbu earthquake, some two-column bents were damaged in the longitudinal and transverse directions. The strength and ductility characteristics of the two-column bents have been studied and the analysis and design method was introduced in the 1996 Design Specifications. Figure 18.21 shows applicable seismic retrofit methods for two-column bents. The concept of the retrofit is to increase flexural strength and ductility as well as shear capacity for columns and cap beams. In the field practices, the axial force in the cap beam is much smaller than that in the columns so that the enhancement of the shear capacity for retrofit of the cap beam is more often essential. Since the jacketing of cap beam is difficult because of existing bearing supports and construction space, the effective retrofit measures for cap beams such as application of fiber sheet jacketing using high elasticity and high strength materials, and out-cable prestressing methods have been developed.

18.5.4 Effectiveness of Seismic Retrofit

18.5.4.1 Recent Damaging Earthquakes

After the 1995 Hyogo-ken nanbu earthquake, several damaging earthquakes have occurred including 2003 Miyagi-ken-hokubu earthquake (M6.4), 2003 Tokachi-oki earthquake (M8.0), 2004 Niigata-ken-chuestu earthquake (M6.8), 2005 Fukuoka-ken-seiho-oki earthquake (M7.0), 2007 Noto-hanto-oki earthquake (M6.9), 2007 Niigata-ken-chuetsu-oki earthquake (M6.9), 2010 Iwate-Miyagi Nairiku earthquake (M7.2) and 2011 Great East Japan earthquake (Mw9.0). Owing to these earthquakes, houses and infrastructure were seriously damaged, although the damage was not so much for bridges except the tsunami effect during the 2011 Great East Japan earthquake. Some of the important examples to discuss the effectiveness of seismic retrofit for bridges are shown in the following (Unjoh, Sugimoto, Sakai, and Okada, 2006).

FIGURE 18.22 Retrofitted Pier P714 of Hanshin Expressway. (From Sato, T. et al., *Proceedings of The 2nd Conference on the Hanshin-Awaji Earthquake*, Jan., 1997.)

FIGURE 18.23 Damage of Pier P715 of Hanshin Expressway. (From Sato, T. et al., *Proceedings of The 2nd Conference on the Hanshin-Awaji Earthquake*, Jan., 1997.)

18.5.4.2 Example 1: Steel Jacketing for Reinforced Concrete Columns

During the 1995 Hyogo-ken nanbu earthquake, the Kobe route, No.3, of the Hanshin expressway was heavily damaged. Some bridges collapsed or nearly collapsed and a number of superstructures, bearings, and columns were seriously damaged. Before the earthquake, based on the 1986/1991 MLIT seismic evaluation and seismic retrofit program, the retrofit project was initiated for selected columns at Tsukimiyama section on the Kobe route (Sato, Taniguchi, Adachi, and Ohta, 1997). Since the area was located 1 km from JR Takatori station, which was one of the heavily damaged areas, the intensity of shaking at this location was estimated to be significant.

The difference in the damage between two piers of P714 and P715, which were adjacent piers with a distance of 30 m (98.4 ft.), is discussed here. They supported PC girders with span lengths of 30 m (98.4 ft.). The height of the pier was 11 m (36 ft.) and the piers were supported by pile foundations with pile lengths of 10 m (32.8 ft.). Soil condition was estimated as Class II medium ground.

Before the earthquake, P714 was already retrofitted using steel jacketing with steel plates of 12 mm (0.47 in.) thickness. P715 was planned to be retrofitted, but was as-built without any retrofit at the time of the earthquake. Figures 18.22 and 18.23 show two piers taken after the earthquake. No damage was found at superstructures and/or bearings. At pier P715, the cracks and spall of cover concrete and the buckling of longitudinal reinforcing bars at midheight section of columns, which was the termination section of the longitudinal reinforcing bars, were found. The pier had not collapsed but the damage was serious and significant. The bottom of the column was investigated after the earthquake by removing the surrounding soils but no damage was found at the bottom. On the other hand, at pier P714, no damage was visible from the outside. No peeling of the coating paint of the steel jacketing was found. After the earthquake, the connection between the steel plate and the inside concrete was checked by the hammering test, and the separation was found at some locations. After removing the steel jacket and detailed investigation, no crack was found in the core concrete. This shows the effectiveness of the seismic retrofit for the column to prevent the bending and shear failure by steel jacketing.

Another example was found during the Niigata-ken-chuetsu earthquake that occurred on October 23, 2004. The magnitude was 6.8 and not so large but the depth was shallow at about 10 km (6.2 miles); strong shaking was observed. The effectiveness of the seismic retrofit for reinforced concrete piers at Shinkumi bridge is shown here. The Shinkumi bridge was constructed in 1989 to overpass the railway as shown in Figure 18.24. The superstructures were of two-span simply-supported steel girders and three-span continuous steel girders. The substructures were RC columns with a circular section and

FIGURE 18.24 Two parallel bridges (left: retrofitted, right: as built).

FIGURE 18.25 Retrofitted columns with steel jacketing (no damage).

FIGURE 18.26 Damaged Pier P5 (as built).

supported by pile foundations. Bearings were of steel plate type. The bridge consisted of two same but completely separate bridges, which had two inbound and downbound lanes, respectively. The columns of one bridge were retrofitted by steel jacketing as shown in Figure 18.25. For the other bridge, the retrofit works were planned to be done later.

The damage was found at the bridge columns without retrofit. The heaviest damage was found at the midheight section of pier P5, which was the termination section of some of the longitudinal reinforcing bars. The cracks, spall-off of cover concrete, and buckling of reinforcing bars were found as shown in Figure 18.26. At other piers of the same as-built bridge, bending and shear cracks were also observed. However, no damage was found at the retrofitted bridge and the retrofit by the steel jacketing was verified to work effectively.

18.5.4.3 Example 2: Unseating Prevention Devices

The Miyagi-ken-hokubu earthquake occurred on July 26, 2003, at Sendai area that is located at the north of the main island of Japan. The effectiveness of unseating prevention devices recognized at the Ono Bridge is shown here. In the past seismic retrofit programs, the unseating prevention devices connecting the adjacent girders and abutments by cables for prestressed concrete were installed at the Ono Bridge to prevent the falling down of superstructures by excessive displacement. The Ono Bridge is located about 2 km (1.24 miles) from the epicenter. The strong motion with the peak acceleration of 440 gal on the ground was observed at the nearest MLIT strong motion observation station, which is located 1 km from the bridge. Because of the strong shaking, all of the bearings at piers and abutments were damaged. Anchor bolts failed in shear or were pulled out, and some of the steel plates of bearings were fractured at the welded section. Then, all girders moved in the longitudinal direction by about 20 cm (7.9 in.). The

FIGURE 18.27 Effectiveness of unseating prevention devices using PC cable.

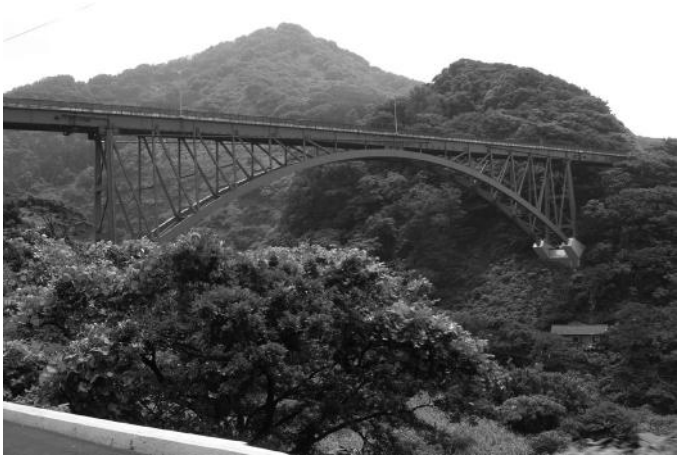

FIGURE 18.28 Retrofit of steel truss arch bridge.

FIGURE 18.29 Springing section of arch ribs retrofitted by concrete jacketing.

largest displacement was found at the abutment but the unseating devices by PC cables worked effectively to restrain further excessive displacement as shown in Figure 18.27.

18.5.4.4 Example 3: Steel Truss Arch Bridges

The Niigata-ken-chuetsu-oki earthquake with a magnitude of 6.8 occurred on July 16, 2007 in the Niigata area. Similar to the 2004 Niigata-chuetsu earthquake, the damage was serious and a number of houses were affected. The nuclear power plant there was also affected by the earthquake. The retrofit for a long-span bridge, namely the Agewa Bridge, is shown here. It should be noted here that a strong motion was observed at the site closest to the bridges, and the peak acceleration was 659 gal. The Agewa Bridge was constructed in 1965. The superstructure was a steel truss arch bridge as shown in Figure 18.28. Simple span steel gerber girders were at the both ends of the arch section. The bridge length was 197 m (646 ft.). The abutments at both ends of girder were gravity type and wall type, and the foundations were spread type and pile foundations. Arch abutments were spread type foundation. The bridge was retrofitted before the earthquake. The arch ribs were strengthened by filling light-weight concrete into the steel hollow section to increase the strength and ductility. At the same time, both the ends of the arch section were retrofitted to be fixed by concrete jacketing from the original pin-type bearings as shown in Figure 18.29.

Owing to the strong shaking during the earthquake, some movement was found at both the expansion joints and abutments, but no remarkable damage was found at the main members including retrofitted arch ribs. Some buckling and deformation was found at connection section of the lower lateral beam. The seismic retrofit to increase the strength and ductility of the arch ribs was estimated to work effectively.

Notations

The following symbols are used in this chapter. The section number in parentheses after definition of a symbol refers to the section where the symbol first appears or is defined.

a = space of tie reinforcements (Section 18.4.7)
A_h = sectional area of tie reinforcement (Section 18.4.7)
A_w = sectional area of shear reinforcement (Section 18.4.7)
b = width of section (Section 18.4.7)
c_B = coefficient to evaluate effective displacement (Section 18.4.9)

c_B = modification coefficient for clearance (Section 18.4.12)
c_{df} = modification coefficient (Section 18.4.10)
c_c = modification factor for cyclic loading (Section 18.4.7)
c_D = modification coefficient for damping ratio (Section 18.4.3)
c_e = modification factor for scale effect of effective height of section (Section 18.4.7)
c_P = coefficient depending on the type of failure mode of a pier (Section 18.4.5)
c_{pt} = modification factor for longitudinal reinforcement ratio (Section 18.4.7)
c_R = factor depending on the bilinear factor r (Section 18.4.5)
c_S = modification factor for nonlinear response characteristics (Section 18.4.5)
c_W = corrective coefficient for ground motion characteristics (Section 18.4.11)
c_Z = modification coefficient for zone (Section 18.4.3)
d = effective height of section (Section 18.4.7)
D = width or diameter of a pier (Section 18.4.7)
D_E = coefficient to reduce soil constants according to F_L value (Section 18.4.11)
E = Young's modules of steel plate (Section 18.4.8)
E_c = elastic modules of concrete (Section 18.4.7)
E_s = elastic modules of reinforcing bar (Section 18.4.7)
E_{des} = gradient at descending branch (Section 18.4.7)
F_L = liquefaction resistant ratio (Section 18.4.11)
$F(u)$ = restoring force of a device at a displacement u (Section 18.4.9)
h = damping ratio (Section 18.4.3)
h = height of a pier (Section 18.4.7)
h_s = height of the center of gravity of girder from the top of bearing (Figure 18.17)
h_B = equivalent damping of a Menshin device (Section 18.4.9)
H_0 = shear force at the bottom of footing (Figure 18.15)
k_{hc} = lateral force coefficient (Section 18.4.5)
k_{hg} = seismic coefficient for the evaluation of liquefaction potential (Section 18.4.11)
k_{hc0} = standard lateral force coefficient (Section 18.4.5)
k_{hp} = lateral force coefficient for a foundation (Section 18.4.10)
K_B = equivalent stiffness of a Menshin device (Section 18.4.9)
L = shear stress ratio during an earthquake (Section 18.4.11)
L_A = redundancy of a clearance (Section 18.4.12)
L_E = clearance at an expansion joint (Section 18.4.12)
L_P = plastic hinge length of a pier (Section 18.4.7)
M_0 = moment at the bottom of footing (Figure 18.15)
P_a = lateral capacity of a pier (Section 18.4.5)
P_c = bending capacity to develop crack (Section 18.4.5)
P_s = shear capacity in consideration of the effect of cyclic loading (Section 18.4.7)
P_{s0} = shear capacity without consideration of the effect of cyclic loading (Section 18.4.7)
P_u = bending capacity (Section 18.4.7)
r = bilinear factor defined as a ratio between the first stiffness (yield stiffness) and the second stiffness (post-yield stiffness) of a pier (Section 18.4.5)
r_d = modification factor for shear stress ratio with depth (Section 18.4.11)
R = dynamic shear strength ratio (Section 18.4.11)
R_D = dead load of superstructure (Section 18.4.12)
R_F = width-thickness ratio for a steel section with plastic behavior (Section 18.4.8)
R_{HEQ} and R_{VEQ} = vertical reactions caused by the horizontal seismic force and vertical force (Section 18.4.12)
R_L = cyclic triaxial strength ratio (Section 18.4.11)
R_t = radius-thickness ratio for a steel section with plastic behavior (Section 18.4.8)

R_U = design uplift force applied to the bearing support (Section 18.4.12)
s = space of shear reinforcements (Section 18.4.7)
S = acceleration response spectrum for level 1 earthquake (Section 18.4.3)
S_c = shear capacity shared by concrete (Section 18.4.7)
S_{I} and S_{II} = acceleration response spectrum for Type-I and Type-II ground motions of level 2 earthquake (Section 18.4.3)
S_0 = standard acceleration response spectrum for level 1 earthquake (Section 18.4.3)
S_{I0} and S_{II0} = standard acceleration response spectrum for Type-I and Type-II ground motions of level 2 earthquake (Section 18.4.3)
S_B = clearance between a deck and an abutment or between two adjacent decks (Section 18.4.12)
S_E = seat length (Section 18.4.12)
S_{EM} = minimum seat length (Section 18.4.12)
S_s = shear capacity shared by shear reinforcements (Section 18.4.7)
T = natural period (Table 18.4)
ΔT = difference of natural periods (Section 18.4.12)
T_1 and T_2 = natural periods of the two adjacent bridge systems (Section 18.4.12)
u_B = design displacement of a device (Section 18.4.9)
u_{Be} = effective design displacement of a device (Section 18.4.9)
u_G = relative displacement of ground along the bridge axis (Section 18.4.12)
u_R = relative displacement developed between a superstructure and a substructure (Section 18.4.12)
u_S = relative displacement developed between adjacent structural components at level 2 earthquake (Section 18.4.12)
V_0 = vertical force at the bottom of footing (Figure 18.15)
W = equivalent weight (Section 18.4.5)
W = elastic strain energy (Section 18.4.9)
W_P = weight of a pier (Section 18.4.5)
W_U = weight of a part of superstructure supported by a pier (Section 18.4.5)
Δ_W = energy dissipated per cycle (Section 18.4.9)
α = safety factor (Section 18.4.7)
α and β = coefficients depending on shape of pier (Section 18.4.7)
α_m = safety factor used in Menshin design (Section 18.4.9)
δ_y = yield displacement of a pier (Section 18.4.5)
δ_R = residual displacement of a pier after an earthquake (Section 18.4.5)
δ_R = relative displacement developed between adjacent structural components at level 1 earthquake (Section 18.4.12)
δ_{Ra} = allowable residual displacement of a pier (Section 18.4.5)
δ_u = ultimate displacement of a pier (Section 18.4.7)
ε_a = allowable strain of a steel pier (Section 18.4.8)
ε_c = strain of concrete (Section 18.4.7)
ε_{cc} = strain of confined concrete at maximum strength (Section 18.4.7)
ε_{cu} = ultimate strain of concrete (Section 18.4.7)
ε_G = ground strain induced during an earthquake along the bridge axis (Section 18.4.12)
ε_s = strain of reinforcements (Section 18.4.7)
ε_{sy} = yield strain of reinforcements (Section 18.4.7)
ε_y = yield strain of steel plate (Section 18.4.8)
θ = angle between vertical axis and tie reinforcement (Section 18.4.7)
θ_{pu} = ultimate plastic angle (Section 18.4.7)
μ_a = allowable displacement ductility factor of a pier (Section 18.4.5)
μ_m = allowable displacement ductility factor of a pier in Menshin design (Section 18.4.9)
μ_r = response ductility factor of a pier (Section 18.4.5)

ρ_s = tie reinforcement ratio (Section 18.4.7)
σ_c = stress of concrete (Section 18.4.7)
σ_{cc} = maximum strength of confined concrete (Section 18.4.7)
σ_{ck} = design strength of concrete (Section 18.4.7)
σs = stress of reinforcements (Section 18.4.7)
σ_{sy} = yield strength of reinforcements (Section 18.4.7)
σ_v = total loading pressure (Section 18.4.11)
σ_v' = effective loading pressure (Section 18.4.11)
τ_c = shear stress capacity shared by concrete (Section 18.4.7)
ϕ_y = yield curvature of a pier at bottom (Section 18.4.7)
ϕ_u = ultimate curvature of a pier at bottom (Section 18.4.7)

Acknowledgments

Great appreciation is given to Prof. Kazuhiko Kawashima, Professor at the Tokyo Institute of Technology. Prof. Kawashima served as the chairman of the committee for drafting the revision of the "Part V Seismic Design" of the "1996 Design Specifications of Highway Bridges." The revision based on the lessons learned from the 1995 Hyogo-ken nanbu earthquake was remarkably important for the seismic design of highway bridges in Japan. Also, all other members of the committee, including Dr. Jun-ichi Hoshikuma and Dr. Jun-ichi Sakai of Public Works Research Institute, are greatly acknowledged.

References

JRA. 1995. *References for Applying Guided Specifications to New Highway Bridge and Seismic Strengthening of Existing Highway Bridges*, Japan Road Association, Tokyo, Japan, June. (in Japanese)

JRA. 1996. *Design Specifications of Highway Bridges, Part I: Common Part, Part II: Steel Bridges, Part III: Concrete Bridges, Part IV: Foundations, and Part V: Seismic Design*. Japan Road Association, Tokyo, Japan.

JRA. 2002. *Design Specifications of Highway Bridges, Part I Common Part, Part II Steel Bridges, Part III Concrete Bridges, Part IV Foundations, and Part V Seismic Design*, Japan Road Association, Tokyo, Japan.

Kawashima, K. 1995. "Impact of Hanshin/Awaji Earthquake on Seismic Design and Seismic Strengthening of Highway Bridges," *Report No. TIT/EERG 95-2*, Tokyo Institute of Technology, Tokyo, Japan.

Kawashima, K. and Unjoh, S. 1990. "An Inspection Method of Seismically Vulnerable Existing Highway Bridges," *Structural Eng./Earthquake Eng.*, 7(7), Proc. JSCE, April, 155–162. (in Japanese)

Kawashima, K. and Unjoh, S. 1997. "The Damage of Highway Bridges in the 1995 Hyogo-ken Nanbu Earthquake and its Impact on Japanese Seismic Design," *J. Earthquake Eng.*, 1(3), 211–240.

Kawashima, K., Unjoh, S. and Mukai H. 1994. "Seismic Strengthening of Highway Bridges," *Proceedings of the 2nd* U.S.-*Japan Workshop on Seismic Retrofit of Bridges*, Berkeley, USA, January 1994, Technical Memorandum of PWRI, No.3276.

Kawashima, K., Nakano, M., Nishikawa, K., Fukui, J., Tamura, K. and Unjoh, S. 1997. "The 1996 Seismic Design Specifications of Highway Bridges," *Proceedings of the 29th Joint Meeting of U.S.-Japan Panel on Wind and Seismic Effects*, UJNR, Technical Memorandum of PWRI, No.3524, Tsukuba, Japan.

MOC. 1995a. *Report on the Damage of Highway Bridges by the Hyogo-ken Nanbu Earthquake*, Committee for Investigation on the Damage of Highway Bridges Caused by the Hyogo-ken Nanbu Earthquake, Ministry of Construction, Tokyo, Japan.

CIVIL ENGINEERING

Bridge Engineering Handbook

SECOND EDITION

SEISMIC DESIGN

Over 140 experts, 14 countries, and 89 chapters are represented in the second edition of the **Bridge Engineering Handbook.** This extensive collection highlights bridge engineering specimens from around the world, contains detailed information on bridge engineering, and thoroughly explains the concepts and practical applications surrounding the subject.

Published in five books: **Fundamentals, Superstructure Design, Substructure Design, Seismic Design,** and **Construction and Maintenance,** this new edition provides numerous worked-out examples that give readers step-by-step design procedures, includes contributions by leading experts from around the world in their respective areas of bridge engineering, contains 26 completely new chapters, and updates most other chapters. It offers design concepts, specifications, and practice, as well as the various types of bridges. The text includes over 2,500 tables, charts, illustrations, and photos. The book covers new, innovative and traditional methods and practices; explores rehabilitation, retrofit, and maintenance; and examines seismic design and building materials.

The fourth book, **Seismic Design** contains 18 chapters, and covers seismic bridge analysis and design.

What's New in the Second Edition:

- Includes seven new chapters: Seismic Random Response Analysis, Displacement-Based Seismic Design of Bridges, Seismic Design of Thin-Walled Steel and CFT Piers, Seismic Design of Cable-Supported Bridges, and three chapters covering Seismic Design Practice in California, China, and Italy
- Combines Seismic Retrofit Practice and Seismic Retrofit Technology into one chapter called Seismic Retrofit Technology
- Rewrites Earthquake Damage to Bridges and Seismic Design of Concrete Bridges chapters
- Rewrites Seismic Design Philosophies and Performance-Based Design Criteria chapter and retitles it as Seismic Bridge Design Specifications for the United States
- Revamps Seismic Isolation and Supplemental Energy Dissipation chapter and retitles it as Seismic Isolation Design for Bridges

This text is an ideal reference for practicing bridge engineers and consultants (design, construction, maintenance), and can also be used as a reference for students in bridge engineering courses.

K12394

ISBN: 978-1-4398-5218-7
90000
9 781439 852187

~StormRG~

CRC Press
Taylor & Francis Group
an informa business
www.crcpress.com

6000 Broken Sound Parkway, NW
Suite 300, Boca Raton, FL 33487
711 Third Avenue
New York, NY 10017
2 Park Square, Milton Park
Abingdon, Oxon OX14 4RN, UK

www.crcpress.com